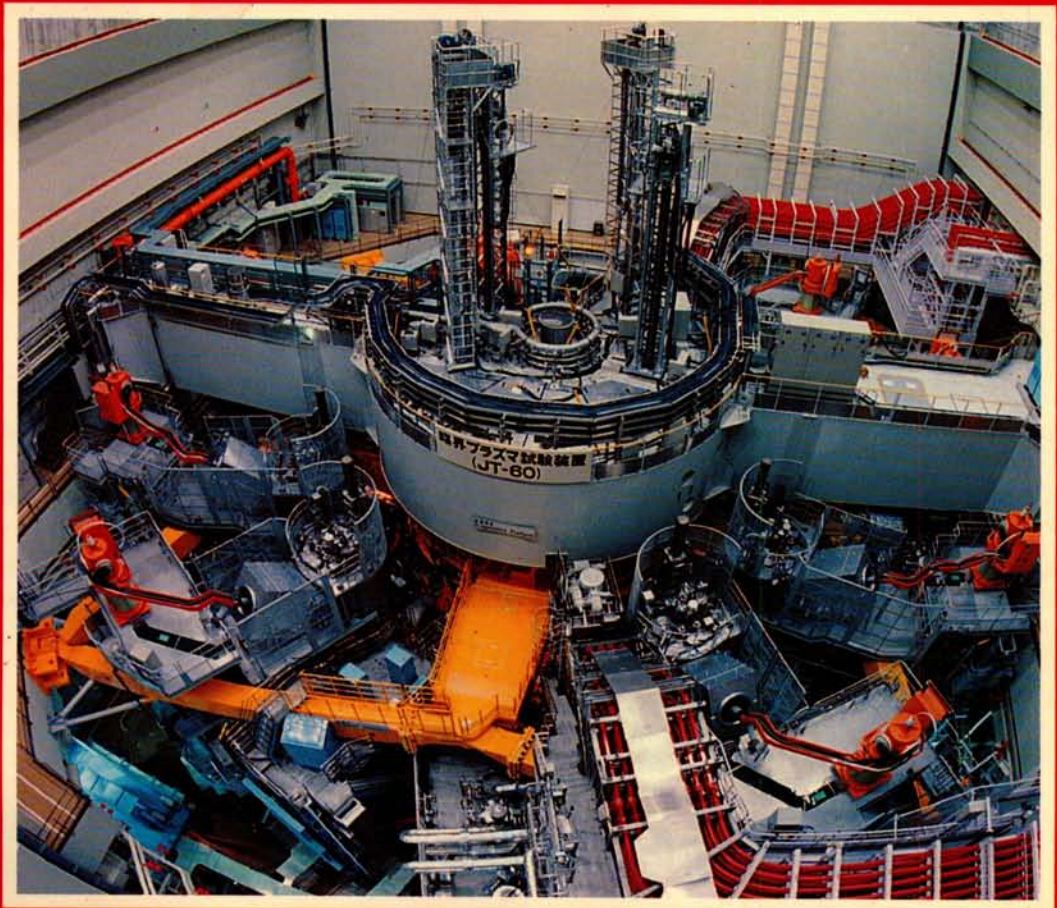


# Plasma Physics and Controlled Nuclear Fusion Research 1986

Vol.1

ELEVENTH CONFERENCE PROCEEDINGS, KYOTO, 13–20 NOVEMBER 1986

Nuclear Fusion, Supplement 1987



INTERNATIONAL ATOMIC ENERGY AGENCY, VIENNA, 1987

The cover picture shows JT-60, one of the largest operational tokamaks.  
By courtesy of the Japan Atomic Energy Research Institute, Tokyo.

PLASMA PHYSICS  
AND CONTROLLED  
NUCLEAR FUSION RESEARCH  
1986

VOLUME 1

The following States are Members of the International Atomic Energy Agency:

AFGHANISTAN	GUATEMALA	PARAGUAY
ALBANIA	HAITI	PERU
ALGERIA	HOLY SEE	PHILIPPINES
ARGENTINA	HUNGARY	POLAND
AUSTRALIA	ICELAND	PORTUGAL
AUSTRIA	INDIA	QATAR
BANGLADESH	INDONESIA	ROMANIA
BELGIUM	IRAN, ISLAMIC REPUBLIC OF	SAUDI ARABIA
BOLIVIA	IRAQ	SENEGAL
BRAZIL	IRELAND	SIERRA LEONE
BULGARIA	ISRAEL	SINGAPORE
BURMA	ITALY	SOUTH AFRICA
BYELORUSSIAN SOVIET SOCIALIST REPUBLIC	JAMAICA	SPAIN
CAMEROON	JAPAN	SRI LANKA
CANADA	JORDAN	SUDAN
CHILE	KENYA	SWEDEN
CHINA	KOREA, REPUBLIC OF	SWITZERLAND
COLOMBIA	KUWAIT	SYRIAN ARAB REPUBLIC
COSTA RICA	LEBANON	THAILAND
COTE D'IVOIRE	LIBERIA	TUNISIA
CUBA	LIBYAN ARAB JAMAHIRIYA	TURKEY
CYPRUS	LIECHTENSTEIN	UGANDA
CZECHOSLOVAKIA	LUXEMBOURG	UKRAINIAN SOVIET SOCIALIST REPUBLIC
DEMOCRATIC KAMPUCHEA	MADAGASCAR	UNION OF SOVIET SOCIALIST REPUBLICS
DEMOCRATIC PEOPLE'S REPUBLIC OF KOREA	MALAYSIA	UNITED ARAB EMIRATES
DENMARK	MALI	UNITED KINGDOM OF GREAT BRITAIN AND NORTHERN IRELAND
DOMINICAN REPUBLIC	MAURITIUS	UNITED REPUBLIC OF TANZANIA
ECUADOR	MEXICO	UNITED STATES OF AMERICA
EGYPT	MONACO	URUGUAY
EL SALVADOR	MONGOLIA	VENEZUELA
ETHIOPIA	MOROCCO	VIET NAM
FINLAND	NAMIBIA	YUGOSLAVIA
FRANCE	NETHERLANDS	ZAMBIA
GABON	NEW ZEALAND	ZIMBABWE
GERMAN DEMOCRATIC REPUBLIC	NICARAGUA	
GERMANY, FEDERAL REPUBLIC OF	NIGER	
GHANA	NIGERIA	
GREECE	NORWAY	
	PAKISTAN	
	PANAMA	

The Agency's Statute was approved on 23 October 1956 by the Conference on the Statute of the IAEA held at United Nations Headquarters, New York; it entered into force on 29 July 1957. The Headquarters of the Agency are situated in Vienna. Its principal objective is "to accelerate and enlarge the contribution of atomic energy to peace, health and prosperity throughout the world".

© IAEA, 1987

Permission to reproduce or translate the information contained in this publication may be obtained by writing to the International Atomic Energy Agency, Wagramerstrasse 5, P.O. Box 100, A-1400 Vienna, Austria.

Printed by the IAEA in Austria  
June 1987

NUCLEAR FUSION, SUPPLEMENT 1987

PLASMA PHYSICS  
AND CONTROLLED  
NUCLEAR FUSION RESEARCH  
1986

PROCEEDINGS OF THE  
ELEVENTH INTERNATIONAL CONFERENCE ON PLASMA PHYSICS  
AND CONTROLLED NUCLEAR FUSION RESEARCH  
HELD BY THE  
INTERNATIONAL ATOMIC ENERGY AGENCY  
IN KYOTO, 13-20 NOVEMBER 1986

*In three volumes*

VOLUME 1

INTERNATIONAL ATOMIC ENERGY AGENCY  
VIENNA, 1987

PLASMA PHYSICS AND CONTROLLED NUCLEAR FUSION RESEARCH 1986  
IAEA, VIENNA, 1987  
STI/PUB/723  
ISBN 92-0-130087-5

## FOREWORD

The IAEA Conferences on Plasma Physics and Controlled Nuclear Fusion Research, organized biennially, are the largest and most important meetings in the field. They are a scientific forum not only for the presentation of the best results achieved in all laboratories performing fusion research but also for the co-ordination of international fusion efforts.

The Eleventh Conference, which was organized in co-operation with the Japanese Atomic Energy Research Institute, was attended by about 650 participants and observers representing 32 countries and two international organizations. About 200 papers were accepted for oral and poster presentations. The Conference opened with the traditional Artsimovich Memorial Lecture.

The Eleventh Conference became an important event for fusion scientists and engineers all over the world, for two special reasons. First, on the basis of the results achieved on several experimental devices, the plans for reaching plasma ignition within the next two years were presented. Second, the Conference not only marked 25 years of international co-operation under the auspices of the IAEA but also represented the starting point for a new international venture — an international thermonuclear experimental reactor.

These Proceedings, which include all the technical papers and five Conference summaries, are published in English as a supplement to the IAEA journal *Nuclear Fusion*.

The Agency promotes close international co-operation among plasma and fusion physicists and engineers of all countries by organizing these regular conferences on controlled nuclear fusion and by holding seminars, workshops and specialists meetings on appropriate topics. It is hoped that the present publication, as part of these activities, will contribute to the rapid demonstration of fusion power as one of the world's future energy resources.

## **EDITORIAL NOTE**

*The Proceedings have been edited by the editorial staff of the IAEA to the extent considered necessary for the reader's assistance. The views expressed remain, however, the responsibility of the named authors or participants. In addition, the views are not necessarily those of the governments of the nominating Member States or of the nominating organizations.*

*Although great care has been taken to maintain the accuracy of information contained in this publication, neither the IAEA nor its Member States assume any responsibility for consequences which may arise from its use.*

*The use of particular designations of countries or territories does not imply any judgement by the publisher, the IAEA, as to the legal status of such countries or territories, of their authorities and institutions or of the delimitation of their boundaries.*

*The mention of names of specific companies or products (whether or not indicated as registered) does not imply any intention to infringe proprietary rights, nor should it be construed as an endorsement or recommendation on the part of the IAEA.*

*The authors are responsible for having obtained the necessary permission for the IAEA to reproduce, translate or use material from sources already protected by copyrights.*

*Material prepared by authors who are in contractual relation with governments is copyrighted by the IAEA, as publisher, only to the extent permitted by the appropriate national regulations.*

## CONTENTS OF VOLUME 1

### ARTSIMOVICH MEMORIAL LECTURE and TOKAMAK EXPERIMENTS (Session A)

Artsimovich Memorial Lecture (IAEA-CN-47/A-0) .....	3
<i>J.F. Clarke</i>	
Recent experiments in JT-60 (IAEA-CN-47/A-I-1) .....	11
<i>JT-60 Team: T. Abe, H. Aikawa, H. Akaoka, H. Akasaka, M. Akiba, N. Akino, T. Akiyama, T. Ando, K. Annoh, N. Aoyagi, K. Arakawa, M. Araki, K. Arimoto, M. Azumi, S. Chiba, M. Dairaku, N. Ebisawa, T. Fujii, T. Fukuda, H. Furukawa, K. Hamamatsu, K. Hayashi, M. Hara, K. Haraguchi, H. Hiratsuka, T. Hirayama, S. Hiroki, K. Hiruta, M. Honda, H. Horiike, R. Hosoda, N. Hosogane, Y. Iida, T. Iijima, K. Ikeda, Y. Ikeda, T. Imai, T. Inoue, N. Isaji, M. Isaka, S. Ishida, N. Itige, T. Ito, Y. Ito, A. Kaminaga, M. Kawai, Y. Kawamata, K. Kawasaki, K. Kikuchi, M. Kikuchi, H. Kimura, T. Kimura, H. Kishimoto, K. Kitahara, S. Kitamura, A. Kitsunozaki, K. Kiyono, N. Kobayashi, K. Kodama, Y. Koide, T. Koike, M. Komata, I. Kondo, S. Konoshima, H. Kubo, S. Kunieda, S. Kurakata, K. Kurihara, M. Kuriyama, T. Kuroda, M. Kusaka, Y. Kusama, S. Maehara, K. Maeno, S. Mase, S. Matsuda, M. Matsukawa, T. Matsukawa, M. Matsuoka, N. Miya, K. Miyati, Y. Miyo, K. Mizuhashi, M. Mizuno, R. Murai, Y. Murakami, M. Muto, M. Nagami, A. Nagashima, K. Nagashima, T. Nagashima, S. Nagaya, H. Nakamura, Y. Nakamura, M. Nemoto, Y. Neyatani, S. Niikura, H. Ninomiya, T. Nishitani, H. Nomata, K. Obara, N. Ogiwara, Y. Ohara, K. Ohasa, T. Ohga, H. Ohhara, M. Ohkubo, T. Ohshima, K. Ohta, M. Ohta, M. Ohtaka, Y. Ohuchi, A. Oikawa, H. Okumura, Y. Okumura, K. Omori, S. Omori, Y. Omori, T. Ozeki, M. Saigusa, K. Sakamoto, A. Sakasai, S. Sakata, M. Satou, M. Sawahata, M. Seimiya, M. Seki, S. Seki, K. Shibamura, R. Shimada, K. Shimizu, M. Shimizu, Y. Shimomura, S. Shinozaki, H. Shirai, H. Shirakata, M. Shitomi, K. Sukanuma, T. Sugie, T. Sugiyama, H. Sunaoshi, K. Suzuki, M. Suzuki, M. Suzuki, N. Suzuki, S. Suzuki, Y. Suzuki, H. Takahashi, M. Takahashi, S. Takahashi, T. Takahashi, M. Takasaki, M. Takatsu, A. Takeshita, H. Takeuchi, S. Tamura, S. Tanaka, K. Tani, M. Terakado, T. Terakado, K. Tobita,</i>	

*T. Tokutake, T. Totsuka, N. Toyoshima, H. Tsuda, T. Tsugita, S. Tsuji, Y. Tsukahara, M. Tsuneoka, K. Uehara, M. Umehara, Y. Uramoto, H. Usami, K. Ushigusa, K. Usui, J. Yagyū, K. Yamada, M. Yamamoto, O. Yamashita, Y. Yamashita, K. Yano, T. Yasukawa, K. Yokokura, H. Yokomizo, H. Yoshida, M. Yoshikawa, Y. Yoshinari, R. Yoshino, I. Yonekawa, K. Watanabe*

Discussion .....	29
JET latest results and future prospects (IAEA-CN-47/A-I-2) .....	31
<i>JET Team: H. Altmann, R.J. Anderson, J. Arbez, W. Bailey, D.V. Bartlett, B. Beaumont, G. Beaumont, K. Behringer, P. Bertoldi, E. Bertolini, C.H. Best, V. Bhatnagar, R.J. Bickerton, A. Boileau, F. Bombarda, T. Bonicelli, S. Booth, A. Boschi, G. Bosia, M. Botman, H. Brelen, H. Brinkschulte, M.L. Browne, M. Brusati, T. Budd, M. Bures, P. Butcher, H. Buttgerit, D. Cacaot, C. Caldwell-Nichols, J.D. Callen, D.J. Campbell, J. Carwardine, G. Celentano, C.D. Challis, A. Cheetham, J.P. Christiansen, C. Christodoulopoulos, P. Chuilon, R. Claesen, J.P. Coad, S.A. Cohen, M. Cooke, J.G. Cordey, W. Core, S. Corti, A.E. Costley, G.A. Cottrell, M. Cox, C. David, J. Dean, L. de Kock, E. Deksnis, G.B. Denne, G. Deschamps, K.J. Dietz, J. Dobbing, S.E. Dorling, D.F. Dücks, G. Duesing, P.A. Duperrex, H. Duquenoy, A.W. Edwards, J. Ehrenberg, W. Engelhardt, S.K. Erents, F. Erhorn, B.T. Eriksson, M. Evrard, H. Falter, N. Foden, M.J. Forrest, C. Froger, K. Fullard, G. Fussmann, M. Gadeberg, A. Galetsas, A. Gallacher, D. Gambier, R. Giannella, A. Giannelli, A. Gibson, R.D. Gill, A. Goede, A. Gondhalekar, C. Gordon, C. Gormezano, N.A. Gottardi, C.W. Gowers, R. Granetz, B. Green, S. Gregoli, F.S. Griph, R. Haange, J.H. Hamnén, C.J. Hancock, P.J. Harbour, N.C. Hawkes, P. Haynes, T. Hellsten, J.L. Hemmerich, R. Hemsworth, F. Hendriks, R.F. Herzog, L. Horton, J. How, M. Huart, A. Hubbard, J. Hugill, M. Hugon, M. Huguét, B. Ingram, H. Jäckel, J. Jacquinet, Z. Jankowicz, O.N. Jarvis, E.M. Jones, P. Jones, T.T.C. Jones, C. Jupén, E. Källne, J. Källne, O. Kaneko, A. Kaye, B.E. Keen, M. Keilhacker, G. Kinahan, S. Kissel, A. Konstantellos, M. Kovanen, U. Kühnnapfel, P. Kupschus, P. Lallia, J.R. Last, L. Lauro-Taroni, K.D. Lawson, E. Lazzaro, R.C. Lobel, P.J. Lomas, N. Lopes-Cardozo, M. Lorenz-Gottardi, C. Lowry, G. Magyar, D. Maisonnier, M. Malacarne, V. Marchese, P. Massmann, G.M. McCracken, P. McCullen, M.J. Mead, P. Meriguet, V. Merlo, V. Mertens, S. Mills, P. Millward, A. Moissonnier, P.L. Mondino, D. Moreau, P.D. Morgan, E.R. Müller, D. Murmann, G. Murphy, M.F. Nave, L. Nickesson, P. Nielsen, P. Noll, S. Nowak, W. Obert, M. Olsson, J. O'Rourke, M.G. Pacco, J. Paillere, S. Papastergiou,</i>	

<i>J. Partridge, D. Pasini, N.J. Peacock, M. Pescatore, J. Plancoulaine, J.-P. Poffé, R. Prentice, T. Raimondi, J. Ramette, C. Raymond, P.H. Rebut, J. Removille, W. Riediker, R. Roberts, D.C. Robinson, A. Rolfe, R.T. Ross, G. Rupprecht, R. Rushton, H.C. Sack, G. Sadler, J. Saffert, N. Salmon, F. Sand, A. Santagiustina, R. Saunders, M. Schmid, F.C. Schüller, K. Selin, R. Shaw, A. Sibley, D. Sigournay, R. Sillen, F. Simonet, R. Simonini, P. Smeulders, J.A. Snipes, K. Sonnenberg, L. Sonnerup, M.F. Stamp, C.A. Steed, D. Stork, P.E. Stott, T.E. Stringer, D.R. Summers, H.P. Summers, A.J. Tagle, G. Tallents, A. Tanga, A. Taroni, A. Terrington, A. Tesini, P.R. Thomas, E. Thompson, K. Thomsen, F. Tibone, R. Tivey, T.N. Todd, P. Trevalion, M. Tschudin, B.J. Tubbing, P. Twynam, E. Usselmann, H. Van der Beken, J.E. Van Montfoort, M. von Hellermann, J. von Seggern, T. Wade, C. Walker, B.A. Wallander, M. Walravens, K. Walter, M.L. Watkins, M. Watson, D. Webberley, A. Weller, J.A. Wesson, J. Wilks, T. Winkel, C. Woodward, M. Wykes, D. Young, L. Zannelli, J.W. Zwart</i>	
Dicussion .....	48
TFTR plasma regimes (IAEA-CN-47/A-I-3) .....	51
<i>R.J. Hawryluk, V. Arunasalam, M.G. Bell, M. Bitter, W.R. Blanchard, N.L. Bretz, R. Budny, C.E. Bush, J.D. Callen, S.A. Cohen, S.K. Combs, S.L. Davis, D.L. Dimock, H.F. Dylla, P.C. Efthimion, L.C. Emerson, A.C. England, H.P. Eubank, R.J. Fonck, E. Fredrickson, H.P. Furth, G. Gammel, R.J. Goldston, B. Grek, L.R. Grisham, G. Hammett, W.W. Heidbrink, H.W. Hendel, K.W. Hill, E. Hinnov, S. Hiroe, H. Hsuan, R.A. Hulse, K.P. Jaehnig, D. Jassby, F.C. Jobes, D.W. Johnson, L.C. Johnson, R. Kaita, R. Kamperschroer, S.M. Kaye, S.J. Kilpatrick, R.J. Knize, H. Kugel, P.H. LaMarche, B. LeBlanc, R. Little, C.H. Ma, D.M. Manos, D.K. Mansfield, R.T. McCann, M.P. McCarthy, D.C. McCune, K. McGuire, D.H. McNeill, D.M. Meade, S.S. Medley, D.R. Mikkelsen, S.L. Milora, W. Morris, D. Mueller, V. Mukhovatov, E.B. Nieschmidt, J. O'Rourke, D.K. Owens, H. Park, N. Pomphrey, B. Prichard, A.T. Ramsey, M.H. Redi, A.L. Roquemore, P.H. Rutherford, N.R. Sauthoff, G. Schilling, J. Schivell, G.L. Schmidt, S.D. Scott, S. Sesnic, J.C. Sinnis, F.J. Stauffer, B.C. Stratton, G.D. Tait, G. Taylor, J.R. Timberlake, H.H. Towner, M. Ulrickson, V. Vershkov, S. Von Goeler, F. Wagner, R. Wieland, J.B. Wilgen, M. Williams, K.L. Wong, S. Yoshikawa, R. Yoshino, K.M. Young, M.C. Zarnstorff, V.S. Zaveryaev, S.J. Zweben</i>	
Discussion .....	63

Experimental studies in JET with magnetic separatrix (IAEA-CN-47/A-I-5) .....	65
<i>A. Tanga, D.V. Bartlett, K. Behringer, R.J. Bickerton, A. Cheetham, J.G. Cordey, A. Gibson, N.A. Gottardi, A. Gondhalekar, P.J. Harbour, H. Jaeckel, M. Keilhacker, E. Lazzaro, V. Martens, P. Noll, S. Nowak, F.C. Schüller, A.J. Tagle, A. Taroni, P.R. Thomas, F. Tibone</i>	
Discussion .....	73
Energy confinement and profile consistency in TFTR (IAEA-CN-47/A-II-1) .....	75
<i>R.J. Goldston, V. Arunasalam, M.G. Bell, M. Bitter, W.R. Blanchard, N.L. Bretz, R. Budny, C.E. Bush, J.D. Callen, S.A. Cohen, S.K. Combs, S.L. Davis, D.L. Dimock, H.F. Dylla, P.C. Efthimion, L.C. Emerson, A.C. England, H.P. Eubank, R.J. Fonck, E. Fredrickson, H.P. Furth, G. Gammel, B. Grek, L.R. Grisham, G. Hammett, R.J. Hawryluk, W.W. Heidbrink, D.B. Heifetz, H.W. Hendel, K.W. Hill, E. Hinnov, S. Hiroe, H. Hsuan, R.A. Hulse, K.P. Jaehnig, D. Jassby, F.C. Jobes, D.W. Johnson, L.C. Johnson, R. Kaita, R. Kamperschroer, S.M. Kaye, S.J. Kilpatrick, R.J. Knize, H. Kugel, P.H. LaMarche, B. LeBlanc, R. Little, C.H. Ma, D.M. Manos, D.K. Mansfield, R.T. McCann, M.P. McCarthy, D.C. McCune, K. McGuire, D.H. McNeill, D.M. Meade, S.S. Medley, D.R. Mikkelsen, S.L. Milora, W. Morris, D. Mueller, V. Mukhovatov, E.B. Nieschmidt, J. O'Rourke, D.K. Owens, H. Park, N. Pomphrey, B. Prichard, A.T. Ramsey, M.H. Redi, A.L. Roquemore, P.H. Rutherford, N.R. Sauthoff, G. Schilling, J. Schivell, G.L. Schmidt, S.D. Scott, S. Sesnic, J.C. Sinnen, F.J. Stauffer, B.C. Stratton, G.D. Tait, G. Taylor, J.R. Timberlake, H.H. Towner, M. Ulrickson, V. Vershkov, S. Von Goeler, F. Wagner, R. Wieland, J.B. Wilgen, M. Williams, K.L. Wong, S. Yoshikawa, R. Yoshino, K.M. Young, M.C. Zarnstorff, V.S. Zaveryaev, S.J. Zweben</i>	
Discussion .....	86
Energy and particle confinement of JT-60 plasmas with high power heating (IAEA-CN-47/A-II-2) .....	89
<i>JT-60 Team: T. Abe, H. Aikawa, H. Akaoka, H. Akasaka, M. Akiba, N. Akino, T. Akiyama, T. Ando, K. Annoh, N. Aoyagi, K. Arakawa, M. Araki, K. Arimoto, M. Azumi, S. Chiba, M. Dairaku, N. Ebisawa, T. Fujii, T. Fukuda, H. Furukawa, K. Hamamatsu, K. Hayashi, M. Hara, K. Haraguchi, H. Hiratsuka, T. Hirayama, S. Hiroki, K. Hiruta, M. Honda, H. Horiike, R. Hosoda, N. Hosogane, Y. Iida, T. Iijima, K. Ikeda, Y. Ikeda, T. Imai, T. Inoue, N. Isaji, M. Isaka, S. Ishida, N. Itige, T. Ito, Y. Ito, A. Kaminaga, M. Kawai, Y. Kawamata, K. Kawasaki, K. Kikuchi, M. Kikuchi, H. Kimura, T. Kimura, H. Kishimoto, K. Kitahara, S. Kitamura, A. Kitsunozaki,</i>	

<p><i>K. Kiyono, N. Kobayashi, K. Kodama, Y. Koide, T. Koike, M. Komata, I. Kondo, S. Konoshima, H. Kubo, S. Kunieda, S. Kurakata, K. Kurihara, M. Kuriyama, T. Kuroda, M. Kusaka, Y. Kusama, S. Maehara, K. Maeno, S. Mase, S. Matsuda, M. Matsukawa, T. Matsukawa, M. Matsuoka, N. Miya, K. Miyati, Y. Miyo, K. Mizuhashi, M. Mizuno, R. Murai, Y. Murakami, M. Muto, M. Nagami, A. Nagashima, K. Nagashima, T. Nagashima, S. Nagaya, H. Nakamura, Y. Nakamura, M. Nemoto, Y. Neyatani, S. Niikura, H. Ninomiya, T. Nishitani, H. Nomata, K. Obara, N. Ogiwara, Y. Ohara, K. Ohasa, T. Ohga, H. Ohhara, M. Ohkubo, T. Ohshima, K. Ohta, M. Ohta, M. Ohtaka, Y. Ohuchi, A. Oikawa, H. Okumura, Y. Okumura, K. Omori, S. Omori, Y. Omori, T. Ozeki, M. Saigusa, K. Sakamoto, A. Sakasai, S. Sakata, M. Satou, M. Sawahata, M. Seimiya, M. Seki, S. Seki, K. Shibamura, R. Shimada, K. Shimizu, M. Shimizu, Y. Shimomura, S. Shinozaki, H. Shirai, H. Shirakata, M. Shitomi, K. Sukanuma, T. Sugie, T. Sugiyama, H. Sunaoshi, K. Suzuki, M. Suzuki, M. Suzuki, N. Suzuki, S. Suzuki, Y. Suzuki, H. Takahashi, M. Takahashi, S. Takahashi, T. Takahashi, M. Takasaki, M. Takatsu, A. Takeshita, H. Takeuchi, S. Tamura, S. Tanaka, K. Tani, M. Terakado, T. Terakado, K. Tobita, T. Tokutake, T. Totsuka, N. Toyoshima, H. Tsuda, T. Tsugita, S. Tsuji, Y. Tsukahara, M. Tsuneoka, K. Uehara, M. Umehara, Y. Uramoto, H. Usami, K. Ushigusa, K. Usui, J. Yagyu, K. Yamada, M. Yamamoto, O. Yamashita, Y. Yamashita, K. Yano, T. Yasukawa, K. Yokokura, H. Yokomizo, H. Yoshida, M. Yoshikawa, Y. Yoshinari, R. Yoshino, I. Yonekawa, K. Watanabe</i></p>	98
<p>Discussion .....</p>	98
<p>Energy confinement in JET with Ohmic heating and strong auxiliary heating (IAEA-CN-47/A-II-3) .....</p>	99
<p><i>J.G. Cordey, D.V. Bartlett, V. Bhatnagar, R.J. Bickerton, M. Bures, J.D. Callen, D.J. Campbell, C.D. Challis, J.P. Christiansen, S. Corti, A.E. Costley, G.A. Cottrell, G. Duesing, J. Fessey, M. Gadeberg, A. Gibson, A. Gondhalekar, N.A. Gottardi, C.W. Gowers, M. von Hellermann, F. Hendriks, L. Horton, H. Jäckel, J. Jacquinet, O.N. Jarvis, T.T.C. Jones, E. Källne, J. Källne, M. Keilhacker, S. Kissel, L. de Kock, P. Lallia, E. Lazzaro, P.J. Lomas, N. Lopes-Cardozo, P.D. Morgan, P. Nielsen, J. O'Rourke, R. Prentice, R.T. Ross, G. Sadler, F.C. Schüller, A. Stabler, P. Smeulders, M.F. Stamp, D. Stork, P.E. Stott, D.R. Summers, A. Tanga, P.R. Thomas, E. Thompson, K. Thomsen, G. Tonetti, B.J. Tubbing, M.L. Watkins</i></p>	
<p>Discussion .....</p>	109

Effect of p and j profiles on energy confinement in ECH experiments on T-10 (IAEA-CN-47/A-II-4) .....	111
<i>V.V. Alikaev, A.A. Bagdasarov, E.L. Berezovskij, A.B. Berlizov, G.A. Bobrovskij, A.A. Borshchegovskij, N.L. Vasin, A.N.I. Vertiporokh, V.V. Volkov, E.P. Gorbunov, Yu.A. Gorelov, Yu.V. Esipchuk, S.L. Efremov, V.S. Zaveryaev, V.I. Il'in, A.Ya. Kislov, P.E. Kovrov, S.Yu. Luk'yanov, Yu.S. Maksimov, A.A. Medvedev, G.E. Notkin, A.B. Pimenov, V.I. Poznyak, I.A. Popov, S.V. Popovichev, K.A. Razumova, P.V. Savrukhin, E.V. Sitar, A.M. Solntsev, M.M. Stepanenko, V.S. Strelkov, A.V. Tarakanov, K.N. Tarasyan, K.B. Titishov, V.M. Trukhin, G.S. Yaramyshev, S.N. Vlasov, A.L. Gol'denberg, V.A. Markelov, V.A. Flyagin, B.V. Shishkin</i>	
Discussion .....	123
Achievement of regimes with high density, low $q_a$ and good confinement on ASDEX (IAEA-CN-47/A-II-5) .....	125
<i>H. Niedermeyer, F. Wagner, G. Becker, K. Büchl, A. Eberhagen, G. Fussmann, O. Gehre, G. von Gierke, O. Gruber, G. Janeschitz, M. Kaufmann, K. Lackner, R. Lang, V. Mertens, H. Murmann, W. Sandmann, E. Speth, K. Steinmetz, G. Vlases, H.S. Bosch, H. Brocken, J. Gerhardt, E. Glock, G. Haas, J. Hofmann, A. Izvozchikov, F. Karger, M. Keilhacker, O. Klüber, M. Kornherr, M. Lenoci, G. Lisitano, F. Mast, H.M. Mayer, K. McCormick, D. Meisel, E.R. Müller, Z.A. Pietrzyk, W. Poschenrieder, H. Rapp, H. Riedler, H. Röhr, J. Roth, F. Ryter, F. Schneider, C. Setzensack, G. Siller, P. Smeulders, F.X. Söldner, K.-H. Steuer, O. Vollmer, D. Zasche</i>	
Discussion .....	136
Studies of the regime of improved particle and energy confinement following pellet injection into Alcator C (IAEA-CN-47/A-III-1) .....	139
<i>M. Greenwald, M. Besen, F. Camacho, C. Fiore, M. Foord, R. Gandy, C. Gomez, R. Granetz, D. Gwinn, S. Knowlton, B. LaBombard, B. Lipschultz, H. Manning, E. Marmor, S.C. McCool, J. Parker, R. Parker, R. Petrasso, P. Pribyl, J. Rice, D. Sigmar, Y. Takase, J. Terry, R. Watterson, S. Wolfe</i>	
Discussion .....	149
Confinement studies of additionally heated plasma in the JFT-2M tokamak (IAEA-CN-47/A-III-2) .....	151
<i>K. Odajima, A. Funahashi, K. Hoshino, S. Kasai, T. Kawakami, H. Kawashima, T. Matoba, T. Matsuda, H. Matsumoto, Y. Miura, M. Mori, H. Ogawa, T. Ogawa, H. Ohtsuka, S. Sengoku, T. Shoji, N. Suzuki, H. Tamai, Y. Uesugi, T. Yamamoto, T. Yamauchi, M. Hasegawa, S. Takada, K. Hasegawa, A. Honda, I. Ishibori, T. Kashimura, Y. Kashiwa, M. Kazawa, K. Kikuchi, Y. Matsuzaki,</i>	

<i>K. Ohuchi, H. Okano, T. Shibata, T. Shibuya, T. Shiina, K. Suzuki, T. Tani, K. Yokoyama</i>	
Discussion .....	157
Initial results from the DIII-D tokamak (IAEA-CN-47/A-III-3) .....	159
<i>J. Luxon, P. Anderson, F. Batty, C. Baxi, G. Bramson, N. Brooks, B. Brown, B. Burley, K.H. Burrell, R. Callis, G. Campbell, T. Carlstrom, A. Colleraine, J. Cummings, J. Davis, J. DeBoo, S. Ejima, R. Evanko, H. Fukumoto, R. Gallix, J. Gilleland, T. Glad, P. Gohil, A. Gootgeld, R.J. Groebner, S. Hanai, J. Haskovec, E. Heckman, M. Heiberger, F.J. Helton, P. Henline, D. Hill, D. Hoffman, E. Hoffmann, R. Hong, N. Hosogane, C. Hsieh, G.L. Jackson, G. Jahns, G. Janeschitz, E. Johnson, A. Kellman, J.S. Kim, J. Kohli, A. Langhorn, L. Lao, P. Lee, S. Lightner, J. Lohr, M. Mahdavi, M. Mayberry, B. McHarg, T. McKelvey, R. Miller, C.P. Moeller, D. Moore, A. Nerem, P. Noll, T. Ohkawa, N. Ohyabu, T. Osborne, D. Overskei, P. Petersen, T. Petrie, J. Phillips, R. Prater, J. Rawls, E. Reis, D. Remsen, P. Riedy, P. Rock, K. Schaubel, D. Schissel, J. Scoville, R. Seraydarian, M. Shimada, T. Shoji, B. Sleaford, J. Smith, Jr., P. Smith, T. Smith, R.T. Snider, R.D. Stambaugh, R. Stav, H. St. John, R. Stockdale, E.J. Strait, R. Street, T.S. Taylor, J. Tooker, M. Tupper, S.K. Wong, S. Yamaguchi</i>	
Discussion .....	168
Pellet injection results during TFTR Ohmic and neutral beam heating experiments (IAEA-CN-47/A-III-4) .....	171
<i>G.L. Schmidt, S.L. Milora, V. Arunasalam, M.G. Bell, M. Bitter, C.E. Bush, S.K. Combs, H.F. Dylla, P.C. Efthimion, E. Fredrickson, R.J. Goldston, B. Grek, L.R. Grisham, G. Hammett, R.J. Hawryluk, W.W. Heidbrink, H.W. Hendel, K.W. Hill, H. Hsuan, D.W. Johnson, L.C. Johnson, P.H. LaMarche, R. Little, D.K. Mansfield, D.C. McCune, K. McGuire, D.M. Meade, S.S. Medley, D. Mueller, W. Morris, E.B. Nieschmidt, J. O'Rourke, D.K. Owens, H. Park, A.T. Ramsey, M.H. Redi, J. Schivell, D. Schuresko, T. Senko, S. Sesnic, F.J. Stauffer, B.C. Stratton, G.D. Tait, G. Taylor, J.R. Timberlake, H.H. Towner, M. Ulrickson, R. Wieland, J.B. Wilgen, M. Williams, M.C. Zarnstorff, S.J. Zweben</i>	
Discussion .....	177
Fast ion losses and plasma confinement in TFR during neutral beam injection (IAEA-CN-47/A-III-5) .....	179
<i>Equipe TFR</i>	
Discussion .....	185
Particle and thermal transport, and resonant field experiments in TEXT (IAEA-CN-47/A-III-6) .....	187
<i>A.J. Wootton, R.D. Bengtson, J.A. Boedo, R.V. Bravenec, K.L. Empson,</i>	

<i>K.W. Gentle, W.L. Hodge, C.C. Klepper, J. Porter, A. Macmahon, S.C. McCool, W.H. Miner, D.M. Patterson, P.E. Phillips, B. Richards, C.P. Ritz, T.L. Rhodes, D.W. Ross, W.L. Rowan, J.C. Wiley, D.L. Brower, S.K. Kim, N.C. Luhmann, W.A. Peebles, J.S. DeGrassie, T.E. Evans, G.L. Jackson, N. Ohyabu, P.H. Diamond, T.S. Hahm, P.W. Terry, Shuping Fan, Yexi He, J.C. Forster, R.L. Hickok, P.M. Schoch, G. Haas, F. Karger, Xuehua Yu, Shaobai Zheng, R.C. Isler</i>	
Discussion .....	194
Impurity production mechanisms and behaviour during additional heating in JET (IAEA-CN-47/A-IV-1) .....	197
<i>K. Behringer, A. Boileau, F. Bombarda, G.B. Denne, W. Engelhardt, M.J. Forrest, G. Fussmann, R. Giannella, N.A. Gottardi, M. von Hellermann, L. Horton, H. Jäckel, C. Jupén, E. Källne, K.D. Lawson, G. Magyar, G.M. McCracken, P.D. Morgan, E.R. Müller, N.J. Peacock, J. Ramette, B. Saoutic, M.F. Stamp, H.P. Summers, G. Tallents, A. Weller</i>	
Discussion .....	205
Impurity and particle transport and control in TFTR (IAEA-CN-47/A-IV-2) .....	207
<i>K.W. Hill, V. Arunasalam, M.G. Bell, M. Bitter, W.R. Blanchard, N.L. Bretz, R. Budny, C.E. Bush, S.A. Cohen, S.K. Combs, S.L. Davis, D.L. Dimock, H.F. Dylla, P.C. Efthimion, L.C. Emerson, A.C. England, H.P. Eubank, R.J. Fonck, E. Fredrickson, H.P. Furth, G. Gammel, R.J. Goldston, B. Grek, L.R. Grisham, G. Hammett, R.J. Hawryluk, W.W. Heidbrink, H.W. Hendel, E. Hinnov, S. Hiroe, H. Hsuan, R.A. Hulse, K.P. Jaehnig, D. Jassby, F.C. Jobes, D.W. Johnson, L.C. Johnson, R. Kaita, R. Kamperschroer, S.M. Kaye, S.J. Kilpatrick, R.J. Knize, H. Kugel, P.H. LaMarche, B. LeBlanc, C.H. Ma, D.M. Manos, D.K. Mansfield, R.T. McCann, M.P. McCarthy, D.C. McCune, K. McGuire, D.H. McNeill, D.M. Meade, S.S. Medley, D.R. Mikkelsen, S.L. Milora, W. Morris, D. Mueller, V. Mukhovatov, E.B. Nieschmidt, J. O'Rourke, D.K. Owens, H. Park, N. Pomphrey, B. Prichard, A.T. Ramsey, M.H. Redi, A.L. Roquemore, P.H. Rutherford, N.R. Sauthoff, G. Schilling, J. Schivell, G.L. Schmidt, S.D. Scott, S. Sesnic, M. Shimada, J.C. Sinnis, F.J. Stauffer, J. Strachan, B.C. Stratton, G.D. Tait, G. Taylor, J.R. Timberlake, H.H. Towner, M. Ulrickson, V. Vershkov, S. Von Goeler, F. Wagner, R. Wieland, J.B. Wilgen, M. Williams, K.L. Wong, S. Yoshikawa, R. Yoshino, K.M. Young, M.C. Zarnstorff, V.S. Zaveryaev, S.J. Zweben</i>	
Discussion .....	216

Impurity and MHD behaviour in JT-60 divertor discharges

(IAEA-CN-47/A-IV-3) .....	217
<i>JT-60 Team: T. Abe, H. Aikawa, H. Akaoka, H. Akasaka, M. Akiba, N. Akino, T. Akiyama, T. Ando, K. Annoh, N. Aoyagi, K. Arakawa, M. Araki, K. Arimoto, M. Azumi, S. Chiba, M. Dairaku, N. Ebisawa, T. Fujii, T. Fukuda, H. Furukawa, K. Hamamatsu, K. Hayashi, M. Hara, K. Haraguchi, H. Hiratsuka, T. Hirayama, S. Hiroki, K. Hiruta, M. Honda, H. Horiike, R. Hosoda, N. Hosogane, Y. Iida, T. Iijima, K. Ikeda, Y. Ikeda, T. Imai, T. Inoue, N. Isaji, M. Isaka, S. Ishida, N. Itige, T. Ito, Y. Ito, A. Kaminaga, M. Kawai, Y. Kawamata, K. Kawasaki, K. Kikuchi, M. Kikuchi, H. Kimura, T. Kimura, H. Kishimoto, K. Kitahara, S. Kitamura, A. Kitsunezaki, K. Kiyono, N. Kobayashi, K. Kodama, Y. Koide, T. Koike, M. Komata, I. Kondo, S. Konoshima, H. Kubo, S. Kunieda, S. Kurakata, K. Kurihara, M. Kuriyama, T. Kuroda, M. Kusaka, Y. Kusama, S. Maehara, K. Maeno, S. Mase, S. Matsuda, M. Matsukawa, T. Matsukawa, M. Matsuoka, N. Miya, K. Miyati, Y. Miyo, K. Mizuhashi, M. Mizuno, R. Murai, Y. Murakami, M. Muto, M. Nagami, A. Nagashima, K. Nagashima, T. Nagashima, S. Nagaya, H. Nakamura, Y. Nakamura, M. Nemoto, Y. Neyatani, S. Niikura, H. Ninomiya, T. Nishitani, H. Nomata, K. Obara, N. Ogiwara, Y. Ohara, K. Ohasa, T. Ohga, H. Ohhara, M. Ohkubo, T. Ohshima, K. Ohta, M. Ohta, M. Ohtaka, Y. Ohuchi, A. Oikawa, H. Okumura, Y. Okumura, K. Omori, S. Omori, Y. Omori, T. Ozeki, M. Saigusa, K. Sakamoto, A. Sakasai, S. Sakata, M. Satou, M. Sawahata, M. Seimiya, M. Seki, S. Seki, K. Shibanuma, R. Shimada, K. Shimizu, M. Shimizu, Y. Shimomura, S. Shinozaki, H. Shirai, H. Shirakata, M. Shitomi, K. Suganuma, T. Sugie, T. Sugiyama, H. Sunaoshi, K. Suzuki, M. Suzuki, M. Suzuki, N. Suzuki, S. Suzuki, Y. Suzuki, H. Takahashi, M. Takahashi, S. Takahashi, T. Takahashi, M. Takasaki, M. Takatsu, A. Takeshita, H. Takeuchi, S. Tamura, S. Tanaka, K. Tani, M. Terakado, T. Terakado, K. Tobita, T. Tokutake, T. Totsuka, N. Toyoshima, H. Tsuda, T. Tsugita, S. Tsuji, Y. Tsukahara, M. Tsuneoka, K. Uehara, M. Umehara, Y. Uramoto, H. Usami, K. Ushigusa, K. Usui, J. Yagyu, K. Yamada, M. Yamamoto, O. Yamashita, Y. Yamashita, K. Yano, T. Yasukawa, K. Yokokura, H. Yokomizo, H. Yoshida, M. Yoshikawa, Y. Yoshinari, R. Yoshino, I. Yonekawa, K. Watanabe</i>	
Discussion .....	224
Density limit and impurity transport investigations in	
DITE tokamak (IAEA-CN-47/A-IV-4) .....	227
<i>J. Allen, G.E. Austin, K.B. Axon, R. Barnsley, M. Dunstan, D.N. Edwards, K.D. Evans, S.J. Fielding, D.H.J. Goodall,</i>	

<i>W. Han, N.C. Hawkes, J. Hugill, P.C. Johnson, G.M. McCracken, G.F. Matthews, W. Millar, N.J. Peacock, C.S. Pitcher, J. Pritchard, A. Sykes, M.F. Turner, J.P. Webber</i>	
Discussion .....	235
Studies of edge plasma phenomena in T-10 (IAEA-CN-47/A-IV-5) .....	237
<i>K.F. Alexander, L. Dietrich, H. Grote, K. Günther, J. Lingertat, E.L. Berezovskij, A.V. Chankin, V.M. Chicherov, S.E. Lysenko, V.A. Medvedev, A.Yu. Pigarov, V.I. Pistunovich, S.V. Popovichev, V. Vershkov</i>	
Discussion .....	246
ALT-I pump limiter behaviour and edge plasma flows during biasing and ICRF heating in the TEXTOR tokamak (IAEA-CN-47/A-IV-6) .....	249
<i>R.W. Conn, D.M. Goebel, W.K. Leung, G.A. Campbell, B. LaBombard, A.K. Prinja, W.L. Hsu, G.J. Thomas, K.H. Dippel, K.H. Finken, R. Reiter, G.H. Wolf, H.L. Bay, G. Bertschinger, W. Bieger, P. Bogen, W. Brussau, Y. Cao, H.G. Esser, G. Fuchs, B. Giesen, E. Graffmann, H. Hartwig, E. Hintz, F. Hoenen, K. Höhker, A. Kaleck, H. Keuer, L. Könen, M. Korten, L. Li, Y.T. Lie, A. Pospieszczyk, A. Rogister, G. Ross, D. Rusbüldt, U. Samm, J. Schlüter, B. Schweer, H. Soltwisch, F. Waelbroeck, G. Waidmann, P. Wienhold, J. Winter, R. Yamauchi, T. Delvigne, P. Descamps, F. Durodie, M. Jadoul, R. Koch, D. Lebeau, A.M. Messiaen, D.I.C. Pearson, P.E. Vandenplas, R. Van Nieuwenhove, G. Van Oost, G. Van Wassenhove, R.R. Weynants</i>	
Discussion .....	261
Current density profiles in the TEXTOR tokamak (IAEA-CN-47/A-V-1) ...	263
<i>H. Soltwisch, W. Stodiek, J. Manickam, J. Schlüter</i>	
Discussion .....	272
Stability and confinement studies in the Princeton Beta Experiment (PBX) (IAEA-CN-47/A-V-2) .....	275
<i>M. Okabayashi, K. Bol, M. Chance, P. Couture, H. Fishman, R.J. Fonck, G. Gammel, W.W. Heidbrink, K. Ida, K.P. Jaehnig, G. Jahns, R. Kaita, S.M. Kaye, H. Kugel, B. LeBlanc, J. Manickam, W. Morris, G.A. Navratil, N. Ohyabu, S. Paul, E. Powell, M. Reusch, S. Sesnic, H. Takahashi</i>	
Discussion .....	290
Stabilization of the tearing mode (IAEA-CN-47/A-V-3) .....	291
<i>T.C. Hender, D.C. Robinson, J.A. Snipes</i>	
Discussion .....	298
Experimental and theoretical studies of circular cross-section high beta tokamaks (IAEA-CN-47/A-V-4) .....	299
<i>G.A. Navratil, Y. Baransky, A. Bhattacharjee, C.K. Chu, A.V. Deniz, A.A. Grossman, A. Holland, T. Ivers, X.L. Li, T.C. Marshall,</i>	

<i>M.E. Mauel, S. Sabbagh, A.K. Sen, J. Van Dam, X.-H. Wang, M. Hughes, M. Phillips, A.M.M. Todd</i>	
Discussion .....	308
Disruption control experiments using local modular multipole field coils (IAEA-CN-47/A-V-5) .....	309
<i>K. Yamazaki, K. Kawahata, Y. Abe, R. Akiyama, T. Amano, R. Ando, Y. Hamada, S. Hirokura, K. Ida, E. Kako, O. Kaneko, Y. Kawasumi, S. Kitagawa, T. Kuroda, K. Masai, K. Matsuoka, A. Mohri, M. Mugishima, N. Noda, I. Ogawa, Y. Ogawa, K. Ohkubo, Y. Oka, K. Sakurai, M. Sasao, K. Sato, K.N. Sato, S. Tanahashi, Y. Taniguchi, K. Toi, T. Watari</i>	
Discussion .....	316
Studies of MHD modes and high frequency fluctuations on the HT-6B and HT-6M tokamaks (IAEA-CN-47/A-V-6) .....	317
<i>Jikang Xie, Jiayu Chen, Wenkang Guo, Yuping Huo, HT-6B Group, HT-6M Group</i>	
Anomalous transport in JET plasmas (IAEA-CN-47/A-VI-1-1) .....	325
<i>D.F. Duchs, T.E. Stringer, A. Taroni, M. Brusati, N.A. Gottardi, T. Hellsten, F. Tibone</i>	
Microinstability based models for confinement properties and ignition criteria in tokamaks (IAEA-CN-47/A-VI-1-2) .....	337
<i>W.M. Tang, C.M. Bishop, B. Coppi, S.M. Kaye, F.W. Perkins, M.H. Redi, G. Rewoldt</i>	
Drift wave models of tokamak confinement (IAEA-CN-47/A-VI-1-3) .....	345
<i>R.E. Waltz, R.R. Dominguez, S.K. Wong, P.H. Diamond, G.S. Lee, T.S. Hahn, N. Mattor</i>	
Discussion on papers IAEA-CN-47/A-VI-1-1 to A-VI-1-3 .....	355
MHD stability and transport of beam heated ASDEX discharges in the vicinity of the beta limit (IAEA-CN-47/A-VI-2) .....	357
<i>O. Gruber, G. Becker, G. von Gierke, K. Grassie, O. Klüber, M. Kornherr, K. Lackner, J.K. Lee, H.P. Zehrfeld, H.S. Bosch, H. Brocken, A. Eberhagen, G. Fussmann, O. Gehre, J. Gernhardt, E. Glock, G. Haas, J. Hofmann, A. Izvozchikov, G. Janeschitz, F. Karger, M. Kaufmann, M. Keilhacker, M. Lenoci, G. Lisitano, F. Mast, H.M. Mayer, K. McCormick, D. Meisel, V. Mertens, E.R. Müller, H. Murmann, H. Niedermeyer, W. Poschenrieder, H. Rapp, H. Riedler, H. Röhr, J. Roth, F. Ryter, F. Schneider, C. Setzensack, G. Siller, P. Smeulders, F.X. Söldner, E. Speth, K.-H. Steuer, O. Vollmer, F. Wagner, D. Zasche</i>	
Discussion .....	371
Beta limit disruptions (IAEA-CN-47/A-VI-3) .....	373
<i>Mingsheng Chu, E.J. Strait, J.K. Lee, L. Lao, R.D. Stambaugh, K.H. Burrell, R.J. Groebner, J.M. Greene, F.J. Helton, J.Y. Hsu,</i>	

<i>J.S. Kim, H. St. John, R.T. Snider, T.S. Taylor</i>	
Discussion .....	384
Sawteeth and temperature profiles in tokamaks (IAEA-CN-47/A-VI-4) .....	387
<i>D.A. Boyd, R.E. Denton, J.Q. Dong, J.F. Drake, P.N. Guzdar,</i> <i>A.B. Hassam, R.G. Kleva, Y.C. Lee, C.S. Liu, F.J. Stauffer</i>	
Discussion .....	398
First results from the HL-1 tokamak (IAEA-CN-47/A-VII-1) .....	399
<i>HL-1 Tokamak Group</i>	
Tokamak current drive via AC magnetic helicity injection (IAEA-CN-47/A-VII-2) .....	407
<i>P.M. Bellan, P.C. Liewer, J.M. Finn, T.M. Antonsen, Jr.</i>	
Study of enhanced confinement and $q = 2$ disruptive modes with fast rising current in the STOR-1M tokamak (IAEA-CN-47/A-VII-3) .....	413
<i>H. Kuwahara, O. Mitarai, E.J.M. Van Heesch, M. Emaami,</i> <i>A.H. Sarkissian, S.W. Wolfe, A. Hirose, H.M. Skarsgard</i>	
Coherent and turbulent fluctuations in TFTR (IAEA-CN-47/A-VII-4) .....	421
<i>K. McGuire, V. Arunasalam, M.G. Bell, M. Bitter, W.R. Blanchard,</i> <i>N.L. Bretz, R. Budny, C.E. Bush, J.D. Callen, M. Chance, S.A. Cohen,</i> <i>S.K. Combs, S.L. Davis, D.L. Dimock, H.F. Dylla, P.C. Efthimion,</i> <i>L.C. Emerson, A.C. England, H.P. Eubank, R.J. Fonck, E. Fredrickson,</i> <i>H.P. Furth, G. Gammel, R.J. Goldston, B. Grek, L.R. Grisham, G. Hammett,</i> <i>R.J. Hawryluk, W.W. Heidbrink, H.W. Hendel, K.W. Hill, E. Hinnov,</i> <i>S. Hiroe, H. Hsuan, R.A. Hulse, K.P. Jaehnig, D. Jassby, F.C. Jobs,</i> <i>D.W. Johnson, L.C. Johnson, R. Kaita, R. Kamperschroer, S.M. Kaye,</i> <i>S.J. Kilpatrick, R.J. Knize, H. Kugel, P.H. LaMarche, B. LeBlanc,</i> <i>R. Little, C.H. Ma, J. Manickam, D.M. Manos, D.K. Mansfield,</i> <i>R.T. McCann, M.P. McCarthy, D.C. McCune, D.H. McNeill,</i> <i>D.M. Meade, S.S. Medley, D.R. Mikkelsen, S.L. Milora, D. Monticello,</i> <i>W. Morris, D. Mueller, E.B. Nieschmidt, J. O'Rourke, D.K. Owens,</i> <i>H. Park, W. Park, N. Pomphrey, B. Prichard, A.T. Ramsey,</i> <i>M.H. Redi, A.L. Roquemore, P.H. Rutherford, N.R. Sauthoff,</i> <i>G. Schilling, J. Schivell, G.L. Schmidt, S.D. Scott, S. Sesnic,</i> <i>J.C. Sinnis, F.J. Stauffer, B.C. Stratton, G.D. Tait, G. Taylor,</i> <i>J.R. Timberlake, H.H. Towner, M. Ulrickson, S. Von Goeler,</i> <i>F. Wagner, R. Wieland, J.B. Wilgen, M. Williams, K.L. Wong,</i> <i>S. Yoshikawa, K.M. Young, M.C. Zarnstorff, S.J. Zweben</i>	
Sawteeth and disruptions in JET (IAEA-CN-47/A-VII-5) .....	433
<i>D.J. Campbell, P.A. Duperrex, A.W. Edwards, R.D. Gill,</i> <i>C.W. Gowers, R. Granetz, M. Hugon, P.J. Lomas, N. Lopes-Cardozo,</i> <i>M. Malacarne, M.F. Nave, D.C. Robinson, F.C. Schüller,</i> <i>P. Smeulders, J.A. Snipes, P.E. Stott, G. Tonetti, B.J. Tubbing,</i> <i>A. Weller, J.A. Wesson</i>	

## PLASMA HEATING AND CURRENT DRIVE

(Session F)

Radiofrequency heating on JET (IAEA-CN-47/F-I-1) ..... 449

*JET Team: H. Altmann, R.J. Anderson, J. Arbez, W. Bailey, D.V. Bartlett, B. Beaumont, G. Beaumont, K. Behringer, P. Bertoldi, E. Bertolini, C.H. Best, V. Bhatnagar, R.J. Bickerton, A. Boileau, F. Bombarda, T. Bonicelli, S. Booth, A. Boschi, G. Bosia, M. Botman, H. Brelen, H. Brinkschulte, M.L. Browne, M. Brusati, T. Budd, M. Bures, P. Butcher, H. Buttgerit, D. Cacaot, C. Caldwell-Nichols, J.D. Callen, D.J. Campbell, J. Carwardine, G. Celentano, C.D. Challis, A. Cheetham, J.P. Christiansen, C. Christodoulopoulos, P. Chuilon, R. Claesen, J.P. Coad, S.A. Cohen, M. Cooke, J.G. Cordey, W. Core, S. Corti, A.E. Costley, G.A. Cottrell, M. Cox, C. David, J. Dean, L. de Kock, E. Deksnis, G.B. Denne, G. Deschamps, K.J. Dietz, J. Dobbing, S.E. Dorling, D.F. Düchs, G. Duesing, P.A. Duperrex, H. Duquenoy, A.W. Edwards, J. Ehrenberg, W. Engelhardt, S.K. Erements, F. Erhorn, B.T. Eriksson, M. Evrard, H. Falter, N. Foden, M.J. Forrest, C. Froger, K. Fullard, G. Fussmann, M. Gadeberg, A. Galetsas, A. Gallacher, D. Gambier, R. Giannella, A. Giannelli, A. Gibson, R.D. Gill, A. Goede, A. Gondhalekar, C. Gordon, C. Gormezano, N.A. Gottardi, C.W. Gowers, R. Granetz, B. Green, S. Gregoli, F.S. Griph, R. Haange, J.H. Hamnén, C.J. Hancock, P.J. Harbour, N.C. Hawkes, P. Haynes, T. Hellsten, J.L. Hemmerich, R. Hemsworth, F. Hendriks, R.F. Herzog, L. Horton, J. How, M. Huart, A. Hubbard, J. Hugill, M. Hugon, M. Huguet, B. Ingram, H. Jäckel, J. Jacquinet, Z. Jankowicz, O.N. Jarvis, E.M. Jones, P. Jones, T.T.C. Jones, C. Jupén, E. Källne, J. Källne, O. Kaneko, A. Kaye, B.E. Keen, M. Keilhacker, G. Kinahan, S. Kissel, A. Konstantellos, M. Kovanen, U. Kühnnapfel, P. Kupschus, P. Lallia, J.R. Last, L. Lauro-Taroni, K.D. Lawson, E. Lazzaro, R.C. Lobel, P.J. Lomas, N. Lopes-Cardozo, M. Lorenz-Gottardi, C. Lowry, G. Magyar, D. Maisonnier, M. Malacarne, V. Marchese, P. Massmann, G.M. McCracken, P. McCullen, M.J. Mead, P. Meriguet, V. Merlo, V. Mertens, S. Mills, P. Millward, A. Moissonnier, P.L. Mondino, D. Moreau, P.D. Morgan, E.R. Müller, D. Murmann, G. Murphy, M.F. Nave, L. Nickesson, P. Nielsen, P. Noll, S. Nowak, W. Obert, M. Olsson, J. O'Rourke, M.G. Pacco, J. Paillere, S. Papastergiou, J. Partridge, D. Pasini, N.J. Peacock, M. Pescatore, J. Plancoulaine, J.-P. Poffé, R. Prentice, T. Raimondi, J. Ramette, C. Raymond, P.H. Rebut, J. Removille, W. Riediker, R. Roberts, D.C. Robinson, A. Rolfe, R.T. Ross, G. Rupprecht, R. Rushton, H.C. Sack,*

<i>G. Sadler, J. Saffert, N. Salmon, F. Sand, A. Santagiustina,</i>	
<i>R. Saunders, M. Schmid, F.C. Schüller, K. Selin, R. Shaw, A. Sibley,</i>	
<i>D. Sigournay, R. Sillen, F. Simonet, R. Simonini, P. Smeulders,</i>	
<i>J.A. Snipes, K. Sonnenberg, L. Sonnerup, M.F. Stamp, C.A. Steed,</i>	
<i>D. Stork, P.E. Stott, T.E. Stringer, D.R. Summers, H.P. Summers,</i>	
<i>A.J. Tagle, G. Tallents, A. Tanga, A. Taroni, A. Terrington, A. Tesini,</i>	
<i>P.R. Thomas, E. Thompson, K. Thomsen, F. Tibone, R. Tivey,</i>	
<i>T.N. Todd, P. Trevalion, M. Tschudin, B.J. Tubbing, P. Twynam,</i>	
<i>E. Usselman, H. Van der Beken, J.E. Van Montfoort,</i>	
<i>M. von Hellermann, J. von Seggern, T. Wade, C. Walker,</i>	
<i>B.A. Wallander, M. Walravens, K. Walter, M.L. Watkins,</i>	
<i>M. Watson, D. Webberley, A. Weller, J.A. Wesson, J. Wilks,</i>	
<i>T. Winkel, C. Woodward, M. Wykes, D. Young, L. Zannelli, J.W. Zwart</i>	
Discussion .....	459
Ion cyclotron heating and lower hybrid experiments on ASDEX (IAEA-CN-47/F-I-2) .....	461
<i>K. Steinmetz, F.X. Söldner, D. Eckhardt, G. Janeschitz,</i>	
<i>F. Leuterer, F. Mast, K. McCormick, J.-M. Noterdaeme, C. Setzensack,</i>	
<i>F. Wagner, F. Wesner, I. Bäumlner, G. Becker, H.S. Bosch,</i>	
<i>M. Brambilla, F. Braun, H. Brocken, H. Derfler, A. Eberhagen,</i>	
<i>H.-U. Fahrbach, G. Fussmann, R. Fritsch, O. Gehre, J. Gernhardt,</i>	
<i>G. von Gierke, E. Glock, O. Gruber, G. Haas, J. Hofmann,</i>	
<i>F. Hofmeister, K. Hübner, A. Izvozchikov, F. Karger, M. Keilhacker,</i>	
<i>O. Klüber, M. Kornherr, K. Lackner, M. Lenoci, G. Lisitano,</i>	
<i>E. Van Mark, H.M. Mayer, D. Meisel, V. Mertens, E.R. Müller,</i>	
<i>E. Münich, H. Murmann, H. Niedermeyer, Z.A. Pietrzyk, W. Poschenrieder,</i>	
<i>S. Puri, H. Rapp, H. Riedler, H. Röhr, J. Roth, F. Ryter, K.H. Schmitter,</i>	
<i>F. Schneider, G. Siller, P. Smeulders, E. Speth, K.-H. Steuer, T. Vien,</i>	
<i>O. Vollmer, H. Wedler, D. Zasche, M. Zouhar</i>	
Discussion .....	474
Ion Bernstein wave heating experiments on PLT (IAEA-CN-47/F-I-3) .....	477
<i>M. Ono, P. Beiersdorfer, R. Bell, S. Bernabei, A. Cavallo, A. Chmyga,</i>	
<i>S.A. Cohen, P. Colestock, G. Gammel, G. Greene, J. Hosea, R. Kaita,</i>	
<i>I. Lehrman, G. Mazzitelli, E. Mazzucato, D.H. McNeill, M. Mori,</i>	
<i>K. Sato, J. Stevens, S. Suckewer, J.R. Timberlake, V. Vershkov,</i>	
<i>J.R. Wilson, A. Wouters</i>	
Discussion .....	484
Confinement studies on TEXTOR with high power, long pulse ICRH (IAEA-CN-47/F-I-4) .....	485
<i>P.E. Vandenplas, T. Delvigne, P. Descamps, F. Durodie, M. Jadoul,</i>	
<i>R. Koch, D. Lebeau, A.M. Messiaen, D.I.C. Pearson,</i>	
<i>R. Van Nieuwenhove, G. Van Oost, G. Van Wassenhove, R.R. Weynants,</i>	
<i>H.L. Bay, G. Bertschinger, W. Bieger, P. Bogen, W. Brussaau,</i>	

<p><i>G.A. Campbell, Y. Cao, R.W. Conn, H. Conrads, K.H. Dippel, H.G. Esser, K.H. Finken, G. Fuchs, B. Giesen, D.M. Goebel, E. Graffmann, H. Hartwig, E. Hintz, F. Hoenen, K. Höthker, W.L. Hsu, A. Kaleck, H. Keuer, L. Könen, M. Korten, W.K. Leung, L. Li, Y.T. Lie, A. Pospieszczyk, D. Reiter, A. Rogister, G. Ross, D. Rusbüldt, U. Samm, J. Schlüter, B. Schweer, H. Soltwisch, G.J. Thomas, F. Waelbroeck, G. Waidmann, P. Wienhold, J. Winter, G.H. Wolf</i></p>	
Experiments on ICRF heating and fast wave current drive in JIPP T-IIU (IAEA-CN-47/F-I-5) .....	495
<p><i>T. Watari, K. Ohkubo, R. Akiyama, R. Ando, D. Eckhardt, Y. Hamada, S. Hirokura, K. Ida, E. Kako, O. Kaneko, K. Kawahata, Y. Kawasumi, S. Kitagawa, T. Kuroda, K. Masai, K. Matsuoka, A. Mohri, S. Morita, M. Mugishima, N. Noda, I. Ogawa, Y. Ogawa, Y. Oka, M. Sakamoto, K. Sakurai, M. Sasao, K. Sato, K.N. Sato, S. Tanahashi, Y. Taniguchi, T. Tetsuka, K. Toi, K. Yamazaki</i></p>	
Discussion .....	501
Electron heating and MHD modes during lower hybrid current drive on PLT (IAEA-CN-47/F-II-1) .....	503
<p><i>S. Bernabei, R. Bell, A. Cavallo, T.K. Chu, P. Colestock, J. Felt, W. Hooke, J. Hosea, F.C. Jobes, E. Mazzucato, E. Meservey, R. Motley, J.A. Murphy, M. Ono, R. Pinsker, J. Stevens, S. Von Goeler, J.R. Wilson</i></p>	
Radiofrequency heating and current drive experiments on Alcator C and Versator II (IAEA-CN-47/F-II-2) .....	509
<p><i>M. Porkolab, P. Bonoli, Kuoin Chen, C. Fiore, R. Granetz, D. Griffin, D. Gwinn, S. Knowlton, B. Lipschultz, S.C. Luckhardt, E. Marmor, M. Mayberry, F.S. McDermott, J. Moody, R. Parker, J. Rice, Y. Takase, J. Terry, S. Texter, S. Wolfe</i></p>	
Discussion .....	523
Current drive by lower hybrid waves at 3.7 GHz in Petula B (IAEA-CN-47/F-II-3) .....	525
<p><i>F. Parlange, D. Van Houtte, H. Bottollier-Curtet, G. Briffod, P. Chabert, M. Clément, C. David, A. Girard, C. Gormezano, W. Hess, M. Hesse, G.T. Hoang, G. Ichtchenko, J.M. Rax, F. Ryter, J.C. Vallet</i></p>	
Discussion .....	531
Experiments on current drive and plasma heating by LH and EC waves in the T-7 tokamak (IAEA-CN-47/F-II-4) .....	533
<p><i>V.V. Alikeev, A.A. Borshchegovskij, V.V. Chist'akov, Yu.A. Gorelov, V.I. Il'in, D.P. Ivanov, N.V. Ivanov, A.M. Kakurin, P.P. Khvostenko, A.Ya. Kislov, V.A. Kochin, P.E. Kovrov, K.I. Likin, Yu.S. Maksimov, I.B. Semenov, A.F. Shigaev, Yu.A. Sokolov, N.L. Vasin, V.V. Volkov, J. Āatlov, V. Kopecký, L. Kryška</i></p>	

Electron cyclotron heating of lower hybrid current driven plasma in the JFT-2M tokamak (IAEA-CN-47/F-II-5) .....	545
<i>T. Yamamoto, A. Funahashi, K. Hoshino, S. Kasai, T. Kawakami, H. Kawashima, T. Matoba, T. Matsuda, H. Matsumoto, Y. Miura, M. Mori, K. Odajima, H. Ogawa, T. Ogawa, H. Ohtsuka, S. Sengoku, T. Shoji, N. Suzuki, H. Tamai, Y. Uesugi, T. Yamauchi, M. Hasegawa, S. Takada, K. Hasegawa, A. Honda, I. Ishibori, T. Kashimura, Y. Kashiwa, M. Kazawa, K. Kikuchi, Y. Matsuzaki, K. Ohuchi, H. Okano, T. Shibata, T. Shibuya, T. Shiina, K. Suzuki, T. Tani, K. Yokoyama</i>	
Discussion .....	551
Electron cyclotron and lower hybrid current drive experiments in the WT-2 and WT-3 tokamaks (IAEA-CN-47/F-II-6) .....	553
<i>S. Tanaka, Y. Terumichi, T. Maekawa, M. Nakamura, T. Cho, A. Ando, K. Ogura, H. Tanaka, M. Iida, S. Ide, K. Oho, S. Ozaki, R. Itatani, H. Abe, Y. Yasaka, M. Fukao, K. Ishii, A. Mohri, S. Kubo</i>	
Discussion .....	562
Improvement of current drive and confinement by combination of LHCD and NBI heating in JT-60 (IAEA-CN-47/F-II-7) .....	563
<i>JT-60 Team: T. Abe, H. Aikawa, H. Akaoka, H. Akasaka, M. Akiba, N. Akino, T. Akiyama, T. Ando, K. Annoh, N. Aoyagi, K. Arakawa, M. Araki, K. Arimoto, M. Azumi, S. Chiba, M. Dairaku, N. Ebisawa, T. Fujii, T. Fukuda, H. Furukawa, K. Hamamatsu, K. Hayashi, M. Hara, K. Haraguchi, H. Hiratsuka, T. Hirayama, S. Hiroki, K. Hiruta, M. Honda, H. Horiike, R. Hosoda, N. Hosogane, Y. Iida, T. Iijima, K. Ikeda, Y. Ikeda, T. Imai, T. Inoue, N. Isaji, M. Isaka, S. Ishida, N. Itige, T. Ito, Y. Ito, A. Kaminaga, M. Kawai, Y. Kawamata, K. Kawasaki, K. Kikuchi, M. Kikuchi, H. Kimura, T. Kimura, H. Kishimoto, K. Kitahara, S. Kitamura, A. Kitsunezaki, K. Kiyono, N. Kobayashi, K. Kodama, Y. Koide, T. Koike, M. Komata, I. Kondo, S. Konoshima, H. Kubo, S. Kunieda, S. Kurakata, K. Kurihara, M. Kuriyama, T. Kuroda, M. Kusaka, Y. Kusama, S. Maehara, K. Maeno, S. Mase, S. Matsuda, M. Matsukawa, T. Matsukawa, M. Matsuoka, N. Miya, K. Miyati, Y. Miyo, K. Mizuhashi, M. Mizuno, R. Murai, Y. Murakami, M. Muto, M. Nagami, A. Nagashima, K. Nagashima, T. Nagashima, S. Nagaya, H. Nakamura, Y. Nakamura, M. Nemoto, Y. Neyatani, S. Niikura, H. Ninomiya, T. Nishitani, H. Nomata, K. Obara, N. Ogiwara, Y. Ohara, K. Ohasa, T. Ohga, H. Ohhara, M. Ohkubo, T. Ohshima, K. Ohta, M. Ohta, M. Ohtaka, Y. Ohuchi, A. Oikawa, H. Okumura, Y. Okumura, K. Omori, S. Omori, Y. Omori, T. Ozeki, M. Saigusa, K. Sakamoto, A. Sakasai, S. Sakata, M. Satou, M. Sawahata, M. Seimiya, M. Seki, S. Seki, K. Shibanuma, R. Shimada, K. Shimizu,</i>	

<i>M. Shimizu, Y. Shimomura, S. Shinozaki, H. Shirai, H. Shirakata, M. Shitomi, K. Sukanuma, T. Sugie, T. Sugiyama, H. Sunaoshi, K. Suzuki, M. Suzuki, M. Suzuki, N. Suzuki, S. Suzuki, Y. Suzuki, H. Takahashi, M. Takahashi, S. Takahashi, T. Takahashi, M. Takasaki, M. Takatsu, A. Takeshita, H. Takeuchi, S. Tamura, S. Tanaka, K. Tani, M. Terakado, T. Terakado, K. Tobita, T. Tokutake, T. Totsuka, N. Toyoshima, H. Tsuda, T. Tsugita, S. Tsuji, Y. Tsukahara, M. Tsuneoka, K. Uehara, M. Umehara, Y. Uramoto, H. Usami, K. Ushigusa, K. Usui, J. Yagyu, K. Yamada, M. Yamamoto, O. Yamashita, Y. Yamashita, K. Yano, T. Yasukawa, K. Yokokura, H. Yokomizo, H. Yoshida, M. Yoshikawa, Y. Yoshinari, R. Yoshino, I. Yonekawa, K. Watanabe</i>	
Discussion .....	573
Current drive, confinement and instability control experiments with ECRH on the CLEO tokamak (IAEA-CN-47/F-III-2) .....	575
<i>D.C. Robinson, N.R. Ainsworth, P.R. Collins, A.N. Dellis, T. Edlington, P. Haynes, S. Iyengar, I. Johnson, B. Lloyd, M. O'Brien, B.J. Parham, A.C. Rivière, D.F.H. Start, T.N. Todd</i>	
Discussion .....	585
Confinement in electron cyclotron heating experiments on Doublet III (IAEA-CN-47/F-III-3) .....	587
<i>R. Prater, S. Ejima, R.W. Harvey, A.J. Lieber, K. Matsuda, C.P. Moeller, and the Doublet III Physics Group</i>	
Discussion .....	597
Electron cyclotron heating on TFR (IAEA-CN-47/F-III-4) .....	599
<i>H.P.L. de Esch, J.A. Hoekzema, W.J. Schrader, E. Westerhof, W. Kooijman, R.W. Polman, T.J. Schep, and Equipe TFR</i>	
Discussion .....	606
Investigation of plasma formation regimes for ICRF heating experiments in the TUMAN-3 tokamak with magnetic compression (IAEA-CN-47/F-III-5) .....	607
<i>L.G. Askinasi, N.E. Bogdanova, V.E. Golant, S.G. Goncharov, M.P. Gryaznevich, V.V. D'yachenko, A. Izvozchikov, E.R. Its, S.V. Krikunov, S.V. Lebedev, B.M. Lipin, I.P. Pavlov, G.T. Razdobarin, V.V. Rozhdestvenskij, N.V. Sakharov, M.A. Khalilov, F.V. Chernyshev, K.G. Shakhovets, O.N. Shcherbinin, S.E. Bender, Yu.A. Kostsov, R.N. Litunovskij, O.A. Minyaev, E.N. Rumyantsev, P.P. Teplov</i>	
Discussion .....	615
Alfvén wave heating and current profile modification in TCA (IAEA-CN-47/F-III-6) .....	617
<i>G. Besson, G.A. Collins, B.P. Duval, C. Hollenstein, A.A. Howling, B. Joye, J.B. Lister, J.-M. Moret, F. Ryter, C.W. Simm, H. Weisen</i>	
Discussion .....	625

Analysis of ICRF heating and current drive in tokamaks (IAEA-CN-47/F-IV-1) .....	627
<i>A. Fukuyama, T. Morishita, Y. Kishimoto, K. Hamamatsu, S.-I. Itoh, K. Itoh</i>	
Double helix ( $\vec{j} \times \vec{b}$ ) current drive in the RF tokamak device RYTHMAC (IAEA-CN-47/F-IV-2) .....	635
<i>M.J. Dutch, A.L. McCarthy</i>	
Dependence of power absorbed in a plasma on Alfvén heating antenna parameters (IAEA-CN-47/F-IV-3) .....	645
<i>A.G. Kirov, V.P. Sidorov, A.G. Elfimov, S.N. Lozovskij, L.F. Ruchko, K.G. Komoshvili, V.V. Onishchenko, V.V. Dorokhov, A.V. Sukachev, V.D. Samushia, L.Ya. Malykh, N.L. Gulasaryan, D.A. Vojtenko</i>	
Recent advances in the theory and modelling of RF heating in inhomogeneous plasmas (IAEA-CN-47/F-IV-4) .....	653
<i>D.G. Swanson, S. Cho, C.K. Phillips, D.Q. Hwang, W. Houlberg, L. Hively</i>	
Electron cyclotron current drive and supra-thermal generation in large tokamaks (IAEA-CN-47/F-IV-5) .....	659
<i>T.J. Schep, R.W. Polman, E. Westerhof, L. Klieb</i>	
Chairmen of Sessions and Secretariat of the Conference .....	669

**Session A**  
**ARTSIMOVICH MEMORIAL LECTURE**  
**AND**  
**TOKAMAK EXPERIMENTS**

**Chairmen of Sessions**

<b>Session A-I</b>	<b>S. MORI</b>	<b>Japan</b>
<b>Session A-II</b>	<b>D.M. MEADE</b>	<b>USA</b>
<b>Session A-III</b>	<b>J.B. LISTER</b>	<b>Switzerland</b>
<b>Session A-IV</b>	<b>M. KEILHACKER</b>	<b>JET</b>
<b>Session A-V</b>	<b>R.A. GROSS</b>	<b>USA</b>
<b>Session A-VI</b>	<b>L.E. ZAKHAROV</b>	<b>USSR</b>

*Papers A-VI-1-1, A-VI-1-2 and A-VI-1-3  
were presented by D.F. Düchs as Rapporteur*

**Session A-VII (Posters)**



## ARTSIMOVICH MEMORIAL LECTURE

J.F. CLARKE  
Associate Director for Fusion Energy,  
Office of Energy Research,  
United States Department of Energy,  
Washington, D.C.,  
United States of America

Mr. Chairman, Ladies and Gentlemen,

I want to thank the International Atomic Energy Agency (IAEA) for asking me to give this address. I consider it an honour to be here, to be speaking to you — scientists of many races and nationalities united by a common effort to provide fusion power to the world. I am especially pleased to join you in honouring the memory of Lev Artsimovich, a man who contributed so much to the achievement of our goal.

This occasion is particularly meaningful to me, because it marks the 25th anniversary of my own involvement in fusion research. In 1961, as a young doctoral candidate in physics at MIT, I was fortunate enough to be offered the opportunity to choose my field of study under masters of almost all of the disciplines of physics. For a young man, the choice was bewildering. After much thought, I finally settled on a field for a most unscientific reason. That field was the relatively undeveloped — and at the time unprestigious — field of plasma physics. The reason for my choice was a simple one. I learned that plasma physics might hold the key to unlimited energy for the people of the world. That possibility engaged the enthusiasm of a young man. I have never regretted that decision. Over the years, the science of plasma physics has grown into a major scientific field and has provided all of the professional satisfaction and excitement a scientist could desire. Moreover, my primary motivation for choosing plasma physics — the benefit that might one day flow from the science — has been strengthened as the reality of the promised contribution to the future well-being of humanity has become more certain.

I believe that this motivation is a distinguishing characteristic that unites fusion scientists. It is widely recognized that all scientists are united by their common professional endeavours. This is certainly true in fusion research. However, in working with fusion scientists and engineers from many countries, I have found a stronger bond than merely sharing scientific skills — a bond that comes from applying those skills in the service of humanity.

This lecture honours the memory of one of our fraternity. A man who exemplified dedication to this higher purpose. Lev Artsimovich will always be remembered as a giant in the development of fusion power. His scientific contributions were certainly important, and yet, his stature rests on more than this. He was a giant

because of his wisdom, courage, skill, and, most of all, his dedication to our common purpose.

Fortunately, he was not alone in these qualities. Throughout the history of fusion development there have been a number of scientist/statesmen who shared the dream of harnessing fusion power, but who also saw the task was beyond the capability of their own laboratory. More importantly, these men had the wisdom to see that — in practical if not in absolute sense — the task was possibly beyond the capability of their own nation.

Over the years, men like Igor Kurchatov, Lev Artsimovich, Evgenij Velikhov, Edward Teller, David Rose, Hans Otto Wüster, Donato Palumbo, Koji Husimi, Tatsuoki Miyajima, and others have advocated international co-operation in the development of fusion power. Moreover, they had the courage to act to make co-operation possible. In honouring these men for their wisdom, we must not ignore their courage. Advocating co-operation takes wisdom. Acting upon it takes courage.

I really began to appreciate the degree of courage required of them as I prepared for this address. Since Artsimovich is identified with international co-operation in fusion, I began to reflect on the very first international meeting on fusion. It took place at Harwell in Great Britain, in 1956 — thirty years ago. The date is important. It was a time of great political tension and rivalry in the world. I have only to mention the places: Indochina, Korea, Formosa, Berlin, Hungary, and Suez, to recall the occasions of confrontation. To heighten the tension — if that were possible — the major world powers had developed and were racing to deploy the new military technologies of the hydrogen bomb and the ICBMs, and the world was on the verge of the space race with the Soviet preparations to launch Sputnik. In a small way, fusion research mirrored these tensions and rivalries. National programmes worked in rivalry and secrecy to achieve the first fusion reaction and thereby obtain for their country a significant technological advantage — unlimited, economical energy or, perhaps, even some military advantage. On an even more human scale, key figures within national programmes struggled to expand their own laboratory's share in a programme that they believed would surely make them Nobel Laureates.

Fortunately, then as now, the leaders of the major nations were seeking ways to improve relations and reduce tensions, and scientists/statesmen were at the forefront of the initiatives. In 1953, President Eisenhower made his Atoms for Peace proposal at the United Nations. By 1954, the United States and the Soviet Union had agreed to consider exchanging atomic energy information, and by 1955, the first Geneva Conference on the Peaceful Uses of Atomic Energy was held. At this Conference, Homi Bhabha of India first alerted the world at large to the potential of fusion research. In 1956, Igor Kurchatov took the next step by openly discussing Soviet fusion work while visiting Great Britain. The result was that by 1958, the time of the Second Geneva Conference on the Peaceful Uses of Atomic Energy, the situation of secrecy and rivalry in fusion had changed. The papers of Artsimovich, Teller, Biermann, Thonemann, and Alfvén summarized previously hidden research in fusion. As a result of these events, the European Countries, the United States, and the Soviet Union agreed to open magnetic fusion research.

Historians of the period record many political factors leading to the change. However, I believe it was mainly a result of the wisdom, courage, and dedication of both national political leaders and the scientific leaders in the national fusion programmes. The scientific leaders realized that fusion would be achieved most directly by uniting the scientific talents of the world. The political leaders recognized that co-operation on fusion — an effort in the interest of all mankind — could help to reduce world tension and rivalry. They had the courage to take the risk and try to establish international co-operation in fusion in spite of political tension and voices of caution in their own countries. They had the wisdom to create useful co-operative mechanisms, such as the IAEA, and the dedication to live up to these commitments for almost three decades.

It is well to reflect on our beginnings and to realize that our scientific success today rests on a remarkable foundation. It is simply that in fusion research, national political leaders and fusion scientific leaders have been able to transcend their own parochial interests in an effort to achieve a plentiful supply of energy for future generations.

Today, we have a situation similar in many ways to that which existed in 1958. Political tensions are high and the power and number of modern weapons has raised the premium on reducing those tensions. On a political level, world leaders are struggling with major issues, such as nuclear disarmament. As in the 1950s, they are also looking toward co-operation on fusion as a means to reduce tensions and increase understanding. Recently, Andronik Petrosyants, Chairman of the Soviet State Committee on the Utilization of Atomic Energy, acknowledge this when he said that, in the view of the Soviet Union, scientific co-operation has great political significance in that it helps to strengthen peace and lessens the danger of new global war.

On the scientific level, fusion leaders are beginning to realize that in order to exploit our successes and complete the development of fusion power, a new degree of collaboration may be necessary that will allow us to build facilities that go beyond the resources available in any one national programme.

These factors led to the discussion of fusion at the Geneva Summit and at the recent Reykjavik meeting. The Reagan-Gorbachev initiative to expand fusion co-operation and the positive reactions of other world leaders to the initiative have provided the political mandate and opportunity to accelerate progress in our field. It urges us to combine our resources in new ways for mutual benefit. The issue for us to decide is "How should we, the international fusion community, respond to this opportunity?"

I would like to discuss this question in the remainder of this lecture. First, it is clear that there is a technical imperative for closer co-operation. This was clearly recognized by Artsimovich from the very beginning. At Geneva, in 1958, he said: "This problem (of fusion) seems to have been created especially for the purpose of developing close co-operation between scientists and engineers of various countries, working at this problem according to a common plan, and continuously exchanging the results of their calculations, experiments, and engineering developments." In the

years since these words were uttered, the nations of the world have developed a remarkable degree of co-operation in fusion. The most outstanding example is, of course, the common fusion programme developed by the European Communities. Within the European Atomic Energy Community, the words of Artsimovich have been borne out to the letter, and the obvious benefits are clearly evident in the achievements of the JET facility.

On the wider international scene, numerous co-operative projects and exchanges have also advanced the field. We have created effective mechanisms for co-operation through the International Atomic Energy Agency, the International Energy Agency (IEA), the USA/Japan and the USA/USSR bilateral agreements in fusion, and, most recently, the Fusion Working Group of the Economic Summit countries. Although fusion co-operation outside of the European Summit countries. Although fusion co-operation outside of the European Communities has not reached the stage of working to a common plan described by Artsimovich, there has been significant movement in that direction over the last few years.

The science of fusion is by no means finished. The remaining scientific steps will require new, expensive facilities and equally expensive operation of these facilities. The relatively new technology research will require perhaps more expensive facilities. If it existed, the common plan envisioned by Artsimovich would allow this work to be shared, duplication to be avoided, and the available technical expertise in the world to be used to best advantage. The practical benefit of this was recognized by Donato Palumbo in his 1980 Artsimovich Lecture. He questioned whether each of the four big programmes could proceed individually to address next generation fusion issues, and at the same time continue other necessary activities along a wider front. A common plan would allow a broader attack on these difficult problems within available resources. With this in mind, the Heads of State of the Economic Summit nations set up the Fusion Working Group (FWG) to examine the fusion development plans of participating countries, in an effort to identify opportunities for working to a common plan.

The Fusion Working Group has agreed that the remaining problems of fusion can be summarized by four critical issues. These issues are: improving magnetic confinement concepts to make them more amenable to practical application, investigating the scientific problems associated with a burning plasma, developing materials suitable for fusion reactors, and solving the problems of fusion nuclear technology. The work of the FWG in joint planning to resolve the four critical issues is not finished, but already its practical effects are evident.

The FWG has examined national plans for addressing the burning plasma issue. They concluded that a machine like the European NET, or the Japanese FER, is needed in the late 1990s to complete the scientific base and to address the technical feasibility of fusion. They concluded that it was valuable and feasible to attempt a short pulse ignition experiment in the early 1990s to gain realistic operating experience with a burning fusion plasma. The United States of America has taken on this latter task and has produced a conceptual design for a Compact Ignition Device

(CIT) which, depending on details of funding, will operate as early as 1993. The Europeans and Japanese have continued to develop designs for a facility with the broader technical aim that might be ready for construction decisions at about the time CIT is completed.

The FWG has also examined the national plans in fusion nuclear technology and materials. In the latter area, their deliberations were aided greatly by a detailed study of the IEA members' fusion materials programmes by an IEA Blue Ribbon Panel, chaired by Professor Amelinckx of Belgium. In both areas, it was found that a co-ordinated international programme was possible and desirable.

Finally, in a recent meeting of the Co-ordinating Committee of the USA/USSR Co-operative Agreement on the Peaceful Uses of Atomic Energy, it was agreed to begin the process of joint planning in order to improve the co-ordination of the US and the USSR fusion programmes.

So, in small steps, using all the mechanisms of co-operation established over the years since Artsimovich made his statement in 1958, we appear to be moving toward his common plan. However, the movement is not without difficulty. I have already remarked on the courage of Artsimovich in making this proposal, considering the time at which it was made. The courage demanded of us is becoming more evident as we face the difficulty of actually implementing his proposal on a world scale.

The difficulty is not technical. The above examples show that technical agreement can be reached if we wish to do so. The real difficulty was well described by Hans-Otto Wüster in testimony to the US Congress in 1985 on the process of achieving a unified European fusion programme. He noted that international collaboration on the scale achieved in Europe is the result of the general insight that, because of resource limitations, research in separate nations could not be as successful as a joint effort. As Wüster so pungently remarked, "After all, if you have a common aim and want to do something, you will find a way to give in to reason." If the world fusion programme has lagged behind the European Communities in achieving a common plan, it is probably due to lack of agreement on the necessity to work more closely together to achieve a common aim within our total financial and human resources. Reaching agreement on the necessity of working together is difficult, because it involves many non-technical factors. It involves the personal ambitions of scientists, as well as institutional ambitions of laboratories. The dedication to a common aim must be very strong to motivate an appropriate balance between such ambitions and more efficient pursuit of our common goal.

In considering how the fusion community should respond to the opportunity presented by the Geneva Summit, we need to look more closely at this question. What aim do we have in common and is it necessary that it be achieved jointly? The heightened necessity for co-operation was perceived as long ago as 1977. David Rose — a man who can justly be called the father of fusion technology — became concerned about the possibility of reaching the goal of fusion power. His worry was not primarily technical, although he recognized — perhaps more clearly than anyone

at the time — the real technical problems that would have to be overcome to demonstrate the scientific and technical feasibility of fusion. No, he foresaw that the solution of these problems would require large, expensive facilities. He knew that these would also take a long time to plan, and operate. Finally, he knew that the practical benefit of fusion would be in doubt until the end of this expensive and long term programme. His worry was that national governments would be reluctant to spend such large sums for these facilities — let alone even more for larger, but essential support programmes — without clearer indication that fusion will work and be more attractive than fission breeders or bulk solar power. His conclusion was that a world fusion programme conducted according to a common plan was needed if these facilities were to be built.

His arguments defining the necessity of intensified co-operation led Director General Sigvard Eklund, of the IAEA, to request the views of member governments on the possibility of greater collaboration, and, in particular, their consideration of how to take the major step after JET, JT-60, T-15, and TFTR — the step that would complete the scientific base and demonstrate the technical feasibility of fusion. In response, very much in the tradition of Artsimovich, Academician Velikhov proposed that a joint group with participants from the European Communities, Japan, the United States, and the USSR should be formed to investigate a project to build a tokamak reactor experiment.

This proposal led, in 1978, to the organization of the INTOR Workshop. Over the last eight years, this Workshop, under the leadership of Sigeru Mori, Günter, Grieger, Weston Stacey and Boris Kadomtsev, has clarified the nature and magnitude of a facility that could complete the scientific base and address the technical feasibility of fusion. Through their pioneering efforts and the steadfast support of the IAEA, we have developed a worldwide appreciation of the key role in fusion development and the technical requirements of such a facility. The INTOR work has been the essential ingredient in creating a world consensus on a major step in fusion.

During the past year, discussions based largely on the INTOR work have taken place among the Economic Summit nations within the framework of the Fusion Working Group, between the USA and the USSR in bilateral meetings, and among key figures from all the world's major fusion programmes in the Director General's International Fusion Research Council. All parties have reached a consensus that a device of the INTOR type, generally known as an Experimental or Engineering Test Reactor (ETR), is the common midterm goal of the world's fusion programmes. As a result, we finally seem to have arrived at agreement on the common aim that Wüster referred to.

However, it remains to be seen whether we will find a way to give in to reason. During the development of the ETR concept through the INTOR Workshop, all the participating nations put a considerable, if not principal, effort on defining their own national versions of this next step — NET in Europe, FER in Japan, OTR in the Soviet Union, and FED, or more recently TIBER, in the United States. Having come so far and having surmounted so many problems in international collaboration, one

could take comfort in the thought that the passage of time will allow a coalescence of these technical approaches. And yet, I cannot ignore the sense that history is pressing upon us to make a decision on how we wish to take this next critical step in fusion development. We should all recall Professor Husimi's gentle reminder in his 1982 Artsimovich memorial lecture, "...the public has for a long time been eagerly waiting to see the production of fusion energy". I am also spurred in a not so gentle way by the knowledge that the world has spent between the equivalent of US \$15 billion and US \$20 billion dollars to date in the quest for that production of fusion energy. Once we have the technical capability, every year that we avoid a decision to move forward to the next step adds roughly another billion dollars to that total. For this reason, I believe we must take every opportunity to move forward as soon as the technical capability becomes available.

Based on recent technical progress, I suspect the technical capability to build an ETR can be attained within a few years. Therefore, it seems reasonable that we should use the opportunity presented by the Geneva initiative to move as far as possible in preparing for an ETR. If the existence of five different technical approaches prevents near term agreement on a common project, we should consider taking the steps necessary to coalesce those technical approaches. If we lack the complete technical base to support commitment to construction, let us consider co-ordinating the research of our programmes to provide the missing information. Preparing one design and co-operating to prepare a sound technical base would not guarantee that an ETR would be built in common. However, it should help guarantee both that it would be built and that whatever nation or group of nations undertook the project would have a maximum chance at success.

Political leaders seem to recognize the need for collaboration in such tasks. In the recent meeting in Reykjavik, President Reagan and General Secretary Gorbachev agreed on a renewed effort to reach agreement on specific actions in expanding fusion co-operation. I am very pleased that on October 30, the United States transmitted a formal proposal to the Economic Summit Nations and the Soviet Union. The proposal was to join together to prepare a conceptual design report (CDR) for an ETR. It recommended that we adopt the suggestion of Director General Hans Blix that we build on the INTOR process to carry out the work. It also advocated that the research and development necessary to support the CDR be undertaken co-operatively through existing agreements. The proposal indicated that the United States was prepared to commit sufficient resources to accomplish this task within three years. If accepted, this proposal could lead to a major focusing on world resources on preparing for an ETR — the most widely accepted element on a common fusion plan.

Lev Artsimovich offered us the vision of scientists in all nations working together on the fusion problem according to a common plan. Just as the vision of a world served by fusion power engaged the enthusiasm of a young man twenty-five years ago, the vision of a world united in a common fusion effort engages the enthusiasm of an older man today. However — perhaps because of age — it is an enthusiasm tempered by realism. Without in the least minimizing the difficulty of the

remaining problems of fusion science and technology, I would suggest that attempting to merge our futures in a common plan may be a more difficult task. I do not know if we can succeed. But then Artsimovich did not know that we would ever overcome the difficult scientific problems to reach reactor-grade plasma conditions in a tokamak. He persevered in spite of the scientific difficulty and uncertainty. I believe we, too, should persevere in spite of the human difficulty and uncertainty. Lev Artsimovich and Hans-Otto Wüster would surely have recognized the difficulties that must be overcome. Remembering what they attempted in their lives, I am tempted to think they might have advised us in words similar to those of Professor Husimi in his 1982 Artsimovich lecture: "Difficulty does not cause despair; difficulty invites courage, particularly when the goal is splendid."

## RECENT EXPERIMENTS IN JT-60

### JT-60 TEAM

*(Presented by M. Yoshikawa)*

T. Abe, H. Aikawa, H. Akaoka, H. Akasaka, M. Akiba, N. Akino, T. Akiyama, T. Ando, K. Annoh, N. Aoyagi, K. Arakawa, M. Araki, K. Arimoto, M. Azumi, S. Chiba, M. Dairaku, N. Ebisawa, T. Fujii, T. Fukuda, H. Furukawa, K. Hamamatsu, K. Hayashi, M. Hara, K. Haraguchi, H. Hiratsuka, T. Hirayama, S. Hiroki, K. Hiruta, M. Honda, H. Horiike, R. Hosoda, N. Hosogane, Y. Iida, T. Iijima, K. Ikeda, Y. Ikeda, T. Imai, T. Inoue, N. Isaji, M. Isaka, S. Ishida, N. Itige, T. Ito, Y. Ito, A. Kaminaga, M. Kawai, Y. Kawamata, K. Kawasaki, K. Kikuchi, M. Kikuchi, H. Kimura, T. Kimura, H. Kishimoto, K. Kitahara, S. Kitamura, A. Kitsunozaki, K. Kiyono, N. Kobayashi, K. Kodama, Y. Koide, T. Koike, M. Komata, I. Kondo, S. Konoshima, H. Kubo, S. Kunieda, S. Kurakata, K. Kurihara, M. Kuriyama, T. Kuroda, M. Kusaka, Y. Kusama, S. Maehara, K. Maeno, S. Mase, S. Matsuda, M. Matsukawa, T. Matsukawa, M. Matsuoka, N. Miya, K. Miyati, Y. Miyo, K. Mizuhashi, M. Mizuno, R. Murai, Y. Murakami, M. Muto, M. Nagami, A. Nagashima, K. Nagashima, T. Nagashima, S. Nagaya, H. Nakamura, Y. Nakamura, M. Nemoto, Y. Neyatani, S. Niikura, H. Ninomiya, T. Nishitani, H. Nomata, K. Obara, N. Ogiwara, Y. Ohara, K. Ohasa, T. Ohga, H. Ohhara, M. Ohkubo, T. Ohshima, K. Ohta, M. Ohta, M. Ohtaka, Y. Ohuchi, A. Oikawa, H. Okumura, Y. Okumura, K. Omori, S. Omori, Y. Omori, T. Ozeki, M. Saigusa, K. Sakamoto, A. Sakasai, S. Sakata, M. Satou, M. Sawahata, M. Seimiya, M. Seki, S. Seki, K. Shibamura, R. Shimada, K. Shimizu, M. Shimizu, Y. Shimomura, S. Shinozaki, H. Shirai, H. Shirakata, M. Shitomi, K. Sugauma, T. Sugie, T. Sugiyama, H. Sunaoshi, K. Suzuki, M. Suzuki, M. Suzuki, N. Suzuki, S. Suzuki, Y. Suzuki, H. Takahashi<sup>1</sup>, M. Takahashi, S. Takahashi, T. Takahashi, M. Takasaki, M. Takatsu, A. Takeshita, H. Takeuchi, S. Tamura, S. Tanaka, K. Tani, M. Terakado, T. Terakado, K. Tobita, T. Tokutake, T. Totsuka, N. Toyoshima, H. Tsuda, T. Tsugita, S. Tsuji, Y. Tsukahara, M. Tsuneoka, K. Uehara, M. Umehara, Y. Uramoto, H. Usami, K. Ushigusa, K. Usui, J. Yagyu, K. Yamada, M. Yamamoto, O. Yamashita, Y. Yamashita, K. Yano, T. Yasukawa, K. Yokokura, H. Yokomizo, H. Yoshida, M. Yoshikawa, Y. Yoshinari, R. Yoshino, I. Yonekawa, K. Watanabe

Naka Fusion Energy Research Establishment,  
Japan Atomic Energy Research Institute,  
Naka-machi, Naka-gun, Ibaraki-ken,  
Japan

### Abstract

#### RECENT EXPERIMENTS IN JT-60.

The paper describes the Joule heating experiment and more recent NBI and ICRF heating and LHRF current drive experiments made in JT-60 in the past three months. JT-60 is a large tokamak with a poloidal divertor using TiC as first wall material. It is currently operated at a level of  $I_p \leq 2.0$  MA,

<sup>1</sup> Princeton Plasma Physics Laboratory, Princeton University, NJ, USA.

$P_{NB} \leq 20$  MW,  $P_{IC} \leq 1.4$  MW,  $P_{LH} \leq 1.2$  MW. The plasma is characterized by a wide range of operational parameters:  $0.1 \times 10^{19} \text{ cm}^{-3} \leq \bar{n}_e \leq 9.7 \times 10^{19} \text{ m}^{-3}$  and  $q_{\text{eff}} \geq 2.2$  and by a very low impurity content,  $Z_{\text{eff}} \geq 1.5$ , and  $P_{\text{rad}} \geq 5\%$ . The energy confinement time is about 0.5 s for Joule heated plasmas at high densities and 0.12 s for NB heated plasmas at high heating power. In the LHRF experiment an LH driven current up to 1.5 MA is obtained, and a synergetic effect of LH current drive and NB heating to enhance current drive and heating efficiency is observed. In the ICRF experiment, the heating has an efficiency of  $0.18 \text{ J} \cdot \text{W}^{-1}$  and is found to reduce the hydrogen recycling.

## 1. INTRODUCTION

JT-60 is a long pulse tokamak device with a plasma of circular cross-section and a poloidal divertor placed radially outside. Three means of intense heating, NBI, LHRF, and ICRF are provided, the latter two of which can also be used for studying RF current drive. The main parameters of JT-60 are listed in Table I. The operation of JT-60 was started in April 1985; it was shut down in July 1985 for the installation of heating systems. After the Joule heating experiment, which took about five months, the heating and current drive experiments were started in August 1986.

The present paper reviews the present status of the JT-60 experiment on Joule heating [1–4], NBI and ICRF heating, and LHRF current drive. The status of JT-60 will be described in the next section, and experimental results will be presented and discussed in later sections.

## 2. STATUS OF JT-60

In this section, we present technical features of JT-60, in particular, those relevant to the description of experimental results. Detailed technical descriptions of JT-60 are provided in Refs [3–5]. Table I compares the designed and the achieved values of the main parameters and shows that JT-60 is now being operated near its maximum performance although more conditioning is required to raise the power handling capability of the RF launchers.

The cross-section of the vacuum vessel is shown in Fig. 1. The toroidal limiters, divertor plates, in-board armour plates, and the protective plates of the divertor coils are made of molybdenum coated with TiC of 20  $\mu\text{m}$  thickness. Protective plates elsewhere are made of Inconel 625, coated with TiC of the same thickness. Since no large horizontal ports are available on the vacuum vessel, profile measurements rely heavily on the four large ports at an angle of  $\pm 4^\circ$  with the midplane as well as on the array of vertical ports.

To block the backflow of discharge gas compressed in the divertor chamber, the gaps between the divertor coils and the vacuum vessel are sealed, except at the pumping ports where deflecting plates are placed to guide the backflow into the pumping ports. Additional Zr-Al getter pumps of an effective total pumping speed

TABLE I. DESIGNED AND ACHIEVED PARAMETERS OF JT-60

## (a) JT-60 Parameters

	Designed	Achieved	
		(Divertor)	(Limiter)
Major Radius	3.0 m	3.10 m	3.04 m
Minor Radius	0.95 m	0.90 m	0.90 m
Toroidal Field*	4.5 T**	4.5 T	4.5 T
Plasma Current	2.7 MA	2.0 MA	2.0 MA
Pulse Length	10 s	10 s	10 s

\* At a major radius of 3 m, \*\* 2.1 MA with divertor

## (b) JT-60 NBI Parameters

	Designed	Achieved	
		(Test)**	(With plasma)
Total power into torus	20 MW	20 MW	20 MW
Number of beamlines	14	14	14
Number of sources	28	28	28
Beam energy	75 keV	~100 keV	≥75 keV
Species power ratio*	-	80:13:7	75:16:9
Pulse length	10 s	10 sec	2 s

\*  $H^0(E): H^0(E/2): H^0(E/3)$  at 75 keV,

\*\* Each beamline tested separately in a test stand

## (c) JT-60 RF Parameters

	Designed	Achieved	
		(Test)*	(With plasma)
<u>Lower Hybrid</u>			
Frequency	1.7-2.23GHz	1.7-2.23GHz	2.0 GHz
Number of units	3	3	1
Power tubes per unit	8 klystrons	8	8
Power at sources	24 MW	24 MW	2.0 MW
Power into torus	15 MW	-	1.2
Power into plasma	7.5 MW	-	-
Pulse length	10 s	10 s	0.75 s
<u>Ion Cyclotron</u>			
Frequency	110-130MHz	110-130MHz	120 MHz
Number of units	1	1	1
Power tubes	8 Tetrodes	8	8
Power at source	6 MW	6 MW	1.6 MW
Power into torus	5 MW	-	1.4 MW
Power into plasma	2.5MW	-	-
Pulse length	10 s	10 s	1.2 s

\* Each unit tested separately

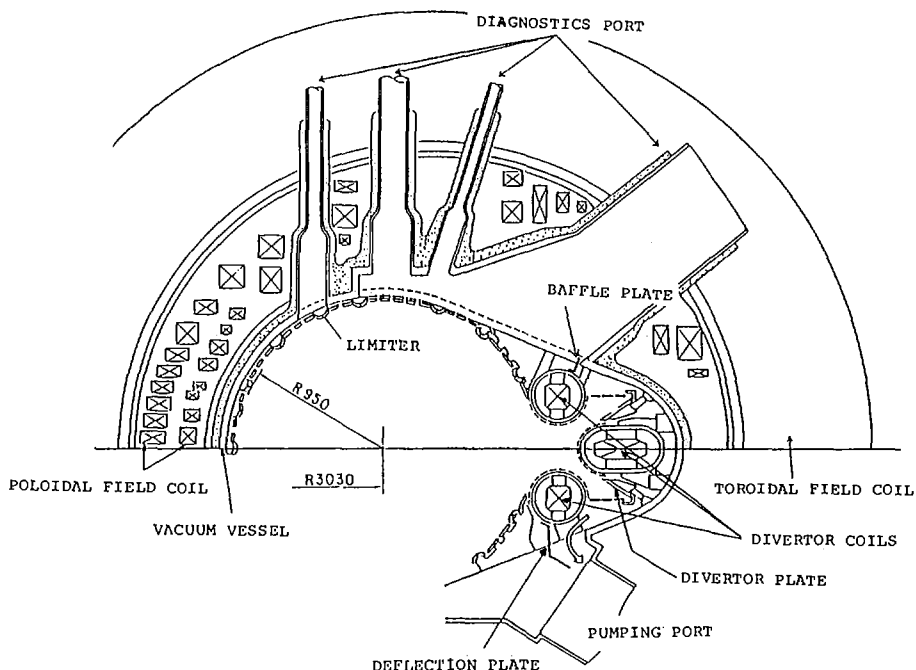


FIG. 1. Cross-section of vacuum vessel.

of  $5 \text{ m}^3 \cdot \text{s}^{-1}$  ( $\text{H}_2$ ) are connected at the divertor chamber to pump the hydrogen gas built up in the chamber.

Nearly the entire diagnostic equipment manufactured is now in working order. Its availability in the experiments is quite high. A list of diagnostic equipment is given in Table II.

### 3. OPERATIONAL CHARACTERISTICS

#### 3.1. Machine operation

Figure 2 shows the time behaviour of typical divertor and limiter discharges in JT-60. In most discharges, hydrogen prefill is used since helium prefill tends to lead to a disruptive discharge during the ramp-up phase. Later in the discharge, gas feed of hydrogen or helium (as in Fig. 2) is performed through gas valves which are placed at the main vacuum vessel or at the divertor chamber. The content of hydrogen in the 'helium' discharge is not precisely known although an estimate from neutral beam shinethrough indicates that the helium ion content is higher than the hydrogen content during the NB heating. In some discharges, the plasma density is feedback controlled so as to evolve according to the instructions before the discharge.

TABLE II. DIAGNOSTICS IN JT-60

Plasma parameter	Sub-systems	
Electron Density	FIR Interferometer 2-mm Interferometer	3ch, CH <sub>3</sub> OH Laser (118.8 $\mu$ m) 1ch
Electron Temperature	Fourier Transform Spectrometer Thomson Scattering System	ECE Multi-pulse Ruby/YAG Laser (6ch)
Ion Temperature	CX Particle Analyser Active Beam Scattering System CX Recombination Spectrometer Neutron Counter	E=0.1 ~ 110keV, E//B 200keV-3.5A, He, $\theta = 7^\circ$ (on Active Beam) E = 1.5 ~ 4 MeV
Impurity	VUV Spectrometer (2) Doppler Spectrometer Crystal Spectrometer Visible Spectrometer I Visible Spectrometer II Grazing Incidence Spectrometer	0.2 ~ 500 $\text{\AA}$ , Holographic Grating 5 ~ 9000 $\text{\AA}$ 0.6 ~ 2.7 $\text{\AA}$ 2000~7000 $\text{\AA}$ , Spectrograph, Photo-Multiplier The same as above, Rotating Mirror 10 ~ 1300 $\text{\AA}$
Radiation Flux	SX High Speed PHA PIN Diode Array Bolometer Array HX Detector	1ch 17ch 16ch
Peripheral Plasma	Visible TV Magnetic Probes, Thermocouples H $\alpha$ Diode Array	3ch 61ch 4ch, 3ch, 1ch
Divertor Plasma	FIR Interferometer Visible Spectrometer VUV Spectrometer H $\alpha$ Diode Array Bolometer Array Thermocouple Array IR & Visible TV	2ch, CH <sub>3</sub> OH Laser 2ch 2 ~ 1200 $\text{\AA}$ , Holographic Grating 4ch 4ch (on Divertor Plate) 2ch

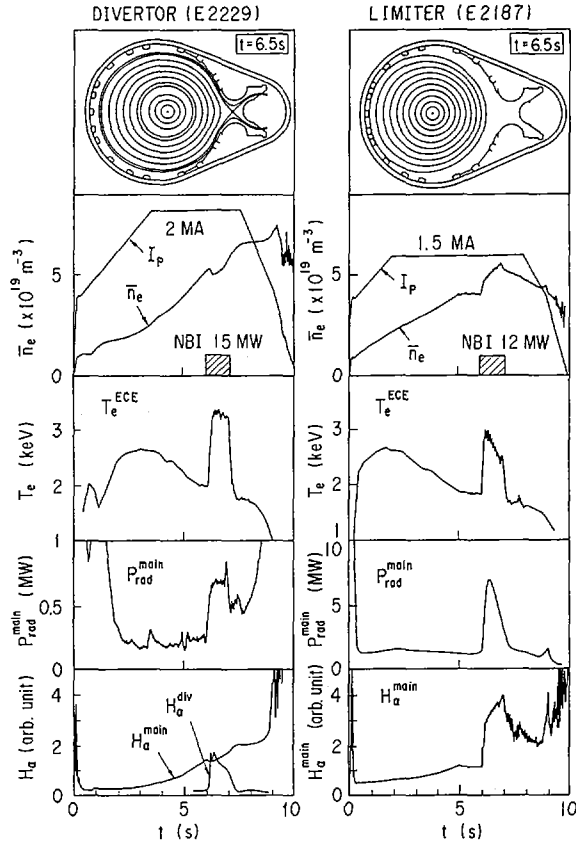


FIG. 2. Divertor and limiter discharges with NB heating.

The discharge is usually initiated as a limiter discharge. In the case of divertor experiments, it is then switched over to a divertor discharge by exciting the divertor coil current with a typical delay of a few hundred milliseconds. Feedback control is applied, with a sampling time of 1 ms, to the plasma current, and the vertical and the horizontal field coil currents. The quadrupole and the divertor coil currents are either preprogrammed (as in Fig. 2) or feedback controlled with special attention to precise positioning of the separatrix magnetic surface with respect to the closest limiter and the divertor plates [1]. In some of the discharges, the intersection of the separatrix magnetic surfaces is swept over a width of several centimetres by modulating the divertor coil current to reduce the peak heat load at the divertor plates.

The supplementary heating power can be applied at any desired time during the discharge. The discharge is terminated by turning off the heating power and the gas feed, and then the plasma current. In hydrogen discharges, the plasma density can be reduced simultaneously with the plasma current, while in helium discharges the

density stays high until the end of the discharge because of the longer effective particle confinement time. The discharge ends as a limiter discharge such as it has been initiated.

### 3.2. Operational regime

JT-60 is rather routinely operated near its maximum rating (Table I), as required by the experimental plan. Statistically, a large fraction of experiments is made near the maximum toroidal magnetic field. The plasma current is usually varied with steps of 0.5 MA up to 2 MA.

The operational regime of JT-60 divertor plasmas extends over a wide range of plasma parameters. Figures 3(a) and 3(b) show the regime for NB heated divertor (D) and limiter (L) discharges as well as for Joule heated hydrogen divertor discharges. The lower limit of  $q_{\text{eff}}$  is about 2.2 in both NB heated and Joule heated discharges. Attempts to reduce  $q_{\text{eff}}$  closer to 2.0 result in disruptive discharges.

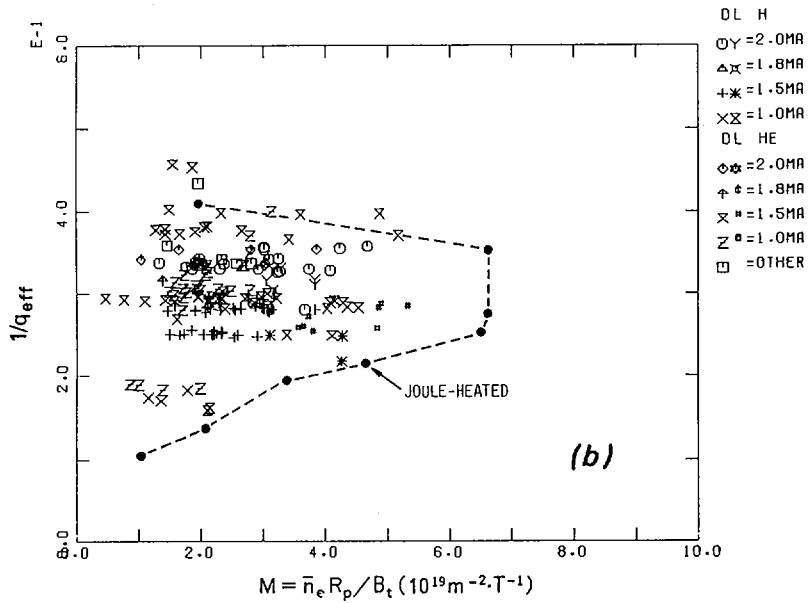
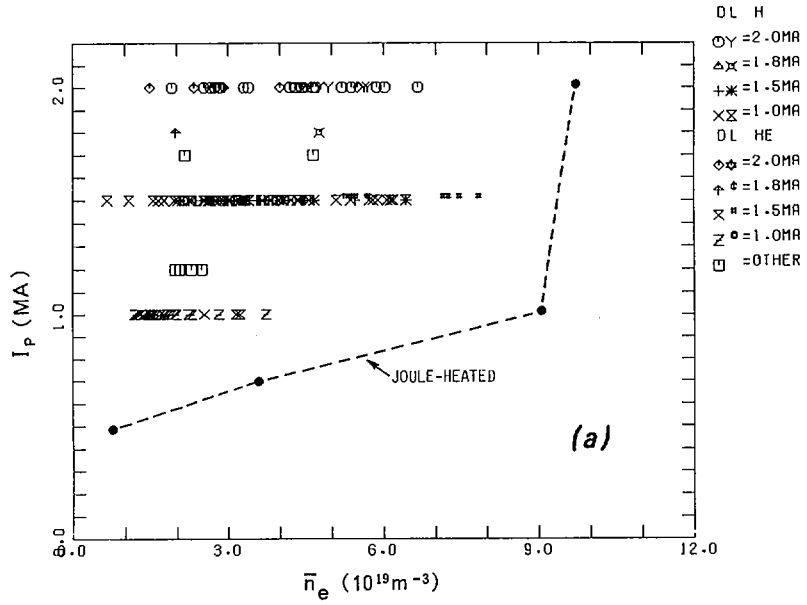
In Joule heated discharges efforts are made to explore the upper limits of  $\bar{n}_e$  and the Murakami parameter  $\bar{n}_e R_p / B_T$ , which are  $9.7 \times 10^{19} \text{ m}^{-3}$  and  $6.6 \times 10^{19} \text{ m}^{-2} \cdot \text{T}^{-1}$ , respectively. The lowest limit of  $\bar{n}_e$  achieved is  $0.1 \times 10^{19} \text{ m}^{-3}$ . On the other hand, in NB heated discharges, no particular efforts are made to raise the upper limits of these parameters. In this sense, the respective limits of  $\bar{n}_e$  and the Murakami parameter, of  $8 \times 10^{19} \text{ m}^{-3}$  and  $5.2 \times 10^{19} \text{ m}^{-2} \cdot \text{T}^{-1}$ , should not be regarded as unsurpassable limits. The lower end of  $\bar{n}_e$  is limited by the shinethrough power allowed by the armour plates of the vacuum vessel.

Figure 3(c) is a plot of NB heated discharges in the diagram of  $\bar{n}_e$  versus  $P_{\text{abs}} = P_{\text{joule}} + P_{\text{inj}} - P_{\text{shinethrough}}$  for both divertor (D) and limiter (L) discharges. It shows that the experiments have covered rather evenly the operational regime shown in this diagram.

### 3.3. Global effects of the divertor

A comparison of radiation losses from the main plasma as shown in Fig. 4 demonstrates the dramatic effect of the divertor in reducing the radiation loss in the NB heated and the Joule heated plasmas. The radiation loss is typically 5–10% of  $P_{\text{abs}}$  in divertor discharges and 30–90% in limiter discharges. It shows that the divertor is particularly effective in reducing the radiation loss of the NB heated plasmas and keeps  $P_{\text{rad}}/P_{\text{abs}}$  below the Joule heating value.

Figure 2 shows a pronounced increase, during NB heating, of hydrogen radiation from the divertor chamber and a small change in the radiation in the main vacuum vessel. This observation indicates that the particle loss in the plasma is enhanced during NB heating and also that the lost particles are efficiently transported to the divertor chamber through the divertor throat similar to the observation made



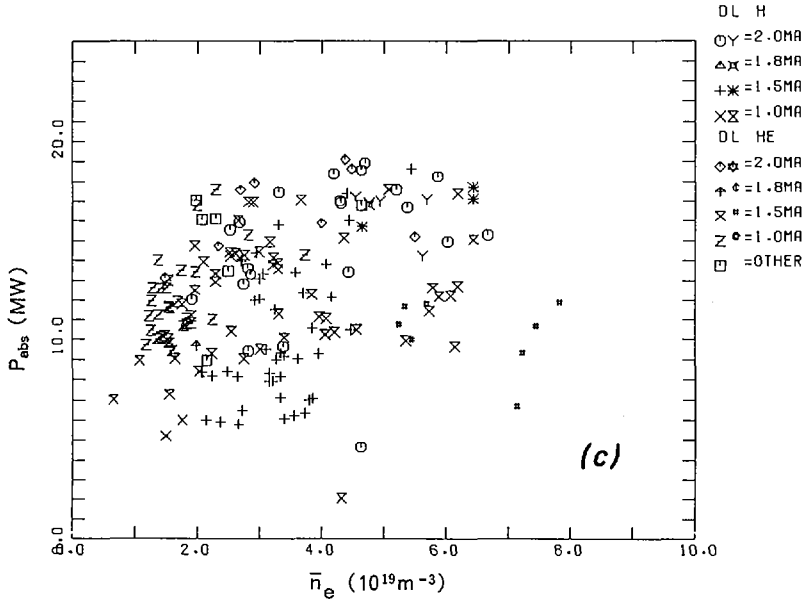


FIG. 3. Operational regime of Joule heated and NB heated plasmas.  
 (a)  $\bar{n}_e$  ( $10^{19} \text{ m}^{-3}$ ) versus  $I_p$  (MA);  
 (b)  $\bar{n}_e R_p / B_t$  ( $10^{19} / \text{m}^2 \text{ T}$ ) versus  $1/q_{\text{eff}}$ ;  
 (c)  $\bar{n}_e$  ( $10^{19} \text{ m}^{-3}$ ) versus  $P_{\text{abs}}$  (MW).

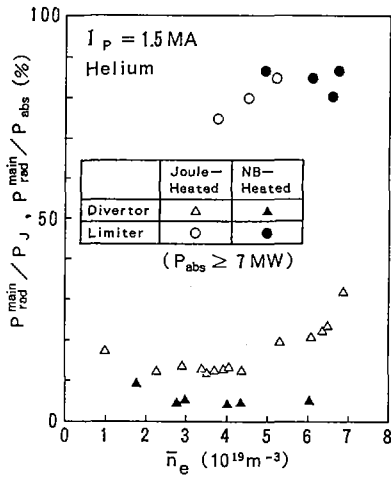
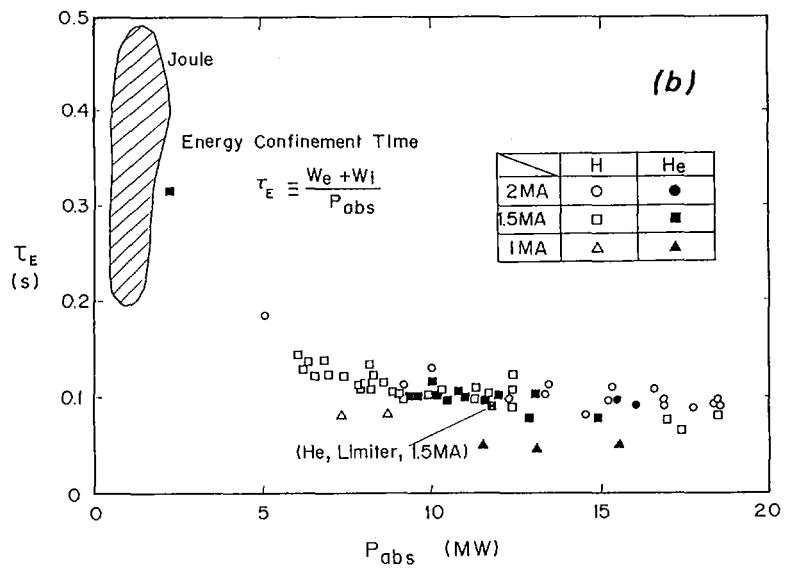
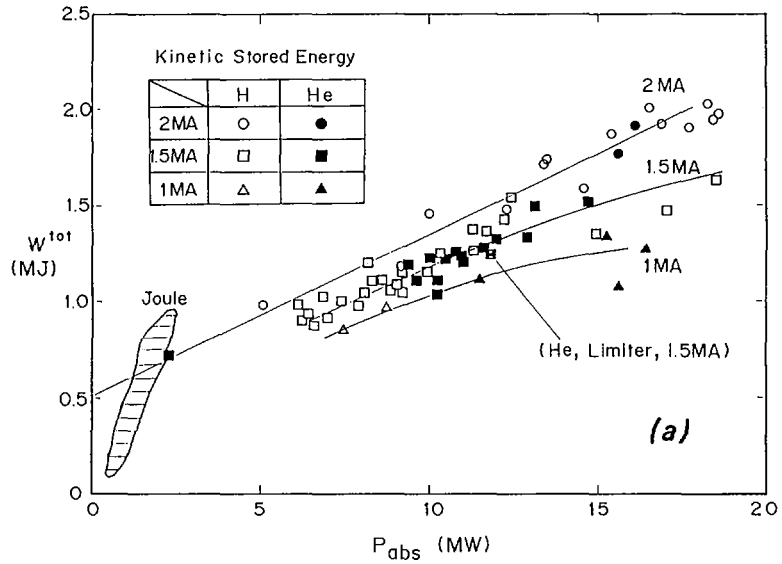


FIG. 4.  $\bar{n}_e$  versus  $P_{\text{rad}}^{\text{main}} / P_{\text{abs}}$  in Joule heated and NB heated plasmas.



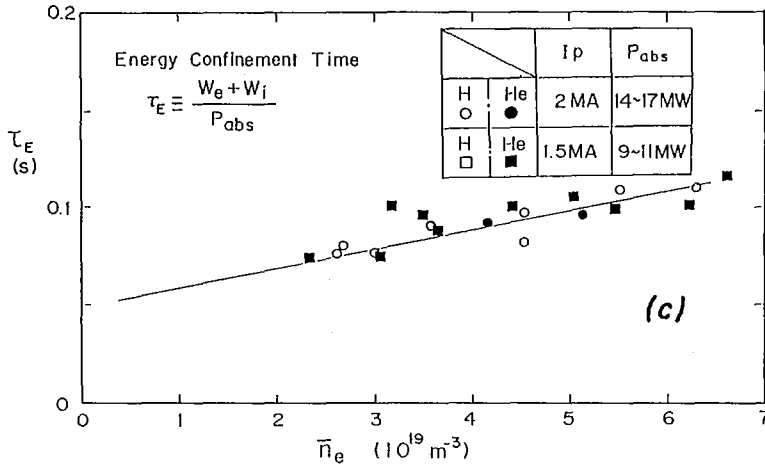


FIG. 5. Confinement in Joule heated and NB heated plasmas:

- (a)  $P_{obs}$  versus  $W^{tot}$ ;  
 (b)  $P_{obs}$  versus  $\tau_E$ ;  
 (c)  $\bar{n}_e$  versus  $\tau_E$ .

in Joule heated plasmas [1, 2, 4]. With respect to heat transport through the throat to the divertor chamber, the temperature rise  $\Delta T$  of the divertor plates is measured during NB heating by a set of thermocouples embedded in the plates. The half-width of the  $\Delta T$  distribution across the separatrix is less than 2 cm, which corresponds to a half-width of less than about 1 cm at the divertor throat, small enough to assure unobstructed transport of heat to the divertor plates.

#### 4. ENERGY CONFINEMENT AND TRANSPORT

Figure 5(a) shows the total kinetic stored energy  $W = W_e + W_i + W_{beam}$  versus  $P_{obs}$  in the NB heated divertor and limiter discharges, as the density is varied. It shows that the stored energy increases as an offset, linear function of  $P_{obs}$  up to a maximum of 2 MJ and that the energy confinement time is reduced by NB heating. This L-mode-like behaviour can also be seen in Figs 5(b) and (c), where the dependence of the energy confinement time  $\tau_E$  on other parameters is shown.  $\tau_E$  decreases from Joule heating values of 0.3–0.5 s, depending on the density [4], to 0.1–0.12 s with NB heating and approaches an asymptotic value. It increases with  $\bar{n}_e$  and  $I_p$ , although the dependence is rather weak. No clear dependence on the ion mass number was observed within the experimental ambiguity, which can be understood in view of the substantial hydrogen content in the helium discharges (see Subsection 3.1). The degradation in the energy confinement in the core region is interpreted as due to the enhancement in the electron conduction since none of the

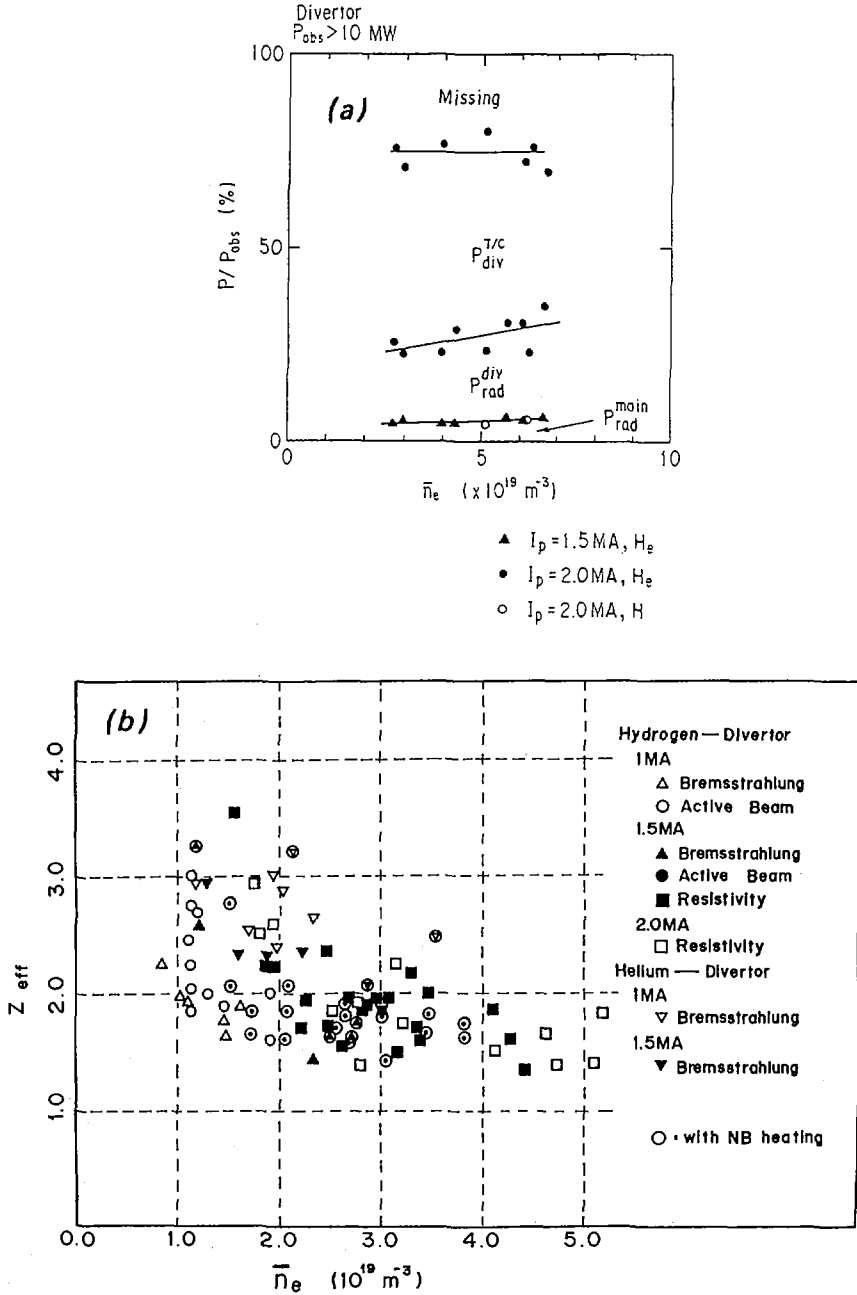


FIG. 6. (a) Energy accounting in the NB heated divertor plasma.

$P_{rad}^{main}$  and  $P_{rad}^{div}$  are the radiation loss from the main and the divertor plasmas, respectively.  $P_{div}^{T/C}$  is the energy loss to the divertor plates measured by thermocouples;

(b)  $Z_{eff}$  versus  $\bar{n}_e$  for Joule heated and NB heated plasmas.

reasonably enhanced neoclassical ion, convection, and radiation losses is large enough to account for the experimentally observed values. More detailed discussions on this subject are given in a companion paper [6].

A typical set of plasma parameters obtained in the NB heated plasmas is  $T_i(0)$  6 keV,  $T_e(0)$  4 keV,  $\bar{n}_e$   $3 \times 10^{19} \text{ m}^{-3}$  at  $P_{\text{abs}}$  14 MW. In an attempt to improve the confinement, a limited number of discharges with H-mode characteristics are obtained. They are, however, not reproducible and need further study.

In Fig. 6(a) the power losses observed in the main vacuum vessel and in the divertor chamber are compared with  $P_{\text{abs}}$ . There is a good accountability between them in the NB heated plasmas as was observed earlier in the Joule heated discharges [1].

## 5. IMPURITIES

Major species of impurities that are observed spectroscopically in hydrogen divertor discharges are oxygen, carbon, titanium (from TiC coating) with and without NB heating. In some of the NB heated plasmas a molybdenum burst is observed during the NB heating, which can, in most cases, be eliminated by sweeping the separatrix magnetic surface over the divertor plates (see Subsection 3.1). The titanium ion content near the axis, estimated from the dominant Ti XXI intensity observed along the viewline through the vessel axis, decreases roughly in inverse proportion to the plasma density although the shot to shot fluctuation is fairly large. The titanium content is about  $1 \times 10^{-5}$  in Joule heated hydrogen divertor plasmas at  $\bar{n}_e$   $2 \times 10^{19} \text{ m}^{-3}$  and  $I_p$  2 MA and increases to about  $2 \times 10^{-5}$  in NB heated plasmas with  $P_{\text{abs}} > 10 \text{ MW}$ . These values are too small to contribute to  $Z_{\text{eff}}$  and  $P_{\text{rad}}$ . In Joule heated hydrogen limiter plasmas, on the other hand, the titanium content is much larger,  $3 \times 10^{-4}$ , which is still too small to affect  $Z_{\text{eff}}$  and may have a small contribution to  $P_{\text{rad}}$ .

The oxygen and carbon contents are not quantified by spectroscopic measurements. However, their combined effects are estimated from the energy distribution of helium scattered near the axis from the helium active beam. The amount thus estimated is equivalent to 1.2% in oxygen or, alternatively, to 2.4% in carbon in Joule heated hydrogen divertor plasmas at  $\bar{n}_e$   $3.4 \times 10^{19} \text{ m}^{-3}$ . With NB heating, it increases up to 1.8% and 3.6%, respectively. These values are naturally consistent with  $Z_{\text{eff}}(0)$  as measured by the helium scattering method to be described below. No direct information is as yet available on the spatial distributions of the impurities.

$Z_{\text{eff}}(0)$  is estimated by three methods: visible bremsstrahlung, helium active beam scattering, and resistivity analyses (assuming Spitzer resistivity; the neoclassical resistivity yields  $Z_{\text{eff}}(0)$  below unity in hydrogen discharges). Figure 6(b) shows  $Z_{\text{eff}}(0)$  in various kinds of discharges with and without NB heating. These methods consistently give  $Z_{\text{eff}}(0)$  1.5–2 for  $\bar{n}_e > 3 \times 10^{19} \text{ m}^{-3}$  hydrogen divertor discharges with and without NB heating.

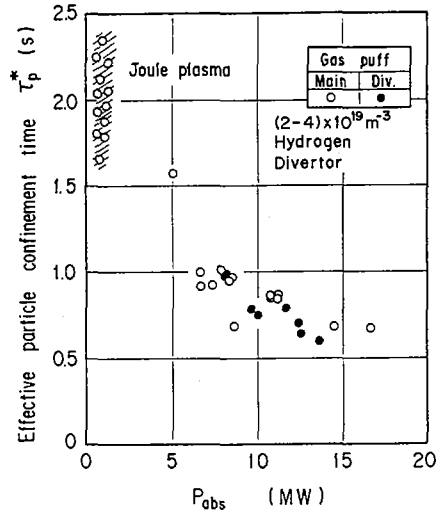
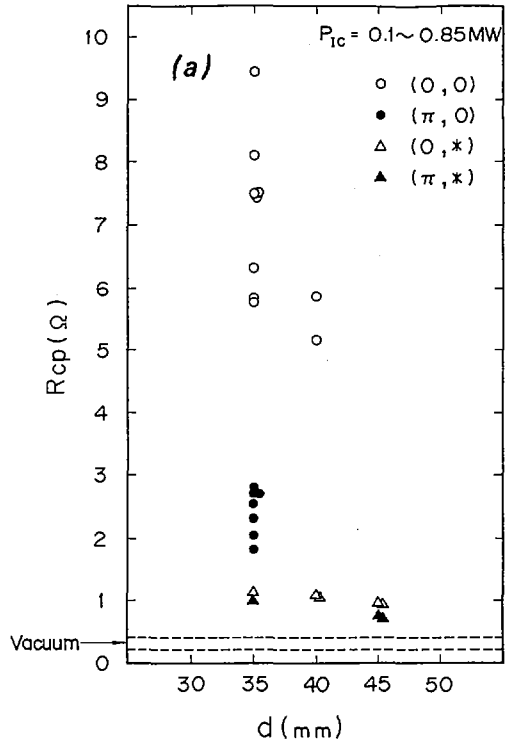


FIG. 7. Effective particle confinement time  $\tau_p^*$  versus  $P_{abs}$ .



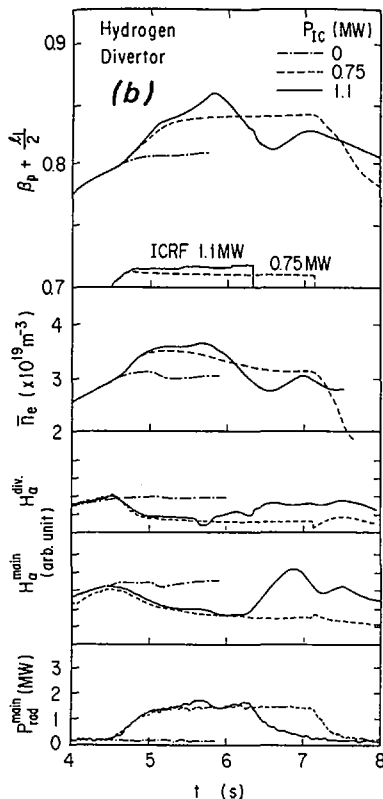


FIG. 8. ICRF heating experiment:

(a) Antenna loading;

(b) Plasma behaviour.

## 6. PARTICLE CONFINEMENT AND TRANSPORT

Particle confinement in the NB heated hydrogen divertor plasmas is evaluated from the density profile and influx of fast (NBI) and slow hydrogen atoms. The diffusion coefficient  $D$  in the plasma core is about  $0.5 \text{ m}^2 \cdot \text{s}^{-1}$  at  $\bar{n}_e = (4.5-5) \times 10^{19} \text{ m}^{-3}$  and  $I_p = 2 \text{ MA}$  for  $P_{\text{abs}} = 20 \text{ MW}$  and increases in proportion to  $P_{\text{abs}}$ , when a shaping parameter of  $C_v = 0$  is assumed. In contrast, the diffusion coefficient is, at least, an order of magnitude smaller in Joule heated plasmas. The diffusion coefficient of titanium impurity in Joule heated plasmas is evaluated from the temporal evolution of titanium lines following an accidental penetration of a minute titanium piece into the plasma and is about  $1 \text{ m}^2 \cdot \text{s}^{-1}$  with  $C_v \sim 0$ .

Recycling behaviour in Joule heated hydrogen plasmas has been reported for both divertor and limiter plasmas [1, 3]. The effective particle confinement time,

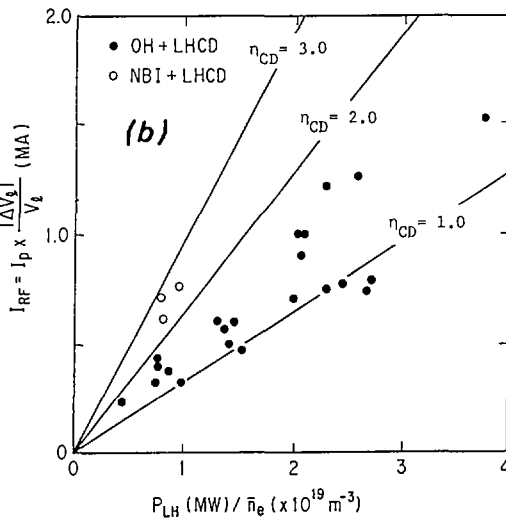
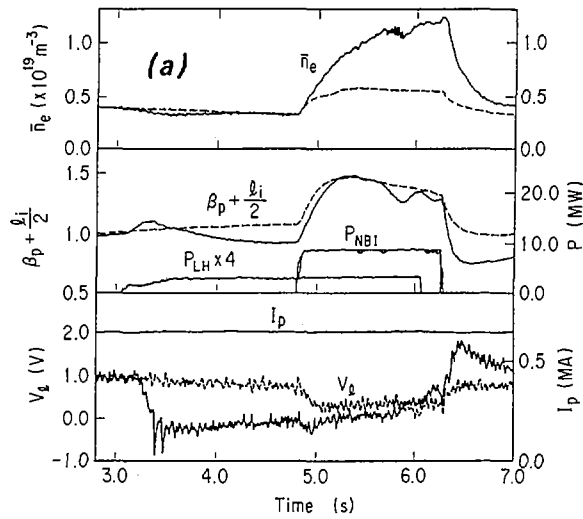


FIG. 9. LHRF current drive experiment:

(a) Plasma behaviour with and without LH power shown by full and broken line, respectively;  
 (b) Efficiency.

$\tau_p^* = \tau_p/(1-R)$ , is about 2 s and 5.5 s, respectively, at a density of  $3 \times 10^{19} \text{ m}^{-3}$  and is proportional to the plasma density.  $\tau_p^*$  in NB heated hydrogen divertor plasmas is plotted in Fig. 7, as a function of  $P_{\text{NB}} = P_{\text{inj}} - P_{\text{shinethrough}}$  for a density range of  $(2-4) \times 10^{19} \text{ m}^{-3}$ . It shows that  $\tau_p^*$  decreases with  $P_{\text{NB}}$  and is independent of the plasma density. The hydrogen pressure,  $P_{\text{div}}$ , in the divertor chamber increases in proportion to  $\bar{n}_e$  in the NB heated plasmas as in the Joule heated plasmas [2, 3], indicating compression of the hydrogen gas in the divertor chamber. The inverse normalized pressure in the divertor chamber,  $\bar{n}_e^2/P$ , decreases with  $P_{\text{NB}}$  and then tends to an asymptotic value. This observation and the aforementioned increase of  $D$  with  $P_{\text{abs}}$  consistently indicate the enhancement of recycling during NB heating, due to degradation of particle confinement.

## 7. ICRF HEATING

The ICRF heating experiment with a  $2\omega_{ci}$  resonance on the axis is conducted with an injected power of  $P_{\text{IC}} \leq 1.4 \text{ MW}$ , injected from a  $2 \times 2$  loop antenna array. Figure 8(a) shows the antenna loading resistance  $R_{\text{cp}}$  as a function of the Faraday shield-to-separatrix distance  $d$  for various choices of the phase difference ( $\Delta\varphi$ ,  $\Delta\theta$ ) of the loops. The plasma is a hydrogen divertor plasma with  $\bar{n}_e = 3 \times 10^{19} \text{ m}^{-3}$  and  $I_p = 1.5 \text{ MA}$  at 4 T.  $R_{\text{cp}}$  as high as  $10 \Omega$  is obtained with (0, 0) phase difference. This value of  $R_{\text{cp}}$  is larger than the values evaluated from a simplified theoretical model [8].

The increase in the kinetic stored energy  $\Delta W$  at  $P_{\text{IC}} = 1.2 \text{ MW}$  is 0.20 MJ, corresponding to  $\Delta W/P_{\text{IC}}$  of  $0.17 \text{ J} \cdot \text{W}^{-1}$ . Figure 8(b) shows the plasma behaviour with and without ICRF heating, in particular, an increase in stored energy and a reduction of the hydrogen radiation from the main and divertor plasmas.

## 8. LHRF CURRENT DRIVE

The current drive experiment is performed by using a  $4 \times 8$  waveguide launcher fed by one of the LHRF power units [9]. Experiments are performed at an injected power  $P_{\text{LH}}$  of up to 1.2 MW at  $I_p = 0.5-1.5 \text{ MA}$  into a hydrogen divertor plasma of  $\bar{n}_e = (0.1-2) \times 10^{19} \text{ m}^{-3}$ . With a phase difference  $\Delta\varphi$  of  $\pi/2$  corresponding to waves peaked at an  $n_{\parallel}$  value of about 1.7, evidence is obtained for a current drive as shown in Fig. 9(a) for two cases with and without LH power. The NB heating is timed so that its effect can be seen clearly. It is interesting to note that NB heating and LH current drive are synergetic. In Fig. 9(b), the driven current  $I_{\text{RF}}$ , estimated as  $I_p |\Delta V_\ell| / V_\ell$  from the loop voltage  $V_\ell$ , is plotted as a function of  $P_{\text{LH}}/\bar{n}_e$ . The current drive efficiency  $\eta_{\text{CD}} = \bar{n}_e R I_{\text{RF}} / P_{\text{RF}}$  is  $(1-1.7) \times 10^{19} \text{ A} \cdot \text{m}^{-2} \text{W}^{-1}$  without NB heating and increases to  $(2-2.8) \times 10^{19} \text{ A} \cdot \text{m}^{-2} \text{W}^{-1}$  with NB heating. The stored energy during the NB heating is improved by 30% throughout the current drive.

## 9. CONCLUSIONS

JT-60, as well as its heating and diagnostics systems, has been operated at near maximum capabilities. The main results obtained in recent experiments are:

- (1) The experiments are carried out over a wide operational regime:  $0.1 \times 10^{19} \text{ m}^{-3} \leq n \leq 9.7 \times 10^{19} \text{ m}^{-3}$ ,  $q_{\text{eff}} \geq 2.2$ , and  $P_{\text{abs}} \leq 20 \text{ MW}$ . A  $W^{\text{tot}}$  of up to 2.0 MJ is obtained.
- (2) The energy confinement time is up to 0.5 s in Joule heated plasmas, depending on the plasma density. With NB heating, it is reduced to 0.12 s at high heating power; it is weakly dependent on density and plasma current. This behaviour is accompanied by a reduction of the particle confinement time.
- (3) The divertor is effective in reducing impurities with  $P_{\text{rad}}/P_{\text{abs}} \geq 5\%$  and  $Z_{\text{eff}} \geq 1.5$  in the NB heated plasmas. This indicates that a first wall material with medium Z can be used at reactor grade plasma parameters. Compression of hydrogen gas in the divertor chamber is observed.
- (4) In the LH current drive experiment a current equivalent to 1.5 MA is driven. The current drive efficiency  $\eta_{\text{CD}}$  is as high as  $(1-1.7) \times 10^{19} \text{ A} \cdot \text{m}^{-2} \text{W}^{-1}$ . The efficiency is further increased to  $(2-2.8) \times 10^{19} \text{ A} \cdot \text{m}^{-2} \text{W}^{-1}$  by NB heating, which is accompanied by the enhancement of the NB heating efficiency by the LH current drive. In the ICRF heating experiment an effective heating of  $\Delta W^*/P_{\text{IC}} \cong 0.17 \text{ J} \cdot \text{W}^{-1}$  is observed and is accompanied by the reduction of hydrogen recycling.
- (5) Attempts to improve confinement are being made.

## ACKNOWLEDGEMENTS

The authors wish to thank the members of JAERI who have contributed to the JT-60 project throughout its progress. They also wish to express gratitude to Drs S. Mori, Y. Iso, and K. Tomabechi for continuous encouragement and support.

## REFERENCES

- [1] JT-60 TEAM (presented by M. Yoshikawa), *Plasma Phys. Controll. Fusion* **28** (1986) 165.
- [2] JT-60 TEAM (presented by S. Tsuji), in *Controlled Fusion and Plasma Physics (Proc. 12th Europ. Conf. Budapest, 1985), Part I, European Physical Society* (1985) 375.
- [3] JT-60 TEAM (presented by S. Tamura), *Plasma Phys. Controll. Fusion* **28** (1986) 1377.
- [4] JT-60 TEAM (presented by H. Kishimoto), in *Plasma-Surface Interactions in Controlled Fusion Devices (Proc. 7th Int. Conf. Princeton, NJ, 1986)*.
- [5] *Nucl. Eng. Des./Fusion (Special Issue)*, to be published.

- [6] JT-60 TEAM (presented by M. Nagami), Paper IAEA-CN-47/A-II-2, these Proceedings, Vol. 1.
- [7] JT-60 TEAM (presented by H. Takeuchi), Paper IAEA-CN-47/A-IV-3, these Proceedings, Vol. 1.
- [8] KIMURA, H., et al., in Heating in Toroidal Plasmas (Proc. 4th Int. Symp. Rome, 1984), Vol. 2, ENEA, Frascati (1984) 1128.
- [9] JT-60 TEAM (presented by T. Imai), Paper IAEA-CN-47/F-II-7, these Proceedings, Vol. 1.

## DISCUSSION

R.J. GOLDSTON: I am interested in your measurements of  $H_{\alpha}$  emission in the main chamber. You showed that it rose very little during neutral injection into divertor discharges. Whereabouts in the main chamber do you measure the  $H_{\alpha}$  emission and how does the emission near the divertor throat behave?

M. YOSHIKAWA: We have an array of  $H_{\alpha}$  detectors to measure the  $H_{\alpha}$  intensity. The signal from the detector in the direction of the throat is much larger than the other signals.

M. KEILHACKER: Since H-mode discharges have been achieved recently in both JET and DIII-D, could you comment on the progress made in H-mode research on JT-60?

M. YOSHIKAWA: We have spent a considerable amount of experimental time investigating the H-mode. Although a small number of shots exhibit characteristics of the H-mode type, we are not convinced that H-mode operation is achieved, since these shots are not reproducible and limited in number.

J.G. CORDEY: Do you have a physical explanation for the improvement in the efficiency of the lower hybrid current drive with the addition of neutral beam injection?

M. YOSHIKAWA: No, we are not yet able to interpret the improvement clearly. One possible explanation is that the electron energy distribution is broadened at the upper end by neutral beam heating and improves the efficiency of the lower hybrid current drive, whereas the ion energy distribution is not disturbed and does not affect the wave power.

B. COPPI: What type of density profile did you observe with Ohmic discharges and auxiliary heated discharges?

M. YOSHIKAWA: The density profile in JT-60 is generally wide. One interesting observation in association with recent TFTR experiments is that the density profile broadens when the confinement of the neutral beam heated plasma is improved by lower hybrid current drive.



## JET LATEST RESULTS AND FUTURE PROSPECTS

### JET TEAM

*(Presented by P.H. Rebut)*

H. Altmann, R.J. Anderson, J. Arbez, W. Bailey, D.V. Bartlett, B. Beaumont<sup>1</sup>, G. Beaumont, K. Behringer, P. Bertoldi, E. Bertolini, C.H. Best, V. Bhatnagar<sup>2</sup>, R.J. Bickerton, A. Boileau<sup>3</sup>, F. Bombarda<sup>4</sup>, T. Bonicelli, S. Booth, A. Boschi, G. Bosia, M. Botman, H. Brelen, H. Brinkschulte, M.L. Browne, M. Brusati, T. Budd, M. Bures, P. Butcher, H. Buttgerit, D. Cacaut, C. Caldwell-Nichols, J.D. Callen<sup>5</sup>, D.J. Campbell, J. Carwardine, G. Celentano, C.D. Challis, A. Cheetham, J.P. Christiansen, C. Christodouloupoulos, P. Chuilon, R. Claesen, J.P. Coad, S.A. Cohen<sup>6</sup>, M. Cooke, J.G. Cordey, W. Core, S. Corti, A.E. Costley, G.A. Cottrell, M. Cox<sup>7</sup>, C. David, J. Dean, L. de Kock, E. Deksnis, G.B. Denne, G. Deschamps, K.J. Dietz, J. Dobbing, S.E. Dorling, D.F. Dücks, G. Duesing, P.A. Duperrex<sup>8</sup>, H. Duquenoy, A.W. Edwards, J. Ehrenberg<sup>9</sup>, W. Engelhardt, S.K. Erents<sup>7</sup>, F. Erhorn, B.T. Eriksson, M. Evrard<sup>2</sup>, H. Falter, N. Foden, M.J. Forrest<sup>7</sup>, C. Froger, K. Fullard, G. Fussmann<sup>9</sup>, M. Gadeberg<sup>10</sup>, A. Galetsas, A. Gallacher, D. Gambier<sup>1</sup>, R. Giannella<sup>4</sup>, A. Giannelli<sup>4</sup>, A. Gibson, R.D. Gill, A. Goede, A. Gondhalekar, C. Gordon, C. Gormezano, N.A. Gottardi, C.W. Gowers, R. Granetz, B. Green, S. Gregoli, F.S. Griph, R. Haange, J.H. Hamnén<sup>11</sup>, C.J. Hancock, P.J. Harbour, N.C. Hawkes<sup>7</sup>, P. Haynes<sup>7</sup>, T. Hellsten, J.L. Hemmerich, R. Hemsworth, F. Hendriks, R.F. Herzog, L. Horton<sup>12</sup>, J. How, M. Huart, A. Hubbard<sup>13</sup>, J. Hugill<sup>7</sup>, M. Hugon, M. Huguet, B. Ingram, H. Jäckel<sup>9</sup>, J. Jacquinet, Z. Jankowicz<sup>14</sup>, O.N. Jarvis, E.M. Jones, P. Jones, T.T.C. Jones, C. Jupén<sup>15</sup>, E. Källne, J. Källne, O. Kaneko<sup>16</sup>, A. Kaye, B.E. Keen, M. Keilhacker, G. Kinahan, S. Kissel, A. Konstantellos, M. Kovanen<sup>17</sup>, U. Kühnnapfel<sup>9</sup>, P. Kupschus, P. Lallia, J.R. Last, L. Lauro-Taroni, K.D. Lawson<sup>7</sup>, E. Lazzaro, R.C. Lobel, P.J. Lomas, N. Lopes-Cardozo<sup>18</sup>, M. Lorenz-Gottardi, C. Lowry<sup>13</sup>, G. Magyar, D. Maisonnier, M. Malacarne, V. Marchese, P. Massmann, G.M. McCracken<sup>7</sup>, P. McCullen, M.J. Mead, P. Meriguet, V. Merlo, V. Mertens<sup>9</sup>, S. Mills, P. Millward, A. Moissonnier, P.L. Mondino, D. Moreau<sup>1</sup>, P.D. Morgan, E.R. Müller<sup>9</sup>, D. Murmann<sup>9</sup>, G. Murphy, M.F. Nave, L. Nickesson, P. Nielsen, P. Noll, S. Nowak, W. Obert, M. Olsson, J. O'Rourke, M.G. Pacco, J. Paillere, S. Papastergiou, J. Partridge<sup>7</sup>, D. Pasini<sup>12</sup>, N.J. Peacock<sup>7</sup>, M. Pescatore, J. Plancoulaine, J.-P. Poffé, R. Prentice, T. Raimondi, J. Ramette<sup>1</sup>, C. Raymond, P.H. Rebut, J. Removille, W. Riediker, R. Roberts, D.C. Robinson<sup>7</sup>, A. Rolfe, R.T. Ross, G. Rupprecht<sup>9</sup>, R. Rushton, H.C. Sack, G. Sadler, J. Saffert, N. Salmon<sup>13</sup>, F. Sand, A. Santagiustina, R. Saunders, M. Schmid, F.C. Schüller, K. Selin, R. Shaw, A. Sibley, D. Sigournay, R. Sillen<sup>18</sup>, F. Simonet<sup>1</sup>, R. Simonini, P. Smeulders, J.A. Snipes<sup>7</sup>, K. Sonnenberg, L. Sonnerup, M.F. Stamp, C.A. Steed, D. Stork, P.E. Stott, T.E. Stringer, D.R. Summers, H.P. Summers<sup>19</sup>, A.J. Tagle, G. Tallents<sup>20</sup>, A. Tanga, A. Taroni, A. Terrington, A. Tesini, P.R. Thomas, E. Thompson, K. Thomsen<sup>10</sup>, F. Tibone, R. Tivey, T.N. Todd<sup>7</sup>, P. Trevalion, M. Tschudin, B.J. Tubbing<sup>18</sup>, P. Twynam, E. Usselmann, H. Van der Beken, J.E. Van Montfoort, M. von Hellermann, J. von Seggern<sup>21</sup>, T. Wade, C. Walker, B.A. Wallander, M. Walravens,

K. Walter, M.L. Watkins, M. Watson, D. Webberley, A. Weller<sup>9</sup>, J.A. Wesson,  
 J. Wilks, T. Winkel, C. Woodward, M. Wykes, D. Young, L. Zannelli,  
 J.W. Zwart  
 JET Joint Undertaking,  
 Abingdon, Oxfordshire,  
 United Kingdom

### Abstract

#### JET LATEST RESULTS AND FUTURE PROSPECTS.

During JET's first three years of operation, experiments have been undertaken with up to ~7 MW of ICRF, ~10 MW of neutral beam and ~18 MW of total input power during combined operation. The latest JET results show many advances made during this period. In particular, the especially good confinement ( $\tau_E$  up to 0.8 s), high temperatures ( $T_e$  up to 5 keV) and fusion product ( $\langle \hat{n}_i \tau_E \hat{T}_i \rangle = 10^{20} \text{ m}^{-3} \cdot \text{s} \cdot \text{keV}$ ) achieved with ohmic heating alone have exceeded expectations. Also, very efficient ion heating has been observed ( $T_i > 12.5 \pm 1.5 \text{ keV}$ ) at moderate neutral beam injection power levels ( $P_{NB} \leq 8 \text{ MW}$ ) and at low average densities ( $\bar{n}_e \sim (1-1.5) \times 10^{19} \text{ m}^{-3}$ ). In addition, a fusion product of ( $\langle \hat{n}_i \tau_E \hat{T}_i \rangle = 2 \times 10^{20} \text{ m}^{-3} \cdot \text{s} \cdot \text{keV}$ ) has been achieved with a separatrix configuration in JET. However, limitations have been encountered in plasma density and electron and ion temperatures because of disruptions and sawtooth oscillations. With additional heating, confinement is degraded, as the electron temperature outside the sawtooth region exhibits only a weak dependence on the input power per particle. As a consequence, additional heating has little impact on the fusion product. The consequent developments to provide significant alpha heating in JET are described.

- 
- <sup>1</sup> CEA, Centre d'études nucléaires de Fontenay-aux-Roses, France.
  - <sup>2</sup> Plasma Physics Laboratory, Association "Euratom-Belgian State" ERM/KMS, Brussels, Belgium.
  - <sup>3</sup> Institut national de la recherche scientifique, Ste-Foy, Québec, Canada.
  - <sup>4</sup> ENEA, Centro Ricerche Energia, Frascati, Italy.
  - <sup>5</sup> Department of Physics, University of Wisconsin, Madison, WI, USA.
  - <sup>6</sup> Princeton Plasma Physics Laboratory, Princeton University, NJ, USA.
  - <sup>7</sup> UKAEA, Culham Laboratory, Abingdon, Oxfordshire, UK.
  - <sup>8</sup> Centre de recherches en physique des plasmas, Ecole polytechnique fédérale de Lausanne, Switzerland.
  - <sup>9</sup> Max-Planck-Institut für Plasmaphysik, Garching, Fed. Rep. Germany.
  - <sup>10</sup> Risø National Laboratory, Roskilde, Denmark.
  - <sup>11</sup> Swedish Energy Research Commission, Stockholm, Sweden.
  - <sup>12</sup> Natural Sciences and Engineering Research Council, Ottawa, Ontario, Canada.
  - <sup>13</sup> Imperial College of Science and Technology, University of London, UK.
  - <sup>14</sup> RCC CYFRONET IAE, Otwock-Świerk, Poland.
  - <sup>15</sup> University of Lund, Sweden.
  - <sup>16</sup> Department of Physics, University of Nagoya, Japan.
  - <sup>17</sup> Department of Physics, Lappeenranta University of Technology, Lappeenranta, Finland.
  - <sup>18</sup> FOM Instituut voor Plasmafysica, Rijnhuizen, Nieuwegein, Netherlands.
  - <sup>19</sup> University of Strathclyde, Glasgow, UK.
  - <sup>20</sup> Research School of Physical Sciences, Australian National University, Canberra, Australia.
  - <sup>21</sup> Kernforschungsanlage Jülich GmbH, Fed. Rep. Germany.

## 1. Introduction

The Joint European Torus (JET) [1,2] is the largest single project of the coordinated fusion research programme of the European Atomic Energy Community (EURATOM). Its main objective is to obtain and study plasmas in conditions and with dimensions approaching those needed for a fusion reactor (ie  $n = 2 \times 10^{20} \text{m}^{-3}$ ;  $T \geq 10 \text{keV}$ , and  $\tau_E = 1\text{-}2\text{s}$ ), and is specifically designed to study D-T reactions in the plasma.

This paper concentrates on experiments and advances during the last 2 years (the first additional heating phase) using ion-cyclotron resonance frequency (ICRF) and neutral beam (NB) heating, both individually and in combined situations, and indicates particular developments and additions to JET that are planned to improve performance further towards the reactor regime.

## 2. Technical Status of the Device

### 2.1. Machine Conditions

Machine conditions have been progressively improved during the operational phase and all machine systems have now met the stringent design specifications. The achieved parameters are compared with the design values in Table I.

The toroidal magnetic field ( $B_T$ ) now operates routinely at its maximum design value of 3.45T. The plasma current ( $\pm < 3\%$ ), horizontal plasma position ( $\pm \leq 10\text{mm}$ ), plasma elongation ( $\epsilon (\pm 5\%)$ ) and shape are all controlled by feedback circuits acting on poloidal field coils. Following considerable work on these systems, stable control has been obtained with elongations in the range 1.2-1.7. However, the plasma vertical position is naturally unstable due to both the quadrupole poloidal field necessary for the elongated plasma and the de-stabilising effect of the iron magnetic circuit. Loss of vertical position feedback control at higher elongations can lead to large vertical forces on the vessel. Some additional vessel support has been introduced, but the plasma current,  $I_p$ , had still to be restricted within the operating regime given by  $I_p^2(\epsilon-1.2) < 5.0(\text{MA})^2$ .

With a plasma elongation limited to 1.4, the plasma current has been increased to 5.1MA (for a period of 3s within a 20s pulse) exceeding the design value of 4.8MA. In addition, plasma currents have been achieved routinely at 4MA with flat-tops of 6s duration. At present, the full inductive flux (34Vs) is not used as the maximum premagnetisation current creates stray fields, which inhibit reliable plasma breakdown. Strengthening of the vacuum vessel, modifying the primary winding and improving the power supply will allow an enhancement of the plasma current to 7MA, at the full elongation of  $\epsilon = 1.7$ . Stable discharges with  $I_p = 3.5\text{MA}$ ,  $B_T = 1.7\text{T}$ ,  $\epsilon = 1.35$  and  $q_\psi = 2.2$  have been studied to simulate 7MA operation.

The vacuum vessel is usually operated with wall temperatures at 250-300°C and with a base pressure of  $10^{-7}\text{mbar H}$  and  $10^{-9}\text{mbar}$  residual impurities. The vessel is conditioned by glow discharge cleaning (GDC) in hydrogen and/or deuterium. To reduce the level of metallic impurities and oxygen, the torus walls are carbonised by glow discharge cleaning in a mixture of hydrogen or deuterium and hydrogenic methane ( $\text{CH}_4$ ) [3].

In most recent experiments, eight carbon plasma limiters have been located symmetrically on the outer equatorial plane of the vessel. Since disruptions mostly terminate on the inner walls, these have been covered by carbon tiles to a height of  $\pm 1\text{m}$  around the mid-plane. Similar tiles also protect the frames of the RF antennae, eight octant joints, and the outer wall from neutral beam shine-through. Additional tiles have been installed at the top and

TABLE I. PRINCIPAL PARAMETERS OF JET:  
DESIGN AND ACHIEVED VALUES

Parameter	Design Values		Achieved Values
Plasma minor radius (horizontal), a	1.25m		0.8—1.2m
Plasma minor radius (vertical), b	2.10m		0.8—2.1m
Plasma major radius, $R_0$	2.96m		2.5—3.4m
Plasma elongation ratio, $\epsilon=b/a$	1.68		1.2—1.7
Flat-top pulse length	Up to 20s		Up to 20s
Toroidal magnetic field (plasma centre)	3.45T		3.45T
Plasma current:			
circular plasma	3.2MA		3.0MA
Elongated plasma	4.8MA		5.1MA
Flux Drive Capability	34 V·s		28 V·s
Additional heating power (in plasma)	1986 Values	Full Values	
RF Power	8MW (3 antenna)	32MW (8 antenna)	<7MW
Neutral beam power	10MW (1 box)	20MW (2 boxes)	<9MW

bottom of the vessel to protect the vessel during X-Point (Separatrix) operation. The total surface area covered is  $45\text{m}^2$ , corresponding to  $\sim 20\%$  of the vacuum vessel area. The inner wall tiles used as limiters and those for X-Point protection have provided powerful pumping (with speeds up to  $100\text{mbar.l.s}^{-1}$ ). This has allowed operation at low density near the plasma edge and was used to reduce the density after neutral injection to avoid disruptions. Recently, helium discharges prior to normal operation have improved the inner wall tiles pumping capacity.

In early 1987, it is planned to extend the coverage in the machine and the existing limiters will be replaced with two toroidal 'belt' limiters (surface area  $\sim 15\text{m}^2$ ), and the existing RF antennae will be replaced with eight water-cooled models. In late 1987, the belt limiter tiles and those from the eight antennae will be replaced by beryllium plates to investigate the expected advantages with this low Z material.

## 2.2. RF Heating System

Since early 1985, three RF antennae have been installed at the outer equatorial wall. Power is transferred to the plasma at a radiation frequency (25-55MHz) equal to the cyclotron resonance of a minority ion species (H or  $\text{He}^3$ ). Each antenna is fed by a tandem amplifier

delivering up to 3MW in matched conditions. The three units have been regularly operated up to 7.2MW for 2s pulses. Experiments with 8s pulse duration have also been performed delivering ~40MJ to the plasma. Recently, a fourth RF generator has been installed so that two generators can be coupled to one antenna [4].

When completed, the JET RF system will have eight generator-antenna units initially delivering 24MW for 20s pulses. Subsequently, each amplifier unit will be upgraded to 4MW, using a more powerful tetrode in the final amplification stage. New water-cooled antennae have been built and tested for insertion inside the toroidal belt limiter.

### 2.3. Neutral Beam System

A long pulse (~10s) neutral beam (NB) injector with eight beam sources and one integrated beam line system has been operated on JET since early 1986. H beams have been injected into D plasmas with particle energies (in the full energy fraction) of up to 65keV. The neutral power fractions were 69%, 23% and 8% in the full, half and one-third energy components, respectively, giving a total beam power of ~5.5MW injected into the torus. D beams have also been injected into D plasmas, with particle energies up to 75keV (injected power fractions of 76%, 17% and 7%) giving a total power up to 10MW. Up to 40MJ have been delivered to the plasma during a pulse. The second neutral injection box will be available for operation on the machine in mid-1987.

### 2.4. Diagnostics

About 30 different diagnostics have been installed on JET, allowing cross measurements of the main plasma parameters and detailed analysis of some of the plasma features such as sawteeth oscillations and MHD behaviour [5]. The ECE diagnostic is the main instrument for providing electron temperature profiles and infra-red interferometry is the main technique for density profiles. The ion temperature is measured by three different techniques; charge-exchange neutrals, Doppler broadening of  $\text{Ni}^{26+}$  and of resonant charge-exchange lines of light impurities. Flux measurements and spectrometry of 2.4MeV neutrons are also used.  $Z_{eff}$  is measured by visible bremsstrahlung and is in agreement with estimates from neoclassical resistivity.

## 3. Experimental Results

### 3.1. Overall Plasma Parameters

Experiments have been performed in JET in different configurations: limiter discharges on the inner or outer walls and X-Point discharges with single or double null. Various heating scenarios have been used ranging from ohmic heating alone to combinations of ohmic, RF and NB. The variation of the main JET parameters is presented in Table II. Several examples of typical pulses under these various conditions are indicated in Fig. 1, which show the density ( $n$ ), electron temperature ( $T_e$ ) and safety factor ( $q$ ) profiles, with ion temperature ( $T_i$ ) measurements where available.

Each heating method has its own characteristic power deposition profile. For ICRF, it is well localised (half width ~30cm), as shown in Ref. [4], and can be varied across the plasma by changing either the toroidal field or the frequency. The NB deposition profiles are usually less peaked on axis, and are quite flat at high densities.

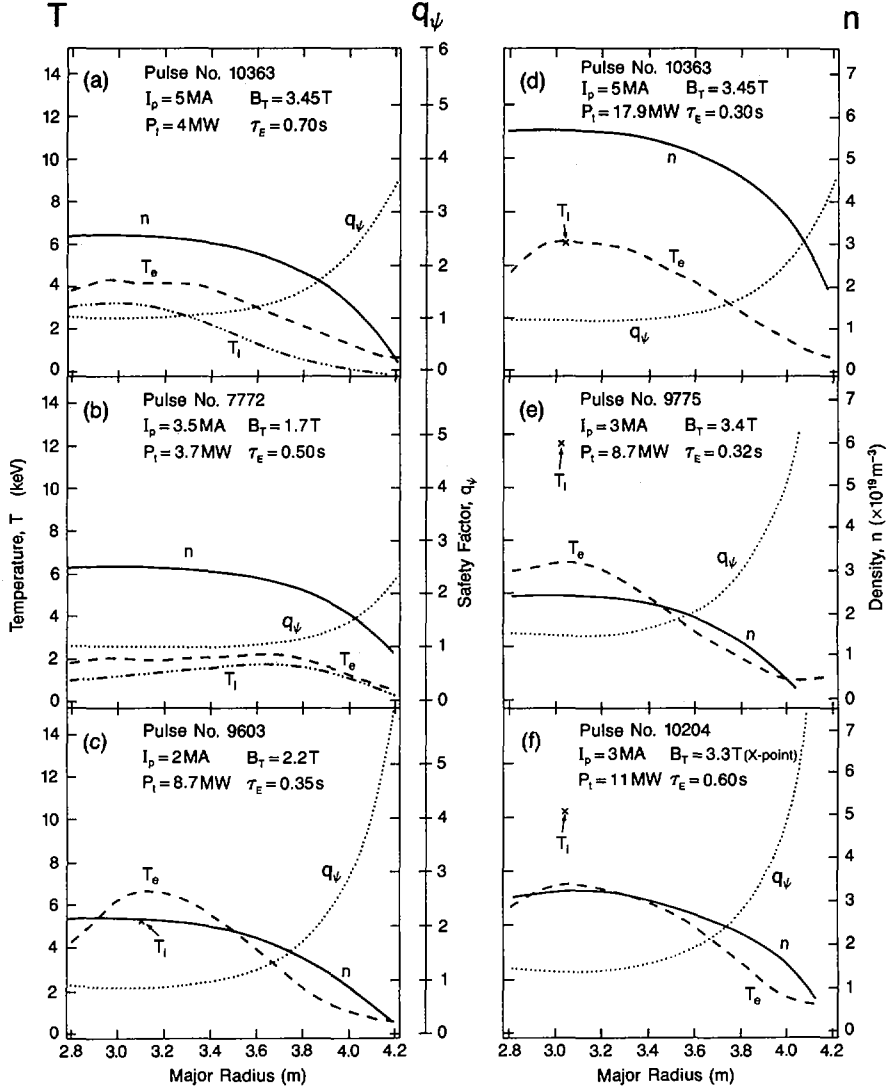
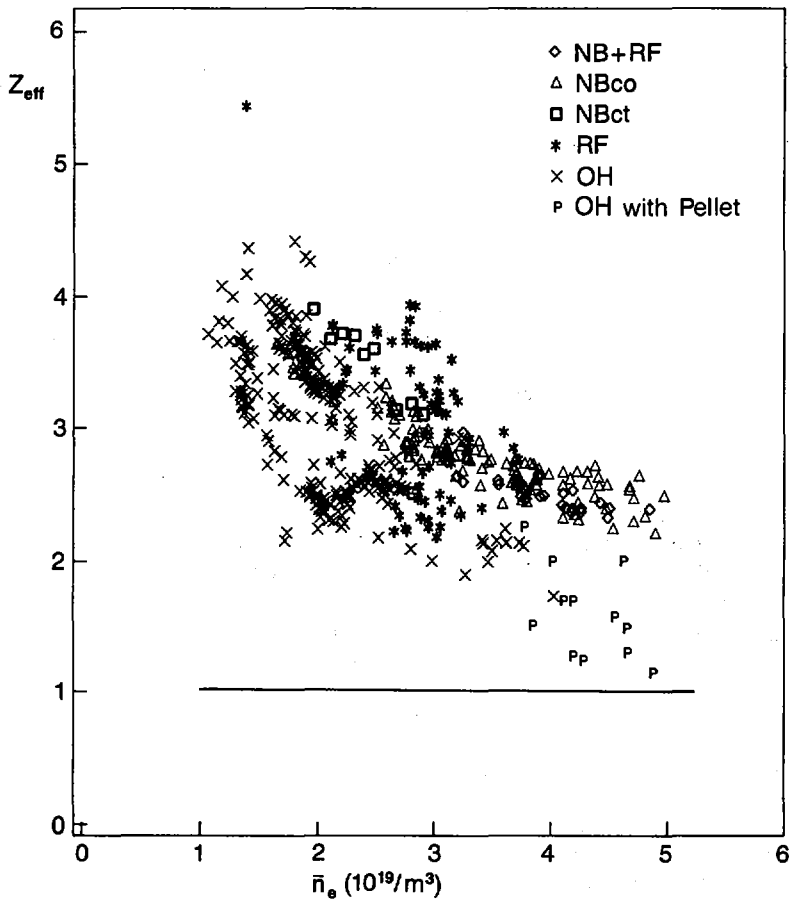


FIG. 1. Density ( $n$ ), electron temperature ( $T_e$ ) and safety factor ( $q$ ) as a function of major radius. The ion temperature ( $T_i$ ) is shown where available. These profiles are indicated for the following cases: (a) 5 MA pulse (No: 10363), ohmic heating only,  $B_T = 3.45 \text{ T}$ . (b) Low  $q$  pulse (No. 7772), ohmic heating only,  $I_p = 3.5 \text{ MA}$ ,  $B_T = 1.7 \text{ T}$ . (c) Monster sawtooth pulse (No. 9603),  $P_{\text{add}} = 6.1 \text{ MW}$ . (d) 5 MA pulse (No. 10363) with 15.2 MW of RF + NB power,  $B_T = 3.45 \text{ T}$ . (e) High  $T_i$  pulse (No. 9775),  $P_{\text{add}} = 8 \text{ MW}$ . (f) X-point configuration pulse (No. 10204),  $I_p = 3 \text{ MA}$ ,  $P_{\text{add}} = 8.2 \text{ MW}$ .

TABLE II. RANGE OF MAIN JET PLASMA PARAMETERS

Parameter	Value
Toroidal field (plasma centre) $B_t$	1.7-3.4T
Plasma current, $I_p$	1-5MA
Flux safety factor at edge, $q_\psi$	2.2-16
Volume averaged density, $\bar{n}_e$	$0.5-5 \times 10^{19} \text{m}^{-3}$
Central electron temperature, $\hat{T}_e$	2-7.5keV
Central ion temperature, $\hat{T}_i$	1.5-12keV
Energy confinement time, $\tau_E$	0.2-0.9s

FIG. 2.  $Z_{\text{eff}}$  as a function of average density for various plasma conditions.

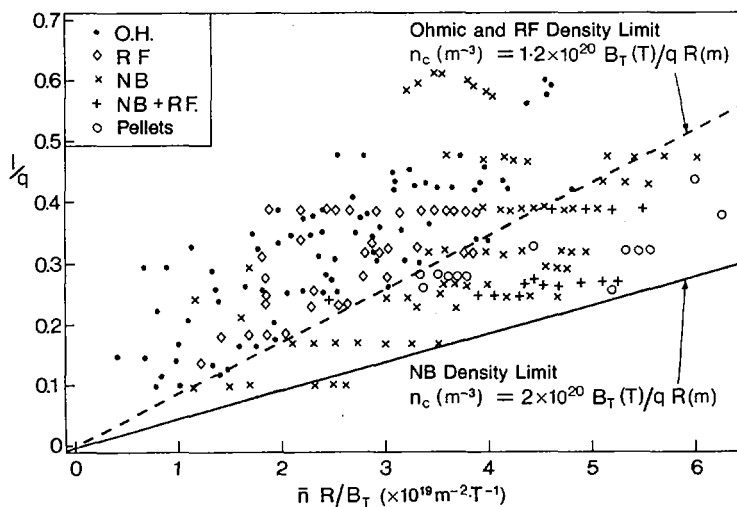


FIG. 3. Normalized current ( $= (2\pi R I_p / AB_T) = l/q$ ) versus normalized density ( $= \bar{n}R/B_T$ ).

The following parameters have been obtained under different conditions:

- (a) With ohmic heating, peak ion and electron temperatures of 3keV and 4keV, respectively, were achieved with a plasma density  $\sim 4.2 \times 10^{19} \text{m}^{-3}$  and energy confinement times exceeding 0.8s;
- (b) With RF heating, the peak electron and ion temperatures have reached 5.5keV with peak ion densities of  $3.5 \times 10^{19} \text{m}^{-3}$ . However, the confinement time has dropped to  $\tau_E = 0.3\text{s}$ ;
- (c) Ion temperatures up to 6.5keV at mean densities of  $3 \times 10^{19} \text{m}^{-3}$  have been produced with neutral beam heating. At lower peak densities ( $\sim 1.5 \times 10^{19} \text{m}^{-3}$ ), ion temperatures  $\geq 12.5\text{keV}$  have been observed (Fig.1(e)). Again, there was a degradation in confinement time down to 0.3-0.4s. In addition, with  $\sim 7\text{MW}$  of neutral beam injection, current drive of 0.4MA has been observed at a mean density of  $2 \times 10^{19} \text{m}^{-3}$ ;
- (d) Combined RF and neutral beam heating has coupled power up to 15MW to the plasma in a 5MA discharge: the plasma energy content was  $\sim 6\text{MJ}$  (Fig.1(d)).

The JET impurity behaviour is similar to that observed in other ungettered tokamaks with graphite limiters [3]. The main impurities in ohmic and neutral beam heated plasmas are carbon and oxygen and principally carbon at high electron density,  $n_e$ . During ICRH, moderate metal concentrations (0.1%  $n_e$ ) are responsible for  $\sim 20\%$  of the total radiation power losses. These can be prevented temporarily by carbonisation. Radiation power losses represent 30-60% of the total heating power,  $P_{tot}$ , during NBH and 40-70% of  $P_{tot}$  for ICRH. Most of the radiated power is emitted from the edge plasma.  $Z_{eff}$  varies from 3.5 at low  $n_e$  to 2.5 at high  $n_e$ . With NB injection,  $Z_{eff}$  falls to values of 2-3 and with pellet injection, it can fall to values close to 1 (see Fig.2).

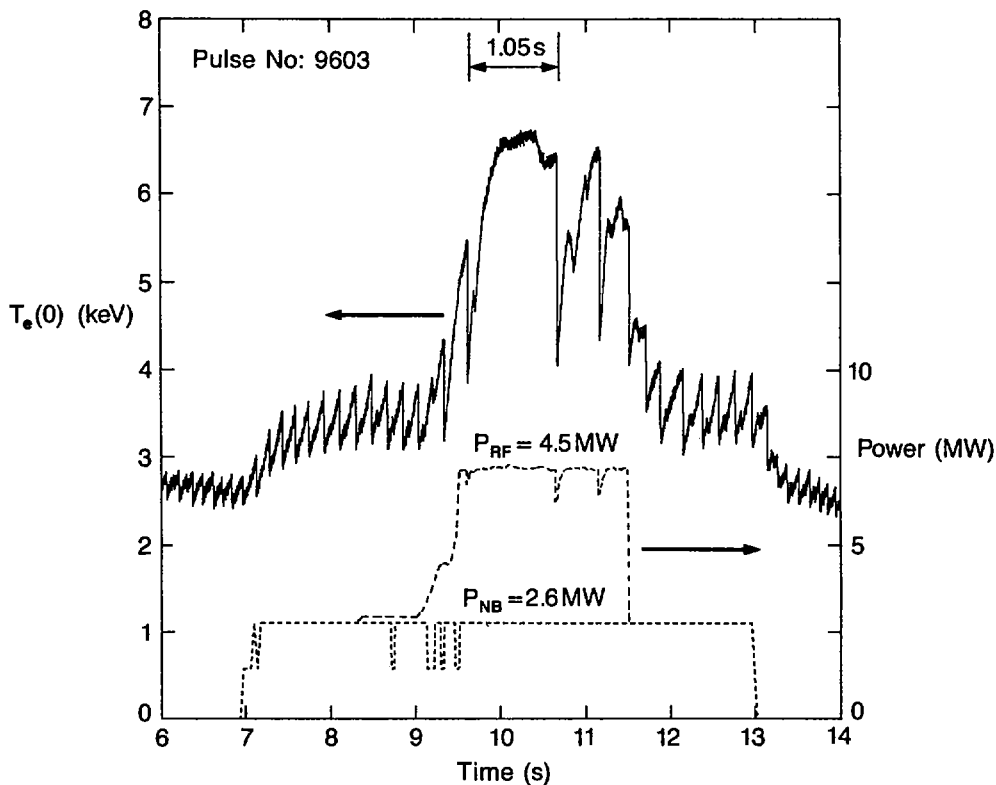


FIG. 4. Sawtooth oscillations of the central electron temperature, showing the effects of NB and RF additional heating.

### 3.2. Density Limits

The Hugill diagram for JET is shown in Fig.3, where the operating domain is limited by disruptive instabilities. In ohmic plasmas, the density limit is  $n_c(\text{OH})(\text{m}^{-3}) = 1.2 \times 10^{20} B_T(T)/qR(\text{m})$ . This limit depends on plasma purity. In RF heated discharges, it is only slightly increased, possibly because the effect of the extra power is cancelled by an increase in impurities. In neutral beam heated plasmas, the limit is substantially increased, as shown in Fig.3, to  $n_c(\text{NB})(\text{m}^{-3}) = 2.0 \times 10^{20} B_T(T)/qR(\text{m})$ . Switching off neutral beams at high density causes the plasma to disrupt, which indicates that the power input plays an important role in the disruption mechanism. Preliminary experiments with a single-shot pellet injector have also exceeded the OH density limit.

Density limit disruptions are always preceded by an increase in the impurity radiation at the plasma edge [6]. This is seen to cause a contraction of the electron temperature profile, which is followed by the growth of coherent MHD activity (principally  $m = 2, n = 1$ ). Alternative theoretical models predict that either the contraction of the temperature profile leads to an unstable current profile [6], or that the increased radiation losses at the  $q = 2$  surface lead to a thermal instability [7], but it is possible that both of these effects

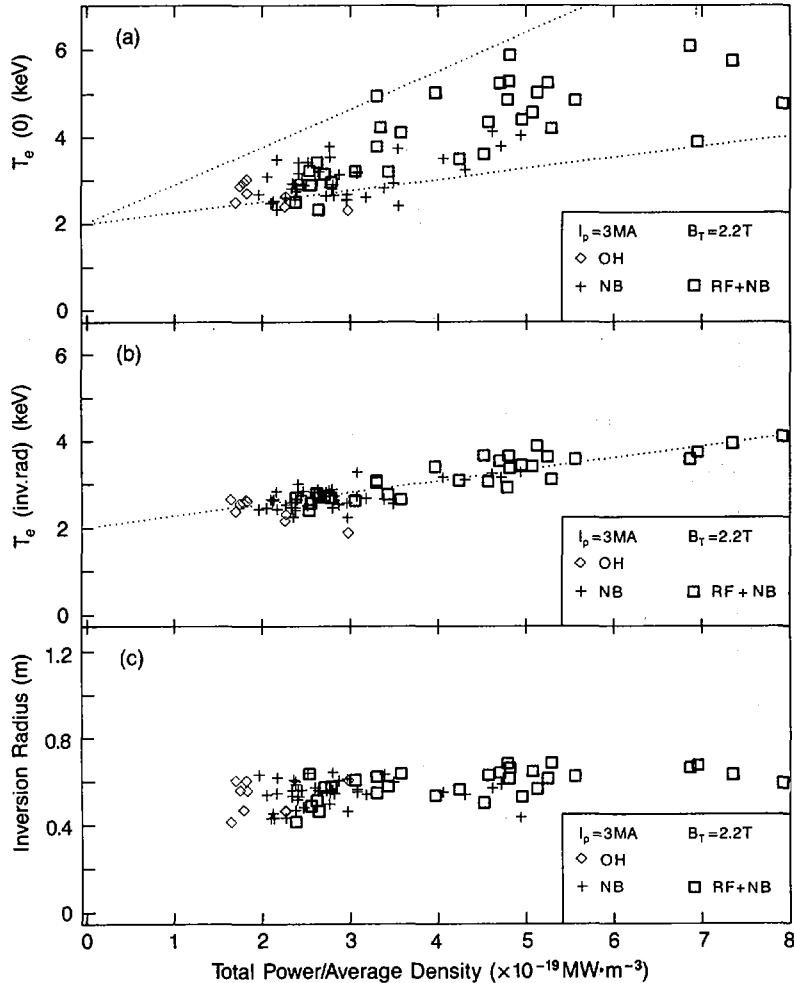


FIG. 5. (a) Electron temperature at the centre, (b) electron temperatures at the inversion radius ( $q \approx 1$ ), and (c) inversion radius as a function of power input per particle, for ohmic, RF, NB and combined heating cases ( $I_p = 3 \text{ MA}$ ;  $B_T = 2.2 \text{ T}$ ).

may be involved [8]. Both models result in the growth of an  $m=2, n=1$  island before the disruption. Observations and theoretical considerations both show that the central plasma density can be increased by deep fuelling.

### 3.3. Temperature Effects

Sawtooth oscillations occur in almost all JET discharges. As these instabilities, in general, limit the peak ion and electron temperatures, and may affect, in certain cases, the global

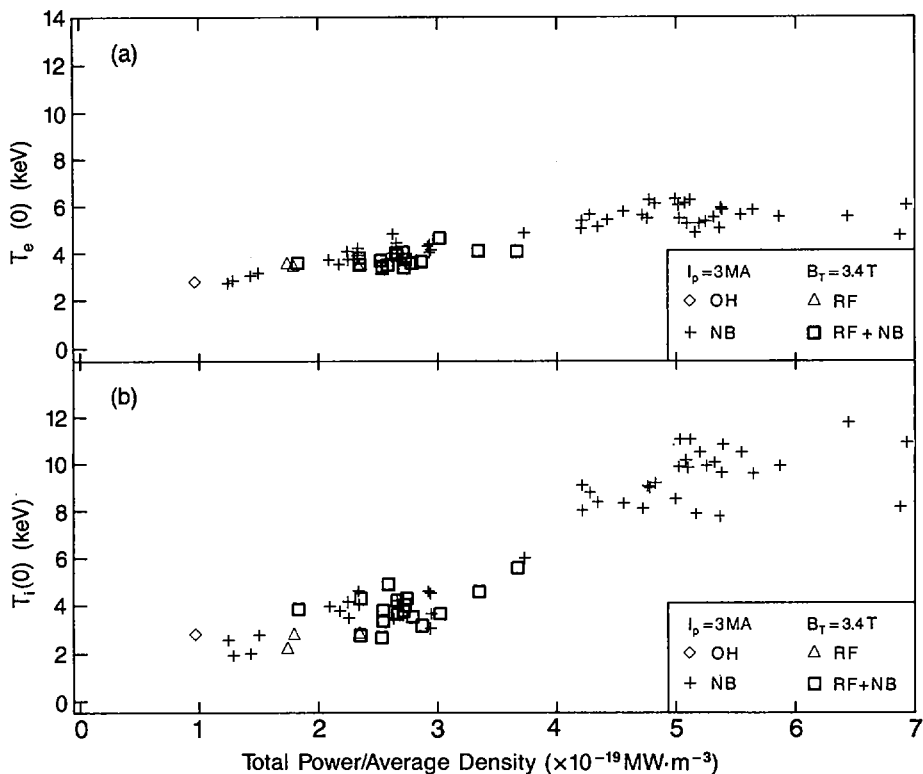


FIG. 6. (a) Electron temperature ( $T_e$ ) at the centre, and (b) ion temperature ( $T_i$ ) at the centre, as a function of power input per particle for various heating scenarios.

energy confinement times, they justify a careful analysis. With central deposition of additional power, sawteeth may develop large amplitudes (up to doubling the central electron temperature) and long periods (up to 0.6s) [6]. In some circumstances, with combined NB and RF, 'monster' sawteeth have been observed (see Fig.4). They are characterised by long durations of 0.8 - 1.2s and strong reduction of the low  $m, n$  numbers MHD activity. The instability mechanism of the sawteeth is described by a model involving ideal MHD [8].

The peak electron temperature  $T_e(0)$  can be raised significantly above the value reached in the ohmic phase as shown in Fig.5(a). The dispersion seen in  $T_e(0)$  is due to sawteething and to variations in profile deposition of the additional power. By contrast, the electron temperature at the inversion radius ( $q \sim 1$  surface) shows only a weak dependence with the power input per particle ( $P/\bar{n}$ ) for a given plasma current and toroidal field (Fig.5(b)), and no explicit density dependence. The radius of inversion is independent of  $P/\bar{n}$  in the range shown (Fig.5(c)).

The ion temperature behaviour appears quite different; the peak ion temperature  $T_i(0)$  (deduced from the X-ray crystal spectrometer) is plotted versus  $P/\bar{n}$  in Fig.6(b). Above  $4 \times 10^{19} \text{ MW} \cdot \text{m}^{-3}$ , the ion temperature can greatly exceed the electron temperature and can reach 12.5keV in JET. A broadening of the ion temperature profile is also observed in cases of off-axis ICRF heating [4].

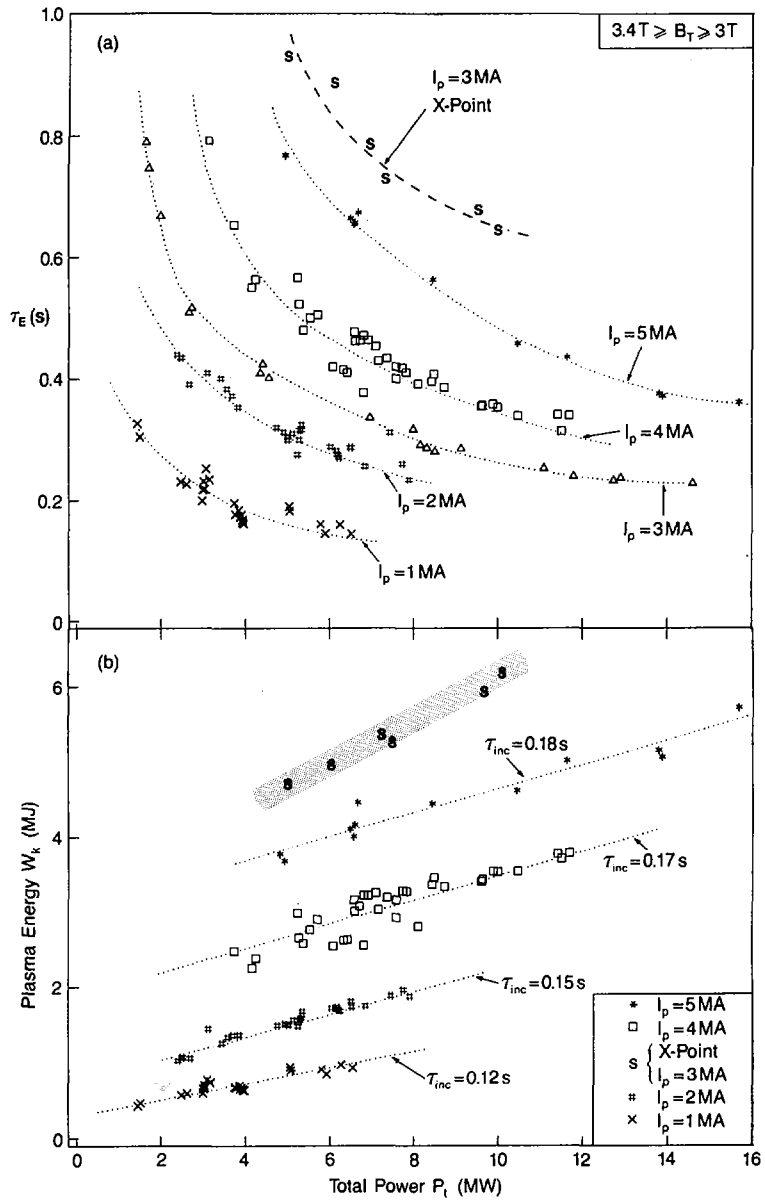


FIG. 7. (a) Energy confinement time  $\tau_E$  as a function of additional heating power (at  $I_p = 1, 2, 3, 4$  and  $5$  MA;  $3.4 T \geq B_T \geq 3.0 T$ ). (b) Plasma energy content  $W_k$  versus total input power  $P_t$  with NBI and ICRF heating ( $I_p = 1, 2, 4$  and  $5$  MA;  $3.4 T \geq B_T \geq 3.0 T$ ). X-point values at  $I_p = 3$  MA are shown for comparison.

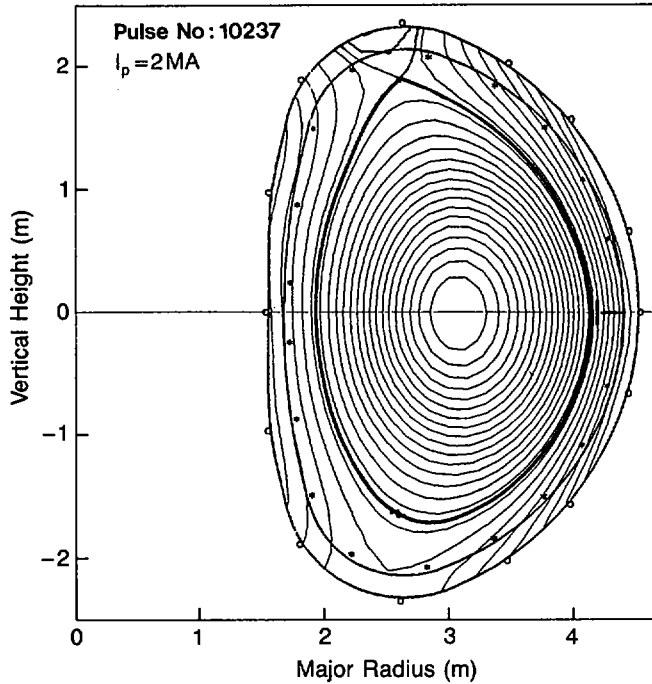


FIG. 8. Single-null X-point configuration at  $I_p = 2.0$  MA.

### 3.4. Confinement Degradation

The definition of the total energy confinement time used at JET is  $\tau_E = W_k / [P_t - dW_k/dt]$ , where  $W_k$  is the kinetic energy and  $P_t$  is the total input power to the plasma without subtracting radiation losses. Reported values of  $\tau_E$  are quasi-stationary.

With additional heating, the confinement time,  $\tau_E$ , degrades with increasing input power (Fig.7(a)), as seen in a number of other experiments. The degradation is independent of type of heating, whether RF, NB or combined. The rate of increase in  $W_k$  with  $P_t$  ( $= \Delta W_k / \Delta P_t$ ) appears to reach a limit of 0.1-0.3 MJ/MW (=s) at high powers (see Fig.7(b)). This suggests a lower limit to the global confinement time,  $\tau_E$ , of 0.1-0.3s in JET, independent of type of additional heating. Confinement time depends weakly on plasma density but scales favourably with plasma current.

Since the plasma energy is a function of  $n_i$ ,  $T_e$  and  $T_i$ , the degradation in confinement time is consistent with the observation that the electron temperature, at the inversion radius ( $q=1$  surface) increases little with power input and only the central temperature ( $T_e(0)$ ) shows an increase dependent on the central input power (see Fig.7(a) and (b)).

### 3.5. X-Point Regime

A better confinement regime with additionally heated plasmas has been observed (H-mode) in some Tokamaks with magnetic limiters or divertors. Stable discharges with magnetic separatrix (or X-Point) inside the vessel have been maintained in JET for several seconds,

TABLE III. MAXIMUM VALUES OF  $\langle n_i(0)\tau_E T_i(0) \rangle$ 

Experimental programme	Peak density	Energy confinement time	Ion temperature	Fusion parameter	$Q_{DT}$ equivalent	Plasma current
	$n_i(0)$ ( $10^{19} \text{ m}^{-3}$ )	$\tau_E$ (s)	$T_i(0)$ (keV)	$\langle n_i(0)\tau_E T_i(0) \rangle$ ( $10^{19} \text{ m}^{-3} \cdot \text{s} \cdot \text{keV}$ )	$Q_{DT}$	$I_p$ (MA)
Ohmic (4.6 MW)	4.2	0.8	3.0	10	0.010	5
ICRF (7 MW)	3.7	0.3	5.4	6	0.012	3
NBI (6 MW)						
High $n_i$	4.4	0.4	4.0	7	0.10 <sup>a</sup>	3
Low $n_i$	1.5	0.4	10	6	0.20 <sup>a</sup>	3
Combined NBI + RF (14 MW)	5.0	0.4	3.5	7	0.10 <sup>a</sup>	3
X-point (NB 10 MW)	5	0.65	6	20	0.15 <sup>a</sup>	3

<sup>a</sup> Beam-plasma reactions are dominant.

at plasma currents up to 3.0MA with a single null (Fig.8) and up to 2.5MA with a double null [9]. While interaction of the discharges with the limiters was curtailed, localised power deposition on the top and bottom target plates has limited the total input power to 10MW. The main objectives of these experiments are (i) to study the conditions of creation of a high density highly radiative region at the X-point capable of screening and isolating the main bulk plasma and (ii) to study the global confinement characteristics in comparison with limiter discharges. Evidence exists of the formation of a dense plasma near the X-Point, with average density  $1-2 \times 10^{20} \text{ m}^{-3}$ , corresponding to an order of magnitude higher than the average value of the main plasma density. There is also evidence that up to 40% of the total input power could be radiated by a  $\sim 20\text{cm} \times 20\text{cm}$  toroidal annulus around the X-Point in the high density discharges with additional power.

As shown in Fig.7, the increase in total energy content (and hence global confinement time) in single-null configurations is observed to be about twice that observed with limiters. In these conditions, both average electron and ion temperatures appear to be higher, and there are indications of changes in edge plasma suggesting an H-mode.

### 3.6. Slide-away Discharges

A preliminary study of slide-away discharges has also started with a view to decoupling currents and electron temperature. In these conditions, a plasma with 3MA and a mean density just below  $10^{19}\text{m}^{-3}$  has been obtained with a good confinement time for these conditions ( $\sim 0.6\text{-}0.7\text{s}$ ). The voltage per turn was 0.2V. When trying to increase the density by gas puffing, the discharge reverted to normal conditions.

### 3.7. Progress Towards Breakeven

Neutron yields  $> 2.8 \times 10^{15}\text{s}^{-1}$  have been obtained with D injection, mainly from beam-plasma D-D reactions. The best ratio of fusion power to input power obtained was  $Q_{DD} = 4 \times 10^{-4}$ , which is equivalent to  $Q_{DT} \sim 0.2$  and would have corresponded to a fusion power production of  $\sim 2\text{MW}$  (see Table II).

Fusion products  $\langle \hat{n}_i \tau_E \hat{T}_i \rangle \approx 10^{20}\text{m}^{-3}\cdot\text{s}\cdot\text{keV}$  have been achieved in JET (compared with the value  $5 \times 10^{21}\text{m}^{-3}\cdot\text{s}\cdot\text{keV}$  required in a reactor) in an ohmic discharge at 5MA and a value of  $2 \times 10^{20}\text{m}^{-3}\cdot\text{s}\cdot\text{keV}$  has been obtained in an X-Point discharge at 3MA current. However, additional heating has not yet been optimized into 5MA discharges. Under optimum conditions at lower currents, the values are similar for ohmic heating only, RF, NB, and combined heating cases, the degradation in  $\tau_E$  with additional heating offsetting gains in other parameters (see Table III).

## 4. Progress in Understanding Heat Transport

JET data have been used to assess the status of theoretical understanding of heat transport [10]. Local fluxes have been derived from measurements and compared with presently available theoretical values. No acceptable agreement has been found. However, the scaling of global energy confinement time with the dimensionless plasma physics parameters suggests that the underlying heat transport is a consequence of resistive MHD instabilities [11]. The topology of the magnetic field including chaotic regions and small islands could account for the heat fluxes observed in JET [12]. Such a model is also consistent with the existence of an H-mode.

As  $\alpha$ -particles mostly heat the electrons, it is imperative to obtain better control of their temperature, especially inside the  $q=1$  surface (ie sawteeth). A possible approach to increase  $T_e(0)$  is to control the profile of current and achieve a flat current distribution ( $q \approx 1$ ,  $q' \approx 0$ ) in the central region, in order to stabilize or at least delay the sawtooth crash significantly.

## 5. The JET Strategy and Future Programme

The JET strategy is to optimize the fusion product  $\langle \hat{n}_i \hat{T}_i \tau_E \rangle$ . Attempts will be made to maintain  $\tau_E$  with additional heating near to present values, and to increase the central density and temperature.

In order to obtain higher levels of performance, additional equipment is required on JET. Fig.9 shows the plasma profiles which are envisaged. They correspond to an energy content of  $\sim 20\text{MJ}$  and would produce  $\sim 10\text{MW}$  of  $\alpha$ -power. If  $\tau_E \sim 0.3\text{-}0.4\text{s}$ ,  $Q_{DT}$  should reach 1  $\sim$  2.

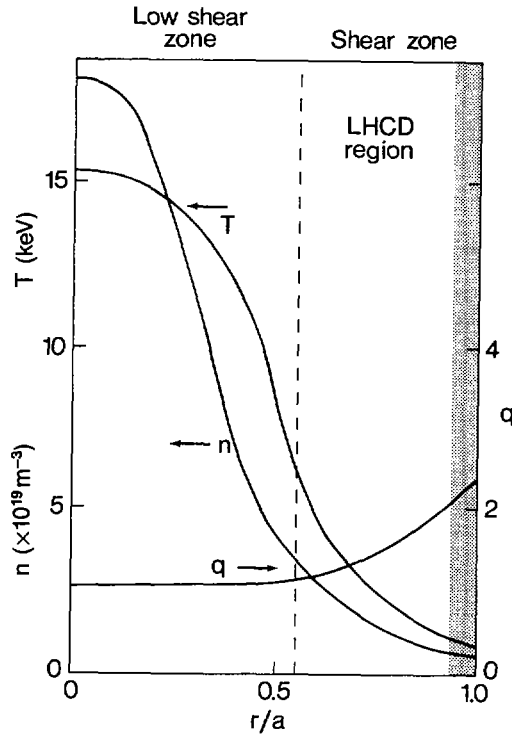


FIG. 9. Density ( $n$ ), temperature ( $T$ ) and safety factor ( $q$ ) profiles aimed for according to the latest JET strategy. The shaded area represents the zone  $q = 2$ .

Such plasma parameters could be obtained in the following ways:

- (i) Sawteeth oscillations should be stabilized or have periods of several confinement times. This should be achieved by flat  $q$  profiles ( $q \geq 1$ ,  $q' = 0$ ) over a large plasma cross-section, working with a low  $q$  boundary and driving part of the current ( $\sim 2\text{-}3\text{MA}$ ) in the outer plasma by Lower Hybrid Current Drive (LHCD) ( $\sim 10\text{MW}$ ) and by NB injection. The ICRF antennae with proper phase control could also be used to launch a travelling wave and provide some additional localised current;
- (ii) Radiation cooling between the  $q=2$  surface and the plasma boundary would be minimised to allow operation below the major disruption limit and to provide high  $T_e$  on the edge. Low  $Z$  material (C or Be) would be used to take advantage of its low ionisation potential;
- (iii) Since the temperature at the  $q \sim 1$  surface is higher when the density is lowered, edge pumping will be used. Further advantages of low densities in the outer region would be the prevention of disruptions and higher efficiency for LHCD;
- (iv) The D-T density on axis would be increased up to  $1\text{-}2 \times 10^{20} \text{m}^{-3}$  by high velocity pellet injection ( $> 5\text{km/s}$ );
- (v) High central temperature ( $\sim 12\text{-}15\text{keV}$ ) would be achieved by a combination of 'on axis' ICRF heating, NBI at  $160\text{keV}$  and current profile control.

This scheme will be tested in two configurations: (a) with a magnetic separatrix at 4MA and (b) with limiters at current values up to 7MA. Such a low-q discharge has been simulated in JET (see Fig.1(b)).

The main aim of JET operation during the next phase will be to reach maximum performance with full additional heating power in deuterium plasmas, before proceeding to the final phase requiring the introduction of tritium. The starting date for D-T operations is linked to the performance reached in the previous phase and is expected in 1991.  $\alpha$ -particle production must be sufficient to analyse its effects on the plasma and to answer the question whether  $\alpha$ -particle heating degrades energy confinement as other heating methods. Although degradation is foreseen, this has direct consequences on the ignition margin and on the size of future devices.

## 6. Implications for a Reactor

Present results suggest that a way for a future reactor is to rely upon tight control of current and density profiles and intense heating inside the  $q=1$  surface to benefit from improved energy confinement and high central temperature (as proposed for JET). Alternatively, a size and current increase could lead to the required ignition temperature, without additional heating. The resulting simplification of the overall system could well compensate for the larger size. Scaling [13] suggests that in a Tokamak with a major radius of  $\sim \times 2.5$  that of JET, plasma volume of  $\sim 2000\text{m}^3$  and magnetic field slightly higher than in JET, a 15keV plasma with a confinement time of 15-25s could be reached with ohmic heating alone at a peak density  $\sim 2 \times 10^{19}\text{m}^{-3}$ , satisfying the ignition criterion. Then, the thermonuclear power output of the D-T burner could be increased by injecting fuel pellets: the thermal insulation should degrade as the additional heating provided by the  $\alpha$ -particles increases without a strong variation of temperature. Burn control would be performed entirely through density control.

## 7. Conclusions

The following conclusions can be drawn at this stage:

- (a) Both ICRF and neutral beam (NB) injection methods are effective in delivering power into the JET plasma with the expected profile depositions. Large central electron and ion temperature increases have been observed;  $T_e$  and  $T_i$  have both reached values of 7.5keV at densities of  $3 \times 10^{19}\text{m}^{-3}$ . At lower density ( $\sim 1.5 \times 10^{19}\text{m}^{-3}$ ),  $T_i \approx 12.5\text{keV}$  has been measured;
- (b) For both heating methods, plasma energy has increased with input power. About 6MJ energy has been achieved in JET plasmas with  $\sim 18\text{MW}$  of total power input. However, the rate of energy increase with power,  $(\Delta W_p / \Delta P_i) \sim 0.1-0.3\text{s}$ , is smaller than the corresponding ohmic confinement times ( $\tau_E \sim 0.6-0.8\text{s}$ ). The fusion product  $\langle n_i \tau_E T_i \rangle$  has reached values in excess of  $10^{20}\text{m}^{-3}\cdot\text{s}\cdot\text{keV}$ , both with ohmic heating at 5MA and with additional heating; the degradation in confinement offsets the gains in density and temperature;
- (c) A higher fusion product value of  $\sim 2 \times 10^{20}\text{m}^{-3}\cdot\text{s}\cdot\text{keV}$  has been obtained in X-point configuration at lower current ( $\sim 3\text{MA}$ ). Values of  $\tau_E \approx 0.6-0.7\text{s}$  and  $T_i$  up 10keV were achieved with neutron production  $\sim 2 \times 10^{15}\text{ns}^{-1}$ , equivalent to a thermal  $Q_{DT}=0.1$ , the total  $Q_{DT}$  being  $\sim 0.15$ ;

- (d) In the central region (inside the inversion radius) between sawtooth collapses, additional heating is effective in increasing the electron temperature of the plasma (cf monster sawteeth);
- (e) Outside this region, electron heating is poor. The electrons seem to be the main energy loss channel, which appears related to confinement properties and not to the heating process;
- (f) Good prospects exist on JET for production of several MW of  $\alpha$ -particle power at a value  $Q_{DT} \approx 1$ ;
- (g)  $\alpha$ -particle heating is expected to behave in a similar fashion to other heating methods. Therefore, a reactor must either: (i) work at moderate currents with sophisticated control of the central region; or (ii) work at high currents without the need for complex control and additional heating.

## REFERENCES

- [1] HUGUET, M., et al., in Fusion Technology (SOFT) (Proc. 13th Symp. Varese, 1984), Vol. 1, Commission of the European Communities, Brussels (1984) 91.
- [2] LALLIA, P.P., et al., Plasma Phys. Contr. Fusion **28** (1986) 55.
- [3] BEHRINGER, K., et al., Paper IAEA-CN-47/A-IV-1, these Proceedings, Vol. 1.
- [4] JACQUINOT, J., et al., Paper IAEA-CN-47/F-I-1, these Proceedings, Vol. 1.
- [5] JET TEAM, Progress Rep. EUR-JET-PR-3 (EUR-10616.EN), Commission of the European Communities, Abingdon (1985).
- [6] CAMPBELL, D.J., et al., Paper IAEA-CN-47/A-VII-5, these Proceedings, Vol. 1.
- [7] REBUT, P.H., HUGON, M., in Plasma Physics and Controlled Nuclear Fusion Research 1984 (Proc. 10th Int. Conf. London, 1984), Vol. 2, IAEA, Vienna (1985) 197.
- [8] WESSON, J.A., et al., Paper IAEA-CN-47/E-I-1-1, these Proceedings, Vol. 1.
- [9] TANGA, A., et al., Paper IAEA-CN-47/A-I-1, these Proceedings, Vol. 1.
- [10] DÜCHS, D.F., et al., Paper IAEA-CN-47/A-VI-1-1, these Proceedings, Vol. 1.
- [11] CORDEY, J.G., et al., Paper IAEA-CN-47/A-II-3, these Proceedings, Vol. 1.
- [12] REBUT, P.H., et al., Paper IAEA-CN-47/E-III-4, these Proceedings, Vol. 2.
- [13] THOMSON, K., et al., in Controlled Fusion and Plasma Heating (Proc. 13th Europ. Conf. Schliersee, 1986), Vol. 10c, Pt 1, European Physical Society (1986) 29.

## DISCUSSION

R.J. GOLDSTON: In your presentation you mentioned the 'hot ion regime' at  $I_p = 3$  MA, which had  $\tau_E = 0.6$  s, for  $P_e \sim 9$  MW. Could you say how this fits into the broader set of data you have for X-point and limiter discharges?

P.H. REBUT: In the case of a pure hot ion mode the confinement time (pulse No. 9775 in Fig. 1(e)) is only 0.32 s. With X-point and H-mode operation, 0.6 s can be reached with a relatively high ion temperature of about 10 keV in the centre. This set of results does fit into the general JET data set.

H. HORA: What was the highest number of fusion neutrons you measured and what was the input energy, i.e. neutral beam plus tokamak operation?

P.H. REBUT: The highest number of neutrons per second emitted from JET is  $2.8 \times 10^{15}$ . The injected power was 8 MW, into a plasma limited on the inner wall.

R.R. WEYNANTS: With regard to the X-point operation, can you comment on, first, the OH plasma confinement, and, second, the existence of a power threshold?

P.H. REBUT: A minimum power of 6–8 MW was needed to obtain good confinement properties in the X-point mode of operation, which is a gain of up to a factor of two. This corresponds to a different plasma regime at the edge, near the separatrix. If this edge regime is not achieved, there is little difference between an X-point configuration and a 'standard' one.

R.J. TAYLOR: For the high ion temperature mode, the electron energy confinement time must be considered separately. What is this time in the case of JET?

P.H. REBUT: I agree that the electron energy confinement time is dominant for a fusion reactor, but without a full profile of the ion temperature and without knowing the ion transport in detail it is difficult to consider the electron confinement time separately. It may be estimated from Fig. 1, taking into account that half of the power might perhaps be transported directly by the ions.

D. OVERSKEI: You indicated that  $\tau_E$  improved with increasing plasma current and with the use of a single-null diverted magnetic configuration. Could you say whether this increase in  $\tau_E$  is due predominantly to an increase in  $T_i(0)$  rather than to better confinement of ions?

P.H. REBUT: The increase in confinement is mainly due to a widening of the profiles and to a pedestal in the electron temperature.

B. COPPI: What values of the streaming parameters did you attain in order to observe the slide-away regime?

P.H. REBUT: We did not make any measurement of the electron temperature. The current was 3 MA and the central density was close to  $10^{19} \text{ m}^{-3}$ .



## TFTR PLASMA REGIMES

R.J. HAWRYLUK, V. ARUNASALAM, M.G. BELL, M. BITTER,  
 W.R. BLANCHARD, N.L. BRETZ, R. BUDNY, C.E. BUSH<sup>1</sup>, J.D. CALLEN<sup>2</sup>,  
 S.A. COHEN, S.K. COMBS<sup>1</sup>, S.L. DAVIS, D.L. DIMOCK, H.F. DYLLA,  
 P.C. EFTHIMION, L.C. EMERSON<sup>1</sup>, A.C. ENGLAND<sup>1</sup>, H.P. EUBANK,  
 R.J. FONCK, E. FREDRICKSON, H.P. FURTH, G. GAMMEL,  
 R.J. GOLDSTON, B. GREK, L.R. GRISHAM, G. HAMMETT,  
 W.W. HEIDBRINK<sup>3</sup>, H.W. HENDEL<sup>4</sup>, K.W. HILL, E. HINNOV, S. HIROE<sup>1</sup>,  
 H. HSUAN, R.A. HULSE, K.P. JAEHNIG, D. JASSBY, F.C. JOBES,  
 D.W. JOHNSON, L.C. JOHNSON, R. KAITA, R. KAMPERSCHROER,  
 S.M. KAYE, S.J. KILPATRICK, R.J. KNIZE, H. KUGEL, P.H. LaMARCHE,  
 B. LeBLANC, R. LITTLE, C.H. MA<sup>1</sup>, D.M. MANOS, D.K. MANSFIELD,  
 R.T. McCANN, M.P. McCARTHY, D.C. McCUNE, K. McGUIRE,  
 D.H. McNEILL, D.M. MEADE, S.S. MEDLEY, D.R. MIKKELSEN,  
 S.L. MILORA<sup>1</sup>, W. MORRIS<sup>5</sup>, D. MUELLER, V. MUKHOVATOV<sup>6</sup>,  
 E.B. NIESCHMIDT<sup>7</sup>, J. O'ROURKE<sup>8</sup>, D.K. OWENS, H. PARK,  
 N. POMPHREY, B. PRICHARD, A.T. RAMSEY, M.H. REDI,  
 A.L. ROQUEMORE, P.H. RUTHERFORD, N.R. SAUTHOFF, G. SCHILLING,  
 J. SCHIVELL, G.L. SCHMIDT, S.D. SCOTT, S. SESNIC, J.C. SINNIS,  
 F.J. STAUFFER<sup>9</sup>, B.C. STRATTON, G.D. TAIT, G. TAYLOR,  
 J.R. TIMBERLAKE, H.H. TOWNER, M. ULRICKSON, V. VERSHKOV<sup>6</sup>,  
 S. VON GOELER, F. WAGNER<sup>10</sup>, R. WIELAND, J.B. WILGEN<sup>1</sup>,  
 M. WILLIAMS, K.L. WONG, S. YOSHIKAWA, R. YOSHINO<sup>11</sup>,  
 K.M. YOUNG, M.C. ZARNSTORFF, V.S. ZAVERYAEV<sup>6</sup>, S.J. ZWEBEN

Princeton Plasma Physics Laboratory,  
 Princeton University,  
 Princeton, New Jersey,  
 United States of America

### Abstract

#### TFTR PLASMA REGIMES.

Significant extensions in the TFTR plasma operating regimes have been achieved with additional heating system capability, installation of a multishot pellet injector, and the development of an enhanced confinement regime. In ohmically heated pellet-fuelled discharges characterized by highly peaked

<sup>1</sup> Oak Ridge National Laboratory, Oak Ridge, TN, USA.

<sup>2</sup> University of Wisconsin, Madison, WI, USA.

<sup>3</sup> GA Technologies, Inc., San Diego, CA, USA.

<sup>4</sup> RCA David Sarnoff Research Centre, Princeton, NJ, USA.

<sup>5</sup> Balliol College, University of Oxford, Oxford, UK.

<sup>6</sup> Kurchatov Institute of Atomic Energy, Moscow, USSR.

<sup>7</sup> EG&G Idaho, Inc., Idaho Falls, ID, USA.

<sup>8</sup> JET Joint Undertaking, Abingdon, Oxfordshire, UK.

<sup>9</sup> University of Maryland, College Park, MD, USA.

<sup>10</sup> Max-Planck-Institut für Plasmaphysik, Garching, Fed. Rep. Germany.

<sup>11</sup> JAERI, Naka-machi, Naka-gun, Ibaraki-ken, Japan.

density profiles, enhancements in  $\tau_E$  have resulted in  $n_e(0)\tau_E(a)$  values of  $1.5 \times 10^{20} \text{ m}^{-3}\cdot\text{s}$ . In neutral beam heated discharges, an operating regime has been developed in which substantial improvements in energy confinement time and neutron source strength are observed. Ion temperatures of about 20 keV and  $n_e(0)\tau_E(a)T_i(0)$  values of  $2 \times 10^{20} \text{ m}^{-3}\cdot\text{s}\cdot\text{keV}$  have been achieved. This enhanced confinement regime is characterized by high values of  $\beta_p$  and low values of collisionality. The observed surface voltage, which is negative during beam injection, is compared with models including beam driven and bootstrap currents.

## I. Introduction

The goals of the TFTR project are (1) to study reactor-grade plasmas with temperatures of order 10 keV and densities of order  $10^{20} \text{ m}^{-3}$ , and (2) to achieve approximate breakeven between the power input to and the fusion output from the plasma ( $Q \sim 1$ ). During the past year, high-power neutral-beam-heating experiments and ohmic-heating experiments utilizing a deuterium pellet injector have significantly extended the operating regimes of TFTR, as measured by the  $n_e(0)\tau_E(a)T_i(0)$  product and the Q-value achieved in neutral-beam-heated discharges.

This paper gives a brief description of the TFTR device status and the operating regimes in gas-fueled and pellet-fueled ohmic discharges. A more extensive discussion of the pellet-fueled discharges is given by Schmidt et al. [1]. Results from neutral-beam-heating experiments in the standard regime are also summarized briefly. A general description is given of the operating characteristics of discharges in the enhanced confinement regime; further information is contained in the papers by Goldston et al.[2], McGuire et al.[3], and Hill et al. [4].

## II. Machine Status

An initial series of experiments with two (co-injecting) neutral beamlines was completed in April 1985, during which TFTR reached its original machine design specifications for plasma current and toroidal field ( $I_p = 2.5 \text{ MA}$  and  $B_T = 5.2 \text{ T}$ ) [5]. Subsequently, two additional  $p$  beamlines were installed; three beamlines are now aimed tangentially in the direction of the plasma current (co-injection), and one opposite (counter-injection). During the recent experiments, the maximum injected power was 20 MW with a full energy component of  $\sim 10 \text{ MW}$ . The maximum beam voltage was 110 kV and the maximum pulse duration 1.0 s. Most of the experiments were conducted with 0.5 s pulse lengths and an average beam voltage of  $\sim 95 \text{ keV}$ . Deuterium injection was used in all of the experiments discussed here. During the last beamline installation, a large-area axisymmetric inner wall limiter was also installed. This limiter is composed of water-cooled Inconel plates covered with graphite tiles. The toroidal inner wall limiter and moveable limiter define the present maximum plasma dimensions as  $R \approx 2.48 \text{ m}$  and  $a \approx 0.82 \text{ m}$ .

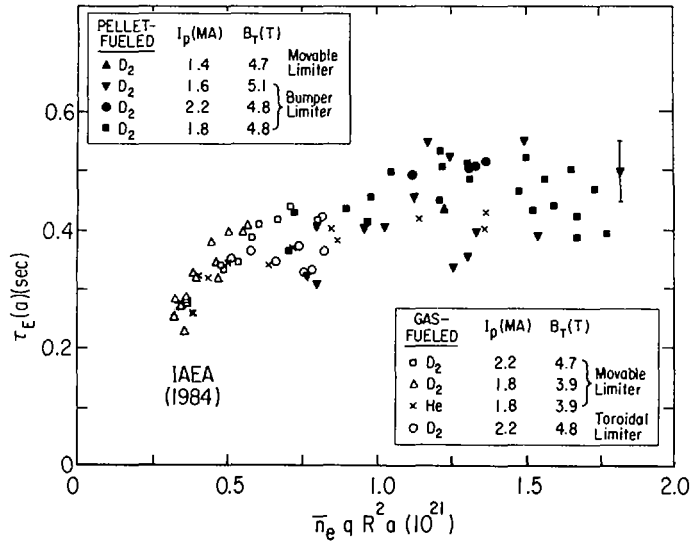


FIG. 1. Gross energy confinement versus  $\bar{n}_e q R^2 a$  for ohmically heated discharges with and without pellet injection. The 1.6 MA discharges had reduced aperture,  $a = 0.7$  m, compared with the other full-size 0.8 m discharges.

### III. Ohmically Heated Discharges

Initial ohmic experiments reported in 1984 [6] at modest toroidal fields ( $\leq 2.8$  T), plasma currents ( $\leq 1.4$  MA), and densities ( $\bar{n}_e < 3 \times 10^{19} \text{ m}^{-3}$ ) demonstrated that the global energy confinement time,  $\tau_E$ , scales consistent with  $\bar{n}_e q R^2 a$ , reaching a maximum value of  $\tau_E \sim 0.3$  s. Subsequent experiments utilizing both gas- and pellet-fueled discharges have concentrated on exploring the applicability of this scaling law over a wider operating range in density, toroidal field, and plasma current.

The analysis of the energy confinement time has relied principally upon a time-independent kinetic analysis code, SNAP, [5] and has been supplemented by magnetic measurements [7]. Figure 1 is a summary of the ohmic-heating studies for full bore plasmas. In gas-fueled deuterium discharges, the confinement time increases up to 0.44 s, in reasonable agreement with  $\bar{n}_e q R^2 a$  scaling for  $\bar{n}_e \leq 4.8 \times 10^{19} \text{ m}^{-3}$ . At higher densities, saturation is found to occur for both helium-gas and deuterium-pellet fueled discharges. In the high density regime, the confinement time is observed to be a weak function of plasma current.

In addition to increasing the line-averaged density, pellet injection produces highly peaked density profiles. A line-averaged density of  $1.4 \times 10^{20} \text{ m}^{-3}$  has been achieved 200 ms after the injection of five 2.7 mm pellets in experiments conducted on

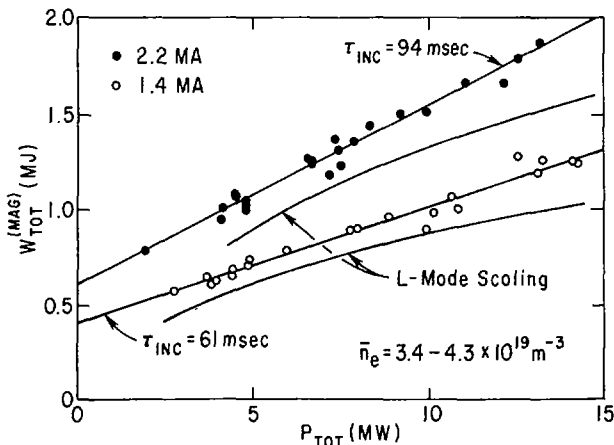


FIG. 2. Variation of the stored energy for 1.4 and 2.2 MA power scans, for a constrained density range and  $B_T = 4.8$  T,  $R = 2.48$  m,  $a = 0.82$  m. Magnetic measurements are compared with prediction of the Goldston L-mode model.

the inner graphite limiter. This corresponds to a Murakami parameter,  $\bar{n}_R/B_T = 6.5 \times 10^{19} \text{ m}^{-2} \text{ T}^{-1}$ . The central electron density was  $2.8 \times 10^{20} \text{ m}^{-3}$  and central electron temperature was 1.4 keV, as measured by Thomson scattering. This peaked density profile was achieved by operating with a reduced plasma minor radius of 0.7 m and a plasma current of 1.6 MA, in order to improve pellet penetration. The energy confinement time was  $\sim 0.50$  s according to kinetic and diamagnetic measurements corresponding to an  $\bar{n}_e(0)\tau_E \approx 1.4 \times 10^{20} \text{ m}^{-3} \cdot \text{s}$ . The energy confinement time is  $\sim 20\%$  greater than that achieved in gas-fueled discharges with the same values of  $I_p$ ,  $R$ , and  $a$ , using either deuterium or helium as the working gas.

#### IV. Neutral-Beam-Heating Studies in the Standard Regime

The variation of energy confinement time with injection power up to  $\sim 15$  MW was studied systematically. These experiments were conducted in the large plasma configuration on the inner wall limiter with deuterium gas fueling, deuterium beams,  $I_p = 1.4$  and 2.2 MA, and  $B_T = 4.8$  T [7]. Figure 2 shows the variation in the total stored energy for the 1.4 and 2.2 MA power scan with a constraint on the density at the end of injection. Kinetic and magnetic measurements (using the techniques described in Ref. 7) are in good agreement. The stored energy increases linearly with heating power; however, the rate of increase of stored energy,  $dW_p/dP_{\text{heat}}$ , is appreciably less than the ohmic confinement time. The gross energy confinement time  $\tau_E(a)$ , defined as  $W_{\text{TOT}}/(P_{\text{TOT}} - dW_{\text{TOT}}/dt)$ , where  $W_{\text{TOT}} = W_e + W_i + W_b$  and  $P_{\text{TOT}} = P_{\text{OH}} + P_{\text{INJ}}$  for the data shown in Fig. 2, can be fitted to a form  $\alpha + \beta/P_{\text{TOT}}$ , where  $\alpha$  is the "incremental" confinement time. In the plasma density

range of  $3.4 < \bar{n}_e < 4.3 \times 10^{19} \text{ m}^{-3}$ ,  $\alpha$  increases with plasma current from 61 ms to 94 ms as the current is increased from 1.4 to 2.2 MA. The energy confinement time is observed to depend weakly upon density; however, a negative scaling of  $\alpha$  with increased density is observed in the 1.4 MA discharges. At low density, the enhancement in stored energy at high power occurs in the beam and thermal ions, since the electron stored energy decreases slowly with decreasing density. The high-power beam heating in this current and density range results are also in fair agreement with the Goldston L-mode model [8] for hydrogen injection into deuterium plasma. Power-law fits to the data shown in Fig. 2 indicate that  $W_{\text{TOT}} \propto P_{\text{TOT}}^{0.46} I_p^{0.91}$  for  $P_{\text{TOT}} > 4 \text{ MW}$  [7].

#### V. Neutral Beam Heating in the Enhanced-Confinement Regime

Previous operation of TFTR at low  $I_p$  (0.4-1.0 MA) and moderate beam power ( $P_b < 6 \text{ MW}$ ) using only co-injection [5] allowed access to a very low-density regime ( $\bar{n}_e \sim 1 \times 10^{19} \text{ m}^{-3}$ ), characterized by high values of ion temperature ( $\sim 9 \text{ keV}$ ) and rapid toroidal rotation velocity (up to  $\sim 7 \times 10^5 \text{ m/s}$ ). Recent experiments in this regime conducted at higher power ( $\leq 20 \text{ MW}$ ), using both co- and counter-injection, have demonstrated enhanced confinement relative to the predictions of L-mode scaling, along with central ion temperatures of  $\sim 20 \text{ keV}$  at  $\bar{n}_e \sim 3 \times 10^{19} \text{ m}^{-3}$  with a central  $n_e(0) \sim 7 \times 10^{19} \text{ m}^{-3}$  [9]. The achievement of this improved performance relative to the previous experiments is due to extensive degassing of the limiter and near-balanced injection ( $P_{\text{ctr}} \sim P_{\text{CO}}$ ).

A procedure that results in a low recycling rate, as shown by decreases in the  $D_\alpha$  emission and edge neutral pressure, is identified to be critical in giving rise to the enhanced confinement regime [4,10]. Both low-density deuterium and helium discharges have been used to degas the inner wall. These high power discharges (0.8-1.8 MA) were not fueled following breakdown. Helium discharges were more effective in reducing the low-density limit and the decay time of the density following a diagnostic gas puff. The density decay time has been decreased from  $> 5 \text{ s}$  to as low as  $\approx 0.15 \text{ s}$  after extensive degassing. The low initial density of the target plasma and relatively high  $Z_{\text{eff}} \sim 6$  is a consequence of the degassing procedure which effectively removes  $D^+$  from the target plasma. The large density rise during injection [ $\bar{n}_e(\text{final})/\bar{n}_e(\text{prior to injection}) \leq 3-4$ ] is accompanied by a decrease in  $Z_{\text{eff}}$  to  $\sim 3$  at the end of injection.

Figure 3 shows a comparison of the temporal evolution of two discharges during neutral beam injection with different initial line-integral densities, different deuterium recycling rates due to different degassing histories, and comparable final line-integral densities. In the discharge with the lower initial density, both the neutron source strength and the stored energy

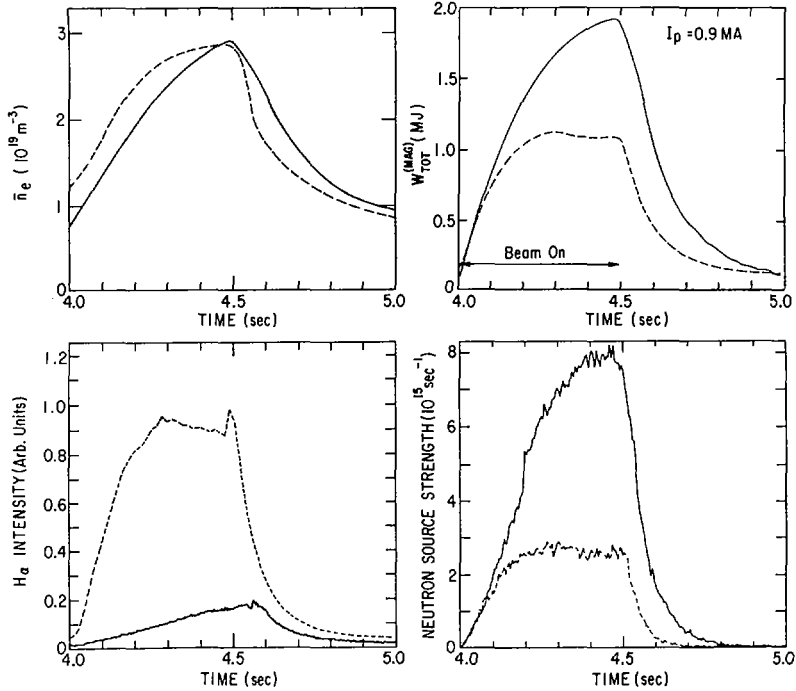


FIG. 3. Comparison of the evolution of line average density, neutron source strength,  $H_\alpha$  emission (which includes both  $H_\alpha$  and  $D_\alpha$  emission) and stored energy for two discharges. The solid curve corresponds to a supershot.  $R = 2.48$  m,  $a = 0.82$  m,  $P_b = 12.5$  MW and  $B_T = 4.7$  T in the supershot discharge, whereas  $P_b = 11.4$  MW and  $B_T = 5.0$  T in the other shot.

increase throughout the 0.5 s neutral-beam pulse. The global energy confinement time is also substantially longer. Discharges that exhibit continually rising stored energy and neutron source strength during the half-second beam-injection have been colloquially termed "supershots". Experiments conducted in the final days of the experimental run demonstrated continued increase in stored energy with 0.7 s duration beam pulses and that the stored energy approached equilibrium with 1.0 s duration pulses. At plasma currents up to 1 MA, values of  $\beta_p = 2.0$  from plasma diamagnetism have been measured. Maximum values of  $\beta_p$  up to 2.2 have been achieved transiently. These high values of  $\beta_p$  result in substantial outward shifts of the magnetic axis  $(R_{mag} - R_{geo})/a \lesssim 0.4$  and distortions of the plasma shape. The vertical elongation,  $\kappa$ , decreases from 1.05 to  $\lesssim 0.9$  in the most extreme cases. Figure 4 shows a comparison of the electron temperature and density profiles measured near the end of the pulse for the discharges shown in Fig. 3. The discharge with the lower initial density (supershot) has a more peaked density profile, with a higher central density and a much broader electron temperature profile. Peak central electron temperatures of  $\sim 6.5$  keV during injection have been obtained in supershots.

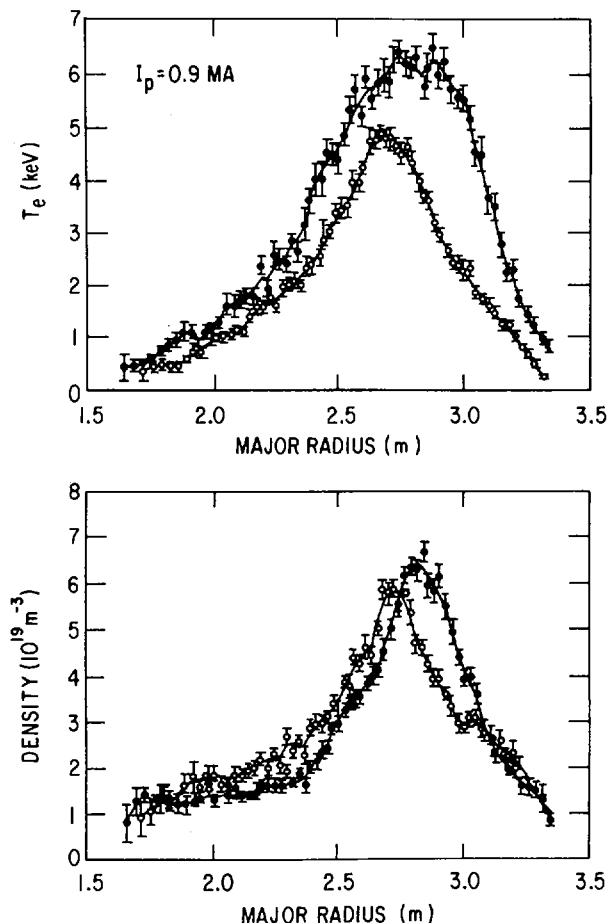


FIG. 4. Comparison of Thomson scattering measurements of the electron temperature and density profiles at 4.45 s for the discharges shown in Fig. 3. The solid points are for the supershot discharge and the open circles are for the other shot.

The central ion temperature is measured using several techniques. X-ray Doppler-broadening measurements have been carried out for Fe XXV and Ni XXVII  $K_{\alpha}$  lines using a horizontally viewing crystal spectrometer and three vertically viewing spectrometers. The horizontal channel is rendered ineffective, due to neutron noise during supershots. In the analysis of the vertical detectors the large shift in magnetic axis needs to be taken into account. For the data shown in Fig. 5, the emitting region viewed by the vertical detector is  $\sim 0.2$  m outside of the magnetic axis. Doppler-broadening measurements in the VUV have also been used to obtain central ion temperatures. The

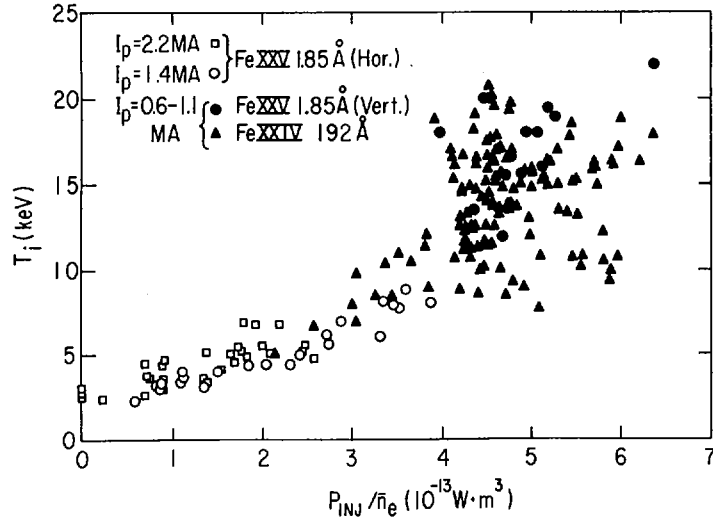


FIG. 5. Ion temperature versus  $P_{INJ}/\bar{n}_e$ . Closed symbols are for  $4.8 < B_T < 5.2$  T,  $0.8 \leq I_p \leq 1.0$  MA,  $R = 2.45$  m and  $a = 0.80$  m, and open symbols are for the discharges shown in Fig. 2.

spectrometer has a horizontal radial view of the plasma. One-dimensional impurity transport simulations including charge-exchange recombination indicate that the mean radius of the emission profile for the lithium-like ions used is  $\sim 0.2$  m. The heating beams have permitted preliminary spectroscopic measurements utilizing carbon lines excited by charge-exchange recombination. Good agreement between the various measurements is achieved.

Figure 5 shows the variation in central ion temperature for discharges in the standard neutral-beam-heating regime ( $I_p = 1.4$  and 2.2 MA) and for both super and non-super low-current discharges ( $0.6 < I_p < 1.1$  MA). In the low-current discharges, considerable variability in the heating results is obtained, reflecting the occurrence of MHD activity, variations in limiter history, and variations in the fraction of power in the co-direction. Taking into account uncertainties in the measurements and the calculated differences between the impurity and hydrogenic ion temperatures which are  $< 2$  keV, these results indicate central bulk ion temperatures of  $\sim 20$  keV. The maximum value of the ion heating efficiency parameter,  $\bar{n}_e \Delta T_i / P_{INJ}$ , is  $\sim 3.8 \times 10^{13}$  keV·W $^{-1}$ ·m $^{-3}$ . This is in comparison with previous experiments [5] in which  $\bar{n}_e \Delta T_i / P_{INJ}$  was  $\sim 1.5 \times 10^{13}$  keV·W $^{-1}$ ·m $^{-3}$ .

Figure 6 shows the scaling of stored energy with power. An important characteristic of the enhanced confinement regime is the fraction of power in the co-direction,  $P_{CO}/P_{INJ}$ . As shown in Fig. 6, at a given power the highest stored energy (and hence  $\tau_E$ ) is

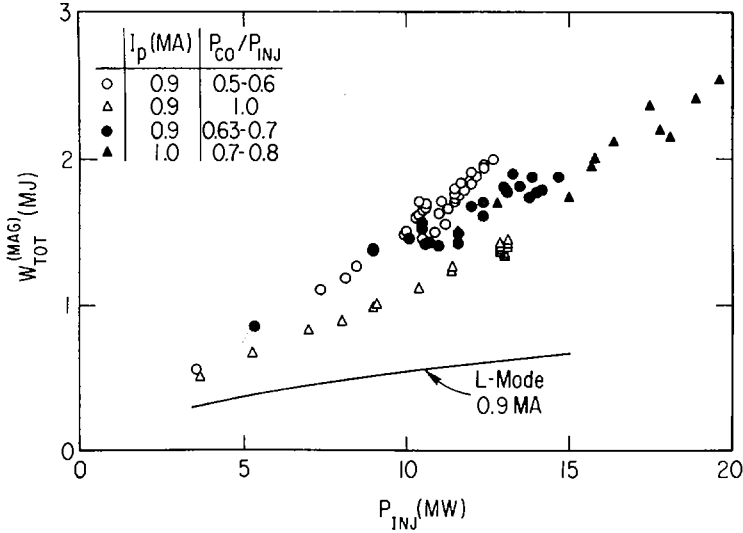


FIG. 6. Variation of stored energy with injected power for different values of fractional power in the co-direction, for  $4.7 < B_T < 5.2$  T,  $2.40 < R < 2.48$  m and  $0.76 < a < 0.82$  m. Magnetic measurements are compared with the prediction of the L-mode model of Goldston.

achieved with nearly balanced injection ( $P_{CO}/P_{INJ} \sim 0.5$ ) in discharges with degassed limiters. In Fig. 6, the data set was constrained to eliminate discharges with very-large-amplitude continuous MHD activity [3]. With nearly balanced injection the stored energy increases linearly with heating power and the incremental confinement time is 0.15 s, comparable to the low-density ohmic confinement time prior to injection. Furthermore, with near balanced injection the global confinement time is not observed to degrade with power: values up to 0.17 s are achieved with 12 MW, as shown in Fig. 7, and the confinement time is up to  $\sim 3$  times the prediction of Goldston L-mode scaling [8]. With the present distribution of beam sources, at full power  $P_{CO}/P_{INJ}$  is  $\approx 0.7$ , which is not optimum, as indicated in Fig. 7. The highest power experiments were conducted at higher current (1.0 MA) to minimize the effects of MHD activity.

The energy stored in the discharge appears to be limited by a maximum  $\beta_p$  value of  $\sim 2$ . Further increases in power at a given current result in either disruptions or MHD activity degrading the stored energy [3]. At low toroidal field and modest  $q_a$  ( $\sim 4-5$ ), the maximum stored energy is in fair agreement with the Troyon  $\beta_T$  limit [ $\beta_T^{\max} \approx (2.2-2.5) \mu_0 I_p / a B_T$ ] [11]. At high toroidal field and  $q_a$  the Troyon  $\beta_T$  limit would permit  $\beta_p$  values up to  $\sim 3.5$ .

At higher plasma current ( $I_p > 1.1$  MA), the favorable characteristics of supershots have not been observed, and the

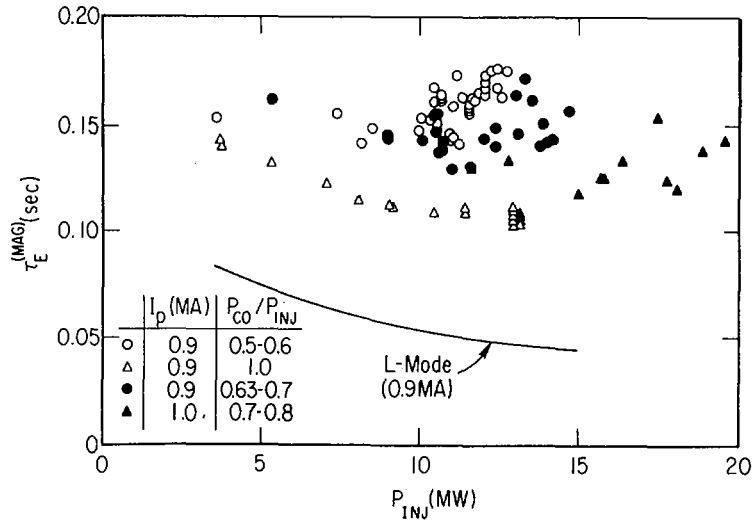


FIG. 7. Variation of global confinement time with injected power for the data set shown in Fig. 6. Magnetic measurements are compared with the prediction of the L-mode model of Goldston.

difference in  $\tau_E$  between balanced and co-only injection at  $P_b = 10$  MW is less than 15%. Supershot characteristics at higher current (1.3 MA with 17 MW of neutral beam power) can be achieved by ramping the current from 0.9 MA during the beam pulse, resulting in  $q_a \approx 5$ . Further extension of the operating regime may be possible with the longer-duration (2.0 s) and higher-full-energy-species-mix beam sources (80% power at full energy) that are currently being installed. Present current-ramp experiments are encouraging in that supershot characteristics are observed even when fairly large current-ramp rates up to 1 MA/sec are applied. By tailoring the beam power waveform and the current ramp, it may be possible to achieve supershots with much higher currents, thus avoiding the  $\beta$  limits.

In discharges in which the plasma current is maintained constant by feedback control, the surface voltage is observed to decrease from the ohmic phase with increasing  $\beta_p$  and co-injected power and is typically  $\sim -0.2$  V at the end of injection. Though the electron temperature increases and broadens and  $Z_{eff}$  decreases, changes in conductivity alone cannot produce a negative voltage. The changes in plasma geometry coupled with changes in conductivity are also not large enough to account for the negative voltage, as determined by a one-and-one-half dimensional magnetic field diffusion calculation. Monte Carlo beam calculations show that neoclassical beam-driven currents [12] contribute to the decrease in surface voltage, but still do not account for the magnitude. The calculations show that, due to the beam orbits, co-injection is more effective in driving current, particularly in

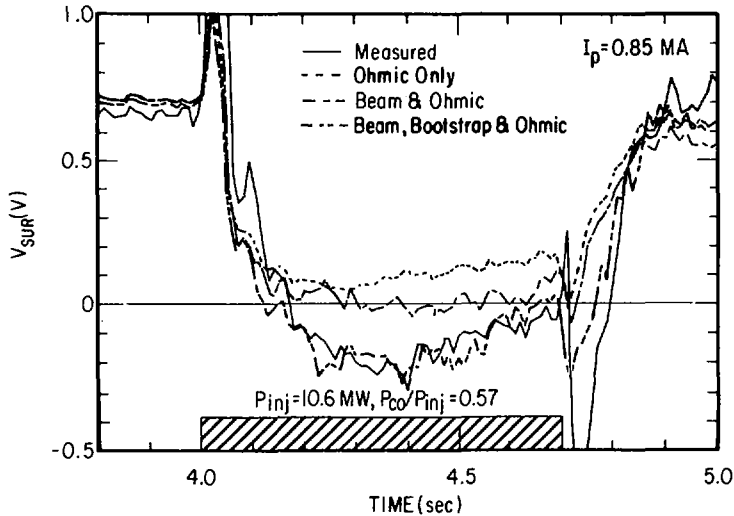


FIG. 8. Comparison of the measured surface voltage with the calculated surface voltage under different assumptions for the role of non-ohmically driven currents. The discharge parameters are  $B_T = 5.2$  T,  $R = 2.45$  m and  $a = 0.8$  m.

outer regions of plasma, than counter-injection; thus, even when the power is nearly balanced, a net beam-driven current effect on the surface voltage is calculated. By including the neoclassical bootstrap current predicted by Galeev and Sagdeev [13] and Bickerton *et al.* [14] as formulated by Hirshman and Sigmar [12], good agreement is obtained between the calculated and measured surface voltage, as shown in Fig. 8. These calculations indicate that for this case approximately 350 kA of bootstrap current is present, compared with 420 kA of co-injected current and -160 kA of counter-injected current. In presently analyzed discharges, the maximum calculated bootstrap current is 440 kA in a 900 kA plasma with 370 kA of calculated beam-driven current. While the driven currents do not exceed the total current, the calculated voltage is negative because the radial distribution of the bootstrap current is broader than that of the ohmic current, exceeding the total current density in the outer region of the plasma.

Operation in the supershot regime has resulted in substantial increases in neutron source strength and equivalent  $Q$ . The maximum neutron source strength of  $1.2 \times 10^{16}$  n/s was achieved with 19.6 MW of beam power, with  $P_{CO}/P_{INJ} = 0.7$ . The maximum  $Q_{DD}$  of  $8.7 \times 10^{-4}$  was achieved with 12.3 MW, when the power was more nearly balanced ( $P_{CO}/P_{INJ} \approx 0.56$ ), corresponding to a source strength of  $8.9 \times 10^{15}$  n/s. In the supershot regime, SNAP and time-dependent (TRANSP) calculations of the neutron flux are in good agreement ( $\pm 25\%$ ) with the measured flux. These calculations indicate that, for the discharge with the highest

value of  $Q_{DD}$ , ~ 17% of the flux is due to beam-beam reactions, ~ 53% due to beam-target, and ~ 30% from the thermalized ions shortly before the end of the beam pulse. In order to estimate the  $Q_{DT}$  which would be achieved with deuterium and tritium, it is necessary to assume a composition for the hydrogenic component of the target plasma. For the hypothetical condition of deuterium beam injection into a tritium plasma (with the same value of  $Z_{eff} = 3.3$ ),  $Q_{DT}$  would be 0.23, due to beam-target reactions. Because beam fueling is clearly very important, a more realistic case would be to consider injection using deuterium and tritium beams into a 50%/50% deuterium/tritium plasma. In this case, the resulting value of  $Q_{DT}$  would be  $\approx 0.18$ . A significant improvement over these values can be expected from the new long-pulse ion sources with better species mix, operation at 120 kV, and nearly balanced injection at full beam power, even without assuming higher injected power and improved plasma parameters.

## VI. Summary

During the past year, substantial progress has been made in expanding the operating range of TFTR. Ohmically heated pellet-fueled discharges have resulted in exceptional central densities and  $n_e(0) \tau_E(a) T_i(0)$  values of  $\sim 2 \times 10^{20} \text{ m}^{-3} \cdot \text{s} \cdot \text{keV}$ . Furthermore, in the saturated regime, the confinement time in pellet-fueled discharges is observed to be longer than that achieved in gas-fueled discharges. In these discharges, the density profile is very peaked,  $n_e(0)/\bar{n}_e \sim 2$ .

In neutral-beam-heated discharges an enhanced confinement regime has been found. This regime is characterized by peaked density profiles, broad electron temperature profiles, high ion temperatures,  $\approx 20 \text{ keV}$ , and high neutron source strengths. In this regime,  $n_e(0) \tau_E(a) T_i(0)$  values of  $\sim 2 \times 10^{20} \text{ m}^{-3} \cdot \text{s} \cdot \text{keV}$  have also been achieved. The operating regime is characterized by a low initial density and deuterium recycling prior to injection, which can only be achieved at low  $I_p$  and after extensive limiter degassing. At high toroidal field ( $B_T = 5.2 \text{ T}$ ), this corresponds to relatively high values of  $q_a$  (in the range of 7-8) and  $\beta_p$  (up to 2). In reduced toroidal field experiments and in current ramp experiments, supershots with  $q_a \sim 4-5$  have been obtained. Significantly improved performance is achieved with nearly balanced injection.

In the high temperature regime, the plasma collisionality is low and  $\beta_p$  is high, so that both beam-driven currents and bootstrap currents are predicted to be important. Calculations including bootstrap current are in better accord with the experimental measurements than those including only the beam-driven currents. If these indications of the bootstrap current are verified by future experiments, the performance of tokamak reactors could be fundamentally enhanced.

### Acknowledgements

We are grateful to D.J. Grove and J.R. Thompson for their advice and support, and to J. Strachan for his many contributions. This work was supported by US DOE Contract No. DE-AC02-76CH03073. The ORNL participants were also supported by US DOE Contract No. DE-AC05-84OR21400 with Martin Marietta Energy Systems, Inc.

### REFERENCES

- [1] SCHMIDT, G., et al., Paper IAEA-CN-47/A-III-4, these Proceedings, Vol. 1.
- [2] GOLDSTON, R.J., et al., Paper IAEA-CN-47/A-II-1, these Proceedings, Vol. 1.
- [3] McGUIRE, K., et al., Paper IAEA-CN-47/A-VII-4, these Proceedings, Vol. 1.
- [4] HILL, K.W., et al., Paper IAEA-CN-47/A-IV-2, these Proceedings, Vol. 1.
- [5] MURAKAMI, M., et al., Plasma Phys. Controll. Fusion **28** (1986) 17.
- [6] EFTHIMION, P.C., et al., in Plasma Physics and Controlled Nuclear Fusion Research 1984 (Proc. 10th Int. Conf. London, 1984), Vol. 1, IAEA, Vienna (1985) 29.
- [7] BELL, M.G., et al., Plasma Phys. Controll. Fusion **28** (1986) 1329.
- [8] GOLDSTON, R.J., Plasma Phys. Controll. Fusion **26** (1984) 87.
- [9] STRACHAN, J.D., et al., submitted to Phys. Rev. Lett., 1986.
- [10] DYLLA, H.F., et al., submitted to Nucl. Fusion, 1986.
- [11] TROYON, F., et al., Plasma Phys. Controll. Fusion **26** (1984) 209.
- [12] HIRSHMAN, S.P., SIGMAR, D.J., Nucl. Fusion **21** (1981) 1079.
- [13] GALEEV, A.A., SAGDEEV, R.Z., Zh. Ehksp. Teor. Fiz. **53** (1967) 348 (Sov. Phys. — JETP **26** (1968) 233).
- [14] BICKERTON, R.J., CONNER, J.W., TAYLOR, J.B., Nat. Phys. Sci. **229** (1971) 110.

### DISCUSSION

A. GIBSON: In the two cases for which you quote the large values of  $\bar{n}_e \tau_E \bar{T}_i$ , what is the ratio  $\bar{n}_D / \bar{n}_e$ ?

R.J. HAWRYLUK: In high density pellet fuelled discharges, the correction factor for depletion is small, since  $Z_{\text{eff}}$  is about one. In the supershot discharge, the depletion factor,  $n_D(0)/n_e(0)$ , is about 0.7.

M. GREENWALD: Are you quite sure of the  $Z_{\text{eff}}$  profiles in your pellet fuelled shots? I ask this because there seems to be evidence of impurity accumulation.

R.J. HAWRYLUK: We do not have  $Z_{\text{eff}}$  profile measurements for the pellet fuelled discharges. In some discharges, there is substantial radiation on axis; however, even small concentrations of impurities would be adequate to explain the power loss.

Further, experiments are required to analyse impurity transport in pellet fuelled discharges and to determine whether accumulation occurs and, if so, under what conditions.

S. ITOH: I would like to ask about the target plasma for the 'supershot'. Is the target plasma in a slide-away regime? Judging by the target parameters, it would seem to be. Secondly, did you see any input power limit or threshold for the injection? The supershot discharges seem to be similar to the ASDEX discharges with slide-away electrons reported at the 1982 Conference.

R.J. HAWRYLUK: In some of the target plasma, electron cyclotron emission measurements indicate the presence of slide-away electrons. However, they are not evident in all of the supershot discharges and the occurrence of a slide-away does not appear to be a critical parameter.

Regarding your second question, at a given current there is an upper power limit present that corresponds to attainment of the  $\beta_p$  limit ( $\beta_p \sim 2$ ) which I discussed. However, higher current operation enables us to inject the available 20 MW of neutral beam power and to maintain supershot characteristics.

K. LACKNER: Troyon-type scalings,  $\beta_{pol, crit} \sim q_0$ , are obtained for current density profiles adjusted to maintain  $q$  on axis at a constant value of about one. A reduction in  $\beta_{pol, crit}$  and independence of it from  $q_a$ , as reported by you for low currents, would follow from theory for a current density profile flatter and non-dependent on  $q_a$ .

R.J. HAWRYLUK: In their paper, McGuire and co-workers\* show that the profiles are not optimal, which is why the experimental beta limit is below that predicted by Troyon. The lack of sawteeth indicates that  $q$  on axis is greater than one. However, since the current penetration time is long compared with the beam duration,  $q$  is not substantially greater than one, according to our analysis.

M. BRUSATI: You have reported degradation of performance correlated with enhanced MHD activity. Can you comment on the kind of MHD spectra that you get?

R.J. HAWRYLUK: The mode number of the continuous MHD activity which degrades performance is typically  $m/n = 2/1$  or  $3/2$ . For further details, I would refer you to the paper by McGuire and co-workers that I have just mentioned.\*

---

\* Paper IAEA-CN-47/A-VII-4, these Proceedings, Vol. 1.

## EXPERIMENTAL STUDIES IN JET WITH MAGNETIC SEPARATRIX

A. TANGA, D.V. BARTLETT, K. BEHRINGER,  
R.J. BICKERTON, A. CHEETHAM, J.G. CORDEY,  
A. GIBSON, N.A. GOTTARDI, A. GONDHALEKAR,  
P.J. HARBOUR, H. JAECKEL, M. KEILHACKER,  
E. LAZZARO, V. MARTENS, P. NOLL, S. NOWAK,  
F.C. SCHÜLLER, A.J. TAGLE, A. TARONI,  
P.R. THOMAS, F. TIBONE  
JET Joint Undertaking,  
Abingdon, Oxfordshire,  
United Kingdom

### Abstract

#### EXPERIMENTAL STUDIES IN JET WITH MAGNETIC SEPARATRIX.

The main objectives of the experiments described are (i) to compare the global confinement characteristics of separatrix and limiter discharges and (ii) to study the conditions for the creation of a high density, highly radiative, cool plasma region near the X-point capable of screening and isolating the bulk plasma. Compared to similar limiter discharges, the thermal energy content of single null X-point discharges (SN) is roughly a factor of two higher. Plasmas with even modest separation between X-point and target plates show typical signatures of H-mode discharges. Multi-channel infrared interferometer measurements provide evidence of the formation of a high density diverted plasma with average density  $\sim 10^{20} \text{ m}^{-3}$ , an order of magnitude higher than the main plasma. Measurements with a bolometer camera array show that, in high density discharges with additional power, up to 40% of the input power is radiated within a  $\sim 0.2 \times 0.2 \text{ m}^2$  toroidal region around the torus.

### 1. INTRODUCTION

The main aim of JET is to study plasmas under conditions approaching those needed for a fusion reactor. At present, in limiter discharges, confinement with additional heating is low (L-mode). Better confinement (H-mode) has been observed in tokamaks with magnetic limiters or divertors. In JET, a magnetic configuration with a separatrix inside the vacuum vessel can be created [1]. Two ("double null configuration", DN) or one ("single null configuration", SN) poloidal field nulls are then produced near the top and/or bottom of the vessel as shown in Figs. 1a and 1b.

In these configurations the plasma is detached from both the limiter and the inner wall and recycling occurs in an open divertor region near the X-point. Experiments have been carried

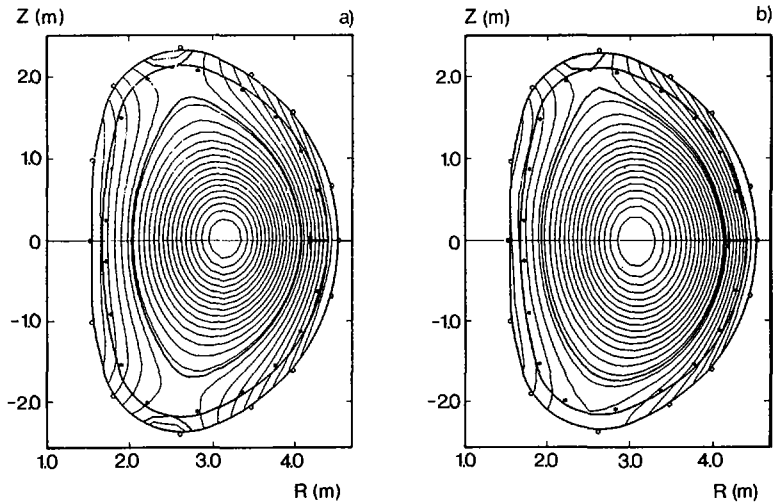


FIG. 1. (a) Flux plot of a double null configuration. Plasma current = 2 MA, toroidal field = 2.8 T, average electron density =  $3 \times 10^{19} \text{ m}^{-3}$ , poloidal beta = 0.44, plasma elongation = 1.8. (b) Flux plot of a single null configuration. Plasma current = 2 MA, toroidal field = 2.2 T, average electron density =  $3 \times 10^{19} \text{ m}^{-3}$ , poloidal beta = 0.6, plasma elongation = 1.65 (#10237,  $t = 13.5 \text{ s}$ ).

out with plasma currents up to 2.5MA in the DN and up to 3.0MA in the SN configuration. A maximum additional power of 9MW has been injected ( $D^{\circ}$  into  $D^{+}$ ).

## 2. FORMATION OF A MAGNETIC SEPARATRIX

A magnetic separatrix can be formed within the vacuum vessel of JET using the multipolar field normally used to control the elongation and triangularity of the plasma cross-section. In the DN configuration, the present poloidal field equipment allows operation at plasma currents up to 2.5MA. The resulting plasma has an elongation of 1.8; the vertical position is unstable with an open loop growth rate of  $150\text{s}^{-1}$ .

The separation between the X-point and the graphite target plates is a linear function of the currents in the shaping coils. For the configuration in Fig.1a the separation is  $\sim 0.1\text{m}$ . In the SN configuration, plasma currents up to 3.0MA have been produced with an elongation of 1.65; the growth rate of the vertical instability is substantially smaller than for the DN configuration.

The maximum separation between the X-point and the target plates obtained so far at 2MA with SN is  $\sim 0.13\text{m}$  and may be increased by displacing the magnetic axis below the midplane.

The radial position of the null point is held constant during the discharge, to within a few centimetres. The distance between the separatrix and the antennae for ICRH is finely controlled by the radial position feedback system and this can allow good coupling of ICRH to the plasma. In both DN and SN configurations, Langmuir probe measurements give the e-folding length for decay of density and temperature as 0.06m and 0.10m, respectively.

The location of the separatrix has been corroborated to within a few centimetres by observations with a bolometer camera array and TV cameras and by the separation between the erosion marks on the graphite target tiles. The magnetic configuration is only slightly sensitive to changes in internal parameters, such as the poloidal beta and internal inductance.

### 3. HIGH RECYCLING IN THE X-POINT REGION

The formation of a magnetic separatrix within the vacuum vessel produces a significant change in the discharge characteristics. For separations between the plasma and the limiter larger than 0.07m, deuterium recycling (monitored by  $D_{\alpha}$  signals) shifts from the limiters to small regions near the X-points. Both the  $D_{\alpha}$  monitors and TV observations in the near infra-red show the formation of bright regions (~0.2m across) coinciding with the X-points. In high density DN discharges, only one bright region is observed. The application of a radial magnetic field shifts the toroidal plasma column vertically and the bright region moves correspondingly, indicating that the formation of only a single bright region is not connected with slight up-down asymmetries in the poloidal field.

Simultaneous with the shift in recycling characteristics, stronger gas-fuelling is needed to sustain the average plasma density,  $Z_{\text{eff}}$  is reduced and the bolometer camera array shows a decrease in bulk plasma radiation and a large increase in the radiation from the X-point region. As shown in Fig.2a for a series of ohmic DN discharges, the total radiated power is in most cases between 70 and 100% of the input power and the power radiated in the X-point region increases with plasma density more rapidly than the total radiated power. SN discharges show similar behaviour with the power radiated from the X-point region, following approximately a density-squared dependence. The size of the highly radiative region in the vicinity of the X-point can be estimated to be  $\leq 0.2 \times 0.2 \text{m}^2$ .

The far infra-red multichannel interferometer suggests a similar small region with high electron density near the X-point. When one of the vertical channels of the interferometer passes through the X-point region, the fringe count for that channel shows a substantial increase over the other channels. This can be interpreted as a measurement of the local X-point line density. In Fig.2b, the difference between

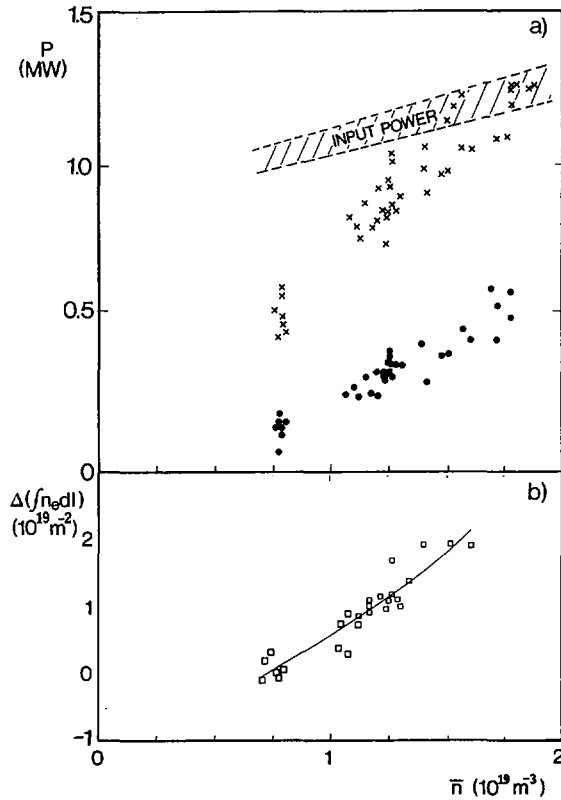


FIG. 2. (a) Radiated power versus line average electron density for Ohmic double null configuration. Dots represent power radiated from X-point, crosses total power radiated from plasma. (b) Difference in line density between two adjacent interferometer channels one of which intercepts the X-point.

two adjacent channels of the interferometer has been plotted against the line average electron density. Assuming that the size of this high density plasma region corresponds to that of the highly radiative region the density in the X-point region is estimated to be  $\sim 10^{20} \text{ m}^{-3}$ . No data are available for average plasma densities larger than  $2 \times 10^{19} \text{ m}^{-3}$  because the channel of the interferometer intercepting the X-point loses fringes.

Assuming that the thickness of the high recycling region corresponds to the mean free path for neutrals,  $\lambda^0$ , the interferometer data provides a measure of [2]

$$n_t \lambda^0 = \frac{v^0}{\langle \sigma v \rangle}$$

where  $v^0$  is the effective speed of the emitted atoms and  $\langle \sigma v \rangle$  is the effective rate coefficient for ionisation. Assuming a

single temperature,  $T_t$ , for electrons, ions and neutrals, the right hand side of this equation is only a function of  $T_t$ .  $T_t \sim 5-10\text{eV}$  is obtained for  $\bar{n}_e > 1 \times 10^{19}\text{m}^{-3}$ . The density,  $n_t$ , may also be estimated from a zero-dimensional model which balances the power flow from the bulk plasma with sonic flow at the high density region in the scrape-off layer. For  $\bar{n}_e > 1 \times 10^{19}\text{m}^{-3}$ ,  $n_t \sim 4 \times 10^{19}\text{m}^{-3}$  is obtained, in reasonable agreement with the estimates made earlier.

This trend towards high recycling is further corroborated by Langmuir probe measurements which suggest that the Mach number of the flow parallel to the magnetic field decreases with increasing plasma density.

#### 4. IMPROVED CONFINEMENT WITH ADDITIONAL HEATING IN THE SINGLE NULL CONFIGURATION

DN X-point discharges show an energy confinement time some 20-30% higher than similar limiter or inner wall discharges. However, no clear H-mode transition was identified as the power levels available. Recent experiments have therefore concentrated on the SN configuration. First results show a substantial improvement of energy confinement in SN X-point discharges compared to similar limiter or inner wall discharges. The experiments have been carried out with neutral beam injection heating with up to 9.0MW power. Ion cyclotron heating has been applied in some of the shots with a power of up to 4MW (but keeping the total input power,  $P_{\text{tot}} = P_{\text{Q}} + P_{\text{NBI}} + P_{\text{RF}} \leq 20\text{MW}$ ).

In Fig.3 the variation of the total plasma thermal energy content with total input power  $P_{\text{tot}}$  for two series of SN X-point discharges at plasma currents of 2MA and 3MA is compared with the corresponding data sets for limiter discharges. While the separation of the X-point and the target plates is  $\sim 0.13\text{m}$  at 2MA this is reduced to  $\sim 0.5\text{m}$  at 3MA and is then rather close to the wall. For either plasma current the energy content of the X-point discharges is up to a factor of 2 larger than that of the corresponding limiter discharge with the same additional power. In general, the trend with increasing heating power is also similar in all cases.

As shown in Fig.4, the electron temperatures (and also the central ion temperatures) for such an X-point H-mode plasma are substantially higher than for a limiter plasma with the same parameters of plasma density, plasma current, toroidal field and  $P_{\text{tot}}$ . It should be noted that the electron temperature profile is broader, with the edge temperature at  $R=4.0\text{m}$  being some 2.5 times higher.

As pointed out already the SN discharges at 2MA exhibit clear indications of a transition into an H-mode [3]. As shown in Fig.5 the edge  $D_{\alpha}$  signal ( $f$ ) drops and the line integrated electron density ( $d$ ) increases more rapidly. These events occur shortly after the crash of a sawtooth when the edge temperature

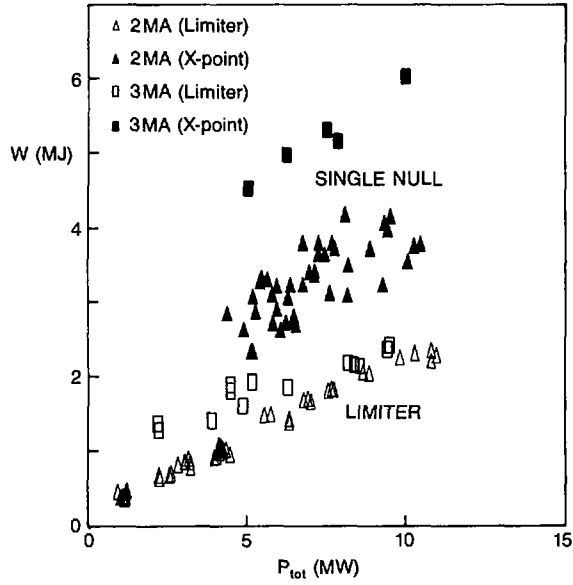


FIG. 3. Total plasma thermal energy content as measured by diamagnetic loop versus total input power for single null and limiter configurations.

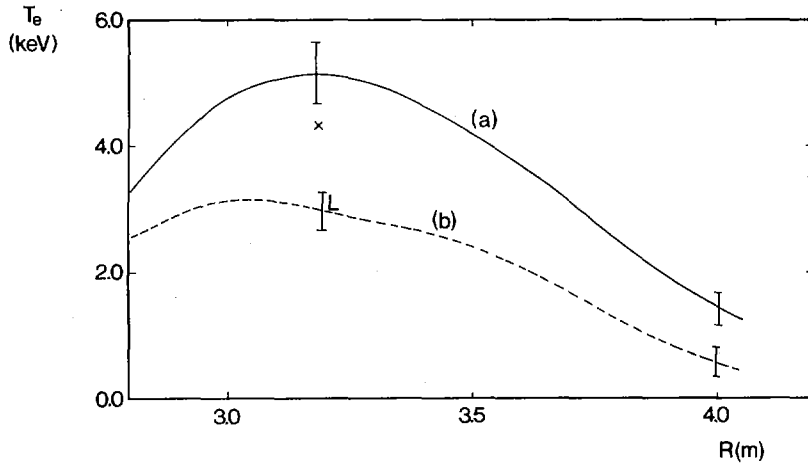


FIG. 4. Electron temperature profiles (a) X-point (#10237,  $t = 13.5$  s) and (b) limiter discharge (#7709). Central ion temperature for SN (X) and Limiter (L) discharge.

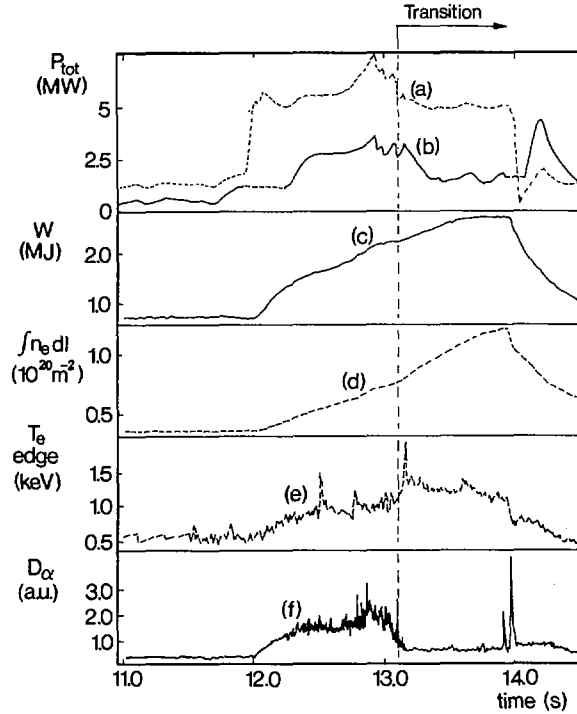


FIG. 5. (a) Total input power  $P_{tot}$ , for #10237;  
 (b) Power conducted to the target plates from, bolometric analysis,  $P_{tot} - P_{rad} - W$ ;  
 (c) Total energy content from the diamagnetic loop,  $W$ ;  
 (d) Line electron density,  $\int n_e dl$ ;  
 (e) Plasma edge electron temperature,  $T_e^{edge}$ ;  
 (f)  $D_{\alpha}$  signal from the plasma boundary.

(e) increases abruptly. The power flow to the target plates (b) is substantially reduced. This phase is subject to an abrupt termination when the average density reaches some limiting value (as evidenced more clearly in other JET Pulses where this event is not obscured by the end of additional heating). The average density, temperature and thermal energy content (c) fall in about 40ms, accompanied by a spike in the X-point radiation. During the H-phase the plasma density profile broadens with steep gradients developing at the edge.

Impurity radiation from the plasma edge (O VI, C IV) falls by about a factor of two at the transition to the H-regime. At this time the ICRH power ceases to be coupled to the plasma (probably due to the changed edge conditions) and the nickel influx from the antenna screen falls to zero. Nevertheless, the total nickel content as observed from the Ni XXV and Ni XXVI

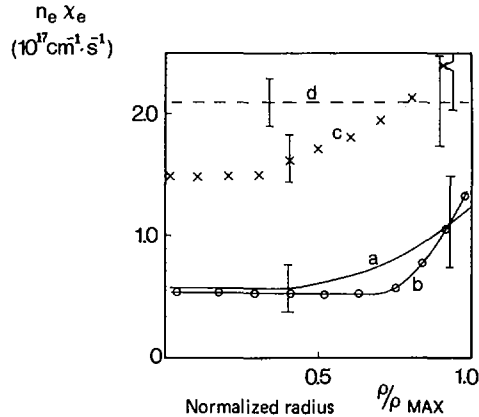


FIG. 6.  $n_e \chi_e$  profiles for SN, limiter and inner wall discharges. (a) OH phases, (b) dots for discharge of Fig. 4 at  $t = 13.8$  s, (c) for reference limiter discharge, (d) for reference discharge lying on the inner wall with NBI heating (#8899), with larger input power but lower energy content than (b).

line intensities remains constant indicating substantially improved confinement of metals in the interior of the plasma. As indicated by the soft X-ray radiation profiles, however, this does not lead to accumulation of impurities.

A preliminary analysis of transport properties comparing SN X-point with limiter and inner wall discharges has been done with the transport code Jetto [4]. Using the transport models described in [5] good simulations of all the relevant measured quantities ( $n_e$ ,  $T_e$ , radiation profiles, central ion temperature,  $Z_{\text{eff}}$ ) have been obtained in the ohmic phase of these three types of discharges. With additional heating, however, a degradation of the coefficient for the electron energy transport must be introduced for the inner wall and limiter case but not for the X-point discharge. The radial profiles of  $n_e \chi_e$  (Fig.6) show that these differences hold over the whole plasma cross-section.

## 5. CONCLUSIONS

Separatrix operation appears to induce substantial changes in the plasma behaviour compared to limiter operation. This is possibly a result of the high shear at the boundary of the plasma. Even with a modest separation of the X-point from the target plates, a high recycling regime has been observed in this region at high plasma densities. With additional heating the stored energy increases substantially above that for corresponding limiter discharges. A further increase in stored

energy is observed for both 2MA and 3MA discharges leading to global energy confinement times in excess of 0.6s, about a factor of two higher than for the corresponding limiter discharges. These discharges also exhibit other signatures (e.g., reduced edge recycling) normally associated with H-modes.

#### ACKNOWLEDGEMENTS

The authors would like to acknowledge the effort of the whole JET team and, in particular, of the RF and NB Divisions.

#### REFERENCES

- [1] TANGA, A., in Controlled Fusion and Plasma Physics (Proc. 12th Europ. Conf. Budapest, 1985), Vol. 1, European Physical Society (1985) 70.
- [2] NEUHAUSER, J., WUNDERLICH, R., in Plasma-Surface Interactions in Controlled Fusion Devices (Proc. 7th Int. Conf. Princeton, NJ, 1986), to be published in J. Nucl. Mater.
- [3] WAGNER, F., et al., Phys. Rev. Lett. **49** (1982) 408; WAGNER, F., et al., in Plasma Physics and Controlled Nuclear Fusion Research 1982 (Proc. 9th Int. Conf. Baltimore, 1982), Vol. 1, IAEA, Vienna (1983) 43.
- [4] DÜCHS, D., et al., in Controlled Fusion and Plasma Physics (Proc. 12th Europ. Conf. Budapest, 1985), Vol. 1, European Physical Society (1985) 22.

#### DISCUSSION

H.P. FURTH: Your results seem to me to be extremely significant as well as encouraging. One could say that you have shown that the quality of confinement in JET need not deteriorate at heating powers much higher than Ohmic, but this would be an understatement.

A critical figure of merit for tokamaks is  $V_H = P_{\text{total}}/I_{\text{plasma}}$ . For Ohmic heating,  $V_H$  is normally less than 1 V. For a practical tokamak reactor,  $V_H$  must exceed 50 V, and even for an ETR,  $V_H$  must exceed  $\sim 10$  V. Your demonstration that JET confinement is unimpaired for  $V_H > 3$  V is therefore a truly major step forward.

A. TANGA: Thank you for the comment.



## ENERGY CONFINEMENT AND PROFILE CONSISTENCY IN TFTR

R.J. GOLDSTON, V. ARUNASALAM, M.G. BELL, M. BITTER,  
W.R. BLANCHARD, N.L. BRETZ, R. BUDNY, C.E. BUSH<sup>1</sup>, J.D. CALLEN<sup>2</sup>,  
S.A. COHEN, S.K. COMBS<sup>1</sup>, S.L. DAVIS, D.L. DIMOCK, H.F. DYLLA,  
P.C. EFTHIMION, L.C. EMERSON<sup>1</sup>, A.C. ENGLAND<sup>1</sup>, H.P. EUBANK,  
R.J. FONCK, E. FREDRICKSON, H.P. FURTH, G. GAMMEL, B. GREK,  
L.R. GRISHAM, G. HAMMETT, R.J., HAWRYLUK, W.W. HEIDBRINK<sup>3</sup>,  
D.B. HEIFETZ, H.W. HENDEL<sup>4</sup>, K.W. HILL, E. HINNOV, S. HIROE<sup>1</sup>,  
H. HSUAN, R.A. HULSE, K.P. JAEHNIG, D. JASSBY, F.C. JOBES,  
D.W. JOHNSON, L.C. JOHNSON, R. KAITA, R. KAMPERSCHROER,  
S.M. KAYE, S.J. KILPATRICK, R.J. KNIZE, H. KUGEL, P.H. LaMACHE,  
B. LeBLANC, R. LITTLE, C.H. MA<sup>1</sup>, D.M. MANOS, D.K. MANSFIELD,  
R.T. McCANN, M.P. McCARTHY, D.C. McCUNE, K. McGUIRE,  
D.H. McNEILL, D.M. MEADE, S.S. MEDLEY, D.R. MIKKELSEN,  
S.L. MILORA<sup>1</sup>, W. MORRIS<sup>5</sup>, D. MUELLER, V. MUKHOVATOV<sup>6</sup>,  
E.B. NIESCHMIDT<sup>7</sup>, J. O'ROURKE<sup>8</sup>, D.K. OWENS, H. PARK,  
N. POMPHREY, B. PRICHARD, A.T. RAMSEY, M.H. REDI,  
A.L. ROQUEMORE, P.H. RUTHERFORD, N.R. SAUTHOFF, G. SCHILLING,  
J. SCHIVELL, G.L. SCHMIDT, S.D. SCOTT, S. SESNIC, J.C. SINNIS,  
F.J. STAUFFER<sup>9</sup>, B.C. STRATTON, G.D. TAIT, G. TAYLOR,  
J.R. TIMBERLAKE, H.H. TOWNER, M. ULRICKSON, V. VERSHKOV<sup>6</sup>,  
S. VON GOELER, F. WAGNER<sup>10</sup>, R. WIELAND, J.B. WILGEN<sup>1</sup>,  
M. WILLIAMS, K.L. WONG, S. YOSHIKAWA, R. YOSHINO<sup>11</sup>,  
K.M. YOUNG, M.C. ZARNSTORFF, V.S. ZAVERYAEV<sup>6</sup>, S.J. ZWEBEN  
Princeton Plasma Physics Laboratory,  
Princeton University,  
Princeton, New Jersey,  
United States of America

<sup>1</sup> Oak Ridge National Laboratory, Oak Ridge, TN, USA.

<sup>2</sup> University of Wisconsin, Madison, WI, USA.

<sup>3</sup> GA Technologies Inc., San Diego, CA, USA.

<sup>4</sup> RCA David Sarnoff Research Center, Princeton, NJ, USA.

<sup>5</sup> Balliol College, University of Oxford, Oxford, UK.

<sup>6</sup> Kurchatov Institute of Atomic Energy, Moscow, USSR.

<sup>7</sup> EG&G Idaho, Inc., Idaho Falls, ID, USA.

<sup>8</sup> JET Joint Undertaking, Abingdon, Oxfordshire, UK.

<sup>9</sup> University of Maryland, College Park, MD, USA.

<sup>10</sup> Max-Planck-Institut für Plasmaphysik, Garching, Fed. Rep. Germany.

<sup>11</sup> JAERI, Naka-machi, Naka-gun, Ibaraki-ken, Japan.

## Abstract

### ENERGY CONFINEMENT AND PROFILE CONSISTENCY IN TFTR.

A new regime of enhanced energy confinement has been observed on TFTR with neutral beam injection at low plasma current. It is characterized by extremely peaked electron density profiles and broad electron temperature profiles. The electron temperature profile shapes violate the concept of profile consistency in which  $\langle T_{e0}/T_e \rangle_v$  is assumed to be a tightly constrained function of  $q_a$ , but they are in good agreement with a form of profile consistency based on examining the temperature profile shape outside of the plasma core. The enhanced confinement regime is only obtained with a highly degassed limiter; in discharges with gas filled limiters convective losses are calculated to dominate the edge electron power balance. Consistent with the constraint of profile consistency, global confinement is degraded in these cases. The best heating results in the enhanced confinement regime are obtained with nearly balanced co- and counter-injection. Much of the difference between balanced and co-only injection can be explained on the basis of classically predicted effects associated with plasma rotation.

## 1. Introduction

A new regime of enhanced energy confinement has been observed on TFTR with neutral beam injection at low plasma current. It is characterized by extremely peaked electron density profiles and broad electron temperature profiles. The best heating results in this regime are obtained with nearly balanced co and counter injection. The properties of these discharges (referred to as "supershots") raise questions about some of the recently achieved understanding of tokamak auxiliary heating physics - electron temperature profile consistency, and the lack of importance of toroidal rotation, among others. In this paper we discuss the implications of our results in these areas. We begin (Sec. 2) by putting the electron stored energy results in this new regime into the context of previous scaling laws and TFTR data, showing that these discharges exhibit enhanced electron energy confinement as well as the high total stored energy and ion temperature discussed in [1]. Next (Sec. 3) we study the electron temperature profile shapes of these enhanced confinement discharges, in comparison with L-Mode and ohmically heated profiles on TFTR. In Section 4 we address issues connected with the electron density profile shape. In Section 5 we discuss the role of rotation and balanced versus unbalanced injection.

## 2. Stored Electron Energy in Supershots

Figure 1 shows the electron energy content from a series of scans of neutral beam power at  $I_p = 0.9, 1.4,$  and  $2.2$  MA, with the plasma resting on the inner-wall carbon limiter. The scans at higher current were performed without any special limiter degassing procedures. They show typical L-Mode behavior: the stored energy reaches equilibrium during the beam pulse, and broad density profiles are observed. The 0.9 MA data were taken after extensive degassing with low density He discharges [2]; they

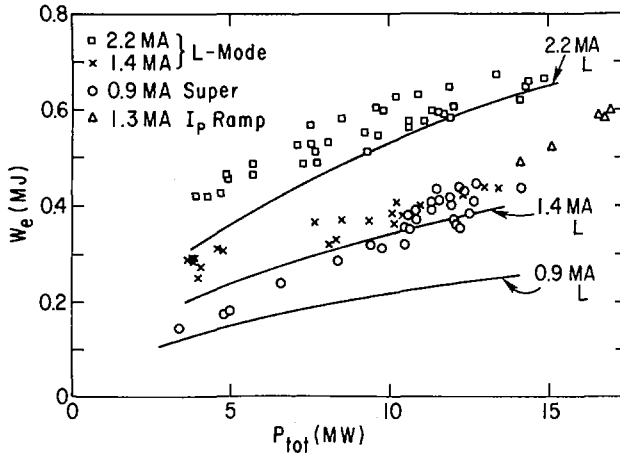


FIG. 1. Electron stored energy versus total heating power for 2.2 MA and 1.4 MA L-mode discharges and for 0.9 MA enhanced confinement discharges. Also shown are enhanced confinement discharges at 1.3 MA achieved by ramping the plasma current up from 0.9 MA during the injection pulse. The curves represent  $0.4 \times w_{tot}^L$ , where  $w_{tot}^L$  is the L-mode scaling prediction [4] for total stored energy (see text).

generally show rising stored energy throughout the beam pulse, and at higher powers they exhibit strongly centrally peaked density profiles. Shots with severe MHD activity [3] which caused the stored energy and neutron flux to fall at the end of the pulse have been excluded from this data set. The higher current data sets have been constrained to  $0.25 < P_{co}/P_{inj} < 0.75$ , while the 0.9 MA data set has been constrained to  $0.35 < P_{co}/P_{inj} < 0.65$ , in order to minimize the effects of unbalanced injection, which are greatest in the low-current region [1]. The current of 0.9 MA was selected because at lower plasma currents ( $I_p = 0.7-0.8$  MA) high power operation is prevented by severe MHD activity and disruptions, while the data set at higher currents ( $I_p = 1 - 1.1$  MA) and  $P_{inj}$  less than 10 MW is very limited. Up to 17 MW of neutral beam power has been injected into discharges with an initial plasma current of 0.9 MA, without inducing strong MHD oscillations or disruptions, by ramping the plasma current up to 1.3 MA during the 0.5 sec beam pulse. Due to our present beam configuration, at these high powers  $P_{co}/P_{inj} > 0.70$ , which has been observed to result in significantly reduced heating compared to balanced injection at lower powers. Also plotted on this figure is the prediction of L-Mode scaling [4] (for  $H^{\circ} \rightarrow D^+$  injection) where the prediction of the scaling law for electron energy has been taken to be 0.4 times the prediction for total stored energy, since this ratio is characteristic of high power TFTR results in the standard regime. While the higher current results approach the L-Mode prediction at high powers, the 0.9 MA

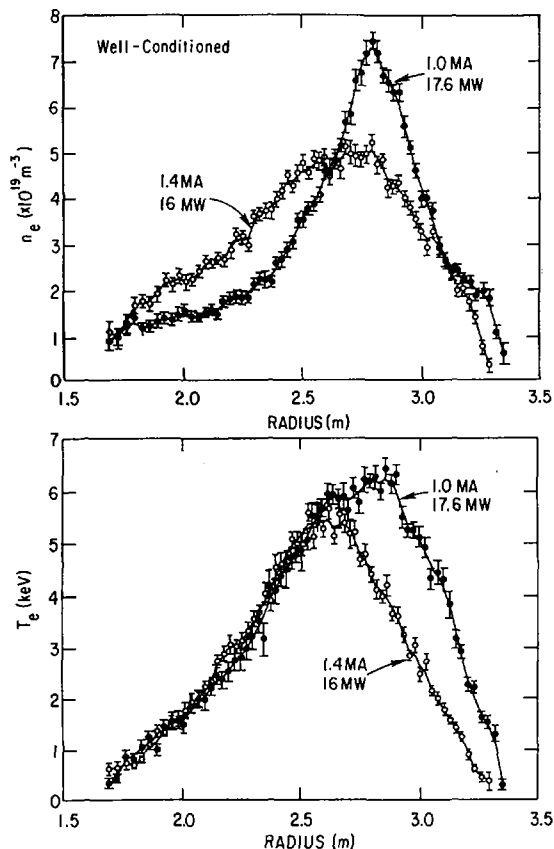


FIG. 2. Electron density and temperature profiles for a 1.0 MA enhanced confinement discharge (solid points) and for a 1.4 MA L-mode discharge (open points). For the enhanced confinement discharge:  $W_e = 0.52$  MJ. For the L-mode discharge:  $W_e = 0.47$  MJ.  $P_{co}/P_{inj} = 0.7$  for both.

supershot results clearly diverge from it. The stored electron energy of the 1.3 MA current-ramp supershots is remarkably close to the standard regime 2.2 MA data. The magnetically-measured total stored energies of enhanced confinement discharges show even more of a gain over standard L-Mode discharges. The total stored energy of 0.9 MA supershots equals that of 2.2 MA standard regime discharges at powers in the range of 11 MW. The fact that kinetic stored energy calculations agree well with the diamagnetic measurement results ( $\pm 5\%$  in the 0.9 MA data set shown here) indicates that the thermal and beam ions gain in stored energy as expected due to the high electron temperatures and peaked density profiles provided by supershots.

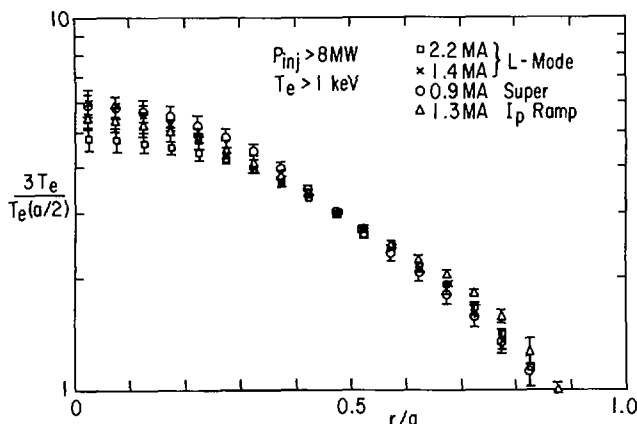


FIG. 3. Electron temperature profile shape normalized to  $r = a/2$  for the data sets of Fig. 1. The factor of three is applied in order to centre the mid-radius on a single decade scale. The error bars represent the root mean square (RMS) variation of the data.

### 3. Electron Temperature Profile Consistency

Figure 2 shows an overlay of the Thomson scattering measurements of  $T_e(R)$  and  $n_e(R)$  from a supershot with  $I_p = 1$  MA,  $B_T = 5$  T, and from a 1.4 MA discharge at the same toroidal field. Both discharges had a well-degassed limiter, but in the 1.4 MA case  $\beta_p$  nonetheless saturated after 0.3 sec into the beam pulse, and the density profile did not gain the peaked shape characteristic of the enhanced confinement mode. These results, and others like them, violate the concept of electron temperature profile consistency in which  $T_e(0)/\langle T_e \rangle_v$  is taken as the measure of profile shape and is postulated to be a tightly-defined, monotonically rising function of  $q_a$ . This measure of profile shape is, however, already suspect as an indicator of microscopic transport mechanisms, since it can be largely enforced by sawtooth oscillations [4,5], if  $\chi_e$  is sufficiently peaked to the outside of the discharge. On TFTR it has been previously observed [6] that the detailed electron temperature profile shape, outside of the core of the plasma and in the region where  $T_e > 1$  keV, shows a remarkable constancy, independent of heating power - and most surprisingly - independent of  $q_a$ . Figure 3 shows electron temperature profile shapes normalized at  $r = a/2$  for the points with  $P_{tot} > 8$  MW in the power scans of Fig. 1. The electron temperatures measured by Thomson scattering have been mapped to flux surfaces, and plotted as a function of midplane minor radius. The two-sided electron temperature measurement ensures that this process unambiguously corrects for the strong Shafranov shift observed in the low current, enhanced confinement regime.

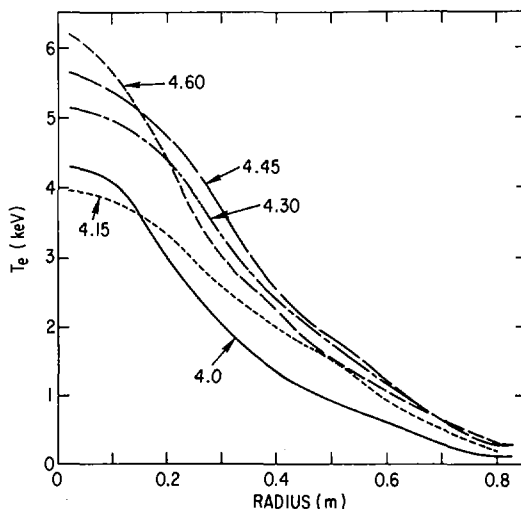


FIG. 4. Time evolution of  $T_e(r)$  from Thomson scattering, mapped to time dependent magnetic flux surfaces for 9.5 MW balanced injection into a 0.8 MA discharge, in enhanced confinement regime. Neutral beam injection heating from  $t = 4.0$  s to 4.5 s.

The error bars indicate the R.M.S. variation of the data. The 0.9 MA supershot temperature profiles line up with the L-Mode profiles in the region outside of  $a/3$ . The few current ramp shots show an approximately 10% higher  $T_e(0.8a)/T_e(0.4a)$  than the others. Whether this is significant is difficult to say. Ohmic discharges at these same currents overlay well with this data, although in their case the selection for  $T_e > 1\text{keV}$  reduces the amount of data available outside 0.7a. In general it is found here, as in the data of [6], that the temperature profiles tend to fall off more steeply in the region where  $T_e < 1\text{keV}$ . This suggests that processes such as impurity radiation, charge-exchange, and convection, which are likely to be more important at the colder edge of the plasma, control  $T_e$  in this region and help set the amplitude for the overall electron temperature profile.

While the mid-region temperature profiles are consistent with previous results in TFTR, the central region of the temperature profile in high-power enhanced confinement discharges is truncated in comparison with high-q ohmic target discharges ( $t = 4.45$  sec versus  $t = 4.0$  sec in Fig. 4), despite the absence of regular sawtooth oscillations during the heating phase [3]. One hypothesis to explain this effect is that the neutral beams provide a large source of cold electrons in the core region. Time-dependent transport analysis of balanced injection shots indicates that core region electron thermal convection losses

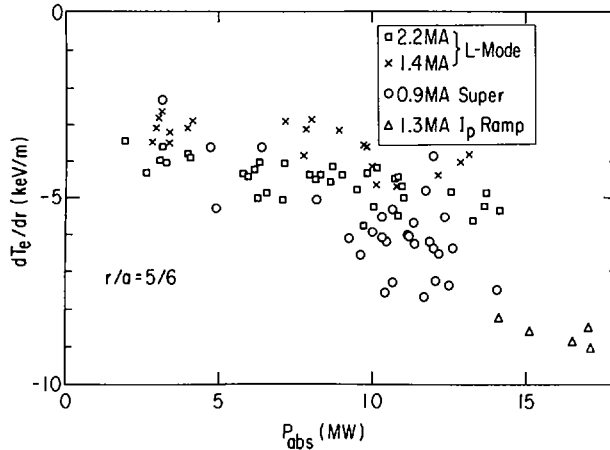


FIG. 5. Edge temperature gradient versus absorbed beam power for the same data sets as in Fig. 1.

( $5/2r_e T_e$ ) are comparable to electron conduction losses at the end of injection. The argument that an effect of this magnitude is adequate to alter  $T_e(r)$  in the core is bolstered by the observation that an even stronger central flattening of  $T_e$  is seen early in the injection pulse ( $t = 4.15$  sec in Fig. 4), when the rapid build-up of central density results in a  $dW_e/dt$  term which is also comparable to conduction, but over a larger region. Furthermore, when the cold electron source is turned off at the end of injection, the central electron temperature rises ( $t = 4.6$  sec in Fig. 4), and the profile shape regains the characteristic central peak of a high- $q$  ohmic discharge. (Issues associated with the  $\Delta'$  stability of these discharges are discussed in [3]).

If the electron temperature profile in the bulk of the minor radius in supershots is controlled by a mechanism of profile consistency such as transport coefficients which depend strongly on  $vT_e/T_e$ , and the core region is possibly clamped by convective losses, then we should look to the outer region for the enhanced confinement properties of supershots. Figure 5 shows  $dT_e/dr$  at  $r = 5a/6$  versus absorbed power for the data set of Fig. 1. As expected for consistency with L-mode current scaling, the 1.4 MA shots show a lower edge temperature gradient than the 2.2 MA shots. However at high power the 0.9 MA supershots have a steeper outer region temperature gradient than even the 2.2 MA shots. On the basis of L-mode scaling, and profile consistency, these gradients would normally be expected to vary inversely with density, since in the L-Mode  $W_e$  is found to depend only weakly on  $\bar{n}_e$ . In the power range of  $P_{inj} > 10$  MW, the 2.2 MA discharges in this data set have  $\bar{n}_e \approx 4.4 \times 10^{19} \text{ m}^{-3}$ , the 1.4 MA shots and the current ramp shots both have  $\bar{n}_e \approx 3.4 \times 10^{19} \text{ m}^{-3}$ , while the 0.9 MA supershots have  $\bar{n}_e \approx 2.7 \times 10^{19} \text{ m}^{-3}$ . The lower line average

density of the supershots is therefore not adequate to explain their steeper edge gradients. This suggests that the reduced recycling coefficient of the degassed limiters, coupled with deep beam fueling, permits a low edge density and less convective losses in the enhanced confinement regime, giving rise to a hotter edge. Absolute  $D\alpha$  measurements, coupled with neutral modeling calculation, indicate  $\tau_D$  of the order of 30 msec for the gas-filled limiter case shown in Figure 4 of [1], and  $dT_e/dr$  at 5a/6 in that case is only 3.5 keV/m. Transport analysis of this discharge indicates that at the edge of the plasma convective losses dominate conduction in the electron power balance (as in high recycling conditions in D-III [7]), explaining the low edge electron temperature and, through the constraint of profile consistency, perhaps the overall reduction in confinement.

#### 4. The Electron Density Profile

The peaked density profiles observed in the enhanced confinement regime appear to be the result of a beam build-up instability [8]. In the discharge illustrated in figure 4, at 0.1 sec into the beam pulse transport analysis calculations indicate that  $n_b(0)/n_e(0) \approx 0.4$ , and the beam density is strongly peaked on axis, contributing most of the core density gradient. As the beam ions slow down the background density builds up, and at the end of the beam pulse  $n_b(0)/n_e(0)$  has dropped to  $\approx 0.2$ . The central electron density rises at about 70% of the beam fueling rate for the first 0.3 sec of injection, and later rises at 20-30% of the source rate. The importance of central beam deposition to this build-up process may explain the sensitivity of the supershot mode to plasma current. The minimum attainable initial target density in cases with a well-degassed limiter is observed to be proportional to  $I_p^{1.5}$  in the range of 0.8-1.2 MA, and the Shafranov shift drops rapidly as a function of current, so that  $\int ndl$  between the edge and the plasma core increases strongly with  $I_p$ . The shift may be especially important, because the tightly compressed outer flux surfaces present a thin target to neutral beam injection, and particles deposited in that region are distributed around the volume of the flux surface, which is largely hidden from the beam by the plasma core. Spectroscopic measurements also indicate higher carbon influx rates at higher currents. This further helps to explain the absence of peaked density profiles and supershot behavior at high current. L-Mode and ohmically heated plasmas generally have more peaked density profiles at  $q_a > 5$  as well, suggesting an increased susceptibility to this process at high  $q_a$ .

There are a number of ways in which a peaked density profile can mediate improved confinement. One natural hypothesis is that the peaked profiles reduce  $\eta_i$  and/or  $\eta_e$  which could be important factors in the instabilities which drive transport ( $\eta_{i,e} \equiv d\ln T_{i,e}/d\ln n_{i,e}$ ).  $\eta_i$  has not been measured on TFTR, but  $\eta_e$  can be calculated from the Thomson scattering data. In the

region inside  $0.4a$   $n_e$  is significantly lower in supershots than in standard discharges, dropping at high powers from values in the range of 1.7 at  $0.4a$  for standard discharges to 1.2 in the enhanced confinement mode. An alternative hypothesis discussed in section 3 above, is that high edge electron temperatures, in the presence of reduced recycling and low edge densities, may result in relatively low values for edge transport coefficients as in the H-mode. In the presence of even constant edge transport coefficients, electron temperature profile consistency arguments which take into consideration the presence of a centrally peaked density profile, but assume that the edge electron thermal diffusivity responds only to the local  $n_e$ , predict a significant improvement in  $W_e$  [9].

##### 5. Balanced vs. Unbalanced Injection and Plasma Rotation

As indicated in [1], the stored energy in supershot plasmas shows a considerable improvement as the beam powers in the co and counter directions are brought into balance. Because of the present configuration of TFTR (3 co-beamlines and 1 counter-beamline for the usual direction of  $I_p$ ) we have not obtained high power data with pure counter-injection and a well-degassed limiter. At low currents (600-800 kA), however, enhanced confinement discharges with favorable time evolution and highly peaked density profiles can be obtained with only 5 MW of balanced injection power, and the full spectrum of  $P_{co}/P_{inj}$  can be explored. We find that the density increase at fixed injection power drops with rising  $P_{co}/P_{inj}$ , but the peakedness of the density profile falls off as one moves away from balanced injection in either direction. Stored energy and especially neutron production fall off as well. Plasma rotation speeds of  $\approx 8 \times 10^5$  m/sec have been measured in co-injected discharges, corresponding to a Mach number of  $\approx 0.7$ . Rotation speeds with counter-injection are lower than with co-injection at the same power.

A number of classically expected factors may lead to reduced density peaking and poorer heating efficiency at high rotation speeds with unidirectional injection [10]. In the rotating plasma frame the beam ions, and especially the fractional energy component beam ions (which constitute about one half of the total beam), have considerably reduced energy. This results in larger atomic cross-sections for beam deposition and a larger fraction of the deposition on hydrogenic species in the form of charge-exchange rather than impact ionization. Because of the lower beam ion velocity in the plasma frame, the beam ion slowing down time and therefore the beam ion density is substantially reduced. In an extreme example (13 MW of co-injection at  $I_p = 0.9$  MA with  $v_\phi(0) = 7.5 \times 10^5$  m/sec) taking these effects into account in somewhat simplified calculations results in a 30% reduction of central electron source rate. The central beam ion density at the end of injection is reduced by a factor of 3. If the presence of

a central peak of circulating beam ions is important for establishing a sharp electron density profile, it is reasonable to expect that this sharpness will be reduced in a rapidly rotating plasma. At the high Mach numbers we have observed, one expects significant centrifuging of plasma density, and especially of impurity density, to the large major radius side of the plasma. Thomson scattering measurements show a definite trend in this direction, correlated with unbalanced injection. Detailed scaling studies have not been made, but effects of the magnitude expected are observed. This centrifuge effect should tend to reduce beam penetration to the center of the plasma. To determine whether these classically expected effects of rotation are enough to explain the differences in the density profiles we observe, without additional changes in central particle diffusivity, will require more detailed calculations and examination of the data. The increased density rise in counter-injected discharges almost certainly also plays a role in the broad density profiles observed in the more slowly rotating counter-injected plasmas.

Lower beam velocity in the plasma frame results in a strong reduction in the beam-target and beam-beam fusion neutron yield; unidirectional injection reduces beam-beam neutron production as well. In the example above the effects of plasma rotation reduce the calculated neutron flux by a factor of 2, and good agreement is obtained with the measurement. The importance of plasma rotation for neutron production is most clearly illustrated by the rapid rise in neutron production observed when a low-current plasma is first heated with 5 MW of co-only injection, and then the co beams are switched off and 5 MW of counter beams turned on. The neutron emission rises by a factor of 2 in 50 msec.

With unbalanced injection a substantial fraction of the beam power is invested in applying torque to the rotating plasma. Much of this power is expected to be returned to the bulk ions via viscous damping mechanisms in the region where the gradients in rotation speed are high, probably close to the plasma surface. In this region ion thermal losses through convection and charge-exchange are large however. Rotational energy may also be partially lost from the plasma via the same mechanisms. In the example discussed above, this process, plus the reduction in beam penetration, results in a 50% reduction of central heating power, and an overall 40% investment of beam heating power in driving rotation. If the power is not coupled back to the plasma, the lower total stored energy observed with co-only injection [1] is reasonably well explained. Central ion temperature measurements in co-only cases are also reduced compared to balanced injection with similar parameters, consistent with the calculated reduced central input power to the ions. Rotational energy is probably coupled back into the bulk thermal plasma with some efficiency, and it is thus a mix of this mechanism and the broader density profiles observed with co-only injection which together result in reduced stored energy.

## 6. Conclusions

A new mode of enhanced energy confinement has been observed on TFTR. It exhibits improved electron stored energy, as well as improved thermal and beam ion stored energy. The broad electron temperature profile shapes observed in this regime at high  $q_a$  do not support a concept of profile consistency based on the assumption that  $T_e(0)/\langle T_e \rangle_v = f(q_a)$ , but do fit with a model based on examining normalized profile shapes outside of the plasma core, independent of  $q_a$  [6, 11]. The observation that increased recycling results in a convection-dominated edge electron power balance, which then correlates with reduced overall confinement, fits well with an understanding of this regime based on profile consistency arguments [9]. On the other hand it is also a reasonable hypothesis that the reduction of  $n_e$  and/or  $n_i$  in the core region plays an important role.

The peaked density profiles observed in this regime appear to be due to a beam build-up process which results in highly centralized beam deposition. Density profiles are most peaked with near-balanced injection, and some classically expected mechanisms have been put forward to explain this, but it is not clear whether other effects are required. Neutron production and beam heating efficiency are also highest with near-balanced injection. Classical calculations including plasma rotation are adequate to explain the difference in neutron production rate with co-only and balanced injection, given the differences in plasma profiles. The fractional power delivered to the plasma in the form of torque on a rotating body is comparable to the fractional difference in stored energy between co-only and balanced injection. Some of this power, however, is probably re-invested in ion heating near the outside in minor radius. The combination of the resulting reduction in heating efficiency and the broader density profiles observed with unbalanced injection together explain the importance of balanced injection for obtaining the best results in the TFTR "supershot" regime.

## ACKNOWLEDGMENTS

We are grateful to D.J. Grove and J.R. Thompson for their advice and support, and to J. Strachan for his many contributions. This work was supported by US DOE Contract No. DE-AC02-76-CHO3073. The ORNL participants were also supported by U.S. Department of Energy Contract No. DE-AC05-84OR21400 with Martin Marietta Energy Systems, Inc.

## REFERENCES

- [1] HAWRYLUK, R.J., et al., Paper IAEA-CN-47/A-I-3, these Proceedings, Vol. 1.
- [2] HILL, K.W., et al., Paper IAEA-CN-47/A-IV-2, these Proceedings, Vol. 1.
- [3] McGUIRE, K., et al., Paper IAEA-CN-47/A-VII-4, these Proceedings, Vol. 1.

- [4] GOLDSTON, R.J., Plasma Phys. Control. Fusion **26** (1984) 87.
- [5] WALTZ, R.E., Comments on Profile Consistency, Rep. GAT-A 18365, Goodyear Atomic Corp., Portsmouth, OH.
- [6] FREDRICKSON, E., et al., in Controlled Fusion and Plasma Heating (Proc. 13th Europ. Conf. Schliersee, 1986), Vol. 1, European Physical Society (1986) 148.
- [7] NAGAMI, M., et al., Nucl. Fusion **24** (1984) 183.
- [8] POST, D.E., private communication, 1978.
- [9] FURTH, H.P., Plasma Phys. Control. Fusion **28** (1986) 1305.
- [10] GOLDSTON, R.J., in Basic Physical Processes of Toroidal Fusion Plasmas (Proc. Course and Workshop Varenna, 1985), Vol. 1, EUR-10418-EN, CEC, Brussels (1986) 165\*.
- [11] MURMANN, H.D., et al., in Controlled Fusion and Plasma Heating (Proc. 13th Europ. Conf. Schliersee, 1986), Vol. 1, European Physical Society (1986) 216.

## DISCUSSION

A. BHATTACHARJEE: I have a comment and a question. In the presence of toroidal rotation, the density on any given flux surface becomes poloidally asymmetric. This, as you know, was observed in PDX. However, the magnitude of toroidal rotation necessary to explain the asymmetry experimentally observed was found to be greater than the rotation actually observed, for example, by S. Semenzato et al. at the Centre de recherches en physique de plasmas, Lausanne. It appears that the same could be said of TFTR.

My question is: why is it that the rotation velocity observed is different for co-injection and counter-injection when the beam power is held fixed?

R.J. GOLDSTON: On TFTR, as on PDX, we do see some in-out asymmetry in the Thomson scattering density profiles, even in Ohmic plasmas. We have found, however, that there is a systematic further asymmetry which correlates with unbalanced injection. The degree of this further asymmetry is roughly in agreement with what would be theoretically expected, but we have not yet carried out detailed scaling studies on the asymmetry.

Counter-injection does indeed drive less central rotation speed than co-injection, for fixed power, but the density is higher. We have not yet measured the radial profile of the rotation, so I am hesitant to suggest an explanation.

B. COPPI: I should just like to comment that the lack of dependence of  $T_c(0)/T\langle T_e \rangle_{av}$  on  $q_a$  when  $q(r=0) > 1$  was in fact pointed out in the original formulation for the principle of profile consistency. Therefore, the observations you

---

\* The last term in Eq. (26) of this reference should read:

$$\begin{aligned}
 & + \frac{\Sigma_i n_i \omega_i^2}{2} \left( \frac{\partial V}{\partial \rho} \right)^{-1} \left\{ \frac{\partial}{\partial \rho} \left[ \langle R^2 (\vec{v}_\rho)^2 \rangle \left( \frac{\partial V}{\partial \rho} \right) n_i \left( \frac{\vec{v}_\rho}{v_\rho} \right) \right] \right. \\
 & \quad \left. - \langle R^2 \rangle \frac{\partial}{\partial \rho} \left[ \langle (\vec{v}_\rho)^2 \rangle \left( \frac{\partial V}{\partial \rho} \right) n_i \left( \frac{\vec{v}_\rho}{v_\rho} \right) \right] \right\}
 \end{aligned}$$

reported do not require a reformulation of this principle. In addition, the temperature profile may deviate considerably from a Gaussian, depending on a variety of factors, for example, the presence of trapped electrons, under the same formulation.

R.J. GOLDSTON: Thank you for the comment.

A. GIBSON: Now that you have the concept of profile consistency with so many 'ifs' and 'buts' and restricted it to such a special region of the profile, do you still believe it has any physical significance, and if so what is it?

R.J. GOLDSTON: Researchers have frequently divided the tokamak into three zones — a central sawtooth zone, a middle 'confinement' zone, and an edge zone dominated by convection and atomic physics. The refinement we proposed at the 13th European Conference in 1986 and which we are discussing here is that the resiliency of the profile applies mostly in the middle 'confinement' zone. Lower hybrid heating experiments certainly show that the presence or absence of sawteeth can strongly attack the core zone, and the H-mode is an example of how the edge can be modified. The fact that modifications of the edge region can have profound effects on core transport strongly suggests a transport mechanism which resists profile shape changes. One example would be a model which includes  $\nabla T_e$  or  $d \ln T_e / dr$  in the electron thermal diffusivity itself.



# ENERGY AND PARTICLE CONFINEMENT OF JT-60 PLASMAS WITH HIGH POWER HEATING

JT-60 TEAM

*(Presented by M. Nagami)*

T. Abe, H. Aikawa, H. Akaoka, H. Akasaka, M. Akiba, N. Akino, T. Akiyama, T. Ando, K. Annoh, N. Aoyagi, K. Arakawa, M. Araki, K. Arimoto, M. Azumi, S. Chiba, M. Dairaku, N. Ebisawa, T. Fujii, T. Fukuda, H. Furukawa, K. Hamamatsu, K. Hayashi, M. Hara, K. Haraguchi, H. Hiratsuka, T. Hirayama, S. Hiroki, K. Hiruta, M. Honda, H. Horiike, R. Hosoda, N. Hosogane, Y. Iida, T. Iijima, K. Ikeda, Y. Ikeda, T. Imai, T. Inoue, N. Isaji, M. Isaka, S. Ishida, N. Itige, T. Ito, Y. Ito, A. Kaminaga, M. Kawai, Y. Kawamata, K. Kawasaki, K. Kikuchi, M. Kikuchi, H. Kimura, T. Kimura, H. Kishimoto, K. Kitahara, S. Kitamura, A. Kitsunozaki, K. Kiyono, N. Kobayashi, K. Kodama, Y. Koide, T. Koike, M. Komata, I. Kondo, S. Konoshima, H. Kubo, S. Kunieda, S. Kurakata, K. Kurihara, M. Kuriyama, T. Kuroda, M. Kusaka, Y. Kusama, S. Maehara, K. Maeno, S. Mase, S. Matsuda, M. Matsukawa, T. Matsukawa, M. Matsuoka, N. Miya, K. Miyati, Y. Miyo, K. Mizuhashi, M. Mizuno, R. Murai, Y. Murakami, M. Muto, M. Nagami, A. Nagashima, K. Nagashima, T. Nagashima, S. Nagaya, H. Nakamura, Y. Nakamura, M. Nemoto, Y. Neyatani, S. Niihara, H. Ninomiya, T. Nishitani, H. Nomata, K. Obara, N. Ogiwara, Y. Ohara, K. Ohasa, T. Ohga, H. Ohhara, M. Ohkubo, T. Ohshima, K. Ohta, M. Ohta, M. Ohtaka, Y. Ohuchi, A. Oikawa, H. Okumura, Y. Okumura, K. Omori, S. Omori, Y. Omori, T. Ozeki, M. Saigusa, K. Sakamoto, A. Sakasai, S. Sakata, M. Satou, M. Sawahata, M. Seimiya, M. Seki, S. Seki, K. Shibanuma, R. Shimada, K. Shimizu, M. Shimizu, Y. Shimomura, S. Shinozaki, H. Shirai, H. Shirakata, M. Shitomi, K. Sugauma, T. Sugie, T. Sugiyama, H. Sunaoshi, K. Suzuki, M. Suzuki, M. Suzuki, N. Suzuki, S. Suzuki, Y. Suzuki, H. Takahashi<sup>1</sup>, M. Takahashi, S. Takahashi, T. Takahashi, M. Takasaki, M. Takatsu, A. Takeshita, H. Takeuchi, S. Tamura, S. Tanaka, K. Tani, M. Terakado, T. Terakado, K. Tobita, T. Tokutake, T. Totsuka, N. Toyoshima, H. Tsuda, T. Tsugita, S. Tsuji, Y. Tsukahara, M. Tsuneoka, K. Uehara, M. Umehara, Y. Uramoto, H. Usami, K. Ushigusa, K. Usui, J. Yagyu, K. Yamada, M. Yamamoto, O. Yamashita, Y. Yamashita, K. Yano, T. Yasukawa, K. Yokokura, H. Yokomizo, H. Yoshida, M. Yoshikawa, Y. Yoshinari, R. Yoshino, I. Yonekawa, K. Watanabe

Naka Fusion Energy Research Establishment,  
Japan Atomic Energy Research Institute,  
Naka-machi, Naka-gun, Ibaraki-ken,  
Japan

---

<sup>1</sup> Princeton Plasma Physics Laboratory, Princeton University, NJ, USA.

## Abstract

### ENERGY AND PARTICLE CONFINEMENT OF JT-60 PLASMAS WITH HIGH POWER HEATING.

Results are reported from initial confinement experiments of divertor and limiter plasmas, carrying a current of up to 2 MA and heated by neutral beam power up to 20 MW, over a wide range of densities  $(0.3\text{--}8) \times 10^{19} \text{ m}^{-3}$ , and toroidal fields, 1.9–4.5 T. Preliminary experiments on the concurrent application of NB heating and ICRF or LHCD are also described. The plasma stored energy has an offset linear relation with the absorbed power, and the energy confinement time (in seconds) scales as  $(0.051 + 0.35/P_{\text{abs}} [\text{MW}]) \times I_p [\text{MA}]^{0.4}$ . The energy and particle confinement times have a similar dependence on the absorbed power. Improved particle and energy confinement is discussed for NB, NB + ICRF, and NB + LHCD discharges.

## 1. INTRODUCTION

This paper discusses confinement results from the initial auxiliary heating experiments. A companion paper [1] provides a review of the JT-60 programme and its experiments. Another companion paper [2] describes impurity and MHD effects. The additional heating and current drive programme started in early August, using either NB heating, ICRF second harmonic (120 MHz) heating or LHCD (2 GHz). The injected NB power ( $P_{\text{inj}}$ ) was raised to 20 MW, the ICRF power to 1.4 MW and the LHCD power to 1 MW, within two to three months from the start of the experiments.

The particle confinement and the energy confinement of NB heated normal discharges are discussed in Sections 2 and 3, respectively. The regimes of improved confinement are described in Section 4. Conclusions are presented in Section 5.

## 2. PARTICLE CONFINEMENT

The line integrated  $H_\alpha$  emission intensity was measured along a chord in the poloidal plane at four different locations each in the main and divertor chambers. Figure 1 shows the time evolution of  $\bar{n}_e$  and four channel  $H_\alpha$  signals for an 8 MW NB heating divertor discharge. With NB injection the main plasma density started to decrease, and the  $H_\alpha$  intensity in the divertor chamber increased by a factor of 5 to 20 from its Ohmic level while the intensity only rose by a factor of two to three in the main chamber. This suggests an enhanced scrape-off plasma flow from the main chamber into the divertor chamber during NB injection.

On the assumption of toroidal symmetry, the global particle confinement time  $\tau_p$  can be determined from an absolute intensity measurement of the  $H_\alpha$  emission at one toroidal location. This assumption is believed to be valid for divertor discharges. For Ohmic discharges,  $\tau_p$  was found to be proportional to  $n_e^{0.7}$  and was 70 ms at  $\bar{n}_e = 3 \times 10^{19} \text{ m}^{-3}$  (Fig. 2(a)). The  $\tau_p$  degraded with increasing  $P_{\text{inj}}$ , and, at 20 MW, was lower than its Ohmic values by a factor of three.

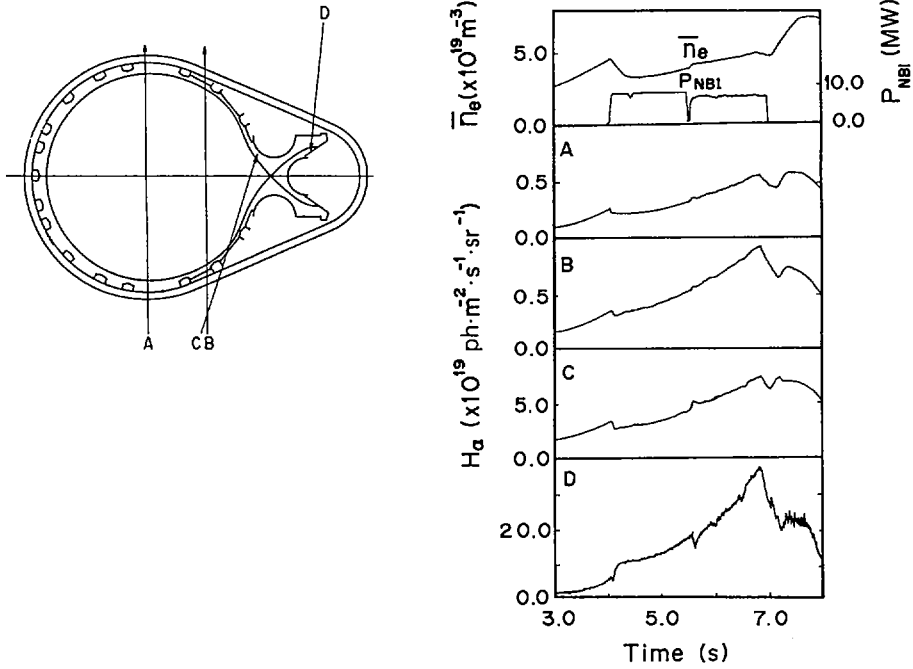


FIG. 1. Evolution of  $\bar{n}_e$  and four channel  $H_\alpha$  signals for NB heated divertor discharge.

The hydrogen neutral pressures measured in the main and divertor chambers are plotted against  $\bar{n}_e$  in Fig. 2(b) for Ohmic and NB heated discharges. The pressure ratio,  $P_{\text{div}}/P_{\text{main}}$ , which is sometimes regarded as an indicator of efficient divertor function, was 30 to 40 for Ohmic discharges, but increased up to 40 to 60 for discharges heated with 10 to 20 MW of NB power. The measured  $P_{\text{div}}$  was proportional to  $\bar{n}_e^2$ . This dependence, together with the experimentally determined  $\bar{n}_e$  dependence of  $\tau_p$ , leads to a conductance of the neutral particle backflow from the divertor to the main chamber which is nearly independent of  $\bar{n}_e$ . The conductance, consistent with the measured  $P_{\text{div}}$  and  $\tau_p$ , was about  $900 \text{ m}^3 \cdot \text{s}^{-1}$  and was one-half to one-third of the calculated mechanical conductance. This difference appears reasonable when the presence of the scrape-off plasma that obstructs the backflow is taken into account. For a constant backflow conductance, the normalized divertor pressure,  $P_{\text{div}}^* = P_{\text{div}}/\bar{n}_e^2$ , is inversely proportional to  $\tau_p$ . The dependence on the absorbed power ( $P_{\text{abs}}$ ) (sum of Ohmic and injected beam power minus shinethrough loss) of  $1/P_{\text{div}}^*$  was similar to that of the energy confinement time (Fig. 2(c)). This resemblance suggests a correlation between the increased scrape-off plasma flow and the degradation of energy confinement.

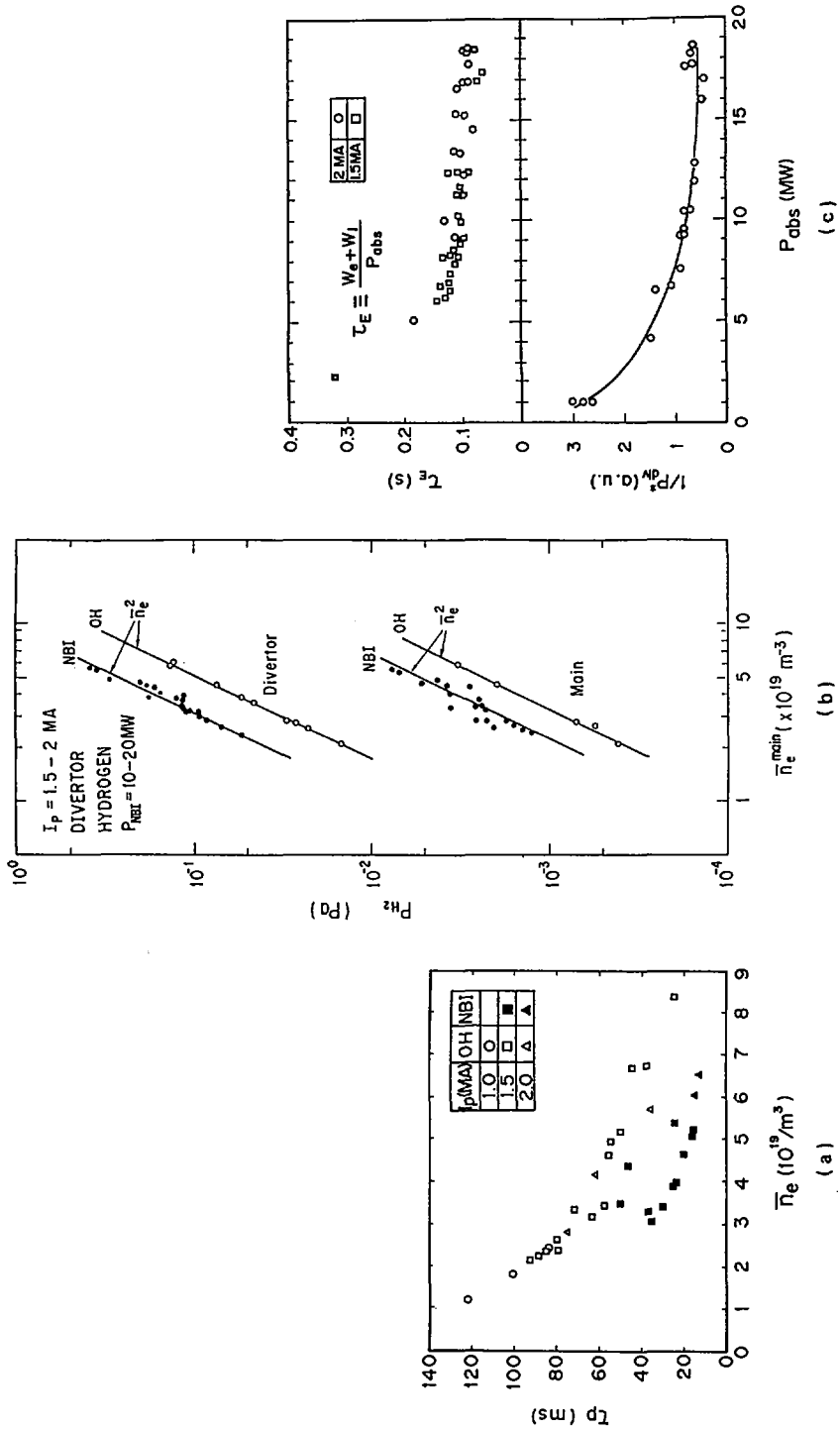


FIG. 2. (a) Plot of  $\tau_p$  against  $\bar{n}_e$  for Ohmic and NB heated discharges; (b) plot of  $P_{main}$ ,  $P_{div}$  against  $\bar{n}_e$  for Ohmic and NB heated discharges; (c) plot of  $\tau_E$  and  $1/P_{div}^*$  against  $P_{abs}$

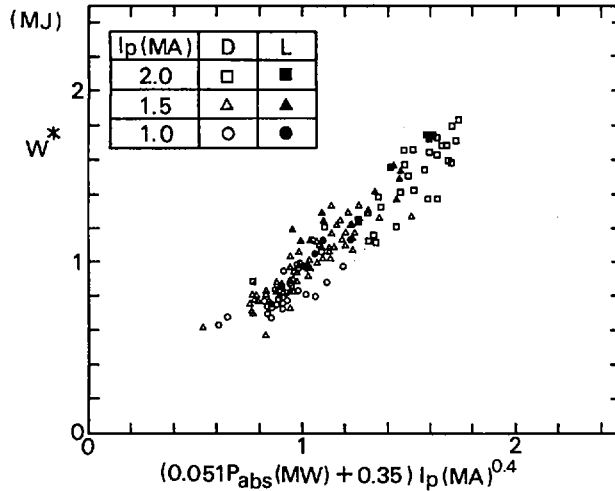


FIG. 3. Plot of  $W^*$  against  $(0.051P_{abs} [MW] + 0.35) I_p [MA]^{0.4}$ .

### 3. ENERGY CONFINEMENT

Hydrogen neutral beam power of up to 20 MW at energies of 50 to 75 keV, was injected into hydrogen or helium plasmas. The fraction of hydrogen in the (nominally) helium plasmas was estimated to be up to one-half, from  $H_\alpha$  emission intensity, beam shintthrough loss and neutral hydrogen flux measurements.

In divertor discharges roughly 80% of the absorbed power can be accounted for. Energy balance in the divertor chamber is accomplished through a bolometer array used to measure the radiation loss and a thermocouple array utilized to measure the divertor plate heat flux. The measurement showed that the divertor chamber radiation accounted for about 20%, the divertor plate heat deposition for about 50% and the main chamber radiation for less than 10% of the absorbed power.

#### 3.1. Energy confinement scaling

The plasma stored energy was evaluated by both kinetic and magnetic means. The kinetic determination of the stored energy was based on a six point Thomson scattering profile of the electron temperature and the spectroscopically determined central ion temperature. When the calculated fast ion energy was added to the kinetically determined stored energy, the sum agreed with the magnetically determined stored energy ( $W^*$ ) within 20%.

The value of  $\tau_E^* = W^*/P_{abs}$  was the same for hydrogen and (nominally) helium discharges and did not depend on the density. A toroidal field ( $B_t$ ) scan from 1.9 to 4.4T at  $I_p = 1MA$  did not yield any obvious dependence of  $\tau_E^*$  on  $B_t$ , or on  $q_{eff}$ .

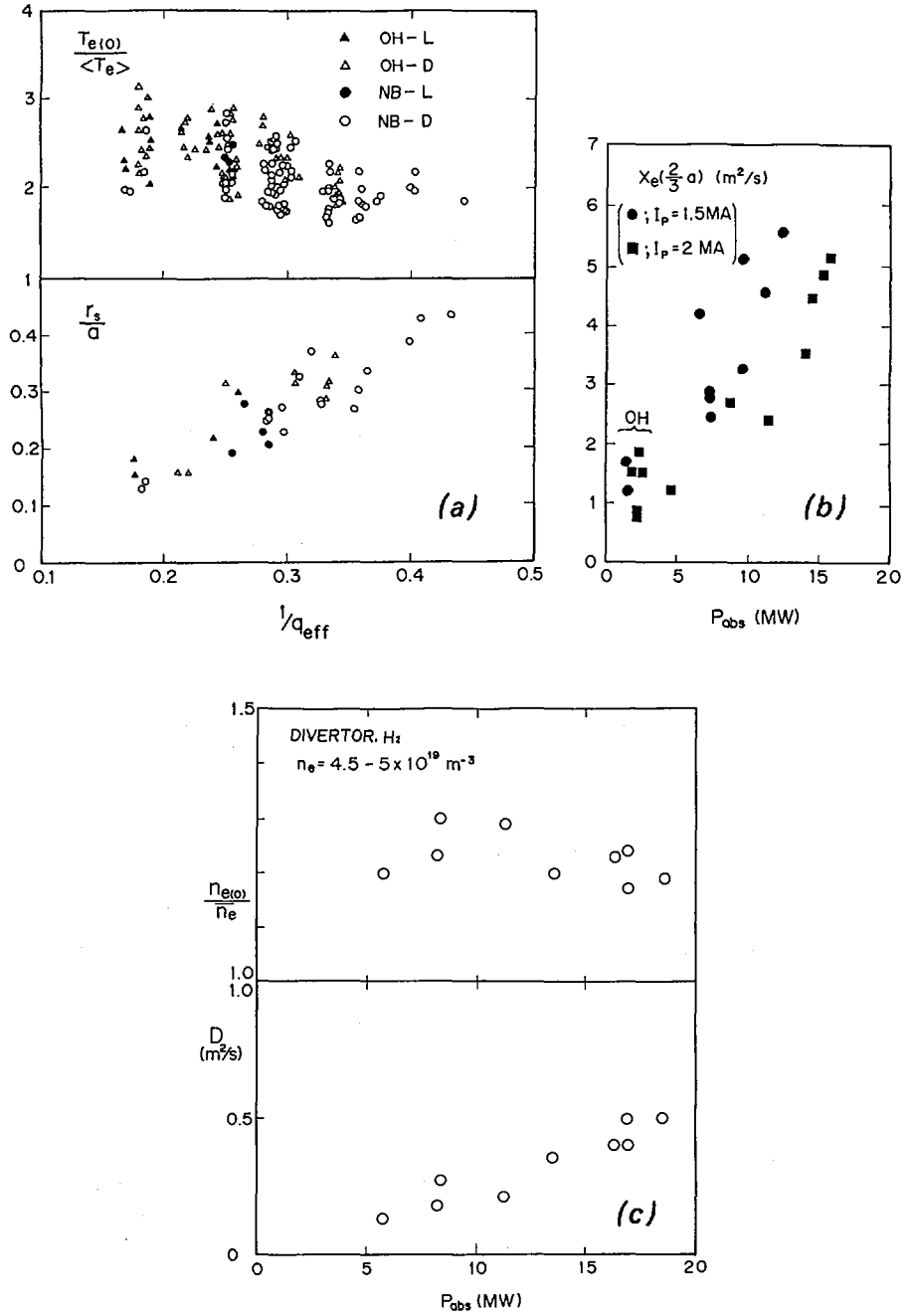


FIG. 4. (a) Plot of  $T_e(0)/\langle T_e \rangle$  and  $r_s/a$  against  $1/q_{eff}$  for ohmically heated divertor and limiter discharges, and NB heated divertor and limiter discharges; (b) plot of electron thermal diffusivity,  $X_e$ , at  $r = 2a/3$  against  $P_{obs}$ ; (c) plot of  $n_e(0)/n_e$  and particle diffusivity ( $D$ ) against  $P_{obs}$ .

which varied from 2.2 to 6. Under similar conditions, the  $W^*$  of the limiter discharges was about the same as that of the divertor discharges. The discharges can be represented by an offset linear relation,  $\tau_E^* [s] = (0.051 + 0.35/P_{abs} [MW])/I_p [MA]^{0.4}$ , which results in an increased confinement time of 50 to 70 ms for  $I_p = 1$  to 2MA (Fig. 3). This relation has a weaker  $I_p$  dependence than the Kaye-Goldston scaling.

### 3.2. Energy transport analysis

The ratio of the central to the volume averaged electron temperature,  $T_e(0)/\langle T_e \rangle$ , and the ratio of the sawtooth inversion radius to the minor radius,  $r_s/a$ , are plotted against  $1/q_{eff}$  in Fig. 4(a). These ratios varied little between Ohmic and NB heated discharges, or between divertor and limiter discharges. This fact may be an indication that the electron temperature profile and the current profile in the core region did not vary substantially.

The energy transfer from the fast ions to the plasma electrons and ions was estimated as a function of the magnetic surface co-ordinate using Monte Carlo beam deposition and fast ion orbit/slow-down calculations. The main ion energy loss channel was the energy transfer to the electrons, and the ion heat conduction played a minor role in the ion energy balance.

The electron heat conduction dominated the energy confinement in the plasma core. The electron thermal diffusivity ( $X_e$ ) at  $r/a = 2/3$ , calculated by the transport analysis assuming that  $X_i$  is three times the Chang-Hinton value, was  $1-2 \text{ m}^2\cdot\text{s}^{-1}$  for Ohmic discharges and increased by a factor of three to five for discharges heated with 20 MW of NB power (Fig. 4(b)). The ratio of the central to the line averaged density,  $n_e(0)/\bar{n}_e$ , is plotted against  $P_{abs}$  in Fig. 4(c). This ratio, which is around 1.2, indicates a very flat density profile, nearly independent of the NB power. The particle diffusivity ( $D$ ) at  $r = 2a/3$ , deduced from NB particle fuelling and density profile evolution, increased with the increase of absorbed power. The convective energy flow made a contribution of approximately 20% in the plasma core, and was estimated to be comparable to the conduction loss in the peripheral regions.

## 4. IMPROVED PARTICLE AND ENERGY CONFINEMENT DISCHARGES

There were three different sets of conditions in which an improvement in either particle or energy confinement was observed.

The first set of conditions was found during an effort made to produce an environment which was considered conducive to the H-mode, based upon the experience from medium sized devices: increasing  $P_{inj}$  to 20 MW, lowering  $B_t$  to 1.9 T, and  $q_{eff}$  to 2.2, maintaining a large separatrix-limiter distance up to 5 cm, maximizing the volume averaged power density by reducing the plasma volume

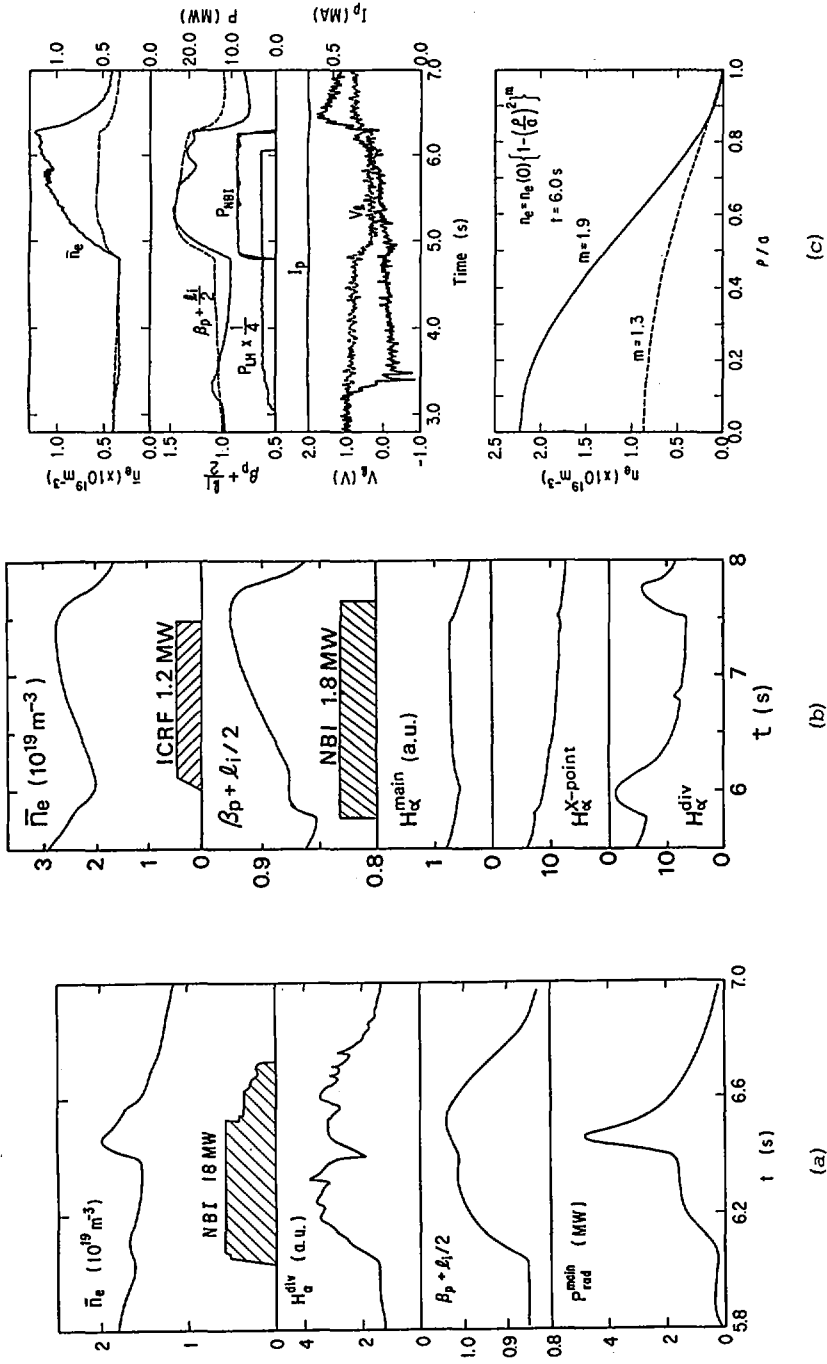


FIG. 5. (a) Evolution of  $\bar{n}_e$ ,  $H_\alpha^{\text{div}}$ ,  $H_\alpha^{\text{main}}$ ,  $\beta_p + \ell_1/2$  and  $P_{\text{rad}}^{\text{main}}$  for an  $I_p = 1.5$  MA divertor discharge with a weak H-mode-like transition; (b) evolution of  $\bar{n}_e$ ,  $H_\alpha$  signals and  $\beta_p + \ell_1/2$  for an  $I_p = 1.5$  MA divertor discharge with NB and ICRF heating; (c) evolution of  $\bar{n}_e$ ,  $\beta_p + \ell_1/2$ ,  $I_p$ ,  $V_t$  and radial  $n_e$  profiles at  $t = 6$  s for two discharges: one (shown by broken lines) is a normal, inductively driven discharge and the other one (solid line) is a discharge driven entirely by LHCD.

(14 MW/31 m<sup>3</sup>), the use of helium instead of hydrogen, fuelling through the divertor chamber, etc. These efforts produced no clear, reproducible H-mode discharges. The example shown in Fig. 5(a) possessed, however, most of the characteristics commonly associated with the H-mode. The discharge was a small minor radius (0.71 m) plasma heated with  $P_{inj} = 18$  MW ( $P_{abs} = 14$  MW) and showed an abrupt reduction of the  $H_\alpha$  emission in the divertor chamber (at 0.37 s into the beam heating phase) and a simultaneous increase in  $\bar{n}_e$  from 1.6 to  $2 \times 10^{19}$  m<sup>-3</sup>, in  $\Delta\beta_p$  by 20%, and in the radiative power from 1.4 to 4.8 MW. Furthermore, this discharge had the best  $\tau_E^*$  among discharges with a similar minor radius. The increase in  $\beta_p$  was, however, insignificant and only a few similar discharges have been obtained to date. Many discharges with similar parameters that can be set by the operator resulted in bursts of radiation, originating from the molybdenum discharge contamination beginning at about the time when the  $H_\alpha$  reduction would have happened.

Reduction of particle recycling in the divertor region was observed during ICRF injection into Ohmic discharges and NB injected discharges with the injection power not greatly exceeding the ICRF power. The second example shown in Fig. 5(b) is a 1.5 MA divertor discharge with NB and ICRF heating. The increased  $H_\alpha$  emission in the divertor with the NB injection turned out to diminish with the start of the ICRF injection, and at the switchoff of the ICRF injection the emission started to increase again, suggesting a reduction of plasma flow into the divertor chamber during ICRF injection. The behaviour of  $H_\alpha$  and  $\bar{n}_e$  signals during ICRF injection is totally different from that in NB heated discharges. The increased energy confinement time of 70 ms during the initial NB injection was extended by 40% at the end of the ICRF injection.

As the third example, two discharges heated with NB are compared in Fig. 5(c): one (shown by broken lines) was a normal, inductively driven discharge and the other one (solid line) was a discharge driven entirely by LHCD. Both discharges were operated at  $B_t = 4$  T,  $I_p = 700$  kA, with no gas feed (prefill only); they were heated by 40 keV, 8.1 MW NB power. A dramatically increased  $\bar{n}_e$  level in the LHCD discharge over the inductively driven discharge indicates improved particle confinement. The three chord density profile measurements showed substantially a peaked  $n_e$  profile ( $n_e(0)/\bar{n}_e = 2.1$ ), suggesting  $\tau_p$  improvement in the plasma core. Also, the increased energy confinement time was raised by 30%. The improvement may be related to the suppression of sawtooth activities and/or a change in current profile. The internal inductance fell by 0.2 from the Ohmic heating level, indicating a flattening of the current profile by LHCD.

## 5. CONCLUSIONS

Energy and particle confinement was studied, by taking full advantage of efficient divertor functions of the JT-60 device that allowed operations over a wide density range by controlling the particle exhaust and impurity contamination, and by

utilizing three different means of additional heating. The divertor was particularly useful in allowing operations at extremely low densities at which LHCD had to operate.

The availability of three different means of additional heating, used individually and in various combinations, allowed investigations of the confinement properties that lead to operating modes with improved confinement.

### ACKNOWLEDGEMENTS

The authors wish to thank the members of JAERI who have contributed to the JT-60 project throughout its progress. They also wish to express their gratitude to Drs S. Mori, Y. Iso, and K. Tomabechi for continued encouragement and support.

### REFERENCES

- [1] YOSHIKAWA, M., Paper IAEA-CN-47/A-I-1, these Proceedings, Vol. 1.
- [2] JT-60 TEAM (presented by H. Takeuchi), Paper IAEA-CN-47/A-IV-3, these Proceedings, Vol. 1.

### DISCUSSION

F. WAGNER: The  $H_{\alpha}$  radiation in the divertor chamber reflects the local ionization equilibrium fuelled by the power flow into it.  $H_{\alpha}$  can transiently drop when the plasma confinement changes. On the other hand,  $H_{\alpha}$  also drops when the power flow into the divertor chamber is reduced by enhanced impurity radiation in the main plasma chamber. To what extent is the  $H_{\alpha}$  intensity reduction which you observed during ICRH caused by enhanced impurity radiation?

M. NAGAMI: Although the radiation loss in the main plasma,  $P_{\text{rad}}^{\text{main}}$ , increased during ICRF, the power flux into the divertor,  $P_{\text{tot}} - P_{\text{rad}}^{\text{main}}$ , also increased. Furthermore, it was experimentally demonstrated that an impurity ( $N_2$ ) injection into an Ohmic discharge or a neutral beam heated discharge does not produce the same  $H_{\alpha}$  reduction as that observed during ICRH.

D.E. POST: Did the divertor operate in a 'high recycling' regime with high neutral compression at the low densities used for lower hybrid current drive?

M. NAGAMI: Neutral particle pressure and recycling in the divertor chamber are low for the low density discharges with lower hybrid current drive.

## ENERGY CONFINEMENT IN JET WITH OHMIC HEATING AND STRONG AUXILIARY HEATING

J.G. CORDEY, D.V. BARTLETT, V. BHATNAGAR<sup>1</sup>, R.J. BICKERTON,  
M. BURES, J.D. CALLEN<sup>2</sup>, D.J. CAMPBELL, C.D. CHALLIS,  
J.P. CHRISTIANSEN, S. CORTI, A.E. COSTLEY, G.A. COTTRELL,  
G. DUESING, J. FESSEY, M. GADEBERG<sup>3</sup>, A. GIBSON,  
A. GONDHALEKAR, N.A. GOTTARDI, C.W. GOWERS,  
M. VON HELLERMANN, F. HENDRIKS, L. HORTON, H. JÄCKEL<sup>4</sup>,  
J. JACQUINOT, O.N. JARVIS, T.T.C. JONES, E. KÄLLNE, J. KÄLLNE,  
M. KEILHACKER, S. KISSEL, L. DE KOCK, P. LALLIA, E. LAZZARO,  
P.J. LOMAS, N. LOPES-CARDOZO<sup>5</sup>, P.D. MORGAN, P. NIELSEN,  
J. O'ROURKE, R. PRENTICE, R.T. ROSS, G. SADLER, F.C. SCHÜLLER,  
A. STABLER<sup>4</sup>, P. SMEULDERS, M.F. STAMP, D. STORK, P.E. STOTT,  
D.R. SUMMERS, A. TANGA, P.R. THOMAS, E. THOMPSON,  
K. THOMSEN<sup>3</sup>, G. TONETTI<sup>6</sup>, B.J. TUBBING<sup>5</sup>, M.L. WATKINS

JET Joint Undertaking,  
Abingdon, Oxfordshire,  
United Kingdom

### Abstract

#### ENERGY CONFINEMENT IN JET WITH OHMIC HEATING AND STRONG AUXILIARY HEATING.

The energy confinement properties with strong auxiliary heating are found to be well described by an offset linear law relating the stored energy  $W$  to the input power  $P$  ( $W = \alpha P + \beta$ ). The scaling of the energy confinement time with the non-dimensional plasma physics parameters suggests that the underlying mechanism is resistive MHD. The heating profile and impurity radiation are identified as making a substantial contribution to the degradation in the global energy confinement time with auxiliary heating.

---

<sup>1</sup> Plasma Physics Laboratory, Association "Euratom-Belgian State" ERM/KMS, Brussels, Belgium.

<sup>2</sup> Department of Physics, University of Wisconsin, Madison, WI, USA.

<sup>3</sup> Risø National Laboratory, Roskilde, Denmark.

<sup>4</sup> Max-Planck-Institut für Plasmaphysik, Garching, Fed. Rep. Germany.

<sup>5</sup> FOM Instituut voor Plasmafysica, Nieuwegein, Netherlands.

<sup>6</sup> Centre de recherches en physique des plasmas, Ecole polytechnique fédérale de Lausanne, Lausanne, Switzerland.

## 1. INTRODUCTION

In this paper the energy confinement properties of the JET plasma with intense auxiliary heating are discussed. In previous papers [1],[2], confinement in ohmically heated plasmas has been reported. The additional heating was provided by neutral beams (60-75keV D and H) at powers up to 9MW and ion cyclotron resonance heating [3] of helium and hydrogen minorities at powers up to 7MW. The two heating methods were also combined to give a total input power of 16MW which was between 4 and 20 times the ohmic input power. The toroidal field B, plasma current I and average density  $\langle n \rangle$  were all varied over a wide range ( $B = 1.7 - 3.4$  T,  $I = 1-5$ MA,  $\langle n \rangle = 0.5 - 5 \times 10^{19} \text{m}^{-3}$ ), with the geometry kept essentially fixed (major radius  $R \sim 3.0$ m, horizontal minor radius  $a = 1.2$ m, elongation  $K = 1.45$ ) so that the dependence of the global energy confinement  $\tau_E$  ( $= W/P - \dot{W}$ ) upon I, B,  $\langle n \rangle$  and the heating scheme could be assessed.

The plasma edge conditions have, however, been varied by limiting the plasma on the outer mid-plane limiters, the inner wall or separatrices (X-points) near the top and bottom of the chamber. Generally, the confinement time  $\tau_E$  degrades with both types of heating from its ohmic value  $\sim 0.5 - 0.8$ s down to  $\sim 0.2-0.4$ s. The smallest degradation occurs for plasmas located on the inner wall or with an X-point.

The remainder of the paper is divided as follows: in section 2.1 a simple empirical scaling law describing the behaviour of the  $\tau_E$  with the plasma parameters is derived and then in section 2.2 the scaling of  $\tau_E$  with the Connor-Taylor [4] dimensionless constraint parameters is determined. In Section 3 the degradation in confinement is discussed. First the question of whether the heat flux is self-regulating to maintain a fixed electron temperature profile or whether it is determined by the local temperature gradient is examined. The latter model is found to be more consistent with the data. Then a procedure is given for correcting the input power for impurity radiation losses and heating profile effects, and it is shown that these can account for a substantial part of the degradation in confinement.

### 2.1. Scaling of $\tau_E$ with Plasma Parameters

The plasma confinement properties with additional heating can be most clearly seen by exhibiting the data in a total (diamagnetic) energy W versus total input power P diagram such as that shown in Fig. 1 where examples of power scans with combined heating at four different currents and toroidal fields are shown. The data in Fig. 1 can be represented by an offset linear scaling of W with P in the form:

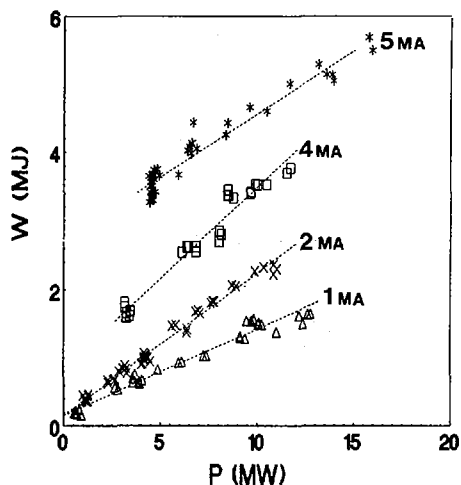


FIG. 1. Total stored energy versus total input power for four different power scans:  
 $I = 5 \text{ MA}$ ,  $B = 3.4 \text{ T}$ ;  $I = 4 \text{ MA}$ ,  $B = 3.4 \text{ T}$ ;  $I = 2 \text{ MA}$ ,  $B = 2 \text{ T}$ ;  $I = 1 \text{ MA}$ ,  $B = 2 \text{ T}$ .

$$W = W(0) + \tau_{\text{inc}} P \quad (1)$$

where the incremental confinement time  $\tau_{\text{inc}}$  and  $W(0)$  are functions of the  $I$ ,  $B$ ,  $\langle n \rangle$ , etc. To make the representation fully general a dependence on power  $P$  has to be included in  $\tau_{\text{inc}}$ . The reason for this is that, although the data in Fig. 1 appear linear with  $P$ , the density  $\langle n \rangle$  is increasing with  $P$  in all the power scans and this could be masking the true power dependence. However, by combining data from scans at different starting densities, we have been able to show that the density dependence in  $\tau_{\text{inc}}$  is weak. A good fit to the NBI data set has been found by use of standard regression techniques; it is:  
 $W(0) = 0.225 n^{0.6} I^{0.5} B^{0.4}$  and  $\tau_{\text{inc}} = 0.047 * I$  (Units: MJ,  $\text{m}^{-3} \times 10^{-19}$ , MA, T). The complete data set (NBI, ICRH and combined heating) is shown against this fit in Fig. 2.

The scatter in the data in Fig. 2 is thought to be mainly due to the method of heating (NBI or ICRH) and the type of confinement, limiter or inner wall. It is found that the fraction of the input power radiated by the impurities is significantly larger for ICRH and limiter confinement than for inner wall with NBI heating.

In Fig. 3 the radiation profiles are shown for three pulses: (A) a typical ohmic discharge. (B) an NBI discharge located on the inner wall, (C) a combined heating discharge on the limiter. Typically 30% of the input power is radiated in the central confinement zone ( $r/a < 0.7$ ) in case (C) and only 8% in case (B); the source and concentration of the

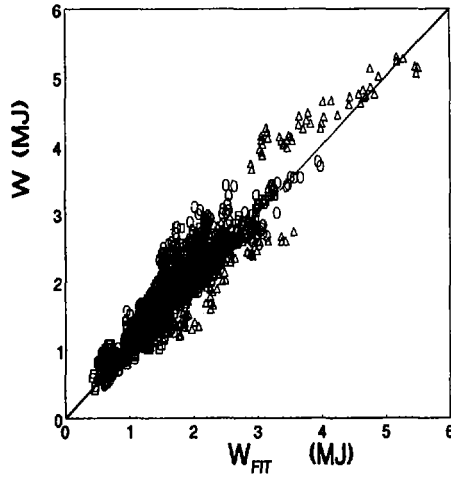


FIG. 2. Total stored energy versus the fit given in Eq. (1). The symbols are:  $\square$  — neutral beam injection heating alone,  $\Delta$  — including ICRH with H minority, and  $\circ$  — including ICRH with He minority.

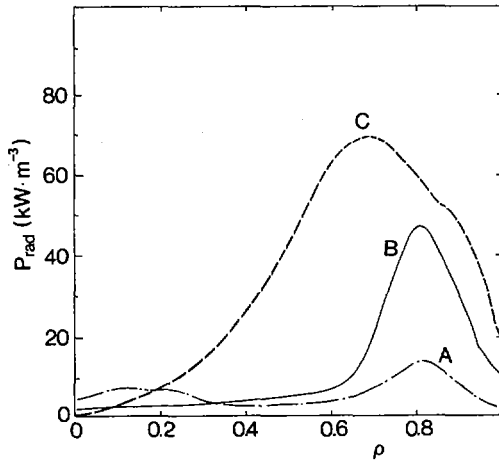


FIG. 3. Radiation profiles for: (A) an ohmic discharge located on the inner wall, (B) an NBI heated (9 MW) discharge located on the inner wall, and (C) a discharge with combined heating (4 WM of ICRH and 5 MW of NBI).

impurities is discussed in detail in ref. [5]. The radial heating profiles of the two schemes are also very different: the ICRH profiles are always peaked, ie. similar to the ohmic heating profile, whilst the NBI profile is usually less peaked, and at high densities the NBI profile is quite flat.

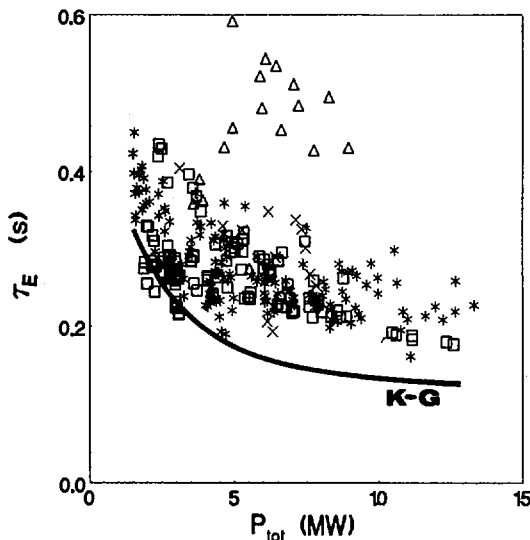


FIG. 4. Energy confinement time versus total power. The symbols are:  $\times$  — X-point with double null,  $\Delta$  — X-point with a single null, \* — inner wall discharges, and  $\square$  — limiter discharges. The solid line is the Kaye-Goldston fit.

The effect on confinement of changing the plasma configuration is shown in Fig. 4, where the global  $\tau_E$  (diamagnetic) is given as a function of power for the complete 2MA data set; also shown on the same figure is the empirical L-mode scaling of Kaye and Goldston [6] derived from data from previous experiments. Although for all configurations and heating schemes the  $\tau_E$  degrades with power, the inner wall and double null X point data with NBI heating are up to a factor 2 above the Kaye-Goldston law. The single null X point data which had clear H mode characteristics was up to a factor 3 larger than the Kaye-Goldston law.

The majority of the NBI experiments have been made with deuterium injection in the co-direction. A few experiments with counter-injection using deuterium and also hydrogen injection in the co-direction have also been made. As far as energy confinement was concerned, there was no apparent difference between co- and counter-injection, and the hydrogen injection results which were reported earlier [2] were similar to the present deuterium injection data.

## 2.2. Scaling of $\tau_E$ with Dimensionless Parameters

The additional heating data have been compared with the Connor-Taylor models [4]. It is found that the low beta models cannot represent the confinement time scaling, especially when

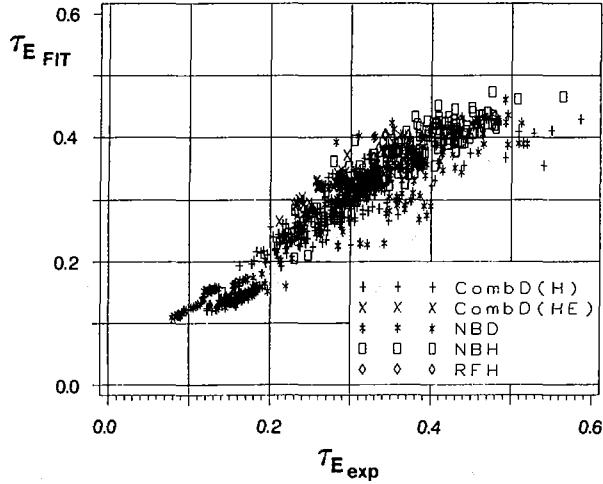


FIG. 5. Energy confinement time versus the fit from the resistive MHD model.

comparison is made with data from smaller devices. The scaling invariants originally given by Connor and Taylor were chosen arbitrarily to represent density, temperature and magnetic field dependences. For the high beta models, it is more appropriate to use the magnetic Reynolds number ( $S = \tau_R/\tau_{AD}$ ), the cyclotron frequency times the poloidal Alfvén time ( $\omega_C \tau_{AD}$ ), and the ratio of total to ohmic powers ( $P_{tot}/P_{ohm}$ ). The latter variable is equivalent to the poloidal beta in power law scaling forms and is used in order to prevent the energy content from appearing in both the dependent and independent variables. This set of scaling variables make the relationship between models more transparent and ensures that geometrical quantities such as safety factor and elongation are included in a natural fashion. The energy confinement time for the collisional high beta model is

$$\tau_E/\tau_{AD} = F(\omega_C \tau_{AD}, S, P_{tot}/P_{ohm}) \quad (2)$$

The collisionless models are obtained by combining the last arguments as  $(P_{tot}/P_{ohm})S^{-1}$  and the fluid models by dropping  $\omega_C \tau_{AD}$ . It is found that the JET data for  $(P_{tot}/P_{ohm}) > 2$  are best represented by the resistive MHD model as

$$\tau_E = 0.91 \tau_{AD} (P_{tot}/P_{ohm})^{-0.5} S^{0.75} \quad (3)$$

The fit is shown in Fig. 5. Data from other machines can be reproduced when the aspect ratio ( $\epsilon = a/R$ ) is included and the resulting scaling law is equivalent to

$$\tau_E = (\tau_R \tau_{AD})^{0.5} (\epsilon \beta_p)^{-1} \quad (4)$$

In view of the surprising simplicity of this form and the absence of any significant normalising constant, it might be concluded that Eq(4) is indicative of the underlying transport mechanism. However, this should be qualified by noting the difficulty in varying  $S$  and  $\beta_p$  in such a way as to clearly confirm the separate dependences in a given device. At first sight, Eq(3) appears to be inconsistent with the offset linear scaling law Eq(1). In fact, the implicit dependence of  $P_{ohm}$  and  $S$  on power make the two indistinguishable.

### 3. DISCUSSION OF CONFINEMENT DEGRADATION

There are many possible explanations for the degradation in confinement and some of these are examined briefly in this section. A current popular explanation is that the heat transport is self-adjusting such that the same electron temperature profile is maintained ('profile consistency'). The evidence for profile consistency in JET data was reviewed by Bartlett et al. [7] recently. The electron temperature profiles in high current ( $I \geq 3MA$ ) discharges certainly exhibit the conventional profile consistency features, that is  $T_e(\rho)/T_e(0)$  is only a function of  $q$  and the profile is unchanged by additional heating, at least at the presently available power levels ( $P_{tot}/P_{ohm} \sim 4$ ). In low current ( $I = 1MA$ ) discharges, where  $P_{tot}/P_{ohm} \sim 20$ , the electron temperature profile appears to respond to the changing heating profile. In Fig.6(a), the temperature profiles are shown for the two cases of low and high current before and during heating, and the corresponding heating profiles are shown in Fig.6(b). In the low current case, the initial ohmically heated profile is substantially broadened by the application of NBI heating, whilst for the higher current pulse the ohmic and NBI heating profiles are rather similar. Although the change in both temperature profiles is small with additional heating, it is consistent with what is expected for the change in heating profile shown in Fig.6(b). Indeed, as Waltz et al. [8] have shown, very large changes in the heating profile only produce small changes in the temperature profile shape for discharges in which the central  $q$  is limited by internal relaxations (sawteeth).

Thus, in summary, there is no really clear evidence that 'profile consistency' plays a deterministic role in heat transport. There is, however, evidence that whilst the confinement time degrades with power input, the underlying heat transport is independent of the auxiliary heating power. First, the fact that the total energy  $W$  increases linearly with power  $P$ , as shown in Fig. 1, means that the incremental confinement time  $\tau_{inc} = \Delta W/\Delta P$  does not vary significantly with power level. For example, at  $I = 3MA$  we have  $\chi_{inc} = ab/4\tau_{inc} \sim 2.9 \pm 0.6m^2/s$ .

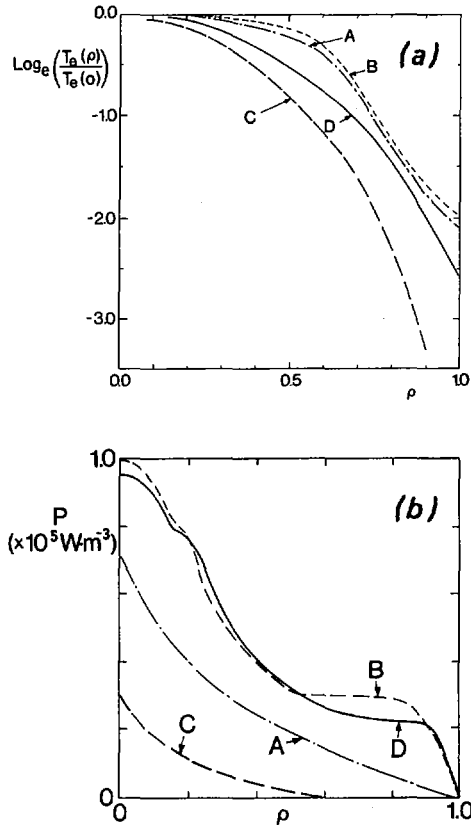


FIG. 6. (a)  $\text{Log}_e(T_e(\rho)/T_e(0))$  versus  $\rho$ , for a 3 MA discharge before heating (curve A) and after 9 MW of NBI heating (curve B), and for a 1 MA discharge before heating (C) and during 9 MW of NBI heating (D). (b) Power input to the electrons versus  $\rho$  for the four cases shown in (a).

Second, as shown in Fig. 7, the electron heat flux per unit density,  $P_e(r)/nA = \int d^3x \Sigma Q/nf dA$ , is proportional to the local temperature gradient. This implies a  $\chi_{\text{flux}} = \Delta(P_e(r)/nA)/\Delta(dT_e/dr) \sim 1.8 - 3.3 \text{ m}^2/\text{s}$  for the 3MA case. (The reason for the large range in  $\chi_e$  is due to the uncertainty in estimating the loss through the ion channel.) Finally, and most locally, the  $\chi_{\text{HP}}$  determined using the heat pulse propagation method [9] is found to be approximately constant (for  $I = 3\text{MA}$ ,  $a = 1.2$ ,  $K = 1.45$ ) at a value of  $2.4 \pm 0.7 \text{ m}^2/\text{s}$ , independent of the heating power [10]. The fact that these three different methods of determining the electron heat diffusivity  $\chi_e$  yield nearly the same power-independent value ( $\chi_{\text{inc}} \sim \chi_{\text{flux}} \sim \chi_{\text{HP}}$ ) implies that the transition from ohmically to auxiliary heated

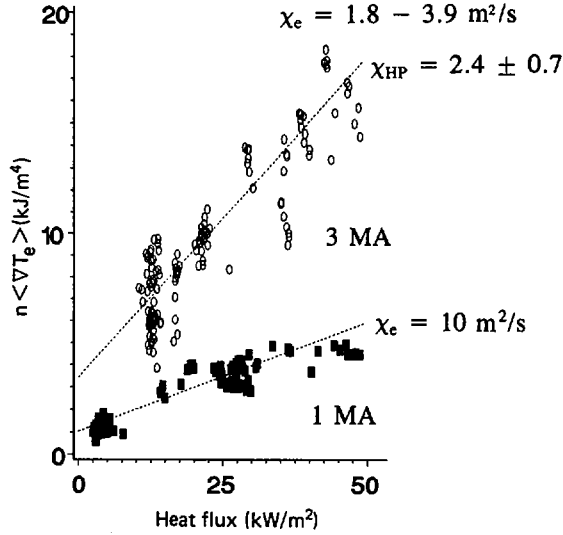


FIG. 7.  $n \langle \nabla T_e \rangle$  at  $\rho = 0.75$  versus heat flux for a 3 MA power scan ( $\circ$ ) and a 1 MA power scan ( $\blacksquare$ ). The dotted lines are the best straight line fits to the data.

discharges may be interpretable in terms of a transport model with electron heat conduction characterised by a constant value of  $\chi_e$ .

An example of such a model will now be developed and used to clarify the heating profile and radiation loss effects. First, assume that the heat flux is given generally by heat conduction plus convection in the form  $\vec{q} = -n\chi\nabla T + \vec{q}_{\text{conv}}$ . Utilising this in the equilibrium heat balance,  $\nabla \cdot \vec{q} = \Sigma Q = Q_{\text{OH}} + Q_{\text{aux}} - Q_{\text{rad}}$ , and assuming that  $\chi$  and  $q_{\text{conv}}$  are not strongly dependent upon  $T$  or  $\nabla T$ , one can integrate once to determine the temperature gradient and once more to calculate the temperature profile. A further integration over the plasma volume gives the total stored energy  $W$ , which in cylindrical geometry has the form

$$\begin{aligned}
 W &= 3\int d^3x n(r) \left[ \int_0^a \frac{dr}{r} \frac{r'}{rn\chi} \int_0^{r'} \Sigma Q(r'') - \int_0^a \frac{dr}{r} \frac{q_{\text{conv}}}{n\chi} \right] \\
 &= \tau_{\text{ex}} \left\{ [P_{\text{ohm}} + P_{\text{aux}} - P_{\text{rad}}]_{\text{eff}} - P_{\text{conv}} \right\} \quad (5)
 \end{aligned}$$

Here,  $\tau_{\text{ex}} = ab/4\chi$ , and the effective power inputs take account of the effects of heating, radiation, density and  $\chi$  profiles on the total stored energy  $W$ . For constant  $n$  and  $\chi$ , one obtains

$P_{\text{eff}} = C_0 \int_0^a r dr (1-r^2/a^2) Q(r)$ , where  $C_0$  is a normalising constant.

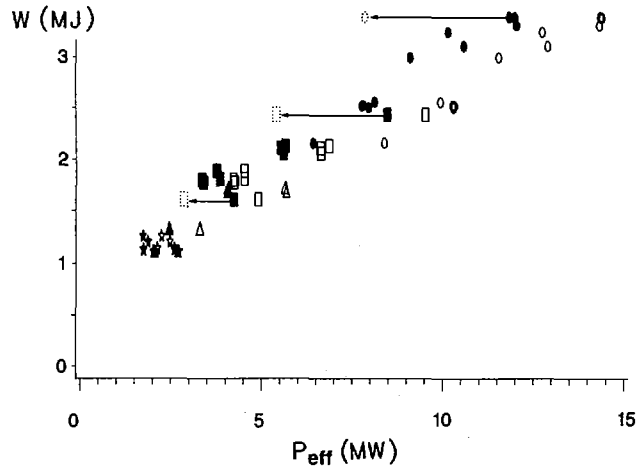


FIG. 8. Total energy density versus effective power.

Symbols:  $\star$  = ohmic heating,  $\square$  = NBI only,  $\Delta$  = ICRH only,  $\circ$  = combined ICRH and NBI. Open symbols: before correction for radiation losses and heating; solid symbols: after correction for radiation; dotted symbols: after correction for radiation and heating profile effects.

The main reason for deriving Eq(5) is that it has the same form as the linear offset model Eq(1) used to represent the data, the offset being identified as the convected power. However, it would be negative in this model, indicating a heat pinch [11]. An alternative heat transport model without a heat pinch ( $q_{conv} = 0$ ) would require a  $\chi$  which, while constant over the usual power input (or  $\nabla T$ ) range, varies strongly at low values of  $\nabla T$  [12],[13]. From Fig. 7, either of these models could fit the present data.

An example of the use of Eq(5) is shown in Fig. 8, where the above profile analysis techniques are applied to an  $I = 3\text{MA}$ ,  $B = 2\text{T}$ , power scan with combined heating. The data is shown before correction for the power lost by radiation (open points) and then after correction for the power lost by radiation (solid points). Correcting for radiation losses reduces the scatter in the data and increases the incremental confinement time by 30%. Correcting for the differing heat deposition profile further increases the incremental confinement time (arrowed points) and the degradation in confinement in going from ohmic to strong auxiliary heating is then much smaller. Now the results in Fig. 8 will depend on the assumptions that are made for the radial profile of  $\chi$ . However, this example does demonstrate qualitatively that the degradation in the confinement time  $\tau_e$  could be due to the broader

deposition profile of NBI and/or enhanced radiation, and a change in the basic heat transport mechanism may not be required.

#### 4. CONCLUSIONS

A simple empirical scaling law, Eq.(1), has been found to adequately describe the energy confinement properties of JET with intense additional heating. The scaling of the energy confinement time with the dimensionless plasma physics parameters suggests that the underlying heat transport is a consequence of resistive MHD instabilities. Electron heat transport with auxiliary heating has been found by three different methods to be describable in terms of a heat flux with a constant coefficient ( $\chi_e \sim 2.5 \pm 1.0 \text{ m}^2/\text{s}$  for 3MA discharges). A substantial contribution to the degradation in global confinement with additional heating is shown to be due to the profiles of radiation and heating.

#### REFERENCES

- [1] CORDEY, J.G., et al., in Controlled Fusion and Plasma Physics (Proc. 12th Europ. Conf. Budapest, 1985), Pt. I, European Physical Society (1985) 26.
- [2] THOMSEN, K., et al. in Controlled Fusion and Plasma Heating (Proc. 13th Europ. Conf. Schliersee, 1986), Vol. 1, European Physical Society (1986) 29.
- [3] JACQUINOT, J., et al., Paper IAEA-CN-47/F-I-1, these Proceedings, Vol. 1.
- [4] CONNOR, J.W., TAYLOR, J.B., Nucl. Fusion **17** (1977) 1047; Phys. Fluids **27** (1984) 2676.
- [5] BEHRINGER, K., et al., Paper IAEA-CN-47/A-IV-1, these Proceedings, Vol. 1.
- [6] KAYE, S.M., GOLDSTON, R.J., Nucl. Fusion **25** (1985) 65.
- [7] BARTLETT, D.V., et al., in Controlled Fusion and Plasma Heating (Proc. 13th Europ. Conf. Schliersee, 1986), Vol. 1, European Physical Society (1986) 236.
- [8] WALTZ, R.E., et al., Rep. GA-A-18365, GA Technologies Inc., San Diego, CA; to be published in Nucl. Fusion.
- [9] CALLEN, J.D., JAHNS, G.L., Phys. Rev. Lett. **38** (1977) 971.
- [10] TUBBING, B.J.D., et al., Heat Pulse Propagation Studies in JET, Report JET Joint Undertaking, Abingdon (to be published).
- [11] FREDRICKSON, E.D., et al., Nucl. Fusion **26** (1986) 849.
- [12] REBUT, P.H., BRUSATI, M., paper presented at 12th Europ. Conf. Budapest on Controlled Fusion and Plasma Physics, 1985.
- [13] THOMAS, P., paper presented at 12th Europ. Conf. Budapest on Controlled Fusion and Plasma Physics, 1985.

#### DISCUSSION

R.J. GOLDSTON: In your model, heat flow is a strictly defined offset linear function of  $n_e \nabla T_e$ . How does this model deal with the heating profile experiments

from T-10, ASDEX, TFTR and JET, and how does it cope with the apparent sensitivity of the confinement to edge parameters, for instance in the H-mode?

J.G. CORDEY: It has been shown by Waltz et al. (paper IAEA-CN-47/A-VI-1-3, these Proceedings) that  $n\chi \nabla T$  can produce 'profile consistency' for  $T_e$  profiles. In the H-mode the magnitude of  $\chi$  in the edge region is greatly reduced and this accounts for the improved confinement.

H. HORA: With regard to your discussion of the inhibition of thermal conduction, have you included in this the effects of electric (inhomogeneity) fields and double layer<sup>1</sup>, since there they provide an explanation for pellet fusion<sup>2</sup> and since the generally predicted fields<sup>3</sup> have now been measured in toroidal plasmas?

J.G. CORDEY: No; this model is only in its infancy and these effects have not been taken into account.

B. COPPI: I do not understand how a theory of purely resistive modes can be applicable to low collisionality regimes (multi-keV), as you have in JET. Could you comment on that?

J.G. CORDEY: Yes, I would expect this theory to apply equally to the low collisionality regimes; however, the data certainly do not appear to fit them. There are two possible explanations: one is that the true dependence of  $\tau_e$  on the plasma parameters is being masked by power deposition and radiation profile effects; the other is that the non-linear development of the general kinetic theory leaves resistive MHD for determining the transport.

R.J. TAYLOR: What does your  $n\tau_E T_i$  function look like for all the JET data versus power input? Does it support Rebut's position regarding the lack of significance of auxiliary heating?

J.G. CORDEY: Until recently, the best  $n\tau_E T_i$  value was obtained with Ohmic heating ( $I = 5$  MA); however, using X-point operation at 3 MA, this value has recently been doubled to  $2 \times 10^{20} \text{ m}^{-3} \cdot \text{s} \cdot \text{keV}$ . We do not yet have its scaling with power.

---

<sup>1</sup> HORA, H., et al., Phys. Rev. Lett. **53** (1984) 1650.

<sup>2</sup> CICCHITELL, L., et al., Laser Part. Beams **2** 4 (1984).

<sup>3</sup> LALOUSIS, P., Phys. Lett., A **99** (1983) 89.

## EFFECT OF $p$ AND $j$ PROFILES ON ENERGY CONFINEMENT IN ECH EXPERIMENTS ON T-10

V.V. ALIKAEV, A.A. BAGDASAROV, E.L. BEREZOVSKIJ,  
A.B. BERLIZOV, G.A. BOBROVSKIJ,  
A.A. BORSHCHEGOVSKIJ, N.L. VASIN,  
A.N.I. VERTIPOROKH, V.V. VOLKOV, E.P. GORBUNOV,  
Yu.A. GORELOV, Yu.V. ESIPCHUK, S.L. EFREMOV,  
V.S. ZAVERYAEV, V.I. IL'IN, A.Ya. KISLOV, P.E. KOVROV,  
S.Yu. LUK'YANOV, Yu.S. MAKSIMOV, A.A. MEDVEDEV,  
G.E. NOTKIN, A.B. PIMENOV, V.I. POZNYAK, I.A. POPOV,  
S.V. POPOVICHEV, K.A. RAZUMOVA, P.V. SAVRUKHIN,  
E.V. SITAR, A.M. SOLNTSEV, M.M. STEPANENKO,  
V.S. STRELKOV, A.V. TARAKANOV, K.N. TARASYAN,  
K.B. TITISHOV, V.M. TRUKHIN, G.S. YARAMYSHEV  
I.V. Kurchatov Institute of Atomic Energy,  
Moscow

S.N. VLASOV, A.L. GOL'DENBERG, V.A. MARKELOV,  
V.A. FLYAGIN, B.V. SHISHKIN  
Institute of Applied Physics of the USSR Academy of Sciences,  
Gorkij

Union of Soviet Socialist Republics

*Presented by B.B. Kadomtsev*

### Abstract

EFFECT OF  $p$  AND  $j$  PROFILES ON ENERGY CONFINEMENT IN ECH EXPERIMENTS ON T-10.

ECH experiments with doubled HF power,  $P_{HF}$ , were carried out on T-10, and the dependence of energy confinement on  $P_{HF}$  was shown to remain the same as in previous T-10 experiments. The dependence of the transport coefficients on the pressure gradient was shown to be strongly non-linear. The results of off-axis heating agree with the idea of pressure (current) profile consistency.

### 1. INTRODUCTION

An ECH experiment with increased HF power has recently been carried out on T-10. The HF set-up consisted of six gyrotrons with  $f = 81$  GHz and provided a  $P_{HF}$  value of up to 2 MW, which was twice as high as previously [1, 2]. Diagnostic measurements showed the absorbed power,  $P_{ab}$ , to be 70 to 75% of  $P_{HF}$ .

The main goal of our recent investigations was to study the influence of the plasma parameter profiles on the energy confinement. The profiles were varied by shifting the ECR zone. The conservation of the  $p$  and  $j$  profiles (i.e. the dependence of the transport coefficient on the  $P_{ab}$  profile [3, 4]), its dependence on  $\nabla p_e$  and the connection of this dependence with the limit profile idea [3] were studied.

The plasma current  $I_p$  was varied from 180 to 230 kA, which corresponded to  $q_L = 6.4$  to 5.0 at  $a_L = 34$  cm. The ratio  $P_{tot}/P_{OH}$  was increased up to 5.5,  $P_{tot}$  being defined as  $P_{ab} + P_{OH}^{ECH}$ .

## 2. PECULIARITIES OF RECENT EXPERIMENTAL CONDITIONS

The experimental conditions differed from those in the previous experiments [1, 2], which resulted in a difference in the Ohmic stages. First, the vacuum chamber was replaced by a new one. Second, two circular carbon limiters were removed because the large amount of graphite has led to hydrocarbon film production on the first wall. This resulted in breakdowns between the wall and the waveguide and in a cut-off of the power input. To prevent this, we needed a great number of training discharges, along with the HF pulses.

In the recent experiment, it was only the movable rail limiter that was made of graphite. The reduction of the quantity of graphite, together with waveguide baking, eliminated arcing and, on the other hand, changed the near wall conditions significantly. The metal impurity influx increased so that the iron density in the centre rose up to  $1\text{--}2 \times 10^{10} \text{ cm}^{-3}$ , i.e. by a factor of five. This seems to be the reason for the increase in radiation power;  $P_{rad} = 0.7 P_{OH}$  at  $\bar{n}_e = 3 \times 10^{13} \text{ cm}^{-3}$  in comparison with  $0.25 P_{OH}$  in [1, 2]. The recycling and the additional particle influx during ECH went down markedly. Figure 1 shows the energy content in the Ohmic plasma,  $W_{OH}$ , as a function of  $\bar{n}_e$  at  $I_p = 180$  kA,  $B_t = 2.9$  T. At the beginning of the experiments (solid line), a saturation in  $W_{OH}(\bar{n}_e)$ , accompanied by a rise in the  $m = 2$  mode activity ( $\bar{B}_p/B_p = 4 \times 10^{-4}$  at  $\bar{n}_e = 3.2 \times 10^{13} \text{ cm}^{-3}$ ) was observed near to the limit value of  $\bar{n}_e$ ,  $\bar{n}_{e,lim} = 3.5 \times 10^{13} \text{ cm}^{-3}$ , above which disruption occurred. The energy confinement time  $\tau_E$  did not exceed 50 ms and was lower than that in [2]. In the course of the experiments, the heavy impurity level, the radiation losses and the loop voltage were going down, apparently because of changes in the wall conditions. The value of  $\bar{n}_{e,lim}$  then rose up to  $4.2 \times 10^{13} \text{ cm}^{-3}$ , MHD activity stopped up to  $\bar{n}_e = 3.6 \times 10^{13} \text{ cm}^{-3}$ , and no evident saturation on the  $W_{OH}(\bar{n}_e)$  graph was observed (Fig. 1, dashed line).  $\tau_E$  increased up to 70 ms.

## 3. ENERGY CONFINEMENT DURING ON-AXIS ECH

In contradiction to the previous experiments [2], the decreased particle influx no longer compensated for the outflux rise caused by the drop of  $\tau_p$  at ECH. As a result,  $\bar{n}_e$  decreased during ECH without additional gas puffing (Fig. 2(a)). The

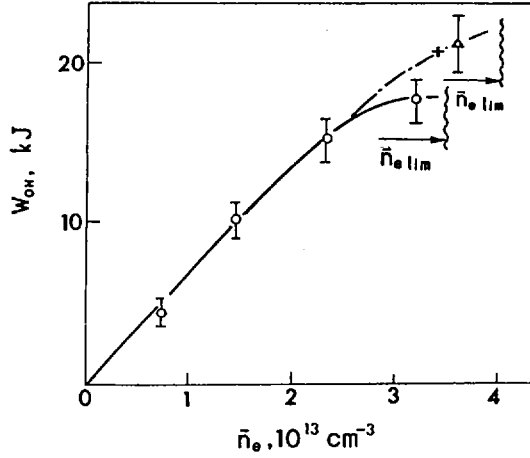


FIG. 1.  $W_{OH}(\bar{n}_e)$  dependence on Ohmic stage of discharges with  $I_p = 180 \text{ kA}$ ,  $B = 2.9 \text{ T}$ . Solid line refers to results obtained at beginning of experiments, dashed line to the final stage.

decrease was stronger at higher  $n_e$  and  $P_{HF}$ . As before [2], the most significant decrease in  $n_e$  was recorded at the plasma centre. It caused  $n_e$  profile flattening (Fig. 3(a)).

The energy content reached its maximum  $W_m$  at  $\Delta t_m = 25 \text{ ms}$  of the ECH pulse (Fig. 2(a)) and went then down while  $T_e$  continued growing during the whole pulse all over the cross-section (Fig. 4(a)). The decrease in energy content (from  $W_m = 37.5 \text{ kJ}$  to  $26 \text{ kJ}$  at  $\Delta t = 65 \text{ ms}$ ) can be explained, within the experimental accuracy, by the dependence  $\tau_E \propto \bar{n}_e$ , which is valid for ECH as has been shown in [1] and was confirmed in the recent experiments. If  $\bar{n}_e$  is maintained constant by an additional puffing during the ECH pulse, there is virtually no change in  $W$  after reaching the stationary value (Fig. 2(b)). The dependence of  $W_m$  on  $P_{tot}$  is displayed in Fig. 5, together with the data of [2]. The  $\tau_E(P_{tot})$  dependence does not, within the experimental accuracy, deviate from that estimated earlier [2]:

$$\tau_E/\tau_{E\text{ OH}} = (P_{tot}/P_{OH})^{-0.55}$$

if the drop in  $n_e$  and the  $\tau_E(\bar{n}_e)$  dependence are taken into account. This result does not contradict the conclusion reached in [2] that the electron energy confinement time for the column as a whole,  $\tau_{Ee}(a_L)$ , is proportional to  $\langle T_e \rangle^{-1/2}$ , which is equivalent to

$$\tau_{Ee}/\tau_{Ee\text{ OH}} = (P_{tot}/P_{OH})^{-1/2}$$

because  $(\beta_i/\beta_e)_{OH} = 0.7$ , and the ions were not heated significantly by ECH in the case considered.

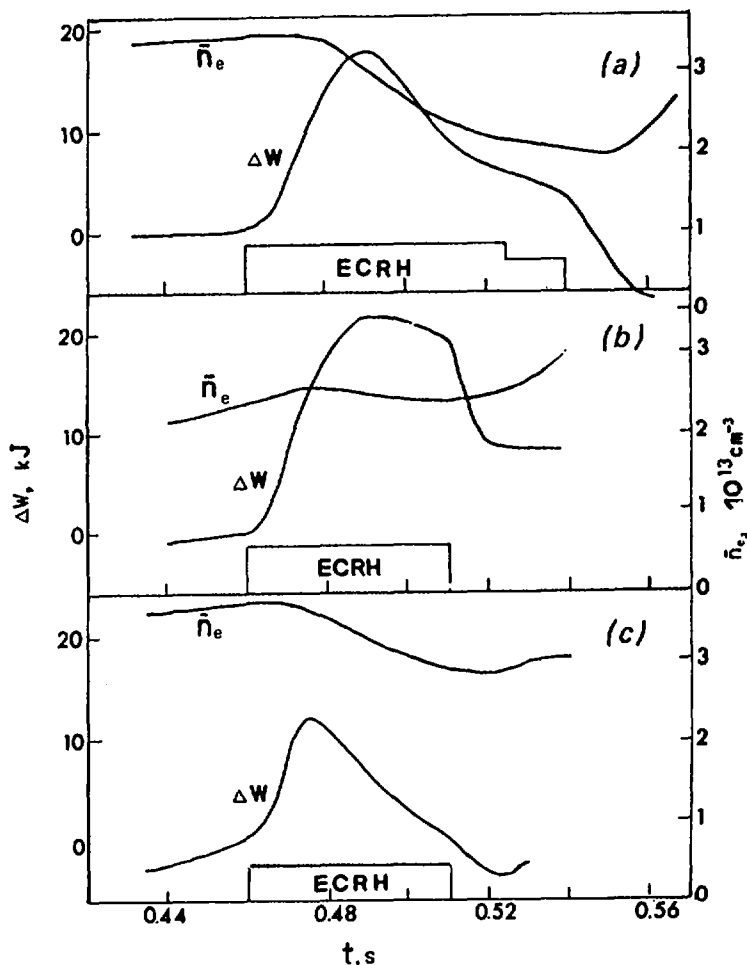


FIG. 2. Time behaviour of energy content increase,  $\Delta W$ , and  $n_e$  during ECH: (a) on-axis heating,  $B_t = 2.9 T$ , 6 gyrotrons, low level gas puffing during ECH; (b) same with high level puffing; (c) off-axis heating,  $B_t = 3.25 T$ , ECR zone shift,  $\Delta R = 18$  cm, 4 gyrotrons.

In summary, the  $P_{HF}$  doubling did not change the scaling for the global confinement time obtained earlier.

#### 4. $T_e$ PROFILE IN ON-AXIS ECH

The electron energy confinement in the core varies more dramatically with the  $P_{tot}$  variations than the global time  $\tau_E$ . The profiles of the relative  $T_e$  increase at the end of the ECH pulse were measured for different numbers of gyrotrons in

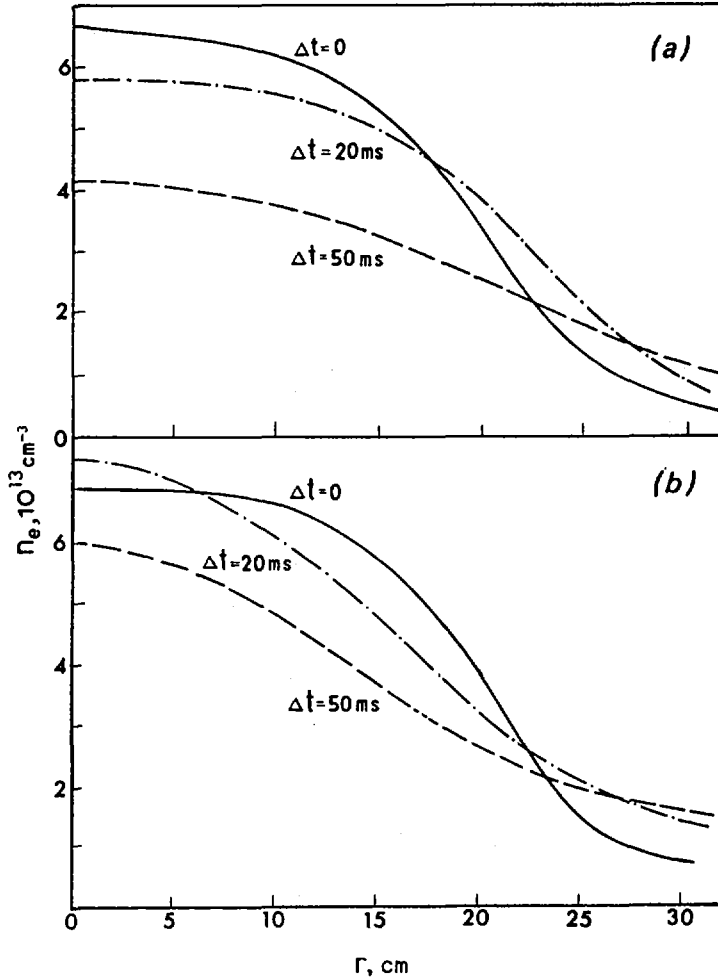


FIG. 3.  $n_e$  profiles at different moments of ECH pulse starting at  $\Delta t = 0$ : (a) same conditions as Fig. 2(a); (b) same conditions as Fig. 2(c).

plasmas with  $\bar{n}_e = (3-3.5) \times 10^{13} \text{ cm}^{-3}$  and are displayed in Fig. 6(a), (b) and (c). EC radiometer data are used. For  $P_{ab} \leq 1 \text{ MW}$ ,  $T_e(0)$  is proportional to  $P_{tot}$  (Fig. 7) and  $T_e/T_{eOH}$  is practically constant along the radius, providing, thus, evidence of a  $T_e$  profile change in a similar way. For higher  $P_{tot}$ ,  $T_e(0)$  almost ceases rising, which indicates a drastic increase of transport in the plasma centre. The  $T_e$  profile tends to flatten (Figs 6(a) and 8), which agrees with the conclusion of [2] that the heat conductivity coefficient  $K_e$  increases less strongly with increasing radius.

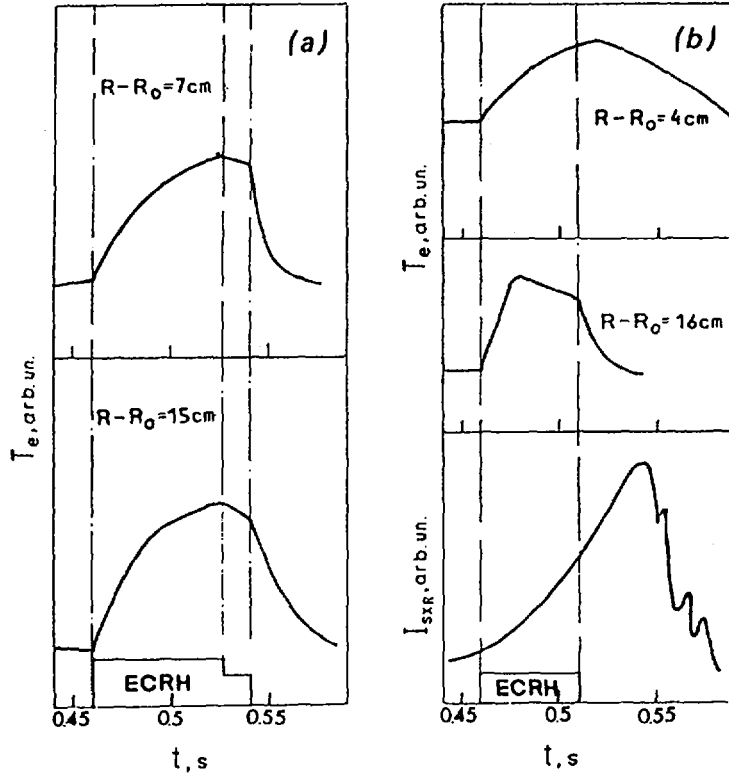


FIG. 4.  $T_e$  time behaviour during ECH at different radii: (a) same conditions as Fig. 2(a); (b) same conditions as Fig. 2(c).  $I_{sXR}$  is soft X-ray intensity emitted by plasma core.

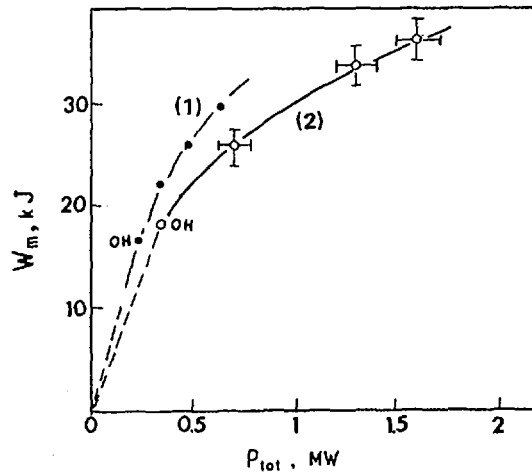


FIG. 5. Dependence of maximum energy content,  $W_m$ , on total heating power,  $P_{tot}$ , (2), together with the data of Ref. [2], (1):  $I_p = 180\text{ kA}$ ,  $B_t = 2.9\text{ T}$ ,  $\bar{n}_e = 2.8 \times 10^{13}\text{ cm}^{-3}$ .

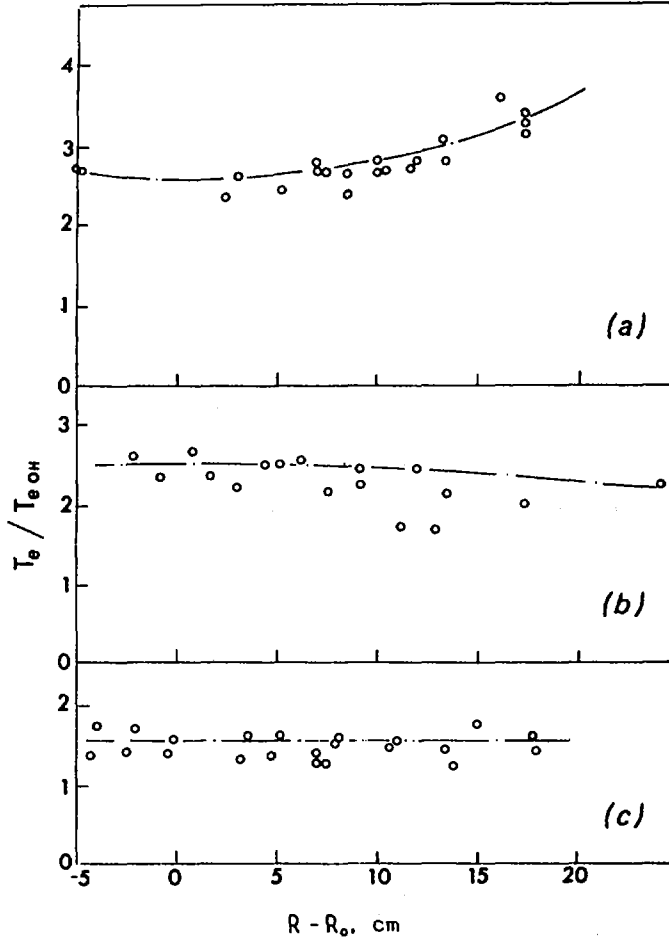


FIG. 6. Relative profiles of electron temperature,  $T_e/T_{eOH}$ , as measured by EC radiometer at end of ECH pulse.  $B_z = 2.9 T$  (on-axis ECH),  $\bar{n}_e = (3-3.5) \times 10^{13} \text{ cm}^{-3}$ . (a), (b) and (c) are for 6, 4 and 2 gyrotrons, respectively.

In Ref. [3], the dependence of  $K_e$  on the pressure gradient,  $\nabla p_e$ , was shown. The new results confirm this dependence and point out its strongly non-linear character, i.e. the existence of a limit gradient near which the transport coefficients rise up significantly. This is illustrated by Fig. 9, where the data obtained for the end of the ECH pulse at different  $P_{tot}$  and  $n_e$  values is displayed. These data relate to the plasma centre ( $r \leq 10 \text{ cm}$ ). The S value,

$$S = \frac{P_{tot}/P_{OH}}{T_e/T_{eOH}^{(0)}} \frac{1}{1 - P_{eiOH}/P_{OH}}$$

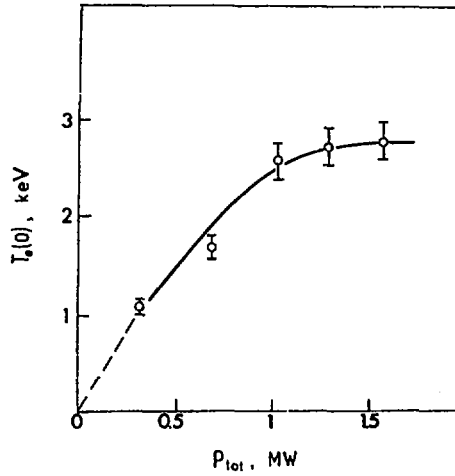


FIG. 7. Dependence of central  $T_e$  on  $P_{tot}$  for end of on-axis ECH ( $B_t = 2.9 T$ ,  $\bar{n}_e = 3.2 \times 10^{13} \text{ cm}^{-3}$ ).

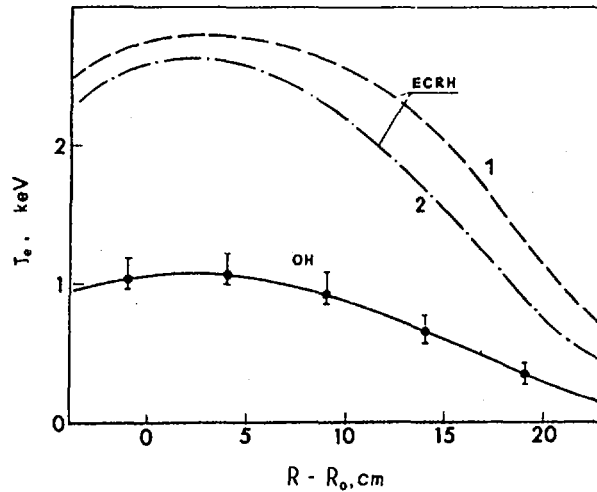


FIG. 8.  $T_e$  profiles for OH and end of on-axis ECH with 6 (1) and 4 (2) gyrotrons.  $B_t = 2.9 T$ ,  $\bar{n}_e = 3.2 \times 10^{13} \text{ cm}^{-3}$ . PHA data are used for  $T_{e,OH}$ .

( $P_{OH}$  is the Ohmic power at the Ohmic stage,  $P_{ei}$  the electron-ion heat transfer) is, in fact, the ratio  $K_e/K_{e,OH}$  if one assumes that the  $T_e$  profile changes only slightly in the plasma core. In Fig. 9,  $\nabla p_e$  is replaced by the central pressure, in accordance with the idea of p profile consistency [3]. The results of the ECH experiment on T-7 are also shown in Fig. 9 [5]. The rise in  $T_e(0)$  from 1.6 to 4.2 keV at low HF power

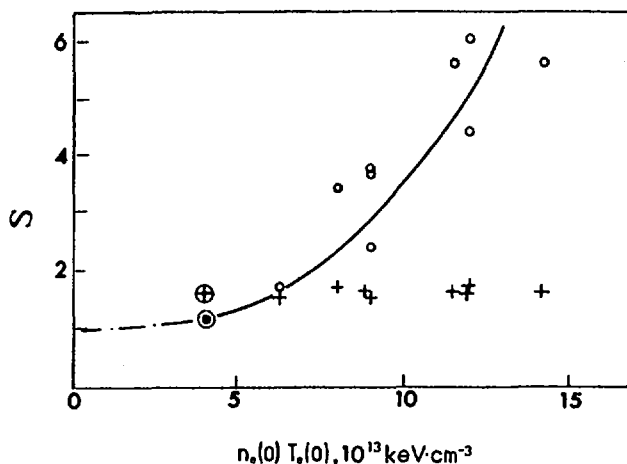


FIG. 9. Increase in  $K_e$  for plasma core ( $r \leq 10$  cm) as a function of pressure gradient (see the text). + - calculations for  $K_e \propto T_e^{0.5}$ ;  $\odot$ ,  $\oplus$  T-7 data [5].

( $P_{\text{tot}} = 0.3$  MW) obtained in this experiment can be explained by the fact that the pressure gradient was far from the limit gradient in T-7, because of low  $\bar{n}_e$  ( $6 \times 10^{12}$  cm $^{-3}$ ).

Could the observed  $K_e(\nabla p_e)$  dependence be interpreted as a relation between their local values? Or is it the result of a distortion of the  $p$  and  $j$  profiles by ECH, i.e. is it determined by the  $P_{\text{ab}}$  profile?

We have not yet enough data to decide which of these explanations is the correct one.

## 5. ON PROFILE CONSISTENCY IN PLASMA (OFF-AXIS ECH)

Consistency of  $p$  and  $j$  profiles in plasma (if it exists) can only be realized through variations of the transport coefficients which would depend on the profile of the heating power,  $P_{\text{ab}}(r)$ . This means that the outward shift of the ECR zone would result in a decrease of the transport coefficients in the plasma core after switching on the ECH pulse, because we apply no additional power there.

To test the hypothesis of profile consistency, the experiment was done with an outward shifted ECR zone ( $\Delta R = 18$  cm). The results are displayed in Figs 2(c), 4(b) and 10. As previously [1, 2], the maximum rise in energy content,  $\Delta W_m$ , is practically the same compared with on-axis ECH at the same  $P_{\text{ab}}$  value, and the confinement degradation observed at the end of the ECH pulse is stronger (Fig. 2(c)). The data presented in Fig. 10(a) show that the rise in  $T_e$  at  $\Delta t_m = 20$  ms is stronger behind the ECR zone, in this case, than with on-axis heating and, hence,  $\Delta W_m$  does not change with the  $\Delta R$  variations, but for  $\Delta t > \Delta t_m$ ,  $T_e$  falls in the plasma

exterior, in contrast to the central ECH. In the plasma core,  $T_e$  rises during the entire ECH pulse (Fig. 4(b)). These results qualitatively indicate the tendency towards pressure profile conservation, especially if  $n_e(r)$  peaking is taken into account (Fig. 3(b)), which is the other difference between on-axis and off-axis ECH. This tendency is confirmed by the energy balance at  $\Delta t = 50$  ms in the plasma core ( $r \leq 9$  cm), which is not supplied with additional power (Fig. 10).  $K_e$  decreases in the core during ECH so that

$$K_e/K_{e\text{ OH}}|_{r=9\text{ cm}} = \frac{(P_{\text{OH}} - P_{\text{ei}} - P_{\text{rad}} - (3/2) \frac{d}{dt} \langle n_e T_e \rangle)_{\text{ECH}}}{(P_{\text{OH}} - P_{\text{ei}} - P_{\text{rad}})_{\text{OH}}} \times \frac{\frac{d}{dr} T_{e\text{ OH}}}{\frac{d}{dr} T_{e\text{ ECH}}} < \frac{1}{2}$$

$$\langle n_e T_e \rangle = 2\pi \int_0^9 n_e T_e r dr; K_{e\text{ OH}} \approx 7 \times 10^{16} \text{ cm}^{-1} \cdot \text{s}^{-1}$$

This estimation is the upper limit of  $K_e$  at ECH because the current profile rebuild which decreases the  $P_{\text{OH}}$  value for off-axis ECH is not taken into account.

The soft X-ray signal traces (Fig. 4(b)) demonstrate rise in  $I_{\text{SXR}}$  at the centre 20 ms after switching off the ECH pulse. This displays a slow decrease in  $T_e(0)$  and a possible continuous accumulation of impurities ('B-regime' on T-10).

The slow rebuild of the  $T_e$  profile in the plasma core during the ECH pulse is connected with the fact that  $P_{\text{OH}}$  is nearly balanced there by the electron energy losses  $P_e$ . From a rough estimate, the characteristic time of profile rebuild is of the order of seconds. So, to confirm the p and j profile conservation, an experiment is needed with longer ECH pulse at lower  $n_e$ , i.e. with a higher value of  $(P_{\text{OH}} - P_e)$ .

It was assumed in [6] that the low  $K_e$  in the plasma core ( $< 10^{17} \text{ cm}^{-1} \cdot \text{s}^{-1}$ ) at high  $n_e/I_p$  values was the result of a balance between diffusivity and convective influx (heat pinch). If balance prevails, then at the beginning of the HF pulse ( $\Delta t = 20$  ms) one could expect a strong rise in the heat flux because both the diffusive flux (Fig. 10(a)) at  $r = 6$  cm and the heat pinch would be directed inward. Hence, the  $K_e$  value measured as the ratio of the total electron heat flux to  $\nabla T_e$  would also rise strongly. However, an energy balance analysis showed that in the plasma core  $K_e$  was at least not higher than in the Ohmic stage. We may conclude that the heat pinch does not play an essential role under these conditions.

## 6. INTERNAL MHD ACTIVITY

A specific MHD activity was detected in recent experiments by pickup coils with good reproducibility (Fig. 11(a)). This activity had also been observed

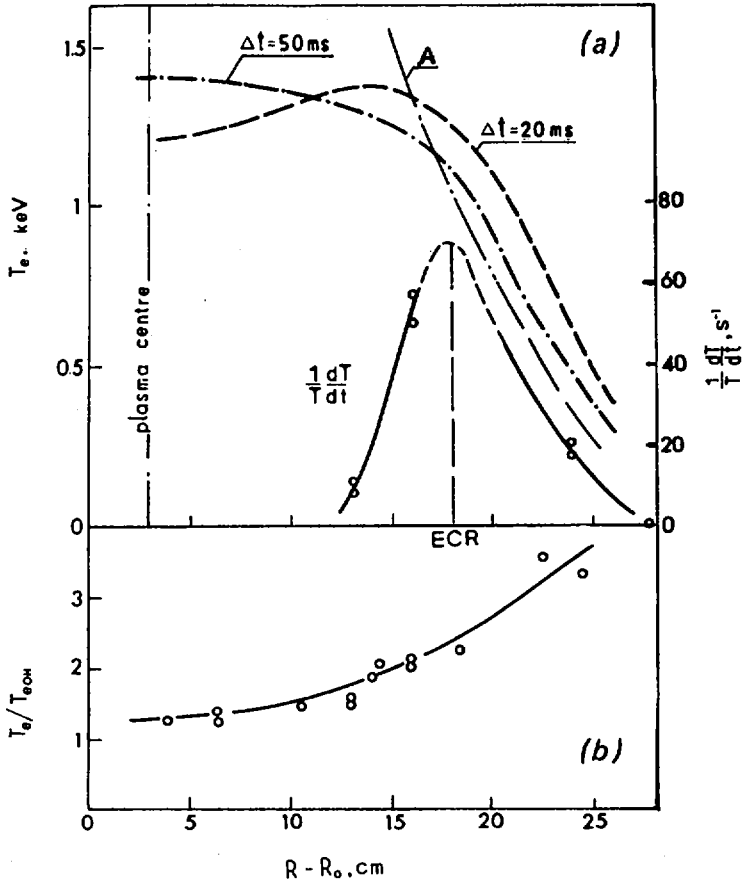


FIG. 10. (a)  $T_e$  profiles at two instants of ECH pulse together with profile of  $T_e^{-1}(dT_e/dt)$  at the start of non-central ECH.  $B_t = 3.25$  T,  $\bar{n}_e = 3.6 \times 10^{13}$   $\text{cm}^{-3}$ , 4 gyrotrons; (b) relative increase of  $T_e$  at end of ECH pulse ( $\Delta t = 50$  ms) for same conditions. A refers to  $T_e$  profile at  $\Delta t = 50$  ms of central heating.

previously. It manifests itself in sinusoidal oscillations on the traces of the EC radiation and of the SXR intensity (Fig. 11(c)) at intermediate radii. The amplitude of  $B_p$  oscillations (see Fig. 11(a) for  $\tilde{B}_p/B_p$ ) is so high that these oscillations would result in a major disruption or in strong confinement degradation if  $m$  were equal to 2 or 3 (Fig. 11(b)). However, this 'quiet' mode does not significantly enhance the plasma-wall interaction (Fig. 11(a)). It results in a drop in  $T_e(0)$  and suppresses the sawteeth, i.e. it exists mainly in the plasma interior. The mode is observed for  $\bar{n}_e = (1.5-2.5) \times 10^{13}$   $\text{cm}^{-3}$  at  $I_p = 200-230$  kA ( $B_t = 3$  T).

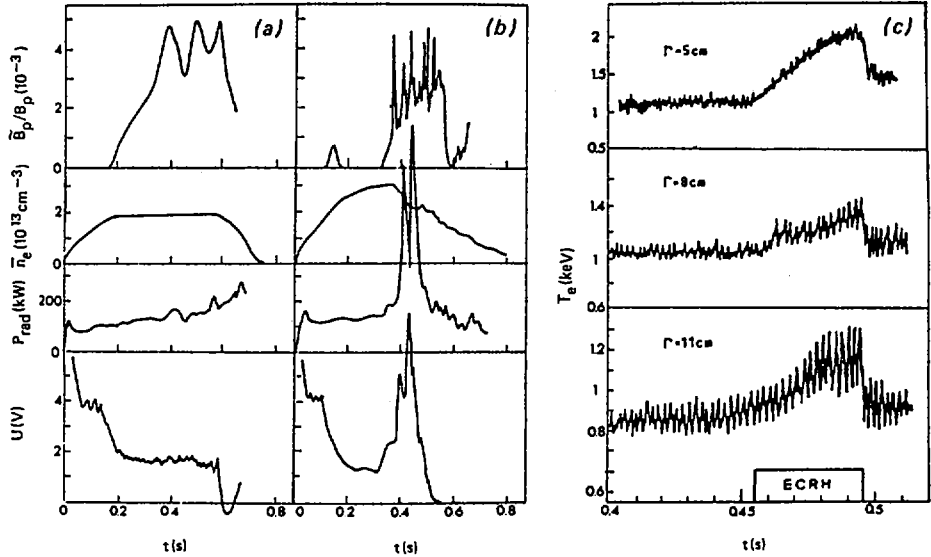


FIG. 11. Time behaviour of MHD activity characterized by  $\bar{B}_p/B_p$  amplitude ( $B_p$  is the poloidal field) and traces of  $\bar{n}_e$ ,  $P_{rad}$  and loop voltage  $U$ : (a) for internal MHD mode; (b) for  $m = 2$  mode; (c) time behaviour of  $T_e$  at different radii of auxiliary-heated discharge (on-axis ECH) with internal MHD mode.

## 7. SUMMARY

1. Doubling the HF power during the ECH experiments on T-10 practically did not change the character of the energy confinement dependence on  $P_{tot}$ , compared to previous experimental results. This dependence does not contradict the 'Ohmic' scaling,  $\tau_{Ee} \propto \langle T_e \rangle^{-0.5}$ .

2. The dependence of  $K_e$  on  $\nabla p_e$  for the plasma core obtained previously is confirmed; it is shown to be essentially non-linear. A limit value of  $\nabla p_e$  exists in the vicinity of which the transport coefficients rise significantly.

3. The results of the off-axis heating experiments do not contradict the idea of  $p$  and  $j$  profile consistency.

4. The low  $K_e$  values in the plasma core which are characteristic for high  $\bar{n}_e/I_p$ , ohmically heated plasmas are shown to be not the result of the existence of a heat pinch.

## ACKNOWLEDGEMENTS

The authors would like to thank B.B. Kadomtsev and V.S. Mukhovatov for fruitful discussions and the T-10 staff for providing the experiments.

## REFERENCES

- [1] ALIKAEV, V.V., et al., in Plasma Physics and Controlled Nuclear Fusion Research 1984 (Proc. 10th Int. Conf. London, 1984), Vol. 1, IAEA, Vienna (1985) 419.
- [2] T-10 GROUP, in Controlled Fusion and Plasma Physics (Proc. 12th Europ. Conf. Budapest, 1985), Vol. 1, European Physical Society (1985) 42.
- [3] ESIPCHUK, Yu.V., RAZUMOVA, K.A., in Controlled Fusion and Plasma Heating (Proc. 13th Europ. Conf. Schliersee, 1986), invited paper.
- [4] ESIPCHUK, Yu.V., KADOMTSEV, B.B., Pis'ma Zh. Ehksp. Teor. Fiz. **43** (1986) 573.
- [5] ALIKAEV, V.V., et al., Paper IAEA-CN-47/F-II-4, these Proceedings.
- [6] T-10 GROUP, in Controlled Fusion and Plasma Physics (Proc. 12th Europ. Conf. Budapest, 1985), Vol. 1, European Physical Society (1985) 38.

## DISCUSSION

R.J. GOLDSTON: This is more a comment than a question. It seems that we are learning how strong the profile conserving mechanism is in the plasma core. It appears to be able to reduce  $\chi_e$  by something like a factor of two, but it does not turn  $\chi_e$  negative, which would correspond to a heat pinch, nor does it even make  $\chi_e$  zero.

B.B. KADOMTSEV: Yes, I quite agree.

M.A. DUBOIS: The absence of a central electron temperature spike during central heating is in sharp contradiction with the TFTR results. Is it certain that the  $q = 1$  surface is present inside those plasmas?

B.B. KADOMTSEV: No, it is not absolutely certain. We do not yet have any experimental data on this point.



## ACHIEVEMENT OF REGIMES WITH HIGH DENSITY, LOW $q_a$ AND GOOD CONFINEMENT ON ASDEX

H. NIEDERMEYER, F. WAGNER, G. BECKER, K. BÜCHL, A. EBERHAGEN,  
G. FUSSMANN, O. GEHRE, G. VON GIERKE, O. GRUBER, G. JANESCHITZ,  
M. KAUFMANN, K. LACKNER, R. LANG, V. MERTENS, H. MURMANN,  
W. SANDMANN, E. SPETH, K. STEINMETZ, G. VLASES<sup>1</sup>, H.S. BOSCH,  
H. BROCKEN, J. GERHARDT, E. GLOCK, G. HAAS, J. HOFMANN,  
A. IZVOZCHIKOV<sup>2</sup>, F. KARGER, M. KEILHACKER<sup>3</sup>, O. KLÜBER,  
M. KORNHERR, M. LENOCI, G. LISITANO, F. MAST, H.M. MAYER,  
K. McCORMICK, D. MEISEL, E.R. MÜLLER<sup>3</sup>, Z.A. PIETRZYK<sup>1</sup>,  
W. POSCHENRIEDER, H. RAPP, H. RIEDLER, H. RÖHR, J. ROTH,  
F. RYTER<sup>4</sup>, F. SCHNEIDER, C. SETZENSACK, G. SILLER,  
P. SMEULDERS<sup>3</sup>, F.X. SÖLDNER, K.-H. STEUER, O. VOLLMER,  
D. ZASCHE

Euratom-IPP Association,  
Max-Planck-Institut für Plasmaphysik,  
Garching, Federal Republic of Germany

### Abstract

#### ACHIEVEMENT OF REGIMES WITH HIGH DENSITY, LOW $q_a$ AND GOOD CONFINEMENT ON ASDEX.

The density limit in ASDEX decreases for  $q_a < 2.7$ . However, in gettered discharges at high current (500 kA), the density limit shows again a steep increase to a higher second maximum ( $M = n_e R/B_t = 7.2 \times 10^{19} \text{m}^{-2} \cdot \text{T}^{-1}$ ) at  $q_a = 2.05$ . The lowest  $q_a$ -value achieved so far in Ohmic and beam heated plasmas is 1.9 ( $M_{OH} = 6.6 \times 10^{19}$ ). With continuous pellet injection, peaked density profiles with very high central values ( $2.2 \times 10^{20} \text{m}^{-3}$ ) were obtained in Ohmic and weakly beam heated discharges. In pellet refuelled discharges,  $\tau_E$ -values of 160 ms are achieved with  $n_e \tau_E = 3.5 \times 10^{19} \text{sm}^{-3}$ . The confinement in the L-regime seem to be governed by the same principles as in the OH-saturation regime.  $\tau_E$  can be increased by deuterium operation or by ICRF instead of NI heating. A recipe for achieving the H-mode has been developed which was successfully applied to the cases of  $q_a \leq 2$ , with ICRH or at high density with pellet refuelling.

<sup>1</sup> University of Washington, Seattle, WA, USA (DOE contract).

<sup>2</sup> Academy of Sciences, Leningrad, USSR.

<sup>3</sup> Present address: JET Joint Undertaking, Abingdon, Oxfordshire, UK.

<sup>4</sup> CEA, Centre d'études nucléaires de Grenoble, Grenoble, France.

### 1. Density limit of gas refuelled discharges

The density limit of ASDEX divertor discharges has been studied at  $q_a$ -values (cylindrical approximation neglecting the separatrix) above 2.2 by ramping up the density to the disruptive limit. Feedback controlled gas puffing has been applied in ohmic and beam heated divertor discharges without gettering [1]. An increase of the density limit with additional heating was achieved both in  $B_T$ - or  $I_p$  ( $1/q_a$ )-scans (see Fig. 1). The density limit, however, increases much less than proportional to the heating power. The Hugill-Murakami scaling was found to be valid in ohmic discharges but not with strong additional heating, where at given  $q_a$ -values  $M = \bar{n}_e R/B_t$  at the density limit scales like  $1/\sqrt{B_t}$ .

In most cases edge cooling is believed to be responsible for the density limit. In low- $q_a$  discharges (below about 2.7) the  $q=2$  surface is obviously destabilized directly while at higher  $q_a$ -values thermal effects cause the current channel to shrink and as a consequence trigger the disruptive  $m=2$ -mode. In these cases the onset of marfes is always observed before the discharge shrinks. This kind of a two dimensional thermal instability increases edge radiation substantially and is thus strongly involved in the shrinking process.

### 2. Pellet discharges

Pellet injection as a tool for more efficient refuelling was expected to reduce edge cooling and permit higher densities. In fact an appreciable increase of the maximum density has been achieved by this method as well as an unexpected improvement of particle and energy confinement. Injection of a series of  $D_2$  pellets with a centrifuge [2], [3] (size corresponding to an averaged density of  $1 \cdot 10^{19} \text{ m}^{-3}$ , velocity of 650 m/s, repetition rate less than 40 per second, penetration depth about  $a/2$ )

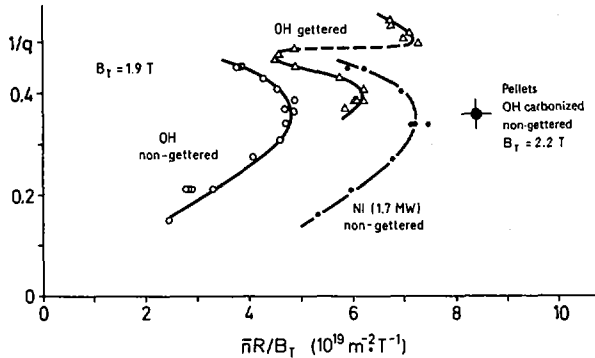


FIG. 1. Maximum achievable densities for different types of divertor discharges plotted in the Hugill diagram.

may cause a peaking of the density profile as already observed in experiments with smaller numbers of pellets /4/, /5/, /6/, /7/. Penetration to the center is not necessary to get triangular density profiles. Sufficient recycling, however, is a necessary condition for the onset of this regime. We attribute the change of the profile to an increased ratio of the inward drift velocity to the particle diffusion constant evidently caused by pellet injection. Unfortunately an accumulation of metal impurities in the plasma center results from the improved particle confinement and now central radiation determines the density limit. With wall carbonisation a Murakami parameter of  $8.5 \cdot 10^{19}$  and a central density above  $2 \cdot 10^{20} \text{ m}^{-3}$  can be achieved in ohmic discharges. Before excessive central radiation arises, the  $T_e$ -profiles are nearly unchanged compared to gas refuelling. With this strongly increased density high confinement times of up to 160 ms in ohmic discharges are obtained. We surmise that the transport properties are changed as shown by the fact that triangular density profiles with nearly constant peak density are sustained for 300 ms after having stopped pellet injection. There are indications that even smaller pellet penetration depths are sufficient to cause

density peaking. High power co-injection prevents peaking of the profiles. The few discharges with counter-injection performed so far show improved particle and energy confinement. This result and a remarkable curvature of the pellet trajectories as observed on photographs suggest that also during the ohmic phase toroidal plasma rotation plays an important role.

### 3. Low- $q_a$ discharges at high densities

With only gas-puff refuelling a Murakami parameter of  $7.2 \cdot 10^{19}$  was reached in gettered divertor discharges at very low  $q_a$ -values of about 2 (cylindrical approximation) performed with a plasma current near the design limit of 500 kA (Fig. 1). In earlier experiments on ASDEX a steep drop of the density limit with decreasing  $q_a$  has been found when approaching  $q_a = 2$  in agreement with all known results of other tokamaks. At small  $q_a$ -values a strong saturated  $m=2$ -mode develops already at moderate densities and increases slowly with increasing density (Fig. 2). Finally it leads to a disruption. Now it has been discovered that at even smaller  $q_a$ -values the  $m=2$ -activity may suddenly drop to a very small level during the slow density rise (Fig. 2). It reappears again but then at much higher densities and determines the density limit.  $q_a$ -values of 1.9 were obtained, however, the optimum  $q_a$  is about 2.0. The only difference in the external parameter settings of the two cases compared in Fig.2 is the plasma current. The attempt to raise the plasma density evidently results in an increase of MHD fluctuations for the lower plasma current, but in their decrease for the higher one. Due to the singularity induced by the stagnation point, the true  $q_\psi = 2$ -surface for the two cases will always be inside and close to the separatrix, but at different locations: the qualitatively different response of the MHD signals might therefore result from the predicted reaction of tearing modes, which are stabilized by flattening

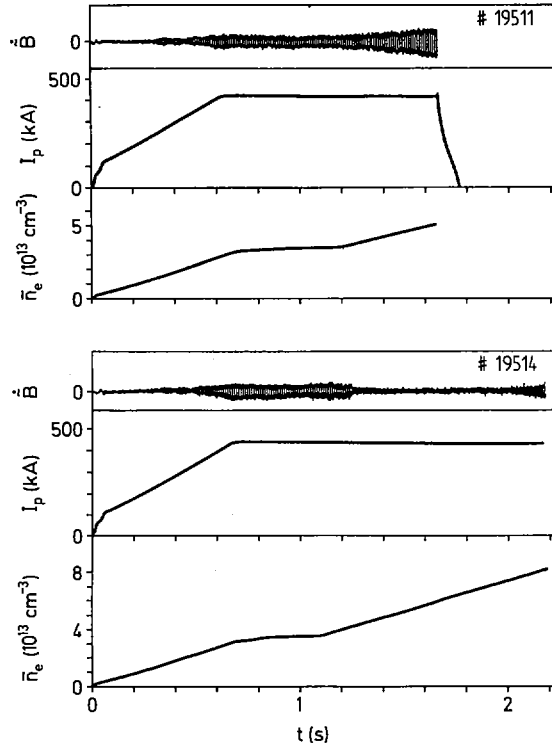


FIG. 2. Time evolution of plasma current, mean density and MHD activity during discharges at  $q_a = 2.15$  ( $I_p = 420$  kA) (top) and  $2.05$  ( $I_p = 440$  kA).

of the current density profile (and hence by cooling) inside the resonant surface, but destabilized by it on the outside. Stable discharges with long density plateaus 5 % below the density limit were run at  $q_a = 1.9$ .  $T_e$  profiles are trapezoidal with the flat central part extending to  $a/2$  in ohmic discharges and high power beam heated discharges. Density profiles are parabolic in ohmic discharges, in beam heated discharges they are rather flat with a very high edge density. Confinement of ohmic discharges is good,  $\tau_E$  is comparable to the  $\tau_E$ -values of the saturation region away from the density limit (80 ms typically), the toroidal beta values rise with increasing density and with decreasing  $q_a$ . At  $q_a = 1.9$ ,  $\beta_t = 0.61$  % was

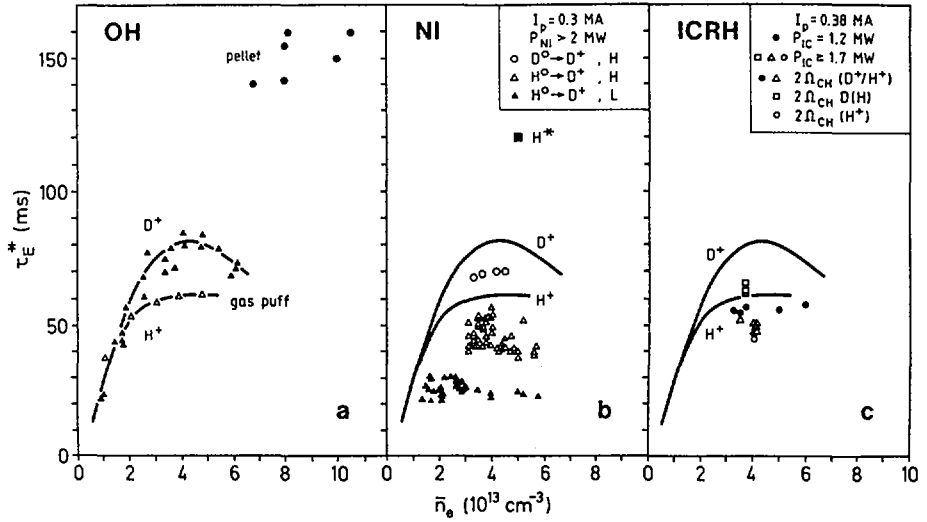


FIG. 3. Survey of confinement time values versus density in (a) ohmically, (b) NI and (c) ICRH heated plasmas. (a)  $B_T = 2.2$  T; gas puff:  $I_p = 420$  kA, pellet:  $I_p = 380$  kA; (b)  $B_T = 2.2$  T; (c)  $B_T = 2.4$  T.

reached compared to 0.43 % at  $q_a = 2.5$ . With beam injection at a power level of 1.7 MW, L-mode confinement is being interrupted by short phases of the H-mode. At 2.6 MW the signature of the H-mode is more clearly pronounced. Measured confinement times of about 50 ms are only slightly higher than those expected from L-mode scaling. This might be attributed to strong impurity radiation present with high power beam heating which was not observed in ohmic discharges.

#### 4. Confinement

On Asdex the most important confinement regimes which seem to be characterized by intrinsically different properties can be realized. Figure 3 summarizes density scans of the global confinement time  $\tau_E$  for ohmic and auxiliary heated discharges.

The ohmic data represent pellet refuelled plasmas and scans in pure hydrogen or deuterium discharges with gas-puff refuelling. The auxiliary heated data comprise density scans of discharges in the L-regime heated either by NI or ICRH, and plasmas in the H-mode for the injection scenarios  $H^0 \rightarrow D^+$  and  $D^0 \rightarrow D^+$ , and finally, the result achieved in the quiescent H-mode when ELMs are suppressed /8/.

The degradation of confinement with ICRH is less severe than that with NI. The reason is not clear but could be due to the better particle confinement with ICRH or the lack of toroidal rotation. Deuterium as working gas is superior to hydrogen both with ohmic and auxiliary heating. This isotope dependence improves the confinement of  $2\Omega_{CH}$  - ICRH applied to basically deuterium plasmas (with the minimum necessary hydrogen concentration of ~20 %) or D(H) - minority heating at the fundamental frequency. Also the H-mode confinement is subject to the isotope effect.

Pellet refuelling yields  $\tau_E$ -values up to 160 ms /9/ and  $\hat{n}_e \tau_E^-$  values up to  $3.5 \cdot 10^{19} \text{ sm}^{-3}$ . In the quiescent H-mode ( $H^*$ ),  $\tau_E = 120 \text{ ms}$  is found. (As the  $H^*$ -mode strongly suffers from impurity accumulation the core-radiation overlapping with the power deposition profile has been corrected for the  $\tau_E$ -analysis.)

#### 4.1. L-Regime

The ohmic saturation and the L-regime are both regimes with degraded confinement. Common features are the lack of density dependence of  $\tau_E$  and a similar improvement with isotope mass. Another aspect common to OH-saturation and L-regime is "profile consistency" /10/: An increase of  $I_p$  (decrease of  $q_a$ ) broadens the  $T_e$  profile in the same way. Figure 4 shows the volume averaged electron temperature  $\langle T_e \rangle$  versus plasma current both for NI-heating at different heating power levels and for OH-heating for two different densities. Irrespective of the heating method

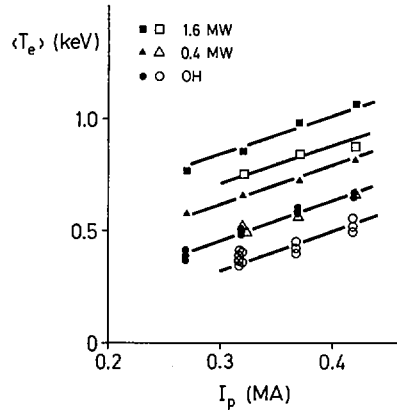


FIG. 4. Volume averaged electron temperature  $T_e$  versus plasma current for different NI power levels and plasma densities. Solid symbols:  $\bar{n}_e = 2 \times 10^{13} \text{ cm}^{-3}$ ; open symbols:  $\bar{n}_e = 3 \times 10^{13} \text{ cm}^{-3}$ .

(OH or NI),  $\langle T_e \rangle$  increases with  $I_p$  in a similar way. These results indicate the same profile broadening and improvement in energy content for OH- and NI-heated plasmas. The broadening of the  $T_e$ -profile with increasing current leads ultimately to the proportionality of  $\tau_E$  and current under auxiliary heating conditions. In the ohmic case, however, the  $\tau_E$  of the saturation regime is independent of current despite the fact that the energy content also increases with current. The difference between ohmic and auxiliary heating is that in the ohmic case the heating power increases linearly with current while it is independent of current with auxiliary heating. Already under ohmic conditions, the heating power degrades confinement as it is known from auxiliary heated plasmas. Both plasma current and heating power are two important parameters which determine the confinement both in the OH-saturation regime and the L-mode with the L-mode being the continuation of the OH-saturation regime towards higher power.

Figure 5 shows the plasma energy content versus power for an ohmic current scan and for two NI-power scans at two current

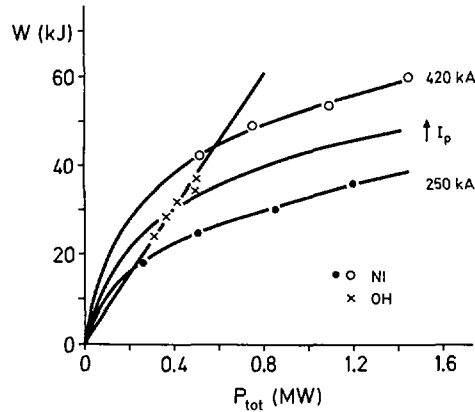


FIG. 5. Variation of energy content  $W$  with heating power  $P$  in Ohmic current scan and with NI at two plasma current values (the first data point of the NI scans represents the OH starting value). Curves represent non-linear relation between  $W$  and  $P$  at constant current; straight line is a fit through Ohmic data points.

values. The solid lines tentatively indicate an inherent non-linear relation between  $W$  and  $P$ . Under OH conditions, this dependence is hidden, because the heating power and the plasma current rise simultaneously /11/. From this analysis it is obvious that there has to be a discontinuity of the slopes in a  $W$  versus  $P$  diagram at the transition from ohmic to auxiliary heating as shown in Fig. 5. The reason for the discontinuity is that an ohmic power scan occurs in a plane where  $I_p/P$  is constant; with auxiliary heating, however, a power scan is continued in an  $I_p = \text{const.}$  plane. The ohmic  $W$  vs.  $P$ -trace is not a scalable relation. The assumption of a special quality of OH-heating does not seem to be justified. The reason for the current scaling which seems to be unique to all auxiliary heated plasmas at higher densities is not the introduction of a new confinement element. Rather it is the disappearance of a common element which is the dominance of the ohmic heating power and its proportionality to plasma current /10/. Therefore also in the H-mode  $\tau_E$  is proportional to  $I_p$  despite distinct

differences in the development of L- and H-phases and in the absolute values of  $\tau_E$ . The operational space with good confinement below the ohmic power is only accessible under highly efficient current drive conditions like with Lower-Hybrid heating or in non-thermal discharges. Indeed, such current drive scenarios indicate improved confinement.

#### 4.2. H-Regime

In spite of the large differences in the profile shapes there are common characteristics of the good pellet discharges and the H-mode, for example the reduction of the divertor recycling, an improvement in runaway electron confinement, the tendency for impurity accumulation, and strong indications of the importance of the plasma edge conditions for confinement /12/. The H-mode is caused by the sudden development of an edge transport barrier /12/ which seems to require an edge electron temperature above 200-300 eV. The deep pellet refuelling obviously prevents the detrimental effect of gas-puff refuelling on plasma edge conditions which leads to the  $\tau_E$  roll-over and the development of the saturation regime.

Apart from the insight in the role of the plasma periphery for the H-transition a recipe for reaching the H-mode emerged from our studies. The crucial element seems to be the increase of  $T_e$ (edge) beyond a threshold requiring a minimal heating power (1.8 MW with NI in the double-null configuration) and giving rise to the preceding L-phase (until  $T_e$ (edge) is sufficiently heated up) /12/. The edge temperature threshold also causes the sensitivity of the H-transition on recycling and impurity radiation cooling. The intrinsically better confinement of deuterium and helium facilitates the H-mode development: In pure hydrogen discharges ( $H^0 \rightarrow H^+$ ) the power threshold is ~3 MW. Owing to the ion-electron coupling, the H-transition is eased when the ion temperature is also high at the edge. Because of

these requirements, recycling has to be kept low and gas refuelling into the divertor instead of the main plasma chamber can reduce the power threshold. With low recycling, neoclassical ion transport may be dominant even at the plasma edge. In this case, a poloidal asymmetry of the energy sink distribution (as realized by the X-point) can reduce the ion heat transport and with it the power requirements for the H-transition /12/. In the poloidally asymmetric situation of the single null (SN) configuration, the power threshold is reduced to 1.2 MW if the ion grad-B-drift is toward the X-point. In the opposite case, the power threshold rises to ~3 MW /12/. With the X-point in the mid-plane, no improvement is expected. The above described recipe has been applied to successfully increase the operational space of the H-mode. (1) In the low  $q_a$ -plasmas, described in Sec. 3, when additionally edge radiation by oxygen is reduced owing to Ti-gettering, the H-mode can be realized in the most attractive corner of the Hugill-diagram (high current and high density); (2) reduced recycling in pellet refuelled discharges allowed an increase of the upper density limit of the H-mode from  $\bar{n}_e = 7-8 \cdot 10^{19} \text{ m}^{-3}$  with gas puff refuelling to  $\bar{n}_e > 1.1 \cdot 10^{20} \text{ m}^{-3}$ . (3) The application of ICRH in the deuterium dominated D(H)-minority heating scheme (instead of  $2\Omega_{CH}$ -heating in hydrogen) yielded the H-mode with a different heating method. In the SN-configuration, 1.7 MW ICRH-power is required. Another improvement in operational space is counter-NI which decreased the power threshold to 0.8 MW. The H-phase, however, is heavily affected by impurity accumulation and therefore transient.

## REFERENCES

- [1] NIEDERMEYER, H., et al., in *Controlled Fusion and Plasma Physics (Proc. 12th Europ. Conf. Budapest, 1985)*, Part 1, European Physical Society (1985) 159.
- [2] AMENDA, W., LANG, R.S., in *Fusion Technology (Proc. 13th Symp. Varese, 1984)*, CEC, Brussels (1984) 243.

- [3] AMENDA, W., LANG, R.S., to be published in *J. Phys., E (London). Sci. Instrum.* **19** (1986).
- [4] GREENWALD, M., et al., in *Controlled Fusion and Plasma Physics (Proc. 11th Europ. Conf. Aachen, 1983), Part 1, European Physical Society (1983)* 7.
- [5] SCHMIDT, G.L., et al., in *Controlled Fusion and Plasma Physics (Proc. 12th Europ. Conf. Budapest, 1985), Part 2, European Physical Society (1985)* 674.
- [6] SENGOKU, S., et al., *Nucl. Fusion* **25** (1985) 1475.
- [7] FONCK, R.J., et al., *J. Nucl. Mater.* **128 & 129** (1984) 330.
- [8] GRUBER, O., JILGE, W., BERNHARDI, H., EBERHAGEN, A., et al., in *Controlled Fusion and Plasma Phys. (Proc. 12th Europ. Conf. Budapest, 1985), Vol. 1, European Physical Society (1985)* 18.
- [9] KAUFMANN, M., *Plasma Phys. Controll. Fusion* **28** (1986) 1341.
- [10] WAGNER, F., GRUBER, O., LACKNER, K., MURMANN, H.D., SPETH, E., et al., *Phys. Rev. Lett.* **56** (1986) 2187.
- [11] WAGNER, F., et al., to be published in *Nucl. Fusion*.
- [12] WAGNER, F., et al., in *Basic Physical Processes of Toroidal Fusion Plasmas (Proc. Workshop Varenna, 1985)*.
- [13] HINTON, F., *Nucl. Fusion* **25** (1985) 1457; WAGNER, F., BARTIROMO, R., BECKER, C., BOSCH, H.S., et al., *Nucl. Fusion* **25** (1985) 1490.

## DISCUSSION

R.J. HAWRYLUK: How was  $q_a$  defined?

F. WAGNER: We used the cylindrical definition, so that  $1/\epsilon$  represents the plasma current.

S. YAMAMOTO: I should like to mention that in JAERI's JFT-2M, H-mode behaviour was observed in the limiter discharge with simultaneous co-NBI and  $2\omega_{ci}$  ICRF. Recently, the limiter H-mode discharge was obtained with only co-NBI. In the limiter H-mode discharge, the plasma is restricted by the inside limiter only, and there should be some clearance between the plasma surface and the vacuum chamber on the low field side.

R.J. GOLDSTON: You showed that the power threshold for the H-mode transition was 1.2 MW for the grad-B drift in the direction of a single null divertor and 3 MW for the reverse configuration. Could you comment on the plasma parameters — radiated power, impurities, edge electron temperature — at, say, about 1 MW of input power in each case.

F. WAGNER: The majority of the experiments were made at higher power (1.6 MW). No striking difference in these parameters has been observed in SN-discharges with different ion grad-B drift directions. But there remains the observation, even in these configurational studies, that the edge electron temperature tends to increase in the correct configuration (in grad-B drift to the X-point), causing H-transition when it exceeds a threshold of 200–300 eV.

J. JACQUINOT: Can you comment on the stationary aspect of the H-mode? I am thinking of a comparison between the duration of good confinement and the duration of the heating pulse.

F. WAGNER: At reduced power, when  $\beta/\beta_{\max} \leq 0.7-0.8$ , the H-mode remains in a quasi-steady state (parameters only modulated edge located discharges). Stationary H-mode phases have been maintained by stacking the beams for  $\sim 10\tau_E$ . Approaching the beta limit, the confinement in the H-mode degrades after a maximum. This might be due to a reduction of the beta limit when the current profile broadens and  $q(0)$  rises on account of the high edge electron temperature.

M.C. ZARNSTORFF: Could you comment on any dependence of the H-mode onset upon the angle of beam injection, i.e. co-injection versus counter-injection?

F. WAGNER: The lowest power threshold for the H-transition occurs with counter-injection ( $\sim 2 \times P_{OH}$ ). Because of the tremendous impurity accumulation under these circumstances, the H-phases are short ( $\sim 50$  ms). The high-Z impurity problems can be avoided by wall carbonization. The required power for H-mode onset is, however, higher in this case.



## STUDIES OF THE REGIME OF IMPROVED PARTICLE AND ENERGY CONFINEMENT FOLLOWING PELLET INJECTION INTO ALCATOR C

M. GREENWALD, M. BESEN, F. CAMACHO, C. FIORE,  
M. FOORD, R. GANDY<sup>1</sup>, C. GOMEZ<sup>2</sup>, R. GRANETZ,  
D. GWINN, S. KNOWLTON, B. LaBOMBARD<sup>3</sup>,  
B. LIPSCHULTZ, H. MANNING<sup>4</sup>, E. MARMAR,  
S.C. McCOOL<sup>5</sup>, J. PARKER<sup>6</sup>, R. PARKER, R. PETRASSO,  
P. PRIBYL<sup>3</sup>, J. RICE, D. SIGMAR, Y. TAKASE, J. TERRY,  
R. WATTERSON<sup>4</sup>, S. WOLFE  
Plasma Fusion Center,  
Massachusetts Institute of Technology,  
Cambridge, Massachusetts,  
United States of America

### Abstract

#### STUDIES OF THE REGIME OF IMPROVED PARTICLE AND ENERGY CONFINEMENT FOLLOWING PELLETT INJECTION INTO ALCATOR C.

Pellet fueling in Alcator C can result in a plasma regime in which both energy and particle confinement are dramatically improved. In this regime, ion thermal losses (highly anomalous in gas fueled plasmas) are reduced to approximately neoclassical values, resulting in increased global energy confinement for high density discharges where ion losses are important. There is little or no change in electron thermal conductivity. The pellet fueled discharges exhibit peaked density profiles, which tends to confirm the importance of the  $\eta_i$  parameter in determining ion thermal diffusivity. At the same time, impurity particle transport is reduced to neoclassical levels, leading to accumulation of impurities and strong peaking of impurity profiles. Confinement of the hydrogenic species in the discharge core is also increased. The modifications of ion thermal transport, central particle transport, and impurity transport are well correlated; there are no discharges where only one or two of these parameters change. In the favourable transport regime, sawteeth are partially or completely suppressed. This is probably due to the strong peaking of low Z impurities which flatten the central current profile by increasing the plasma resistivity. Radiation does not play an important role in the power balance of these discharges. For plasmas in which the sawteeth are suppressed, the improved confinement is sustained for the remainder of the discharge.

---

<sup>1</sup> Auburn University, AL, USA.

<sup>2</sup> Los Alamos National Laboratory, NM, USA.

<sup>3</sup> University of California, Los Angeles, CA, USA.

<sup>4</sup> Science Research Laboratory, Somerville, MA, USA.

<sup>5</sup> Texas University, Austin, TX, USA.

<sup>6</sup> Lincoln Laboratory, Lexington, MA, USA.

## 1. Introduction

Previous work on Alcator C demonstrated that pellet fueling could increase global energy confinement in the "saturated" regime of ohmic discharges [1]. Detailed analysis showed that pellet fueling reduces ion thermal transport to levels near the predictions of neo-classical theory [2,3] (FIG. 1). It is important to note that for gas fueling in Alcator C, the ion transport is always anomalous. The confinement saturation becomes apparent at high densities where significant power is lost through the ion channel. The effect of pellets is to reduce ion losses at all densities which causes the observed increase in global confinement at high density. These results are consistent with theories of ion temperature gradient driven turbulence [4], the so-called  $\eta_i$  or ion-mixing modes [5,6]. Our latest experiments have concentrated on the behavior of particle transport with pellet fueling. A coherent picture has emerged, in which particle and energy confinement are inextricably linked and which may shed light on the mechanisms of anomalous transport for both electrons and ions. Recent results from ASDEX and TFTR have shown some of these same features and comparisons may yield additional insights [7,8].

## 2. Particle transport experiments

There were a number of reasons to expect little change in particle transport with pellet fueling. Conventional wisdom has linked particle

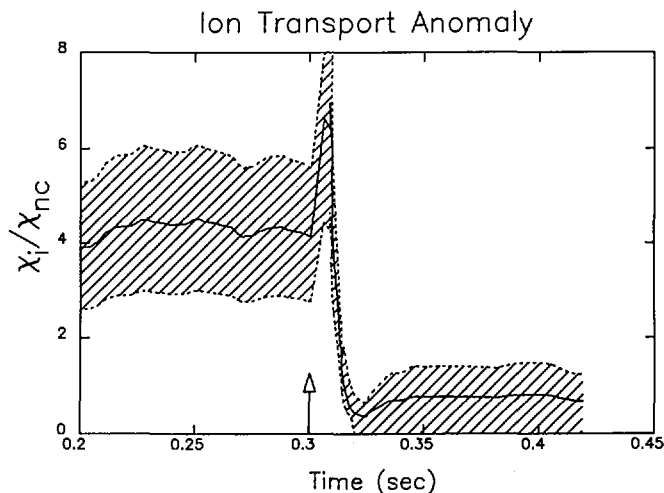


FIG. 1. Anomaly factor for neo-classical ion transport versus time. A single pellet is injected at 0.3 sec.

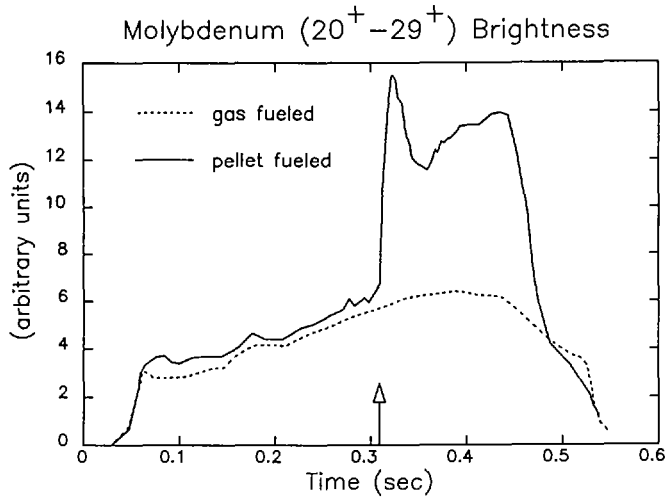


FIG. 2. Brightness of lines from highly ionized molybdenum versus time. Pellet injection at 0.3 sec.

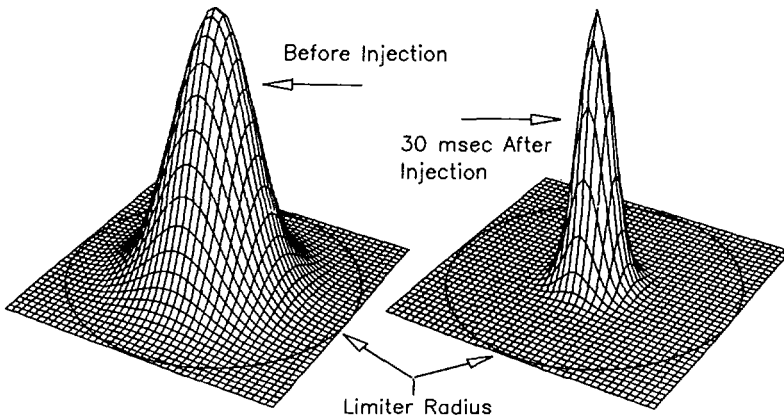


FIG. 3. Profiles of soft X-ray emission before and after injection.

diffusivity to anomalous electron thermal conductivity in impurity free plasmas, ( $D_p \propto \chi_e$ ), which is unchanged in our experiments. Empirical studies of impurity confinement in impure plasmas have shown scalings quite different from those for electron energy transport [9]:

$$\tau_1 \propto \frac{m_{bg} Z_{eff}}{q Z_{bg}}$$

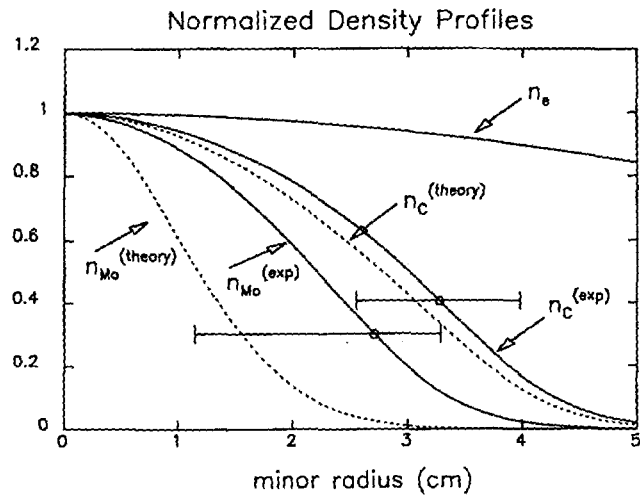


FIG. 4. Carbon and molybdenum profiles inferred from X-ray data and a comparison with neo-classical theory.

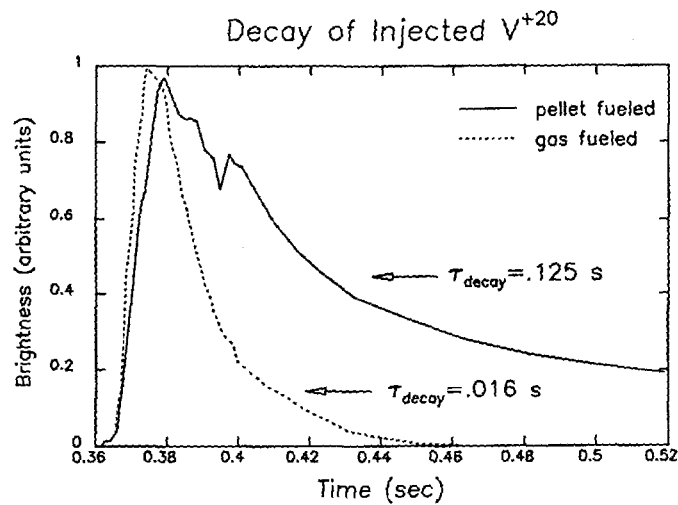


FIG. 5. Comparison of decay times for injected vanadium before and after pellet fueling.

where  $m_{bg}$  and  $Z_{bg}$  are, respectively, the atomic mass and charge of the background plasma. None of the parameters in this expression is significantly altered by pellet fueling. In contrast, the experiments demonstrate that particle confinement is substantially increased by pellet fueling. Transport coefficients for hydrogen cannot be unambiguously obtained for the gas fueled discharges, but analysis of density profiles after injection

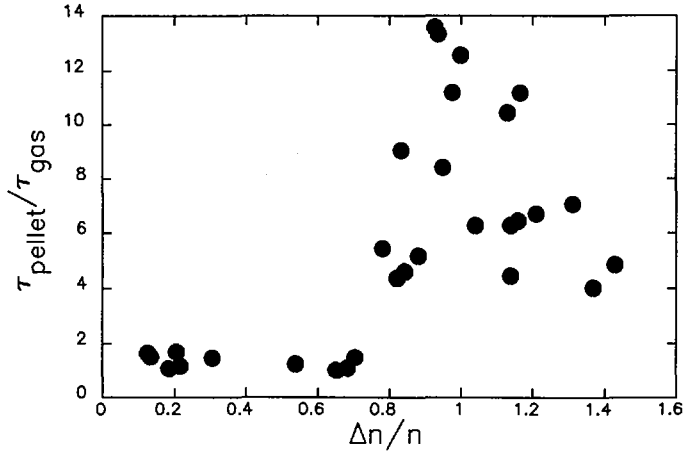


FIG. 6. Enhancement of impurity confinement with pellet fueled density increase.

shows an increase in the ratio of inward convection to diffusion and indicates an increase in central particle confinement of about a factor of 2. Densities of intrinsic impurities, mainly carbon and molybdenum, begin to increase substantially in the plasma core after pellet injection. This can be seen in FIG. 2, which shows the time history of lines of highly ionized molybdenum. The source, as indicated by the intensity of lines from low ionization states of these impurities, shows little change.

Further evidence of the improved impurity confinement is seen in data from arrays of soft x-ray diodes. Radiation in this spectral range is sensitive to plasma density, temperature, and impurity concentration. After an initial drop due to plasma cooling by the pellet, the signals increase and peak strongly as the impurities build up on axis (FIG. 3). The impurity peaking is even greater than would be apparent at first glance, since the x-ray profile is dominated by the electron temperature profile before the pellet and by the impurities afterwards. Careful analysis of data from arrays with different spectral filtering has determined the time histories of profiles of carbon and molybdenum [10] and shown them to be in reasonably good agreement with the theory of neo-classical impurity transport [11] FIG. 4. Experimental values for the diffusivity  $D$  and convective velocity  $V$  of the carbon were  $300 \text{ cm}^2/\text{s}$  and  $1000 \text{ cm}/\text{s}$ , respectively. Comparisons of plasmas before and after injection indicate that the principal change is a drop in  $D$  by about an order of magnitude.

These observations are confirmed by measuring the confinement of injected impurities [12]. In these experiments, trace quantities of non-intrinsic, non-recycling impurities are injected by the laser blow-off method

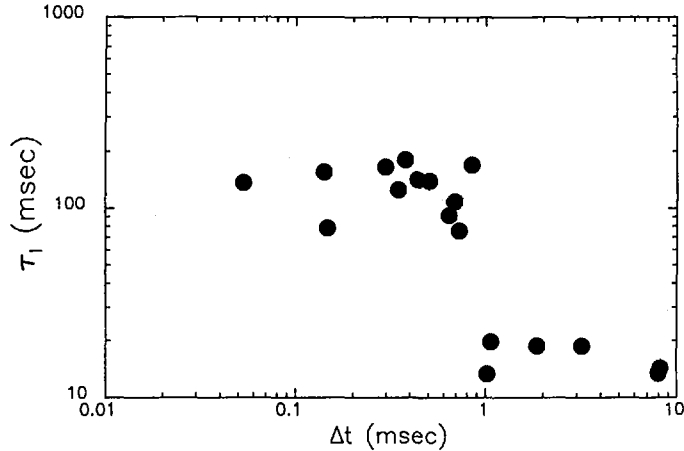


FIG. 7. Correlation of  $\tau_I$ , the impurity confinement time, and  $\tau_{Te}$ , the relaxation time for the central electron temperature.

and their time histories followed by UV and X-ray spectroscopy [9]. Figure 5 shows results of such an experiment which compares the confinement of injected vanadium in pellet and gas fueled plasmas. The vanadium confinement time before injection is 16 msec, which is in agreement with the empirical scaling law. After injection, the time increases to 125 msec. (Actually, the empirical law would predict a slight decrease since in this case the deuterium plasma was diluted with hydrogen from the pellet.) Typically, the increases are factors of 5 - 20. When the increase in injected impurity confinement is plotted against the normalized density increase ( $\Delta n/n$ ) a threshold is seen at about  $\Delta n/n = 1$  (FIG. 6). This same threshold is also observed for the accumulation of intrinsic impurities, the reduction of ion thermal transport and for peaking of the electron density profile.  $\Delta n/n$  is not a unique parameter for characterizing the threshold. Because of the relationship between pellet size and ablation rate [13], the threshold could also be expressed in terms of the pellet penetration depth.

This same threshold is seen in an apparently unrelated measurement, the rate of fall of the central electron temperature in the first few hundred  $\mu$ seconds after injection. The pellets in these experiments were injected at about  $8.0 \times 10^4$  cm/sec and were completely evaporated after traveling less than 8 - 12 cm, thus they never reached the magnetic axis (or even the sawtooth mixing radius). The expected result would have been a cold annulus of plasma surrounding an unperturbed hot core. With ordinary (albeit anomalous) heat transport,  $\chi_e \sim 1 - 2 \times 10^3$  cm<sup>2</sup>/s, the

relaxation time would be a few msec. Nonetheless, the central temperature, as measured by electron cyclotron emission and Thomson scattering, typically fell much more rapidly, maintaining its shape and reaching equilibrium in as little as 100  $\mu\text{sec}$  [14,15]. The surprising result is that the relaxation time shows the same threshold and is strictly correlated with the confinement improvements described above (FIG. 7). This observation suggests that the bifurcation in plasma regimes occurs immediately after injection. The transport analysis is consistent with models where transport coefficients change promptly at injection.

### 3. Sawtooth effects

A common feature of pellet fueled discharges is the modification of the sawtooth oscillations [16]. Typically the sawteeth continue through the injection, initially with little change in period or amplitude. Gradually the period increases, culminating in either one or more very large sawteeth or in their complete suppression. The variation in behavior is correlated with the peaking of the electron and impurity densities and thus with particle confinement; plasmas with the most peaked profiles have no sawteeth. Sorting out cause and effect is difficult. It appears that the sawteeth do not have a direct influence on the regime of particle transport but rather the reverse. As impurities peak on axis the central resistivity increases. The effect on the plasma current profile can be seen by considering the equation for the evolution of the poloidal field

$$\frac{\partial r B_p}{\partial t} = \frac{c^2}{4\pi} \left[ r \frac{\partial}{\partial r} \left( \frac{1}{r\sigma} \frac{\partial r B_p}{\partial r} \right) \right]$$

where  $\sigma$  is the Spitzer conductivity  $\sim T^{3/2}/Z_{\text{eff}}$ ; substituting, one obtains

$$\frac{\partial r B_p}{\partial t} = \frac{c^2}{4\pi\sigma} \left[ r \frac{\partial}{\partial r} \left( \frac{1}{r} \frac{\partial r B_p}{\partial r} \right) - \left( \frac{3}{2} \frac{1}{T} \frac{\partial T}{\partial r} - \frac{1}{Z} \frac{\partial Z}{\partial r} \right) \frac{\partial r B_p}{\partial r} \right]$$

The first term is diffusive and tends to flatten the current profile. The second and third terms are convective and lead to growth or damping depending on their relative sizes. Ordinarily, the term proportional to temperature gradient will dominate and give rise to the thermal instability which drives the sawteeth. However, after injection, with impurity densities becoming strongly peaked, the third term can dominate, flatten the current profile, raise  $q(0)$ , and turn off the sawteeth. A series of simulations were run to solve for the simultaneous evolution of an impurity species (carbon) and current density. In these simulations, Spitzer

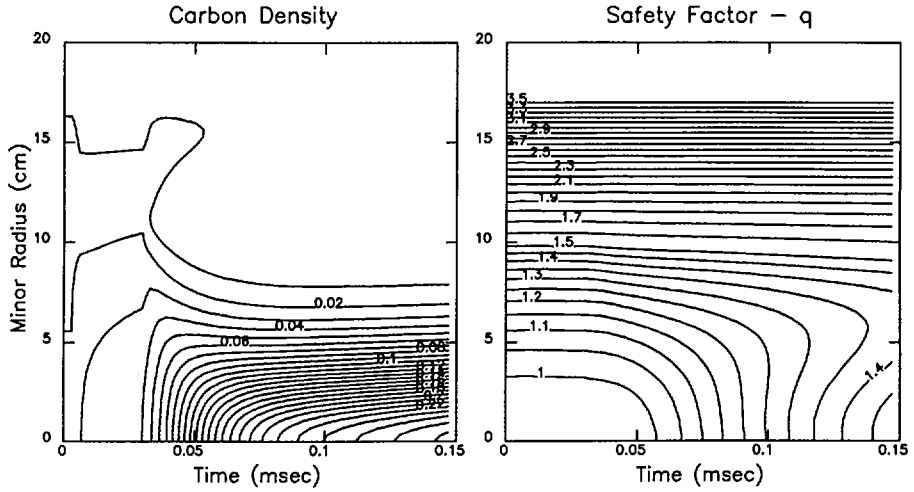


FIG. 8. Contours of carbon density and plasma  $q$  from a simulation of impurity and current diffusion.

resistivity was used for the current diffusion and the particle transport coefficients were adjusted to match experimental data. The results can be seen in FIG. 8 where contours of carbon density and plasma safety factor  $q$  are plotted against space and time. After a single pellet, injected at 30 msec, the central value of  $q$  goes from an initial value of .95 to above 1.0 in 25 msec. This is in agreement with our observations of sawtooth suppression. It should be noted that in the plasmas considered here, radiation has negligible effect on central power balance. We also note that sawteeth can have an indirect effect on the transport regime. If the sawteeth are not completely eliminated, they flatten the density profile and the plasma reverts to the pre-injection confinement mode.

#### 4. Density limit studies

Pellet injection has also provided a tool to study the physics of the density limit. For gas fueling, a limit  $n_e \propto I_p$  has been seen on most tokamaks [17]. The standard explanation for this limit is that high plasma densities lead to a radiative collapse of the plasma column to an unstable MHD equilibrium [18]. This explanation does not seem consistent with the relative insensitivity of the limit to auxiliary power or  $Z_{\text{eff}}$ . (The limit considered here must be distinguished from the Murakami limit with  $n_e \sim B/R$  which is sensitive to both these factors [19].) Analysis of the density decay after pellet fueling showed that the central particle confinement degraded markedly as the density limit was approached. With pellets, the limit could be surpassed (briefly) without disruption, but the

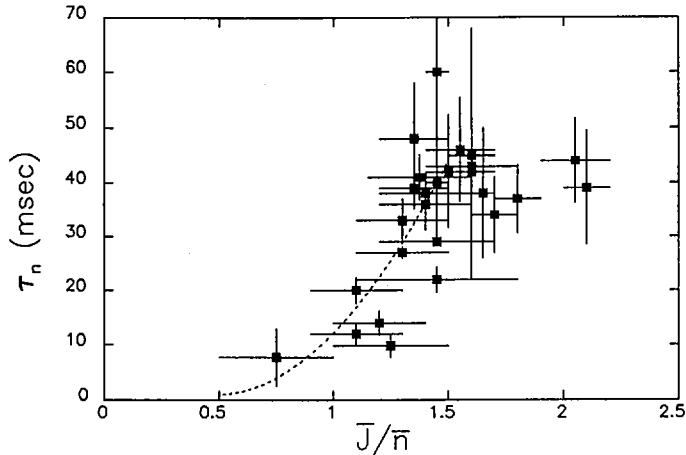


FIG. 9. Density decay time after pellet injection plotted versus  $\bar{J}/\bar{n}$ , the average current density (MA/m<sup>2</sup>) over average density ( $10^{14}$  cm<sup>-3</sup>).

plasma shed the excess particles extremely rapidly. Figure 9 shows the decay time vs  $\bar{J}/\bar{n}_e$ , where  $\bar{J}$  is the plasma current divided by the plasma cross-sectional area. This suggests that this density limit is due to the degradation of particle confinement, and the disruptive limit that is commonly observed with gas puffing occurs when the plasma is "choked" with gas that it cannot absorb [20]. The same scaling may explain the onset of Marfes at densities somewhat below the limit. As particle confinement degrades with respect to energy confinement, the average energy of an edge particle drops and triggers a thermal/radiative collapse.

## 5. Discussion and Summary

Several features of these experiments have implications for theories of plasma transport. The observation that ion thermal conductivity decreases as the density gradient is increased (with constant temperature profiles) is consistent with theories of the  $\eta_i$  mode. However, electron thermal transport, if driven by drift wave turbulence [21,22], should increase under these conditions and this is not observed. Further, ion energy and particle transport appear to be tightly coupled and both uncoupled from electron energy confinement. Electron, ion and impurity particle fluxes are always tied through the ambipolarity constraint, with net particle flux limited by the less diffusive species. It seems reasonable that the electrons, which remain highly anomalous, are "held back" by the ions and that particle confinement is governed by the same mechanisms which determine ion energy transport. (The  $\eta_i$  modes are predicted to

drive particle diffusion in collisionless plasmas [23] and an inward pinch in the collisional regime [5].) The decoupling of particle and electron thermal transport might suggest that electron transport is not driven by purely electrostatic modes which would give rise to intrinsically ambipolar particle transport through the  $E \times B$  drift. With this interpretation, the experimental observation can be taken as support for electron transport driven by electro-magnetic mechanisms [24].

In summary, with pellet fueling we have attained a regime in which the ion species show nearly neo-classical transport. The improvement seems to be linked to steep density profiles and may be related to suppression of  $\eta_i$  modes. This could have important implications for future machines as these modes are predicted to seriously degrade ion energy confinement as the reactor regime is approached. On the other hand, suppression of this turbulence and the ensuing neo-classical accumulation of impurities presents problems for long pulse ignited plasmas.

#### ACKNOWLEDGEMENT

This work was supported by the United States Department of Energy, under Contract No. DE-AC02-78ET51013.

#### REFERENCES

- [1] GREENWALD, M., et al., Phys. Rev. Lett. **53** 4 (1984) 352.
- [2] WOLFE, S., et al., Nucl. Fusion **26** (1986) 329.
- [3] CHANG, C.S., HINTON, F.L., Phys. Fluids **25** 9 (1982) 1493.
- [4] LEE, G.S., DIAMOND, P.H., Rep. IFSR-209, Institute for Fusion Studies, Texas Univ., Austin (1986); Phys. Fluids **29** 10 (1986) 3291.
- [5] COPPI, B., SPIGHT, C., Phys. Rev. Lett. **41** 8 (1978) 551.
- [6] ANTONSEN, T., COPPI, B., ENGLADE, R., Nucl. Fusion **19** (1979) 641.
- [7] KAUFMANN, M., in Controlled Fusion and Plasma Heating (Proc. 13th Europ. Conf. Schliersee, 1986), Vol. 28, No. 9A, European Physical Society (1986) 1341.
- [8] SCHMIDT, G.L., MILORA, S.L., et al., in Controlled Fusion and Plasma Physics (Proc. 12th Europ. Conf. Budapest, 1985), Vol. 2, European Physical Society (1985) 674.
- [9] MARMAR, E., et al., Nucl. Fusion **22** (1982) 1567.
- [10] PETRASSO, R., et al., Phys. Rev. Lett. **57** 6 (1986) 707.
- [11] HIRSHMAN, S.P., SIGMAR, D.J., Nucl. Fusion **21** (1981) 1079.
- [12] TERRY, J., et al., Particle Transport Following Pellet Injection into the Alcator C Tokamak, Rep. PFC/JA-86-23, Plasma Fusion Center, Massachusetts Inst. of Tech., Cambridge (1986).
- [13] MILORA, S.L., FOSTER, C.A., et al., Nucl. Fusion **20** (1980) 1491.
- [14] GREENWALD, M., et al., in Controlled Fusion and Plasma Physics (Proc. 11th Europ. Conf. Aachen, 1983), Vol. 1, European Physical Society (1983) 7.

- [15] GOMEZ, C., Study of Electron Temperature Evolution during Sawtooth and Pellet Injection Using Thermal Electron Cyclotron Emission in the Alcator C Tokamak, Rep. PFC/RR-86-8, Plasma Fusion Center, Massachusetts Inst. of Tech., Cambridge (1986).
- [16] GREENWALD, M., et al., in Plasma Physics and Controlled Nuclear Fusion Research 1984 (Proc. 10th Int. Conf. London, 1984), Vol. 1, IAEA, Vienna (1985) 45.
- [17] AXON, K.B., et al., in Plasma Physics and Controlled Nuclear Fusion Research 1980 (Proc. 8th Int. Conf. Brussels, 1980), Vol. 1, IAEA, Vienna (1981) 413.
- [18] WESSON, J., et al., in Controlled Fusion and Plasma Physics (Proc. 12th Europ. Conf. Budapest, 1985), Vol. 1, European Physical Society (1985) 147.
- [19] MURAKAMI, M., CALLEN, J.D., BERRY, L.A., Nucl. Fusion **16** (1976) 347.
- [20] GREENWALD, M., et al., A New Look at Density Limits in Tokamaks, Rep. PFC/JA-86-22, Plasma Fusion Center, Massachusetts Inst. of Tech., Cambridge (1986).
- [21] PERKINS, F., in Heating in Toroidal Plasmas (Proc. 4th Int. Symp. Rome, 1984), Vol. 2, ISPP and ENEA (1984) 977.
- [22] TANG, W., et al., in Plasma Physics and Controlled Nuclear Fusion Research 1984 (Proc. 10th Int. Conf. London, 1984), Vol. 2, IAEA, Vienna (1985) 213.
- [23] DIAMOND, P.H., presented at Int. Workshop on Small Scale Turbulence in Magnetized Plasmas, Cargese, July 1986.
- [24] CALLEN, J.D., Phys. Rev. Lett. **39** 24 (1977) 1540.

## DISCUSSION

F. WAGNER:  $\tau_E$  in the Ohmic saturation regime depends on the isotopic mass of the target plasma. It had been shown in the ALCATOR and ASDEX devices that  $\tau_E$  is smaller for hydrogen than for deuterium. This scaling is different from the scaling of neoclassical ion transport and I wonder whether the ion transport in the saturation regime should be described by an enhancement factor  $\chi_i^{NC}$ .

M. GREENWALD: I agree. I don't think ion transport at levels that are three to six times those of neoclassical transport is really neoclassical. It is simply a way to benchmark the discrepancy between experiment and theory. In our experiments, the anomalous ion confinement does not have neoclassical scaling either concerning the plasma current or the isotope chosen.

M. KAUFMANN: I would like to comment on your statement that the improved energy confinement in pellet fuelled discharges might be due to  $\eta_e$ . On ASDEX we also observed that confinement was enhanced while the temperature profile remained unchanged. In cases with relatively small pellets and moderate penetration we found a remarkable improvement in the particle confinement as well as in the energy confinement before  $\eta_e$  changed.



## CONFINEMENT STUDIES OF ADDITIONALLY HEATED PLASMA IN THE JFT-2M TOKAMAK

K. ODAJIMA, A. FUNAHASHI, K. HOSHINO, S. KASAI,  
T. KAWAKAMI, H. KAWASHIMA, T. MATOBA,  
T. MATSUDA, H. MATSUMOTO, Y. MIURA, M. MORI,  
H. OGAWA, T. OGAWA, H. OHTSUKA, S. SENGOKU,  
T. SHOJI, N. SUZUKI, H. TAMAI, Y. UESUGI,  
T. YAMAMOTO, T. YAMAUCHI, M. HASEGAWA<sup>1</sup>,  
S. TAKADA<sup>2</sup>, K. HASEGAWA, A. HONDA, I. ISHIBORI,  
T. KASHIMURA, Y. KASHIWA, M. KAZAWA,  
K. KIKUCHI, Y. MATSUZAKI, K. OHUCHI, H. OKANO,  
T. SHIBATA, T. SHIBUYA, T. SHIINA, K. SUZUKI,  
T. TANI, K. YOKOYAMA

Japan Atomic Energy Research Institute,  
Tokai-mura, Naka-gun, Ibaraki-ken, Japan

### Abstract

CONFINEMENT STUDIES OF ADDITIONALLY HEATED PLASMA IN THE JFT-2M TOKAMAK.

The H-mode can be achieved in NBI and/or ICRF heated open divertor discharges, and an H-transition with improved energy confinement is also observed in limiter discharges with both heating methods. The gross energy confinement time  $\tau_{EG}$  in the H-mode recovers that of the Ohmic plasma. A large improvement in gross energy confinement is also observed after injection of a single pellet into an NBI heated plasma, where during the first 40 ms after pellet injection 70% of the NBI power is stored in the plasma.  $\tau_{EG}$  reaches 70 ms, which is about twice the Ohmic value. In an additionally heated plasma, the incremental stored energy behaves as if it had its own energy confinement time  $\tau_{ad}$ , which is independent of the heating power. In some cases of H-modes,  $\tau_{ad}$  is equal to the doubled L-mode value.

### 1. INTRODUCTION

Recent additional heating experiments in JFT-2M have been devoted to the improvement of energy confinement and to the understanding of its properties during additional heating. This paper reports the achievement of the H-mode in both diverted and limiter bounded discharges, with NBI and/or ICRF heating, and of improved confinement with pellet injection. The confinement properties of the H- and L-modes are discussed on the basis of the concept of stored energy.

<sup>1</sup> Mitsubishi Electric Corp., Tokyo, Japan.

<sup>2</sup> Mitsubishi Electric Computer System Corp., Tokyo, Japan

## 2. EXPERIMENTAL ARRANGEMENT

JFT-2M is a tokamak with a D-shaped vacuum vessel of major radius 1.31 m, inside which both D-shaped limiter and open single or double null divertor configurations have been realized [1]. The minor radius is 0.35 m with full size D-shaped limiter and 0.26 m for the smallest diverted discharges. The divertor plates and both the fixed poloidal and the movable rail limiters are made of graphite. The working gas is deuterium in the  $H^0$  NBI heating experiment or mixed gas ( $H/D = 0.4$ ) in the ICRF heating experiments. NBI heating experiments using hydrogen gas as a working gas exhibit the same phenomena as are described in this paper, except for a slightly poorer confinement and a slightly higher threshold power for the transition.

The ICRF heating power  $P_{ICH} = P_G(R_P - R_V)/R_P$  by definition, where  $R_P$  and  $R_V$  are the loading resistance of the antennas, with and without plasma, respectively, and the  $P_G$  is the generator output power. The NBI heating power  $P_{NBI}$  is defined by  $P_{NBI} = P_{torus} - P_{loss}$ , where  $P_{torus}$  is the measured input power to the torus and  $P_{loss}$  represents the shinethrough, ion orbit and charge exchange losses.  $P_{loss}$  is calculated to be  $0.1P_{torus}$ . The total stored energy  $W_T$  is determined from  $\beta_P [= \Lambda - (\ell_i - 1)/2]$  by a poloidal magnetic field fitting code using 24 magnetic probes and eight saddle loops [1] and the value determined in this way is cross-checked by a diamagnetic measurement.

## 3. ACHIEVEMENT OF H-MODE

JFT-2M has achieved the H-mode in the open divertor configuration with NBI heating [2]. Later, H-like transitions were observed not only in ICRF heated, open divertor discharges [3], but also in D-shaped, limiter bounded plasmas [4]. Figure 1-A shows an example for H-transition (thick line) with ICRF heating. After reaching the quasi-steady state,  $W_T$  increases again simultaneously with an abrupt decrease in the  $H_\alpha/D_\alpha$  line emission. Following the transition, the electron density  $\bar{n}_e$  increases, which is in contrast to the case without transition. The radiation losses  $P_R$  after an initial small dip also increase strongly. As is shown in Fig. 1-A-e, an increased emission from highly ionized metals near the centre correlates with increased radiation losses in spite of a decrease in the emission from metals in the low ionization states (Fig. 1-A-f). This indicates a decrease in the impurity influx and an impurity accumulation by the improved confinement. The dip in  $P_R$  at the transition is due to the sudden decrease of the impurity influx, at first overcompensating the increase of the radiation loss due to central accumulation.

In the case of D-shaped limiter discharges, an example for H-like transition is shown in Fig. 1-B (thick lines). For the H-transition in a limiter discharge, an inner shift of the plasma is necessary. Following the abrupt decrease of the  $H_\alpha/D_\alpha$  line emission, we also observe an increase in  $W_T$ ,  $\bar{n}_e$  and  $P_R$ . At the transition,  $P_R$  also dips briefly. These observations clearly show that the transition has the same properties as are observed in diverted discharges. In some cases, ELM-like spikes [5] in

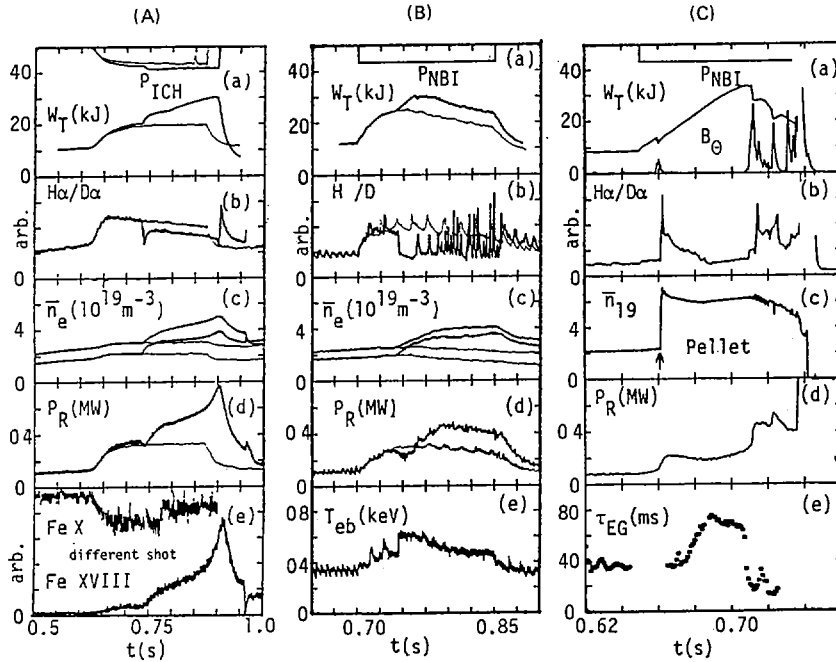


FIG. 1. Temporal behaviour of plasma parameters of: (A) 0.74 MW, ICRF heated H-mode in single null diverted discharge.  $I_p = 220$  kA,  $B_T = 1.27$  T,  $a = 0.30$  m,  $\kappa = 1.4$  (note that line emission of Fe X is obtained in different shots, where the H-transition occurs at different times); (B) H-like transition in limiter D-shaped discharge with 0.65 MW NBI.  $I_p = 220$  kA,  $B_T = 1.18$  T,  $a = 0.32$  m,  $\kappa = 1.4$ ,  $T_{eb}$  is measured at  $R = 1.03$  m (limiter at  $R = 0.96$  m); (C) Improvement after injection of single pellet into 0.7 MW, NBI heated divertor discharge.  $I_p = 220$  kA,  $a = 0.26$  m,  $\kappa = 1.4$ . Traces of  $n_e$  are at central chord for the larger values and at  $r = 21$  cm chord for the smaller ones.

the  $H_\alpha/D_\alpha$  emission are observed, and the appearance of the spikes suppresses the further increase in stored energy and radiation losses.

In Fig. 1-B-e, the electron temperature near the edge of the plasma  $T_{eb}$  is shown. At the transition,  $T_{eb}$  increases abruptly, which indicates the formation of a temperature pedestal. The line average density traces in Figs 1-A-c and 1-B-c suggest the formation of a density pedestal: at the transition, the line density  $\bar{n}_e$  at the central chord increases gradually, while  $\bar{n}_e$  at the  $r = 21$  cm chord first increases strongly. Later on, the increase becomes slower than that of the central chord.

The difference between the H- and L-modes in Fig. 1-A is the heating power, and in Fig. 1-B is the strength of the magnetic field,  $B_T$ . By increasing the ICRF power from 0.70 MW to 0.74 MW in the former case, and by decreasing  $B_T$  from 1.21 T to 1.18 T at the same plasma current in the latter case, H-transition occurs. The minimum power required for the H-transition is 0.2 MW for optimized single

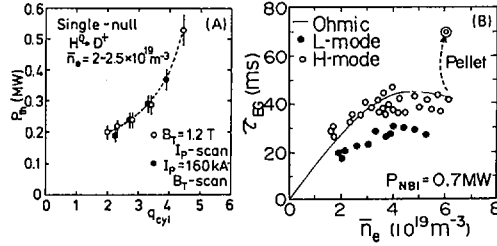


FIG. 2. (A) Threshold power for H-transition  $P_{th}$  versus cylindrical  $q$  value,  $q_{cyl}$ ; (B) Gross energy confinement time  $\tau_{EG}$  as a function of  $\bar{n}_e$  in H- and L-modes. The improvement with pellet injection is also plotted.  $I_p = 220$  kA,  $B_T = 1.18$  T,  $a = 0.26$  m,  $\kappa = 1.4$ ,  $P_{NBI} = 0.7$  MW.

null diverted and 0.5 MW for limiter discharges and is roughly the same for NBI and ICRF heating. A low  $q_a$  value is more favourable to the transition and the threshold power decreases as  $q_a$  decreases as is shown in Fig. 2-A.

#### 4. IMPROVED CONFINEMENT WITH PELLET INJECTION

Confinement improvement is also observed transiently with pellet injection into an NBI heated divertor discharge [6], as is shown in Fig. 1-C. If a single pellet is injected before the H-transition occurs, the stored energy starts increasing linearly. During the first 40 ms after pellet injection, about 70% of NBI power is stored in the plasma.  $W_T$  reaches 35 kJ, and then the plasma collapses, because of the growth of an MHD instability. The gross energy confinement time,  $\tau_{EG}$ , defined as  $\tau_{EG} = W_T / (P_T - \dot{W}_T)$ , increases up to 70 ms (Fig. 1-C-e), which is about three times as high as Kaye-Goldston scaling [7] and is twice the Ohmic value at the same density. For a smaller pellet,  $W_T$  also increases linearly with the same slope, but then saturates abruptly, following the growth of an MHD fluctuation. This saturation level of  $W_T$  is almost the same as the value achieved in the gas fuelled H-mode.

#### 5. CONFINEMENT PROPERTIES IN H- AND L-MODES

The gross energy confinement times,  $\tau_{EG}$ , of the H- and L-modes are plotted as a function of  $\bar{n}_e$  in Fig. 2-B. The improvement by pellet injection is also shown in this figure. The NBI heating power is 0.7 MW, which is four to five times the Joule heating power. To obtain the L-mode at the same heating power for the sake of comparison, a lower rail limiter is inserted near the separatrix. In the optimized H-mode,  $\tau_{EG}$  is almost the same as in an Ohmic plasma over the whole density range, which is in contrast to the deterioration in the L-mode plasma.

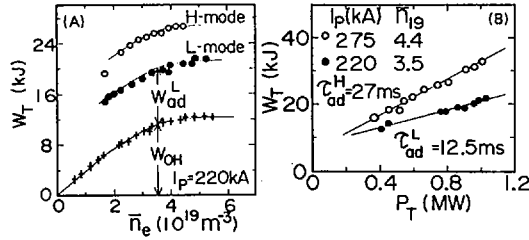


FIG. 3. (A) Total stored energy  $W_T$  as a function of  $\bar{n}_e$ , for the same conditions as in Fig. 2-B; (B) Total stored energy  $W_T$  as a function of total input power  $P_T$  in H- and L-modes with NBI heated, single null divertor discharge, with  $a = 0.28 \text{ m}$  and  $\kappa = 1.45$  (note that the L- and H-data are at different plasma currents, but for  $I_p > 200 \text{ kA}$ , in the L-mode, the dependence of  $\tau_{ad}$  on current is weak).

If we study the confinement properties from the point of view of the total stored energy, we see some features of the energy confinement. Figure 3-A shows  $W_T$  as a function of  $\bar{n}_e$ . The dependence of  $W_T$  on density with additional heating parallels that in the Ohmic phase. This indicates that the following model is plausible:  $W_T = W_{OH} + W_{ad}$ , where  $W_{OH}$  is the stored energy of the Ohmic base plasma and  $W_{ad}$  is the incremental stored energy from the additional heating with its own confinement time,  $\tau_{ad}$  ( $= \Delta W_T / \Delta P_T |_{\bar{n}_e = \text{const}}$ ). Earlier experiments in JFT-2M have shown that  $\tau_{ad}$  is almost independent of  $\bar{n}_e$  and  $I_p (> 200 \text{ kA})$  as well as of  $P_T$  in the L-mode [8]. Taking into account the above model, we infer, from Fig. 3-A, the following features of energy confinement: (1) If  $\bar{n}_e$  is affected by the heating, then the increase in  $W_T$  becomes the sum of  $W_{ad}$  and  $\Delta W_{OH}$  (because of its dependence on density); therefore, the apparent increase in  $W_T$  is affected by the change in  $\bar{n}_e$ ; (2) in the high  $n_e$  region, where the increase in  $W_{OH}$  with  $\bar{n}_e$  saturates and/or in the high  $P_{ad}$  region, where  $W_{ad} \gg W_{OH}$ ,  $W_T$  and  $\tau_{EG}$  are independent of  $\bar{n}_e$ ; (3) in the low density region, where  $\tau_{OH} \approx \tau_{ad}$ , no deterioration of  $\tau_{EG}$  with additional heating is seen, as compared to  $\tau_{OH}$ ; this can also be seen from the L-mode of Fig. 2-B, where  $\tau_{EG}$ , with additional heating, approaches  $\tau_{OH}$  with decreasing  $\bar{n}_e$ .

In the H-mode, the incremental stored energy,  $W_{ad}$ , of the plasma can amount to the double value of that of the L-mode plasma, as is shown in Fig. 3-A. Figure 3-B shows  $W_T$  versus  $P_T$  with fixed  $\bar{n}_e$  on the H- and L-modes in NBI heated, diverted discharges. The power dependence of  $W_T$  is almost linear, and the slope gives  $\tau_{ad} = 27 \text{ ms}$  and  $\tau_{ad} = 12.5 \text{ ms}$ , for the H- and L-modes, respectively. In the case of Fig. 3-B, the H-transition, thus, improves  $\tau_{ad}$  by a factor of two. In the other cases, the improvement factor takes different values and is closely correlated with the decrease in  $H_\alpha/D_\alpha$  emission. A large decrease in the  $H_\alpha/D_\alpha$  emission yields good improvement, and a small decrease, or a spiked emission, results in poor improvement.

## 6. SUMMARY AND DISCUSSIONS

- (1) An H-mode plasma is demonstrated in NBI and/or ICRF heated open divertor discharges, and an H-like transition with improved energy confinement is also observed in limiter discharges with both heating methods, separately and combined. Therefore, we may conclude that the H-transition does not depend on the microscopic nature of the heating method, and that a diverted magnetic configuration is not a necessary condition for an H-transition.
- (2) A large improvement in gross energy confinement is observed after injection of a single pellet into an NBI heated plasma, where during the first 40 ms after pellet injection 70% of the NBI power is stored in the plasma.  $\tau_{EG}$  reaches 70 ms, which is twice the Ohmic value.
- (3) At the H-transition, suddenly temperature and density pedestals are formed before the total stored energy increases. This fact suggests that the energy and particle transport near the plasma edge are abruptly improved at the transition. If this is really the case, the H-transition provides evidence that the energy confinement of the tokamak is determined by transport effects in the edge region of the plasma [9, 10].
- (4) In an additionally heated plasma, the incremental stored energy behaves as if it had its own energy confinement time  $\tau_{ad}$ , which is independent of the heating power. In some cases to the H-mode,  $\tau_{ad}$  is doubled with respect to the L-mode.

## ACKNOWLEDGEMENTS

The authors are grateful to Drs M. Tanaka, K. Tomabechi, and S. Mori for continuous encouragement. They also thank Dr. J.-M. Noterdaeme for useful discussions.

## REFERENCES

- [1] SHOJI, T., et al., in *Controlled Fusion and Plasma Physics (Proc. 11th Europ. Conf. Aachen, 1983)*, Vol. 1, European Physical Society (1983) 55.
- [2] SENGOKU, S., et al., Confinement and fuelling studies during additional heating phase in JFT-2M tokamak, in *Plasma-Surface Interaction (Proc. 7th Conf. Princeton, 1986)*, to be published in *J. Nucl. Mater.*
- [3] MATSUMOTO, H., et al., Improved Confinement during ICRF Heating on JFT-2M, Rep. JAERI-M-86-147 (submitted to *Nucl. Fusion*).
- [4] SENGOKU, S., et al., Regime of improved confinement in neutral-beam-heated limiter discharge of the JFT-2M tokamak, submitted to *Phys. Rev. Lett.*
- [5] WAGNER, F., et al., *Phys. Rev. Lett.* **42** (1982) 1408.
- [6] MIURA Y., et al., Characteristics of Improved Confinement and High Beta in Pellet and Neutral-Beam Injected Single Null Divertor Discharges of the JFT-2M Tokamak, Rep. JAERI-M-86-148, Japan Atomic Energy Research Institute, Tokyo (1986).

- [7] KAYE, S.M., GOLDSTON, R.J., Nucl. Fusion **25** (1985) 65.
- [8] ODAJIMA, K., et al., Scaling of incremental energy confinement time in the JFT-2M, to be published in Phys. Rev. Lett.
- [9] OHYABU, N., et al., Nucl. Fusion **23** (1986) 593.
- [10] FURTH, H.P., Plasma Phys. Controll. Fusion **28** (1986)1305.

## DISCUSSION

K. McGUIRE: In your H-mode limiter discharges, does the plasma contact the inner limiter during the H-mode phase and is the inner shift of the plasma important in obtaining the H-mode in limiter discharges?

K. ODAJIMA: Yes, in our H-mode limiter discharges the plasma is bounded only by the inner limiter and is always in contact with the limiter during the H-phase. But we cannot really say whether a point contact with the limiter or a separation from the outer limiter is important or not to obtain the H-mode.

J. JACQUINOT: Have you observed the H-mode with circular plasmas lying on the inner wall?

K. ODAJIMA: Yes, we have observed H-transition in circular plasmas with ICRF heating.

A. GONDHALEKAR: In your pellet injection experiments, there is an apparent increase in the energy confinement time. The duration of the apparent increased confinement is shorter than the confinement time itself. What significance do you attach to this increase in energy confinement time?

K. ODAJIMA: The saturation value of  $W_T$  before the collapse is almost the same as that in gas fuelled H-mode discharges or slightly higher. Hence, no improvement has been brought about in the steady state phase with pellet injection so far.



## INITIAL RESULTS FROM THE DIII-D TOKAMAK\*

J. LUXON, P. ANDERSON, F. BATTY<sup>1</sup>, C. BAXI, G. BRAMSON,  
N. BROOKS, B. BROWN, B. BURLEY, K.H. BURRELL, R. CALLIS,  
G. CAMPBELL, T. CARLSTROM, A. COLLERAINE, J. CUMMINGS,  
L. DAVIS, J. DeBOO, S. EJIMA, R. EVANKO, H. FUKUMOTO<sup>2</sup>, R. GALLIX,  
J. GILLELAND, T. GLAD, P. GOHIL, A. GOOTGELD, R.J. GROEBNER,  
S. HANAI<sup>3</sup>, J. HASKOVEC, E. HECKMAN, M. HEIBERGER, F.J. HELTON,  
P. HENLINE, D. HILL<sup>4</sup>, D. HOFFMAN<sup>1</sup>, E. HOFFMANN, R. HONG,  
N. HOSOGANE<sup>5</sup>, C. HSIEH, G.L. JACKSON, G. JAHNS, G. JANESCHITZ<sup>6</sup>,  
E. JOHNSON, A. KELLMAN, J.S. KIM, J. KOHLI, A. LANGHORN, L. LAO,  
P. LEE, S. LIGHTNER, J. LOHR, M. MAHDAVI, M. MAYBERRY,  
B. McHARG, T. McKELVEY, R. MILLER, C.P. MOELLER, D. MOORE,  
A. NEREM, P. NOLL<sup>7</sup>, T. OHKAWA, N. OHYABU, T. OSBORNE,  
D. OVERSKEI, P. PETERSEN, T. PETRIE, J. PHILLIPS, R. PRATER,  
J. RAWLS, E. REIS, D. REMSEN, P. RIEDY, P. ROCK, K. SCHAUBEL,  
D. SCHISSEL, J. SCOVILLE, R. SERAYDARIAN, M. SHIMADA<sup>5</sup>, T. SHOJI<sup>2</sup>,  
B. SLEAFORD, J. SMITH, Jr., P. SMITH, T. SMITH, R.T. SNIDER,  
R.D. STAMBAUGH, R. STAV, H. St. JOHN, R. STOCKDALE, E.J. STRAIT,  
R. STREET, T.S. TAYLOR, J. TOOKER, M. TUPPER, S.K. WONG,  
S. YAMAGUCHI<sup>8</sup>

GA Technologies Inc.,  
San Diego, California,  
United States of America

### Abstract

#### INITIAL RESULTS FROM THE DIII-D TOKAMAK.

The DIII-D tokamak was designed to exploit both (a) the strong dependence of limiting beta values and plasma energy confinement on high current, and (b) the effectiveness of the divertor configuration in obtaining good confinement. Initial operation of the device has resulted in Ohmic confinement ( $\tau \approx 150$  ms) comparable to that of other large tokamaks and in low levels of plasma impurities ( $Z_{\text{eff}} = 1.5$  at  $\bar{n}_e = 6 \times 10^{19} \text{ m}^{-3}$ ). Both single null divertor and elongated dee shaped limiter plasmas have been produced. The paper reports both attaining H-mode confinement during beam heating of plasmas in open divertor configurations and values of the Troyon scaling quantity ( $I/aB \approx 2$ ) large enough to allow future studies of beta limits in regimes heretofore unattainable.

\* Work sponsored by the United States Department of Energy, under Contract No. DE-AC03-84ER51044, and by the Japan Atomic Energy Research Institute, under a co-operative agreement.

<sup>1</sup> Oak Ridge National Laboratory, Oak Ridge, TN, USA.

<sup>2</sup> On leave from Hitachi Ltd., Japan.

<sup>3</sup> On leave from Toshiba Corp., Japan.

<sup>4</sup> Lawrence Livermore National Laboratory, Livermore, CA, USA.

<sup>5</sup> Japan Atomic Energy Research Institute, Japan.

<sup>6</sup> Euratom-IPP Association, Max-Planck-Institut für Plasmaphysik, Garching, Fed. Rep. Germany.

<sup>7</sup> JET Joint Undertaking, Abingdon, Oxfordshire, United Kingdom.

<sup>8</sup> On leave from Mitsubishi Electric Corp., Tokyo, Japan.

## 1. INTRODUCTION

The DIII-D device has been in operation since February 1986 [1], and is now operating at parameters comparable to other large tokamaks. Doublet III [2,3,4] and other devices have demonstrated the role of plasma current in attaining high beta and good confinement, and the importance of the divertor in attaining regimes of good confinement with neutral beam heating. The DIII-D was designed to exploit this understanding.

DIII-D is a non-circular cross section, low aspect ratio tokamak designed to achieve high performance in a modest sized device (Fig. 1) [1]. The parameters of the device are presented in Table I. The indicated design capability of the device is attainable with additional shaping power supplies, auxiliary plasma heating, and internal vessel protection armor.

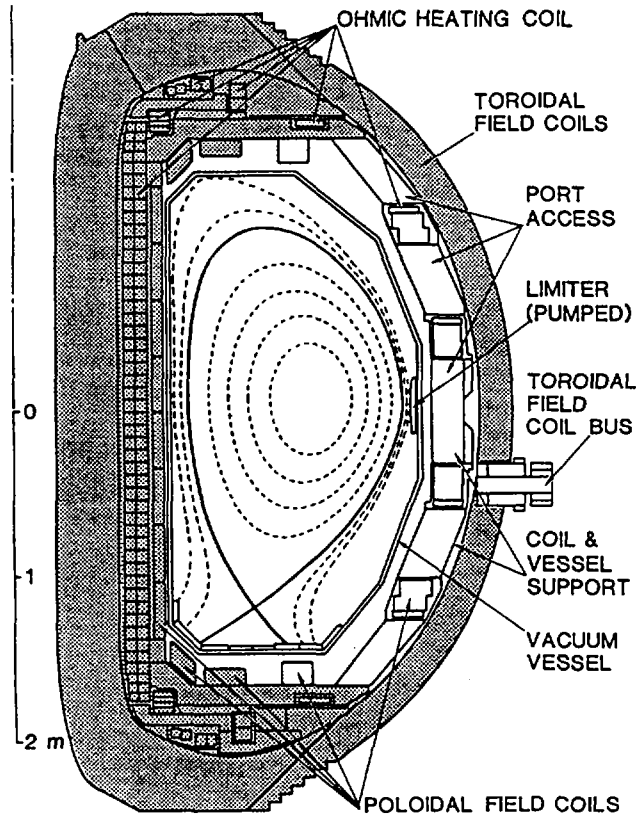


FIG. 1. Cross-section of the DIII-D device. Areas not shown in gray are new. Superimposed is the MHD equilibrium of a high beta divertor discharge (Fig. 3 at 2280 ms).

TABLE I. DIII-D PARAMETERS

	Oct. 1986	1987	Design Capability
Major radius (m)	1.67	1.67	1.67
Minor radius (m)	0.67	0.67	0.67
Vessel elongation	2.0	2.0	2.0
Aspect ratio	2.5	2.5	2.5
Maximum toroidal field on axis (T)	2.2	2.2	2.2
Maximum plasma current (MA)			
Limiter	2.5	3.5	5.0
Divertor	2.0	2.5	3.5
Neutral beam power (MW)	6	12	14
Neutral beam pulse length (s)	0.4	0.7	5
ICRH power at 30–60 MHz (MW)	—	2	20
ECH power at 60 GHz (MW)	—	1.8	10

Neutral beam injection is the principal source of auxiliary heating power. The beamlines have been reconstructed to improve beam transmission and to accommodate the new 5 sec sources which are now being delivered. The beamlines inject at an average angle of  $19.5^\circ$  from radial in the co-direction. The results reported here were obtained using two of the beamlines fitted with 0.5 sec sources producing up to 6.0 MW of power at energies up to 70 keV for 0.45 sec pulses into the plasma. Conversion to long pulse sources with a capability of up to 14 MW of power should be complete in the spring of 1987.

## 2. NON-CIRCULAR PLASMA PRODUCTION AND SHAPING

Both divertor and limiter plasmas with elongations up to 2.1 have been formed in the device (Fig. 2). The shape and position of the plasma is controlled by the 18 independently powered shaping coils. The low error fields and precise field nulling which can be attained with the coil system allows discharges to be routinely initiated with one-turn voltages of 11 volts or less. Owing to the small amount of field due to the ohmic heating coil in the plasma region and the precise control afforded by the plasma shaping coils, the chosen plasma configuration can be maintained over the entire duration of the discharge. The position, elongation and triangularity are separately controlled, and the plasmas exhibit no vertical instability over the range of configurations tested ( $\kappa = 1.2$  to 2.1).

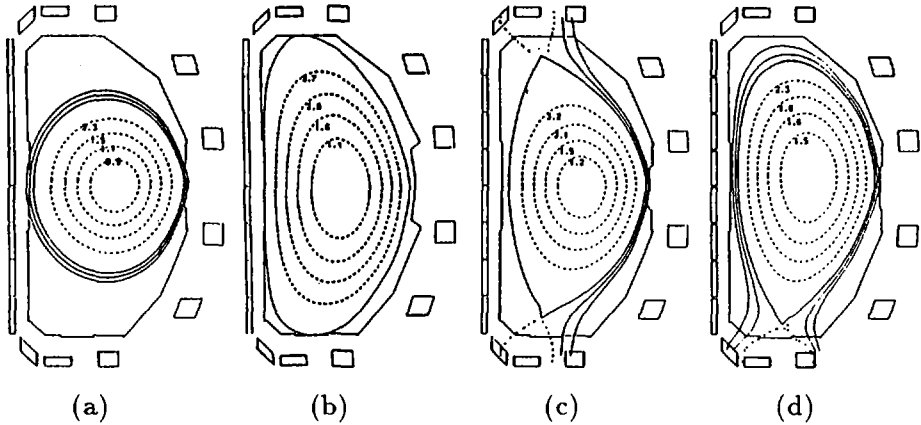


FIG. 2. MHD equilibrium cross-sections for Ohmic discharges produced in DIII-D. (a)  $\kappa = 1.2$  limiter discharge, (b)  $\kappa = 2.1$  dee shaped discharge, (c) double null divertor, (d) single null divertor.

Single null divertor configurations have been obtained with elongations  $\kappa$  from 1.6 to 1.97 and triangularities of up to 0.35. The separatrix flux surfaces intersect two toroidal bands of graphite armor at the bottom of the vacuum vessel (see Fig. 1). The spacing between the X-point and the vessel bottom is controlled to an accuracy of 1 cm within a range of from 8 to 30 cm. Currents of as high as 2.0 MA have been achieved in divertor configurations, and currents of 1 MA have been maintained for 4 sec. Values of  $I/aB$  of up to 1.9 have been attained ( $q^* = 3.3$ ), making them particularly attractive for auxiliary heating. Double null divertor configurations have also been produced, but extensive use of these configurations must await the installation of protective armor in the upper inside corner of the vacuum vessel.

Limiter plasma configurations have been obtained with elongations of from 1.2 to 2.1. These discharges have been run on both the inside wall graphite armor and the outside limiters. A current of 2.5 MA has been achieved using the dee-shaped configuration of Fig. 2 with a flattop duration of 0.5 sec. This resulted in  $I/aB = 1.8$  with  $q_\psi = 4.1$  and triangularity of  $\delta = 0.5$ .

The flux necessary to reach a given plasma current is supplied by both the ohmic heating coil (total capacity 12 V-s) and the plasma shaping system which contributes about 1.0 V-s/MA essentially from the vertical field. The flux required from the ohmic heating coil transformer is found to be 2.1 V-s/MA and constant over a variety of plasma shapes and currents. This indicates adequate flux is available to reach plasma currents of 5 MA.

### 3. CONFINEMENT AND PLASMA HEATING

Vessel cleanup has progressed significantly in the last nine months. The vessel is constructed of Inconel with Inconel protective plates (35% of surface) and graphite armor (15%) used to protect the interior surface of the vessel in areas of high heat flux. The limiters consist of two  $0.4 \times 0.8$  m shaped graphite blades located on the outside midplane. Vacuum pumping rates of up to  $10,000$   $\ell/s$  are obtained using two turbo molecular and two cryo pumps. The partial pressure of non-hydrogen components stands at  $\sim 5 \times 10^{-9}$  torr with a leak rate for air of less than  $5 \times 10^{-5}$  torr $\cdot\ell/s$ .

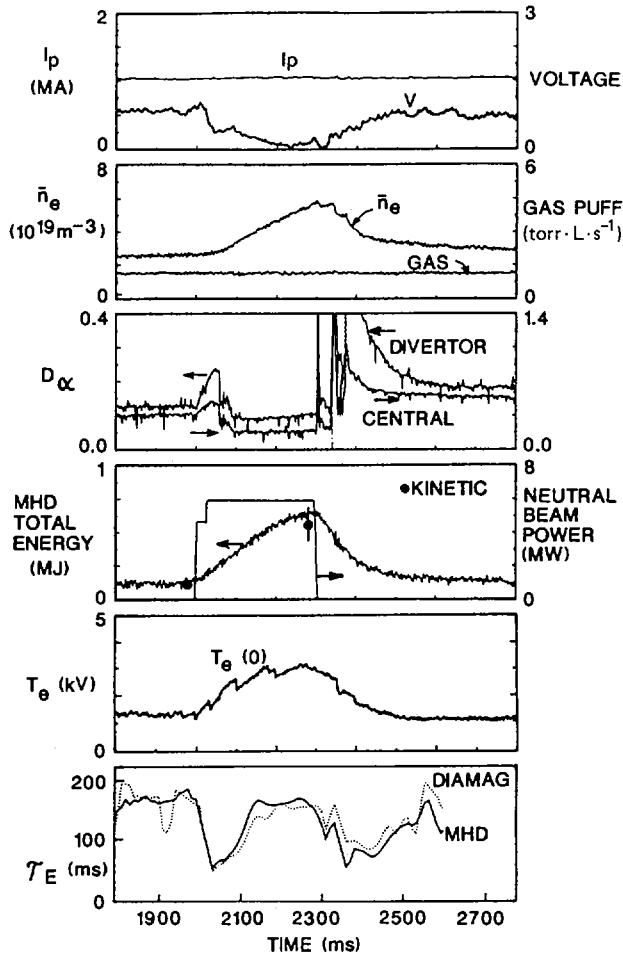


FIG. 3. Time history of a beam heated discharge exhibiting H- and L-mode behaviour. The start of the current rise is time = 0.

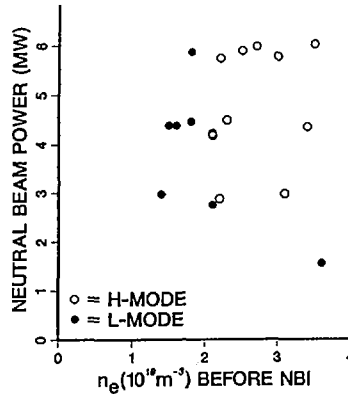


FIG. 4. Characterization of the H-mode threshold for divertor discharges with  $I_p = 1.0 \text{ MA}$ ,  $B_T = 2.1 \text{ T}$ .

Hydrocarbons cleaned up rapidly with baking to  $400^\circ\text{C}$ . Baking, glow discharge cleaning, and rapid pulse discharge cleaning are used to clean up water and other sources of oxygen. Substantial cleanup time including tokamak discharges is required after the vessel is exposed to air. After one to two months,  $Z_{eff} = 1.5$  can be attained in ohmic discharges at  $n_e \sim 3 - 6 \times 10^{19} \text{ m}^{-3}$ . The principal impurity is oxygen. No gettering of the vessel walls has been done.

Ohmic DIII-D discharges exhibit the characteristics of clean tokamak discharges. The ohmic confinement observed in DIII-D is comparable to that seen in other larger tokamaks. The confinement in ohmic hydrogen discharges is estimated from magnetic measurements to be  $\tau_E = 150 \pm 50 \text{ ms}$  for densities in the range  $\bar{n}_e = 0.7 - 5 \times 10^{19} \text{ m}^{-3}$ . This produces values of  $\tau_E/\bar{n}_e$  which equal or exceed those expected from the scaling  $\tau_E/\bar{n}_e = 1.92 R^{2.04} a^{1.04}$  [5]; the explicit dependence of  $\tau$  on  $n$  has not been demonstrated from the limited operation to date.

Initial application of up to 6.0 MW of hydrogen neutral beam power to single null diverted deuterium discharges ( $B_T = 2.1 \text{ T}$ ) has resulted in attaining regimes of good confinement commonly referred to as H-mode [6]. The time history of the parameters for an H-mode discharge is shown in Fig. 3, and the MHD equilibrium is shown in Fig. 1. The plasma current is maintained constant, and the one-turn voltage is measured at the surface of the plasma. The onset of the H-mode is characterized by a rapid, to date uncontrolled, rise in the line average plasma density. The gas puff to the plasma was held constant. The  $D_\alpha$  radiation in both the divertor X-point region and the central plasma also drops to a fraction of the ohmic value. The central electron temperature is seen to rise, and

the total energy rises dramatically as the global energy confinement time returns to values comparable to the ohmic confinement.

A well defined threshold in both plasma density and neutral beam power must be exceeded in order to attain H-mode confinement, otherwise poor (L-mode) confinement is obtained (Fig. 4). At a current of 1 MA the power threshold is less than 2.8 MW and the density must exceed  $2 \times 10^{19} \text{ m}^{-3}$ . The transition to the H-mode is delayed from the initial application of beam power. This period is characterized by little density rise, a sharp increase in  $D_\alpha$  radiation, and a period of poor (L-mode) confinement.

The ion temperature profile  $T_i(r)$  from charge exchange recombination and the electron temperature profile  $T_e(r)$  from absolutely calibrated electron cyclotron emission are shown in Fig. 5 at 2280 ms. The line average density is determined from a single vertical  $\text{CO}_2$  interferometer chord. The absolutely calibrated visible bremsstrahlung radiation (dependent on  $T_e$ ,  $n_e$ , and  $Z_{eff}$ ) is measured along 16 chords. These data were combined along with the assumption  $Z_{eff} = \text{const.}$  to obtain the set of profiles shown in Fig. 5 for the ohmic ( $t = 2000$ ,  $\bar{n}_e = 2.5 \times 10^{19} \text{ m}^{-3}$ ,  $Z_{eff} = 1.5$ ), and H-mode ( $t = 2280$ ,  $\bar{n}_e = 5.2 \times 10^{19} \text{ m}^{-3}$ ,  $Z_{eff} = 2.9$ ) phases of the discharge.

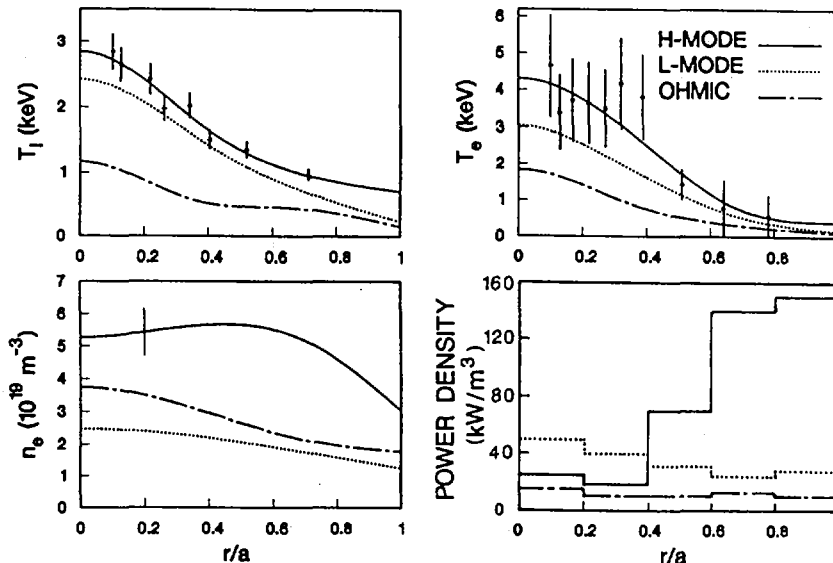


FIG. 5. Temperature, density, and radiated power profiles: H-mode from the discharge of Fig. 3 at 2280 ms; Ohmic at 2000 ms. L-mode is from a similar discharge ( $P = 4.5 \text{ MW}$ ).

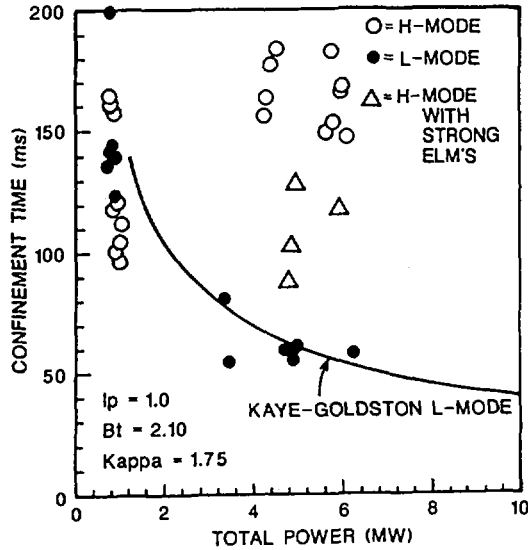


FIG. 6. Confinement time for L-mode and H-mode discharges and a comparison to Kaye-Goldston scaling for divertor discharges with  $I_p = 1$  MA and  $B_T = 2.1$  T.

Data for a similar L-mode discharge ( $\bar{n}_e = 1.8 \times 10^{19} \text{ m}^{-3}$ ,  $Z_{eff} = 4.6$ ) is also shown. During the H-mode, the estimated peak kinetic total energy including calculated fast ion contributions is  $700 \pm 140$  kJ and is indicated in Fig. 3. This results in  $\beta = 1.4\%$  and  $\beta_p = 1.1$ .

The radiated power increases above ohmic for both H- and L-mode with neutral beam heating. The radiated power distribution for the main body of the plasma is shown in Fig. 5. In L-mode the radiation remains centrally peaked, accounts for  $\sim 35\%$  of the power, and is about equally distributed between the main body of the plasma and the divertor region. In the H-mode  $\sim 45\%$  of power is radiated with the majority of the power being radiated from the main body of the plasma.

Preliminary indications are that the scaling of confinement time with power in the L-mode follows that expected from Kaye-Goldston L-mode scaling [7]. Figure 6 illustrates this for a case with current fixed at 1 MA,  $B_T = 2.1$  T and  $\kappa = 1.75$ . However, once the H-mode is established, confinement improves dramatically reaching values of as much as three times the L-mode confinement and equaling or exceeding the initial ohmic ( $P \sim 1$  MW in Fig. 6) confinement. The confinement times indicated here are global energy confinement times based on magnetic measurements and corrected for the time rate of change of the energy. Those discharges with the best confinement do not reach steady state with the available beam pulse durations.

Spikes occur in the  $D_\alpha$  radiation during the H-mode coincident with the rapid expulsion of substantial amounts (up to 15%) of energy and particles. These losses appear to propagate from the edge into the plasma. The discharge described in Fig. 3 only exhibited this feature after the power was turned off. Initial evidence is that these bursts are likely associated with edge localized modes (ELM) [6]. The highest values of total plasma energy  $W_T$  occur in discharges with no  $D_\alpha$  bursts.

Additional information on the nature of the ELM can be obtained from ICH coupling experiments carried out using cavity wave launchers constructed by Oak Ridge National Laboratory. Satisfactory loading can be achieved in both ohmic limiter and divertor plasmas, but with H-mode heating the loading drops by a factor of  $\sim 2$  from the L-mode coupling. However, this loading is seen to increase abruptly by a factor of 2 or more coincident with the  $D_\alpha$  bursts. These results suggest particularly low density in the region outside the separatrix during H-mode and a sharp rise in this density associated with the ELM.

Once H-mode confinement has been attained, it remains for the entire duration of the neutral beam pulse. H-mode confinement has been sustained for up to 740 ms with 3 MW of power applied. Burst free H-mode has been sustained for 300 ms before the heating ended. H-modes have been achieved over the entire current range  $0.7 \leq I_p \text{ (MA)} \leq 2.0$  and toroidal field range  $1.2 \leq B_T \text{ (T)} \leq 2.1$  studied to date. The maximum line average density attained is  $8.4 \times 10^{19} \text{ m}^{-3}$ .

#### 4. SUMMARY

The first nine months of DIII-D operation have demonstrated that the tools necessary to carry the study of confinement and beta into new regimes will be available in the upcoming years. Discharges with good (H-mode) confinement have been demonstrated with neutral beam heating in the open divertor configuration. H-mode confinement times are comparable to ohmic confinement times and about three times the L-mode confinement ( $\tau_E^H \sim \tau_E^{OH} \sim 3 \tau_E^L \simeq 175 \text{ ms}$ ). This result clearly shows that this important confinement improvement can be scaled to larger devices. It also shows that this enhanced confinement can be achieved in simplified divertor configurations which can be more readily incorporated into larger devices. The substantial range of divertor shapes available, including the double null, along with the precise control demonstrated by the shaping system, should allow the role of cross sectional shape in attaining good confinement to be thoroughly explored.

DIII-D has demonstrated the tools necessary for an aggressive study of plasma shape in attaining high values of beta. Values of  $I/aB \sim 2$  have already been attained in both limiters and divertors, and substantially higher values are anticipated in the future. The plasma cross section can be precisely controlled in both space and time over a range of elongations from near circular to elongations greater than two. Triangularity can be independently varied. With the addition of the new long pulse sources beam heated discharge durations are anticipated to be sufficiently long to attain quasi steady state conditions.

It is anticipated that during the next year the tokamak will be operated in regimes of high current and high  $I/aB$  (Table I) and that all of the neutral beamlines will be brought into operation and fitted with long pulse sources capable of a total of 14 MW of power with multisecond pulse durations. This capability should allow extension of confinement studies to substantial values of current and power and a definitive test of the beta limits of the machine.

ECH outside launch heating experiments in both the extraordinary and ordinary mode are planned through early 1987. This system will be capable of 1.4 MW of power at 60 GHz and will allow profile control experiments using edge heating to be carried out. Installation of inside launch ECH with a total of 2 MW of power is anticipated in late 1987. This will allow both edge heating and current drive experiments. The present ICH coupling experiments will be complete in early 1987, and 2 MW of heating using cavity resonators to couple power at 30-60 MHz is planned for late 1987.

## REFERENCES

- [1] LUXON, J.L., DAVIS, L.G., *Fusion Technol.* **8** (1985) 441.
- [2] STAMBAUGH, R.D., in *Plasma Physics and Controlled Nuclear Fusion 1984* (Proc. 10th Int. Conf. London, 1984), Vol. 1, IAEA, Vienna (1985) 217.
- [3] BURRELL, K.H., *ibid.*, p. 131.
- [4] KITSUNEZAKI, A., *ibid.*, p. 57.
- [5] PARKER, R.R., et al., *Nucl. Fusion* **25** (1985) 1127.
- [6] WAGNER, F., et al., *Phys. Rev. Lett.* **49** (1982) 1408.
- [7] KAYE, S.M., et al., *Nucl. Fusion* **24** (1984) 1303.

## DISCUSSION

Y. SHIMOMURA: Did you observe the H-mode in the hydrogen plasma?

J. LUXON: No, we have not yet had an opportunity of doing so.

M. KEILHACKER: I would like to make a comment. The recent observation of H-mode discharges in large tokamak experiments, such as JET and DIII-D, allows

the size scaling of H-mode confinement times to be studied. A comparison of DIII-D and JET results with those from ASDEX seems to indicate that the global energy confinement time of H-mode discharges scales linearly with total plasma current, but has no additional separate size scaling.

F. WAGNER: Dr. Luxon, you mentioned in your presentation that the H-mode is often preceded by an L-phase. Having in mind the previous D-III results where the L- and H-modes were different, from the very beginning of the beam pulse, I would like to know whether there are still cases without a preceding L-phase. Do you attribute the difference in H-mode development between D-III and BIG-D to the change in the ion grad-B drift direction?

J. LUXON: At present, the onset of the H-mode is always preceded by some period of delay, although the duration varies. The ion grad-B drift is into the divertor for DIII-D and away from the divertor for Doublet III. But I think that there are so many other differences that we should carry out the experiment rather than infer the result.



## PELLET INJECTION RESULTS DURING TFTR OHMIC AND NEUTRAL BEAM HEATING EXPERIMENTS\*

G.L. SCHMIDT, S.L. MILORA<sup>1</sup>, V. ARUNASALAM, M.G. BELL,  
M. BITTER, C.E. BUSH<sup>1</sup>, S.K. COMBS<sup>1</sup>, H.F. DYLLA, P.C. BFTHIMION,  
E. FREDRICKSON, R.J. GOLDSTON, B. GREK, L.R. GRISHAM,  
G. HAMMETT, R.J. HAWRYLUK, W.W. HEIDBRINK<sup>2</sup>, H.W. HENDEL,  
K.W. HILL, H. HSUAN, D.W. JOHNSON, L.C. JOHNSON, P.H. LaMARCHÉ,  
R. LITTLE, D.K. MANSFIELD, D.C. McCUNE, K. McGUIRE, D.M. MEADE,  
S.S. MEDLEY, D. MUELLER, W. MORRIS<sup>3</sup>, E.B. NIESCHMIDT<sup>4</sup>,  
J. O'ROURKE<sup>5</sup>, D.K. OWENS, H. PARK, A.T. RAMSEY, M.H. REDI,  
J. SCHIVELL, D. SCHURESKO<sup>1</sup>, T. SENKO, S. SESNIC,  
F.J. STAUFFER<sup>6</sup>, B.C. STRATTON, G.D. TAIT, G. TAYLOR,  
J.R. TIMBERLAKE, H.H. TOWNER, M. ULRICKSON, R. WIELAND,  
J.B. WILGEN<sup>1</sup>, M. WILLIAMS, M.C. ZARNSTORFF, S.J. ZWEBEN

Princeton Plasma Physics Laboratory,  
Princeton University,  
Princeton, New Jersey,  
United States of America

### Abstract

#### PELLET INJECTION RESULTS DURING TFTR OHMIC AND NEUTRAL BEAM HEATING EXPERIMENTS.

In Ohmic discharges, pellet injection experiments on TFTR have increased density limits and energy confinement. Injecting multiple pellets sustains the improved confinement and increases the central density and peaked character of the profile, producing significant increases in  $n_e(0)\tau_E(a)$ . A value of  $(1.4 \pm 0.3) \times 10^{20} \text{ m}^{-3}\cdot\text{s}$  has been achieved at a central electron temperature of 1.4 keV. Decay of the central density for strongly peaked profiles in Ohmic discharges is consistent with central particle diffusion coefficients of  $0.1 \text{ m}^2/\text{s}$  and flow velocities on the order of neoclassical velocities. Concentrations of scandium injected following pellet injection ( $n_{Sc}/n_e$ ) exhibit an extended rise time and then remain roughly constant during the subsequent slow decay of the electron density. In pellet-fueled discharges heated by tangential neutral beams at high density, heating profiles vary from a flat radial shape to a profile that is peaked near the  $q = 2$  radius. Global confinement is comparable to that obtained in gas-fueled discharges with similar total input power but with heating profiles more strongly peaked on axis. Central confinement in pellet-fueled discharges exceeds values obtained in gas-fueled discharges.

\* Research sponsored by the Office of Fusion Energy, United States Department of Energy, under Contract No. DE-AC02-76-CHO-3073 with Princeton University and under Contract No. DE-AC05-84OR21400 with Martin Marietta Energy Systems, Inc.

<sup>1</sup> Oak Ridge National Laboratory, Oak Ridge, TN, USA.

<sup>2</sup> GA Technologies Inc., San Diego, CA, USA.

<sup>3</sup> Balliol College, Oxford University, Oxford, United Kingdom.

<sup>4</sup> EG&G Idaho, Inc., Idaho Falls, ID, USA.

<sup>5</sup> JET Joint Undertaking, Abingdon, Oxfordshire, United Kingdom.

<sup>6</sup> University of Maryland, College Park, MD, USA.

## 1. INTRODUCTION

Fueling by injection of single and multiple pellets of frozen deuterium at speeds up to 1500 m/s has been carried out in TFTR Ohmic and neutral-beam-heated discharges using gas-driven injectors developed at Oak Ridge National Laboratory [1,2]. A carbon inner wall with a large surface area, conditioned by extensive operation with helium plasmas, has been used as the discharge limiter. Operation in Ohmic discharges at  $\bar{n}_e > 2 \times 10^{19} \text{ m}^{-3}$  is characterized by minimal metal impurities and significant pumping of recycling plasma [3].

## 2. OHMIC DISCHARGES

### 2.1. Overview

Injection of multiple pellets produces increased penetration of successive pellets as the plasma is cooled by the introduction of pellet mass. The final pellets penetrate to the plasma magnetic axis, as illustrated in Fig. 1. Penetration calculations, based on a neutral gas shielding model modified to include a Maxwellian distribution of electrons, a cold plasma shield extending along the magnetic field lines, and a finite electron heat bath, reproduce this effect and correctly predict penetration at 3 keV.

Deep pellet penetration produces strongly peaked density profiles at higher line-average density than is attainable by gas puffing. Central densities up to  $4 \times 10^{20} \text{ m}^{-3}$  have been produced. This is roughly four times the highest value obtained with gas puffing [4]. Plasma line-average densities of  $1.4 \times 10^{20} \text{ m}^{-3}$  have been obtained, corresponding to a value of  $\bar{n}_e R / B\tau = 6.5 \times 10^{19} \text{ m}^{-2} \cdot \text{T}^{-1}$ , twice that achieved with gas puffing.

As illustrated in Fig. 1, central electron temperatures decrease from approximately 3 keV to  $< 1$  keV immediately following the injection sequence. Temperature profiles broaden, with volume-average electron temperatures decreasing by a smaller factor than central temperatures. However, plasma pressures increase with pellet injection, becoming strongly peaked during the initial reheat. Neutron rates up to  $5 \times 10^{13} \text{ N/s}$  have been obtained in 2.2-MA discharges, roughly four times the maximum rate in gas-fueled discharges.

Changes in discharge MHD behavior have been associated with these strong temperature perturbations in smaller devices with shorter inductive time-scales [5]. Similar effects are observed in TFTR. During pellet ablation (0.5 ms) a high-frequency fluctuation,  $f > 160 \text{ kHz}$ , is observed on Mirnov loops located at the vessel wall. Following this period, a 1/1 mode, possibly associated with poloidal and toroidal propagation of the pellet density perturbation [6,7], is often observed. The mode decays on a 1- to 10-ms time-scale and propagates at roughly the ion sound speed. During an extended period following the pellet perturbation, sawtooth oscillations either can dominate the MHD behavior or are suppressed. When sawtooth oscillations are dominant, they appear shortly after the pellet event, are of large amplitude, and have a period of roughly 100 to 200 ms, compared with 20 to 50 ms before pellet injection. In discharges associated primarily with strong pellet penetration, sawtooth oscillations

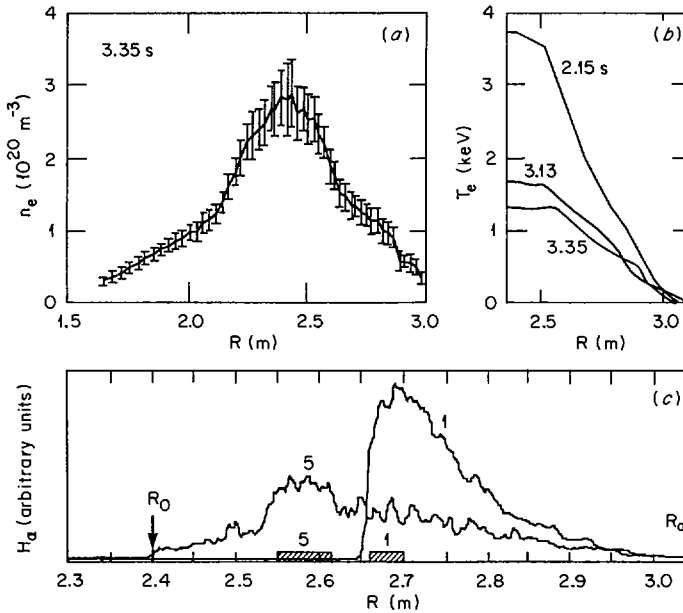


FIG. 1. (a) Density profile at 3.35 s, after injection of five 2.67 mm pellets. (b) Electron temperature profiles at 2.15 s, before injection of first pellet; at 3.13 s, before injection of fifth pellet; and at 3.35 s. (c) Measured light during pellet ablation, indicating penetration depths of the first and fifth pellets. Calculated penetration depths, allowing for a 10% uncertainty in electron temperature, are indicated by the bars.

can be suppressed for a period of 1 s. These discharges either exhibit no mode structure or are dominated by strong, continuous  $m = 1$  oscillations. In these cases a large and very narrow central x-ray peak forms during the plasma reheat. During this period, off-axis, sawtooth-like relaxations that do not alter the central peak can be observed. Such events imply a broad, flat  $q$ -profile within the plasma core. In some discharges that initially exhibit these characteristics, sawtooth oscillations can reappear. When this occurs, the continuous  $m = 1$  oscillations cease, the formation of the strong central x-ray emission is terminated, and the discharge becomes sawtooth dominated.

## 2.2. Particle transport

Following pellet injection, particle content in strongly peaked discharges decays on a 1- to 2-s time-scale, while central density initially decays on a time-scale greater than 2 s. A strong interior density gradient forms during the first phase of this decay, as does a density pedestal with the approximate profile shape of gas-fueled discharges. Such a case is shown in Fig. 2. The central density profile decay under these conditions is reproduced by calculations assuming a fixed particle diffusion coefficient of  $0.1 \text{ m}^2/\text{s}$  for  $r/a < 0.5$  [ $D = 0.1 + (r/a)^6 \text{ m}^2/\text{s}$ ].

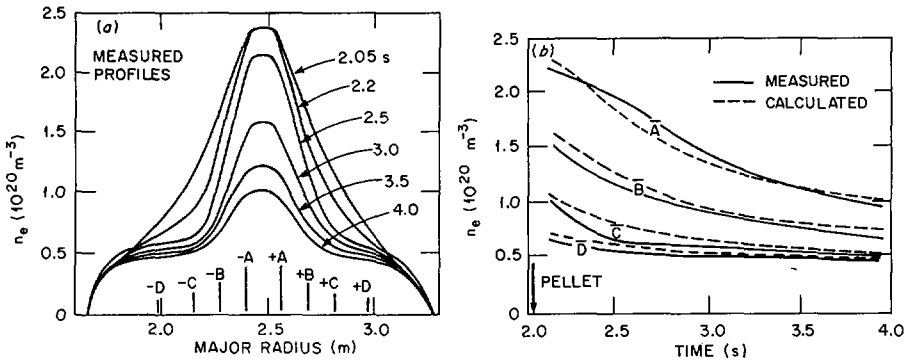


FIG. 2. (a) Electron density profile evolution following pellet injection, obtained from Abel inversion of FIR laser interferometer data (10 channels). (b) Measured and calculated decay of  $n_e$  at four radial positions  $r$ :  $\pm 0.08$  m (A),  $\pm 0.2$  m (B),  $\pm 0.3$  m (C), and  $\pm 0.5$  m (D), averaged about the plasma center.

The inward pinch term determined by this diffusion coefficient and the measured ratio  $D/v$  evaluated at 3.7 s is less than 0.3 m/s within this region. This value is roughly only five times the neoclassical value. These terms represent a time average of the transport. They are consistent with results from a similar discharge based on a least-squares fit to  $\alpha$  and  $\beta$  in the equation  $\Gamma = \alpha n + \beta dn/dr$ . Data are fitted over a range of time separately at a given radius;  $\Gamma$  is obtained from a calculation using measured values of  $n_e(r, t)$  and a computed source term. As indicated in the figure, the initial transport deviates from the average, with density decaying slowly at the center and more rapidly at larger radii, suggesting some variation about the average values.

Impurity transport during this decay has been evaluated with scandium injection. Scandium concentrations ( $n_{Sc}/n_e$ ) within the plasma core have been deduced from pulse-height analyzer measurements, assuming the same profile shape for scandium and electron densities within this region. When scandium is injected following pellet injection, concentrations are found to increase over an extended period of 300 to 500 ms after scandium injection and then to remain roughly constant during the subsequent slow decay of the electron density.

### 2.3. Energy confinement

Confinement properties of pellet-fueled and gas-fueled discharges have been compared using (1) magnetic and kinetic measurements of the plasma stored energy; (2) calculations of the resistive input power, including corrections due to changes in the internal plasma inductance obtained from measurements of the diamagnetic flux  $\beta_{p, \text{diamag}}(t)$  and the equilibrium magnetic field  $\lambda(t)$ ; and (3) calculations of the global confinement, including corrections to the input power term due to the time rate of change in stored energy. Comparisons were made primarily at 1.6 MA, where operation with deuterium gas puffing was

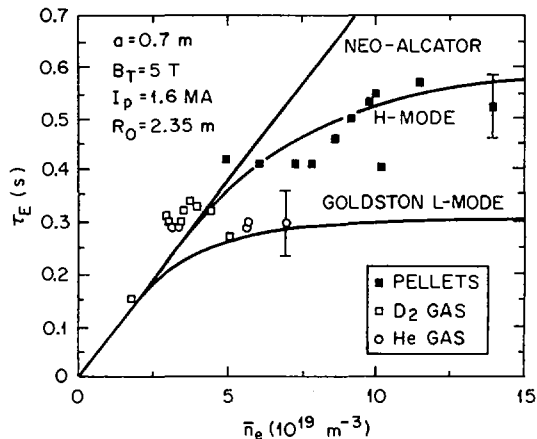


FIG. 3. Global energy confinement in deuterium and helium gas-fueled and deuterium pellet-fueled discharges. Plasma stored energy was obtained from  $\beta_p$ , diamag

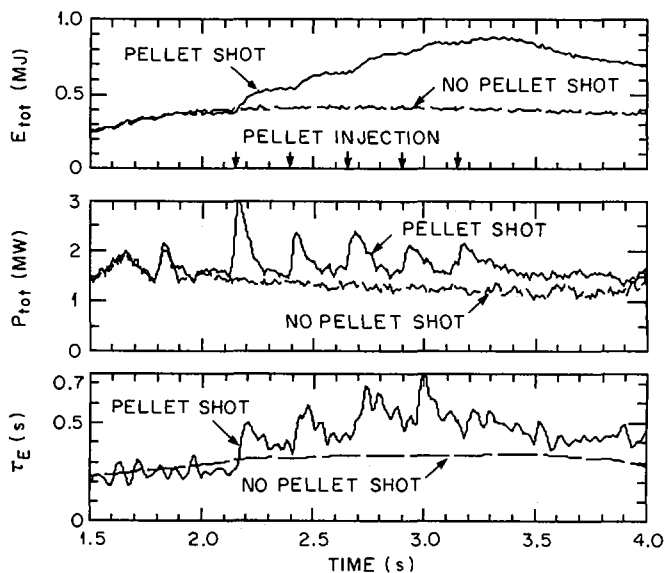


FIG. 4. Time history of plasma stored energy  $E_{\text{tot}}$ , calculated input power, and global confinement for a deuterium gas-fueled discharge and a deuterium pellet-fueled, 1.6 MA discharge.

limited to  $\bar{n}_e < 5 \times 10^{19} \text{ m}^{-3}$  by "Marfe-like" phenomena and high radiative power. Operation in helium extended the density limit to  $\sim 7 \times 10^{19} \text{ m}^{-3}$ . As shown in Fig. 3, although the confinement times for gas puffing saturate at  $\bar{n}_e \approx 4 \times 10^{19} \text{ m}^{-3}$ , the pellet-fueled discharges exhibit improved energy confinement at substantially higher densities. The data are compared with Goldston empirical scaling [8] at fixed  $P_{\text{tot}} = 1.6 \text{ MW}$ . The gross energy confinement time is expressed in terms of Ohmic ( $\tau_{\text{NA}}$ ) and auxiliary ( $\tau_{\text{aux}}$ ) heating components,  $1/\tau_E^2 = \tau_{\text{NA}}^2 + \tau_{\text{aux}}^2$ , where  $\tau_{\text{NA}} = 7.1 \times 10^{-22} \bar{n}_e (\text{cm}^{-3}) a (\text{cm})^{1.04} R (\text{cm})^{2.04} q^{0.5}$ ,  $\tau_{\text{aux}} = [6.4 \times 10^{-8} C R^{1.75} a^{-0.37} I_p (\text{A}) / P_{\text{tot}} (\text{W})^{0.5}]^2 / \tau_E$ , and  $C$  is a constant determined by the confinement regime and the plasma isotope effect. Good agreement with the pellet fueling data is obtained for an "H-mode-like" confinement factor of  $C = 2.66$  [4]. The gas fueling confinement times are more typical of L-mode results ( $C = 1.33$ ).

This improved confinement appears qualitatively similar to the Alcator-C results [9]. However, if ion transport is neoclassical, ion heat conduction losses represent only  $\sim 15\%$  of the total power flow at the half-radius. Plasma convective losses and uncertainties in the radiated power from within the plasma core, which is a significant part of power balance, affect the accuracy with which the upper limit of the ion neoclassical anomaly factor can be determined. At present, we estimate the upper limit of this factor to be  $\sim 2$ – $3$ , and we cannot determine whether ions or electrons play the dominant role in heat conduction losses. Calculations were made for a representative experiment, fueled by three pellets, using the BALDUR code with models for radiative and convective power losses corresponding to the measured radiation and density decay and for electron transport based on dissipative trapped electron modes [10]. These calculations simulate the measured global confinement with a neoclassical anomaly factor of 1.

The improved confinement obtained with pellets can be sustained by injecting multiple pellets, as shown in Fig. 4. The plasma stored energy rises with successive pellets, the global confinement increases with the first pellets and then is sustained by continued injection, and the central density increases. The increase in stored energy is partially due to higher resistive power, but the primary contribution is a roughly 70% increase in  $\tau_E$ , which in this case remains above the 0.5-s level for 0.7 s.

### 3. AUXILIARY HEATING

Auxiliary heating on TFTR is currently produced by tangential injection of 80- to 100-keV deuterium beams. Heating powers up to 11 MW have been used for pellet experiments. At high density, beam geometry and attenuation result in modest central input power levels even at high total input power. Heating profiles vary from flat to strongly peaked near the radius at which  $q = 2$ . Nonetheless, global confinement is comparable to that obtained in gas-fueled discharges with similar total input power but with heating profiles more strongly peaked on axis. This general result suggests a radial dependence of the energy confinement, which has been confirmed by detailed analysis of results at 6 MW [4]. Application

of ion cyclotron heating in the coming year will provide increased central input power levels in pellet-fueled discharges, permitting tests of possible enhanced confinement scenarios [11].

#### 4. SUMMARY

Pellet injection experiments on TFTR have increased density limits and energy confinement in Ohmic discharges. Injecting multiple pellets sustains the improved confinement and increases the central density and peaked character of the profile, producing significant increases in  $n_e(0)r(a)$ . A value of  $(1.4 \pm 0.3) \times 10^{20} \text{ m}^{-3}\cdot\text{s}$  has been achieved at a central electron temperature of 1.4 keV. Decay of the central density for strongly peaked profiles in Ohmic discharges is consistent with central particle diffusion coefficients of  $0.1 \text{ m}^2/\text{s}$  and with flow velocities on the order of neoclassical velocities. Concentrations of scandium injected following pellet injection ( $n_{Sc}/n_e$ ) exhibit an extended rise time and then remain roughly constant during the subsequent slow decay of the electron density.

#### REFERENCES

- [1] COMBS, S.K., MILORA, S.L., FOUST, C.R., et al., Rev. Sci. Instrum. **56** (1985) 1178.
- [2] COMBS, S.K., MILORA, S.L., "Pneumatic pellet injectors for TFTR and JET", Fusion Technology (Proc. 11th Symp. Avignon, 1986), in press.
- [3] HILL, K.W., TFTR Group, Paper IAEA-CN-47/A-IV-2, these Proceedings, Vol. 1.
- [4] MILORA, S.L., SCHMIDT, G.L., ARUNASALAM, V., et al., Plasma Phys. Controll. Fusion **28** (1986) 1435.
- [5] MILORA, S.L., FOSTER, C.A., THOMAS, C.E., et al., Nucl. Fusion **20** (1980) 1491.
- [6] HEIDBRINK, W.W., et al., Nucl. Fusion **24** (1984) 3.
- [7] PARÉ, V.K., COLCHIN, R.J., MILORA, S.L., BELL, S.D., FREDRICKSON, E., MCGUIRE, K., SCHMIDT, G.L., Bull. Am. Phys. Soc. **30** (1985) 1522.
- [8] GOLDSTON, R.J., Plasma Phys. Controll. Fusion **26** (1984) 87.
- [9] GREENWALD, M., GWINN, D., MILORA, S., et al., in Plasma Physics and Controlled Nuclear Fusion Research 1984 (Proc. 10th Int. Conf. London, 1984), Vol. 1, IAEA, Vienna (1985) 45.
- [10] TANG, W.M., BISHOP, C.M., COPPI, B., et al., Paper IAEA-CN-47/A-VI-1-2, these Proceedings, Vol. 1.
- [11] FURTH, H.P., Plasma Phys. Controll. Fusion **28** (1986) 1305.

#### DISCUSSION

F.X. SÖLDNER: You told us that you compared the confinement times from the experiment with different scalings. Which scaling law did you apply for the H-mode in this case?

S.L. MILORA: We used Goldston scaling, with an auxiliary heating confinement time multiplier of 2.66 to account for pure deuterium operation ( $\times 1.33$ ) and H-mode confinement ( $\times 2$ ).

A. GIBSON: Is it still true that the highest  $\hat{n}_D \tau_E \hat{T}_i$  in TFTR is obtained with Ohmic heating and pellet fuelling, and without additional heating?

S.L. MILORA: The two experiments exhibit nearly identical values of  $n_e \tau_E T_i$ . However, the deuteron concentration on axis is higher in the pellet fuelling case and consequently its  $n_D \tau_E T_i$  value is still higher.

J.G. CORDEY: Do your electron temperature profiles show profile consistency for the case of pellet injection and neutral beam injection?

S.L. MILORA: Profile consistency applies in the case of moderate density pellet fuelled discharges with neutral beam injection. At higher densities, the electron temperature profiles can become hollow in the centre since radiation from low-Z impurities exceeds the input power density.

R.S. PEASE: How do the results you report depend on the current used? And how close can you get to the value  $\beta_p = 1$ ?

S.L. MILORA: Similar values of the confinement time, namely 0.5–0.6 s, have been attained at higher currents (up to 2.2 MA). These are lower than we expected. However, the experiments were performed with one or two pellets only and so we cannot say that we have reached the peak plasma energy. For the 1.6 MA discharges,  $\beta_p = 0.31$ .

# FAST ION LOSSES AND PLASMA CONFINEMENT IN TFR DURING NEUTRAL BEAM INJECTION

EQUIPE TFR

Association Euratom-CEA sur la fusion,  
Département de recherches sur la fusion contrôlée,  
Centre d'études nucléaires de Cadarache,  
Saint-Paul-lez-Durance, France

*Presented by J.-P. Roubin*

## Abstract

### FAST ION LOSSES AND PLASMA CONFINEMENT IN TFR DURING NEUTRAL BEAM INJECTION.

Neutral beam injection experiments on carbon limited discharges in TFR exhibit a strong ion heating saturation with increasing additional power and negligible electron heating. These results seem to be inconsistent with the usual L-mode scaling. To identify a possible beam specific mechanism limiting the power before complete thermalization of the fast ions, an exhaustive check of the whole coupling chain from the neutral beam sources to the bulk plasma has been made. The coupling of the neutral beams with the plasma is analysed and shown to be as expected. Fast ion thermalization is investigated by different methods (active charge exchange, neutron production in  $D^0$ -D experiments). It is concluded that a spatial diffusion mechanism causes saturation of the central fast ion density with power at the very beginning of the slowing-down process. Finally, the heating results are interpreted, taking into account the fast ion losses. While the electron confinement appears to deteriorate, the central ion confinement time remains constant with power.

## INTRODUCTION

Recent NBI experiments [1] on carbon limited discharges in TFR, in the  $P_{\text{add}}/P_{\text{Ohm}}$  range  $\leq 3$ , exhibit a strong ion heating saturation with increasing additional power density and negligible electron heating. These results seem to be inconsistent with the usual L-mode scaling. When the classical deposition profile computed by Monte Carlo or Fokker-Planck codes is used, energy transport analysis shows a strong decrease of  $\tau_i$  compared with the Ohmic level (up to a factor of three at high power). To identify a possible beam specific mechanism limiting the power before complete thermalization of the fast ions, an exhaustive check of the whole coupling chain from the neutral beam sources to the bulk plasma has been made.

## 1. BEAM INPUT ACCOUNTABILITY

### 1.1. Power transmission into the torus

A water cooled calorimeter has been installed on the inner wall of TFR, in front of one neutral beam port. With this calorimeter the total space and time integrated beam power entering the torus can be accurately measured. The operation of the calorimeter without plasma gives the transmission efficiency  $\eta_T$  of the injectors (ions + neutrals) when the toroidal field is off, and the global neutral transmission efficiency  $\eta_G$ , expressed as  $\eta_G = \eta_T \cdot \eta_N$  (where  $\eta_N$  is the species averaged neutralization efficiency) when the toroidal field is on.

The values of  $\eta_T$  and  $\eta_G$  are found to be constant and independent of the extracted power and to be close to the expected values [2]:  $\eta_G = 0.38$ ,  $\eta_T = 0.60$  and hence  $\eta_N = 0.63$ . This rules out re-ionization of the neutrals before they enter the torus and any other conceivable saturation mechanism inside the injector with increasing power.

### 1.2. Capture of fast neutrals by the plasma

The calorimeter can also be operated in the presence of plasma; its contribution is then monitored by a second calorimeter [3]. Since the actual neutral beam power at the plasma boundary is known, the measurement of the 'shine-through' fraction of this power can be used to check if the fast neutral ionization mechanisms are the expected ones.

The experimental shine-through fractions are shown in Fig. 1 as a function of line density. For identical plasma conditions the results are the same for the case with two sources in operation and for the case with four sources in operation. This shows that the power input to the plasma grows linearly with the extracted power.

Comparison with theoretical values computed on the basis of the usual capture cross-sections [4, 5] shows that the experimental results can be explained by a small increase (+13% at  $\bar{n} = 8 \times 10^{19} \text{ m}^{-3}$ ,  $E = 34 \text{ keV}$ ) of these cross-sections. A higher increase of the cross-section (+24%) due to multi-step ionization mechanisms has been predicted theoretically [6, 7].

In any case, under TFR conditions, the power density in the plasma centre is almost unaffected by these corrections and hence full accountability of the beam input is assessed experimentally. Consequently, the observed low heating efficiency and saturation are due to fast ions and/or bulk plasma confinement problems.

## 2. BEHAVIOUR OF FAST IONS

Direct information on the beam ion distribution function and its dependence on injected power has been obtained in the following experiment.

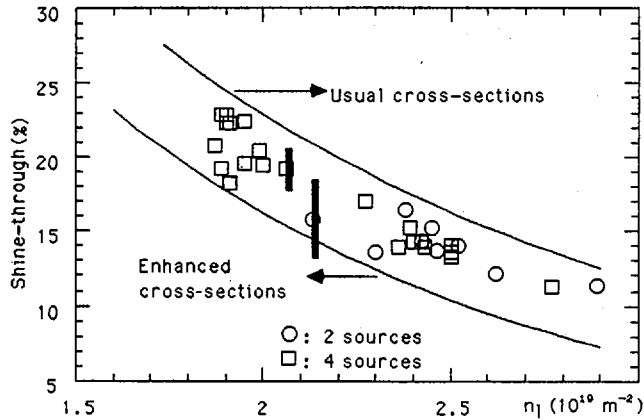


FIG. 1. Experimental shine-through values versus line density and comparison with theory (solid lines).

## 2.1. Active charge exchange measurements

### 2.1.1. Measurements during the stationary phase

The distribution function of central fast ions has been measured using an auxiliary modulated doping beam which crosses the line of sight of a multi-channel neutral particle analyser at the plasma centre. Fourier analysis of the modulated experimental signals at the modulation frequency gives an amplitude proportional to the fast ion density at a given energy. A comparison of the signals at various power levels, with the other experimental parameters ( $T_e$ ,  $n_e$ , MHD,  $Y_{eff}$ ) kept constant, has been made [8].

It is concluded that the fast ion density does not increase with power as expected. Since saturation appears already at the highest analysed energy (30 keV, only 3 keV below the injection energy) and then remains constant with energy, it follows that the saturating mechanism mainly affects the most energetic ions at the beginning of their slowing-down process and transfers them towards peripheral regions.

### 2.1.2. Measurements after beam cut-off

Using the same experimental set-up and holding the doping beam constant during the fast simultaneous cut-off of the neutral beams, information on the slowing-down kinematics of the fast ions can be obtained. The temporal behaviour of the decrease of the energetic neutral flux is compared with a simulation based on a numerical solution of the homogeneous time dependent Fokker-Planck equation. The experiments are in good agreement with theory over the whole range of density and

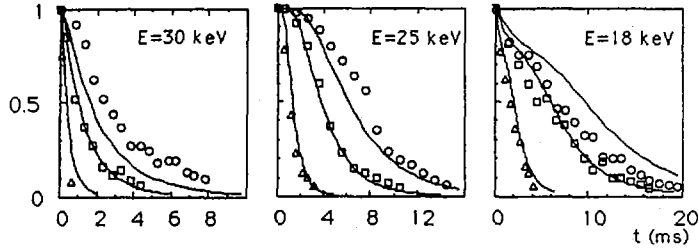


FIG. 2. Comparison between theoretical (solid lines) and experimental fast neutral signals after beam cut-off for three different densities and three analyser energies.

$\Delta$ :  $n_e(0) = 1.3 \times 10^{20} \text{ m}^{-3}$ ,  $\square$ :  $n_e(0) = 0.5 \times 10^{20} \text{ m}^{-3}$ ,  $\circ$ :  $n_e(0) = 0.3 \times 10^{20} \text{ m}^{-3}$ .

power (Fig. 2) and show that the fast ions which remain in the centre of the discharge after the beginning of their slowing-down phase (from 33 keV to  $\approx 30$  keV) continue to be classically coupled to the plasma. This confirms that, independent of the exact nature of the mechanism in connection with saturation, this mechanism necessarily acts only at the highest fast ion energy.

## 2.2 Neutron production in $\text{D}^0$ -D experiments

On TFR, the neutron production in  $\text{D}^0$ -D experiments is largely dominated by beam-plasma interaction. These neutron fluxes can serve as a monitor of the highest part of the fast ion distribution function (because of the energy dependence of the fusion cross-section) in the plasma centre (because of the peaked profiles of density and slowing-down time). Since on TFR the ion sources can be tilted in a vertical plane, the neutron production dependence can be studied for various deposition profiles at different power levels [9] and under similar plasma conditions. The beams can be aimed on axis ( $\delta = 0$  cm) as well as off axis ( $\delta$  up to  $a/2 = 10$  cm).

For operation with a single source the neutron yields and their dependence upon  $\delta$  are in excellent agreement with numerical simulations, but a comparison of data for operation with one, two and four sources under the same plasma conditions ( $T_e$ ,  $Z_{\text{eff}}$ ) shows that the increase of neutron yield with power is less than expected. Moreover, the saturation is strongest for the most peaked deposition profiles ( $\delta=0$ ) and thus for the highest fast ion density (Fig. 3). The numerical simulation fits the high power cases only with artificially broadened fast ion profiles.

This confirms the spatial diffusion of the fast ions as indicated by active charge exchange experiments.

## 2.3. A possible mechanism

For the very rapid loss of beam ions a mechanism is required which can transport the ions on a time-scale much shorter than the slowing-down time. Such a

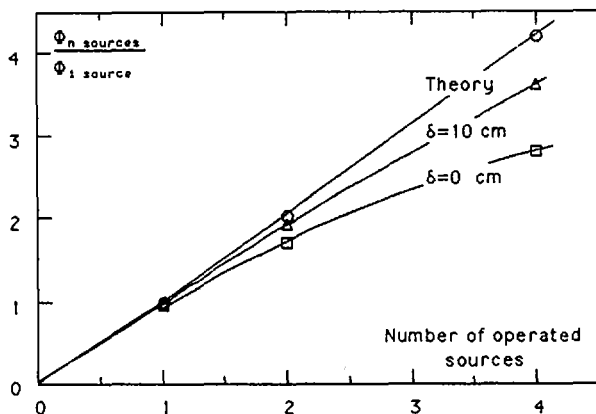


FIG. 3. Theoretical and experimental evolution of neutron yield with power for central deposition ( $\delta=0$ ) and more peripheral deposition ( $\delta=10$  cm).

mechanism is the fishbone instability observed in high beta experiments with perpendicular NBI.

In our low beta case, an electrostatic trapped-ion instability can occur, driven by resonance with the magnetic drift of beam ions [10]. The target plasma is in a collisional regime and responds adiabatically.

In the simplest approximation, the dispersion relation is:

$$2 \frac{n_p}{T_p} = \int_{\mathcal{E}} d\mathcal{E} \frac{\partial f}{\partial \mathcal{E}} \frac{\omega_D}{\omega - \omega_D}$$

where  $\omega_D = \frac{\ell q}{r} \frac{E}{eBR}$  is the precession frequency,  $\ell$  is the toroidal mode number, and

$q$  is the beam ion distribution. With TFR parameters, we find an  $\ell=1$  mode unstable for

$$\frac{n_B}{n_p} \approx \frac{E_B}{T_p} \left( \frac{\Delta E}{E_B} \right)^2$$

where  $\Delta E/E_B$  is the relative width of  $f$ .

This mode is very similar to a bump-in-tail instability. Its low frequency and large wavelength scale render direct observation with the existing diagnostics difficult. It is known that this type of resonance causes a rapid outward transport of the ions as they lose energy to the wave [11].

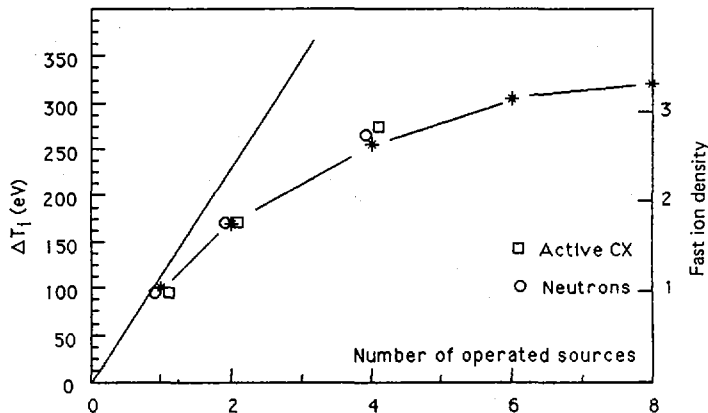


FIG. 4. Ion temperature increase (\*) versus power and fast ion density calibrated for operation with one source.

### 3. POWER BALANCE WITH EXPERIMENTAL FAST ION LOSSES

From the above observations it follows that the central power density used in central energy balance analysis has to be corrected. The actual power, as given by charge exchange or neutron flux experiments, increases only by a factor of 2.8 going from one to four sources. The saturation of the ion temperature increase is quite similar to the actual power saturation (Fig. 4), and, for central ion heating simulations using the corrected power, no decrease of the Ohmic  $\tau_i$  is required any more.

However, since classical slowing-down of the remaining central fast ions has been proved, it follows that, for TFR conditions, the power input to electrons and ions is similar. A strong decrease of  $\tau_e$  is needed to explain the poor electron heating. No specific mechanism for such a decrease has yet been identified, but a strong correlation of this process with the density fluctuation level has been clearly established experimentally [12].

In conclusion, the ion energy balance is dominated by a radial diffusion mechanism of the injected fast ions which is non-linear with input power and affects mainly the most energetic ions. Thus, bulk ion heating saturation does not imply enhanced ion heat conduction. On the other hand, strong confinement deterioration of the electrons has been shown.

### REFERENCES

- [1] EQUIPE TFR, in Plasma Physics and Controlled Nuclear Fusion Research 1984 (Proc. 10th Int. Conf. London, 1984), Vol. 1, IAEA, Vienna (1985) 103.
- [2] KIM, J., HASELTON, H.H., J. Appl. Phys. **50** 6 (1979) 3802.

- [3] EQUIPE TFR, Power transmission and shine-through calorimetry during NBI in TFR, to be published in Plasma Phys.
- [4] RIVIERE, A.C., Nucl. Fusion **11** (1971) 363.
- [5] OLSON, R.E., SALOP, A., Phys. Rev., A **16** (1977) 531.
- [6] PERRAUDIN, J.-C., PhD Thesis, Orléans Univ., 1977.
- [7] BOLEY, C.D., et al., Phys. Rev. Lett. **52** (1984) 534.
- [8] EQUIPE TFR, in Controlled Fusion and Plasma Physics (Proc. 12th Europ. Conf. Budapest, 1985), Vol. 2, European Physical Society (1985) 308.
- [9] EQUIPE TFR, in Controlled Fusion and Plasma Heating (Proc. 13th Europ. Conf. Schliersee, 1986), Vol. 2, European Physical Society (1986) 285.
- [10] TAGGER, M., LAVAL, G., PELLAT, R., Nucl. Fusion **17** (1977) 109.
- [11] TAGGER, M., PELLAT, R., Plasma Phys. **24** (1982) 753.
- [12] TFR GROUP and TRUC, A., Nucl. Fusion **26** (1986) 1303.

## DISCUSSION

R. J. GOLDSTON: I don't know what the injection angle was for these experiments, nor do I know how the toroidal rotation speed varied with beam power in TFR, but don't you think that many of the effects you describe could perhaps be explained by rotation effects?

J.-P. ROUBIN: Unfortunately, we have no measurements of the toroidal rotation, but in view of the quasi-perpendicular injection angle ( $15^\circ$ ) and the high toroidal ripple value on TFR, these effects are probably not dominant.

M.C. ZARNSTORFF: Do you have any measurements of the fast ion slowing-down spectrum off axis during central heating to show the radial fast ion motion?

J.-P. ROUBIN: No, but we have measured greater ripple losses of fast ions than expected from the calculations and this may be an indication of an enhanced radial diffusion of fast ions.



## **PARTICLE AND THERMAL TRANSPORT, AND RESONANT FIELD EXPERIMENTS IN TEXT**

A.J. WOOTTON, R.D. BENGTON, J.A. BOEDO, R.V. BRAVENEC,  
K.L. EMPSON, K.W. GENTLE, W.L. HODGE, C.C. KLEPPER,  
J. PORTER, A. MACMAHON, S.C. McCOOL, W.H. MINER,  
D.M. PATTERSON, P.E. PHILLIPS, B. RICHARDS, C.P. RITZ,  
T.L. RHODES, D.W. ROSS, W.L. ROWAN, J.C. WILEY  
Fusion Research Center,  
The University of Texas at Austin,  
Austin, Texas, United States of America

D.L. BROWER, S.K. KIM, N.C. LUHMANN, W.A. PEEBLES  
University of California,  
Los Angeles, California, United States of America

J.S. DeGRASSIE, T.E. EVANS, G.L. JACKSON, N. OHYABU  
GA Technologies, Inc.,  
San Diego, California, United States of America

P.H. DIAMOND, T.S. HAHM, P.W. TERRY  
Institute for Fusion Studies,  
The University of Texas at Austin,  
Austin, Texas, United States of America

Shuping FAN, Yexi HE  
Institute of Plasma Physics,  
Hefei, China

J.C. FORSTER, R.L. HICKOK, P.M. SCHOCH  
Rensselaer Polytechnic Institute,  
Troy, New York, United States of America

G. HAAS, F. KARGER  
Max-Planck-Institut für Plasmaphysik,  
Garching, Federal Republic of Germany

Xuehua YU, Shaobai ZHENG  
Institute of Physics,  
Chinese Academy of Sciences,  
Beijing, China

R.C. ISLER  
Fusion Energy Division,  
Oak Ridge National Laboratory,  
Oak Ridge, Tennessee, United States of America

### Abstract

#### PARTICLE AND THERMAL TRANSPORT, AND RESONANT FIELD EXPERIMENTS IN TEXT.

Particle and energy confinement have been studied on TEXT. Characteristics of the turbulence are presented, and scalings of global confinement times and local transport coefficients discussed. At the edge the measured electrostatic component of the turbulence plays a major role in particle transport. In the interior the measured density fluctuation levels are used in drift wave turbulence models to compare measured and theoretical transport coefficients. Resonant fields are used to produce ergodic layers and coherent island chains. Ergodic layers enhance radial electron heat flux and reduce the edge temperature, while islands allow increased limiter particle collection.

### PARTICLE TRANSPORT

Transport is studied on TEXT [1], an ohmically heated tokamak with major and minor radii  $R = 1m$ ,  $a = 0.27m$ , at plasma currents  $I_p \leq 400$  kA, toroidal fields  $B_t \leq 2.8T$  and densities  $\bar{n}_e \leq 1 \times 10^{20}m^{-3}$ . The working particle flux  $\Gamma$ , deduced from flux surface averages (FSA) of the asymmetric  $H_\alpha$  or  $D_\alpha$  emission [2], is characterized by the particle confinement time  $\tau_p = N/\Gamma(a) \sim 10ms$ . The  $I_p$  and  $B_t$  dependencies are approximately  $\tau_p \propto 1/q(a)$ .  $\tau_p$  peaks at  $\bar{n}_e \sim 4 \times 10^{19}m^{-3}$ .

The turbulence-driven fluxes  $\Gamma^f$  were measured using electrostatic probes. The associated confinement time,  $\tau_p^f = N/\Gamma^f(a)$ , agrees with  $\tau_p$  in both magnitude and functional dependence. Poloidal asymmetries of a factor 2 are observed, but do not affect the scalings. An exception to the agreement is that  $\tau_p^f$ , unlike  $\tau_p$ , shows little dependence on plasma position. For large radial diffusion coefficient  $D_r$  (i.e.,  $q^2 D_r / (eD_\parallel) \geq 0.01$ ) this could be explained by the interaction of a localized source (following plasma displacement) and a poloidally asymmetric  $D_r$  or inward convection velocity  $v$ .

The generally anisotropic edge turbulence does not satisfy the Boltzmann relationship. For  $r < a$ , probes and an ion beam show  $\int e\tilde{\phi}(\omega)n/(\bar{n}(\omega)kT_e)d\omega > 1$ , integrated from  $\omega/2\pi = 50$  to 150kHz, the dominant frequency range of the fluxes. Changing the edge potential  $\phi$  by biasing limiters changes edge confinement [3]: a 30% decrease in both  $\Gamma^f(a)$  and  $\Gamma(a)$  (i.e., increasing  $\tau_p^f$  and  $\tau_p$ ) follows a decrease in  $E_r$  ( $25 < r < 28cm$ ) from  $\sim 30Vcm^{-1}$  to  $\sim -80Vcm^{-1}$ .

Figure 1 shows the radial fluxes  $\Gamma$  (from  $H_\alpha$ ) and  $\Gamma^f$  (from probes) [4]. For  $r \geq a = 27cm$  there is agreement if a parallel loss term is used to account for flow to the limiter. However for  $r < 27cm$ ,  $\Gamma^f$  is too large, and continuity is apparently not satisfied. This can be resolved by invoking probe perturbations, asymmetries, or an additional inward convection with  $v \sim 10^2ms^{-1}$ . An ergodic region could couple the limiter to  $r \sim 25cm$ , but

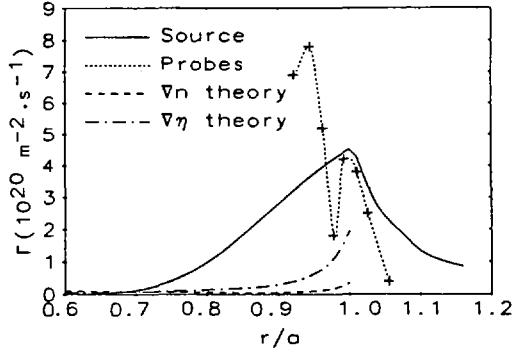


FIG. 1. Profiles of the radial particle flux  $\Gamma$  for  $I_p = 200$  kA,  $B_t = 2$  T,  $\bar{n}_e = 3.5 \times 10^{19} \text{ m}^{-3}$ . Both experimental (from  $H_\alpha$  and probes) and theoretical ( $\nabla n$  and  $\nabla \eta$ ) cases are shown.

then absolute agreement between  $\tau_p$  and  $\tau_p^f$  would not be found. Also shown are the fluxes expected from resistivity gradient driven [5] ( $\nabla \eta$ , related to the rippling mode) and collisional drift wave [6] ( $\nabla \eta$ ) turbulence. The  $\nabla \eta$  mode, for which line tying behind the limiter is a stabilizing effect, is the least unlikely candidate. It correctly predicts the scalings of  $\Gamma$  with  $I_p$ ,  $B_t$  and  $q$ , but not the scalings with  $\bar{n}_e$ , the observed  $|b_r|$  (see below) or the inequality  $e\bar{\phi}/(kT) > \bar{n}/n$ . The sensitivity to  $E_r$  is under investigation.

In the interior, both impurity ( $z$ ) and working particle ( $i$ ) profiles and transient responses can be characterized by  $\Gamma = -D_r \nabla n + n v_0 r/a$ , with constant  $D_r$  and inward  $v_0$ , except for working ions near the density limit. For  $H^+$  or  $D^+$ , variations with  $B_t$ ,  $I_p$  and  $\bar{n}_e$  are approximated by the expressions [7]  $D_r(i)$ ,  $v_0(i) \propto 1/(\bar{n}_e q(a))$ : typically  $D_r(H^+) \sim 1.4 D_r(D^+) \sim 1 \text{ m}^2 \text{ s}^{-1}$ , while  $v_0(H^+) \sim v_0(D^+) \sim 10 \text{ ms}^{-1}$ . For impurities (Sc, Ti, Fe) the global confinement  $\tau_z \propto Z_{\text{eff}} m_{bg}^{0.5} B_t^{-1} \sim 25 \text{ ms}$ , with  $D_r(z) \propto m_{bg}^{-0.5} \sim 1 \text{ m}^2 \text{ s}^{-1}$  and  $v_0(z) \propto Z_{\text{eff}} m_{bg}^{-0.5} B_t^{-1} \sim 10 \text{ ms}^{-1}$ .  $v_0(z)$  is consistent with neoclassical predictions if reasonable functional forms for impurity concentration  $n_z(r)$  and charge are assumed. As the operational boundaries are approached, impurity accumulation is observed [8], a result of increasing  $|v_0|$ .

## ENERGY TRANSPORT

Behind the limiter the radial energy flux  $q_T = q_{\text{conduction}} + q_{\text{convection}}$  is deduced from power balance, with a parallel sink included to model flow to the limiter. With  $\bar{n}_e = 2 \times 10^{19} \text{ m}^{-3}$ ,  $\chi_e(a) \sim 10 \text{ m}^2 \text{ s}^{-1}$ , and  $q_{\text{convection}}/q_T = 0.15$  [4]. If only electrostatic turbulence is to account for

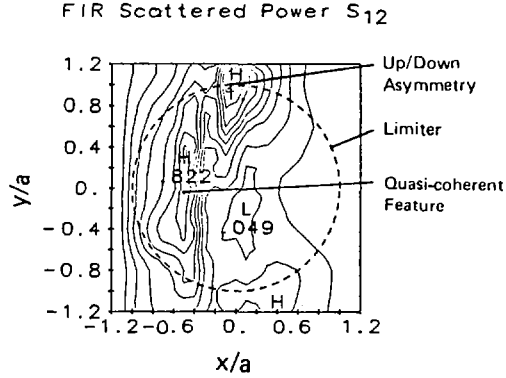


FIG. 2. Contours over a poloidal cross-section of scattered power  $S_{12}$  from FIR Thomson scattering, for  $I_p = 300$  kA,  $B_t = 2.8$  T,  $\bar{n}_e = 3.5 \times 10^{19} \text{ m}^{-3}$ . Incremental values are 0.1; high (H) and low (L) are distinguished. Results are normalized to 1.0 at  $x/a = 0$ ,  $y/a = 1$ , where  $\bar{n}/n = 0.15$ .

$q_T$ , then  $\tilde{T}_e/T_e \sim 1$  is required, an unreasonably high value. Magnetic fluctuation levels ( $b_r^{\text{rms}}/B_t \sim 10^{-4}$  between 20 and 500 kHz) do not contribute significantly:  $\chi_e^b \sim 0.03\chi_e$ . To allow additional  $q$  without increasing  $\Gamma$  (already explained by  $\Gamma^J$ ), either a stationary  $b_r$  or nonthermal parallel flow could be invoked. As  $\bar{n}_e$  is increased,  $q_{\text{convection}}/q_T$  increases, but increasing experimental uncertainties prohibit scaling.

In the interior a power balance shows  $\chi_e \approx 1/(\bar{n}_e q(a))$ ,  $\sim 2.5$  to  $5 \times D_r$ .  $\chi_e$  from sawtooth propagation is  $\sim 3$  times larger. The predictions of three drift wave turbulence models [6,9] are compared with the experimental results, using the spatially and spectrally resolved  $\tilde{n}$  values obtained from Thomson scattering. Figure 2 shows normalized contours of the frequency integrated scattered power with  $k \sim 12 \text{ cm}^{-1}$ ,  $S_{12}$ :  $\tilde{n}/n \propto \sqrt{\int S(k) dk}$ . There is a broadband background spectrum with  $\Delta\omega/\omega$  and  $\Delta k/k \geq 1$ , which is up/down asymmetric [10] and sensitive to both  $I_p$  direction and limiter configuration, suggesting a role is played by toroidal asymmetries.  $\tilde{n}/n \propto \bar{n}_e^0 B_t^{-1}$ : the  $I_p$  dependence is  $\propto I_p^0$  in the interior and  $\propto I_p^{-1}$  at the edge. A quasi-coherent feature [11] with  $\Delta\omega/\omega \leq 0.2$  and  $\Delta k/k \leq 0.5$  is found in the high field region, with  $\tilde{n}/n \propto I_p^0 \bar{n}_e^0 B_t^1$ . As  $\bar{n}_e$  is increased from  $2$  to  $8 \times 10^{19} \text{ m}^{-3}$  the ratio of drift contributions in the electron to ion direction changes from 10/1 to 2/1: a clear peak appears in the ion direction.

A comparison between  $\chi_e$  experiment and theory is shown in Fig. 3. Theoretical results, shown only where applicable, are obtained either using the FSA values of  $\tilde{n}/n$  derived from the contour plots of  $S$  (Fig. 2) or using theoretical estimates for the saturated levels. The FSA values of  $\tilde{n}/n$  are overestimated in the confinement zone because the data is not

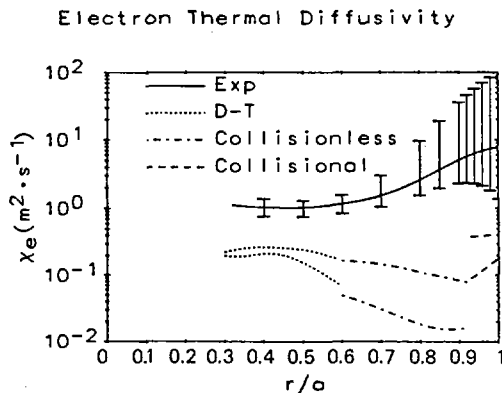


FIG. 3. Profiles of  $\chi_e$  for  $I_p = 300$  kA,  $B_t = 2.8$  T,  $\bar{n}_e = 3.5 \times 10^{19} \text{ m}^{-3}$ . Results are shown from a power balance analysis and from three theoretical models for drift wave turbulence (collisional, collisionless and dissipative trapped electron, DT) using estimated (upper curves) and measured (lower curves) values of the saturated  $\bar{n}/n$ .

deconvolved from the instrument function, and because the assumption of a spatially independent  $k$ -distribution overestimates the importance of the quasi-coherent feature. Disagreement both in amplitude and spatial dependence is found. Using measured  $\bar{n}/n$  increases the disagreement because  $\bar{n}/n$  ( $\sim 1\%$  at  $r = 15\text{cm}$ ,  $> r_{q=1}$ ) is less than the usual estimate of saturation level ( $3\rho_s/L_n \sim 15\%$  at  $r = 15\text{cm}$ ). The models also fail to explain the measured  $D_r$ .

## RESONANT FIELDS

Externally imposed resonant fields have been used [12] both to create ergodic layers (proposed as a means of extracting heat and reducing impurities) and single island chains. Coils at  $r = 33\text{cm}$  with an  $m = 7$ ,  $n = 3$  or 2 structure are computed (vacuum fields only) to produce an ergodic region for  $r \geq 22\text{cm}$  when the multiple sidebands produce overlapping magnetic islands: at  $r = 24\text{cm}$  a coil current  $I_h \sim 5\text{kA}$  produces FSA  $\langle |b_r| \rangle \sim 1.5 \times 10^{-3} T$ . Edge parameters become highly asymmetric: e.g. the probe saturation current,  $\propto n\sqrt{T}$ , varies by a factor  $\sim 10$  over  $\Delta\theta \sim 25^\circ$  behind the limiter. Plasma potential (ion beam, probe) is modified, with  $E_r$  increasing from  $-45\text{Vcm}^{-1}$  to  $-13\text{Vcm}^{-1}$  for  $0.6 < r/a < 1$ . Figure 4 shows  $T_e(r)$  for  $I_h = 0$  and  $4\text{kA}$ , and one point for  $I_h = 7\text{kA}$ :  $T_e(a)$  is reduced without affecting  $T_e(0)$ . For  $0.9 < r/a < 1$ ,  $\chi_e$  increases from 10 to  $50 \text{ m}^2\text{s}^{-1}$ : this increase is larger than the maximum incremental value expected for a diffusive process,  $\Delta\chi = \langle (b_r/B_t)^2 \rangle \chi_{e\parallel} = 20 \text{ m}^2\text{s}^{-1}$ , suggesting

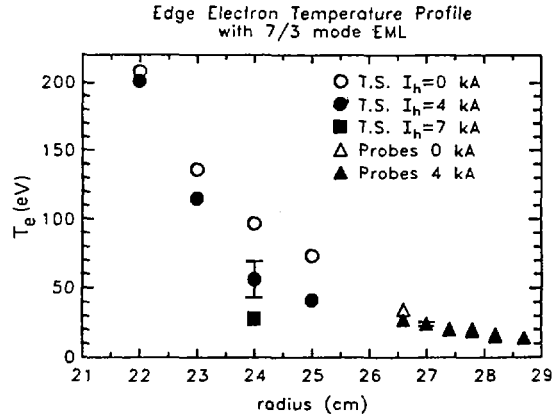


FIG. 4. Profiles of  $T_e$  from Thomson scattering (T.S.) and Langmuir probes near the plasma edge for different imposed resonant field coil currents  $I_h$ .  $I_p = 280$  kA,  $B_t = 2$  T,  $\bar{n}_e = 3 \times 10^{19} \text{ m}^{-3}$ .

the intrinsic  $\chi_e$  has also increased. Significant experimental uncertainties, including poloidal asymmetries, complicate this comparison. No evidence for an increased  $n_e(a)$  concomitant with the reduced  $T_e(a)$  has been found; as predicted by simple momentum balance along field lines. The large intrinsic transport ( $D_i \sim 1 \text{ m}^2 \text{ s}^{-1}$ ) may explain this.

Particle confinement is also affected by the resonant fields.  $\Gamma(a)$  from  $H_\alpha$  increases for conditions without computed island overlap, but decreases once computed overlap starts. Impurity line emission with  $r < 22$  cm is reduced, while with  $r > 26$  cm it is increased. Predictive transport code calculations show these emissions characterize  $n_z$ , the central reduction being explained by a combination of a reduced source and an increased outward flow in the ergodic layer.

Coherent island structures are proposed to enhance particle collection to limiters. Using the  $m = 7$ ,  $n = 2$  resonance coils, coherent island structures with width  $\sim 2$  cm are computed. A pressure gauge inside an apertured limiter shows  $\sim 30\%$  increase when the limiter is inserted to 20 cm, inside an island at the O-point. Thermography demonstrates diversion of the heat flux from the leading edge to the limiter stem, where it is more readily dissipated.

## CONCLUSIONS

Working particle confinement time scalings have been found. The values agree both in amplitude ( $\pm 50\%$ ) and scaling with those deduced from

probe measurements of electrostatic turbulence, suggesting a causal relationship. The radial profiles of the fluxes agree at and behind the limiter tip. Resistivity gradient driven turbulence is the least unlikely candidate investigated to date.

In the main plasma the working and impurity ion histories can usually be explained using a constant  $D_r$  and inward  $v_0$  model. For the working gas, both coefficients  $\propto 1/(\bar{n}_e q(a))$ . Impurity accumulation at low  $B_t$  is explained by an increasing  $v_0$ .

Behind the limiter, at low density, energy transport cannot be explained solely by convection. Magnetic fluctuations contribute insignificantly to the conduction.

Within the main plasma,  $\chi_e$  deduced from power balance  $\propto 1/(\bar{n}_e q(a)) \sim 2.5-5 \times D_r$ . Using spatially and spectrally resolved values of  $\bar{n}/n$ , drift wave turbulence models are shown to underestimate  $\chi_e$  and predict incorrect scalings. At high densities an ion feature has been identified.

Resonant coils have been used to produce both ergodic edge layers and coherent islands. Where island overlap is expected,  $T_e(a)$  is reduced from 100 to 30eV and interior impurity levels are reduced. Coherent island structures have been used to enhance pressure collection within an aperture limiter.

## ACKNOWLEDGMENTS

This work was supported by the U.S. Department of Energy contracts DE-AC05-78ET-53043, DE-AS05-85ER-53193 and DE-AC03-84ER-53158.

## REFERENCES

- [1] GENTLE, K., Nucl. Technol./Fusion **1** (1981) 479.
- [2] ROWAN, W.L., et al., Rep. No. 281, Fusion Research Center, Texas Univ., Austin (1986), to be published in Nucl. Fusion.
- [3] PHILLIPS, P., et al., Rep. No. 291, Fusion Research Center, Texas Univ., Austin (1986).
- [4] RITZ, C., et al., *ibid.*
- [5] HAHM, T.S., et al., Rep. No. 180, Institute for Fusion Studies, Texas Univ., Austin (1985), submitted to Phys. Fluids.
- [6] TERRY, P.W., et al., Phys. Fluids **28** (1985) 1419.
- [7] GENTLE, K.G., et al., Europhysics Conf. Abstr. **10C** Pt 2 (1986) 244.
- [8] ISLER, R.C., et al., Phys. Rev. Lett. **55** (1985) 2413.
- [9] PERKINS, F.W., in Heating in Toroidal Plasmas (Proc. 4th Int. Symp. Rome, 1984), Vol. 2, Int. School of Plasma Physics, Varenna (1984) 977.
- [10] BROWER, D.L., et al., Phys. Rev. Lett. **54** (1985) 689.
- [11] BROWER, D.L., et al., Phys. Rev. Lett. **55** (1985) 2579.
- [12] OHYABU, N., et al., Nucl. Fusion **25** (1986) 1684.

## DISCUSSION

A. REGISTER: I would like to make two points: First, the theory of the rippling instability in toroidal geometry predicts an important up-down asymmetry of the spectrum of the linear density eigenfunction<sup>1</sup> consistent with that measured on TEXT. Theoretically, this asymmetry is a consequence of the magnetic drifts and, incidentally, there might be a connection here with the observation reported in Dr. Wagner's paper<sup>2</sup> on the asymmetric threshold for the transition to the H-mode in ASDEX.

Second, you mentioned that the electron heat conduction coefficient calculated from the measured density fluctuation ( $\delta n/n$ ) is too small to account for the observed transport. A similar conclusion was reached in TFR turbulence studies. However,  $\chi_e$  is not simply proportional to  $(\delta n/n)^2$ , but involves an integral over the poloidal spectrum, which includes a stronger weighting factor for large  $k_\theta$  than the integral appearing in  $(\delta n)^2$ . In the case of TFR, I found agreement between theory and experiment when the proper calculation was performed.

H.P. FURTH: Towards the edge of your plasmas, you seem to find that various theoretical transport mechanisms are too weak to account for the observed transport rates. To be self-consistent, you should really modify transport theory to include the effect of ionization and charge exchange on the modes that are being considered as candidates to explain the transport. It is easy to see that in a recycling plasma these effects cannot be neglected unless  $k \gg d \log n/dr$ . Have you looked into this question?

A.J. WOOTTON: We have not yet applied any formulae for the edge particle or heat fluxes from models which include these considerations.

B. COPPI: Do you have any report to make on the particle diffusion and inflow at the centre of the plasma column?

A.J. WOOTTON: Yes. We have used an oscillating gas puff, with the FIR interferometer system, to determine  $D$  and  $v_0$ , where  $\Gamma = -D \nabla n + n v \cdot r/a$ . Assuming a constant  $D$  and  $v_0$ , we find that both  $D$  and  $v_0$  scale approximately as  $1/(\bar{n}_e q_a)$ , with typical values of  $D \approx 1 \text{ m}^2 \cdot \text{s}^{-1}$  and  $v_0 \approx 10 \text{ ms}^{-1}$ . However, there are cases where the fitting of the results to the expression is poor, suggesting it is incorrect to assume that these coefficients are constant.

F. WAGNER: There may be experimental evidence that the transition from the Ohmic linear regime to the Ohmic saturation regime depends on the edge plasma parameters. Is the transitional density range affected by the ergodic limiter and are there characteristic changes in the Langmuir probe fluctuation signals at the transition?

A.J. WOOTTON: We have not made a careful study of this transition with the applied resonant fields. Concerning the fluctuations at the edge, we have a problem. Initial results from probes suggested no change in edge electrostatic turbulence with the resonant fields, as long as the edge density was held constant in the comparison. However, the discovery of large poloidal asymmetries in ion saturation current —

only with applied resonant fields — means we must make the measurements as a function of poloidal angle before we can answer this question.

D.C. ROBINSON: What fraction of the thermal transport is accounted for by your measured electrostatic turbulent convection, and to what extent do other transport processes, such as magnetic field fluctuations, account for the edge thermal transport?

A.J. WOOTTON: We have only made this determination at lower densities ( $\bar{n}_e < 3 \times 10^{19} \text{ m}^{-3}$ ) because of the large uncertainties in the power balance estimation of the total energy transported at the edge. Here we find that perhaps 20% of the total heat flux is accounted for by convection. Behind the limiter the values of both  $\bar{T}$  and  $\bar{b}$ , in the frequency range up to 250 kHz, are too small to explain the remaining 80%. The only possible candidates would appear to be a stochastic magnetic field region, or non-concentric potential and density surfaces. The latter, if present, would negate our agreement between total flux and turbulence driven flux. Behind the limiter a suprathreshold electron component might transport more parallel heat than we have estimated. There is no evidence for such a component.

---

<sup>1</sup> ROGISTER, A., HASSELBERG, G., Paper IAEA-CN-47/E-III-1, these Proceedings, Vol. 2.

<sup>2</sup> NIEDERMEYER, H., WAGNER, F., et al., Paper IAEA-CN-47/A-II-5, these Proceedings, Vol. 1.



# IMPURITY PRODUCTION MECHANISMS AND BEHAVIOUR DURING ADDITIONAL HEATING IN JET

K. BEHRINGER, A. BOILEAU<sup>1</sup>, F. BOMBARDA<sup>2</sup>, G.B. DENNE,  
W. ENGELHARDT, M.J. FORREST<sup>3</sup>, G. FUSSMANN<sup>4</sup>,  
R. GIANNELLA<sup>2</sup>, N.A. GOTTARDI, M. VON HELLERMANN,  
L. HORTON, H. JÄCKEL<sup>4</sup>, C. JUPÉN<sup>5</sup>, E. KÄLLNE,  
K.D. LAWSON<sup>3</sup>, G. MAGYAR, G.M. McCracken<sup>3</sup>,  
P.D. MORGAN, E.R. MÜLLER<sup>4</sup>, N.J. PEACOCK<sup>3</sup>, J. RAMETTE<sup>6</sup>,  
B. SAOUTIC<sup>6</sup>, M.F. STAMP, H.P. SUMMERS<sup>7</sup>,  
G. TALLENTS, A. WELLER<sup>4</sup>  
JET Joint Undertaking,  
Abingdon, Oxfordshire,  
United Kingdom

## Abstract

### IMPURITY PRODUCTION MECHANISMS AND BEHAVIOUR DURING ADDITIONAL HEATING IN JET.

Impurities in JET are investigated by spectroscopic and plasma edge diagnostics. Impurity influxes are measured by visible spectroscopy, allowing identification of impurity sources and conclusions on production mechanisms. Metals and carbon in JET plasmas originate mainly from the limiters; physical sputtering is the release mechanism. Oxygen originates from the walls, presumably by photon or neutral particle desorption. During ICRH, antenna screen material is released by a process not yet understood. Transport studies yield  $D \approx 1 \text{ m}^2/\text{s}$  for impurities. Ohmic and neutral beam heated plasmas are dominated by light impurities (C, O), in particular by oxygen at high  $\bar{n}_e$ . Moderate metal levels (0.1%  $n_e$ ) during ICRH are responsible for radiation losses of  $\approx 20\% P_{\text{tot}}$ . These can be prevented temporarily by carbonization. Radiative power losses are 30–60%  $P_{\text{tot}}$  for NBI and 40–70%  $P_{\text{tot}}$  for ICRH.  $Z_{\text{eff}}$  ranges between 3.5 at low  $\bar{n}_e$  and 2.5 at higher  $\bar{n}_e$ . During magnetic separatrix operation, a reduction of metals and carbon is observed. The bulk plasma radiation drops compared to limiter discharges, but there is an additional contribution from the X-point regions. To date, no accumulation has been observed during NB counter-injection.

---

<sup>1</sup> Institut national de la recherche scientifique, Québec, Canada.

<sup>2</sup> Euratom-ENEA Association, Centro Ricerche Energia, Frascati, Italy.

<sup>3</sup> Euratom-UKAEA Association, Culham Laboratory, Abingdon, Oxfordshire,  
United Kingdom.

<sup>4</sup> Euratom-IPP Association, Max-Planck-Institut für Plasmaphysik, Garching,  
Fed. Rep. Germany.

<sup>5</sup> University of Lund, Lund, Sweden.

<sup>6</sup> Euratom-CEA Association, Centre d'études nucléaires de Fontenay-aux-Roses, France.

<sup>7</sup> University of Strathclyde, Glasgow, United Kingdom.

## 1. INTRODUCTION

Impurities in JET plasmas are studied by a variety of spectroscopic diagnostics, from the visible to the X-ray range [1], by bolometers and soft X-ray cameras, and by charge-exchange recombination spectroscopy (CXRS).  $Z_{\text{eff}}$  is derived from visible bremsstrahlung. Hydrogen and impurity influxes,  $\phi_{\text{H,D}}$  and  $\phi_{\text{I}}$ , are measured at various locations in the torus by visible spectroscopy. For this purpose, line excitation rate coefficients and intensities of specific impurity lines have been computed relating the number of emitted photons to the influx rate [2]. Surface analysis of collector probes, long-term samples and limiter tiles provides information on the status of surfaces in contact with the plasma and on the consequences of cleaning procedures and carbonisation. Langmuir probes are used to measure the plasma edge parameters. The limiter surface temperatures are monitored by infra-red cameras [3].

## 2. IMPURITY TRANSPORT AND IMPURITY CONFINEMENT

Emission shells of light impurities and low metal ionisation stages in JET are clearly transport dominated, requiring a diffusion coefficient  $D \approx 1 \text{ m}^2/\text{s}$  in order to explain their position and width [4]. Information about transport was also obtained from accidental injections of iron and nickel. At  $\bar{n}_e = 2 \cdot 10^{19} \text{ m}^{-3}$ , simulations using  $D = 1 \text{ m}^2/\text{s}$  agree best with the observed rise and decay of nickel line intensities, as shown in Fig.1 for Ni XXVI. There are indications that  $D$  decreases with electron density and increases during additional heating. Investigations of hydrogen particle transport [5] result in similar transport coefficients as found for the impurities.

$D = 1 \text{ m}^2/\text{s}$  and a drift velocity  $V_D = -2Dr/a^2$  are used in standard interpretation of VUV and X-ray spectra and for calculating radiated power losses of individual impurity species by means of an impurity transport code [6]. The resulting, moderately peaked total ion density profiles are confirmed within a factor of two by analysis of a number of metal ionisation stages at different radial positions (eg Ni XVII-Ni XXVII). Sawteeth, observed on lines of higher ionisation stages, can only be partly explained by pertinent variation of electron temperature profiles. It must be assumed that impurities are expelled from within the  $q=1$  surface during the sawtooth crash.

Both the radiated power  $P_{\text{rad}}$  and  $Z_{\text{eff}}^{-1}$  are roughly proportional to the square of the nuclear charge  $Z$  and the concentration of the impurity species. Therefore, normalized, average radiation losses per unit surface area have been defined

$$P_{\text{norm}} = P_{\text{rad}}/A \bar{n}_e^2 (Z_{\text{eff}}^{-1}) \quad (1)$$

(neglecting hydrogen radiation) where  $A$  is the plasma surface area.  $P_{\text{norm}}$  has been calculated by the impurity transport code for a variety of JET plasma conditions and for the important JET

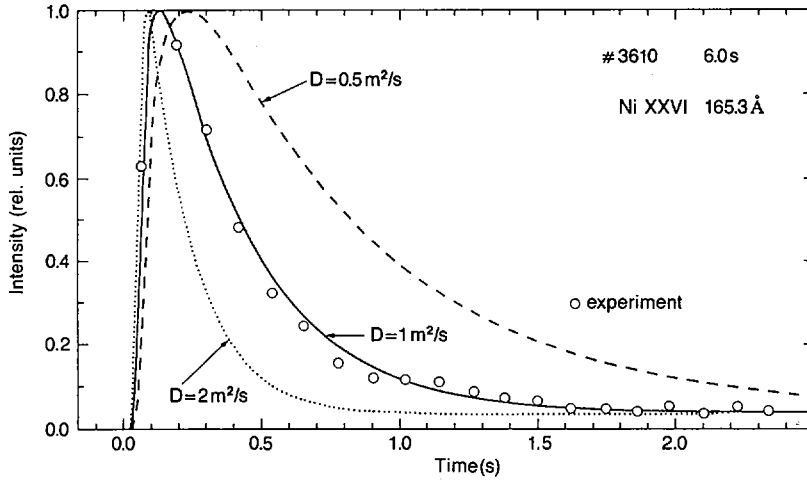


FIG. 1. Ni XXVI intensity after accidental nickel injection ( $\bar{n}_e = 2 \times 10^{19} \text{ m}^{-3}$ ,  $I_p = 2.8 \text{ MA}$ ). Simulations using different  $D$ -values are shown ( $V_D = -2Dr/a^2$ ). Recycling at the limiters leads to a finite level after the event.

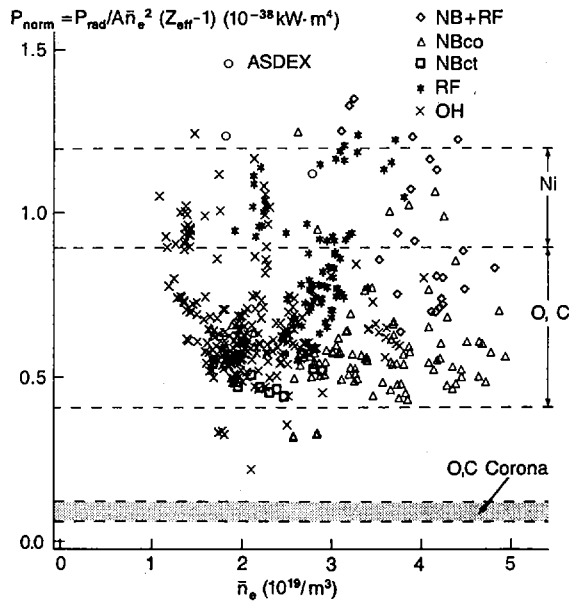


FIG. 2. Normalised power per unit surface area for 1986 JET limiter plasmas. The ranges of  $P_{\text{norm}}$  predicted by the transport code ( $D = 1 \text{ m}^2/\text{s}$ ) for O, C and metals are indicated. Corona assumption leads to much lower  $P_{\text{norm}}$  values for O and C. One point each is shown for ASDEX limiter and divertor discharges [7].

impurities.  $P_{\text{norm}}$  is found to be about  $0.4-0.9 \cdot 10^{-38}$  kW·m<sup>4</sup> for light impurities and about  $0.9-1.2 \cdot 10^{-38}$  kW·m<sup>4</sup> for metals. The lower end of the range corresponds to peaked  $n_e$  profiles and high  $T_e$  values, the upper end to flat  $n_e$  profiles and low  $T_e$  values. The assumption of corona ionisation equilibrium reduces  $P_{\text{norm}}$  by a factor of 5-10 for light impurities, because the radiation shell is then located in the scrape-off layer at low electron and impurity ion densities. A summary of experimental  $P_{\text{norm}}$  values as a function of  $\bar{n}_e$  is shown in Fig.2 for JET 1986 limiter discharges (500 data points). The vast majority of measured values is found in the predicted range. Fig.2 proves clearly the necessity of including transport in the plasma simulation. Two ASDEX data points [7] demonstrate the validity of the scaling with surface area. The detailed behaviour of  $P_{\text{norm}}$  with respect to the different heating schemes will be discussed below.

Impurity particle confinement times, derived from measured influxes and concentrations, agree roughly with calculations on the basis of a simple diffusion model [2] and  $D=1$  m<sup>2</sup>/s, if an energy of a few eV is assumed for the neutral particles produced at the limiters. A good correlation of impurity influxes and densities has been observed throughout the JET operation, both as a function of plasma parameters and of vessel conditions.

Occasionally, when a steep increase in the Cr influx was observed, due to chromium evaporation, the metal concentration in the bulk plasma did not change [2]. These slow particles are ionised in the immediate vicinity of the limiter surfaces and have a high redeposition probability before entering the plasma. This observation demonstrates that the usual impurity influxes of C, O and metals must have a significant kinetic energy to give rise to the measured impurity concentrations.

### 3. IMPURITY PRODUCTION

The impurity behaviour of JET limiter discharges was dominated by the limiter fluxes (wall contribution = 20% during OH). Metal concentrations were only significant ( $> 0.1\%$   $n_e$ ) if the carbon limiters were metal-coated after accidental melting and evaporation of wall material (Inconel droplets and  $\geq 2 \cdot 10^{21}$  m<sup>-2</sup> uniform coverage [8]). Recently, this has been prevented by covering large areas of the torus by carbon protection plates. A particular metal problem during ICRH will be discussed later.

The release of metals from the limiters can be explained by a combination of sputtering by deuterium and by light impurities, taking into account the respective surface coverage of the carbon tiles ( $\phi_M/\phi_D = 0-0.02$ ). The metal fluxes decrease with  $\bar{n}_e$  and increase with  $I_p$ ; they are inversely correlated with the light impurity behaviour. These trends, observed before on many other tokamaks, are due to the temperature dependence of the metal sputtering yields. In JET, gettering of oxygen by chromium has been observed to be a further reason for this anti-correlation.

The carbon concentration in JET has been consistently at a level of a few %  $n_e$  throughout operation periods. The carbon production rate behaves similarly to the metal release, but the dependencies are less pronounced [2]. This observation and the fact that the produced C-particles must have significant kinetic energy suggest physical sputtering as the prevailing production mechanism. Furthermore, during temperature excursions of the limiter surface from 300°C to over 1000°C, no change in carbon production rate was observed, which means that chemical sputtering, expected to manifest itself by an increased yield at about 600°C, is not an important process. There is some evidence for carbon sputtering by oxygen, but only at unusually high oxygen levels [2]. The carbon yields measured ( $\phi_C/\phi_D \approx 0.05-0.1$ ) can be explained by a combination of deuterium, oxygen and self-sputtering at high  $T_e(a)$  values ( $>100$  eV).

The oxygen fluxes and concentrations in JET varied primarily with vessel conditions. The vessel walls constitute the most important oxygen source and, once in the plasma, oxygen recycles at the limiters. This is apparent from the tendency of oxygen limiter fluxes to increase throughout a discharge, even if other parameters are stationary. If the recycling occurs in the form of CO molecules, the O atoms must gain energy in Franck-Condon or charge-exchange processes. Since no dependence of the oxygen yield on plasma parameters is observed, the energy threshold for the respective production mechanism must be very low. During  $^3\text{He}$  discharges, carbon fluxes remained unchanged ( $\phi_C/\phi_{\text{He}} \approx 0.13$ ) while oxygen was substantially reduced. Therefore, chemical processes or CX neutrals must be responsible for the O production.

Due to the above trends, JET plasmas were metal dominated at low electron densities, if there was significant metal deposition on the limiters, otherwise carbon was the most important impurity. At high electron densities, metals disappeared, carbon was reduced, and oxygen dominated. Oxygen concentrations increased, particularly close to the density limit, due to enhanced plasma-wall interaction.  $Z_{\text{eff}}$  fell steeply with  $\bar{n}_e$  when metals were important and was a weak function of  $\bar{n}_e$  for metal-free plasmas. During discharges limited by the inner-wall protection tiles, these took over the role of the limiters leading essentially to the same plasma behaviour.

During ICRF heating on JET, screen material (Cr, Ni) has been observed to enter the plasma from the ICRH antennae [2,3]. The measured chromium flux from a Cr coated antenna ( $10^{16} \text{ cm}^{-2} \cdot \text{s}^{-1} / \text{MW}$ ) decreased by a factor 5 during five months' operation and was reduced temporarily (some 10 discharges) by two orders of magnitude by means of heavy carbonisation (15%  $\text{CH}_4$ , 12 hrs). In the course of ICRH operation, screen material was deposited on the limiters and eroded again by the plasma, resulting in higher basic metal levels during an ICRH campaign. The metal coverage of the limiter carbon tiles was removed by a few OH or NBI discharges, in accord with model predictions [9]. The release mechanism of the screen material is not yet understood.

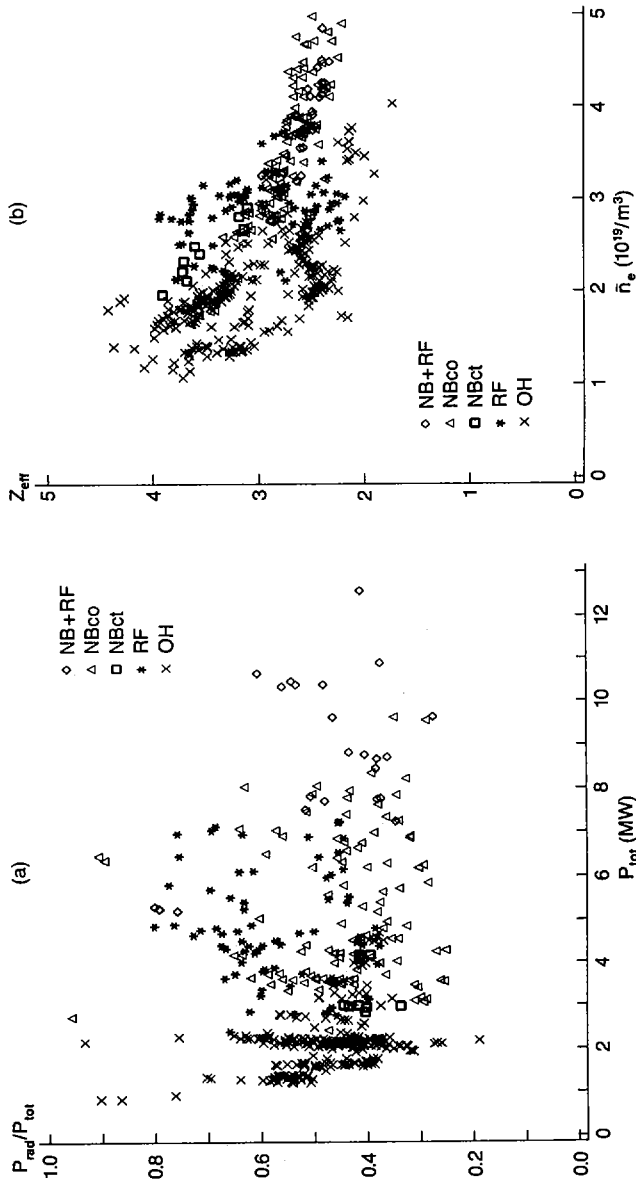


FIG. 3. JET 1986 limiter discharges.  $P_{\text{rad}}/P_{\text{tot}}$  as a function of  $P_{\text{tot}}$  (a), and  $Z_{\text{eff}}$  versus  $\bar{n}_e$  (b), for OH, ICRH (RF), co- and counter-NBI, and combined heating (NB+RF).

#### 4. ICRH AND NB CO-INJECTION

Both hydrogen and impurity influxes increased during additional heating, leading to a substantial increase in  $\bar{n}_e$ , unless the plasma was at the inner wall, which appears to have an efficient pumping capability. Although the wall fluxes gained in importance, the plasmas were still dominated by the limiters. The  $n_e$ -profile flattened during ICRH; it was unchanged or peaked during NBI. The hydrogen and impurity particle confinement times decreased in both cases.

Due to the higher electron densities during NBI, oxygen was the most important impurity. The increase in the O/C ratio is well demonstrated by the CXRS results [10], the trends of which are in excellent agreement with the usual VUV spectroscopic results, while they tend to give somewhat higher carbon concentrations.  $Z_{eff}$  dropped during NBI, but not to a lower level than that of OH discharges at the respective higher densities. For constant  $\bar{n}_e$ , the radiated power fraction  $P_{rad}/P_{tot}$  fell with increasing NBI power. However, due to the pertinent  $\bar{n}_e$ -evolution, radiation losses remained around 45%  $P_{tot}$ , on average. These radiation losses were caused by light impurities, in particular by oxygen (1-2%  $n_e$ ). Due to the latter fact and a tendency to peaked  $n_e$ -profiles during NBI,  $P_{norm}$ -values are at the lower end of the range in Fig.2.

The metal release from the antenna screens during ICRH led to significant metal densities in the plasma ( $\approx 0.1\%$   $n_e$ , contribution to  $P_{rad} \approx 20\%$   $P_{tot}$ , see also [11]) except immediately after heavy carbonisation.  $Z_{eff}$  remained essentially at the OH value before RF, i.e. there was no benefit of the higher electron densities. For individual campaigns, the radiated power fraction increased somewhat with  $P_{RF}$  and was generally in the range 40-70%  $P_{tot}$ . Hydrogen minority heating led to higher metal densities in the plasma than  $^3\text{He}$  minority heating, but the difference in  $P_{rad}$  is within the scatter of the data points. Due to some metal contribution and flatter  $n_e$ -profiles, the  $P_{norm}$  values for ICRH in Fig.2 are at the upper end of the predicted range.

During combined NBI and ICRH, the consequences of the two heating schemes essentially added. The metal densities in the plasma corresponded to the respective RF power. Basic metal levels and limiter coverage built up as during ICRH alone.  $Z_{eff}$  and  $P_{rad}/P_{tot}$  values for OH plasmas and additional heating are summarised in Fig.3 for 1986 JET limiter discharges. At higher electron densities,  $Z_{eff}$  was about 2.5 for NBI, ICRH and combined heating, essentially caused by oxygen and carbon.

#### 5. MAGNETIC SEPARATRIX

The magnetic separatrix configuration has been successfully generated in JET (X-point plasmas [12]). In this case, the top and bottom vessel protection tiles act as X-point neutraliser plates. Even when these plates consisted of Inconel (June 1985),

no significant metal concentrations were detected in X-point plasmas. With carbon plates, the carbon level was reduced compared to the respective limiter discharges during the OH phase. During NBI, carbon concentrations increased, in contrast to the behaviour of limiter discharges as demonstrated again by CXRS [10]. The behaviour of carbon and metals indicates a low plasma temperature in front of the neutraliser plates during OH discharges and therefore a low sputtering yield. After argon puffing into X-point plasmas, no retention of Ar in the X-point regions was observed, ie the same amount was found in the bulk of X-point and corresponding limiter discharges, in contrast to the Doublet III results [13].

The oxygen concentration was not different from limiter plasmas ( $\approx 1.5\% n_e$ ). Since metal concentrations were generally low, X-point operation resulted only in a minor reduction of  $Z_{\text{eff}}$  ( $Z_{\text{eff}} \approx 3$  at  $\bar{n}_e = 1.5 \cdot 10^{19} \text{ m}^{-3}$  and  $I_p = 2 \text{ MA}$ ). The radiation losses of the bulk plasma were also somewhat lower, but there was an additional contribution of the X-point regions of  $\approx 50\% P_{\text{bulk}}$ . The total radiation losses amounted to  $\approx 50\% P_{\Omega}$  at low densities ( $\bar{n}_e = 1 \cdot 10^{19} \text{ m}^{-3}$ ) and approached 100% at higher densities. NBI into X-point plasmas led to a low level of wall material in the plasma, probably due to CX particles hitting the walls. The oxygen concentration did not change significantly during NBI.

#### 6. NB COUNTER-INJECTION

Counter-injection, both into limiter and X-point plasmas, has been studied for a limited period in JET. The impurity behaviour of these discharges was virtually indistinguishable from the corresponding co-injection cases (see Figs 2 and 3). Some peaking of soft X-ray emission profiles was observed and the line intensities of higher metal ionisation stages appeared to increase more than the lower ones. However, the standard analysis taking into account the respective  $n_e$ - and  $T_e$ -distributions resulted in the usual impurity ion density profiles within the experimental error bars. For the present NBI power levels ( $< 7 \text{ MW}$ ) and plasma parameters, no accumulation of impurities has been observed.

#### 7. CONCLUSION

The JET impurity situation is not significantly different from that of other ungettered tokamaks with carbon limiters. Metal concentrations in the plasma were very low during OH and NBI discharges, due to coverage of large areas of the wall by carbon tiles. An exception was ICRF heating, where screen material entered the plasma from the antennae. This will be prevented in the future by a carbon or beryllium coating of the Faraday screens presently under investigation. The carbon concentration was high at moderate electron densities, but, due to the fact that physical sputtering is the production mechanism, it decreased at high densities, which are aimed for anyway. At

high  $\bar{n}_e$ , radiation losses were mainly caused by oxygen. Well below the density limit,  $P_{\text{rad}}/P_{\text{tot}}$  was typically 50% radiated from the plasma edge, while the bulk plasma was transport dominated. A primary aim of future operation must be the reduction of oxygen levels, which could be most easily achieved by gettering. Accumulation of impurities has not been observed in JET.

## REFERENCES

- [1] BEHRINGER, K., Rev. Sci. Instrum. **57** (1986) 2000.
- [2] BEHRINGER, K., J. Nucl. Mater. **145-147** (1987) 145.
- [3] ENGELHARDT, W., Plasma Phys. Controll. Fusion **28** (1986) 1401.
- [4] BEHRINGER, K., et al., in Basic and Advanced Fusion Plasma Diagnostic Techniques (Proc. Workshop Varenna, 1986), CEC, Brussels (1987).
- [5] CHEETHAM, A., et al., in Controlled Fusion and Plasma Heating (Proc. 13th Europ. Conf. Schliersee, 1986), Vol. 10C, Part I, European Physical Society (1986).
- [6] BEHRINGER, K.H., CAROLAN, P.G., DENNE, B., et al., Nucl. Fusion **26** (1986) 751.
- [7] MULLER, E.R., Nucl. Fusion **22** (1982) 1651.
- [8] BEHRISCH, R., et al., J. Nucl. Mater. **145-147** (1987) 731.
- [9] McCracken, G.M., et al., J. Nucl. Mater. **145-147** (1987) 621.
- [10] VON HELLERMANN, M.G., et al., in Basic and Advanced Fusion Plasma Diagnostic Techniques (Proc. Workshop Varenna, 1986), CEC, Brussels (1987).
- [11] JACQUINOT, J., et al., paper IAEA-CN-47/F-I-1, these Proceedings, Vol. 1.
- [12] TANGA, A., et al., Paper IAEA-CN-47/A-I-1, these Proceedings, Vol. 1.
- [13] MAHDAVI, M.A., et al., Phys. Rev. Lett. **47** (1981) 1602.

## DISCUSSION

S. KONOSHIMA: Can you describe the entire experimental impurity profile from the centre up to the edge by a single value of the transport coefficient  $D \sim 1 \text{ m}^2/\text{s}$ ? And is there a significant difference in these values between the H-mode and the L-mode, especially near the edge?

K. BEHRINGER: Within the error bars, the impurity density profiles in JET can be described by a constant diffusion coefficient  $D = 1 \text{ m}^2/\text{s}$  — the value from impurity injection — and an inward drift velocity  $v_D \sim -2Dr/a^2$ . We have no proof that other models — for example with both  $D$  and  $v_D$  varying with radius — could not provide an equally good description.

There are indications that  $D$  increases during the L-mode. During the H-mode, particle confinement is clearly improved, but there are no systematic studies yet with respect to the individual transport parameters.

F. WAELBROECK: You attribute the appearance of carbon impurity ions to physical sputtering. I would therefore like to ask why there is no chemical erosion in JET, i.e. metal-carbon bonds at the limiter surface. Furthermore, other devices, for example TEXTOR, show molecular band emission near the limiter. What happens in the case of JET?

K. BEHRINGER: Chemical sputtering cannot be excluded completely. If it does take place, the respective particles must be redeposited before being ionized and are thus not detected by emission spectroscopy. The important flux entering the plasma does not originate from chemical effects.

Molecular band emission near the limiter is observed in JET, but the respective intensities are very low.

R.J. TAYLOR: Is it possible to fabricate a limiter for JET on which no recycling of hydrogen or impurities would take place?

K. BEHRINGER: We do not know of any such limiter material, but we would be grateful for any proposals.

## IMPURITY AND PARTICLE TRANSPORT AND CONTROL IN TFTR

K.W. HILL, V. ARUNASALAM, M.G. BELL, M. BITTER, W.R. BLANCHARD, N.L. BRETZ, R. BUDNY, C.E. BUSH<sup>1</sup>, S.A. COHEN, S.K. COMBS<sup>1</sup>, S.L. DAVIS, D.L. DIMOCK, H.F. DYLLA, P.C. EFTHIMION, L.C. EMERSON<sup>1</sup>, A.C. ENGLAND<sup>1</sup>, H.P. EUBANK, R.J. FONCK, E. FREDRICKSON, H.P. FURTH, G. GAMMEL, R.J. GOLDSTON, B. GREK, L.R. GRISHAM, G. HAMMETT, R.J. HAWRYLUK, W.W. HEIDBRINK<sup>2</sup>, H.W. HENDEL<sup>3</sup>, E. HINNOV, S. HIROE<sup>1</sup>, H. HSUAN, R.A. HULSE, K.P. JAEHNIG, D. JASSBY, F.C. JOBES, D.W. JOHNSON, L.C. JOHNSON, R. KAITA, R. KAMPERSCHROER, S.M. KAYE, S.J. KILPATRICK, R.J. KNIZE, H. KUGEL, P.H. LaMARCHE, B. LeBLANC, C.H. MA<sup>1</sup>, D.M. MANOS, D.K. MANSFIELD, R.T. McCANN, M.P. McCARTHY, D.C. McCUNE, K. McGUIRE, D.H. McNEILL, D.M. MEADE, S.S. MEDLEY, D.R. MIKKELSEN, S.L. MILORA<sup>1</sup>, W. MORRIS<sup>4</sup>, D. MUELLER, V. MUKHOVATOV<sup>5</sup>, E.B. NIESCHMIDT<sup>6</sup>, J. O'ROURKE<sup>7</sup>, D.K. OWENS, H. PARK, N. POMPHREY, B. PRICHARD, A.T. RAMSEY, M.H. REDI, A.L. ROQUEMORE, P.H. RUTHERFORD, N.R. SAUTHOFF, G. SCHILLING, J. SCHIVELL, G.L. SCHMIDT, S.D. SCOTT, S. SESNIC, M. SHIMADA<sup>8</sup>, J.C. SINNIS, F.J. STAUFFER<sup>9</sup>, J. STRACHAN, B.C. STRATTON, G.D. TAIT, G. TAYLOR, J.R. TIMBERLAKE, H.H. TOWNER, M. ULRICKSON, V. VERSHKOV<sup>5</sup>, S. VON GOELER, F. WAGNER<sup>10</sup>, R. WIELAND, J.B. WILGEN<sup>1</sup>, M. WILLIAMS, K.L. WONG, S. YOSHIKAWA, R. YOSHINO<sup>8</sup>, K.M. YOUNG, M.C. ZARNSTORFF, V.S. ZAVERYAEV<sup>5</sup>, S.J. ZWEBEN

Princeton Plasma Physics Laboratory,  
Princeton University,  
Princeton, New Jersey,  
United States of America

- 
- <sup>1</sup> Oak Ridge National Laboratory, Oak Ridge, TN, USA.  
<sup>2</sup> GA Technologies Inc., San Diego, CA, USA.  
<sup>3</sup> RCA David Sarnoff Research Centre, Princeton, NJ, USA.  
<sup>4</sup> Balliol College, University of Oxford, Oxford, UK.  
<sup>5</sup> Kurchatov Institute of Atomic Energy, Moscow, USSR.  
<sup>6</sup> EG&G Idaho, Inc., Idaho Falls, ID, USA.  
<sup>7</sup> JET Joint Undertaking, Abingdon, Oxfordshire, UK.  
<sup>8</sup> JAERI, Naka-machi, Naka-gun, Ibaraki-ken, Japan.  
<sup>9</sup> University of Maryland, College Park, MD, USA.  
<sup>10</sup> Max-Planck-Institut für Plasmaphysik, Garching, Fed. Rep. Germany.

## Abstract

### IMPURITY AND PARTICLE TRANSPORT AND CONTROL IN TFTR.

Degassing of the TFTR graphite limiter by low density deuterium or helium discharges enables the limiter to pump deuterium, thereby reducing recycling and improving energy confinement in neutral-beam-heated discharges. During a helium degassing sequence the hydrogen influx decreased by a factor of 20. As a consequence of degassing sequences the low density limit in 0.8 MA deuterium discharges decreased from  $1 \times 10^{19} \text{ m}^{-3}$  to  $0.5 \times 10^{19} \text{ m}^{-3}$ , the density decay time dropped from greater than 10 s to 0.15 s, and the recycling coefficient dropped from nearly 1 to less than 0.4.  $Z_{\text{eff}}$  values in 2.2 MA L-mode discharges on the toroidal limiter with neutral-beam-heating power up to 15 MW are between 2 and 3 if the pre-beam plasma has low  $Z_{\text{eff}}$  (high density), but can be as high as 4.5 if the pre-beam plasma has high  $Z_{\text{eff}}$  (low density).  $Z_{\text{eff}}$  values in enhanced confinement shots drop from 7 during the ohmic phase to 3 with neutral beam heating. The radiated power drops from 60-70% of total heating power to 30-35% for beam powers from 10 to 20 MW.

## I. Introduction

Operation of TFTR plasmas on the toroidal graphite limiter at neutral beam powers up to 20 MW has provided new data on plasma-limiter interactions at near reactor temperatures and densities. Discovery of a new regime of enhanced energy confinement in beam-heated discharges [1] has improved prospects for achieving breakeven in TFTR and has provided new insights into the role of edge particle control. Degassing of the limiter to achieve low recycling and documentation of the effect of the degassing on plasma confinement have been a focus of recent experiments [2,3].

A second aspect of plasma-limiter/wall interactions is impurity production and influence of the resulting contamination on the plasma. Plasma impurity levels in L-mode and enhanced confinement discharges with neutral beam powers up to 20 MW are discussed. Impurity transport rates have been inferred by injecting impurities into the plasma and studying the time behavior of their radiation.

## II. Conditioning for Particle and Impurity Control

The large area toroidal limiter [2] required special conditioning techniques to achieve satisfactory plasma operation [4]. Following installation, 130 hours of glow-discharge cleaning (GDC) and 175 hours of pulse-discharge cleaning (PDC) were performed during a six-week period, with the vacuum vessel heated to 150 C. After this conditioning, discharges were severely affected by outgassing of the limiter following a disruption. Additional PDC and a newly developed technique, disruptive discharge cleaning (DDC), were used to heat the limiter surface sufficiently (~1000 C) to effect outgassing of water vapor and hydrocarbons. The DDC consisted of a sequence of tokamak discharges with flat-top currents increasing from 0.6 to 2.5 MA.

The flat-top current was increased progressively by 0.2 MA after a forced disruption at each current did not affect the succeeding discharge. When recovery was easy after a 2.5 MA disruption, ohmic discharges at 2.2 MA had a radiated power fraction less than 50% and  $Z_{\text{eff}} \leq 1.5$  for  $\bar{n}_e > 4 \times 10^{19} \text{ m}^{-3}$ . Following a one-week opening of the vacuum vessel, DDC, in addition to GDC and PDC, was again required to eliminate excessive limiter outgassing caused by a 2.2 MA disruption.

In contrast, only standard GDC and PDC techniques were required to prepare both the vacuum vessel and the movable limiter for high power operation, prior to installation of the toroidal graphite limiter [5]. Following 100-200 discharges, the radiated power fraction and  $Z_{\text{eff}}$  in ohmic fiducial discharges ( $I_p = 1.4 \text{ MA}$ ,  $\bar{n}_e = 2.4 \times 10^{19} \text{ m}^{-3}$ ) dropped to 60 - 70% and 2, respectively.

The initial enhanced confinement neutral-beam-heated discharges were obtained only after degassing the graphite limiter by several tens of low density helium and deuterium discharges. Evidently, desorption of deuterium from the normally saturated near-surface region of the graphite enabled the limiter to retain

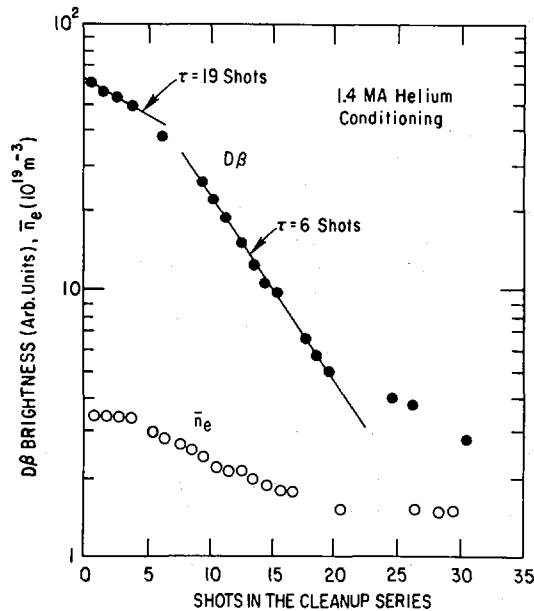


FIG. 1.  $D\beta$  emission intensity and line-averaged electron density during a sequence of low density 1.4 MA helium limiter degassing discharges. A decrease in the deuterium influx of a factor of 20 indicates depletion of deuterium from the surface and near surface regions of the limiter.

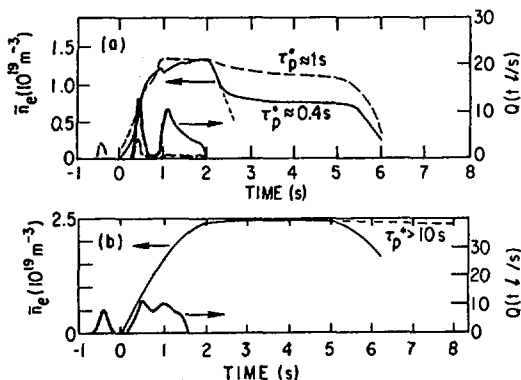


FIG. 2. Line-averaged electron density and gas fueling rate as a function of time during fiducial shots on: (a) a well conditioned limiter (solid line) and a deconditioned limiter (dashed line), and (b) an unconditioned limiter.

incident hydrogen efficiently and substantially reduced recycling. In combination with intense central fueling by neutral beam injection, the lower recycling produced a more peaked density profile. During normal enhanced-confinement operation, daily sequences of about 10 degassing shots were used to keep plasma performance optimized. About 20-30 degassing shots were required to recover from gas loading caused by pellet-fueled [6] or detached plasmas [7].

The hydrogen degassing by a series of 1.4 MA helium conditioning discharges on the toroidal limiter is illustrated by Fig. 1. The brightness of the deuterium D $\beta$  line ( $n = 4-2$  transition), which is a measure of the deuterium influx into the plasma, decreased by a factor of 20 during this sequence. The minimum achievable line-averaged electron density also decreased by a factor of two, as shown, and oxygen radiation decreased by an order of magnitude. This suggests that conditioning discharges also remove oxygen, possibly in the form of water vapor or CO. The intensity of carbon radiation changed little during the sequence.

Two important consequences of the limiter degassing are a smaller low-density limit and a shorter density-decay time, constant or effective particle confinement time  $\tau_p^*$ , indicated by faster density pumpout. Both effects are illustrated in Fig. 2a, which shows the time evolution of the central-chord line-averaged electron density and the gas input rate for 2 shots, one before and one after a 25-shot 0.8 MA deuterium degassing sequence. In contrast, a large value of  $\tau_p^*$  ( $> 10$  s) characterized the toroidal limiter before conditioning sequences were begun (Fig. 2b). In these fiducial discharges the gas feed is controlled by feedback to produce a preselected density at  $t = 2$  s

and is then shut off. Figure 2a depicts 0.8 MA discharges programmed to  $\bar{n}_e = 1.3 \times 10^{19} \text{ m}^{-3}$ , whereas Fig. 2b is a 1.4 MA discharge programmed to  $\bar{n}_e = 2.4 \times 10^{19} \text{ m}^{-3}$ . The density decays exponentially to a baseline which is determined by recycling. The density decay time is determined by the intercept of the dashed lines, which characterize the initial decay rate, with the minimum density baseline.

Decay time constants as small as 0.15 s were obtained after applying helium degassing sequences frequently over a 1000-shot interval. The sequences were interspersed with series of neutral-beam-heated shots to test the effectiveness of conditioning on improving beam fueling and energy confinement. During this period the minimum line-averaged density achievable in 0.8 MA deuterium discharges decreased from  $0.9 \times 10^{19} \text{ m}^{-3}$  to  $0.55 \times 10^{19} \text{ m}^{-3}$ .

The recycling coefficient in ohmic discharges, R, is determined from  $\tau_p^*$  and the particle confinement time,  $\tau_p$ , by the equation

$$\tau_p^* = \frac{\tau_p}{1-R} \quad (1)$$

$\tau_p$  as measured by the absolute intensity of the  $D\alpha$  emission is on the order of 0.1 s. Thus, the fastest density decay times, 0.15 - 0.3 s, correspond to a recycling coefficient of  $R < 0.5$ .

Helium discharges with  $I_p = 1.4$  and 1.8 MA were more effective in degassing the limiter than were 0.8 MA deuterium discharges. A few shots in deuterium are required to expel the residual helium, but the succeeding discharges have lower densities than can be achieved following conditioning by deuterium discharges. There are indications that higher current helium discharges are more effective than lower current discharges.

The limiter degassing effect is easily reversed by exposure to higher density deuterium plasmas. An estimated 100 torr-liters ( $7.1 \times 10^{21}$  atoms) of total gas input over a few discharges will increase the recycling coefficient to approximately 1. Deuterium gas-fueled 0.8 MA ohmic discharges with  $\bar{n}_e$  as low as  $1.2 \times 10^{19} \text{ m}^{-3}$  can produce a noticeable degradation.

The limiter degassing is believed to result from desorption of hydrogen from the graphite by energetic carbon and helium ion bombardment. Graphite can absorb hydrogen up to a H/C ratio of 0.4 at room temperature. Spectroscopic measurements and  $Z_{\text{eff}}$  values of six to seven show that the carbon density in degassing discharges is high. Recent measurements by Wampler *et al.* [8] show that bombardment of saturated graphite by carbon, helium, or hydrogen ions with energies of 3, 0.6 and 0.3 keV, respectively (consistent with the edge electron temperature and sheath potential in these discharges) removes 5, 2 and 1 hydrogen atoms per incident ion, the latter case resulting in replacement, with

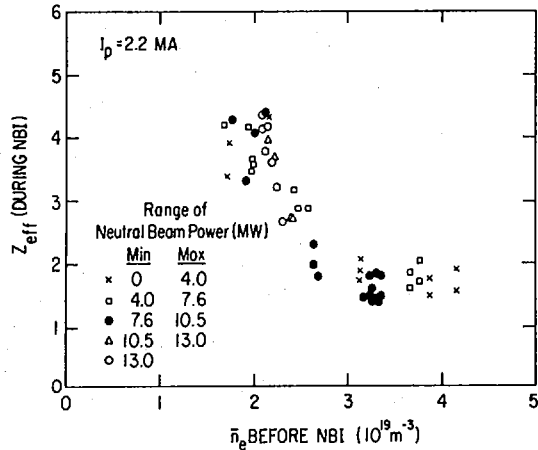


FIG. 3.  $Z_{eff}$  during neutral-beam injection as a function of electron density before injection, sorted by ranges of neutral-beam power. The values are near the pre-NBI  $Z_{eff}$  values, but somewhat reduced owing to neutral-beam fueling.

no net removal of hydrogenic species. Also, the yields for sputtering carbon atoms from graphite are 0.5, 0.09 and 0.025 atoms/ion for these three ions. Thus the degassing process is aided by the low density, high edge temperature, and the resultant high levels of carbon impurities.

### III. Plasma Impurity Concentrations in the Standard Regime

Impurity concentrations and  $Z_{eff}$  have been measured by x-ray and vacuum ultraviolet spectroscopy and visible bremsstrahlung; the total radiated power has been measured by bolometer arrays. These measurements have documented the effectiveness of impurity control techniques, provided quantitative data on the variation of impurities over a wide range of plasma parameters, and provided additional information on impurity sources and impurity production mechanisms [9-11].

The impurity situation in ohmically heated TFTR discharges is discussed in Refs [9-11]. Impurity concentrations were low ( $Z_{eff} = 1.2$ ) at high density, but were significant ( $Z_{eff} = 5-6$ ) at the low-density limit for 2.2 MA plasmas on either the movable or toroidal limiter. Discharges on the toroidal limiter had lower  $Z_{eff}$  at intermediate densities than those on the movable limiter [12]. The low-Z impurities, carbon and oxygen, ranged from about 10% of electron density (at low  $n_e$ ) to 1% (high  $n_e$ ) and were the dominant contributors to  $Z_{eff}$  and radiated power. The ratio of carbon to oxygen was about 10 at low density and 1 at high density. Oxygen increased with density and dominated the radiated power at the high density limit [11]. Metals (Cr, Fe, Ni) were generally negligible contributors to  $Z_{eff}$  and radiated power.

Impurity behavior in 2.2 MA neutral-beam-heated plasmas on the movable limiter with beam power up to 5.6 MW has been discussed previously [11]. In a beam-power scan at constant final density ( $\bar{n}_e = 4.5 \times 10^{19} \text{ m}^{-3}$ ),  $Z_{\text{eff}}$  near the end of the 0.5 s heating pulse increased from less than 2 to about 3 as beam power increased to 5.6 MW. During a discharge, metal and carbon densities remained constant from the pre-beam to the beam-heated phase. Thus, higher  $Z_{\text{eff}}$  at higher power results mainly from the lower pre-beam density (and therefore higher  $Z_{\text{eff}}$ ) required to keep the final density constant. The fraction of total input power radiated decreased from about 50% in the ohmic phase to 30% at a beam power greater than 3 MW.

$Z_{\text{eff}}$  values in 2.2 MA, L-mode beam-power scans on the toroidal limiter also correlated much more strongly with the electron density in the pre-beam ohmic heating phase of discharges than with beam power or with density at the end of injection (Fig. 3). The data, measured by x-ray pulse-height analysis, have been sorted according to ranges of beam power. Low  $Z_{\text{eff}}$  values ( $\leq 2$ ) are achieved during neutral-beam injection (NBI) if the ohmic target plasma is clean ( $\bar{n}_e > 3 \times 10^{19} \text{ m}^{-3}$ ), while higher  $Z_{\text{eff}}$  values during NBI occur if the ohmic plasma is dirty (low density). The trend is similar to that of pre-beam  $Z_{\text{eff}}$  versus  $\bar{n}_e$ , although shifted slightly lower, due to dilution of impurities by neutral-beam fueling.  $Z_{\text{eff}}$  values measured from visible bremsstrahlung emission were on the average 15% higher than the values from pulse-height analysis for most of these shots.

The radiated-power fraction in these L-mode discharges on the toroidal limiter decreased to about 20% for neutral beam powers greater than 10 MW.

#### IV. Impurity Concentrations in Enhanced Confinement Plasmas

The pre-injection target plasmas in enhanced confinement discharges are carbon dominated, with a total  $Z_{\text{eff}}$  of six to eight and a  $Z_{\text{eff}}$  contribution of 0.3 - 1.5 from metals. The carbon concentration is about 15% of the electron density. The deuteron fraction is estimated to be between 10% and 20%, based on the increase in neutron emission following a small gas puff. During neutral beam injection,  $Z_{\text{eff}}$  from visible bremsstrahlung drops to 2-4 (Fig. 4 and earlier data). The earliest enhanced confinement plasmas had  $Z_{\text{eff}}$  values of 2-3 during the beam-heating phase, with a negligible contribution from metals. Subsequent limiter conditioning and plasma operation, spanning 1000 discharges over a period of five weeks, increased the metal levels by a factor of 10, presumably by depositing metals removed from inconel hardware near the limiter onto the graphite surface.

During neutral beam heating, the fueling by the beam neutrals increases the deuteron fraction to 50-60% of electron density and decreases the carbon fraction to 5-8%. The fraction

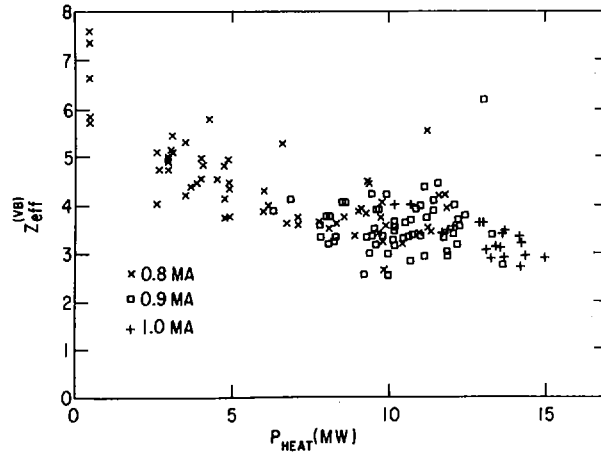


FIG. 4.  $Z_{\text{eff}}$  as a function of total heating power in enhanced confinement discharges.

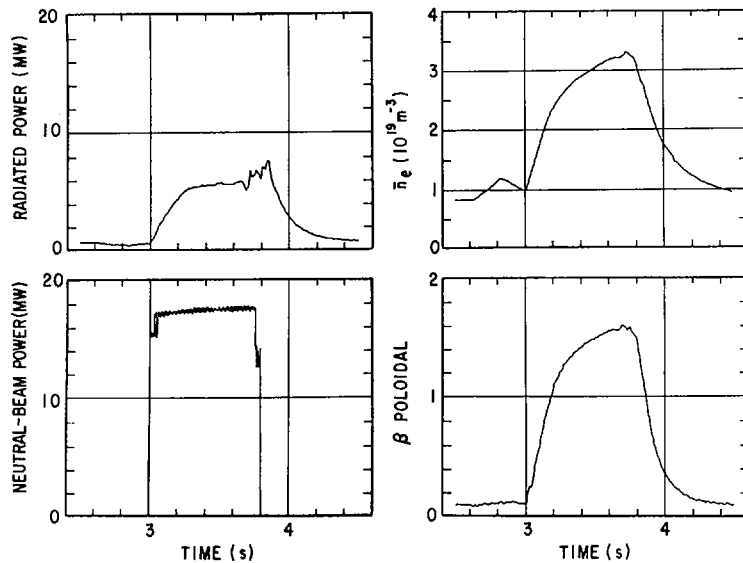


FIG. 5. Total radiated power, line-averaged electron density, neutral-beam power and poloidal beta, as a function of time during a 1.1 MA enhanced confinement discharge with a 0.7 s beam-heating pulse.

of total heating power radiated decreases from 60-70% during the ohmic phase to about 30% for beam powers greater than 10 MW. For longer pulse (0.7 s) beams the total radiated power saturates while electron density and  $\beta_p$  are still rising, as shown in Fig. 5.

The impurity transport during beam heating in enhanced confinement discharges appears to be similar to that during the ohmic phase. Transport rates were inferred from the time evolution of vacuum-ultraviolet lines emitted by germanium injected into the plasma by laser ablation. Comparison of these intensities with numerical impurity transport code predictions [13] yielded a diffusion coefficient (assumed to be radially constant) and convective velocity at the limiter radius of 0.65  $m^2/s$  and 0 - 0.1 m/s, respectively, in the ohmic phase, and 0.75  $m^2/s$  and 0.1 - 0.2 m/s, respectively, during neutral beam injection. The uncertainty in the convective velocity is a factor of 2. The impurity confinement time in both cases was approximately 0.25 s.

#### V. Summary and Conclusions

A disruptive discharge cleaning procedure, in addition to glow- and pulsed-discharge cleaning, was found necessary following atmospheric exposure to remove water vapor from the large-area graphite toroidal limiter and permit satisfactory plasma operation.

Low density deuterium or helium discharges were found to be effective in degassing the limiter, allowing it to pump hydrogen and, thus, reduce recycling and permit improved confinement in neutral-beam-heated discharges. High carbon concentrations and  $Z_{eff}$  appear to aid degassing by causing high edge temperatures and leading to desorption of deuterium by energetic carbon ion bombardment.

Relatively low  $Z_{eff}$  values (about 2) were attained in high density L-mode discharges on the toroidal limiter, with beam powers up to 10 MW, and values of 2.5 - 3 were found at beam powers up to 15 MW. The trends suggest, however, that the purity of the pre-beam target plasma is a more important determinant of impurity concentrations during NBI than is beam power or final density.

Enhanced confinement plasmas are characterized by a  $Z_{eff}$  of six to seven before neutral beam injection and two to four during injection.  $Z_{eff}$  decreases with beam power, presumably due to the dominance of beam fueling in these plasmas.

There is no evidence of significant changes in impurity transport between ohmic and enhanced confinement discharges.

### Acknowledgments

We are grateful to J.R. Thompson and D. Grove for their support. This work was supported by US DOE Contract No. DE-AC02-76-CH03073. The ORNL participants were also supported by US DOE Contract No. DE-AC05-84OR21400 with Martin Marietta Energy Systems, Inc.

### REFERENCES

- [1] STRACHAN, J.D., et al., submitted to Phys. Rev. Lett.
- [2] HAWRYLUK, R.J., et al., paper IAEA-CN-47/A-I-3, these Proceedings, Vol. 1.
- [3] GOLDSTON, R.J., et al., Paper IAEA-CN-47/A-I-4, these Proceedings, Vol. 1.
- [4] DYLLA, H.F., et al., submitted to Nucl. Fusion.
- [5] LA MARCHE, P.H., et al., J. Nucl. Mater. **145&146** (1987).
- [6] MILORA, S.L., et al., paper IAEA-CN-47/A-III-4, these Proceedings, Vol. 1.
- [7] STRACHAN, J., et al., in Controlled Fusion and Plasma Physics (Proc. 12th Europ. Conf. Budapest, 1985), Pt. I, European Physical Society (1985) 339.
- [8] WAMPLER, W., DOYLE, B., BRYCE, D., submitted for publication.
- [9] HILL, K.W., et al., Nucl. Fusion **26** (1986) 1131.
- [10] DYLLA, H.F., et al., J. Nucl. Mater. **145&146** (1987).
- [11] STRATTON, B.C., et al., submitted to Nucl. Fusion.
- [12] BELL, M.G., et al., Plasma Phys. Contr. Fusion **28** (1986) 1329.
- [13] STRATTON, B.C., et al., J. Nucl. Mater. **145&146** (1987).

### DISCUSSION

F.C. SCHÜLLER: It is normally accepted that the high density limit for disruptions decreases with increasing  $Z_{\text{eff}}$ . You quote for the high density Ohmic discharges a  $Z_{\text{eff}}$  which is considerably lower than that in JET, whilst your density limit is lower. Do you get 100% radiation just before disruption?

K.W. HILL: In Ohmic discharges, the high density limit in TFTR is higher than that in JET; however, the Murakami parameters are comparable. The good agreement in the  $Z_{\text{eff}}$  determination between the various diagnostics, as described in the paper, gives us confidence in our low values of  $Z_{\text{eff}}$  at high density. At the density limit the power radiated is about 100%. The question then arises whether the usual Murakami/Hugill parameter coupled with  $Z_{\text{eff}}$  determines the operating boundary accurately. Perhaps the operational limit depends, in addition, on plasma elongation and on the toroidal field — in a manner other than that implied by the relationship given by the Murakami/Hugill parameter.

## IMPURITY AND MHD BEHAVIOUR IN JT-60 DIVERTOR DISCHARGES

JT-60 TEAM

*(Presented by H. Takeuchi)*

T. Abe, H. Aikawa, H. Akaoka, H. Akasaka, M. Akiba, N. Akino, T. Akiyama, T. Ando, K. Annoh, N. Aoyagi, K. Arakawa, M. Araki, K. Arimoto, M. Azumi, S. Chiba, M. Dairaku, N. Ebisawa, T. Fujii, T. Fukuda, H. Furukawa, K. Hamamatsu, K. Hayashi, M. Hara, K. Haraguchi, H. Hiratsuka, T. Hirayama, S. Hiroki, K. Hiruta, M. Honda, H. Horiike, R. Hosoda, N. Hosogane, Y. Iida, T. Iijima, K. Ikeda, Y. Ikeda, T. Imai, T. Inoue, N. Isaji, M. Isaka, S. Ishida, N. Itige, T. Ito, Y. Ito, A. Kaminaga, M. Kawai, Y. Kawamata, K. Kawasaki, K. Kikuchi, M. Kikuchi, H. Kimura, T. Kimura, H. Kishimoto, K. Kitahara, S. Kitamura, A. Kitsunezaki, K. Kiyono, N. Kobayashi, K. Kodama, Y. Koide, T. Koike, M. Komata, I. Kondo, S. Konoshima, H. Kubo, S. Kunieda, S. Kurakata, K. Kurihara, M. Kuriyama, T. Kuroda, M. Kusaka, Y. Kusama, S. Maehara, K. Maeno, S. Mase, S. Matsuda, M. Matsukawa, T. Matsukawa, M. Matsuoka, N. Miya, K. Miyati, Y. Miyo, K. Mizuhashi, M. Mizuno, R. Murai, Y. Murakami, M. Muto, M. Nagami, A. Nagashima, K. Nagashima, T. Nagashima, S. Nagaya, H. Nakamura, Y. Nakamura, M. Nemoto, Y. Neyatani, S. Niikura, H. Ninomiya, T. Nishitani, H. Nomata, K. Obara, N. Ogiwara, Y. Ohara, K. Ohasa, T. Ohga, H. Ohhara, M. Ohkubo, T. Ohshima, K. Ohta, M. Ohta, M. Ohtaka, Y. Ohuchi, A. Oikawa, H. Okumura, Y. Okumura, K. Omori, S. Omori, Y. Omori, T. Ozeki, M. Saigusa, K. Sakamoto, A. Sakasai, S. Sakata, M. Satou, M. Sawahata, M. Seimiya, M. Seki, S. Seki, K. Shibanuma, R. Shimada, K. Shimizu, M. Shimizu, Y. Shimomura, S. Shinozaki, H. Shirai, H. Shirakata, M. Shitomi, K. Sugauma, T. Sugie, T. Sugiyama, H. Sunaoshi, K. Suzuki, M. Suzuki, M. Suzuki, N. Suzuki, S. Suzuki, Y. Suzuki, H. Takahashi<sup>1</sup>, M. Takahashi, S. Takahashi, T. Takahashi, M. Takasaki, M. Takatsu, A. Takeshita, H. Takeuchi, S. Tamura, S. Tanaka, K. Tani, M. Terakado, T. Terakado, K. Tobita, T. Tokutake, T. Totsuka, N. Toyoshima, H. Tsuda, T. Tsugita, S. Tsuji, Y. Tsukahara, M. Tsuneoka, K. Uehara, M. Umehara, Y. Uramoto, H. Usami, K. Ushigusa, K. Usui, J. Yagyu, K. Yamada, M. Yamamoto, O. Yamashita, Y. Yamashita, K. Yano, T. Yasukawa, K. Yokokura, H. Yokomizo, H. Yoshida, M. Yoshikawa, Y. Yoshinari, R. Yoshino, I. Yonekawa, K. Watanabe

Naka Fusion Energy Research Establishment,  
Japan Atomic Energy Research Institute,  
Naka-machi, Naka-gun, Ibaraki-ken,  
Japan

<sup>1</sup> Princeton Plasma Physics Laboratory, Princeton University, NJ, USA.

### Abstract

#### IMPURITY AND MHD BEHAVIOUR IN JT-60 DIVERTOR DISCHARGES.

The diffusion coefficient ( $D_A$ ) and the inward peaking factor ( $C_V$ ) of titanium are estimated from the experimental evolution of the titanium lines and the calculational result of a simulation code:  $D_A = 1.0 \text{ m}^2 \cdot \text{s}^{-1}$  and  $C_V = \sim 0$  for ohmically heated plasmas and  $D_A = 0.6\text{--}0.8 \text{ m}^2 \cdot \text{s}^{-1}$  and  $C_V = 0$  to 1 for neutral beam (NB) injection heated plasmas. No difference in titanium transport is observed with respect to the direction (co- or counter-) of NB injection. There is no strong titanium pinch at the centre in divertor discharges, either with or without sawtooth oscillation. — In discharges with Ohmic and NB heating, various MHD activities are observed. The transition from single to compound sawteeth took place at a resistive diffusion time of  $\tau_R = \mu_0 r_i^2 / \eta \geq 3.5 \text{ s}$ . It is confirmed that the inversion radius observed in a wide range of  $q_{\text{eff}} = 2.6\text{--}6$  depends linearly on  $1/q_{\text{eff}}$ , but is independent of density, radius, plasma current or heating power.

## 1. INTRODUCTION

To attain an equivalent breakeven plasma condition, impurities and MHD activity are the most important factors resulting in a degradation of confinement properties. A single null poloidal divertor has been installed in JT-60 in order to eliminate the impurities from the main plasma; the MHD activity in the JT-60 divertor configuration was investigated.

Plasma heating experiments with a neutral beam (NB) heating power of up to 20 MW were started in August 1986 with an injection energy of  $E_b = 50\text{--}70 \text{ keV}$ , a beam pulse length of up to 3 s, by eight co- and six counter-injection units with nearly perpendicular angle ( $78^\circ$  to the magnetic axis). Hydrogen or helium plasmas in divertor or limiter configurations in the range of  $1 \leq I_p \leq 2 \text{ MA}$  and  $1.9 \leq B_t \leq 4.5 \text{ T}$  were used as the target. This paper reports impurity and relevant MHD behaviour of ohmically and NB heated plasmas in divertor discharges.

In Section 2, quantity and species of the impurities and their behaviour are described. Section 3 is devoted to the MHD behaviour of compound sawtooth and fluctuation during NB heating. These results will be discussed and summarized in the last section.

## 2. IMPURITY BEHAVIOUR

Figure 1 shows typical spectra in the wavelength range of 5 to 500 Å measured by a unit type flat field grazing incidence spectrometer in a divertor hydrogen discharge with  $B_t = 4.5 \text{ T}$  and  $I_p = 2 \text{ MA}$ . The major impurities were identified to be oxygen, carbon and titanium, which were the coating materials of the first wall. A small amount of nickel, iron and chromium was observed in divertor discharges; molybdenum lines were also identified in limiter discharges.

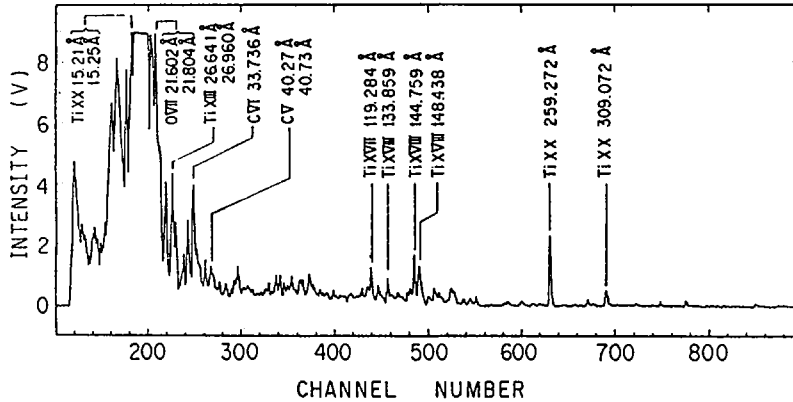


FIG. 1. Typical VUV spectrum recorded by unit type spectrometer, integrated over 20 ms for  $B_t = 4.5$  T,  $I_p = 2$  MA in divertor discharge.

The amount of titanium was estimated from soft X-ray measurements. In ohmically heated discharges, the amount of titanium was around  $1 \times 10^{-3}\%$  and  $8 \times 10^{-3}\%$  at  $\bar{n}_e = 2 \times 10^{13} \text{ cm}^{-3}$  in hydrogen and helium discharges, respectively. The ratio of titanium to line averaged electron density decreased with the increase in electron density. For NB heated hydrogen plasmas, the ratio of titanium to electron density became about twice that in ohmically heated plasmas. And the quantities of nickel, iron and chromium were below 1/10 to 1/100 of that of titanium.

The amount of light impurities in hydrogen discharges was measured by a Rutherford particle scattering technique, using a diagnostic helium beam with an energy of 170 keV. This scattering technique is insensitive to metal impurities, for the present plasma parameters, and does not distinguish between light impurity species. The ratio of light impurity to proton density was 1.2% or 2.4% if the species were assumed to be totally oxygen or carbon, respectively.  $Z_{\text{eff}}$  as obtained by this method was 1.5, which was equal to the values obtained from visible bremsstrahlung and simple Spitzer resistivity. Therefore, it was suggested that light ions were the dominant impurities in JT-60, although the main species contributing to  $Z_{\text{eff}}$  were not yet identified by the spectroscopic measurements.  $Z_{\text{eff}}$  decreased with the increase in electron density, and the  $Z_{\text{eff}}$  values of NB heated plasmas were slightly higher than those of ohmically heated plasmas.

The metal impurity (titanium) in plasmas in the limiter configurations is much higher than that in divertor configurations; this difference was exploited to intentionally inject titanium into the plasma. Specifically, when a titanium injection into a divertor discharge was needed the configuration was converted from a divertor to a limiter configuration within 50 ms, remained in the limiter configuration for 50 ms and then again became a divertor configuration.

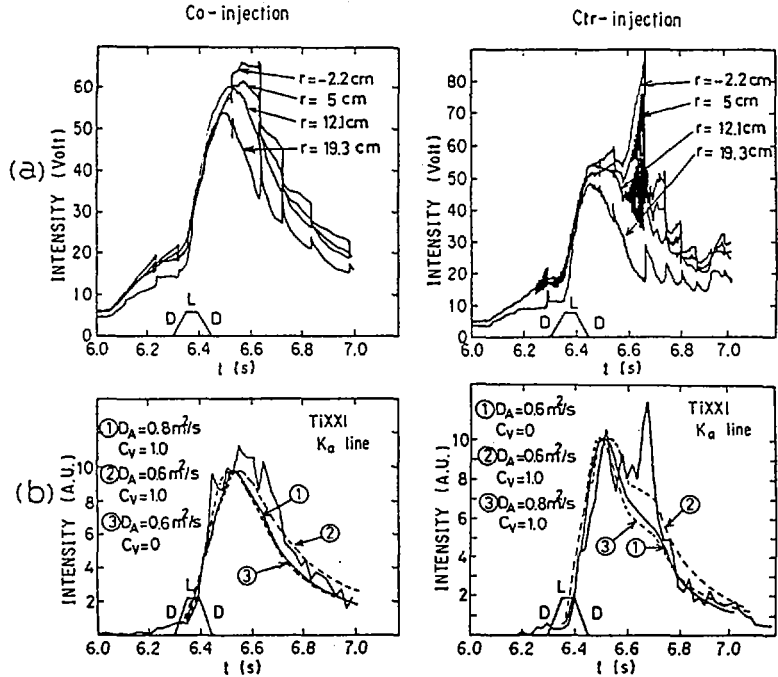


FIG. 2. Comparison of evolutions of (a) soft X-ray, (b) Ti XXI with co- and counter-NB injection. Titanium is injected intentionally by switching from divertor to limiter configuration and back to divertor configuration.

Figure 2 shows the time evolution of 15-channel soft X-ray diode array signals and the Ti XXI line intensity as measured by a Johan type crystal spectrometer. In this figure, a NB heating pulse of 7.7 to 8.4 MW, either in co- or counter-direction, was started at 6.0 s from the start of the discharge, and the titanium injection procedure of 150 ms as described above was started at 6.3 s. The targets were hydrogen plasmas with  $\bar{n}_e \cong 5 \times 10^{19} \text{ m}^{-3}$ ,  $I_p = 1.5 \text{ MA}$  and  $B_t = 4.5 \text{ T}$ . The Ti XXI line intensity decreased with a decay time of  $\sim 200 \text{ ms}$  if the minor disruptions were smoothed out, and there was no difference in decay time for different injection angles. A large  $m = 1/n = 1$  oscillation was observed as the precursor of internal disruptions in the discharges with counter-injection. The toroidal rotation speed of the plasma was also calculated with MHD oscillation data, assuming an  $m = 1/n = 1$  mode; the results were  $\sim 4 \times 10^4 \text{ m} \cdot \text{s}^{-1}$  and  $\sim 8 \times 10^4 \text{ m} \cdot \text{s}^{-1}$  for 8.4 MW co- and 7.7 MW counter-injection, respectively.

The decay of the Ti XXI line intensity was simulated by a 1-D impurity transport code [1]. The best fittings were obtained with  $D_A = 0.8 \text{ m}^2 \cdot \text{s}^{-1}$  and  $C_V = 1$  for the co-injection case, and with  $D_A = 0.6 \text{ m}^2 \cdot \text{s}^{-1}$  and  $C_V = \sim 0$  for the counter-injection case. Considering that  $D_A = 1.0 \text{ m}^2 \cdot \text{s}^{-1}$  and  $C_V = \sim 0$  for

ohmically heated discharges [2], it was concluded that there was no significant difference in impurity transport among these three cases. At the same time, it was suggested that the impurity transport was not affected by a toroidal rotation of  $(4-8) \times 10^4 \text{ m}\cdot\text{s}^{-1}$ .

### 3. MHD BEHAVIOUR

In the current flat top phase, the onset of sawtooth oscillations was normally observed around 2–4 s after breakdown. These sawteeth were observed in the soft X-ray, ECE (electron cyclotron emission) and line electron density signals in both hydrogen and helium discharges. As is shown in Fig. 3(a), large  $m = \text{odd}$  successor and precursor oscillations were observed in the local and full reconnection phases during a compound sawtooth. The frequency of these oscillations was in the range of 0.2–1.2 kHz, and the density fluctuations were found to be clearly correlated to the soft X-ray signals. The repetition times of the normal sawtooth oscillation discharges in ohmically heated plasmas were 25–30 ms for  $I_p = 1 \text{ MA}$  and 50–80 ms for  $I_p = 2 \text{ MA}$ , as is shown in Fig. 4, and the compound sawteeth with a repetition time of 70–140 ms were also frequently observed in discharges with a large plasma current ( $I_p > 1.5 \text{ MA}$ ).

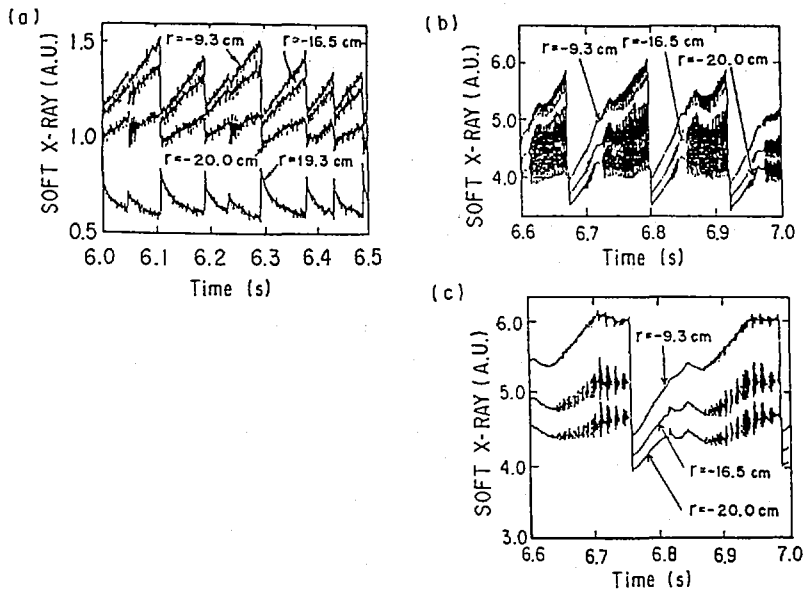


FIG. 3. Characteristics of JT-60 MHD behaviour. (a) Soft X-ray signal in ohmically heated divertor discharge of hydrogen gas. Soft X-ray signal of (b) continuous and (c) MHD burst during NB heating.

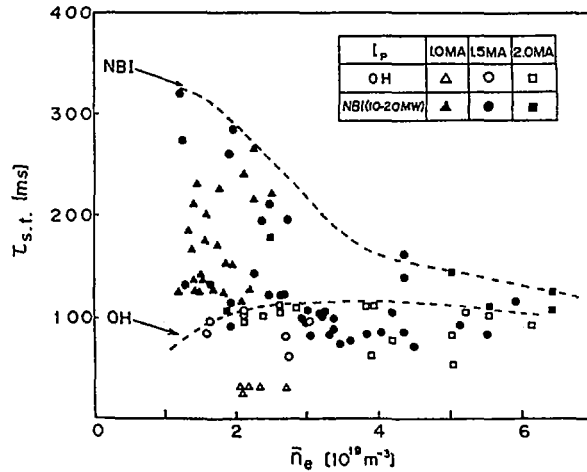


FIG. 4. Dependence of sawtooth period  $\tau_{st}$  on line averaged electron density in divertor discharge with Ohmic and NB heating.

The transition of the normal sawtooth to the compound oscillation one was analysed by the 1-D tokamak code incorporating the multi-tearing instability. The onset condition for the compound sawtooth oscillation in JT-60 given by this simulation was that the resistive diffusion time  $\tau_R > 3.0$  s. This value nearly agreed with the experimental results ( $\tau_R \geq 3.5$  s) of the critical plasma current for the onset of the compound oscillation and was also consistent with the experimental result that the compound oscillation was only rarely observed in helium discharges.

Except for dirty discharges, enhanced sawtooth activity as shown in Fig. 3(b) was observed in discharges with high power NB heating. Magnetic fluctuations were measured with a magnetic probe array of 11 coils located at about 5 cm from the limiter surface. The fluctuation level of  $\delta B_p/B_p$  was higher than 0.02%, with a frequency of  $\sim 1$  kHz. The mode was identified as  $m = 4$  and synchronized with the central  $m = \text{odd}$  oscillation.

MHD bursts as shown in Fig. 3(c) were observed for a NB heating power of over 17 MW and a beam energy of over 70 keV. The central fluctuation observed with soft X-ray diodes was a compound of an  $m = \text{odd}$  mode with 1 kHz and a higher mode fluctuation. In one of two cases, the  $m = 3$  magnetic fluctuation of 4 kHz was synchronized with the higher frequency mode of the central fluctuation, and in the other case the magnetic fluctuation was synchronized with the lower frequency mode of the central fluctuation. Considering that the toroidal rotation frequency, from MHD measurements, was comparable to the trapped particle precession frequency and that the central deposition of the intense neutral beam results in the generation of deeply trapped fast ions, and also considering the relatively high poloidal beta in these discharges, it turned out that the MHD bursts were a result of mode-particle

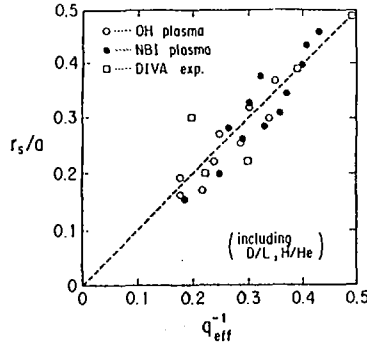


FIG. 5. Dependence of inversion radius  $r_s$  on  $1/q_{\text{eff}}$ , where

$$q_{\text{eff}} = \frac{2\pi a^2 B_t}{\mu_0 I_p R} \left[ 1 + \left( \frac{a}{R} \right)^2 \left\{ 1 + \frac{1}{2} (\beta_p + \ell_l/2)^2 \right\} \right]$$

resonance such as the fishbone [3]. However, the inferred flux of fast ions ejected from the plasma by the instability was not detected with the charge exchange neutral particle analysers, probably because of a low sampling rate and the viewing angle of the analyser which is looking at the plasma centre and is insensitive to the ejected fast ions. No significant effect of this instability on plasma confinement has been observed so far, but more investigations of this instability are needed in the future.

Figure 4 shows the sawtooth repetition time  $\tau_{\text{st}}$  as a function of the line averaged electron density for discharges with Ohmic and NB heating. No difference in  $\tau_{\text{st}}$  was observed between hydrogen and helium plasmas. Apparently, the repetition time for the ohmically heated plasmas is almost independent of the electron density, the enhancement of the repetition time due to NB heating was longer in the low density regime and the repetition time for NB heated plasmas approached that of ohmically heated plasmas at  $\bar{n}_e > 5 \times 10^{19} \text{ m}^{-3}$ .

Figure 5 shows the normalized inversion radius of the sawtooth  $r_s/a$  as a function of the inverse of the safety factor  $1/q_{\text{eff}}$ , where  $r_s$ ,  $a$  and  $q_{\text{eff}}$  are the inversion radius, the plasma minor radius and the safety factor, respectively. The verified data of JT-60 for discharges with various parameters are plotted in Fig. 5. The DIVA data [4] are also plotted in the figure. Figure 5 indicates that  $r_s/a$  depends only on  $1/q_{\text{eff}}$  and is independent of all other parameters such as plasma configuration, heating power, ion species, etc.

#### 4. DISCUSSION AND SUMMARIES

Clean plasmas were obtained in divertor configurations, and the major impurities were identified to be oxygen, carbon and titanium. The diffusion coefficient and

the peaking factor, were estimated to be  $D_A = 1.0 \text{ m}^2 \cdot \text{s}^{-1}$ ,  $C_V \sim 0$  in ohmically heated plasmas and  $D_A = 0.8 \text{ m}^2 \cdot \text{s}^{-1}$ ,  $C_V \sim 1$  and  $D_A = 0.6 \text{ m}^2 \cdot \text{s}^{-1}$ ,  $C_V \sim 0$  in discharges with sawtooth oscillation with co- and counter- NB injection, respectively. The difference in the direction of the NB injection did not bring about any significant difference in titanium impurity transport.

Considering the values of  $D_A$  and  $C_V$  in ohmically heated discharges without sawteeth, it is indicated that there was no significant difference in the impurity transports between ohmically heated plasmas without sawteeth and NB heated plasmas with sawteeth. The difference in the heating method or the existence of sawtooth oscillations does not affect the above conclusion. In NB heated plasmas, magnetic fluctuations with  $\delta B_p/B_p \geq 0.02\%$  do not seem to enhance the impurity influx, probably because of the sufficient thickness of the scrape-off layer.

The sawteeth had a compound structure in high current discharges and tended to have large  $m = 1$ , continuous oscillations or large MHD bursts in NB heated discharges. The transition from the normal to the compound sawtooth took place at a resistive diffusion time of  $\tau_R \geq 3.5 \text{ s}$ . The repetition time of the sawteeth in ohmically heated plasmas was almost constant, for a wide range of plasma densities. The repetition time in the NB heated plasmas was enhanced in the low plasma density region and tended to approach that of the ohmically heated plasmas with high plasma density. The inversion radius of the sawteeth was determined experimentally in a wide range of parameters,  $q_{\text{eff}} = 2.6\text{--}6$ ,  $\bar{n}_e = (1\text{--}9) \times 10^{19} \text{ m}^{-3}$ ,  $I_p = 1\text{--}2 \text{ MA}$ ,  $P_{\text{NB}} = 5\text{--}20 \text{ MW}$  in divertor and limiter configurations. The normalized inversion radius  $r_s/a$  depends only on  $1/q_{\text{eff}}$  and is independent of all other parameters.

### ACKNOWLEDGEMENTS

The authors wish to thank the members of JAERI who have contributed to the JT-60 project throughout its progress. They further wish to express their gratitude to Drs S. Mori, Y. Iso, and K. Tomabechi for continued encouragement and support.

### REFERENCES

- [1] HIRAYAMA, T., et al., in Plasma-Surface Interactions in Controlled Fusion Devices (Proc. 7th Int. Conf. Princeton, 1986) (to be published).
- [2] HIRAYAMA, T., et al., Rep. JAERI-M 86-161 (October 1986).
- [3] McGUIRE, K., et al., Phys. Rev. Lett. **50** (1983) 891.
- [4] DIVA GROUP, Nucl. Fusion **20** (1980) 271.

### DISCUSSION

R.J. GOLDSTON: You discussed oscillations at high beam power which you thought might be related to PDX fishbones. Could you tell us how their frequency is related with the fast ion precession frequency?

H. TAKEUCHI: The fast ion precession frequency is comparable to the toroidal rotation frequency from MHD measurements.

K. McGUIRE: I noticed that your soft X-ray signal showed a very large increase in the first second. Do you have a large influx of impurities during this time?

H. TAKEUCHI: The JT-60 discharge started with the limiter configuration, and at 0.33 s the limiter configuration was switched to divertor type configuration. After the switching, the impurity flux was gradually reduced by the divertor effect.



## DENSITY LIMIT AND IMPURITY TRANSPORT INVESTIGATIONS IN DITE TOKAMAK

J. ALLEN, G.E. AUSTIN, K.B. AXON, R. BARNESLEY<sup>1</sup>,  
M. DUNSTAN, D.N. EDWARDS, K.D. EVANS<sup>1</sup>,  
S.J. FIELDING, D.H.J. GOODALL, W. HAN, N.C. HAWKES,  
J. HUGILL, P.C. JOHNSON, G.M. McCracken,  
G.F. MATTHEWS, W. MILLAR, N.J. PEACOCK,  
C.S. PITCHER, J. PRITCHARD, A. SYKES,  
M.F. TURNER, J.P. WEBBER  
Euratom-UKAEA Fusion Association,  
Culham Laboratory,  
Abingdon, Oxfordshire,  
United Kingdom

### Abstract

#### DENSITY LIMIT AND IMPURITY TRANSPORT INVESTIGATIONS IN DITE TOKAMAK.

The processes leading to disruption with increasing density have been studied. The discharge remains in thermal equilibrium but there is a slow profile contraction as the density is raised because of a deterioration in edge confinement relative to the centre. This is only partly explained by radiation losses. — The central confinement time of impurities injected by laser ablation has been measured. At high density in ohmically heated discharges, it can be varied by more than a factor of five by changing the gas feed rate. The largest values occur for refuelling by recycling only. Substantial differences also occur with co- and counter-neutral beam injection, which are not sensitive to the gas feed rate in this case. These differences cannot be mainly ascribed to plasma rotation because they are not removed by switching on the bundle divertor, which reduces the rotation speed by an order of magnitude. An accumulation of intrinsic impurities is observed in discharges with long impurity confinement times. The effects described are much reduced or absent at low density.

### 1. INTRODUCTION

Recent experimental work on DITE tokamak has concentrated on studies of the limit set by disruption at high density and the confinement of impurities with and without the bundle divertor. The main machine parameters used were: major radius,  $R=1.17\text{m}$ ; poloidal carbon limiter radius =  $0.26\text{m}$ ; adjustable rail limiter and divertor separatrix radius =

---

<sup>1</sup> University of Leicester, Leicester, UK.

0.21m; toroidal field,  $B_T = 2.0-2.6T$ ; plasma current,  $I_p = 0.1-0.25MA$ ; tangential neutral H beam injection,  $P_{inj} \lesssim 1.6MW$  at  $E = 25$  keV. The working gas was generally helium for highest density operation, with some lower density work in deuterium.

Preliminary results on the density limit were given previously [1]. Here, we summarise the main conclusions of more recent work. Studies of impurity transport were intended to complement previous work on energy and particle exhaust in diverted discharges [2] and to explain the generally lower intrinsic impurity levels observed with both ohmic and beam heating. Non-diverted discharges used for comparison purposes showed some interesting new behaviour which is reported in Section 3.

## 2. INVESTIGATION OF THE DENSITY LIMIT

Disruption at high density is almost invariably preceded by rapidly growing poloidal field oscillations of low mode number. The aim of the present study is to identify the processes leading to their destabilisation: in particular to determine whether there is a radial collapse of the discharge due to thermal instability or a sudden change in transport due to the onset of other instabilities, such as ballooning modes. Relatively high  $q$ -values of 4-8 were employed to avoid effects due to operation near  $q=3$  and  $q=2$ .

In ohmically heated discharges there is a gradual narrowing of the plasma current and temperature profiles. A reduction in peripheral temperature is measured by probes and Marfes [3] may appear, especially in helium. The soft X-ray sawtooth inversion radius increases and the radial positions of peaks in line radiation from low charge states of carbon and oxygen ions move inwards. These last two effects are illustrated in Fig.1. For  $q \geq 6$  profile narrowing leads to the appearance of detachment from the limiter [4]. However, there is no rapid profile contraction due to an unstable thermal equilibrium. Detached discharges can be maintained for times  $> 20 \tau_E$ .

Disruption is preceded by a rapid growth ( $\gamma \geq 10^3 \text{ s}^{-1}$ ) in the amplitude of poloidal field fluctuations, usually

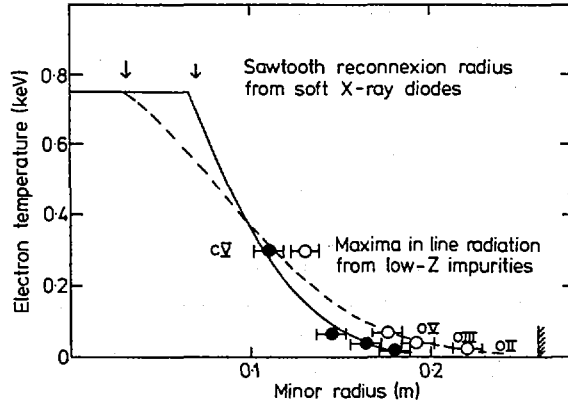


FIG. 1. Profile narrowing in deuterium discharge at  $I_p = 102$  kA,  $B_T = 2.5$  T, as evidenced by SXR and impurity line radiation. Curves are model profiles consisting of truncated Gaussians with the same total Spitzer resistance. For line radiation data, abscissa represents excitation energy. ---,  $\circ - n_e = 1.5 \times 10^{19} \text{ m}^{-3}$ ; —,  $\bullet - n_e = 2.7 \times 10^{19} \text{ m}^{-3}$ .

following sawtooth relaxation. The principal mode numbers are  $m=2$ ,  $n=1$  with a smaller component at 3,2 and possibly others. Estimated pressure gradients are at least a factor of 2 too small to destabilise ideal ballooning modes.

Profile narrowing may be partly explained by radiation losses, which are relatively stronger in the periphery. A numerical simulation [5] assuming constant thermal conductivity, increased  $100 \times$  for  $q < 1$ , and coronal radiation losses from 0.1% Fe, 1% O and 2% C shows gradual profile contraction due to increasing radiation loss as the density is increased. The  $q=2$  surface is typically unstable to a tearing mode but, at low density, flattening of the current density across the magnetic island limits its growth. At a critical density the solution becomes non-linearly unstable, with oscillating and overlapping islands from 2,1 and 3,2 modes. This model shows that radiation losses of  $\sim 75\%$  at  $q=4$  can indeed produce sufficient contraction to destabilise tearing modes to the point of disruption (overlapping of 2,1 and 3,2 modes) without producing thermal instability. It is deficient in predicting a 2,1 tearing mode island at low density which is not observed.

The experimentally measured radiation loss at disruption is ~65% at  $q=4$  rising to ~80% at  $q>6$ . However, the limiters receive only about 10% of the input power, the remainder being so far unaccounted for. Line radiation from a large Marfe indicates local temperatures in the range 5-15eV and can account for up to 50% of the total radiation. A substantial fraction of the input power must be conducted to the periphery of the discharge in this case to support the losses in the Marfe. Attempts to raise the peripheral temperature by applying neutral beam injection heating produce instead an increase in radiation from the Marfe. The density limit is increased but not indefinitely. At  $q=4$  the Murakami parameter increases from 2.2 to 4.0 in deuterium and from 3.8 to 5.3 in helium, with up to 1.5 MW of neutral beam power. The Marfe can be avoided by adjusting the plasma position in the limiter aperture but this does not affect the density limit appreciably. It appears to be a symptom of low edge temperature rather than the cause of it.

In detached discharges the Marfe is usually absent. However, probe measurements of Mach number inside the limiter radius, which show no appreciable flow in normal discharges, reveal substantial flow along the magnetic field (up to Mach 0.4) in detached discharges. These measurements indicate large scale convection in the peripheral plasma whose flow pattern however, could not be fully explored with the existing probes.

### 3. IMPURITY TRANSPORT IN NON-DIVERTED DISCHARGES

#### 3.1 Experimental method

The transport of impurities was investigated using pulsed sources of impurity, principally aluminium introduced by laser ablation. A Bragg X-ray spectrometer [6] yielded most of the spatial, temporal and spectral survey information about central impurities. Additional data was provided by instruments covering the ultraviolet and visible spectral regions and by two orthogonal soft X-ray cameras and a bolometer camera.

Spatial scans show that Al XII and Al XIII emission lines originate from the discharge centre. We find that  $T_e(o)$  varies little during the period of measurement and thus the rate of decay of either line, after correction for the density variation, provides a direct measurement of the central impurity confinement time,  $\tau_{imp}$ .

### 3.2 Ohmically heated discharges

A new result is the strong dependence of  $\tau_{imp}$  on the discharge dynamics at high density [7]. Fig.2 shows  $\tau_{imp}$  versus  $\bar{n}_e$  for two density scans in helium. In one scan  $\bar{n}_e$  was maintained approximately constant by recycling.  $\tau_{imp}$  increases with  $\bar{n}_e$  and reaches values in excess of 150ms. At high density an accumulation of intrinsic impurities is deduced from the soft X-ray and bolometer camera data, similar to that seen on Pulsator [8] and more recently in B-regime discharges on T-10 [9]. In the second scan  $\bar{n}_e$  was ramped by additional gas feed during the period of measurement. At low density  $\tau_{imp}$  is not affected but it reaches a maximum and then decreases as  $\bar{n}_e$  is raised. The latter dependence is similar to

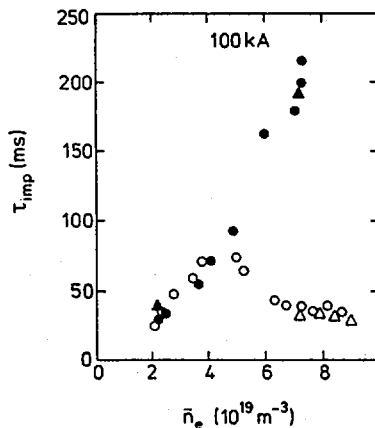


FIG. 2. Variation of impurity confinement time with mean line of sight density for aluminium injection in Ohmic limiter discharges.  $\circ$ ,  $\Delta$  — rising density ( $d\bar{n}_e/dt > 1.5 \times 10^{20} \text{ m}^{-3}\cdot\text{s}^{-1}$ );  $\bullet$ ,  $\blacktriangle$  — constant density ( $d\bar{n}_e/dt < 2.5 \times 10^{19} \text{ m}^{-3}\cdot\text{s}^{-1}$ ).  $\circ$ ,  $\bullet$  — Al XII;  $\Delta$ ,  $\blacktriangle$  — Al XIII.

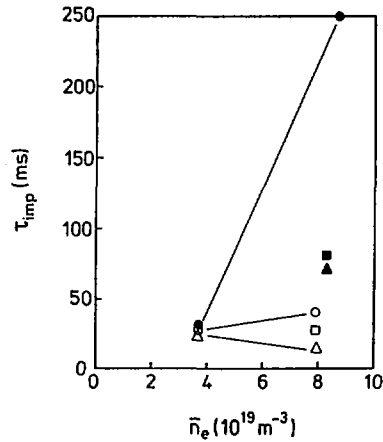


FIG. 3. Variation of impurity confinement time with mean line of sight density for aluminium injection in neutral beam heated limiter discharges.  $\circ$ ,  $\square$ ,  $\triangle$  — co-injection;  $\bullet$ ,  $\blacksquare$ ,  $\blacktriangle$  — counter-injection.  $\circ$ ,  $\bullet$  — 0.4 MW;  $\square$ ,  $\blacksquare$  — 0.8 MW;  $\triangle$ ,  $\blacktriangle$  — 1.1 MW.

that in Alcator, which resulted in a scaling for  $\tau_{\text{imp}}$  independent of  $\bar{n}_e$  [10]. The density at which the two scans diverge is about 50% of the disruptive limit and increases by a factor of 1.5 when the current is raised from 100kA to 150kA. In spite of the factor of five variation in  $\tau_{\text{imp}}$  at high density, there is no indication of corresponding changes in energy transport, as observed in T-10 [9]; and there is no change in the period of sawtooth oscillations, which is approximately proportional to  $\bar{n}_e$ .

### 3.3 Beam heated discharges

The variation of  $\tau_{\text{imp}}$  with  $\bar{n}_e$  in discharges heated by co- and counter-injection is shown in Fig.3. In this case refuelling by the beams cannot be avoided and additional gas feed does not affect  $\tau_{\text{imp}}$ . Toroidal rotation speeds of  $\sim 10^5 \text{ ms}^{-1}$  are found, decreasing with increasing density. At low density co- and counter-injection give similar values for  $\tau_{\text{imp}}$ , as observed on PLT [11]. However, at high density, counter-injection gives higher values of  $\tau_{\text{imp}}$  than co-injection, as seen on ISX-B [12], and  $\tau_{\text{imp}}$  decreases, for both directions, as the injection power is raised.

## 4. IMPURITY BEHAVIOUR WITH BUNDLE DIVERTOR

### 4.1 Ohmically heated discharges

The confinement of injected impurities in diverted discharges is broadly similar to that in limiter discharges. The highest values of  $\tau_{imp}$  again occur without gas feed, which results in a falling density due to particle exhaust. The amount of injected impurity reaching the centre is not reduced by the divertor, thus the reduction of intrinsic impurity content [2] is not explained by a screening effect. It is consistent with a decrease in impurity generation at the walls and limiters due to the divertor exhaust.

### 4.2 Beam heated discharges

At high density, diverted plasmas have somewhat larger values of  $\tau_{imp}$  for co-injection, but a substantial difference between co- and counter-injection remains. Since the divertor field reduces the speed of rotation produced by injection by an order of magnitude [13] it is clear that rotation is not the only factor producing this difference.

## 5. CONCLUSIONS

### 5.1 Density limit

Disruption at high density is preceded by a gradual narrowing of the temperature and current profiles, while the discharge remains in thermal equilibrium. Disruption is immediately preceded by a rapidly growing 2/1 mode. Profile contraction is partly explained by radiation losses but there is evidence that increased peripheral transport losses also play a role.

### 5.2 Impurity transport

At high density,  $\tau_{imp}$  is strongly affected by refuelling and by the direction (and magnitude) of neutral beam injection. With no gas feed or with counter-injection large

values of  $\tau_{imp}$  and accumulation of intrinsic impurities are observed. These effects are reduced or absent at low density.

Application of the divertor has no significant effect on  $\tau_{imp}$  in ohmically heated discharges. The toroidal rotation produced by beam injection is reduced by an order of magnitude, however substantial differences in  $\tau_{imp}$  for co- and counter-injection remain. Thus the role of rotation in impurity transport remains to be clarified.

Although the variation in  $\tau_{imp}$  in high density ohmically heated discharges is produced experimentally by changes in edge conditions, the effect appears to be associated with the central transport of background plasma rather than with edge processes.

#### ACKNOWLEDGEMENTS

We would like to acknowledge the contribution of D. Bell, R.W. Storey and the operations team in maintaining and operating the DITE experiment and neutral beam injectors.

#### REFERENCES

- [1] ALLEN, J.M., et al., Plasma Phys. Control. Fusion **28** (1986) 101.
- [2] JOHNSON, P.C., et al., in Plasma Physics and Controlled Nuclear Fusion Research 1984 (Proc. 10th Int. Conf. London, 1984), Vol. 1, IAEA, Vienna (1985) 239.
- [3] LIPSCHULTZ, B., et al., Nucl. Fusion **24** (1984) 977.
- [4] McCRACKEN, G.M., et al., to be published in J. Nucl. Mater. (1987).
- [5] HOPCRAFT, K.I., TURNER, M.F., Phys. Rev. Lett. **56** (1986) 2372.
- [6] BARNSLEY, R., et al., Rev. Sci. Instrum. **57** (1986) 2159.
- [7] BARNSLEY, R., FIELDING, S.J., HAWKES, N.C., et al., submitted to Phys. Rev. Lett.
- [8] ENGELHARDT, W., et al., in Plasma Physics and Controlled Nuclear Fusion Research 1978 (Proc. 7th Int. Conf. Innsbruck, 1978), Vol. 1, IAEA, Vienna (1979) 123.
- [9] BAGDASAROV, A.A., et al., in Controlled Fusion and Plasma Physics (Proc. 12th Europ. Conf. Budapest, 1985), Vol. 9F/1, European Physical Society (1985) 207.
- [10] MARMAR, E.A., RICE, J.E., ALLEN, S.L., Phys. Rev. Lett. **51** (1983) 455.
- [11] SUCKEWER, S., et al., Nucl. Fusion **24** (1984) 815.
- [12] ISLER, R.C., et al., Nucl. Fusion **23** (1983) 1017.
- [13] HAWKES, N.C., PEACOCK, N.J., Nucl. Fusion **25** (1985) 971.

## DISCUSSION

K. IDA: Is the impurity transport observed in DITE neoclassical transport? If so, can you use the neoclassical theory to explain the long confinement time for impurity injected into the plasma with constant density and the difference in impurity transport between the co-injection case and the counter-injection case?

P.C. JOHNSON: Some of the observed effects can be explained using arguments based on neoclassical theory, for example the switching on and off of a temperature gradient screening term in the Ohmic high density cases. However, we do not have profile data of sufficient accuracy for a detailed comparison of experiment with neoclassical theory. The results with central beam heating suggest that processes other than neoclassical ones are important.



## STUDIES OF EDGE PLASMA PHENOMENA IN T-10

K.F. ALEXANDER, L. DIETRICH, H. GROTE,  
K. GÜNTHER, J. LINGERTAT  
Akademie der Wissenschaften der DDR,  
Zentralinstitut für Elektronenphysik,  
Berlin, German Democratic Republic

E.L. BEREZOVSKIJ, A.V. CHANKIN, V.M. CHICHEROV,  
S.E. LYSENKO, V.A. MEDVEDEV, A.Yu. PIGAROV,  
V.I. PISTUNOVICH, S.V. POPOVICHEV, V. VERSHKOV  
I.V. Kurchatov Institute of Atomic Energy,  
Moscow, Union of Soviet Socialist Republics

### Abstract

#### STUDIES OF EDGE PLASMA PHENOMENA IN T-10.

A scoop limiter equipped with Langmuir and heat flux probes in its scoop channels has been operated in T-10. Results concerning the properties of the scoop plasma and the neutral gas pressure in the pump duct are reported together with a Monte Carlo simulation of the neutral component which fairly well agrees with the observations. A 3-D model of the scrape-off layer (SOL) in tokamaks has been developed and evaluated with respect to plasma density, taking into account the multiplicity of connection lengths due to the complex interplay of the q-dependent magnetic topology and the particular limiter geometry (rail limiter in T-10). It turns out that such a SOL is highly non-uniform in accordance with experimental data from direct Langmuir probing, limiter thermography and a post mortem investigation of limiter damage. Results of a 2-D Monte Carlo calculation (geometry of T-10) of the distribution of neutrals originating from the limiter by recycling, considering the effect of backscattering, show good agreement with corresponding measurements and, furthermore, can explain the discrepancy between the neoclassical and the observed magnitude of ion heat transport: it is the neutrals that are the carriers of the additional efflux of ion energy in question.

#### 1. Further results of measurements with a scoop limiter

Fig.1a shows the sketch of a scoop limiter with instrumentation which has been used in T-10 to study the scoop plasma and the neutral gas in the pump duct in dependence on discharge parameters. Details of the experiment and main results have already been reported [1].

In typical T-10 regimes the electron density,  $n_e$ , in the scoop channels on the electron and ion drift sides increases with growing  $\bar{n}_e$  (Fig.1.b) while the electron temperature  $T_e$  decreases down to about 5 eV, which leads to an only weak  $\bar{n}_e$ -dependence of  $J_s$ , the sum of saturation currents of the probes at the entrances of both channels ( $J_s \propto n_e \sqrt{T_e}$ ), for  $\bar{n}_e > 10^{19} \text{ m}^{-3}$ . With the two

pairs of probes at different minor radii ( $\Delta r = 1$  cm) it was possible to determine the decay length  $\lambda$  (e-folding length for  $J_s$ ). Fig.1c,d shows a strong e-i-side asymmetry of  $\lambda$  depending on the direction of the magnetic field.  $\lambda$  is always larger on that side of the limiter where the plasma influx comes from the outer side of the torus, in accord with an argument given in [1] about the preponderance of plasma escape to the outer torus side.

By comparison of the signals from the outer and inner probes in each channel it turned out that the electron temperature is largely constant along a channel. The mean value of the floating potentials of the probes on both sides of the neutralizer plate was not much different from the limiter potential, indicating ambipolarity of the plasma flow in the channels. The heat flux probes (thermocouples) at the neutralizer plate generally displayed an average power input equal to  $7J_s T_e/e$ .

As to the gas pressure,  $p_d$ , in the pump duct, the finding [1] that  $p_d$  depends non-linearly on the plasma influx into the channel can be reproduced by Monte-Carlo calculations. The plates are the source of the neutral gas. In the equilibrium the production rate of neutrals balances the plasma flux into the channel  $\Phi_0 = n_e c_s$ , where  $c_s$  is the sound velocity. The trajectories of neutrals were simulated in two dimensions using the code DDC-83 [4,5], which takes into account the processes of dissociation, charge exchange, stepwise ionization, backscattering, and reemission. The calculated dependence of the gas pressure in the pump duct on the plasma influx  $\Phi_0$  is shown in Fig.1e for two values of the plasma temperature. Especially at low temperatures ( $T = 5$  eV) the gas pressure rises considerably faster than  $\Phi_0$  above a critical value of  $\Phi_0$ . This can be qualitatively explained by the fact that a great deal of neutral gas near the plates and inside the duct consists of molecules produced by reemission. The molecules interact strongly with electrons even at relatively low temperatures. The atoms produced by dissociation of the molecules are emitted isotropically and return in part to the plates or go into the duct, thus increasing the pressure  $p_d$ . At higher temperatures ( $T > 7$  eV) ionization of atoms and dissociation of molecules with ion production become important. Consequently, a smaller number of neutrals relative to  $\Phi_0$  can reach the pump duct and the pressure rise is not so steep.

More realistically, it was assumed that the temperature decreases with increasing  $\Phi_0$  as observed experimentally. The dependence of  $p_d$  on  $\Phi_0$  was calculated with the assumption that the plasma temperature decreases from 20 eV to 4 eV while the plasma density increases from  $5 \times 10^{17} \text{ m}^{-3}$  up to  $1.5 \times 10^{19} \text{ m}^{-3}$ . The results (Fig.1e) fairly well match the experimental data.

## 2. The inherent structure of a rail-limiter scrape-off layer (SOL): a 3-D approach to plasma density

In view of growing experimental evidence for the occurrence of a non-uniform structure of the SOL in tokamaks [2,3,6,7,8],

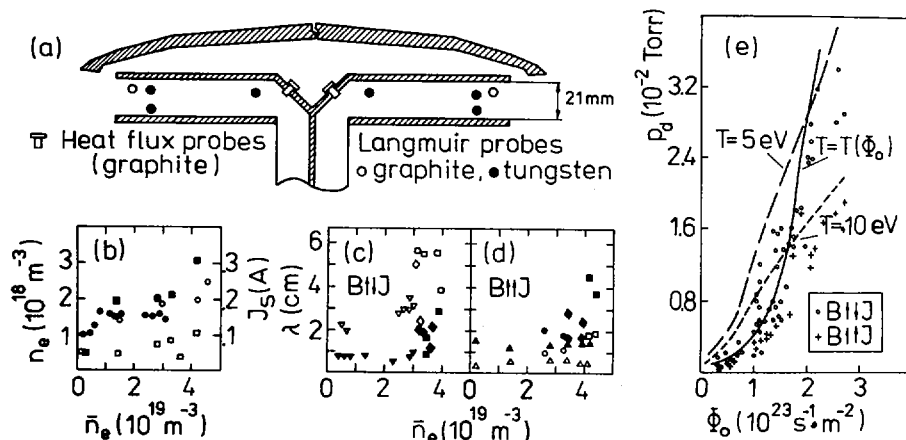


FIG. 1. Results of scoop limiter operation in T-10. (a) Limiter design (section in toroidal direction). (b) Electron density in the two scoop channels ( $\square$  electron side,  $\blacksquare$  ion side) and sum of saturation currents of channel entrance probes ( $\circ$  for  $B_{t11}J_p$ ,  $\bullet$  for  $B_{t11}J_p$ ) as a function of line averaged density  $\bar{n}_e$  in the discharge ( $B_t = 2.1\text{--}2.5$  T,  $J_p = 200\text{--}250$  kA,  $a = 28$  cm). (c), (d) Radial decay length referring to saturation current as a function of  $\bar{n}_e$  for normal (c) and reversed (d) magnetic field (open symbols: electron side, closed symbols: ion side). Symbol shape indicates different discharge regimes ( $B_t = 2.2\text{--}3.0$  T,  $J_p = 200\text{--}350$  kA,  $a = 26.5\text{--}28.0$  cm). (e) Gas pressure in scoop limiter pump duct as a function of plasma influx at channel entrance. Experimental data and model calculations.

the symmetry-breaking effect of limiter configurations is of particular interest. While an aperture limiter leads to a relatively simple two-dimensional situation in cylindrical geometry [2], the case of a single rail limiter as used in T-10 can only be met by a 3-D approach with properly taking account of the magnetic topology in dependence on the safety factor  $q(r)$ .

## 2.1. Theory

Fig.2 illustrates the problem. The "reference cross-section" (RCS) shown on the left is defined as the minor cross-section at the toroidal position opposite to the limiter, ie  $180^\circ$  away from it. The different connection lengths,  $L_{\parallel}$ , of flux tubes give rise to a poloidal variation of plasma parameters in addition to the radial one, and the numerical treatment of cross-field transport requires a sufficiently fine grid in polar coordinates. Along each field line, however, there will be no great variation within half a revolution round the torus, ie up to the limiter section, because the flux tubes usually have a length of several revolutions:  $L_{\parallel} = L_0 N = 2\pi R_0 N$ . This may justify our taking the whole torus circumference along a field line ( $\approx L_0$ ), beginning and ending at the limiter section, as the elementary interval  $\Delta x$  for the treatment of parallel transport along the coordinate  $x$ . Thus, each point in the RCS stands for a flux tube segment of length  $L_0$ , and a complete flux tube is described by a sequence of points

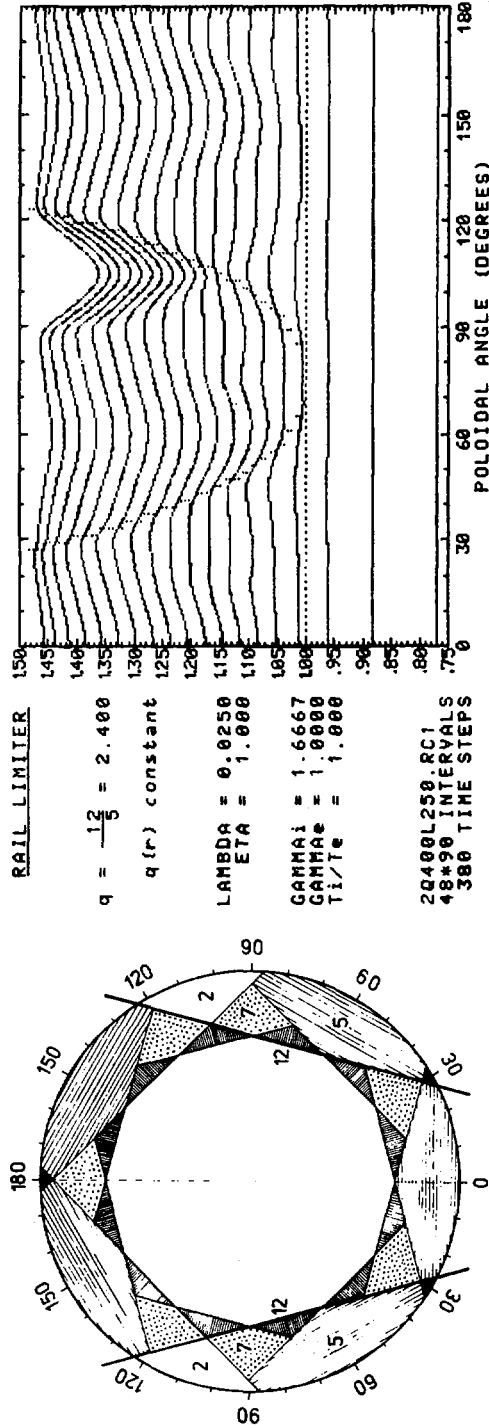


FIG. 2. Topology of rail limiter SOL and resulting density distribution (minor cross-section 180° away from a bottom rail limiter). Limiter edge shadows marked by heavy lines (left) and dots (right). Left: All panels with same type of shading represent single bundle of open flux tubes of uniform connection length described by number,  $N$ , of revolutions round torus ( $N$  values given in the limiter front and back areas). Each bundle, on running round the torus, appears  $N$  times in cross-section considered. Right:  $r, \delta$ -map of isodensity with logarithmic scaling ( $\Delta \ln n = 0.5$  from line to line). Dashed line indicates boundary between plasma and SOL.

in the RCS which are found by means of the rotational transformation corresponding to  $\mathbf{q}(r)$ . On the other hand, a 2-D map of, eg, the density in the RCS, as shown in Fig.2 through Fig.4, describes the entire 3-D field of density owing to the rotational transformation which has to be applied according to the toroidal position under consideration.

Aiming at the structural aspects first of all, we have only solved the continuity equation by time evolution to obtain the stationary plasma density  $n$ :

$$\frac{L_o}{2c_s} \left( \frac{\partial n}{\partial t} + \frac{\partial un}{\partial x} \right) = \frac{L_o}{2c_s} \nabla_{\perp} \cdot \vec{D}_{\perp} \cdot \nabla_{\perp} n = \lambda_o^2 \left( \frac{1}{r} \frac{\partial}{\partial r} r \frac{\partial}{\partial r} + \frac{\eta}{r^2} \frac{\partial^2}{\partial \vartheta^2} \right) n$$

$$\lambda_o^2 = \frac{L_o D_r}{2c_s}, \quad L_o = 2\pi R_o, \quad c_s^2 = \frac{1}{m_i} (\gamma_i T_i + \gamma_e T_e)$$

The velocity,  $u(x)$ , of parallel flow can be expressed by  $n(x)$ , using an analytical solution to the momentum balance equation,

$$\frac{\partial un}{\partial t} + \frac{1}{m_i + m_e} \frac{\partial (T_i + T_e) n}{\partial x} + \frac{\partial u^2 n}{\partial x} = \nabla_{\perp} u \cdot \vec{D}_{\perp} \cdot \nabla_{\perp} n + \nabla_{\perp} n \cdot \vec{\mu}_{\perp} \cdot \nabla_{\perp} u$$

with the boundary condition  $u(\pm L_{\parallel}/2) = \pm c_s$ , setting  $\nabla_{\perp} u = 0$  (as well as  $\partial u/\partial t = 0$ ). The occurrence of sufficiently large  $r, \vartheta$ -regions of uniform  $L_{\parallel}$  (Fig.2) warrants and requires this approximation by contrast with a traditional approach of complete neglect of the momentum sources. Additionally, we have made use of  $T(x) \propto [n(x)]^{\gamma-1}$  with the standard choice  $\gamma_i = 5/3$  (adiabatic expansion) and  $\gamma_e = 1$  (isothermic expansion). As to the stagnation point temperatures  $T_{i0}$  and  $T_{e0}$ , equality and constancy with respect to  $r$  and  $\vartheta$  has been assumed for the sake of simplicity.

## 2.2. Results, discussion, and experimental evidence

Fig.2 visualizes what turns out upon assuming, for the sake of demonstration, that  $\mathbf{q}(r)$  is constant. (i) There is a fundamental symmetry which shortens the calculation. (ii) The distributions on both sides of the limiter are asymmetric with respect to  $\vartheta$ , show mirror symmetry to each other, and are simply exchanged by  $B_t$ -field inversion. (iii) In the limiter shadow area the average  $n$  and the associated effective decay length  $\lambda$  (apparent SOL thickness) are smaller than the corresponding total SOL averages owing to a bias in statistical weight: each flux tube bundle appears exactly once in the limiter area, but counts just  $N$  times in the total average; however, the larger  $N$  the greater  $\lambda$  and  $n$ . Additionally, the general character of the density profile  $n(x)$  for each flux tube enhances this important effect. It implies a "self-protection" of the limiter (SOL acts as a "by-pass") and shows that probing the SOL by means of the limiter itself (thermography) may be misleading (accountability of power; see [10]). All these statements remain valid when taking into account the actual dependence of  $\mathbf{q}$  on  $r$  (cf the following examples).

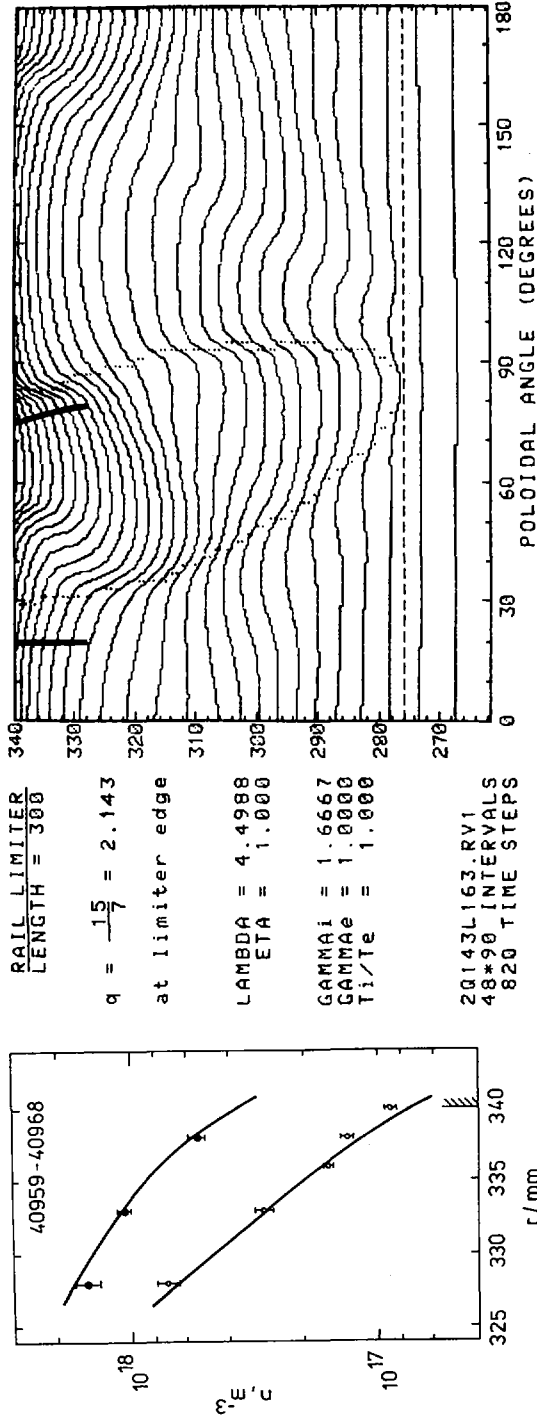


FIG. 3. Radial density profiles measured with Langmuir probe (circles) at two poloidal positions compared with theoretical prediction (curves). Complete density map for reference cross-section (RCS) with heavy bars indicating the two sites probed ( $\Delta$  in  $n = 0.25$ ; see caption of Fig. 2).

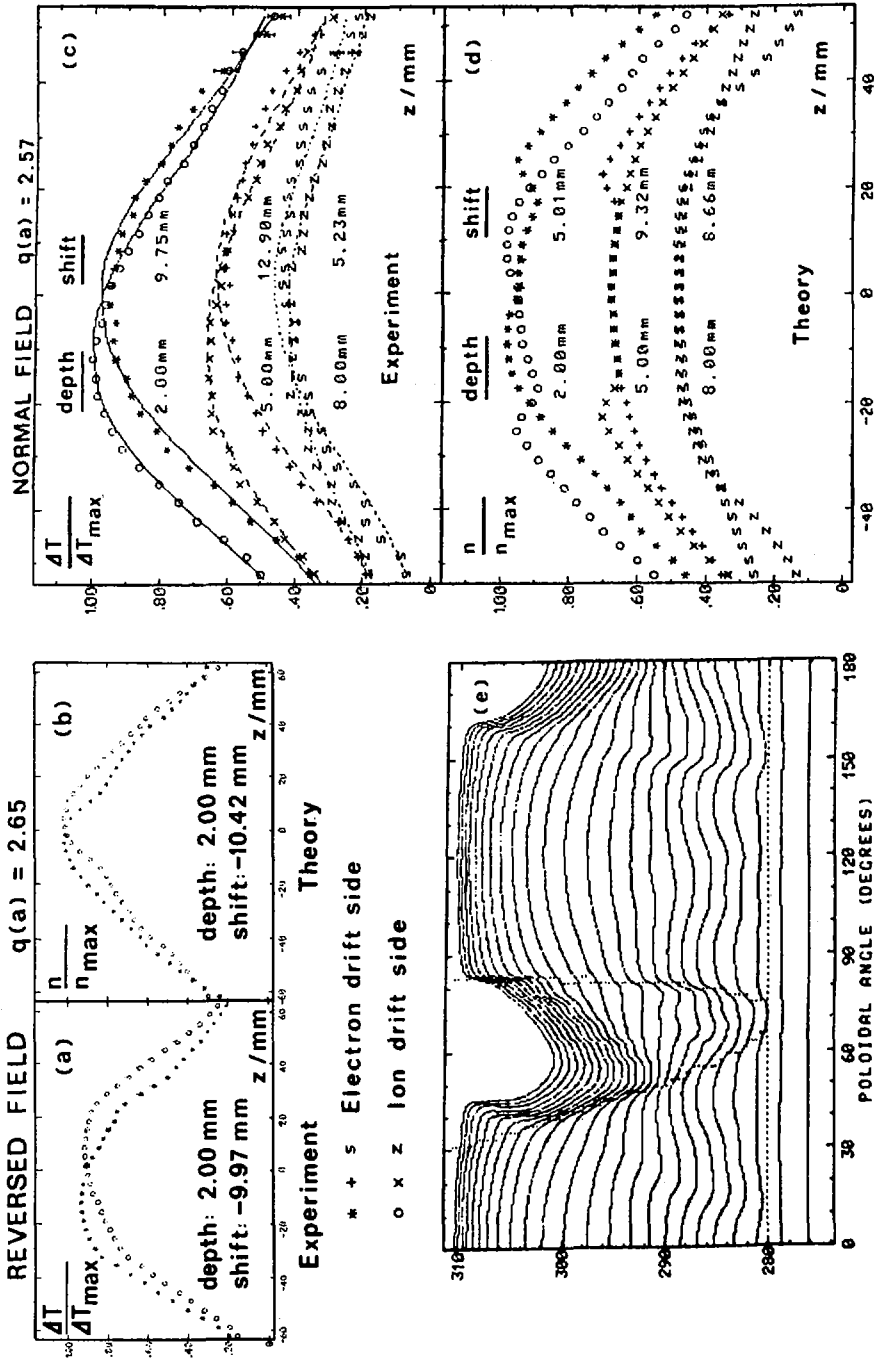


FIG. 4. Profiles along chords in minor cross-section parallel to bottom rail limiter edge (torus centre to the right). For details see text. Density map with  $\Delta \ln n = 0.25$  (see caption of Fig. 2).

The high degree of non-uniformity of the SOL exhibited by the density map in Fig.3 has been confirmed by a Langmuir probe experiment on T-10 (different probe positions by field inversion). The only adjustable parameter in the calculation is  $\lambda_0$ . The value that proved appropriate (4.5 mm) corresponds to  $D_r = 0.2 \text{ m}^2/\text{s}$  for  $T = 8.5 \text{ eV}$ , which just equals the Bohm coefficient ( $B_t = 2.5 \text{ T}$ ).

In earlier reports [6,7] on thermographic measurements on T-10 rail limiters we have pointed out the existence of a shift between the temperature peaks on both sides of the limiter. This phenomenon has now been studied systematically by evaluating the temperature profiles along straight lines parallel to the ridge of the span-roof-like limiter surface [7] on both the electron and ion drift sides. In the minor cross-section these lines are horizontal chords whose distance from the limiter edge is called "depth". Fig.4 shows an example (a) compared with the theoretical prediction (b). Although both data are intrinsically incommensurate, the similarity is striking (a smaller value of  $\lambda_0$  has been used to simulate the influence of temperature decay). There is an obvious mutual mirror symmetry of the asymmetric peaks.

In a uniform exponential-decay SOL the profiles in question should read  $\Delta T(z) \propto \exp[-(z-z_0)^2/2a\lambda]$ . We have used this expression complemented with a third-order asymmetry term to fit the experimental profiles as well as the theoretical ones, mainly to obtain a unique measure of the shift: the difference of  $z_0$  values for both of the limiter sides. Fig.4c,d shows an example together with the corresponding density map (e). The entire set of data examined ( $q(a)$  between 2 and 3.3) has shown that the theory in any case yields the correct sign of the shift for a small depth (always positive for normal field direction and vice versa) and, thus, also accounts for previous results of a post-mortem investigation of a T-10 rail limiter [11] which has shown the same e-i-side shift of limiter load by ablation and cracks.

It can be concluded that the phenomenon of asymmetry in question is actually due to the kind of SOL structure our model accounts for. Remaining discrepancies can clearly be attributed to the experimental uncertainty of  $q(a)$  on the one hand and the shortcomings of the model on the other hand: (i) A complete two-fluid theory in terms of  $n, u, T_i, T_e$  is needed. (ii) True toroidal geometry must be used. (iii) Cross-field motions (eg,  $E \times B$ ) must be considered. (iv) The effect of loop voltage should be included. None of these requirements is too difficult to meet.

### 3. Toroidally localized neutral particle distributions

The limiter as the main sink for the plasma efflux is at the same time the main source of neutrals by recycling. This leads to strong inhomogeneities in the spatial distribution of neutrals both in the plasma column and in the SOL. Taking into account the actual geometry of T-10, we have simulated the neutral particle transport in the vicinity of the poloidal aperture limiter by a Monte-Carlo procedure. Since a large percentage of neutral atoms

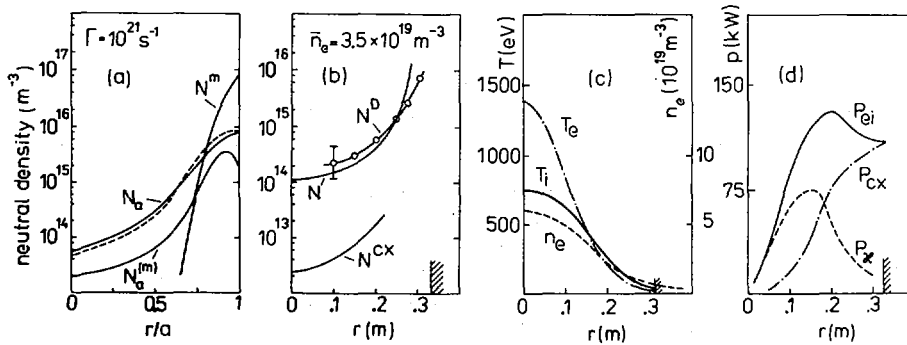


FIG. 5. Neutral particle density in T-10. (a) Calculated radial distributions at position of poloidal aperture limiter.  $N_b$ : limiter produced atoms (dashed line: analytical solution);  $n^m$ : molecules from gas puff;  $N_a^m$ : molecules from gas puff;  $N_a^n$ : atoms produced by dissociation of gas molecules. (b) Experimentally determined radial distribution of atoms.  $N^D$ : from  $D_\beta$  radiation in limiter section ( $N$ : calculated for limiter produced neutrals).  $N^{CX}$ : from charge exchange spectra  $90^\circ$  away from limiter section. (c) Experimental temperature and density profiles typical for T-10 Ohmic discharges. (d) Calculated contributions to radial ion energy efflux due to twice the neoclassical ion heat conduction ( $P_e$ ) and charge exchange neutrals ( $P_{CX}$ ), which sum up to total flux corresponding to net energy input in ion component ( $P_{ei}$ ).

leaving the limiter are backscattered neutralized ions, the penetration depth of these neutrals into the plasma core is considerably larger than it is in the case of neutrals originating from cold gas molecules desorbed from the wall or puffed into the chamber. Results for both cases ("fast" neutral atom source and "slow" molecular source normalized to the same global particle flux), referring to one of the standard regimes of T-10 [9], are given in Fig.5a. The Monte-Carlo calculations were used to fit neutral density profiles obtained with the one-dimensional model of consecutive generations [12] by varying the energy of the primary neutrals. An energy of 20 eV gives a good overall fit to the Monte-Carlo profile for limiter-produced neutral atoms. This profile is confirmed by comparison with experimental data for the limiter section (Fig.5b), while the low values measured far from the latter are in keeping with the calculated density peak at the limiter to decay steeply in toroidal direction.

#### 4. Ion heat transport by charge-exchange with neutrals

An important effect, ordinarily not considered in energy transport calculations, is the additional heat conduction caused by the charge-exchange interaction of neutral atoms with plasma ions. This process can contribute substantially to the ion heat transport in the outer region of the plasma column, considering the enhanced penetration depth of fast primary neutrals coming from the limiter via recycling. A thorough investigation of ion temperature measurements in the presence of kinetic convective

ripple transport of ions [13] revealed that the ion temperature profiles in T-10 have a more pronounced peak than thought before. The ion heat conductivity derived from these profiles deviates strongly from the neoclassical scaling for  $r > 0.7a$ . This behaviour can be attributed to the additional heat conduction by neutral atoms.

The plasma energy balance has been calculated for the experimental data in Fig.5c. Assuming neoclassical ion heat conductivity multiplied by  $K_{an} = 2$  and including the heat transport by neutral atoms based on the above-mentioned Monte-Carlo calculations, one obtains the curves in Fig.5d which shows that the apparent high anomaly of the ion heat conductivity for  $r > a/2$  is actually heat conduction by neutrals.

## REFERENCES

- [1] VERSHKOV, V.A., GRASHIN, S.A., CHANKIN, A.V., in Plasma-Surface Interactions in Controlled Fusion Devices (Proc. 7th Int. Conf. Princeton, NJ, 1986), Report 7.5 (in press).
- [2] SAMM, U., et al., *ibid.*, Report 1.6 (in press).
- [3] WAN, A.S., et al., *ibid.*, Report 1.3 (in press).
- [4] IGITKHANOV, Yu.L., et al., Dokl. Akad. Nauk SSSR **278** (1984) 338.
- [5] KUKUSHKIN, A.S., PIGAROV, A.Yu., USSR Contribution to the INTOR Phase-Two-A Workshop, Group A, p. 20.
- [6] LINGERTAT, J., et al., in Plasma Physics and Controlled Nuclear Fusion Research 1984 (Proc. 10th Int. Conf. London, 1984), Vol. 1, IAEA, Vienna (1985) 265.
- [7] GÜNTHER, K., et al., in Controlled Fusion and Plasma Physics (Proc. 12th Europ. Conf. Budapest, 1985), Vol. 2, European Physical Society (1985) 567.
- [8] BOGEN, P., et al., *ibid.*, p. 527.
- [9] ALIKAEV, V.V., et al., *ibid.*, p. 160.
- [10] LINGERTAT, J., et al., *ibid.*, p. 559.
- [11] HILDEBRANDT, D., et al., in Controlled Fusion and Plasma Physics (Proc. 10th Europ. Conf. Moscow, 1981), Vol. 1, European Physical Society (1981) J-12.
- [12] DNESTROVSKY, Yu.N., KOSTOMAROV, D.P., Numerical Simulation of Plasmas, Springer-Verlag, Berlin, Heidelberg (1986).
- [13] BEREZOVSKIJ, E.L., et al., Nucl. Fusion **23** (1983) 1575.

## DISCUSSION

H. WOBIG: The limiter introduces inhomogeneities not only into the density but also into the electric potential. This may lead to additional convective motion in the vicinity of the limiter. Did you take into account this effect?

K.F. ALEXANDER: No, we did not take this effect into account in the present work, but we will do this in future. In the experiments with the scoop limiter, differences in the floating potential of several volts between the electron and ion drift sides were observed.

R.J. GOLDSTON: In your model of the scrape-off plasma you don't seem to need asymmetric sources to explain an asymmetric scrape-off plasma. In some auxiliary heating experiments, asymmetries have been attributed to the physical loss mechanisms. Could you perhaps comment on this and tell us what has been observed during ECH on T-10?

K.F. ALEXANDER: Our model assumes a poloidally and toroidally homogeneous plasma source feeding the scrape-off layers. The asymmetries produced by the rail limiter discussed here are only due to the topology of open field lines of different connection lengths within the scrape-off layers.

During ECH, additional asymmetries are certainly observed, for instance in limiter thermography. I would refer you in this connection to the paper by J. Lingertat which he presented at the 1984 Conference<sup>1</sup>.

---

<sup>1</sup> LINGERTAT, J., et al., in Plasma Physics and Controlled Nuclear Fusion Research 1984 (Proc. 10th Int. Conf. London, 1984), Vol. 1, IAEA, Vienna (1985) 265.



# ALT-I PUMP LIMITER BEHAVIOUR AND EDGE PLASMA FLOWS DURING BIASING AND ICRF HEATING IN THE TEXTOR TOKAMAK

R.W. CONN, D.M. GOEBEL, W.K. LEUNG, G.A. CAMPBELL,  
B. LaBOMBARD, A.K. PRINJA

Center for Plasma Physics and Fusion Engineering,  
University of California<sup>1</sup>,  
Los Angeles, California, United States of America

W.L. HSU, G.J. THOMAS  
Sandia National Laboratories<sup>2</sup>,  
Livermore, California, United States of America

K.H. DIPPEL, K.H. FINKEN, R. REITER, G.H. WOLF, H.L. BAY,  
G. BERTSCHINGER, W. BIEGER, P. BOGEN, W. BRUSSAU, Y. CAO,  
H.G. ESSER, G. FUCHS, B. GIESEN, E. GRAFFMANN, H. HARTWIG,  
E. HINTZ, F. HOENEN, K. HÖTHKER, A. KALECK, H. KEVER, L. KÖNEN,  
M. KORTEN, L. LI, Y.T. LIE, A. POSPIESZCZYK, A. REGISTER, G. ROSS,  
D. RUSBÜLDT, U. SAMM, J. SCHLÜTER, B. SCHWEER, H. SOLTWISCH,  
F. WAELBROECK, G. WAIMANN, P. WIENHOLD, J. WINTER,  
R. YAMAUCHI

Euratom-KFA Association,  
Institut für Plasmaphysik,  
Kernforschungsanlage Jülich GmbH,  
Jülich, Federal Republic of Germany

T. DELVIGNE, P. DESCAMPS, F. DURODIE, M. JADOUL, R. KOCH,  
D. LEBEAU, A.M. MESSIAEN, D.I.C. PEARSON, P.E. VANDENPLAS,  
R. VAN NIEUWENHOVE, G. VAN OOST, G. VAN WASSENHOVE,  
R.R. WEYNANTS

Laboratoire de physique des plasmas —  
Laboratorium voor Plasmafysica,  
Association Euratom-Etat Belge —  
Associatie Euratom-Belgische Staat,  
Ecole royale militaire — Koninklijke Militaire School,  
Brussels, Belgium

<sup>1</sup> Work supported by the United States Department of Energy, under Contract No. DE-RG03-85-ER51069.

<sup>2</sup> Work supported by the United States Department of Energy, under Contract No. DE-AC04-76DP00789.

## Abstract

### ALT-I PUMP LIMITER BEHAVIOUR AND EDGE PLASMA FLOWS DURING BIASING AND ICRF HEATING IN THE TEXTOR TOKAMAK.

Experiments have been performed in the TEXTOR tokamak, using the ALT-I pump limiter with strong electrical biasing and ICRF heating. With negative biasing (up to  $-450$  V) of ALT-I, the flux to ALT-I increases moderately (about 10%) at the front face of the limiter but very significantly (up to 250%) in the throat. The pressure and removal rate increase by a factor of two or more. Simultaneously, total  $D_\alpha$  light from the surface of other recessed limiters and the liner decreases by a factor of up to two. Some shots show no change in the loop voltage signal, while others show an increase. With positive bias (up to  $+450$  V), generally opposite effects occur. The flux and pressure at ALT-I decrease, while  $D_\alpha$  light at the liner increases by a factor of two. The O VI signal likewise jumps and the loop voltage increases by 80% in 0.5 s. The net current drawn to the power supply ends at 120 A for negative bias and about 220 A for positive bias. With up to 1.6 MW of ICRF heating, negative biasing of ALT-I causes a decrease in recycling at the antenna. However, no change in plasma energy confinement scaling using ALT-I relative to previously reported results was found in a systematic study.

## 1. INTRODUCTION

Core plasma density control and heat removal are primary reasons for investigating pump limiters [1-3] in fusion devices. As part of the ALT-I program [4] in the TEXTOR tokamak [5,6], pump limiters of several designs and materials have been used in experiments to explore the physics of plasma exhaust [7-10], impurity and helium flows [10], the nature of the plasma edge [11], the performance of different limiter materials [12,13], and pump limiter operation during ICRF heating [14].

In this paper, we report experiments in which the ALT-I pump limiter is electrically biased both positively (to  $+450$ V) and negatively (to  $-450$ V) with respect to the other limiters and the liner. Early work on the role of DC radial electric fields in plasma transport was reported by Taylor et al. [15] and recent experiments using limiter biasing were performed in the PDX [16] and TEXT [17] tokamaks. The experiments in TEXTOR were performed during ohmic and ICRF heated (up to 1.6MW) discharges. General ICRF heating studies in TEXTOR are reported in references [18] and [19]. We describe here studies of ICRF heating with ALT-I operated as a pump limiter or, with its exhaust channels closed, as a regular limiter. Limiter biasing during ICRF heating will also be discussed.

## 2. LIMITER BIASING EXPERIMENTS

### 2.1. EXPERIMENTAL ARRANGEMENT AND DIAGNOSTICS

The general TEXTOR experimental arrangement and diagnostics are described in references [5, 6]. The ALT-I

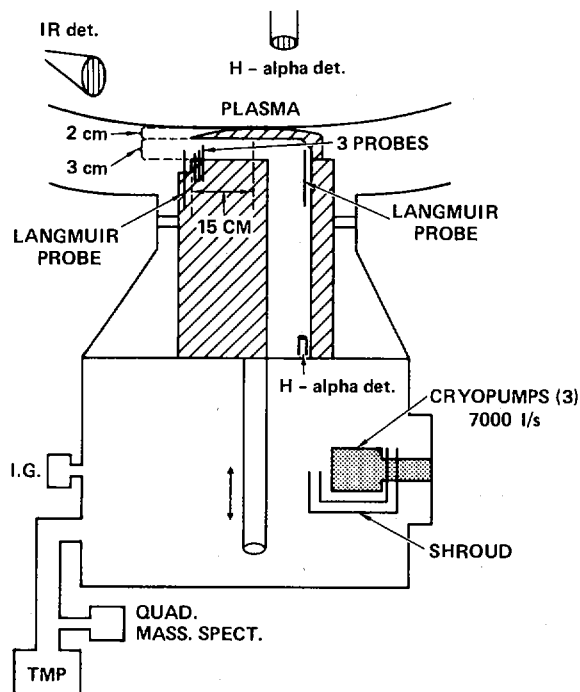


FIG. 1. ALT-I pump limiter, showing position of Langmuir probes,  $D_{\alpha}$  viewing positions, the pumping chamber, and position of pressure measurements.

limiter has the design first reported in ref. [4] and is made of a carbon-carbon composite weave. The design and location of various diagnostics are given in Fig. 1. For the experiments reported here, ALT-I limits the plasma to a radius of 42 cm. Approximately  $90^{\circ}$  toroidally from ALT-I are three main limiter segments made of carbon, each subtending approximately  $30^{\circ}$  poloidally and located top, bottom and midplane outside. They are retracted to a minor radius of 48 cm, i.e. 6 cm radially beyond ALT-I. The ICRF antennas are two half-turn loops located  $40^{\circ}$  toroidally from ALT-I in the opposite direction of the main limiters. The protective carbon limiters of the antennas form a full poloidal ring beginning at 48.8 cm. The liner is at 55 cm and the tokamak is generally conditioned by carbonization [20]. Experiments were also performed with ALT-I at other radial locations, but we restrict the discussion here to the geometrical arrangement just described.

Key diagnostics which will be referred to in the paper include  $D_{\alpha}$  monitors viewing the liner, the ICRF ring limiters, and the upper main limiter. In addition,  $D_{\alpha}$  emission is monitored at the face of the ALT-I head and at the deflector

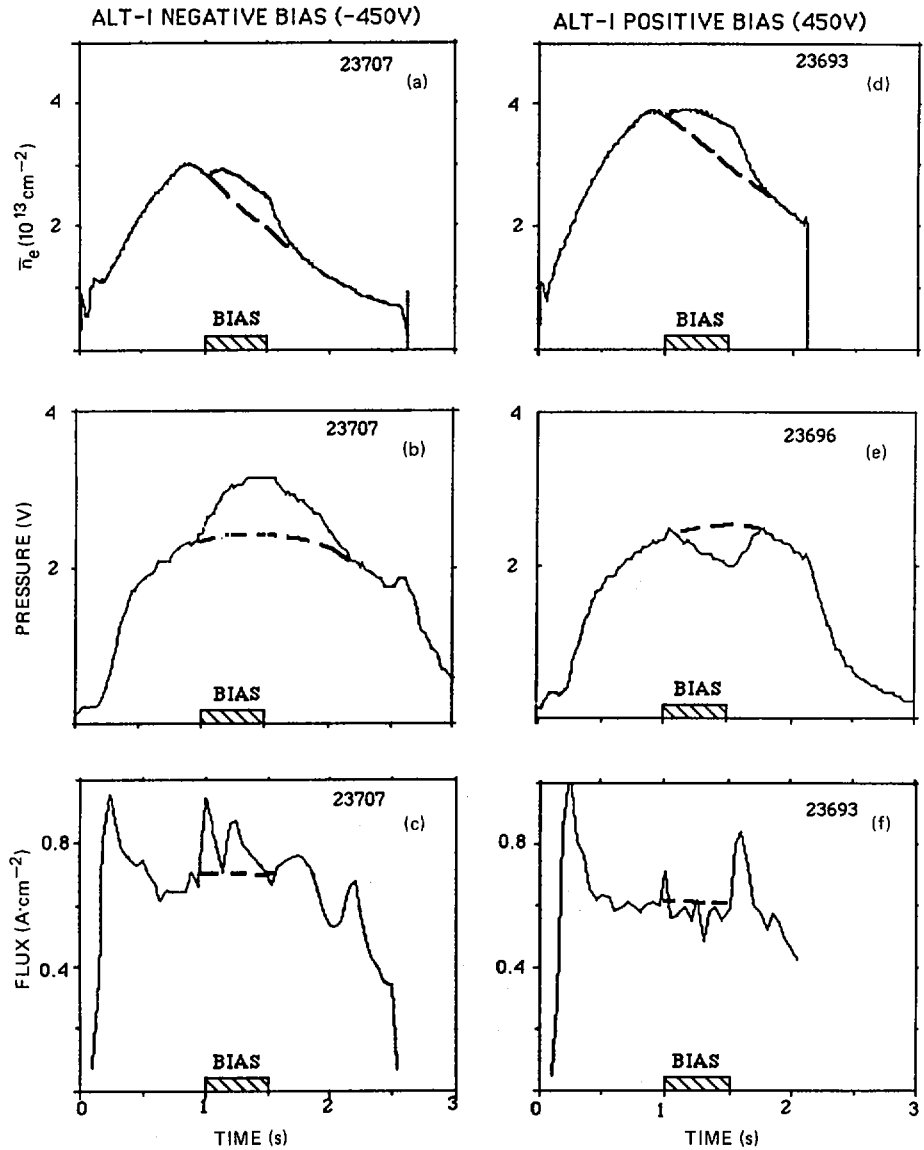


FIG. 2. Core plasma density, pressure in the pump limiter and flux into the pump limiter throat, as a function of time. Negative or positive bias to ALT-I is applied from 1 s to 1.5 s. The dashed curve indicates signal values without bias.

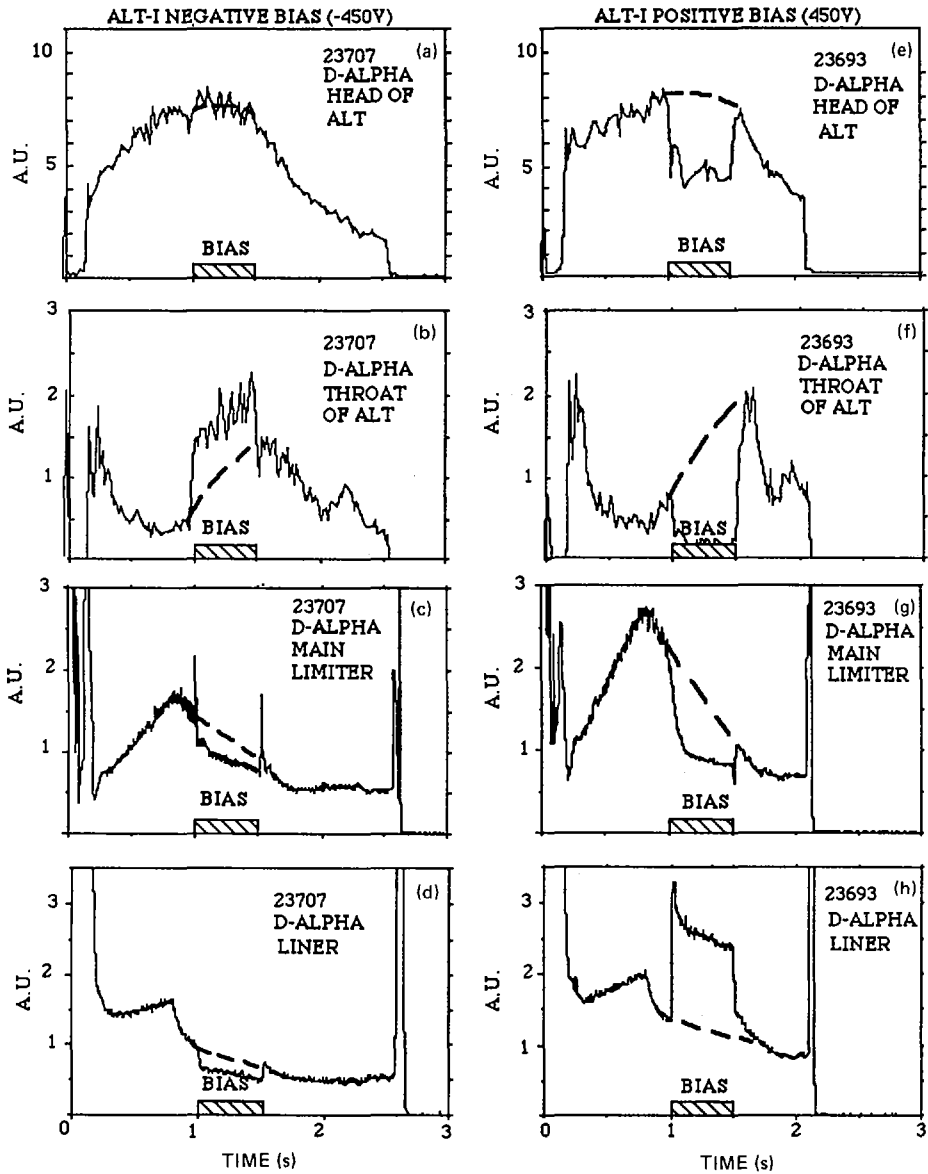


FIG. 3.  $D_\alpha$  signals viewing various locations in ALT-I, at the main limiters, and at the liner, as a function of time. Bias is applied from 1 s to 1.5 s. The dashed lines indicate the signal values without bias.

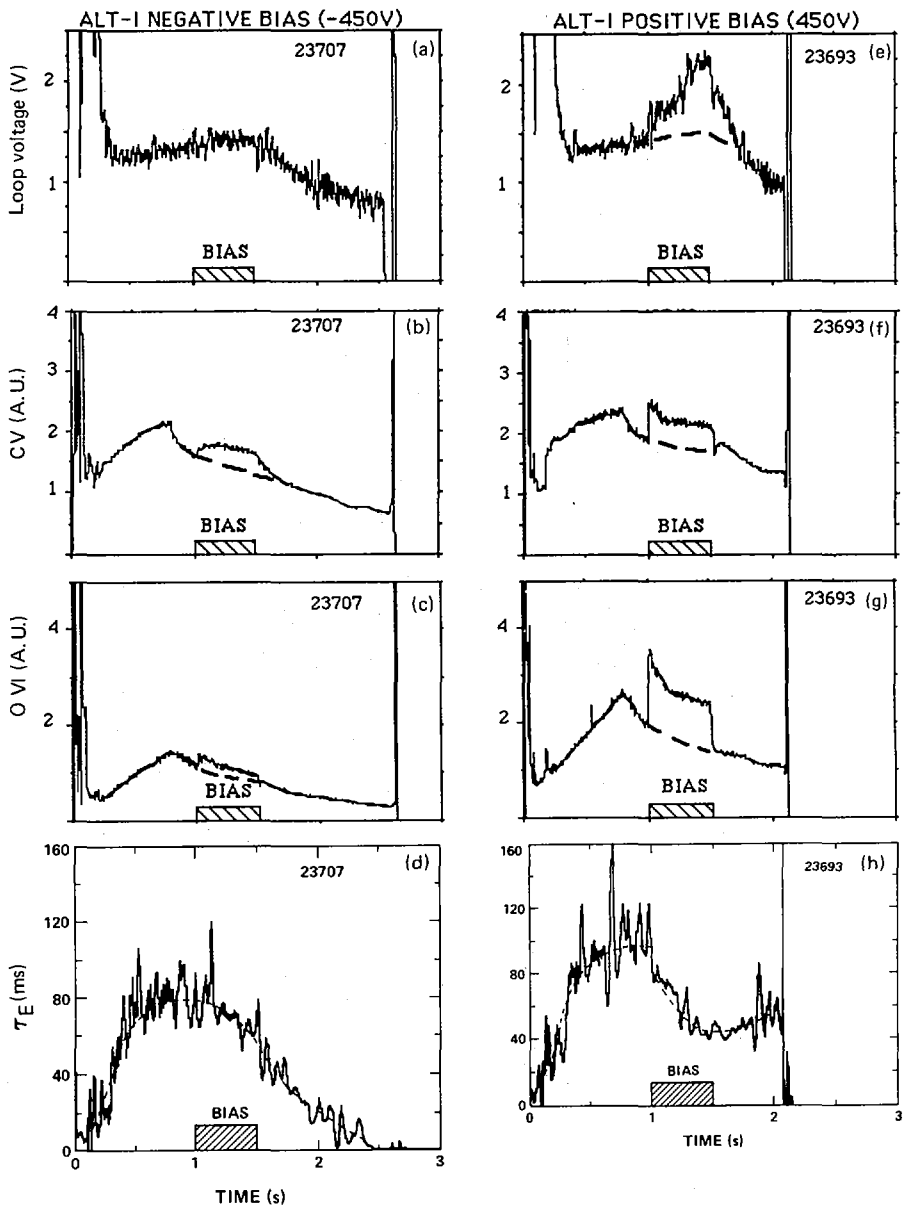


FIG. 4. Loop voltage, O VI and CV signals, and energy confinement time as a function of time. Bias is applied from 1 s to 1.5 s. The dashed lines indicate signal values without bias.

plate where plasma terminates inside the pump limiter. Plasma fluxes are measured with Langmuir probes and the neutral pressure is measured in the pump limiter chamber.

## 2.2. RESULTS FOR OHMIC DISCHARGES

Key results from various diagnostics are summarized in Figs 2, 3 and 4, where signals are plotted versus time during a discharge. Generally, the gas puff is on until 0.8 s, the bias is applied from 1 s to 1.5 s, the plasma current is constant from 0.5 s to 1.6 s, and the discharge generally terminates in a "soft landing" at 3.0 to 3.5 s [5,6].

Fig. 2 shows that the central line-averaged density increases at bias turn-on for both positive and negative bias. The relative increase is largest with positive bias and in each case the increase appears to be due to impurity introduction. (See Fig. 4, to be discussed shortly.) For negative bias, the flux into the throat of the pump limiter increases sharply at bias turn-on and both the pressure signal and the plasma removal rate in the pump limiter increase by 50 to 100%. (See Fig. 2.) By contrast, we see from Fig. 3 that the  $D_{\alpha}$  signals at the other limiters and particularly at the liner decrease. The  $D_{\alpha}$  signal at the front face of ALT-I increases, but by a smaller amount than the signals in the throat. The increase in the CV signal shown in Fig. 4 appears to be due to carbon from the limiter and correlates with the density rise.

These results indicate that during negative biasing, ion flow is preferentially to ALT-I and, in particular, into the throat. A measurement by Pospieszczyk and Ross [21] of the density profile in the plasma boundary layer, taken at 1.4 s into the discharge and while bias is on, is shown in Fig. 5. During negative bias, a density bump occurs between 45 and 48 cm, suggesting that cross-field transport is inhibited as the plasma approaches the main limiters (48 cm). The main limiters are the first objects radially beyond ALT-I and are positive relative to it. The impedance to cross-field flow appears to be related to a radial potential barrier.

Generally, opposite effects occur during positive bias. Following turn-on of positive bias, decreases are observed in the  $D_{\alpha}$  signals at the ALT-I face and at the deflector plate. No bump in the boundary layer density occurs (see Fig. 5) and the density in front of the main limiter at 48 cm is somewhat lower than with no bias. The  $D_{\alpha}$  signals at the other limiters do not change much, but four of the five  $D_{\alpha}$  monitors at the liner show increases of a factor of 2 or more. We do find that the liner  $D_{\alpha}$  signals strongly depend on toroidal location. Some signal changes are illustrated in Fig. 6, where  $\Delta$  (signal) corresponds to the signal value just after bias minus the value just prior to bias, normalized to the value just before bias.

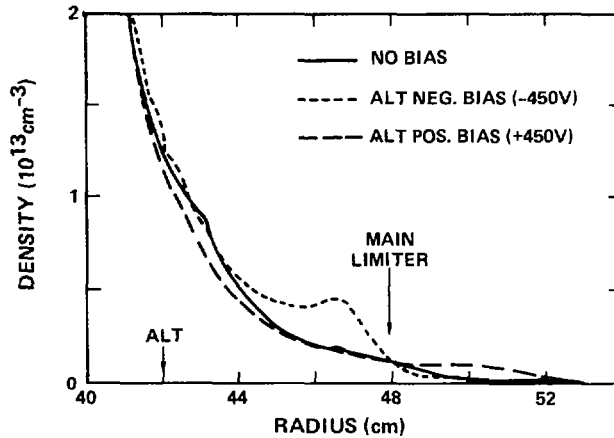


FIG. 5. Edge plasma density profile at 1.4 s into discharges, with positive bias, negative bias or no bias applied to ALT-I. The radial position of ALT-I and the main limiters are shown.

The increased flux to the liner is correlated with a prompt increase in the OVI and CV signals in the plasma edge, indicating that there is a flux-induced release of oxygen and carbon. The loop voltage shown in Fig. 4 increases linearly over the 0.5 s positive bias time, suggesting impurity accumulation. The value of global energy confinement,  $\tau_E$ , correspondingly decreases, apparently due to increased levels of low Z radiation. For negative bias, the oxygen signal increases slightly, but the loop voltage and confinement time show little change. We deduce that the source of oxygen impurity is desorption from the liner, not from ALT-I. During negative bias, the source of carbon must be ALT-I.

The I-V trace of current and voltage at the bias power supply, shown in Fig. 6, indicates that the current limits to a net value of 110A for strong negative bias and about 220A for strong positive bias. The floating potential is 50-90V relative to the wall. The 110-120A current level during negative bias is within a factor of 2 to 3 of the estimated ion current diffusing from the core plasma for this particular arrangement of limiters. This estimate assumes  $\tau_p$  is 0.1s, consistent with results reported earlier [22].

A possible picture to explain the edge plasma flows during biasing is to view the plasma potential as following the potential applied to ALT. (This is similar to the observation reported by Taylor et al. [15].) The system then effectively acts as a double probe of unequal areas, with ALT-I as one electrode and the liner as the other. The net current in the power supply circuit is determined by the plasma potential in the scrape-off layer plasma relative to the two electrodes.

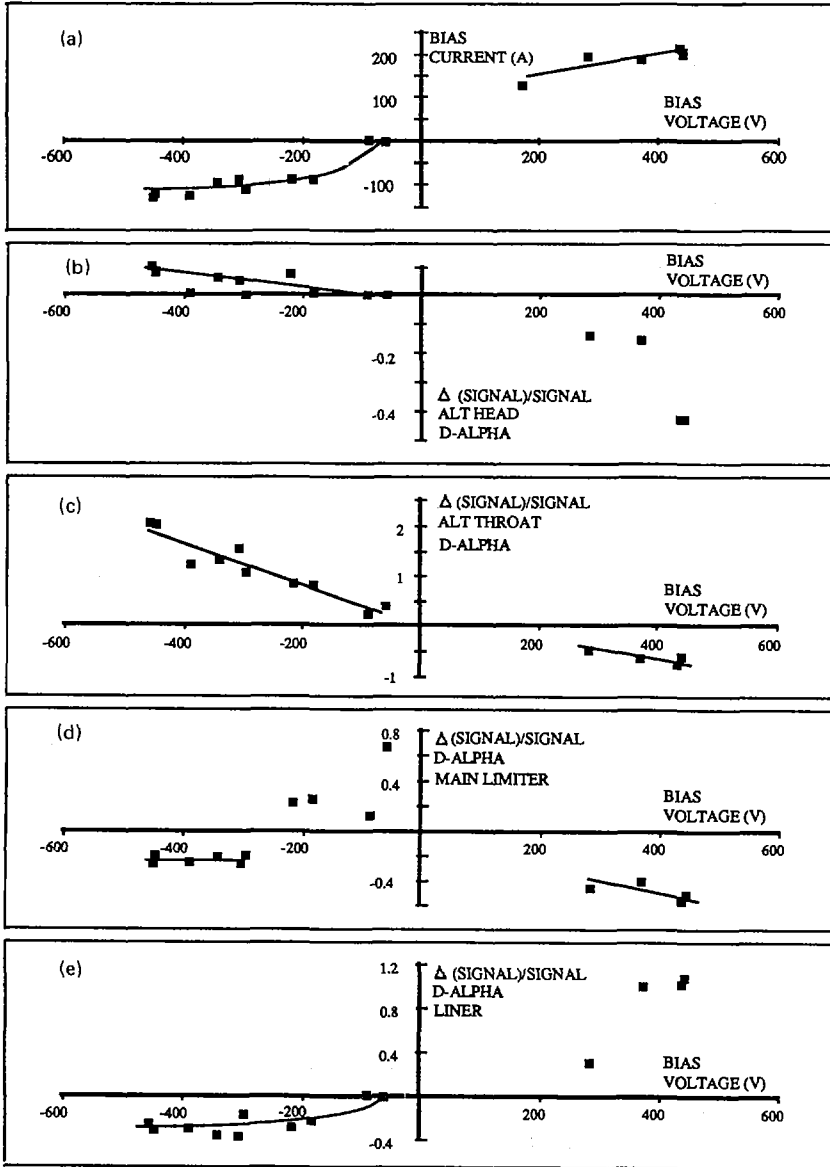


FIG. 6. (a) Current through the power supply versus bias voltage applied to ALT-I.  
 (b, c, d, e) Relative changes in  $D_{\alpha}$  signals at various locations.  $\Delta(\text{signal})/\text{signal}$  is the value just after turn-on of bias, minus the value just prior to bias, normalized to the value before bias.

During negative bias of ALT, the plasma potential decreases relative to the wall, creating a potential barrier between the plasma edge and the main limiters at 48 cm and the liner at 55 cm. The density bump reported in Fig. 5, and the decrease in the  $D_{\alpha}$  signals at the other limiters and liner are consistent with this potential barrier. For positive bias, the plasma potential increases relative to the wall, but is now below the ALT potential. The 220A of current in the circuit is determined by the amount of current that flows across the magnetic field in the edge and reaches the main limiters and liner, and not by the random electron flux in the edge near ALT. Overall, we conclude that plasma flows in the boundary are significantly modified by plasma potential changes, without requiring excessive currents in the power supply. In general, limiter biasing is a specific technique to alter wall recycling in tokamaks and a means to alter the plasma flux to various limiters and the liner.

### 3. PUMP LIMITER AND ICRF HEATING

First results on ALT-I behavior during ion cyclotron resonance heating (ICRF) [18,19] were reported earlier [14]. Here, we report a systematic comparison of ICRF heating using ALT-I as a pump limiter (PL mode) or, with its throat closed, as a regular limiter (RL-mode). Particular emphasis is given to the influence, if any, of pump limiter operation on core energy confinement time and of negative limiter biasing.

The analysis of energy confinement time is that of Messiaen et al. [18], in which the global energy confinement time,  $\tau_E$ , is determined from

$$\tau_E = \frac{E_{dia}}{P_{OH} + P_{RF} - \frac{dE_{dia}}{dt}}$$

where  $E_{dia}$  is the plasma energy determined from the diamagnetic loop signal,  $P_{OH}$  is the ohmic heating power during the ICRF heating, and  $P_{RF}$  is the RF power radiated into the tokamak vessel. A reasonable estimate of the RF power coupled to the plasma is 85% of the RF power delivered by the generator.

Results are given in Fig. 7, where  $\tau_E$  is plotted versus the total heating power,  $P_{OH} + P_{ICRH}$ , evaluated during a typical 0.5 second RF heating pulse. The open circles are values of  $\tau_E$  for ALT-I in the PL-mode, while solid circles denote  $\tau_E$  for RL-mode operation. No systematic difference is found. This is so, even though operation in the PL-mode reduces the degree of core density rise which normally accompanies the ICRH pulse. Though not shown here,  $\tau_{OH}$  follows an Alcator-like scaling with

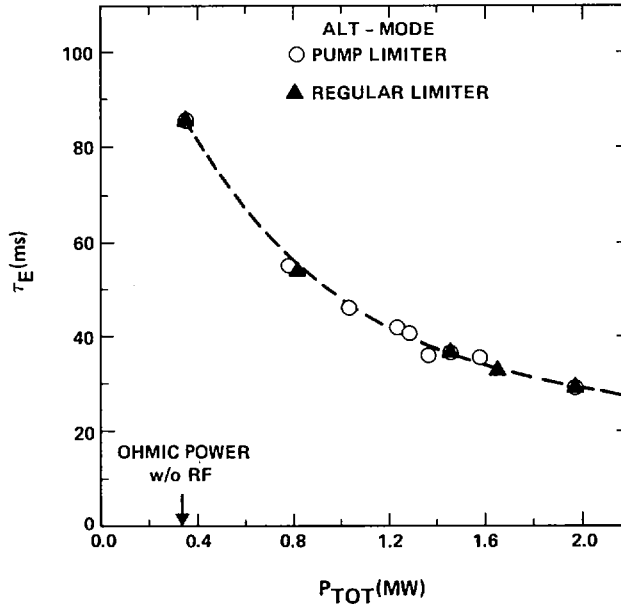


FIG. 7. Global energy confinement time as a function of total input power, determined midway through an ICRF power pulse. Open circles are for ALT-I as a pump limiter and triangles are for ALT-I as a regular limiter (with its throat closed).

density. No difference in  $\tau_{OH}$  scaling is found when operating ALT-I in either the PL- or RL-modes.

Negative limiter biasing during ICRH heating is found to reduce the recycling plasma flux at the RF antenna and, operationally, fewer breakdown/interruptions in the antennas are observed. Nevertheless, no differences in global  $\tau_E$  are found during ICRF heating and limiter biasing.

#### 4. CONCLUSIONS

Plasma edge flows can be strongly affected by limiter biasing. Plasma exhaust is increased (by a factor of 2 in this work) during negative bias, while flows to the liner, other limiters and the RF antennas generally decrease. No strong change in energy confinement is observed. The strong exhaust increase follows from a bump in the edge density profile which may be due to a radial potential barrier. Positive bias increases flow to the walls, decreases flow to the pump limiter, decreases plasma exhaust, and appears to induce impurity accumulation. No bump is found in the edge radial density profile.

During ICRH heating, negative biasing of ALT-I causes a decrease in recycling at the RF antenna and results in fewer antenna breakdowns/interruptions. However, no change in core plasma confinement is observed, relative to earlier results [18,19], when using ALT-I as a regular or a pump limiter.

#### ACKNOWLEDGEMENT

The authors gratefully acknowledge the help of the TEXTOR operations team and the support staff of UCLA, Sandia Labs and the ERM, Brussels.

#### REFERENCES

- [1] MIODUSZEWSKI, P.J., *J. Nucl. Mater.* **111&112** (1982) 253.
- [2] CONN, R.W., *J. Nucl. Mater.* **128&129** (1984) 407.
- [3] GOEBEL, D.M., *Fusion Technol.* **10** (1986) 761.
- [4] CONN, R.W., et al., in *Fusion Technology 1982* (Proc. 12th Symp. Jülich, 1982), Vol. 1, Pergamon Press, Oxford (1983) 497.
- [5] WAIDMANN, G., BAY, H.L., BERTSCHINGER, G., et al., in *Plasma Physics and Controlled Nuclear Fusion Research 1984* (Proc. 10th Int. Conf. London, 1984), Vol. 1, IAEA, Vienna (1985) 193.
- [6] WOLF, G., et al., *Plasma Phys. Controll. Fusion* **28** (1986) 1413.
- [7] PONTAU, A.E., et al., *J. Nucl. Mater.* **128&129** (1984) 434.
- [8] CAMPBELL, G.A., et al., *The Influence of Plasma-Neutral Interactions on the Behaviour of a Pump Limiter*, Rep. PPG-958, Univ. of California, Los Angeles (1986).
- [9] FINKEN, K.H., et al., *J. Nucl. Mater.* **145&146** (1987).
- [10] DIPPEL, K.H., FINKEN, K.H., GUTHRIE, S.E., et al., in *Plasma Physics and Controlled Nuclear Fusion Research 1984* (Proc. 10th Int. Conf. London, 1984), Vol. 1, IAEA, Vienna (1985) 249.
- [11] GOEBEL, D.M., et al., *Langmuir Probe Measurements in the TEXTOR Tokamak during ALT-I Pump Limiter Experiments*, Rep. PPG-945, Univ. of California, Los Angeles (1986).
- [12] McGRATH, R.T., et al., *J. Nucl. Mater.* **145&146** (1987).
- [13] DOYLE, B.L., McGRATH, R.T., PONTAU, A.E., *Nucl. Instrum. Methods Phys. Res., Sect. B* (1987).
- [14] LEUNG, K., et al., Rep. PPG-968, Univ. of California, Los Angeles (1986).
- [15] TAYLOR, R.J., JAMES, B.W., JIN, S.X., et al., in *Plasma Physics and Controlled Nuclear Fusion Research 1982* (Proc. 9th Int. Conf. Baltimore, 1982), Vol. 3, IAEA, Vienna (1983) 251.
- [16] SHIMADA, M., et al., *Bull. Am. Phys. Soc.* **30** (1985) 1439.
- [17] PHILLIPS, P.E., et al., *J. Nucl. Mater.* **145&146** (1987).
- [18] MESSIAEN, A., et al., *Plasma Phys. Controll. Fusion* **28** (1986) 71.
- [19] VANDENPLAS, P.E., DELVIGNE, T., DESCAMPS, P., et al., *Paper IAEA-CN-47/F-I-4*, these Proceedings, Vol. 1.
- [20] WINTER, J., *J. Nucl. Mater.* **145&146** (1987).
- [21] POSPIESZCZYK, A., ROSS, G., TEXTOR Group, private communication.
- [22] SAMM, U., et al., in *Fusion Engineering* (Proc. 11th Symp. Austin, TX, 1985), Vol. 1, IEEE-CAT. No. CH2251-7, IEEE, New York (1986) 66.

## DISCUSSION

R.J. HAWRYLUK: In your experiments, the confinement time in ICRF heated discharges was unaffected by the pump limiter. Did limiter biasing affect the confinement time?

R.W. CONN: At present, we have no evidence of improved energy confinement using limiter biasing with ICRF heating. However, no systematic experiments on this point have yet been undertaken.

A. GIBSON: On the basis of your results, would you care to offer a prognosis for the future of pump limiters?

R.W. CONN: Pump limiters have been shown in earlier work to be effective in controlling plasma density and also to have efficient exhaust capability. The key issue ultimately will be to achieve improved confinement, such as is now possible with divertors. The results presented in this paper demonstrate that plasma edge flows are strongly influenced by limiter biasing. This can be combined with material conditioning and pump limiter exhaust capability to produce low recycling operation — a key to achieving better confinement. Also, we have heard at this Conference that such improved confinement (H-mode) with a limiter has been achieved on JFT-2M. Given the inherent simplicity and low cost of limiters, the future for pump limiters is reasonably bright.



## CURRENT DENSITY PROFILES IN THE TEXTOR TOKAMAK

H. SOLTWISCH<sup>1</sup>, W. STODIEK<sup>2</sup>,  
J. MANICKAM<sup>2</sup>, J. SCHLÜTER<sup>1</sup>

<sup>1</sup> Euratom-KFA Association,  
Institut für Plasmaphysik der  
Kernforschungsanlage Jülich GmbH,  
Jülich, Federal Republic of Germany

<sup>2</sup> Princeton Plasma Physics Laboratory,  
Princeton University,  
Princeton, New Jersey,  
United States of America

### Abstract

#### CURRENT DENSITY PROFILES IN THE TEXTOR TOKAMAK.

Current density and hence safety factor profiles have been measured by the Faraday rotation method in the TEXTOR tokamak. The profiles of sawtooth dominated discharges appear marginally stable for all modes and have stationary values of  $q$  on axis less than unity, in some conditions as low as  $2/3$ . The profiles assume a roughly universal shape which is determined in the central region by the stability of the  $m = 1$  tearing mode and in the outer region by the general heat transport and thermal stability of the plasma column.

### 1. INTRODUCTION

The tokamak magnetic structure for low  $\beta$  plasmas is determined by "external" parameters: magnetic axis major radius, toroidal magnetic field strength, total plasma current and an "internal" parameter: the poloidal field distribution, adjusted to fulfil macroscopically MHD (at least near) stable equilibrium.

In general, the radial temperature profile is determined by balancing the ohmic heating with the plasma heat loss. The thermal instability<sup>1</sup> will cause the current channel to shrink if the plasma edge is set by a "virtual" limiter.<sup>2</sup> This shrinking process is halted, leading to a stationary state, through clamping of the local current density by additional local transport introduced by sawtooth activity near the plasma axis.<sup>3</sup> The sawtooth activity is connected with instability of the  $m=1$ ,  $n=1$  internal tearing mode, originating near the  $q=1$  radius.

Under steady state conditions with sawtooth activity the radius of the  $q=1$  surface and the current density profile (the "internal" tokamak parameter) are thus determined by the dependence of the stability of the  $m=1, n=1$  tearing mode on the current density profile.

The experimental investigation of this relationship is the subject of this paper.

The recent development on TEXTOR Tokamak of the Faraday rotation method<sup>4</sup> for poloidal magnetic field measurements has enabled us to follow the evolution of the current density distribution and in particular to determine the quasi-stationary profiles, especially near the plasma axis, for various "external" tokamak parameters. A direct measurement of the current density in this area is preferable to, for instance, inference from plasma conductivity, because of the intricacies of the sawtooth activity.<sup>5</sup>

The TEXTOR tokamak plasmas considered are ohmically heated, circular with aspect ratio of 3.5-4, and have an effective charge of 1.5-3. The "external" parameters varied are toroidal field and total plasma current.

Theoretically, tearing mode stability is determined by analyzing the observed profiles for  $m > 1$  modes with a cylindrical tearing mode code,<sup>6</sup> which is sufficient for this problem. The  $m=1, n=1$  mode, ideally unstable in cylindrical geometry,<sup>7</sup> requires toroidal analysis, which has been carried out with the Princeton resistive PEST code.<sup>8</sup>

The experimental results indicate that the plasma current density increases and the column radius decreases in time, until the  $q=1$  radius is well inside the plasma column. As a general trend, this has been derived from conductivity measurements with soft x-ray techniques permitting simultaneously the determination of electron temperature and  $Z_{\text{eff}}$  profiles. A direct determination of greater accuracy was carried out with the Faraday rotation method. Under these conditions the value of  $q$  on axis is measured to be considerably less than unity.

Such profiles have been found experimentally stable, that is, no modes of any  $m$  or sawtooth activity are observed. In many cases these profiles are hindered from further shrinkage by centrally located impurities. If the profile shrinks further (for instance by loss of impurities from the center), predominantly the  $m=1$  mode, with accompanying sawtooth activity, develops periodically, and now the sawtooth mechanism, on the average, becomes the controlling mechanism for the central conductivity.

The exact theoretical criteria for the onset of the  $m=1$  instability, as function of the  $q$ -profile and aspect ratio, are not

yet clear in detail.<sup>9</sup> Stability is favored by a plateau in the current density distribution, suggesting that, in toroidal geometry, stability can be obtained through nonlinear saturation and profile modification. This is supported by the observation that  $m=1$ ,  $n=1$  modes exist with stationary, large amplitudes for hundreds of plasma rotation periods.<sup>10</sup> For profiles with  $q=2.1$  at the limiter and  $q(0)=0.66$ , these plateaus could be resolved in our experiments, due to their dimensions relative to the apparatus. We find these profiles to be near marginal stability, using the PEST code, in agreement with the experiments.

We observe that in stationary conditions in sawtooth discharges, current density and  $q$ -profile assume a unique shape. This can be expressed in reduced coordinates (depending only on the "external" tokamak parameters  $R$ ,  $B_T$  and  $I$ ) as a result of the critical effect of the  $m=1$  tearing mode on transport:

$$j / [\frac{1}{\mu_0} (B_T/R)], \quad r / \sqrt{I / [\frac{1}{\mu_0} (B_T/R)]}$$

The universal profile is overall tearing mode marginally stable in the cylindrical approximation.

Thus the profiles may be interpreted as fine-scale heat conduction profiles, intrinsically marginally stable to higher- $m$  tearing modes, clamped only by the very critical  $m=1$  mode, through sawtooth activity, to the external tokamak parameters. With the  $q=1$  radius fixed, the total profile and thus the "internal" tokamak parameter is then determined.

## 2. ACCURACY OF THE FARADAY ROTATION METHOD TO DETERMINE THE VALUE OF $q$ AND $j$ AT THE MAGNETIC AXIS

To prove experimentally the stability of the  $m=1$  tearing mode, it is necessary to show that stability exists for  $q(0)$  considerably less than one. This requires sufficient spatial resolution of the polarimeter diagnostic inside the  $q=1$  radius to derive the value of  $q$  on axis by Abel inversion. For larger  $q=1$  radii this is possible in TEXTOR with the existing probing beam spacing of 10 cm. For plasmas with high  $q$  at the limiter and a small  $q=1$  radius, the effective number of probing beams can be increased by slowly moving the plasma relative to the beam system by about  $\pm 1/3$  beam distance. Even for small  $q=1$  radii we find generally agreement between the two methods. At present obtainable accuracies for  $q$  and  $j$  are given in Fig. 1 and are about  $\pm 15\%$  on axis. Thus, at this time the question of the stability of the  $m=1$  mode can be unambiguously decided only for cases of  $q$ -values considerably less than unity.

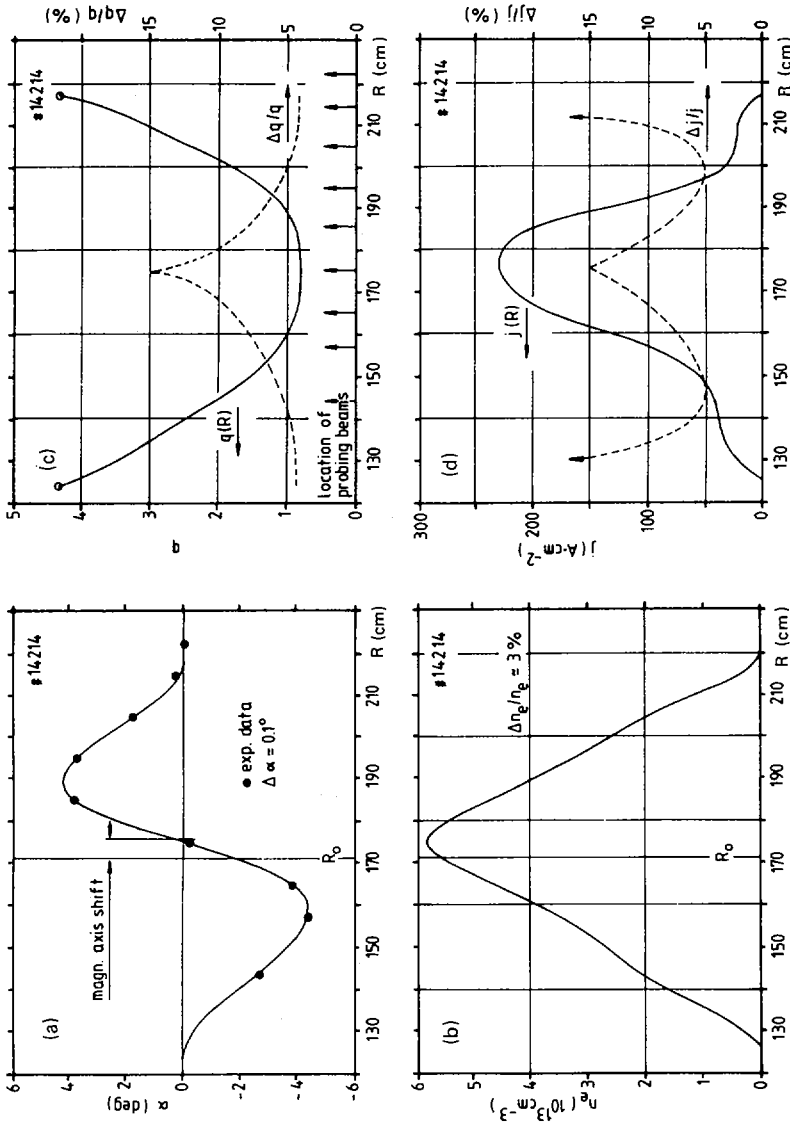


FIG. 1. (a) Faraday rotation angles and (b) radial electron density profile as obtained from the nine-channel polar interferometer during quasi-steady-state conditions of a non-sawtooth Ohmic discharge ( $I = 335 \text{ kA}$ ,  $B_T = 2 \text{ T}$ ). (c) Corresponding safety factor profile and (d) current density distribution derived from the interpolated rotation profile. The accuracy of  $q$  improves towards the plasma edge ( $\Delta q/q$ ) being determined by the small errors in  $I$ ,  $B_T$  and  $a$ ), whereas the accuracy of  $j$  rapidly deteriorates beyond  $r/a \sim 0.7$ .

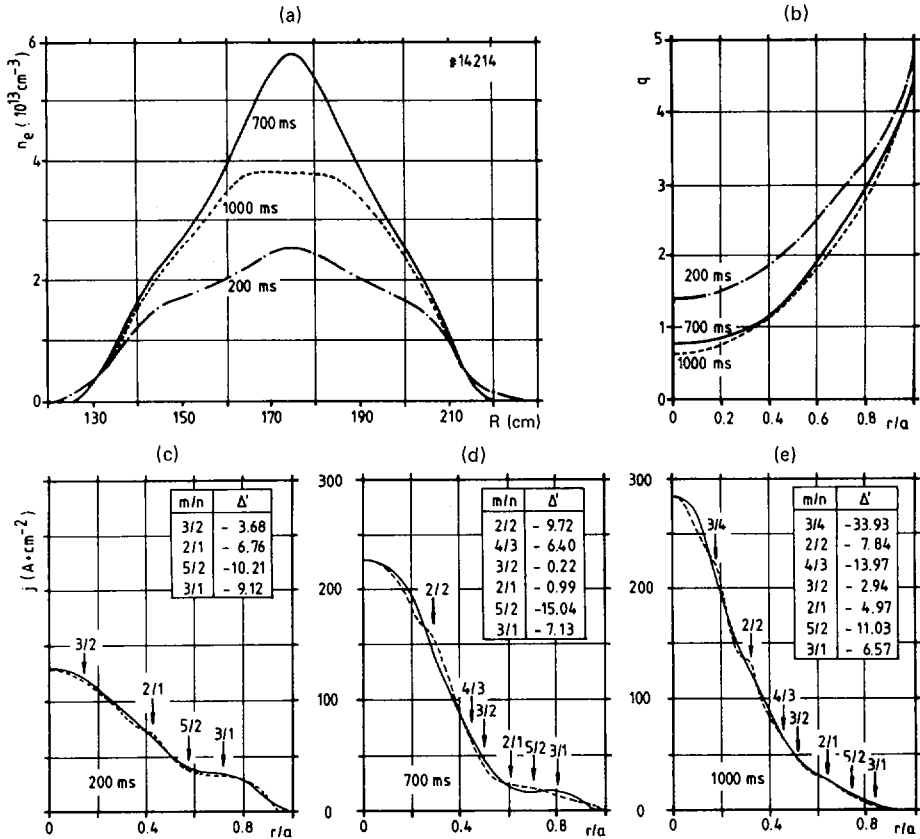


FIG. 2. (a) Electron density, (b) safety factor and (c-e) current density profiles at the end of current ramp-up (200 ms;  $\dot{I} = 625 \text{ kA} \cdot \text{s}^{-1}$ ,  $I = 300 \text{ kA}$ ) and in quasi-stationary conditions (700 ms, 1000 ms;  $I = 335 \text{ kA}$ ,  $B_T = 2 \text{ T}$ ). A non-destructive disruption occurring between 700 ms and 1000 ms changes the discharge characteristics from a non-sawtooth plasma of relatively high metal content to a cleaner sawtooth discharge. Safety factor and current density are plotted versus normalized flux surface radius  $r/a$  to allow a comparison with linear tearing mode stability theory in cylindrical geometry. Dashed curves represent computed stable profiles with  $\Delta'$ -values as listed.

### 3. DEVELOPMENT OF THE CURRENT DENSITY PROFILE IN TIME

An example of the development of the current distribution profile in time is shown in Fig. 2 for nearly constant total plasma current. Under the influence of the thermal instability the distribution contracts until the stationary profile with  $q$  on axis of about 0.6 is reached. The values of the stability criteria  $\Delta'$  of linear tearing mode theory in cylindrical approximation are given in the inserts for the individual modes, indi-

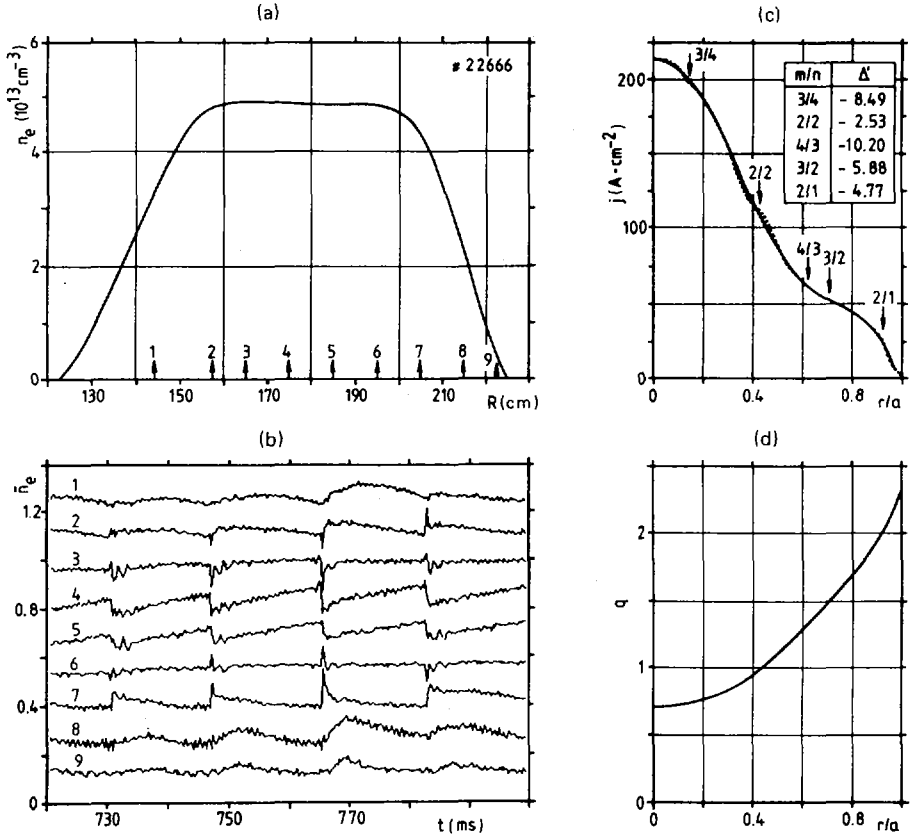


FIG. 3. Quasi-stationary low- $q$  discharge ( $I = 476 \text{ kA}$ ,  $B_T = 1.7 \text{ T}$ ,  $q(a) = 2.33$ ).  
 (a) Electron density distribution. (b) Fluctuations of line-integrated electron densities along the chords indicated in frame (a) ( $n_e$  in units of  $6.6 \times 10^{14} \text{ cm}^{-2}$ ). (c) Current density distribution. (d) Safety factor profile presented as in Fig. 2.

cated by the arrows (note that the  $m=1, n=1$  mode cannot be treated by this method). During the development in time the profiles always show small negative values of  $\Delta'$ , indicating marginal stability. It must be concluded that at the time of 700 msec the  $m=1$  mode is also stable because no  $m=1$  or sawtooth activity is observed, but the  $q=1$  radius is clearly at  $r/a = 0.3$ . This is accompanied by a peaked electron density profile indicated in frame a of Fig. 2. At 1000 msec the  $j$ -profile has further steepened, and sawtooth activity connected with the marginally unstable  $m=1$  mode occurs with the accompanied flattening of the electron density profile.

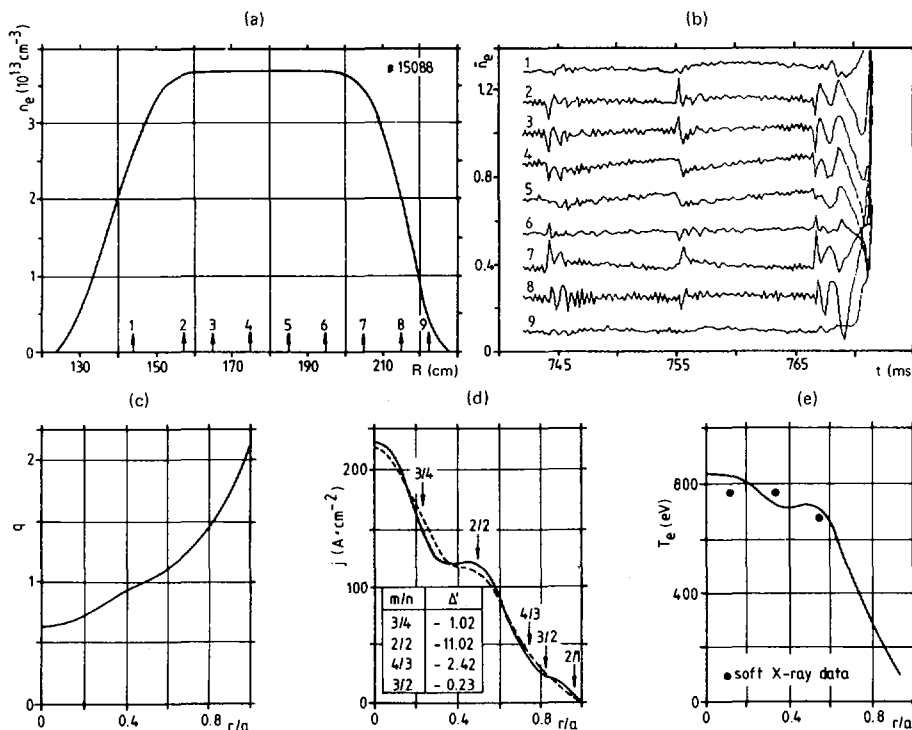


FIG. 4. Low- $q$  discharge ( $I = 485$  kA,  $B_T = 1.57$  T,  $q(a) = 2.1$ ) suddenly developing a large  $m = 1$  mode after about 500 ms of stationary behaviour (frame (b) showing the fluctuations of line-integrated electron densities at the chord positions indicated in frame (a)). Profiles about 25 ms before this event: (a) electron density, (c) safety factor, (d) current density, showing a pronounced shoulder at the  $q = 1$  radius, and (e) electron temperature calculated from the  $j$ -profile using neoclassical resistivity with  $U_\parallel = 1.50$  V and  $Z_{\text{eff}} = 2$  (dots represent average temperatures in the time interval 400–800 ms measured by soft X-ray pulse height analysis).

#### 4. PLASMAS WITH $q$ AT LIMITER NEAR 2

In Fig. 3, a current distribution with a limiter  $q$ -value near 2.3 is shown. The profile is maintained by the  $m=1$  instability-induced sawtooth activity. The  $m=1$  mode must be marginally stable. The  $\Delta'$  values of the higher- $m$  modes derived for the cylindrical model are all negative. In this case the  $q$ -value on axis is so low that even without the plasma shift method the accuracy is sufficient to definitely exclude a value of  $q(0)=1$ .

A case with  $q$  at limiter of 2.1 is shown in Fig. 4. The current distribution is held stationary by the increased transport caused by sawtooth activity initiated by marginal instability of the  $m=1$  mode. The  $q=1$  radius has moved out to  $r/a \sim 0.5$ .

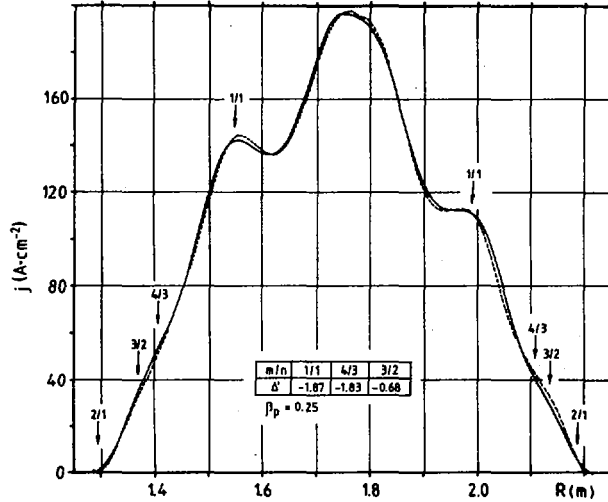


FIG. 5. Current density profile stable to the  $m = 1$  resistive mode in toroidal geometry ( $a/R_0 = 0.46/1.75$ ,  $B_T = 1.49$  T) with a finite  $\beta_p$  of 0.25 according to the Princeton PEST III code. Full line: experimental profile of Fig. 4, used to calculate the required input information  $q(\psi)$ ; dashed line: stable profile after self-consistent equilibrium recalculation.

The  $q(0)$  is about  $0.6 \pm 15\%$ . Frame e of Fig. 4 gives an indication of the electron temperature from soft X-ray measurements (dots). The solid curve represents the temperature profile derived from the current density profile using neoclassical electron conductivity.

For this steep profile the nonlinear stability behaviour of the  $m=1$  mode is so strong that an actually measurable plateau occurs in the  $j$ -profile. The precarious stability situation is evident by the rapidly growing  $m=1$  mode (at 767 msec) which (in contrast to the small local  $m=1$  modes which may produce sawtooth activity without affecting the current distribution) produces, by total reconnection, a complete disruption of the plasma column.

The current density profile of Fig. 4 has been analyzed with respect to tearing mode stability with the PEST code in toroidal geometry<sup>11</sup>. Figure 5 shows the result. The solid curve is the experimental profile which was entered into the code as a  $q(\psi)$ -profile. The dotted line represents as a check the recomputed  $j$ -profile for the recalculated plasma equilibrium. The computed values of  $\Delta'$  for the 1/1, 4/3, 3/2 modes are all slightly negative, indicating marginal stability including the 1/1 mode. As expected, stability cannot be obtained in cylindrical geometry.<sup>11</sup> From the experimental results as well as from

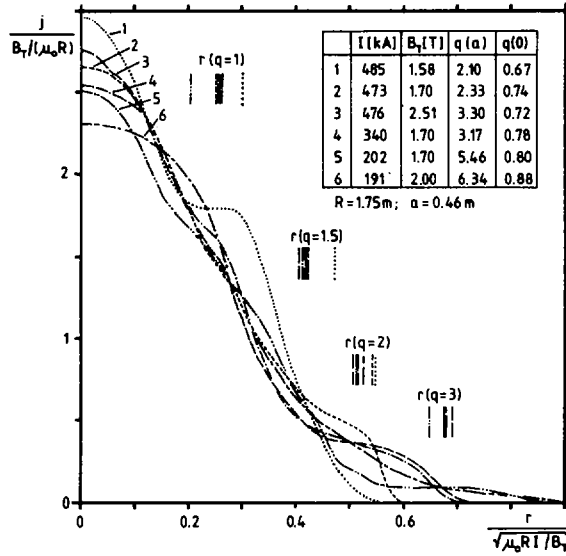


FIG. 6. Superposition of normalized current density profiles measured in a variety of quasi-stationary sawtoothing Ohmic discharges (see insert). In reduced co-ordinates the profiles resemble roughly a universal profile.

this first theoretical result we conclude that the  $m=1, n=1$  resistive mode can be linearly or at least nonlinearly stable in toroidal geometry. The dependence on geometry and other profile effects is under investigation.<sup>11</sup>

## 5. PROFILE SHAPE

The experimental profiles show a dependence of the effective minor radius on the plasma current and current density on axis. With the current density clamped inside the  $q=1$  radius, the profile outside the  $q=1$  radius is also fairly well fixed by the restriction of the thermal transport. It is thus convenient to display the experimental profiles for various external tokamak parameters in appropriate coordinates. Figure 6 shows that they can roughly be represented by one profile. This effective minor radius dependence requires the effectiveness of the virtual or radiation limiter, which in the investigated cases was assured by the presence of a small amount of light impurities (carbon). Theoretically the situation around the  $q=1$  radius is still not completely clear, and thus the  $q=1$  radius cannot be determined precisely because the  $m=1$  stability criteria are not sufficiently well known to warrant numerical calculations.

## SUMMARY

In stationary state plasmas with sawtooth activity,  $q(0)$  is found to be considerably below unity. In most cases, but not exclusively, sawtooth activity is not connected with complete reconnection, which would increase  $q(0)$  to near unity. Experimentally, the  $m=1$ ,  $n=1$  tearing mode is intermittently stable or at least saturated at an undetectable level. Theoretical estimates with the PEST code confirm these results in the cases investigated. The effect of current density clamping near the axis results in a general shape of the stationary, sawtooth dominated, current distribution and determines the effective minor radius.

## ACKNOWLEDGEMENT

This work was in part supported by U.S. DoE Contract No. DE-AC02-76-CH0-3073.

## REFERENCES

- [1] BISHOP, A.S., HINNOV, E., in Plasma Physics and Controlled Nuclear Fusion Research (Proc. Conf. Culham, 1965), Vol. 2, IAEA, Vienna (1966) 673.  
GRISHAM, L.R., BOL, K., Nucl. Fusion **18** (1978) 315.  
YOSHIKAWA, S., CHANCE, M.S., Bull. Am. Phys. Soc. **31** (1986) 14.
- [2] FURTH, H.P., ROSENBLUTH, M.N., RUTHERFORD, P.H., STODIEK, W., Phys. Fluids **13** (1970) 3020.
- [3] VON GOELER, S., STODIEK, W., SAUTHOFF, N.R., Phys. Rev. Lett. **33** (1974) 1201.
- [4] SOLTWISCH, H., Rev. Sci. Instrum. **57** 8 (1986) 1939.
- [5] ALLADIO, F., MAZZITILLI, G., TUCILLO, A.A., VLAD, G., in Controlled Fusion and Plasma Physics (Proc. 12th Europ. Conf. Budapest, 1985), Vol. 9F, Part I, European Physical Society (1985) 138.
- [6] LACKNER, K., private communication. (This code was provided by Dr. Karl Lackner, Max-Planck-Institut für Plasmaphysik, Garching, and installed by A. Kaleck, Jülich.)
- [7] FURTH, H.P., RUTHERFORD, P.H., SELBERG, H., Phys. Fluids **16** 7 (1973) 1054.
- [8] GRIMM, R.C., DEWAR, R.L., MANICKAM, J., JARDIN, S.C., GLASSER, A.H., CHANCE, M.S., in Plasma Physics and Controlled Nuclear Fusion Research 1982 (Proc. 9th Int. Conf. Baltimore, 1982), Vol. 3, IAEA, Vienna (1983) 35.
- [9] MANICKAM, J., Phys. Rev. Lett. **51** (1983) 1959.
- [10] JAHNS, G., Nucl. Fusion **22** (1982) 1049.
- [11] MANICKAM, J., Bull. Am. Phys. Soc. **31** (1986) 1431.

## DISCUSSION

A. GIBSON: Can you clarify whether your observed universal current density profile also holds good for discharges with large additional heating, especially in the case of off-axis heating?

H. SOLTWISCH: So far we have not made any systematic studies of the current profiles during ICRH on TEXTOR.

R.J. GOLDSTON: We have a ten-channel interferometer on TFTR, and when we carry out Abel inversion, we find significant in-out asymmetries that cannot be explained by a picture in which  $n_e = n_e(\psi)$ . We attribute this result to asymmetries in the scrape-off plasma. Of course, our limiter geometry is different from yours, but I wonder whether there are any uncertainties due to effects of this sort which can interfere with your measurement of  $q$ ?

H. SOLTWISCH: For standard Ohmic discharges, especially at moderate  $\bar{n}_e$ , we have no indication that  $n_e$  varies considerably on a flux surface. Lithium beam measurements of  $n_e$  in the scrape-off layer usually match the  $n_e$  profiles obtained by interferometry quite well.



## STABILITY AND CONFINEMENT STUDIES IN THE PRINCETON BETA EXPERIMENT (PBX)\*

M. OKABAYASHI, K. BOL, M. CHANCE, P. COUTURE<sup>1</sup>,  
H. FISHMAN, R.J. FONCK, G. GAMMEL, W.W. HEIDBRINK<sup>2</sup>,  
K. IDA<sup>3</sup>, K.P. JAEHNIG, G. JAHNS<sup>2</sup>, R. KAITA, S.M. KAYE,  
H. KUGEL, B. LeBLANC, J. MANICKAM, W. MORRIS<sup>4</sup>,  
G.A. NAVRATIL<sup>5</sup>, N. OHYABU<sup>2</sup>, S. PAUL, E. POWELL,  
M. REUSCH, S. SESNIC, H. TAKAHASHI  
Princeton Plasma Physics Laboratory,  
Princeton University,  
Princeton, New Jersey,  
United States of America

### Abstract

STABILITY AND CONFINEMENT STUDIES IN THE PRINCETON BETA EXPERIMENT (PBX).

Values of  $\beta_1$  in excess of 5% were achieved in the PBX tokamak by producing plasmas with indentations  $\geq 20\%$ . Despite the high beta equilibria achieved, the plasmas still remained within the first regime of stability. Comparisons of data with theoretical analyses were made in order to evaluate the MHD stability properties for plasmas close to the Troyon-Gruber limit at all  $q$ . At the low  $q$  and high  $\beta_1$ , the plasmas were limited by hard disruptions whose characteristics were generally consistent with those expected from ideal external kink modes. At higher  $q$ , a wide variety of internal and edge MHD modes were found to be associated with loss of both thermal and fast ion energy. This MHD activity included fishbones, internal sawtooth-like disruption, Edge Relaxation Phenomena (ERPs), coupled disruptions, and the 'tangential equivalent' of fishbones. Most of the activity was associated with internal  $m/n = 1/1$  modes. At low plasma density, the tangential instabilities observed in discharges with pure tangential and mixed tangential and perpendicular neutral beam injection, led to fast ion losses that were comparable to those associated with fishbones in purely perpendicular injection.

---

\* Work supported by the United States Department of Energy, under Contract No. DE-AC02-76CHO-3073.

<sup>1</sup> Institut de la recherche d'Hydro-Québec, Canada.

<sup>2</sup> GA Technologies Inc., San Diego, CA, USA.

<sup>3</sup> University of Nagoya, Nagoya, Japan.

<sup>4</sup> Balliol College, University of Oxford, Oxford, UK.

<sup>5</sup> Columbia University, New York, NY, USA.

## 1. Introduction

Recent theoretical results [1,2] indicate that the bean-shaped configuration can lead to high- $\beta_t$  plasmas in the second stability regime for both ballooning and internal kink modes. The PBX [3] has achieved values of  $\beta_t$  in excess of 5% in plasmas that have indentations  $>20\%$ . While the  $\beta_t$  values are greater than those previously achieved on conventional tokamaks, the plasmas still reside within the first regime of stability, as defined empirically by the relation  $\beta_t < 2.5\beta_c$ , where  $\beta_c = \mu_0 I_p / (a_{mid} B_t)$ , with  $a_{mid}$  the midplane half radius [4,5]. Extensive theoretical and experimental analyses have been carried out in order to evaluate the MHD phenomena associated with the present operational  $\beta_t$  limit. This paper summarizes the results of these studies and, in addition, compares the MHD properties and energetics of plasmas with purely perpendicular injection to those with purely tangential injection. The final topic is a brief discussion of the confinement and transport properties of H-mode plasmas.

The experimental conditions near the Troyon-Gruber  $\beta_t$  limit are summarized in Fig. 1. While Fig. 1(a) contains the data points over all experimental conditions, the data in Fig. 1(b) and 1(c) were limited, for purposes of clarity, to discharges with  $\beta_t > 1.5 \beta_c$ . At high  $\beta_c$ , discharges were obtained with indentations of 18 to 22%; here the indentation  $i_n$  is defined as  $i_n = d / (2 a_{mid} + d)$ , where  $d$  is the radial depth of the indentation. At lower  $\beta_c$ , the highest attainable indentations were progressively less, and the edge  $q$  values were higher.

Along the  $\beta_t$  boundary, the various MHD phenomena and plasma characteristics that were observed depended on the value of  $\beta_c$ . At the highest  $\beta_c$ , plasmas were limited by hard disruptions exhibiting little MHD activity until just before the disruption. At lower values of  $\beta_c$  (0.8 to 1.3),  $\beta_t$  saturation, sometimes with subsequent  $\beta_t$  collapse, was observed. The  $\beta_t$ -saturation phase of the discharge was associated with internal and external MHD bursts, while the collapse phase was associated with a more continuous, saturated amplitude mode in addition to ERP's. Much, but not all, of the MHD activity during both phases of these discharges exhibited internal  $m/n = 1/1$  activity. Examples of high- and low- $\beta_c$  discharges are shown in Fig. 2(a) ( $\beta_t = 5.3\%$ ,  $\beta_c = 2.5$ ,  $i_n = 20\%$ ) and Fig. 2(b) ( $\beta_t = 2.8\%$ ,  $\beta_c = 1.0$ ,  $i_n = 10\%$ ). The high- $\beta_t$  configuration could be produced only by ramping the current at a rate of  $>1.5$  MA/sec. For the  $\beta_t$  collapse discharges, the current was held relatively constant during the neutral-beam pulse.

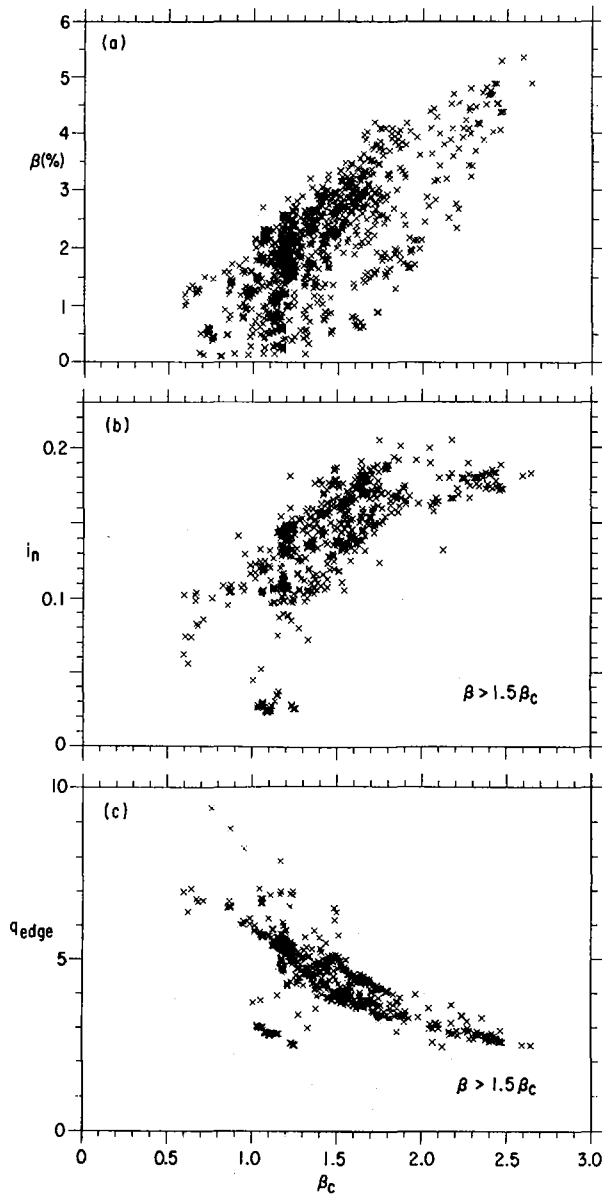


FIG. 1. Range of experimental parameters. (a) Achieved  $\beta_t$  versus Troyon-Gruber parameter  $\beta_c$ , including all experimental conditions; (b) indentation  $i_n$  versus  $\beta_c$  only for  $\beta \geq 1.5 \beta_c$ ; (c)  $q_{edge}$  versus  $\beta_c$  only for  $\beta \geq 1.5 \beta_c$ .

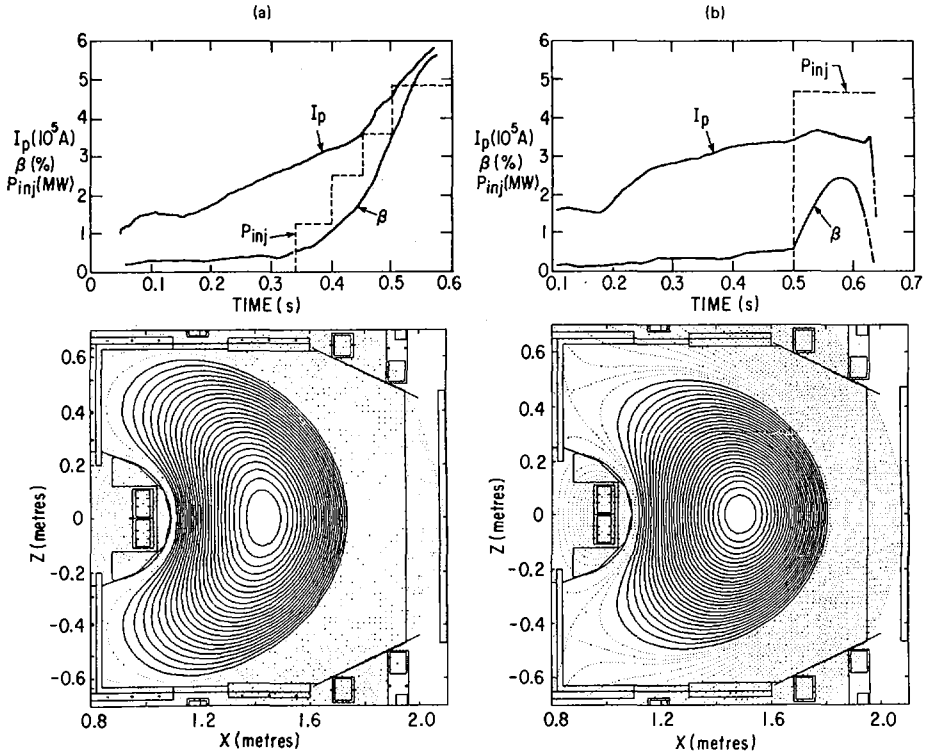


FIG. 2. Examples of discharges with (a) high  $\beta_c$  (high  $\beta$ , and low  $q$  with large current ramp) and (b) low  $\beta_c$  (medium  $\beta$ , and medium  $q$  with low current ramp). Equilibrium was calculated at  $t = 560$  ms for high  $\beta_c$  (a) and  $t = 575$  ms for low  $\beta_c$  (b).

## 2. Discharges Near the $\beta_t$ Limit

In an attempt to delineate the mode or modes responsible for the experimental  $\beta_t$  limit, theoretical  $\beta_t$  limits were calculated using equilibria based on the experimental conditions (Fig. 3). Calculations were performed in which the following parameters were matched to the experimental measurements: coil and plasma currents, poloidal flux, diamagnetic signal, and a total pressure profile taken to be proportional to the electron pressure profile measured by Thomson scattering. In some cases these pressure profiles were cross checked against the pressure profiles determined by the time dependent, generalized geometry transport code, TRANSP. Three cases at various  $\beta_c$  were chosen as representative. In this calculation  $q(0)$  was fixed at 0.8. The calculations focused on three instabilities: the internal and external kink and the

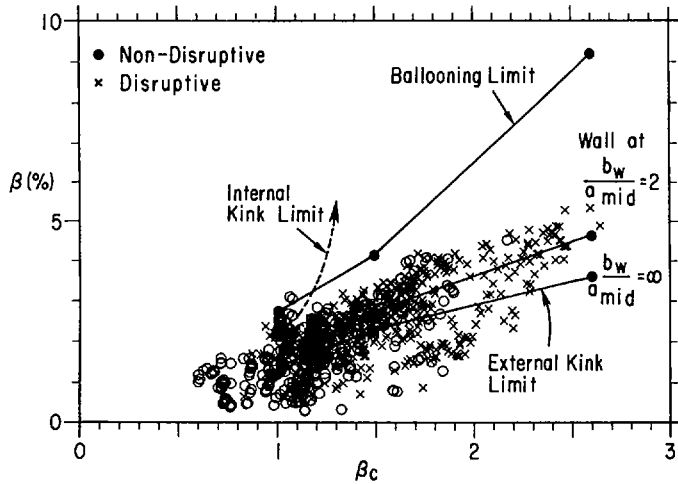


FIG. 3. Comparison of experimentally achieved  $\beta$  values and onset of various ideal MHD instabilities. Cases chosen as representative are: (1)  $\beta_c = 2.5$ ;  $\beta = 5.3\%$ ;  $i_n = 20\%$ ; (2)  $\beta_c = 1.5$ ;  $\beta = 3.1\%$ ;  $i_n = 17\%$ ; (3)  $\beta_c = 1.0$ ;  $\beta = 2.8\%$ ;  $i_n = 10\%$ .

high- $n$  ballooning modes. For high  $\beta_c$  and hence high indentation, the internal kink mode is completely stable and the marginal  $\beta_t$  for ballooning modes is between 8 and 9%. However, without a conducting shell, the external kink goes unstable at 3.5%, but with a conducting shell at one plasma midplane half-width,  $b_w/a_{mid} = 2$ , the marginal  $\beta_t$  for stability is increased to 4.5-5%, close to the observed value.

At slightly lower  $\beta_c$  ( $\beta_c \approx 1.5$ ,  $\beta_t = 3.1\%$ ,  $i_n = 17\%$ ), the relative stability of the three modes is similar to that at higher  $\beta_c$ . At the lowest  $\beta_c$ , with the lower indentation ( $\beta_c = 1.1$ ,  $\beta_t = 2.7\%$ ,  $i_n = 10\%$ ), the internal kink is unstable, indicating a more peaked pressure profile than that assumed in previous theoretical studies [2]. With these pressure and  $q$  profiles consistent with the experimental results, the external kink and ballooning modes can be destabilized at relatively low values of  $\beta_t$  (1.5 to 2.5%).

### 3. MHD Activity

#### 3.1 High $\beta_c$

High  $\beta_c$  ( $\beta_c \approx 2.5$ ) discharges were produced by employing a large current ramp of  $>1.5$  MA/sec for a period of up to 140 msec during neutral-beam injection, resulting in discharges

similar to the one shown in Fig. 2(a). The plasma parameters for this discharge were  $I_p = 570$  kA,  $n_e(0) = 6.0 \times 10^{13} \text{ cm}^{-3}$ ,  $T_e(0) = 2.0$  keV, and  $T_i(0) = 4.5$  keV at  $t = 570$  msec [6]. All discharges at these high  $\beta_c$  terminated in a hard disruption. The disruption, at the highest  $\beta_c$  (and lowest  $q$ ), was characterized by rapid growth (150  $\mu\text{sec}$ ) of magnetic activity leading to a simultaneous loss of plasma energy and current. At slightly lower  $\beta_c$ , growth of magnetic activity led first to the partial (30%) loss of plasma energy with no loss of current [7], but with several msec delay to the loss of both current and the remainder of the energy. The amplitude of the  $m/n = 1/1$  component was smaller in the case of the shorter delays. The delay period was determined to be a period of non-oscillating exponential growth of an  $n = 1$  mode locked in phase with a specific toroidal orientation, presumably due to some field misalignment.

The poloidal mode structure of the magnetic activity agrees well with that calculated from PEST for the external kink with some of the ideal MHD constraints relaxed [8]. Strong coupling across the discharge results in a spectrum of  $m$  components, including an  $m/n = 1/1$  component near the center. The amplitude of this component is theoretically expected to depend strongly on the exact value of  $[q(0) - 1]$ .

At still lower  $\beta_c$  (1.5 to 2.0), the internal  $m/n = 1/1$  crash was accompanied by a smaller energy loss, and it did not necessarily lead to a current termination [7].

### 3.2 Low $\beta_c$

At values of  $\beta_c \approx 1$  ( $i_n \approx 10\%$ ), stability calculations indicate that the plasmas may be unstable to external or internal kink or ballooning modes depending on the specific  $\beta_t$  value (Fig. 3). Experimentally these plasmas exhibited a variety of internal and edge MHD phenomena, some of which were associated with losses of thermal and/or fast-ion energy. An example of this is shown in Fig. 4; for this discharge four neutral beams were injected (two perpendicular and two parallel) with a total injected power of 5.2 MW. The diamagnetic signal shows  $\beta_t$  increasing and then saturating at about 590 msec and finally collapsing at about 640 msec. During the time of  $\beta_t$  saturation, there were various MHD modes excited: internal disruptions with  $m/n = 1/1$  precursors (582, 590, 598, and 620 msec), fishbones (606, 608, 610, and 615 msec), and edge relaxation phenomena -- ERP's [9-12], causing energy loss predominantly from the outer plasma region (e.g. 592 msec). Associated with the collapsing phase in the plasma  $\beta_t$  was a continuous, saturated amplitude mode that exhibited an  $m/n = 1/1$  internal structure and, depending on the exact

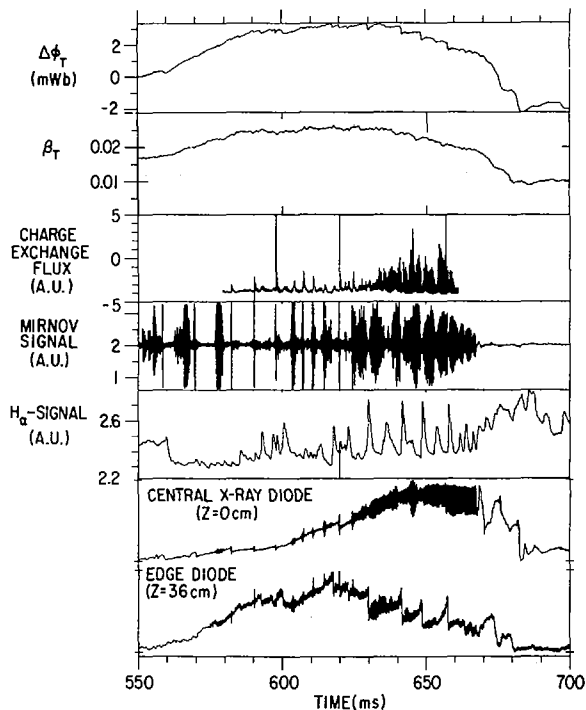


FIG. 4. Characteristics of low  $\beta_c$  discharges.  $\Delta\phi_T$  is diamagnetic flux loop signal, and  $\beta_t$  is determined from  $\Delta\phi_T$  and flux loop measurements.

discharge, either an  $n = 1$ ,  $m = 2$  or a higher- $m$  coupled mode structure as deduced from the magnetic probe measurements. The plasma stored energy dropped even more dramatically when the mode locked ( $t = 667$  msec) and, after locking, grew exponentially.

### 3.2.1 $\beta_t$ -Saturation Phase

While the  $m/n = 1/1$  precursor to the internal disruption during the  $\beta_t$ -saturation phase is similar in some respects (frequency and growth rate) to that of a typical sawtooth, other features point to their marked difference. Figure 5(a) shows the amplitude and phase of the precursor oscillations as measured by the horizontally viewing soft X-ray array. The relative amplitude of the oscillations,  $\tilde{s}/s$ , exhibits a broad structure and shows a gradual phase change across the plasma center unlike the typical sawtooth which exhibits a clear  $180^\circ$  jump in phase [Fig. 5(b)]. Here  $\tilde{s}/s$  is defined as the ratio of the precursor amplitude  $\tilde{s}$  to the average X-ray signal

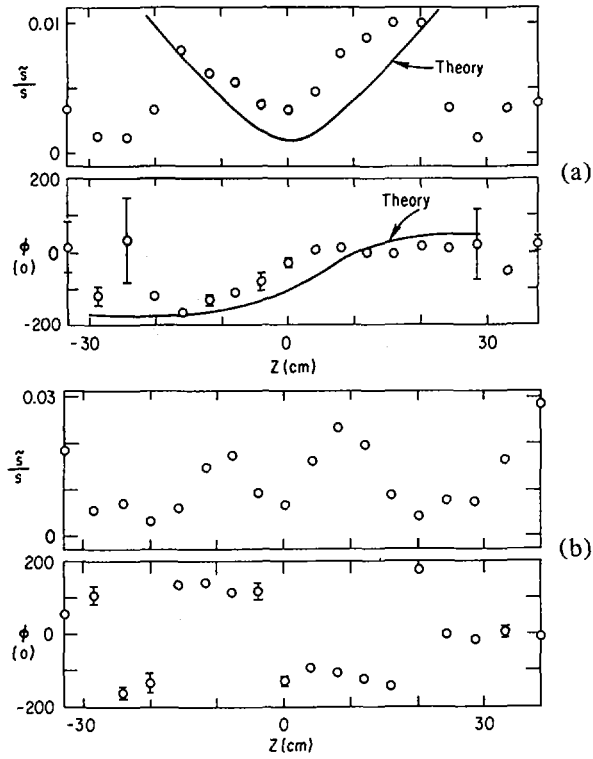


FIG. 5. (a) Amplitude and phase of precursor with two perpendicular and two parallel injectors (at  $t = 620$  ms). Solid lines are theoretical values predicted with PEST code. (b) Behaviour of typical sawtooth.

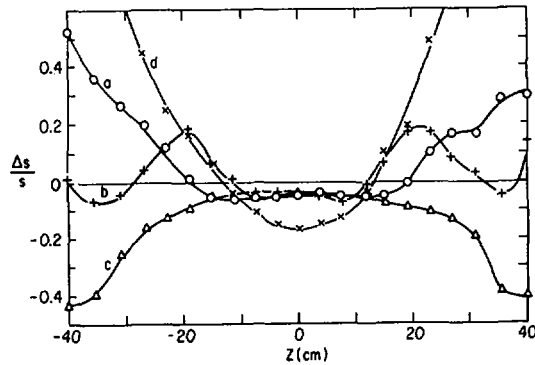


FIG. 6. Change of soft X-ray radial profile before and after mode crash. (a) Crash of internal mode producing ERP with several ms delay; (b) crash of internal mode having additional inversion around  $q = 2$  surface; (c) crash with ERP event; (d) typical sawtooth crash.

amplitude  $s$ . Another difference between the internal disruptions shown here and the typical sawtooth was the profile of the heat redistribution at the time of the "crash," as shown in Fig. 6. In the figure, the  $\Delta s/s$  for various types of events are shown, where  $\Delta s/s$  is the drop in the X-ray signal at the crash normalized to the average value. While the sawtooth exhibits a relatively large drop in the plasma center and an inversion near the  $q = 1$  radius (curve d), one type of internal disruption exhibits only a small, but broad, drop in the center, with large positive  $\Delta s/s$  beyond (curve a). The normalized amplitude  $\Delta s/s$  did not decrease within the field of view. Occasionally, an additional inversion was observed near  $z \approx 40$  cm, close to the estimated location of  $q = 2$  surface as shown on curve b. The "coupled disruption" events [curve (b)] coincided with spikes in the  $H_{\alpha}/D_{\alpha}$  emission. The type of crash that does not exhibit a second inversion (curve a) tended to cause the ERP event (curve c) within a few msec, most likely due to the development of a large temperature gradient at a larger minor radius following the internal disruption. The large temperature gradient did not develop in the second type of internal disruption (curve b) because of the double inversion; therefore, this "coupled disruption" event did not lead to an ERP. There is also a possibility that coincident with the coupled disruption, a small ERP occurred which might have been masked in our measurement by the  $q = 2$  disruption. The energy loss evaluated from the diamagnetic flux signal at the ERP events was 3 to 4% of the stored energy. This value was consistent with the thermal energy loss estimated from the change of the soft X-ray signal.

To test the relation between the observed internal oscillations and the ideal MHD prediction, the soft X-ray array signals were calculated using the simulation from the ideal-MHD code, PEST, assuming that the emissivity was proportional to the integral along the sight of the square of the pressure. As shown by the solid line in Fig. 5(a), theory predicts a broad phase shift presumably due to the strong coupling to the higher- $m$  components. This compares well with the experimental observation. Furthermore, it was recently pointed out [13] that pressure-driven internal modes are unstable at high  $\beta_t/\beta_c$ , even for  $q(0) > 1$  if the shear is reduced around the magnetic axis. Under that condition the mode tends to couple to the plasma periphery; the experimental profiles were not far from the onset condition.

### 3.2.2 $\beta_t$ -Collapse Phase

The actual collapse of  $\beta_t$  occurs during an otherwise steady-state portion of the discharge. Associated with the

beginning of the loss of plasma and beam energy during this time was a continuous mode, as observed on various magnetic pick-up coils, with a frequency of up to 15 kHz and locked to the plasma rotation. This continuous mode grew after several internal disruptions and/or fishbones. The internal structure of this mode was similar to that of the internal disruption precursor, exhibiting  $m/n = 1/1$  behavior. Dependent on the precise discharge, however, the strength of the internal  $m/n = 1/1$  varied. For discharges in which the continuous  $m/n = 1/1$  was dominant internally, the magnetic loops observed higher  $m$  (4 to 6)/ $n = 1$  components, indicating a strong toroidal coupling of the internal mode. However, for discharges in which the internal  $m/n = 1/1$  was not dominant (e.g., higher amplitude  $m \geq 2$  components observed on the soft X-rays), the magnetic loops indicated  $m/n = 2/1$  structure of the continuous modes. During the continuous modes, the excitation of ERP's occasionally coincided with a decrease in frequency (at constant  $\tilde{B}_0$  signal amplitude) of the mode.

The continuous oscillations were observed to slow down during the discharge, corresponding to a slowing down of the plasma rotation. Once locked, however, the  $n = 1$  mode grew (it is difficult to identify  $m$  numbers due to slow rotation), as observed from a toroidal array of  $B_r$  loops, and was associated with a large loss of energy. As was the case in the low- $q$  disruption, the mode locked in phase with the same toroidal orientation mentioned earlier in connection with the high- $\beta_t$  disruption.

### 3.3 Tangential Beam-Driven Instability at Modest Indentation and Low Density

With purely tangential injection for plasmas with  $\beta_c = 1.0$  to 1.2 and low indentation, a loss of fast ions associated with bursts of low-frequency (20 to 30 kHz) and high-frequency (150 to 220 kHz) MHD activity was observed [14]. As shown in Fig. 7 the fast-ion loss, detected on both the neutron and the neutral charge-exchange detectors, caused a significant power loss only in low density ( $n_e \leq 1.5 \times 10^{13} \text{ cm}^{-3}$ ) plasma, where there was a correspondingly high ratio of beam ion pressure to plasma thermal pressure. The fast-ion losses occurred during periods of either low plus high-frequency activity or high-frequency activity alone. The range of high frequencies was comparable to the transit frequency of tangentially moving beam ions, indicating a resonant interaction between the fast particles and the mode similar to fishbone loss [15]. The greatest particle loss occurred during the combined low- and high- frequency events. The low-frequency portion exhibited a growing  $m/n = 1/1$  structure and led to a "crash" that had a much

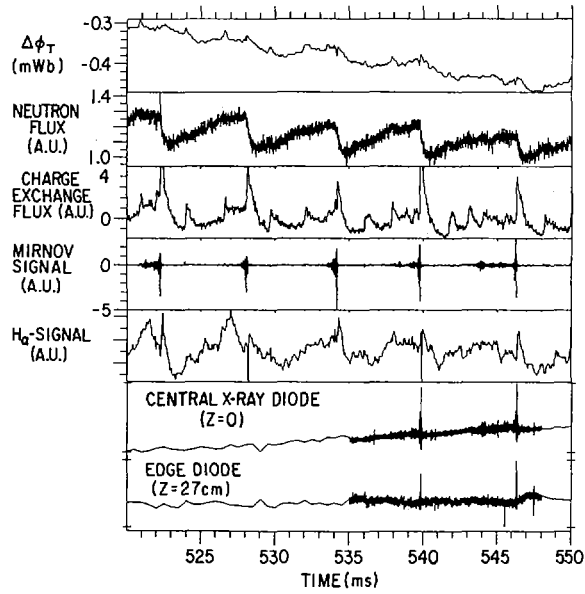


FIG. 7. Characteristics of parallel injection.

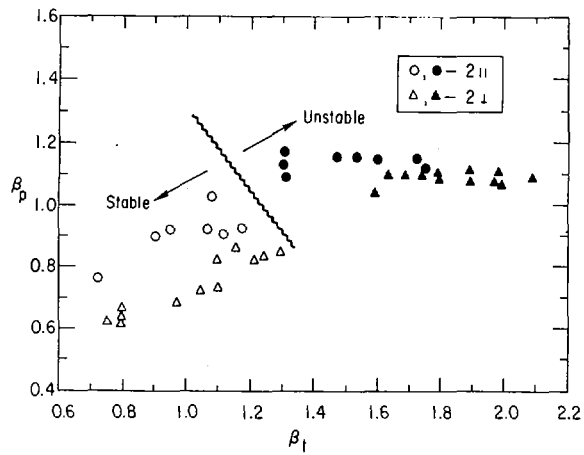


FIG. 8. Comparison of onset dependence of fast ion loss on  $\beta_p$ ,  $\beta_t$  for perpendicular and parallel injections.

smaller central drop and much broader inversion radius than a typical sawtooth, but was similar to that of the internal disruption cases. The average energetic ion confinement time, inferred from the drops in the neutron emission, differed little from that associated with the fishbone instability during purely perpendicular injection. In addition, the values of  $\beta_t$  and  $\beta_p$  for which the tangential and fishbone modes go unstable are similar (Fig. 8).

#### 4. Confinement and Transport in H-Mode

PBX plasmas limited by a magnetic separatrix internal to the vessel rather than by a material surface were produced by using a flat or only slightly increasing ( $<1$  MA/sec) plasma current. These plasmas, with indentations up to 18%, exhibited H-mode transitions typical of the observed diverted plasmas in ASDEX and PDX: a sudden drop in the  $H_\alpha/D_\alpha$  signal associated with a continual rise in plasma density at constant gas puff rate. Both effects indicate an increase in the effective particle confinement time. However, what did not necessarily follow the H-mode transition in PBX was a sustainable enhancement of the energy confinement time. For instance, at the lower toroidal fields ( $<1.2$  T), energy confinement times increased by 50% above the nominal L-mode value at the time of the transition, but decayed back to the L-mode values within 50 to 100 msec. One, but not the only, cause of the H-mode confinement deterioration in many of the lower toroidal-field discharges was radiative loss due to central accumulation of metallic impurities. In these discharges, central radiative power densities of up to  $1 \text{ W/cm}^3$  were observed, and this power density was consistent with that expected assuming neoclassical transport of the impurities [16].

At higher toroidal fields, a sustainable confinement enhancement was achieved, as shown in Fig. 9. The steady-state confinement time after the H-mode transition is plotted as a function of  $B_t$  in Fig. 9(a). At 1.0 T, the  $\tau_E$  values are similar to those of L-mode plasmas, while at 1.8 T, the  $\tau_E$  values are approximately 60% higher than the L-mode, and scale as  $(I_p \kappa^{1/2})/9$ , which is comparable to the good H-mode plasmas produced in PDX. The ability to sustain the enhanced  $\tau_E$  at the higher  $B_t$  value is associated with an increase in the ratio of the divertor to midplane recycling, as is seen in Fig. 9(b).

The transport properties of these H-mode plasmas have been investigated using the TRANSP code, in particular to address the issue of the relationship between the experimentally deduced  $\chi_i$  profile and the neoclassical one.

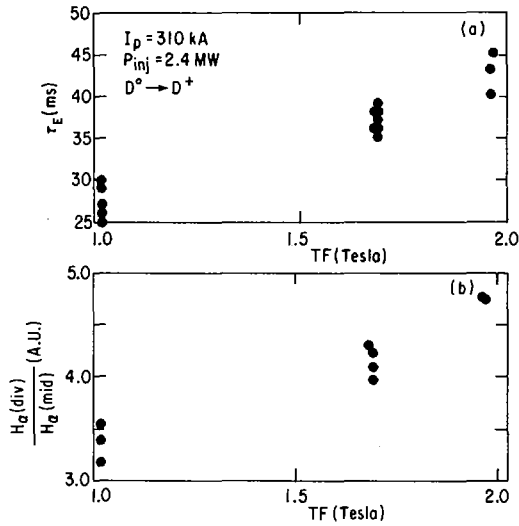


FIG. 9. Dependence of H-mode confinement time on toroidal field.

An analysis of  $T_i$ -profile data on DIII has indicated that the ion thermal diffusivity is neither neoclassical-like in magnitude nor in form [17]. The DIII results indicated that while  $\chi_i$  was of the order of the neoclassical value in the center of the discharge, it could be as much as ten times the neoclassical value halfway out, and that ion thermal conduction, under these conditions, could dominate the electron and ion power balance.

Radial ion temperature profiles from charge-exchange recombination of  $O^{8+}$  [18] have allowed the further investigation of this topic in these PBX H-mode plasmas. An example of the results of these analyses is shown in Fig. 10. Figure 10(a) shows the  $T_i$  and  $T_e$  profiles, while Fig. 10(b) shows the corresponding diffusivities. The  $T_i$  profile labeled  $\alpha\chi_i^{\text{ch}}$  was calculated in the traditionally standard fashion: the neoclassical multiplier  $\alpha$  was adjusted in order to match the measured central  $T_i$ , and it was assumed to be constant across the plasma in order to determine the remainder of the  $T_i$  profile [19]. For the case shown,  $\alpha = 0.5$  when the Chang-Hinton neoclassical  $\chi_i$  is assumed [Fig. 10(b)]. The second  $T_i$  profile is the measured one, and this was used directly to deduce  $\chi_i$  from the ion power balance. The shaded region corresponds to the band of  $\chi_i$  deduced in this fashion. Rather than plot a  $\chi_i$  from a single power balance calculation,

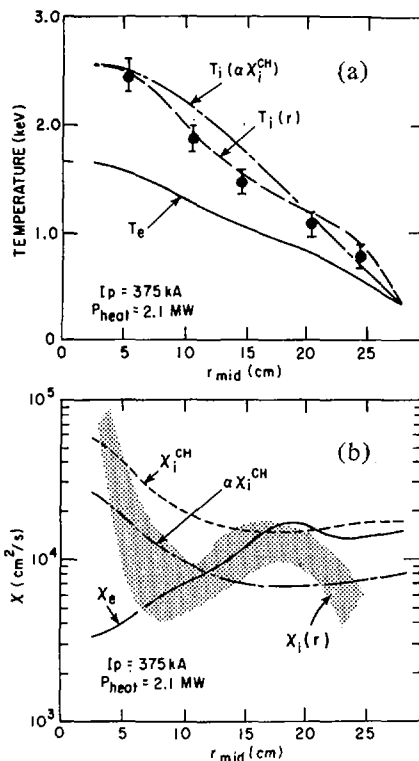


FIG. 10. (a) Calculated (—) and measured (---)  $T_i$  profiles; (b) thermal diffusivity.

several calculations were performed, each with a  $T_i$  profile varied randomly within the experimental uncertainties. The shaded area, then, is the envelope of  $X_i$ 's as determined from these various calculations. Because of uncertainties in  $T_i(r)$  and  $T_e(r)$ , the  $X_i(r)$  inside  $r_{mid} = 5$  cm and beyond 20 cm should be ignored.

It is clear from Fig. 10(b) that the two  $X_i$  profiles [ $0.5 \times X_i^{ch}$  and  $X_i(r)$ ] are not dramatically different in magnitude unlike the DIII result. In fact, the computed  $X_i$  is less than the neoclassical value in the inner half of the discharge rather than greater. In addition, to within the uncertainties in the data and the calculation, the difference in the two  $X_i$  profiles is not reflected in the  $T_i$  profiles; the  $T_i(r)$  determined from the assumption of  $0.5 \times X_i^{ch}$  is consistent with the measured profile. The reason for this is that in the

discharges analyzed, the ion thermal conduction loss never dominates and is responsible for, at most, 30% of the total energy loss.

## 5. Summary

An extensive study was carried out to evaluate the MHD behavior of plasmas residing along the first stability boundary. At the highest  $\beta_c$ , the achievable  $\beta_t$  is limited by hard disruptions produced by external kink modes or substantial energy loss due to the large internal disruption. At lower  $\beta_c$  and lower plasma indentations, various MHD modes, all with  $m/n = 1/1$  internal activity, grow and are associated with loss of thermal and fast-ion energy. The growth of these modes is consistent with the onset of internal kink modes. In addition to the internal modes, edge phenomena, such as ERP's and the edge inversions in the coupled disruptions, lead to thermal energy loss. Purely tangential injection excites low-frequency modes similar to fishbones, but which rotate with the plasma, and high-frequency modes that appear to be responsible for fast-ion loss through some resonant process. The presence and locking of the continuous mode clearly indicates that non-ideal MHD effects must play an important role during the saturated MHD activities in the  $\beta_t$ -collapse phase. Finally, transport analyses of H-mode plasmas with the observed  $T_i(r)$  profile did not indicate a large difference between measured and neoclassical  $\chi_i$  values.

## REFERENCES

- [1] CHANCE, M., JARDIN, S., STIX, T., Phys. Rev. Lett. **51** (1983) 1963.
- [2] MANICKAM, J., GRIMM, R., OKABAYASHI, M., Phys. Rev. Lett. **51** (1983) 1959.
- [3] OKABAYASHI, M., et al., in Plasma Physics and Controlled Nuclear Fusion Research 1984 (Proc. 10th Int. Conf. London, 1984), Vol. 1, IAEA, Vienna (1985) 229.
- [4] TROYON, F., GRUBER, J., Phys. Lett. A **110** (1985) 29.
- [5] SYKES, A., TURNER, M.F., PATEL, S., in Controlled Fusion and Plasma Physics (Proc. 11th Europ. Conf. Aachen, 1983), Pt. II, European Physical Society (1983) 363.
- [6] BOL, K., et al., Phys. Rev. Lett. **57** (1986) 1891.
- [7] TAKAHASHI, H., et al., Rep. PPPL-2391, Princeton Plasma Physics Laboratory (1986).
- [8] OKABAYASHI, M., et al., in Proc. Int. School of Plasma Physics, Varenna, Italy, 1985 (to be published).
- [9] KAYE, S., BELL, M., BOL, K., BOYD, D., BRAU, K., et al., J. Nucl. Mater. **121** (1984) 115.
- [10] FONCK, R.J., BEIRSDORFER, P., BELL, M., BOL, K., BOYD, D., et al., in Heating in Toroidal Plasmas (Proc. 4th Int. Symp. Rome, 1984), Vol. 1, ENEA, Frascati (1984) 37.
- [11] WAGNER, F., BECKER, G., BEHRINGER, K., CAMPBELL, D., EBERHAGEN, A., Phys. Rev. Lett. **49** (1982) 1408.
- [12] MCGUIRE, E., et al., in Plasma Physics and Controlled Nuclear Fusion Research (Proc. 10th Int. Conf. London, 1984), Vol. 1, IAEA, Vienna (1985) 117.

- [13] MANICKAM, J., et al., private communication (1986).
- [14] HEIDBRINK, W., et al., Phys. Rev. Lett. **57** (1986) 835.  
HEIDBRINK, W., et al., Rep. PPPL-2405, Princeton Plasma Physics Laboratory, Princeton, NJ (1986).
- [15] KAITA, R., et al., Plasma Phys. Contr. Fusion **28** (1986) 1319.
- [16] IDA, K., et al., Rep. PPPL-2313, Princeton Plasma Physics Laboratory (1986).
- [17] GROEBNER, R., PFEIFFER, W., BLAU, F., BURRELL, K., FAIRBANKS, E., et al., Nucl. Fusion **26** (1986) 543.
- [18] GAMMEL, G., KAITA, R., FONCK, R.J., JAEHNIG, K., POWELL, E., Rev. Sci. Instrum. **57** (1986) 1800.
- [19] KAYE, S.M., GOLDSTON, R., BELL, M., BOL, K., BITTER, M., et al., Nucl. Fusion **24** (1984) 1303.

## DISCUSSION

G. BECKER: When studying ballooning stability in ASDEX discharges, it was found that the results depended appreciably on the beam contribution to the pressure profile and the time evolution of the current density profile. Did you include these effects in your ballooning mode analysis?

M. OKABAYASHI: Our MHD analysis was carried out with the equilibria matched with the current and pressure profiles evaluated, first, from Thomson scattering  $T_e(r)$  and  $n_e(r)$  data, and, second, from the output of the TRANSP analysis. The ballooning mode was stable for both profiles.

# STABILIZATION OF THE TEARING MODE

T.C. HENDER, D.C. ROBINSON, J.A. SNIPES  
 Euratom-UKAEA Fusion Association,  
 Culham Laboratory,  
 Abingdon, Oxfordshire,  
 United Kingdom

## Abstract

### STABILIZATION OF THE TEARING MODE.

Various methods of stabilizing MHD instabilities in tokamaks are examined and compared with experiments. The intrinsic stabilizing effect of average curvature on the tearing mode is discussed, with particular reference to JET. Stabilization by RF current drive/heating and induced helical fields is considered. It appears possible to stabilize all gross resistive instabilities in the tokamak at moderate beta.

## 1. INTRODUCTION

The  $m = 2$  tearing mode in the tokamak has been shown both theoretically [1] and experimentally [2] to play a dominant role in causing the major disruption. Control of this mode may lead to suppression of the major disruption and to an extension of the operating regime of the tokamak (higher  $I$ ,  $N$ ,  $\beta$ ). Control of the  $m = 1$  mode could permit more peaked pressure profiles, better control of the  $m = 2$  mode and avoidance of the problems associated with the sawtooth collapse.

## 2. STABILIZATION BY PROFILE AND PARAMETER CONTROL

In this section we consider the intrinsic stabilizing effect of the average curvature on the tearing mode [3], which is particularly pronounced on JET because of its tight aspect ratio, high conductivity temperature and high beta potential. We also consider the stabilizing effect of local RF current drive/heating modifications to the equilibrium current profile.

The studies discussed in this section are conducted using the linear stability code FAR [4, 5]. This code solves the compressible (or incompressible) resistive MHD equations in full toroidal geometry with no ordering assumptions.

### 2.1. The $m = 2$ tearing mode

The tight aspect ratio and the high degree of shaping in JET lead to strong toroidal coupling between the  $m = 2$  harmonic and its resonant side-bands ( $m = 3, 4 \dots$

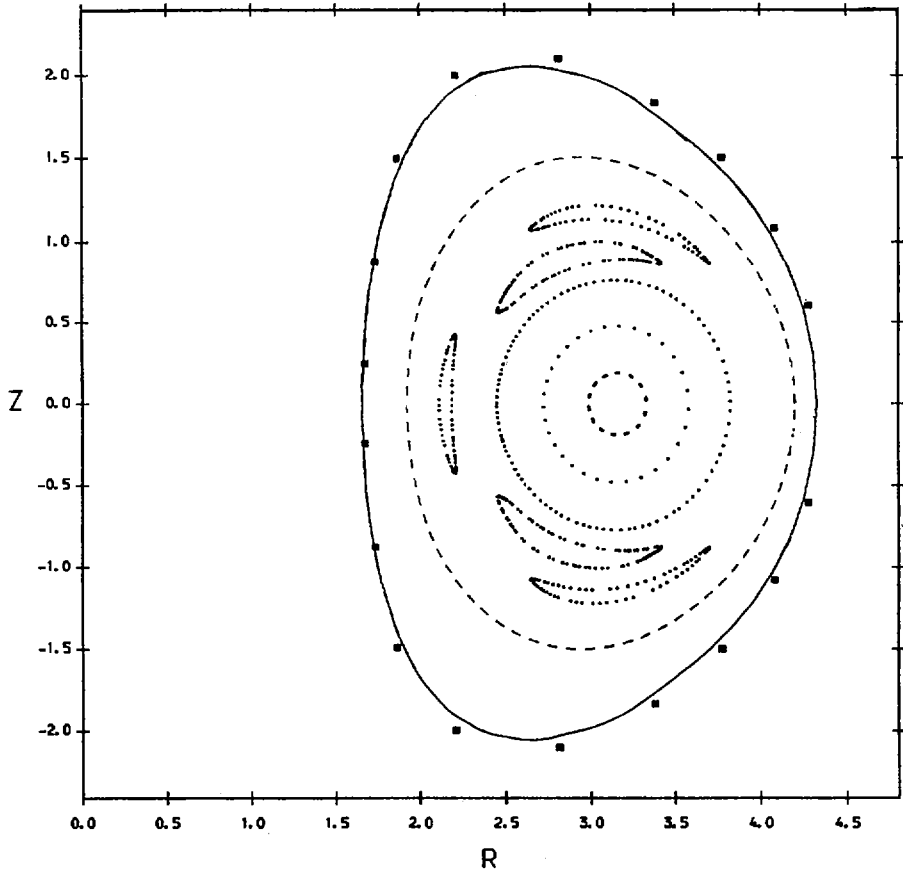


FIG. 1.  $m = 2$  and  $m = 3$  toroidal side-band islands. The solid ellipse is the liner location, the broken ellipse is the plasma-vacuum interface and the squares are the locations of poloidal coils.

for  $q_0 > 1$ ). Figure 1 shows the magnetic island structure in a constant toroidal angle plane for JET shortly before a density limit disruption when the  $n = 1$  mode is growing linearly and is not rotating. The poloidal field strength at the liner is  $\delta B_\theta/B_\theta = 1\%$ . In this case,  $q$  varies between 1.08 at the axis and 4.6 at the plasma edge. The dominant  $m = 2$  islands and the toroidal side-band  $m = 3$  islands are clearly visible. The toroidal coupling is weakly stabilizing; decreasing the aspect ratio at constant  $q$  (which strengthens the coupling) lowers the growth rate. A far stronger stabilization, however, arises from the average curvature effects which increase with beta [3]. As the magnetic Reynolds number ( $S$ ) increases (and the growth rate  $\gamma$  decreases) the relative importance of the stabilizing average curvature terms ( $D_R < 0$ ) increases. Figure 2 shows how the  $n = 1$  growth rate varies

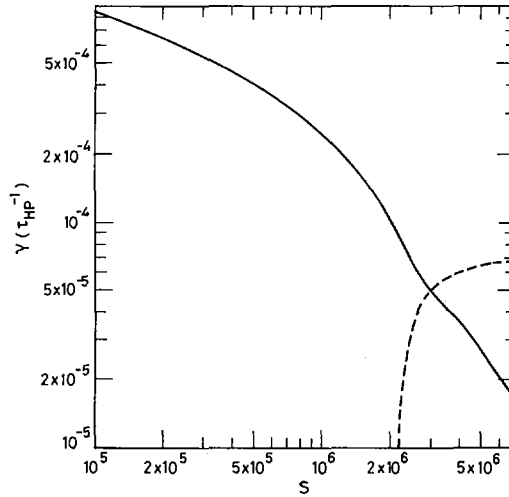


FIG. 2. Growth rate versus  $S$  for JET, with  $q = 1.08 (1 + (\rho/0.508)^8)^{1/4}$  (solid line is growth rate, broken line is frequency).

with  $S$  for a typical JET discharge with  $b/a = 1.4$ ,  $\beta_0 = 0.7\%$  and  $q = 1.08 (1 + (\rho/0.508)^8)^{1/4}$ . This case is moderately unstable in the cylindrical limit ( $\Delta' = 4.7$ ). The growth rate of the tearing mode is strongly reduced with increasing  $S$  and becomes overstable at high  $S$  (as predicted in Ref. [3]). For values of  $S$  consistent with the flat-top in JET ( $\sim 3 \times 10^7$ ) this case is approximately marginally stable to the  $n = 1$  mode. The strength of the average curvature terms also increases with beta (since  $D_R \propto \beta$ ) and complete stability to the  $n = 1$  mode occurs at  $\beta_0 = 1.1\%$  when  $S = 10^5$ , for this case. It should be noted that, in part, this stabilization is probably also due to a decrease in  $\Delta'$  as beta increases.

This inherent stability to tearing modes may be related to the absence of  $m = 2$  oscillations and the low level of coherent MHD activity ( $\delta B_\theta/B_\theta \sim 3 \times 10^{-5}$ ) which is observed for the majority of the time in JET discharges with  $q_\psi > 2.3$ . During the  $q$  and density limit pre-disruption phase, in which strong  $m = 2$  activity ( $\delta B_\theta/B_\theta \sim 1\%$ ) is observed, the temperature (and therefore  $S$  and beta) at the  $q = 2$  surface decrease. Since the critical  $\Delta'$  is proportional to  $(a^2 T^2 \beta_0^2/R_0)^{1/3}$ , the tearing mode is rapidly destabilized by falling  $\beta_0$  and  $S$ , in agreement with the experimental observations.

For cases in which  $m = 2$  activity is observed on JET, we have compared the theoretically predicted and the experimentally measured phase and amplitude variations of the poloidal fluctuations ( $\delta B_\theta$ ) at the liner. Figure 3 shows a comparison of the amplitude variation of  $\delta B_\theta$  with poloidal angle between the experimental measurements on JET and the predictions from the FAR code. The theoretical results

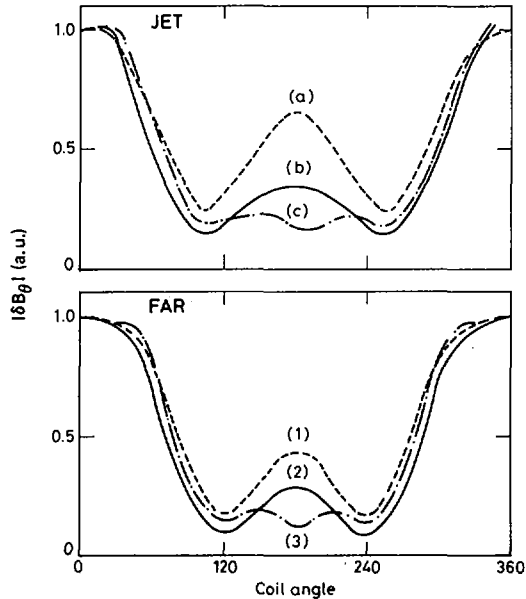


FIG. 3. Fluctuating poloidal field amplitude variation for JET.

(a) RF shot with  $q_\psi \sim 5$ , (b) OH shot with  $q_\psi \sim 7.0$ , (c) NBI shot with  $q_\psi \sim 6.5$ ; with FAR predictions for increasingly peaked current profiles: (1)  $(1 + (\psi/0.4)^4)^{-1.5}$ , (2)  $(1 + (\psi/0.4)^2)^{-2}$ , (3)  $(1 - \psi/0.85)$ ,  $q_0 = 1.08$  at  $\beta_0 = 0.8\%$ .

reproduce the strong in-out ballooning asymmetry shown by the experiment and indicate that the in-out ratio becomes stronger for more peaked current profiles. Between the liner and limiter surfaces (in the FAR calculations) we have imposed the equilibrium constraints  $P = J_z = 0$  and, to match experimental observations, used a high resistivity ( $5 \times 10^4$  relative to its central value). The locations of the liner, the plasma-vacuum interface and the poloidal field coils are shown in Fig. 1 for the same case as shown in Fig. 3, curve (2).

We have also investigated the effects of localized heating and/or current drive, which allows us to tailor the current profile near the  $q = 2$  surface. A possible scheme for JET is to use ECRH downshifted by 60 GHz, which leads to a localized unidirectional driven current [6]. We have added a Gaussian perturbation to the toroidal equilibrium current to simulate the driven current ( $\delta I$ ). We find that the stabilization is very sensitive to the radial location of the current perturbation and that it is optimized when it is centred on the  $q = 2$  surface; this is in agreement with experimental results from T-10 [7]. From examining a range of  $q$ -profiles we conclude that  $\delta I/I \sim 5\%$  should be sufficient to stabilize the  $m = 2$  tearing mode in JET, in all but the most extreme cases. Ray-tracing and Fokker-Planck calculations

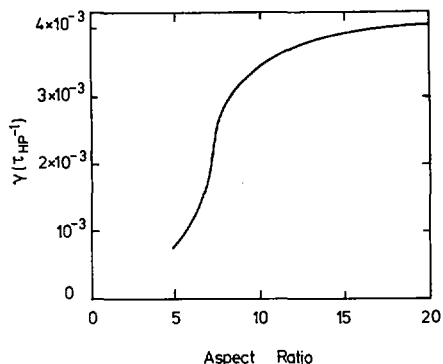


FIG. 4. Stabilization of the resistive  $m = 1$  mode by lowering the aspect ratio when  $q' = 0$ ,  $S = 10^5$ .

indicate that such a current can be achieved with 2 MW of ECRH [6]. It should be noted that the intrinsic stability of the tearing mode in JET means that cylindrical estimates of  $\delta I/I$  necessary to stabilize a given case would be much larger.

## 2.2. The $m = 1$ sawtooth mode

Because of the different physics of the toroidal  $m = 1$  mode, stabilization techniques that are applicable to  $m \geq 2$  instabilities will not necessarily work for the  $m = 1$  mode.

At  $\beta < \beta_{\text{crit}}$ , with monotonically increasing  $q$ -profiles and  $q_0 < 1$ , the ideal internal kink mode is stable [8]. In these cases, however, the generally large values of  $\Delta'$  ( $\sim 100$ ) result in a resistive kink instability with  $\gamma \propto S^{-1/3}$ , a result which has been confirmed numerically [9]. The resistive  $m = 1$  kink mode has been proposed as providing an explanation for the sawtooth [10], though experiments on JET suggest a much faster scaling [11]. The rapid growth of the resistive  $m = 1$  kink mode means that the average curvature terms do not stabilize this mode. With a tight aspect ratio (which makes the ideal energy strongly stabilizing) and high  $S$  it is possible for the  $m = 1$  mode to have a tearing mode scaling ( $\gamma \propto S^{-3/5}$ ) [9]. However, extreme values of  $S$  ( $\sim 10^8$ ) and aspect ratio ( $\sim 1.5$ ) are required to achieve this. Also the average curvature terms, which are stabilizing when  $\gamma \propto S^{-3/5}$  (provided  $p' < 0$  and  $q' > 0$  at  $q = 1$ ), tend to be weak because the toroidal curvature vanishes at  $q = 1$  and also the local aspect ratio is generally quite large.

It is possible to reduce the growth rate, and in some cases to achieve complete stability to the resistive  $m = 1$  mode, by reducing  $q'$  near  $q = 1$ . In practice, this may be achieved by RF current drive or indeed it may be the profile which the plasma chooses in some cases [12]. Figure 4 shows the growth rate of the  $n = 1$  mode as

a function of aspect ratio for the profile  $q = 1 - 0.2(1 - (\rho/0.58)^2)^3$ , with  $S = 10^5$  and  $\beta = 0$ . For this  $q$ -profile there is a very strong stabilizing effect when the aspect ratio is decreased. This stabilization is a toroidal effect. For the same  $q$ -profile in the cylindrical limit the  $m = 1$  mode is destabilized when the aspect ratio is reduced (i.e. the ratio of length to radius). This is partly because in the cylindrical limit the ideal internal kink mode is unstable at zero beta [8]. This method of stabilizing the  $m = 1$  resistive mode appears to be sensitive to the form of the  $q$ -profile; for other  $q$ -profiles, with  $q' = 0$  at  $q = 1$ , we have not been able to achieve complete stability.

### 3. STABILIZATION WITH HELICAL FIELDS

In this section we examine the effects of resonant fields induced by saddle coils external to the plasma, as studied on Pulsator [13] and TOSCA [14]. Because of the complex boundary conditions we use in this case the reduced tokamak MHD equations. Single helicity non-linear calculations show that if we apply a (2, 1) helical current such that its  $x$ -points and the 0-points of an existing (2, 1) plasma island are aligned, then the island width first decreases. However, the final saturated state is such that the  $x$ -points of the saddle coil and of the plasma island are aligned and, because of the influence of the saddle coil, the island width increases slightly. We can exploit the initial decrease in island width by using a pair of orthogonal coils to actively stabilize the (2, 1) mode. This scheme seems particularly attractive for a locked or slowly rotating ( $\sim 400$  Hz) (2, 1) mode such as that which precedes the disruption in JET. We have also examined the effect of adding a static saddle coil current to a toroidally rotating plasma. For a (2, 1) saddle coil perturbation which gives vacuum islands that are significantly smaller than the intrinsic saturated plasma island, the island continues to rotate and has a slightly enhanced width. For larger saddle coil currents the plasma island locks to the phase of the imposed perturbation and the island width is slightly increased. Experimentally it has been observed on machines such as Pulsator [13] and TOSCA [14] that large (2, 1) saddle coil currents will lock the mode and may cause a disruption (and indeed the mode lock observed on JET may be caused by a similar phenomenon, with the mode locking to small inhomogeneities in the external fields). Lower currents, however, have been observed experimentally to stabilize the mode without phase locking. It appears that this stabilization must be due to effects not included in our simulation (quasi-linear modifications to the resistivity, toroidal coupling, etc.).

### 4. CONCLUSIONS

Various methods for stabilizing MHD instabilities in the tokamak have been examined. For the  $m = 2$  tearing mode the average curvature (i.e. beta) is strongly

stabilizing — an effect which is particularly pronounced at tight aspect ratio and high conductivity temperatures. The average curvature terms are also stabilizing in the non-linear Rutherford regime [15]. This stabilization effect, however, depends strongly on the details of the MHD equations within the resistive layer and may therefore be affected by kinetic effects.

Local flattening of the current (and  $q$ ) with RF current drive/heating can stabilize the resistive  $m = 1$  and  $m = 2$  modes. For the  $m = 1$  mode this is a purely toroidal effect.

The  $m = 2$  mode can be stabilized with an applied (2, 1) helical field, using an active feedback system of two orthogonal coil sets. A static saddle coil perturbation, with the induced saddle coil island widths comparable to the intrinsic plasma island, will phase lock a rotating mode; this is in agreement with experiment.

### ACKNOWLEDGEMENTS

The authors are indebted to the ORNL MHD Group for providing them with a copy of the FAR code and for their continued collaboration and help. The authors would also like to thank R.J. Hastie for numerous useful discussions and suggestions.

This work was performed under a Task Agreement between the JET Joint Undertaking and Culham Laboratory.

### REFERENCES

- [1] WADDELL, B.V., et al., *Phys. Rev. Lett.* **41** (1978) 1386.
- [2] ROBINSON, D.C., MCGUIRE, K., *Nucl. Fusion* **19** (1979) 115.
- [3] GLASSER, A.H., et al., *Phys. Fluids* **18** (1975) 875.
- [4] HENDER, T.C., HASTIE, R.J., ROBINSON, D.C., submitted to *Nucl. Fusion*.
- [5] CHARLTON, L.A., et al., *J. Comput. Phys.* **63** (1986) 107.
- [6] O'BRIEN, M., et al., in *Controlled Fusion and Plasma Heating* (Proc. 13th Europ. Conf. Schliersee, 1986), Vol. 2, European Physical Society (1986) 270.
- [7] ALIKAEV, V.V., ARSENTIEV, Yu.I., BAGDASAROV, A.A., et al., in *Plasma Physics and Controlled Nuclear Fusion Research 1984* (Proc. 10th Int. Conf. London, 1984), Vol. 1, IAEA, Vienna (1985) 419.
- [8] BUSSAC, M.N., et al., *Phys. Rev. Lett.* **35** (1975) 1638.
- [9] HASTIE, R.J., HENDER, T.C., CHARLTON, L.A., HOLMES, J.A., CARRERAS, B.A., submitted to *Phys. Fluids*.
- [10] WADDELL, B.V., et al., *Nucl. Fusion* **18** (1978) 735.
- [11] EDWARDS, A.W., et al., Rep. JET-P(86)12, Culham Laboratory, Abingdon (1986).
- [12] SOLTWISCH, H., SCHLÜTER, J., STODIEK, W., MANICKAM, J., Paper IAEA-CN-47/A-V-1, these Proceedings, Vol. 1.
- [13] KARGER, F., WOBIG, H., CORTI, S., et al., in *Plasma Physics and Controlled Nuclear Fusion Research 1974* (Proc. 5th Int. Conf. Tokyo, 1974), Vol. 1, IAEA, Vienna (1975) 207.

- [14] ELLIS, J.J., HOWLING, A.A., MORRIS, A.W., ROBINSON, D.C., in Plasma Physics and Controlled Nuclear Fusion Research 1984 (Proc. 10th Int. Conf. London, 1984), Vol. 1, IAEA, Vienna (1985) 363.
- [15] KOTSCHENREUTHER, M., et al., Phys. Fluids **28** (1985) 294.

## DISCUSSION

M. PORKOLAB: It is possible that we have already observed the effect you propose to use for stabilization of the sawteeth, namely to flatten the current profile near the  $q = 1$  surface. In contrast to results for ASDEX, the inductance  $\mathcal{L}$  increases during lower hybrid current drive in ALCATOR C. Nevertheless, the sawteeth are stabilized. We believe that the current is driven just outside the  $q = 1$  surface and that it flattens the current profile there, while reducing the current density in the outer layers, thereby increasing the self-inductance. The total current remains constant. This observation is described in my paper<sup>1</sup>.

---

<sup>1</sup> Paper IAEA-CN-47/F-II-2, these Proceedings, Vol. 1.

# EXPERIMENTAL AND THEORETICAL STUDIES OF CIRCULAR CROSS-SECTION HIGH BETA TOKAMAKS\*

G.A. NAVRATIL, Y. BARANSKY, A. BHATTACHARJEE,  
 C.K. CHU, A.V. DENIZ, A.A. GROSSMAN, A. HOLLAND,  
 T. IVERS, X.L. LI, T.C. MARSHALL, M.E. MAUEL,  
 S. SABBAGH, A.K. SEN, J. VAN DAM<sup>1</sup>, X.-H. WANG  
 Plasma Physics Laboratory,  
 Columbia University,  
 New York, New York

M. HUGHES, M. PHILLIPS, A.M.M. TODD  
 Grumman Corporation,  
 Princeton, New Jersey  
 United States of America

## Abstract

EXPERIMENTAL AND THEORETICAL STUDIES OF CIRCULAR CROSS-SECTION HIGH BETA TOKAMAKS.

The paper presents the first results from Columbia University's high beta tokamak, HBT, demonstrating the production of plasmas with poloidal beta of the order of the aspect ratio,  $\beta_p \sim R/a = \epsilon^{-1}$ . Results from a theoretical study of equilibrium, stability and transport in a conceptual second regime experiment, SRX, are also presented. Methods to access the second regime and the advantages of large aspect ratio, second regime operation for tokamak fusion reactors are discussed.

## 1. Introduction

Conventional tokamak experiments have been limited to levels of volume average beta,  $\langle\beta\rangle$ , less than  $\beta_c \equiv 0.035 I_p(\text{MA})/aB_t$ , which corresponds to the theoretically predicted onset of external kink instabilities and internal ballooning modes[1,2]. Although it has been shown theoretically that these instabilities restabilize at higher beta under certain conditions[3-5], no tokamak experiment has operated in this "second stability" regime. The second regime is characterized by large values of the poloidal beta,  $\epsilon\beta_p \approx 1$ , and, in this paper, we report experimental and theoretical results relevant to these high  $\beta_p$  plasmas. The

---

\* Work supported by United States Department of Energy, Grants Nos. DE-FG02-86ER53222 and DE-FG02-86ER53236, and by Grumman Corporation.

<sup>1</sup> Present address: Institute for Fusion Studies, Austin, TX, USA.

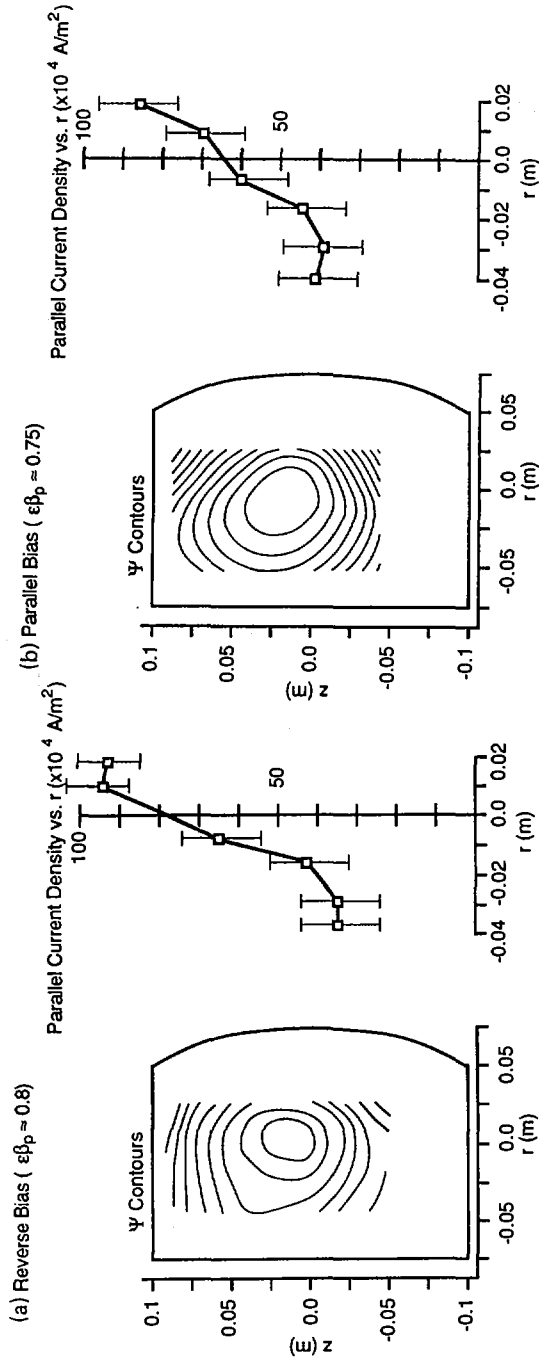


FIG. 1. Contours of poloidal flux and current density for (a) a reverse bias plasma with  $\epsilon\beta_p \approx 0.8$ , and (b) a parallel bias plasma with  $\epsilon\beta_p \approx 0.75$ . For both examples, the predicted shift is  $\Delta \approx 0.2a \approx 0.01m$ .

experimental results were observed with the HBT tokamak, and they demonstrate the existence of tokamak equilibrium with  $\epsilon\beta_p \sim 1$  and  $\langle\beta\rangle > \beta_c$  for as many as 20 Alfvén transit times ( $\tau_A = qR/V_A$ ). To explore the physics of high  $\beta_p$  plasmas more completely, the theoretical work has described tokamak equilibrium, stability and transport for a conceptual second regime experiment (SRX) sustained with auxiliary heating.

## 2. HBT Experiment

The HBT experiment is a pulsed, high-beta tokamak replacing the earlier Torus II device[6]. HBT can produce very high beta plasmas ( $\langle\beta\rangle < 30\%$ ,  $B_t \leq 0.4T$ ) by rapidly reversing the toroidal field (reverse bias), or lower beta plasmas ( $\langle\beta\rangle < 4\%$ ,  $B_t \leq 0.7T$ ) by rapidly increasing the toroidal field (parallel bias). A quartz vacuum chamber surrounds the plasma, allowing fast programming ( $<2\mu\text{sec}$ ) of the applied magnetic fields. We have operated primarily with circular cross-section plasmas, maximizing  $\beta_p$ . By adjusting the magnitude of the initial toroidal field, the ohmic coil current or the neutral gas pressure, the plasma's inverse aspect ratio ( $0.1 < \epsilon < 0.3$ ), cylindrical safety factor ( $0.5 \leq q_{\text{cyl}} < 9$ ) and collisionality can be systematically changed. Typically, at low to medium densities of helium or hydrogen ions, we find  $\langle n_i \rangle \approx 10^{21}\text{m}^{-3}$ ,  $\langle T_e \rangle \approx \langle T_i \rangle \approx 25\text{eV}$ ,  $R = 0.24\text{m}$ ,  $a \approx 0.05\text{m}$ , and  $\langle\beta\rangle \approx 10\%$ . For these plasmas, both external and internal ideal MHD modes are predicted to be unstable. The plasma parameters are measured with a multi-point Thomson scattering system, a two-channel  $\text{CO}_2$  laser interferometer, infrared bremsstrahlung tomography[7], and internal and external magnetic probes[8].

### 2.1. Observation of high $\beta_p$ plasmas in HBT

The first experiments with HBT have documented plasmas with high poloidal beta, and they illustrate the outward-shifted poloidal flux surfaces and non-concentric profile of the parallel current density expected in ideal MHD high-beta equilibria.

Fig. 1 illustrates the results of these measurements for both reverse bias and parallel bias formation methods. The contours of constant poloidal flux and parallel current density are reconstructed from internal magnetic probe measurements. They clearly indicate shifted poloidal flux surfaces and non-concentric current density profiles. These measurements can be compared to the expected magnitude of the Shafranov shift,  $\Delta$ , by estimating the poloidal beta from the condition for major radial force balance

$$\frac{d}{dt} M \frac{dR}{dt} = \frac{1}{2} \mu_0 J_p^2 [\ln(8R/a) - 1 + (l_i + \beta_p + \mu_i)/2] - 2\pi R I_p B_v \quad (1)$$

In Eq. (1), the plasma size ( $R$ ,  $a$ ), mass ( $M$ ), diamagnetism ( $\mu_i$ ), current ( $I_p$ ), and the applied vertical field ( $B_v$ ) can be measured as a function of time to determine the poloidal beta. For the reverse bias case (Fig. 1a), Eq. (1) gives  $\epsilon\beta_p \approx 0.8$  and, for the parallel bias case (Fig. 1b),  $\epsilon\beta_p \approx 0.75$ . The expected Shafranov shift for both examples is of the order of  $\Delta \approx 0.2a = 0.01\text{m}$ , comparable with measured shifts. When plasmas with lower  $\beta_p$  are produced, nearly concentric flux surfaces are observed as expected[8].

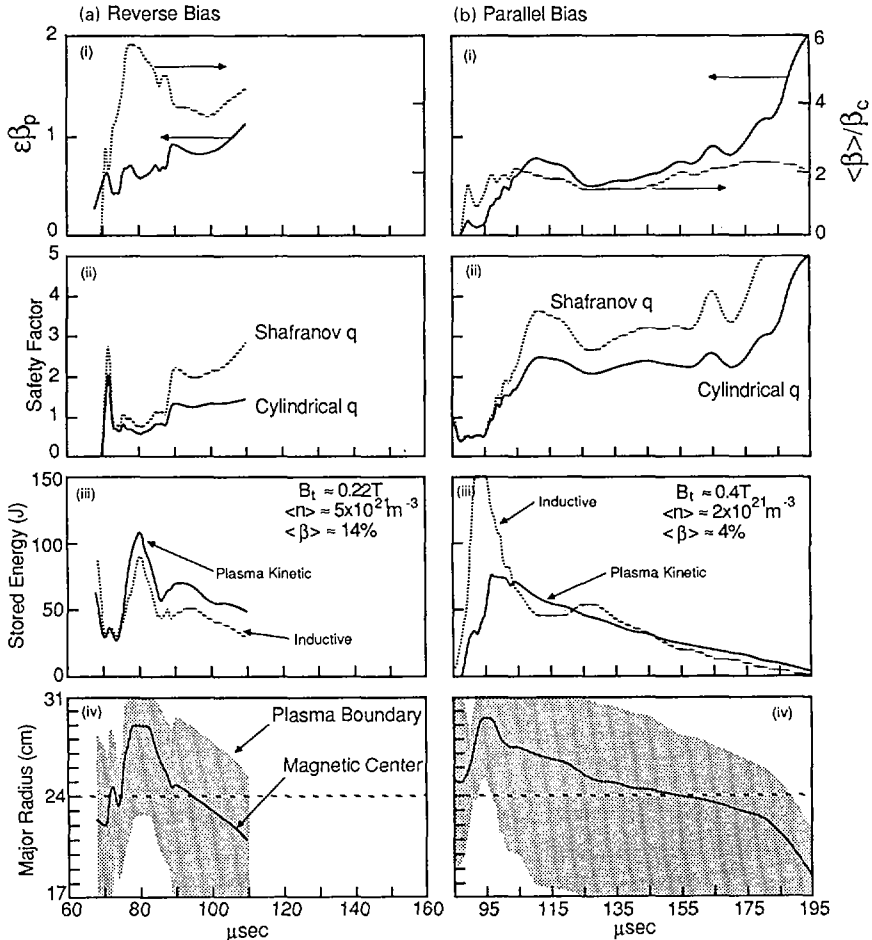


FIG. 2. Time evolution of (a) a reverse bias discharge made with 80 mtorr He fill pressure, and (b) a parallel bias discharge with 22 mtorr H<sub>2</sub> fill pressure, showing the transition from low  $\epsilon\beta_p$  to high  $\epsilon\beta_p$ . For each discharge, the four plots illustrate: (i) the evolution of  $\epsilon\beta_p$  and  $\langle\beta\rangle/\beta_c$ , (ii) the cylindrical safety factor ( $q_{cyl} \equiv 2\pi a^2 B_v / \mu_0 I_p R$ ) and the Shafranov safety factor ( $q_\psi \equiv q_{cyl} \{1 + \epsilon^2 [1 + 0.5(l/2 + \beta_p)^2]\}$ ), (iii) the total inductive and kinetic stored energies, and (iv) the position of the magnetic center and outer edge of the plasma.

## 2.2. Investigation of the transition from low to high $\epsilon\beta_p$

Eq. (1) can also be used to calculate the time evolution of the discharge parameters, allowing the investigation of the transition to high  $\epsilon\beta_p$  from low  $\epsilon\beta_p$ , as summarized in Fig. 2. For the first example (Fig. 2a), the toroidal field is reversed at  $t = 70\mu\text{sec}$ , inducing several MA of poloidal currents and coupling 300J into the plasma. After ionization and heating,  $W_p \equiv 0.375\beta_p R \mu_0 I_p^2 \approx 100\text{J}$ ,  $\langle\beta\rangle \approx 4\beta_c$  and  $\epsilon\beta_p \approx 0.5$ . As the discharge continues, both the inductive stored energy ( $W_I = 0.5LI_p^2$ , where  $L$  is the plasma's inductance) and  $W_p$  gradually decrease, although  $W_I$  is observed to decrease more rapidly than  $W_p$ , leading to an increase in  $\epsilon\beta_p$ . After  $30\mu\text{sec}$ , the safety factor,  $q$ , has increased to 2 and  $\epsilon\beta_p$  has increased to 1. The poloidal flux contours shown in Fig. 1a correspond to the plasma shown in Fig. 2a at  $t = 95\mu\text{sec}$ .

Fig. 2b shows the parallel bias example. With this formation method, a rapid compression of the plasma occurs at the same time as the plasma current is rapidly increased. Although this method couples less total energy to the plasma as does reverse bias, by reducing the gas fill pressure and substituting  $\text{H}_2$  for He, parameters similar to the previous case can be achieved. As shown in the figure, the initially high current dissipates shortly after formation, raising  $q$  from slightly less than one to more than 2.5. Thereafter, the plasma current and energy decay with a time-constant of  $\approx 60\mu\text{sec}$  while maintaining a high beta configuration ( $\epsilon\beta_p \approx 0.8$ ,  $\langle\beta\rangle \approx 2\beta_c$ ) for more than  $80\mu\text{sec}$ . With  $B_t = 0.4\text{T}$  and  $\langle n_i \rangle \approx 2 \times 10^{21}\text{m}^{-3}$ , this corresponds to 20 Alfvén transit times.

For both of the examples shown in Fig. 2, the plasma was observed to evolve without macroscopic instability and to terminate when the resistive decay of the vertical field,  $B_v$ , was unable to center the plasma within the vacuum vessel. Although these experiments establish that high  $\epsilon\beta_p$  plasmas can be maintained for times long compared to  $\tau_A$ , we do not yet know whether these equilibria are stable as the plasma's collisionality is reduced. Investigating MHD stability at higher temperatures and reduced collisionality remains a current research activity of the HBT experiment.

## 3. Large Aspect Ratio, Second Regime Tokamak

When operating in the second stability regime, a large aspect ratio tokamak can provide significant advantages for a fusion reactor[9]. With large aspect ratio and circular cross-section, a tokamak can access the second stability regime at lower  $\langle\beta\rangle$  than a conventional tokamak. This is seen by examining a simple estimate of  $\epsilon\beta_p$  shown in Eq. (2)

$$\epsilon\beta_p \sim 2(q_0 q_a / \epsilon) \{ (1 + \kappa^2) / 2 \}^{1/2} \langle\beta\rangle \quad (2)$$

TABLE I. TARGET PARAMETERS FOR THE SRX EXPERIMENT

$\langle\beta\rangle = 3.68\%$	$R/a = 9$	$B_T = 1 \text{ T}$
$\varepsilon\beta_p = 1.16$	$\kappa = 1$	$(b/a)_c^{n=1} = 0.25-0.3$
$\beta/\beta_c = 4.2$	$\delta = 0$	$(b/a)_c^{n=2} = 0.15-0.2$
$q_0 = 1.01$	$a = 0.175 \text{ m}$	$(b/a)_c^{n=3} = 0.05-0.1$
$q_a = 4.1$	$P_{aux} = 2-3\text{MW}$	$(b/a)_c^{n>3} = \infty$
$q(\psi) \propto \psi^{2.5}$	$I_p = 51.2 \text{ kA}$	

To minimize the  $\langle\beta\rangle$  required for second regime access ( $\varepsilon\beta_p \sim 1$ ), we should reduce  $\varepsilon$ , choose a circular cross-section ( $\kappa = 1$ ), and operate with high  $q$ . The results of equilibrium, stability and transport calculations for a second regime experiment (SRX) based on this concept are described below. In addition, extensions to the theories describing transition into the second regime from low beta using either energetic particles or toroidal rotation are discussed.

### 3.1. Equilibrium and Stability Boundaries

Ideal MHD stability analysis has defined the target parameters for the second stable region of SRX, and these are shown in Table I. Low toroidal mode number,  $n$ , ballooning modes, driven by the pressure gradient in the low shear region, require a close fitting conducting shell,  $0.5 < (b/a)_c^{n=3} < 0.10$ , for stability [10]. Here,  $(b/a)$  is the shell displacement from the plasma edge normalized to the plasma radius. Raising the axis shear to balance high and low  $n$  internal instabilities would increase the critical wall position. The fact that modes with  $n > 1$  set the minimum requirement, and that  $(b/a)_c$  is observed to increase rapidly for all modes when  $\varepsilon\beta_p > 1$ , indicate that the pressure gradient rather than the parallel current is the dominant instability driver.

Current or safety factor,  $q(\psi)$ , programming has been suggested as a method to improve second region access[10]. We have demonstrated stable access for all ideal MHD modes in SRX when  $q_0 < 3.1$ ,  $q_a = 4.1$ ,  $(b/a) > 0.05$ ,  $p(\psi) \propto \psi^{2.5}$ , and  $q(\psi) \propto \psi^{4.0}$ . Again, stability of the  $n = 3$  mode defines the minimum wall position as  $\varepsilon\beta_p$  is increased. The minimum wall requirement applies only in the middle of the unstable region. Restabilization, as described above, is again observed at higher  $\varepsilon\beta_p$ . Even in the absence of a completely stable access path, current programming can significantly reduce the  $\varepsilon\beta_p$  required for second region operation (e.g.  $\varepsilon\beta_p < 0.7$  for  $q_0 \sim 2$ ). This technique could then be used in conjunction with the other mechanisms discussed in Section 3.3.

### 3.2. Transport Modeling and Power Requirements

A flux surface averaged transport code[11] has been used to estimate the auxiliary heating power necessary to obtain the second regime SRX design point plasma of Table I with neutral beam injection. The transport model includes neoclassical coefficients supplemented by a microinstability model of anomalous diffusion[12]. Similar models have been used to match PBX[13] and TFTR[14] results. Electromagnetic effects (*e.g.* ballooning modes), which are expected to play an important role at high  $\langle\beta\rangle$ , are not included in the present transport

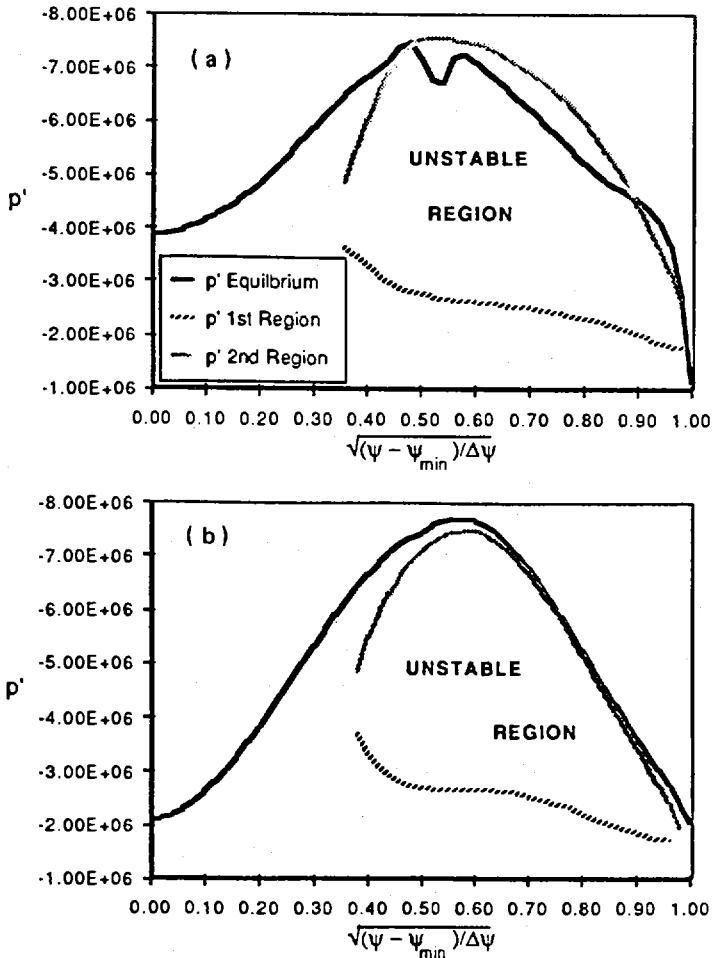


FIG. 3. Profiles of  $p'$ : (a) calculated from a 1.5-D transport code with 5 MW of neutral beam power, and (b) corresponding to the stable second regime design point of Table I.

model. However, the analysis does provide an estimate of the required power for an SRX plasma with a stable access path to the second regime. The confinement times obtained from this code are similar to those predicted by L-mode scaling. Shown in Fig. 3a is the  $p'$  profile generated by the transport code and in Fig. 3b the  $p'$  profile for the stable design point equilibrium. The corresponding pressure profiles for these two cases are nearly identical. Our results suggest that a device based on the design parameters of Table I can exceed  $\beta_c$  by a substantial factor ( $>4$ ) and that the target parameters can be achieved with a neutral beam power of 2 to 3 MW.

### 3.3. Stabilization Mechanisms for Second Regime Access

We have examined and extended two proposed stabilization schemes for transition from the first to the second regime: (1) energetic particle stabilization, and (2) induced toroidal rotation[9]. The original work on energetic particle stabilization showed that highly energetic particles introduced into the bad curvature region of a tokamak could improve the stability of the system against ideal ballooning modes[16]. We have extended this work to include finite aspect ratio effects in an analytic equilibrium with scalar pressure and an anisotropic energetic particle pressure. Even without aspect ratio corrections, an additional region of ballooning instability exists beyond the so-called "drift reversal line" (see Ref. 16). When the energetic particle beta is comparable to the plasma beta, finite aspect ratio effects can completely remove the original ballooning unstable region, but the new instability region persists. This may limit the magnitude of the local  $p'$  in a high beta plasma stabilized using this technique.

A WKB theory has been developed for  $n = \infty$  ballooning modes in an equilibrium with large rigid toroidal rotation, and sufficient conditions for stability, which extend earlier work[17], have been obtained. For large flow velocities on the order of Mach 1, a possible stabilization mechanism is provided by the centrifugal separation of the surfaces of constant mass density and pressure. In the central part of the equilibrium, the density gradient caused by the centrifugal force may offset the destabilizing effects of the pressure gradient.

## 4. Fusion Reactor Applications

In order to quantify the differences between a conventional first regime reactor and a large aspect ratio second regime reactor, zero-dimensional calculations based on a model developed by Uckan and Sheffield[18] have been used to directly compare the two configurations. By limiting the magnetic field at the toroidal field coil to 12T, limiting the neutron wall loading to 5MW/m<sup>2</sup>, and considering "Starfire-sized" reactors with net electrical output of 1.2GW, very similar operating parameters and costs were observed for first regime reactors

with elongation and triangularity sufficient to raise  $\beta_c > 6\%$  ( $\kappa \approx 2$ ,  $\delta \approx 0.4$ ) and for second regime reactors with large aspect ratios ( $R/a > 6$ ). However, the large aspect ratio reactor can operate (1) at half the field strength at the toroidal field coils, allowing the use of NbTi superconductors, and (2) with 16 times less inductive energy stored in plasma current, reducing the potential for disruption-induced damage. The high  $\langle \beta \rangle$  and magnetic field utilization of the large aspect ratio second regime reactors also permit cost effective compact reactors (with net electrical output of the order of 300MW) and may also make a reasonably sized tokamak reactor burning advanced fuels feasible. Indeed, by increasing  $\langle \beta \rangle$  to 30% and  $B_t$  to 10T,  $\langle \beta \rangle^2 B_t^4$  can increase by a factor of 150 over that needed for DT fusion. The zero-dimensional reactor model has also been used to estimate the confinement needed for DT ignition by extrapolating present empirical scaling laws to high beta and large aspect ratio. As in first regime reactors, it is observed that only a limited subset of these scaling laws predict ignition for reasonably sized reactors, and these have been used to specify the confinement which must be observed in the conceptual SRX experiment to demonstrate trends leading to ignition[19].

## REFERENCES

- [1] BERNARD, L.C., HELTON, F.J., MOORE, R.W., Nucl. Fusion **23** (1983) 1475.
- [2] TROYON, F., GRUBER, R., SAURENMANN, H., SEMENZATO, S., SUCCI, S., Plasma Phys. **26** (1984) 209.
- [3] MERCIER, C., in Plasma Physics and Controlled Nuclear Fusion Research 1978 (Proc. 7th Int. Conf. Innsbruck, 1978), Vol. 1, IAEA, Vienna (1979) 701.
- [4] CHANCE, M.S., JARDIN, S.C., STIX, T.H., Phys. Rev. Lett. **51** (1983) 1963.
- [5] COPPI, B., CREW, G.B., RAMOS, J.J., Comments Plasma Phys. Controll. Fus. **8** (1983) 11.
- [6] CHU, C.K., DENIZ, A., GEORGIU, G.E., GROSS, R.A., GROSSMANN, A.A., et al., Nucl. Fusion **25** (1985) 1109.
- [7] HOLLAND, A., NAVRATIL, G.A., Rev. Sci. Instrum. **57** (1986) 1557.
- [8] DENIZ, A.V., MARSHALL, T.C., IVERS, T., LI, X., MAUEL, M., Phys. Fluids **29** (1986) 4119.
- [9] NAVRATIL, G.A., MARSHALL, T.C., Comments Plasma Phys. Controll. Fus. **10** 4 (1986).
- [10] TODD, A.M.M., et al., Paper IAEA-CN-47/E-III-11, these Proceedings, Vol. 2.
- [11] BATEMAN, G., Proc. International Centre for Theoretical Physics, Trieste, 1985.
- [12] TANG, W.M., Rep. PPPL-2311, Plasma Physics Lab., Princeton Univ., NJ (1986).
- [13] JARDIN, S.C., et al., Rep. PPPL-2358, Plasma Physics Lab., Princeton Univ., NJ (1986).
- [14] REDI, M., Rep. PPPL-2368, Plasma Physics Lab., Princeton Univ., NJ (1986).
- [15] KAYE, S.M., GOLDSTON, R.J., Nucl. Fusion **25** (1985) 65.
- [16] ROSENBLUTH, M.N., et al., Phys. Rev. Lett. **51** (1983) 1967.
- [17] HAMEIRI, E., LAURENCE, P., J. Math. Phys. **25** (1984) 296.
- [18] UCKAN, N.A., SHEFFIELD, J., Rep. ORNL/TM-9722, Oak Ridge National Lab. (1985). Also in Tokamak Startup (KNOEPFEL, H., Ed.), Plenum Press, New York and London (1986) 45.
- [19] MAUEL, M.E., submitted to Nuclear Fusion.

**DISCUSSION**

D.C. ROBINSON: In your HBT experiments with  $\epsilon\beta_p \sim 1$ , was the discharge characterized by central  $q$  values greater or less than one?

G.A. NAVRATIL: We have produced discharges with central  $q$  greater than one, but for those discussed here the central  $q$  was near one.

D.C. ROBINSON: Could I also ask how you account for the absence of strong MHD instabilities in your plasmas with  $\epsilon\beta_p \sim 1$ , given such central  $q$  values?

G.A. NAVRATIL: We have computed the stability of equilibria similar to these and expect them to be unstable. Two effects which may reduce the growth rate of these modes come from the collisional nature of these plasmas and the presence of a conducting halo plasma with finite pressure.

## DISRUPTION CONTROL EXPERIMENTS USING LOCAL MODULAR MULTIPOLE FIELD COILS

K. YAMAZAKI, K. KAWAHATA, Y. ABE, R. AKIYAMA,  
T. AMANO, R. ANDO, Y. HAMADA, S. HIROKURA,  
K. IDA, E. KAKO, O. KANEKO, Y. KAWASUMI,  
S. KITAGAWA, T. KURODA, K. MASAI, K. MATSUOKA,  
A. MOHRI, M. MUGISHIMA, N. NODA, I. OGAWA,  
Y. OGAWA, K. OHKUBO, Y. OKA, K. SAKURAI, M. SASAO,  
K. SATO, K.N. SATO, S. TANAHASHI, Y. TANIGUCHI,  
K. TOI, T. WATARI  
Institute of Plasma Physics,  
Nagoya University,  
Nagoya, Japan

### Abstract

#### DISRUPTION CONTROL EXPERIMENTS USING LOCAL MODULAR MULTIPOLE FIELD COILS.

In the JIPP T-IIU tokamak, major disruptions have been successfully suppressed by using compact local sets of  $\ell = 3$  modular multipole field coils with an  $m = 3/n = 2$  dominant helical component. It is found that stabilization can be attributed to the excitation of a 'mini-disruption' induced by the  $3/2$  helical field perturbation before the catastrophic stage that leads to a major disruption. Because of the quick but mild ergodization of the  $m = 2/n = 1$  magnetic islands by this mini-disruption, temperature flattening is impeded and a two-step disruption that would lead to disruptive current termination is avoided. This system is easily applicable to larger tokamaks because of compact coil utilization, slow pulse application and quick stabilization response. It has also been demonstrated that this coil system can be used for edge plasma control with an ergodic limiter configuration.

### 1. INTRODUCTION

The usefulness of the superposition of weak external helical field perturbations on tokamak plasmas for stability studies [1] and transport studies [2] has already been widely recognized. The stabilization of the  $m = 2/n = 1$  island by an  $m = 2/n = 1$  resonant helical field ( $m$  and  $n$  are the poloidal and toroidal mode numbers) with gradual current profile modification or fast in-phase feedback schemes has been demonstrated. Stabilization by a non-resonant helical field has also been tried with the production of an ergodic region outside the  $q = 2$  surface. In contrast to these previous experiments, in our experiments we investigated the effect of ergodization inside and/or outside the  $q = 2$  surface. We found a new, quick stabilization process through excitation of a small disruption ('mini-disruption') induced by

the helical field. In contrast to a configuration with complicated purely helical coils or saddle coils, the coil configuration used here is rather compact. With this coil set, tests of both core ergodization for disruption control and edge ergodization for ergodic limiter experiments have been carried out.

## 2. HELICAL FIELD CONFIGURATION

Two sets of toroidally localized multipole ( $\ell = 3$ ) field coils ('local helical coils', Fig. 1(a)) have been used; they are mounted on two vacuum vessel sectors of  $30^\circ$  at opposite sides of the torus. These coils were installed initially with the aim of achieving  $m = 3/n = 1$  ergodic limiter configurations [3]. When the coil currents are driven in the anti-parallel direction, an  $m = 3/n = 2$  helical field with  $1/1$ ,  $2/2$  and  $4/2$  side-band components (A (anti) mode: core ergodization mode) is produced; when the coil currents are driven in the parallel direction, an  $m = 3/n = 1$  field with  $2/1$ ,  $4/1$  and  $4/3$  components (D (dual) mode: edge ergodization mode) is produced (Fig. 1(b)).

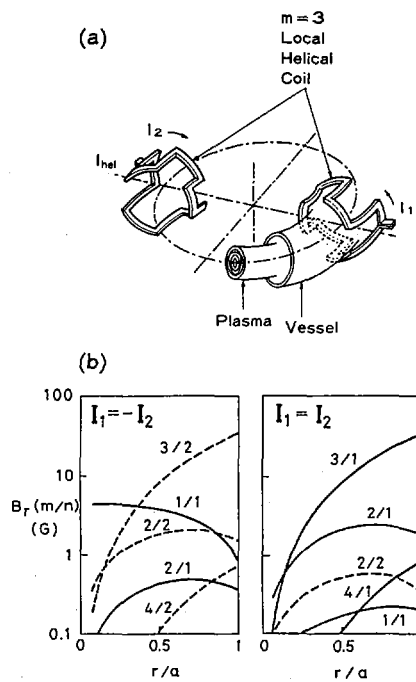


FIG. 1. (a) Configuration of the local helical coil. (b) Radial field components of the local helical coil for an A-mode pulse with an  $m = 3/n = 2$  dominant component ( $I_1 = -I_2$ ), and for a D-mode pulse with an  $m = 3/n = 1$  dominant component ( $I_1 = I_2$ ), with  $I_{hel} = 15$  kA.

The JIPP T-IIU machine ( $R = 91$  cm,  $a = 24$  cm) was operated at  $1 \text{ T} \leq B_t \leq 3 \text{ T}$  and  $100 \text{ kA} \leq I_p \leq 300 \text{ kA}$ . The applied 3/2 radial perturbation field strength at the plasma surface,  $B_{r3/2}(a)$ , is about 30 G at a maximum helical coil current  $I_{\text{hel}}$  of 15 kA (Fig. 1(b), left). The ratio of this perturbation field to the poloidal field of the plasma current,  $B_{r3/2}(a)/B_\theta(a)$ , is about 1.0–1.5%.

### 3. DISRUPTION CONTROL EXPERIMENTS:

#### *Pulse application to unstable discharges*

The changes in MHD activity during pulse application are measured mainly by single, 10- and 20-channel Mirnov coil poloidal arrays, a 10-channel grating polychromator receiving second harmonic electron cyclotron emission (ECE), and a 7-channel soft-X-ray (SXR) pin diode poloidal array.

The typical discharge waveforms with and without pulse application to the mildly unstable discharges are shown in Fig. 2. Figure 3 is a plot of the time variations of the electron temperature profile  $T_e^{1.5}(r)$ , before pulse application, without a pulse and with a pulse; third-order spline-fitting curves are used; the current profile  $j(r)$  can be roughly estimated from the electron temperature profile ( $j(r) \propto T_e^{1.5}(r)$ ).

Without pulse application (Fig. 2(a)) the plasma current ( $q_a \approx 3.2\text{--}3.4$  and  $n_e \approx 2 \times 10^{13} \text{ cm}^{-3}$ ) is terminated by a few pre-disruptions and by the subsequent major disruption. In this case, the discharge proceeds with successive phenomena characterized by the stages of initial 'precursor oscillation', 'soft mode locking', 'pre-disruptions', 'major disruption' and 'current quench' (Fig. 2(a)). The peaked electron temperature profile at  $t \approx 90$  ms is changed to the flattened profile near the centre by the onset of precursor oscillations (Fig. 3(a)). During the precursor oscillation phase, the strong 2/1-mode toroidal 'co'-rotation (rotation in the plasma current direction) gradually comes to a standstill and then leads to the pre-disruption. According to the magnetics, SXR and ECE temperature fluctuation measurements, a pure  $m = 2/n = 1$  mode ( $R \approx 100$  cm) accompanied by 1/1 deformation ( $R \approx 88$  cm) grows, and an  $m = 1/n = 1$  island quickly develops with double mode frequency on this 1/1-deformed surface just before the pre-disruption. The ECE temperature decay during the pre-disruption is initiated mainly near the  $q = 2$  surface as a result of 2/1–1/1 interaction, as predicted by theory [4]. The island width of the 2/1 mode is not reduced by this pre-disruption and finally the plasma current is terminated through the two-step disruption process. Although the  $T_e^{1.5}(r)$  profile does not correspond exactly to the  $j(r)$  profile, it is suggested from the flat profile (Fig. 3(b)) that the central  $q_0$  before the major disruption in the case without a pulse is larger than 1.3 [5]; this is consistent with the theoretical prediction of 'bubble' formation [6].

When an A-mode pulse ( $m = 3/n = 2$  dominant) is applied during the unstable period (Fig. 2(b)), the  $m = 2$  mode toroidal rotation gradually comes to an end and

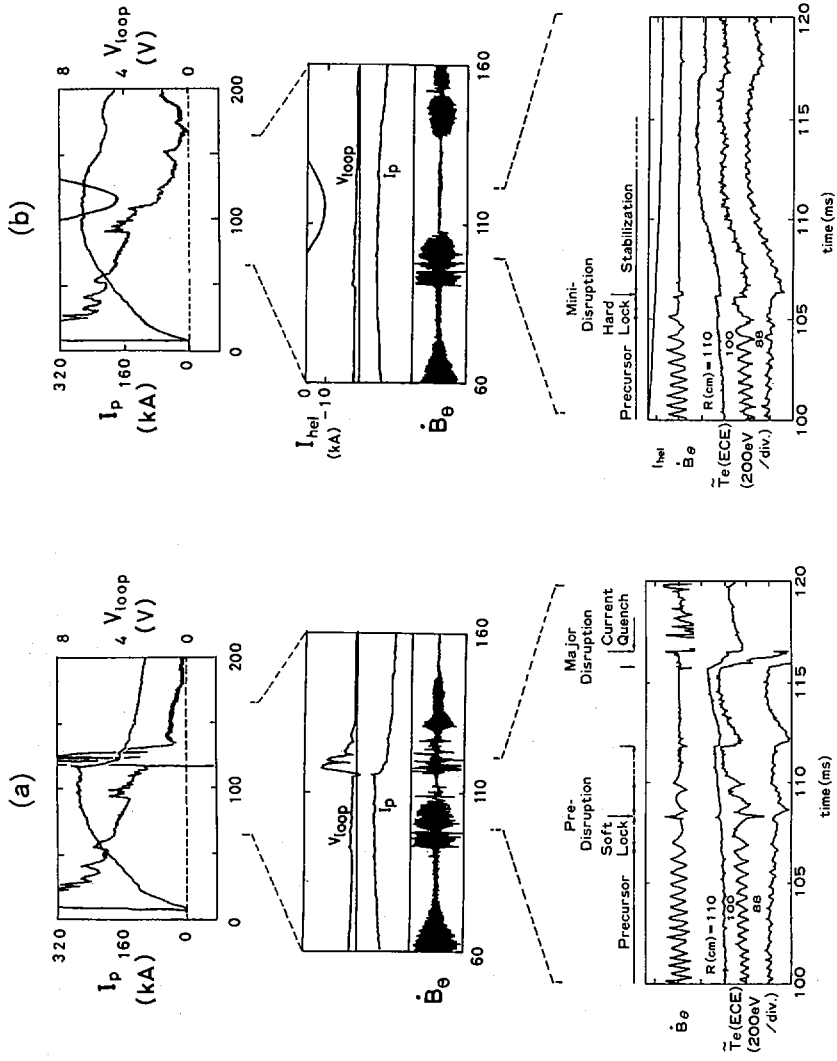


FIG. 2. Time behaviour of discharge parameters and expanded typical Mirnov signals and ECE temperature fluctuations: (a) without a pulse and (b) with an A-mode pulse;  $V_{loop}$  is loop voltage,  $I_p$  is plasma current,  $I_{hel}$  is helical coil current and  $\dot{B}_\theta$  is Mirnov signal.

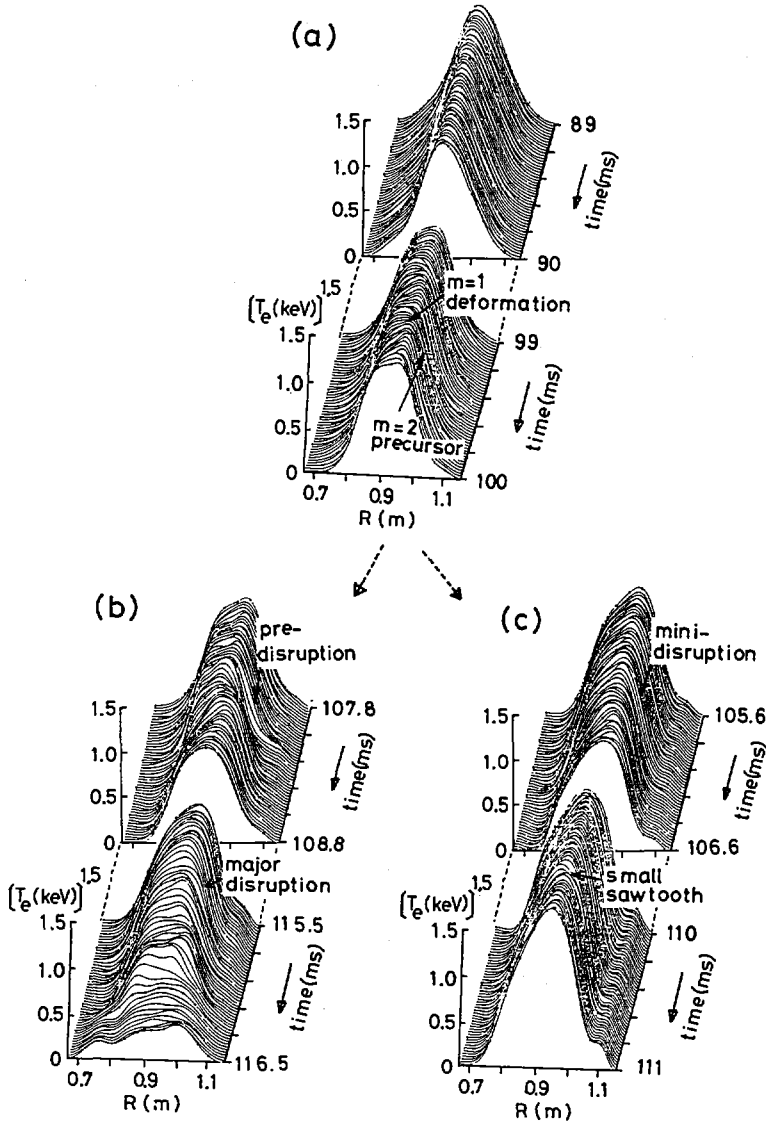


FIG. 3. Time evolution of the one-half power of the electron temperature profile  $T_e^{1.5}$ : (a) before pulse application ( $t < \sim 100$  ms), (b) without a pulse ( $t > \sim 100$  ms) and (c) during an A-mode pulse ( $t > \sim 100$  ms).

is finally more tightly locked in phase than it is without pulse application. A mini-disruption is excited before the above-mentioned pre-disruption in the case without a pulse; this mini-disruption is characterized by a mild and global change in the plasma profile. The 2/1 magnetic island disappears in this mini-disruption stage, whereas it did not disappear in the pre-disruption stage when no pulse was applied.

After one or two mini-disruptions the plasma current channel becomes more peaked than in the case without a helical pulse, which often leads to the occurrence of small sawtooth oscillations. In contrast to the situation existing in the case without a pulse, the profile after the mini-disruption induced by the A-mode pulse remains almost constant, except just during pre-disruption, and does not change to the flat profile (Fig. 3(c)). This quick rearrangement of the magnetic configuration due to the favourable mini-disruption helps avoid disruptive current terminations.

The D-mode pulse ( $m = 3/n = 1$  dominant), however, is not effective in suppressing major disruptions and sometimes the discharge is destabilized. This may be due to the fact that the 3/1-dominant field does not directly affect the 2/1-1/1 interaction and that it causes undesirable disturbances on the  $q = 3$  surface or the plasma edge surface.

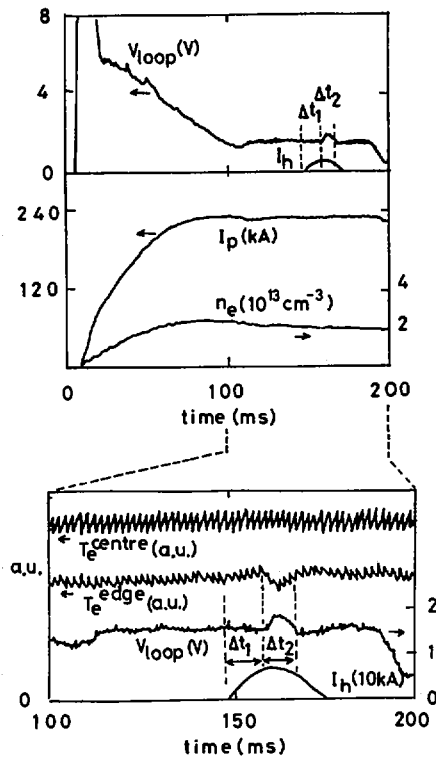


FIG. 4. Ergodic limiter experiments with application of a D-mode pulse.

#### 4. ERGODIC LIMITER EXPERIMENTS:

##### *Pulse application to stable discharges*

Helical magnetic field perturbations are also applied to stable discharges with  $q_a \approx 3-4$  in order to clarify the effect of ergodization on the transport process. When a D-mode pulse is applied, a hard-X-ray burst due to loss of runaway electrons, a decrease of the C-IV, C-V, O-V and Fe-IX line intensities, and a decay of edge ECE temperature are observed, with a time delay  $\Delta t_1$  after pulse application (see Fig. 4). Ergodization of the edge confinement region and a resultant favourable effect of impurity influx suppression in the time interval  $\Delta t_2$  are suggested. The quick onset and duration of this ergodization depend on the pulse height and the width of the helical perturbations, which suggests the existence of an ergodization threshold.

On the other hand, an A-mode pulse does not significantly influence the stable discharges, even with a maximum coil current of 15 kA.

#### 5. CONCLUSIONS

In the JIPP T-IIU tokamak experiment it has been demonstrated that the  $m = 3/n = 2$  dominant helical field perturbation produced by toroidally localized multipole field coils induces one or two mini-disruptions in the tokamak plasma and that the 2/1 magnetic island is ergodized by this mini-disruption. Temperature flattening is interrupted and two-step disruption is avoided. With this scenario, a compact local helical coil system producing 'dirty' spectral field components is used instead of complicated purely toroidal helical coils. This may be acceptable in a large tokamak because it reduces the probability of disruptive current terminations through slow feedback.

Also, preliminary ergodic magnetic limiter experiments have been carried out using the local helical coil system with an  $m = 3/n = 1$  dominant helical component. The favourable effect of edge ergodization on the edge temperature drop has been confirmed and the effectiveness of this coil configuration for transport and stability control verified.

#### REFERENCES

- [1] KARGER, F., WOBIG, H., CORTI, S., et al., in Plasma Physics and Controlled Nuclear Fusion Research 1974 (Proc. 5th Int. Conf. Tokyo, 1974), Vol. 1, IAEA, Vienna (1975) 207.
- [2] OHYABU, N., et al., Nucl. Fusion **25** (1985) 1684.
- [3] KAWAMURA, T., et al., J. Nucl. Mater. **111&112** (1982) 268.
- [4] TURNER, M.F., WESSON, J.A., Nucl. Fusion **22** (1982) 1069.
- [5] YAMAZAKI, K., et al., Quick Profile Reorganization Driven by Helical Field Perturbation for Suppressing Tokamak Major Disruptions, Res. Rep. IPPJ-796, Inst. of Plasma Physics, Nagoya Univ. (1986).
- [6] KLEVA, R.G., et al., Phys. Fluids **29** (1986) 457.

## DISCUSSION

K. McGUIRE: In your A-mode type stabilization of the major disruption, could you improve the density limit or the low  $q_a$  limit?

K. YAMAZAKI: No, we have not yet managed to extend the operating region. The density limit was somewhat improved, but not substantially. The reason why the present system was not effective is that in the case of low  $q_a$ /high density the growth of the MHD mode is too fast to be controlled by the present slow pulse coil system outside the vacuum vessel. Another reason might be that the disruption mechanism for low  $q_a$ /high density is different from the  $2/1 - 1/1$  interaction of mildly unstable medium  $q$  and medium density discharges. However, we are still trying to improve the operational regime by using the present 'mini-disruption' scheme with other helical field components.

D.C. ROBINSON: I noticed that your A-mode coil configuration ( $m = 3$ ,  $n = 2$ ) had a significant  $m = 1$ ,  $n = 1$  component. Did you observe any significant effect of this coil configuration on sawtooth activity?

K. YAMAZAKI: We applied the A- and D-mode helical pulses to stable OH and ICRF heated discharges with sawteeth, but did not observe any significant changes in sawtooth behaviour. We think the  $m = 1/n = 1$  component is still too small to modify the sawtooth activity. We plan, however, to add new coils and to perform further sawtooth stabilization experiments.

# STUDIES OF MHD MODES AND HIGH FREQUENCY FLUCTUATIONS ON THE HT-6B AND HT-6M TOKAMAKS

Jikang XIE, Jiayu CHEN, Wenkang GUO, Yuping HUO,  
HT-6B GROUP, HT-6M GROUP  
Institute of Plasma Physics,  
Academia Sinica,  
Hefei, Anhui, China

## Abstract

STUDIES OF MHD MODES AND HIGH FREQUENCY FLUCTUATIONS ON THE HT-6B AND HT-6M TOKAMAKS.

Detailed studies of MHD modes have been performed on the HT-6B tokamak by means of weak resonant helical fields (RHF). The experimental results show that the MHD behaviour cannot be explained by the current tearing mode theory. A very interesting point is that a weak RHF (about 0.5% of  $B_p$ ) could significantly influence sawtooth processes and thereby change the global thermal properties of the plasma. A series of voltage pulses were applied to HT-6M plasma. The investigations included low frequency MHD modes, high frequency magnetic fluctuations,  $H_\alpha$  line emission and ECE signals. High frequency fluctuations have been suppressed by the voltage pulses.

## 1. INTRODUCTION

Plasma parameters for conditions close to ignition have already been achieved in tokamaks. However, there are still many important processes of the plasma besides transport which are not yet clear. There are many reports on high frequency fluctuations, but no conclusion has been reached as to their physical origin, their relation with other plasma processes and the way of control. Low frequency MHD perturbations, which are directly related with plasma disruptions and which have an influence on the global thermal properties of the plasma, have long been regarded as tearing modes [1]. Recently, this theory has been questioned because of some experimental results [2]. It seems necessary to find a new explanation, also for sawtooth processes. Therefore, a careful study of such processes is certainly of value for the further development of tokamaks.

To obtain more information and to investigate different aspects of MHD modes and high frequency fluctuations, we studied the changes of these modes under the influence of external disturbances [3, 4]. When  $\ell = 2$  and  $\ell = 3$  weak resonant helical fields (RHF) were used as active magnetic probes, many new phenomena could be observed; these seem to give a physical picture for the low frequency modes which is totally different from the usual one. Also, when skin current pulses were applied, some new properties of high frequency fluctuations were found.

The HT-6B is an air-core transformer tokamak with  $\ell = 2$  and  $\ell = 3$  windings on its vacuum chamber. The operational parameters are:  $R = 45$  cm,  $a = 12.5$  cm,  $B_t = 6\text{--}8$  kG,  $I_p < 40$  kA,  $n_e = (0.7\text{--}3) \times 10^{13}$  cm $^{-3}$ ,  $T_{e0} = 150\text{--}250$  eV,  $Z_{\text{eff}} < 2$ . The diagnostics of HT-6B are nearly all conventional, including multichannel soft-X-ray fluctuation measurements, multichannel spectroscopy, five-channel ECE,  $\cos m\theta$  coils and more than twenty magnetic probes.

The HT-6M is a new air-core transformer tokamak with the following parameters:  $R = 65$  cm;  $a = 20$  cm;  $B_t = 15$  kG,  $I_p < 120$  kA,  $Z_{\text{eff}} = 1.5\text{--}2.5$ ,  $T_e = 400\text{--}700$  eV,  $n_e = (0.9\text{--}2) \times 10^{13}$  cm $^{-3}$ . It is equipped with  $\ell = 3$  helical windings and a second Ohmic heating winding just outside the vacuum chamber.

## 2. MHD MODE STUDIES WITH A RESONANT HELICAL FIELD

The helical windings on HT-6B can produce steady or pulsed RHF with a magnitude of 0.5–5% of  $B_p$ . Without an RHF we observed all the typical MHD phenomena which appear also on other devices. The main results of experiments with RHF are as follows:

(a) The fact that different  $n, m$  modes always have the same frequency has long been observed on all tokamaks including the HT-6B. Normally, this is explained by the rotation of the magnetic islands which can be observed by the phase shifts of signals of Mirnov probes located at different poloidal positions. On HT-6B, the rotation of the magnetic island was stopped by a weak RHF, as shown in Fig. 1; the RHF was turned on at 6 ms and turned off at 12 ms. In some cases, non-rotating Mirnov signals or signals without any phase relation were observed even without an RHF. Obviously, this means that the frequency (about 20 kHz on HT-6B) is not entirely due to magnetic island rotation.

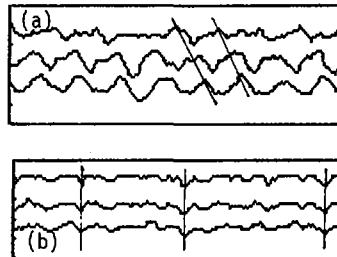


FIG. 1. Phase shifts on adjacent Mirnov probes, (a) without RHF and (b) with RHF.

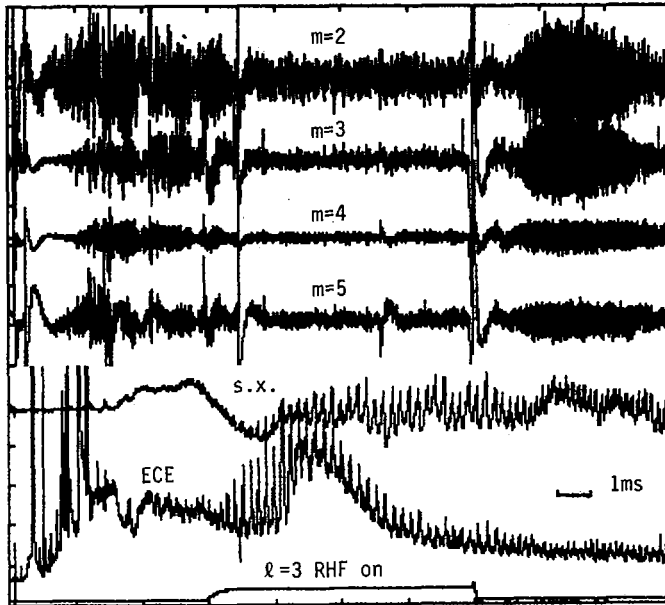


FIG. 2. Suppression of  $m = 2, 3, 4, 5$  modes, and enhancement of sawteeth on soft-X-ray and ECE signals by an  $\ell = 3$  RHF.

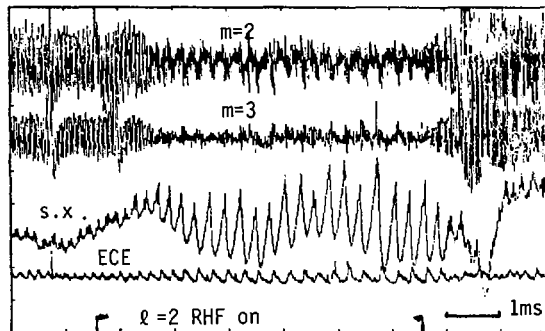


FIG. 3. Changes of  $m = 2$  and  $m = 3$  modes, soft-X-ray signals and ECE signals when an  $\ell = 2$  RHF is turned on.

(b) The weak  $\ell = 3$  RHF of about 1%  $B_p(a)$  can suppress all  $m = 2, 3, 4$  modes effectively when  $q(a) > 3$  (Fig. 2). Oscillations of the same frequency in soft-X-ray and spectroscopic signals are also suppressed. In the case of a weak  $\ell = 2$  RHF with  $q(a) > 2.5$  the same phenomena could be observed (Fig. 3). It should be emphasized that our RHF's were rather weak so that only the magnetic structure close to the corresponding resonance surface could be changed. This local

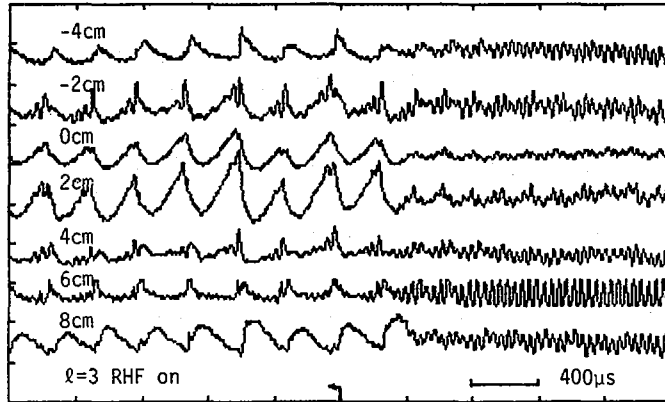


FIG. 4. Reduction and relaxation of sawteeth on soft-X-ray signals to 20 kHz Mirnov oscillations when the RHF is turned off.

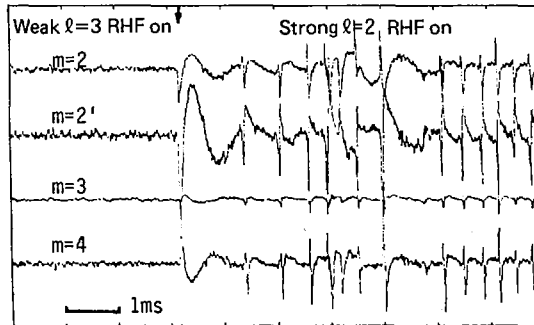


FIG. 5. Application of a strong  $\ell = 2$  RHF to an  $\ell = 3$  stabilized plasma, causing a new mode on  $\cos m\theta$  coil signals.

resonant interaction of the RHF with the plasma has been proven by two facts: (1) when the direction of the toroidal magnetic field was reversed, the weak helical field could not influence the plasma fluctuations; and (2) in the case of  $q(a) < 3$ , the  $\ell = 3$  helical current could not suppress the MHD modes. Since the magnetic islands of different  $m$ -modes did not overlap in our experiments, it is difficult to explain why such localized disturbances could suppress the  $m = 2, 3, 4, 5$  modes, each of which is concentrated only near the corresponding resonant surface according to tearing mode theory.

(c) The sawtooth oscillations which appeared on HT-6B in soft-X-ray signals, ECE signals and, in some cases, even in magnetic signals, were dramatically modified by a weak RHF. Mostly, an RHF ( $\ell = 3$  or  $\ell = 2$ ) increased the sawtooth

amplitude and prolonged the repetition period, as shown in Fig. 2. The ECE signals showed an increment of the central electron temperature. In extreme cases, an RHF moved the inverse surface of a sawtooth ( $q = 1$  surface) outwards, and the sawtooth oscillation appeared even in the soft-X-ray signal of the edge chord. In some discharge regimes without an RHF there was no sawtooth oscillation, only a 20 kHz fluctuation in the soft-X-ray signals. After the weak RHF was turned off, the large amplitude sawteeth disappeared with a 1 ms delay (see Fig. 4). All these facts seem to indicate that the very localized changes of the magnetic structure caused by a weak RHF could bring about a strong resonant change of the energy process of the plasma, especially in the inner part.

(d) A relatively strong  $\ell = 2$  RHF in some cases increased the 20 kHz oscillation and suppressed sawteeth, but did not disrupt the discharge. When the  $\ell = 2$  RHF was larger than 2%  $B_p(a)$ , the discharge deteriorated immediately. An experiment was performed in which two RHF's ( $\ell = 2$  and  $\ell = 3$ ) were combined. The MHD fluctuations were stabilized by a suitable  $\ell = 3$  RHF; in this way the discharge could be prevented from suddenly turning on a strong  $\ell = 2$  RHF, as shown in Fig. 5. When the  $\ell = 2$  RHF was turned on, there were suddenly more  $m = 2$  and  $m = 4$  perturbations, but the  $\ell = 3$  mode remained stable.

(e) Similar effects on RHF's have also been observed on the HT-6M tokamak.

### 3. SKIN CURRENT PULSE EXPERIMENTS ON HT-6M

In an attempt to change the edge conditions, four voltage pulses (V-pulses), 0.2–1 ms wide, with 10–100 V loop voltage, were applied to the plasma during the discharges via the second Ohmic heating winding. Pulse currents,  $\tilde{I}_p$ , of up to 15 kA (20% of  $I_p$ ) were induced in the co-direction and the counter-direction with regard to  $I_p$  (Fig. 6). Some of the preliminary results are as follows:

(a) The amplitudes of the  $m = 2, 3, 4, 5$  MHD modes did not change much during the pulse process with  $\tilde{I}_p$  up to 15% of  $I_p$  (Fig. 7). When  $\tilde{I}_p$  was slightly larger than 15%  $I_p$ , the amplitudes of the  $m = 2$  mode were enlarged, but those of the  $m = 3$  mode were not enlarged. Usually, the discharge was interrupted immediately after a fast rise of the  $m = 2$  mode amplitude, with  $\tilde{I}_p$  more than 20% of  $I_p$ . It was found that the instant of the enhancement of the  $m = 2$  mode or the low frequency magnetic oscillation  $\tilde{B}_r$  (see below) was at the set-up of a positive electric field of the V-pulse, i.e. in the direction of  $I_p$ .

(b) A broad-band high frequency magnetic fluctuation was observed by a small  $B_r$  coil close to the edge of the plasma. The amplitude of this fluctuation was  $\tilde{B}_r/B_p(a) = 10^{-5}$  to  $10^{-4}$ . In many cases there was a large component of about 250 kHz. Suppression of these fluctuations by a V-pulse was observed (Fig. 8). After the V-pulse was switched on, the high frequency fluctuation  $\tilde{B}_r$  gradually disappeared, but a low frequency (about 10 kHz) magnetic oscillation began to grow;

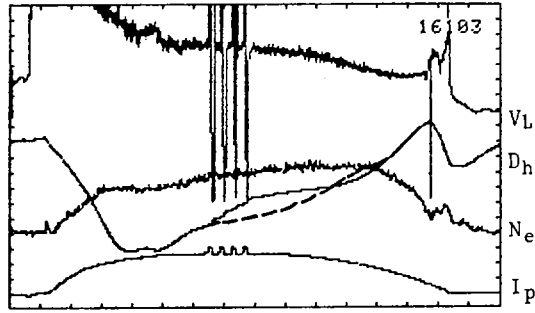


FIG. 6. Discharge with  $V$ -pulse, plasma current  $I_p$  (20.4 kA/div.), loop voltage  $V_L$  (6.26 V/div.), position of plasma  $D_h$  (10.5 kA·cm/div.) and electron density  $N_e$  ( $3.5 \times 10^{12}$  cm $^{-3}$ /div.). The dashed line denotes the position of the plasma without a  $V$ -pulse, time 3.84 ms/div.

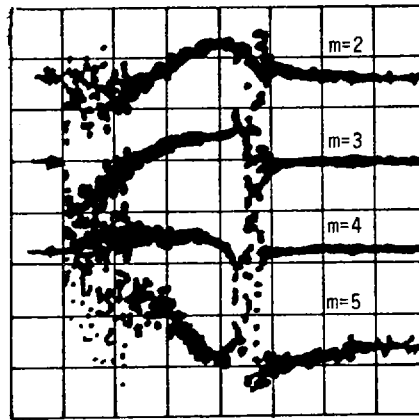


FIG. 7. Waveforms of the  $m = 2, 3, 4, 5$  MHD modes during a  $V$ -pulse, time 200  $\mu$ s/div.

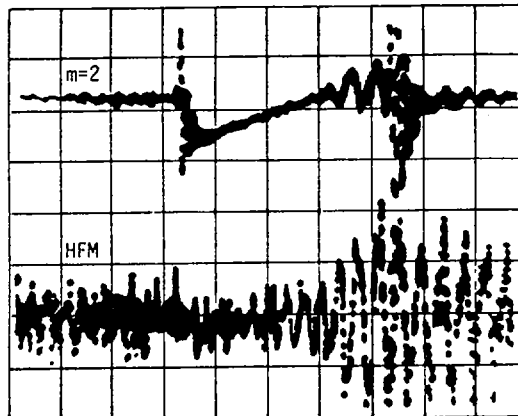


FIG. 8. Waveforms of the  $m = 2$  MHD mode and the high frequency magnetic fluctuation (HFM) during a  $V$ -pulse, time 200  $\mu$ s/div.

this was not correlated with the MHD modes mentioned before. The amplitude of this oscillation increased with increasing voltage.

(c) The horizontal displacement of the plasma underwent a shift during the pulse processes and did not recover after the V-pulse had passed by (Fig. 6). The delay of the shift may be related to the slight change in the profile of the plasma current density.

It was found that the  $H_{\alpha}$  line emission from the edge as well as the line density of the plasma did not increase during the V-pulse process. The edge heating effect was observed by ECE measurements.

#### 4. DISCUSSION

Low frequency MHD oscillations are very complicated phenomena which depend sensitively on the discharge conditions, such as electron density, impurities and wall conditions. Also, the discharge conditions have an influence on the effectiveness of the RHF. Although the experimental RHF results discussed above can only be reproduced in some discharge regimes, they show that the observed 'MHD oscillations' cannot be properly explained by the tearing mode theory; however, they give some clues to finding the mode structures.

Our experimental RHF results can be partly explained by assuming that the observed mode was a single mode which extended through the whole plasma. From a recent study of profile consistency it became clear that the RHF strongly influences sawtooth processes through this mode.

Our skin current experiments also showed the complexity of the low frequency magnetic fluctuations. We still do not know the real nature of the observed 10 kHz mode, but it is obvious that the high frequency fluctuation is of electromagnetic origin.

#### REFERENCES

- [1] WHITE, R.B., MONTICELLO, D.A., ROSENBLUTH, M.N., WADDELL, B.V., in Plasma Physics and Controlled Nuclear Fusion Research 1976 (Proc. 6th Int. Conf. Berchtesgaden, 1976), Vol. 1, IAEA, Vienna (1977) 569.
- [2] CAMPBELL, D.J., GILL, R.D., GOWERS, C.W., et al., Sawtooth Activity in Ohmically Heated JET Plasmas, Rep. JET-P(86)05, JET Joint Undertaking, Abingdon, Oxfordshire (1986).
- [3] ZHAO, Qingchu, CHEN, Jiayu, XIE, Jikang, et al., in Plasma Physics and Controlled Nuclear Fusion Research 1984 (Proc. 10th Int. Conf. London, 1984), Vol. 1, IAEA, Vienna (1985) 345.
- [4] HT-6B GROUP, Paper ASIPP/11, presented at 12th Europ. Conf. on Controlled Fusion and Plasma Physics, Budapest, 1985.



## ANOMALOUS TRANSPORT IN JET PLASMAS

D.F. DÜCHS, T.E. STRINGER, A. TARONI, M. BRUSATI,  
 N.A. GOTTARDI, T. HELLSTEN, F. TIBONE  
 JET Joint Undertaking,  
 Abingdon, Oxfordshire,  
 United Kingdom

### Abstract

#### ANOMALOUS TRANSPORT IN JET PLASMAS.

Local thermal fluxes have been determined experimentally for ohmic, RF wave and neutral beam heated JET plasmas through direct power balance calculations and through a modified application of 'predictive' equilibrium transport codes. A realistic way of describing the RF power deposition profile has been developed. Free-boundary plasmas, important for magnetic limiter cases in JET, can now be computed fully self-consistently. The experimental local fluxes have been compared with available analytically derived fluxes, but no acceptable agreement could be found. Many discharges can, however, be modelled empirically by modifying the electron thermal transport equation so that the steady state  $T_e$  profile is constrained to fit the observed canonical shape, with both ohmic and additional heat sources.

### 1. INTRODUCTION

In this paper we attempt to assess the status of theoretical understanding of anomalous transport in JET plasmas. This is done by deriving local fluxes from measurements and comparing them with presently available theoretical ones which are applicable under JET conditions. Sections 2 and 3 present the experimental values which are obtained firstly by the usual method of the integrated power balance and secondly by applying a full predictive transport code in steady state. The chosen cases include JET discharges where the plasma is heated ohmically, by ion cyclotron waves, and by neutral injection. Those discharges have been selected where a maximum number of diagnostics were available with reliable results so that the uncertainties on the fluxes could be minimised. In Section 4, a number of proposed theoretical formulae are reviewed and checked against JET data. Finally, in Section 5, an empirical approach is outlined by which also the plasma evolution in time is modelled successfully. The highlights are summarised in Section 6.

### 2. FLUXES FROM INTEGRATED POWER BALANCE

If  $V_\psi$  denotes the volume inside a chosen magnetic flux surface  $S_\psi$ , we define the average primary electron thermal energy flux density at time point  $t$  as

$$f_e(\psi, t) = \frac{1}{S_\psi} \int_{S_\psi} \left( \frac{3}{2} n_e T_e \vec{v}_e + \vec{q}_e \right) \cdot d\vec{S}_\psi \quad (1)$$

consisting of a convective and a conductive term. We prefer this quantity  $f_e$  rather than  $\chi_e$  (or  $\chi_i$ ) because it is closer to the actual measurements and avoids special assumptions and errors connected with local gradients. The flux is calculated as a function of  $\psi$  from the power balance

$$f_e(\psi, t) = \frac{1}{S_\psi} \left\{ - \frac{\partial}{\partial t} \int_{V_\psi} \frac{3}{2} n_e T_e dV \right. \\ \left. - \int_{V_\psi} p_{\text{rad}} dV - \int_{V_\psi} n_e \frac{T_e - T_i}{t_{\text{eq}}} dV \right. \\ \left. + \int_{V_\psi} \eta j^2 dV + \int_{V_\psi} P_{\text{RF}} dV + \int_{V_\psi} P_{\text{NBI}} dV \right\} \quad (2)$$

An analogous equation holds for  $f_i(\psi, t)$ . Additional possible terms (e.g. ionisation, adiabatic compression, etc.) were estimated as negligible. The geometry, i.e.  $\psi$ ,  $S_\psi$  and  $V_\psi$ , are taken from solutions of the Grad-Schlüter-Shafranov equation which agree with outside magnetic probe measurements. These solutions also provide the ohmic heating term. The bolometer array signals deliver the radiation loss term after the charge exchange neutral share is computed and subtracted.

Only the electron part of the ion cyclotron heating in the central region can be estimated experimentally. Therefore, the total deposition profile is calculated using the global wave code LION [1]. This code calculates wave propagation for the magnetosonic wave in toroidal geometry, assuming the plasma species to be Maxwellian. In the case of on-axis heating of hydrogen minority at its fundamental cyclotron resonance, the distortion of the velocity distribution of the heated minority ions becomes strong [2]. At low density, the heating of the minority species outside the central region is still high enough to produce strong Doppler broadening of the resonance, which broadens the power deposition. The power transfer to the electrons and ions from that absorbed by the minority ions is calculated with the Fokker-Planck code BAFIC [2]. Direct electron heating has been neglected. The power deposition on the electrons is then checked against measurements, and generally good agreement is found. At high temperatures, significant ion heating occurs, due to second harmonic absorption by the deuterons.

Also the power deposition from neutral beams cannot be measured directly and has been computed by Monte-Carlo or pencil beam codes, with the total power, temperature and density profiles, and  $Z_{\text{eff}}$  as measured input [3]. A major source of uncertainty is the ion temperature profile which we took from the neutral particle analyser diagnostics [4] when available.

These profiles suffice to determine the remaining terms in eq. (2) if the equilibration ( $t_{\text{eq}}$ ) is assumed to be classical.

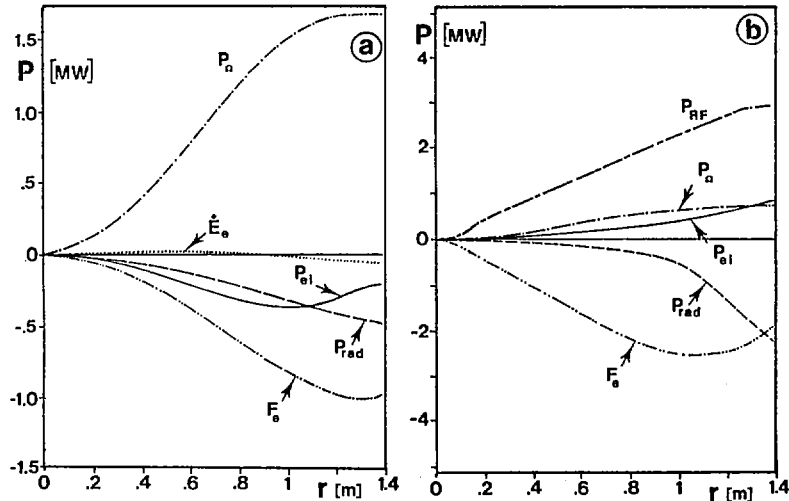


FIG. 1. Local power balance (integrals over magnetic flux surface volume inside  $r$ ) for a JET pulse during (a) ohmic heating and (b) RF heating.  $I_p = 2$  MA,  $B_t = 2.2$  T, H minority ( $n_H/n_D \sim 2\%$ ) heating in (b).

Figure 1 shows the individual terms of eq. (2) for an ohmically (1a) and an RF heated (1b) JET plasma. The average minor radius  $r$  is used here as a flux surface label, i.e. it specifies  $S_\psi$  and  $V_\psi$ . The integrated ohmic input power is denoted by  $P_\Omega$ , the RF input by  $P_{RF}$ , the power exchanged between electrons and ions by  $P_{ei}$ , the radiation loss by  $P_{rad}$ , and the temporal change in thermal (electron) energy content by  $\dot{E}_e$ . The result of the balance is  $F_e = f_e \cdot S_\psi$ .

These cases have been chosen because  $F_e$  is a significant term (i.e. not only a difference of large numbers) over the whole cross-section.

In order to set off the difference between ohmic and additionally heated plasmas, the figures 1 to 3 refer to two different time slices of the same discharge with a total plasma current  $I_p = 2$  MA and a toroidal field (on axis) of 2.2 T.

Figure 2 presents a typical result obtained through the above procedure for the ohmic case. Figure 2a shows the measured plasma characteristics, i.e. density, temperature and  $q$ -profiles, while the local mean thermal fluxes are given in Fig. 2b. The same quantities for a neutral beam heated case are shown in Fig. 4.

The error margin for these fluxes is assessed by varying the terms in eq. (2) within the experimental errors.

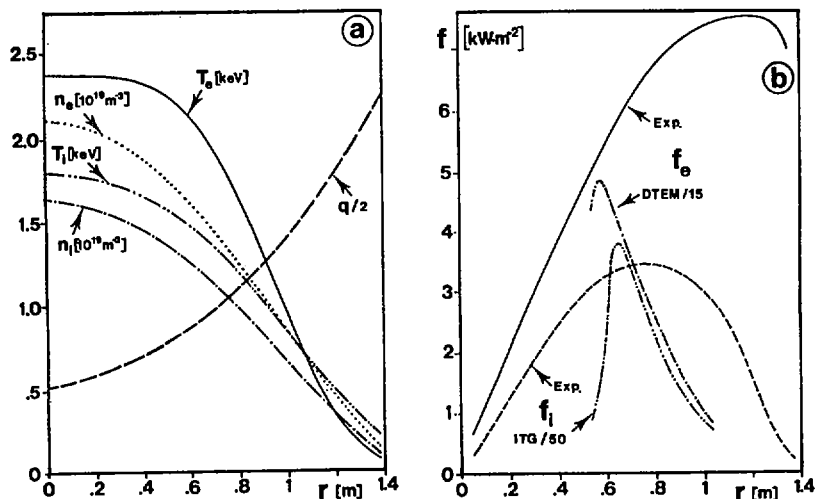


FIG. 2. (a) Plasma parameter profiles, and (b) measured surface averaged thermal fluxes  $f$  for electrons and ions, for the ohmically heated JET plasma (Fig. 1(a)). Theoretical results for the dissipative trapped electron mode (DTEM), scaled down by a factor of 50, and for the ion temperature gradient (ITG) instability, scaled down by a factor of 50, are also shown.

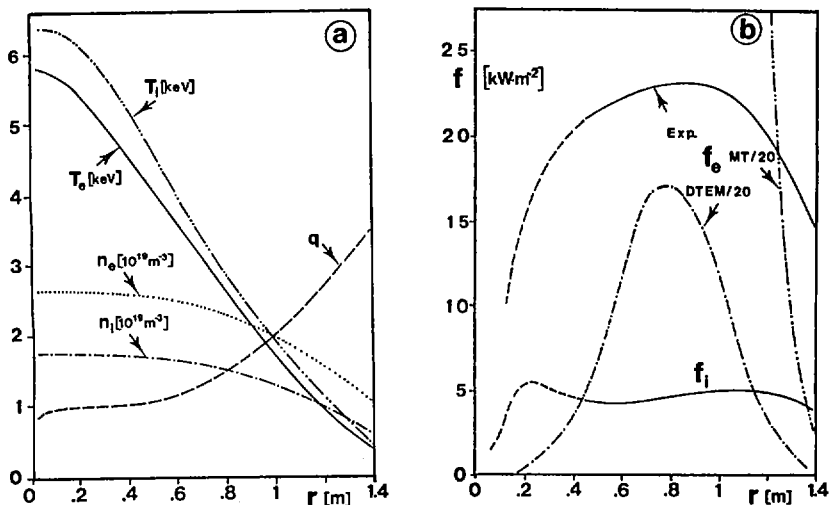


FIG. 3. (a) Plasma parameter profiles for an RF heated JET plasma, and (b) surface averaged thermal fluxes  $f$  as derived (Section 3) for electrons and ions. The uncertainty of  $f$  is enhanced within the sawtooth region (dashed curves). The electron heat fluxes predicted for the dissipative trapped electron mode (DTEM) and the microtearing (MT) mode are also shown.

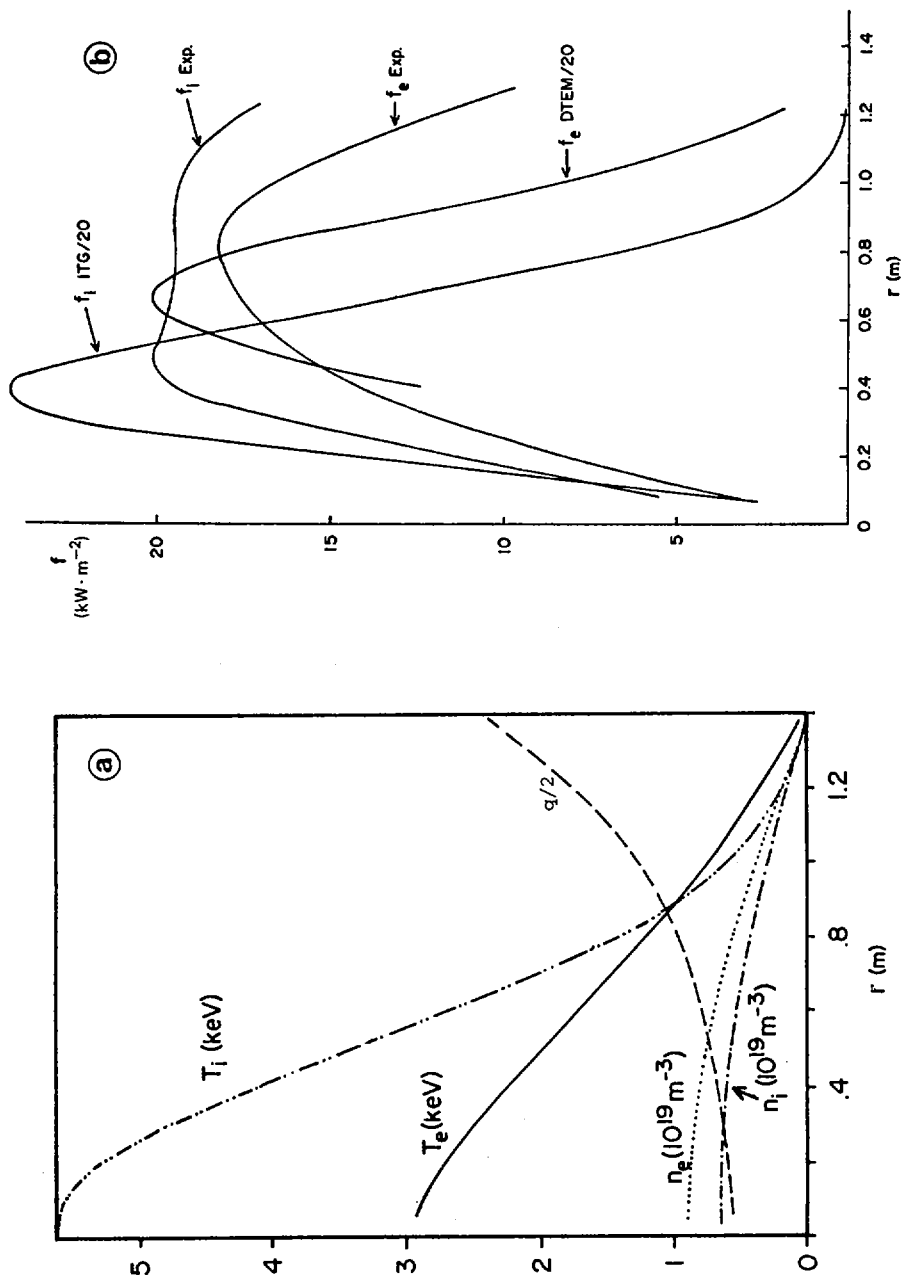


FIG. 4. (a) Plasma parameter profiles for a neutral beam heated (NBI) JET plasma, and (b) surface averaged thermal fluxes  $f$  as derived (Section 3) for electrons and ions ( $P_{\text{inj}} = 5.4 \text{ MW}$ ,  $I_p = 3 \text{ MA}$ ,  $B_1 = 3.5 \text{ T}$ ). For comparison, scaled down theoretical results for the dissipative trapped electron mode (DTEM) and the ion temperature gradient (ITG) mode are also shown.

### 3. FLUXES FROM EQUILIBRIUM/TRANSPORT CODES IN STEADY STATE

Our second method to obtain measured fluxes uses a full equilibrium/transport code (in  $\psi(R,Z),t$ ) containing more detailed physics. For example, this code has been restructured to allow fully consistent free-boundary equilibrium transport calculations. The mathematical methods have been published recently [5]. The code interacts with the external coils, which is especially important for magnetic limiter cases in JET. In the interpretative application it is, of course, used to reproduce the measured magnetic (probe, loop) signals, thus checking whether the equilibria are consistent with (transport) pressure and current density profiles. In addition, it contains detailed modelling of impurity diffusion and radiation, neutral atom distributions, the sawtooth region, and boundary conditions.

The present method of application is as follows: The measured basic plasma parameters (densities, temperatures, fields) are inserted as initial values. The measured complex quantities, such as radiation losses, neutron yields, charge exchange neutrals, are examined immediately through the models for their consistency with the basic parameters; this leads either to corrections or to an assessment of error bars. In the spirit of "shooting methods" an ansatz for the desired fluxes is guessed and programmed; for example, the result of the previous (cruder) power balance method could be chosen, or any function of the basic parameters and their derivatives. The code is then stepped forward in time, and, in stationary state, must reproduce the input initial value profiles, provided that our ansatz for the fluxes was suitable, otherwise it is to be modified. This method lends itself readily to sensitivity studies by determining those terms which predominantly cause deviation from steady state.

The method can, of course, also be applied to non-stationary conditions, except that then several sets of measurements at consecutive time slices are required.

Figure 3 presents the fluxes for an RF-heated JET plasma evaluated by this method.

We have analysed many other cases which are being collected, with some attempts at "scaling" for a forthcoming JET report [6].

### 4. COMPARISON WITH THEORY

Expressions for the anomalous transport, derived analytically for different instabilities, have been evaluated for JET parameters and compared with the measured fluxes. The extensive review in Ref. [11] and more recent literature has been taken into account. Only those modes which may be unstable in JET conditions, and for which predicted loss rates are available, will be discussed. Space does not permit these expressions to be reproduced here, they may be found in the references quoted. The notation here is the same as in the references.

a) Electron transport

A significant level of agreement has recently been achieved [7,8] between the global energy confinement times measured on several tokamaks and prediction based on the dissipative trapped electron mode (DTEM). However, when the predicted local thermal diffusivity [8], including  $Z_{\text{eff}}$  in the collision frequency  $\nu_{e1}$ , is compared with the experimental value in JET, the predicted value is typically an order of magnitude too high within the region where the DTEM should be dominant (see Fig.2b). Because of the strong dependence of the diffusivity on temperature ( $\chi_e \sim T_e^{-7/2}$  for the DTEM and  $\chi_e \sim T_e^{-3/2}$  for the collisionless trapped electron mode) and on the characteristic lengths  $r_n$  and  $r_T$ , the global confinement time is sensitive to the temperature profile and cannot be adequately expressed in terms of the peak or mean temperature.

It is questionable whether the temperature in JET is low enough, even in the edge region, to satisfy the criteria for the rippling instability [9]. In any case, the predicted diffusivity turns out to be too low by about two orders of magnitude.

The microtearing mode (MT) [10] could develop under JET conditions for mode numbers  $m$  such that

$$m < 10^{-11} \frac{r r_n n B_T Z_{\text{eff}}}{T_e^{5/2}}$$

in MKS units and eV. The predicted electron thermal diffusivity,  $\chi_e \sim T_e^{-7/2} / n Z r_n^2 B^2$ , has a parametric dependence similar to the DTEM, and is larger in magnitude. Close to the plasma edge in JET its value is comparable to the experimental value, but as one moves into the plasma it exceeds the experimental value by a rapidly increasing factor, as illustrated in Fig. 3b.

Collisional drift wave transport [13] could occur in the JET edge region; however, the magnitude of the flux comes out too small by 1-2 orders of magnitude.

Stochastic transport due to electrostatic trapping in drift waves has been proposed in Ref [14]. It could occur within the operating range of JET. However, as most of the other models, it reproduces neither the spatial dependence nor the scaling with global parameters obtained in JET.

b) Ion transport

The neoclassical ion heat diffusivity [15] is a factor 1-8 below the experimental value in JET. For example, in Fig. 3b best fit was obtained with once neoclassical.

The observed saturation in  $\tau_E$  at higher densities has been reproduced in several tokamaks by including in the transport code the diffusivity derived for the ion temperature gradient

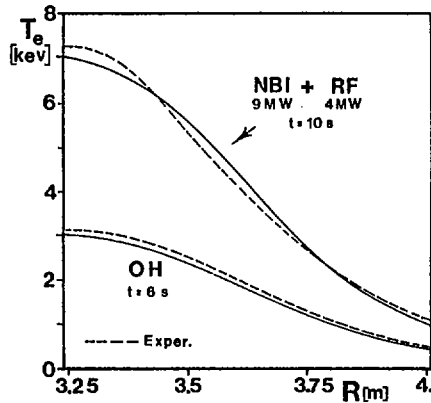


FIG. 5. Comparison between measured and empirically modelled (evolving)  $T_e$  profiles for combined ion cyclotron heating (H minority) and neutral beam heating of a JET plasma ( $I_p = 2$  MA,  $B_t = 2.2$  T).

instability (ITG) [7,8]. However, the predicted thermal diffusivity for this mode in JET is more than an order of magnitude higher than the experimental value (see Fig. 2b).

## 5. EMPIRICAL FLUX DESCRIPTION

In view of the obvious lack of satisfactory transport theory the development of empirical prescriptions [16] has been pursued further.

A widely applicable prescription is based on the experimental finding that, largely independent of additional heating and radiation losses, two parameters suffice to describe the electron temperature profile  $T_e(\rho)$  in all steady states (for  $q_b \leq 7$ ) by

$$T_e(\rho) = T_e(\rho_b) \exp\{\alpha[1 - (\rho/\rho_b)^2]\} \quad (4)$$

or an expression with similar profile characteristics.

The flux surface coordinate ("radius")  $\rho_b$  lies towards the inside of the radiation dominated layer, for most JET discharges close to the limiter radius. The parameter  $\alpha$  can vary between

$$1.5 < \alpha < 2.2$$

with a strong peak around  $\alpha = 1.9$ , and no clear dependence on other plasma parameters.

All rigorously derived transport equations are based on the assumption that the parameters of the system tend towards thermodynamic equilibrium, e.g. flat profiles for vanishing sources. It is possible to restructure the balance equations so

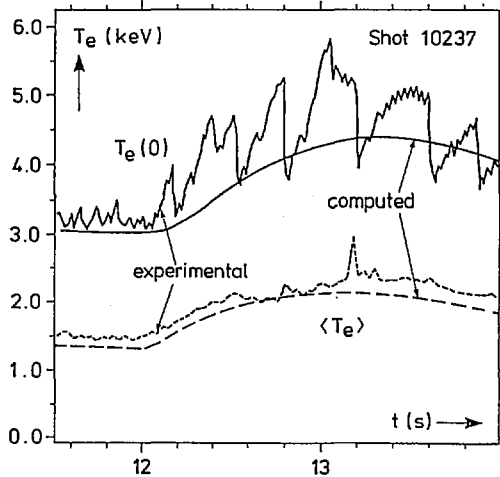


FIG. 6. Evolution of on-axis electron temperature  $T_e(0)$  and volume averaged electron temperature  $\langle T_e \rangle$ . Comparison of measured values computed with empirical ('profile consistent') fluxes.

that the parameters, here  $T_e$ , always approach prescribed equilibrium profiles, e.g. the ones given above in formula (4).

Such apparent neglect of thermodynamic principles might indicate that not all important parameters are computed self-consistently, i.e. that we are dealing with an open thermodynamic system.

A physically consistent model to solve this problem, based on partial ergodisation of the magnetic field, is being developed by P.H. Rebut et al. [12,17].

A restructured balance equation for the electron thermal energy does, of course, allow for temporal deviations from the given equilibrium profiles. In comparison with the experiment it must satisfy two constraints:

- a) The equilibrium profiles for  $T_e(\rho)$ , obtained from

$$\frac{\partial}{\partial t} \left( \frac{3}{2} n_e T_e \right) = 0, \quad \text{i.e. (integrated once over } \rho) \text{ from}$$

$$0 = \rho f_e(\rho) + \int_0^\rho (n j^2 + P_{RF} + P_{NBI} - P_{rad} - P_{ei}) \rho \, d\rho \quad (5)$$

must coincide with formula (4), and

- b)  $f_e$  should reproduce the observed rate of relaxation towards the given equilibrium profile (or the maximum deviation from it for given sources).

It is not clear whether these requirements lead to a unique solution, nor is a sufficiently wide data base available yet for point b.

An application of this procedure to particle transport is given by the popular anomalous inward particle flux term [18,19].

Several practical approaches to solve the above problem for  $T_e$  have been reported [20,21], and the connections to widely used empirical formulae have been pointed out. Our method [21] has, in the meantime, been successfully checked against a number of JET discharges including strong additional combined RF and neutral beam heating and X-point plasmas. Figure 5 shows an example of "profile consistency". Figure 6 demonstrates good agreement with the measured time evolution of the electron temperature.

## 6. CONCLUSIONS

Measured local thermal fluxes in JET plasmas are presented. A vital ingredient is the power deposition for the various heating schemes. For the RF deposition the theoretical model which has been developed shows good agreement with measurements.

The JET code now allows transport calculations with fully consistent free boundary equilibria. The application of predictive transport codes to obtain experimental local fluxes is outlined.

Previous studies have mostly compared measured and predicted global energy confinement times. The comparison of local energy fluxes made here is a more exacting test of theory. The low collisionality regime accessible to JET also extends the parameter range. Our comparison shows that theoretically predicted loss rates do not agree with the observed radial variation in the fluxes.

Empirically the temporal evolution of discharges in JET can be reproduced well by a prescription which enforces a certain shape of the  $T_e$  profile in ohmic and additionally heated steady state plasmas.

## ACKNOWLEDGEMENTS

We are indebted to W.G.F. Core, S. Corti, M. von Hellerman, F. Romanelli and E. Springmann for their help and useful discussions.

## REFERENCES

- [1] APPERT, K., et al., Plasma Phys. Controll. Fusion **28** (1986) 133.
- [2] SUCCI, S., et al., Comput. Phys. Commun. **40** (1986) 137.
- [3] WATKINS, M.L., et al., in Controlled Fusion and Plasma Heating (Proc. 13th Europ. Conf. Schliersee, 1986), Part I, European Physical Society (1986) 156.
- [4] CORTI, S., et al., *ibid.*, p. 109.

- [5] CENACCHI, G., TARONI, A., in Computational Physics (Proc. 8th Europ. Conf. Eibsee, 1986), European Physical Society (1986) 57.
- [6] DÜCHS, D.F., et al., JET Report, to be published.
- [7] DOMINGUEZ, R.R., WALTZ, R.E., Rep. No. GA-A-18184, General Atomic, San Diego, CA (1986).
- [8] ROMANELLI, F., TANG, W.M., WHITE, B.B., Rep. PPPL-2310, Plasma Physics Lab., Princeton Univ., NJ (1986).
- [9] GARCIA, L., DIAMOND, P.H., CARRERAS, B.A., CALLEN, J.D., Phys. Fluids **28** (1985) 2147.
- [10] DRAKE, J.F., GLADD, N.T., LIU, C.S., CHANG, C.L., Phys. Rev. Lett. **44** (1980) 994.
- [11] LIEWER, P.C., Nucl. Fusion **25** (1985) 543.
- [12] REBUT, P.H., BRUSATI, M., Plasma Phys. Controll. Fusion **28** (1986) 113.
- [13] TERRY, P.W., DIAMOND, P.H., Phys. Fluids **28** (1985) 1419.
- [14] HORTON, W., CHOI, D.-I., YUSHMANOV, P.N., PARAIL, V.V., to be published.
- [15] CHANG, C.S., HINTON, F.L., Phys. Fluids **25** (1982) 1493.
- [16] COPPI, B., Comments Plasma Phys. Controll. Fusion **5** (1980) 261.
- [17] REBUT, P.H., et al., Paper IAEA-CN-47/E-III-4, these Proceedings, Vol. 2.
- [18] COPPI, B., SHARKY, N., Nucl. Fusion **21** (1981) 1363.
- [19] BEHRINGER, K., et al., in Divertors and Impurity Control in Tokamaks (Proc. IAEA Tech. Comm. Mtg Garching, 1981), Max-Planck-Institut für Plasmaphysik, Garching (1981).
- [20] TANG, W.M., Rep. PPPL-2311, Plasma Physics Lab., Princeton Univ., NJ (1986).
- [21] TARONI, A., TIBONE, F., in Controlled Fusion and Plasma Heating (Proc. 13th Europ. Conf. Schliersee, 1986), Part I, European Physical Society (1986) 160.



## MICROINSTABILITY BASED MODELS FOR CONFINEMENT PROPERTIES AND IGNITION CRITERIA IN TOKAMAKS

W.M. TANG, C.M. BISHOP<sup>1</sup>, B. COPPI<sup>2</sup>, S.M. KAYE,  
F.W. PERKINS, M.H. REDI, G. REWOLDT  
Princeton Plasma Physics Laboratory,  
Princeton University,  
Princeton, New Jersey,  
United States of America

### Abstract

#### MICROINSTABILITY BASED MODELS FOR CONFINEMENT PROPERTIES AND IGNITION CRITERIA IN TOKAMAKS.

The results of theoretical studies are reported for: (1) the use of microinstability based thermal transport models to interpret the anomalous confinement properties observed in key tokamak experiments such as TFTR, and (2) the likely consequences of the presence of such instabilities for future ignition devices. Transport code simulations using profile consistent forms of anomalous thermal diffusivities due to drift type instabilities have yielded good agreement with the confinement times and temperatures observed in TFTR under a large variety of operating conditions including pellet fuelling in both Ohmic and neutral-beam-heated discharges. With regard to achieving an optimal ignition margin, the adverse temperature scaling of anomalous losses caused by drift modes leads to the conclusion that it is best to operate at the maximum allowable density while holding the temperature close to the minimum value required for ignition.

#### ANALYSIS OF ANOMALOUS THERMAL CONFINEMENT IN TOKAMAKS

Identification of the primary physical processes responsible for the anomalous thermal transport properties currently observed in tokamaks is vitally important not only for the effective development of methods to improve performance in existing devices but also for the proper planning of future ignition experiments. In recent work [1-4] it has been demonstrated that if realistic profile constraints are invoked, then most of the significant confinement trends in low-beta tokamaks can be explained by electrostatic ( $E \times B_0$ ) transport caused by drift-type microinstabilities. Anomalous thermal transport models based on the associated physics have yielded predictions in very favorable agreement with a substantial experimental data base with respect to both the scaling and the magnitude of the energy confinement time ( $\tau_E$ ) and the central electron temperature ( $T_{e0}$ ).

---

<sup>1</sup> Culham Laboratory, Abingdon, Oxfordshire, UK.

<sup>2</sup> Massachusetts Institute of Technology, Cambridge, MA, USA.

In the present studies, the profile-consistent microinstability models derived in Ref. [2] have been used in the BALDUR (time-dependent, 1D) transport code [5] for the purpose of interpreting experimental results from TFTR including ohmic heating, neutral-beam-injection (NBI) heating, and pellet-fuelling in both ohmic and NBI-heated discharges. The theoretical expressions for the anomalous thermal diffusivities ( $\chi_e$ ,  $\chi_i$ ) are based on the presence of trapped-electron drift modes and/or toroidal ion temperature gradient ( $\eta_i$ ) modes in the bulk region of optimal thermal insulation (roughly located between the  $q = 1$  and  $q = 2$  surfaces in the plasma). They incorporate the familiar mixing length estimate for the magnitude of the fluctuations and also include the assumption that a temperature "profile consistency" constraint [6] is satisfied. The latter is required here because the present state of development of nonlinear toroidal microinstability theories cannot provide reliable scaling with non-dimensional parameters such as  $q$  and because mechanisms outside the realm of microinstabilities could be playing a prominent role outside the  $q = 2$  region. If the parameter,  $\eta_i \equiv d\ln T_i/d\ln n_i$ , remains below a critical magnitude,  $(\eta_i)_c$  (roughly about 2), then the dominant instability is the trapped-electron mode, and the associated form of the electron diffusivity can be expressed as

$$\chi_e^{TE} (\text{cm}^2/\text{sec}) = \frac{0.4(1+0.25\alpha_n)10^4 P^{0.8} F_H(r)}{n_{e0} R^{1.2} a^{0.1} Z^{0.2} B_T^{0.4} q_a^{0.9}} \quad (1)$$

with

$$F_H(r) = \frac{[1-\exp(-\alpha_q)] \exp(2\alpha_q r^2/3a^2) \int_0^{r/a} dx h(x)}{[n_e(r)/n_{e0}] (r^2/a^2) \int_0^1 dx h(x)}$$

where  $\alpha_q = q_a + 0.5$ ,  $P(\text{MW})$  is the total equilibrated ("steady-state") value of the input power (minus radiation losses),  $h(x)$  is the energy deposition profile,  $n_{e0}$  ( $10^{14} \text{ cm}^{-3}$ ),  $R(\text{m})$ ,  $a(\text{m})$ ,  $B_T(\text{T})$ , and  $\alpha_n$  is the usual parabolic density profile parameter. In arriving at Eq. (1), the intrinsic temperature dependence has been eliminated in terms of a power dependence through an assumed thermal steady state [2]. The influence of these modes on  $\chi_i$  tends to be masked by the usual ion neoclassical transport [2]. However, if  $\eta_i > (\eta_i)_c$ , then the toroidal  $\eta_i$ -modes become dominant [7], and the associated profile-consistent form of the anomalous ion diffusivity becomes

$$\chi_i(r) = \frac{10^3 (P/n_{e0})^{0.6}}{(RB_T q_a)^{0.8} (a)^{0.2}} F_H(r) \quad (2)$$

For a sufficiently collisionless plasma,  $\chi_e$  also scales as Eq. (2). On the other hand, for values of  $v_{*e}$  (the usual banana

regime collisionality parameter)  $\geq 0.1$  to 0.2, the electron loss channel remains sensitive to collisions in the presence of  $\eta_i$ -modes. This is due to the fact that even though it does not strongly affect these instabilities, the non-adiabatic trapped-electron response does determine  $\chi_e$ . Hence, the associated form of  $\chi_e$  tends to be very similar to Eq. (1).

Simulations of nearly two dozen TFTR discharges covering a wide range of experimental conditions were carried out with the BALDUR transport code using  $\chi_e = \chi_e^{\text{NEO}} + \chi_e^{\text{TE}}$ ,  $\chi_i = \chi_i^{\text{NEO}} + \chi_i^{\eta_i}$  (with  $\chi_i^{\eta_i} = 0$  if  $\eta_i \leq 1.5$  at  $q = 1.5$ ). Other important effects, such as sawteeth behavior inside the  $q = 1$  region, radiation processes, etc. have also been included and are described in Ref. [5]. With regard to particle transport, empirical models were constructed to produce density profiles approximating the Thomson-scattering-measured density data. In particular,  $D = D^{\text{NEO}} + D^{\text{ANOM}}$  and  $v = v^{\text{NEO}} + v^{\text{ANOM}}$ . For example, in simulating the pellet-fuelled cases,  $D^{\text{ANOM}}(\text{cm}^2/\text{sec}) = 4 \times 10^{16}/n_e(r)$  with  $v^{\text{ANOM}} = 2D^{\text{ANOM}}/r/a^2$  before and  $v^{\text{ANOM}} = 0$  after the pellets are injected. The results from the predictive simulations of numerous TFTR large plasma discharges are summarized on Fig. 1 and Table 1. On Fig. 1 the calculated energy confinement times are plotted as a function of the familiar neoAlcator parameter and compared with the experimental results from a large number of gas-fuelled ohmically-heated discharges (crosses) as well as from pellet-fuelled ohmic cases (open diamonds). For the gas-fuelled cases it is quite clear that the anomalous enhancement of  $\chi_i$  associated with  $\eta_i$ -modes (solid circles) can account for the observed saturation of  $\tau_E$  at values below those predicted by calculations using only  $\chi_i^{\text{NEO}}$  (open circles). The result from the simulation of an ohmic PDX plasma is also displayed to indicate consistent size-scaling at a small value of the neoAlcator parameter. With regard to the pellet-fuelled cases the simulation results are again in very good agreement with the experimental data. As shown on Fig. 1, the first pair of diamonds correspond to values of  $\tau_E$  at two points in time after the injection of a single pellet, and the second pair of diamonds to the analogous situation for a three-pellet experiment. The higher  $\tau_E$  in each pair represents the confinement at the time closer to the time of injection. In these cases the global confinement times are lower than those for the gas-fuelled experiments because of larger energy losses associated with convection and radiation. However, the simulations also indicate that the central confinement is significantly improved after pellet injection because of the resultant peaking in the density profile. This trend, which is in agreement with that found in the TRANSP data analysis, is likely due to  $\chi_e$  scaling as  $1/n_e(r)$  and to the fact that the  $\eta_i$ -driven anomalous enhancement of  $\chi_i$  can be eliminated (e.g. in the 3-pellet case). Results for  $\tau_E$  and  $T_e$  from simulations of a representative set of NBI-heated TFTR discharges are given in Table 1 and show good agreement with the experimental values. These include a pellet-injection NBI case

TABLE 1. PARAMETERS OF SIMULATED NEUTRAL BEAM HEATED TFTR SHOTS

Shot	$I_p$ (MA)	$B_z$ (T)	R (m)	a (m)	$\bar{n}_e$ ( $10^{19} \text{ m}^{-3}$ )	$P_{inj}$ (MW)	$Z_{eff}$	$q_a$	$T_e^{exp}$ (keV)	$T_e^{Sim}$ (keV)	$\tau_E^{exp}$ (s)	$\tau_E^{Sim}$ (s)	$\nu_e$ ( $q=1.5$ )
14727	2.2	4.8	2.56	0.82	4.8	5.3	2.6	2.8	4.0	3.6	0.20	0.18	0.19
14773	2.2	4.7	2.57	0.82	3.0 (7.0 <sup>a</sup> )	5.7	1.9	2.8	2.4	2.8	0.14	0.19	0.29
19965	2.2	4.8	2.49	0.83	4.2	8.8	3.2	3.0	3.8	3.7	0.11	0.11	0.25
22014	0.8	4.6	2.55	0.82	3.2	11.3	2.5	7.6	5.8	3.5	0.12	0.06	0.13
										6.2 <sup>b</sup>		0.14 <sup>b</sup>	

<sup>a</sup> After pellet injection.<sup>b</sup> Collisional model.

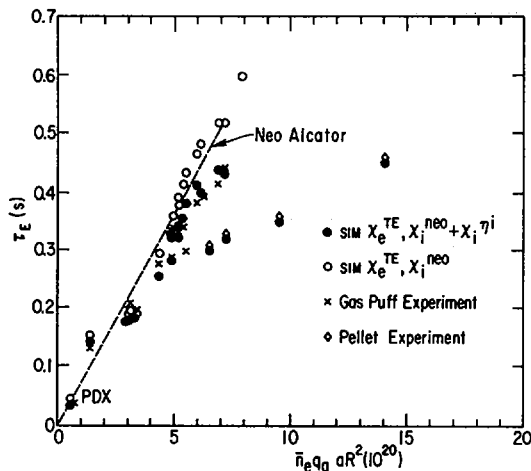


FIG. 1. Results of simulations of neutral beam heated TFTR shots.

(shot 14773) and a typical "supershot" discharge (shot 22014). All of the results displayed in Fig. 1 and Table 1 were computed using Eq. (1). With regard to the "supershot" case, preliminary calculations using a more realistic version of  $\chi_e(r)$  (which takes into account only the power into the electron channel and the proper transition into the collisionless regime) has yielded close agreement with the experimental values given in Table 1; i.e.  $\tau_E = 0.14s$  and  $T_e = 6.2$  keV. In addition, all of the computed temperature profiles correlated well with the data, and comparisons of the theoretical  $\chi_e(r)$  given by Eq. (1) and those obtained from TRANSP data analysis studies of a number of ohmic and NBI-heated TFTR discharges have also indicated reasonable agreement.

Before proceeding with the further development and application of the profile-consistent models just described to the important class of H-mode NBI-heated divertor plasmas, it is necessary to first establish the proper behavior of the microinstabilities invoked under such conditions. In previous studies involving comprehensive kinetic toroidal computations [8], it was demonstrated that the weaker pressure gradients in the interior region of H-mode plasmas led to correspondingly weaker instabilities. Although this reduction in the local anomalous thermal diffusivity in the inner zone is consistent with the observed improvement in  $\tau_E$ , it leaves open the question of the nature of the transport properties in the very steep gradient region near the edge. Specifically, in order to be consistent with the thermal fluxes calculated in the interior, the local thermal diffusivity in the edge zone must be greatly reduced.

This issue has been addressed in the present work by interfacing the kinetic stability code [8] with a model tokamak equilibrium with a separatrix [9]. The equilibrium here takes into account the enhanced local shear effects near the separatrix and is basically an extension of the familiar "s- $\alpha$  model" [10] whose finite-beta properties are primarily governed by the magnitude of the local pressure gradient. Fully electromagnetic calculations of the dominant toroidal microinstabilities were carried out using as input parameters the edge data obtained from careful measurements of H-mode and L-mode PDX tokamak discharges. The results generally indicate that the proximity of the separatrix to the magnetic surface considered has a significant stabilizing influence. This effect is considerably stronger for the H-mode cases with their characteristically steeper edge profiles. In particular, the finite-beta-modified drift-type electrostatic modes are found to be stable over a region extending several centimeters inside the separatrix for the H-mode profiles but over a much smaller range for the L-mode. These enhanced local stability properties near the separatrix thus serve to support the notion that thermal transport properties in H-mode plasmas are reconcilable with microinstability-based models.

#### CONSEQUENCES OF MICROINSTABILITIES FOR IGNITION IN TOKAMAKS

The favorable correlations between the confinement trends observed under a large variety of tokamak operating conditions and the results from the anomalous transport studies just described as well as from previous work [1-4] serve to emphasize the importance of addressing the consequences of drift-type instabilities for future ignition devices. Under steady-state conditions, the simplest form of the basic homogeneous (zero-dimensional) thermal energy balance equation is given by

$$P_h = P_{Le} + P_{Li} + P_R - P_\alpha \quad (3)$$

where  $P_h$  is the external heating power density,  $P_{Le}$  and  $P_{Li}$  represent the losses due to electron and ion conductivity,  $P_R$  represents radiation losses, and  $P_\alpha$  is the  $\alpha$ -particle heating term. In earlier calculations [11,12] it was demonstrated that the familiar Murakami density limit represents a balance between radiation losses ( $P_R$ ) and ohmic heating input power ( $P_h$ ). However, since the fusion power ( $P_\alpha$ ) will offset  $P_R$  at temperatures characteristic of ignition conditions ( $T_0 > 6$  keV), this limit should not be relevant. Instead, attention needs to be focused on the influence of enhanced forms of  $P_{Le}$  and  $P_{Li}$  caused by the presence of microinstabilities. First consider the situation where the dominant terms in Eq. (1) are  $P_\alpha$ ,  $P_R$  (from bremsstrahlung), and  $P_{Le}$  from anomalous losses associated with the dissipative trapped-electron modes. Using the simple local form

for  $\chi_e$  given in Ref. [1] and applying the boundary conditions of sawtooth flattening for  $q \leq 1$  and  $T_e = 0$  for  $q \geq 2$ , the corresponding 1-D radial equation yields eigenvalue solutions which can be expressed in the form of an ignition criterion,

$$[n_0(10^{15} \text{ cm}^{-3})B_T(10 \text{ T})]^2 [a(\text{m})]^{2.5} [R(\text{m})]^{1.5} > 14.6(3/q_a)^{1.5} \alpha_n^2 \quad (4)$$

Since  $P_{Le}$  is independent of density in the dissipative trapped-electron regime, it can be concluded that for ignition experiments falling in this regime, the density can be increased to the point where the criterion given by Eq. (4) can be satisfied, provided external power ( $P_h$ ) is supplied to compensate for the heat capacity of the increased density and to maintain  $T_0 > 6$  keV so that  $P_\alpha > P_R$ . The power required to balance the thermal conduction losses is estimated to be  $P_{\text{crit}}(\text{MW}) = 120(3/q_a)^{2.75} (T_0/6 \text{ keV})^{4.5} \alpha_n^2 / (ZB_T^2(\text{aR})^{0.5})$ . These results clearly suggest that the optimal ignition scenario would involve operating at (i) the lowest allowable temperature (consistent with ignition), (ii) the highest allowable density (consistent with MHD  $\beta$ -limits but not the Murakami limit), and (iii) the flattest density profiles (because of the strong  $\alpha_n$ -dependence in the local model used for  $\chi_e$ ). However, with regard to (iii), it should be strongly cautioned that if the density profiles are allowed to be too flat, then  $\eta_i$  can easily exceed  $(\eta_i)_c$ . The consequent enhancement of  $P_{Li}$  due to  $\eta_i$ -instabilities can then pose a very restrictive density constraint in the ignition temperature regime. In order to simply illustrate this point, it is convenient to express Eq. (3) in a schematic form highlighting the density and temperature dependences in each term, i.e. (taking  $T_i = T_e = T$ )

$$P_h - \gamma_{TE} T^{9/2} = n^2 (\gamma_{BN} T^{1/2} - \gamma_\alpha T^{5/2}) + n \gamma_{\eta_i} T^{5/2} \quad (5)$$

with  $\gamma_{TE} T^{9/2}$  being the dissipative trapped-electron losses,  $n^2 T^{1/2} \gamma_{BN}$  being losses due to bremsstrahlung and ion neoclassical conduction,  $\gamma_\alpha T^{5/2} = P_\alpha$ , and  $n \gamma_{\eta_i} T^{5/2}$  being the  $\eta_i$ -mode losses. In the absence of the last term, Eq. (5) clearly indicates that, provided  $P_h > \gamma_{TE} T^{9/2}$ , there would indeed be no density limit for  $T \geq T_{MI}$ , with  $T_{MI} = (\gamma_{BN}/\gamma_\alpha)^{1/2} =$  minimum ignition temperature. However, if present, this density-dependent loss term would force operating below an upper density bound at  $T \leq T_{MI}$  and above a lower density bound at  $T > T_{MI}$ . The latter situation simply corresponds to requiring  $P_\alpha > n \gamma_{\eta_i} T^{5/2}$ . Estimates from Eq. (5) indicate that the external power  $n^2$  needed to reach ignition is proportional to  $T_{MI}^{9/2}$ . Hence, in order to avoid such stringent constraints, pellet-injection fuelling procedures could be adopted to produce density profiles sufficiently peaked to suppress the  $\eta_i$ -modes. After exceeding the required ignition temperature, a

less discriminating fuelling system would be adequate since  $P_\alpha$  could then offset any ensuing anomalous losses of this type. In general, for  $T > T_{mI}$ , the power losses resulting from drift modes increase at least as rapidly with  $T$  as the fusion power. Consequently, the optimum path to ignition should exploit favorable scalings with  $B_T$ , density, size, etc., while holding  $T$  close to  $T_{mI}$ .

#### ACKNOWLEDGMENTS

We are indebted to P.C. Efthimion, G.L. Schmidt, D.R. Mikkelsen, and the TFTR physicists for providing the data as well as valuable assistance needed to carry out the BALDUR simulations. Special thanks are extended to S. Hiroe, B. LeBlanc, and B. Grek for providing the profile data from PDX used in the H-mode calculations.

This work was supported by United States Department of Energy Contract No. DE-AC02-76-CHO-3073 and for F. Perkins also by NASA Contract No. NAGW-91 and by the National Bureau of Standards.

#### REFERENCES

- [1] PERKINS, F.W., in Heating in Toroidal Plasma (Proc. 4th Int. Symp. Rome, 1984), Vol. 2, Int. School of Plasma Physics, Varenna (1984) 977.  
PERKINS, F.W., SUN, Y.C., Rep. PPPL-2261, Plasma Physics Lab., Princeton Univ., Princeton, NJ (1985).
- [2] TANG, W.M., Nucl. Fusion **26** (1986) 1605.
- [3] DOMINGUEZ, R.R., WALTZ, R.E, Rep. GA-18184, GA Technologies, Inc., San Diego, CA (1986).
- [4] ROMANELLI, F., TANG, W.M., WHITE, R.B., Nucl. Fusion **26** (1986) 1515.
- [5] SINGER, C.E., et al., Rep. PPPL-2073, Plasma Physics Lab., Princeton Univ., Princeton, NJ (1986).
- [6] COPPI, B., Comments Plasma Phys. Controll. Fusion **5** (1980) 261.
- [7] TANG, W.M., REWOLDT, G., CHEN, Liu, Phys. Fluids **29** (1986) 3715.
- [8] TANG, W.M., et al., Nucl. Fusion **25** (1985) 151.  
REWOLDT, G., et al., Phys. Fluids **25** (1982) 480.
- [9] BISHOP, P.M., Rep. CLM-P-764, UKAEA Culham Lab., Abingdon (1985).
- [10] CONNOR, J.W., et al., Phys. Rev. Lett. **40** (1978) 396.
- [11] PERKINS, F.W., HULSE, R.A., Phys. Fluids **28** (1985) 1837.
- [12] COPPI, B., TANG, W.M., Rep. PPPL-2343, Plasma Physics Lab., Princeton Univ., Princeton, NJ (1986).

## DRIFT WAVE MODELS OF TOKAMAK CONFINEMENT

R.E. WALTZ, R.R. DOMINGUEZ, S.K. WONG<sup>1</sup>,  
GA Technologies, Inc.,  
San Diego, California

P.H. DIAMOND, G.S. LEE<sup>2</sup>, T.S. HAHM, N. MATTOR  
Institute for Fusion Studies,  
University of Texas,  
Austin, Texas

United States of America

### Abstract

DRIFT WAVE MODELS OF TOKAMAK CONFINEMENT.

Drift wave models are used to explain the observed tokamak confinement scaling with density, power, size and magnetic field. Some additional edge mechanism is required to obtain the observed scaling with safety factor and to account for H-mode transitions.

### 1. INTRODUCTION

Simple scaling models for  $\tilde{E} \times B_0$  transport from drift wave turbulence have had considerable recent success in explaining many universally observed features of tokamak confinement. This paper summarizes those successes and discusses the remaining difficulties of such models. The theory is broken into drift wave models for the bulk plasma which control the scaling of confinement time with power (temperature), density, size, and magnetic field, and models for the edge plasma which control the scaling of confinement time and temperature profiles with safety factor,  $q$ , and possibly transitions to improved divertor (H-mode) confinement.

We report first on the application of some simple mixing length models in a standard tokamak transport code [1]. Then, as an example of much recent work on the theory and simulation of drift wave turbulence itself, we summarize an analytic re-examination of ion temperature gradient mode turbulence [2]. Finally, we discuss several models for the edge plasma, their difficulties and their promises.

---

<sup>1</sup> Jaycor, San Diego, CA, USA.

<sup>2</sup> Oak Ridge National Laboratory, Oak Ridge, TN, USA.

## 2. TRANSPORT CODE SIMULATIONS

In the bulk plasma, turbulent transport from two drift mode branches is important: the dissipative trapped electron (DTE) mode for  $\omega_*/\nu_{\text{eff}} < 1$  or the collisionless trapped electron (CTE) mode for  $\omega_*/\nu_{\text{eff}} > 1$ , and the ion temperature gradient ( $\eta_i$ ) mode. At the plasma edge, the collisional circulating electron (CCE) mode for  $\nu_e/\omega_{te} > 1$  or possibly the universal circulating electron (UCE) mode for  $\nu_e/\omega_{te} < 1$  may be important. In our transport code simulations we have assumed that these have  $\gamma/k_x^2$  diffusivities scaling respectively as

$$\hat{D}_{TE} = \epsilon^{1/2} (\omega_*/k_x^2) \cdot [(\omega_*/\nu_{\text{eff}}), 1]_{\text{min}} \quad (1a)$$

$$\hat{D}_i = (\omega_*/k_x^2) \cdot [(2/\tau) \cdot (L_n/R) \cdot (L_n/L_{T_i})]^{1/2} \quad (1b)$$

$$\hat{D}_{CE} = (\omega_*/k_x^2) \cdot (\omega_*/\omega_{te}) \cdot [(\nu_e/\omega_{te}), 1]_{\text{max}} \quad (1c)$$

where  $\gamma$  is the linear growth rate and  $k_x = (1/\Delta x_k)$  is the inverse mixing length. We assumed  $k_x$  equal to an rms poloidal wavenumber  $k_\theta = 0.3 \rho_s^{-1}$ . [The notation is standard:  $\epsilon = r/R$ ,  $\omega_* = k_\theta (cT_e/eB)/L_n$ ,  $\nu_{\text{eff}} = \nu_e/\epsilon$ ,  $\nu_e$  is the electron collision frequency,  $\tau = T_e/T_i$ ,  $L_n$  and  $L_T$  are density and temperature gradient lengths,  $\omega_{te} = v_e/Rq$ , with  $v_e = (2T_e/m_e)^{1/2}$ ,  $\rho_s = c_s/\Omega_i$  with  $c_s = (T_e/m_i)^{1/2}$  and  $\Omega = eB/m_i c$ .]

To specify the model further, we took the turbulent heat diffusivities to be  $\chi_e = c \cdot 5/2 \cdot (\hat{D}_{TE} + \hat{D}_{CE}) (1 + \bar{c}_{ei} f_i \cdot L_n/R \cdot L_n/L_T)$  and  $\chi_i = c \cdot 5/2 \cdot [\hat{D}_i f_i + \bar{c}_{ie} (\hat{D}_{TE} + \hat{D}_{CE})]$ , where  $\bar{c}_{ei} = 3$  represents electron transport driven by the ion modes and  $\bar{c}_{ie} = 1$  represents ion transport driven by electron modes.  $f_i = 1(0)$  for  $\eta_i = L_n/L_{T_i} \gg (\ll) \eta_{\text{ith}} \geq 1$ , the ion mode threshold. A small and generally unimportant electron to ion exchange  $\Delta = \bar{c}_{ie} \cdot nT \cdot c (\hat{D}_{TE} + \hat{D}_{CE})/L_n^2$ , was included.  $c$  is the "fit" coefficient (e.g.,  $c = 1$  for DIII, Alcator-A and -C, JET, and  $c = 0.3$  for ISX-A). While the model was designed to fit DIII, subsequent simulations of ohmic Alcator density scans showed premature density saturation due to the electron driven CCE-mode scaling. This suggests that we assume the electron branch of the scaling to be stabilized by electron temperature gradients  $\eta_e$  except on the extreme edge. Neoclassical ion heat loss, classical exchange, Spitzer's relation between current and voltage, as well as sawteeth degradation inside  $q = 1$  were included. Edge losses from convection, and charge exchange were not explicitly included, and, more importantly, radiation was also not included.

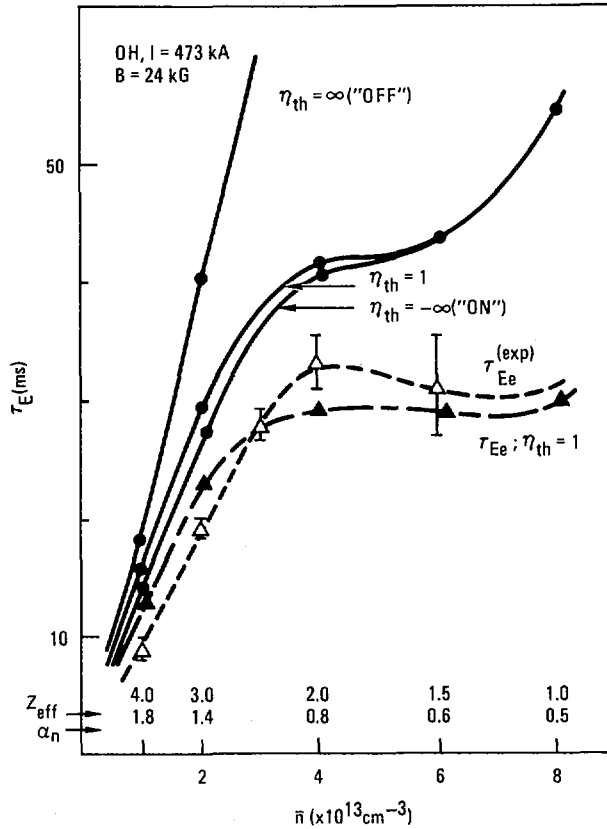


FIG. 1. DIII density scan with Ohmic heating, showing total energy confinement time  $\tau_E$  with  $\eta_i$  mode "on" and "off" and electron energy confinement time  $\tau_{Ee}$  in comparison with experiment;  $n = n(0) (1 - r^2/a^2)^{\alpha_n}$ .

In low density ohmically heated plasmas, the DTE mode provides the confinement time scaling ( $\tau_E \propto a^2/\chi$ )  $\tau_{EOH}^{low-n} \propto na^{1.04}R^{1.79}q^{1.16}B^{-0.33}Z^{-0.17}(L_n/a)^{0.83}$ , which is very close to the established neo-Alcator scaling. At higher densities, many tokamaks (e.g., DIII, Alcator-C gas) have progressively flatter density profiles ( $L_n$  large) with  $\eta_i$  increasing past the threshold. This causes the ion channel to be degraded well below the neoclassical confinement limit, as often observed (e.g., ISX-A, Alcator-A, Alcator-C pellet), and  $\tau_{EOH}^{high-n}$  to saturate. This is illustrated in Fig. 1 for DIII. Radiation effects are needed for final saturation of  $\tau_E$  as the Murakami ohmic density limit is approached.

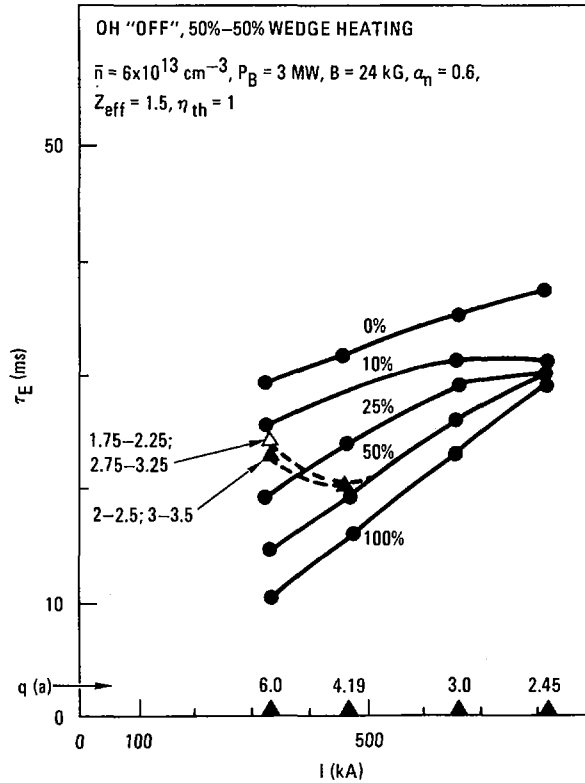


FIG. 2. DIII confinement time  $\tau_E$  versus current at fixed power; 0% with no tearing mode short circuit; 50% partial tearing mode short circuit; 100% complete short circuit  $q > 2$  (see Ref. [3]); dashed lines indicate data for short circuit only at  $q = 2$  and 3.

DIII (and several other tokamaks) typically beam heat from the  $\eta_i$  saturated ohmic regime. The power scaling from this mode when acting alone is  $\tau_{EB} \propto P^{-0.6} n^{0.6} I^{0.8} a^{2.2} (a/R)^{-1.6} q^{0.8}$ . With sufficient power or steepening density profile, the electron confinement may saturate with nearly identical CTE mode scaling [3]. Accounting for the beam penetration effect modifies the density scaling from  $n^{0.6}$  to  $n^{0.0}$ , as observed. Simulations at low density show an improvement in  $\tau_E$  with beam power as the (classical) hot ion channel opens up in accord with experiment (e.g., ASDEX). Thus the scaling with density ( $n$ ), power ( $P$ ), and size ( $a$  or  $R$ ) are consistent with experiment. The scaling with current ( $I$ ) and field ( $B$ ) are consistent, apart from the  $q^{0.8}$  factor which gives a favorable  $B$  rather than the observed favorable  $I$  scaling. This is the principal failure of the bulk drift wave models.

Some edge mechanism must be found to degrade the edge confinement at high  $q$ , making the effective size smaller than  $a$  and canceling the  $q^{0.8}$  factor [3]. The CCE mode with  $\chi \propto q^2 R^2 B^{-2} L_n^{-2} n Z T^{-1/2}$  has these qualitative properties. However, when acting alone with the bulk drift waves, it produces only a modest current scaling (no more than  $\tau \propto I^{0.4}$ ). Some additional high- $q$  mechanism is needed. If we assume that low- $m$  tearing modes short-circuit the heat flow near integer  $q$ -surfaces ( $q = m$  to  $m + VB$ ,  $m = 2, 3, 4 \dots$ , and  $VB$  is the fractional amount between adjacent rational surfaces that is short-circuited), then the observed scaling  $\tau \propto IB^0$  can be obtained for  $VB = 0.50$ . The current scaling of these models is illustrated by DIII simulations shown in Fig. 2.

In addition to controlling the  $q$ -scaling, the edge mechanism must cool the edge sufficiently to force current to the center, thereby producing sawteeth and maintaining  $q(0) \simeq 1$ . [The drift wave models alone are not sufficient and the tearing mode short circuits are needed to force sawteeth at high  $q$ .] We have shown [4] that  $q(0) = 1$  and Spitzer's law are sufficient to bound the temperature profile to  $q(a) \geq T(0)/\langle T \rangle \geq q(a)^{2/3}$  and provide the so-called principle of profile consistency. In fact, both ohmic and beam heated discharges from DIII and TFTR have  $T(0)/\langle T \rangle \simeq q(a)^{2/3}$ , the minimum requirement for sawteeth, and recent high- $q$  Alcator discharges without sawteeth fall well below the peakedness bounds.

### 3. THEORY OF ION TEMPERATURE GRADIENT MODE TURBULENCE

$\eta_i$ -mode turbulence or ion pressure gradient driven turbulence (IPGDT) is of interest, not only because of its crucial role in tokamak confinement scaling described above, but also as a paradigm for saturated multifield turbulence. It has a long history [5], with contributions from many workers. To facilitate analytic progress, the more tractable sheared slab model is considered here rather than the toroidal model [6]. The latter includes ion curvature drifts ( $\propto 1/R$ ) in addition to ion parallel motion. Special emphasis is placed on the validity of the mixing length estimates and the relation of ion thermal transport to electron heat and particle confinement.

IPGDT develops from unstable  $\eta_i$ -modes, which result from the coupling of sound waves to radial ion temperature gradients. For

$\eta_i \gg \eta_{i \text{ crit}} > 1$ , IPGDT can be described by coupled equations for vorticity ( $\nabla_{\parallel}^2 \hat{\phi}$ ), parallel flow velocity ( $\hat{v}_{\parallel}$ ), and ion pressure ( $\hat{p}$ ). In a field with shear length  $L_s = Rq/\hat{s}$  ( $\hat{s} = d \ln q / d \ln r$ ) and with  $L_n^2/L_s L_T \ll 1$ , the characteristic growth rates of the longwave hydrodynamic modes are  $\gamma_k \simeq [(1 + \eta_i)/\tau] \omega_* \cdot L_n/L_s$ . In general, the characteristic length of the modes is  $\Delta x_k \sim [(\gamma_k/\omega_*)/(L_n/L_s)]^{1/2} \rho_s$ . Shorter wavelength modes develop frequencies  $\omega_r \sim \gamma$  as  $k_{\theta} \rho_s \rightarrow 1$ . Ultimately, ion Landau damping, represented in the fluid model as a parallel ion viscosity  $\mu_{\parallel} \simeq (c_s^2/\tau)/|\gamma_k|$ , truncates the spectrum at  $k_{\theta} \rho_s \sim 1$ .

A natural description of the nonlinear fluctuation dynamics of IPGDT utilizes coupled equations for the energies  $E_w \sim \langle \hat{\phi}^2 + (\nabla \hat{\phi})^2 \rangle$ ,  $E_K \sim \langle \hat{v}_{\parallel}^2 \rangle$ ,  $E_p \sim \langle \hat{p}^2 \rangle$ , thus ensuring consistency with the conservation laws and constraints of the system. The energy evolution is determined by physical processes characterized by three time-scales, which are  $\tau_{ck} = (D_k/\Delta x_k^2)^{-1}$ , the nonlinear interaction time;  $\tau_{\text{eq},k} = \{[(1 + \eta_i)/\tau]^{1/2} \gamma_k\}^{-1}$ , the sound wave energy equipartition time; and  $\tau_{dk} = [\mu_{\parallel} k_{\theta}^2 \Delta x_k^2/L_s^2]^{-1}$ , the dissipation time-scale. For IPGDT, the time-scales follow the ordering  $\tau_{\text{eq},k} < \tau_{ck} < \tau_{dk}$ . Hence, exploiting the fact that all nonlinearities are convective, the energy equations may be added so that the total energy  $\mathcal{E}$  is determined by

$$(\partial/\partial t) \mathcal{E} - \mu_{\parallel} \nabla_{\parallel}^2 \mathcal{E} + T_{1,2}[\mathcal{E}] = S_{1,2}^{(0)} \quad (2)$$

Here  $T_{1,2}$  and  $S_{1,2}^{(0)}$  refer schematically to the  $\hat{E} \times B_0$  nonlinearity triplet and the pressure gradient source terms, respectively. Thus, saturated IPGDT results from the nonlinear coupling of robust, hydrodynamic ( $\gamma > \omega_r$ ) long wavelength modes with marginal or damped short wavelength modes with  $k_{\theta} \rho_s \sim 1$ .

Standard methods of renormalized turbulence theory have been used to solve Eq. (2). A "Reynolds number"  $\text{Re} = \|T_{1,2}\| / \|\mu_{\parallel} \nabla_{\parallel}^2\| \sim \tau_{dk}/\tau_{ck} \simeq (1 + \eta_i)$  can be defined. As  $\text{Re} > 1$ , the turbulence saturates by coupling to smaller scales, with typical scales  $k_d \sim (\text{Re})^{1/2} k_0$ , where  $k_0 \rho_s \sim 0.4$ , the rms wave number with weak parametric dependence. The predicted ion thermal diffusivity  $\chi_i = |C(\text{Re})|^2 \chi_i^{\text{ML}}$ , where  $\chi_i^{\text{ML}} = \gamma_{k_0} (\Delta x)_{k_0}^2$  is the mixing-length prediction, and  $C(\text{Re}) = (\pi/2) \ln(\text{Re})$ . Note that  $\chi_i$  depends weakly on the dissipation  $\mu_{\parallel}$ . This is in contrast to mixing-length estimates, which effectively balance  $T_{1,2}[\mathcal{E}] \sim S_{1,2}^{(0)}$ . However, dependence on  $\mu_{\parallel}$  is to be expected since

even if "inertial range" properties are insensitive to  $\mu_{\parallel}$ , macroscopic observables are determined by spectrum sums whose limits of integration depend on dissipation. Indeed,  $C(\text{Re}) \rightarrow \infty$  as  $\mu_{\parallel} \rightarrow 0!$

Several transport coefficients of practical interest have been derived using the theory of IPGDT. The ion thermal diffusivity is given by

$$\chi_i = 0.4 |C(\text{Re})|^2 (\rho_s^2 c_s / L_s) [(1 + \eta_i) / \tau]^2 \quad (3)$$

Using the dissipative trapped electron response (for  $\nu_{*e} < 1$ ), the accompanying electron thermal  $\chi_e$  diffusivity and particle diffusion  $D_n$  are obtained from quasilinear theory [ $\chi_e, D_n \propto |e\phi/T|^2$ ], with  $\tilde{n}/n \sim e\tilde{\phi}/T \sim |C(\text{Re})|^2 (\gamma_k/\omega_*) \cdot (\Delta x_k/L_n)$ :

$$\chi_e = 3.2 \sqrt{\epsilon} |C(\text{Re})|^4 (c_s^2 \rho_s^2 / \nu_{\text{eff}} L_s^2) [(1 + \eta_i) / \tau]^3 \quad (4a)$$

$$D_n = \sqrt{\epsilon} |C(\text{Re})|^4 (c_s^2 \rho_s^2 / \nu_{\text{eff}} L_s^2) [(1 + \eta_i) / \tau]^3 \cdot (1 + 3\eta_e/2) \quad (4b)$$

For collisional electrons, the IPGDT-driven particle flux is given by

$$\begin{aligned} \Gamma_n = n_0 |C(\text{Re})|^4 [\hat{\chi}_e + (1 + \alpha_T)^2] [1 - (\eta_e/\eta_{e \text{ crit}})] \\ \times (m_e/m_i) (0.51/\hat{\chi}_e) (\nu/L_n) \rho_s^2 [(1 + \eta_i) / \tau]^2 \end{aligned} \quad (5)$$

where  $\hat{\chi}_e = 1.61$ ,  $\alpha_T = 0.71$ , and  $\eta_{e \text{ crit}} = 1.77$ . For  $\eta_e > \eta_{e \text{ crit}}$ , an inward flow results. A normally outward heat conduction flow with similar scaling is induced by IPGDT at the edge.

There are several correlations with experiments. IPGDT drives a toroidal flow viscosity  $\mu_{\perp} \simeq \chi_i$ , which may explain the DIII observation that toroidal flow damping times  $\tau_{\phi}$  are comparable to  $\tau_E$  in co-injection heated plasmas. In addition, impurity gradients can have a significant effect on IPGDT. In particular, for an impurity species with density  $n_{oI}$  and scale length  $L_{nI}$ , IPGDT transport is modified according to the substitution  $(1 + \eta_i) \rightarrow \Lambda(1 + \eta_i)$ , where  $\Lambda = [1 + Z(n_{oI}/n_{oi}) (L_{ni}/L_{nI})]^{-1}$ . Thus, impurity distributions peaked at the edge enhance IPGDT, while distributions peaked on axis quench it. In particular, the inward par-

ticle flux at the edge ( $\nu_{*e} > 1$ ) is strongly enhanced,  $\Gamma_n \rightarrow \Lambda^3 \Gamma_n$ , for edge-peaked impurity profiles. This enhancement may underlie the density profile steepening and improved particle confinement following impurity puffing observed during the Z-mode of the ISX-B tokamak.

From the previous intermediate formulas, alternative scalings can be obtained in other physical limits. For example, in the extremely flat density profile limit,  $L_n^2/L_s L_T \gg 1$ .  $\gamma_k \simeq \omega_* [(L_n/L_s)(1 + \eta_i)/\tau]^{1/2}$ , giving the mixing length estimate  $\chi_i \sim [(1 + \eta_i)/\tau] \rho_s^2 c_s / L_n$ , apart from logarithmic factors. In the extreme toroidal limit,  $\gamma_k \simeq \omega_* [2(L_n/R)(1 + \eta_i)/\tau]^{1/2}$ , with  $\chi_i \sim [2(L_s/R)(1 + \eta_i)/\tau] \cdot \rho_s^2 c_s / L_n$ , using the shear mixing length [6]. [The latter formula differs from the toroidal scaling Eq. (1b) [7,8] where a shearless mixing length  $\Delta_x = 3\rho_s$  was used.] These formulas differ most significantly from Eq. (3) in their dependence on  $L_s$ . However, they are difficult to distinguish experimentally because  $q(r)/\hat{s}(r)$  is a weak function of  $q(a)$  in the bulk plasma where  $\eta_i$  mode turbulence is dominant.

#### 4. THE EDGE PLASMA

Our understanding of the edge plasma and the mechanism for controlling  $q$ -dependence remains unsatisfactory. Other models have been considered in place of the CCE-mode scaling with only partial success. For example, limiting the edge pressure gradient to the critical ideal value ( $P' < P'_{\text{crit}} \propto B^2 q^{-2}$ ) [9] is a high- $q$  mechanism with similar behavior when acting in concert with the low- $m$  tearing mode short circuit model. Unfortunately we have not been able to theoretically justify the latter. High- $q$  modes ( $q = 4, 5, 6 \dots$ ) in particular are difficult to destabilize even with thermal effects from radiative cooling at the edge.

Other models for dissipative fluid turbulence (DFT) at the edge have been only partially explored. However, they have some noteworthy common features which may be relevant to understanding the H-mode. For example, a heuristic derivation for magnetic transport from microtearing modes has, in the collisional limit,  $\chi_e \simeq L_s^2 \nu_e \rho_e^2 / L_T^2$ . This is identical (apart from the replacement of  $L_n$  by  $L_T$ ) to the CCE-mode scaling Eq. (1c). Perhaps more promising is a recent result for  $\vec{E} \times B_0$  transport from resistivity gradient driven turbulence (rippling modes) [10]:

$$\begin{aligned} \chi_e &= 7.1 [(c/B_T) E_{\parallel} (L_s/L_T)]^{4/3} (\nu_{ii} r^2 L_s^2/c_s^2)^{1/3} \\ &\propto \hat{s}^{-2} q^2 R^2 (E_{\parallel}/B)^{4/3} T^{-5/6} n^{1/3} L_T^{-4/3} a^{2/3} \end{aligned} \quad (6)$$

where  $E_{\parallel} = V_{\text{loop}}/2\pi R = \eta_{\parallel} J_{\parallel}$ . (This scaling is at fixed mode number  $\langle m \rangle_{\text{rms}}$  suggested by numerical calculations. It also includes impurity effects.) These diffusivities from DFT all have favorable  $T$ -scaling (in contrast to transport from bulk drift waves) and  $\chi \propto L_s^2 \propto \hat{s}^{-2} q^2$ . We speculate that both features may be used to explain the improved edge confinement layer just inside the separatrix of the ASDEX H-mode. Diverted plasmas naturally have a hotter edge on closed field lines exploiting the favorable  $T$ -dependence. Perhaps more importantly, it can be shown [11] that while  $q$  diverges logarithmically near a separatrix,  $\hat{s}^{-2} q^2$  vanishes algebraically as  $(1 - r^2/r_{\text{sep}}^2)^2$ , allowing a steep gradient in  $T$  as well as  $n$  to be supported as  $r \rightarrow r_{\text{sep}}$ . Also, the steepening density gradient may allow ideal ballooning modes to be diamagnetically stabilized. Indeed, using  $\omega = \omega_{*i}/2 \pm (\omega_{*i}^2 - 4\gamma_{\text{MHD}}^2)^{1/2}/2$ , modes with  $k_{\theta}^2 \rho_i^2 > (2L_n^2/L_p R) [1 - (L_p/\beta)(\beta/L_p)_{\text{crit}}]$ , corresponding to the full range of "high- $n$ " modes for ASDEX parameters, are stable.

## ACKNOWLEDGMENT

This is a report of work sponsored by the U.S. Department of Energy under Contract Nos. DE-AC03-84ER53158 and DE-FG05-80ET53088.

## REFERENCES

- [1] DOMINGUEZ, R.R., WALTZ, R.E., Nucl. Fusion **27** (1987) 65.
- [2] LEE, G.S., DIAMOND, P.H., Phys. Fluids **29** (1986) 3291.
- [3] PERKINS, F.W., in Heating in Toroidal Plasmas (Proc. 4th Int. Symp. Rome, 1984), Int. School of Plasma Physics, Varenna (1984).  
TANG, W.M., CHENG, C.Z., KROMMES, J.A., et al., in Plasma Physics and Controlled Nuclear Fusion Research 1984 (Proc. 10th Int. Conf. London, 1984), Vol. 2, IAEA, Vienna (1985) 213.
- [4] WALTZ, R.E., WONG, S.K., GREENE, J.M., DOMINGUEZ, R.R., Nucl. Fusion **26** (1986) 1729.
- [5] POGUTSE, O.P., Sov. Phys. — JETP **25** (1967) 498.
- [6] COPPI, B., ROSENBLUTH, M.N., SAGDEEV, R.Z., Phys. Fluids **10** (1967) 582.
- [6] HORTON, W., CHOI, Duk-In, TANG, T.M., Phys. Fluids **24** (1981) 1077.

- [7] ANTONSEN, T., COPPI, B., ENGLADE, R., Nucl. Fusion **19** (1979) 641.
- [8] WALTZ, R.E., Phys. Fluids **29** (1986) 3684.
- [9] CONNOR, J.W., TAYLOR, J.B., TURNER, M.F., Nucl. Fusion **25** (1985) 65.
- [10] HAHM, T.S., TERRY, P.W., DIAMOND, P.H., Rep. IFSR-180, Inst. for Fusion Studies, Texas Univ., Austin (1985), submitted to Phys. Fluids.
- [11] HAHM, T.S., DIAMOND, P.H., Rep. IFSR-230, Inst. for Fusion Studies, Texas Univ., Austin (1986); Phys. Fluids (in press).

## DISCUSSION

### ON PAPERS IAEA-CN-47/A-VI-1-1 TO A-VI-1-3

B.P. LEHNERT: Did you take into account interaction of plasma and neutral gas in the edge region? The reason for my question is that even small amounts of recycling neutral gas could have an effect on the plasma profiles in a quasi-steady state. As an example, an increasing average plasma density will lead to a decreasing penetration length of the neutral gas, and this in turn will lead to a growing plasma pressure gradient in the edge region.

D.F. DÜCHS: Neutral gas is self-consistently included in both the JET model and the Princeton model. The model developed by GA Technologies explicitly excludes neutral gas. We do not believe that it affects our results very much.

G. BECKER: One problem with electron heat diffusivities derived from drift wave turbulence is that their scalings differ from the scalings of the coefficients determined from the experiments by local transport analysis or transport modelling. Discrepancies occur with the dependence on the ion mass number and the main magnetic field, and in neutral beam heated plasmas also with the current or  $B_p$ . I therefore conclude that the present drift wave models do not explain the experimental behaviour observed.

D.F. DÜCHS: As I have shown, our comparisons would lead to the same conclusion. However, if global profile consistency is considered, for example including constraints, the dependent variables, such as  $T_e$  in the expression for  $\chi_e$ , can be expressed in terms of  $B_T$ . Such scaling shows good agreement with the experimental results. In this sense, one should not rule out unstable drift waves as possible turbulence mechanisms.

K. ITOH: Did you observe that the discrepancy between the experimentally derived heat flux and the theory, for example in the dissipative trapped electron mode, scaled with the plasma size? In other words, when comparing the data with the experiment, did you find that an 'intermittence of the scale length' appeared in  $\chi_e$ ?

D.F. DÜCHS: In our JET calculations we did not vary the plasma rise very much. However, we know from experience that, for example, 'Venetian blinds' effectively reduce the plasma radius.

B. COPPI: The nature of the  $\eta_i$  modes changes considerably over the  $\eta_i$  range 1 - 4. In addition, the spatial mode localization is an important factor to be considered in assessing the relevant transport. How is all this accounted for in the expression for  $\chi_i$  presented by the group from GA Technologies?

D.F. DÜCHS: The range of validity of the  $\eta_i$  theory presented is:  $\eta_{i,crit.} < \eta_i < L_\delta/L_T$ . Clearly, the theory fails for  $\eta_i \sim \eta_{i,crit.}$ , where detailed kinetic analysis is needed, and for  $\eta_i > L_\delta/L_T$ , with a weaker dependence on  $\eta_i$ . The latter regime may be relevant for some of the JET cases. For  $\eta_{i,crit.} < \eta_i < L_\delta/L_T$ ,  $\chi_i$  is well approximated by the given expression. In the codes, a threshold turn-on function, varying rapidly with  $\eta_i$ , is used as an approximation for reasons of practicality.



## MHD STABILITY AND TRANSPORT OF BEAM HEATED ASDEX DISCHARGES IN THE VICINITY OF THE BETA LIMIT

O. GRUBER, G. BECKER, G. von GIERKE, K. GRASSIE, O. KLÜBER,  
M. KORNHERR, K. LACKNER, J.K. LEE<sup>1</sup>, H.P. ZEHRFELD, H.S. BOSCH,  
H. BROCKEN, A. EBERHAGEN, G. FUSSMANN, O. GEHRE,  
J. GERNHARDT, E. GLOCK, G. HAAS, J. HOFMANN, A. IZVOZCHIKOV<sup>2</sup>,  
G. JANESCHITZ, F. KARGER, M. KAUFMANN, M. KEILHACKER<sup>3</sup>,  
M. LENOCI, G. LISITANO, F. MAST, H.M. MAYER, K. McCORMICK,  
D. MEISEL, V. MERTENS, E.R. MÜLLER<sup>3</sup>, H. MURMANN<sup>3</sup>,  
H. NIEDERMEYER, W. POSCHENRIEDER, H. RAPP, H. RIEDLER,  
H. RÖHR, J. ROTH, F. RYTER<sup>4</sup>, F. SCHNEIDER, C. SETZENSACK,  
G. SILLER, P. SMEULDERS<sup>3</sup>, F.X. SÖLDNER, E. SPETH, K.-H. STEUER,  
O. VOLLMER, F. WAGNER, D. ZASCHE

Euratom-IPP Association,  
Max-Planck-Institut für Plasmaphysik,  
Garching, Federal Republic of Germany

### Abstract

#### MHD STABILITY AND TRANSPORT OF BEAM HEATED ASDEX DISCHARGES IN THE VICINITY OF THE BETA LIMIT.

Neutral beam heated H mode discharges in ASDEX exhibit a beta limit at  $\beta_c = 2.8 I_p / (aB_t)$  [% , MA, m, T] in agreement with theoretical predictions. A 'hard  $\beta$  saturation' is always observed nearly without prior confinement deterioration up to  $\beta_{max}$ . Enhanced losses set in after the attainment of  $\beta_{max}$ , causing a subsequent decrease of the energy content by typically 30%. Analyses with the TRANSP and BALDUR codes using measured plasma parameters reveal this transport enhancement to be mainly due to electron heat conduction and convection losses. Impurity accumulation is correlated with the time evolution of  $\beta$ . It can be ruled out as directly responsible energy loss channel, but may cause enhanced current density flattening and a consequent reduction in the maximum stable  $\beta$  values. Using the pressure and current density profiles from the transport analyses, the authors try to identify the responsible instabilities theoretically. Low  $m$  ( $\leq 6$ ) pressure driven tearing modes are predicted by the 3-D CART code and are seen in Mirnov coil signals, but show no clear experimental correlation with the observed  $\beta$  limitation. The solution of the full ideal MHD ballooning equation predicts these plasmas to be stable, leaving resistive ballooning modes in an intermediate range of wavenumbers (between 30 and 50) as a possible cause of the observed behaviour.

<sup>1</sup> GA Technologies, San Diego, CA, USA.

<sup>2</sup> Academy of Sciences, Leningrad, USSR.

<sup>3</sup> JET Joint Undertaking, Culham, Oxfordshire, UK.

<sup>4</sup> Centre de recherches en physique des plasmas, Ecole polytechnique fédérale de Lausanne, Lausanne, Switzerland.

## 1. Introduction

In the divertor tokamak ASDEX neutral beam-heated H mode discharges allow, due to their superior confinement, a test of the  $\beta$  limits over a large range of magnetic fields ( $1.2 < B_t < 2.7$  T) and plasma currents ( $0.2 < I_p < 0.48$  MA) with the available modest beam powers of up to 4.5 MW. A clear "operational" beta limit at  $\beta_c = 2.8 I_p / (a B_t)$  [% , MA, m, T] is observed /1/ ( $2a \approx 0.8$  being the horizontal plasma diameter). In the L mode even combined neutral beam and ion cyclotron resonance heating with powers up to 5 MW allowed - possibly restricted by the limited heating time /1/ - only values of  $\beta_{max} \leq 0.85\beta_c$ . H discharges with a maximum beta value  $\beta_{max}$  below  $0.75\beta_c$  display a nearly constant time behaviour of beta after reaching  $\beta_{max}$ . Their normalized beta,  $\beta/\beta_c$ , is found to be proportional to the normalized heating power  $P_N = 3P/(bR_0B_t)$  [MW, m, T], where P is the total heating power (absorbed beam plus ohmic heating power),  $2b$  is the vertical plasma diameter ( $b/a \approx 1$ ) and  $R_0$  is the toroidal major radius ( $\approx 1.65$  m). The resulting energy replacement time  $\tau_E^*$  depends only on the plasma current. Various combinations of P,  $I_p$ , and  $B_t$  produce no gradual reduction of confinement when  $\beta$  is increased, but a "hard  $\beta$  saturation limit" when  $\beta_c$  is approached. Such a hard saturation is also seen in the time evolution of discharges with  $\beta_{max} > 0.8\beta_c$ , which also exhibit only a small confinement deterioration before  $\beta_{max}$  (see Fig.1 and Ref. /1, 2/). After attainment of  $\beta_{max}$  the beta values of these discharges decay to about  $0.7\beta_c$  and often reach a new stationary state at this level (see Section 2). This saturation near the  $\beta_c$  limit without disruption is a peculiarity of the ASDEX discharges. Disruptions, however, may occur both during the rise and the fall of beta especially at values of the cylindrical  $q_a$  below three.

A  $\beta_c$  limit similar to the one observed in ASDEX and other experiments /3, 4/ has been predicted by MHD stability calculations for low m surface kinks /5/ and ballooning modes /6/. For parameters and profiles of an actual ASDEX discharge series with  $\beta_{max} = 0.9 \beta_c$  stability was found both with respect to ideal kink modes (using the ERATO code /2/) and to ideal ballooning modes (by applying the criterion in the approximation for circular, concentric magnetic surfaces:

$$\alpha_M = - \frac{2 \mu_0 R_0 q^{*2}}{B_t^2} \left( \frac{d p}{d r} \right)_M = f(s) \quad (1)$$

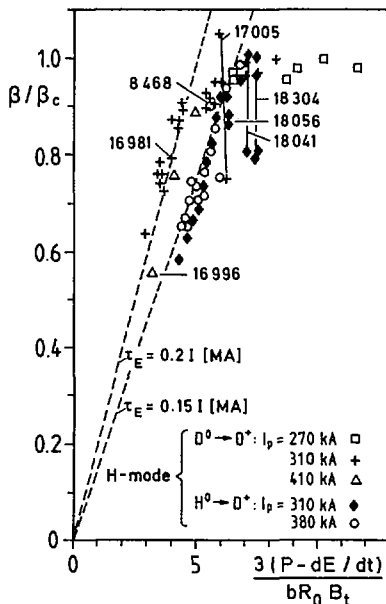


FIG. 1. Maximum normalized  $\beta$  values  $\beta/\beta_c$  (from diamagnetic  $\beta_{p,\perp}$ ) as a function of normalized heating power  $P_N = 3(P - dE/dt)/(b R_0 B_t)$  for NI heated H mode discharges. Points connected by lines indicate  $\beta$  decrease, after  $\beta_{max}$  of the corresponding discharge.

where  $f(s)$  is a known function of the shear  $s = (r/q^*) dq^*/dr / I$ ,  $p$  is the total pressure,  $q^* = 5B_t r^2 / (2\pi R_0) \int_0^r j_t r dr$  [T, m, MA], and  $j_t$  is the toroidal plasma current density).

After these initial results, stability and transport studies of ASDEX divertor discharges at the  $\beta$  limit have been intensified applying refined diagnostics (e.g. detailed measurements of electron density and temperature profiles and of Mirnov and soft X-ray signals) and more detailed theoretical analysis. Based on measured profiles, plasma transport properties have been investigated by means of the PPPL analysis code TRANSP /8/ and of a modified version of the predictive transport code BALDUR /9/ (see Sections 2 and 3). The pressure and current profiles obtained from transport computations were then used to calculate consistent MHD equilibria (see Section 4), which were in turn subjected to stability analysis by the 3-D CART code /10/ (see Section 5) and by an exact solution of the ballooning mode equation (see Section 6).

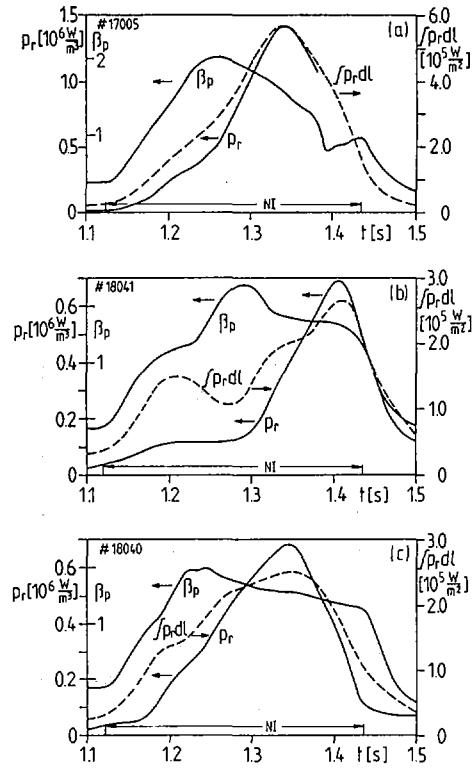


FIG. 2. Time evolution of  $\beta_p$ , central non-inverted chord intensity  $\int p_r dl$  of bolometer array and central radiation power density  $p_r$ , obtained by Abel inversion for a  $D^0 \rightarrow D^+$  discharge (No. 17005) and two  $H^0 \rightarrow D^+$  discharges (No. 18040, No. 18041) with the same discharge parameter.

## 2. Current density profile and $\beta$ limit

The  $\beta$  decrease after reaching transiently  $\beta_c$  happens on a time-scale of about 30 to 50 ms (see Fig.2). An explanation for this behaviour, advanced in /11/, consisted in a reduction of the ballooning mode limited beta due to broadening of the toroidal current density profile with time. In fact, integration of Eq. (1) over the whole cross-section yields a maximum attainable value of  $\beta q_a^* / \epsilon$  increasing with  $q_a^* / q_0$  /12/ or the internal inductance  $l_i$  /11/ but depending only weakly on the finer details of the current density distribution (here  $\epsilon = a/R_0$ ,  $q_a^* = q^*(a)$ ,  $q_0 = q(r=0)$ ). Indeed, during the high-beta phase, an increase of  $q_0$  is indicated by the

disappearance of sawteeth, and an  $I_t$  decrease can be deduced from magnetic measurements, although the characteristic time for current diffusion due to neoclassical resistivity significantly exceeds the time-scale of the  $\beta$  changes.

There are two possibilities for reducing this apparent discrepancy of time-scales. First, the instability which causes the  $\beta$  limit might also give rise to an anomalously fast current flattening. Measurements suggest an additional, more classical explanation. In H mode discharges with improved energy and particle confinement a central accumulation of metal impurities takes place [1] yielding strongly peaked radiation power densities  $p_r$ . Spectroscopy and soft X-ray diagnostics confirm that the evolution of the central peak of the bolometric profiles given in Fig. 2 is mainly due to increasing line radiation of highly ionized iron and does not result from density changes. In  $\beta$  limit shots using  $H^0$  into  $D^+$  injection the radiated central power density is smaller (see Figs. 2b and 2c), due to particle confinement deterioration with respect to the  $D^0 \rightarrow D^+$  discharges of Fig. 2a. Although the central  $p_r$  values become comparable to the local beam heating of the electrons, the globally radiated power rises at most by about 25% and remains always less than one third of the total heating power. This implies that radiation itself is not responsible for the beta limitation. But central  $Z_{\text{eff}}$  values above 4 are easily deduced if iron is assumed to cause the central radiation losses and if the temperature-dependent radiative power loss function including CX recombination with beam neutrals is applied [13]. This increase in  $Z_{\text{eff}}$  at  $r < 15$  cm can explain an enhanced and accelerated broadening of  $j_t$ : TRANSP calculations in this case predict during the  $\beta$  decay of the  $D^0 \rightarrow D^+$  discharge an increase of  $q_0$  from 1.1 to 1.45 (rather than to only 1.2 as would result for a fixed  $Z_{\text{eff}}(r, t) = 1.5$ ) and an  $I_t$  decrease from 1.2 to 1.04.

This postulated influence of impurity accumulation and the consequent  $j_t$  broadening is supported further by the clear correlation of the central radiation intensity with the time evolution of beta close to  $\beta_{\text{max}}$ . For the same values of  $I_p$ ,  $B_t$ ,  $R_0$  and  $\bar{n}_e$  discharges in which the central radiation increases earlier - this may happen due to an earlier L to H transition or a longer ELM(edge-localized mode)-free H-phase - reach only smaller values of  $\beta/\beta_c$ . Subsequently however betas decay to similar plateau values for both cases (see Figs. 2b and 2c). Overall, this time behaviour is consistent with the conjecture that the plasma stays at a marginal stability limit governed by current density profiles.

### 3. Transport in H mode discharges close to the $\beta$ limit

Detailed transport analyses have been carried out for all the discharges indicated in Fig.1. Input data used were:

the electron density profiles  $n_e(r, t)$  measured by a 4-channel HCN laser interferometer and a 16-spatial channel multi-pulse Thomson scattering system which provides profiles every 17 ms,

electron temperature profiles  $T_e(r, t)$  from 4-channel ECE diagnostic and multi-pulse Thomson scattering,

the ion temperature  $T_i$  measured by passive and active CX diagnostic, Doppler broadening of CX recombination lines and neutron production rates,

the bolometrically measured profiles of the radiation losses and global parameters like the loop voltage  $V_L$ ,  $I_p$ ,  $\beta_{p\perp} = \beta_{p\perp}^{th} + \beta_{p\perp}^{beam}$  from diamagnetic flux measurements and  $\beta_{p\parallel} + I_p/2$  with  $\beta_{p\parallel} = \beta_{p\parallel}^{th} + .5(\beta_{p\perp}^{beam} + \beta_{p\parallel}^{beam})$  deduced from the poloidal fields and fluxes. The calculated kinetic pressures include the contributions due to the anisotropic fast beam ions ( $p_{\parallel}^{beam} \approx 2p_{\perp}^{beam}$ ) and are in good agreement with the magnetically measured ones.

Beam-heated H mode discharges staying below  $\beta_C$  show energy replacement times comparable in magnitude to the ohmic ones (see Fig. 3) with (for  $q_a^* > 3$ ) a scaling  $\tau_E^* = 0.1 I_p A_i$  [s, MA,  $A_i$  = ion mass number] independent of the heating power (see Fig.1). For these high confinement times and consequently high plasma energies the convective losses  $P_{conv}/P \approx 5/2 \Gamma k (T_e + T_i) / (G \cdot E_0)$  (with  $\Gamma$  the particle flux and  $\langle E \rangle$  the medium energy of the injected neutrals) and the ion conduction losses become comparable to the electron conduction losses. So, over a large part of the plasma cross-section in  $D^0 \rightarrow D^+$  discharges  $P_{cond,e}$  amount to only between 0.2 ( $I_p = 310$  kA,  $q_a^* = 4$ ) and 0.35 ( $I_p = 410$  kA,  $q_a^* = 2.7$ ) of the total heating power compared to  $P_{cond,e} = (0.5 \dots 0.65) \cdot P$  in ohmic and L mode discharges /14/. Ion heat conduction  $\chi_i$  is taken throughout as 3 times the neoclassical value as calculated by C. Chang and F. Hinton for all discharge phases (OH, L, H), which gives the best fit to the  $T_i$  measurements.

In discharges coming close to  $\beta_C$  transport analyses confirm that additional energy losses set in just after  $\beta_{max}$  has been reached. This confinement degradation can be seen by the time evolution of the confinement times in the  $D^0 \rightarrow D^+$  discharge

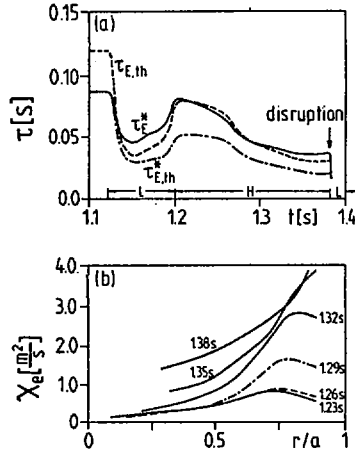


FIG. 3. (a) Time behaviour of energy replacement times  $\tau_E^* = E/(P - dE/dt)$  with ( $\tau_E^*$ ) and without ( $\tau_{E,th}^*$ ) fast ions, and of thermal energy confinement time  $\tau_E = E/(P_{cond} + P_{conv})$  for a  $D^0 - D^+$  discharge (No. 17005).

(b) Evolution of electron thermal diffusivity  $\chi_e(r, t)$  for the same discharge.

shown in Fig. 3a. For these discharges the ion heating by the beams,  $P_{bi}$ , exceeds the electron heating,  $P_{be}$ , ( $P_{bi} \leq 3P_{be}$ ) and the beam contributes about 25 % to the total  $\beta$  during the rise phase. The latter fact results in the difference of the  $\tau_E^*$  values with and without beam contribution. The confinement time  $\tau_E$  is defined including only the conductive and convective losses and illustrates, when compared to  $\tau_E^*$ , the influence of the radiation and CX losses.

These additional losses have to be attributed to an enhanced electron heat conduction and partly to the convection associated with the density decrease. This is shown by the time variation of the radial profiles of the electron heat diffusivity  $\chi_e$  given in Fig. 3b which are found to be nearly time-independent in the H mode during the  $\beta$  rise phase, but are increased over the whole plasma during the  $\beta$  decrease. As  $n_e$  and  $T_e$  decrease during the latter phase, this translates only into an approximate doubling of the electron heat conduction losses, which, at  $r = 0.75a$  increase from 450 kW at 1.26 s to 900 kW at 1.38 s. An assumed additional increase of the ion heat conduction losses by 30 % brings the computed kinetic variation of  $\beta_{p\perp}$  and  $\beta_{p\parallel} + 1/2$  in agreement with magnetic measurements.

A transport simulation of the  $H^0 \rightarrow D^+$  discharge (see Fig.2b) by the predictive BALDUR code reproduces the measured evolution of the  $n_e$ ,  $T_e$  and  $T_i$  profiles and of  $\beta_p$  up to the  $\beta$  limit if transport scalings derived from H-regime discharges well below  $\beta_c/15$  are applied:  $\chi_e^H(r) = 1.3 a^2 / (R_0 r_n I_p)$  [ $m^2/s$ , m, MA], particle diffusivity  $D^H(r) = 0.4 \chi_e^H(r)$  and anomalous pinch velocity  $v_{in}^H(r) = -0.5 D^H(r) r_{Te}^{-1}$  [ $m/s$ , m] (with  $r_n = -n / (\partial n / \partial r)$  and  $r_{Te} = -T_e / (\partial T_e / \partial r)$ ). After the attainment of  $\beta_{max}$  also here the electron heat diffusivity in the region  $r < 0.7a$  has to be enhanced by a factor of 4 to simulate the measurements.

#### **4. MHD equilibria for stability analyses**

The above transport analyses produce profiles of the total plasma pressure  $p(r, t) = p^{th} + 1/2 (p_{||}^{beam} + p_{\perp}^{beam})$  and - by solving the poloidal field diffusion equation - of the current density profile  $j_t(r, t)$ . These profiles are used to calculate MHD equilibria whose stability is then analyzed. For given currents in the external conductors a static plasma equilibrium configuration is uniquely determined, if profiles of pressure  $p(V)$  and of the total toroidal current inside a given flux surface  $I(V)$  are prescribed as functions of the volume  $V$  enclosed by it. The toroidal current density can then be described in an unambiguous form as

$$j_t = 2 \pi R \left\{ 1 / R^2 \langle 1 / R^2 \rangle^{-1} + \beta_p \langle 1 - 1 / R^2 \langle 1 / R^2 \rangle^{-1} \rangle \right\} \frac{dI}{dV} \quad (2)$$

where  $\beta_p$  is a local beta poloidal value given by  $\beta_p = dp/d\psi \cdot dV/dI$ ,  $\psi$  is the poloidal magnetic flux and  $\langle \rangle$  denotes the usual flux surface average. The corresponding equilibria are then calculated by using the Garching free-boundary flow equilibrium code NIVA. In order to make the radial data  $p(r)$  and  $I(r)$  suitable for a use in the two-dimensional equilibrium calculations we relate the normalized small radius  $r/a$  to the volume  $V$  enclosed by a magnetic surface by  $r/a = (V/V_a)^{1/2}$ , where  $V_a$  is the total plasma volume.

#### **5. Low m mode stability**

Our investigations of low m MHD activity are based on results from Mirnov probe measurements /15/ and two-dimensional soft XR tomography /16/ and on their

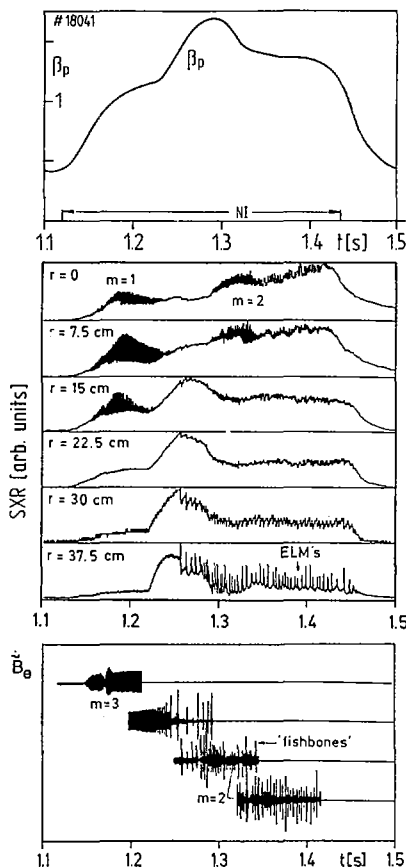


FIG. 4. Time behaviour of diamagnetic poloidal beta, line integrated soft X-ray radiation at various tangential radii and Mirnov signals at torus outside.

comparison with stability calculations using the 3-D code CART developed at GA, which is capable of treating the linear and nonlinear evolution of ideal and resistive MHD instabilities at finite  $\beta_p \approx R_0/a$ .

The measurements show that the observed modes always have a toroidal mode number  $n = 1$ . During the L phase of beam-heated ASDEX discharges a "continuous" mode develops, whose amplitude decreases after the L to H transition to a low level. Both an  $m = 1$  (detected by soft X-ray) and an  $m = 3$  component (from Mirnov signals) are present at the same frequency in the range of 10 to 20 kHz (see Fig. 4). During the H phase ELM's occur [1] and additionally MHD bursts are observed with a "fishbone-like" character. The fishbone amplitudes are much smaller than those of the continuous mode and exhibit an  $m = 3$  to 4 structure at lower  $\beta_p$  values

( $\beta/\beta_C < 0.6$ ) and an  $m \approx 6$  structure near the  $\beta$  limits (from Mirnov signals). This poloidal mode number is above the value of  $q$  at the boundary of an equivalent circular discharge at finite  $\beta$   $q_a \approx q_a^* (1 + \epsilon^2 (1 + .5 (\beta_p + 1/2)^2))$ , so that the resonant surfaces  $m = q$  should lie close to, but inside the separatrix. The frequency of the mode is observed to increase with heating power and  $\beta_p$  up to  $\approx 25$  kHz. Both the continuous and the fishbone-like mode show an amplitude ratio up to 20 between torus outside and inside and propagate with the central toroidal rotation velocity. Sometimes, during the  $\beta$  decay, a strong  $m = 2$  to 3 mode with  $f = 5$ - 10 kHz develops (seen in soft XR and Mirnov coils, see Fig. 4), triggered by an ELM, which frequently leads to a disruption especially at low  $q$  values [16].

The low- $m$  MHD activity observed seems to be mainly due to tearing modes. Moving a conducting wall to the plasma surface in the CART stability analyses of these discharges does not significantly change the perturbed linearized  $n = 1$  magnetic flux function  $\Psi$  or the linear growth rates  $\gamma$ . An indication for the driving mechanism of this instability was obtained from the dependence of the computed  $\gamma$ -values on the resistivity  $\eta$ . In simulations of our low  $\beta_p$  discharges  $\gamma$  scales like  $\eta^{3/5}$ , as is expected for current-driven tearing modes. From simulation of discharges near the  $\beta$  limit a scaling  $\gamma \propto \eta^{1/3}$  is derived which suggests that pressure-driven modes are involved.

For a direct comparison of numerical results with the Mirnov signals we have calculated the poloidal component of the perturbed magnetic field  $B_\theta$  as a function of the poloidal (see Fig. 5) and toroidal position. The nonlinear treatment, allowing for superposition of all toroidal Fourier components  $n$ , confirms the measured dominance of the  $n = 1$  modes. Within the poloidal region accessible to measurements not only the  $m$  numbers but also the amplitudes are reproduced by the code, whereas differences in the poloidal mode pattern exist. The code also predicts the shift in the mode pattern to higher  $m$  numbers with increasing plasma pressure actually shown by the measurements.

However no clear correlation between the observed  $n = 1$  mode activity and the  $\beta_C$  limit or the  $\beta$  decrease can be detected in the experiments. The strong  $m = 2$  to 3 mode sometimes observed during the  $\beta$ -decay seems to be no necessary prerequisite for it, but may be produced by the increase of  $q_0$  during the high- $\beta$  phase described in Sect. 2, which shifts the  $q = 2$  surface further to the plasma boundary. The

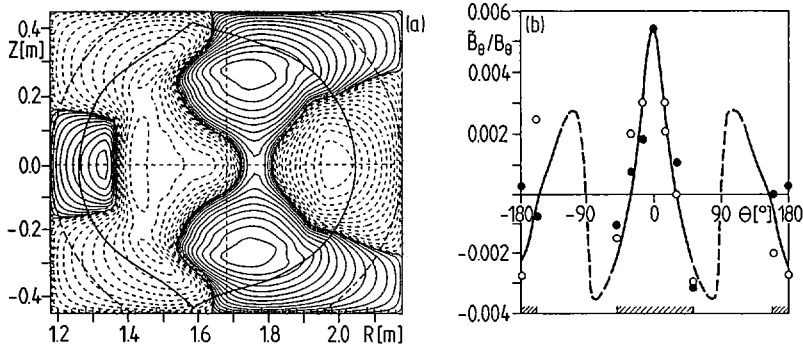


FIG. 5. (a) Perturbed magnetic flux contours for unstable  $n = 1$  mode of discharge with  $\beta/\beta_c = 0.6$ . Full line shows magnetic separatrix and dotted line circle where Mirnov coils are seated. (b) Comparison of calculated magnetic fluctuation amplitude (full line inside, dotted line outside computational box of (a), with measurements ( $m = 4$  mode:  $\bullet$ ,  $m = 3$  mode:  $\circ$ ). Hatched region shows poloidal range covered by probes.

contribution of this mode - if present - to the  $\beta$  decrease is hard to state. Finally, the energy losses due to the ELM's are already present in medium beta H mode discharges showing no beta decrease and are therefore not responsible for the additional losses at the beta limit.

## 6. Ballooning mode stability

A ballooning mode stability analysis of true ASDEX equilibria has been done by solving the corresponding Sturm-Liouville problem for magnetic surfaces with volume values  $V \varepsilon (O, V_a)$ . Written in the form

$$\frac{d}{d\Theta} \left\{ S(\Theta) \frac{du}{d\Theta} \right\} + \beta_p (C_1(\Theta) + \beta_p C_2(\Theta)) u = 0 \quad (3)$$

the ballooning equation can be conceived as having an explicit dependence on the local  $\beta_p$ , and an implicit one via the coefficients  $S$ ,  $C_1$ , and  $C_2$  depending on the total equilibrium. In order to obtain information on the presumably attainable marginal value we have, based on a given equilibrium configuration, modified the explicitly appearing local  $\beta_p$  until a marginal solution of equation (3) with a  $\beta_p$  value  $\beta_M$  was obtained. Fig. 6 shows the calculated beta ratio  $\beta_p/\beta_M = p'/p'_M$  (with  $' = d/d\psi$ ) as function of  $r/a$  for the already described  $D^0 \rightarrow D^+$  and  $H^0 \rightarrow D^+$  discharges with  $\beta = \beta_c$  at the time of  $\beta_{max}$ .

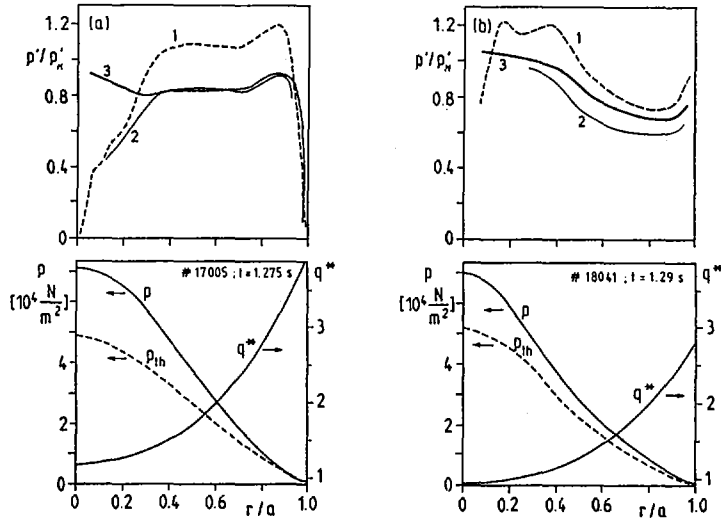


FIG. 6. Radial dependence of pressure gradient  $p'$  normalized to marginally stable one  $p'_M$ , due to ideal ballooning modes ( $\alpha(S)$  criterion: 1, large aspect ratio expansion: 2, exact solution: 3), together with pressure and  $q$  profiles used ( $p = p_{th} + 1/2 (p_{\perp}^{beam} + p_{\parallel}^{beam})$ ) for a  $D^0 \rightarrow D^+$  (No. 17005) and a  $H^0 \rightarrow D^+$  (No. 18041) discharge at  $\beta_{max}$ .

Besides the general evaluation of equation (3), we have also performed a large aspect ratio expansion of the coefficients  $S$ ,  $C_1$  and  $C_2$ . Although assuming circular flux surfaces we have taken here into account the correct differential displacement of the magnetic surfaces due to toroidal curvature  $r/R_0$ ,  $\beta_p = 2 \mu_0 (p - p_{th})/B_p^2$  and inductivity coefficient  $l_i$ :

$$\Delta'(x) = \frac{d\Delta}{dr} = - \frac{r}{R_0} (\beta_p + 1 + l_i/2) \quad (4)$$

with the average being defined by  $p = \int_0^V p dV / V = 2 \int_0^r p r' dr / r^2$ . This treatment is different from that in /7/ (see eq.(1)), where the quantities  $\alpha$  and  $s$  are the only free parameters of the problem, as well as from that in ref./18/, where a special functional form of the differential displacement was assumed. Except for the neighbourhood of the magnetic axis we find the results of our large aspect ratio expansion in good agreement with those of the complete treatment; both these refined approaches yield however  $p'/p'_M$  values about 20 - 30 % lower than given by the simple the  $\alpha = f(s)$  criterion when  $p'$  is in the vicinity of the marginal limit (see Fig.6). Broader current density profiles having higher  $q_0$  values are more

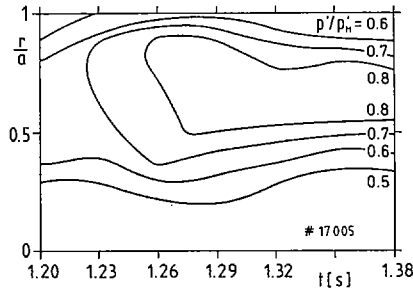


FIG. 7. Contours of constant pressure gradient  $p'$  normalized to marginally stable one  $p'_M$ , due to ideal ballooning modes (large aspect ratio expansion) as a function of time and normalized radius  $r/a$  for a  $D^0 \rightarrow D^+$  discharge (No. 17005).

susceptible to ballooning instabilities, due to their lower shear and vice versa. This manifests itself for the given  $p$  profiles more by a  $p'/p'_M$  profile variation than by an increase of its maximum value, which stays always below 0.9 for  $0.8 \leq q_0 < 1.2$ . (The differences in the  $p(r)$  profiles of Figs. 6a and 6b are due to the different penetration of 40 keV  $D^0$  and  $H^0$  neutrals).

The time development of the ideal ballooning stability according to our large aspect ratio expansion in the  $D^0 \rightarrow D^+$  discharge is illustrated in Fig. 7. At the time of maximum beta (about 1.26s), the discharge reaches a normalized pressure gradient  $p'/p'_M = 0.8$  in the region  $0.5 < r/a < 0.9$ . This is also the region where the enhanced plasma losses start according to the TRANSP analysis as demonstrated in Fig. 3b. During the  $\beta$  decrease between 1.28 to 1.38 s, the  $p'/p'_M = 0.8$  region shrinks only slightly, but the maximum value of  $p'/p'_M$  stays below 0.9. Using the general evaluation of equation (3) yields for  $0.15 < r/a < 0.85$  a region with  $p'/p'_M$  values between 0.7 and 0.85 during the beta decrease. The pressure gradient decreases in fact, but so does  $p'_M$  due to the broadening of the current density profile (the latter being calculated using classical resistivity and the increase in the central  $Z_{eff}$  described in Sect. 2). For discharges with  $\beta_{max} < 0.8 \beta_c$  the  $p'/p'_M$  values remain significantly below unity with maximum values being smaller than the corresponding global  $\beta/\beta_c$  ratio.

In the ASDEX discharges close to the  $\beta$  limit the resistivity is very small but finite so that, strictly speaking, the modes to be studied are resistive ballooning instabilities. The influence of these modes and resistive interchange modes on the  $\beta$  limit was investigated near the plasma axis ( $r \leq 0.1a$ ) /19/. There the ratio

$S = \tau_R / \tau_A$  amounts to  $10^8$ , where  $\tau_R$  is the resistive time and  $\tau_A$  is the poloidal Alfvén time. For  $r = 0.1$  a and mode numbers  $20 < n < 40$  that are not yet stabilized by the finite ion Larmor radius effects the critical beta due to resistive ballooning modes is 25 to 40 % below the ideal MHD limit. It is concluded that the discharges under investigation are ideal ballooning stable but may be marginal with respect to resistive ballooning modes with high wave numbers. This would also explain the near-invariance of the  $p/p_M$  profiles during the  $\beta$  decrease.

## 7. Summary

The good confinement of H mode discharges has allowed the investigation of the  $\beta_c = 2.8 I_p / (a B_T)$  limit derived on the basis of ideal MHD stability calculations. The maximum betas are only reached transiently - normally without any disruption - and beta decreases thereafter, saturating at a level of 0.7 to  $0.8\beta_c$ . Nearly no degradation of confinement is observed when approaching the limiting  $\beta$ : additional energy losses not following the usual H mode transport scaling set in near  $\beta_c$  leading to a "hard" saturation. These losses persist, leading to a subsequent decrease in  $\beta$ , surmised to be a consequence of the reduction in the marginally stable  $\beta$  due to a flattening of the current density profile. Global MHD modes with  $m \approx 6$  and of pressure-driven tearing-mode type are observed, but no clear correlation between their appearance and the  $\beta$  development has been identified. Though the  $\beta$  limit discharges seem to be stable against ideal ballooning modes, resistive ones with high wave numbers  $m > 20$  might be unstable.

## REFERENCES

- [1] KEILHACKER, M., et al., in Plasma Physics and Controlled Nuclear Fusion Research 1984 (Proc. 10th Int. Conf. London, 1984), Vol. 1, IAEA, Vienna (1985) 71; KEILHACKER, M., et al., Plasma Phys. Controll. Fusion **28** (1986) 29.
- [2] BECKER, G., et al., Nucl. Fusion **25** (1985) 705.
- [3] STRAIT, E.J., et al., in Controlled Fusion and Plasma Heating (Proc. 13th Europ. Conf. Schliersee, 1986), Vol. 10C, Part I, European Physical Society (1986) 204.
- [4] McGUIRE, K., et al., in Plasma Physics and Controlled Nuclear Fusion Research 1984 (Proc. 10th Int. Conf. London, 1984), Vol. 1, IAEA, Vienna (1985) 117.
- [5] TROYON, F., et al., Plasma Phys. Controll. Fusion **26** (1984) 209.
- [6] SYKES, A., et al., in Controlled Fusion and Plasma Physics (Proc. 11th Europ. Conf. Aachen, 1983), Vol. 7D, Part II, European Physical Society (1984) 363.

- [7] CONNOR, J.W., et al., Phys. Rev. Lett. **40** (1978) 396;  
LORTZ, D., NÜHRENBERG, J., Phys. Lett. **A68** (1978) 49.
- [8] HAWRYLUK, R., in Physics of Plasmas Close to Thermonuclear Conditions (Proc. Course Varenna, 1979), Vol. 1, Rep. EUR-FU-BRU/XII/476/80, CEC, Brussels (1980).
- [9] POST, D.E., SINGER, C.E., MCKENNEY, A.M., BALDUR: A One-dimensional Plasma Transport Code, Rep. 33, PPPL Transport Group, TFTR Physics Group, Princeton, NJ (1981).
- [10] LEE, J.K., Nucl. Fusion **26** (1986) 955.
- [11] VON GIERKE, G., et al., in Controlled Fusion and Plasma Heating (Proc. 13th Europ. Conf. Schliersee, 1986), Vol. 10C, Part I, European Physical Society (1986) 33.
- [12] LACKNER, K., SYKES, A., private communication.
- [13] HULSE, R.A., et al., J. Phys., B (London). At. Mol. Phys. **13** (1980) 3895.
- [14] GRUBER, O., et al., in Controlled Fusion and Plasma Heating (Proc. 13th Europ. Conf. Schliersee, 1986), Vol. 10C, Part I, European Physical Society (1986) 248.
- [15] BECKER, G., Nucl. Fusion **24** (1984) 1364.
- [16] KLÜBER, O., et al., in Controlled Fusion and Plasma Heating (Proc. 13th Europ. Conf. Schliersee, 1986), Vol. 10C, Part I, European Physical Society (1986) 136.
- [17] KORNHERR, M., et al., *ibid.*, p. 140.
- [18] CHOE, W.H., FREIDBERG, J.P., Phys. Fluids **29** (1986) 1766.
- [19] CORREA-RESTREPO, D., Plasma Phys. Controll. Fusion **27** (1985) 565.

## DISCUSSION

M. OKABAYASHI: You reported that fishbone instabilities were excited during beta collapse. What is the actual power input if you include the fast ion losses due to these fishbone instabilities?

O. GRUBER: We do not observe fast ion losses with the passive charge exchange energy measurements. So I don't believe that the observed fishbone modes contribute to the energy loss. Moreover, these modes are also present in discharges with  $\beta \leq 0.7 \beta_c$ , showing a dependence of constant  $\beta$  on time and, therefore, no increased losses.

K. MCGUIRE: The edge relaxation phenomena can cause a large energy loss, as was pointed out by Dr. Okabayashi<sup>1</sup>. What is the effect of the edge relaxation phenomena and of core radiation on the beta saturation in ASDEX?

O. GRUBER: The total radiated power has no influence on the global balance, despite the increased central radiation power density. Edge localized modes might be almost absent before  $\beta_{max}$ , or are present after the H-transition during the whole beta increase. This does not affect the beta limit observed in ASDEX discharges. We find edge localized modes also in the case of power beta values. Their contribution to the power losses is included in our normal H-mode scaling.

D. OVERSKEI: Can you say what the thermal plasma contribution to the pressure gradient is? And what is the ratio of  $p'_{thermal}$  to  $p'_{critical}$  as a function of radius? In addition, how does the fast ion contribution to  $p \sim (\beta)$  vary in time and space during this relaxation?

<sup>1</sup> Paper IAEA-CN-47/A-V-2, these Proceedings, Vol. 1.

O. GRUBER: For the  $D^0 \rightarrow D^+$  injection cases,  $\beta^{\text{beam}}$  is up to 25% of the total beta before  $\beta_{\text{max}}$  is reached. Afterwards the beam contribution increases owing to the decay of the thermal energy content until a new saturation level is reached. The contribution of  $p'_{\text{thermal}}$  to  $p'_M$  is about 70% in the  $D^0 \rightarrow D^+$  cases, having a radial profile similar to the total  $p'/p'_M$ . For the  $H^0 \rightarrow D^+$  cases, fast particles are deposited further inwards and the thermal contribution to  $p'$  near the centre is reduced.

## BETA LIMIT DISRUPTIONS\*

Mingsheng CHU, E.J. STRAIT, J.K. LEE, L. LAO,  
 R.D. STAMBAUGH, K.H. BURRELL, R.J. GROEBNER,  
 J.M. GREENE, F.J. HELTON, J.Y. HSU, J.S. KIM,  
 H. St. JOHN, R.T. SNIDER, T.S. TAYLOR  
 GA Technologies, Inc.,  
 San Diego, California,  
 United States of America

### Abstract

#### BETA LIMIT DISRUPTIONS.

Temporal behavior of disruptions in the maximal  $\beta_t$  discharges in Doublet III is analyzed systematically by using ideal and resistive MHD models. These discharges disrupt at beta values predicted by the Troyon-Sykes-Wesson limit. The basic disruption mechanism is identified as the overlapping of the central sawtooth mixing zone with the edge stochastic zone. This overlap is predicted theoretically to be greater for more square current profiles and also to be enhanced at larger values of beta. This suggests that in order to find a disruption-free path to high beta, the current profile must be made broader as beta increases. Eventually, even the broadened profile will become unstable to tearing modes, at an average beta value lower than that of a profile optimized for stability against ballooning modes alone, resulting in disruptions. This scenario is consistent with the experimental results. Discharges which successfully approach the beta limit have a lower internal inductance (broader profiles) than similar discharges at lower beta. For long periods preceding the disruptions, a significant portion of the profile is calculated to be at or slightly beyond marginal stability for ballooning modes. This long stable period argues against the ballooning modes as the cause of the disruption. As beta increases, the window for avoiding the overlap of the sawtooth mixing zone and the edge stochastic zone becomes narrower, until finally no way can be found to avoid the disruption; this defines the 'operational' beta limit.

## 1. INTRODUCTION

The maximum achievable  $\beta_t$  value is the most important parameter determining the suitability of the tokamak as an energy producing fusion device. A number of groups have published first stable regime  $\beta_t$  scaling laws of the form  $\beta_t (\%) = CI(\text{MA})/a(\text{m}) B(\text{T})$ . The constant

---

\* This is a report of work sponsored by the United States Department of Energy, under Contract No. DE-AC03-84ER53158.

$C$  varies from 2.8 for ideal external kink modes with no wall stabilization [1] to 4.4 for ideal ballooning modes with optimized profiles [2]. The physical basis for the parametric dependence of this limit has been elucidated by Wesson and Sykes [3] who have pointed out that if tearing mode stability is taken into account,  $C$  is reduced to 2.2 without an external conducting wall.

Experimentally, a value of  $C = 3.5 \pm 0.5$  was obtained in Doublet III [4] covering a range of elongation  $1.0 \leq \kappa \leq 1.6$  and triangularity  $-0.1 \leq \delta \leq 0.9$ . Concurrently, the parametric dependence of the experimentally achievable beta value has been analyzed by Bernard, Helton, Moore and Todd [5]. They used the ideal MHD theory and assumed that the plasma should be stable to both the localized ballooning mode and the external kink mode with an external conducting wall located at 1.5 plasma radius. A scaling law was deduced which explained the limit of the achievable beta in Doublet III. Experimentally, it is invariably found in the Doublet III experiments that the plasma ends in disruption. Because of the narrow range of the theoretical predictions about the experimental value for  $C$ , it is not possible to identify the mode causing the  $\beta_t$  limit disruptions on the basis of the value of  $C$  alone. We must therefore examine the details of the  $\beta_t$  limiting process. We have carried out such a program of detailed examination of the observed phenomena leading to the disruption, using both linear and nonlinear, and ideal and resistive MHD stability calculations for the particular equilibria obtained in the experiment.

A general pattern emerged in which the probable cause of the  $\beta_t$  limit is the unchecked growth of the  $m=2, n=1$  tearing mode shortly after the last sawtooth. This 2/1 mode growth is caused by the finite  $\beta$  effect of shifting the current centroid and steepening the edge current density gradient, and is triggered by the drop of the last sawtooth. Finite  $\beta$  also enhanced the field line stochasticity in the sawtooth mixing region and around the 2/1 island. In low  $q_t$  ( $\leq 3.1$ ) discharges, the ideal ballooning mode  $\beta$  limit of the configuration has not been reached, whereas at high  $q_t \geq 3.5$ , the ballooning mode stability limit was violated over a large portion of the inner region of the plasma. The destabilization of the ballooning modes in the central region is consistent with the experimental observation from the soft x-ray signal that the sawtooth mixing region was greatly extended in the last sawtooth before disruption. It is proposed here that the overlapping of this central stochastic region with the edge stochastic region centered around the  $q=2$  surface is the direct cause of the  $\beta$  limit disruptions.

## 2. $\beta$ LIMIT DISRUPTIONS IN DOUBLET III

The  $\beta$  limits in Doublet III were investigated by stepwise increasing the neutral beam heating power in consecutive discharges or in the same discharge until the  $\beta_t$  limit disruption was produced [6]. No specific operational techniques were successful in trying to prevent these disruptions except copious gas puffing which degraded  $\tau_E$  and so limited the energetically achievable  $\beta$ . A predisruption interval of 10 to 20 ms preceded the disruption. This interval is initiated by the drop of the last sawtooth. During the interval, the global energy confinement becomes poorer, the measured high frequency magnetic perturbation signals on the Mirnov probe are replaced by the signal of a low frequency 2/1 mode, and intense interaction with the limiter ensues with large signals in the  $H_\alpha$  limiter light. Prior to the predisruption interval, the discharges have increasingly large sawteeth and constant heating efficiency ( $\Delta W/\Delta P$ ) as the NBI power and  $\beta_t$  rise. The current profile steadily broadens, as evidenced by a decreasing  $\ell_i$ .

### 2.1. Current Profile and Beta Optimization

In this section we try to elucidate the importance of plasma current profile and finite  $\beta$  effects in determining the maximum achievable  $\beta$  value.

We explore first the  $\beta$  limit for a specific class of current profiles for a large aspect ratio circular tokamak. The effect of  $\beta$  on the current profile is temporarily ignored. This problem was first studied by Wesson and Sykes [3]. They emphasized the optimization with respect to all profiles with fixed  $q_0$  and  $q_\ell$ . In this paper, we aim at understanding the generic relationship among profiles which are not yet optimized with respect to ballooning modes. A convenient parameterization is given by

$$j = j_0 \left[ \frac{1 - P_d}{1 + \left(\frac{r}{r_0}\right)^\lambda} + P_d \right]^{3/2} \left[ 1 - \left(\frac{r}{a}\right)^{\lambda_e} \right]^{3/2}$$

$\lambda$  is a current peakedness parameter, which is higher for a peaked current profile. At fixed  $q_0$  and  $q_\ell$ ,  $r_0$  increases slightly with increasing  $\lambda$ .  $P_d$  represents an amount of current pedestal,  $\lambda_e$  is used to make the current at the plasma edge vanish. Shown in the inset of Fig. 1 (a) are the typical current profile variations for  $q_0 = 1$ ,  $q_\ell = 3.05$ ,  $P_d = 0$ , and  $\lambda = 2$  and 10. Higher  $\lambda$  corresponds to a more square current profile. The  $\beta_t$  limit

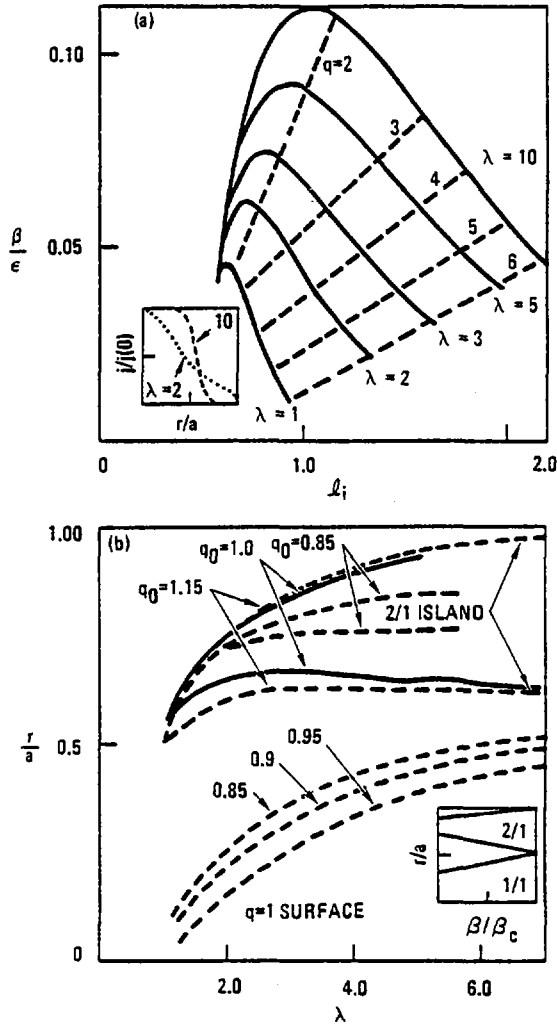


FIG. 1. (a) Maximum  $\beta/\epsilon$  versus  $l_i$  for a class of current profiles, low  $\lambda$  for flat current profile, high  $\lambda$  for square current profile. Shown in the inset are the typical current profiles for  $\lambda = 2$  and  $\lambda = 10$ . (b) Location of the  $q = 1$  surface and the  $2/1$  island size with  $q_0$  as a parameter for different current peakedness. The enlargement of the  $1/1$  and  $2/1$  stochastic regions as a function of  $\beta/\beta_c$  is shown schematically in the inset.

for a particular current profile for infinite  $n$  ideal ballooning mode is given by [3]

$$\beta_m = \frac{-0.30}{Ra^2} \int_0^a \frac{\partial}{\partial r} \left( \frac{1}{q^2} \right) r^3 dr$$

Shown in Fig. 1 (a) is the  $\beta_m$  versus  $\ell_i$ , with  $\lambda$  as a parameter.  $\lambda_e$  has been fixed at 30, with  $q_0 = 1$  and  $P_d = 0$ . It is observed that a peaked current profile will admit of a larger  $\beta_m$  value, whereas a flatter current profile will accommodate a smaller  $\beta_m$  value. With  $P_d$  nonzero, the ranges of  $\beta_m$  and  $\ell_i$  are somewhat reduced. If we could achieve optimization only with respect to the ballooning mode without an effect on tearing modes, we could aim at peaked current profiles with large  $\ell_i$  values.

Shown in Fig. 1 (b) is the location of the  $q=1$  surface and the quasilinear  $m=2$  island size for a  $q_\ell = 3.05$  plasma with  $P_d = 0$ . Before the sawtooth drop, the plasma central  $q$  normally has  $1 > q \sim 0.95$ , and the sawtooth mixing region has a radius  $\sim\sqrt{2}$  larger than the  $q=1$  surface. After the sawtooth, the central  $q$  rises above 1 to a value of  $\sim 1.0$  to 1.2. Starting with a current profile with  $\lambda = 4$ , which is more square than the experimental profiles, and with central  $q \sim 0.95$ , after the sawtooth there will be an overlapping of the 2/1 island and the sawtooth mixing region. For a less square current profile ( $\lambda \lesssim 3$ ), the 2/1 island and the sawtooth mixing region could be well separated. For a very broad current profile ( $\lambda \lesssim 2$ ), the plasma becomes unstable to external kink modes at low  $q_\ell$  ( $\leq 3$ ). Therefore, in order to optimize  $\beta_t$  for ideal ballooning modes while avoiding the overlapping of the 1/1 mixing region and the 2/1 island, we should aim at achieving the highest  $\ell_i$  value which does not cause a mixing of the two zones. Experimental discharges in DIII were almost always optimized to obtain sawtooth oscillations because of their favorable property of expelling impurities from the central region of the plasma. The resultant experimental profiles therefore had a relatively high  $\ell_i$  value corresponding to  $\lambda \lesssim 3$ .

For a finite aspect ratio and finite  $\beta_t$  tokamak, increasing  $\beta_t$  while keeping the total current and  $q_0$  constant reduces  $\ell_i$ . This reduction is brought about by the increased toroidal shift of the current centroid and thus the reduction of the central current density. At the same time, the edge current density gradient on the outboard side of the torus is enhanced and the 2/1 tearing mode destabilized. In contrast to the zero-beta cylindrical theory, the drop in  $\ell_i$  associated with finite  $\epsilon\beta_p$  is a destabilizing effect. Further, the finite  $\epsilon\beta_p$  effect enhances the coupling to the side-band harmonics and increases the magnetic field line stochasticity both at the edge of the sawtooth mixing zone and around the 2/1 islands. This could be visualized in Fig. 1 (b) by enlarging both the central mixing zone and the 2/1 stochastic zone. For a fixed current profile this increasing stochasticity is expected to close the stable

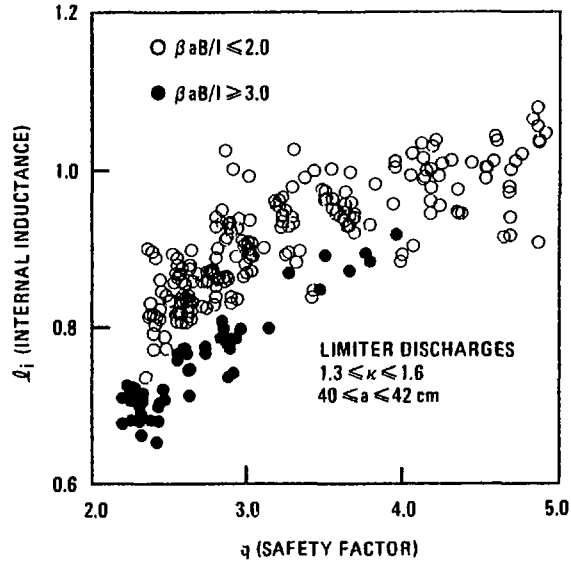


FIG. 2. Experimentally obtained  $\ell_i$  as a function of safety factor. Higher  $\ell_i$  values have lower normalized  $\beta$ .

operating window, as shown schematically in the inset of Fig. 1 (b). This is confirmed by numerical computations with increasingly large plasma pressure. It is observed that as the pressure increases, the 2/1 instability generates a stochastic region with increasingly large size until a critical  $\beta$  value is reached, at which the whole plasma region becomes stochastic. For this reason, in order to optimize  $\beta_t$ , we need to start with profiles with even lower  $\ell_i$  as determined from the cylindrical theory, to avoid the overlapping of 2/1 and 1/1 in the finite  $\beta_t$  plasma.

Experimentally, the statistical behavior of  $\ell_i$  as a function of  $q_t$  is given in Fig. 2 for a large number of discharges during the high  $\beta$  studies. It is seen that for discharges in which disruption is postponed by broadening the profile, a higher  $\beta$  is achieved. As beta increases, the window for disruption-free operation becomes narrower, until finally no way can be found to avoid the disruption. This defines the "operational" beta limit.

Another route which could be adopted is to eliminate the 1/1 region by raising the central  $q$  or stabilizing the 2/1 region by using a current pedestal and to aim at higher  $\ell_i$  with higher  $\beta_t$  values [7,8].

## 2.2. Detailed Comparison Between Theory and Experiment

To further ascertain the  $\beta_t$  limit disruption process, a detailed comparison between theory and experiment is necessary. Stability against ballooning modes [9] was investigated using the stability code MBC [10]. The current and pressure profiles were obtained from the MHD equilibrium analysis using EFIT [11]. An analysis using equilibria incorporating kinetic data does not result in substantially different results. EFIT is an ideal MHD equilibrium code for determining arbitrary noncircular plasma cross-section and current profiles separating  $\beta_p$  and  $\ell_i$  values. In discharges near the  $\beta_t$  limit at high  $q_\ell > 3.5$ , the inner portion ( $r/a < 0.7$  to  $0.8$ ) was found to be unstable to high  $n$  localized ballooning modes. Crossing this theoretical threshold was found to permit the achievement of stationary  $\ell_i$  and  $\beta_t$  values before the disruption. The edge region of the plasma [where  $q(r) \geq 2$ ] remains stable to ballooning modes throughout the discharge. For low  $q_\ell < 3$ , marginal stability is reached only just before the disruption, with steadily rising  $\beta_t$  and decreasing  $\ell_i$ . Modes that were consistent with localization at a resonant surface ( $m/n=2/1, 4/2, 6/3$ ) were observed near the  $\beta_t$  limit.

This difference in the approach to the maximum  $\beta$  is shown for the high  $q_\ell$  ( $\sim 5$ ) discharge 36288 in Fig. 3 (a) and for the low  $q_\ell$  ( $\sim 2.6$ ) discharge 43481 in Fig. 3 (b). It is seen that at low  $q_\ell$  the trend of the  $\ell_i$ ,  $\beta_t$  and  $\beta^*$  development does not change until the disruption time, whereas at high  $q_\ell$  all these quantities show that a stationary value was reached. The achievement of the stationary values of the plasma equilibria quantities correlates with the ballooning stability criterion development shown in Fig. 4 for high and low  $q_\ell$ . At high  $q_\ell$  the stability criterion is violated over a large region for a time much longer than the energy confinement time, whereas at low  $q_\ell$  the stability criterion is only marginally violated.

A last sawtooth drop initiated the predisruption interval. This last sawtooth is characterized by an increased size of the sawtooth inversion region as determined from soft x-ray emission signals. A particularly large inversion radius enhancement is observed to occur at high  $q_\ell$  shots which violated the ballooning stability criterion. Thus an extended central mixing zone is produced by this last sawtooth. This predisruption interval was shorter than the normal sawtooth. The central soft x-ray signal also fails to rise to a comparable level. These findings support the hypothesis that in this central mixing zone, flux surfaces did not completely reform.

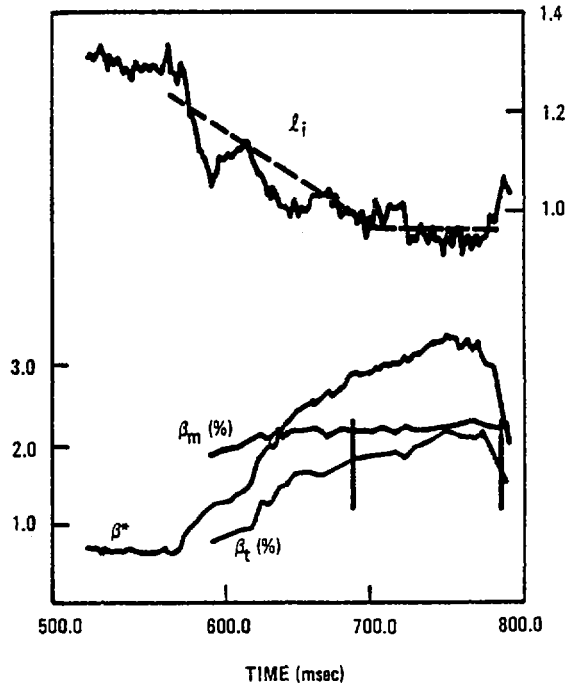


Fig. 3a. Behaviour of  $l_i$  (internal inductance),  $\beta_m$  (maximum theoretically stable  $\beta$ ),  $\beta_t$  (toroidal  $\beta$ ), and  $\beta^*$  [ $=\beta(aB/l)$ ] for a high  $q$  discharge, showing saturation behavior of  $l_i$ . The vertical line indicates the time at which the localized ballooning mode threshold is first crossed.

In the predisruption interval, high frequency and/or high mode number MHD activity gives way to a low frequency mode with  $m = 2$ ,  $n = 1$  in the magnetic probe data and  $m = 1$  in the soft x-ray data. The details of the experimental data traces are shown in Ref. [6]. After the last sawtooth, MHD equilibrium code fits indicate that the toroidal current density gradient and the pressure gradient have increased near  $q=2$  surface. Calculations using the ordinary  $\Delta'$  analysis or using the reduced MHD stability code CART [12] predict that a tearing mode with dominant  $m=2, n=1$  character in  $\tilde{\psi}$  should be unstable. Shown in Fig. 5 are a typical perturbed magnetic flux function and perturbed pressure patterns. The amplitude of the magnetic perturbation measured at the Mirnov probes indicates that sizable ( $\sim 20\%$  of minor radius)  $2/1$  islands were excited. In resistive MHD simulations, toroidal and  $\beta_p$  coupling ( $\epsilon\beta_p \sim 0.4$ ) with continued mode growth induces large field line stochasticity outside of the  $q=2$  surface which would result in a degradation in confinement over that region. Poorer edge confinement may be the cause of the observed enhanced limiter interaction, as indicated

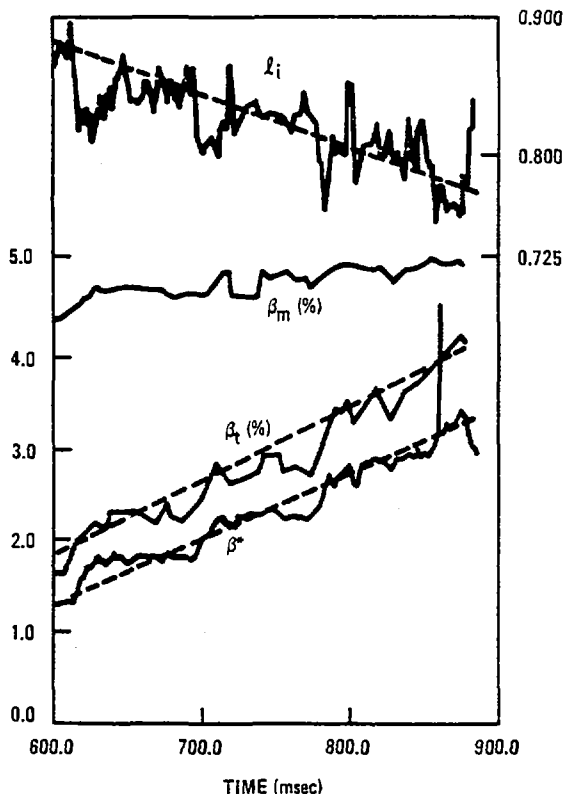


FIG. 3b. Same as Fig. 3a, showing the corresponding behavior for a low  $q$  discharge; no apparent saturation of  $l_i$ ,  $\beta$ , or  $\beta^*$ .

by the increased level of the  $H_{\alpha\text{lim}}$  light. This is also correlated with the fact that the frequency of magnetic perturbations is drastically reduced, indicating loss of charge by the plasma and the resultant poor angular momentum confinement of the predisruption plasma. Material recycled from the limiter may cause the edge and the 2/1 island center to cool. Code simulations with enhanced resistivity in the island center give enlarged island sizes and enhanced higher order island overlapping in the edge region [13]. It is observed that this enlarged edge stochastic region can overlap the central sawtooth mixing region [14].

We conclude that there is agreement between experiment and theory, confirming that an overlapping of the edge stochastic region and the central sawtooth mixing region is the crucial event that leads to disruption.

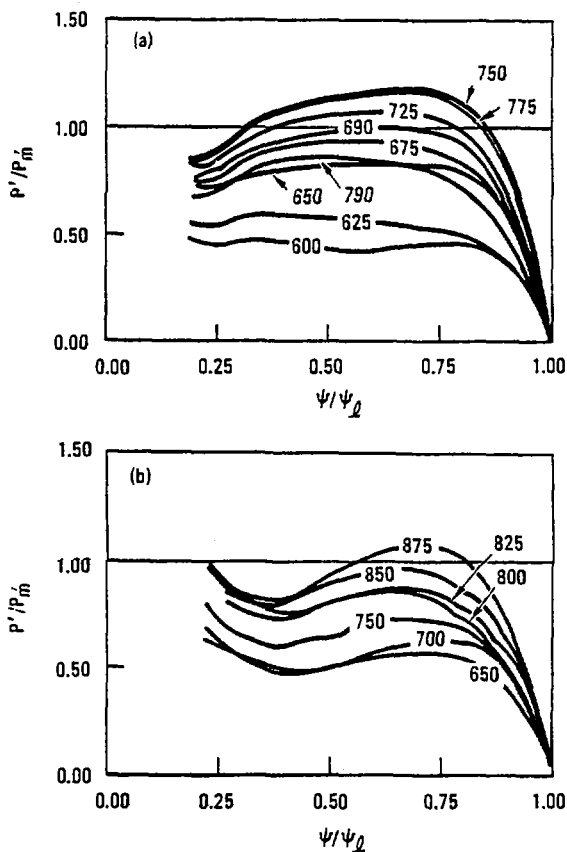


FIG. 4. Temporal development of  $P'/P'_m$  as a function of the normalized flux function.  $P'$  is the pressure gradient and  $P'_m$  is the maximum pressure gradient stable to the infinite  $n$  ballooning modes. Times in milliseconds are indicated (a) for a high  $q_t$  ( $\approx 5$ ) discharge, and (b) for a low  $q_t$  ( $\approx 2.6$ ) discharge.

### 3. CONCLUSION AND SUMMARY

We have performed systematically an analysis of the sequence of events leading to the high  $\beta$  disruptions in the neutral beam heated plasmas in Doublet III. It is found that the path through which the high  $\beta$  values were reached was consistent with avoiding disruption throughout the experiment, except at the very end.

It is found that the disruption interrupts the process of pressure and profile broadening through which the plasma reaches the ballooning mode limit. At high  $q$  ( $\gtrsim 3.5$ ), the pressure gradient was able to develop

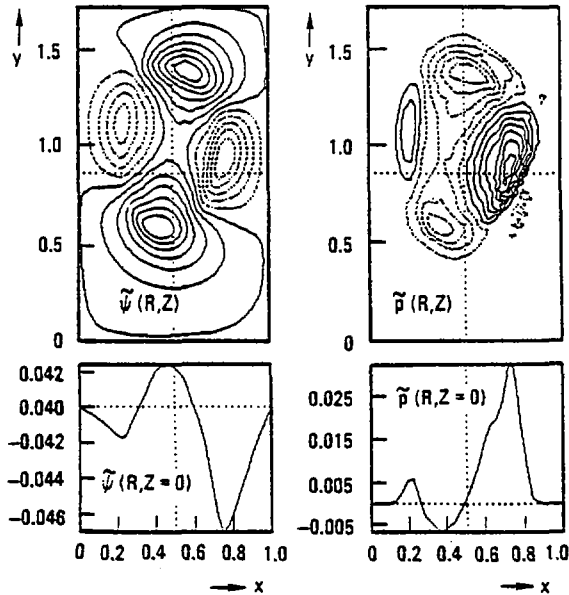


FIG. 5. Perturbed magnetic flux function and pressure distribution from the resistive MHD code CART computed for the low  $q$  discharge 43481 for equilibria during the predisruption period.

to the maximum allowed by the ideal ballooning modes over a large portion of the plasma interior, whereas at low  $q$  ( $\lesssim 3.1$ ), the ballooning mode limit was barely reached. The general trend of increasing  $\beta$  in a sawtoothing plasma is to destabilize the 2/1 region and to enlarge the sawtooth mixing and 2/1 stochastic zones. The immediate cause of the disruption is triggered by a sawtooth instability which causes the plasma current gradient to further steepen around the  $q=2$  surface, thus exciting a large 2/1 island. The accompanying loss of charge slows down the island rotation and enhances the interaction of the island with the limiter. Then, either a thermal island growth follows or the profile change induces other edge resonance modes. The further growth of the islands causes the enlarged edge stochastic region and the sawtooth mixing regions to overlap; this leads to disruption.

As beta increases, the profile window for disruption-free operation becomes narrower, until finally no way can be found to avoid the disruption. This defines the experimental "operational" limit.

## REFERENCES

- [1] TROYON, F., GRUBER, R., SAURENMANN, H., SEMENZATO, S., SUCCI, S., *Plasma Phys. and Contr. Fusion* **26** (1984) 209.
- [2] SYKES, A., TURNER, M.F., PATEL, S., in *Controlled Fusion and Plasma Physics* (11th Euro. Conf. Aachen, European Physical Society), Vol. 7D, Part II (1983) 363.
- [3] WESSON, J.A., SYKES, A., *Nucl. Fusion* **25** (1985) 85.
- [4] STAMBAUGH, R.D., MOORE, R.W., BERNARD, L.C., KELLMAN, A.G., STRAIT, E.J., et al., in *Plasma Physics and Controlled Nuclear Fusion Research* (Proc. 10th Int. Conf. London, 1984) Vol. 1, IAEA, Vienna (1985) 217.
- [5] BERNARD, L.C., HELTON, F.J., MOORE, R.W., TODD, T.N., *Nucl. Fusion* **23** (1983) 1475.
- [6] STRAIT, E.J., CHU, M.S., JAHNS, G.L., KIM, J.S., KELLMAN, A.G., et al., in *Controlled Fusion and Plasma Heating* (Proc. 13th European Conf., Schliersee, 1986), *Europhysics Conference Abstracts* **10C**, Part I, 204.
- [7] HINTON, F.L., CHU, M.S., DOMINGUEZ, R.R., HARVEY, R.W., LAO, L., et al., in *Plasma Physics and Controlled Nuclear Fusion Research* (Proc. 10th Int. Conf. London, 1984) Vol. 2, IAEA, Vienna (1985) 3.
- [8] GIERKE, G.V., BECKER, G., BOSCH, H.S., BROCKEN, H., BÜCHL, K., et al., in *Controlled Fusion and Plasma Heating* (Proc. 13th European Conf., Schliersee, 1986), *Europhysics Conference Abstracts* **10C**, Part I, 33.
- [9] CHU, M.S., LAO, L.L., MOORE, R.W., ST. JOHN, H., STAMBAUGH, R.D., STRAIT, E.J., TAYLOR, T.S., GA Technologies Rep. GA-A18546, submitted to *Nucl. Fusion*.
- [10] MOORE, R.W., MBC, A Ballooning Stability Code for Finite Toroidal Mode Number, GA Technologies Rep. GA-A16234 (1981).
- [11] LAO, L.L., ST. JOHN, H., STAMBAUGH, R.D., KELLMAN, A.G., PFEIFFER, W., *Nucl. Fusion* **25** (1985) 1611.
- [12] LEE, J.K., *Phys. Fluids* **29** (1986) 1629; *Nucl. Fusion* **26** (1986) 955.
- [13] KIM, J.S., CHU, M.S., GREENE, J.M., GA Technologies Rep. GA-A18586, submitted to *Nucl. Fusion*.
- [14] CHU, M.S., GREENE, J.M., KIM, J.S., LAO, L., SNIDER, R.T., STAMBAUGH, R.D., STRAIT, E.J., TAYLOR, T.S., GA Technologies Rep. GA-A18579, submitted to *Nucl. Fusion* (1986).

## DISCUSSION

O. GRUBER: I would like to mention that we do not have sawteeth during the H-mode phase of ASDEX, so overlapping of  $m = 1/n = 1$  islands and  $m = 2/n = 1$  islands is not possible in our beta limit shots. My question is as follows. In the paper you presented at the 13th European Conference in 1986 it was stated that the ideal ballooning mode limit is violated only near the plasma centre, whereas it is strongly stable over the major part of the plasma cross-section. Now you have violation of the ideal ballooning limit in the outer part of the plasma. How are the different pressure profiles determined?

Mingsheng CHU: If we use the kinetic hot ion pressure determined directly from the hot ion deposition profile, then the central pressure gradient becomes very large and seriously violates the ballooning criterion at the centre. This is not very reasonable. Therefore we use the magnetically determined pressure profile. The ballooning criterion is only moderately violated. This is more satisfactory. A more self-consistent hot ion pressure deposition profile is definitely called for.

M.A. DUBOIS: For your conclusions to be valid, you need to measure the  $q = 2$  island size, for instance by a full Fourier analysis of the  $m = 2, n = 1$   $\delta B$  components measured by the Mirnov coils. Are you sure that such a direct measurement of the  $q = 2$  island width using Mirnov coils has been made on Doublet III?

Mingsheng CHU: In Doublet III, the magnitude of the magnetic perturbation is routinely measured by Mirnov probes located close to the plasma boundary. The signal measured is compared with the computed magnetic perturbation amplitude at that particular location in order to determine the  $m = 2, n = 1$  island size. For instance, shot 46167 is computed to have an island size greater than  $0.31a$  at the time of disruption. The  $q = 2$  surface is at  $0.83a$ , and the sawtooth mixing region with radius  $\approx 0.52a$  remains flat in terms of temperature throughout the predisruption period, as determined from the soft X-ray emissions.



## SAWTEETH AND TEMPERATURE PROFILES IN TOKAMAKS

D.A. BOYD, R.E. DENTON, J.Q. DONG, J.F. DRAKE,  
P.N. GUZDAR, A.B. HASSAM, R.G. KLEVA, Y.C. LEE,  
C.S. LIU, F.J. STAUFFER

Laboratory for Plasma and Fusion Energy Studies,  
University of Maryland,  
College Park, Maryland,  
United States of America

### Abstract

#### SAWTEETH AND TEMPERATURE PROFILES IN TOKAMAKS.

A detailed theoretical/experimental study of sawteeth, electron confinement, and temperature profiles in tokamaks has been completed.

### 1. INTRODUCTION

A theoretical/experimental study of sawteeth, electron confinement, and temperature profiles in tokamaks has been completed. Temperature profiles in TFTR discharges are distinctly trapezoidal (flat in the centre with a constant slope in the outer regions) at low values of the safety factor at the limiter,  $q_L$ . For a given  $q_L$ , the profiles are insensitive to auxiliary injected power as well as other plasma parameters. Such profiles result from sawtoothing at the plasma centre with anomalous cross-field thermal conduction in the outer plasma which depends strongly on the electron temperature gradient,  $\nabla T_e$ . Such trapezoidal profiles cause skin currents to form during the sawtooth cycle. The resulting current profiles produce compound as well as normal sawteeth and enable us to simply explain the many discrepancies between experimental observations of sawteeth and the standard Kadomtsev model. A theoretical model of anomalous transport resulting from a short wavelength  $\nabla T_e$  driven mode produces the observed scaling of central electron temperature in TFTR and produces profiles in agreement with observations.

### 2. ELECTRON TEMPERATURE PROFILES IN TFTR

An experimental study of electron temperature profiles in TFTR discharges has been completed. Measured temperature profiles were normalized by the following prescription: all minor radial co-ordinates were divided by the limiter radius and all

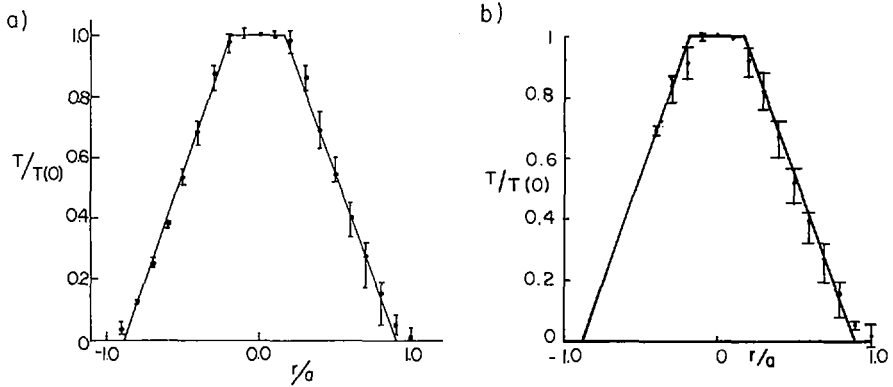


FIG. 1. (a)  $T/T(0)$  versus  $r/a$  for six low  $q_L$  Ohmic discharges. Here  $q_L = 2.65, 2.65, 2.70, 2.79, 3.39, 3.41$ ;  $\{ndl = 4.8, 6.6, 4.0, 2.1, 2.0 \times 10^{19} \text{ m}^{-2}\}$ ;  $B = 4.66, 4.66, 4.80, 4.70, 5.81, 3.05 \text{ T}$ ;  $R = 2.59, 2.59, 2.56, 2.57, 2.07, 2.79 \text{ m}$ ;  $a = 0.80, 0.80, 0.82, 0.82, 0.41, 0.58 \text{ m}$ .

(b)  $T/T(0)$  versus  $r/a$  for four low  $q_L$  neutral beam heated discharges. Here  $q_L = 2.65, 2.65, 2.67, 2.65$ ;  $\{ndl = 6.9, 8.7, 9.9, 9.3 \times 10^{19} \text{ m}^{-2}\}$ ;  $B = 4.66, 4.66, 4.83, 4.79 \text{ T}$ ;  $R = 2.59, 2.59, 2.49, 2.49 \text{ m}$ ;  $a = 0.8, 0.8, 0.83, 0.83 \text{ m}$ ; the injected power  $P_B = 4.20, 4.26, 10.50, 9.56 \text{ MW}$ .

temperatures by the temperature at  $r = 0$ , so that graphs of  $T/T(0)$  versus  $r/a$  could be produced. Thus the shapes of profiles with very different temperatures and limiter radii could be compared. The profiles were measured with a fast scanning Michelson interferometer utilizing the second harmonic of the electron cyclotron emission spectrum [1].

Two basic profile shapes have been identified. The parameter that seems to have the strongest influence in determining the shape is the limiter safety factor,  $q_L$ .

The plot of  $T/T(0)$  versus  $r/a$  for six low  $q_L$ , ohmically heated discharges is shown in Fig. 1(a). These discharges range over a factor of 2.2 in density, 1.9 in toroidal field strength, 1.35 in major radius, and a factor of 2 in minor radius. The cylindrical  $q_L$ 's vary from 2.65 to 3.41. The average  $T/T(0)$  values are plotted with the error bars showing the full range of  $T/T(0)$  at each  $r/a$ . The plot reveals a basically trapezoidal shape: flat within the sawtooth region and then a linear decrease in temperature until the limiter is approached. The solid line is a trapezoid fitted to the data.

Figure 1(b) shows a similar plot for low  $q_L$  discharges that are heated by neutral beam injection. In this case a four shot average is shown. The density varies by over a factor of 1.4 and the injected power varies from 4.2 to 10.5 MW. Although the density increases by a factor up to 1.4 and the temperature up to 1.36 under injection, the profile shape barely changes (the trapezoid from Fig. 1(a) is shown for comparison).

High and mid  $q_L$  discharges have a different shape. A plot for three high  $q_L$ ,  $q_L > 7$ , ohmically heated discharges is shown in Fig. 2(a). The shape shows strong central peaking and from  $0.1 < r/a < 0.6$  the shape can be fitted with an exponen-

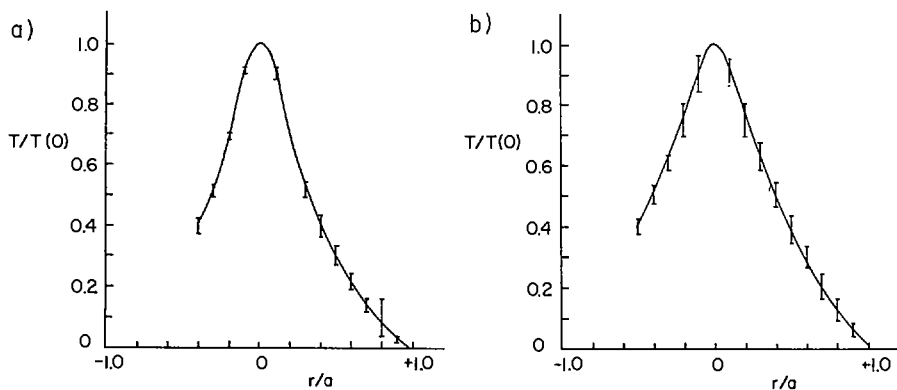


FIG. 2. (a)  $T/T(0)$  versus  $r/a$  for three high  $q_L$  Ohmic discharges. Here  $q_L = 7.47, 7.87, 7.88$ ;  $\int ndl = 1.0, 1.3, 1.4 \times 10^{19} \text{ m}^{-2}$ ;  $B = 3.90, 4.72, 4.72 \text{ T}$ ;  $R = 2.55, 2.56, 2.56 \text{ m}$ ;  $a = 0.82, 0.82, 0.82 \text{ m}$ .

(b)  $T/T(0)$  versus  $r/a$  for six mid high  $q_L$  neutral beam heated discharges. Here  $q_L = 7.91, 7.88, 4.70, 4.73, 4.72, 4.72$ ;  $\int ndl = 2.2, 3.5, 4.8, 4.9, 4.7, 4.9 \times 10^{19} \text{ m}^{-2}$ ;  $B = 4.72, 4.73, 4.8, 4.8, 4.7, 4.8 \text{ T}$ ;  $R = 2.56, 2.55, 2.48, 2.48, 2.48, 2.48 \text{ m}$ ;  $a = 0.82, 0.82, 0.83, 0.83, 0.83, 0.83 \text{ m}$ ;  $P_B = 4.23, 4.91, 11.0, 10.49, 11.31, 10.42 \text{ MW}$ .

tial [2] with a characteristic normalized length of  $\Delta r/a = 0.36$ . Mid  $q_L$  ( $\sim 4.7$ ) discharges are often sawtoothing and have a flattened central region, but outside this region the shape is again exponential with the same characteristic length.

When subjected to neutral beam injection, high and mid  $q_L$  discharges develop broadened electron temperature profiles. The sawtoothing ceased during injection for the mid  $q_L$  discharges and so their data could be combined with the high  $q_L$  data. A six shot average has been plotted in Fig. 2(b). For these discharges the density varies by a factor 2.2, the central electron temperature by 1.8, and the injected power from 4.2 to 11.3 MW. With high power injection the density increases by a factor of 2.3 and the temperature by 1.25. The profile can still be fitted with an exponential, but the characteristic length is now  $\Delta r/a = 0.45$ .

Over a very broad range of operating conditions TFTR electron temperature profile shapes have two distinct forms: trapezoidal at low limiter  $q$  and exponential at mid and high  $q_L$ . Strong neutral beam heating does not modify the profile shape. Interestingly, at mid  $q_L$  with high power neutral beam heating, the electron temperature drops when the beams turn on; the profile broadens and becomes trapezoidal. When the electrons reheat and the temperature saturates the profile is once again of the exponential form.

### 3. SAWTEETH

The sawtooth cycle [3] results from the thermal runaway of the plasma column which causes the central current density  $J$  to rise. In the Kadomtsev mode [4] the

crash occurs when  $q = rB_0/RB_\theta < 1$ : the  $m = n = 1$  tearing mode grows from the  $q = 1$  radius until it encompasses the entire central plasma and expels the hot plasma to the outside. Significant discrepancies between the Kadomtsev model and experimental observations of sawteeth have been noted. The precursor oscillation measured prior to the crash could be quite small, indicating that the  $m/n = 1$  magnetic island was very small [5]. Moreover, a successor oscillation is often seen after the crash [5]. Very short crash times, apparently independent of resistivity [6, 7], and compound sawteeth [8] also did not fit the Kadomtsev model. We show that in discharges with good central confinement, the current profile develops a distinct skin current which causes  $q$  to fall below one at a finite radius  $r_s$ . Compound and normal sawteeth are produced which are consistent with the experimental observations.

We integrate the 2-D reduced resistive MHD equations for helical perturbations with a self-consistent evolution equation for the electron temperature:

$$\begin{aligned} d\nabla_\perp^2 \phi/dt - \mu \nabla_\perp^4 \phi &= \bar{\mathbf{B}} \cdot \nabla \mathbf{J} \\ \nabla_\perp^2 \psi &= \mathbf{J} - 2n/m; \quad \partial\psi/\partial t = \bar{\mathbf{B}} \cdot \nabla \phi + \eta \mathbf{J} \\ dT/dt - \nabla_\perp \cdot \kappa_\perp \nabla_\perp T - \kappa_\parallel (\bar{\mathbf{B}} \cdot \nabla)^2 T &= \Omega \eta \mathbf{J}^2 \end{aligned}$$

where  $d/dt = \partial/\partial t + \bar{\mathbf{v}} \cdot \nabla$ ,  $\bar{\mathbf{v}} = \hat{\mathbf{z}} \times \nabla \phi$ ,  $\bar{\mathbf{B}} = \hat{\mathbf{z}} \times \nabla \psi$ ,  $\phi$  and  $\psi$  being the stream and helical flux functions,  $\Omega = a^2 B_0^2 / 4\pi n R^2 \hat{T}$  with  $\hat{T}$  an arbitrary normalization for  $T$ ,  $\eta = \hat{\eta}/T^{3/2}$ , and other notation standard. Times are normalized to the Alfvén time,  $\tau_A = R/c_A$ , and perpendicular scales to the minor radius,  $a$ . The perpendicular conduction  $\kappa_\perp = \kappa_{\perp 0} (1 + \alpha |\nabla T|^2)$ , with the parameters  $\alpha$ ,  $\kappa_{\perp 0}$ ,  $\hat{\eta}$ ,  $\mu$  and  $\kappa_\parallel$  all constants. This form for  $\kappa_\perp$  allows us to reduce the central perpendicular conduction ( $\kappa_{\perp 0}$ ) compared with that at the edge and produces the trapezoidal temperature profiles measured at low edge  $q$  (Fig. 1(a)). A theoretical model which justifies such a form is presented in Section 3 of this paper.

We first demonstrate that the structure of the sawteeth in our simulations is controlled by the resistivity (temperature) profile and therefore the profile of  $\kappa_\perp$  [9]. In Fig. 3(a) we show the time dependence of  $T$  ( $r = 0$ ) for a typical run with constant  $\kappa_\perp$  ( $\alpha = 0$ ). Other parameters are  $\hat{\eta} = 2 \times 10^{-5}$ ,  $\Omega = 1$ , and  $\kappa_\parallel = 60$ . The sawteeth in this simulation are in excellent agreement with the Kadomtsev model ( $q$  first falls below one at  $r = 0$ ) but the discrepancies with experiment remain. In Fig. 3(b) there is a similar trace of  $T(t)$  for a typical simulation with  $\kappa_\perp$  reduced around the centre of the plasma column ( $\alpha = 1$ ). Figure 4 shows profiles of  $T$ ,  $\mathbf{J}$ , and  $q$  at three times during the sawtooth rise from this run. The rate of rise of  $T$  is now nearly constant until the crash, while the central temperature profile remains rather flat, in agreement with the TFTR observations. More significantly, the current profile develops a skin current causing  $q$  to first fall below one at a finite radius  $r_s$ . For

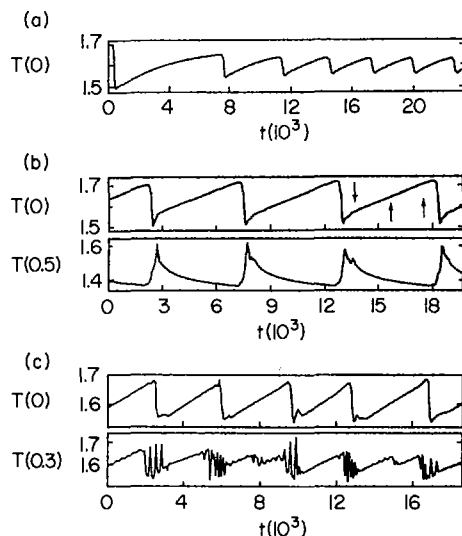


FIG. 3. Temperature versus time for (a) constant  $\kappa_{\perp}$ , (b) reduced  $\kappa_{\perp}(0)$  and (c) reduced  $\kappa_{\perp}(0)$  with lower resistivity.

such a  $q$  profile, all the previously mentioned experimental discrepancies with the Kadomtsev model can be understood easily.

We first focus on the sawtooth crash. For a  $q$  profile of the form shown in Fig. 4(c) with  $\Delta q_0 = 0$ , the helical flux is reversed only in a narrow band  $\Delta r$  around  $r_s$  (Fig. 5(a)). Resistivity allows the reversed flux to reconnect as shown in Fig. 5(b). At this point the tension in the helical field drives the plasma toward the circular bubble configuration (Fig. 5(c)). Since no topological change in the magnetic configuration is required for this transition to occur, the formation time of the bubble is the helical Alfvén time,  $\tau = \tau_A / \Delta q_s$ . Finally, on the same helical MHD time-scale the bubble moves to the centre of the plasma column, causing the crash of the central electron temperature observed experimentally. Detailed MHD simulations of the crash have been completed for several values of  $\Delta q_s$  over a range of resistivity from  $10^{-4}$  to  $6 \times 10^{-7}$ . The crash velocity  $V_c$  from these simulations (points) are compared with the theoretical value,  $V_c = \Delta q_s r_s / \tau_A$  (solid curve), in Fig. 6. The error bars represent the scatter of points over the range of resistivities studied. This figure confirms that the crash time is given by the helical Alfvén time, independent of resistivity. Values of  $\Delta q_s$  as small as 0.004 can cause the  $50 \mu s$  crash time recently documented on TFTR [7].

When  $\Delta q_0 \neq 0$  but  $\Delta q_0 \ll \Delta q_s$ , the formation of the bubble is essentially unaffected by the central helical flux. The stronger magnetic field in the bubble simply pushes aside the weak central flux (Fig. 5(d)), producing a large residual magnetic island following the crash. Over a longer resistive time-scale the flux in

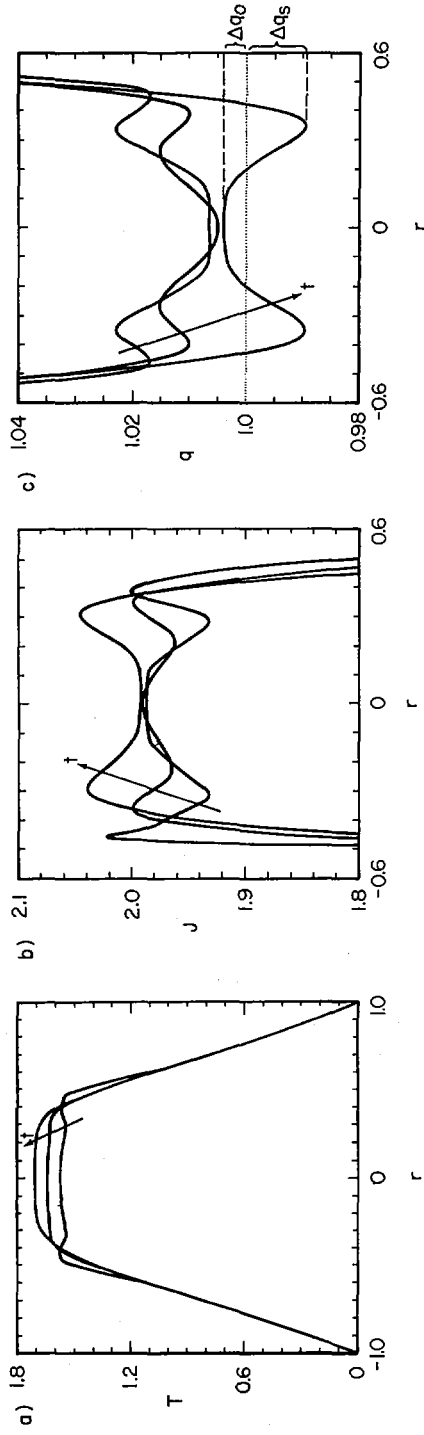


FIG. 4. Profiles of  $T$ ,  $J$ , and  $q$  at the three times shown by arrows in Fig. 3(b).

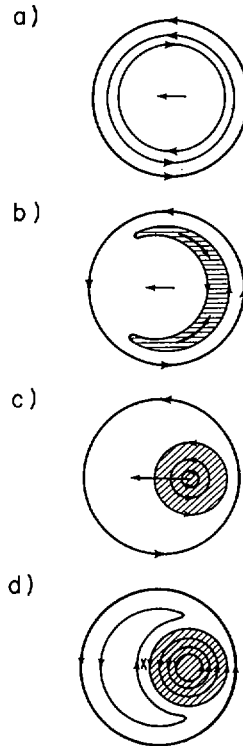


FIG. 5. Schematic of evolution of helical flux for current profile with skin currents and  $q(0) = 1$  [(a), (b), (c)] and  $q(0) \geq 1$  (d).

the residual island reconnects with that in the bubble and the column returns to a symmetric state. This residual magnetic island produces the successor oscillations which are often seen experimentally.

When  $\Delta q_0 > \Delta q_s \Delta r / r_s$ , the helical flux in the central plasma of Fig. 5(d) exceeds that in the bubble and the central temperature does not fall during the crash. Such a 'subordinate' crash occurs during compound sawteeth. An example of this phenomenon is shown in Fig. 3(c) from a simulation with  $\hat{\eta} = 10^{-5}$ ,  $\alpha = 1$ ,  $\Omega = 2$ , and  $\kappa_1 = 100$ . The third and fifth sawteeth are compound with subordinate crashes occurring near  $t = 7500$  and  $15\,000$ . Compound sawteeth occur at low edge  $q$  when  $\kappa_{\perp 0}$  and  $\hat{\eta}$  are small.

We emphasize that the magnetic island present prior to the crash can be very small as shown in Fig. 3(b). Since the area within the closed helical flux is conserved during the formation of the bubble from Fig. 3(b) to (c), an expression relating the bubble radius  $r_b$  to the island width  $w$  of the precursor is easily computed:  $w \approx r_b^2 / 2r_s$ . In recent observations of sawtooth crashes on JET, the formation of a bubble much like that shown in Fig. 5 was observed with no obvious precursor [6].

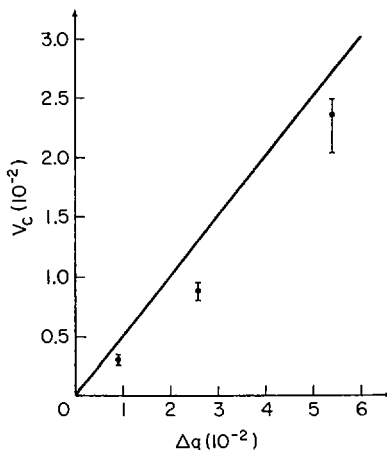


FIG. 6. Crash velocity versus  $\Delta q$ , for  $\Delta q_0 = 0$ .

However, in their experiment  $r_b \sim r_s/3$  and therefore  $w \sim r_s/18$  so that the precursor would be extremely small. It has been suggested that the pressure driven internal kink is responsible for the sawtooth crashes in the JET experiment [10]. The competition between reconnection and the pressure driving forces in causing the sawtooth crash is currently under investigation.

#### 4. A THEORETICAL MODEL FOR ENERGY TRANSPORT

The formation of trapezoidal temperature profiles similar to those observed on TFTR in our sawtooth simulations with a model cross-field conduction  $\kappa_{\perp} \propto |\nabla T|^2$  provides strong evidence for the role of the electron temperature gradient in causing anomalous transport. The electron temperature gradient is known to be an important source of free energy for instabilities causing such transport. The electron temperature gradient destabilizes the collisional trapped electron modes. However, the transport coefficient derived for such modes decreases very rapidly with increasing  $r$  contrary to experimentally inferred  $\chi_e$  profiles. Recently we have found [11] that the electron temperature gradient modes can also destabilize modes with wavelengths between the electron and the ion gyroradii. A systematic study of the mode in a sheared slab magnetic field geometry together with full gyrokinetic and finite beta effects yields modes with a threshold  $\eta_e = d \ln T_e / d \ln n \approx 1.0$ . Here,  $T_e$  is the electron temperature and  $n$  the density. The mode frequency ranges from 0.05 to 0.4 times the electron diamagnetic frequency  $\omega_{ne}^* = k_y c T_e / e B_0 L_n$  where  $L_n$  is the density scale length, and  $k_y$  is the azimuthal wavenumber.

Following a quasilinear theory, the anomalous electron energy coefficient is estimated to be

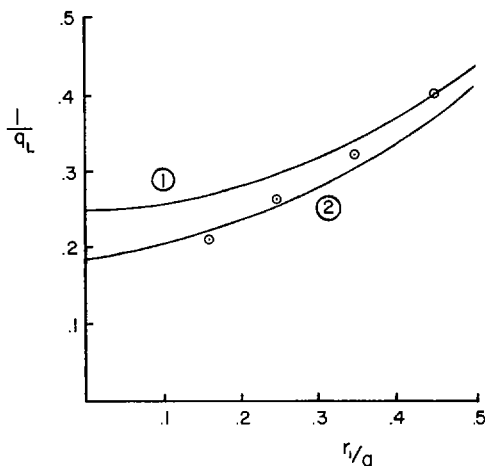


FIG. 7.  $1/q_L$  versus  $r_1/a$ : ① analytic model; ② numerical model; and ⊙ experimental points for TFTR [12].

$$\chi_e = 0.1 c^2 \hat{s} v_e \eta_e (1 + \eta_e) / \omega_{pe}^2 q R$$

where  $c$  is the velocity of light,  $v_e$  is the electron thermal velocity,  $\omega_{pe}$  the plasma frequency, and  $\hat{s} = d \ln q/d \ln r$ . One interesting feature that emerges from the above expression is that the temperature gradient dependence is similar to that used in the sawteeth studies.

We introduce this  $\chi_e$  into the steady state equations for electron energy transport in an ohmically heated tokamak. We assume that the density gradient is given by  $n = n_0 \exp(-\alpha r^2/a^2)$ ; here,  $\alpha \approx 2$ . From our numerical studies it is found that the central electron temperature  $T(0)$  scales as

$$T(0) \propto B_0^{2/3} R^{-1/3} a^{2/3} q_L^{0.19} \gamma^{1/3}(Z_{eff})$$

where  $\gamma(Z_{eff}) = Z_{eff}[0.29 + 0.46/(1.08 + Z_{eff})]$ . This is in reasonable agreement with the TFTR scaling [12].

$$T(0) \propto B_T^{0.6} R^{-0.1} a^{0.7} q_L^{0.2} Z_{eff}^{0.5}$$

Another interesting consequence of this thermal conduction coefficient is the relationship between  $r_1$ , the inversion radius for sawtoothing, and the limiter safety factor as shown in Fig. 7. Curve 1 corresponds to a simple analytical model, curve 2 to the full numerical model and the points correspond to data from TFTR [12]. Furthermore, we find that  $r_1/a = 0$  for  $q_L = 5.6$ . Thus for  $q_L > 5.6$  the discharges should

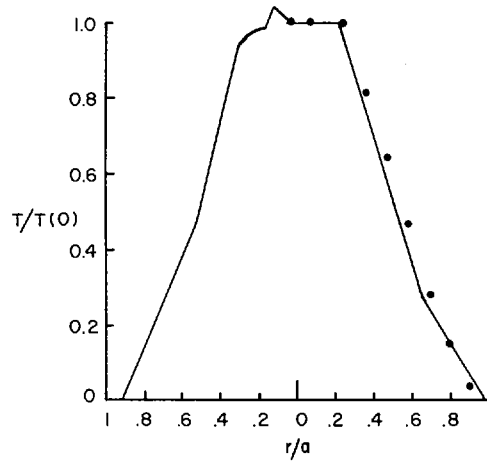


FIG. 8.  $T/T(0)$  versus  $r/a$ . Solid line is experimental data from TFTR ECE diagnostic for  $q_L = 3.3$ ,  $B = 3.04$  T,  $R = 2.79$  m,  $a = 0.55$  m.

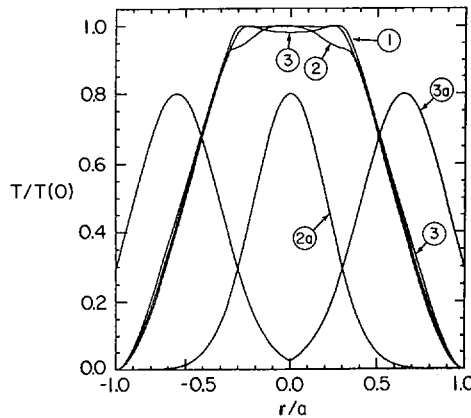


FIG. 9.  $T/T(0)$  versus  $r/a$  for  $q_L = 3.0$ ,  $\alpha = 2.5$ :  $\odot$  Ohmic profile;  $\ominus$  profile with auxiliary heating deposition profile given by  $\ominus$ ;  $\oplus$  profile with auxiliary heating deposition profile given by  $\oplus$ .

stop sawtoothing. Experimentally, for TFTR and Alcator it is found that the transition to non-sawtoothing discharges occurs around  $q_L = 7.0$ . Figure 8 shows a plot of the normalized temperature  $T/T(0)$  against  $r/a$  for TFTR from the ECE diagnostics. The dots correspond to the theoretical profile.

Next, we investigate the influence of auxiliary power on the temperature profiles. The theoretical expression for  $\chi_e$  has been incorporated into the sawtooth code. The profiles halfway up the sawtooth rise are shown in Fig. 9. Curve 1

corresponds to the Ohmic temperature profile. Curve 2 is the auxiliary heated plasma temperature profile for the same  $q_L$  as the Ohmic case and an auxiliary power profile given by curve 2a. The amount of auxiliary power is assumed to be four times the initial Ohmic power. Curve 3 is the auxiliary heated temperature profile for the auxiliary power deposition profile given by curve 3a. As can be seen, the only significant changes in the profile occur inside the inversion radius. These changes become even more significant as one goes to higher limiter safety factors. Thus for low  $q_L$  the present model shows that the electron temperature profiles are nearly invariant with different heat deposition profiles. However, as one goes to higher values of the limiter safety factor, the profiles can be modified significantly.

In conclusion, we may summarize that we have derived a transport coefficient for short wavelength temperature gradient driven instabilities which explain many facets of ohmically and auxiliary heated discharges.

### ACKNOWLEDGEMENTS

This work was supported in part by the US Department of Energy. It is a pleasure for us to acknowledge the support of PPPL and, particularly, the TFTR experimental group.

### REFERENCES

- [1] STAUFFER, F.J., BOYD, D.A., CUTLER, R.C., McCARTHY, M.P., *Rev. Sci. Instrum.* **56** (1985) 925.
- [2] FREDRICKSON, E., et al., in *Controlled Fusion and Plasma Physics (Proc. 13th Europ. Conf. Schliersee, 1986)*, Vol. 10, Part I, European Physical Society (1986) 41.
- [3] VON GOELER, S., STODIEK, W., SAUTHOFF, N.R., *Phys. Rev. Lett.* **33** (1974) 1201.
- [4] KADOMTSEV, B.B., *Fiz. Plazmy* **1** (1975) 710; *Sov. J. Plasma Phys.* **1** (1975) 389.
- [5] DUBOIS, M.A., MARTY, D.A., POCHELON, A., *Nucl. Fusion* **20** (1980) 1355.
- [6] EDWARDS, A.W., et al., *Phys. Rev. Lett.* **57** (1986) 210.
- [7] McGUIRE, K., private communication.
- [8] PFEIFFER, W., *Nucl. Fusion* **25** (1985) 673; CAMPBELL, D.J., et al., *Nucl. Fusion* **26** (1986) 1085; YAMADA, H., et al., Rep. PPPL-2213, Princeton Plasma Physics Laboratory (1986); KIM, S.B., private communication.
- [9] DENTON, R.E., DRAKE, J.F., KLEVA, R.G., BOYD, D.A., *Phys. Rev. Lett.* **56** (1986) 2477.
- [10] WESSON, J.A., *Plasma Phys. Controll. Fusion* **28** (1986) 243.
- [11] LEE, Y.C., DONG, J.Q., GUZDAR, P.N., LIU, C.S., Rep. No. 86-023, Maryland Univ., Baltimore (1986).
- [12] TAYLOR, G., et al., *Nucl. Fusion* **20** (1986) 339.

## DISCUSSION

L.E. ZAKHAROV: Have you any comment to make regarding the obvious contradiction between your theory of internal disruption and the TEXTOR  $q(0)$  measurements?

J.F. DRAKE: We are in the process of including toroidal effects in our code. There are two important points about sawteeth which will need to be carefully studied. The first point is the competition between the ideal and resistive modes. Both of them will produce similar signatures as far as the experiments are concerned. Which of them is used in the actual machine remains to be seen. The second point is the TEXTOR results, which require an appropriate explanation.

O. GRUBER: In Ohmic discharges the time behaviour of the electron temperature rise when the sawtooth drops is linear and in beam heated L-mode discharges it shows a saturation point. The latter behaviour is not present in your calculated  $T_e$  traces. Can you comment on this?

J.F. DRAKE: We do not always have a linear temperature rise. If the confinement is degraded in the centre of the plasma, the sawteeth distinctly rise. In our first simulations, all the sawteeth rounded out and virtually stopped rising during the rise phase. At least for the Ohmic case we found we had to reduce the condition in the centre in order to get the linear rise. And if your confinement is being degraded in beam heating, you also get saturation of the sawteeth.

R.E. WALTZ: The advantages of the  $\eta_e$  mode model for transport when describing profiles have been emphasized. I think, however, I should point out the disadvantages of this model in explaining the scaling of the confinement time. Firstly, the model has an Ohmic confinement time scaling roughly equal to  $\tau_{OH} \propto na^2Rq$ , in contrast to experiments (and dissipative trapped electron drift mode scaling), where it is  $\tau_{OH} \propto naR^2q$ . Secondly, and more seriously, the model has almost no relation to the scaling of the auxiliary heated confinement time  $\tau_{aux}$ . Thirdly, the model has weak power degradation,  $p^{-0.3}$ , as compared with  $p^{-0.6}$  for the  $\eta_i$  drift mode scaling. Most importantly, the model has no favourable scaling with field strength  $B$  or current  $I \propto B/q$ , as distinct from the  $\eta_i$  drift mode scaling, which fails to explain  $\tau_{aux}$  only by a dimensionless factor.

# FIRST RESULTS FROM THE HL-1 TOKAMAK

HL-1 TOKAMAK GROUP

(Presented by Shangjie Qian)

Southwestern Institute of Physics,  
Leshan, Sichuan,  
China

## Abstract

### FIRST RESULTS FROM THE HL-1 TOKAMAK.

The medium sized HL-1 tokamak (major radius  $R = 102$  cm, plasma minor radius  $a = 20$  cm), operating up to a toroidal field of 2.6 T and plasma currents of 150 kA, has produced sawtoothed plasmas of a line averaged electron density of  $3.3 \times 10^{13} \text{ cm}^{-3}$ , an average electron temperature of 700 eV and a global energy confinement time of 13 ms, without gas puffing. Its electromagnetic system, including a particularly heavy copper stabilizing shell (thickness  $d = 5$  cm,  $d/a = 1/4$ ,  $d/R = 1/20$ ) and closely packed, wedge shaped toroidal field coils, with a comparatively uniform toroidal field and well compensated stray fields, ensures maintaining stable discharge currents in equilibrium for a duration of over 1 s.

## 1. INTRODUCTION

The HL-1 tokamak has been in exploratory plasma operation for two experimental run seasons, April to August 1985 and May to August 1986. Preliminary experimental results obtained are reported in this paper.

HL-1 is the largest of the nine small and medium sized tokamaks currently being operated in China (Fig. 1). Its principal parameters are:

Parameter	Design value [1]	Used to date
Major radius, R (cm)	102	102
Plasma minor radius, a (cm)	20	up to 20
Toroidal field, $B_t$ (T)	5	0.3-2.8
Plasma current, $I_p$ (kA)	400	up to 150
Discharge duration (s)		up to 1.04
Toroidal field flat-top (s)		up to 2.8
Stray fields in plasma (T)	$2.5 \times 10^{-3}$	$\sim 10^{-4} B_t$
Toroidal field power supply (MW)	160	up to 66

The HL-1 tokamak is an axisymmetric device of circular plasma minor cross-section, with inductive current drive and Ohmic heating using a 1.75 volt-second flux swing iron core transformer, a 0.7 MJ capacitor bank, a DC flywheel generator and

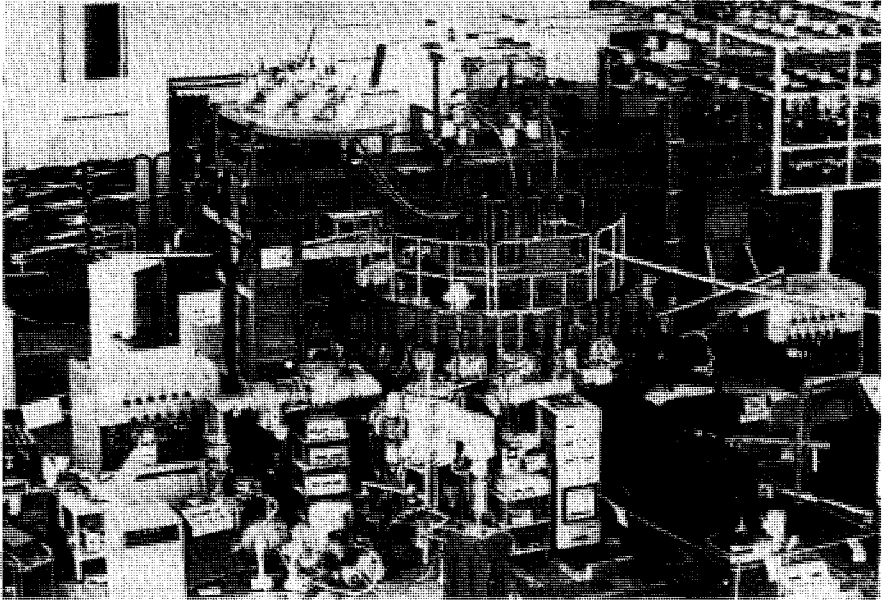


FIG. 1. HL-1 tokamak.

a 4.5 MJ energy storage inductor pulsed for a flat-top of several hundred milliseconds [2]. The inner vacuum chamber consists of four sections of bellows mechanically jointed and made of 0.5 mm thick Inconel-type alloy GH39 [3].

HL-1 features: (1) a copper stabilizing shell of record thickness  $d = 5$  cm ( $d/a = 1/4$ ,  $d/R = 1/20$ ), used also as the outer vacuum chamber, which, in combination with the wedge shaped and closely packed  $B_z$  coils (toroidally 82% to 90% copper covered, with total copper thickness of 13.6 cm), gives a skin eddy field diffusion time of well over 0.5 s; (2) a comparatively uniform  $B_z$  with 0.6% ripple at the magnetic axis; (3) stray fields (with compensation) of  $\sim 10^{-4} B_z$ ; (4) capability of long pulse operation.

## 2. OPERATING RANGE AND PLASMA PARAMETERS

The present exploratory phase of plasma experiments (1985–1986) aims at bringing out the basic capability and operating regimes of HL-1. To date, HL-1 has operated its toroidal field in the range of 0.3 to 2.8 T with plasma currents of up to 150 kA.

In summary, for stable discharges in hydrogen, we have obtained:

line averaged electron density, $\bar{n}_e$	$0.5\text{--}3.3 \times 10^{13} \text{ cm}^{-3}$
average electron temperature, $T_e$	700 eV
average ion temperature, $T_i$	$\sim 300 \text{ eV}$
global energy confinement time, $\tau_E$	13 ms
effective ionic charge, $Z_{\text{eff}}$	2.5–3
safety factor at limiter, $q(a)$	2.5–8

The diagnostics in use are magnetic and electric probes, bolometers, a 4 mm microwave interferometer, optical and VUV spectrometers, hard X-ray detectors and gold-silicon barrier soft X-ray detectors, and data acquisition with a computer having a total storage of about one billion bytes.

The average ion temperatures have been estimated by several methods, including SIMS analysis of the depth profile of hydrogen atoms implanted in movable silicon probes; the results, up to about 300 eV, are roughly in accord with the Artsimovich formula.

The global energy confinement time is given by

$$\tau_E = W/(P_\Omega - dW/dt), \quad W = 3\pi^2 R a^2 \bar{n}_e (T_e + T_i)$$

The experimental values, increasing with  $q(a)$ , ranged from 3 to 13 ms. For medium  $Z_{\text{eff}}$ , medium radiation power and sawtooth discharges with which we have been working, adopting Goldston's values [4] for the exponentials of  $R$  and  $a$ , we find the following scaling:

$$\tau_E(\text{ms}) = 7.9 \times 10^{-6} \bar{n}_e^{0.8} (10^{13} \text{ cm}^{-3}) R^{2.04}(\text{cm}) a^{1.04}(\text{cm}) q^{0.8}(a)$$

The average electron temperatures are found to scale with  $I_p/\bar{n}_e a^2$ .

### 3. DISCHARGE CHARACTERISTICS: TRANSIENT ELECTROMAGNETICS

After a great deal of breakdown experiments, field adjustments and vacuum conditioning [5, 6], some 2400 tokamak discharges have been documented preliminarily. They fall into two categories:

- (1) regular discharges, more than 95% of all shots;
- (2) disrupted and irregular discharges.

The regular discharges were the well adjusted and properly driven discharges. They are stable, well centred and reproducible for each fixed set of operating conditions. Figure 2 gives a historical sketch of the improvement in plasma currents.

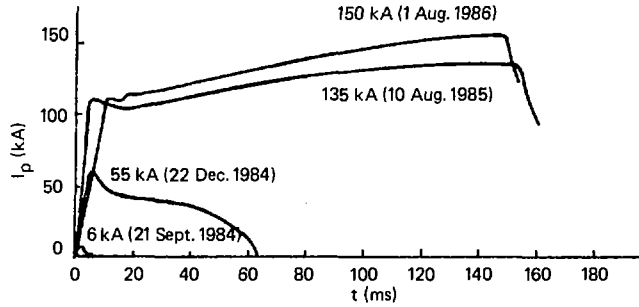


FIG. 2. Improvements in HL-1 plasma current.

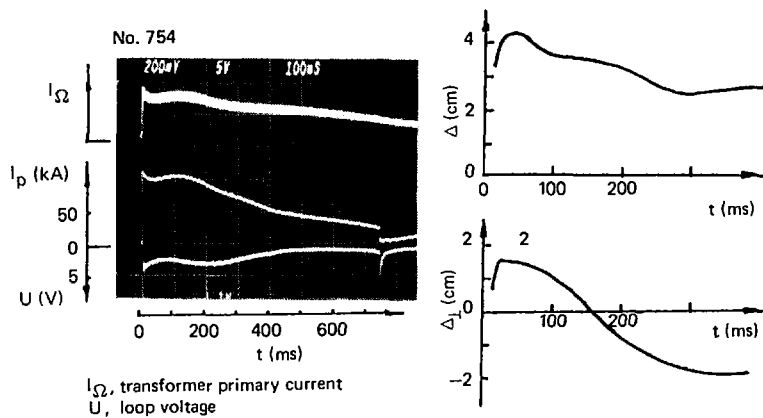


FIG. 3. Typical discharge in HL-1 (No. 754, hydrogen filling pressure =  $8.5 \times 10^{-4}$  torr,  $B_t = 2.0$  T).

A typical discharge is shown in Fig. 3. Each of these discharges consists of a fast current rise of 4 to 24 ms, usually with a slight overshoot, a current plateau of 150 to 200 ms, then turning into a stable, long decay of a duration that varies between 300 and 800 ms, finally terminated by loss of equilibrium. The whole discharge lasted for about 500 ms to 1040 ms.

The plasma current rise and plateau of these discharges were similar in pulse shape and duration, varying somewhat with the individual operating condition. The reproducibility and the similarity between the discharge currents during the 200 ms rise and plateau indicate that they were determined inherently by the electromagnetic system of the device.

The HL-1 plasma equilibrium is maintained by a set of quasi-DC (25 s) externally located vertical field coils, a set of fast pulsing internally located vertical field coils, and the copper shell and surrounding conductors. The toroidally directed

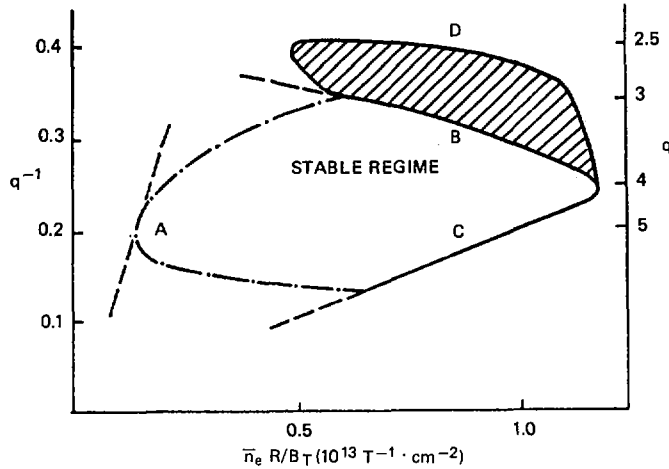


FIG. 4. Experimentally determined stable operation regime of HL-1. (A) runaway boundary, not determined; (B) low  $q$  operation boundary; (C) high density operation boundary; (D) low  $q$  operation boundary with gas puffing.

discharge current and all its surrounding conductors form a poloidally close coupled system, the secondary of the Ohmic transformer. The transformer primary power is fed into and drives the plasma current  $I_p$ . During the fast current rise, because of  $dI_p/dt$ , the main eddy currents in the copper shell, etc., are established simultaneously. By the end of the plateau, the iron core has exhausted its volt-seconds and begins working as an air core. The transformer primary circuit keeps on inputting, but much less effectively, some power into the discharge current up to over a second.

After the plateau, the discharge current, essentially, decays freely, its detailed shape being modified by the specific electron velocity distribution and current profile. Experimental indications are that there is a strong component of runaway electrons in many of the regular discharges.

#### 4. STABILITY

The MHD behaviour in HL-1 has been surveyed by using multi-location magnetic probes with Fourier analysers, and hard and soft X-ray detectors.

Figure 4 shows the experimentally determined stable operation regime for HL-1.

Figure 5(a) shows a sawtooth oscillation with a period of 0.9 ms. The relations

$$r_s(\text{cm}) = 0.5 a(\text{cm})/q^{1/2}(a) \quad \text{and} \quad \tau_s(\text{ms}) = n_{e0} (10^{13} \text{ cm}^{-3}) r_s^2(\text{cm}) R(\text{cm})$$

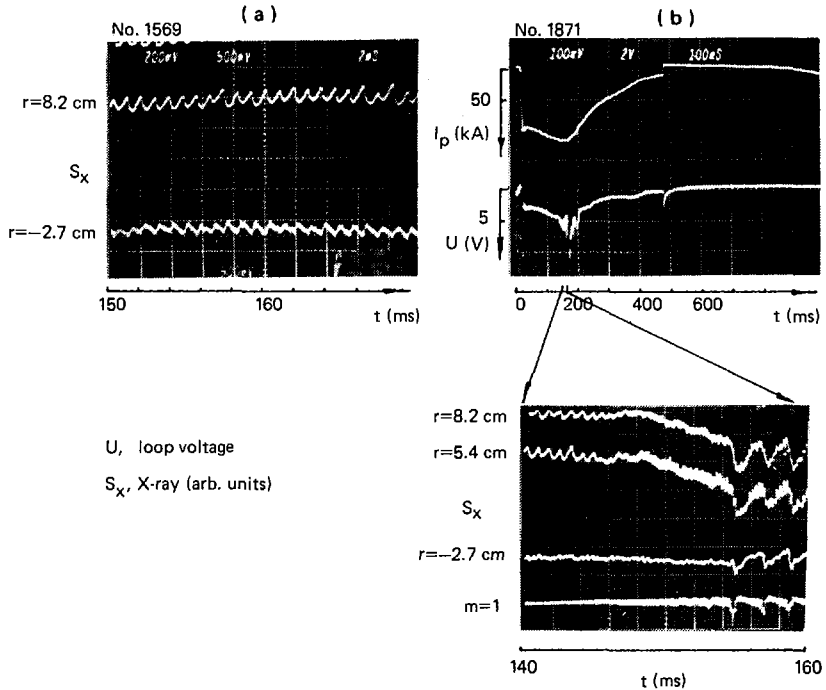


FIG. 5. Sawtooth oscillations from soft X-ray data: (a) steady sawtooth oscillation (No. 1569, hydrogen filling pressure =  $8 \times 10^{-4}$  torr,  $B_t = 2.0$  T); (b) changeover of sawtooth oscillations with internal disruption, accompanied by  $m = 1$  disturbance (No. 1871, hydrogen filling pressure =  $6 \times 10^{-4}$  torr,  $B_t = 2.5$  T). Negative value of minor radius refers to inboard position.

give 0.74 ms. Figure 5(b) shows the changeover of a sawtooth oscillation into another one, with larger amplitude and about twice the period. The event was marked by the occurrence of an internal disruption, accompanied by a growing  $m = 1$  disturbance.

Weak instabilities developed in a number of discharges. These usually occurred near the end of or after the plasma current plateau. Some of them were observed to be associated with  $m = 2$  or  $m = 2$  and  $m = 3$  precursors, appearing during the current rise. There were only rarely  $m = 3$  precursors alone.

In general, we may state that the MHD activities were observed to be impurity related. However, for operating densities of up to  $3.3 \times 10^{13} \text{ cm}^{-3}$ , very few discharges terminated in major (hard) disruptions. These occurred when a new movable limiter was put in without careful precleaning or when the horizontal fields were accidentally or intentionally off adjustment.

## 5. CONCLUSIONS

We arrive at the following conclusions concerning HL-1:

(1) Engineering performance, fabrication and assembly of the device prove to be gratifying, meeting and, in some respects, even surpassing the design requirements.

(2) Exploratory plasma operation has demonstrated the basic capability of HL-1 as designed and has provided a range of good plasmas for subsequent physics investigation.

(3) HL-1 could be a suitable device for studies of current drive by combining its inductive drive and long pulse capability with non-inductive drives, e.g. to study the production and evolution of suprathreshold electron populations and profile effects.

(4) Heavy conducting surroundings over a tokamak plasma, in conjunction with fine plasma profile control and adjustment, might offer some interesting possibilities for confinement experiments.

## ACKNOWLEDGEMENTS

The authors gratefully acknowledge the design and construction of HL-1 in the former HL-1 Division headed by He Chengxun; the diagnostics from the former Experiments Division led by Sun Xiang; early conceptual framework as established by Gu Yongnian's group. Numerous workers both inside and outside SWIP have contributed to this project.

## REFERENCES

- [1] LI, Zhengwu, in *Controlled Fusion and Plasma Physics* (Proc. 9th Europ. Conf. Oxford, 1979), Inv. Papers, UKAEA, Culham Laboratory, Abingdon (1979) 485.
- [2] ZE, M.R., CHENG, J.S., in *Fusion Engineering* (Proc. 11th Symp. Austin, TX, 1985), IEEE, New York (1986) 707.
- [3] ZHU, Y.K., et al., *J. Nucl. Mater.* **128&129** (1984) 784.
- [4] GOLDSTON, R.J., *Plasma Phys. Controll. Fusion* **26** (1984) 87.
- [5] LI, G.D., et al., *Nucl. Fusion Plasma Phys.* **6** (1986) 23 (in Chinese).
- [6] YANG, H.R., et al., in *Plasma-Surface Interactions in Controlled Fusion Devices* (Proc. 7th Int. Conf. Princeton, 1986), Paper 8.6.



# TOKAMAK CURRENT DRIVE VIA AC MAGNETIC HELICITY INJECTION

P.M. BELLAN, P.C. LIEWER  
California Institute of Technology,  
Pasadena, California

J.M. FINN, T.M. ANTONSEN, Jr.  
Laboratory for Plasma and Fusion Energy Studies,  
University of Maryland,  
College Park, Maryland

United States of America

## Abstract

### TOKAMAK CURRENT DRIVE VIA AC MAGNETIC HELICITY INJECTION.

With AC helicity injection, low frequency modulations of toroidal and/or poloidal magnetic fields produce an effective steady DC toroidal electromotive force which can sustain a DC toroidal current. Both toroidal-poloidal and poloidal-only modulation schemes are discussed. For the toroidal-poloidal scheme, analysis (in both one-dimensional and axisymmetric toroidal geometry) of the effect of the motion of the plasma-vacuum boundary shows that this motion may largely cancel the DC electromotive force. Thus, if toroidal-poloidal helicity injection is to work, there must be (i) no moving boundary or (ii) a less symmetric geometry. A low power toroidal-poloidal experiment (Caltech Encore tokamak) shows a change  $\Delta I$  in plasma current that is dependent on toroidal-poloidal phasing, but, because of an offset,  $\Delta I$  is always negative. The poloidal-only scheme is based upon the experimentally observed anomalous skin penetration during the startup phase of tokamaks. Analytic and numerical results indicate feasibility, and scaling of steady state current and power dissipated with frequency and plasma resistivity is presented. This scheme is potentially more efficient in terms of current generated per unit power dissipated than other current drive schemes. It is shown that the resistive MHD activity responsible for anomalous current penetration (and therefore required for the success of this current drive scheme) must be fully three-dimensional. A comparison of the effectiveness of this scheme with that of F- $\theta$  pumping in reversed field pinches is presented.

## 1. INTRODUCTION

AC magnetic helicity injection has been recently proposed [1]-[3] as a method for obtaining steady state toroidal current drive. This method utilizes AC modulations of the poloidal and/or toroidal magnetic fields at very low frequencies ( $\omega \ll \omega_{ci}$ ). Modulations of a few percent at frequencies of  $10^1$ - $10^2$  Hz could drive the current in a fusion reactor provided there is anomalous current penetration. In this paper we discuss both toroidal-poloidal modulation schemes (Caltech authors, Sections 2-3) and poloidal-only schemes (U. Maryland authors, Section 4).

## 2. EFFECT OF A MOVING BOUNDARY ON HELICITY INJECTION

Bellan [4] interpreted toroidal-poloidal AC helicity injection as resulting from the beating of two normal modes of the tokamak plasma: (1) modulation of the plasma minor radius driven by toroidal field modulation and (2) classical resistive diffusion (having skin depth penetration) driven by poloidal field modulation. This beating would produce a DC toroidal emf which could drive a DC toroidal current. The process was strictly one-dimensional (radial dependence only) and the resulting DC toroidal current was predicted to be a skin current; reconnection (a three-dimensional process) would be necessary to make the skin current penetrate.

References [1]-[3] implicitly assumed that plasma continuously filled the vacuum chamber right up to the wall. Yet, Ref. [4] showed that toroidal modulation should compress the plasma minor radius, so that plasma should detach from the wall, leaving behind a vacuum region. We have studied [5] the effect of the motion of the plasma-vacuum boundary using a one-dimensional slab model and found that this motion makes the current drive significantly less than predicted by Refs [1]-[4].

To obtain the one-dimensional slab model, zero-pressure resistive MHD equations in rectangular coordinates were used with  $x$  (radial) dependence only. The radial velocity  $U_x$  of the plasma was the  $\vec{E} \times \vec{B}$  velocity associated with the time-varying, but spatially uniform, toroidal field (long wavelength limit of the compressional Alfvén wave). The evolution of the total (DC plus AC) poloidal magnetic field  $B_y(x,t)$  was described by

$$\frac{\partial B_y}{\partial t} = - \frac{\partial}{\partial x}(U_x B_y) + \frac{\eta}{\mu_0} \frac{\partial^2 B_y}{\partial x^2} \quad (1)$$

This equation is valid only in the plasma, but not in the adjoining vacuum region. By including oscillation of the plasma boundary, this model conserves total plasma throughout the cycle. To complete the model, equations for  $B_y$  in the vacuum region between the plasma and the wall and in a region corresponding to the central hole of a tokamak are also included.  $B_y$  cannot be specified at the wall because it contains an unknown DC component. Instead, the current in the external poloidal field coil is specified, which then gives a jump in  $B_y(x,t)$  at the coil.

The solution of this system of equations and boundary conditions shows that the driven DC poloidal magnetic field scales as  $\bar{B}_y \bar{B}_x / B_0$  and thus, the driven DC poloidal field is always much smaller than  $\bar{B}_y$ . This is in contrast to the expectations of Ref. [4] which suggested that the driven DC poloidal field could be comparable to or larger than  $\bar{B}_y$ . When Eq. (1) was

solved with the effect of the moving boundary neglected (e.g. assuming plasma filled the region up to the wall throughout the oscillation cycle), then a significantly larger DC poloidal field was obtained. Note that plasma is not conserved when the moving boundary is neglected. In a real plasma experiment there is never a true vacuum region between the plasma and the wall because of ionization and cross-field diffusion. However, this plasma is likely to be highly resistive and thus the vacuum treatment may be more realistic.

The importance of a moving boundary is also manifested [6] by an apparent discrepancy between the helicity conservation equations of Jensen and Chu [3]

$$\frac{dK}{dt} + \int dS \cdot (\phi \vec{B} + \vec{E} \times \vec{A}) = -2 \int \eta \vec{J} \cdot \vec{B} d^3r \quad (2)$$

and of Moffatt [7]

$$\frac{dK}{dt} + \int dS \cdot \vec{B} (\phi - \vec{A} \cdot \vec{U}) = \eta \int d^3r (\vec{B} \cdot \nabla^2 \vec{A} + \vec{A} \cdot \nabla^2 \vec{B}) \quad (3)$$

which turn out to differ by a Lagrangian (i.e. moving boundary) term. Using Moffatt's equation (which incorporates a moving boundary) it is possible to show [6] that no DC current can be driven in an axisymmetric plasma having circular flux surfaces. It is still possible to inject net helicity in this situation, but the injected helicity does not drive DC currents because it is exactly consumed by the increase in helicity dissipation associated with the oscillating fields producing the injected helicity.

It is crucial to find whether (i) non-conservation of plasma makes it possible for the plasma to be compressed without producing a moving plasma-vacuum boundary, or (ii) non-axisymmetric mode structures would allow helicity injection in excess of the increased helicity consumption associated with the modes, because then the optimistic predictions of Refs [1]-[4] would hold.

### 3. EXPERIMENTS

Experimental studies of helicity injection are underway on the Caltech Encore high repetition rate research tokamak. Typical parameters are: H plasma,  $n \sim 10^{12} \text{ cm}^{-3}$ ,  $T_i \sim 1-10 \text{ eV}$ ,  $T_e \sim 5-15 \text{ eV}$ ,  $B \sim 100-300 \text{ G}$ ,  $I \sim 1-3 \text{ kA}$ , shot duration 1-3 msec, repetition rate 10-30 shots/sec,  $R=38 \text{ cm}$ ,  $a=10 \text{ cm}$ , poloidal and toroidal modulations 1-10% at 24 kHz, gap long way around in one torus quadrant.

Preliminary results, obtained at low power using signal averaging techniques, indicate a change in plasma current  $\Delta I$  dependent on the relative phas-

ing of the toroidal and poloidal modulations. However,  $\Delta I$  always has a negative offset so that only phase-dependent reductions in plasma current are observed. In agreement with theoretical prediction, the phase dependence flips sign when the DC toroidal field is reversed. However, for certain values of plasma current or toroidal field, the flipping of sign fails to occur (this is associated with a resonance in  $\Delta I$ ).

#### 4. CURRENT DRIVE USING POLOIDAL FIELD MODULATION ONLY

Motivated by the phenomenon of anomalous current penetration during tokamak startup, we investigate theoretically whether steady state current can be driven by oscillating the poloidal (Ohmic heating) coils only. If double tearing modes indeed cause anomalous penetration, the induced skin current parallel to the bulk current may penetrate anomalously, whereas the skin current induced in the other half of the cycle should be stable to tearing modes, and so penetrate only classically. This scheme is related to helicity injection by toroidal-poloidal modulation [1]-[3] (also called F- $\Theta$  pumping), but has the advantage that only one field (poloidal) is modulated. In the present scenario, the injected helicity is provided by the relaxations that are assumed to occur preferentially in one part of the cycle. This scheme is inherently low frequency because full nonlinear resistive MHD activity must occur within one cycle.

In our model the plasma is treated classically throughout the quiescent part of the cycle, in 1D (cylindrical) geometry. The double tearing activity is idealized by flattening the  $j_z$  profile ( $q$  profile) while conserving the magnetic helicity and the poloidal flux at the plasma edge, i.e. the flux linking the torus. The toroidal flux is assumed to remain constant throughout the process. Using this model it can be shown, by analytic and numerical means, that steady state current can indeed be driven, i.e. that no oscillation of the toroidal field is required. From the point of view of helicity injection, current can be driven against resistive decay, even though no helicity is injected by external circuits, for the following reason: when the skin current induced by the oscillating OH is negative, i.e. opposite to the main current, the rate of change of helicity  $dK/dt = -2\int \vec{E} \cdot \vec{B} dV$  is positive. On the other half of the cycle, the skin current penetrates, conserving helicity, so that the net change due to resistive decay of skin currents is positive.

The scaling of this scheme with frequency and resistivity can be estimated as follows. Balancing the resistive decay of helicity with the injection of helicity due to the decay of skin current, we find

$$\bar{I}_p \sim \frac{2\pi a (\omega \eta_e)^{\frac{1}{2}} \tilde{\psi}}{\langle \eta \rangle}$$

Thus, for a given flux swing  $\tilde{\psi}$  the mean current  $\bar{I}_p$  increases as the square root of frequency. The mean current is also enhanced if the edge resistivity  $\eta_e$  greatly exceeds the average resistivity  $\langle \eta \rangle$ . Here,  $a$  is the minor radius. If the flux swing  $\tilde{\psi}$  is the limiting factor, the optimum frequency is the highest frequency for which the double tearing modes can completely reconnect in one cycle. The ratio of the mean current to the magnitude of the oscillating skin current can also be estimated to be  $\bar{I}_p / |I_p| \sim \eta_e / \langle \eta \rangle$ , which is independent of frequency and can be made large if the edge resistivity is considerably higher than the average. The scaling for  $\bar{I}_p / P$ , the ratio of steady state current driven to the power deposited, can be obtained by similar arguments. The power deposited in the plasma is  $P = \int \vec{E} \times \vec{B} \cdot \hat{n} dS \sim \omega \bar{I}_p \tilde{\psi} L$ , where  $L$  is the plasma length  $L = 2\pi R$ . Therefore, we find

$$\frac{P}{\bar{I}_p} \sim \frac{\langle \eta \rangle^2 \bar{I}_p L}{\eta_e a \Delta_s}$$

where  $\Delta_s = \sqrt{\eta_e / \omega}$  is the skin depth. Recalling that  $P //$  for Ohmic heating is  $I_p^2 R / I_p \sim \langle \eta \rangle I_p L / \pi a^2$ , we see that the power dissipated in oscillating current drive, compared to pure inductive (OH) current drive producing the same current, scales as  $a \langle \eta \rangle / (\Delta_s \eta_e)$ . This dissipation is not much larger than pure Ohmic dissipation.

We have also investigated whether anomalous skin penetration and any oscillating current drive scheme based upon it can be due to single helicity  $m/n$  modes, behaving as  $\exp(im\theta - in\phi)$ , where  $\theta, \phi$  are poloidal and toroidal angles, respectively, or whether multiple helicity (3D) effects are required. We conclude that single helicity activity with  $m \geq 2$  cannot explain the results and such activity with  $m = 1$  modes is unlikely to do so. This conclusion is based upon the observation that the  $\vec{U} \times \vec{B}$  term for modes with  $m \geq 2$  cannot change the flux at the magnetic axis (the Cowling theorem). Modes with  $m=1$  can experience a change in flux at the magnetic axis, by Kadomtsev reconnections, but double Kadomtsev reconnections reduce the flux at the axis. That is, if anomalous current penetration is due to resistive MHD modes, fully three-dimensional behavior is required. Thus, magnetic surfaces may not exist in some areas in the plasma. This may lead to a natural flattening of the current profile, but may also allow transport of heat along ergodic magnetic field lines. It is an open question whether this latter phenomenon may lead to very poor energy confinement or whether the region of destroyed magnetic surfaces may be confined to a part of the plasma volume.

It is interesting to compare this oscillating current drive proposal for tokamaks to F- $\Theta$  pumping for RFP's. As we have discussed, the former scheme depends upon preferential MHD relaxation activity in one part of the cycle, whereas the latter scheme depends upon external injection of helicity. The helicity absorbed by the plasma in a cycle in F- $\Theta$  pumping is  $\Delta K_{\text{rfp}} = 4\pi^2 L \epsilon \bar{\psi} \bar{\phi}$ , where  $\bar{\psi}$  and  $\bar{\phi}$  are the amplitudes of the oscillating poloidal and toroidal fluxes, respectively. Also,  $\epsilon$  is an efficiency factor that is typically somewhat less than unity and depends critically upon the edge resistivity and the number of relaxations per cycle [8]. This efficiency is related to the loss of helicity in F- $\Theta$  pumping due to decay of skin currents. On the other hand, for this tokamak scheme, the helicity injected is of order  $\Delta K_{\text{tok}} = 4\pi^2 L B_z a \bar{\psi} \sqrt{(\eta(a)/\omega)}$ , from the scaling arguments above. From these relations it is clear that the current drive scaling is quite favorable compared to that for F- $\Theta$  pumping. Essentially,  $\Delta K_{\text{tok}}$  is first order in oscillating fluxes and  $\Delta K_{\text{rfp}}$  is second order. It appears, therefore, that there is little advantage to oscillating the toroidal field in a tokamak for this scheme.

In summary, we have shown that if relaxations flattening the skin profiles occur preferentially in that part of the cycle where the skin current is parallel to the bulk current, current drive can be achieved. Estimates based upon nominal parameters give 1 MA of steady state current driven per voltsec (amplitude) of oscillated flux, and dissipation comparable to Ohmic.

#### ACKNOWLEDGEMENT

This work was supported by the United States Department of Energy.

#### REFERENCES

- [1] BEVIR, M.K., GREY, J.W., in Proc. Reverse Field Pinch Theory Workshop, Vol. 3, Los Alamos Scientific Laboratory (1981) paper A-3.
- [2] SCHOENBERG, K.F., et al., Phys. Fluids 27 (1984) 548.
- [3] JENSEN, T.H., CHU, M.S., Phys. Fluids 27(1984) 2881.
- [4] BELLAN, P.M., Phys. Rev. Lett. 54 (1985) 1381.
- [5] LIEWER, P.C., GOULD, R.W., BELLAN, P.M., One-dimensional modeling of DC current drive by AC helicity injection, submitted to Phys. Fluids.
- [6] BELLAN, P.M., The adverse consequences of a moving vacuum-plasma boundary on axisymmetric helicity injection, Phys. Rev. Lett. 57 (1986) 2383.
- [7] MOFFATT, H.K., Magnetic Field Generation in Electrically Conducting Fluids, Cambridge University Press, Cambridge (1978) 43-45.
- [8] FINN, J.M., Phys. Fluids 29 (1986) 2630.

# STUDY OF ENHANCED CONFINEMENT AND $q = 2$ DISRUPTIVE MODES WITH FAST RISING CURRENT IN THE STOR-1M TOKAMAK

H. KUWAHARA, O. MITARAI<sup>1</sup>, E.J.M. VAN HEESCH,  
M. EMAAMI, A.H. SARKISSIAN, S.W. WOLFE,  
A. HIROSE, H.M. SKARSGARD  
Plasma Physics Laboratory,  
University of Saskatchewan,  
Saskatoon, Saskatchewan,  
Canada

## Abstract

STUDY OF ENHANCED CONFINEMENT AND  $q = 2$  DISRUPTIVE MODES WITH FAST RISING CURRENT IN THE STOR-1M TOKAMAK.

The STOR-1M tokamak can operate in three different modes — as a normal tokamak, as a tokamak with a fast current pulse superimposed on the normal plasma current, and as an AC tokamak. Magnetohydrodynamic activity is observed during the fast pulse which gives access to  $q(a)$  as low as 1.5. The fast pulse also produces delayed increases in density and temperature, possibly as a result of improved containment properties due to current profile modification. Recent results on AC operation with gas puffing are also presented.

## I. INTRODUCTION

STOR-1M is a small tokamak in which a fast current pulse (~20  $\mu$ sec duration) can be superimposed on the normal plasma current. The current pulse provides turbulent heating of the plasma. In addition it can provide a rapid variation of  $q(a)$  over a wide range, passing quickly through  $q$ -values that would normally lead to termination of the discharge. MHD activity can thus be observed on this fast time-scale, particularly in the important  $q=2$  range. In addition, the fast pulse can provide, on a longer time-scale governed by the magnetic diffusion time, a modification of the current density profile which can influence the plasma properties. Finally, the STOR-1M tokamak has also been operated in an AC mode; recent results on the beneficial effects of gas puffing on the AC operation are included in this report.

---

<sup>1</sup> Department of Electrical Engineering, Kumamoto Institute of Technology,  
4-22-1, Ikeda, Kumamoto 860, Japan.

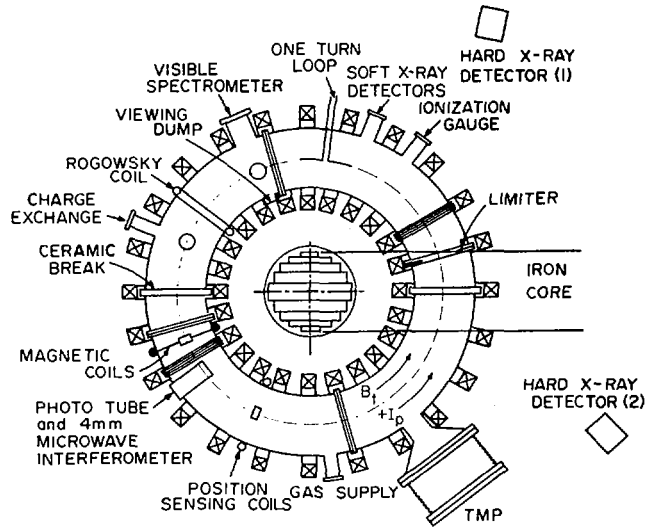


FIG. 1. Schematic diagram of the STOR-1M tokamak including diagnostics.

STOR-1M has major and minor radii of 22 cm and 3.5 cm respectively. The duration of the fast pulse is typically 20  $\mu$ sec and its maximum ramp rate exceeds  $10^9$  A/sec. The radial plasma position is controlled by a position feedback system, except during the turbulent heating pulse when the vacuum chamber acts as a conducting shell (field penetration time  $\approx$  130  $\mu$ sec). The duration of the ohmic discharge is about 5 msec. Typical plasma parameters are: initial filling pressure  $9 \times 10^{-4}$  Torr of hydrogen,  $I_p = 4$  to 7 kA,  $\bar{n}_e \lesssim 3 \times 10^{13}$   $\text{cm}^{-3}$ ,  $T_e \lesssim 100$  eV,  $Z_{\text{eff}} = 2$  to 3,  $q(a) \gtrsim 3.5$  and  $B_t = 0.5 - 1.0$  T. Diagnostic instruments include a 4 mm microwave interferometer, hard and soft x-ray detectors, a charge exchange analyzer and an optical spectrometer in addition to various standard magnetic coils as shown in Fig. 1.

## 2. MHD ACTIVITY DURING THE FAST PULSE

Previous studies of tokamak operation at low  $q$ -values show that some tokamaks can operate [1,2] below  $q=2$  while others exhibit major disruption [3,4] for  $q \sim 2$  to 2.5. The range of unstable  $q$ -values and the growth rate of the disruptive mode are still not well understood.

The turbulent heating pulse in STOR-1M is superimposed on the flat top portion of the ohmic discharge current where  $q(a) = 5.6$  at  $B_t = 1.0$  T, or  $q(a) = 4.5$  at  $B_t = 0.8$  T are chosen for

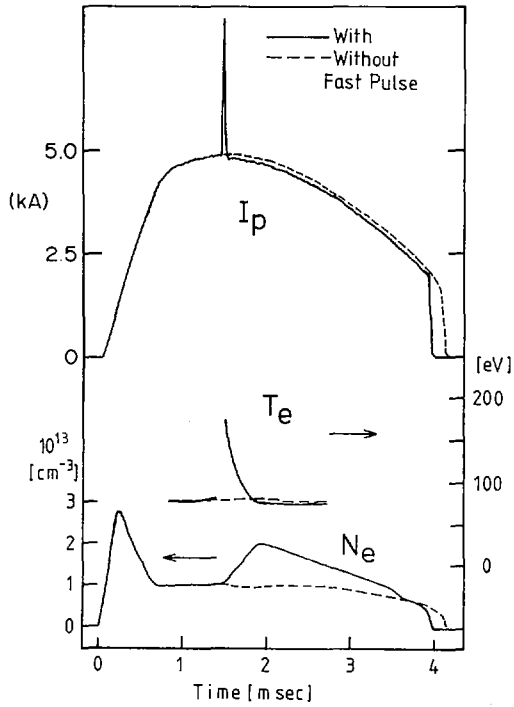


FIG. 2. Typical discharges with and without the fast turbulent heating pulse.

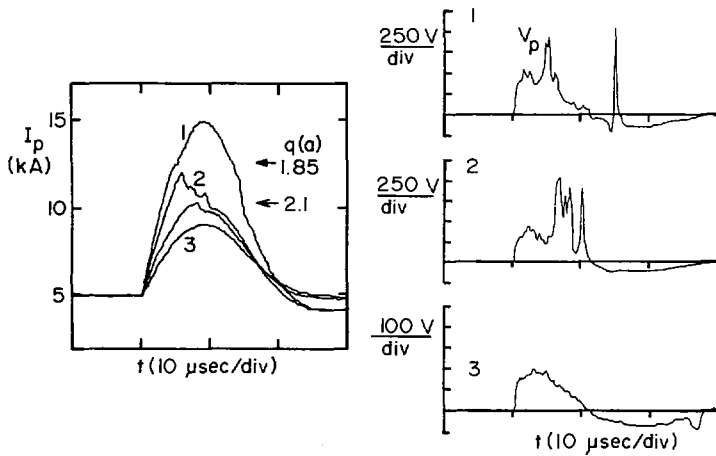


FIG. 3. Current and voltage traces during the fast pulse; large voltage spikes are observed for  $1.85 \leq q(a) \leq 2.1$ .

the initial conditions. Typical discharges with and without turbulent heating are shown in Fig. 2. By varying the charging voltage of the turbulent heating capacitor bank, the current ramp rate can be changed up to a maximum of  $1.8 \times 10^9$  A/sec.

As shown in Fig. 3, when  $q(a)$  is above 2.1, there are no large voltage spikes and the discharge is stable. Voltage spikes appear below  $q(a) = 2.1$  and disruptions begin to be noticeable on the plasma current trace. When the plasma remains below  $q(a) = 2.1$  for a longer time, higher voltage spikes are observed and complete termination of the plasma current occasionally takes place. The plasma becomes stable, with no voltage spikes, below  $q(a) = 1.85$  if the ramp rate exceeds  $4 \times 10^8$  A/sec at  $q(a) = 2.1$ ; stable discharges at  $q(a)$  as low as 1.5 have been achieved. After the peak current, voltage spikes are apparent as the plasma current decrease takes  $q$  through the unstable region ( $1.85 \leq q(a) \leq 2.1$ ).

In the unstable region, MHD activity is monitored with magnetic coils. Plasma disruption is preceded by rapid growth of a magnetic perturbation whose growth time ( $\sim 500$  nsec) is still 100 times longer than the Alfvén time. The largest magnetic perturbation observed is  $\tilde{B}_\theta/B_\theta \sim 0.03\%$  at the coil ( $r = 5$  cm). The magnetic island width ( $m=2/n=1$ ) estimated from this amplitude [5] is  $\leq 5\%$  of the minor radius, insufficient to cause disruption.

In the LT-4 tokamak an  $n=1$  mode was detected, whose amplitude was also not large enough to cause the observed disruption [4]. (Although its  $m$ -number was not determined, the central portion of the hot plasma core showed an asymmetric profile before a major disruption.) Thus the growth of magnetic perturbations prior to disruption may not play an important role in causing the disruption.

### 3. PLASMA HEATING

So far, noise problems have prevented us from measuring the electron and ion temperature increase during the heating pulse itself. An indication of effective heating is found from measurements of the resistivity at peak current (Fig. 4). The resistivity increase with applied voltage demonstrates the enhanced power input ( $P_{in} \propto \Delta I_p^n$ ;  $n > 2$ ) due to current-driven turbulence.

Electron temperature measurements are available after 0.15 msec from the heating pulse. For moderate applied voltage the temperature reproducibly decays within  $\sim 0.3$  msec, from  $\sim 200$  eV down to the value ( $\sim 100$  eV) measured without the fast pulse.

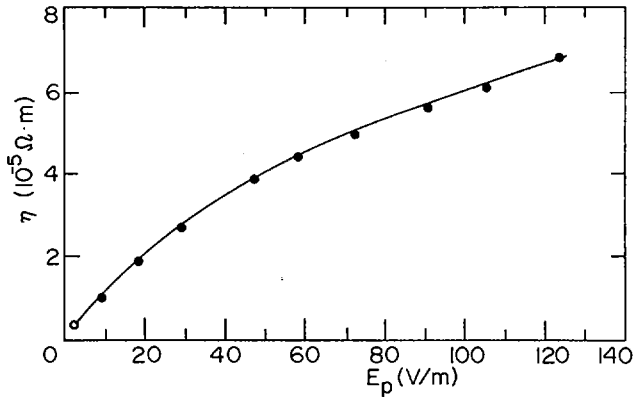


FIG. 4. Plasma resistivity during the fast pulse as a function of the applied voltage (O — in the ohmic discharge).

When the applied voltage is increased to  $\geq 60$  V/m the electron temperature, instead of decaying with time, shows a double-hump behaviour, the second peak coinciding approximately with the observed peak in  $n_e(t)$  (see Fig. 2). It is as though the containment is improving, leading to an increase in the energy density  $nT$ . The implied improvement in containment is generally greater, the larger the applied voltage, although reproducibility deteriorates at the highest voltages. ( $q(a) > 2.1$  for the range of voltages employed.)

A possible explanation for enhanced global confinement is the change in the current density profile produced by the fast current pulse. Until the magnetic diffusion ( $\tau \sim 0.15 - 0.6$  msec) can redistribute the current perturbation, the current density profile is flattened somewhat.

A similar observation of delayed "heating" following the turbulent heating pulse has been observed in the TORTUR tokamak [6]. In that case it has been attributed to a conversion of magnetic energy into thermal energy, supposing that the current channel expands again from a contracted state which is assumed to be formed just after the application of the fast pulse. Accurate measurements of the time variation of the current density profile may be required in order to choose between the two proposed explanations.

The case of a turbulent heating current pulse applied in the opposite direction to the ohmic heating current was also studied in STOR-1M. Although there is a small density increase

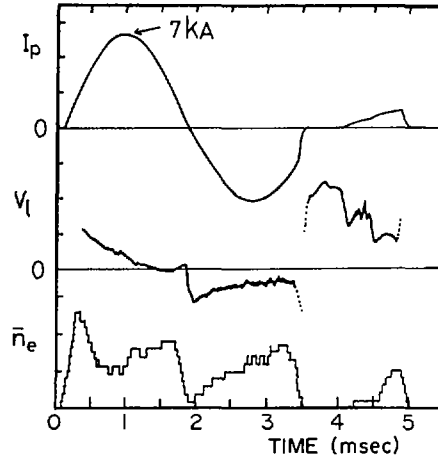


FIG. 5. AC tokamak discharge with gas puffing.  
 $I_p$  (2.64 kA/div),  $V_t$  (10 V/div),  $n_e$  ( $2 \times 10^{12}$  cm $^{-3}$ /step),  $B_z = 1$  T.

after the pulse, no plasma heating is observed with this arrangement. Apparently the current density profile produced by the negative fast pulse is not favourable either for heating or confinement.

#### 4. AC OPERATION WITH GAS PUFFING

Since 1984, AC operation has been studied in STOR-1M as a possible approach to quasi-continuous tokamak operation. Stable reproducible AC discharges have been obtained without disruptive behaviour or plasma extinction during current reversal [7], even with reversal times  $2I_{p0}(dI_p/dt)^{-1}$  an order of magnitude longer than the energy containment time. Synchronization of the zero crossing time for the vertical magnetic field and the plasma current is the most important single factor in achieving AC operation.

The original experiments, with no gas puffing, exhibited a density decay to  $\sim 2 \times 10^{12}$  cm $^{-3}$  at reversal, followed by a slight increase (to  $\sim 4 \times 10^{12}$  cm $^{-3}$ ) in the reverse half-cycle. Gas puffing has now been employed in an attempt to improve the density behaviour. Typical results are shown in Fig. 5. With appropriate activation of the piezoelectric valve the electron density now reaches approximately the same value in the first and second half-cycles of AC operation. It is also possible to

achieve current reversal at higher plasma currents ( $I_{po} \leq 8$  kA instead of 6 kA). The density at current reversal, however is still about the same as without gas puffing.

This work was supported by the Natural Sciences and Engineering Research Council of Canada.

### REFERENCES

- [1] MIRNOV, S.V., SEMENOV, I.B., Sov. Phys. — JETP **33** (1971) 1134.
- [2] DIVA Group, Nucl. Fusion **20** (1980) 271.
- [3] TOI, K., et al., Nucl. Fusion **22** (1982) 465.
- [4] KUWAHARA, H., et al., private communication, 1986.
- [5] TFR Group, Rep. EUR-CEA-FC-1151, Groupe de recherches sur la fusion contrôlée, Association Euratom-CEA, Centre d'études nucléaires de Fontenay-aux-Roses (1982).
- [6] DE KLUIVER, H., et al., "Plasma heating in the TORTUR tokamak by low-frequency toroidal current pulses", Controlled Fusion and Plasma Physics (Proc. 12th Europ. Conf. Budapest, 1985), Vol. 2, European Physical Society (1985) 272.
- [7] MITARAI, O., et al., Bull. Am. Phys. Soc. **29** 8 (1984) 1337; Rep. PPL-75, Plasma Physics Laboratory, University of Saskatchewan (1984).



## COHERENT AND TURBULENT FLUCTUATIONS IN TFTR

K. McGUIRE, V. ARUNASALAM, M.G. BELL, M. BITTER,  
 W.R. BLANCHARD, N.L. BRETZ, R. BUDNY, C.E. BUSH<sup>1</sup>, J.D. CALLEN<sup>2</sup>,  
 M. CHANCE, S.A. COHEN, S.K. COMBS<sup>1</sup>, S.L. DAVIS, D.L. DIMOCK,  
 H.F. DYLLA, P.C. EFTHIMION, L.C. EMERSON<sup>1</sup>, A.C. ENGLAND<sup>1</sup>,  
 H.P. EUBANK, R.J. FONCK, E. FREDRICKSON, H.P. FURTH,  
 G. GAMMEL, R.J. GOLDSTON, B. GREK, L.R. GRISHAM, G. HAMMETT,  
 R.J. HAWRYLUK, W.W. HEIDBRINK<sup>3</sup>, H.W. HENDEL<sup>4</sup>, K.W. HILL,  
 E. HINNOV, S. HIROE<sup>1</sup>, H. HSUAN, R.A. HULSE, K.P. JAEHNIG,  
 D. JASSBY, F.C. JOBES, D.W. JOHNSON, L.C. JOHNSON, R. KAITA,  
 R. KAMPERSCHROER, S.M. KAYE, S.J. KILPATRICK, R.J. KNIZE,  
 H. KUGEL, P.H. LaMARCHE, B. LeBLANC, R. LITTLE, C.H. MA<sup>1</sup>,  
 J. MANICKAM, D.M. MANOS, D.K. MANSFIELD, R.T. McCANN,  
 M.P. McCARTHY, D.C. McCUNE, D.H. McNEILL, D.M. MEADE,  
 S.S. MEDLEY, D.R. MIKKELSEN, S.L. MILORA<sup>1</sup>, D. MONTICELLO,  
 A.W. MORRIS<sup>5</sup>, D. MUELLER, E.B. NIESCHMIDT<sup>6</sup>, J. O'ROURKE<sup>7</sup>,  
 D.K. OWENS, H. PARK, W. PARK, N. POMPHREY, B. PRICHARD,  
 A.T. RAMSEY, M.H. REDI, A.L. ROQUEMORE, P.H. RUTHERFORD,  
 N.R. SAUTHOFF, G. SCHILLING, J. SCHIVELL, G.L. SCHMIDT,  
 S.D. SCOTT, S. SESNIC, J.C. SINNIS, F.J. STAUFFER<sup>8</sup>, B.C. STRATTON,  
 G.D. TAIT, G. TAYLOR, J.R. TIMBERLAKE, H.H. TOWNER,  
 M. ULRICKSON, S. VON GOELER, F. WAGNER<sup>9</sup>, R. WIELAND,  
 J.B. WILGEN<sup>1</sup>, M. WILLIAMS, K.L. WONG, S. YOSHIKAWA,  
 K.M. YOUNG, M.C. ZARNSTORFF, S.J. ZWEBEN

Princeton Plasma Physics Laboratory,  
 Princeton University,  
 Princeton, New Jersey,  
 United States of America

---

<sup>1</sup> Oak Ridge National Laboratory, Oak Ridge, TN, USA.

<sup>2</sup> University of Wisconsin, Madison, WI, USA.

<sup>3</sup> GA Technologies Inc., San Diego, CA, USA.

<sup>4</sup> RCA David Sarnoff Research Center, Princeton, NJ, USA.

<sup>5</sup> Balliol College, University of Oxford, Oxford, UK.

<sup>6</sup> EG&G Idaho, Inc., Idaho Falls, ID, USA.

<sup>7</sup> JET Joint Undertaking, Abingdon, Oxfordshire, UK.

<sup>8</sup> University of Maryland, College Park, MD, USA.

<sup>9</sup> Max-Planck-Institut für Plasmaphysik, Garching, Fed. Rep. Germany.

## Abstract

### COHERENT AND TURBULENT FLUCTUATIONS IN TFTR.

Classification of the sawteeth observed in the TFTR tokamak has been carried out to highlight the differences between the many types observed. Three types of sawteeth are discussed: "simple", "small", and "compound". During the enhanced confinement discharges on TFTR, sawteeth related to  $q = 1$  are usually not present, but a sawtooth-like event is sometimes observed. Beta approaches the Troyon limit only at low  $q_{cyl}$  with a clear reduction of achievable  $\beta_n$  at high  $q_{cyl}$ . This suggests that a  $\beta_p$  limit, rather than the Troyon-Gruber limit, applies at high  $q_{cyl}$  in the enhanced confinement discharges. These discharges also reach the stability boundary for  $n \rightarrow \infty$  ideal MHD ballooning modes. Turbulence measurements in the scrape-off region with Langmuir and magnetic probes show strong edge density turbulence,  $\bar{n}/n = 0.3 - 0.5$ , with weak magnetic turbulence,  $\bar{B}_\theta/B_\theta > 5 \times 10^{-6}$ , measured at the wall, but these measurements are very sensitive to local edge conditions.

### 1. Introduction

Near-term achievement of ignition in tokamaks depends on overcoming anomalous heat conduction and/or control of the central energy transport due to sawteeth. Sawteeth in TFTR have been studied (Section 2) in an attempt to understand the mechanism that causes the sawtooth crash and gives rise to enhanced heat pulse propagation. The MHD activity observed in enhanced confinement discharges (locally known as supershots) and the constraints imposed by the Troyon and the  $\beta_p$  limit are discussed in Sections 3 and 4. In Section 5, a summary of turbulence measurements carried out on TFTR is presented, and the correlation between edge turbulence and gross confinement is examined. Finally in Section 6, we summarize the results of the coherent and turbulent fluctuations measured in TFTR.

### 2. Sawtooth Activity

Three types of sawtooth activity have been identified in TFTR: (1) simple or normal sawteeth, (2) small sawteeth, and (3) compound sawteeth. Simple sawtooth oscillations, as observed in most tokamaks, are a series of  $m/n = 0/0$  relaxations, each with an  $m/n = 1/1$  precursor mode, where  $m$  and  $n$  are poloidal and toroidal mode numbers, respectively. Figure 1a shows a simple sawtooth which is observed in TFTR plasmas with a small  $q = 1$  radius and high  $q_a$ . Small sawteeth (Fig. 1b) are similar to simple sawteeth in period, but the  $m/n = 1/1$  mode is different. While the precursor oscillations before the  $m/n = 0/0$  crash are usually not present or have very small amplitude, the successor oscillations have a large amplitude. Compound (sometimes called "double") sawtooth activity (Fig. 1c) has been observed recently in many tokamaks [1-3]. Each compound sawtooth consists of a subordinate relaxation followed by a large (up to 20% in central  $T_e$ ) main relaxation with a smaller inversion radius. Compound sawteeth appear frequently in ohmically heated plasmas with high plasma

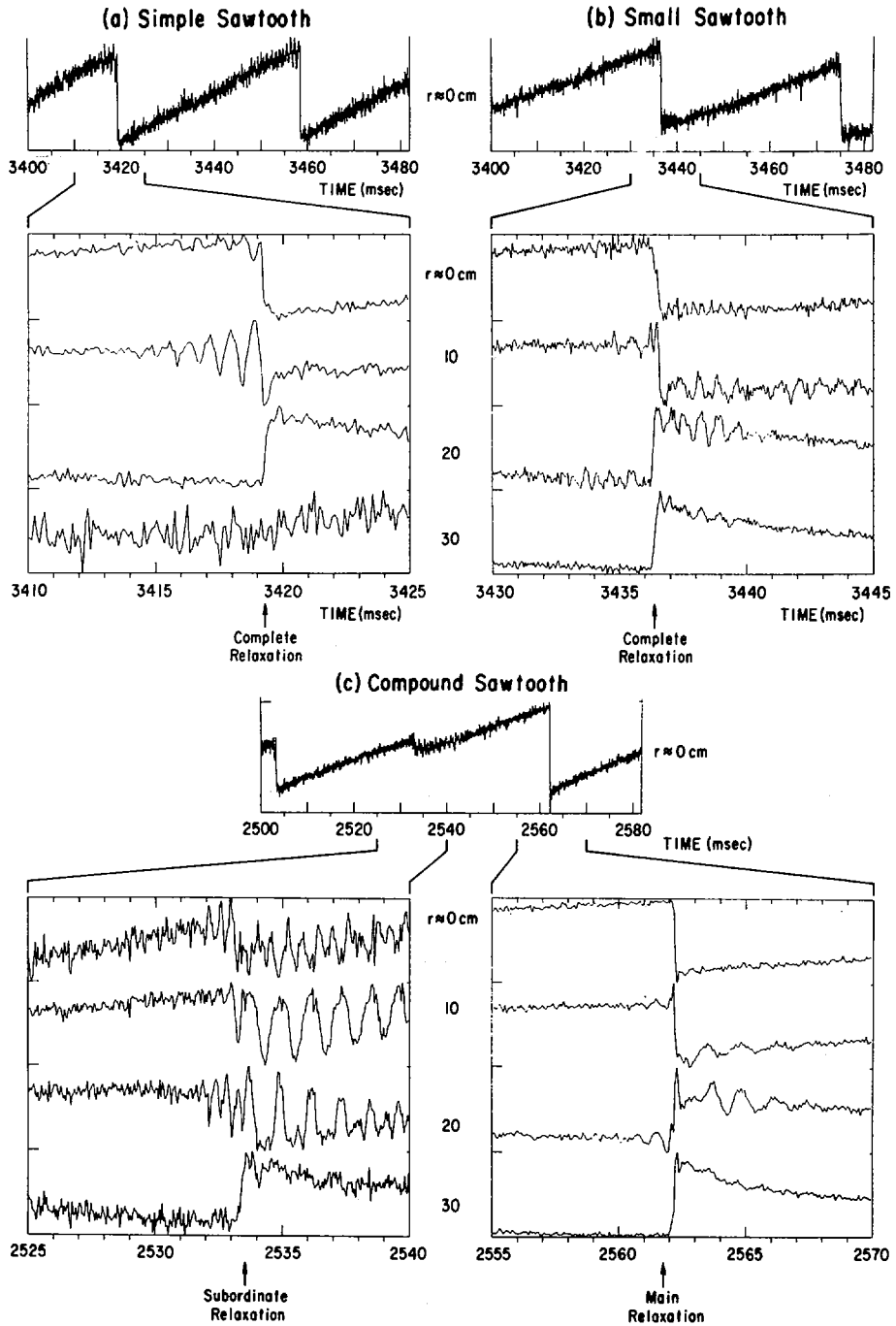


FIG. 1. Soft x-ray emissivity signals, indicating the three main types of sawteeth observed in TFTR. (a) Simple or normal sawtooth, (b) small sawtooth, and (c) compound sawtooth.

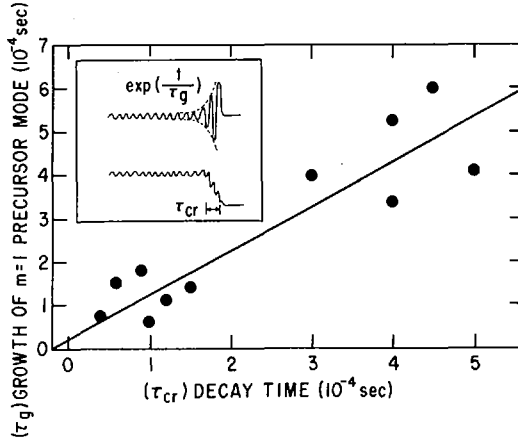


FIG. 2. Comparison between the growth time of the  $m = 1$  mode at the crash of the sawtooth and the crash time of the sawtooth, as measured by the central soft x-ray signal.

current ( $I_p > 1.0$  MA) and/or high density ( $\bar{n}_e > 2.0 \times 10^{19} \text{ m}^{-3}$ ). Sawteeth may switch from compound to small during the steady phase of a discharge, although global parameters such as averaged temperature, density,  $Z_{\text{eff}}$ , and even the inversion radius of the sawtooth do not change [2]. This suggests that small or localized changes of plasma parameters affect the characteristics of sawteeth significantly. The subordinate relaxation and the small amplitude of the  $m = 1$  precursor indicate that compound sawteeth and small sawteeth cannot be explained by the Kadomtsev model [4]. It has been found that the duration of the crash ( $\tau_{\text{cr}}$ ) is proportional to the final growth time ( $\tau_g$ ) of an  $m = 1$  mode during the crash phase itself (Fig. 2). Note that  $\tau_{\text{cr}}$  appears to be completely determined by  $\tau_g$ . Possible explanations include fast transport or reconnection due to: a) small perturbations at the  $q = 1$  surface, b) two  $q = 1$  surfaces [5] or c) a flat  $q$  profile with  $q_0$  close to 1 [1,6].

### 3. MHD Activity in Enhanced Confinement Discharges

Recent experiments on TFTR at low  $I_p$  and high-power balanced neutral beam injection (NBI) have achieved enhanced confinement relative to the predictions of L-mode scaling [7,8]. These discharges are remarkable from the MHD viewpoint, the most obvious feature being the lack of sawteeth during NBI for  $q_{\text{cyl}} > 5$ . This may be due to the removal of the  $q=1$  surface from the plasma (some data show  $r_{\text{inv}} \rightarrow 0$ ), but  $q_{\text{cyl}} < 5$  enhanced confinement discharges with sawteeth have  $r_{\text{inv}}$  unchanged. During enhanced confinement plasmas with  $q_{\text{cyl}} > 5$ , there are occasional sawtooth-like events which are similar to the subordinate relaxations described in

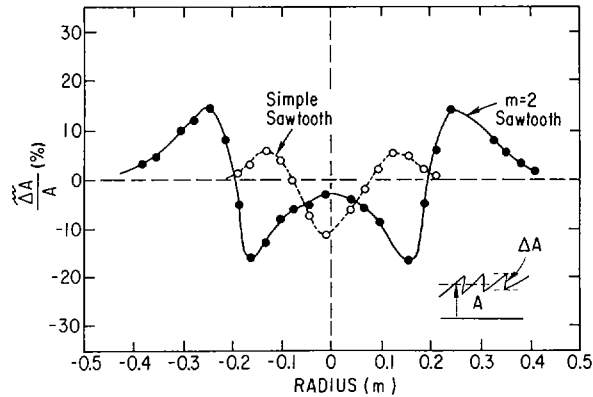


FIG. 3. Plot of  $\Delta A/A$  of the sawtooth crash versus radius, for an  $m/n = 1/1$  sawtooth in an L-mode,  $I_p = 900$  kA discharge with 3.4 MW of counter NBI, and an  $m/n = 2/1$  sawtooth in an  $I_p = 800$  kA enhanced confinement discharge with 10 MW of balanced NBI. The  $m = 2$  sawtooth-like event has an inversion at 0.2 m which is close to the calculated  $q = 2$  radius.

Section 2. They have only a small perturbation on axis and an inversion close to the calculated location of the  $q = 3/2$  or  $2/1$  surfaces. Figure 3 shows an  $m = 2$  sawtooth-like event which was observed in an enhanced confinement discharge with  $I_p = 0.8$  MA,  $q_{cyl} = 7.6$  and 10 MW of balanced NBI; the calculated  $q = 2$  radius for this discharge was about 0.25 m. In Fig. 3 the line-averaged soft x-ray inversion radius was about 0.20 m for the  $m = 2$  sawtooth, which was larger than the  $m = 1$  inversion radius observed at an  $m/n = 1/1$  sawtooth in an  $I_p = 0.9$  MA,  $q_{cyl} = 7.3$ , and  $P_{inj} = 3.6$  MW counter-injection L-mode discharge. The mode amplitude and the phase on the x-ray diodes clearly show an  $m = 2$  mode structure, also a small amplitude odd  $m$ -mode was present near the center. The magnetic signals at the wall show a clear  $m/n = 2/1$  mode with no coupled mode structure. These  $m = 2$  sawteeth are infrequent, with an irregular period, and they do not appear to affect the confinement of the discharge. The off-axis sawtooth events can occur during a period of continuous  $m/n = 3/2$  or  $2/1$  activity (detected by magnetic measurements at the wall) with no interruption of the oscillation. Similar type sawteeth have also been observed in pellet injection discharges during a period of continuous  $m = 1$  mode activity.

For identical operating conditions, enhanced confinement discharges can vary substantially, depending on the MHD activity. Figure 4 shows two such discharges, one with  $m/n = 2/1$  activity, the other without MHD activity. The correlation of the MHD activity with the drop in total stored energy and neutron emission is very clear. This can occur with  $m/n = 2/1$  alone, or  $m/n = 3/2$  alone. Figure 5 shows the coherent MHD activity versus the rate

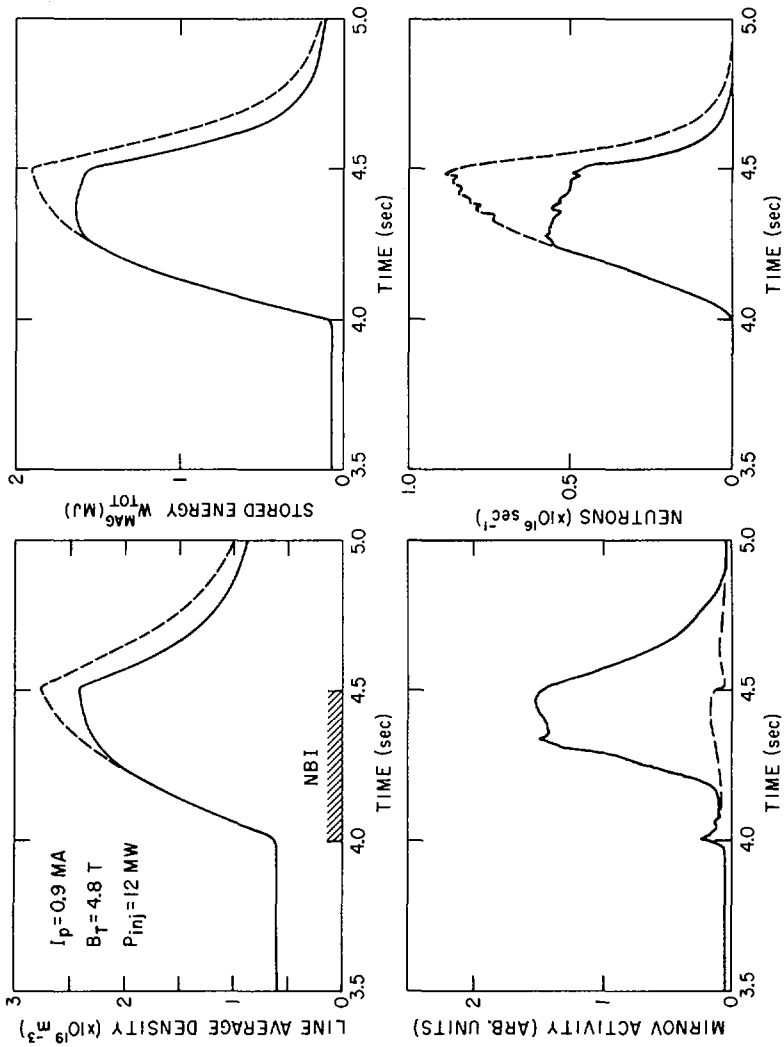


FIG. 4. Illustration of the effect of MHD activity on enhanced confinement discharges.

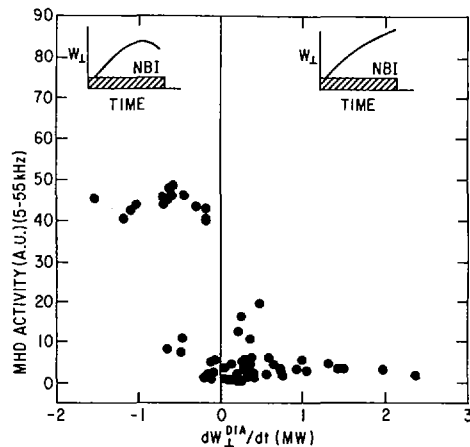


FIG. 5. MHD activity between 5 and 55 kHz versus  $dW_{\perp}^{DIA}/dt$ , 50 ms before the end of the beam pulse. These data include only enhanced confinement discharges. No similar correlation of MHD activity and confinement is seen for L-mode-type discharges.

of change of stored energy (calculated from the diamagnetic signal) 50ms before the end of the beam pulse. It is clear that a large amplitude of MHD activity is correlated with negative  $dW_{\perp}^{DIA}/dt$ . From delta-prime calculations on the  $j(r)$  profiles calculated by the TRANSP code [9] it is found that the profiles are sometimes unstable to the  $m/n = 2/1$  and/or  $m/n = 3/2$  modes. This implies that the  $j(r)$  profile may play an important role in the energy balance inside the  $q = 2$  surface for the enhanced confinement discharges on TFTR [10].

At lower  $q_{cyl}$  ( $< \sim 7$ ), bursts of  $m = 1$  activity are seen in the center of the plasma on the soft x-ray detectors. This mode couples out as  $m/n \sim 6/1$  on the Mirnov coils, similar to the fishbone oscillations observed on PDX. This is in contrast with the  $2/1$  and  $3/2$  modes which appear as  $m/n = 2/1$  and  $3/2$ , respectively, on the Mirnov coils, even though the mode amplitude peaks at a similar radius (0.1 - 0.3 m). There is no measurable effect on the neutron emission, due to  $m = 1$  activity at the levels observed to date, although we have observed coherent (5 kHz) oscillations in the charge-exchange neutral signals.

Enhanced confinement discharges which disrupt can lose most of the plasma energy in as little as 20 - 100  $\mu s$ , with only a low amplitude or no detectable MHD activity preceding them. The temperature on the inner wall, as measured by  $1.0 \mu m$  radiation, can rise to over  $1200^{\circ}C$  in 20  $\mu s$  after a high  $\beta_p$  disruption. In a

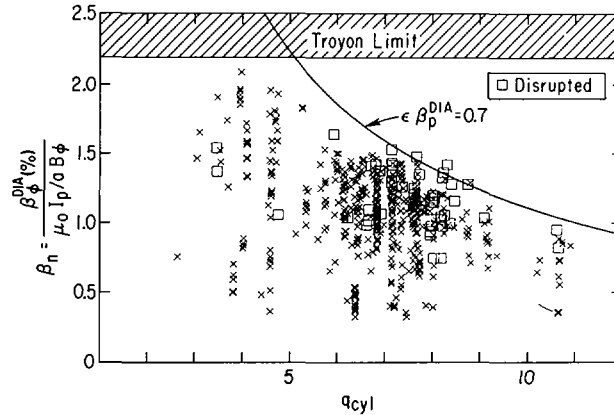


FIG. 6. The present enhanced confinement regime of TFTR on a plot of  $\beta_n$  versus  $q_{cyl}$ . The square symbols show discharges that disrupted during the neutral beam pulse. Also shown is a curve representing  $\epsilon \beta_p^{DIA} = 0.7$ , which fits the high  $q_{cyl}$  data better than the optimized Troyon limit.

few disruptive discharges, a 40 kHz mode growing on a 50  $\mu$ s time-scale, with an  $m = 1$  structure in the center and  $m > 4$ ,  $n = 1$  on the magnetic signals, has been observed. Although the bulk of the plasma energy is lost rapidly, the current disruption occurs up to 0.5 s later, after a narrowing of the  $T_e$  and X-ray emission profiles. It is also observed that few major disruptions take place for  $q_{cyl} < 5$ ; here the continuous 3/2 and/or 2/1 modes are detected and the energy is lost slowly, as in Fig. 4.

#### 4. BETA Limits

Enhanced confinement discharges with  $q_{cyl} < 5$  have values of normalized toroidal beta,  $\beta_n = \beta_\phi / \beta_c$  ( $\beta_c = \mu_0 I_p^2 / a B_\phi$ ), which approach the limit found from optimized ideal MHD kink stability theory [11,12]. This limit has previously been confirmed on other devices with NBI (DIII, PDX, ASDEX, ISX-B, for example). The experimental limit from these devices is  $\beta_n = 2.2 \sim 2.5$ , approximately independent of plasma shape, but only for a small range of aspect ratio and  $q_{cyl}$ . Figure 6 shows  $\beta_n$  for the enhanced confinement regime of TFTR versus  $q_{cyl}$ . Diamagnetic  $\beta_\phi^{DIA}$  (assuming a circular cross-sectional plasma) is used in Fig. 6 and, since the NBI is tangential, this underestimates the total  $\beta$  ( $< 10\%$  at high  $\beta_p$ ). It is seen that there is a clear fall of the achievable  $\beta_n$  with  $q_{cyl}$ . There is little published data from other auxiliary heated tokamaks in the high- $\beta_n$  high- $q$  region [13]. At high  $q_{cyl}$ , the limit appears to be disruptive, but at  $q_{cyl} < 5$  the  $\beta_n$  limit is associated with coherent MHD activity. Attempts to reach higher  $\beta_n$  by reducing  $(I_p, B_\phi)$  at constant  $q_{cyl}$  have not been successful. For a current ramp-down experiment with

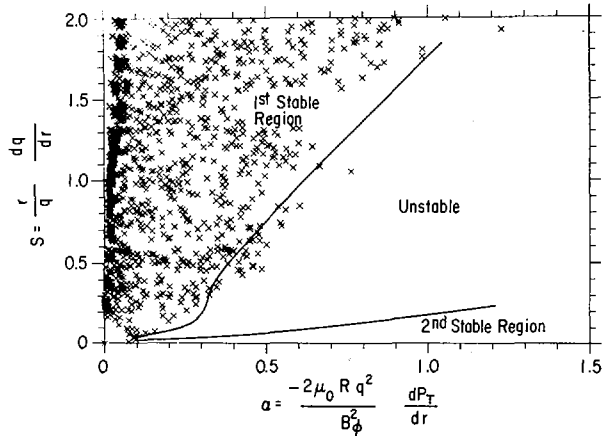


FIG. 7. Data from TFTR profiles on an  $S$ - $\alpha$  diagram for various types of discharge. The pressure profile used is the total pressure,  $(P_{\parallel} + P_{\perp})/2$ , calculated by the TRANSP code [9].

NBI,  $\beta_p$  reached 2.65 before the discharge disrupted; this  $\beta_p$  was not maintained in equilibrium. There appears to be a hard  $\beta_p$  limit at 2 - 2.2 or an  $\epsilon\beta_p \approx 0.7$  limit, as illustrated in Fig. 6. However, the range of the inverse aspect ratio  $\epsilon$  for the TFTR data is from 0.28 to 0.33 and it is not clear from this data whether  $\epsilon$  is an important parameter in the  $\beta$  limit.

The profiles of enhanced confinement discharges have been examined for violation of the high- $n$  ballooning mode stability criterion. Figure 7 shows points on the profile in the  $S$ - $\alpha$  diagram [14] (where  $S = r(dq/dr)/q$ ,  $\alpha = -2\mu_0 q^2 R(dP_T/dr)/B_\phi^2$ ) for various types of discharges. The pressure profile,  $(P_{\parallel} + P_{\perp})/2$  from the TRANSP code [9], which includes calculated beam and thermal ion pressure profiles and anisotropy, is used for  $dP_T/dr$  ( $\alpha_{\text{beam}} < 0.7 \alpha_{\text{total}}$ ). The beam-driven and bootstrap currents have been included in the calculation of  $q$ . The profile of maximum  $\beta_p$  hovers close to the curve for the large-aspect-ratio circular tokamak  $n \rightarrow \infty$  ideal ballooning-mode stability limit [14]. Though the profiles may be at the ballooning limit, these discharges are not the optimum for  $n \rightarrow \infty$  ballooning stability [15] ( $j(r)$  is not optimum). It is well known [16] that FLR, finite- $n$ , toroidicity, and pressure anisotropy effects can all lead to significant movement of the stability boundary, and it is likely that TFTR is stable to modes with  $n > 10$  under these conditions. Higher- $n$  modes ( $m > 3$  and  $n > 3$ ) have been observed on soft x-ray diodes viewing the center of the plasma in TFTR at  $q_{\text{cyl}} \approx 5 - 7$  and at high injection power. These high- $n$  modes are not observed before disruptions at high  $\beta_p$ .

### 5. Turbulence in TFTR

Langmuir probes in the scrape-off region outside the last closed flux surface have revealed broadband turbulent fluctuations in the frequency range 10 - 200kHz, with fluctuation levels typically  $\tilde{n}/n = 0.3 - 0.5$  and  $\tilde{\phi}/T_e = 0.1$ . Imaging of D-alpha light at the inner wall also shows large amplitude fluctuations [17] in this frequency range, with typical poloidal wavelengths  $\lambda_{pol} = 0.03 - 0.07m$ , but with  $\lambda_{tor} > 1.0m$ . Measurements of the magnetic fluctuations 0.11m outside the plasma edge show that the amplitude at 100kHz increases by a factor of 4 to  $\tilde{B}_\theta/B_\theta = 5 \times 10^{-6}$  during neutral beam injection for both L-mode and enhanced confinement discharges. Since the distance of the coils from the plasma boundary varies for different coils, a radial e-folding distance can be measured; for most conditions this distance is about 0.05m. A strong dependence of the turbulent fluctuations on local edge conditions is found. For example, a gas puff of 5 Torr·l/s or a burst of low frequency  $m/n = 5/1$  or  $4/1$  mode activity in an ohmically heated discharge can decrease the turbulent fluctuations by a factor of 10. From this result it is clear that turbulent fluctuations measured outside the plasma are not generally appropriate for direct correlation with global energy confinement.

The broadband spectra of  $\tilde{n}$ ,  $\tilde{\phi}$  and  $\tilde{B}_\theta$  in the frequency range 10 - 250kHz have an approximate power-law dependence  $P(f) \propto f^\gamma$ , where  $-1 > \gamma > -2$ . Short radial decay lengths are found for  $\tilde{n}$  and  $\tilde{B}_\theta$  in the range corresponding to "mode numbers"  $m > 15$ , i.e., small-scale compared with the plasma size. The amplitude of the broadband fluctuations of  $\tilde{n}$  and  $\tilde{B}_\theta$  increased with NBI both in the L-mode and enhanced confinement mode.

### 6. Conclusions

On TFTR, three different types of sawteeth have been identified. The main differences are in the precursor and successor oscillation amplitudes. Possible explanations include extensions of the Kadomtsev model with two  $q = 1$  surfaces and partial reconnection. Turbulence measured in the scrape-off region shows large amplitude fluctuations in the frequency range 10-250kHz, with fluctuation levels typically  $\tilde{n}/n = 0.3-0.5$  and  $\tilde{\phi}/T_e = 0.1$ . It is also found that the measured edge fluctuations of  $\tilde{n}$  and  $\tilde{B}_\theta$  can be extremely sensitive to local edge conditions.

The enhanced confinement discharges on TFTR have values of  $\beta_n$  at low  $q_{cyl}$  which approach the limit found from ideal kink stability theory. At higher  $q_{cyl}$  it appears that the beta limit is better described by  $\epsilon\beta_p^{DIA} \approx 0.7$ . In addition,  $dP_T/dr$  in these discharges is close to the  $n \rightarrow \infty$  large aspect ratio ideal ballooning stability limit. High frequency modes at  $> 60kHz$  with  $m > 3$ ,  $n > 3$  have been observed in the core of discharges with

high  $\beta_p$  and high neutral beam power. Deterioration of confinement in the enhanced confinement discharges appears to be associated more with coherent modes ( $m/n = 2/1$  and  $3/2$ ). Major disruptions at high  $\beta_p$  can have fast thermal energy decay ( $< 100 \mu\text{sec}$ );  $n = 1$  modes (with many coupled  $m$ -modes) are sometimes observed, but high- $n$  modes are not detected by the magnetic coils or soft x-ray diodes during these disruptions.

### ACKNOWLEDGEMENTS

The authors are grateful to D.J. Grove and J.R. Thompson for their advice and support, and to J. Strachan for his many contributions.

This work was supported by the United States Department of Energy, under Contract No. DE-AC02-76-CHO3073. The ORNL participants were also supported by the United States Department of Energy, under Contract No. DE-AC05-84OR21400 with Martin Marietta Energy Systems, Inc.

### REFERENCES

- [1] PFEIFFER, W., Nucl. Fusion **25** (1985) 673.
- [2] McGUIRE, K., et al., in Controlled Fusion and Plasma Physics (Proc. 12th Europ. Conf. Budapest, 1985), Part 1, European Physical Society (1985) 134.
- [3] CAMPBELL, D., et al., Nucl. Fusion **26** (1986) 1085.
- [4] KADOMTSEV, B., Fiz. Plazmy **1** (1975) 710.
- [5] DENTON, R., et al., Phys. Rev. Lett. **56** (1986) 2477.
- [6] PARAIL, V., PEREVERZEV, G., Fiz. Plazmy **6** (1980) 27.
- [7] HAWRYLUK, R.J., et al., Paper IAEA-CN-47/A-I-3, these Proceedings, Vol. 1.
- [8] GOLDSTON, R.J., et al., Paper IAEA-CN-47/A-II-1, these proceedings, Vol. 1.
- [9] HAWRYLUK, R.J., in Physics of Plasmas Close to Thermonuclear Conditions (Proc. Course Varenna, 1979), Rep. EUR/FU/BRU/XII/476/80, CEC, Brussels (1980) 503.  
GOLDSTON, R.J., et al., J. Comput. Phys. **43** (1981) 61.
- [10] FURTH, H., Plasma Phys. Controll. Fusion **28** (1986) 1305.
- [11] TROYON, F., et al., Plasma Phys. Controll. Fusion **26** (1984) 209.
- [12] MANICKAM, J., et al., Nucl. Fusion **24** (1984) 595.
- [13] ROBINSON, D.C., et al., in Plasma Physics and Controlled Nuclear Fusion Research 1984 (Proc. 10th Int. Conf. London, 1984), Vol. 1, IAEA, Vienna (1985) 205.
- [14] LORTZ, D., et al., Phys. Lett., A **68** (1978) 49.  
CHOE, W., et al., Phys. Fluids **29** (1986) 1766.
- [15] SYKES, A., et al., in Controlled Fusion and Plasma Heating (Proc. 11th Europ. Conf. Aachen, 1983), Pt. 11, European Physical Society (1984) 363.
- [16] BISHOP, C., et al., Nucl. Fusion **24** (1984) 643.  
TANG, W., et al., Nucl. Fusion **21** (1981) 891.
- [17] ZWEBEN, S., et al., J. Nucl. Mater. **145-147** (1987).



## SAWTEETH AND DISRUPTIONS IN JET

D.J. CAMPBELL, P.A. DUPERREX<sup>1</sup>, A.W. EDWARDS,  
 R.D. GILL, C.W. GOWERS, R. GRANETZ, M. HUGON,  
 P.J. LOMAS, N. LOPES-CARDOZO<sup>2</sup>, M. MALACARNE,  
 M.F. NAVE, D.C. ROBINSON<sup>3</sup>, F.C. SCHÜLLER,  
 P. SMEULDERS, J.A. SNIPES<sup>3</sup>, P.E. STOTT, G. TONETTI<sup>1</sup>,  
 B.J. TUBBING<sup>2</sup>, A. WELLER<sup>4</sup>, J.A. WESSON  
 JET Joint Undertaking,  
 Abingdon, Oxfordshire,  
 United Kingdom

### Abstract

#### SAWTEETH AND DISRUPTIONS IN JET.

The behaviour of magnetohydrodynamic phenomena associated with sawteeth and major disruptions has been studied for a wide range of discharge conditions with Ohmic, neutral beam and ion cyclotron heating. The sawtooth collapse has been investigated in detail and found to be inconsistent with models based on resistive reconnection. Disruptions set limits to JET operation at low  $q$  and high density, and the detailed evolution of disruptions at these limits has been studied. A hard operational limit is found at  $q_{\psi} = 2.0 \pm 0.1$ . The highest value of the Murakami parameter achieved in Ohmic plasmas is  $nR/B_T = 7.2 \times 10^{19} \text{ m}^{-2} \cdot \text{T}^{-1}$ , but neutral beam heating leads to a substantial increase ( $\sim 50\%$ ) in the density limit. Finally, during high power neutral beam heating combined with ion cyclotron heating, 'monster' sawteeth are observed in which MHD activity of modes with low  $m$  and  $n$  becomes quiescent for periods  $\sim 1$  s.

#### INTRODUCTION

Sawteeth and disruptions are well known phenomena in all tokamaks and define the limits on the mhd stability of the discharge. They have been studied extensively in JET and there are some important new features in the results which will be reported here.

Our studies of these phenomena have used all of the JET diagnostics, but in particular we have made detailed measurements of the mode structures using: magnetic pick-up

<sup>1</sup> Centre de recherches en physique des plasmas, Ecole polytechnique fédérale de Lausanne, Lausanne, Switzerland.

<sup>2</sup> FOM Instituut voor Plasmafysica, Nieuwegein, Netherlands.

<sup>3</sup> UKAEA, Culham Laboratory, Abingdon, Oxfordshire, UK.

<sup>4</sup> Max-Planck-Institut für Plasmaphysik, Garching, Fed. Rep. Germany.

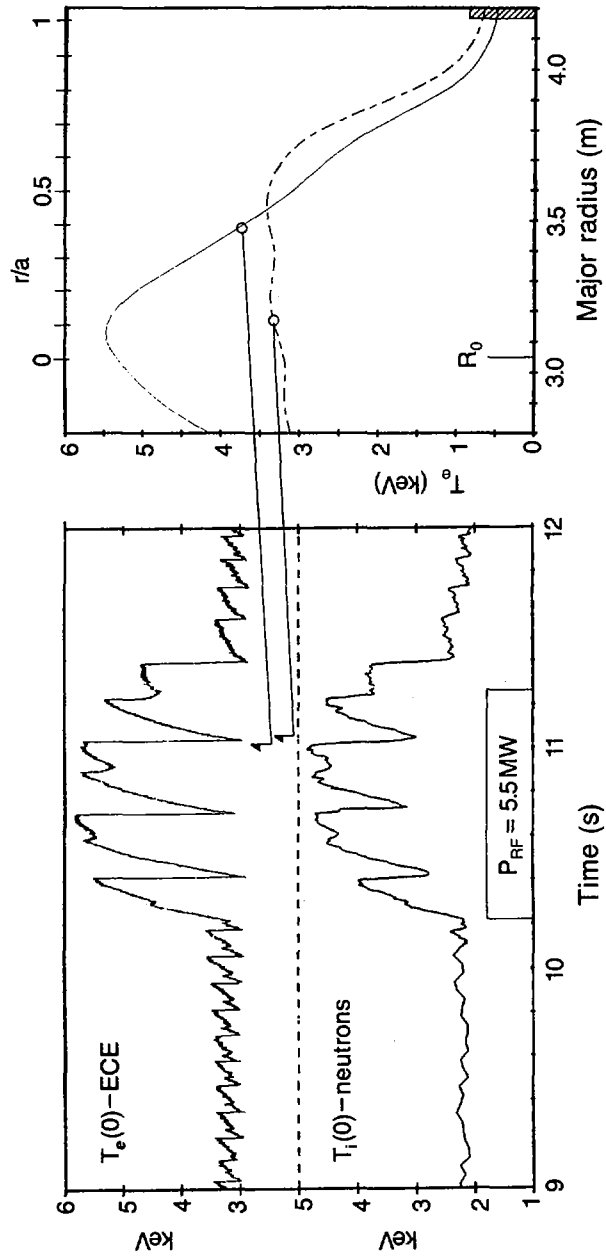


FIG. 1. Central electron and ion temperatures showing increase in sawtooth modulation and period with 5.5 MW of ion cyclotron heating. Electron temperature profiles before and after sawtooth collapse are shown.

coils and loops outside the plasma boundary; electron cyclotron emission to measure local electron temperatures; and orthogonal arrays of X-ray diodes combined with tomographic analysis to measure the soft X-ray emissivity.

#### SAWTEETH

Sawteeth are observed in almost all JET discharges. Their general features which have been discussed in earlier papers [1,2] will only be summarised here. In ohmically heated plasmas the modulation of the central electron temperature is up to 20% and the period is between 30 and 250ms. In discharges with ion cyclotron heating (Fig. 1) or co-injected neutral beams the modulation is increased up to 50% and the period extended up to 600ms, whereas with counter injected beams both the modulation and the period are reduced. With combined ion cyclotron and neutral beam heating we have sometimes seen "monster" sawteeth lasting for more than 1s. We have attempted to determine the scaling of the period with various tokamak parameters, but the only clear trend is that in ohmic discharges the period increases with plasma density. Most JET sawteeth show a compound structure with one or more partial collapses occurring between the main collapses.

As we have reported elsewhere [1] the main collapse of sawteeth in JET occurs on a much shorter time scale (typically ~ 100 $\mu$ s) than would be consistent with resistive reconnection models. In ohmic discharges the collapse usually occurs spontaneously without any precursor oscillations but often we see successor oscillations. The behaviour is very similar in ion cyclotron heated discharges, but with neutral beam heating we usually see a precursor either as a growing oscillation or sometimes as a saturated mode. When there are precursors, the main collapse appears to be a continuation of the precursor. This suggests that the precursor and main collapse are the same instability, but this has not been proved conclusively.

The collapse mechanism appears to be the same in all JET discharges despite these differences in precursor activity. Detailed studies [3] with the X-ray and ECE diagnostics show that the collapse has an  $m=n=1$  structure and involves the displacement in minor radius of the hot central core of plasma (Fig. 2a). The displaced core spreads poloidally around the magnetic axis into a crescent shaped region (Fig. 3) and at the same time there is a rapid outflow of plasma energy. The successor oscillations are seen to be the rotation of a residual asymmetry in the collapsed state. The soft X-ray emission profiles after the collapse are sometimes slightly hollow. The time scale of the collapse and the detailed

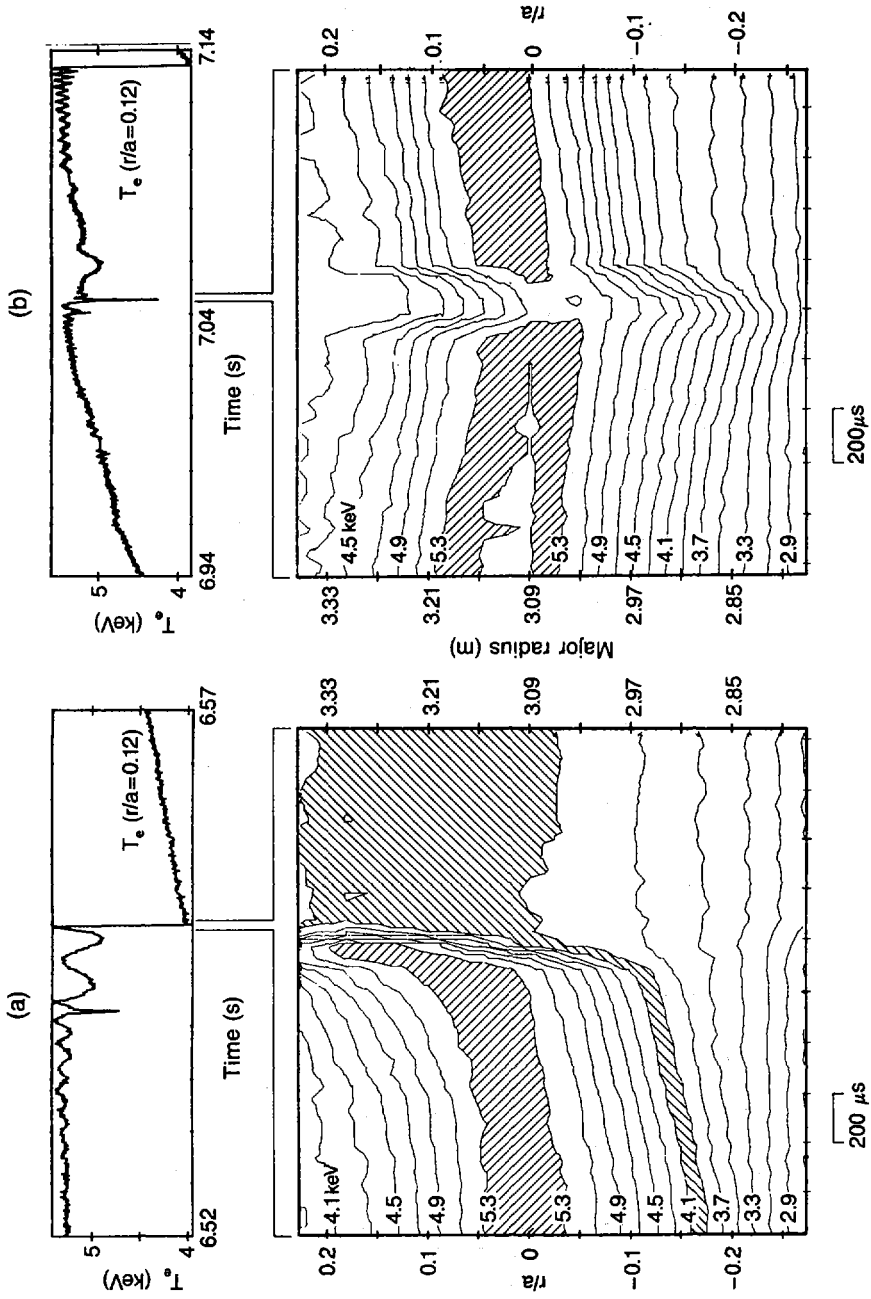


FIG. 2. Temperature contours (each line representing an interval of 0.2 keV) during (a) main collapse, (b) partial collapse. Displacement of core is seen in both cases, but is smaller for partial collapse and does not lead to complete core cooling.

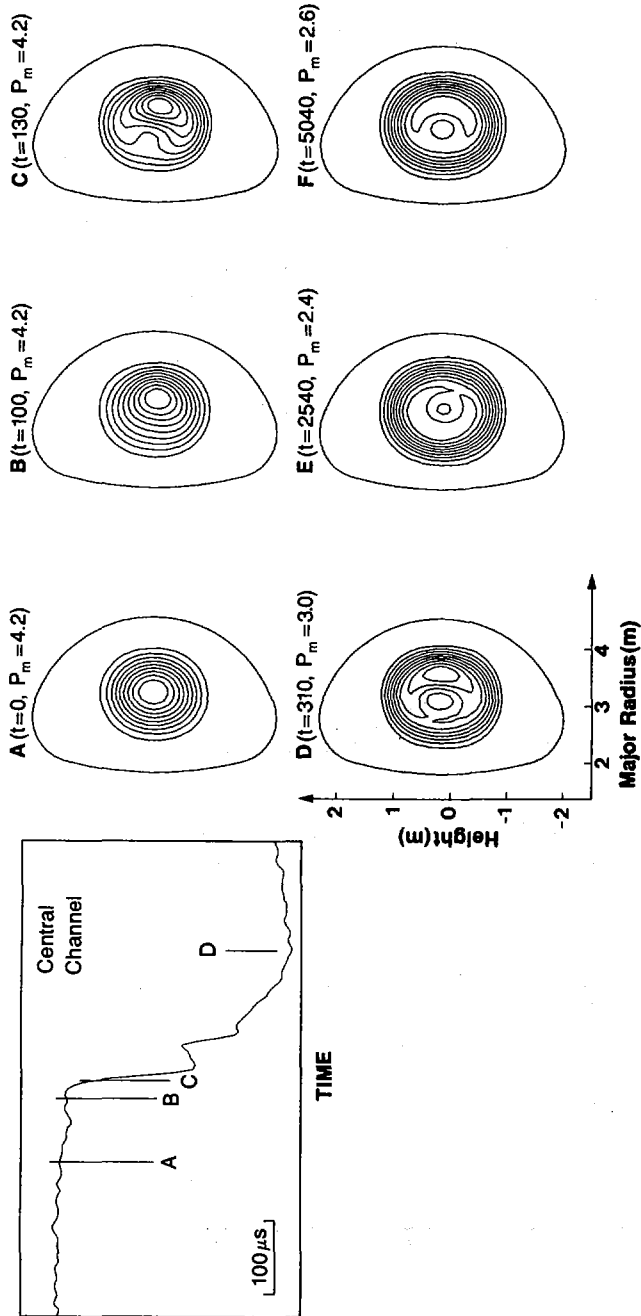


FIG. 3. Contour plots of X-ray emissivity (at relative times in  $\mu\text{s}$ ) during main collapse. Core displacement is seen in frames A and B and poloidal spreading in frame C. The fall in peak emissivity  $P_m$  ( $\text{kWhm}^{-3}$ ) between frames C and D corresponds to rapid core cooling. Frames E and F show residual asymmetry at times 2.4 and 4.9 ms after collapse.

displacement and spreading of the hot core are in agreement with the predictions of the model by Wesson [4] where the sawtooth collapse is an ideal mhd instability. A magnetic signal with  $n=1$  is detected simultaneously with the collapse [5].

Partial collapses show a wider range of behaviour in precursor and successor oscillations and are more difficult to classify, but there appear to be at least two general types. One is similar to the main collapse, with a sudden ( $\sim 100\mu\text{s}$ ) but smaller displacement of the hot core (Fig. 2b), and the subsequent propagation of a heat pulse outside the central region. The second type is a much softer relaxation on a longer timescale  $\sim 10\text{ms}$  with an  $m = 1$  oscillation which shifts inwards but does not lead to a central collapse. Both types of partial collapse have very little overall effect on the central temperature.

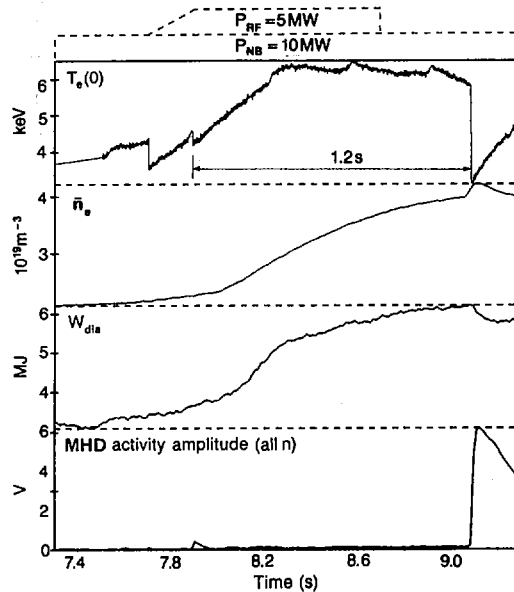


FIG. 4. Evolution of central electron temperature  $T_e(0)$ , line integral of electron density  $\int n_e dl$ , total plasma energy from diamagnetic measurements  $W_{dia}$ , and amplitude of total MHD activity during 5 MA discharge with a monster sawtooth lasting 1.2 s.

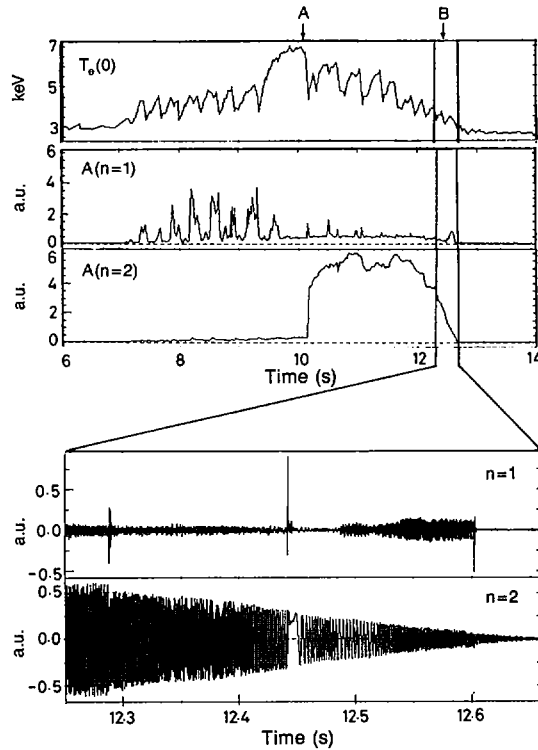


FIG. 5. After monster sawtooth collapses at time A, large amplitude  $n = 2$  mode persists until end of neutral beam heating pulse at time B.

### MONSTER SAWTEETH

In discharges with combined ion cyclotron and neutral beam heating some sawteeth have very long duration (up to 1.26s). These were first seen in relatively low current discharges ( $I_p \sim 2\text{MA}$ ), but similar long duration ("monster") sawteeth have now been seen in discharges with an internal separatrix ( $I_p = 2\text{MA}$ ) and at high currents ( $I_p = 5\text{MA}$ ) as shown in figure 4. These are not simply sawteeth with particularly long periods, as they are characterised by low levels of coherent mhd activity suggesting that the  $m=1$  mode has been stabilised. However after the sawtooth collapse the plasma remains in an unstable state characterised by a large  $m = 3$ ,  $n=2$  mode which oscillates for several seconds and often persists until the end of the neutral beam pulse (Fig. 5). This seems to prevent the growth

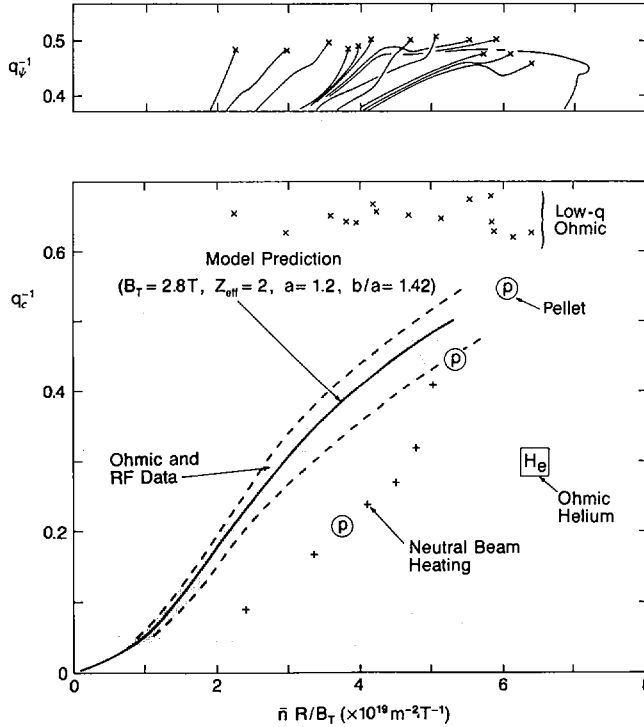


FIG. 6. Hugill diagram summarizing the limits of stable operation in JET. Preliminary results of single pellet injection into Ohmic discharges which did not disrupt are also shown. Low  $q$  limit is more consistently plotted in terms of  $q_p$  as shown in upper figure.

of a second monster sawtooth in the same pulse, although there may be several normal sawteeth. The conditions for monster sawteeth have not yet been fully explored, but simultaneous ion cyclotron and neutral beam heating appear to be required. The ratio of ion cyclotron to neutral beam power does not appear to be critical but there does appear to be a threshold of total additional power which increases with plasma current. A possible explanation is that the current profile is modified by the beam driven current which may be enhanced by the ion cyclotron heating.

#### LOW $q$ DISCHARGES AND DISRUPTIONS

Reproducible, stable ohmic discharges with  $I_p = 3.5\text{MA}$ ,  $B_T = 1.7\text{T}$ ,  $R = 2.97\text{m}$ ,  $a = 1.2\text{m}$ ,  $b/a = 1.35$ ,  $q_p = 2.2$  and  $q_c = (5 \times 10^6 \text{ ab} B_T / R I_p) = 1.59$  have been studied to simulate the

planned operation of JET at  $I_p = 7\text{MA}$  and  $B_T = 3.4\text{T}$ . The sawtooth inversion radius is  $0.55a$ . The global energy confinement time of  $0.45\text{s}$  is consistent with normal JET scaling. These discharges reach the highest value of the Murakami parameter  $\bar{n} R/B_T = 7.2 \times 10^{19} \text{ m}^{-2} \cdot \text{T}^{-1}$  obtained for JET ohmic plasmas (Fig. 6).

When  $q_\psi$  is lowered either by raising  $I_p$ , lowering  $B_T$ , or by reducing  $a$  or  $b/a$ , a lower limit to stable operation is always found at  $q_\psi = 2.0 \pm 0.1$ . These low  $q$  disruptions are initiated by a sawtooth collapse and have precursors only on a time scale shorter than the sawtooth period. The total radiated power remains less than the ohmic power input and there is no contraction of the current profile.

#### DISRUPTIONS AT THE DENSITY LIMIT

Disruptions at the density limit in discharges with  $q_\psi \geq 3$  are preceded by signs of deterioration for up to  $1\text{s}$  before the final energy quench. The radiated power rises to equal the total power [6], and although the ohmic power increases due to increased plasma resistance, it fails to keep pace with the radiation. The discharge contracts until just before the quench there is virtually no current flowing outside the  $q=2$  surface. Combining these observations with the assumption that all the energy loss outside  $q=2$  is due to low  $Z$  impurity radiation gives an expression for the density limit in JET. An earlier calculation [7] has now been extended to include the effect of additional heating and a more accurate model [8] of the impurity radiation. The predicted high density limit for low  $Z$  dominated discharges with gas refuelling is

$$\bar{n}_{\text{crit}} = 3.5 \times 10^{16} \left( \frac{P q_c}{(Z_{\text{eff}} - 1) R a b (q_c - 2a/b)} \right)^{1/2} \text{ m}^{-3}$$

where  $P$  is the total power input (watts). This model clearly breaks down when  $Z_{\text{eff}}$  is close to 1 and other cooling mechanisms become important. There is good agreement between this expression and observed density limits for disruptions during the current flat top [6], but disruptions during the current rise and decay phases generally occur at lower and higher densities respectively than the predicted values. The model also indicates that the weakness of the increase in the density limit with ion cyclotron heating is due to the observed increase in  $Z_{\text{eff}}$  with increasing power, whereas the substantial increase in the density limit with beam heating is slightly assisted by the reduction of  $Z_{\text{eff}}$  by the beam particles.

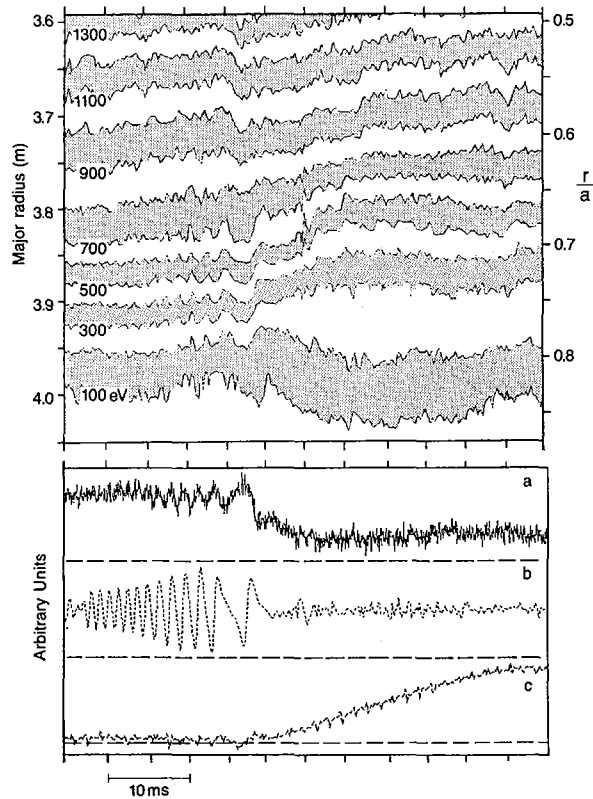


FIG. 7. Contours of electron temperature (at 100 eV intervals) versus time during magnetic activity which precedes disruption. Lower traces show (a) electron temperature at  $R = 3.95$  m ( $r/a = \sim 0.8$ ), and amplitudes (b) of  $m = 2, n = 1$  oscillation (c) of locked mode.

#### DETAILED STUDIES OF DISRUPTIONS

Detailed studies are being made of the sequence of events which precede a density limit disruption [9]. In a typical case ( $I_p = 3$  MA,  $B_T = 3.4$  T,  $q_\psi = 5.7$ ) the significant magnetic activity, shown in Figure 7, starts about 700 ms before the energy quench with a mode which is predominantly  $m=2, n=1$ . This activity grows for about 30 ms. The mode then stops rotating and locks in a fixed toroidal position when  $\bar{B}_\theta$  at the wall is  $10^{-3}$  T. During the locked phase the mode continues to grow in amplitude. ECE measurements show that the temperature profile shrinks before the start of the mhd activity. After the mode locks the temperature profile flattens slightly at a minor

radius of 0.95 m which is close to the calculated position of the  $q=2$  surface. This is consistent with the growth of a non-rotating magnetic island (the ECE diagnostic views close to the calculated position of the 'O' point) and there may be similar evidence from the soft X-ray emission, but the analysis is at a preliminary stage and there could be other interpretations. The spatial resolution of the ECE diagnostic (at present 40mm in the radial direction) is not quite sufficient to determine whether the 'O' point is colder than the surrounding plasma as predicted by the thermal instability model of disruptions [10].

The locked mode persists for several hundred ms until the final energy quench. This has been studied in detail for the last few ms before the energy quench using the soft X-ray diode arrays. A contour plot (Fig. 8) of the X-ray emission from the vertical camera shows that 2ms before the quench the central core of the discharge is eroded. The emission following the final termination is probably due to contact of the plasma with the walls and limiter. Tomographic analysis of the X-ray emission shows the growth of a large  $m=1$  asymmetry in the plasma centre. This structure appears to be locked in a specific toroidal phase for most disruptions which suggests that it is  $n=1$  and coupled to the locked  $m=2$  mode observed magnetically.

#### MAGNETIC FLUCTUATIONS

The magnetic pick-up coils detect incoherent fluctuations as well as coherent mhd activity. These incoherent fluctuations have a broadband spectrum over the whole measured frequency range from 5 to 60kHz.

During typical conditions the frequency dependence of the spectrum is  $f^{-1.6 \pm 0.2}$  and the total normalised fluctuation amplitude is  $\bar{B}_\theta / B_\theta \sim 10^{-5}$ . The magnetic fluctuations have a short growth and decay time. A strong correlation is observed in the direction parallel to  $\vec{B}$ . The normalised amplitude is seen to increase with additional heating power which may indicate a possible link with reduced confinement [11].

#### CONCLUSIONS

Detailed studies of sawteeth, disruptions and magnetic fluctuations are being made in JET with the aim of improving our understanding of these phenomena. The detailed mechanisms involved in the collapse of sawteeth have been investigated and found to be in agreement with an ideal mhd model of the

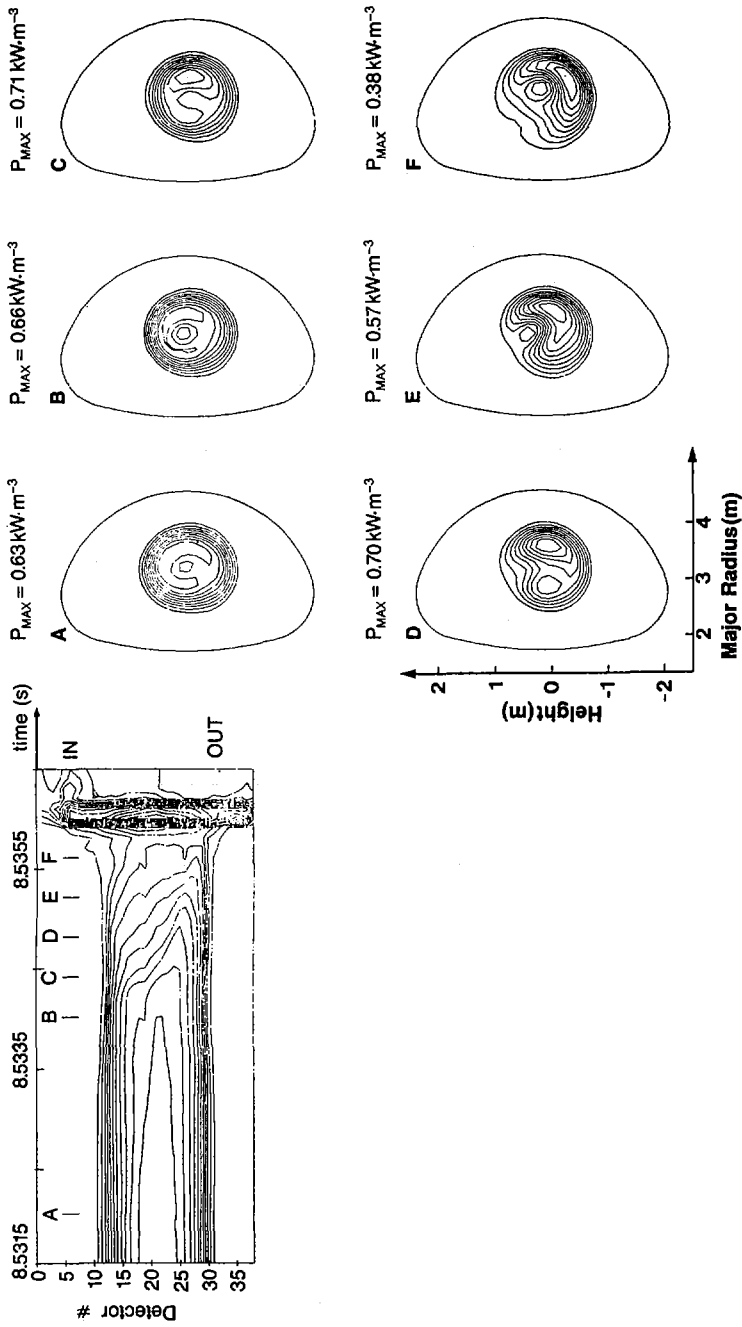


FIG. 8. X-ray emission during the last 5 ms before disruption. Left hand part of figure shows contours of the integrated emission versus time; tomographically inverted contours at various times are shown on the right. Development of  $m = 1$  mode is clearly seen.

collapse. A new regime which appears to be stable to low  $m$  and  $n$  modes for more than 1s has been observed with combined ion cyclotron and neutral beam heating. The operational limits to stable operation at low  $q$  and high density have been explored and the detailed mechanisms leading to disruptions have been studied. This work is proceeding with the objective of fully understanding the nature of disruptions and attempting to stabilise them by various means.

#### ACKNOWLEDGEMENTS

It is a pleasure to acknowledge contributions to this work and many helpful discussions with our colleagues in the JET project.

#### REFERENCES

- [1] CAMPBELL, D.J., et al., Nucl. Fusion **26** (1986) 1085.
- [2] GILL, R.D., et al., in Controlled Fusion and Plasma Heating (Proc. 13th Europ. Conf. Schliersee, 1986), Vol. 1, European Physical Society (1986) 21.
- [3] EDWARDS, A.W., et al., Phys. Rev. Lett. **57** (1986) 210.
- [4] WESSON, J., Plasma Phys. Controll. Fusion **28** (1986) 243.
- [5] DUPERREX, P.A., et al., in Controlled Fusion and Plasma Physics (Proc. 12th Europ. Conf. Budapest, 1985), Vol. 1, European Physical Society (1985) 126.
- [6] WESSON, J., et al., *ibid.*, p. 147.
- [7] SCHÜLLER, F.C., et al., *ibid.*, p. 151.
- [8] BEHRINGER, K., et al., Paper IAEA-CN-47/A-IV-1, these Proceedings, Vol. 1.
- [9] HENDER, T.C., ROBINSON, D.c., SNIPES, J.A., paper IAEA-CN-47/A-V-3, these Proceedings, Vol. 1.
- [10] REBUT, P.H., HUGON, M., in Plasma Physics and Controlled Nuclear Fusion Research 1984 (Proc. 10th Int. Conf. London, 1984), Vol. 2, IAEA, Vienna (1985) 197.
- [11] MALACARNE, M., DUPERREX, P.A., JET Preprint-P(86)31, JET Joint Undertaking, Abingdon (1986).



## **Session F**

### **PLASMA HEATING AND CURRENT DRIVE**

#### **Chairmen of Sessions**

<b>Session F-I</b>	<b>O.S. PAVLICHENKO</b>	<b>USSR</b>
<b>Session F-II</b>	<b>R.R. PARKER</b>	<b>USA</b>
<b>Session F-III</b>	<b>F.G. PREVOT</b>	<b>France</b>
<b>Session F-IV (Posters)</b>		



## RADIOFREQUENCY HEATING ON JET

### JET TEAM<sup>1</sup>

*(Presented by J. Jacquinot)*

H. Altmann, R.J. Anderson, J. Arbez, W. Bailey, D.V. Bartlett, B. Beaumont<sup>1</sup>, G. Beaumont, K. Behringer, P. Bertoldi, E. Bertolini, C.H. Best, V. Bhatnagar<sup>2</sup>, R.J. Bickerton, A. Boileau<sup>3</sup>, F. Bombarda<sup>4</sup>, T. Bonicelli, S. Booth, A. Boschi, G. Bosia, M. Botman, H. Brelen, H. Brinkschulte, M.L. Browne, M. Brusati, T. Budd, M. Bures, P. Butcher, H. Buttgereit, D. Cacaut, C. Caldwell-Nichols, J.D. Callen<sup>5</sup>, D.J. Campbell, J. Carwardine, G. Celentano, C.D. Challis, A. Cheetham, J.P. Christiansen, C. Christodoulopoulos, P. Chuilon, R. Claesen, J.P. Coad, S.A. Cohen<sup>6</sup>, M. Cooke, J.G. Cordey, W. Core, S. Corti, A.E. Costley, G.A. Cottrell, M. Cox<sup>7</sup>, C. David, J. Dean, L. de Kock, E. Deksnis, G.B. Denne, G. Deschamps, K.J. Dietz, J. Dobbing, S.E. Dorling, D.F. Dücks, G. Duesing, P.A. Duperrex<sup>8</sup>, H. Duquenoy, A.W. Edwards, J. Ehrenberg<sup>9</sup>, W. Engelhardt, S.K. Erents<sup>7</sup>, F. Erhorn, B.T. Eriksson, M. Evrard<sup>2</sup>, H. Falter, N. Foden, M.J. Forrest<sup>7</sup>, C. Froger, K. Fullard, G. Fussmann<sup>9</sup>, M. Gadeberg<sup>10</sup>, A. Galetsas, A. Gallacher, D. Gambier<sup>1</sup>, R. Giannella<sup>4</sup>, A. Giannelli<sup>4</sup>, A. Gibson, R.D. Gill, A. Goede, A. Gondhalekar, C. Gordon, C. Gormezano, N.A. Gottardi, C.W. Gowers, R. Granetz, B. Green, S. Gregoli, F.S. Griph, R. Haange, J.H. Hamnén<sup>11</sup>, C.J. Hancock, P.J. Harbour, N.C. Hawkes<sup>7</sup>, P. Haynes<sup>7</sup>, T. Hellsten, J.L. Hemmerich, R. Hensworth, F. Hendriks, R.F. Herzog, L. Horton<sup>12</sup>, J. How, M. Huart, A. Hubbard<sup>13</sup>, J. Hugill<sup>7</sup>, M. Hugon, M. Huguet, B. Ingram, H. Jäckel<sup>9</sup>, J. Jacquinot, Z. Jankowicz<sup>14</sup>, O.N. Jarvis, E.M. Jones, P. Jones, T.T.C. Jones, C. Jupén<sup>15</sup>, E. Källne, J. Källne, O. Kaneko<sup>16</sup>, A. Kaye, B.E. Keen, M. Keilhacker, G. Kinahan, S. Kissel, A. Konstantellos, M. Kovanen<sup>17</sup>, U. Kühnappel<sup>9</sup>, P. Kupschus, P. Lallia, J.R. Last, L. Lauro-Taroni, K.D. Lawson<sup>7</sup>, E. Lazzaro, R.C. Lobel, P.J. Lomas, N. Lopes-Cardozo<sup>18</sup>, M. Lorenz-Gottardi, C. Lowry<sup>13</sup>, G. Magyar, D. Maisonnier, M. Malacarne, V. Marchese, P. Massmann, G.M. McCracken<sup>7</sup>, P. McCullen, M.J. Mead, P. Meriguet, V. Merlo, V. Mertens<sup>9</sup>, S. Mills, P. Millward, A. Moissonnier, P.L. Mondino, D. Moreau<sup>1</sup>, P.D. Morgan, E.R. Müller<sup>9</sup>, D. Murmann<sup>9</sup>, G. Murphy, M.F. Nave, L. Nickesson, P. Nielsen, P. Noll, S. Nowak, W. Obert, M. Olsson, J. O'Rourke, M.G. Pacco, J. Paillere, S. Papastergiou, J. Partridge<sup>7</sup>, D. Pasini<sup>12</sup>, N.J. Peacock<sup>7</sup>, M. Pescatore, J. Plancoulaine, J.-P. Poffé, R. Prentice, T. Raimondi, J. Ramette<sup>1</sup>, C. Raymond, P.H. Rebut, J. Removille, W. Riediker, R. Roberts, D.C. Robinson<sup>7</sup>, A. Rolfe, R.T. Ross, G. Rupprecht<sup>9</sup>, R. Rushton, H.C. Sack, G. Sadler, J. Saffert, N. Salmon<sup>13</sup>, F. Sand, A. Santagiustina, R. Saunders, M. Schmid, F.C. Schüller, K. Selin, R. Shaw, A. Sibley, D. Sigournay, R. Sillen<sup>18</sup>, F. Simonet<sup>1</sup>, R. Simonini, P. Smeulders, J.A. Snipes<sup>7</sup>, K. Sonnenberg, L. Sonnerup, M.F. Stamp, C.A. Steed, D. Stork, P.E. Stott, T.E. Stringer, D.R. Summers, H.P. Summers<sup>19</sup>, A.J. Tagle, G. Tallents<sup>20</sup>, A. Tanga, A. Taroni, A. Terrington, A. Tesini, P.R. Thomas, E. Thompson, K. Thomsen<sup>10</sup>, F. Tibone, R. Tivey, T.N. Todd<sup>7</sup>, P. Trealion, M. Tschudin, B.J. Tubbing<sup>18</sup>, P. Twynam, E. Usselmann, H. Van der Beken, J.E. Van Montfoort, M. von Hellermann, J. von Seggern<sup>21</sup>, T. Wade, C. Walker, B.A. Wallander, M. Walravens,

K. Walter, M.L. Watkins, M. Watson, D. Webberley, A. Weller<sup>9</sup>, J.A. Wesson, J. Wilks, T. Winkel, C. Woodward, M. Wykes, D. Young, L. Zannelli, J.W. Zwart

JET Joint Undertaking,  
Abingdon, Oxfordshire,  
United Kingdom

### Abstract

#### RADIOFREQUENCY HEATING ON JET.

High power ICRF,  $P \leq 7.2$  MW, has been coupled to the JET plasma in a variety of conditions: outboard limiters, inner wall, combined operation with neutral beams and pellet injection. Long pulse modulation experiments (10 s) yield a precise deposition which is extremely localized, in agreement with expectations. The best heating efficiency is obtained when the minority resonance crosses the magnetic axis. With off-axis heating, the ion temperature profile broadens more than the electron temperature profile. A new operating regime called 'monster sawtooth' has been found during combined RF and NBI heating. The MHD quiet regime can last 1.26 s and the central electron temperature rises to 7.4 keV with a D-D reaction rate of  $4 \times 10^{15} \text{ s}^{-1}$ . The temperature profile steepens over the entire profile and  $\tau_E$  is enhanced by a factor of 2.5 for a combined power of 10 MW. RF heating of plasma fuelled with a single mildly penetrating pellet exhibits the normal L-mode behaviour. In combination with NBI, the input power reaches 16 MW and the plasma stored energy reaches 5.8 MJ at the highest plasma current of 5 MA. Recent experiments in single-null X-point configuration with combined heating have shown the transition to an enhanced confinement regime (H-mode).

<sup>1</sup> CEA, Centre d'études nucléaires de Fontenay-aux-Roses, France.

<sup>2</sup> Plasma Physics Laboratory, Association "Euratom-Belgian State" ERM/KMS, Brussels, Belgium.

<sup>3</sup> Institut national de la recherche scientifique, Ste-Foy, Québec, Canada.

<sup>4</sup> ENEA, Centro Ricerche Energia, Frascati, Italy.

<sup>5</sup> Department of Physics, University of Wisconsin, Madison, WI, USA.

<sup>6</sup> Princeton Plasma Physics Laboratory, Princeton University, NJ, USA.

<sup>7</sup> UKAEA, Culham Laboratory, Abingdon, Oxfordshire, UK.

<sup>8</sup> Centre de recherches en physique des plasmas, Ecole polytechnique fédérale de Lausanne, Switzerland.

<sup>9</sup> Max-Planck-Institut für Plasmaphysik, Garching, Fed. Rep. Germany.

<sup>10</sup> Risø National Laboratory, Roskilde, Denmark.

<sup>11</sup> Swedish Energy Research Commission, Stockholm, Sweden.

<sup>12</sup> Natural Sciences and Engineering Research Council, Ottawa, Ontario, Canada.

<sup>13</sup> Imperial College of Science and Technology, University of London, UK.

<sup>14</sup> RCC CYFRONET IAE, Otwock-Świerk, Poland.

<sup>15</sup> University of Lund, Sweden.

<sup>16</sup> Department of Physics, University of Nagoya, Japan.

<sup>17</sup> Department of Physics, Lappeenranta University of Technology, Lappeenranta, Finland.

<sup>18</sup> FOM Instituut voor Plasmafysica, Rijnhuizen, Nieuwegein, Netherlands.

<sup>19</sup> University of Strathclyde, Glasgow, UK.

<sup>20</sup> Research School of Physical Sciences, Australian National University, Canberra, Australia.

<sup>21</sup> Kernforschungsanlage Jülich GmbH, Fed. Rep. Germany.

## 1. INTRODUCTION

Initial ICRF heating experiments on JET have recently been reported [1,2]. Performed at a maximum power level of 5MW, these experiments revealed a degradation in energy confinement with increased power, following a behaviour previously observed in Tokamaks with a cold plasma edge. It appeared difficult to raise the electron temperature outside the  $q=1$  surface above the ohmic heating value.

The heating sources have now been increased up to 7.2MW using three ICRF antenna-generator units [3] and to 10MW with NBI [4]. Combined ICRF and NBI heating to a maximum power of 16MW has successfully been achieved, and a wider variety of operating regimes have been investigated. These results are summarised below. Experiments performed with ICRF alone are addressed in the first three sections, in which emphasis is placed on power modulation to deduce the deposition profile, on off-axis heating and on the effect of antenna phasing. The last sections described specific aspects of combined ICRF, NBI and Pellet operation. In particular, injected beam ions appear to be accelerated when the RF is applied and, in some conditions, the internal sawteeth are stabilized and a high central electron temperature is achieved ('Monster' mode).

## 2. MODULATION EXPERIMENT AND POWER DEPOSITION PROFILE

The power deposition profile can be inferred from the change of slope of the temperature evolution during the sharp rise of the applied heating source. A variant is to observe the slope of internal sawteeth [5]. The signal-to-noise ratio is generally mediocre and the method could only be applied to heating on axis at high power density. Experiments with long and amplitude modulated heating pulses offer the opportunity to use noise rejection techniques, such as the box-car or the fast Fourier transform. The frequency of modulation  $\nu_M$  can be scanned across the characteristic energy exchange and transport frequencies to reveal the dominant energy channels. In these experiments,  $\nu_M$  was between 5-62Hz, the heating pulse lasted during 10s and the peak-to-peak modulation was about 1MW. The local perturbation of the electron temperature was measured with a 12-channel polychromator.

When the modulation frequency is high enough, the response of the electron species is adiabatic and it is possible to deduce directly the power density  $P_e$  transferred to the electrons, as shown in Fig. 1a,b. In both cases, the peak response is close to the location of the cyclotron resonance and the width of the deposition (FWHM) is  $\sim 60$ cm for on-axis heating and  $\sim 20$ cm for off-axis heating.

The experimental result is compared with theoretical descriptions using either the ray tracing technique [6] or full wave solutions [7]. Both models take into account the D-shape cross-section and the actual plasma parameters. These both predict that most of the coupled power is first transferred to the minority species, as observed, and is subsequently redistributed by collisions according to Table I. In the ray tracing model, part of the power ( $\sim 20\%$ ) is not absorbed and is assumed lost in the wall or the edge. A very small part ( $\approx 5\%$ ) goes directly to the electrons and ions. In the full wave model, the pressure anisotropy of the minority is taken into account. A significant fraction of the power is directly coupled to the deuterons (10 to 20%).

Note that electron heating prevails with heating on-axis, but, as the power density decreases with off-axis heating ion heating increases. At high power, electron heating tends to dominate in all cases. Both models give a good representation of the observed deposition profile (Fig.1a,b). The agreement is excellent for off-axis heating. Central heating is somewhat broader than predicted.

The observed temperature modulation decreases rapidly with  $\nu_M (\bar{T}_e \propto \nu_M^{-2})$ . Such a law can only be obtained theoretically if the RF power first transits via the minority before reaching the electron species (direct electron heating would imply  $\bar{T}_e \propto \nu_M^{-1}$ ). The measurement

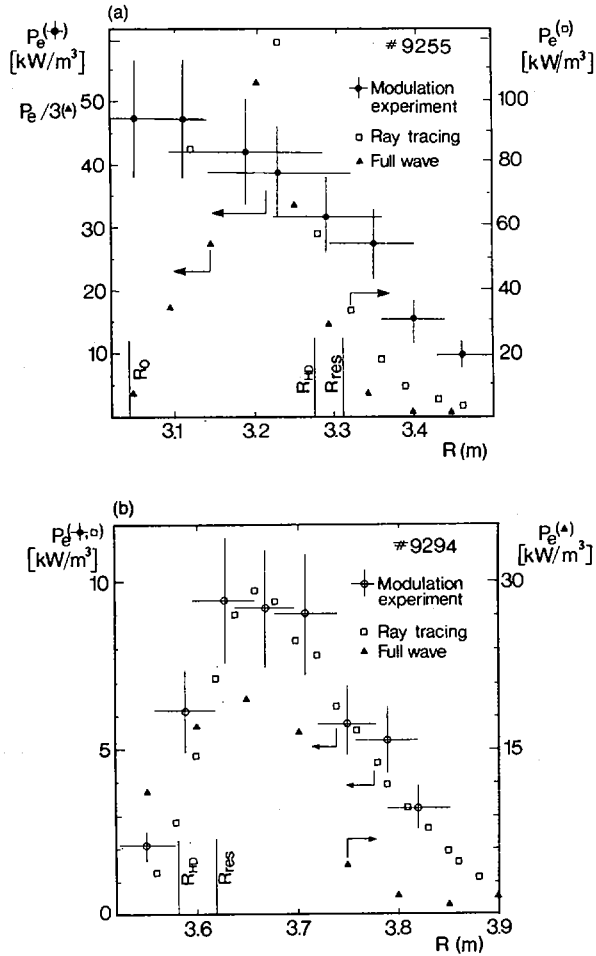


FIG. 1. Net power density  $P_e$  transferred to electrons, deduced from the adiabatic modulation of  $T_e$  during long pulse ICRF modulation experiments: 1.3 MW peak modulation, 12.5 Hz, H minority. Comparison with theory: (a) on-axis heating  $B_\phi = 3.4$  T,  $\nu = 47.7$  MHz, (b) off-axis heating  $B_\phi = 2.9$  T,  $\nu = 37$  MHz. Heating via the minority is demonstrated by comparison with theory.

of  $\tilde{T}_e = f(\nu_M)$  has been used to determine the power coupled to the minority. Results are given in Table I.

### 3. OFF-AXIS HEATING

The importance of power localisation has been studied in two series of experiments. In the first [2, 8], the minority resonance position is scanned by ramping down the toroidal magnetic field during the RF pulse. In the second, the same effect is obtained by varying the wave frequency in the same plasma conditions. Moreover, the experiment was carried out after a

TABLE I. TRANSFER OF POWER  
Comparison of two models with experiment

Power input ( $P_c$ ) 1.3MW	Directly to Minority H ( $P_m/P_c$ )	To electrons ( $P_e/P_c$ )	To deuterons ( $P_d/P_c$ )
On-axis	0.75	0.42	0.39
Ray tracing			
Off-axis	0.71	0.15	0.60
On-axis	0.80	0.34	0.66
Full wave			
Off-axis	0.90	0.25	0.75
On-axis	$0.6 \pm 0.12$	$\geq 0.31 \pm 0.06$	not
Observed			measured
Off-axis	$0.7 \pm 0.15$	$\geq 0.15 \pm 0.03$	

heavy carbonisation to avoid the radiated power increase when the resonance is far off-axis and with long pulses ( $\approx 8$ s) to avoid transient effects. Both series give similar results, for example:

- Large amplitude sawteeth on both  $T_e$  and  $T_i$  were observed only when the ion-ion hybrid resonance was inside the inversion radius [2, 8]. The sawteeth do not disappear with far off-axis heating, but become small and short.
- The largest increase of central temperature and stored energy was achieved with central heating (Fig. 2). The increase of  $T_e$  was only weakly dependent on the resonance location [2].

The deuteron temperature profile (from NPA) appears to broaden with heating off-axis (Fig. 3b). On the contrary, the electron temperature profile is only slightly broadened (Fig.3a) outside the  $q=1$  volume.

Transport code simulations of off-axis heating cases indicate that the energy transport coefficient,  $\chi_e$ , re-adjusts itself to try to conserve a similar  $T_e$  profile, by lowering  $\chi_e$  inside the heating region and by further increasing it outside the heating zone.

#### 4. ANTENNA PHASING AND EDGE EFFECTS

Among the three antennas, two are of the dipole-quadrupole type [1] and internal phasing of the two coupling elements allows the launching of a  $k_{||}$  spectrum which is peaked either for  $k_{||}=0$  or for  $k_{||}=7\text{m}^{-1}$ . In addition, these two antennas, located on either side of a large horizontal port, can be phased relative to each other. When the dipoles are out of phase, two peaks at  $k_{||}=2\text{m}^{-1}$  and  $7\text{m}^{-1}$  are emitted;  $90^\circ$  phase difference produces a small portion of travelling wave (directivity  $\approx 5\%$ ). All these phasing conditions have been compared, using a target plasma which maximizes the impurity effects with ICRF (low density  $\approx \langle n_e \rangle = 1.1 \times 10^{19}\text{m}^{-3}$ , no carbonisation for several months). The following observations were made:

- Phasing between the two adjacent antennas, each being in the dipole mode ( $k_{||}=0$ ) did not produce any measurable difference on wave coupling, edge plasma or plasma heating.

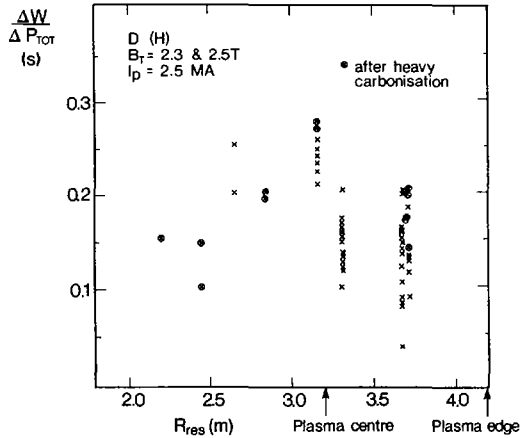


FIG. 2. Incremental confinement time versus position of the H resonance. The frequency was varied between 25 and 48 MHz. Data points following a heavy carbonisation are identified.

- Phasing internally in the quadrupole mode produced not only reduced coupling resistance [1] but also a marked reduction of specific ICRF effect on the edge plasma. In particular, the flattening of scrape-off-layer density and temperature profiles observed with dipoles disappears with the quadrupole, and the increase of metallic ions originating from the activated screen (Cr for one antenna, Ni for the other [9]) is about halved. The density evolution was also different in the two cases: the average density increased more with the quadrupole. Despite this higher density, the radiated power  $P_{rad}$  was significantly lower and the carbon released from the wall was typically  $\times 2-3$  smaller. The heating efficiency defined by the incremental confinement time  $\tau_{inc} = (\Delta W / \Delta P)$  was higher in the quadrupole phasing by typically 25% for similar plasma conditions. Table II summarizes this comparison between the two phasing conditions, in which  $I_{Ni}$ ,  $I_{Cr}$  are the intensities of Ni XXVI and Cr XXII lines and  $\phi$  is total neutral flux.

It is clear from these experiments that the edge modification induced with dipole phasing is considerably reduced with the quadrupole. The metallic impurity emitted by the activated screen and the insensitiveness of phasing between adjacent antennas suggest that the RF field pattern immediately in front of each antenna screen plays a key role.

## 5. HIGH POWER EXPERIMENTS : OPERATING REGIMES

With ICRF alone, it is difficult to couple large amounts of power when the plasma current is low (e.g. at  $I_p = 1$  MA). The plasma disrupts at only 1 MW, as the density rise during ICRF approaches the density limit. At  $I_p \geq 2$  MA, no power limit was found. Combined ICRF and NBI operation removed the power limitations at 1 MA.

Experiments with long pulses (5 MW, 8 s) have shown that quasi-stationary conditions are reached after about 2 s. No serious accumulation of high-Z impurity was observed and the plasma central temperatures remained constant after the initial rise.

Neutral beam injection increased the antenna coupling resistance. This increase can be highly beneficial; for instance, when the plasma is in contact with the inner wall and 5 cm away from the antenna, the coupling resistance more than doubled. The technical difficulty of coping with large changes of coupling resistance meant that it can be difficult to maintain constant

TABLE II. COMPARISON OF DIPOLE AND QUADRUPOLE PHASING  
1 MW coupled power and identical starting plasma conditions

	$\frac{\Delta I_{Ni}}{\langle n_e \rangle}$ (a.u.)	$\frac{\Delta I_{Cr}}{\langle n_e \rangle}$ (a.u.)	$\Delta P_{rad}$ (MW)	$\Delta Z_{eff}$	$\Delta n_e d l$ ( $10^{19} \text{m}^{-2}$ )	$\Delta \phi$ ( $10^{21} \text{s}^{-1}$ )	$\tau_{inc}$ (s)
Dipole	1.8	3.1	0.74	0.34	0.49	0.05	0.17
Quad- rupole	1.2	1.5	0.57	0.14	0.79	0.58	0.23

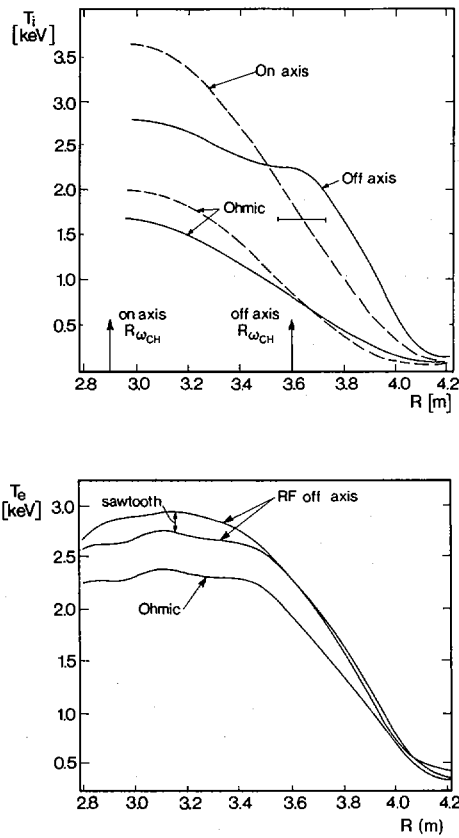


FIG. 3. Electron and ion temperature profiles during the ohmic phase (before RF) and during on-axis or off-axis RF heating. The main effect of off-axis heating is a broadening of the  $T_i$  profile.

on-axis:  $B_\phi = 2.3 \text{ T}$ ,  $\nu = 37 \text{ MHz}$ ,  $P_e = 3 \text{ MW}$ ,  $I_p = 2.5 \text{ MA}$ ,  $q(a) = 3.25$

off-axis:  $B_\phi = 2.5 \text{ T}$ ,  $\nu = 31.8 \text{ MHz}$ ,  $P_e = 5 \text{ MW}$ ,  $I_p = 2.5 \text{ MA}$ ,  $q(a) = 3.55$ .

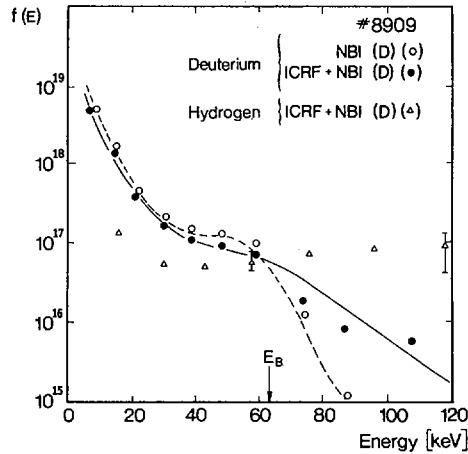


FIG. 4. Deuterium and hydrogen energy spectra before and during a 'monster sawtooth' ( $P_{NBI} = 2.5$  MW, 65 keV;  $P_{RF} = 7$  MW).  $I_p = 2$  MA,  $B_\phi = 2.13$  T,  $\nu = 31.8$  MHz. Acceleration of beam injected ions up to 120 keV is observed.

RF power when the beams are switched on during a RF pulse. Injecting RF power during a NBI pulse is normally straightforward. The variation of coupling resistance with the crash of the large sawteeth is often a factor limiting the power during the pulse.

## 6. COMBINED RF AND PELLETT INJECTION

Combining ICRF with pellet injection did not raise any special technical problems. 6MW RF could be applied at the time of injection of a mildly penetrating pellet (3.6 mm,  $1\text{km}\cdot\text{s}^{-1}$ ). The power was ramped up over 0.5s. The change of coupling resistance due to the pellet was hardly noticeable. The ratio of radiated power to input power increased only slightly by 10-20% despite a doubling of the average density. The pellet increased the density from  $\langle n_e \rangle = 1.9 \times 10^{19} \text{ m}^{-3}$  to  $3.7 \times 10^{19} \text{ m}^{-3}$ . Without RF, the density decayed typically on a 1s time scale. With RF, the density was sustained at its maximum level and even slightly increased for the duration of the RF pulse (2s). The increase of  $T_i(0)$  and  $T_e(0)$  with  $P_{RF}/\langle n_e \rangle$  was comparable with the largest increments obtained in the similar discharges without the pellet. The energy confinement during RF was not modified by pellet injection. The incremental confinement time with the pellet becomes  $\tau_{inc} = 0.2$ s. Large sawteeth appear early in the reheat phase. The pellet penetration was not changed by the presence of ICRF.

## 7. COMBINED HEATING AND BEAM ACCELERATION

Generally, ICRF plasma heating on the outboard limiters behaves according to the L-mode scaling law [1,2]. Recent combined NBI and ICRF heating up to 16MW has been performed. The energy confinement scaling is reported in [10]. Again L-mode behaviour is found, although inner wall operation and high -q operation perform somewhat better than the 'Goldston L-mode scaling'. Both H and  $\text{He}^3$  minority scenarios have been tested, but the stored energy increase is not appreciably different in the two cases.

In combined RF and NBI heating, the H minority scenario has a distinctive feature: power can be coupled to the energetic D beam ions at the harmonic cyclotron resonance. It is calculated [11] that the NBI current drive will be enhanced by ICRF. The beam acceleration also enhances the fusion reactivity.

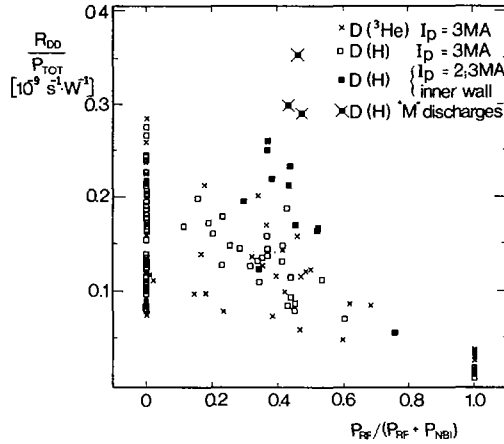


FIG. 5. Fusion D-D reaction rate normalized to the total input power versus the ratio of RF to total additional power. The beam plasma reaction is maintained proportional to the additional power, independently of its origin, provided  $P_{RF}/(P_{NBI} + P_{RF}) \leq 0.5$ . Monster sawteeth give a larger fusion yield.

Figure 4 demonstrates beam acceleration by ICRF. The slope of the energy distribution function above the injection energy increases from 5keV to 16keV. Simulation by a Fokker-Planck calculation [12] requires that a substantial fraction of the incident RF power is coupled to the beam ions. However, note that the high energy tail of the proton still exceeds the D tail (Fig. 4) and most of coupled power is still transferred to the protons. The fraction of power directly transferred to the beam ions is estimated [13] to be about 10%. It is expected to increase non-linearly with RF power.

The fusion reactivity in these D → D injection experiments is dominated by beam-plasma reactions. RF heating increases the reactivity roughly in proportion to the total heating power (cf. Fig. 5) provided the RF power does not exceed the NBI power. Comparison between the He<sup>3</sup> and H minority shows that a higher reactivity is obtained in the H minority experiments ( $n_H/n_D \sim 2 \times 10^{-2}$ ).

## 8. MONSTER SAWTOOTH

Unusually long sawteeth and high fusion reactivity have been observed in the so-called 'Monster sawtooth' regime in the following conditions:

- $I_p = 2 - 2.2$  MA,  $B_\phi = 2.1 - 2.2$  T, Plasmas lying on the inner wall. H minority, RF alone or combined with beams
- $I_p = 5$  MA,  $B_\phi = 3.4$  T, He<sup>3</sup> minority, combined heating
- $5 \text{ MW} \leq (P_{RF} + P_{NBI}) \leq 15 \text{ MW}$
- $2 \times 10^{19} \text{ m}^{-3} < \bar{n}_e < 3.5 \times 10^{19} \text{ m}^{-3}$

Fig. 6 illustrates such a regime when the RF is applied on top of NBI injection. The internal relaxations stop and the plasma is remarkably free from MHD activity for  $\sim 1$  s.  $T_e(0)$  more than doubles and a peak temperature of 7.4 keV has been obtained with 10MW of additional power. The  $T_e$  gradient steepens in the entire profile. The inversion radius appears to expand up to mid-radius. In many cases, the stored energy does not saturate before the crash, even

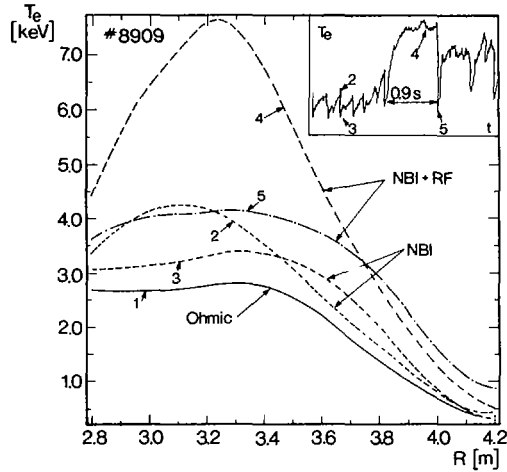


FIG. 6.  $T_e$  profile before heating (ohmic) during  $P_{NBI}$  (2.5 MW) and during a 'monster sawtooth' ( $NBI = 2.5$  MW,  $P_{RF} = 7$  MW). In each case, the curves represent the top and bottom of a sawtooth. Note the increase of the inversion radius.

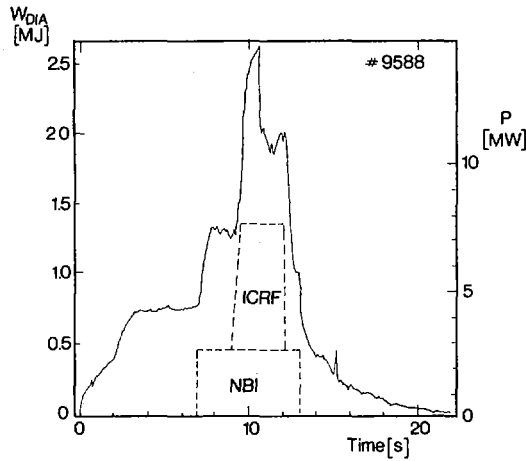


FIG. 7. Evolution of the stored energy during the longest 'monster sawtooth' (1.26 s). Although  $T_e$  saturates, the density and the stored energy keep increasing.  $P_{NBI} = 2.6$  MW (80 keV),  $P_{RF} = 5.5$  MW,  $I_p = 2.2$  MA,  $B_\phi = 2.18$  T.

after 1.26s (Fig. 7). The incremental confinement time  $\tau_{inc} = \Delta W / \Delta P_{RF}$  is somewhat improved over the usual conditions. Typically,  $\tau_{inc} = 250$  ms at the end of the 'Monster' instead of 200ms in normally sawteething discharges. The pressure anisotropy is mild:  $\beta_{p\perp} = 1.13$   $\beta_{p\parallel} = 0.5$ . The crash of the monster releases 30% of the stored energy. Thereafter, the MHD activity is high (mostly  $n = 2$  modes) and the confinement appears degraded. In these experiments, the poloidal beta reached 0.5 and the ion temperature was between 5 and 7keV.

## 9. TRANSITION TO AN 'H-MODE'

Preliminary experiments with combined heating in a single null X-point configuration exhibited the change of edge and bulk plasma parameters in the Asdex H-mode behaviour. The transition occurred with 7 MW of combined heating in the Hydrogen minority regime. After the transition, the density rose, the temperature remaining constant, and the confinement time increased from 0.35 s to 0.6 s.

## 10. CONCLUSIONS

After a year of operation on JET, ICRF heating has reached record levels of RF power and electron temperatures in a Tokamak. Eight water cooled antennas will be installed in 1987 and connected to a 32 MW power source. Recent results give confidence that JET will demonstrate a fusion output comparable to the heating power input.

## REFERENCES

- [1] JACQUINOT, J., et al., *Plasma Phys. Controll. Fusion* **28** (1986) 1.
- [2] LALLIA, P.P., et al., *Plasma Phys. Controll. Fusion* **28** (1986) 1211.
- [3] KAYE, A.S., in *Fusion Engineering (Proc. 11th Symp. Austin, TX, 1985)*, Vol. 2, IEEE, New York (1986) 1204.
- [4] DUESING, G., et al., *Plasma Phys. Controll. Fusion* **28** (1986) 1429.
- [5] GAMBIER, D., et al., in *Controlled Fusion and Plasma Physics (Proc. 12th Europ. Conf. Budapest, 1985)*, Vol. 9F, Part II, European Physical Society (1985) 152.
- [6] BHATNAGAR, V.P., KOCH, R., GEILFUS, P., KIRKPATRICK, R., WEYNANTS, R.R., *Nucl. Fusion* **24** (1984) 955.
- [7] HELLSTEN, T., APPERT, K., in *Controlled Fusion and Plasma Heating (Proc. 13th Europ. Conf. Schliersee, 1986)*, Vol. 10C, Part II, European Physical Society (1986) 129.
- [8] SAND, F., et al., *ibid.*, p. 197.
- [9] BEHRINGER, K., et al., Paper IAEA-CN-47/A-IV-1, these Proceedings, Vol. 1.
- [10] CORDEY, J.G., et al., Paper IAEA-CN-47/A-II-3, these Proceedings, Vol. 1.
- [11] HAMNEN, H., et al., in *Controlled Fusion and Plasma Heating (Proc. 13th Europ. Conf. Schliersee, 1986)*, Vol. 10C, Part II, European Physical Society (1986) 425.
- [12] CORE, W., et al., *ibid.*, p. 73.
- [13] COTTRELL, G., private communication, 1986.

## DISCUSSION

R.J. GOLDSTON: Do you have any idea why the duration of the 'monster sawtooth' before the crash is so long?

J. JACQUINOT: We first thought this might be due to NBI current drive enhanced by the local increase in  $T_e$  produced by ICRF. The recent observation that good 'monster sawteeth' with similar input powers are also obtained with RF alone weakens this model very much and leaves us without a clear physical picture to offer as an explanation.

K. ITOH: During the 'monster sawtooth', the time behaviour of the electron temperature indicates that the electron energy confinement is not improved, while the total stored energy increases continuously. Do you observe any increase in ion energy which is due to the appearance of the 'monster sawtooth'? And do you conclude that ion energy confinement is improved by 'monster sawteeth'?

J. JACQUINOT: The improvement of confinement during a 'monster sawtooth' seems to be related with the continuous increase in electron density and in the size of the  $q = 1$  surface. The additional stored energy is mainly in the electrons.

# ION CYCLOTRON HEATING AND LOWER HYBRID EXPERIMENTS ON ASDEX

K. STEINMETZ, F.X. SÖLDNER, D. ECKHARTT, G. JANESCHITZ,  
F. LEUTERER, F. MAST, K. McCORMICK, J.-M. NOTERDAEME,  
C. SETZENSACK, F. WAGNER, F. WESNER, I. BÄUMLER, G. BECKER,  
H.S. BOSCH, M. BRAMBILLA, F. BRAUN, H. BROCKEN, H. DERFLER,  
A. EBERHAGEN, H.-U. FAHRBACH, G. FUSSMANN, R. FRITSCH,  
O. GEHRE, J. GERNHARDT, G. von GIERKE, E. GLOCK, O. GRUBER,  
G. HAAS, J. HOFMANN, F. HOFMEISTER, K. HÜBNER<sup>1</sup>,  
A. IZVOZCHIKOV<sup>2</sup>, F. KARGER, M. KEILHACKER<sup>3</sup>, O. KLÜBER,  
M. KORNHERR, K. LACKNER, M. LENOCI, G. LISITANO,  
E. VAN MARK, H.M. MAYER, D. MEISEL, V. MERTENS, E.R. MÜLLER,  
E. MÜNICH, H. MURMANN, H. NIEDERMAYER, Z.A. PIETRZYK<sup>4</sup>,  
W. POSCHENRIEDER, S. PURI, H. RAPP, H. RIEDLER, H. RÖHR, J. ROTH,  
F. RYTER<sup>5</sup>, K.H. SCHMITTER, F. SCHNEIDER, G. SILLER,  
P. SMEULDERS<sup>3</sup>, E. SPETH, K.-H. STEUER, T. VIEN, O. VOLLMER,  
H. WEDLER, D. ZASCHE, M. ZOUHAR

Euratom-IPP Association,  
Max-Planck-Institut für Plasmaphysik,  
Garching, Federal Republic of Germany

## Abstract

### ION CYCLOTRON RESONANCE HEATING AND LOWER HYBRID EXPERIMENTS ON ASDEX.

A summary is given of recent experimental investigations with ICRH and LH on the divertor tokamak ASDEX. Hydrogen second harmonic heating ( $2\Omega_{\text{CH}}$  at 67 MHz), hydrogen minority heating (D(H) at 33.5 MHz), and ICRH in combination with neutral beam injection (NI) are compared in detail at different parameters ( $P_{\text{IC}} \leq 2.6$  MW,  $P_{\text{NI}} \leq 4.4$  MW,  $I_{\text{p}} = 250$  to 450 kA,  $\bar{n}_{\text{e}} = 2$  to  $9 \times 10^{13}$  cm<sup>-3</sup>). Heating and current drive with waves have been studied in Ohmic target plasmas and in combination with NI heating up to a total heating power of 4 MW ( $P_{\text{NI}} \leq 3$  MW plus  $P_{\text{LH}} \leq 1$  MW).

<sup>1</sup> University of Heidelberg, Heidelberg, Fed. Rep. Germany.

<sup>2</sup> Academy of Sciences, Leningrad, USSR.

<sup>3</sup> JET Joint Undertaking, Abingdon, Oxfordshire, UK.

<sup>4</sup> University of Washington, Seattle, WA, USA.

<sup>5</sup> CEA, Centre d'études nucléaires de Grenoble, France. Present address: Centre de recherches en physique des plasmas, Ecole polytechnique fédérale de Lausanne, Lausanne, Switzerland.

### ION CYCLOTRON RESONANCE HEATING

Various heating schemes have been investigated on ASDEX: Hydrogen second harmonic heating ( $2\Omega_{CH}$ , 67 MHz, in pure hydrogen or D/H mixtures), hydrogen minority heating (D(H), 33.5 MHz,  $n_H/n_e \approx 5\%$ ), neutral beam injection ( $H^0 \rightarrow H^+$ ,  $H^0 \rightarrow D^+$ ,  $D^0 \rightarrow H^+$ ,  $D^0 \rightarrow D^+$ ) and the combination of NI with ICRH. Thus, a thorough comparison with respect to heating, confinement, and plasma performance in a wide range of parameters can be provided.

#### H-mode with pure ICRF heating

The H-mode has been realized - for the first time - with ICRH alone in the D(H)-minority scheme at an absorbed RF power of about 1.1 MW /1, 2/. Thus, it appears that the dominant confinement regimes of auxiliary heated plasmas are found to be independent of the heating method. At that power level the H-mode is achieved just marginally as shown in Fig. 1 where a typical example of an ICRF heated discharge is displayed in comparison to an L-type plasma. The H-mode, developing out of an L-phase with sawteeth, shows all characteristic features like a distinct drop in the  $H_\alpha$ -signal in the divertor chamber (which is mostly a measure of the reduced power flux into the divertor), rising electron density (indicating an improved particle confinement), enhanced plasma energy content (owing to improved energy confinement), a significantly enhanced edge electron temperature (rising from about 50 eV to 250 eV at  $r/a = 0.98$ ; not shown in Fig. 1), and the existence of the typical MHD-phenomenon, called ELMs (edge localized modes) /3/. The sudden occurrence of ELM-free phases (marked by H\*) changed the antenna coupling to such an extent that always one of the generators terminated operation by voltage breakdown. Unfortunately, this technical difficulty could not be avoided so far.

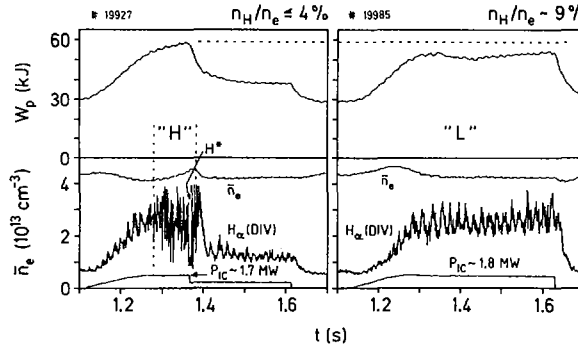


FIG. 1. Plasma energy, line averaged electron density, and  $H_{\alpha}$  signal of ICRF heated discharges with/without H-mode transition.

### Hydrogen minority and second harmonic heating

Wall carbonisation prevented disruptions otherwise caused by excessive impurity radiation and allowed the ICRH to work up to maximal power ( $P_{IC} \approx 15 P_{OH}^*$ ) without NI assistance. Thus, confinement conditions of purely ICRF heated plasmas could be studied. At high power in standard (double-null) configuration both RF scenarios follow essentially an L-type scaling where the D(H)-scheme appears to be slightly better. Figure 2 summarizes the energy confinement times normalized to the values of the Ohmic phases (which eliminates isotope effects on  $\tau_E^*$ ) for the D(H)-scheme and for  $2 \Omega_{CH}$  in hydrogen and hydrogen/deuterium mixture plasmas. The confinement degradation of both RF schemes seems, however, less severe than with beam heating. This is supported by the observation that, with ICRH, the particle confinement does only weakly degrade with respect to the Ohmic phase which is indicated by the constancy of the plasma density during the ICRH pulse, and is supported by an increased impurity confinement during ICRH with respect to the NI L-phase (see also Fig.3).

Figure 3 illustrates the decay (transport) times of TiXX, injected into the plasma by laser blow-off, indicating similar

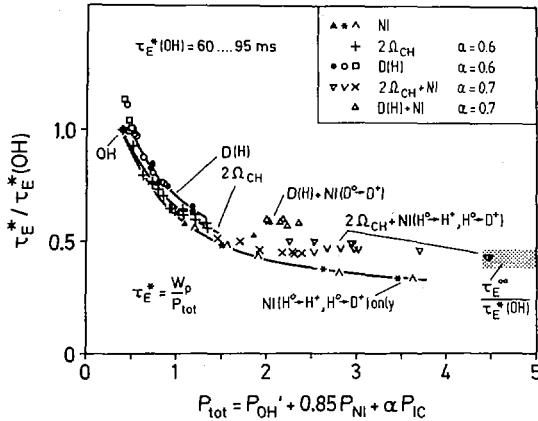


FIG. 2. Energy confinement times (normalized to the value of the Ohmic phase) versus total power.

trends for impurity/particle transport and confinement. The transport analysis suggests an enhancement of the inward drift rather than a reduction of the diffusion coefficient with respect to NI. It is not yet clear whether the improved particle confinement or the absence of plasma rotation during ICRF heating has an influence on the degree of energy confinement degradation.

#### Combination of ICRH and NI

Both RF heating schemes have been combined with neutral beam injection up to total heating power of  $P_{\text{tot}} \approx 4.5 \text{ MW} \approx 50 P_{\text{OH}}'$ . The injection of either deuterium or hydrogen together with  $2\Omega_{\text{CH}}$ -launching clearly indicated bulk heating as the main ICRF absorption scenario. Heating by direct coupling of the wave with the injected particles was found to be negligible [1, 9]. When combining ICRH + NI the degradation of confinement at high power seems to be again less severe than with beam heating alone (Fig. 2). In particular, ICRH + NI data indicate the existence of a substantial residual energy confinement at high

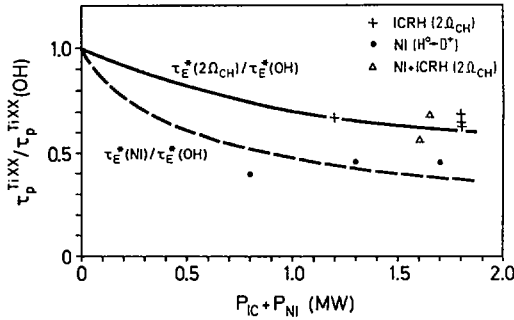


FIG. 3. Transport times of Ti XX compared to global energy confinement.

power ( $\tau_E^*$ -plateau). The corresponding values  $\tau_E^* / \tau_E^*(OH) = 0.43 - 0.50$ , where  $\tau_E^* = W_p / (P_{OH}' + \alpha P_{IC} + 0.85 P_{NI})$ , are consistent with a  $\tau_E^\infty$ -analysis modelling the increase of plasma energy content following an RF power step by  $W_p(t) = W_p(OH) + \Delta W_p^{IC} \cdot (1 - \exp(-t/\tau_E^\infty))$  which gives - under certain assumptions - a measure of the ultimate energy confinement time at "infinitely" large auxiliary heating power. In these experiments the plasma energy content has been increased by a factor of 5, from 26 kJ at  $P_{OH} = 0.4$  MW to 123 kJ at 4.4 MW total heating power. The improved confinement of the combined scenario is also supported by a reduced impurity transport (Fig. 3).

#### Hydrogen second harmonic heating of two-species plasmas

Second harmonic heating has also successfully been applied to H/D mixtures of hydrogen concentrations where conventional hydrogen minority heating at the fundamental frequency does no longer work. In H/D mixtures where the resonant species ( $H^+$ ) is a relatively small fraction of the total particle content the RF heating efficiency, defined as increase of plasma energy content per MW launched power ( $\Delta W_p^{IC} / P_{IC}$ ), is found to be strongly enhanced beyond that of pure hydrogen operation (Fig. 4) probably due to the isotope effect on confinement as

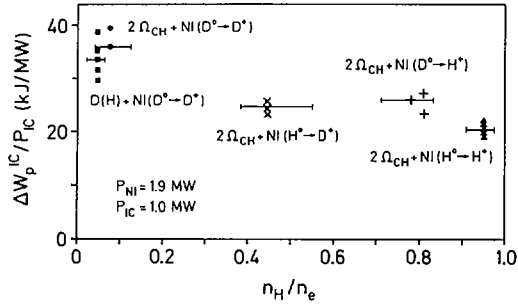


FIG. 4. ICRF heating efficiency at various hydrogen concentrations.

observed also with NI heating. At the lowest hydrogen concentrations ( $n_H/n_e \approx 0.1$ ) the heating efficiency of the " $2\Omega_{CH}$ -minority" scenario /1/ ( $\approx 36$  kJ/MW) compares well with that of the conventional D(H)-hydrogen minority mode ( $\approx 35$  kJ/MW) and is well above that of  $2\Omega_{CH}$ -heating in pure hydrogen ( $\approx 21$  kJ/MW). Unsuccessful application of  $2\Omega_{CH}$  to helium and pure deuterium plasmas clearly ruled out the possibility of 4th harmonic heating.

On the basis of these results second harmonic heating appears as an attractive scenario for a reactor-like DT-plasma where efficient heating is expected to be performed much easier in the  $2\Omega_{CT}$ -scheme than in a three species minority scenario (e.g. hydrogen minority in a DT-mixture) owing to the probably difficult control of the minority concentration within a tight window of  $n_H/n_e$ .

#### Impurity behaviour

The ICRF related reduction of particle and impurity transport with respect to NI (see Fig. 3) leads to an enhanced impurity level which is dominated by iron released from the torus walls /4/. The power radiation of about 35 %, mainly originating from the plasma centre (Fig. 5), limits high power ICRF operation to

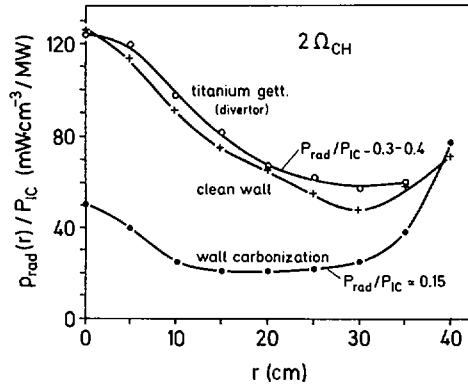


FIG. 5. Radiation density profiles for different torus wall conditions.

$P_{IC} < 1.5$  MW if no wall carbonisation or NI preheating is provided. Carbonisation of the torus wall allowed an almost iron free plasma with a radiation level of about 15 % (Fig. 5) where the residual peaking sometimes observed in the radiation profile results mainly from an imperfect carbon coating. In addition, another mechanism of impurity release has been determined which is related to wave absorption: Conditions of poor central wave absorption have always been accompanied by a particular large central radiation as verified at e.g.  $2\Omega_{CH}$  in helium or pure deuterium discharges. The anti-correlation of central wave absorption and central radiation level indicates that RF power absorbed in the outer region of the plasma, leading to strongly enhanced CX fluxes at the plasma edge /9/ and thereby increasing the metal impurity release, might play a deleterious role in terms of ICRH induced impurity generation.

### Lower Hybrid Experiments

Heating and current drive with Lower Hybrid (LH) waves at  $f_o = 1.3$  GHz have been studied in Ohmic target plasmas and in combination with NI-heating ( $P_{NI} \leq 3$  MW) for various LH wave

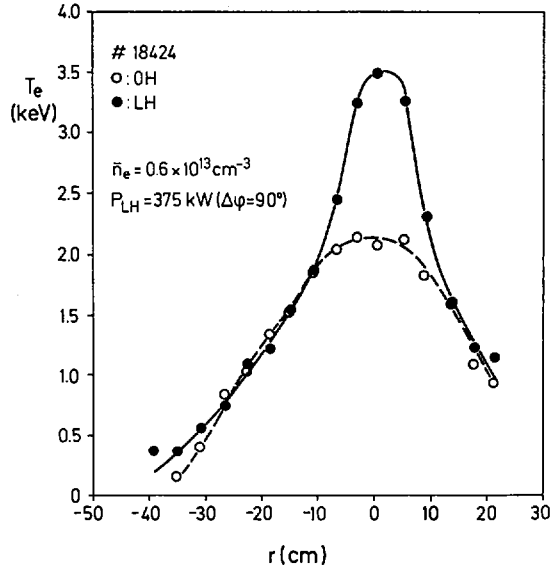


FIG. 6. Radial electron temperature profiles during Ohmic and complete LH current drive ( $U_1 = 0$ );  $I_p = 300 \text{ kA}$ .

spectra with transmitted power up to  $P_{LH} = 1 \text{ MW}$  and pulse duration  $\tau \leq 1.5 \text{ s}$ . Efficient modification of the current density profile can be achieved by appropriate shaping of the LH wave spectrum.

#### Lower Hybrid Heating

Strong electron heating is obtained when LH waves are absorbed by suprathermal electrons below the onset of ion interaction ( $\bar{n}_e \leq 3 \times 10^{13} \text{ cm}^{-3}$  on ASDEX). At low density the electron temperature profile peaks with the central value strongly increasing. In Fig. 6 the  $T_e(r)$  profiles are shown during the Ohmic phase and during complete steady state LH current drive ( $U_1 = 0$ ) at  $\bar{n}_e = 0.6 \times 10^{13} \text{ cm}^{-3}$  ( $P_{OH} = 240 \text{ kW}$ ,  $P_{abs}^{LH} = 375 \text{ kW}$ ). With LH current drive much higher temperatures are observed in the central region inside  $r \approx 10 \text{ cm}$  ( $a = 40 \text{ cm}$ ) with  $T_e(0)$ :  $2 \rightarrow 3.5 \text{ keV}$ . Qualitatively similar results are obtained in the

LH heating mode with stationary wave spectra. The zone of temperature increase in all these cases seems to be restricted to the region inside the  $q = 1$  surface. The observed strong central heating is not due to the suppression of sawteeth which is only attained in the case of LHCD but not in the heating mode.

Power balance calculations are carried out for the LH heating and current drive modes (LHH, LHCD). The absorption coefficient, as determined from the rate of change of the plasma energy content at the beginning of the RF pulse, decreases from about 0.8 at  $\bar{n}_e = 1 \times 10^{13} \text{ cm}^{-3}$  to about 0.3 at  $\bar{n}_e = 2 \times 10^{13} \text{ cm}^{-3}$ . This could be explained by a decrease of the RF power accessible to the plasma centre /5/. The absorption coefficient also decreases with increasing RF power, thus indicating saturation effects. The energy confinement with LHH and LHCD is improved at low density above the Ohmic values ( $\bar{n}_e = 0.6 \times 10^{13} \text{ cm}^{-3}$ ,  $I_p = 300 \text{ kA}$ :  $\tau_E^{\text{OH}} \approx 25 \text{ ms} \rightarrow \tau_E^{\text{LH}} \approx 50 \text{ ms}$ ). With increasing RF power the energy confinement time decreases. The region of improved confinement seems to be limited to the parameter range where the total power input with application of LH is reduced below the power input in the Ohmic phase.

LHH and LHCD have been combined with NI at high power levels:  $P_{\text{LH}} \leq 1 \text{ MW}$ ,  $P_{\text{NI}} \leq 3.4 \text{ MW}$ . At low density the same L scaling for the confinement is found for NI and for the combination with LH as shown in Fig. 7. LH heating itself is improved by preheating from NI, mainly due to an additional direct interaction of LH waves with the beam ions in the plasma centre. These are accelerated up to twice the injection energy as observed in charge exchange measurements /9/.

#### Lower Hybrid Current Drive

Efficient saving of voltseconds in the primary OH transformer can be obtained in the mode of combined RF and inductive

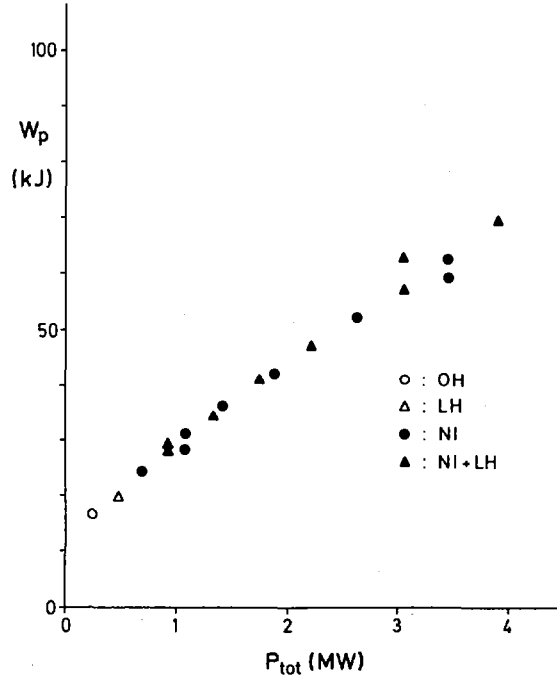


FIG. 7. Plasma energy content  $W_p$  versus total injected heating power  $P_{tot}$  for NI, LHCD and the combination of both ( $\bar{n}_e = 1.1 \times 10^{13} \text{ cm}^{-3}$ ,  $I_p = 300 \text{ kA}$ ).

current drive. The fraction of OH power replaced by LH power ( $-\Delta P_{OH}^{LH}/P_{OH}^{OH}$ ) and the corresponding conversion rate ( $-\Delta P_{OH}^{LH}/P_{LH}^{LH}$ ) are shown in Fig. 8 as functions of  $P_{LH}$  for different densities. The total plasma current is kept constant in all these experiments by a feedback regulation of the OH primary circuit. High efficiencies for replacement of OH power by LH power can be achieved at low  $P_{LH}$  where the LH generated suprathermal electrons increase the electrical conductivity and thereby improve the OH current drive efficiency [6]. At low densities a large reduction in OH power can be obtained with a high conversion rate for the LH power:  $-\Delta P_{OH}^{LH}/P_{OH}^{OH} \approx 1$  with  $-\Delta P_{OH}^{OH}/P_{LH}^{LH} \approx 1$  for  $\bar{n}_e \leq 0.5 \times 10^{13} \text{ cm}^{-3}$ .

In combination with NI the LH current drive efficiency is reduced, as shown in Fig. 9 where the drop in OH power upon

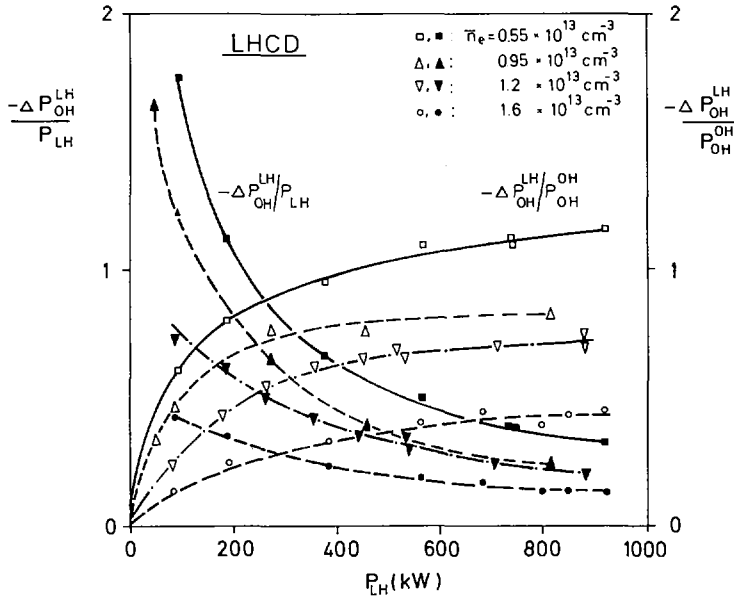


FIG. 8. Drop in OH power input  $-\Delta P_{OH}^{LH} / P_{OH}^{OH}$  during LHCD and corresponding conversion rate of LH power  $-\Delta P_{OH}^{LH} / P_{LH}$  versus  $P_{LH}$ ;  $I_p = 300 \text{ kA}$ .

LHCD is plotted versus  $P_{NI}$ : It decreases with increasing beam power, probably due to the direct absorption of LH power by the beam ions which then reduces the power flow to the electrons. This is also indicated by the strong drop in hard X-ray intensity and suprathreshold ECE emission from fast electrons during the presence of fast beam ions in the plasma.

#### Current Profile Modification

The current profile  $j(r)$  during LHCD is no longer determined by Spitzer resistivity. The  $T_e(r)$  and the  $j(r)$  profiles are decoupled by LHCD in OH target plasmas and in NI heated plasmas. The current profile broadens while the  $T_e(r)$  profile peaks. The broadening of  $j(r)$  as derived from the drop in internal inductance  $l_i$  normally increases with the amount of the RF-driven current. A different behaviour is found in experiments

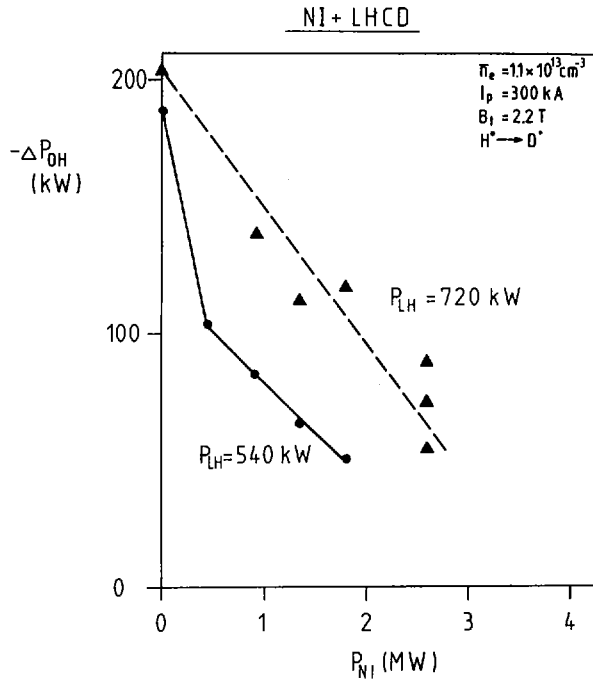


FIG. 9. Drop in OH power input with LHCD in combination with NI as function of  $P_{NI}$ .

where the form of the LH wave spectrum was changed gradually, by shifting power from high to low phase velocities, with the total power kept constant. This leads to a gradual decrease of the total RF-driven current whereas the drop in  $l_1$  increases in the same way /7/. The LH waves with lower phase velocities therefore seem to be absorbed closer to the plasma periphery. The local off-axis LH-current drive then leads to the stronger broadening of  $j(r)$ . An external control of the local plasma current distribution by LH-current drive with an appropriate wave spectrum and the related deposition profile seems therefore possible.

By broadening  $j(r)$  such that the central  $q$ -value increased above 1, sawteeth could be stabilised with LH-current drive in OH- and NI-heated plasmas /8/. With normal current drive

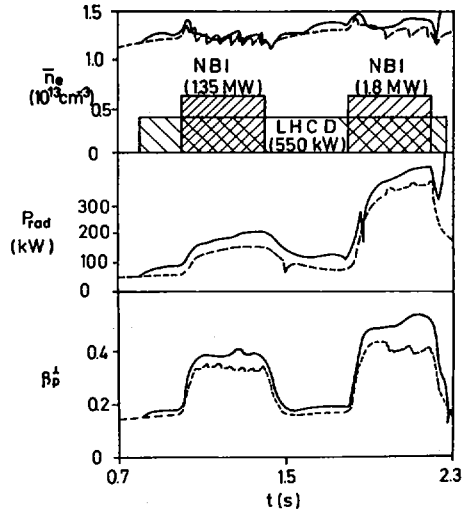


FIG. 10. Waveforms of density  $\bar{n}_e$ , total radiated power  $P_{rad}$  and diamagnetic  $\beta_p$  for a sawtoothing NI heated discharge (dashed lines) and for a sawtooth-free discharge with NI and LHCD (solid lines);  $I_p = 380$  kA,  $B_t = 2.2$  T,  $q(a) = 2.75$ .

spectra for this about half the power of complete LH-current drive is necessary when LH is applied to OH plasmas. With NI the LH power required for sawtooth suppression decreases with increasing beam power. Stabilisation of the sawteeth results in higher central electron temperatures and in slightly improved global energy confinement as seen from Fig. 10.

## SUMMARY

The application of waves in the frequency range of ICRH or LH on ASDEX has been proved as a useful tool for either heating or current drive. ICRH efficiently heats the plasma in various  $2\Omega_{CH}$ - and D(H)-regimes where the H-mode has also been achieved. In combination with NI,  $\tau_E^*$  is improved above the usual L-type scaling where at high power a substantial residual energy confinement is observed. Strong electron heating is found with LH in the suprathreshold electron regime with confinement better than

Ohmic at low density. In combination with NI, acceleration of beam ions is observed. Decoupling of  $T_e(r)$  and  $j(r)$  by LHCD allows independent control of current and heat deposition profiles.

## REFERENCES

- [1] STEINMETZ, K., et al., in *Controlled Fusion and Plasma Heating* (Proc. 13th Europ. Conf. Schliersee, 1986), Vol. 2, European Physical Society (1986) 21.
- [2] WAGNER, F., et al., *Plasma Phys. Controll. Fusion* **28** (1986) 1225.
- [3] KEILHACKER, M., et al., *Plasma Phys. Controll. Fusion* **26** (1984) 49.
- [4] JANESCHITZ, G., et al., in *Controlled Fusion and Plasma Heating* (Proc. 13th Europ. Conf. Schliersee, 1986), Vol. 1, European Physical Society (1986) 407.
- [5] SÖLDNER, F., et al., in *Controlled Fusion and Plasma Physics* (Proc. 12th Europ. Conf. Budapest, 1985), Vol. 2, European Physical Society (1985) 244.
- [6] LEUTERER, F., et al., *Plasma Phys. Controll. Fusion* **27** (1985) 1399.
- [7] LEUTERER, F., et al., in *Controlled Fusion and Plasma Heating* (Proc. 13th Europ. Conf. Schliersee, 1986), Vol. 2, European Physical Society (1986) 409.
- [8] SÖLDNER, F., et al., *Phys. Rev. Lett.* **57** (1986) 1137.
- [9] RYTER, F., et al., in *Controlled Fusion and Plasma Heating* (Proc. 13th Europ. Conf. Schliersee, 1986), Vol. 1, European Physical Society (1986) 101.

## DISCUSSION

S.-I. ITOH: In your summary you said that the confinement structure was not dependent on the heating method. On the other hand, in the case of the particle confinement time (obtained by  $T_i$  line radiation), there is a discrepancy between neutral injection and ICRF heating. What kind of confinement is it that is not dependent on the heating method?

Secondly, with respect to LH heating you stated that the heating was restricted inside the  $q = 1$  surface. Did you see any MHD instabilities due to the sudden rise in  $T_e$  and/or  $\nabla T_e$  inside the  $q = 1$  surface.

K. STEINMETZ: Non-dependence of the confinement structure on the auxiliary heating method means the general existence of an L-type and H-mode behaviour with NI as well as with ICRH. With respect to  $\tau_E$  or  $\tau_p$ , both heating schemes exhibit the same type of scaling, as shown in Fig. 3 of the paper, although the confinement for ICRH is slightly improved compared to that for NI. So there is no discrepancy in terms of the global confinement structure.

No MHD stabilities due to the central electron heating by LH waves were seen. For application of LH alone, the heating efficiency is similar in the current drive mode without sawteeth and in the heating mode in the presence of sawteeth.

H. MATSUMOTO: In your conclusions you said that you have observed an improvement in confinement during ICRF second harmonic heating and during NBI heating through an increase in the heating power. However, this may simply be due to an improvement in absorption of the wave at the second harmonic resonance when the plasma beta was increased. What is your opinion?

My second question is, did you use the constant power absorption coefficient  $\alpha$  when evaluating the RF heating power input to calculate the global confinement time in Fig. 3? And further, how did you determine  $\alpha$ ?

K. STEINMETZ: When the plasma beta was increased by neutral beam injection, the experimentally derived effective ICRH power absorption was found to increase from  $\alpha_{IC} \approx 0.6$  to  $\alpha_{IC} \approx 0.7$ . Since the experimental values of  $\alpha$  are used to calculate  $\tau_E^*$ , the observed improvement in confinement of ICRH plus NI, with respect to NI only, cannot be attributed to the measured change of  $\alpha$ .

For pure ICRH heating,  $\alpha = 0.6$  is taken, while for the combined ICRH plus NI scheme,  $\alpha = 0.7$ , as shown in Fig. 2 of the paper. The effective power absorption is derived via the rate of change in the plasma beta,  $d\beta/dt$ , when the RF is switched on or off, and by modelling the increase in the plasma energy content following an RF power step (see the paper presented by our group at the 13th European Conference in 1986).

R.R. WEYNANTS: Does the effectively absorbed power,  $\alpha$ , change significantly when going from one ICRH heating scenario to the other?

K. STEINMETZ: No. The ICRH absorption coefficient  $\alpha_{IC} \approx 0.6$  is about equal in the  $2\Omega_{CH}$  and the D(H) minority regimes. When ICRH is combined with neutral beam injection, the effective ICRH absorption increases to  $\alpha_{IC} \approx 0.7$ . I should note that we have cross-checked our procedures used to determine  $\alpha$  by applying them to purely NI-heated plasmas and found good agreement between the numerically computed values using a beam deposition code and the experimentally derived values of  $\alpha_{NI} \approx 0.9-1$ .



## ION BERNSTEIN WAVE HEATING EXPERIMENTS ON PLT

M. ONO, P. BEIERSDORFER, R. BELL, S. BERNABEI,  
A. CAVALLO, A. CHMYGA<sup>1</sup>, S.A. COHEN, P. COLESTOCK,  
G. GAMMEL, G. GREENE, J. HOSEA, R. KAITA,  
I. LEHRMAN, G. MAZZITELLI<sup>2</sup>, E. MAZZUCATO,  
D.H. McNEILL, M. MORI<sup>3</sup>, K. SATO<sup>4</sup>, J. STEVENS,  
S. SUCKEWER, J.R. TIMBERLAKE, V. VERSHKOV<sup>1</sup>,  
J.R. WILSON, A. WOUTERS  
Princeton Plasma Physics Laboratory,  
Princeton University,  
Princeton, New Jersey,  
United States of America

### Abstract

#### ION BERNSTEIN WAVE HEATING EXPERIMENTS ON PLT.

Ion Bernstein wave heating (IBWH) has been investigated on PLT, with up to 800 kW of RF power applied to the antenna. A plasma antenna loading of 2-4  $\Omega$  has been observed, resulting in 80-90% of the RF power being coupled to the plasma. An ion heating efficiency of  $\Delta T_i(0) \bar{n}_e / P_{RF} = 6 \text{ eV} \times 10^{13} \text{ cm}^{-3} / \text{kW}$ , without high energy tail ions, has been observed, up to the maximum coupled RF power of 650 kW ( $P_{OH} = 550 \text{ kW}$ ). The particle confinement during high power IBWH increases significantly (as much as 300%). Associated with this increase are a longer confinement time of the injected impurity, a reduced drift wave turbulence activity, frequency shifts of drift wave turbulence and the development of a large negative edge potential. The energy confinement time, however, shows some degradation from the Ohmic value, which can be attributed to the enhanced radiation loss observed during IBWH. The ion heating and energy confinement time are relatively independent of plasma current.

### 1. INTRODUCTION

Plasma heating by externally launched ion Bernstein waves (IBWH) has been investigated as an alternative to conventional ICRF heating. Because of their relatively short wavelength, ion Bernstein waves can heat the bulk ions even at relatively high harmonic frequencies [1].

<sup>1</sup> Kharkov Physico-Technical Institute, Ukrainian SSR.

<sup>2</sup> Associazione Euratom-ENEA sulla Fusione, Centro Ricerche Energia Frascati, Frascati, Rome, Italy.

<sup>3</sup> Japan Atomic Energy Research Institute, Tokai-mura, Naka-gun, Ibaraki-ken, Japan.

<sup>4</sup> Institute of Plasma Physics, Nagoya University, Nagoya, Japan.

To preferentially excite ion Bernstein waves (as opposed to fast waves), a  $B_\theta$ - $E_z$  type loop antenna [2] was used to simulate lower-hybrid-like waveguide fields. The RF current for this antenna flows in the toroidal direction, whereas the current for the fast wave antenna flows in the poloidal direction. In 1985, experiments were performed with such a loop antenna, and various efficient heating regimes were identified, including  $5\Omega_D$ , H minority,  $^3\text{He}$  minority, and  $3/2\Omega_D$  [3, 4]. The RF power in these experiments was 100–150 kW. The observed ion heating quality factor  $\Delta T_i(0) \bar{n}_c/P_{\text{RF}}$  was about  $3\text{--}6 \text{ eV} \times 10^{13} \text{ cm}^{-3}/\text{kW}$  for these regimes. These initial experiments demonstrated that:

- IBWH heats relatively high harmonics of the ion cyclotron frequency — a property that is attractive for a compact IBWH waveguide launcher;
- IBWH interacts non-linearly with subharmonic frequencies [2, 4], giving rise to new heating scenarios;
- IBWH produces very few high energy tail ions. The heating is essentially bulk ion heating, which is of interest for an understanding of plasma confinement with auxiliary heating.

## 2. HIGH POWER IBWH ANTENNA

Since these results were encouraging, in 1986 further IBWH experiments were performed on PLT to investigate the higher power regime ( $P_{\text{RF}} > P_{\text{OH}}$ ) where plasma confinement issues can be tested during IBWH. It was of particular interest to study the confinement properties for bulk ion heating in comparison with those for high energy ion heating such as fast wave ICRF heating or neutral beam heating. Two high power IBWH antennas were installed on PLT. The new high power antennas are 60 cm long and 5 cm wide. The antenna design is very similar to that of the PLT high power ICRF antenna. The distance from the current strip to the back plate is 5 cm, providing adequate flux linkage to the plasma. The antenna is covered with Macor cover plates. Between the Macor plates and the plasma there are two layers of stainless steel Faraday shields. The antenna is protected by graphite plates placed toroidally on both sides of the antenna. Up to 500 kW of RF power can be applied to one antenna. The plasma loading for these antennas is 2–4  $\Omega$ , resulting in 80–90% of the applied RF power being coupled to the plasma. The overall antenna performance is similar to that of the PLT high power fast wave antenna.

## 3. IBWH ION HEATING

IBWH at high power levels was performed on PLT in the  $^3\text{He}$  and  $3/2\Omega_D$  regimes utilizing the existing ICRF 30 MHz transmitter. A typical heating result is shown in Fig. 1(a) where the time evolution of the ion temperature is shown for

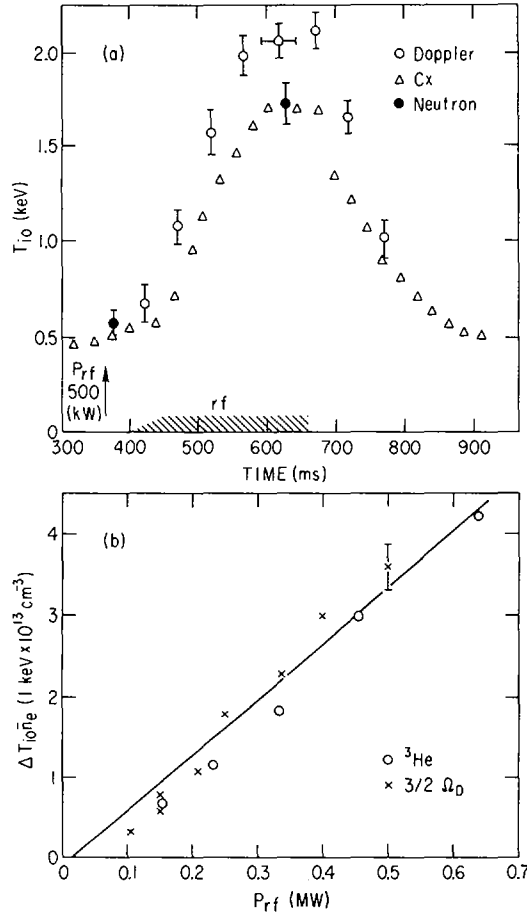


FIG. 1. (a) Typical time evolution of ion temperature.  $P_{RF} = 500 \text{ kW}$ ,  $F = 30 \text{ MHz}$ ,  $B_0 = 29 \text{ kG}$ ,  $3/2 \Omega_D$ ,  $\bar{n}_e = 3.0 \times 10^{13} \text{ cm}^{-3}$ . Other parameters are given in Fig. 2(a-c).

(b) Ion heating as a function of RF power for  $^3\text{He}$  minority ( $B_0 = 32 \text{ kG}$ , 10%  $^3\text{He}$ ) and  $3/2 \Omega_D$  ( $B_0 = 29 \text{ kG}$ , 0%  $^3\text{He}$ ) regimes.

$3/2 \Omega_D$  heating at 500 kW. Three  $T_i$  diagnostic techniques — Doppler broadening (Ti XXI), charge exchange (CX), and neutron emission — are in good general agreement within the uncertainties of each diagnostic. The charge exchange velocity distribution is Maxwellian, without any high energy tail ions up to the highest power level. The ion temperature profile as measured by the Doppler broadening of various ion lines is similar to the Ohmic profile. The ion heating efficiency as shown in Fig. 1(b) is nearly linear up to 650 kW, with a heating quality factor of  $\Delta T_i \bar{n}_e / P_{RF} = 6-7 \text{ eV} \times 10^{13} \text{ cm}^{-3} / \text{kW}$ . It is interesting to note that  $^3\text{He}$  heating and  $3/2 \Omega_D$  heating have similar heating efficiencies. The toroidal magnetic field for

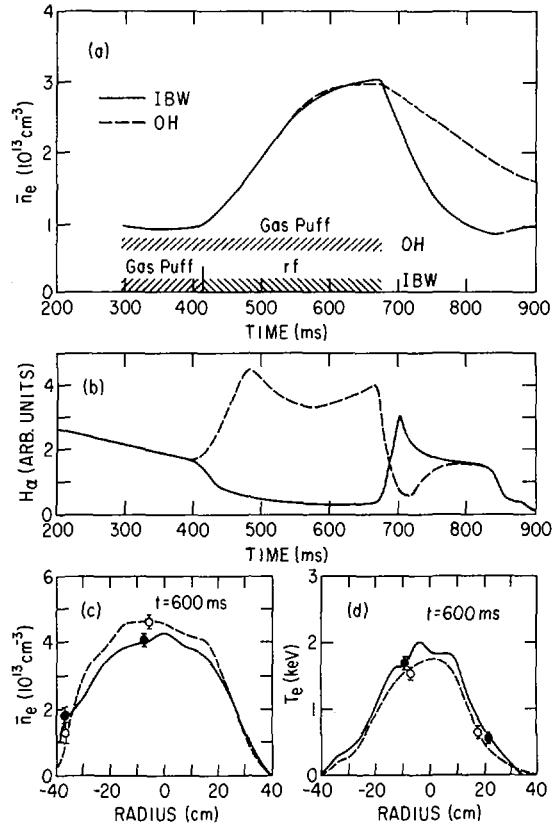


FIG. 2. (a) Density time evolution for the IBWH case (solid curve) shown in Fig. 1(a) and for the Ohmic case (dashed curve) in which gas puffing was used to simulate the density rise of the IBWH case. (b) Time evolution of  $H_\alpha$  emission for the IBWH case and the simulated Ohmic case, near the antenna-limiter region. (c) Density profiles at  $t = 600$  ms for the IBWH case and the simulated Ohmic case shown in Fig. 2(a). (d) Corresponding electron temperature profiles.

$3/2 \Omega_D$  heating is about 10% lower than that for  $^3\text{He}$  heating, and, of course, for the  $3/2 \Omega_D$  regime no  $^3\text{He}$  injection is required. In the 500–600 kW range, the central Doppler ion temperature reaches about 2 keV, which exceeds the central television Thomson scattering (TVTS) electron temperature. The time evolution of the plasma density is shown in Fig. 2(a). The density and electron temperature TVTS profiles at  $t = 600$  ms are shown in Fig. 2(c,d). The dashed curves are for an Ohmic case with the gas feed programmed to yield a similar density evolution. As can be seen, the density and electron temperature profiles are very similar for the two cases.

#### 4. IMPROVED PARTICLE CONFINEMENT DURING IBWH

During IBWH, the particle confinement is significantly improved [5]. A good example is shown in Fig. 2(a). The plasma density increases by more than a factor of three, without active gas puffing and without increasing particle recycling, as indicated by a drop in the  $H_{\alpha}$  emission. The largest drop occurs near the antenna, limiter and gas valve regions. As shown in Fig. 2(b), the  $H_{\alpha}$  emission near the antenna-limiter region (where much of the recycling takes place) during IBWH (solid curve) is considerably less than in the simulated OH case (dashed curve). The density profiles during IBWH are similar to those for the simulated Ohmic case, as shown in Fig. 2(c). The rapid density drop after IBWH as compared with the Ohmic case demonstrates the reduced particle recycling ratio resulting from the reduced total particle inventory in the system. It should be emphasized that the density rise during IBWH is not correlated with the impurity influx as measured by various spectroscopic instruments — a bremsstrahlung based 'Z'-meter and a scanning bolometer. Also, the large increase in the neutron level (a factor of 500) shows that the incremental density is due mainly to deuterium.

In connection with this improvement in particle confinement (or reduced recycling) a number of interesting phenomena were observed. During IBWH, the low energy neutral flux levels (at energies less than 1 keV) decrease significantly [6]. This drop may be related to the drop in the  $H_{\alpha}$  emission. For a further understanding of the particle transport processes during IBWH, a very small amount of selenium was injected with a laser blow-off impurity injector. As shown in Fig. 3(a), the decay time of the Se XXV radiation increases by a factor of two from the Ohmic level (from 50 ms to 100 ms). Since during the observation time the central electron density and temperature are similar and nearly constant for both cases, the selenium line behaviour gives an indication of the central selenium confinement. A similar behaviour was observed with a helium gas puff. When a given amount of helium is injected with a pre-programmed fast gas valve, the net density rise during IBWH is at least twice that in the case without RF, which again suggests an improvement in the particle confinement time. The high ionization states of carbon (C V, C VI) do not rise during IBWH (they may even drop); this represents an exceptional case [6].

Another striking effect of IBWH is the change of the low frequency turbulence activity in the plasma. A microwave scattering system was used to investigate the turbulence in the half-radius region between the  $q = 1$  and  $q = 3$  surfaces ( $r = 25 \pm 10$  cm). Figure 3(b) shows the time evolution of the scattering signals at 100 kHz for the IBWH case and the simulated Ohmic case (the scattered wave-number is  $6-8 \text{ cm}^{-1}$ ). One can see a significant drop in the turbulence level during IBWH as compared with the simulated Ohmic case. In the insert, the frequency spectrum for each case is shown at the end of RF ( $t = 700$  ms). A frequency shift as well as an amplitude reduction occur during IBWH. Since the plasma density profiles are very similar in the two cases, the possibility of a change in the scattering volume can be ruled out. From the frequency shift, one can infer a net increase of

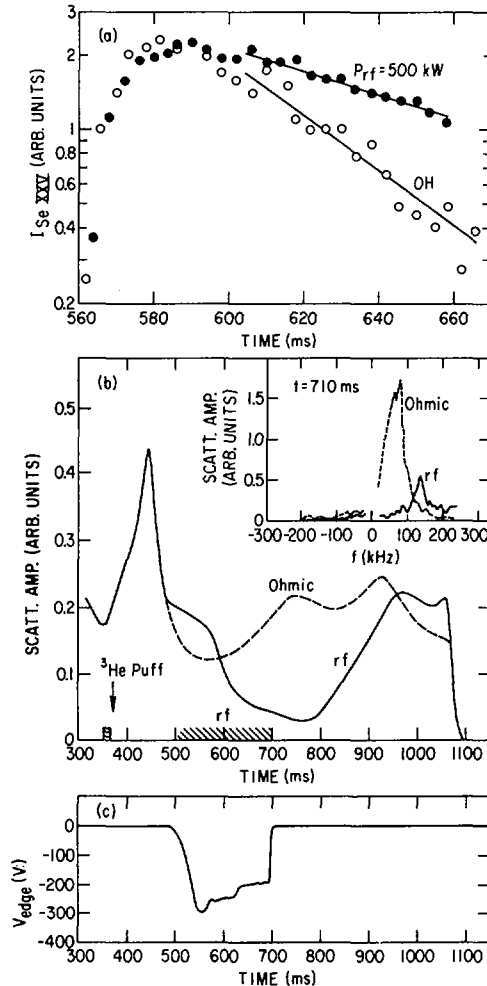


FIG. 3. (a) Time evolution of the selenium XXV resonance line intensity for the IBWH case and the simulated Ohmic case. The selenium was injected at  $t = 550 \text{ ms}$ .

(b) Time evolution of the integrated low frequency turbulence level at 100 kHz for the two cases;  $k(\text{scatt}) = 6\text{--}8 \text{ cm}^{-1}$  at  $r = 25 \pm 10 \text{ cm}$ .

Insert: Frequency spectrum at  $t = 700 \text{ ms}$  for the two cases.

(c) Time evolution of the plasma edge floating potential.

the poloidal rotational velocity of approximately  $5 \times 10^4 \text{ cm/s}$  in the electron diamagnetic drift direction. The net result is a near doubling of the electron diamagnetic drift velocity. This drift velocity corresponds to an electric field of 15 V/cm in the radially inward direction. It should be noted that this reduction in the drift wave activity correlates well with the long impurity particle confinement time. Measurements with an RF-shielded Langmuir probe in the plasma edge have shown that

during IBWH a large floating potential develops which is negative with respect to the chamber wall (Fig. 3(c)). This is correlated with the appearance of the frequency shift in the turbulence spectrum.

## 5. ENERGY CONFINEMENT TIME DURING IBWH

Plasma confinement during IBWH is of interest because of the bulk ion heating properties of ion Bernstein waves. To investigate the scaling of energy confinement with plasma current, the current was varied between 200 kA ( $q_{\text{edge}} = 10$ ) and 630 kA ( $q_{\text{edge}} = 3$ ), with a constant RF power level of 250 kW. Note that the ratio of the RF power to the Ohmic power increases with decreasing current, reaching 1 for the 200 kA case. For a given RF power, the ion temperature increase remains constant down to the lowest current of 200 kA. The normalized energy confinement time,  $\tau_E/\bar{n}_e$ , also remains constant. This may be due to the characteristic of IBWH bulk ion heating that fast ion losses are negligible, even for the low current case. For a given current,  $I_p = 500$  kA, the power scaling shows a gradual degradation of confinement time with increasing RF power. At 650 kW, the confinement time is about 40 ms at  $4.5 \times 10^{13} \text{ cm}^{-3}$ , which is significantly below the Ohmic value of 50–55 ms but is higher than the L-mode scaling time of about 33 ms. This drop in the global confinement time can be attributed to an increase in the electron loss channel. However, in view of increased radiation losses during IBWH, the electron thermal diffusivity still appears to be Ohmic like.

## 6. IMPURITY INFLUX DURING IBWH

During IBWH, an increase in the influx of metallic impurities (predominantly iron) was observed. This high-Z impurity influx, together with the longer particle confinement time, can result in non-negligible central radiation losses during high power (high density) IBWH. Thus, for a successful high power IBWH experiment it is important to reduce the iron influx level as much as possible. To find the source of the iron impurities, the outer Faraday shields of one of the antennas were coated with a 20  $\mu\text{m}$  thick carbon film. This antenna was compared with an uncoated antenna. For the same RF power level, the carbon coated antenna produced half as much iron influx (and half as much central bolometric radiation) as the uncoated antenna. The ion heating efficiency and the density rise, however, remained similar for the two antennas. This indicates that at least half of the iron influx originated from the Faraday shields. The other half may have come from the vacuum chamber wall or the uncoated inner Faraday shield. An antenna with both inner and outer carbon coated Faraday shields is being prepared and will be used in an investigation of this point.

## 7. CONCLUSIONS

Efficient ion heating by IBWH was observed in the  ${}^3\text{He}$  and  $3/2 \Omega_D$  regimes, up to the highest power level ( $P_{\text{RF}} = 650 \text{ kW}$ ). With the application of IBWH, significant improvement in the particle confinement time was observed. Associated with this improvement were a longer confinement time of the injected selenium, a reduced low frequency turbulence level, frequency shifts of drift wave turbulence and the development of a large negative edge potential. The global plasma energy confinement time at the highest power levels showed some degradation from the Ohmic level, which is attributed to the increases in the electron loss channel that are due mainly to the radiative losses. The ion heating and the energy confinement remained relatively constant with plasma current. The ion energy distribution remained Maxwellian for the entire power range.

## REFERENCES

- [1] ONO, M., WURDEN, G.A., WONG, K.L., Phys. Rev. Lett. **52** (1984) 40.
- [2] ONO, M., WATARI, T., et al., Phys. Rev. Lett. **54** (1985) 2339.
- [3] WILSON, J.R., et al., in Radiofrequency Plasma Heating (Proc. 6th Top. Conf. Callaway Gardens, GA, 1985), American Institute of Physics, New York (1985) 8.
- [4] ONO, M., et al., *ibid.*, p. 83.
- [5] HOSEA, J.C., et al., Plasma Phys. Contr. Fusion **28** (1986) 1241.
- [6] WILSON, J.R., et al., J. Nucl. Mater. **145&146** (1986).

## DISCUSSION

R. KOCH: Where does the power limitation come from in your experiment?

M. ONO: At present, the power limitation is due to an arc in one of the two ion Bernstein wave antennas. With an improved antenna and with more operational experience, the power limit can be raised relatively easily.

## CONFINEMENT STUDIES ON TEXTOR WITH HIGH POWER, LONG PULSE ICRH

P.E. VANDENPLAS, T. DELVIGNE, P. DESCAMPS, F. DURODIE,  
M. JADOUL, R. KOCH, D. LEBEAU, A.M. MESSIAEN<sup>1</sup>, D.I.C. PEARSON,  
R. VAN NIEUWENHOVE, G. VAN OOST, G. VAN WASSENHOVE,  
R.R. WEYNANTS<sup>1</sup>

Laboratoire de physique des plasmas — Laboratorium voor Plasmafysica,  
Association Euratom—Etat belge — Associatie Euratom—Belgische Staat,  
Ecole Royale Militaire — Koninklijke Militaire School,  
Brussels, Belgium

H.L. BAY, G. BERTSCHINGER, W. BIEGER<sup>2</sup>, P. BOGEN, W. BRUSSAU,  
G.A. CAMPBELL<sup>3</sup>, Y. CAO<sup>4</sup>, R.W. CONN<sup>3</sup>, H. CONRADS, K.H. DIPPPEL,  
H.G. ESSER, K.H. FINKEN, G. FUCHS, B. GIESEN, D.M. GOEBEL<sup>3</sup>,  
E. GRAFFMANN, H. HARTWIG, E. HINTZ, F. HOENEN, K. HÖTHKER,  
W.L. HSU<sup>5</sup>, A. KALECK, H. KEVER, L. KÖNEN, M. KORTEN,  
W.K. LEUNG<sup>3</sup>, L. LI<sup>4</sup>, Y.T. LIE, A. POSPIESZCZYK, D. REITER,  
A. ROGISTER, G. ROSS<sup>6</sup>, D. RUSBÜLDT, U. SAMM, J. SCHLÜTER,  
B. SCHWEER, H. SOLTWISCH, G.J. THOMAS<sup>5</sup>, F. WAELBROECK,  
G. WAIDMANN, P. WIENHOLD, J. WINTER, G.H. WOLF

Euratom—KFA Association,  
Institut für Plasmaphysik,  
Kernforschungsanlage Jülich GmbH,  
Jülich, Federal Republic of Germany

### Abstract

#### CONFINEMENT STUDIES ON TEXTOR WITH HIGH POWER, LONG PULSE ICRH.

A detailed analysis of the confinement properties of TEXTOR with ICRH is made by means of (i) power, density, plasma current and toroidal magnetic field scans, for which the other plasma parameters are chosen to be as constant as possible, and (ii) RF amplitude modulation at different frequencies. The results can be interpreted on the assumption that the total energy can be split into two parts, each following its own confinement law; the residual OH part  $E'_{OH}$ , obeying the neo-Alcator type scaling of TEXTOR, and the additional heating contribution  $E_{AUX}$ , depending on an auxiliary confinement time  $\tau_{AUX}$ . The observed time evolution of the total energy during the discharges can be well accounted for by two uncoupled first order differential equations describing, respectively,  $E'_{OH}$  and  $E_{AUX}$ . In this way, a complete power or current scan during a single shot can be simulated accurately.

<sup>1</sup> Senior research associate at Fonds national de la recherche scientifique, Brussels, Belgium.

<sup>2</sup> Fachhochschule Jülich, Jülich, Fed. Rep. Germany.

<sup>3</sup> University of California, Los Angeles, CA, USA.

<sup>4</sup> Institute of Plasma Physics, Academia Sinica, Hefei, China.

<sup>5</sup> Sandia National Laboratories, Livermore, CA, USA.

<sup>6</sup> INRS-ENERGIE, Varennes, Québec, Canada.

It is found that  $\tau_{\text{AUX}}$  increases linearly with  $I_p$ , is insensitive to the density and decreases slightly with the RF power. The effectiveness of an increase of OH power at constant density is compared to that of ICRH.

## 1. INTRODUCTION

The general characteristics of ICRH and of stationary long pulse ( $\sim 1$  s), low impurity ICRH operation have been reported previously [1-3]. This paper reports on a detailed analysis of TEXTOR confinement by means of scans of the main parameters of the heated discharge: plasma current,  $I_p$ ; central chord density,  $\bar{N}_{e0}$ ; RF power radiated by the antenna,  $P_{\text{RF}}$ ; and toroidal magnetic field,  $B_t$ . The measurements are made either in steady state plasmas or during the dynamic evolution of the discharges through comparison with simulation programs. For the present analysis, TEXTOR was operated with main and antenna carbon limiters and with a hot carbonized liner [4]. The heating regime is either the minority (or  $2\omega_{\text{CD}}$ ) regime ( $C_H/C_D < 1\%$ ) or the mode conversion regime ( $C_H/C_D \approx 5\%$ ). While the relative electron and ion energy increases are different for the two heating regimes [3], the total plasma energy increases are nearly the same for identical main discharge parameters; the two regimes are, therefore, not distinguished. The operating range is  $1.5 < \bar{N}_{e0} < 6 \times 10^{13} \text{ cm}^{-3}$ ,  $0.2 < I_p < 0.5 \text{ MA}$ ,  $0 < P_{\text{RF}} < 2.2 \text{ MW}$ ,  $B_t \approx 2 \text{ T}$ ; small radius  $a = 0.46 \text{ m}$ , large radius  $R_0 = 1.75 \text{ m}$ .

## 2. INTERPRETATION 'ANSATZ'

The very different behaviour of the total plasma energy content  $E$  with OH power,  $P_{\text{OH}} = I_p V_t$  ( $V_t$  is the loop voltage), and with auxiliary ICRH power has suggested to us [2] to split  $E$  according to the 'ansatz'

$$E = E'_{\text{OH}} + E_{\text{AUX}} \quad (1)$$

where  $E'_{\text{OH}}$  is that part of the energy that is due to the remaining OH power,  $P'_{\text{OH}} = V_t I_p$ , and  $E_{\text{AUX}}$  is the part due to  $P_{\text{RF}}$ .  $V_t$  is the reduced loop voltage in the presence of ICRH. We further assume that  $E_{\text{AUX}} = \tau_{\text{AUX}} P_{\text{RF}}$  and  $E'_{\text{OH}} = \tau_{\text{OH}} P'_{\text{OH}}$  where  $\tau_{\text{OH}} = F_{\text{OH}} \bar{N}_{e0} Q_a^\alpha$  is the neo-Alcator OH confinement law of TEXTOR. The auxiliary confinement time  $\tau_{\text{AUX}}$  is determined for steady state conditions from

$$\tau_{\text{AUX}} = (E - V_t I_p \tau_{\text{OH}}) / P_{\text{RF}} \quad (2)$$

and will be shown to be well approximated by Eq. (5).

When the plasma parameters are time dependent,  $E'_{OH}$  and  $E_{AUX}$  are described by:

$$dE'_{OH}/dt = P'_{OH} - E'_{OH}/\tau_{OH}; \quad dE_{AUX}/dt = P_{RF} - E_{AUX}/\tau_{AUX} \quad (3)$$

These two equations are only coupled through  $V'_b$ , which depends on  $P_{RF}$ . The single law  $dE/dt = P_{tot} - E/\tau_E$ , where  $P_{tot} = P'_{OH} + P_{RF}$  and  $\tau_E$  is the global confinement time, cannot describe all aspects of the observed energy evolution. When  $P_{RF}$  is amplitude modulated, the set of Eqs (3) allows not only the value of  $\tau_{AUX}$  to be checked, but, if the total radiated power  $P_{RF}$  is well coupled to the plasma, is also relevant in the following manner: (i) at a sharp switchoff of  $P_{RF}$ , we have  $\Delta(dE/dt) = \Delta(P_{RF} + P'_{OH})$ ; (ii) immediately after the switchoff, the energy decay is essentially governed by  $dE_{AUX}/dt = -E_{AUX}/\tau_{AUX}$ ; (iii) with sine modulation of  $P_{RF} = P_{RF0} + \tilde{P}_{RF} \exp(-i\omega t)$ , we have

$$\tilde{E}_{AUX} = \tilde{P}_{RF} \tau_{AUX} (1 + \omega^2 \tau_{AUX}^2)^{-1/2} \exp(i\phi), \quad \text{with } \phi = \arctan(\omega \tau_{AUX}) \quad (4)$$

and a similar expression for  $\tilde{E}_{OH}$ , which is negligible for the cases considered. Then the phase difference between  $\tilde{E} \simeq \tilde{E}_{AUX}$  and  $\tilde{P}_{RF}$  is a measure of  $\tau_{AUX}$  and, if we use the value of  $\tau_{AUX}$ , the amplitude of  $\tilde{E}$  determines  $|\tilde{P}_{RF}|$ . If the value of  $|\tilde{P}_{RF}|$  obtained in this way agrees with that actually radiated by the antenna, it is confirmed that the radiated power is well coupled to the bulk of the plasma and represents the  $P_{RF}$  value to be used in Eqs (2) and (3). Another evidence for the coupling of  $P_{RF}$  to the plasma bulk results from the fact that the thermal load remains, with ICRH, at least proportional to  $P_{tot}$  [2].

Let us, finally, note that, when  $I_p$  and  $\bar{N}_{e0}$  are held constant, the incremental confinement time  $\tau_{inc}$  is linked to  $\tau_{AUX}$  by

$$\tau_{inc} = dE/dP_{tot} = (\tau_{OH} dP'_{OH}/dP_{RF} + \tau_{AUX}) (dP_{tot}/dP_{RF})^{-1}$$

### 3. STEADY STATE ANALYSIS

The energy content is measured by four different methods: (i) diamagnetism, (ii)  $\beta_p$  computation from an equilibrium code using as input the current in the vertical field coils and the plasma current profile obtained from polarimetry, (iii) the cosine coil method [5], (iv) kinetic evaluation using the data from the HCN interferometer-polarimeter, from ECE and the neutron yield for  $T_{i0}$ , identical  $T_i$  and  $T_e$  profiles being assumed. The four methods agree well to within  $\pm 7$  kJ.

$\tau_{AUX}$  is computed from Eq. (2) by using for  $\tau_{OH}$  the neo-Alcator law defined in Eq. (1) with  $\alpha = 0.8$  and the value of  $F_{OH}$ , which fits the observed  $\tau_{OH}$  value just before the RF pulse (depending on the particular shot,  $10 < F_{OH} < 14$ ). Note that lower values of  $\alpha$  (e.g.  $\alpha = 0.5$ ) with the appropriate adjustment of  $F_{OH}$  would also give a reasonable fit of the OH behaviour.

**(i) Power scan**

To decouple the effect of the density increase from the effect of the total power increase, a careful selection of shots is made with the same value of  $\bar{N}_{e0}$  during ICRH. As was already stated in Refs [2, 3], the results agree well with a constant value of  $\tau_{AUX}$ , and the global confinement time obeys the relation  $\tau_E = (1 - P_{RF}/P_{tot}) \tau_{OH} + (P_{RF}/P_{tot}) \tau_{AUX}$ , resulting from Eq. (1). For some sets of data, there is, however, a modest decrease of  $\tau_{AUX}$  with power (<30% for  $0.1 < P_{RF} < 2$  MW).

**(ii) Density scan**

The global confinement time  $\tau_E = E/P_{tot}$  is shown versus  $\bar{N}_{e0}$  in Fig. 1(a) for different values of  $P_{tot} = P'_{OH} + P_{RF}$ . The OH curve exhibits the linear dependence of  $\tau_{OH}$  on  $\bar{N}_{e0}$ . The density dependence of  $\tau_E$  diminishes as  $P_{RF}$  increases, and the computed value of  $\tau_{AUX}$ , which corresponds to the limit  $P_{RF} \rightarrow \infty$ , does not, within the accuracy of measurement, depend on the density.

**(iii) Current scan**

Figure 1(b) exhibits the linear dependence of  $\tau_{AUX}$  on the plasma current. We have

$$\tau_{AUX} = F_{AUX} I_p \quad (5)$$

with  $50 < F_{AUX} < 70$  (ms, MA). In contrast to this,  $\tau_{OH}/\bar{N}_{e0}$  decreases  $\propto q_a^\alpha$  when  $I_p$  increases. This is also shown in Fig. 1(b).

**(iv) Magnetic field scan**

For a given plasma composition, the RF power deposition profile can be crudely tailored by moving the mode conversion surface over the plasma cross-section, and conditions can be achieved where the major fraction of power is no longer deposited in the bulk. The central confinement then increases such that the overall energy increment, nevertheless, remains fairly constant.

**4. DYNAMIC ANALYSIS**

The energy evolution is simulated by integrating Eqs (3) with  $\bar{N}_{e0}(t)$ ,  $I_p(t)$ ,  $P_{RF}(t)$ ,  $B_i(t)$  as input data. An approximate empirical expression, derived from steady state data, is taken for  $V'_i$  (i.e.  $V'_i \propto (1 - BP_{RF})(1 + CI_p)$  in the operating range).

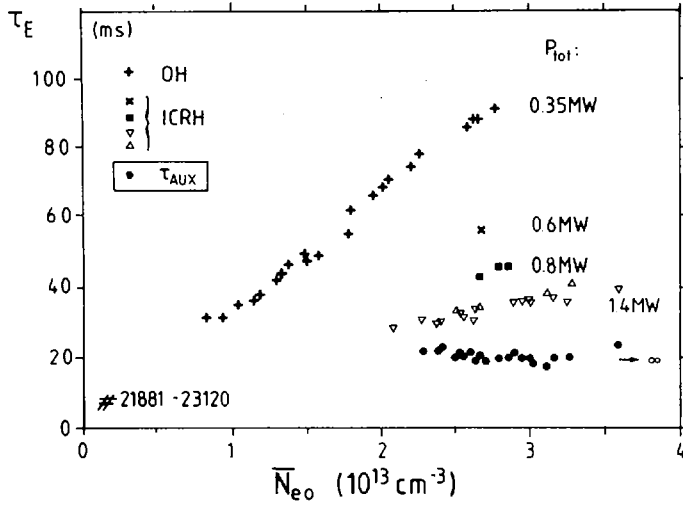


FIG. 1. (a) Density scan results for different values of  $P_{tot} = P_{OH} + P_{RF}$  and constant plasma current,  $I_p = 350 \text{ kA}$ . Curve labelled OH corresponds to pure Ohmic heating case; curve  $\tau_{AUX}$  is computed from Eq. (2).

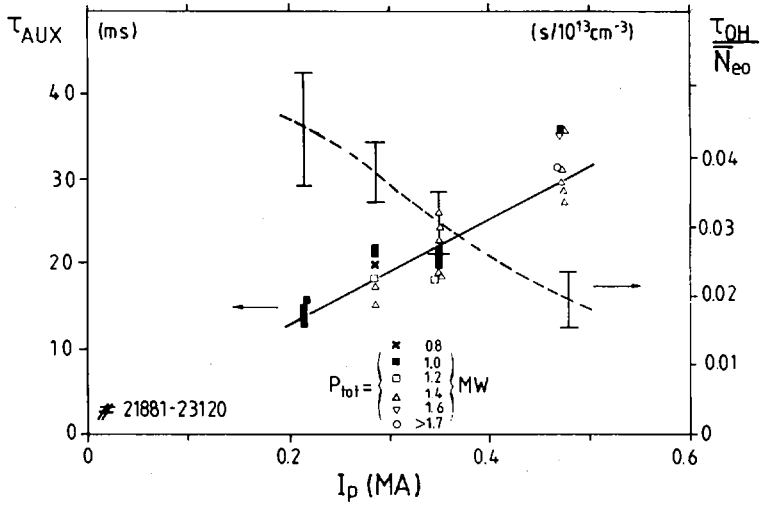


FIG. 1. (b) Evolution of  $\tau_{AUX}$  and  $\tau_{OH}/\bar{N}_{e0}$  versus  $I_p$ .

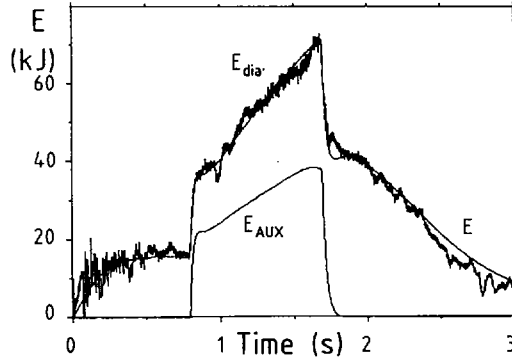


FIG. 2. (a) Complete dynamic current scan made in one shot (No. 23 114).  $E_{dia}$  is the diamagnetic and  $E$  the corresponding simulated energy ( $F_{OH} = 11$ ;  $F_{AUX} = 53$ ;  $P_{RF} = 1.57$  MW). The part corresponding to  $E_{AUX}$  is also displayed.

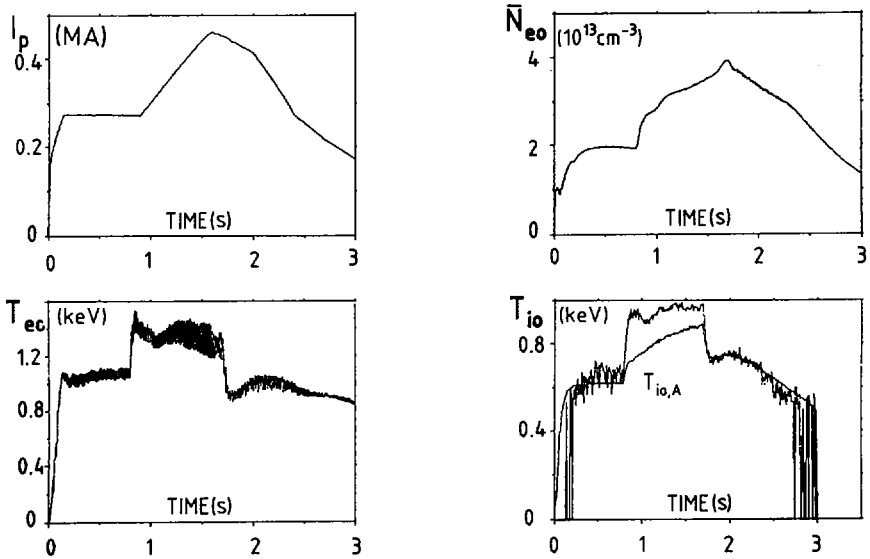


FIG. 2. (b) Corresponding time evolution of  $I_p$ ,  $\bar{N}_{e0}$  (HCN),  $T_{e0}$  (ECE) and  $T_{i0}$  (neutrons). Curve  $T_{i0,A}$  is computed equipartition value from  $\bar{N}_{e0}$ ,  $T_{e0}$ ,  $I_p$  and  $B_i$  measurements.

We take  $\tau_{OH} = F_{OH} \bar{N}_{e0} q_a^{0.8}$  and  $\tau_{AUX} = F_{AUX} I_p$ , where the exact value of  $F_{OH}$  is adjusted around 12 and that of  $F_{AUX}$  around 60 (ms,  $10^{13}$  cm $^{-3}$ , MA) to provide the best fit with the experimental evolution described by the diamagnetic signal. A careful measurement of the time response of the raw diamagnetic energy signal  $E_{dia,r}$  (see Appendix) gives a time constant of  $\tau_{dia} = 12$  ms, which is used to obtain  $E_{dia} = E_{dia,r} + \tau_{dia} dE_{dia,r}/dt$  as corrected experimental energy signal.

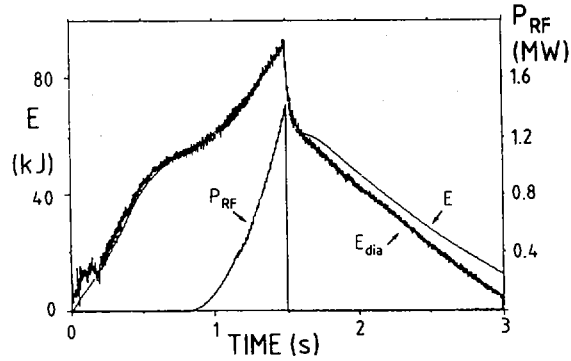


FIG. 3. (a) Dynamic power scan in one shot (No. 24 257).  $E_{dia}$  is compared to simulated  $E$  ( $F_{OH} = 12.3$ ;  $F_{AUX} = 58.5$ ;  $I_p = 480$  kA);  $P_{RF}$  is also shown. Decay of  $I_p$  starts at end of RF heating.

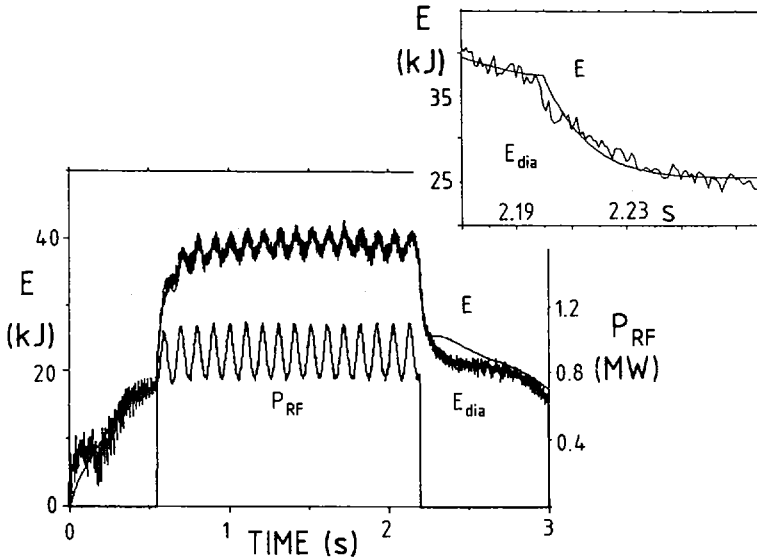


FIG. 3. (b)  $E_{dia}$  compared to simulated  $E$  ( $F_{OH} = 12.8$ ;  $F_{AUX} = 58$ ;  $I_p = 280$  kA) for amplitude modulated RF pulse.  $P_{RF}$  is also shown. Inset shows enlargement of  $E_{dia}$  decay as compared to  $E$  after abrupt ending of RF pulse (No. 24 467).

Figure 2(a) shows a comparison of the simulation with a complete current scan in one shot;  $E_{AUX}$  is also displayed. The time evolution of  $I_p$ ,  $\bar{N}_{e0}$ , the central electron temperature  $T_{e0}$  and the ion temperature  $T_{i0}$  is shown in Fig. 2(b). The value of  $T_{i0,A}$  as computed from equipartition with the electrons agrees well with the experimental value of  $T_{i0}$  (obtained from the neutron yield) during the OH parts of the shot. The simulated  $E$  and the observed  $E_{dia}$  are compared in Fig. 3 for shots

with an amplitude modulated ICRH pulse. Figure 3(a) displays a complete power scan, and Fig. 3(b) the results of sinusoidal amplitude modulation. The insert of Fig. 3(b) shows the good fit during the energy decay after the sharp switchoff of the RF pulse. Also, the phase shift between  $\tilde{E}_{\text{dia}}$  and  $\tilde{P}_{\text{RF}}$  is in agreement with the simulated phase shift.

## 5. CONCLUSIONS

From our investigations, we conclude:

(1) The chosen 'ansatz' in which the effects of  $P_{\text{RF}}$  and  $P'_{\text{OH}}$  are decoupled, can accurately describe the evolution of  $E$  during the shot in a large variety of situations.

(2) The validity of the parametric dependence taken for  $\tau_{\text{AUX}} \propto I_p$  and  $\tau_{\text{OH}} \propto \bar{N}_{e0} q_a^\alpha$  for TEXTOR is confirmed.

(3) The value of  $\tau_{\text{AUX}}$  is very different from that of  $\tau_E = E/P_{\text{tot}}$ , showing that the supplied auxiliary energy has its own behaviour.

(4) It is verified that essentially all radiated  $P_{\text{RF}}$  power is coupled to the plasma bulk when optimum values of  $B_t$  and the H/D ratio are chosen.

The different nature of the confinement properties of OH and of RF additional heating is again very apparent in the comparison of the incremental heating efficiencies  $\eta = \Delta E/\Delta P_{\text{tot}}$  for OH and ICRH. Figure 4 displays, at constant  $\bar{N}_{e0}$ , the OH energy evolution versus  $P_{\text{OH}}$  as  $I_p$  is increased, together with the different evolution of the energy curve at the onset of ICRH, starting from OH for various values of  $I_p$ .

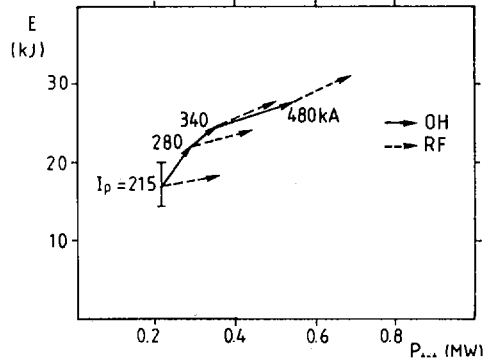


FIG. 4. Evolution, at constant density  $\bar{N}_{e0} = 2.35 \times 10^{13} \text{ cm}^{-3}$ , of  $E_{\text{OH}}$  versus  $P_{\text{OH}}$  when plasma current is increased from 215 to 280, 340, 480 kA successively (plain line arrows). Dotted arrows also indicate, for each value of plasma current, how total energy  $E$  evolves from  $E_{\text{OH}}$  at onset of ICRH.

While for the  $\bar{N}_{e0}$  value considered  $\eta_{OH} > \eta_{ICRH}$  at low  $I_p$  (200 kA), and  $\eta_{OH} \approx \eta_{ICRH}$  ( $I_p = 350$  kA), we have  $\eta_{ICRH} > \eta_{OH}$  at high  $I_p$  ( $\sim 500$  kA). Apparently, the heating efficiency of ICRH exceeds that of OH when  $I_p/\bar{N}_{e0}$  is sufficiently large.

### Appendix

#### MEASUREMENT OF THE TIME RESPONSE OF THE DIAMAGNETIC SIGNAL

The time constant of TEXTOR's diamagnetic signal [6] has been determined by varying the frequency  $\Omega$  of the amplitude modulation of the ICRH pulses (Fig. 3(b)) and measuring the amplitude ratio and the phase difference between  $E_{dia,r}$  and  $\bar{P}_{RF}$ . From these measurements, using a least squares fit procedure, it follows that  $\bar{E}_{dia,r}/\bar{P}_{RF} \propto [(1 + i\Omega\tau_1)(1 + i\Omega\tau_2)]^{-1}$ , with  $\tau_2 \approx \tau_{AUX}$  and  $\tau_1 \approx 12$  ms. The time  $\tau_1$ , whose value is close to the wall time constant, is considered to be the time constant  $\tau_{dia}$  intrinsic to the diamagnetic measurement system.

#### ACKNOWLEDGEMENTS

The authors would like to thank Drs T. Shoji and S. Okamura for suggesting the power modulation experiment in combination with the diamagnetic measurements.

#### REFERENCES

- [1] WEYNANTS, R.R., et al., Radiofrequency Plasma Heating (Proc. 6th Top. Conf. Callaway Gardens, GA, 1985), American Institute of Physics, New York (1985) 40.
- [2] MESSIAEN, A.M., et al., Plasma Phys. Controll. Fusion **28** (1986) 71.
- [3] WOLF, G.H., et al., Plasma Phys. Controll. Fusion **28** (1986) 1413.
- [4] WINTER, J., et al., J. Nucl. Mater. (1986).
- [5] SWAIN, D., NEILSON, G., Nucl. Fusion **22** (1982) 1015.
- [6] FUCHS, G., et al., Rep. KFA-IPP-IB-1/84, Kernforschungsanlage Jülich GmbH (1984).



## EXPERIMENTS ON ICRF HEATING AND FAST WAVE CURRENT DRIVE IN JIPP T-IIU

T. WATARI, K. OHKUBO, R. AKIYAMA, R. ANDO,  
D. ECKHARTT<sup>1</sup>, Y. HAMADA, S. HIROKURA, K. IDA,  
E. KAKO, O. KANEKO, K. KAWAHATA, Y. KAWASUMI,  
S. KITAGAWA, T. KURODA, K. MASAI, K. MATSUOKA,  
A. MOHRI, S. MORITA, M. MUGISHIMA, N. NODA, I. OGAWA,  
Y. OGAWA, Y. OKA, M. SAKAMOTO, K. SAKURAI, M. SASAO,  
K. SATO, K.N. SATO, S. TANAHASHI, Y. TANIGUCHI,  
T. TETSUKA, K. TOI, K. YAMAZAKI

Institute of Plasma Physics,  
Nagoya University, Nagoya,  
Japan

### Abstract

#### EXPERIMENTS ON ICRF HEATING AND FAST WAVE CURRENT DRIVE IN JIPP T-IIU.

The paper summarizes two years' progress on ICRF heating and current drive experiments in JIPP T-IIU. In the heating experiments, a new ion Bernstein wave heating regime called Mode II was examined; efficient electron heating was observed. In high power ICRF heating experiments, a five element antenna array was used, improving the quality of the heating. High power ICRF heating ( $2 \text{ MW} \cdot \text{m}^{-3}$ ) was successfully utilized by suppressing high Z impurity contamination, using a carbonization technique. The energy confinement time scaling has been established, with moderate degradation compared to that of neutral beam injection. Current drive was demonstrated by injection of the fast waves in the lower hybrid frequency range. A four element dipole antenna array was used, and a current drive efficiency as high as that of slow wave current drive was achieved. The fast wave was applied to achieve stabilization of the  $m = 2/n = 1$  tearing mode, causing suppression of major disruptions in various conditions. In another effort undertaken to find a density limit free current drive method, electron beam injection was also examined.

### 1. ION BERNSTEIN WAVE HEATING (MODE II)

At the previous IAEA Conference (1984), a success in ion Bernstein wave heating was reported (Mode I) when a layer with  $\omega = 3\omega_{\text{CD}}$  (or  $\omega = (3/2)\omega_{\text{CH}}$ ) was established at the central plasma vertical chord [1]. Unexpectedly, a half integer cyclotron harmonic heating process was found to exist. A new regime called Mode II is dealt with in this paper where the  $\omega = \omega_{\text{CH}}$  layer is aligned on the central

<sup>1</sup> On leave from Max-Planck-Institut für Plasmaphysik, Garching, Fed. Rep. Germany.

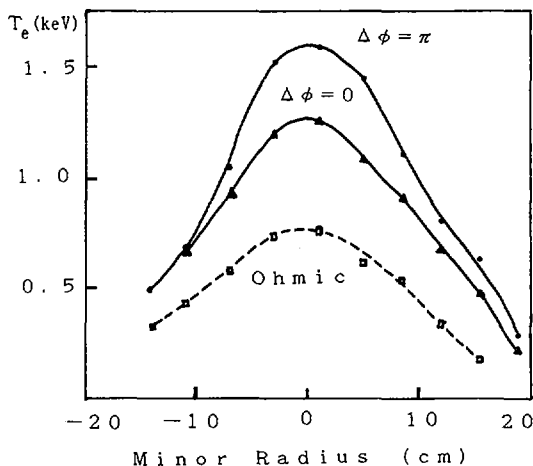


FIG. 1. Electron temperature profile changes for varying phasing angle.

chord. The outstanding feature observed here is a rapid rise in the electron temperature just after the RF power has been turned on, followed by a gradual rise in the ion temperature [2]. This constitutes a pronounced difference with respect to the Mode I experiment. Through a power balance analysis of the experimental data, the conclusion is reached that the input RF power is mostly absorbed by electrons.

## 2. CONFINEMENT STUDY IN HIGH POWER ICRF HEATED PLASMAS

A five element antenna array was installed for  $k_{\parallel}$ -tailoring on which the quality of heating may depend. One expectation was the reduction of impurity content at  $\Delta\varphi = 180^{\circ}$ , associated with the co-axial mode. In the experiment, however, changes are observed neither in the line radiation from impurity ions nor in the spatially resolved bolometer signals. However, the heating efficiency clearly depends on the phasing angle. The central electron temperature shows maximum rise and a peaked profile for  $\Delta\varphi = 180^{\circ}$  (Fig. 1). The neutron yield and the ion temperature also rise to maximum values for  $\Delta\varphi = 180^{\circ}$ . The stored energy as determined from magnetic measurements supports these kinetic data. A computer code developed by Fukuyama et al. [3] is used to study the wave propagation and the power deposition profile. A wave with large  $k_{\parallel}$  tends to be absorbed centrally and is produced when  $\Delta\varphi = 180^{\circ}$ . Therefore, the observed effects are understood in the framework of wave physics as  $k_{\parallel}$  is controlled through the phasing of the antenna.

JIPP T-IIU high power experiments have been applying new methods of impurity control such as carbon limiters, synchronized gas puffing, and a second current rise [4]. Their effectiveness was, however, decreasing with increased injection power

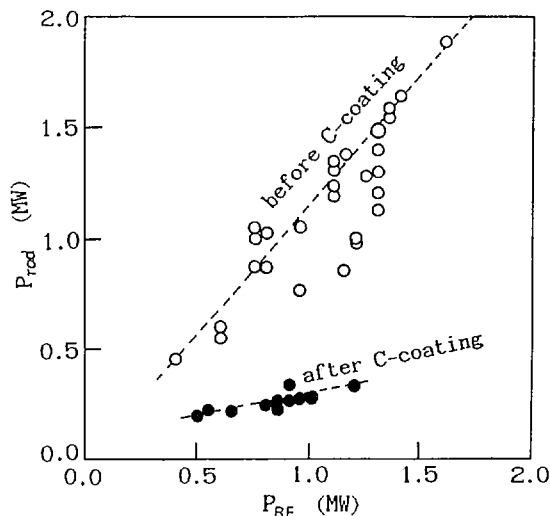


FIG. 2. Radiation loss versus injected RF power (open circles: before carbon coating; solid circles: after carbon coating).

(2 MW max.), i.e. with high power density ( $2 \text{ MW} \cdot \text{cm}^{-3}$ ) which has not been attained elsewhere. A carbonization technique [5] was then employed and found to be very effective in impurity suppression (Fig. 2). Fe lines, which have been the main radiation loss channel in the hot core region, were reduced in intensity by an order of magnitude.

The key question is whether or not ICRF heated plasmas show degradation of confinement as do NBI heated plasmas. The parametric dependences of  $\tau_E$  are studied by varying  $I_p$  from 200 kA to 320 kA and  $P_{RF}$  up to 2 MW with  $\bar{n}_c$  fixed around  $7 \times 10^{13} \text{ cm}^{-3}$  (Fig. 3(a)). There is a degradation of confinement with increasing power and a marked improvement with increasing  $I_p$ . A power law fit to the data yields a scaling  $\tau_E \propto I_p^\alpha P_{tot}^{-\beta}$  with  $\alpha \approx 1$  and  $\beta \approx 0.42$ . This is generally in good agreement with Kaye-Goldston scaling [6]; the encouraging feature of this result is its indication of milder degradation than that due to Kaye-Goldston scaling.

An offset linear plot [7] is likewise suitable to the same data set (Fig. 3(b)). The offset linear  $\tau_E$  is determined to be 8 ms. While  $\tau_E$ , from this definition, predicts a milder degradation with increasing power, there is the problem that it may not be improved by increasing  $I_p$ . With  $\tau_E$  values provided by various machines of different size, the JIPP T-IIU data contribute to the determination of the  $\tau_E$  scaling to the plasma volume. The offset  $\tau_E$  seems to have a  $V^{3/4}$  dependence on the machine size as Kaye-Goldston scaling has with constant  $q$ .

Based on precise measurements of  $T_e(r)$ ,  $n_e(r)$  and sawtooth activity, the power deposition profile  $P(r)$  and the electron heat diffusivity  $X_e(r)$  have been studied. The deposition profile is important because not only may it deeply affect the confinement

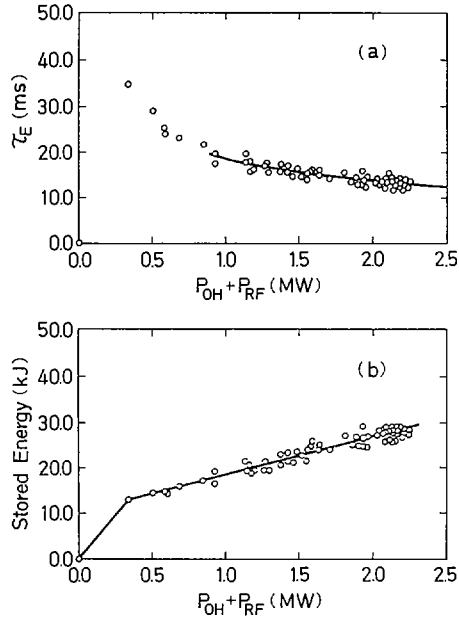


FIG. 3. Confinement time  $\tau_E$  of ICRF heated plasma: (a) power law fit and (b) offset linear fit;  $I_p \approx 280$  kA and  $\bar{n}_e \sim 7 \times 10^{13}$  cm $^{-3}$ .

properties but also provides an interesting interface between experiment and wave physics. It is found to be a peaked deposition profile for medium density plasmas ( $\leq 5 \times 10^{13}$  cm $^{-3}$ ) and a broader profile in the higher density cases ( $\sim (7-8) \times 10^{13}$  cm $^{-3}$ ). The results agree qualitatively with the analysis from the RF power deposition code [3].

### 3. FAST WAVE CURRENT DRIVE EXPERIMENTS

Attention has been focused on fast wave current drive [8-10], because of its attractiveness as a current drive method which may be utilized in high temperature and density plasmas.

The fast wave current drive is studied experimentally by using a four element dipole antenna with a double Faraday shield. The RF frequency is 800 MHz, and  $B_T$  is 2.6 to 2.96 T. The antenna is designed to produce only  $E_y$  and  $B_z$  fields so that, preferentially, the fast wave is excited. Global reflections of the plasma loaded antenna show a minimum at  $\Delta\varphi = 0^\circ$ , where  $\Delta\varphi$  is the phase difference between the dipoles. The reflections decrease also with increasing  $\bar{n}_e$  and by moving the antenna closer to the plasma. These types of behaviour are those of a fast wave, where a decrease in the evanescent region improves the loading characteristics. The pump RF

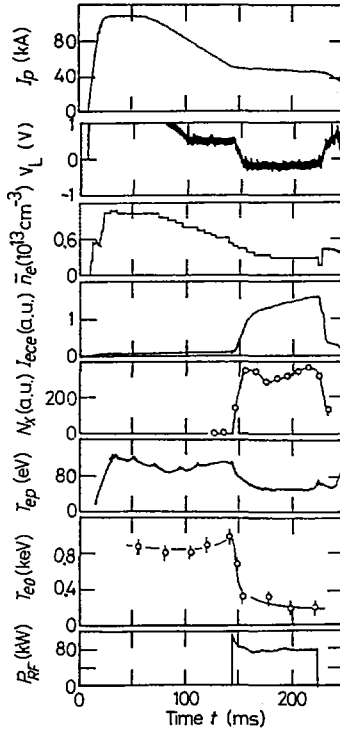


FIG. 4. Time behaviour of plasma parameters for injection of fast waves: plasma current,  $I_p$ , loop voltage,  $V_L$ , line averaged electron density,  $\bar{n}_e$ , microwave emission near the second electron cyclotron harmonic,  $I_{ece}$ , integrated counts of X-ray (10–300 keV),  $N_X$ , peripheral electron temperature deduced from the ratio of the O V lines,  $T_{ep}$ , central electron temperature,  $T_{e0}$  and RF net power,  $P_{RF}$ .

amplitude is monitored with an electrostatic RF probe in the scrapeoff region,  $90^\circ$  toroidally from the antenna. The pump RF field, normalized to the injected RF power, increases by about 15 dB as  $\Delta\varphi$  is shifted from  $180^\circ$  to  $0^\circ$ . This is ascribed to the increased portion of excited waves not satisfying the accessibility condition.

When 80 kW of net RF power,  $P_{RF}$ , is applied with  $\Delta\varphi = 0^\circ$ , a plasma current  $I_p$  of about 50 kA is sustained with a negative loop voltage at constant  $\bar{n}_e = 3 \times 10^{12} \text{ cm}^{-3}$  (Fig. 4). The efficiency of current drive by fast waves,  $\eta = I_p \bar{n}_e R / P_{RF}$ , is  $1.7 \times 10^{-2}$  ( $10^{20} \text{ kA} \cdot \text{m}^{-2} \cdot \text{kW}^{-1}$ ), which is as high as that of slow waves in the JIPP T-IIU tokamak.

In the low OH current discharge, a density limit ( $\bar{n}_e \approx 8 \times 10^{12} \text{ cm}^{-3}$ ) is observed, contrary to theoretical expectations based on linear wave propagation. We conclude that the disappearance of the slide-away electron tail which exists before applying RF and the power flow to the ion tail via a parametric instability resulting from mode conversion must be responsible for the density limit [10].

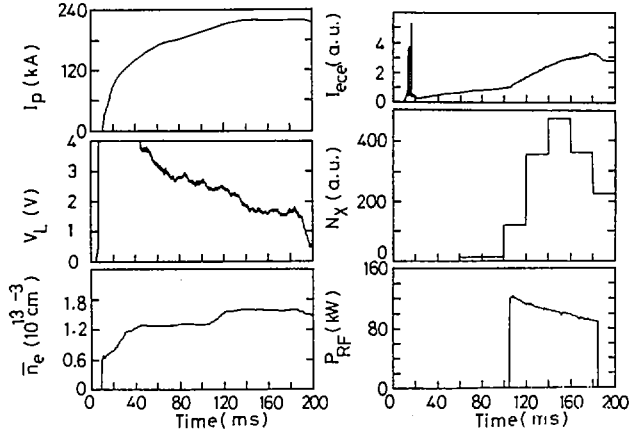


FIG. 5. Discharge characteristics of RF injected plasma in the high density regime where  $\omega_{LH}(r=0) > \omega$ .

When fast waves are injected into a high OH current plasma, the hard X-ray emission in the energy range higher than 30 keV is strongly enhanced in the high density regime  $\omega_{LH}(r=0) > \omega$  (Fig. 5). In this discharge, an enhanced electron cyclotron emission is also observed, while the bulk electron temperature (Thomson scattering) remains constant or decreases slightly. The hard X-ray emission is sharply localized near the plasma centre. These results indicate that fast waves propagate into the high density plasma and interact intensely with the high energy electrons which exist already in a plasma with high OH current. This result is quite encouraging, in the sense that the density limit encountered in the low current plasmas can be overcome if high energy seed electrons are amply provided by slow waves and/or electron cyclotron waves, in place of an inductive electric field.

The RF current drive has a large potential for controlling the current density profile, which governs tearing mode stability and confinement properties. The suppression of  $m=2$  tearing mode and major disruptions was studied using RF current drive and/or production of high energy electrons by fast waves [11]. Stabilizing effects are found in the following regime:  $q(a) = 2.5\text{--}3.5$ ,  $B_z = 1.2\text{--}2.4$  T and  $\bar{n}_e = 0.5\text{--}1.5 \times 10^{13} \text{ cm}^{-3}$ . The RF power required to suppress the major disruption is about 20 to 40% of the Ohmic input power, which is close to the theoretical predictions [12].

#### 4. ELECTRON BEAM INJECTION (EBI)

A current drive experiment with EBI has been performed by using a newly developed injector working for a long duration ( $>4$  ms). Here, the 'plasma anode method' was used to generate the electron beam. The parameters of the target plasma

were  $B_t = 2$  T,  $\bar{n}_e = 1.5 \times 10^{13} \text{ cm}^{-3}$  and  $I_p = 80$  kA. When an electron beam of current  $I_k = 240$  A at an energy 1.1 keV is injected,  $I_p$  rises quickly by 4 kA [13]. The driven current remains constant for 4 ms, and the multiplication factor,  $\Delta I_p/I_k$ , is about 20.

### ACKNOWLEDGEMENTS

The authors thank Dr. Y. Sakamoto and all collaborators who contributed to the success of the carbon coating experiment.

### REFERENCES

- [1] ONO, M., et al., Phys. Rev. Lett. **54** (1985) 2239.
- [2] KAWAHATA, K., et al., in Controlled Fusion and Plasma Heating (Proc. 13th Europ. Conf. Schliersee, 1986), Vol. 10c, Part II, European Physical Society (1986) 169.
- [3] FUKUYAMA, A., et al., Nucl. Fusion **23** (1983) 1005.
- [4] TOI, K., et al., in Plasma Physics and Controlled Nuclear Fusion Research (Proc. 10th Int. Conf. London, 1984), Vol. 1, IAEA, Vienna (1985) 532.
- [5] NODA, N., et al., Jpn. J. Appl. Phys. **25** (1986) L397.
- [6] KAYE, S.M., GOLDSTON, R.J., Nucl. Fusion **25** (1985) 65.
- [7] ODAJIMA, K., et al., to be published in Phys. Rev. Lett.
- [8] GOREE, G., et al., Phys. Rev. Lett. **55** (1986) 1669.
- [9] McWILLIAMS, R., et al., Phys. Rev. Lett. **56** (1986) 835.
- [10] OHKUBO, K., et al., Phys. Rev. Lett. **56** (1986) 2040.
- [11] TOI, K., et al., in Controlled Fusion and Plasma Heating (Proc. 13th Europ. Conf. Schliersee, 1986), Vol. 10c, Part II, European Physical Society (1986) 457.
- [12] RUTHERFORD, P.H., Rep. PPPL-2277, Plasma Physics Lab., Princeton Univ., NJ (1985).
- [13] MOHRI, A., et al., in High-Power Particle Beams (Proc. 6th Int. Conf. Kobe, 1986) P-A-1.

### DISCUSSION

J.-M. NOTERDAEME: Was there any indication in the phasing experiments that radiation losses depend on phasing as the carbonization wears off, or in an uncarbonized machine?

T. WATARI: We carried out our phasing experiment under three sets of conditions, namely before carbon coating, after carbon coating and after removal of the coating. In all three cases, the impurity contents were insensitive to the phasing angle.



## ELECTRON HEATING AND MHD MODES DURING LOWER HYBRID CURRENT DRIVE ON PLT

S. BERNABEI, R. BELL, A. CAVALLO, T.K. CHU,  
P. COLESTOCK, J. FELT, W. HOOKE, J. HOSEA,  
F.C. JOBES, E. MAZZUCATO, E. MESERVEY, R. MOTLEY,  
J.A. MURPHY, M. ONO, R. PINSKER, J. STEVENS,  
S. VON GOELER, J.R. WILSON  
Princeton Plasma Physics Laboratory,  
Princeton University,  
Princeton, New Jersey,  
United States of America

### Abstract

ELECTRON HEATING AND MHD MODES DURING LOWER HYBRID CURRENT DRIVE ON PLT.

Lower hybrid waves of up to 1 MW power from a 2.45 GHz source were applied to ohmic discharges in the PLT tokamak. Highly efficient current drive ( $I_{\text{H}}/R/P \approx 1.4$ ) was obtained from long, multi-element grills (8 and 16 element) producing a narrow, high velocity wave spectrum. Above a certain power level, dependent on the plasma density, the lower hybrid waves suppress sawtooth oscillations. Further increase in power level to about 500 kW (the original ohmic power level) and beyond suppresses the  $m = 1$  oscillation at  $\bar{n}_e \approx 10^{13} \text{ cm}^{-3}$  and results in strong electron heating in the core region ( $T_e$  increases from 2 to 4-6 keV). The  $m = 2$  oscillation does not manifest itself unless the limiter  $q$  is reduced to below 2.5. Enhanced sawtooth amplitude driven by up to 1 MW of ICRF heating ( $D-^3\text{He}$  minority) can also be suppressed by the lower hybrid waves. Preliminary experiments to drive current with fast waves by a phased loop array are described. These experiments, however, did not exhibit efficient current drive effects.

### 1. INTRODUCTION

The application of lower hybrid waves to tokamak discharges in the past few years has led to a variety of new, incompletely understood phenomena, including current drive, sawteeth suppression, and strong electron heating [1-5]. These effects are the result of the formation of a suprathreshold electron tail by the RF waves which creates a new tokamak equilibrium in which the current distribution and the electron temperature distribution are uncoupled. The PLT experiment has been devoted to the study of this new equilibrium, which is still largely uncharted because of the large number of free parameters, such as the direction and

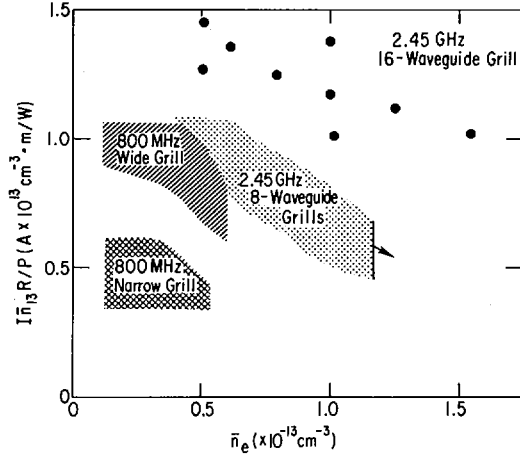


FIG. 1. Current drive figure of merit,  $\bar{I} \bar{n}_{13} R/P$ , versus electron density, for 800 MHz, 6-element, wide and narrow grills, and 2.45 GHz, 8-element and 16-element grills.

phase of the lower hybrid waves, the intensity of the induced electric field in the plasma and the conditions of the target plasma.

## 2. THE EXPERIMENT

The PLT Tokamak, with major and minor radii of  $R = 132$  cm and  $a = 40$  cm, has been operated with a toroidal field  $B = 20$ – $32$  kG, a plasma current  $I$  of 300–700 kA ( $2 < q_L < 6$ ) in the density range  $\bar{n}_e = 0.2$ – $4 \times 10^{13} \text{ cm}^{-3}$ . The RF system consists of three 2.45 GHz klystrons capable of delivering 1 MW of power to the plasma. The waves are coupled to the plasma by means of two grills, one an 8-waveguide array positioned on the top and the other a 16-element array on the outside of the torus. The principal diagnostics include multi-point laser Thomson scattering for  $T_e$ , soft and hard X-rays,  $2\Omega_{ce}$  radiation, and Mirnov loops.

## 3. RESULTS

CURRENT DRIVE. Comparison of results with the present 2.45 GHz system with those of the past 800 MHz, 6-waveguide grill [6] enable us to check the scaling of the density limit and the effect of the wave spectrum. On the first point, the density limit at 2.45 GHz is  $\sim 4 \times 10^{13} \text{ cm}^{-3}$ , at least 6 times greater than at 800 MHz. As shown in Fig. 1, the current drive figure of merit  $\bar{I} \bar{n}_{13} R/P$  is greatest for the higher frequency system launching the fastest waves with the

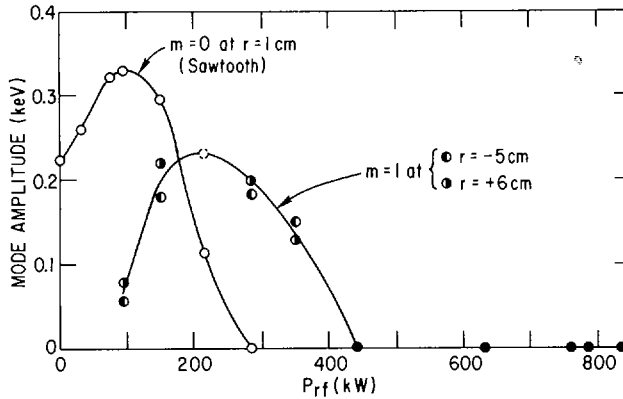


FIG. 2. Mode amplitude of  $m = 0$  (sawtooth) at  $r = 0$ , and of  $m = 1$  at  $r = -5$  cm and  $6$  cm, as a function of lower hybrid power as determined from  $2\Omega_{ce}$  emission;  $\bar{n}_e \approx 10^{13} \text{ cm}^{-3}$ ,  $B = 29$  kG,  $I = 500$  kA.

narrowest wave spectrum (6 WG,  $\Delta n_{||} = 1.5$  and  $2.7$ ; 8 WG,  $\Delta n_{||} = 1.4$ , and 16 WG,  $\Delta n_{||} = 0.5$ ). In all cases the phase velocity was optimized for maximum efficiency. The decrease in efficiency with density is probably due to diminished wave accessibility to the center of the torus. Experiments above  $\bar{n}_e = 1 \times 10^{13} \text{ cm}^{-3}$  show that the efficiency improves with increasing plasma current and electron temperature.

**STABILITY.** If the current drive efficiency is high, lower hybrid power can strongly affect the MHD modes of the tokamak plasma. Above a certain power threshold, which depends on the density, the RF waves suppress sawteeth activity at the center of the plasma while the off-center  $m=1$  mode becomes dominant, as shown in Fig. 2. Further increase in the RF power, however, leads to suppression of the  $m=1$  mode also.

**ELECTRON HEATING.** In spite of the broadening of the current profile, as determined from the change of internal inductance, the central electron temperature rises dramatically, forming a peaked temperature profile apparently decoupled from the current profile (Fig. 3). The stability characteristics of this type of discharge are still largely unexplored by theorists.

As shown in Fig. 4, the temperature rise continues up to  $\sim 500$  kW, and then appears to saturate. Stored energy for the electrons increases with power, but at a rate less than expected from ohmic discharges. The temperature increase becomes smaller as the plasma density rises, as shown in Fig. 5. Above  $\bar{n}_e = 3 \times 10^{13} \text{ cm}^{-3}$  the available RF power is insufficient to eliminate the sawteeth oscillations.

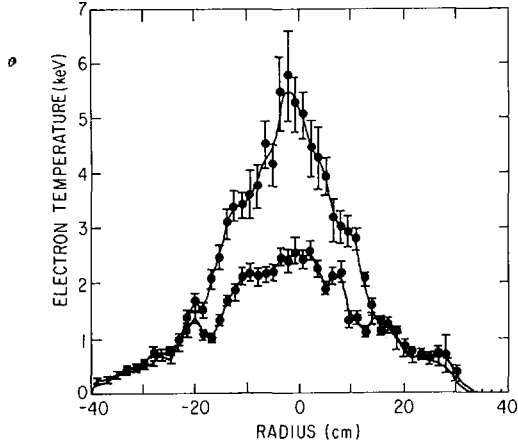


FIG. 3. Temperature profiles during ohmic discharges (lower curve) and lower hybrid discharges measured by laser Thomson scattering.  $B = 30$  kG,  $I \approx 500$  kA and  $\bar{n}_e \approx 10^{13}$  cm $^{-3}$ . (The  $T_e$  profiles are measured along a fixed vertical chord which cannot follow any outward shift of the axis.)

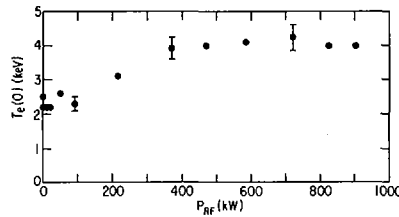


FIG. 4. Laser Thomson scattering measurements of  $T_e(0)$  with RF power input.  $\bar{n}_e \approx 10^{13}$  cm $^{-3}$ ,  $B = 30$  kG,  $I \approx 500$  kA.

The electron energy confinement time at  $\bar{n}_e = 10^{13}$  cm $^{-3}$  rises initially with RF power and then slowly decreases to the ohmic level at an RF power level comparable to the ohmic power. The electron energy confinement time, which is proportional to  $\bar{n}_e$  for ohmic discharges for  $\bar{n}_e < 3 \times 10^{13}$  cm $^{-3}$ , increases with  $\bar{n}_e$  at a rate of  $\sim 1/3$  of that of the ohmic discharge during lower hybrid current drive.

During operation with  $q_L > 2.5$ , the RF power suppresses the  $m=0$  and  $m=1$  modes without driving up the  $m=2$  mode or causing a disruption. As  $q_L$  is reduced below 2.5, the  $m=2$  mode tends to grow in bursts during the RF pulse. Operation near  $q_L = 2$  results in strong  $m=2$  activity and disruptions in both ohmic and RF drive.

Ion cyclotron minority heating (D- $^3$ He) at 1 MW increases the sawteeth amplitude from 0.20 to 0.5 keV because of the

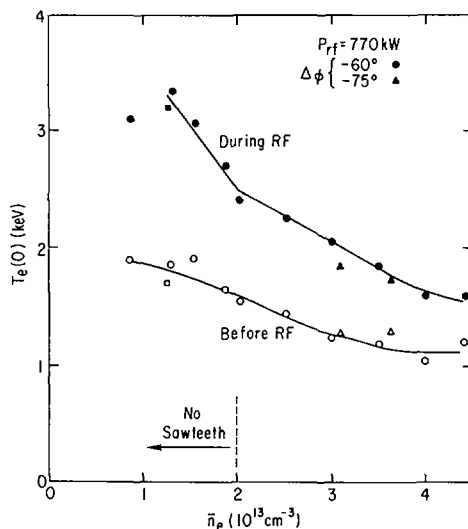


FIG. 5. Electron temperature measured with soft X-rays before and during lower hybrid heating at 770 kW.

central power deposition and electron- $^3\text{He}$  coupling [7]. The application of lower hybrid wave power suppresses these enhanced sawteeth; the minimum lower hybrid power for suppression is almost independent of ICRF power (up to 1 MW).

FAST WAVE. A 6-element loop array has been installed on PLT to launch the fast wave at 800 MHz, to determine whether current drive is possible beyond the normal density limit. Measureable currents have been driven with up to 80 kW of power, but this power level is too low to establish the density scaling of the current drive. The dependence of the loading of the antenna on density and the appearance of parametric decay spectra at  $\bar{n}_e > 1 \times 10^{13} \text{ cm}^{-3}$  are similar to those seen previously with the slow wave coupler, so that the excitation of the fast wave is in doubt. A  $3 \times 4$  dielectric waveguide is now being installed on PLT to enable direct comparison of the slow and fast wave characteristics with a better defined launching configuration.

## REFERENCES

- [1] GORMEZANO, C., BLANC, P., BOTTOLLIER, P., et al., "Experimental studies of lower hybrid heating and current drive on the Petula-B tokamak", Radiofrequency Plasma Heating (Proc. 6th Top. Conf. Callaway Gardens, GA, 1985), American Institute of Physics, New York (1985) 111.
- [2] CHU, T.K., BELL, R., BERNABEI, S., et al., *ibid.*, p. 131.

- [3] CHU, T.K., BELL, R., BERNABEI, S., et al., Nucl. Fusion **26** (1986) 666.
- [4] SOLDNER, F., McCORMICK, K., ECKHARTT, D., et al., Phys. Rev. Lett. **57** (1986) 1137.
- [5] HOSEA, J., WILSON, J.R., HOOKE, W., et al., "RF experiments on PLT", Controlled Fusion and Plasma Heating (Proc. 13th Europ. Conf. Schliersee, 1986), European Physical Society (1986).
- [6] BERNABEI, S., DAUGHNEY, C., EFTHIMION, E., et al., Phys. Rev. Lett. **49** (1982) 1255.
- [7] MAZZUCATO, E., BELL, R., BITTER, M., et al., in Plasma Physics and Controlled Nuclear Fusion Research 1984 (Proc. 10th Int. Conf. London, 1984), Vol. 1, IAEA, Vienna (1985) 433.

## RADIOFREQUENCY HEATING AND CURRENT DRIVE EXPERIMENTS ON ALCATOR C AND VERSATOR II

M. PORKOLAB, P. BONOLI, Kuoin CHEN, C. FIORE,  
R. GRANETZ, D. GRIFFIN, D. GWINN, S. KNOWLTON,  
B. LIPSCHULTZ, S.C. LUCKHARDT, E. MARMAR,  
M. MAYBERRY<sup>1</sup>, F.S. McDERMOTT, J. MOODY,  
R. PARKER, J. RICE, Y. TAKASE, J. TERRY,  
S. TEXTER<sup>2</sup>, S. WOLFE  
Plasma Fusion Center,  
Massachusetts Institute of Technology,  
Cambridge, Massachusetts,  
United States of America

### Abstract

RADIOFREQUENCY HEATING AND CURRENT DRIVE EXPERIMENTS ON ALCATOR C AND VERSATOR II.

Lower hybrid heating and current drive experiments on the Alcator C tokamak ( $R = 0.64$  m,  $a = 0.165$  m, molybdenum limiters) were performed at a frequency of 4.6 GHz, with net injected RF powers up to  $P_{rf} \leq 1.5$  MW. Recent experiments have focused on energy confinement studies in lower hybrid current driven (LHCD) and LHRF heated Ohmic discharges, and sawtooth stabilization in combined LHCD-OH driven discharges at densities  $\bar{n}_e \leq 1.4 \times 10^{20}$  m<sup>-3</sup>. Ion Bernstein wave heating experiments were also carried out in Alcator C, at a frequency of  $f = 183$  MHz and at power levels  $P_{rf} \leq 200$  kW. Significant heating ( $\Delta T_i \leq 400$  eV) was observed at  $\omega/\omega_{CH} \approx 1.5, 2.5$ , and  $\omega/\omega_{CD} = 2.5$ , at densities  $\bar{n}_e \approx 1 \times 10^{20}$  m<sup>-3</sup>. In the Versator II tokamak, particle confinement improvement (by factors of about two) was observed in the presence of 2.45 GHz lower hybrid current drive.

### Energy Confinement in LHCD Plasmas in Alcator C

The energy confinement properties of lower hybrid current driven (LHCD) plasmas, heated and maintained entirely by rf-driven currents have been investigated in the parameter range  $\bar{n}_e = 0.1 - 0.8 \times 10^{20}$  m<sup>-3</sup>,  $I_p = 100 - 200$  kA,  $B_T = 8 - 11$  T,  $q_l = 8 - 17$ ,  $Z_{eff} = 1.5 - 2.2$ , hydrogen gas [1]. Electron temperature profile measurements were obtained with a 5-channel ruby Thomson scattering system and ion temperatures by neutral charge-exchange analysis. The energy of the current carrying

<sup>1</sup> GA Technologies Inc., La Jolla, CA, USA.

<sup>2</sup> TRW Inc., Los Angeles, CA, USA.

superthermal electron population was inferred from plasma hard x-ray spectral analysis and measurements of the equilibrium quantity  $\beta_p + \ell_i/2$ . Confinement measurements from LHCD plasmas were compared with very similar ohmic discharges. The bulk thermal energy content of LHCD plasma was nearly identical to that of a similar ohmic plasma, while the energy content of the superthermal electron tail in LHCD discharges could account for up to half the total kinetic energy of the plasma at the lower range of densities. The global confinement time, defined as  $\tau_E = W_{tot}/P_{in}$ , where  $W_{tot}$  is the total kinetic energy of the bulk and the superthermal particles (LHCD plasmas), and  $P_{in}$  is the net input rf or ohmic power, is plotted vs. density in Fig. 1. Over this range of densities, the ohmic power remained constant, and the ohmic confinement time rises linearly with density. The rf power required to maintain the rf driven discharge increases nearly linearly with density [2]. The quantity  $\tau'_E \equiv W_{Bulk}/P_{in}$ , where  $W_{Bulk}$  is the thermal energy of the bulk LHCD plasma, is also plotted. The difference between  $\tau'_E$  and  $\tau_E$  of the LHCD plasmas indicates the relative importance of the electron tail in the overall energy balance. At densities  $\bar{n}_e \lesssim 0.3 \times 10^{20} \text{ m}^{-3}$ , the confinement time of LHCD plasmas is somewhat greater than that of ohmic plasmas, due to the substantial fraction of energy carried by the superthermal electron distribution. At higher densities, the LHCD confinement time degrades relative to that of the ohmic plasmas. The experimental scaling of the LHCD confinement time with density and input power is comparable with the predictions of the empirical Kaye-Goldston scaling law for NBI-heated plasmas [3]. Such an agreement suggests that similar agents may be affecting the transport of different types of auxiliary heated plasmas, including ones purely maintained by LHCD. Combined ray tracing and transport code studies [4] indicate that the present results at high densities could be explained by a degradation of  $\chi_e$  (bulk) relative to its ohmic value [1].

The confinement time of energetic tail electrons has been estimated by combining measurements of hard x-ray spectra and theoretical calculations of the absorbed power provided by the code [5]. After collisional losses are subtracted, the confinement time of the fast electrons above 100 keV is found to be comparable to the global energy confinement time and increases with energy.

### Lower Hybrid Electron Heating Experiments in Alcator C

Heating experiments have been carried out in ohmically maintained deuterium plasmas for  $B_T = 5.5 - 8.0 \text{ T}$ ,  $I_p = 150 - 375 \text{ kA}$ ,  $\bar{n}_e \leq 2.0 \times 10^{20} \text{ m}^{-3}$ , using molybdenum limiters. In previous experiments using SiC coated graphite limiters, significant electron ( $\Delta T_{e0} \simeq 1.0 \text{ keV}$ ) and ion

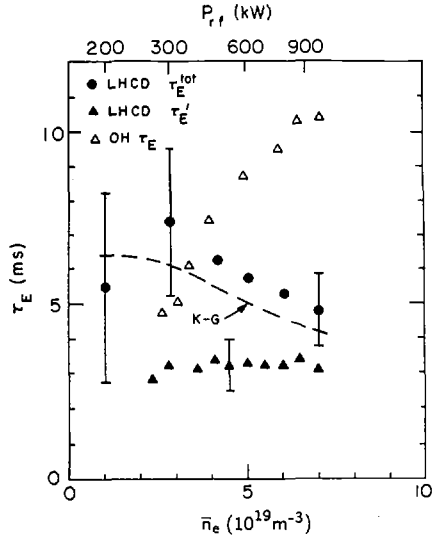


FIG. 1.  $\tau_E$  versus  $\bar{n}_e$  for LHCD (solid circles) and Ohmic (open triangles) hydrogen plasmas, for  $B_T = 8$  T,  $I_p = 140$  kA.  $\tau_E^i = W_{Bulk}/P_{in}$  (solid triangles) for the LHCD plasmas. The dashed line represents the Kaye-Goldston scaling law.

( $\Delta T_{io} \lesssim 0.7$  keV) heating was observed [6]. However, these results were accompanied by rather large rises in  $Z_{eff}$  ( $\Delta Z_{eff} \lesssim 3$ ). Bulk electron heating due to electron Landau damping and subsequent ion heating due to collisional relaxation are observed in the present experiments over the density range  $\bar{n}_e = 0.6 - 1.7 \times 10^{20} \text{ m}^{-3}$ . Temperature increases of  $\Delta T_{eo} = 0.7$  keV and  $\Delta T_{io} = 0.3$  keV are recorded for  $P_{rf} = 1.0$  MW at  $B_T = 5.5$  T,  $I_p = 260$  kA,  $\bar{n}_e = 1.4 \times 10^{20} \text{ m}^{-3}$  with  $\Delta Z_{eff} \lesssim 0.5$  [7]. As seen in Fig. 2, comparable heating efficiencies are obtained with waveguide phasings of  $\Delta\phi = 90^\circ$  (current drive) and  $180^\circ$  (heating mode), and the electron temperature profiles are similar to those in ohmic plasmas in both cases. Figure 2 shows that the energy confinement in LH-heated plasmas is degraded relative to that in ohmic discharges. As in the case of LHCD plasma, the confinement scaling with rf power is consistent with the Kaye-Goldston formula [3]. In the current drive mode sawteeth were stabilized [7, 8]; however, no significant improvement in the global energy confinement is observed when the sawteeth are suppressed. The radiated power estimated by spectroscopic means increased with rf power but was limited to  $P_{rad} \lesssim 150$  kW. Bolometric measurements show a similar trend but higher radiated power levels. However, radiation alone cannot explain the deterioration of  $\tau_E$  with power. Numerical code modelling [4] indicates that 75% of the injected rf power is absorbed by electron Landau damping,

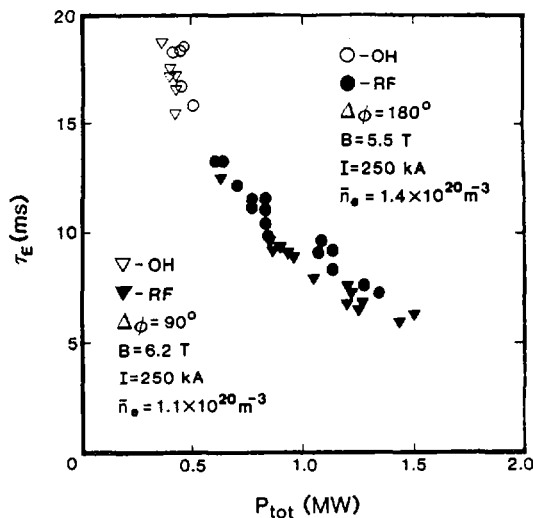


FIG. 2. Energy confinement times in OH driven plasmas with LH heating mode ( $\Delta\phi = 180^\circ$ ) and with LH current drive phasing ( $\Delta\phi = 90^\circ$ ).

with the remainder being lost to collisional absorption near the plasma edge. Modelling indicates that a 30% degradation of  $\chi_e$ , the electron thermal diffusivity, is sufficient to explain the present results.

### Sawtooth Stabilization with LH Current Drive in Alcator C

Stabilizing sawteeth by means of rf current drive has been studied in Alcator plasmas at higher densities ( $\bar{n}_e = 0.6 - 1.2 \times 10^{20} \text{m}^{-3}$ ,  $I_p = 250 - 325 \text{kA}$ ,  $q_l = 4 - 6$ ) than in other tokamaks [9-11]. The major diagnostic of the sawtooth behavior is a 16-channel soft x-ray diode array sensitive in the range 1.5 to 15 keV. The sawtooth period is found to lengthen during lower hybrid wave injection, and with sufficient rf power ( $P_{rf}^{crit} \gtrsim 550 \text{kW}$  for  $\bar{n}_e = 1.1 \times 10^{20} \text{m}^{-3}$ ,  $I_p = 250 \text{kA}$ ,  $B_T = 6.2 \text{T}$ ) the sawteeth are entirely suppressed [7, 8]. Sawtooth suppression has only been achieved in the current drive mode of operation, i.e. with the relative phase between waveguides of  $\Delta\phi = +90^\circ$ ; stabilization is not observed with symmetric ( $\Delta\phi = 180^\circ$ ) or anti-current drive ( $\Delta\phi = -90^\circ$ ) phasings for the range of rf powers used in this experiment. It has been noted that as the rf power is increased above  $P_{rf} \approx 900 \text{kW}$ , the sawteeth recur after 40-50ms, which is comparable to the characteristic L/R time [7]. In contrast to stabilization experiments on low density plasmas in ASDEX and PLT [9, 10], in the current drive mode ( $\Delta\phi = 90^\circ$ ) the

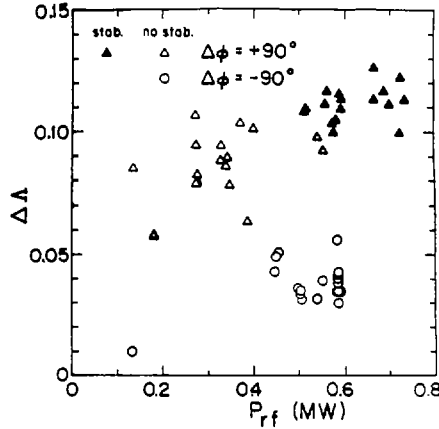


FIG. 3. Change in  $\Delta$  ( $= \beta_p + \ell_i/2 - 1$ ) versus rf power for  $\Delta\phi = +90^\circ$  (triangles) and  $\Delta\phi = -90^\circ$  (circles);  $B_T = 6.0$  T,  $\bar{n}_e = 0.8 \times 10^{20} \text{ m}^{-3}$ ,  $I_p = 275$  kA,  $q(a) = 4.7$ .

sawtooth period increases monotonically (by up to a factor of two) with rf power until stabilization is achieved. In all cases, the sawtooth inversion radius inferred from the x-ray measurements remains at  $r/a \simeq 0.2$  at all rf powers for which sawteeth are observed. For  $\Delta\phi = +90^\circ$  at rf power levels near the threshold, high frequency oscillations are often superimposed on the x-ray sawteeth. In these circumstances, the sawtooth crash times, as observed on the central soft x-ray channel, can be as long as 1 msec (compared to the usual crash times of  $\tau \lesssim 100 \mu\text{sec}$  in both ohmic and LH heated plasmas). The  $m = 1$  oscillations are sometimes observed in fully stabilized discharges as well. As shown in Fig. 2, equally efficient electron and ion heating are observed for both  $\Delta\phi = 90^\circ$  and  $180^\circ$ , as well as for  $\Delta\phi = -90^\circ$  (not shown).

The change in  $\beta_p + \ell_i/2$  versus rf power has been measured and is shown in Fig. 3. During rf injection,  $\beta_p + \ell_i/2$  increases by 0.11 for  $\Delta\phi = +90^\circ$  but only by 0.04 for  $\Delta\phi = -90^\circ$ , in contrast to results from the low density stabilization experiments on ASDEX [9]. From the kinetic measurements, the thermal  $\beta_p$  is estimated to increase by 0.04 – 0.05 in both cases. A likely explanation of the difference in the measured values of  $\beta_p + \ell_i/2$  between the two phasings is an increase in the plasma internal inductance for the current-drive case. This conclusion is supported by comparison of the time evolution of  $\beta_p + \ell_i/2$  for the two phases. While  $\beta_p + \ell_i/2$  increases for both phases, the slowest time evolution, which most likely represents the change in the internal inductance, is negative for  $\Delta\phi = -90^\circ$  and positive for  $\Delta\phi = +90^\circ$ . A possible explanation of this behavior is that rf current is driven at  $r/a \approx 0.2 - 0.4$ , outside the  $q = 1$  surface. Consequently, the current profile shrinks in the outer regions of

the plasma ( $r/a \sim 0.6 - 0.8$ ), resulting in an increased inductance, but is flattened near the center such that  $q(r) > 1$  everywhere.

### Ion Bernstein Wave Heating Experiments in Alcator C

Ion Bernstein wave (IBW) heating experiments have been carried out in Alcator C in order to test the effectiveness of this technique for heating high density plasmas ( $\bar{n}_e \gtrsim 1 \times 10^{20} m^{-3}$ ). Efficient ion heating with IBW has been reported at lower plasma densities in tokamaks by Ono and coworkers [12]. However, the heating mechanism remained somewhat controversial and, in addition to minority heating, nonlinear absorption mechanisms have also been advocated to explain the observed results [13,14]. The present work indicates that both nonlinear absorption and improved ion energy confinement could play a significant role in the ion heating process.

Ion Bernstein waves were launched by a low field side, center fed, moveable T-shaped loop antenna, with the center conductor aligned parallel to the toroidal magnetic field, and surrounded by a double layered Faraday shield. The outer dimensions of the stainless steel antenna are: width  $\lesssim 0.04$  m, length  $\lesssim 0.25$  m, and maximum power transmitted  $P_{rf} \lesssim 200$  kW at  $f = 183$  MHz. Due to significant metallic impurity generation at high powers, most of the data were obtained at  $P \lesssim 150$  kW. The experiments were carried out in three different plasma configurations, with the minor radius (set by molybdenum limiters) set at  $a = 0.115$  m,  $0.120$  m or  $0.125$  m ( $4.8 \leq B(T) \leq 11.0$ ). Optimal coupling was obtained with the front surface of the Faraday shield being  $\Delta r \sim 5$  mm behind the limiter surface. Although heating studies were carried out in a range of magnetic fields, here we shall concentrate on discussing three regimes corresponding to magnetic fields  $B(0) \simeq 5, 7.5,$  and  $9.3-10.3$ T, such that  $\ell_H^{(0)} \equiv \omega/\omega_{CH}(0) \simeq 2.5, 1.5$  or  $1.25$  (and hence  $\ell_D^{(0)} \equiv \omega/\omega_{CD}(0) \simeq 5, 3,$  and  $2.5$  whenever deuterium minority is injected into the hydrogen majority plasma) where  $\ell_H^{(0)}$  ( $\ell_D^{(0)}$ ) designates the hydrogen (deuterium) harmonic numbers in the plasma interior near  $r = 0$ . It should be noted that for  $\ell_H^{(0)} = 2.5$  the resonant layers  $\ell_H = 2, 3$  are just outside of the plasma column. In addition, by adjusting the magnetic field the  $\ell_H = 3$  layer was moved behind the antenna. In the case of  $\ell_H^{(0)} = 1.5$ , both the  $\ell_H = 1, 2$  resonances were outside of the plasma column (and again behind the antenna). However, for the  $\ell_H^{(0)} = 1.25$  ( $\ell_D^{(0)} = 2.5$ ) case, the  $\ell_H = 1.5$  (or  $\ell_D = 3$ ) layer could have been in front of the antenna, and in fact in many successful heating shots it was located 1-2 cm inside the plasma column. Under such circumstances linear and nonlinear absorption of the

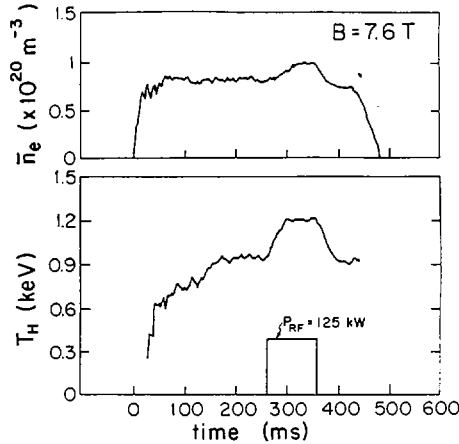


FIG. 4. Time sequence of a typical shot with rf injection in the IBW regime,  $B = 7.5$  T,  $I_p = 240$  kA.

incoming IBW wave at the plasma edge should be complete. Nevertheless, even in such cases efficient central bulk hydrogen and deuterium minority ion heating was observed.

A typical shot during IBW launching at  $B=7.6$ T is shown in Fig.4. The hydrogen bulk temperature rises by an amount  $\Delta T_H \simeq 300$  eV for  $P_{rf} = 125$  kW as measured by standard mass-resolving charge exchange neutral analysis. The density rises by 30%, the loop voltage,  $Z_{eff}$  and the electron temperature remain nearly constant. The ion temperature profile is centrally peaked, and is quite similar to the initial ohmic profile.

Plots of the increase in the bulk hydrogen temperature versus RF power at three different values of the magnetic field (corresponding to the three regimes discussed before) are shown in Fig.5. The most efficient ion heating is recorded for the case of  $B = 9.3$  T (or  $\ell_H^{(0)} = 1.25$ ,  $\ell_D^{(0)} = 2.5$ ). The typical range of densities corresponding to these data were  $\bar{n}_e \simeq (0.7 - 1.1) \times 10^{20} m^{-3}$ . Typical heating rates corresponding to these cases are  $\Delta T(eV)/P(kW) \simeq 2.2-3.3$  at a density of  $\bar{n}_e \simeq 1.0 \times 10^{20} m^{-3}$ . In all cases a threshold power is apparent before heating is observed (namely  $P_{th} \simeq 20$  kW for  $\ell_H^{(0)} = 2.5$ ,  $P_{th} \simeq 35$  kW for  $\ell_H^{(0)} = 1.5$ , and  $P_{th} \lesssim 10$  kW for  $\ell_H^{(0)} = 1.25$ ).

In general, significant heating at any magnetic field is observed only at densities  $\bar{n}_e \lesssim 1.5 \times 10^{20} m^{-3}$ . This is demonstrated in Fig.6, where heating data are shown at  $B = 7.6$  T. Note that no heating was observed above the density limit  $\bar{n}_e \simeq 1.5 \times 10^{20} m^{-3}$ . Measurements indicate that at  $B = 5$  T ( $\ell_H^{(0)} = 2.5$ ,  $\ell_D^{(0)} = 5$ ), even when a deuterium minority species

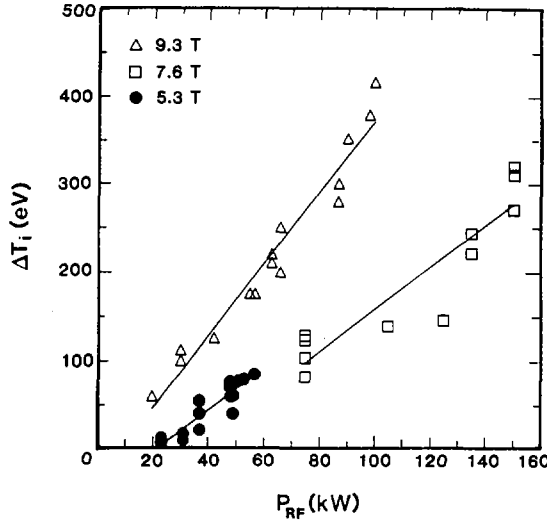


FIG. 5.  $\Delta T_i$  versus  $P_{RF}$  for three values of  $B$ . At  $B = 9.3$  T,  $\ell_H^{(0)} = 1.25$ ; at  $B = 7.5$  T,  $\ell_H^{(0)} = 1.50$ ; at  $B = 5$  T,  $\ell_H^{(0)} = 2.5$ ,  $\bar{n}_e = (0.7 - 1.1) \times 10^{20} \text{ m}^{-3}$ .

is present,  $T_D \simeq T_H$ . In particular, the hydrogen ion temperature rise is independent of the presence of deuterium, indicating that nonlinear absorption is operative in this regime [14]. However, to some extent at  $\ell_H^{(0)} = 1.5$ , and especially at  $\ell_H^{(0)} = 1.25$  the deuterium temperature (with typical concentrations of 0.5-10%) may achieve significantly higher values than the hydrogen majority component. For example, at  $B = 9.3$  T,  $T_D \lesssim 3.5$  keV while  $T_H \lesssim 1.5$  keV during RF injection. A radial scan of the charge exchange analyzer indicates that the deuterium component is always peaking on axis, decays slowly in time, and that the central hydrogen and deuterium heating maximize at the same time. It should be noted that at  $\bar{n}_e > 1.5 \times 10^{20} \text{ m}^{-3}$ ,  $T_e$  often decreased owing to increasing values of radiation. Nevertheless,  $T_i$  does not decrease, and the electron to ion temperature ratio may approach unity (in contrast to pure ohmic discharges where  $T_e > T_i$ ). This phenomena is observed at densities up to  $\bar{n}_e \simeq 2 \times 10^{20} \text{ m}^{-3}$  at both  $B = 7.5$  T ( $\ell_H^{(0)} = 1.5$ ) and  $B = 9.3$  T ( $\ell_H^{(0)} = 1.25$ ). These results clearly indicate the importance of direct rf heating of ions (as long as  $T_e > T_i$ , collisional heating of ions due to confinement improvement cannot be ruled out).

In most discharges for which  $\bar{n}_e < 2.5 \times 10^{20} \text{ m}^{-3}$ , IBW injection results in a significant increase in the global particle confinement time,  $\tau_p$ . Typically, a large increase in electron density, accompanied by a decrease in the particle source rate as inferred from the  $H_\alpha$  emission, is observed.

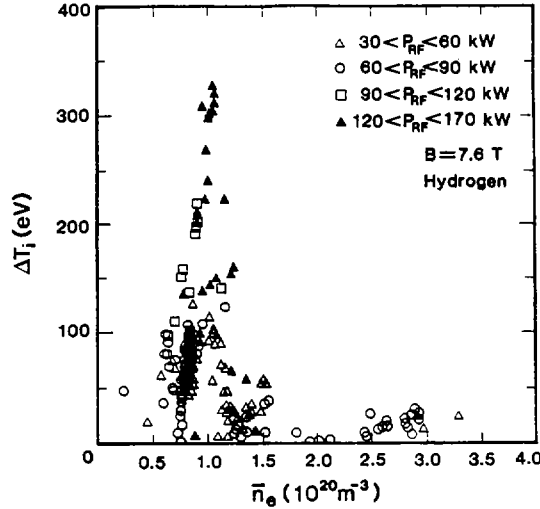


FIG. 6.  $\Delta T_i$  versus  $\bar{n}_e$  for  $B = 7.6$  T; hydrogen ions.

When compared with discharges in which the density is increased by gas puffing alone, the  $\tau_p$  during IBW is as much as three times larger. Improved  $\tau_p$  are observed for both  $B \sim 7.6$  T and  $B \sim 9.4$  T. At  $B = 5$  T, smaller (10%-20%) improvement of  $\tau_p$  was observed, perhaps due to the lower injected powers. The increases in  $\tau_p$  are strongly dependent upon the density of the target plasma. The maximum fractional increase in  $\tau_p$  occurs in target plasmas whose line averaged density is  $\sim 0.7 \times 10^{20} \text{ m}^{-3}$ . As the pre-rf target density is increased, the enhancement in  $\tau_p$  is reduced until above  $\bar{n}_e > 2.5 \times 10^{20} \text{ m}^{-3}$ , no effect upon  $\tau_p$  is observed. This dependence is shown clearly in Fig.7. The changes in global particle confinement time were associated with similar improvements in the central plasma (and not just near the periphery which dominates the global  $\tau_p$ ). Central impurity particle confinement times were measured by injecting trace amounts of Si using the laser blow-off technique. The impurity confinement times also increased during IBW injection, typically by a factor of  $\sim 1.5 - 2$ , but sometimes by as much as a factor of 2.8. Before IBW injection,  $\tau_p$  is found to be 3-6 ms at  $\bar{n}_e \sim 0.9 \times 10^{20} \text{ m}^{-3}$ , with large fractional increases occurring with IBW injection, as described above. Using these values of  $\tau_p$ , at lower densities ( $\bar{n}_e < 1 \times 10^{20} \text{ m}^{-3}$ ) the convection term could be important in the ion energy balance.

In the present experiments, the excitation, propagation and absorption of directly launched ion Bernstein waves (IBW) were studied using  $\text{CO}_2$  laser scattering [15]. The scattering volume was located at the same toroidal location as the IBW antenna. The identification of the IBW was

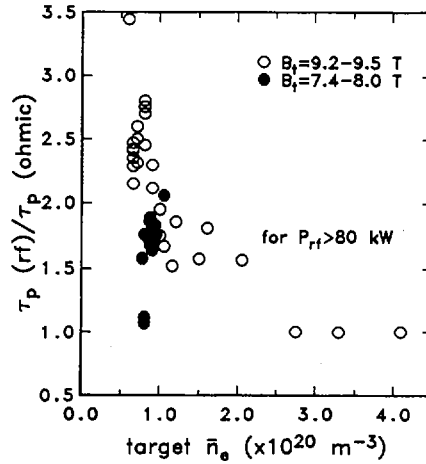


FIG. 7. Particle confinement time with and without IBW injection versus density.  $B = 9.4 \text{ T}$ .

made by mapping out the dispersion relation. The excitation of the IBW is optimized when  $\ell_H$  evaluated at the antenna is just below an integer value, as expected from theory. The scattered  $\text{CO}_2$  signal intensity at  $x/a \simeq +0.4$ ,  $B = 7.5\text{T}$ , is shown as a function of density in Fig. 8a. A sharp decrease of the scattered signal is observed above  $\bar{n}_e \simeq 1 \times 10^{20} \text{ m}^{-3}$ . This density corresponds to the ion heating “density limit”, and the loss of ion heating may be attributed to the inaccessibility of the IBW to the plasma interior. To check this hypothesis, the level of low-frequency fluctuations was measured near the plasma edge by  $\text{CO}_2$  scattering. The relative magnitude of these fluctuations is plotted on Fig. 8b. A strong correlation between the increased level of low frequency edge fluctuations and the decreased level of IBW in the plasma interior is observed as the density is increased above  $\bar{n}_e > 1 \times 10^{20} \text{ m}^{-3}$ . In the present case a minimum in the low frequency fluctuation activity is observed at  $\bar{n}_e \sim 1 \times 10^{20} \text{ m}^{-3}$ , and at the same density IBW and ion heating (see Fig.6) maximize in the plasma interior. Thus, the density limit for IBW heating may be associated with strong scattering by low frequency density fluctuations [16].

A brief discussion regarding the physics of IBW heating in Alcator C is in order. As shown in Ref. 14, we expect that nonlinear absorption should dominate (even in the presence of minority species) at the resonances  $\ell_H^{(0)} = 2.5$  ( $m = 5$ ,  $B = 5\text{T}$ ) and  $\ell_H^{(0)} = 1.5$  ( $m = 3$ ,  $B = 7.5\text{T}$ ). The situation at  $B=9.3\text{T}$  is more complex. In particular, both nonlinear and linear absorption can take place near the plasma edge where  $\ell_H^{(a)} = 1.5$  ( $m = 3$ ) and  $\ell_D^{(a)} = 3$ , or nonlinear absorption can take place near the

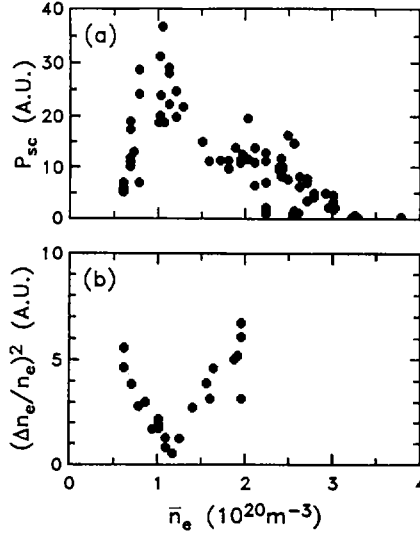


FIG. 8. Scattered  $CO_2$  power versus  $\bar{n}_e$  from (a) IBW at  $r/a = 0.4$ , and (b) low frequency fluctuations,  $(\Delta n/n)^2$  at  $r/a = 0.83$ . Hydrogen plasma,  $B = 7.5$  T.

center on the deuterium minority where  $\ell_D^{(0)} = 2.5$  ( $m = 5$ ) (this may be the only possible process at  $B \geq 10$ T). The nonlinear threshold for one e-fold decay of the transmitted power in a single pass is given by [14]

$$\frac{1.14 \times 10^{19} W k_{\perp}^2 R(m) (P(kW)/S(m^2))}{\omega n(m^{-3}) T_i(keV) Y^2} \geq 1$$

where  $W$  is the nonlinear matrix element whose values are given in Fig.9 for  $m=3, 5$ .  $P/S$  is the transmitted power density, and  $Y = (k_{\perp}/2)(\omega_{ci}^2/\omega_{pi}^2) \times (\partial \epsilon_R / \partial k_{\perp})$  is a quantity proportional to the group velocity. Typical values of  $Y$  vary from  $Y \simeq 0.3 - 0.1$  for  $k_{\perp} r_{ci} \simeq 1.2 - 2$ . The other plasma parameters are in standard notation, including  $R$ , the major radius. The calculated threshold powers for each regime are listed in Table 1. Here we assumed an effective power transmission area of  $S=2A$ , where  $A$  is the antenna surface. We see that the calculated thresholds are in reasonable agreement with the observed values at  $B=5$ T and  $B=7.5$ T. The situation at  $B=9.3$ T is complicated by the presence of the surface absorption layer at  $r \simeq 10$  cm ( $r/a \simeq 0.83$ ). In order to explain the observed energetic deuterium component, at least part of the wave power penetrates to the plasma center. This phenomena is not well understood at present, especially since linear absorption is also effective at the plasma edge. If edge absorption is operative, it also produces significant central bulk heating

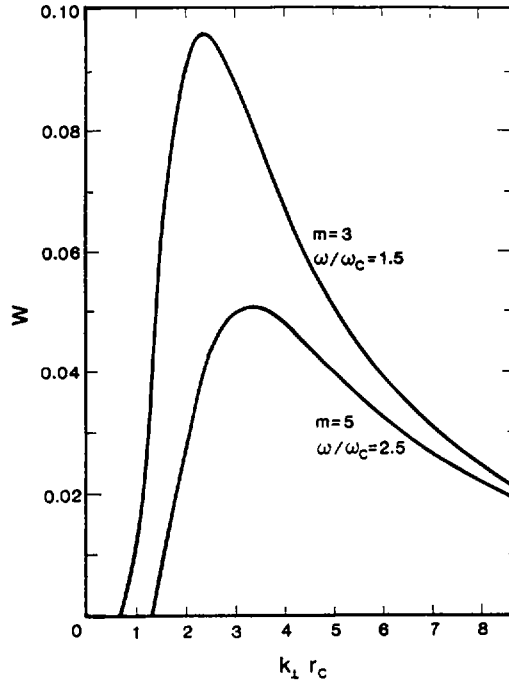


FIG. 9. Non-linear cyclotron damping matrix element,  $W$ , versus  $k_{\perp} r_{ci}$  for IBW.

of hydrogen, apparently by improving energy confinement of ions near the center. In addition, tens of kW s of power would be transferred to the H majority by collisional equilibration from the energetic deuterium minority component. Further complications arise from significant ponderomotive forces at the surface. Detailed theoretical and transport code studies of these complex phenomena are underway.

### Particle Confinement in LHCD Plasmas in the Versator II Tokamak

We have reported previously that significant density increases (up to factors of two) observed during combined ohmic and 800 MHz LHCD at densities  $\bar{n}_e \lesssim 6 \times 10^{18} m^{-3}$  were due to the improvement of global particle confinement [17]. Recently the RF frequency was raised to 2.45 GHz, and RF current drive was demonstrated at densities  $\bar{n}_e \lesssim 2 \times 10^{19} m^{-3}$  [18]. Significant density increases ( $(\Delta\bar{n}_e/\bar{n}_e) \sim 1$ ) have also been ob-

TABLE 1. THRESHOLD POWERS

$B(0)$ (T)	$m$	Resonance at $(r/a)$	Ion Species absorbing	$n(r)$ ( $10^{20}m^{-3}$ )	$T_i(r)$ (keV)	$P_{th}$ (kW)
5.2	5	0.5	H (maj)	0.8	0.4	16
	5	0.5	D (min)	0.8	0.4	0
7.6	3	-0.3	H (maj)	0.8	0.7	36
	3	-0.3	D (min)	0.8	0.7	0
9.3	3	0.9	D (min)			0
	3	0.9	H (maj)	0.1	0.1	0.1
	5	0	2% D (min)	1.0	1.0	30

served during injection of the 2.45 GHz RF power, even at densities  $\bar{n}_e \gtrsim 1 \times 10^{19} cm^{-3}$ . In Fig. 10, the line-averaged density,  $\bar{n}_e$ , is shown to increase from  $\bar{n}_e \sim 1.3 \times 10^{19}$  to  $\sim 1.9 \times 10^{19} cm^{-3}$  when 60 kW of 2.45 GHz RF power is applied in the current drive mode ( $\Delta\phi = 90^\circ$  relative waveguide phasing). The density profile is broadened and increased while the  $H_\alpha$  profile height is decreased during RF injection. Since emissions from carbon and oxygen impurities did not show any increase during RF injection, the electron source term  $S$  is dominated by ionization of hydrogen neutrals. The global confinement can be calculated from the particle balance equation,  $dN_e/dt = S - N_e/\tau_p$ . The particle confinement time is found to increase by a factor of  $\sim 2.2$  during RF injection. The density increase is largest for a relative waveguide phasing of  $\Delta\phi = \pi/2$  (current drive direction) and is smallest when  $\Delta\phi = -\pi/2$  (anti-current drive direction). It should be noted that the improved confinement regime coincides with the current drive density regime, i.e.,  $\bar{n}_e \lesssim 2 \times 10^{19} m^{-3}$ . The upper value of the density at which particle confinement improvement is observed also depends on the toroidal magnetic field. For example, when the magnetic field is raised from 0.9T to 1.1T, the upper density limit

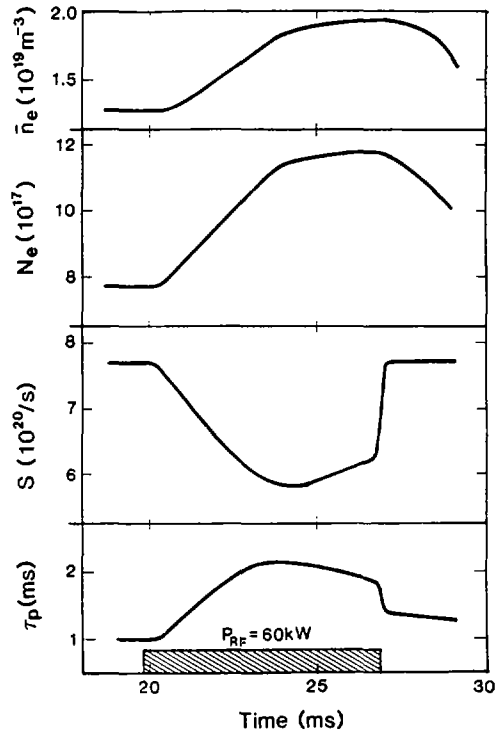


FIG. 10. Temporal evolution of the line-averaged density  $\bar{n}_e$ , the total electron number  $N_e$ , the ionization source term  $S$  deduced from  $H_\alpha$  emissivity profiles, and the calculated global particle confinement time  $\tau_p$  in Versator II during LHCD.

value is increased from  $1.6 \times 10^{19} \text{ cm}^{-3}$  to  $2.0 \times 10^{19} \text{ cm}^{-3}$ . This dependence may be explained by improved wave access when the magnetic field is increased, in agreement with other current drive effects. The exact physical mechanism responsible for the improved confinement during RF current drive has not been identified yet.

#### ACKNOWLEDGEMENTS

The authors are grateful to the Alcator and Versator technical staff for their help in these experiments. They also thank Dr. S. McCool and Dr. R. Watterson for their contributions to the Thomson scattering experiments.

This work was supported by the United States Department of Energy, under Contract No. DE-AC02-78ET51013.

## REFERENCES

- [1] KNOWLTON, S., et al., Phys. Rev. Lett. **57** (1986) 1529;  
TAKASE, Y., et al., Nucl. Fusion **27** (1987) 53.
- [2] PORKOLAB, M., et al., Phys. Rev. Lett. **53** (1984) 450.
- [3] KAYE, S.M., GOLDSTON, R.J., Nucl. Fusion **25** (1985) 65.
- [4] BONOLI, P., ENGLADE, R., PORKOLAB, M., in Heating in Toroidal Plasmas (Proc. 4th Int. Symp. Rome, 1984), Vol. 2, Int. School of Plasma Physics, Varenna (1984) 1311.
- [5] TEXTER, S., Ph.D. Thesis, 1986; Rep. PFC/JA-86-10, Plasma Fusion Center, Massachusetts Inst. of Tech., Cambridge (1986).
- [6] PORKOLAB, M., et al., Phys. Rev. Lett. **53** (1984) 1229.
- [7] PORKOLAB, M., et al., in Controlled Fusion and Plasma Heating (Proc. 13th Europ. Conf. Schliersee, 1986), Vol. 2, European Physical Society (1986) 445.
- [8] PORKOLAB, M., et al., Bull. Am. Phys. Soc. **30** (1985) 1493.
- [9] SÖLDNER, F., et al., Phys. Rev. Lett. **57** (1986) 1137.
- [10] CHU, T.K., et al., Nucl. Fusion **26** (1986) 666.
- [11] VAN HOUTTE, D., et al., Nucl. Fusion **24** (1984) 1485.
- [12] ONO, M., et al., Phys. Rev. Lett. **54** (1985) 2339.  
HOSEA, J., et al., Plasma Phys. Controll. Fusion **28** (1986) 1241.
- [13] ABE, H., et al., Phys. Rev. Lett. **53** (1984) 1153.
- [14] PORKOLAB, M., Phys. Rev. Lett. **59** (1985) 434.
- [15] TAKASE, Y., et al., Bull. Am. Phys. Soc. **31** (1986) 1587.
- [16] ONO, M., Phys. Fluids **25** (1982) 990.
- [17] LUCKHARDT, S.C., et al., Phys. Fluids **29** (1986) 1985.
- [18] MAYBERRY, M.J., et al., Phys. Rev. Lett. **55** (1985) 829.

## DISCUSSION

R.J. GOLDSTON: The Alcator team has previously identified ion thermal losses as the cause of the deterioration of confinement at high density. Now you have a tool to heat ions or perhaps to improve their confinement. How do the electrons respond when the ion temperature rises?

M. PORKOLAB: The electron temperature remains nearly constant as the RF power is injected. In some instances, at the highest power levels,  $T_e$  may decrease by 10–20% because of radiation losses associated with injection of high  $Z_i$  impurities. In all cases, however,  $T_e \geq T_i$  is observed. Since we heat ions exclusively, it is hard to say anything about electron confinement.

K. UEHARA: Did you observe a relationship between the energy confinement time and  $P_{RF}$  in the low density regions where  $\tau_E$  is better than in the OH case? And what was  $\tau_E$  in the low density region as compared with  $\tau_E$  during injection of RF power?

M. PORKOLAB: Our Thomson scattering equipment does not operate reliably at densities below  $3 \times 10^{19} \text{ m}^{-3}$ . Hence, we have no information on confinement at very low densities, i.e. below  $1 \times 10^{19} \text{ m}^{-3}$ . However, if the trend in our data remained the same, I would expect  $\tau_E(\text{RF}) > \tau_E(\text{OH})$  at these low densities. This would be consistent with observations in other machines.



## CURRENT DRIVE BY LOWER HYBRID WAVES AT 3.7 GHz IN PETULA B

F. PARLANGE<sup>1</sup>, D. VAN HOUTTE<sup>1</sup>,  
H. BOTTOLLIER-CURTET, G. BRIFFOD, P. CHABERT<sup>1</sup>,  
M. CLÉMENT, C. DAVID<sup>2</sup>, A. GIRARD, C. GORMEZANO<sup>2</sup>,  
W. HESS<sup>1</sup>, M. HESSE<sup>1</sup>, G.T. HOANG<sup>1</sup>, G. ICHTCHENKO,  
J.M. RAX<sup>1</sup>, F. RYTER<sup>3</sup>, J.C. VALLET<sup>1</sup>

Association Euratom-CEA,  
Département de recherches sur la fusion contrôlée,  
Centre d'études nucléaires de Grenoble,  
Grenoble, France

### Abstract

CURRENT DRIVE BY LOWER HYBRID WAVES AT 3.7 GHz IN PETULA B.

The density limit for lower hybrid current drive is extended to  $8 \times 10^{13} \text{ cm}^{-3}$  by increasing the frequency from 1.3 to 3.7 GHz. When the density is increased above  $2 \times 10^{13} \text{ cm}^{-3}$ , the plasma current cannot be replaced entirely by RF current, because of limited power and wave absorption saturation. Even with partial current replacement, sawteeth can be suppressed with rather low power. In some cases, this may be due to a broadening of the current profile and the vanishing of the  $q = 1$  surface. In other cases, there is some evidence that relaxations may be suppressed while  $q < 1$  on axis.

### 1. INTRODUCTION

The capability of lower hybrid current drive to produce more stable discharges than inductive drive is of great interest at present, in view of the high temperature relaxation limiting performances in today's experiments [1]. The spatial distribution of wave driven currents is a priori different from that in the Ohmic case. In addition, the existence of fast electrons having the wave velocity affects the plasma DC conductivity. Therefore, even partial sustainment of a discharge by waves should modify the stability of tokamak plasmas against MHD resistive modes and sawtooth relaxations.

These effects were demonstrated in an early work on Petula [2] and are currently being observed on other tokamaks [3-5]. Up to now, experiments on Petula were limited to low densities,  $n_e \leq 1.5 \times 10^{13} \text{ cm}^{-3}$ , because of the low RF frequency of 1.3 GHz and critical density phenomena.

<sup>1</sup> CEA, Centre d'études nucléaires de Cadarache, Saint-Paul-lez-Durance, France.

<sup>2</sup> JET Joint Undertaking, Abingdon, Oxfordshire, UK.

<sup>3</sup> Association Euratom-Confédération Suisse, Ecole polytechnique fédérale de Lausanne, Lausanne, Switzerland.

Current drive studies in Petula are now being extended to high densities of up to  $10^{14} \text{ cm}^{-3}$ , by adding a new lower hybrid equipment at 3.7 GHz [6] (500 kW/50 ms). The grill with  $2 \times 9$  waveguides is of the multijunction type and emits a well defined  $N_{\parallel}$  spectrum which can be varied from 2.7 to 1.5.

Experiments were made with the following parameters:  $R = 0.72 \text{ m}$ ,  $a = 0.165 \text{ m}$ ,  $B_T = 2.8 \text{ T}$ ,  $I_p = 100\text{--}170 \text{ kA}$ ,  $\bar{n}_e = (0.5\text{--}10) \times 10^{13} \text{ cm}^{-3}$ .

## 2. DENSITY LIMIT

At low densities ( $\bar{n}_e \sim (0.8\text{--}1.6) \times 10^{13} \text{ cm}^{-3}$ ), the current drive efficiency is similar to what was obtained at 1.3 GHz. The usual figure of merit is  $nIR/P_{\text{RF}} \sim 10^{19} \text{ A} \cdot \text{m}^{-2} \cdot \text{W}^{-1}$ . At higher densities, where current drive is no longer observed at 1.3 GHz because of the density limit effect, a significant decrease in loop voltage, at constant plasma current, is still measured during the 3.7 GHz RF pulse, up to the practical operating density of Petula,  $\bar{n}_e \sim 10^{14} \text{ cm}^{-3}$  (Fig. 1).

However, no complete replacement of the Ohmic current is obtained for densities higher than  $\bar{n}_e \sim 2 \times 10^{13} \text{ cm}^{-3}$ , owing to the  $1/n_e$  density scaling of the lower hybrid current drive and, possibly, other phenomena such as wave accessibility or absorption saturation.

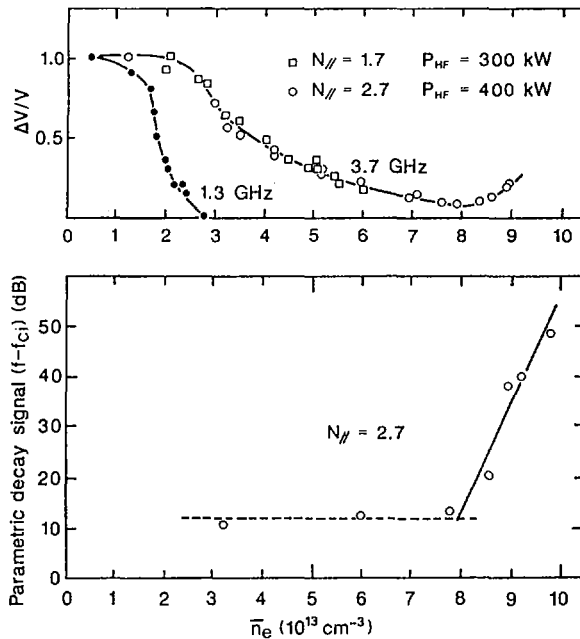


FIG. 1. Relative loop voltage drop and parametric decay wave excitation during lower hybrid current drive.

In particular, the small effect on loop voltage at  $n_e = 8 \times 10^{13} \text{ cm}^{-3}$  could equally be explained by the limited power available,  $P \leq 400 \text{ kW}$ , or by the density limit. On the other hand, parametric decay wave excitation starts increasing sharply above noise level, for densities higher than  $8 \times 10^{13}$ . By similarity with the 1.3 GHz case, this was considered to be a criterion for the density limit. This value, when compared to the value for the 1.3 GHz waves, is in agreement with a scaling  $n = f^\alpha$ , where  $1.7 < \alpha < 2$ , which so far has only been inferred from measurements made on other devices [7].

### 3. CURRENT DRIVE EFFICIENCY AND SATURATION

If all available power were absorbed, the plasma response to the electric field  $E$  and the RF power launched into the torus,  $P$ , would be given by [8, 9]:

$$J \approx \sigma E + \eta \alpha P + \eta^2 E \alpha P$$

where  $\sigma$  is the Spitzer conductivity,  $\eta$  the current drive efficiency given in [8] and  $\alpha$  the fraction of power fulfilling the accessibility condition. The third term on the right hand side describes the RF enhanced conductivity.

This formula gives reasonable agreement for results obtained with a mean wave index  $N_{||} = 2.7$ , up to some power where the voltage drop saturates (Fig. 2), at least for densities lower than  $4 \times 10^{13} \text{ cm}^{-3}$ . The power threshold for saturation is

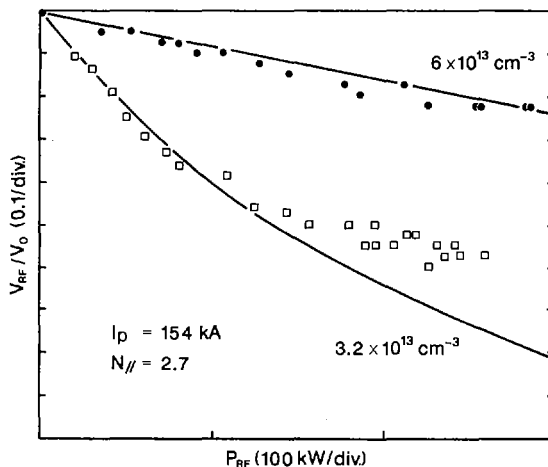


FIG. 2. Loop voltage during the RF pulse for two different densities. Solid line is the result of simulation.

an increasing function of density. Saturation is also observed for the same power on electron cyclotron emission [10]. This saturation is interpreted as a limitation in power absorption when collisions are not sufficient to prevent the formation of a plateau in the electron distribution function.

In short, compared to the linear relation  $I = n \alpha P$ , the experimental points in Fig. 2 show an improved efficiency at low power, due to enhanced conductivity and degradation at high power because of limited absorption.

For  $N_{\parallel} = 1.7$ , accessibility becomes a severe problem preventing propagation of power to the plasma centre for  $\bar{n}_e \geq 4 \times 10^{13} \text{ cm}^{-3}$  ( $\alpha = 0$ ) and giving  $\alpha = 5\%$  for  $\bar{n}_e = 3.2 \times 10^{13} \text{ cm}^{-3}$ . Nevertheless, the experimental curves are quite similar to the  $N_{\parallel} = 2.7$  case and can be fitted by taking  $\alpha = 10\%$ , which corresponds to accessibility at mid-radius. Saturation is observed, as well.

#### 4. SUPPRESSION OF INTERNAL DISRUPTIONS

Studies of sawtooth activity during lower hybrid current drive were carried out with an array of soft X-ray diodes supplemented, for some shots, by fast IR interferometry and ECE emission.

For the whole density range of 1 to  $6 \times 10^{13} \text{ cm}^{-3}$ , the soft X-ray emission is strongly affected by the lower hybrid current drive and may increase by a factor of three above the Ohmic level, on the central chord.

The sawtooth and MHD behaviour during current drive on Petula depends on the density:

- (1) For densities lower than  $3 \times 10^{13} \text{ cm}^{-3}$ , the sawtooth suppression is associated with the triggering of an  $m = 2$  mode in a way similar to the 1.3 GHz case [2]. When the density is increased, the MHD oscillations are triggered later and later until, for  $n_e = 3 \times 10^{13} \text{ cm}^{-3}$ , they cannot be observed any longer during a 100 ms RF pulse. Soft X-ray emission starts increasing in the plasma centre but levels off when the  $m = 2$  mode is present.
- (2) In the  $(3-4.5) \times 10^{13} \text{ cm}^{-3}$  density range, amplitude and period of the sawteeth increase at low RF power (Fig. 3). As the RF power is raised, the sawteeth disappear for some time and may start again. The sawtooth structure becomes more complicated. For sufficiently high power, complete stabilization is achieved from the beginning of the RF pulse. On the central chord, the X-ray level goes to a maximum within 8 to 15 ms, after which the emission is redistributed to the external parts of the plasma. This results in a highly peaked emission for the first 10 ms, which relaxes to a profile much broader than the Ohmic one (Fig. 4). The broadening of the SXR emission seems to be triggered by an  $m = 1$  mode, which is detected slightly before the maximum at the centre and may last for the rest of the RF pulse.

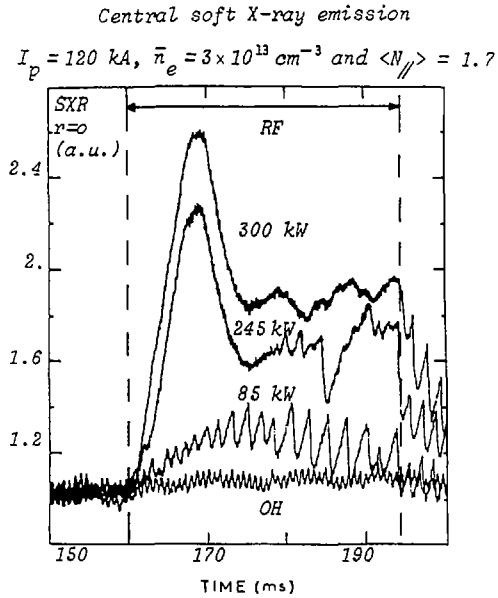


FIG. 3. Soft X-ray signal on central chord at three different powers compared to Ohmic case. Noise on two highest power traces is  $m = 1$  MHD oscillation.

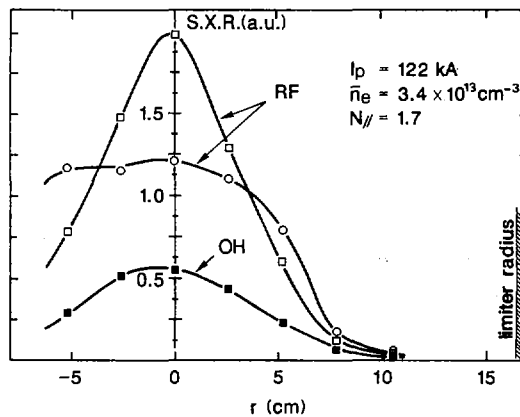


FIG. 4. Soft X-ray emission profile for  $\bar{n}_e = 3.2 \times 10^{13} \text{ cm}^{-3}$ . Before RF pulse (solid circles), 10 ms (circles) and 25 ms (squares) after beginning of RF pulse.

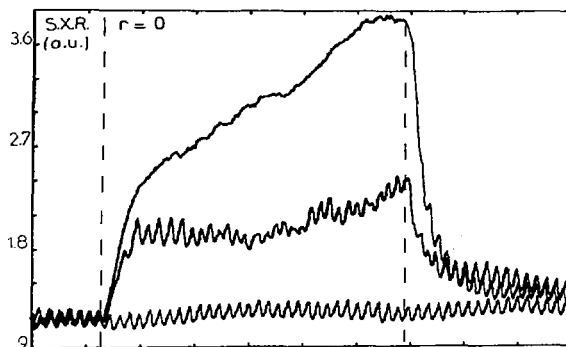


FIG. 5. Soft X-ray signal as a function of time for  $n_e = 6 \times 10^{13} \text{ cm}^{-3}$ . Bottom to top: Ohmic discharge, 150 kW RF discharge, 240 kW RF discharge. Time-scale is 8 ms/div.

The inversion radius of the sawtooth discharges has been determined for different RF powers. Up to the power threshold for stabilization, this radius remains roughly constant and close to its value for the Ohmic case, although amplitude and period of the sawteeth have been increased by a large factor.

These two facts — constancy of inversion radius and presence of  $m = 1$  oscillations — lead to the conclusion that sawteeth can be inhibited with central  $q$ -value smaller than one. Alfvén wave measurements [12] indicate, on the other hand, a decrease in the internal inductance but their interpretation is not yet clear.

- (3) At higher densities,  $n_e = (4.5\text{--}6.5) \times 10^{13} \text{ cm}^{-3}$ , the picture is much simpler. At low RF level, the total soft X-ray emission increases without much effect on sawtooth amplitude and frequency. For sufficiently high power ( $\sim 240 \text{ kW}$ ), internal disruptions disappear completely, and the soft X-ray level may increase for the duration of the RF pulse without the large emission rearrangement observed at lower densities (Fig. 5).  $m = 1$  oscillations with low amplitude are sometimes observed. At the highest densities, the RF pulse is clearly too short for a stationary situation to be established.

All these observations refer to the case of  $N_{||} = 1.7$ . It is to be noted that sawteeth could not be suppressed at high density, with the  $N_{||} = 2.7$  spectrum, although the effects were quite similar for low powers, for the two spectra.

## 5. CONCLUSIONS

Current drive effects were observed up to  $8 \times 10^{13} \text{ cm}^{-3}$ . The Ohmic current replacement was limited by the high power required for high density and absorption saturation, which impairs the apparent efficiency, in the intermediate density range.

Even at the highest densities, temperature relaxation is suppressed with moderate power levels, compared to what would be required for complete replacement of the inductive drive ( $\Delta V/V \sim 25\%$ ).

The power requirements could be further reduced by using the accessibility properties of the lower hybrid waves to deliberately generate an off-axis current [11]. Experiments along this line in Petula were difficult to interpret. Even at the highest densities, the efficiency of waves with fast phase velocities,  $N_{\parallel} = 1.7$ , remains high although accessibility would localize these waves in the plasma periphery. Moreover, the presence of  $m = 1$  oscillations, already observed on PLT [5], indicates that sawtooth stabilization mechanisms more complex than the simple decrease in central current density have to be considered.

### ACKNOWLEDGEMENTS

The authors wish to thank Mr. Agarici and Mr. Panzarella for their technical support and the RF team for the design and operation of the RF system.

### REFERENCES

- [1] LALLIA, P.P., JET TEAM, *Plasma Phys. Controll. Fusion* **28** (1986) 1211.
- [2] VAN HOUTTE, D., et al., *Nucl. Fusion* **24** (1984) 1485.
- [3] PORKOLAB, M., et al., in *Controlled Fusion and Plasma Heating* (Proc. 13th Europ. Conf. Schliersee, 1986), Vol. 2, European Physical Society (1986) 445.
- [4] SÖLDNER, F.X., et al., *Phys. Rev. Lett.* **57** (1986) 1137.
- [5] HOSEA, J., et al., *Plasma Phys. Controll. Fusion* **28** (1986) 1241.
- [6] REY, G., et al., in *Controlled Fusion and Plasma Heating* (Proc. 13th Europ. Conf. Schliersee, 1986), Vol. 2, European Physical Society (1986) 339.
- [7] WEGROWE, J.G., TONON, G., *Non-Inductive Current Drive in Tokamaks* (Proc. IAEA Techn. Comm. Meeting Culham, 1983), Vol. 2, Culham Laboratory, Abingdon (1983) 343.
- [8] FISCH, N.J., *Phys. Fluids* **28** (1985) 245.
- [9] RAX, J.M., *Saturation Induction and Radiation in Wave-Driven Plasmas*, Rep. EUR-CEA-FC-1298, Association Euratom-CEA sur la fusion, Centre d'études nucléaires de Cadarache, Saint-Paul-lez-Durance (1986).
- [10] GIRARD, A., et al., in *Controlled Fusion and Plasma Heating* (Proc. 13th Europ. Conf. Schliersee, 1986), Vol. 2, European Physical Society (1986) 374.
- [11] BRIFFOD, G., et al., *ibid.*, p. 453.
- [12] COLLINS, G.A., et al., submitted to *Plasma Phys. Controll. Fusion*.

### DISCUSSION

F.X. SÖLDNER: In your sawtooth stabilization results you report that for some cases there is a continuous increase in the intensity of the soft X-ray emission after suppression of the sawteeth. You attribute this to the occurrence of one giant sawtooth. Could it not be just a continuous acceleration of the fast electrons generated by your low  $N_{\parallel}$  spectrum in the DC electric field?

F. PARLANGE: The giant sawtooth was mentioned only to stress the fact that we do not have a stationary situation and that the X-ray level could not go on increasing for ever if the RF pulse was longer. As far as the continuous acceleration of fast electrons is concerned, it should be noted that this occurs only at high density ( $6 \times 10^{19} \text{ m}^{-3}$ ) and not at lower densities ( $< 4 \times 10^{19} \text{ m}^{-3}$ ), and that the hard X-ray signal is quite flat.

K. McGUIRE: Do you observe improved confinement time or increased stored energy when you stabilize the sawtooth oscillation?

F. PARLANGE: Neither electron cyclotron emission nor X-rays can be used to measure the electron temperature profile during current drive because of the presence of the energetic tail. Furthermore, Thomson scattering was not reliable during the 3.7 GHz campaign, so that we have no possibility to measure the stored energy.

## EXPERIMENTS ON CURRENT DRIVE AND PLASMA HEATING BY LH AND EC WAVES IN THE T-7 TOKAMAK

V.V. ALIKAEV, A.A. BORSHCHEGOVSKIJ,  
V.V. CHIST'AKOV, Yu.A. GORELOV, V.I. IL'IN,  
D.P. IVANOV, N.V. IVANOV, A.M. KAKURIN,  
P.P. KHVOSTENKO, A.Ya. KISLOV, V.A. KOCHIN,  
P.E. KOVROV, K.I. LIKIN, Yu.S. MAKSIMOV,  
I.B. SEMENOV, A.F. SHIGAEV, Yu.A. SOKOLOV,  
N.L. VASIN, V.V. VOLKOV  
I.V. Kurchatov Institute of Atomic Energy,  
Moscow, Union of Soviet Socialist Republics

J. ĎATLOV, V. KOPECKÝ, L. KRYŠKA  
Institute of Plasma Physics,  
Czechoslovak Academy of Sciences,  
Prague, Czechoslovakia

*Presented by F. Záček*

### Abstract

#### EXPERIMENTS ON CURRENT DRIVE AND PLASMA HEATING BY LH AND EC WAVES IN THE T-7 TOKAMAK.

A microwave set in the ECR range, including two gyrotrons with  $\lambda = 4.8$  mm and a total power of about 400 kW, was added to the lower hybrid set (600 kW,  $f = 900$  MHz), for further development of current drive experiments in T-7. Experimental results on the application of LH and EC power are presented in this paper. The initial stage, where gas breakdown was performed by an EC wave, was followed by LH current ramp-up. In the experiments on LH current sustainment, attention was paid to the dependence of current drive efficiency on electron temperature and to a study of the plasma power characteristics. Application of ECRH allowed a rise of the electron temperature from 1 to 4 keV, at plasma densities within a range of  $n_e = (5-7) \times 10^{12} \text{ cm}^{-3}$ . In this case, a rise in the current drive efficiency was observed. The LH current drive was accompanied by substantial electron heating. The electron energy confinement time for the LH and EC heating techniques is well described by an 'Ohmic' scaling law.

## 1. INTRODUCTION

In further developing the LHCD experiments in the T-7 tokamak [1, 2], grill waveguide conditioning by glow discharge was used which enabled us to raise the LH power launched. In addition to the LH system, the tokamak was supplied with an EC system including two gyrotron generators operating at  $f = 63$  GHz. The output power of each gyrotron is 200 kW for a pulse duration of 100 ms. 90% of the gyrotron power is radiated as an electromagnetic wave with a polarization corresponding to the ordinary wave in the plasma. The power from the gyrotrons is launched into the tokamak chamber along oversized cylindrical waveguides, 80 mm in diameter, through a horizontal port. A mode converter, which converts the incident radiation with ordinary polarization into a radiation with a polarization corresponding to the extraordinary wave, is installed at the chamber wall opposite to the waveguides. The reflected radiation mainly propagates at an angle  $80^\circ$  to the toroidal magnetic field.

The main parameters of the T-7 tokamak are: the major and minor chamber radii are 122 and 35 cm. The main ring-like limiter has a radius of 31.5 cm, the rail limiter is located at the bottom part of the chamber at a distance of  $a = 25$ –31.5 cm from the chamber axis. The toroidal magnetic field in most cases was  $B_T = 2.3$  T, the discharge current was  $I \leq 200$  kA in deuterium. The magnitude of the longitudinal moderation of the LH wave related to the spectral power distribution maximum at the grill mouth for a relative phase shift of  $90^\circ$  corresponded to  $N_{\parallel} \approx 3$ .

The set of diagnostics enabled us to record the plasma parameters including the diamagnetic flux, the electron density along six chords, and the X-ray spectra in the energy range of 2–150 keV (with two germanium detectors). One detector was located in the horizontal port and the other in the vertical port. The line of sight of each detector could be scanned so that the spatial X-ray spectra distributions could be determined. The radiation losses were recorded by a wide angle pyroelectric detector. The impurity spectral line intensities were recorded by optical instruments in the visible area of the spectrum. The ion temperature at the plasma column axis was recorded by a five channel charge exchange neutral spectrum analyser.

## 2. NON-INDUCTIVE DISCHARGE STARTUP

Experiments, in which gas breakdown, ramp-up and sustainment of the toroidal current were performed by RF methods only, were recently carried out in some tokamaks [3, 4]. Using these techniques, one can expect startup and continuous plasma sustainment in tokamaks without inductors or, at least, substantial savings in the inductor magnetic flux.

Only ECR power — 360 kW — was launched into the tokamak at the first stage of the gas breakdown experiments. A toroidal field of 2.3 T, corresponding to the ECR zone position near the tokamak chamber axis, was used. The primary winding of the tokamak was short circuited; deuterium was the working gas.

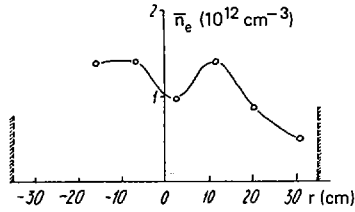


FIG. 1. Spatial distributions of average (over vertical chords) plasma density.

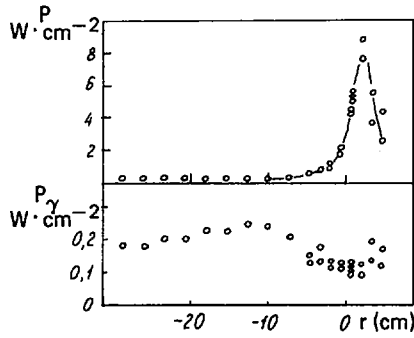


FIG. 2. Signals of pyroelectric detectors versus position of ECR point.

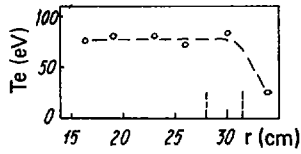


FIG. 3. Spatial distribution of electron temperature.

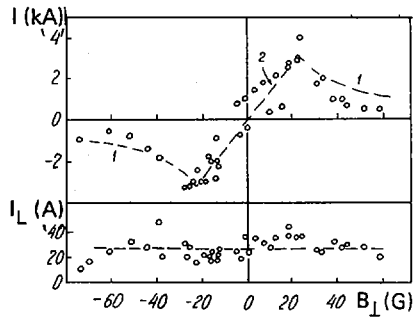


FIG. 4. Toroidal and limiter currents versus  $B_{\perp}$ .

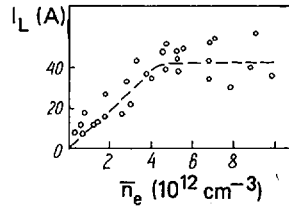


FIG. 5. Rail limiter current versus plasma density.

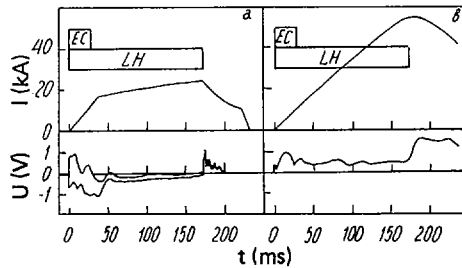


FIG. 6. Oscillograms of toroidal current and loop voltage.

Effective gas ionization occurred under ECR power injection into the tokamak chamber. An almost unchanged plasma density, depending on the initial neutral gas pressure, prevailed up to the end of the microwave pulse, after a 10–15 ms transient process. A typical spatial plasma density distribution at a pressure of  $3 \times 10^{-5}$  torr is shown in Fig. 1. At pressures  $\geq 10^{-4}$  torr, gas ionization occurred non-simultaneously in different chamber regions; signals from the interferometer channels located at  $r = -15.5$  cm and at  $r = -6.5$  cm increased with  $\approx 5$  ms delay in comparison with the signals from the other channels.

The signals from two wide angle pyroelectric detectors placed in the upper diagnostic port versus the toroidal field (and hence the ECR zone position) are represented in Fig. 2. The first detector  $r = 0$  recorded the energy losses,  $P$ , from the plasma by radiation and charged particles, the second detector ( $r = -10$  cm) measured the losses by radiation only,  $P_\gamma$ . The direction of the magnetic field corresponded to the upward direction of electron toroidal drift. The electron temperature as measured by a double Langmuir probe was 70–80 eV (Fig. 3).

A toroidal current depending on the vertical magnetic field  $B_\perp$  (Fig. 4) was generated when the ECR power was injected in case the tokamak primary winding was short circuited. In magnitude and direction, this current coincided with the current which should be driven as a result of electron accumulation on top due to toroidal drift and their drain-off along the inclined magnetic field lines:

$I = a^2 n_e v_d B_T / B_\perp$  (lines 1 in Fig. 4). For low  $B_\perp$ , the driven current should be limited at a level where the field produced by this current reaches a value  $\approx B_\perp$ :  $I = acB_\perp/2$ , which is observed in the experiment (line 2 in Fig. 4). The current  $I_L$  passing between rail limiter and chamber wall is shown in the same figure. The direction of this current corresponds to the toroidal drift direction of charged particles, and its value depends on the plasma density, as is shown in Fig. 5.

The breakdown was followed by a stage of toroidal plasma current ramp-up by the lower hybrid wave. ECR and LH systems were switched on simultaneously in this experiment. The ECR system was under operation for 30 ms, and the LH system for 150 to 200 ms, at a power of 300 kW.

If the primary tokamak winding was short circuited, the current rose up to 15–20 kA in 30–40 ms, after which the current rise was decelerated substantially (Fig. 6(a)). The current trace virtually did not depend on the duration of ECR system operation. Probably, ramp-up deterioration was caused by the self-inductive electric counter field in the plasma which affects hot electrons with energies of  $mc^2/2N_H^2$ . The time of their appearance must be of the order of magnitude of the Coulomb collision time for the electrons of such energies, i.e.  $\tau \approx 40$  ms.

Changing the sign of the loop voltage to positive ( $U \approx 0.5$  V) by means of primary tokamak winding current control made it possible to retain the high rate of the plasma current ramp-up during the entire time of LH system operation (Fig. 6(b)).

### 3. TEMPERATURE DEPENDENCE OF LOWER HYBRID CURRENT DRIVE EFFICIENCY

The question of the dependence of LHCD efficiency on the plasma electron temperature seems to be very important for a better understanding of the LHCD phenomenon as well as from the point of view of application of LHCD to a tokamak reactor. The efficiencies obtained in experiments carried out so far (see, e.g. [1, 2, 5, 6]) are not sufficiently high for a reactor, and previous theoretical considerations [7] of the current drive mechanism do not predict any change in efficiency when we go over from temperature values of  $T_e \approx 1$  keV that are typical of present experiments to reactor scale values of  $T_e \approx 10$  keV. However, an analysis of the experimental data suggests that these considerations are not quite accurate and that the current drive efficiency should depend on the electron temperature in the conditions of a real experiment.

In fact, it was shown in Refs [2, 8] that, in contrast to Ref. [7], the lower velocity limit,  $V_1$ , of the quasi-linear plateau on the electron distribution function does not coincide with the short wavelength boundary of the spectrum of the LH waves launched into the plasma from an external source. The probable reason is the development, in the plasma, of some mechanism of LH wave spectrum broadening towards parallel phase velocity reduction. This broadening continues until a balance

is reached between the input RF power transferred to the resonant electrons and their power lost by Coulomb collisions. In the case where the whole current is driven by LH waves, the value of  $V_1$  can be found from the known current density which approximately corresponds to the condition  $q(0) = 1$ , from the equation

$$j = \frac{en_e}{\sqrt{\pi} V_{Te}} \frac{V_2^2 - V_1^2}{2} e^{-V_1^2/V_{Te}^2} = \frac{cB}{2 \pi R} \quad (1)$$

Here,  $n_e$  is the electron density,  $V_{Te}$  is the electron thermal velocity, and  $V_1$  and  $V_2$  are the limits of the quasi-linear plateau on the electron distribution function. For ordinary experimental conditions, Eq. (1) yields the approximate solution  $V_1 \approx 2V_{Te}$ , which is only weakly dependent on the other plasma parameters. As a result, an electron temperature dependence appears in the expression for the current drive efficiency:

$$\eta = \frac{Z_{eff} + 5}{6} \frac{\bar{n}_e I_{LH} R}{P + I_{LH} U} = \frac{m}{18 \pi^2 e^3 L} \frac{V_2^2 - V_1^2}{\ln(V_2/V_1)} \quad (2)$$

where  $U$  is the loop voltage,  $I_{LH} = I \Delta U / U_0$  the driven current,  $P_{LH}$  the LH power, and  $L$  is the Coulomb logarithm. In formula (4), the driven current is assumed to flow near the plasma column axis, where the plasma density  $n_e \approx 1.5 \bar{n}_e$ .

To verify experimentally the dependence of the efficiency  $\eta$  on the electron temperature we compare results obtained in three tokamak operation regimes. In the first regime (toroidal field  $B_T = 19$  kG, plasma current  $I = 110$  kA, effective charge  $Z_{eff} = 2.5$ , and LH power  $P_{LH} = 40$  kW), the electron temperature was  $T_e = 0.8$  keV. The temperature increased up to  $T_e = 2.3$  keV in the second regime ( $B_T = 23$  kG,  $I = 180$  kA,  $Z_{eff} = 2.5$ ,  $P_{LH} = 180$  kW) and reached a value of 3.5 keV in the third regime ( $B_T = 23$  kG,  $I = 180$  kA,  $Z_{eff} = 5$ ,  $P_{LH} = 180$  kW), which differed from the other regimes in that ECRH was applied. The plasma density in all three regimes was  $\bar{n}_e = (3-7) \times 10^{12} \text{ cm}^{-3}$ . The electron temperature and the effective plasma charge were determined from the results of X-ray spectroscopy measurements in the energy range of 3–10 keV.

The results of measurements of current drive efficiency in the above regimes are given in Fig. 7. The power input into the wave propagating parallel to the current forming electron flux was used as  $P_{LH}$  in determining the efficiency. According to calculations, this power amounted to  $\approx 70\%$  of the total LH power input into the plasma, in our case. The result of calculating the dependence of efficiency on temperature, by formula (4), is also shown in Fig. 7 by the dashed curve. A characteristic phase velocity of the launched LH wave of  $V_2 = 10^{10} \text{ cm} \cdot \text{s}^{-1}$  was chosen in these calculations. It will be seen from Fig. 7 that in the temperature range investigated the efficiency tends to rise with  $T_e$ . This increase agrees, within experimental accuracy, with the result of calculation by formula (4).

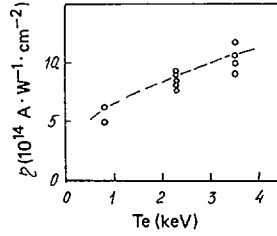


FIG. 7. Dependence of LHCD efficiency on electron temperature. Result from calculation by formula (4) is shown by dashed line.

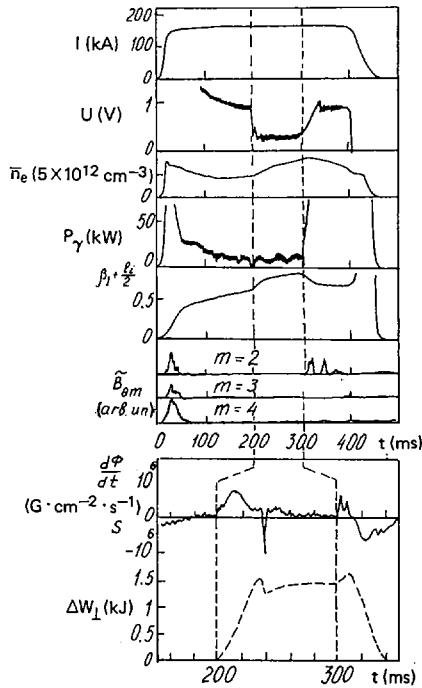


FIG. 8. Oscillograms of main discharge parameters under LHCD. LH pulse duration is shown by dashed lines.

#### 4. LH AND EC HEATING

Here, we consider the energy balance of a plasma when LHCD is applied to a discharge that was formed by the ordinary OH method. Typical oscillograms of the integral discharge parameters are shown in Fig. 8. A fast drop in the loop voltage was observed upon LH power launching. This voltage drop was followed by a

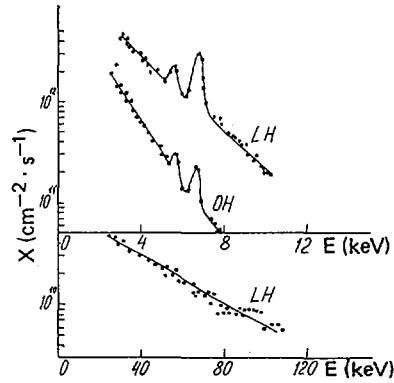


FIG. 9. X-ray spectra in Ohmic regime and during LH pulse.

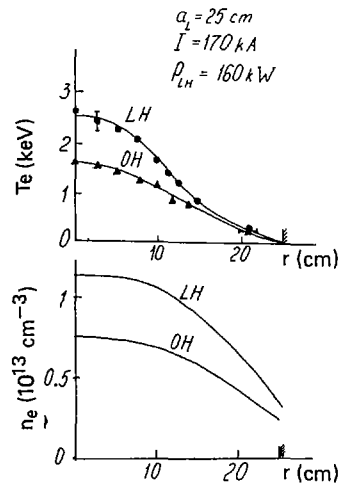


FIG. 10. Spatial distributions of electron temperature and density in Ohmic regime and during LH pulse.

transient process lasting  $\approx 30$  ms, and then the loop voltage was established at a quasi-stationary, almost constant level. This level was 0–0.3 V, depending on the discharge parameters  $\bar{n}_e$ ,  $I$  and on the launched LH power. The loop voltage in the Ohmic discharge stage was  $U \approx 0.8$  V in these experiments.

Regimes with a discharge current of  $I = 170$  kA were studied in detail. The typical X-ray spectra recorded in the Ohmic discharge and during the LH pulse are shown in Fig. 9, where we see that, during the LH pulse, besides the appearance of X-ray radiation within the energy range of 20–150 keV, the slope of this spectrum

from 2 to 10 keV is changed substantially. The radial electron temperature distributions, obtained from the X-ray spectra, and  $n_e(r)$  before the LH power launch and 50 ms after its triggering, are shown in Fig. 10. We see that a rise in the electron temperature takes place upon LH power deposition ( $\Delta T_e = 1$  keV in the central part of the plasma column),  $n_e$  rises by 30–40% and reaches  $10^{13}$  cm $^{-3}$  at the plasma column axis. The obtained distributions  $n_e(r)$  and  $T_e(r)$  show a considerable rise, by a factor of about two, in the thermal electron energy. This result is confirmed by diamagnetic measurements (Fig. 8).

Measurements with pyroelectric detectors showed that the radiation losses remained virtually unchanged during the LH pulse and were equal to 10% of the OH power deposition. No changes were obtained in the charge exchange neutral spectra in this case, the ion temperature being  $T_i(0) = 250$  eV at the plasma column axis.

Thus, in the regimes under study, electron heating was observed besides the current drive. Let us find the LH power absorbed in the plasma,  $P_{LH}$ , and the electron energy confinement time,  $\tau_{Ee}^{LH}$ .  $P_{LH}$  can be calculated from the equation for the change in the plasma column energy:

$$\frac{dW_{LH}}{dt} - \frac{dW_{OH}}{dt} = P_{LH} + \Delta UI \quad (3)$$

Here,  $dW_{OH}/dt$  and  $dW_{LH}/dt$  are the time derivatives of the plasma total energy in the OH regime and just after the LH system triggering, obtained from a combined consideration of the diamagnetic signal and the plasma equilibrium signals.  $\Delta U$  is the change in loop voltage. The electron energy confinement time during the LH pulse is found from the equation describing the power balance for the quasi-stationary state:

$$\frac{W_T^{LH}}{\tau_{Ee}^{LH}} = P_{LH} + U_{LH}I \quad (4)$$

where  $W_T^{LH}$  is the electron thermal energy obtained by integrating the  $n_e(r)$  and  $T_e(r)$  distributions (Fig. 10). We note that the energy transfer from electrons to ions in (6) is neglected. The results of calculations of  $P_{LH}$ ,  $W_T^{LH}$  and  $\tau_{Ee}^{LH}$ , together with the corresponding parameters in the Ohmic regime, are given in Table I. An evaluation of the parameters of the electron beam produced by LH waves yields 0.8 kJ and 0.2–0.3 kJ for the longitudinal and transverse beam energies and 90 kA for the current transported by the electron beam.

The ECRH technique was studied in the next portion of this run. The experiments were done with discharge parameters close to those in which the LH current drive was conducted. This enabled us to compare the efficiencies of the two heating techniques.

The oscillograms of the integral discharge parameters shown in Fig. 11 show that the loop voltage drops,  $(\beta_1 + \ell/2)$  rises and  $\bar{n}_e$  increases after the gyrotrons are

TABLE I. LH EXPERIMENT

	I (kA)	$\bar{n}_e$ ( $10^{12} \text{ cm}^{-3}$ )	$P_{OH} = UI$ (kW)	$P_{LH}$ (kW)	$W_T$ (kJ)	$\tau_{Ee}$ (ms)
OH	170	4.6	140	—	1.3	9
LH	17	6.6	40	160	2.5	12

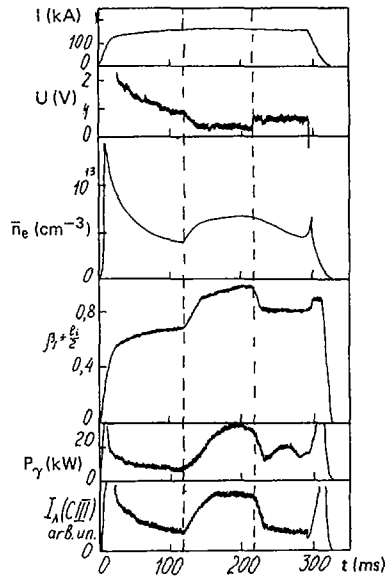


FIG. 11. Oscillograms of main discharge parameters under ECRH. ECRH pulse duration is shown by dashed lines.

switched on. The power losses recorded by the pyroelectric detector and the carbon line intensities rise, in this case. A comparison of the X-ray spectra obtained for the Ohmic discharge and during the ECR pulse shows that the electron temperature rises from 1.5 keV to 4 keV and the effective charge rises from  $Z_{eff} = 1.3$  to  $Z_{eff} = 3$ . The  $T_e(r)$  distributions obtained from the X-ray spectra and  $n_e(r)$  are shown in Fig. 12. The power absorbed in the plasma,  $P_{ECR}$ , and the energy confinement time of the electrons,  $\tau_{Ee}^{ECR}$ , were found to characterize this heating. According to Fig. 11, a substantial rise in  $(\beta_1 + l/2)$  takes place during ECRH. As the calculations based on  $T_e(r)$  and  $Z_{eff}(r)$ , assuming Spitzer conductivity with neoclassical corrections, have shown, the current density profile does not change when the ECR

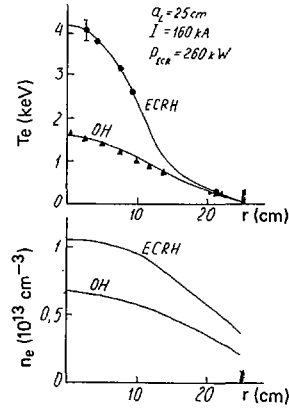


FIG. 12. Spatial distributions of electron temperature and density in Ohmic regime and during ECRH pulse.

TABLE II. ECR EXPERIMENT

	I (kA)	$\bar{n}_e$ ( $10^{12} \text{ cm}^{-3}$ )	$P_{\text{OH}} = UI$ (kW)	$P_{\text{ECR}}$ (kW)	$W_T$ (kJ)	$\tau_{\text{Ee}}$ (ms)	$\tau_{\text{Ee}}^{\text{MM}}$ (ms)
OH	160	4	135	—	1.1	8	7
ECR	160	6	50	260	3.4	11	12

power is launched; hence, the change in internal inductance  $\Delta \ell = 0$ . In this condition the time derivative  $(d/dt)(\beta_1 + \ell/2)$  immediately after switching the ECR power on yields the power absorbed in the plasma,  $P_{\text{ECR}}$ . The increase in thermal energy in the electrons 50 ms after switching ECRH on is 2.3 kJ. The energy content is found from an integration of  $n_e(r)$  and  $T_e(r)$  (Fig. 12).

The electron energy confinement time under ECRH is found for the quasi-stationary state from the energy content  $W_T^{\text{ECR}}$  and  $P_{\text{ECR}}$ :

$$\tau_{\text{Ee}}^{\text{ECR}} = \frac{W_T^{\text{ECR}}}{P_{\text{ECR}} + U_{\text{ECR}} I} \quad (5)$$

where  $U_{\text{ECR}}$  is the loop voltage during the ECR pulse. The values of  $W_T^{\text{ECR}}$ ,  $P_{\text{ECR}}$  and  $\tau_{\text{Ee}}^{\text{ECR}}$  are shown in Table II. In the table we see that  $\tau_{\text{Ee}}^{\text{ECR}} > \tau_{\text{Ee}}^{\text{OH}}$ . This is partly due to the increase in electron density during ECRH. The plasma parameters  $U$ ,  $\bar{n}_e$ ,  $\beta_1$

and  $\tau_{Ec}$  obtained from a numerical simulation are in good agreement with the experimental data. The calculations were based on the T-11 transport coefficients [9]; the difference between the OH and ECRH power deposition profiles was taken into account.

Thus, comparing LH and ECRH results, we note that the power absorption coefficients for LH and EC power are approximately the same and equal to 0.7–0.8. A rise in the electron energy confinement time is observed under LHCD and ECRH which is due to the increase in  $\bar{n}_e$ . The values of  $\tau_{Ec}^{LH}$  and  $\tau_{Ec}^{ECR}$  are close to the Ohmic value  $\tau_{Ec}^{MM}$ , in this case.

## REFERENCES

- [1] ALIKAEV, V.V., et al., in *Plasma Physics and Controlled Nuclear Fusion Research 1982 (Proc. 9th Int. Conf. Baltimore, 1982)*, Vol. 1, IAEA, Vienna (1983) 227.
- [2] ALIKAEV, V.V., et al., *Fiz. Plazmy* **11** (1985) 53 (in Russian).
- [3] TANAKA, S., et al., in *Plasma Physics and Controlled Nuclear Fusion Research 1984 (Proc. 10th Int. Conf. London, 1984)*, Vol. 1, IAEA, Vienna (1985) 623.
- [4] TOI, K., et al., *Phys. Rev. Lett.* **52** (1984) 2144.
- [5] LLOYD, B., et al., in *Non-Inductive Current Drive (Proc. IAEA Tech. Comm. Mtg Culham, 1983)*, Vol. 1, UKAEA, Culham Laboratory, Abingdon (1983) 250.
- [6] MOTLEY, R., et al., *ibid.*, Vol. 2, p. 299.
- [7] FISCH, N.J., *Phys. Rev. Lett.* **41** (1978) 873.
- [8] IVANOV, N.V., *Vopr. Atomn. Nauki Tekh., Ser. Termoyadernyj Sintez* **3** (1985) 22 (in Russian).
- [9] MEREZHKIN, V.G., MUKHOVATOV, V.S., *Pis'ma Zh. Ehksp. Teor. Fiz.* **33** (1981) 463 (in Russian).

## ELECTRON CYCLOTRON HEATING OF LOWER HYBRID CURRENT DRIVEN PLASMA IN THE JFT-2M TOKAMAK

T. YAMAMOTO, A. FUNAHASHI, K. HOSHINO, S. KASAI,  
T. KAWAKAMI, H. KAWASHIMA, T. MATOBA, T. MATSUDA,  
H. MATSUMOTO, Y. MIURA, M. MORI, K. ODAJIMA,  
H. OGAWA, T. OGAWA, H. OHTSUKA, S. SENGOKU,  
T. SHOJI, N. SUZUKI, H. TAMAI, Y. UESUGI, T. YAMAUCHI,  
M. HASEGAWA<sup>1</sup>, S. TAKADA<sup>2</sup>, K. HASEGAWA, A. HONDA,  
I. ISHIBORI, T. KASHIMURA, Y. KASHIWA, M. KAZAWA,  
K. KIKUCHI, Y. MATSUZAKI, K. OHUCHI, H. OKANO,  
T. SHIBATA, T. SHIBUYA, T. SHIINA, K. SUZUKI, T. TANI,  
K. YOKOYAMA

Naka Fusion Energy Research Establishment,  
Department of Thermonuclear Fusion Research,  
Japan Atomic Energy Research Institute,  
Tokai-mura, Naka-gun, Ibaraki-ken, Japan

### Abstract

ELECTRON CYCLOTRON HEATING OF LOWER HYBRID CURRENT DRIVEN PLASMA IN THE JFT-2M TOKAMAK.

The second harmonic electron cyclotron heating of a lower hybrid current driven plasma has been investigated in the JFT-2M tokamak to evaluate its potential for optimizing RF current drive. It is observed that the extraordinary mode effectively couples to electrons at largely down shifted frequencies. From measuring the soft X-ray radiation parallel and perpendicular to the toroidal magnetic field, the existence of selective perpendicular heating of electrons with parallel velocities satisfying the relativistic cyclotron resonance condition is concluded. Initial results on 200 MHz fast wave experiments are also reported. It is observed that, in a discharge combined with electron cyclotron heating, the fast waves launched by a phased two loop antenna array couple to energetic electrons.

### 1. INTRODUCTION

Current drive by lower hybrid (LH) waves has been achieved in a number of tokamaks. These experiments have shown that the LH waves produce a current carrying fast electron tail. Recently, electron cyclotron heating (ECH) in the presence of a mildly relativistic electron tail has received a lot of interest, because of the need for supplementary heating and current profile control in high phase velocity RF current driven plasmas and because of possible improvements, using ECH, of the current drive by LH waves (LHCD) and electron cyclotron (EC) waves [1, 2].

<sup>1</sup> On leave from Mitsubishi Electric Corp., Japan.

<sup>2</sup> On leave from Mitsubishi Electric Computer System Corp., Tokyo, Japan.

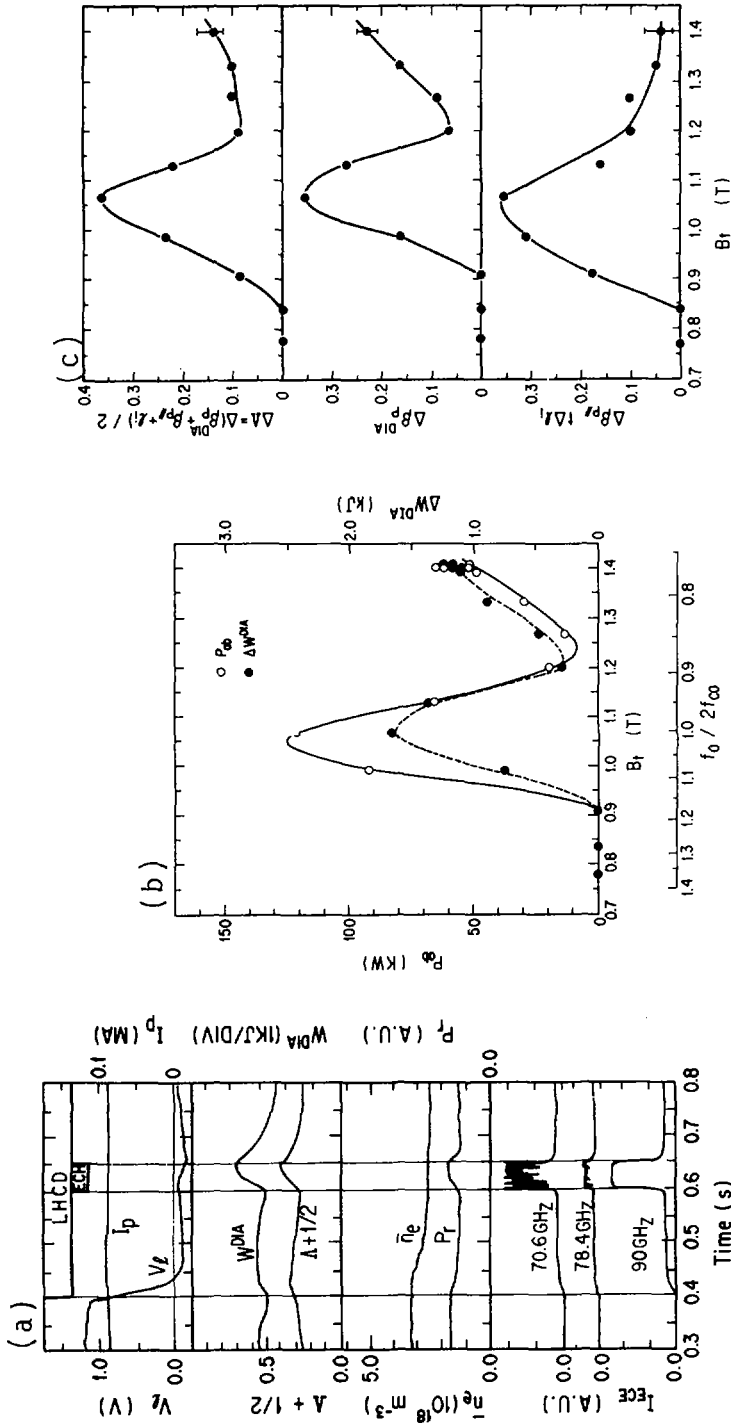


FIG. 1. (a) Time behaviour of plasma parameters at  $B_1 = 1.4$  T for ECH and LHCD combination discharge.  $P_{ECH} = 240$  kW,  $P_{LH} = 140$  kW.  $B_1$  dependence of (b)  $P_{ab}$  and  $\Delta W_{DIA}$ , (c)  $\Delta\beta_p$ ,  $\Delta\beta_p^{DIA}$ , and  $\Delta\beta_p^{DIA} + \Delta\beta_p$ .

On the other hand, in a high temperature and density fusion plasma, LH waves can only drive a skin current since for a plasma with large  $f_{pe}^2/f_{ce}^2$  the lower bound of the allowed parallel refractive index  $N_{\parallel}$  is restricted to relatively high values and the wave power is then absorbed near the plasma surface. Fast waves (FW) in the frequency range of  $f_{ci} < f_0 < f_{LH}(0)$  ( $f_{LH}(0)$  is the maximum LH resonance frequency in the plasma) can, however, penetrate into the plasma core, even if the plasma is hot and dense. The current drive by fast waves (FWCD) is based on the same mechanism as LHCD, i.e. the current carrying electrons are accelerated through Landau damping; this mechanism is expected to be applicable to fusion plasmas.

## 2. EXPERIMENTAL SET-UP

The JFT-2M tokamak has a D-shaped vacuum vessel with a major radius of  $R_0 = 1.31$  m and a  $0.415$  m  $\times$   $0.595$  m minor cross-section [3]. The ECH system consists of two gyrotrons and two oversized waveguide transmission lines [4]. The RF power is generated by a Varian gyrotron capable of producing 200 kW at 60 GHz for up to 0.1 s. The extraordinary mode is radiated at an injection angle of  $\theta = 80^\circ$  to the direction of the toroidal magnetic field from a conical horn antenna propagating the  $TE_{11}$  mode. The horn antennas are placed outside the torus in the midplane. The LH waves are launched by a four waveguide array, which is fed by four 0.75 GHz klystrons. The phase difference between adjacent waveguides is set at  $90^\circ$ , and thus the Brambilla RF spectrum is concentrated between  $N_{\parallel} = 1$  and 5. The fast wave system consists of a 200 MHz RF source capable of 100 kW for up to 0.1 s feeding to a phased two loop antenna array [5]. The RF power is divided into the two lines by a 3 dB hybrid coupler. The phase difference between the antennas,  $\Delta\Phi_{FW}$ , is adjusted by a line stretcher. The impedance of each line is matched by using  $\lambda/8$  double stub tuners.

## 3. EXPERIMENTAL RESULTS

### 3.1. Selective electron cyclotron heating

Experiments with a radiated ECH power of  $P_{ECH} = 240$  kW and a pulse width of  $t_d = 50$  ms have been carried out to investigate the EC wave interaction with mildly relativistic electrons [6]. Figure 1(a) shows the time evolution of the relevant plasma parameters during a typical shot with a central toroidal magnetic field at which no cyclotron resonance layer lies in the plasma column ( $B_t = 1.4$  T, corresponding to  $f_0/(2f_{c0}) = 0.76$ ). For this discharge, the target plasma has a D-shaped cross-section ( $a = 0.34$  m,  $b = 0.46$  m) and the plasma current  $I_p$  kept constant by feedback control. With application of ECH power during the LH pulse, noticeable increases in  $\Lambda = \beta_p + \ell/2 - 1$ , in the stored plasma energy,  $W^{DIA}$ , and in

the EC emissions,  $I_{\text{ECE}}$ , are observed, with no increase in the line averaged electron density  $\bar{n}_e$ , as is shown in Fig. 1. The value of  $\Lambda$  is evaluated from a poloidal magnetic field fitting code, and  $W^{\text{DIA}}$  is estimated from the diamagnetic measurement, assuming isotropic pressure of the plasma.

The  $B_t$  dependence of the change in the relevant plasma parameters is shown in Figs 1(b) and (c). Figure 1(b) shows the absorbed ECH power,  $P_{\text{ab}}$ , and the increase,  $\Delta W^{\text{DIA}}$ , due to ECH. The value of  $P_{\text{ab}}$  is estimated from  $dW^{\text{DIA}}/dt$  at the initiation of the ECH pulse. The experimental conditions are the same as in Fig. 1(a), except for the toroidal magnetic field. It is found that  $P_{\text{ab}}$  and  $\Delta W^{\text{DIA}}$  have a peak around  $B_t = 1.07$  T (corresponding to  $f_o/(2f_{c0}) = 1.0$ ) and increase with  $B_t$  for  $B_t > 1.25$  T. Figure 1(c) shows the changes in  $\Lambda$ ,  $\beta_p^{\text{DIA}}$  and  $\beta_{p\parallel} + \ell_i$  as a function of the toroidal magnetic field, where  $\beta_p^{\text{DIA}}$  is the perpendicular component estimated from the diamagnetic measurement, and  $\beta_{p\parallel} + \ell_i$  is obtained from the relation  $\Delta\Lambda = \Delta(\beta_{p\parallel} + \ell_i)/2$ . Most of  $\Delta\Lambda$  is likely to result from the enhanced  $\beta_p$ , since the change in  $\ell_i$  during the ECH pulse duration of 50 ms, which is much shorter than the current diffusion time,  $t_{\text{diff}} > 1$  s, can be neglected. For  $B_t = 1.07$  T,  $\Delta\beta_p^{\text{DIA}}$  is found to be approximately equal to  $\Delta\beta_{p\parallel}$ , while  $\Delta\beta_p^{\text{DIA}}$  is about six times as large as  $\Delta\beta_{p\parallel}$  for  $B_t = 1.4$  T. This result demonstrates selective perpendicular heating of the fast electrons for  $B_t = 1.4$  T. Therefore, taking account of anisotropic plasma pressure, we obtain  $P_{\text{ab}} = 37$  kW and a resulting absorption efficiency of  $\eta_{\text{ab}} = P_{\text{ab}}/P_{\text{ECH}} = 0.15$  at  $B_t = 1.4$  T.

Figures 2(a), (b) and (c) show the time evolution of the soft X-ray photon counts integrated over different energy ranges for three viewing angles,  $\theta_{\text{sx}} = 0^\circ$ ,  $90^\circ$  and  $180^\circ$ , respectively, at  $B_t = 1.34$  T. The X-ray radiation parallel ( $\theta_{\text{sx}} = 0^\circ$ ) and perpendicular ( $\theta_{\text{sx}} = 90^\circ$ ) to the magnetic field is measured simultaneously by two

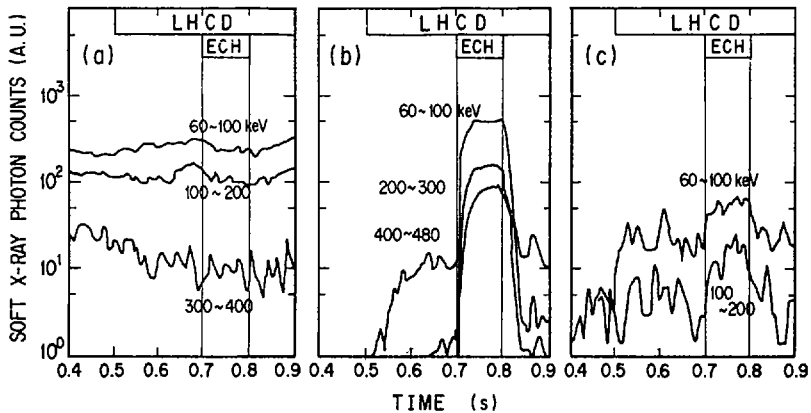


FIG. 2. Time evolution of soft X-ray photon counts integrated over different energy ranges for three different viewing angles: (a)  $\theta_{\text{sx}} = 0^\circ$ , (b)  $\theta_{\text{sx}} = 90^\circ$ , (c)  $\theta_{\text{sx}} = 180^\circ$ .  $B_t = 1.34$  T,  $I_p = 100$  kA,  $\bar{n}_e = 2 \times 10^{18} \text{ m}^{-3}$ ,  $P_{\text{LH}} = 100$  kW,  $P_{\text{ECH}} = 100$  kW.

intrinsic germanium detectors with pulse height analyser systems. The forward-backward ( $\theta_{sx} = 180^\circ$ ) radiation is also measured by changing the direction of the plasma current. It is seen that ECH produces remarkable enhancement of the perpendicular radiation, appreciable increase in the backward radiation and a little decrease in the forward radiation. This result indicates selective EC perpendicular heating of the energetic electrons but no enhanced absorption efficiency of the LH power, which is consistent with the magnetic measurement mentioned above. The noticeable increase in the photon counts in the backward radiation as well as the decrease in the low energy component in the forward radiation during the ECH pulse suggests the generation of an inverse electric field, which decelerates the current carrying electrons and produces a backward stream of fast electrons. It is noted that an additional current drive generates the inductive electric field. From the energy spectra obtained from the data shown in Figs 2(a) to (c) we can infer enhancement of the fast electrons having an energy of  $\sim 100$  keV, which satisfies the relativistic EC resonance condition at the plasma centre.

Meanwhile, the Fisch and Boozer formula [7] predicts that the selective ECH of fast electrons yields an additional current drive due to an asymmetric plasma resistivity effect with high efficiency. From the calculation under the experimental conditions as shown in Fig. 1(a) [6], 90 kA of additional driven current,  $I_{ECH}$ , concentrated around the plasma centre and 28 kW of absorbed ECH power in a single path are expected. Specifically, the current drive efficiency is  $\eta_{CD} = I_{ECH}/P_{ab} = 3.2$  ( $A \cdot W^{-1}$ ). No appreciable additional current drive has, however, been observed from the measurement of the loop voltage. The reason for this could be that the pulse width of ECH has no sufficient duration for the inductive electric field to diffuse to the plasma surface.

### 3.2. Current drive by fast waves

In this section, initial experimental results using a 200 MHz fast wave are presented. Figure 3(a) shows the time behaviour of the relevant plasma parameters for two typical discharge shots at  $n_e = 1.5 \times 10^{19} \text{ m}^{-3}$  and  $B_t = 1.32 \text{ T}$ . The solid line indicates the result of FW combined with ECH, and the dashed line represents the result of independent application of ECH and FW pulses in a shot. The radiated ECH and FW powers are  $P_{ECH} = 100 \text{ kW}$  and  $P_{FW} = 40 \text{ kW}$ , respectively. The value of  $\Delta\Phi_{FW}$  is set at  $135^\circ$ , and the RF spectrum of the fast waves is thus calculated to have a mild peak around  $N_{||} = 3$  in the direction of the current carrying electron drift. The working gas is deuterium, and the plasma current is kept constant at  $I_p = 200 \text{ kA}$ . The present plasma parameters yield 1.1–5 for the accessible  $N_{||}$  at the plasma centre and  $r/a = 0.9$  for the radial position of the LH resonance layer at 200 MHz. The combination of ECH and FW pulses is seen to make an appreciable increase in the EC emissions with frequencies of 50.4 GHz and 78.4 GHz, which correspond to  $f_r/(2f_{c0}) = 0.68$  and 1.06, respectively. Note that the emission at 50.4 GHz comes from non-thermal electrons since 50.4 GHz is not the electron

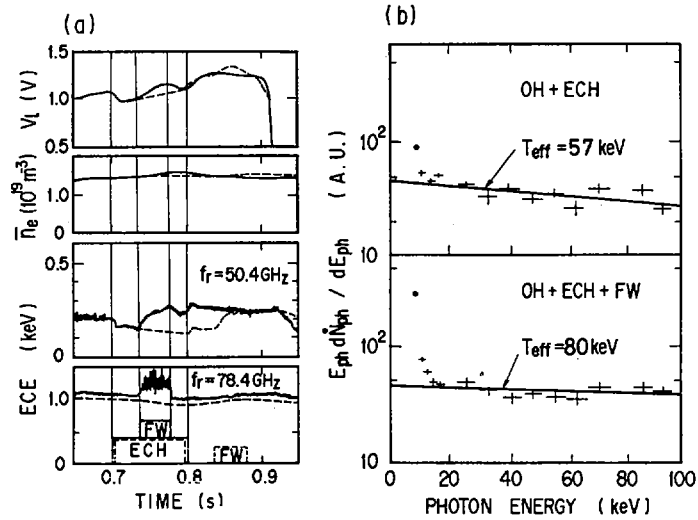


FIG. 3(a). Time evolution of relevant plasma parameters with and without (solid and dashed lines) FW power of 40 kW during ECH pulse.  $B_t = 1.32 \text{ T}$ ,  $I_p = 200 \text{ kA}$ ,  $P_{ECH} = 90 \text{ kW}$ ; (b) energy spectra of soft X-rays without and with (upper and bottom) FW power during ECH pulse. Experimental conditions are the same as in Fig. 3(a).

cyclotron frequency in the plasma. The emission in the extraordinary mode was measured in the horizontal direction with a calibrated heterodyne receiver. A little increase in the loop voltage is also seen during the FW pulse, in both shots. At the same time, an increase in the line intensity of metal impurities was observed.

We have also measured the soft X-ray radiation under the same conditions as those of Fig. 3(a). The measured energy spectra of the forward radiation with and without FW pulse during the ECH pulse are shown in Fig. 3(b). The spectrum is time averaged over the duration of the FW pulse and is superposed for two identical discharges. From this figure, we conclude that energetic electrons exist in the plasma and the application of the FW pulse leads to a noticeable increase in the electron tail in the range of 40 to 100 keV.

The observed results indicate an appreciable interaction of fast waves and energetic electrons, leading to current drive at higher density. No indication of FWCD has, however, been obtained from measuring the loop voltage. The reason for this could be that the RF power and the shape of the RF spectrum are not sufficient to overcome the increase in loop voltage due to enhanced impurity flux. From the calculation [8], a driven current less than 10 kA is predicted in the present experimental conditions assuming 1% of the fraction of the energetic electrons with a temperature of 40 keV. This would, by itself, result in a relative drop of the loop voltage of only a few per cent.

#### 4. SUMMARY

The experimental results can be summarized as follows:

- (1) An absorption efficiency of  $\eta_{ab} = 0.15$  of the ECH power is obtained at a largely down shifted cyclotron frequency of  $f_0/(2f_{c0}) = 0.76$ , when ECH is applied into an LH current driven plasma.
- (2) The measurement of the soft X-ray radiation parallel and perpendicular to the magnetic field demonstrates selective electron cyclotron perpendicular heating of the fast electrons, generated by the LH waves, with the parallel velocity satisfying the relativistic resonance condition.
- (3) It is observed from the measurements of the electron cyclotron emission and the soft X-ray radiation that the 200 MHz fast waves launched from the phased two loop antennas interact with the energetic electrons — in contrast to the LH waves, at high densities.

#### ACKNOWLEDGEMENTS

The authors are grateful to Drs M. Tanaka, K. Tomabechi, and S. Mori for continuous encouragement, and to Dr. J.-M. Noterdaeme for fruitful discussions.

#### REFERENCES

- [1] FIDONE, I., et al., in Heating in Toroidal Plasmas (Proc. 4th Int. Symp. Rome, 1984), Vol. 2, Int. School of Plasma Physics, Varenna (1984) 872.
- [2] KRIVENSKI, V., et al., Nucl. Fusion **25** (1985) 127.
- [3] SHOJI, T., et al., in Controlled Fusion and Plasma Physics (Proc. 11th Europ. Conf. Aachen, 1983), Vol. 1, European Physical Society (1983) 55.
- [4] HOSHINO, K., et al., Design Concepts and Performance Tests of the 60 GHz Electron Cyclotron Heating (ECH) System for the JFT-2M Tokamak, Rep. JAERI-M-85-169, Japan Atomic Energy Research Institute, Tokyo (1985).
- [5] UESUGI, Y., et al., Coupling to Fast Waves via a Phased Loop Antenna Array for Fast Wave Current Drive in the JFT-2M Tokamak, Rep. JAERI-M-86-103, Japan Atomic Energy Research Institute, Tokyo (1986).
- [6] YAMAMOTO, T., et al., in Controlled Fusion and Plasma Heating (Proc. 13th Europ. Conf. Schliersee, 1986), Vol. 10 C, Part II, European Physical Society (1986) 437.
- [7] FISCH, N.J., BOOZER, A.H., Phys. Rev. Lett. **45** (1980) 720.
- [8] YAMAMOTO, T., et al., Numerical Study of the Electron Heating and Current Drive by the Fast Waves, Rep. JAERI-M-86-115, Japan Atomic Energy Research Institute, Tokyo (1986).

#### DISCUSSION

M. PORKOLAB: It appears to me that in Fig. 3(a), showing combined ECH/FW pulses, the loop voltage increases when the fast wave is applied. This is

perhaps due, as you say, to impurity injection. If so, the increased DC electric field in the plasma could enhance the electron tail and hence the ECH emission, rather than the fast wave. In view of this, I am not certain that you have really demonstrated FW current drive.

T. YAMAMOTO: It can be seen in Fig. 3(a) that the ECE does not increase, even when the loop voltage increases during the ECH pulse alone. In addition, no increase in ECE accompanied by an increase in the loop voltage has been observed when the FW power is applied to the plasma with  $\bar{n} \lesssim 1 \times 10^{19} \text{ m}^{-3}$ . These results indicate that the increase in the ECE stems from FW heating and not from the increase in the loop voltage.

No FW current drive has been observed from the measurement of the loop voltage. We have observed appreciable interaction between fast waves and fast electrons, which would lead to FW current drive.

T. CHO: During ECH, it is reasonable to expect the perpendicular soft X-rays to increase, since the lobe of the X-ray inclines in the electron accelerated direction owing to the relativistic effect. However, because of this relativistic effect, the X-ray emission parallel to the magnetic field should be increased by LH current drive alone in the energy range of the quasi-linear Landau-damped resonant particles. How would you interpret the only slight change in the X-ray emission parallel to the magnetic field during slow-wave LHCD with the parallel refractive index  $N_{\parallel} = 2$ ?

T. YAMAMOTO: In the present discharge, the target plasma already includes many runaway electrons and most of the soft X-ray radiation comes from these. When LH power is applied to the plasma, the LH current drive causes a drop in the loop voltage which reduces the production rate of the runaway electrons, while the LH waves accelerate the resonant electrons. As a result, the amount of runaway electrons does not change. Thus, the LH pulse does not contribute to an appreciable enhancement of the soft X-ray radiation. In the case of a discharge which includes a few fast electrons, a remarkable increase in soft X-ray radiation has been observed.

# ELECTRON CYCLOTRON AND LOWER HYBRID CURRENT DRIVE EXPERIMENTS IN THE WT-2 AND WT-3 TOKAMAKS

S. TANAKA, Y. TERUMICHI, T. MAEKAWA,  
M. NAKAMURA<sup>1</sup>, T. CHO<sup>2</sup>, A. ANDO, K. OGURA,  
H. TANAKA, M. IIDA, S. IDE, K. OHO, S. OZAKI,  
R. ITATANI<sup>3</sup>, H. ABE<sup>3</sup>, Y. YASAKA<sup>3</sup>, M. FUKAO<sup>3</sup>,  
K. ISHII<sup>3</sup>, A. MOHRI<sup>4</sup>, S. KUBO<sup>4</sup>

Department of Physics, Faculty of Science,  
Kyoto University, Kyoto,  
Japan

## Abstract

ELECTRON CYCLOTRON AND LOWER HYBRID CURRENT DRIVE EXPERIMENTS IN THE WT-2 AND WT-3 TOKAMAKS.

An electron cyclotron (EC) driven current is generated in two types of toroidal plasmas: an ohmically heated (OH) plasma and a lower hybrid (LH) driven current sustained plasma. In the former case, by injecting microwave  $P_{EC}$  near the EC frequency into an OH plasma, after OH power has been shut off in the WT-2 tokamak, the plasma current is sustained and ramped up by the EC wave only, without OH power. Here, the EC driven current is generated by EC heating of suprathermal electron beam in the OH plasma. In the latter case, when  $P_{EC}$  is injected into the LH driven current sustained plasma, the plasma current  $I_p$  and its ramp-up rate increase, and the increased  $I_p$  is kept after  $P_{EC}$  is shut off. Here, the EC driven current is generated by EC heating of the mildly relativistic electrons in the LH driven plasma. On the other hand, the current  $I_p$  and its ramp-up rate decrease when the bulk electrons are EC heated. This selective EC heating of the bulk or the mildly relativistic electrons is performed by changing the radial position of EC resonance layer in the plasma column. Further, the electron beam (EB) is injected by using the plasma anode method. EB injection into a currentless ECR plasma forms a toroidal current, which is nine times the injected beam current.

## 1. INTRODUCTION

Recently, experiments on non-inductive current drive (CD) have shown that the plasma current is started up, ramped up and sustained by the LH wave in many tokamaks [1]. Meanwhile, other non-inductive CD methods have been suggested theoretically. Fisch et al. [2] have predicted that the plasma current can be produced by quasi-linear cyclotron damping of the EC wave. This current drive, ECCD, is achieved by creating an asymmetric electron distribution function along the field,

<sup>1</sup> Osaka Institute of Technology, Osaka, Japan.

<sup>2</sup> Plasma Research Center, University of Tsukuba, Ibaraki, Japan.

<sup>3</sup> Faculty of Engineering, Kyoto University, Kyoto, Japan.

<sup>4</sup> Institute of Plasma Physics, Nagoya University, Nagoya, Japan.

whose mechanism is quite different from LHCD. Here, we report on experiments in the WT-2 tokamak, in which the plasma is sustained by the EC driven current only, without OH power. Furthermore, the plasma current is produced by EC heating of the mildly relativistic electron beam present in the LH driven current sustained plasma. In addition, an experiment on plasma current drive by injection of an electron beam is presented.

The WT-2 tokamak has an aluminium shell and an iron core, major and minor radii of  $R_0 = 40$  and  $a = 9$  cm, respectively, a toroidal field of  $B_T \leq 15$  kG, and a plasma current of  $I_p \leq 30$  kA [3, 4]. A microwave from a gyrotron ( $\omega/2\pi = 35.6$  GHz,  $P_{EC} \leq 120$  kW, pulse width  $t \leq 10$  ms) is fed from the low field side through circular waveguides to a Vlasov antenna with parabola reflector placed along the major radius. By rotating the antenna around the guide axis, a linearly polarized electromagnetic wave (EMW), propagating parallel or antiparallel to the field  $B_T$  with an angle of  $\pm 48^\circ$  to  $B_T$ , is emitted as the extraordinary (X) mode. To achieve LHCD, RF from a magnetron (0.915 GHz,  $P_{LH} \leq 100$  kW,  $t \leq 20$  ms) is launched into the plasma with a phased array of four waveguides (inner dimension,  $13 \times 185$  mm<sup>2</sup>).

The operation of the new toroidal machine WT-3 ( $R = 65$  cm,  $a = 22$  cm and  $B_T = 1.7$  T) was started in June 1986 for a study of RF heating and current drive. The RF sources are 200 kW, 56 GHz for ECH and 350 kW, 2 GHz for LHH and 500 kW, 12–30 MHz for ICH.

## 2. ELECTRON CYCLOTRON CURRENT DRIVE AFTER OH PLASMA [5]

In Figs 1(a) to (g), the temporal evolution of plasma parameters with and without  $P_{EC}$  is plotted. First, a low density slide-away discharge (dotted curves) with bulk electron density  $\bar{n}_e \approx 2 \times 10^{12}$  cm<sup>-3</sup> and temperature  $T_e \approx 70$  eV, is produced by an OH discharge with EC resonance preionization. When  $P_{EC}$  is injected after the primary voltage  $V_1$  of OH transformer has been short-circuited, the plasma parameters change drastically, and the constant plasma current  $I_p$  continues to flow with a loop voltage of  $V_L = 0$  as long as  $P_{EC}$  is applied (full curves). The data show that the plasma is sustained by the EC driven current only since no OH current flows for  $V_L = 0$ . It is noticeable that in this ECCD plasma strong hard X-ray  $I_{HX}$  appears and both the soft X-ray  $I_{SX}$  (0.85 keV) and the second electron cyclotron emission  $I_\mu$  (68 GHz) increase to more than ten times the values in the OH plasma. The result suggests that a suprathermal electron beam carrying the EC driven current is generated. After  $P_{EC}$  has been turned off,  $V_L$  changes abruptly to a positive value, and  $I_p$  falls off in a short time. Here,  $I_{HX}$  increases strongly, suggesting that the suprathermal electrons are accelerated by the positive  $V_L$ . On the other hand, the pyroelectric signal  $I_{pyro}$  and the light intensity of impurity line  $I_L$  (O II - O V) decrease gradually, suggesting that the temperature of bulk electrons is nearly the same as that in OH plasma.

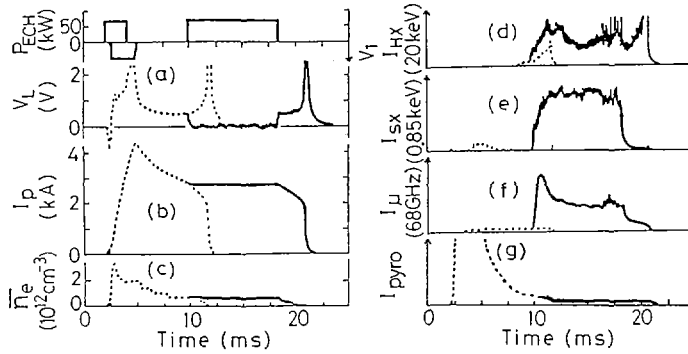


FIG. 1. Temporal evolution of (a) loop voltage  $V_L$ , (b) plasma current  $I_p$ , (c) electron density  $\bar{n}_e$ , (d) hard X-ray emission  $I_{HX}$  (20 keV), (e) soft X-ray  $I_{SX}$  (0.85 keV), (f) electron cyclotron emission  $I_\mu$  (68 GHz), and (g) pyroelectric signal  $I_{pyro}$ . Full curves are with ECH power,  $P_{EC}$  (parallel injection) and dotted curves without  $P_{EC}$ .  $p = 2 \times 10^{-5}$  torr in  $H_2$ , additional gas comes from puffing during injection of  $P_{EC}$ .  $B_T = 12$  kG.

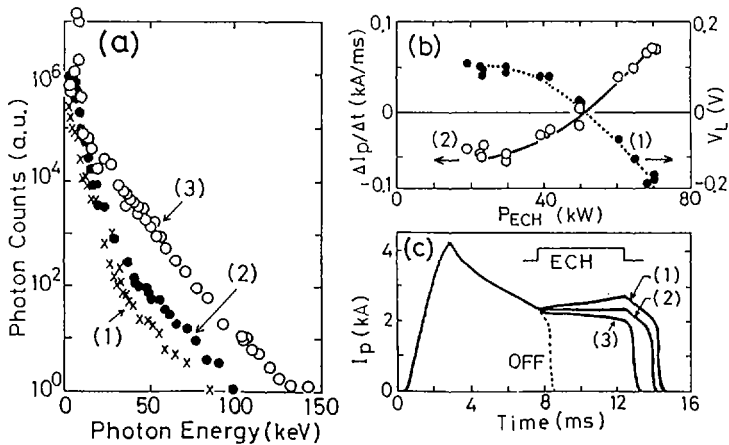


FIG. 2. (a) X-ray energy spectra emitted from plasma as shown in Fig. 1, during: (1) time  $t = 0-5$  ms (startup stage), (2)  $t = 5-10$  ms (OH stage) and (3)  $t = 10-15$  ms (ECCD stage); (b) (1) loop voltage  $V_L$  and (2) ramp-up rate as a function of  $P_{EC}$ ; (c) EC driven current ramp-up, flat-top and decrease for (1)  $P_{EC} = 70$  kW, (2) 50 kW, (3) 30 kW.

The X-ray energy spectra emitted from ECCD as well as OH plasmas are measured, and plotted in Fig. 2(a). The slope of the X-ray spectrum is about 15 keV, and the energy extends to 150 keV in the ECCD plasma. Thus, it is concluded that in the ECCD plasma the electrons are composed of bulk electrons with  $T_e \approx 70$  eV,  $\bar{n}_e \approx 0.5 \times 10^{12} \text{ cm}^{-3}$  and suprathermal electrons with  $T_e \sim 15$  keV,  $n_e \sim 10^{10} \text{ cm}^{-3}$ , which are carrying  $I_p \sim 3$  kA. In addition, the fact that SX-rays up to 100 keV are emitted from the initial OH plasma suggests that weakly suprathermal electrons are present and are necessary for the formation of ECCD plasma.

As  $P_{EC}$  increases, the current  $I_p$  due to ECCD changes from a decreasing curve to flat-top and then to ramp-up as is shown in Figs 2(b) and (c). Correspondingly, the voltage  $V_L$  changes from a positive value to a negative one. This behaviour shows that  $I_p$  is fully sustained by ECW. These flat-top discharges due to ECCD, without OH power, are also obtained in WT-3, where  $I_p = 10$  kA for  $n_e \approx 10^{12} \text{ cm}^{-3}$ ,  $B_T = 1.6$  T, and  $P_{EC} = 70$  kW.

The effect of ECH is examined for various  $B_T$  and ECW injection methods. The flat-top or ramp-up discharge is obtained when the ECR layer is located on the inner side of the torus. Inefficient ECCD under strong  $B_T$  may correspond to the theoretical prediction that the EC heated electrons become trapped on the outer side of the torus. The ECCD efficiency with ECW, propagating parallel to the electron drift, is better than that with ECW, propagating antiparallel or perpendicular to  $B_T$ , and ramp-up discharges are only formed in the former case. Radial profiles of  $I_{SX}$  have rather broad peaks near the plasma centre, and  $\Omega_e$  at peaks is somewhat smaller than  $\omega$ . It is concluded that plasma current is generated by EC heating of the suprathermal electron beam formed in the initial OH plasma. Such a unidirectional electron beam may eliminate the cancelling effect of EC driven current on the opposite side.

The above mentioned ECCD mechanism is also demonstrated in the microwave discharge at ECR in WT-2, where a weak current  $I_p$  is generated [6]. Here, the toroidal drift of electrons circulating in one direction is cancelled by superposing a vertical field  $B_v$ , and an electron beam is formed. The EC driven current is generated in the direction determined by  $B_v$ , independent of the propagation direction of ECW.

### 3. ELECTRON CYCLOTRON CURRENT DRIVE IN RF TOKAMAK [7]

In contrast to the OH plasma, in the LHCD plasma, high energy electrons in the mildly relativistic range, which carry the current  $I_p$ , are produced. Highly efficient ECCD is expected in the LHCD plasma, since ECW is strongly absorbed by such high energy electrons and their collisionality decreases further. As shown in the dotted curves in Figs 3(a) to (k), when  $P_{LH}$  is injected into an initial ECR plasma, the current  $I_p$  starts up rapidly and attains  $I_p = 4$  kA at the end of  $P_{LH}$  and the

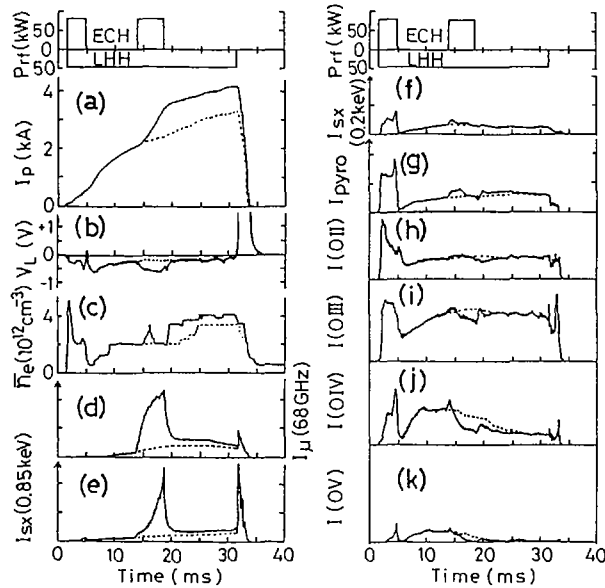


FIG. 3. Temporal evolution of (a) plasma current  $I_p$ , (b) loop voltage  $V_L$ , (c) electron density  $\bar{n}_e$ , (d) electron cyclotron emission  $I_\mu$ , (e) and (f) soft X-ray emission  $I_{sx}$ , (g) pyroelectric detector signal  $I_{pyro}$ , and (h) to (k) impurity line radiations O II, III, IV, V, respectively. Full curves are with  $P_{EC}$  and dotted curves without  $P_{EC}$ . The ECR layer is set at  $r = r_{ECR} = +8.2$  to  $+6.3$  cm, changing during ECH pulse according to  $B_T$  change in time ( $B_{T0} = 15.3$ – $14.7$  kG at  $r = 0$  cm),  $P_{EC} = 80$  kW, and  $P_{LH} = 48$  kW.  $p = 6 \times 10^{-5}$  torr in  $H_2$ ; additional gas comes from puffing during  $P_{LH}$ .

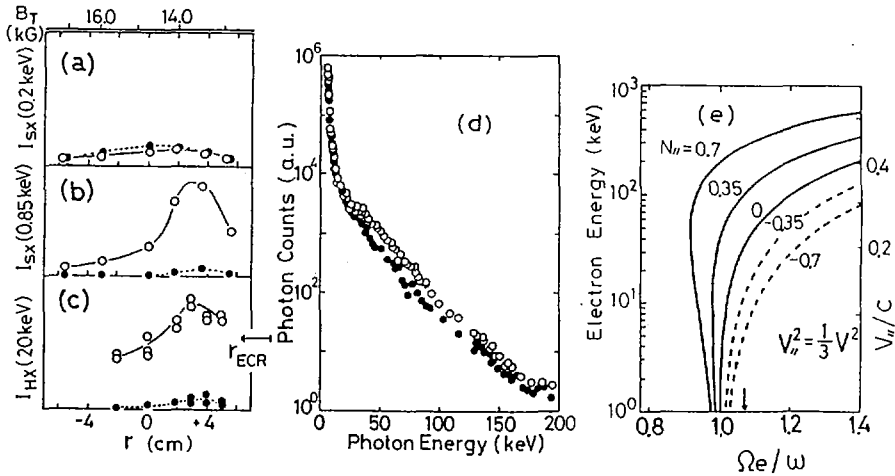


FIG. 4. Radial profile of (a), (b) soft and (c) hard X-ray emissions at the end of ECH pulse ( $t = 5$  ms) in Fig. 3. Solid (dotted) curves are with (without) ECH; (d) soft and hard X-ray spectra with (solid) and without (dotted) ECH pulse, (e) ECR condition.

tokamak plasma is formed by RF power alone, without Ohmic heating power (so-called RF tokamak [8]). When  $P_{EC}$  is applied to the RF tokamak plasma the ramp-up rate of current,  $\Delta I_p/\Delta t$ , increases and  $I_p$  attains a value higher than that without  $P_{EC}$  (solid curve) after termination of the  $P_{EC}$  pulse. This increment of  $I_p$  is ascribed to the EC driven current and the voltage  $V_L$ , the direction of which is opposed to that of electron drift, increases in proportion to  $\Delta I_p/\Delta t$ . The electron density  $\bar{n}_e$  remains constant. The X-ray emission  $I_{SX}$  (0.85 keV),  $I_{HX}$  and non-thermal ECE  $I_\mu$  increase drastically during ECH, while  $I_{pyro}$ ,  $I_{SX}$  (0.2 keV) and  $I_L$  (O II–O V) do not change or even decrease slightly. The results suggest that high energy electrons are generated by ECH although there is no effect on the bulk electrons.

Measurements show that this EC driven current is generated and the emissions  $I_\mu$  and  $I_{SX}$  (0.85 keV) increase strongly when  $B_T$  is strong and the ECR layer ( $\omega = \Omega_e$ ) is on the outer side of the torus ( $r_{ECR} \geq 5$  cm). In Fig. 4(a) the radial profile of  $I_{SX}$  (0.2 keV) is plotted, which is very similar to the density profile of the bulk electrons. The radial profiles of  $I_{SX}$  (0.85 keV) and  $I_{HX}$  (20 keV), representing the profile of high energy electrons, show peaks on the high field side of the ECR layer. When ECH is applied to the RF tokamak, both  $I_{SX}$  (0.85 keV) and  $I_{HX}$  (20 keV) increase drastically near the peaks of their profiles without  $P_{EC}$ , while there is no change of  $I_{SX}$  (0.2 keV). Here, the ECR layer is on the outer side of plasma ( $r_{ECR} \approx 0.3$  a), and the radial position of the peaks of  $I_{SX}$  (0.85 keV) and  $I_{HX}$  is not at the ECR layer, but is shifted slightly towards the high field side, where  $\Omega_{ce} = 1.07 \omega$ .

In the RF tokamak, high energy electrons are present, and strong X-rays up to 300 keV are emitted. The energy spectrum is composed of the steep slope part ( $\sim 15$  keV) in the low energy range and the gentle slope part ( $\sim 45$  keV) in the high energy range as is shown in Fig. 4(d) [9]. When  $P_{EC}$  is injected, the X-ray emission increases by a factor of three in the high energy range of 20–200 keV, while there is no change below 20 keV. Considering the relativistic effect and the Doppler shift, the ECR condition is given by

$$1 - (N_{\parallel} v_{\parallel})/c = (\Omega_e/\omega) \{1 - (v_{\parallel}^2 + v_{\perp}^2)/c^2\}^{1/2}$$

As the electron density increases, the relativistic effect dominates the Doppler shift and resonance occurs at  $\Omega_e/\omega > 1$ , even if  $N_{\parallel}/v_{\parallel} > 0$ . A calculation shows that in the field region of  $\Omega_e/\omega = 1.07 \pm 0.05$  the energy of the resonant electrons is 20–150 keV for  $N_{\parallel} = 0.23 \pm 0.1$  and 2–50 keV for  $N_{\parallel} = -(0.23 \pm 0.1)$ , where  $v^2 = 2v_{\parallel}^2$  is assumed (Fig. 4(e)). It is concluded that mildly relativistic electrons generated by LHW and drifting along one direction of  $B_T$  are accelerated efficiently in the perpendicular direction by ECW, then these electrons become more collisionless and carry the EC driven current efficiently. The collision time of electrons of 50 keV is about 60 ms ( $\bar{n}_e = 2 \times 10^{12}$  cm $^{-3}$ ,  $Z_{eff} = 2$ ) and much longer than the ECH pulse. Thus, in Fig. 4(d), the enhancement of X-ray emission due to  $P_{EC}$  in

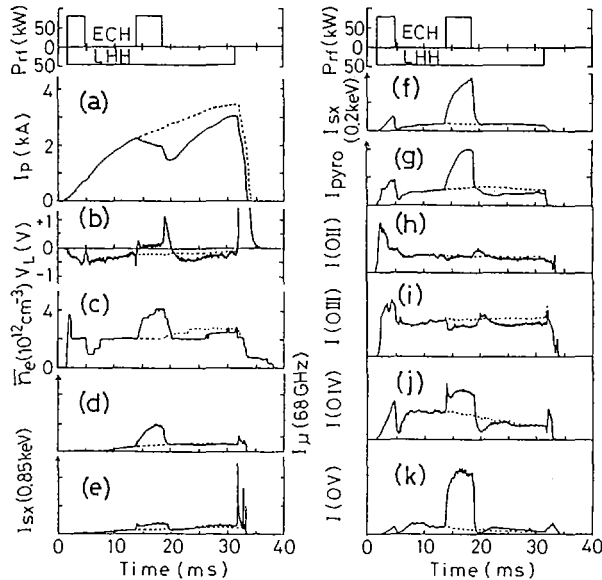


FIG. 5. Temporal evolution of plasma parameters as in Fig. 3. Here, ECR layer is set at  $r = r_{\text{ECR}} = -2.0$  to  $-4.8$  cm ( $B_{T0} = 12.1$ – $11.2$  kG).

the high energy range is maintained after  $P_{\text{EC}}$  has been switched off. Correspondingly, the increased current  $I_p$  due to ECCD does not decay after  $P_{\text{EC}}$  has been switched off in Fig. 3(a).

The change of  $I_p$  due to ECCD in RF tokamak is measured for various  $B_T$ . When  $B_T$  is weak and the ECR layer is located on the inner side ( $r_{\text{ECR}} \approx -0.3$  a), the effects of ECH are quite different from those observed in Fig. 3. During the  $P_{\text{EC}}$  pulse,  $I_p$  continues to decrease,  $\Delta I_p / \Delta t$  becomes negative, and  $I_p$  is smaller than the dotted values after termination of  $P_{\text{EC}}$  in Fig. 5(a). The loop voltage  $V_L$  is zero or slightly positive. The electron density  $\bar{n}_e$  increases. The increment of  $I_\mu$  (68 GHz) and  $I_{\text{SX}}$  (0.85 keV) is small, but  $I_{\text{SX}}$  (0.2 keV) and  $I_{\text{pyro}}$  increase strongly during  $P_{\text{EC}}$ . The line intensities of low excitation energy (O II, O III) do not change or even decrease slightly compared with the dotted curves, in spite of the increase of  $\bar{n}_e$ , but curves of high energy (O IV, O V) increase strongly. It is roughly estimated that the bulk electron temperature increases from 20 to 70 eV by comparing the line intensities with those of no ECH. This behaviour suggests that the heating of bulk electrons occurs at  $\Omega_e / \omega \approx 1$  and no high energy electrons are produced. The dependence of  $I_p$  due to ECCD on  $B_T$  is similar for various methods of  $P_{\text{EC}}$  injection: parallel, antiparallel, perpendicular and top injection although the absolute value of  $\Delta I_p / \Delta t$  is different. The reason why the LH driven current  $I_p$  decreases during bulk electron heating is unknown although it may be ascribed to an enhancement of return current.

## 4. EFFICIENCY OF ECCD

In the ECR plasma, the dependence of EC driven current  $I_p$  on  $P_{EC}$  and  $n_e$  is investigated, and the relation,  $I_p = \eta P_{EC}/n_e R$ , is demonstrated experimentally. Then, the figure of merit of ECCD is obtained as  $\eta \approx 1.2 \times 10^{-3}$  ( $10^{19} \text{ m}^{-2} \text{ kA} \cdot \text{kW}^{-1}$ ). Furthermore, by using the experimental data of the flat-top discharge due to ECCD after OH plasma in Fig. 2(c), the efficiency is calculated to be  $\eta \approx 1 \times 10^{-3}$ . These values are small, compared with  $\eta \approx 6 \times 10^{-2}$  for LHCD in WT-2 [10]. The experimental value of  $\eta$  obtained from the flat-top discharge due to ECCD is calculated to be  $\eta = 0.8 \times 10^{-2}$ , while  $\eta \approx 1 \times 10^{-1}$  for LHCD ( $I_p \approx 45 \text{ kA}$ ,  $P_{LH} = 100 \text{ kW}$ ,  $n_e = 2.6 \times 10^{12} \text{ cm}^{-3}$ ) in WT-3. According to the quasi-linear theory of ECCD, the efficiency is given by  $\eta = 0.306 (j/p) (T_e/10 \text{ keV})/\ln \Lambda$ . The expression for normalized efficiency ( $j/p$ ) is given by Fisch et al. [2] and Cordey et al. [11]. Substituting the experimental values of resonant electrons,  $T_{e \text{ supra}} = 15 \text{ keV}$ , and the bulk electrons,  $T_e = 70 \text{ eV}$ , we obtain  $\eta = 2 \times 10^{-1}$ , which is two orders larger than for the experimental values of WT-2.

Next, the efficiency of ECCD is examined for RF tokamak. In Fig. 6 is plotted the ramp-up rate  $\Delta I_p/\Delta t$  as a function of  $P_{RF}$  ( $P_{LH}$  or  $P_{EC}$ ). For the RF tokamak discharge ( $P_{EC} = 0$ ), as  $P_{LH}$  increases the ramp-up rate increases at first, then attains a constant value (curve 1). When a constant  $P_{EC}$  is superposed, the ramp-up rate increases with  $P_{LH}$  (curve 2) and exceeds that with  $P_{EC} = 0$ . When the RF tokamak is sustained by a constant  $P_{LH}$ , the current ramp-up rate increases with  $P_{EC}$  and attains a constant value (curve 3). Unfortunately, the present pulse of  $P_{EC}$  is too short for  $I_p$  to attain a quasi-stationary state. If it is assumed that the change of the ramp-up rate with respect to  $P_{RF}$ ,  $d(\Delta I_p/\Delta t)/dP_{RF}$ , is proportional to the efficiency of RFCD,  $\eta_{RF}$ , then both  $\eta_{EC}$  with a constant  $P_{LH}$  and  $\eta_{LH}$  with a constant  $P_{EC}$

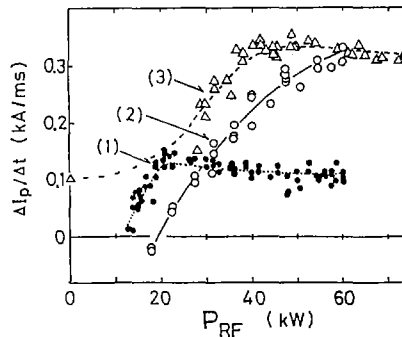


FIG. 6. Ramp-up rate as a function of  $P_{RF}$  ( $P_{EC}$  or  $P_{LH}$ ) in the cases of (1)  $P_{EC} = 0$ , (2)  $P_{EC} = 62 \text{ kW}$  and (3)  $P_{LH} = 60 \text{ kW}$ ;  $B_T = 15 \text{ kG}$ .

are nearly equal to  $\eta_{LH}$  without  $P_{EC}$  in the unsaturated region. It is suggested theoretically that

$$\eta_{EC}/\eta_{LH} \sim (3/4) \{1 + (v/2v_{th})^2\}^{-1} \sim 1$$

which is consistent with the experimental results. As has been noted, when  $P_{EC}$  is superposed on the RF tokamak, the ramp-up rate exceeds that for  $P_{HL}$  alone. Such an enhancement of LHCD efficiency combined with ECH is consistent with the theoretical predictions by Fidone et al. [12].

## 5. CURRENT DRIVE BY INJECTION OF ELECTRON BEAM [13]

By the plasma anode method, an electron beam (EB) is injected into a currentless ECR plasma in WT-2. The peak current of EB is  $I_k = 0.46$  kA, and the pulse width is 5 ms. The energy of EB decreases from 2 to 0.4 keV during the pulse. The plasma current  $I_p$  reaches 4 kA at 0.7 ms after EB injection. Here, the current amplification ratio  $I_p/I_k$  is about 9 at this peak. When EB is injected, the plasma density increases considerably,  $n_e = (2.5 \rightarrow 60) \times 10^{12} \text{ cm}^{-3}$ , and the  $I_{pyro}$  radiation rises rapidly. This abrupt increase in  $n_e$  and  $I_{pyro}$  is attributed to the inflow of impurities produced at the cathode during EB injection. However, it should be noted that  $I_p$  continues to flow during EB injection although the slowing down time of EB is very short, e.g.,  $\tau_s \sim 0.1 \mu\text{s}$  in the case where  $n_e = 6 \times 10^{13} \text{ cm}^{-3}$ ,  $Z_{eff} = 5$  and an EB energy of about 0.5 keV is assumed. As  $B_v$  is varied, the peak value of  $I_p$  changes, and its maximum value is  $I_p = 4$  kA at  $B_v = 1.6 \times 10^{-3}$  T for  $B_T = 1.13$  T.

## 6. CONCLUSIONS

EC driven current is generated in two types of plasmas. First, such a current is generated by ECH of suprathreshold electrons in the OH plasma, and the current  $I_p$  is sustained or ramped-up when  $P_{EC}$  is injected into the plasma after OH power has been switched off. This EC driven current is generated in the ECR plasma. Secondly, EC driven current is generated by ECH of the mildly relativistic electron beam present in LH driven current sustained plasma, and the ramp-up rate of  $I_p$  increases when  $P_{EC}$  is injected into RF tokamak. Such an enhancement of LHCD efficiency combined with ECH is quite important for a new, useful and efficient method of RFCD.

When an electron beam of moderate energy, 0.4 to 2 keV, is injected into a currentless ECR plasma with density  $2.5 \times 10^{12} \text{ cm}^{-3}$  at  $B_T = 1.1$  T, a toroidal current of 4 kA, which is nine times the injected beam current, is formed.

## REFERENCES

- [1] Non-Inductive Current Drive in Tokamaks (Proc. IAEA Tech. Comm. Meeting, Culham, 1983), Vols 1 and 2, Culham Laboratory, Abingdon (1983).
- [2] FISCH, N.J., BOOZER, A.H., Phys. Rev. Lett. **45** (1980) 720.
- [3] TANAKA, S., et al., in Plasma Physics and Controlled Nuclear Fusion Research 1982 (Proc. 9th Int. Conf. Baltimore, 1982), Vol. 1, IAEA, Vienna (1983) 199.
- [4] TANAKA, S., et al., in Plasma Physics and Controlled Nuclear Fusion Research 1984 (Proc. 10th Int. Conf. London, 1984), Vol. 1, IAEA, Vienna (1985) 623.
- [5] ANDO, A., et al., Phys. Rev. Lett. **56** (1986) 2180; J. Phys. Soc. Jpn. **56** (1986).
- [6] SHIMOZUMA, T., et al., J. Phys. Soc. Jpn. **54** (1985) 1360.
- [7] ANDO, A., et al., Nucl. Fusion **26** (1986) 107.
- [8] KUBO, S., et al., Phys. Rev. Lett. **50** (1983) 1994.
- [9] OGURA, K., et al., J. Phys. Soc. Jpn. **55** (1986) 13.
- [10] NAKAMURA, M., et al., J. Phys. Soc. Jpn. **53** (1984) 3399.
- [11] CORDEY, J.G., et al., Plasma Phys. **24** (1982) 7.
- [12] FIDONE, I., GIRUZZI, G., GRANATA, G., MEYER, R.L., Phys. Fluids **27** (1984) 2486.
- [13] TANAKA, H., et al., Jpn. J. Appl. Phys. **24** (1985) 644.

## DISCUSSION

A.C. RIVIERE: In the case of electron cyclotron current drive, did you make an experiment with the antenna in the opposite toroidal direction? If so, what was the difference in current between the two antenna orientations?

S. TANAKA: Yes, we did perform such an experiment. When the antenna was in the opposite toroidal direction, we could not obtain a flat-top or ramp-up discharge, although a weak EC driven current did appear.

# IMPROVEMENT OF CURRENT DRIVE AND CONFINEMENT BY COMBINATION OF LHCD AND NBI HEATING IN JT-60

JT-60 TEAM

*(Presented by T. Imai)*

T. Abe, H. Aikawa, H. Akaoka, H. Akasaka, M. Akiba, N. Akino, T. Akiyama, T. Ando, K. Annoh, N. Aoyagi, K. Arakawa, M. Araki, K. Arimoto, M. Azumi, S. Chiba, M. Dairaku, N. Ebisawa, T. Fujii, T. Fukuda, H. Furukawa, K. Hamamatsu, K. Hayashi, M. Hara, K. Haraguchi, H. Hiratsuka, T. Hirayama, S. Hiroki, K. Hiruta, M. Honda, H. Horiike, R. Hosoda, N. Hosogane, Y. Iida, T. Iijima, K. Ikeda, Y. Ikeda, T. Imai, T. Inoue, N. Isaji, M. Isaka, S. Ishida, N. Itige, T. Ito, Y. Ito, A. Kaminaga, M. Kawai, Y. Kawamata, K. Kawasaki, K. Kikuchi, M. Kikuchi, H. Kimura, T. Kimura, H. Kishimoto, K. Kitahara, S. Kitamura, A. Kitsunezaki, K. Kiyono, N. Kobayashi, K. Kodama, Y. Koide, T. Koike, M. Komata, I. Kondo, S. Konoshima, H. Kubo, S. Kunieda, S. Kurakata, K. Kurihara, M. Kuriyama, T. Kuroda, M. Kusaka, Y. Kusama, S. Maehara, K. Maeno, S. Mase, S. Matsuda, M. Matsukawa, T. Matsukawa, M. Matsuoka, N. Miya, K. Miyati, Y. Miyo, K. Mizuhashi, M. Mizuno, R. Murai, Y. Murakami, M. Muto, M. Nagami, A. Nagashima, K. Nagashima, T. Nagashima, S. Nagaya, H. Nakamura, Y. Nakamura, M. Nemoto, Y. Neyatani, S. Niiikura, H. Ninomiya, T. Nishitani, H. Nomata, K. Obara, N. Ogiwara, Y. Ohara, K. Ohasa, T. Ohga, H. Ohhara, M. Ohkubo, T. Ohshima, K. Ohta, M. Ohta, M. Ohtaka, Y. Ohuchi, A. Oikawa, H. Okumura, Y. Okumura, K. Omori, S. Omori, Y. Omori, T. Ozeki, M. Saigusa, K. Sakamoto, A. Sakasai, S. Sakata, M. Satou, M. Sawahata, M. Seimiya, M. Seki, S. Seki, K. Shibanuma, R. Shimada, K. Shimizu, M. Shimizu, Y. Shimomura, S. Shinozaki, H. Shirai, H. Shirakata, M. Shitomi, K. Sukanuma, T. Sugie, T. Sugiyama, H. Sunaoshi, K. Suzuki, M. Suzuki, M. Suzuki, N. Suzuki, S. Suzuki, Y. Suzuki, H. Takahashi<sup>1</sup>, M. Takahashi, S. Takahashi, T. Takahashi, M. Takasaki, M. Takatsu, A. Takeshita, H. Takeuchi, S. Tamura, S. Tanaka, K. Tani, M. Terakado, T. Terakado, K. Tobita, T. Tokutake, T. Totsuka, N. Toyoshima, H. Tsuda, T. Tsugita, S. Tsuji, Y. Tsukahara, M. Tsuneoka, K. Uehara, M. Umehara, Y. Uramoto, H. Usami, K. Ushigusa, K. Usui, J. Yagyū, K. Yamada, M. Yamamoto, O. Yamashita, Y. Yamashita, K. Yano, T. Yasukawa, K. Yokokura, H. Yokomizo, H. Yoshida, M. Yoshikawa, Y. Yoshinari, R. Yoshino, I. Yonekawa, K. Watanabe

Naka Fusion Energy Research Establishment,  
Japan Atomic Energy Research Institute,  
Naka-machi, Naka-gun, Ibaraki-ken,  
Japan

<sup>1</sup> Princeton Plasma Physics Laboratory, Princeton University, NJ, USA.

## Abstract

### IMPROVEMENT OF CURRENT DRIVE AND CONFINEMENT BY COMBINATION OF LHCD AND NBI HEATING IN JT-60.

First results of the lower hybrid current drive (LHCD) experiment on JT-60 are presented, in which maximum RF driven currents of 1.7 MA with an RF power of 1.2 MW at 2 GHz are obtained for 2 s. High current drive efficiency,  $\eta_{CD} = \bar{n}_e [10^{19} \text{ m}^{-3}] R[m] I_{RF}[MA] / P_{LH}[MW] = 1-1.7$  for Ohmic plasma is reliably attained. An enhancement of  $\eta_{CD}$  is obtained with the combination of LHCD and NBI heating and a value of  $\eta_{CD} = 2-2.8$  is reached. Improvement in confinement because of the synergetic effect of combined LHCD and NBI is also observed. The energy confinement time during NBI heating is not degraded, compared with that in Ohmic discharges.

## 1. INTRODUCTION

Improvement in current drive efficiency and reduction of confinement degradation during auxiliary heating are crucial problems of the next large tokamak aiming at a steady state tokamak reactor. Recent progress in current drive, heating and suppression of MHD activities making use of RF power makes us hope that we shall be able to overcome these problems. As a result of successful heating and current drive experiments in the Lower Hybrid Range of Frequencies (LHRF) on the JAERI tokamaks (JFT-2, JFT-2M) [1-3], a scaling-up programme with high power LHRF heating from 24 MW source power has started in JT-60. The major objectives of the JT-60 LHRF system are the production of a reactor grade plasma with a combination of 20 MW Neutral Beam Injection (NBI) and 6 MW Ion Cyclotron Range of Frequencies (ICRF) heating, and current drive in low and medium density plasmas, in order to ascertain the physics feasibility of stationary or quasi-stationary operation of the tokamak reactor.

In this paper, the first results of lower hybrid current drive in Ohmic and NBI heated plasmas in JT-60 will be described, in which enhancement of current drive efficiency by combination of LHCD and NBI heating and an improvement of confinement are obtained.

## 2. LHRF SYSTEM

Since the performance of JT-60 and the NBI heating system are described in companion papers [4, 5], only a brief description of the LHRF system will be given here. The LHRF heating system produces 24 MW RF power at about 2 GHz (1.7-2.23 GHz) with three units of the eight klystron amplifier subsystems, where the 1 MW klystrons developed in JAERI are used. The line-up of the amplifier chain is shown in Fig. 1(a). One of three  $4 \times 8$  phased array launchers, which are installed in JT-60 at present, is designed for current drive and has additional passive waveguides [6]. The results obtained here are from this launcher, whose  $N_{\parallel}$  spectra,

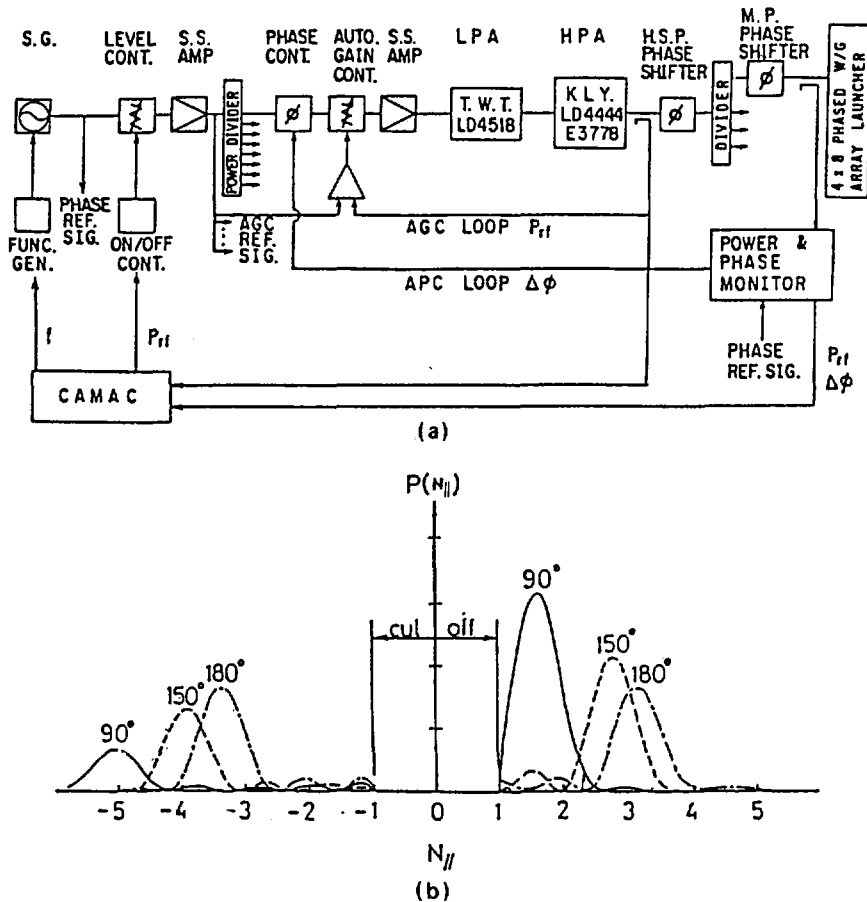


FIG. 1. (a) Line-up of JT-60 LHRF system amplifier chain; (b)  $N_{\parallel}$  spectra for current drive launcher from Brambilla theory (waveguide width  $b = 16$  mm).

from Brambilla theory, are shown in Fig. 1(b). The peak of the  $N_{\parallel}$  spectrum is 1.7, with a phase difference of adjacent waveguides of  $\Delta\phi = 90^\circ$ , and an efficient coupling to the high energy electrons of  $>100$  keV is expected. The radial position of the launcher front is usually at  $r = 945$ – $950$  mm.

### 3. CURRENT DRIVE IN OHMIC PLASMA

The current drive effect in Ohmic plasma is reliably obtained in JT-60, when the lower hybrid wave is coupled unidirectionally to the low density plasma. A typical time evolution of loop voltage  $V_1$ , plasma current  $I_p$ , Ohmic primary

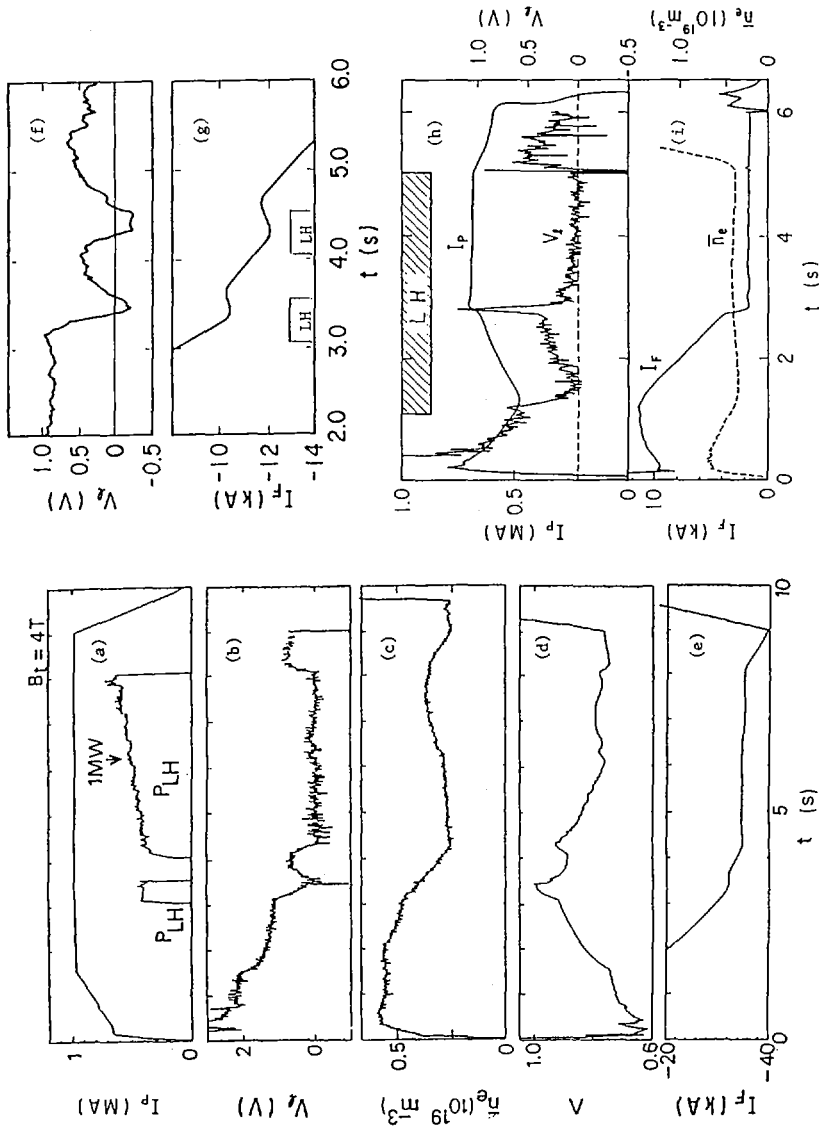


FIG. 2. Time evolution of relevant plasma parameters during LHCD. (a)-(e):  $P_{LH} = 1$  MW; (f), (g):  $P_{LH} = 570$  kW, where feedback control of constant  $I_p$  is done everywhere except for (h) and (i). (h), (i): Current sustainment without Ohmic power supply ( $I_F = 0$ ), where  $\bar{n}_e = 0.37 \times 10^{19} m^{-3}$  and  $B_T = 4 T$ .

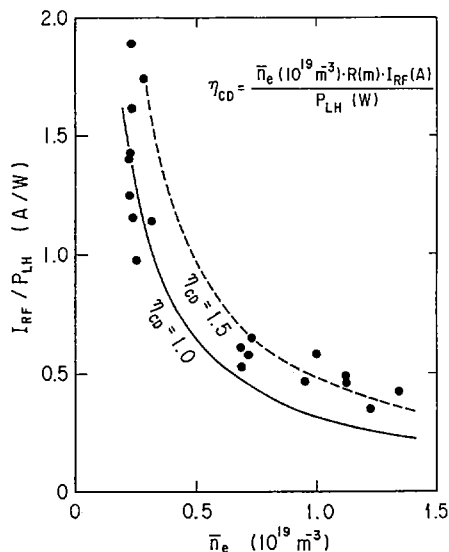


FIG. 3. Density scan of RF driven current normalized by RF power, where  $I_{RF} = I_p |\Delta V_1 / V_1|$ .

current  $I_F$ , electron line average density  $\bar{n}_e$  and  $\Lambda (= \beta_p + \ell_i / 2 - 1)$  in a discharge with RF power  $P_{LH} = 1$  MW is shown in Fig. 2(a)–(e), where  $\beta_p$  and  $\ell_i$  are the poloidal beta and the internal inductance, respectively. Two RF pulses from 3 to 3.5 s and from 4 to 8.0 s are injected during one shot. The  $V_1$  drops sharply to zero or negative values at the RF pulses, and  $I_F$  stays constant. The RF driven currents ( $I_{RF}$ ) as estimated from the drop of the loop voltage ( $\Delta V_1$ ) at the second pulse are:  $I_{RF} \equiv I_p |\Delta V_1| / V_1 \approx 1$  MA. The current drive efficiency as defined by  $\eta_{CD} \equiv \bar{n}_e [10^{19} \text{ m}^{-3}] R[\text{m}] I_{RF}[\text{MA}] / P_{LH}[\text{MW}]$  is given by  $\eta_{CD} \approx 1$ , from  $I_{RF}$  and Fig. 2.

The change in  $\Lambda$  of Fig. 2(d) suggests a reorganization of the current distribution  $j(r)$  during LHCD, since  $\ell_i$  is dominant in  $\Lambda$  because of the low density.  $\Lambda$  at the end of RF pulse is lower than that at  $t = 3.0$  s. Therefore, it is indicated that  $j(r)$  is broadened by LHCD. The effect of  $j(r)$  flattening due to LHCD will be discussed later, in Section 5, in connection with MHD activities and confinement.

Recharging effects of the OH primary coil are clearly seen in a discharge with smaller plasma current and lower density as shown in Fig. 2(f, g).  $\dot{I}_F > 0$  is clearly observed during the RF pulse. Current sustainment without Ohmic supply is also demonstrated in Fig. 2(h). RF currents of 0.7 MA are only sustained by RF power of 0.76 MW, during 2 s. The maximum RF current obtained so far is 1.7 MA, as will be shown in Fig. 5(a).

The density dependence of  $I_{RF}$  ( $\equiv I_p |\Delta V_1| / V_1$ ) is shown in Fig. 3.  $I_{RF}$  is roughly proportional to  $1/\bar{n}_e$ , as usual, since our present density regime is lower

than the density limit. It may be stated that an efficient current drive of  $\eta_{CD} = 1-1.7$  in an Ohmic target plasma is obtained although the estimation of the RF currents ( $I_{RF}$ ) contains some error bar due to the change in  $\xi$  (roughly 20%). These values are appreciably larger than previous results obtained in other small and medium size tokamaks. The theoretical current drive efficiency is given by  $\eta_{TH} = K\mu fg$  [7], where  $\mu = 1/N_1^2 (1 - N_1^2/N_2^2)/\log(N_2/N_1)$ ,  $N_1$  and  $N_2$  being accessibility limit of  $N_{||}$  and the upper limit of the  $N_{||}$  spectrum of radiated power;  $f$  is a directivity factor,  $g$  is the portion of the accessible wave, and  $K$  is a constant factor if  $Z_{eff}$  is constant. The factors  $\mu$ ,  $f$  and  $g$  are not very different among various tokamaks if the  $N_{||}$  spectrum is optimized for current drive. Therefore, the reason for our improved efficiency lies elsewhere. The effect of electron temperature does not explicitly appear in  $\eta_{TH}$ . However, since we need some secondary mechanism to fill up the spectral gap between the wave phase velocity and the thermal velocity in order to explain the effective current drive results obtained previously in many tokamaks, this secondary effect necessarily brings about some reduction in efficiency. Therefore, the electron temperature must play an important role in determining the efficiency, because the higher the electron temperature, the smaller the spectral gap if we optimize  $\mu$ . From this conclusion, we can achieve a more efficient current drive in higher temperature plasmas, which can be realized by NBI heating.

#### 4. IMPROVEMENT OF $\eta_{CD}$ WITH NBI HEATING

As was discussed in Section 3, higher current drive efficiency is expected in NBI heated plasma. Figure 4 shows the time evolution of the relevant plasma parameters in a typical LHCD + NBI shot, where the RF and NBI powers are 0.88 and 8.8 MW, respectively, and  $I_p = 1$  MA. The  $I_{RF}$  current is estimated in the same manner as that in the case of an Ohmic target plasma. Here, the increment of the loop voltage after the RF pulse, while the NBI power is still on, is used as  $\Delta V_1$ . An interesting feature shown in Fig. 4 is that the loop voltage drop ratio ( $\Delta V_1/V_1$ ) does not change much before and after NBI is turned on, while  $n_e$  increases by more than a factor of 2.5. As is seen from the figure,  $|\Delta V_1|/V_1 = 1.25$ , because of LHCD before NBI, and 0.75 during the NBI pulse and, hence  $I_{RF} = 1.25$  and 0.75 MA, in the respective cases. Using  $\bar{n}_e = 0.35 \times 10^{19} \text{ m}^{-3}$  (OH + LHCD),  $0.9 \times 10^{19} \text{ m}^{-3}$  (LHCD + NBI) and  $R = 3.1$  m,  $\eta_{CD} = 1.5$  in an Ohmic plasma and 2.4 in an NBI heated plasma are obtained. The estimated RF current,  $I_{RF}$ , for various cases is plotted in Fig. 5(a), where the currents in an Ohmic target plasma are also plotted. As is seen from the figure,  $\eta_{CD}$ , for NBI + LHCD, is 2-2.8, while for OH + LHCD, it is 1-1.7. The efficiency is almost doubled by NBI. This efficiency enhancement is also supported by measurements of the hard X-ray intensity,  $I_{HX}$ , and the electron cyclotron emission intensity,  $I_{ECE}(3f_{ce})$ . The linear correlation between  $I_{RF}$  and the hard X-ray increment during LHCD  $\Delta I_{HX}$  is obtained from Fig. 5(b). Figure 5(c) shows the transition of  $\Delta I_{HX}$  from OH + LHCD to

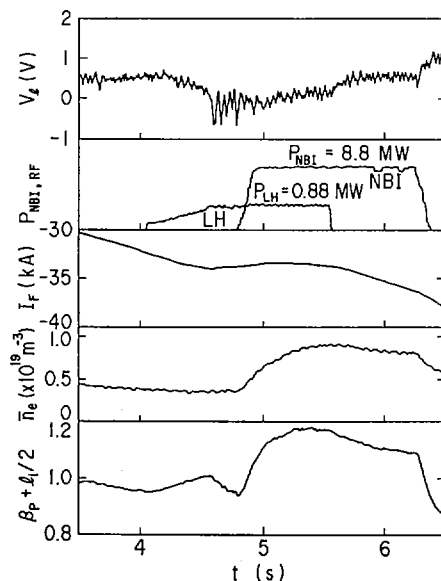


FIG. 4. Time evolution of loop voltage and relevant plasma parameters in discharge with LHCD + NBI heating.

LHCD + NBI in the same shot. Since  $\Delta I_{HX} \propto I_{RF}$  and  $I_{RF} \propto 1/\bar{n}_e$ ,  $\Delta I_{HX} \propto 1/\bar{n}_e$  if RF power and efficiency are constant. But the data in Fig. 5(c) indicate that  $\Delta I_{HX}$  is not simply proportional to  $1/\bar{n}_e$ , when LHCD is combined with NBI heating. The relative enhancement of  $\Delta I_{HX}$  due to NBI heating is seen when the data before and after NBI in the same shot are compared. A similar effect is observed in  $\Delta I_{ECE}$ .

The above-given result is very important and promising for a future application of RF current drive and makes steady state tokamak operation a hopeful device.

## 5. IMPROVEMENT OF CONFINEMENT

As was described in Section 2, the  $j(r)$  in the LHCD plasma seems to be broader than that in the OH plasma. Therefore, improved confinement due to current profile control by LHCD is expected. Actually, sawtooth oscillation and/or  $m = 1$  mode are stabilized during LHCD, as is also observed in other, smaller tokamaks. The effect should be applied to NBI heated plasmas.

Figure 6 shows the time evolution of  $\Lambda$  and other relevant parameters of the OH + NBI shot (Fig. 6(a)) and the LHCD + NBI shot (Fig. 6(b)), where  $I_p = 1.0$  MA and  $B_T = 4$  T with NBI power of  $P_{NBI} = 3.4$  and 4.4 MW, respectively. The total stored energies estimated from the  $\Lambda$  for both shots are

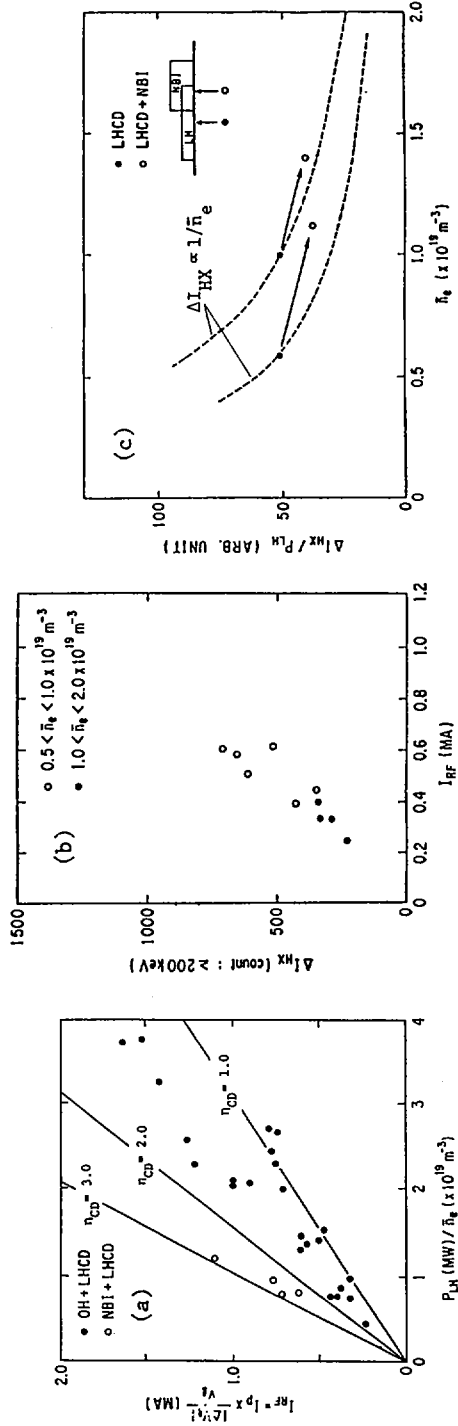


FIG. 5. (a) Power dependence of  $I_{RF}$  in Ohmic plasma (closed circles) and in NBI heated plasmas (open circles); (b) increment of hard X-ray intensity versus  $I_{RF}$ ; (c) normalized hard X-ray increment ( $\Delta I_{HX}/P_{LH}$ ) versus  $\bar{n}_e$ .

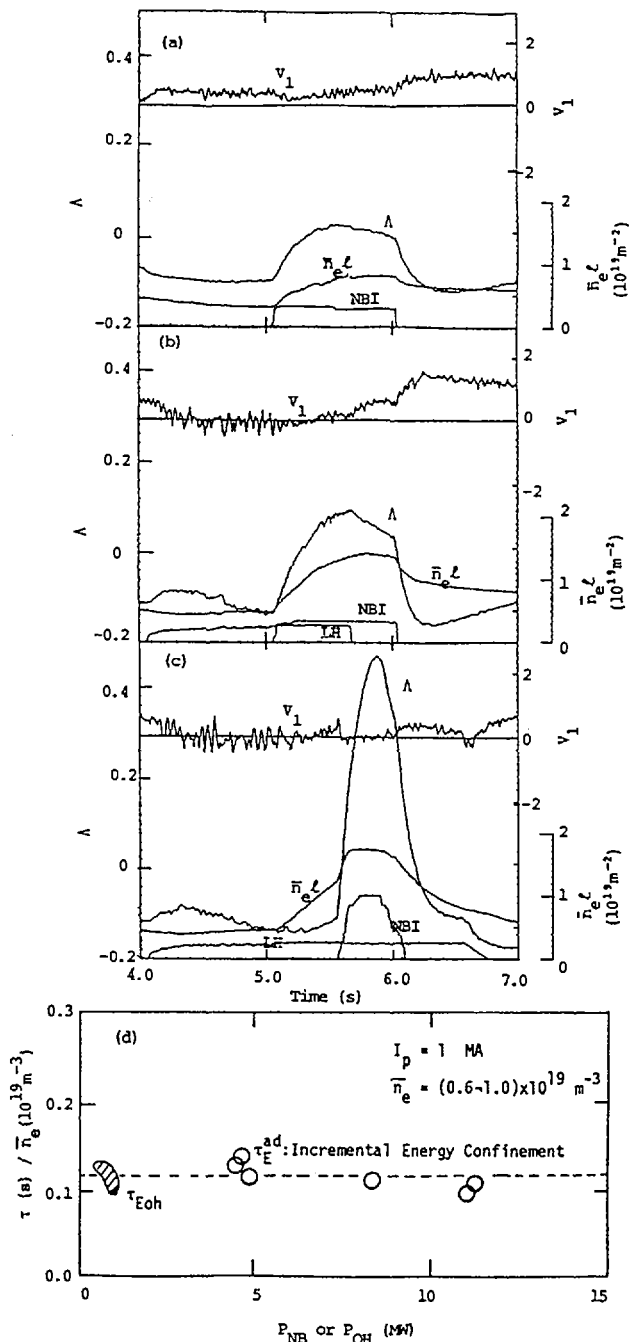


FIG. 6. Time evolution of  $V_1$ ,  $\Delta$  and  $\bar{n}_e \ell$  in case of (a) OH + NBI with  $P_{NBI} = 3.4$  MW and (b) LHCD + NBI with  $P_{LH} = 1$  MW,  $P_{NBI} = 4.4$  MW. (c) LHCD + NBI with  $P_{NBI} = 11$  MW. Energy confinement time with LHCD + NBI is not degraded from Ohmic values (d).

$W^*$  [OH + NBI] = 0.26 MJ and  $W^*$  [LHCD + NBI] = 0.4 MJ, assuming  $\Delta\ell_i$  due to NBI  $\approx 0$ . A substantial enhancement of the stored energy by the combination of LHCD and NBI heating is found from these values. The confinement time for the incremental stored energy during NBI heating increases by 20–30% in the LHCD plasma. A remarkable increase in stored energy is obtained with the higher NBI power of 11 MW in the LHCD plasma, and  $W^*$  reaches 1.1 MJ, from Fig. 6(c). Surprisingly, the global energy confinement time is approximately equal to that in the Ohmic discharge and is 2.5 times larger than that from Kaye–Goldston scaling. The confinement is not degraded by high power NBI ( $P_{\text{NBI}} \gg P_{\text{OH}}$ ) in LHCD plasma, even if hydrogen is dominant. The particle confinement is also improved, since density profile peaking is observed in the LHCD + NBI discharge [5]. These profile reorganizations of  $j(r)$ ,  $n_e(r)$  and possibly  $T_e(r)$  in the LHCD plasma seem to play an important role in confinement and make a new H-mode regime using RF current drive a very promising device.

## 6. CONCLUSIONS

Up to 1.2 MW of LHRF power is launched unidirectionally in toroidal direction into Ohmic and NBI heated plasmas in JT-60. Our results may be summarized as follows:

- (1) Maximum RF currents of 1.7 MA are obtained.
- (2) Efficient RF current drive ( $\eta_{\text{CD}} = 1\text{--}1.7$ ) is obtained in Ohmic plasmas.
- (3) A substantially improved current drive efficiency ( $\eta_{\text{CD}} = 2\text{--}2.8$ ) is observed in plasmas with high power NBI heating, due to the increase in electron temperature.
- (4) The degraded energy confinement in NBI heated plasmas is improved by LHCD.

Although more detailed studies should be done in the future, the results presented in this paper are very important and promising with respect to a future large tokamak. In particular, items (3) and (4) seem to be highly relevant to a steady state tokamak reactor.

## ACKNOWLEDGEMENTS

The authors wish to thank the members of JAERI who have contributed to the JT-60 project. They also wish to express their gratitude to Drs S. Mori, Y. Iso, and K. Tomabechi for continued encouragement and support.

## REFERENCES

- [1] NAGASHIMA, T., FUJISAWA, N., in Heating in Toroidal Plasmas (Proc. 1st Joint Varenna-Grenoble Int. Symp. Grenoble, 1978), Vol. 2 (1978) 281.
- [2] IMAI, T., et al., in Radiofrequency Plasma Heating (Proc. 4th Top. Conf. Austin, TX, 1981), American Institute of Physics, New York (1981).
- [3] YAMAMOTO, T., et al., Phys. Rev. Lett. **45** (1980) 716.
- [4] YOSHIKAWA, M., et al., Paper IAEA-CN-47/A-I-1, these Proceedings, Vol. 1.
- [5] JT-60 TEAM (presented by NAGAMI, M.), Paper IAEA-CN-47/A-II-2, these Proceedings, Vol. 1.
- [6] NAGASHIMA, T., et al., JT-60 radiofrequency heating system: Description and R&D results, to be published in Nucl. Eng. Des./Fusion.
- [7] FISCH, N.J., Phys. Rev. Lett. **41** (1978) 873.

## DISCUSSION

F.X. SÖLDNER: The confinement times are derived from  $\Lambda$ , the sum of poloidal equilibrium beta and internal inductance. Can you rule out an increase in the internal inductance during combined LHCD + NBI in the case of lower NBI power for which you have shown  $\Lambda$  curves for comparable cases of NBI alone and for NBI + LHCD?

Further, what kind of enhancement of the energy confinement is left if you include the injected LH power, i.e. if you scale plasma energy versus total power input?

T. IMAI: We cannot completely rule out a difference in  $\Delta\Lambda$  between cases with NBI + LHCD and NBI alone, for medium NBI power, as seen in Fig. 6(a) and (b), since no kinetic measurements were made because of the low density. In order to avoid this ambiguity, we conducted a higher power experiment and obtained the result shown in Fig. 6(c), where an improvement in confinement can be clearly seen. In addition, we did not observe any evidence of an abrupt increase in internal inductance. If it occurred, a substantial increase in loop voltage should also have been observed.

As to your second point, in our  $\tau_E$  calculation we disregarded both the absorbed LH power and the increase in stored energy due to the LH power  $\Delta W_{LH}^*$ , since we have not yet been able to determine  $\Delta W_{LH}^*$ . However, our estimate of  $\tau_E$  is valid if  $P_{LH} \ll P_{NBI}$ , as in our present experiments. If you compare the incremental energy confinement time,  $\tau_E^{ad} = \Delta W_{NB}^*/P_{NB}$ , you also find an enhancement of  $\tau_E^{ad}$  in the LHCD plasma.

R.J. GOLDSTON: In contrast to the H-mode, one imagines that most of the extra stored energy in this regime lies in the centre of the discharge. The electron temperature profile must be very impressive. Do you have any data on this that you could show us?

T. IMAI: Unfortunately, our density regime in this series of experiments is still low, since the available LH power is not yet high enough to drive a current in a high density plasma. So it is very difficult, for the time being, to produce a temperature profile by Thomson scattering.

K. LACKNER: I would like to recall that the TEXTOR results presented by Dr. Vandenplas<sup>1</sup> for fairly low density also seemed not to show any deterioration of the additional heating, compared to Ohmic confinement times. Your results probably fall into the same category. In your plot, comparing  $\tau_E$  with NBI to NBI/LHCD, the former cases appear to lie at higher densities. Was the change in particle confinement time associated with the addition of LHCD?

T. IMAI: Yes, we observed an improvement in particle confinement for NBI heated plasma with LHCD. This point was dealt with in the paper of Dr. Nagami<sup>2</sup>.

---

<sup>1</sup> Paper IAEA-CN-47/F-I-4, these Proceedings, Vol. 1.

<sup>2</sup> Paper IAEA-CN-47/A-II-2, these Proceedings, Vol. 1.

## CURRENT DRIVE, CONFINEMENT AND INSTABILITY CONTROL EXPERIMENTS WITH ECRH ON THE CLEO TOKAMAK

D.C. ROBINSON, N.R. AINSWORTH, P.R. COLLINS,  
A.N. DELLIS, T. EDLINGTON, P. HAYNES, S. IYENGAR<sup>1</sup>,  
I. JOHNSON, B. LLOYD, M. O'BRIEN, B.J. PARHAM,  
A.C. RIVIERE, D.F.H. START, T.N. TODD  
Euratom-UKAEA Fusion Association,  
Culham Laboratory  
Abingdon, Oxfordshire,  
United Kingdom

### Abstract

CURRENT DRIVE, CONFINEMENT AND INSTABILITY CONTROL EXPERIMENTS WITH ECRH ON THE CLEO TOKAMAK.

Electron cyclotron resonance heating has been carried out on CLEO ( $R/a = 7$ ,  $R = 0.9$  m) using the second harmonic extraordinary mode at both 28 GHz and 60 GHz to investigate current drive, confinement and instability control. With the 28 GHz source, at low collisionality ( $\nu_c^* \sim 0.01$ ) and with a non-thermal population of electrons the confinement is enhanced relative to that in ohmic plasmas, whereas with the 60 GHz source and  $\nu_c^* \sim 0.1$  the confinement degrades with little non-thermal electron production. No evidence for current drive has so far been obtained at 28 GHz, but at 60 GHz a different loop voltage response was obtained when either the antenna direction or the plasma current direction relative to the antenna pattern was changed, indicating a driven current of about 5 kA for 150 kW of absorbed power. Low mode number MHD activity has been controlled in a number of experiments, allowing an increase in the disruptive density limit and control of sawtooth activity.

### INTRODUCTION

A series of experiments with 28 and 60 GHz ECRH has been carried out on CLEO using a variety of different waveguide technologies and modes, to study confinement, current drive, MHD control, preionisation and  $\beta$ -limits in tokamak, stellarator and hybrid configurations.

Current drive experiments have been carried out using second harmonic extraordinary mode radiation launched from the low field side at both 28 [1] and 60 GHz. Considerable development work has been aimed at producing high quality antenna patterns at high power for the current drive experiments at 60 GHz and recent results are detailed below.

<sup>1</sup> Commonwealth Universities scholar.

Low- $m$  MHD mode control has been achieved in a variety of experiments, including stabilisation of the 2,1 tearing mode to raise the disruptive density limit and control of the 1,1 mode affecting the sawtooth period and amplitude.

## ENERGY CONFINEMENT

For CLEO tokamak the plasmas associated with  $2\omega_{ce}$  ECRH at 28 and 60 GHz lie in a large aspect ratio, low density regime where conventional ohmic heating scalings (eg. neo-Alcator) predict significantly lower confinement time than those of auxiliary heating, while the resulting data fall between these predictions and are therefore not easily categorised as simply L-mode or ohmic. Energy confinement was generally better in the bi-Maxwellian (thermal plus 13 keV tail) 28 GHz ECRH plasmas [2] than in their OH targets, even at absorbed power to initial ohmic heating power ratios ( $P_{abs}/P_{OH}$ ) of  $> 10$ . Work on other machines [3] has also correlated confinement enhancement with distorted electron distributions. In the more thermal 60 GHz ECRH cases, with similar  $P_{abs}/P_{OH}$  ratios, the confinement degrades and the data indicate a scaling of  $W_{TOT} \sim I^{\alpha} P_{abs}^{1/2}$  with  $\alpha \sim 0.8$  and with the resonance in the plasma centre.

For 28 GHz,  $2\omega_{ce}$  heating, the fairly weak sensitivity of the energy content to resonance position was accompanied by clear in-out asymmetry in electrical conductivity, consistent with a strong trapped particle population when heating on the low field side. Surface barrier diode array data show that the slowing-down time of this non-thermal trapped particle group is essentially classical [4], while the particles would have to slow down much more rapidly if they were to account for the observed anomalous electron energy loss. Lowering the plasma density raised the stored energy, anisotropy and the population of the 13 keV tail.

At 60 GHz the higher densities and lower temperatures made the ECRH plasmas much less collisionless, resulting in essentially Maxwellian isotropic distributions, while the density dependence of  $\tau_E$  or  $W_{tot}$  became weakly positive up to the cut-off and the sensitivity to resonance position became more critical. At both frequencies the stored energy increase rose with plasma current, saturating near  $q \sim 2$  with the

TABLE I. PARAMETERS OF OHMIC HEATING TARGET PLASMA AND OF THE RESULTANT ECRH PLASMA

$$I_p = 10 \text{ kA}, B_\phi = 1.07 \text{ T}$$

	Ohmic heating	ECRH
$T_c(0)$	400 eV	1250 eV
$n_c(0)$	$8 \times 10^{18} \text{ m}^{-3}$	$6 \times 10^{18} \text{ m}^{-3}$
$\beta_p$	0.7	2.7
$P_{\text{OH/RF}}$	14 kW	155 kW
$\tau_E$	2.3 ms	0.9 ms

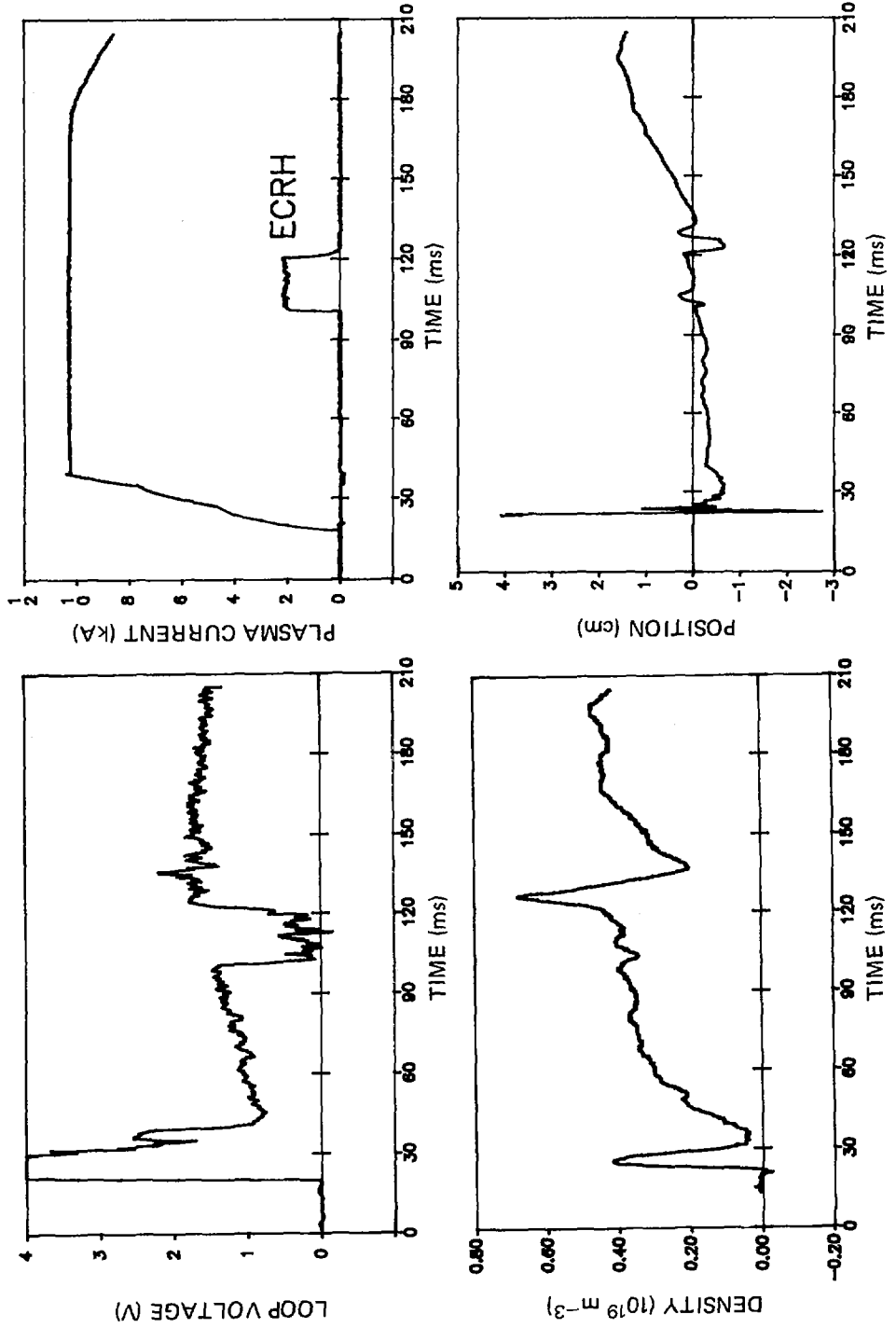
RF-dominated 28 GHz case and at higher  $q$  with the 60 GHz case, where the stored energy of the target plasma became significant. The effect on this current scaling of adding vacuum rotational transform using the  $\lambda=3$  stellarator windings was investigated at 28 GHz, with the conclusion that an improvement was realised only when a significant relative contribution was made by the vacuum transform.

The parameters of the ohmic heating target plasma and of the resultant ECRH plasma at 60 GHz are summarised in Table I and typical waveforms are shown in Fig 1. The ohmic plasmas feature sawteeth and  $Z_{\text{eff}} < 2$ . RF probes indicate that about 85% of the incident RF power is absorbed. The confinement degradation seems to be stronger than the Merezhkin scaling [5] but similar to the L-mode.

With gettering, good vacuum conditions and constant gas injection rates, ECRH in CLEO invariably produces a fall in line averaged density, reaching a factor  $> 2$  when the initial density is a little above the nominal cut-off. However, measurements with a two-channel interferometer show that part of this fall is due to a broadening of the density profile.  $H_\alpha$  measurements show that the particle confinement decreases by a factor  $\sim 2$ .

In CLEO the stored energy ( $\beta_p + \lambda_i/2$ ), SXR flux, etc. in general do not relax during the RF pulse (usually 20-50ms in duration) even when the resonance is displaced off axis.

Fundamental heating has been directly compared with second harmonic heating at the same toroidal field using 28 and 60 GHz.



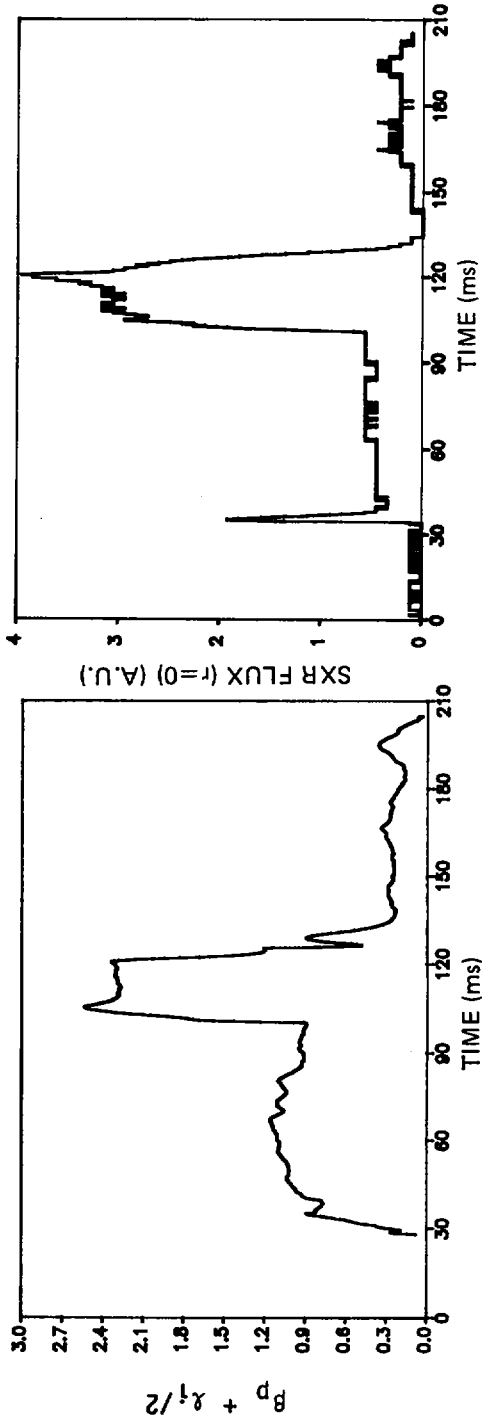


FIG. 1. Typical waveforms during high power current drive experiments at 185 kW, for  $V_L$ ,  $n_e$ ,  $\beta_p + \alpha_1/2$ ,  $I_p$ , horizontal position and SXR flux.

For an 11 kA plasma current at  $\bar{n}_e \sim 3.6 \times 10^{18} \text{ m}^{-3}$  and  $B_\phi \sim 1.04 \text{ T}$  the central electron temperature rise was practically the same: 450 eV (ohmic)  $\rightarrow$  1 keV for 28 GHz and 450 eV  $\rightarrow$  1.15 keV for 60 GHz. However, the range of parameters over which the heating is effective is greater with second harmonic heating.

## CURRENT DRIVE

At 28 GHz the wave was launched in the median plane at about  $80^\circ$  to the magnetic field parallel or anti-parallel to  $I_p$ . The directed launch was obtained by mixing  $TE_{01}$  and  $TE_{11}$  modes and checked by launching the gyrotron output through the entire waveguide system into free space, with far-field antenna patterns recorded on heat sensitive paper. The principal antenna lobe was directed with and against the plasma current, but no discernible differences in the current or loop voltage behaviour appeared, despite a theoretically predicted current of  $\sim 10 \text{ kA}$  (for the far-field launch angles).

60 GHz ECRC experiments utilised a Vlasov antenna, converting a  $TE_{02}$  mode to a single crescent-shaped launch pattern, angled at about  $70^\circ$  to the magnetic field. This theoretical pattern was verified in detail using a real-time

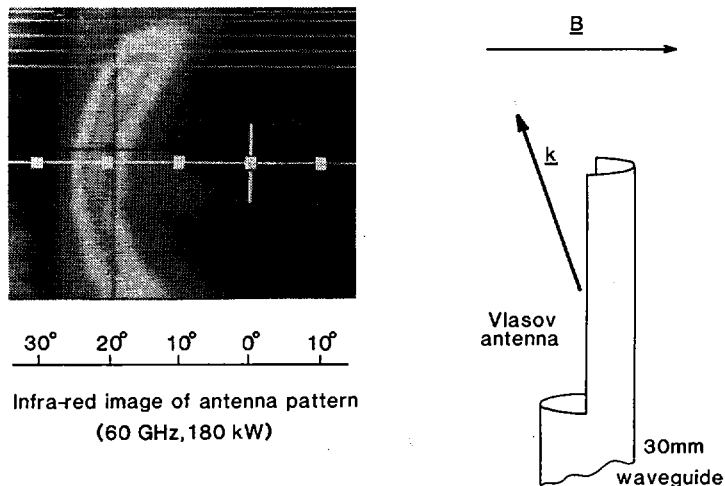


FIG. 2. Far-field infra-red image of antenna pattern for the Vlasov antenna.

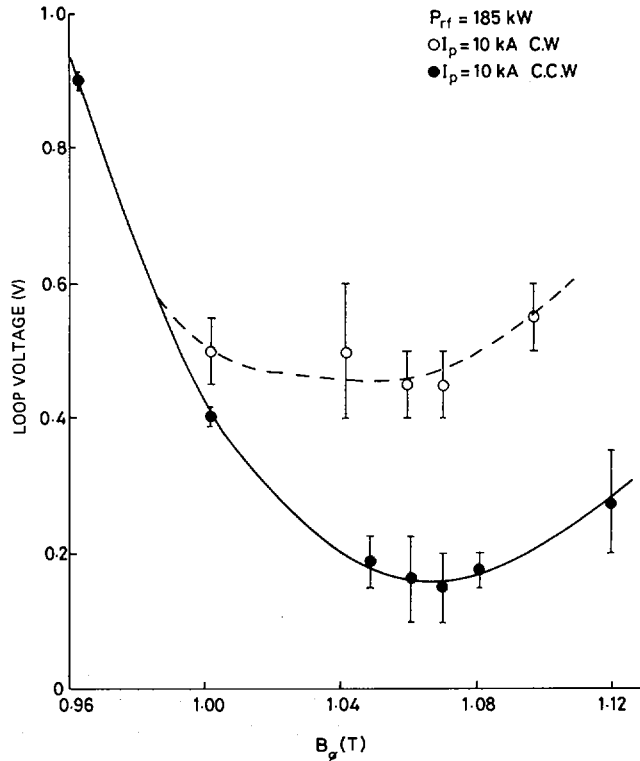


FIG. 3. Loop voltage during ECRH for clockwise and anticlockwise plasma current as a function of toroidal field.

temperature-analysing infra-red camera to look at the result of launching the gyrotron output onto large absorbent tiles, as shown in Fig 2. Calorimetric measurements indicate that 185 kW is radiated into the torus with this directivity, from one 200 kW gyrotron 32 metres, 3 bends and 2 convertors away.

Current drive experiments with this configuration were carried out at  $\bar{n}_e \sim 3.5 \times 10^{18} \text{ m}^{-3}$  (see Fig. 1) and with essentially Maxwellian central temperatures of 1.3 keV at  $I_p = 10 \text{ kA}$  and 1.5 keV at  $I_p = 15 \text{ kA}$ , as deduced from SXR spectra. Reversing the servo-controlled plasma current or the antenna direction produced a clear and consistent difference in loop voltage. Figure 3 shows the difference for a toroidal field scan with both current directions. The theoretical assumption that the ECRH current is essentially the same for each plasma current direction allows its magnitude to be unfolded from the

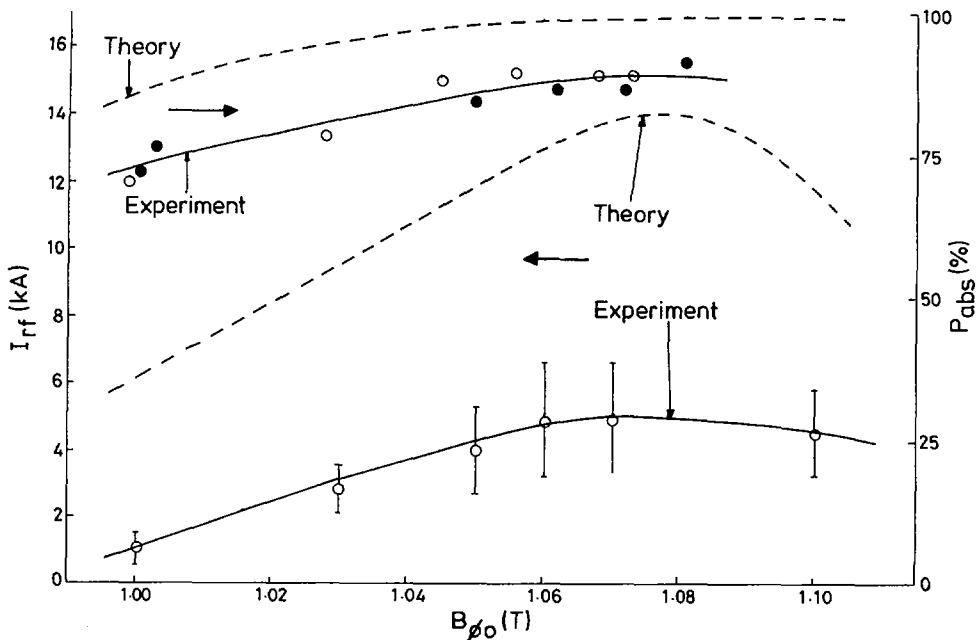


FIG. 4. Comparison of experimental and theoretical values for deduced RF driven current as a function of toroidal field, and percentage absorption as a function of  $B_{\phi}$ , for  $I_p = 10$  kA and  $P_{RF} = 185$  kW. For percentage absorption, the open and closed circles correspond to clockwise and counter-clockwise plasma current, respectively.

loop voltage difference, with the result shown in Fig. 4. The deduced RF current increases with plasma current from 2.5 kA at 5 kA to 5 kA at 15 kA.

A calibrated 'horn receiver' detecting the magnitude of 60 GHz radiation in the torus has been used to estimate the unabsorbed gyrotron power. The absorbed power is typically 80-90% and only a weak function of  $B_{\phi}$ ,  $I_p$  and  $\bar{n}_e$ , indicating the importance of wall reflections for absorption, as theoretically predicted. The wave driven current, however, varies more strongly with  $B_{\phi}$  and  $I_p$ , as shown for example in Fig. 4.

Theoretical calculations of the RF driven current in these experiments have been made using a ray tracing code which includes a current drive model allowing for trapping effects and the weakly relativistic resonance condition [6]. The radiation pattern shown in Fig. 2 was modelled by a bundle of 270 rays.

Plasma profiles of the form  $n_e = n_{e0} (1-r^2/a^2)^2$  and  $T_e = T_{e0} (1-r^2/a^2)^3$  ( $n_{e0}$  and  $T_{e0}$  typically  $0.8 \times 10^{19} \text{ m}^{-3}$  and  $1.3 \text{ keV}$ , respectively) and a hot-core shift of up to 4 cm were assumed, in accordance with the experimental data. The calculations including wall reflections predict greater than 80% absorption, in reasonable agreement with the 'horn receiver' measurements as shown in Fig. 4. With the resonance in the hot core the driven current profile has a half-width of about 3 cm, with an efficiency of typically 60 A/kW. This leads to predicted currents of approximately three times the observed values in the hot core (Fig. 4). As the heating and driven current profiles are somewhat broader than the high- $q$  displaced ohmic profiles, sawteeth suppression is to be expected. In general, this is observed at 15 kA, but, at 10 kA with gas puffing, sawtooth activity has been observed several msec after the RF is applied, with a period  $\sim \tau_E$  and with individual sawteeth showing strong saturation. SXR profile broadening is observed with ECRH at 5, 10 and 15 kA. For these plasmas,  $\bar{\beta}/\beta_{\text{Troyon}} \sim 0.3$ . The calculations show that positioning the resonance away from the magnetic axis leads to broader driven current profiles but only a modest fall in absorption.

The observed loop voltage response to co- and counter-directions is in satisfactory agreement with the predictions of 1D heat and current diffusion calculations using deposition profiles calculated from the ray tracing code.

The interpretation of these results as current drive needs to be treated with caution. Preferential loss of fast electrons carrying toroidal current in one direction could give rise to some of the observed voltage difference, as observed on previous stellarator experiments on CLEO. With a symmetric antenna at 10 kA (but only weakly at 15 kA) the loop voltage response to the ECRH varies with plasma current direction, indicating a preferential loss current in the opposite direction to the net RF currents seen with the Vlasov antenna. The line averaged density and SXR flux profiles are similar for each current direction during the RF but not the  $H\alpha$  emission. In addition, the profiles are sensitive to whether gas puffing is applied to compensate the apparent fall in line density.

The bootstrap current is in the same sense as the total current, and for  $\beta_p \gtrsim 2$ ,  $v_e^* \sim 0.1$ , and with the inferred profiles

it should be  $\sim 6$  kA with a hollow distribution. In the experiment the bootstrap current must be much smaller, as the average decrease in loop voltage corresponds closely to the rise in temperature if the resistivity is neoclassical.

### MODE CONTROL

Experiments on CLEO using 60 GHz  $2\omega_{ce}$  near-axis ECRH have succeeded in raising the disruptive limit for 9 kA discharges at 1.07 T by  $\sim 70\%$ , attaining an I/N value of  $1.0 \times 10^{-14}$  A·m (where  $N = \pi a^2 \bar{n}$ ). Adding vacuum rotational transform to perturb the relative locations of the current density gradients and the  $q=2$  surface has been similarly successful, although the density limit remained disruptive and could only be improved at high  $q$  [7].

Four saddle coils have been added to CLEO, capable of operation at up to 6 kiloampere-turns per winding in four configurations producing predominantly  $(m,n)$ : 1,1; 2,1; 1,0 (3,2) or 2,0 (2,2) (the principal resonant modes of the  $n=0$  options being shown in brackets). Following the successful stabilisation of ohmic heating sawteeth by 1,1 magnetic perturbations in TOSCA [8], experiments have been conducted on CLEO to investigate sawteeth stabilisation using the 1,1 perturbations in the presence of high power  $2\omega_{ce}$  ECRH on axis at 28 GHz since this produces strong sawteeth at high central temperatures. Preliminary results, however, indicate only interference of the sawtooth process and not full stabilisation.

### CONCLUSIONS

ECRH current drive experiments at 60 GHz have shown an asymmetric current component of up to  $\approx 5$  kA for 185 kW injected power. For 28 GHz, second harmonic heating with  $v_e^* \sim 0.01$  and a non-Maxwellian electron distribution function, the energy confinement time is better than the ohmic target plasma, while at 60 GHz with  $v_e^* \sim 0.1$ , near-Maxwellian distributions are obtained but with some confinement degradation. Low- $m$  MHD mode control has been demonstrated in a variety of ways,

significantly raising the disruptive density limit and achieving a measure of sawteeth control, both by using localised ECRH and externally imposed helical fields.

#### ACKNOWLEDGEMENT

The authors would like to thank the CLEO operating team for their valuable support in these studies.

#### REFERENCES

- [1] EDLINGTON, T., et al., in Controlled Fusion and Plasma Heating (Proc. 13th Europ. Conf. Schliersee, 1986), Part II, European Physical Society (1986) 219.
- [2] ROBINSON, D.C., et al., in Plasma Physics and Controlled Nuclear Fusion Research 1984 (Proc. 10th Int. Conf. London, 1984), Vol. 1, IAEA, Vienna (1985) 205.
- [3] SÖLDNER, F., et al., in Controlled Fusion and Plasma Physics (Proc. 12th Europ. Conf. Budapest, 1985), Part II, European Physical Society (1985) 244.
- [4] ROBINSON, D.C., "Small scale turbulence and anomalous transport in magnetized plasmas", in Magnetic Reconnection (Proc. Workshop Corsica, 1986).
- [5] MUKHOVATOV, V., JETP Lett. **33** (1981) 463.
- [6] FERREIRA, A., O'BRIEN, M.R., START, D.F.H., Plasma Phys. Contr. Fusion **26** (1984) 1565.
- [7] TODD, T.N., et al., in Controlled Fusion and Plasma Physics (Proc. 12th Europ. Conf. Budapest, 1985), Suppl., European Physical Society (1985) 76.
- [8] MCGUIRE, K., ROBINSON, D.C., in Controlled Fusion and Plasma Physics (Proc. 9th Europ. Conf. Oxford, 1979), Vol. 1, UKAEA, Culham Lab., Abingdon (1979) D2.7.

#### DISCUSSION

M.C. ZARNSTORFF: How much of your  $\beta_p$  is due to fast electrons? And what is your anisotropy?

D.C. ROBINSON: According to diamagnetic loop and  $\beta_p + \ell/2$  measurements, there is no significant anisotropy in these 60 GHz experiments. The SiLi detector measurements of the electron distribution function show only a slight distortion from Maxwellian at energies of a few times thermal (1.5 keV); thus we believe there is no significant  $\beta_p$  contribution from the fast electrons.

M.C. ZARNSTORFF: After the ECH pulse,  $\beta_p + \ell/2$  dropped to far below the initial Ohmic value. What is the reason for this?

D.C. ROBINSON: In this particular case, the charge came from the toroidal field, which led to some pick-up in the diagnostic; thus the low  $\beta_p + \ell/2$  value is erroneous in this case. With  $\beta_a$  held constant,  $\beta_p + \ell/2$  returns to the previous Ohmic value after the ECRH pulse.

M.A. DUBOIS: On TFR, we have also suppressed sawteeth with ECRH, but our explanation is very different. You say the temperature profile broadens; what diagnostic do you use to measure this?

D.C. ROBINSON: In these experiments the sawtooth is suppressed by current drive and heating. Theoretical calculations predict current and temperature broadening. Broadening of the temperature profile is deduced from soft X-ray measurements with surface barrier diodes and, when combined with density profile measurements, with SiLi detectors.

## CONFINEMENT IN ELECTRON CYCLOTRON HEATING EXPERIMENTS ON DOUBLET III

R. PRATER, S. EJIMA, R.W. HARVEY,  
A.J. LIEBER, K. MATSUDA, C.P. MOELLER,  
and the DOUBLET III PHYSICS GROUP  
GA Technologies Inc.,  
San Diego, California,  
United States of America

### Abstract

CONFINEMENT IN ELECTRON CYCLOTRON HEATING EXPERIMENTS ON DOUBLET III.

Electron cyclotron heating (ECH) experiments have been performed on the Doublet III tokamak in the expanded boundary divertor configuration. Effective ECH is found even at densities twice the cutoff density, with no decrease in the global energy confinement time when the cutoff is exceeded. Analysis of the behaviour of the sawteeth and of the soft x-ray emission indicates that for the overdense discharges ECH takes place near the plasma edge. A simplified transport analysis indicates that the electron thermal transport coefficient decreases by a factor of 2 when the heating is near the edge, while it increases by a factor of 2.5 when the heating is centrally localized. The transport analysis is confirmed by the behaviour of the propagation of the heat pulse when ECH is initiated. The edge heating results in a large improvement in energy confinement over the inner two thirds of the plasma.

### INTRODUCTION

Improvement of energy confinement in tokamaks remains a central objective of the fusion program. Attainment of a mode of improved confinement (the H-mode) has been associated with changes in the plasma edge in previous experiments using neutral injection in tokamaks [1]. Experiments using Electron Cyclotron Heating (ECH) on the Doublet III tokamak have suggested means of improving confinement through direct heating of the plasma edge.

In results presented here, Doublet III was run in the expanded boundary divertor configuration with elongation of 1.5–1.7. The working gas was deuterium. The ECH experiments [2] were carried out using a 60 GHz source with power delivered to the plasma in the range 0.5 to 0.7 MW, for pulses of typical duration 250 msec. The frequency corresponds to a gyroresonance at a field of 2.14 T. The power was launched from the vessel inner wall at the plasma midplane, using oblique launch (30° from the radial at the inner wall) of the extraordinary mode with better than 90% mode purity [3]. The measured launching pattern of the elliptically polarized TE<sub>01</sub> mode has a divergence of 12° FWHM in the vertical plane and 16° in the horizontal plane.

Ray tracing calculations have been performed for this mode and geometry, using the TORAY code [4] for experimentally determined density profiles. In these calculations, the ray trajectory is determined using the cold plasma dispersion relation, and the absorption is integrated along the ray. It is found that the single-pass damping of a group of rays representing the distribution pattern of the antenna is strong up to a line-averaged density of  $\bar{n}_e = 5.6 \times 10^{19} \text{ m}^{-3}$ , at which density the absorption drops rapidly with increasing density, due to refraction of the rays away from the plasma center and to the decrease of the absorptivity with density. This critical density constitutes an effective cutoff density. The maximum local density at which the dispersion relation permits propagation of any polarization or angle is  $8.8 \times 10^{19} \text{ m}^{-3}$  at 60 GHz.

## EXPERIMENTAL RESULTS

In order to experimentally test the anticipated cutoff density, the plasma density was scanned over a wide range,  $1 \leq \bar{n}_e \leq 11 \times 10^{19} \text{ m}^{-3}$ , with ECH power in the range of 0.5–0.7 MW and with the gyroresonance near the plasma axis. The central electron temperature determined from Thomson scattering, Fig. 1a, shows the largest increase at low density near  $2 \times 10^{19} \text{ m}^{-3}$ , where  $\Delta T_e \approx 2 \text{ keV}$ . As the density increases,  $\Delta T_e$  decreases to about 0.3 keV near the critical density, but at densities above the critical density (“overdense”) the temperature increase remains constant at that value.

Similarly, the total plasma energy  $W$ , Fig. 1b, increases by about 20 kJ for all densities above  $2 \times 10^{19} \text{ m}^{-3}$ , with no change as the critical density is exceeded. The plasma energy is determined from MHD equilibrium analysis, using signals from magnetic flux loops and probes. The error in this analysis is estimated to be about 0.1 in  $\beta_p$ , or about 15% in the ECH case. The values for  $W$  generated from measurements of plasma diamagnetism agree with those from MHD analysis within 20%.

The energy confinement time  $\tau_E$ , determined simply from the expression  $\tau_E = W / (P_{OH} + P_{ECH})$ , also shows no degradation as the critical density is exceeded. This behavior is shown in Fig. 1d. In this calculation of  $\tau_E$  the conservative assumption is made that all power incident on the plasma is absorbed, and therefore the plotted  $\tau_E$  value is its lower bound. At the highest densities, the drop in loop voltage during the ECH phase generates a decrease in the ohmic input power which is comparable to the ECH power. For these discharges the incremental confinement time  $\tau_{inc} = \Delta W / \Delta P$  is divergent.

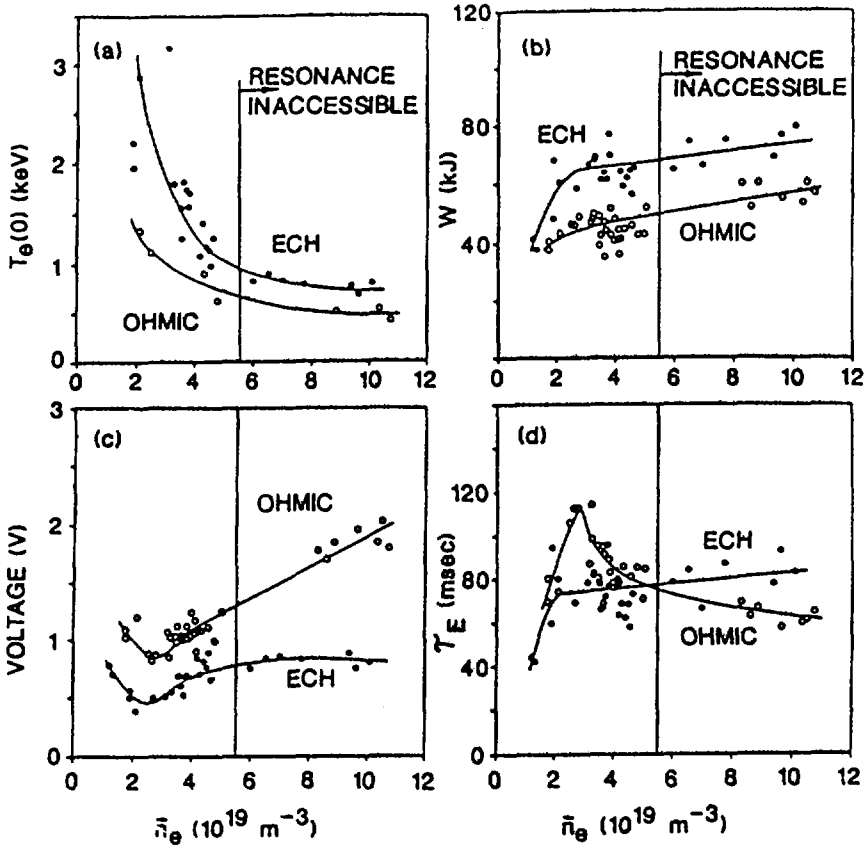


FIG. 1. (a) Central electron temperature from Thomson scattering, (b) total plasma energy from MHD equilibrium analysis, (c) loop voltage on the plasma, and (d) gross energy confinement time, as a function of line averaged density. The hollow circles are taken from ohmic times and the filled circles are from ECH times. The toroidal field is 2.1 T and the plasma current is 500 kA.

The improvement in confinement time over the ohmic confinement time for the overdense heating case may not be significant, since the ohmic phase of the discharge is rather unusual. In particular, it is characterized by the presence of a volume of very high density (a "Marfe" [5]) at the inner wall of the plasma chamber. This high density region can be clearly identified in the radiated power signals from the bolometer, which examines 21 chords in a plane of constant toroidal azimuth from the outside midplane. The Marfe appears to have a crucial role in the development of the ohmic discharge and in the attainment of densities nearly a factor two beyond the usual experimental density limit for Doublet III of  $\bar{n}_e (10^{19} \text{ m}^{-3}) \leq 27 \times B_T/Rq$  (in MKS units), but it also

seems to cause a reduction in confinement similar in magnitude to that of a transition from divertor to limiter configuration [6]. The  $D_\alpha$  radiation from the top of the plasma is also similar in magnitude to that found near a limiter in normal limiter discharges. When the ECH is applied, the Marfe moves rapidly downwards into the divertor region where it dissipates [7], and within 6 msec from the start of the ECH the discharge has evolved into a normal well-behaved divertor configuration, except that it has unusually high density.

An immediate question arises regarding the overdense heating case: does the ECH power get absorbed near the plasma center where the gyroresonance lies, but where the dispersion relation forbids propagation, or is the power absorbed at some other location where the resonance condition is met but the density is lower?

One way to address this question is to examine the behavior of the sawteeth when ECH is applied. At densities low enough that refraction is not important, the ECH power can be concentrated within a few cm of the magnetic resonance. When the gyroresonance is located near the plasma center the ECH power density can be much larger than the ohmic power density, with the result that the power applied to the volume within the  $q=1$  surface increases and that the gradient of the electron temperature evaluated at the  $q=1$  surface tends to increase. Both of these effects may be expected to decrease the sawtooth period  $\tau_{st}$  [8]. Similarly, placing the ECH power outside the  $q=1$  surface by shifting the location of the resonance reduces the power input within that surface

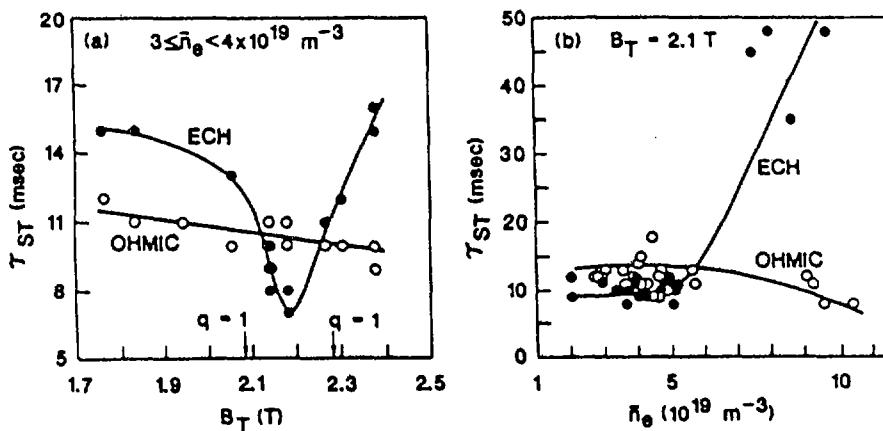


FIG. 2. Sawtooth period as a function of (a) toroidal field, for  $I_p = 350$  kA and  $3.0 < \bar{n}_e < 4.0 \times 10^{19} \text{ m}^{-3}$ , and (b) density, for  $I_p = 500$  kA and  $B_T = 2.1$  T. ECH power is 0.5–0.7 MW.

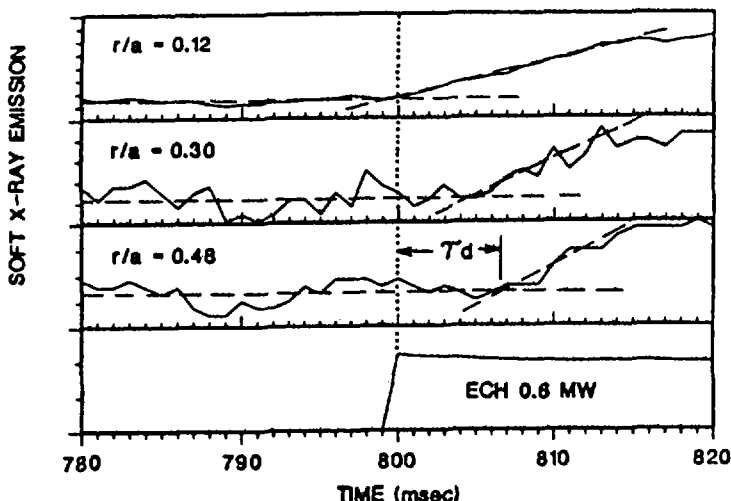


FIG. 3. SXR emission temporal response along three chords. The ECH is initiated at 800 msec. The toroidal field is 2.2 T, the plasma current is 350 kA, and the density is  $\bar{n}_e = 3.5 \times 10^{19} \text{ m}^{-3}$ .

since the loop voltage drops when the ECH is added. It also tends to flatten the electron temperature profile near the  $q=1$  surface. This should result in an increase in the sawtooth period. These effects are observed in ECH experiments in moderate density plasmas when the resonance is scanned across the plasma, Fig. 2a. Placing the resonance within the  $q=1$  surface results in a decrease in  $\tau_{st}$ , and placing the resonance outside the  $q=1$  surface results in an increase in  $\tau_{st}$ .

When the resonance is maintained near the plasma center and the density is scanned,  $\tau_{st}$  displays the expected decrease from the ohmic phase to the ECH phase consistent with central heating when the density lies below the critical density, as shown in Fig. 2b. But above the critical density the sawtooth period exhibits an increase of a factor five when ECH is added. This suggests that when the critical density is exceeded, the radius of power deposition shifts from the plasma center to much further out on the temperature profile.

Evidence of a more direct nature comes from the soft x-ray (SXR) emission behavior of the plasma when ECH is initiated. Propagation of the ECH-generated heat pulse through the plasma can be followed by plotting the delay in the first appearance of increase in the SXR emission on the various chords. This method has also been used in ECH experiments on T-10 [9].

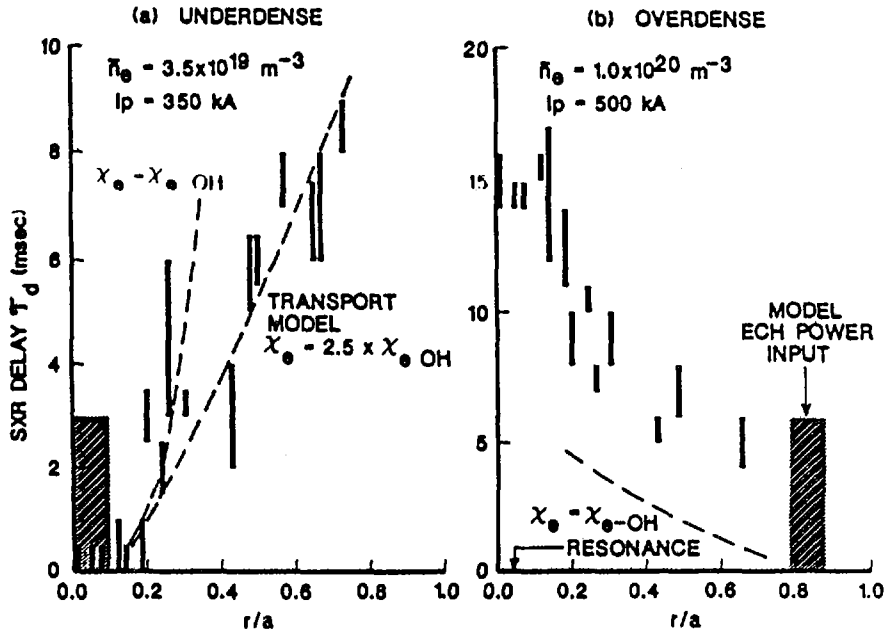


FIG. 4. SXR delay time  $\tau_d$  (defined in Fig. 2) plotted against relative minor radius: (a) underdense discharge ( $\bar{n}_e = 3.5 \times 10^{19} \text{ m}^{-3}$ ) from Fig. 2, and (b) overdense discharge ( $\bar{n}_e = 1.0 \times 10^{20} \text{ m}^{-3}$ ,  $n_e(0) = 1.6 \times 10^{20} \text{ m}^{-3}$ ), with  $B_T = 2.1 \text{ T}$  and  $I_p = 500 \text{ kA}$ . The dashed lines show the results from a transport model for various values of  $\chi_e$ . Also shown is the assumed location (shaded area) of the input ECH power used in the model.

An example of SXR data from a discharge with density well below the critical density ( $\bar{n}_e \approx 3.0 \times 10^{19} \text{ m}^{-3}$ ) and with centrally located resonance is shown in Fig. 3. The 32 SXR chords, which lie in a plane of constant azimuth, are parameterized by the relative minor radius  $r/a$  of the flux surfaces to which they are tangent. The increase in SXR emission is prompt from chords with  $r/a \leq 0.15$  but delayed for chords away from center, and the delay increases with distance. Outside of about  $r/a \approx 0.7$  the signal-to-noise ratio becomes too small for this type of analysis.

The direction and magnitude of the propagation speed of the heat pulse can be determined from a plot of the SXR delay  $\tau_d$  as a function of minor radius. Figure 4a shows  $\tau_d$  for the same low density discharge as Fig. 3, and Fig. 4b shows data from an overdense discharge. It is clear from Fig. 4 that in the underdense case the heat propagates radially outward from the center, while for the overdense case the heat propagates in an inward direction, at least for  $r/a \leq 0.7$ . It may be concluded

from this that for the underdense case the ECH power is being deposited within a radius of 0.15 while for the overdense case the ECH power is deposited somewhere outside of  $r/a=0.7$ .

## Modeling

The ONETWO transport code [10] has been used to model transport in ECH discharges in Doublet III. The inputs to the code include the directly measured quantities, such as the toroidal field, the plasma current, the plasma geometry from the MHD equilibrium analysis, the electron temperature profile, the density profile, and the radiated power profile. The electron temperature profile is measured using second harmonic electron cyclotron emission, and the density profile is determined by unfolding data from a three-channel interferometer, using the actual flux surface geometry to determine chordal path lengths. The radiated power profile is measured by the 21-channel bolometer. For these sawtooth discharges, the central  $q(0)$  is input as 1. The impurity density is assumed to be oxygen, and it is adjusted in an iterative manner to obtain  $q(0)=1$  given the loop voltage  $V_L$ . Further inputs are the ECH power profile as calculated by TORAY and the assumption that the ion thermal conductivity is neoclassical [11]. The time-dependent electron and ion heat equations and the current density diffusion equation using Spitzer conductivity are solved, keeping the density profiles constant. Code outputs are  $\chi_e(r)$ ,  $T_i(r)$ ,  $V_L$ , plasma kinetic energy  $W$ , and global energy confinement time  $\tau_E$ , which are compared with the experimental data.

Analysis of discharge #44055, from which data in Fig. 2 was taken, showed that a good fit to  $T_e(r)$ ,  $V_L$  and  $W$  was obtained with  $\chi_e$  nearly constant across the profile, for the ECH power deposited within  $r/a=0.15$ . The value of  $\chi_e$  so determined during the ECH steady state phase is  $0.8 \text{ m}^2/\text{sec}$ , about 2.5 times its value during ohmic heating in the same discharge, which accounts for the observed decrease in gross energy confinement time from 100 msec before ECH to 54 msec during ECH. The change in the global confinement time when ECH is added represents the transition from the ohmic scaling to the scaling for discharges dominated by auxiliary heating, which is obtained whether the auxiliary heating is ECH or neutral beam injection [12].

An alternative way to determine  $\chi_e$  is to follow the propagation of the heat pulse at the onset of ECH. The ONETWO code calculates the

SXR emission along the chords corresponding to the SXR diode array geometry, and the delay between the application of ECH and the start of the rise of the calculated emission can be compared with experiment. This delay  $\tau_d$  is plotted for two values of  $\chi_e$  as the dashed lines in Fig. 4a. It is clear from the figure that  $\tau_d$  is sensitive to the value of  $\chi_e$  used in the calculation, and that the value for  $\chi_e$  of 2.5 times that of the ohmic heating phase is a good fit to the data. This implies that the magnitude of the thermal conductivity as determined by heat pulse propagation is close to that determined by analysis of the final steady state, and that the increase in  $\chi_e$  from ohmic to ECH occurs throughout the plasma on the time-scale of the heat pulse propagation.

The overdense ECH discharges have also been analyzed using the ONETWO code, although  $T_e$  profiles from electron cyclotron emission are not available, due to cutoff of the  $2\omega_{ce}$  radiation. In order to proceed with analysis, the thermal conductivity is assumed to be spatially constant and the  $T_e$  profile is calculated (assuming a boundary temperature  $T_{eb}$ ). Following the conclusion from Fig. 4b that the heat propagates inward, the ECH power is modeled as being deposited near  $r/a=0.8$ . The requirement that the central temperature and the total plasma energy match the experiment places a constraint on the  $T_e(r)$  shape, with the principal uncertainty coming from the ion transport (mainly through the assumed value of  $\chi_i$ ) and from the uncertainty in  $T_{eb}$ . If the calculated electron temperature profile is parameterized for convenience of discussion as  $T_e(r) = (T_{e0} - T_{eb})(1 - r^2/a^2)^{\alpha_T} + T_{eb}$ , and assuming  $T_{eb}=0.2$  keV, this constraint places the limits  $2.0 \leq \alpha_T \leq 2.5$  on the profile parameter, which means that the  $T_e$  profile remains rather peaked during the ECH. Lower  $T_{eb}$  produces fits with smaller  $\alpha_T$ , but even  $T_{eb} = 0$  implies that  $\alpha_T > 1.5$ , in order for the plasma energy to match experiment. The conclusion that the electron temperature profile remains rather peaked is also consistent with the determination of the internal inductance,  $l_i \approx 1.5$ , which doesn't change much during the ECH.

The value of the average  $\chi_e$  determined from this simplified treatment is about  $1 \text{ m}^2/\text{sec}$  during ohmic heating, and during ECH it decreases a factor two to  $0.5 \text{ m}^2/\text{sec}$ . Although Fig. 4b clearly shows propagation of the heat pulse toward the plasma center, comparison with the model is considerably complicated by the process of the dissipation of the Marfe, which takes about 6 msec. In addition, for the model the determination of  $\tau_d$  for locations near the plasma center is ambiguous, due to smearing out of the leading edge of the heat pulse. Nevertheless, it may be concluded from Fig. 4b that the thermal diffusivity determined from heat propagation is not larger than that during the ohmic phase.

## DISCUSSION AND SUMMARY

In the overdense heating case, the central energy confinement time improves dramatically. The behavior of both the sawtooth period and the SXR emission imply that the ECH power is not being deposited near the resonance at the plasma center, in violation of the dispersion relation, but rather that the plasma edge is being heated. The drop in the loop voltage from 2 V prior to ECH to 0.8 V during ECH, Fig. 1c, indicates that the ohmic power decreases at the plasma center; however, the classical skin time is longer than the ECH pulse length, and the plasma modeling for this case indicates that a central voltage drop to 1.3 V takes place at the plasma center during ECH. But the measured central density is constant and the central electron temperature increases from about 0.5 keV to 0.8 keV. These observations imply that the central energy confinement time increases from 70 msec before ECH to 190 msec during ECH.

A similar conclusion may be reached concerning the plasma within  $r/a=0.7$ : the confinement time for this volume of plasma increases by a factor 2 to 2.5, with the caveat that the electron temperature profile is only inferred from the measurement of central temperature and of total plasma energy. The conclusion that confinement strongly improves is not very sensitive to the details of the electron temperature profile, but depends mainly on the absence of ECH power within  $r/a=0.7$  [7].

Shifting the location of the resonance by changing  $B_T$  for underdense plasma produces a similar effect. Over the range  $1.8 \leq B_T \leq 2.5$  T, for which the resonance moves from  $r/a = -0.5$  to  $+0.5$ , the global energy confinement is constant [2]. (This result has also been seen in T-10 ECH experiments [13].) This implies improvement in the central energy confinement as the heating is moved off axis. Neutral beam heating experiments on TFTR [14] and ASDEX [15] have also shown similar results when the depth of the neutral beam penetration is reduced by operating with high plasma density or reduced beam energy. In those cases, a very long energy confinement time near the axis was observed. The high density heating case reported here with power deposition at  $r/a > 0.7$  may correspond to an extreme case of these results.

The physical bases behind these observations are not well understood. It is possible that a heat diffusivity which is dependent on the gradient in  $T_e$  may account for this behavior. A heat diffusivity which is proportional to  $(\nabla T_e)^2$  has been derived [16], and this strong dependence on the profile could result in the observed independence of the increase in stored energy on the profile of the heating. At the same time, it is observed that the transition to H-mode is closely associated

with changes in the plasma edge. It may be that direct edge heating is an important ingredient in the mix of conditions that produces the H-mode. Experiments aimed at edge heating in DIII-D at low density using second harmonic ECH are planned to try to clarify this.

### ACKNOWLEDGMENT

This work was supported jointly by the U.S. Department of Energy and by the Japanese Atomic Energy Research Institute under Contract Nos. DE-AT03-84ER51044 and DE-AT03-80SF11512. We would like to thank T. Ohkawa and D. Overskei for their encouragement during this work. ECH engineering support from D. Remsen and D. Bell and operational support from R. Callis and his group are also gratefully acknowledged.

### REFERENCES

- [1] WAGNER, F., et al., Phys. Rev. Letters **49** (1983) 1408.
- [2] PRATER, R., BURRELL, K.H., EJIMA, S., JAHNS, G.L., LIN, S.H., MOELLER, C.P., Summary of Electron Cyclotron Heating Physics Results from the Doublet III Tokamak, GA Technologies Report GA-A17939 (1985).
- [3] MOELLER, C.P., PRATER, R., LIN, S.H., The 60 GHz Transmission System for the Doublet III ECH Experiment, GA Technologies Report GA-A16979 (1983).
- [4] KRITZ, A.H., HSUAN, H., GOLDFINGER, R.C., BATCHELOR, D.B., Proc. 3rd Joint Varenna-Grenoble International Symposium on Heating in Toroidal Plasmas, Grenoble (Euratom Report EUR7979 EN), v. II (1982) 707.
- [5] LIPSHULTZ, B., LABOMBARD, B., MARMAR, E.S., PICKRELL, M.M., TERRY, J.L., et al., Nucl. Fusion **24** (1984) 977.
- [6] OHYABU, N., BURRELL, K.H., DeBOO, J., EJIMA, S., GROEBNER, R., et al., Nucl. Fusion **25** (1985) 49.
- [7] EJIMA, S., PRATER, R., Interpretation of Electron Cyclotron Heating Results in Overdense Plasma in Doublet III, GA Technologies Report GA-A18535 (1986), submitted to Nuclear Fusion.
- [8] McGUIRE, K., ROBINSON, D.C., Nucl. Fusion **19** (1979) 505.
- [9] ALIKAEV, V.V., RAZUMOVA, K.A., in Course and Workshop on Applications of RF Waves to Tokamak Plasmas (International School of Plasma Physics, Italy EUR 10333 EN), v. I (1985) 377.
- [10] PFEIFFER, W., et al., GA Technologies Report GA-A16178 (1980).

- [11] CHANG, C.S., HINTON, F.L., Phys. Fluids 25 (1982) 1493.
- [12] BURRELL, K.H., PRATER, R., EJIMA, S., et al., in Plasma Physics and Controlled Nuclear Fusion Research (Proc. 10th Int. Conf. London, 1984), IAEA, Vienna, v. I (1985) 131.
- [13] ALIKAEV, V.V., ARSENTIEV, Yu.I., BAGDASAROV, A.A., BEREZOVSKIJ, E.L., BORSHEGOVSKIJ, A.A., et al., in Plasma Physics and Controlled Nuclear Fusion Research (Proc. 10th Int. Conf. London, 1984), IAEA, Vienna, v. I (1985) 419.
- [14] MURAKAMI, M., ARUNASALEM, V., BELL, J.D., BELL, M.G., BITTER, M., et al., Plasma Physics and Controlled Fusion 28 (1986) 17.
- [15] WAGNER, F., GRUBER, O., LACKNER, K., MURMANN, H.D., SPETH, E., et al., Phys. Rev. Letters 56 (1986) 2187.
- [16] GUZDAR, P.N., LIU, C.S., DONG, J.Q., LEE, Y.C., Bull. Am. Phys. Soc. 31 (1986) 1100.

#### DISCUSSION

R.J. GOLDSTON: There is an inductive term in the power balance of the form  $\frac{1}{2} I_p^2 (d/dt) L_i$ .  $L_i$  can be measured from MHD fitting, or from a combination of MHD fitting and diamagnetism in a high density isotropic plasma. Could you comment on the size of this inductive term?

R. PRATER: This term is quite small since very little change is found in the internal inductance during ECH, even with off-axis heating.



## ELECTRON CYCLOTRON HEATING ON TFR

H.P.L. DE ESCH, J.A. HOEKZEMA, W.J. SCHRADER,  
E. WESTERHOF, W. KOOIJMAN, R.W. POLMAN, T.J. SCHEP  
Association Euratom-FOM,  
FOM Instituut voor Plasmafysica,  
Rijnhuizen, Nieuwegein, Netherlands

### EQUIPE TFR

Association Euratom-CEA sur la fusion,  
CEA, Centre d'études nucléaires de Cadarache,  
Saint-Paul-lez-Durance, France

*Presented by M.A. Dubois*

### Abstract

#### ELECTRON CYCLOTRON HEATING ON TFR.

Results are presented of the joint Euratom-CEA, Euratom-FOM electron cyclotron heating experiments on TFR (March 1985 to June 1986). Up to 500 kW of 60 GHz power was launched into TFR; with central heating, a central electron temperature up to 5 keV was obtained.

#### 1. INTRODUCTION

The ECRH facility on TFR comprised three 60 GHz gyrotrons, each delivering over 200 kW for 100 ms in the TE<sub>02</sub>-mode. In the three transmission lines conversion to TE<sub>11</sub> was realized with an efficiency of approximately 70% (0-mode into TFR over gyrotron output) [1]. The open oversized waveguide antennae were located in the same poloidal cross-section, in the horizontal plane and at + and -15°, and were aimed at the toroidal axis [1]. The full 3 dB beam width on axis was about 3 cm. Facing two of the antennae was a concave corrugated reflector (10° oblique), converting transmitted power into the extraordinary mode at 20° off the meridian plane. The third, upper, antenna had a 16° angle with the meridian plane.

Experiments began in March 1985 with one gyrotron at 100 kW, 30 ms with a smooth, concave, roof-top-shaped reflector (angles ± 10°) on the inboard torus wall [2]. Full power (500 kW into TFR for 100 ms) experiments were done between September 1985 and June 1986 [3,4,5]. TFR was operated with carbon limiters. The parameters in the ohmic regime varied over the range:

$$B(0) = 1.8 \text{ to } 2.7 \text{ T}; n_e(0) = (1 \text{ to } 5) \times 10^{19} \text{ m}^{-3}; I_p = 40 \text{ to } 160 \text{ kA}$$

Under iron-free plasma conditions, two ohmic regimes were obtained: At low plasma current ('L.C.':  $I_p < 105$  kA) no MHD activity was observed and  $\tau_E \geq 8$  ms, while at high current ('H.C.':  $I_p > 105$  kA) strong saturated MHD activity coincided with  $\tau_E \leq 5$  ms. When iron was present (due to a calorimeter in the shadow of the limiter), the iron-dominated regime ('I.D.') showed no such clearcut differences with  $I_p$ , and MHD, when present, tended to be erratic or explosive.

## 2. HEATING

When the resonance is located near the magnetic axis, for average ohmic plasma parameters 60-70% of the power should theoretically be absorbed in the first pass. Because of  $T_e$  increase during ECRH, this figure should rise over 90%. Measurements of the transmitted power, using small holes in the mirror, indicate that at least the expected absorption takes place. For the  $\tau_E$ -calculation, we have assumed that the total injected power is absorbed. This is probably slightly pessimistic since over 10% of the power is injected in the X-mode. When the resonance is set off-centre, a large fraction of the power is transmitted through the plasma. Especially at low densities, the reflected, X-mode power is mostly absorbed by suprathermal electrons, for which confinement can be completely different from that of the bulk. Experimentally it is found that the increase of plasma energy (not counting a possible suprathermal population) has a maximum around central heating and falls abruptly when the resonance is displaced off-centre by more than  $a/3$ . This is illustrated in Fig. 1, which is valid irrespective of the regime (although in the I.D. regime the off-centre displacement was limited to  $\pm a/3$  due to disruptions [4]).

For central heating, the degradation of confinement with ECRH power in the different regimes is shown in Fig. 2 for intermediate density. It is clear that in the L.C. regime the confinement is substantially degraded even with a small amount of additional heating; with ECRH, the difference between the regimes disappears. At lower density, the degradation of energy confinement is much less (apart from the disappearance of the L.C. regime): confinement may even improve, while at higher densities the degradation is worse. This is due for a large part to density behaviour: at high density, a strong pump-out is observed in the centre, while at low density an increase of density is seen. Combining discharges at different densities in the ohmic phase to obtain the  $\tau_E$ -value at constant density for different power levels, we find only a limited reduction of  $\tau_E$  (Fig. 2).

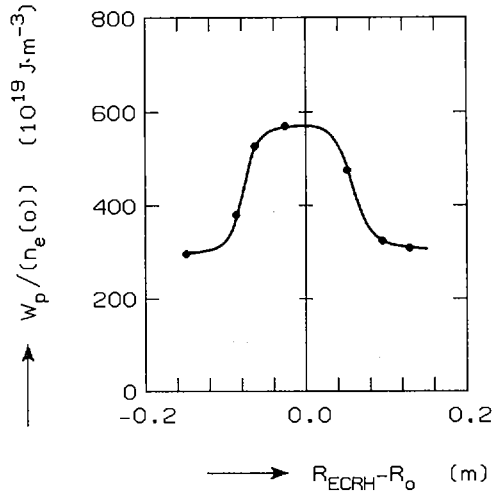


FIG. 1. Plasma kinetic energy ( $T_e$  from Thomson scattering) as a function of resonance layer position  $I_p = 90$  kA,  $n_e(0) = 2 \times 10^{19} \text{ m}^{-3}$ ,  $P_{\text{ECRH}} = 250$  kW,  $P_0 = 110$  kW (without ECRH).

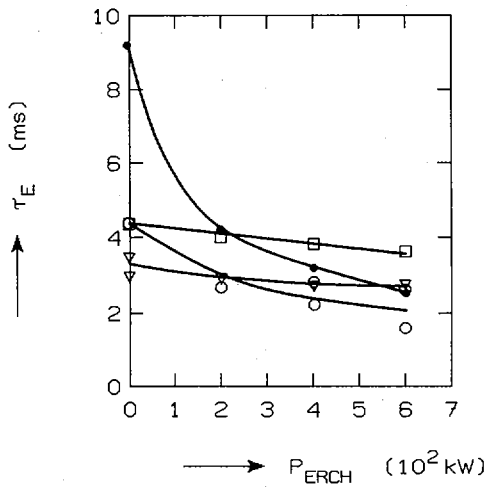


FIG. 2. Energy confinement time as a function of centrally deposited ECRH power in three different regimes, at  $\bar{n}_e \approx (1-1.5) \times 10^{19} \text{ m}^{-3}$ :

- L.C.,  $I_p \approx 100$  kA
- ▽ H.C.,  $I_p \approx 115$  kA
- I.D.
- I.D. at constant central density:  $n_e(0) = 2.8 \times 10^{19} \text{ m}^{-3}$ .

Transport simulations using the MAKOKOT code were presented [4,5] with the conclusions that with ECRH,  $\chi_e$ -scaling is proportional to  $rT_e^{1/2}/(n.q)$  and that the pump-out can be explained by a combination of the  $rT_e^{1/2}/(n.q.)$  dependence of the diffusion coefficient, the decrease of the neoclassical pinch velocity, and enhanced recycling. Besides, the energy confinement time dependence with injected power is well described by this scaling. Simulations with the ICARUS code have also been performed, and a very good agreement is obtained both at high and low density in the I.D. regime for

$$\chi_e = 4 \times 10^{19} \cdot \frac{T_e^{1/2}(r)}{n_e(0)} \cdot \exp\{-3.2(1 - \frac{r^2}{a^2})\}$$

see Fig. 3. This  $\chi_e$ -profile is very close to twice the value proposed by TANG [6].

At low density where diffraction of the ECRH beam in the plasma is weak, a very high central temperature ( $T_e$  up to 5 keV as measured by Thomson scattering and ECE) is obtained in a narrow central spike, too narrow for the ECE spatial resolution. Using discharges with the resonance on the magnetic axis but at slightly different horizontal positions, a fine central  $T_e$ -profile was obtained from the central channel of Thomson scattering: Fig. 4.

The width of the central  $T_e$ -spike (3 cm) is in agreement with the antenna pattern. The height of the spike indicates that confinement inside  $q=1$  is degraded but, despite the very large  $\nabla T_e$ , not dramatically. The inequality  $R \cdot \nabla T_e \leq 13$  keV is fulfilled outside  $q=1$ , as proposed in [7], but much larger gradients can be obtained inside  $q=1$ . This is a strong incentive to stabilize sawteeth on larger machines where the energy content inside  $q=1$  is considerable.

In our experiment, although gradients inside  $q=1$  can reach very high values, sawteeth are not very conspicuous: even when  $T_e(0)$  is larger than 3 keV, the sawtooth drop  $\delta T_e(0)$  is less than 700 eV: the temperature is not flattened completely inside  $q=1$ . When heating is applied outside  $q=1$ , sawteeth are not affected. When heating is applied in the centre, sawteeth are also unaffected, except at high density, in which case the period decreases. More interesting is sawtooth behaviour when the ECRH layer is at the radius of the surface  $q=1$ : in those conditions, an increase of the sawtooth period is observed, corresponding to a larger delay between  $m=1$  growth and internal disruption: the crash is triggered for a larger island size than in ohmic regimes. At high density, sawteeth can disappear, replaced by a saturated  $m=1$  mode. This behaviour can be attributed to a local modification of the  $T_e(r)$ - (and hence  $j(r)$ -) profile. It is a direct effect on the sawtooth trigger and not a mere modification of the regeneration slope as in other experiments.

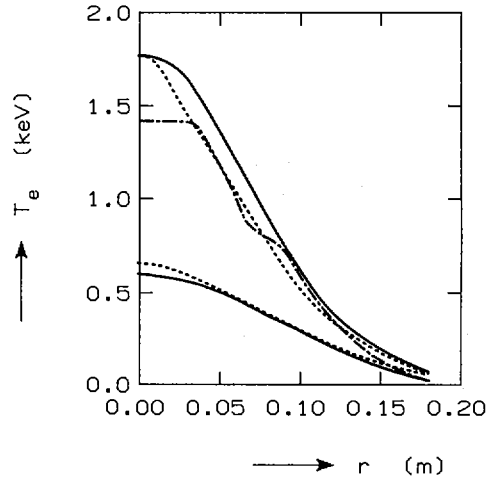


FIG. 3. Electron temperature profiles in the Ohmic regime and with full ECRH power at high density ( $\bar{n}_e = 2.2 \times 10^{19} \text{ m}^{-3}$ ) in the I.D. regime and resonance located at the centre:  
 — ECE  
 - - - Thomson scattering  
 ..... profiles from transport code simulation (ICARUS).

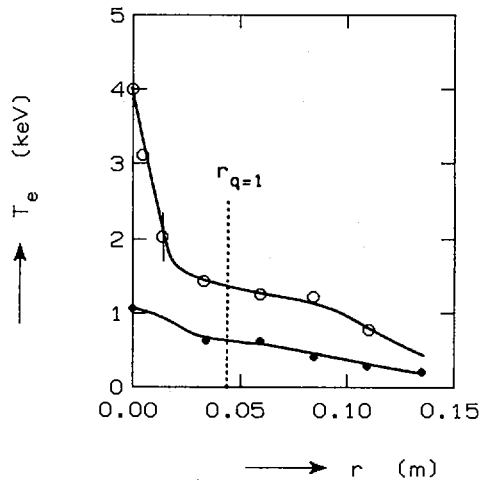


FIG. 4. Thomson scattering  $T_e$  profile (for a low-density discharge ( $\bar{n}_e \approx 0.8 \times 10^{19} \text{ m}^{-3}$ ) at full central ECRH ( $\circ$ ) and with ohmic heating only ( $\bullet$ ).

An estimate of the ECRH deposition profile can be obtained from a measurement of the immediate change of the local  $T_e$  after ECRH switch-on. The soft X-ray emission profile was used to determine this profile and confirms the localization, in case of central heating, mainly within a radius of 2 cm. Analysis of heat pulse propagation experiments is not yet completed and will be published later on.

### 3. IMPURITY BEHAVIOUR

With central heating, no deleterious effect in impurity production is observed during ECRH. A slight enhancement of metal production is suspected from preliminary numerical simulations, but lower than 50%. Highly ionized ion lines (e.g. Fe XXIII) appear during ECRH, indicating increased ionization degree as a consequence of the strong electron heating. When the ECRH layer is far off-centre,  $B\phi \sim 1.8$  T or  $B\phi \sim 2.4$  T ( $2.14$  T = central heating) strong increase of line radiances is observed implying increased central ion densities by a factor of  $\sim 2$  for light impurities and  $\sim 2$  to  $3$  for metal impurities, probably as a result of transmitted power.

### 4. STABILIZATION

In the H.C. regime, where in the ohmic regime saturated  $m=2$  modes are present, application of microwave power has been shown able to suppress the  $q=2$  tearing mode in two different situations:

- when the resonance is applied on the magnetic axis: energy increase leads to an outward shift and, contact with the inner limiter being reduced, the  $q=2$  mode disappears as  $q_a$  increases. In some cases where low-power ECRH was applied in comb-like pulses, stabilization was obtained without a marked outward shift, but coincided with a better horizontal position regulation induced by ECRH: here also, interaction with the limiter was reduced.
- when the power is applied just outside the  $q=2$  surface [2,3], the mode is also suppressed. The absorbed power is very small and does not directly explain an outward shift. Two explanations are then possible: 1) local temperature gradient modification leads to a  $j(r)$  change and, hence, to tearing-mode stabilization. The subsequent confinement improvement allows ohmic heating to increase the particle and energy content, leading to outward shift; 2) the non-absorbed power falls on the vacuum vessel, causing enhanced degassing and, consequently, a density and energy increase, which leads to an outward shift and subsequent stabilization. A careful analysis shows that  $m=2$  activity starts to decrease as soon

as  $q_a$  rises above a critical value ( $\sim 3.3$ ) and rises again when  $q_a$  drops below a sometimes different value (3.1 to 3.3). If the current is too high, the change of  $q_a$  induced by ECRH is too small to cross this value, and MHD activity persists. So, although stabilization has been routinely achieved with ECRH, and even with a feedback loop [3], we are led to conclude that at least when the mode-converting mirror was in use, the first mechanism is occulted by the second, which is of less physical interest. A better prospect will be open with larger machines at higher densities and temperatures.

## 5. SUPRATHERMAL GENERATION AND PELLET ABLATION

Creation of suprathermal electrons has been demonstrated at low densities. As previously mentioned, they outlast the ECRH pulse [2], showing the good quality of confinement inside  $q=1$ . In low-density regimes, even a short ECRH pulse can trigger the discharge to a suprathermal  $2\omega_{ce}$  emission regime. For  $n_e(0)$  below  $1.5 \times 10^{19} \text{ m}^{-3}$ , the ECE is completely dominated by suprathermals; between  $1.5$  and  $2.5 \times 10^{19} \text{ m}^{-3}$  ECE profiles show an asymmetry which is most likely due to suprathermal trapped electrons. Above, the ECE and Thomson-scattering  $T_e$ -profiles are similar.

A natural step was to try current-drive experiments with ECRH. The result [3] is negative: all the effects observed between 2.14 and 2.40 T are explainable by the resistivity decrease due to bulk heating. At higher fields, no effect is observed. As has been explained previously [5] this negative result is likely to be due to a depletion effect of the electron distribution function when the resonance is applied far from the bulk of the maxwellian. This depletion effect at intermediate energies, seen on the SiLi diagnostic and confirmed in numerical simulations, is accompanied by population increase at higher energies, mainly in the perpendicular direction, which is responsible for the suprathermal  $2\omega_{ce}$  emission. A direct evidence for this very energetic tail is the behaviour of deuterium pellets injected into ECRH-heated plasmas: they are sublimated differently than in normal ablation cases, and the radius at which they are sublimated is directly linked to the ECRH layer.

## ACKNOWLEDGEMENT

The Netherlands' contribution to this work was performed under the Euratom-FOM association agreement with financial support from ZWO and Euratom.

## REFERENCES

- [1] VAN DER GEER, C.A.J., *et al.*, and CRENN, J.P., *et al.*, in *Fusion Technology* (Proc. 14th Symp. Avignon, 1986), Pergamon Press, Oxford (1987).
- [2] FOM-ECRH TEAM and TFR GROUP, in *Controlled Fusion and Plasma Physics* (Proc. 12th Europ. Conf. Budapest, 1985), Vol. 9F-II, European Physical Society (1985) 60.
- [3] TFR-GROUP, HOEKZEMA, J.A., *et al.*, in *Electron Cyclotron Emission and Electron Cyclotron Resonance Heating* (Proc. 5th Int. Workshop San Diego, CA, 1985) 154.
- [4] TFR-GROUP and FOM-ECRH-TEAM, in *Controlled Fusion and Plasma Heating* (Proc. 13th Europ. Conf. Schliersee, 1986), Vol. 2, European Physical Society (1986) 207.
- [5] JACQUET, J., PAIN, M., *ibid.*, p. 215.
- [6] TANG, W.M., *Microinstabilities Based Confinement Model for Enhanced Transport*, Rep. PPPL-2311, Princeton Plasma Physics Laboratory (1986).
- [7] TFR GROUP, *Plasma Phys. Contr. Fusion* **28** (1986) 85.

## DISCUSSION

A. GIBSON: Is there any threshold power for the sawtooth stabilization which you describe, and are you able to compare the power required for stabilization with any theoretical expectation?

M.A. DUBOIS: A strong effect was observed even when one gyrotron only was used with ECRH on  $q = 1$  (power  $\sim 150$  kW). We did not try to use a lower power level. I do not expect any threshold, but rather a linear relationship at low power, namely, the increase in the sawtooth period is approximately equal to the ECRH power.

A.C. RIVIERE: In connection with the observation of a narrow high peak in  $T_e$  for central resonance, how far did you have to move the resonance off axis so that this steep narrow peak in  $T_e$  disappeared? Further, how important were the sawtooth oscillations for these measurements?

M.A. DUBOIS: The peak was maximum and narrowest for central heating, but a really visible peak existed as long as ECRH was applied inside  $q = 1$ .

With regard to your second question, the maximum amplitude we observed was less than 600–700 eV, and usually it was much less. A considerable peak subsisted after the sawtooth crash, showing that the flattening of the temperature profile was far from being complete.

# INVESTIGATION OF PLASMA FORMATION REGIMES FOR ICRF HEATING EXPERIMENTS IN THE TUMAN-3 TOKAMAK WITH MAGNETIC COMPRESSION

L.G. ASKINASI, N.E. BOGDANOVA, V.E. GOLANT,  
 S.G. GONCHAROV, M.P. GRYAZNEVICH,  
 V.V. D'YACHENKO, A. IZVOZCHIKOV, E.R. ITS,  
 S.V. KRIKUNOV, S.V. LEBEDEV, B.M. LIPIN, I.P. PAVLOV,  
 G.T. RAZDOBARIN, V.V. ROZHDESTVENSKIJ,  
 N.V. SAKHAROV, M.A. KHALILOV, F.V. CHERNYSHEV,  
 K.G. SHAKHOVETS, O.N. SHCHERBININ  
 A.F. Ioffe Physico-Technical Institute,  
 Leningrad

S.E. BENDER, Yu.A. KOSTSOV, R.N. LITUNOVSKIJ,  
 O.A. MINYAEV, E.N. RUMYANTSEV, P.P. TEPLOV  
 D.V. Efremov Scientific Research Institute  
 of Electrophysical Apparatus,  
 Leningrad

Union of Soviet Socialist Republics

*Presented by O.S. Pavlichenko*

## Abstract

### INVESTIGATION OF PLASMA FORMATION REGIMES FOR ICRF HEATING EXPERIMENTS IN THE TUMAN-3 TOKAMAK WITH MAGNETIC COMPRESSION.

The effect of fast current increase on the plasma parameters is studied. A remarkable increase in the peripheral density and a growth of MHD activity are observed. During the current rise period for a low magnetic field, Thomson scattering measurements yield hollow electron temperature distributions, which are rapidly transformed into a peaked distribution just after the current maximum. The method of plasma formation studied leads to stable discharges with a low safety factor,  $q(a) \approx 2$ . Experimental data on ICR heating with  $P < 0.5$  MW in a plasma formed by a fast current rise are reported. A simultaneous increase in the ion temperature by a factor of 1.4 and in the density by a factor of 1.7 are recorded during the RF pulse.

## 1. INTRODUCTION

The first experiments on fast current increase after magnetic compression were carried out in the TUMAN-3 tokamak in 1983 [1]. The experiments were mainly devoted to an evaluation of the time needed for the current to penetrate into the plasma core, but the conclusion that anomalously quick skin current dissipation takes place could not be considered to be very reliable without any detailed measurements of the electron temperature. In contrast to our data, later TFTR [2] and JET [3] results have shown that the rate of current density redistribution corresponds to the classical Spitzer resistivity. The experiments [1] have also demonstrated the influence fast current input has on the main plasma characteristics. For example, the ion temperature was 1.5 times higher than the temperature measured in a quasi-stationary Ohmic discharge with the same values of  $I_p$ ,  $B_T$ , and  $\bar{n}$  [4].

The new set of measurements described in this paper aimed at studying the mechanism of additional current penetration and the time evolution of the electron temperature profiles during current rise. A plasma column that was separated from the wall was formed by a rapid shift along the major radius (R-compression) [5], whereas, in previous experiments, minor radius compression had been used. The plasma obtained in this way is supposed to be used as an initial plasma in ICRF heating experiments.

## 2. EXPERIMENT

The main diagnostics used for recording the plasma parameters are as follows: a microwave interferometer ( $\lambda = 2$  mm) 'looking' through the plasma along ten vertical chords, a Thomson scattering apparatus including ruby laser and polychromator with four space points, five energy channel neutral particle analysers capable of recording charge exchange fluxes within  $\pm 16$  cm from the equatorial plane. In addition, measurements of soft X-rays, vacuum spectral line intensities, radiation losses and several electromagnetic parameters were performed.

The time behaviour of the plasma parameters in a discharge with fast current increase is shown in Fig. 1. At the initial stage, the plasma is formed near the outer chamber wall. According to the magnetic flux measurements, the discharge axis is at  $R = 61$  cm (Fig. 1(b)). The low field side limiter is placed at the radius  $R = 75$  cm, the high field side limiter at the radius  $R = 31$  cm. The plasma current  $I_p = 43$  kA (Fig. 1(a)), the average density  $\bar{n} \approx 0.6 \times 10^{13}$  cm<sup>-3</sup> (Fig. 1(d)), the ion temperature  $T_i(0) = 100$  eV (Fig. 1(e)). At 25 ms, a specially programmed equilibrium control system moves the plasma column to the radius  $R = 53$  cm, during 1.5 ms. At 25.5 ms, switching on an additional capacitor battery provides a plasma current rise up to 120 kA during 4 ms. Then, the current decreases at a rate that corresponds approximately to the decay of the toroidal field (Fig. 1(c)). The evolution of the plasma parameters was studied for two values of the toroidal field:  $B_T(0) = 5$  kG (Fig. 1) and  $B_T(0) = 7$  kG (Fig. 2).

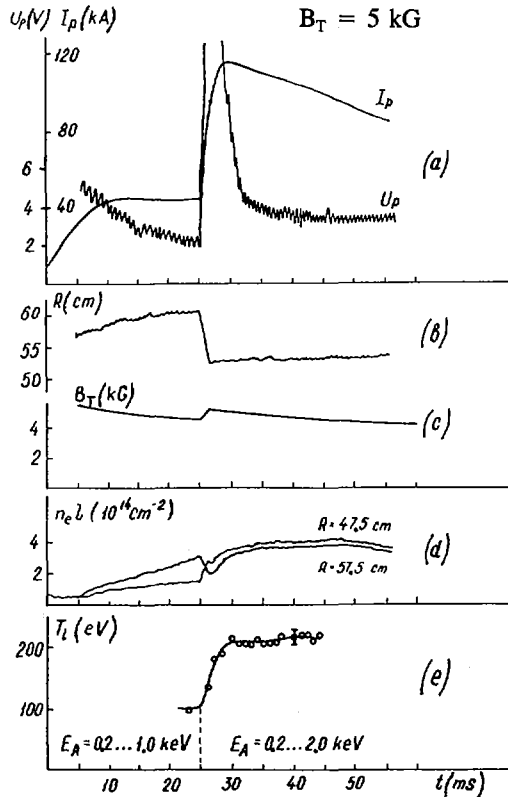


FIG. 1. Time behaviour of different plasma parameters in discharge with fast shift and current rise at  $B_T(0) = 5$  kG.

The interferometer data yield the chord distributions of the plasma density at different times (Fig. 3). A comparison between the positions of the  $n_e \ell(R)$  maxima and the values of the major radius  $R$  obtained from magnetic measurements demonstrates sufficient accuracy of the electromagnetic diagnostics, even for a significant column shift. This enables the use of electromagnetic diagnostics in the equilibrium control system.

### 3. RESULTS

The current rise disturbs the plasma parameters substantially. During the time interval from 25 to 32 ms, the total number of particles,  $N$ , increases by a factor of 1.7 in discharges with  $B_T(0) = 5$  kG and by a factor of 1.4 in discharges with

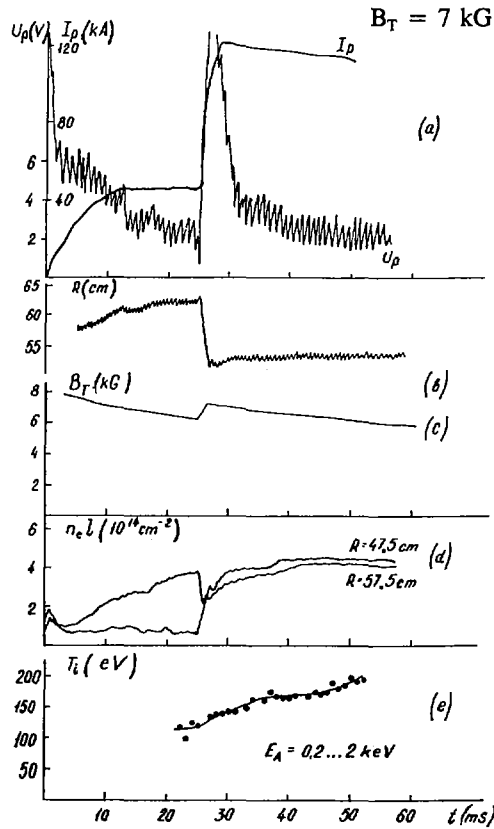


FIG. 2. Time behaviour of different plasma parameters in discharge with fast shift and current rise at  $B_T(0) = 7$  kG.

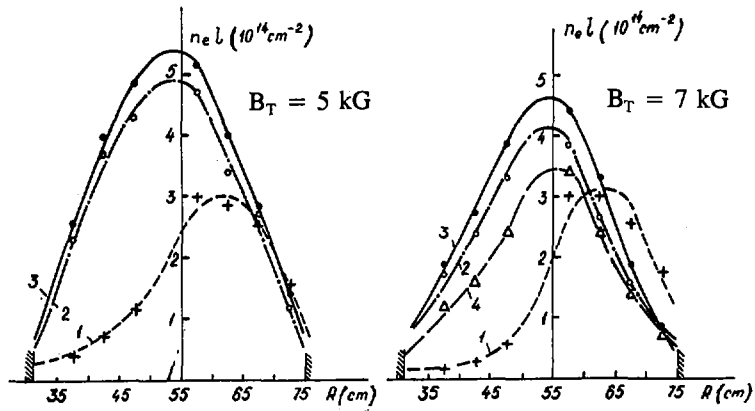


FIG. 3. Chord distributions of density during current rise at  $B_T(0) = 5$  kG and  $B_T(0) = 7$  kG. Curve 1: 25 ms, curve 2: 32 ms, curve 3: 41 ms, curve 4: 32 ms of discharge with major radius compression without current rise.

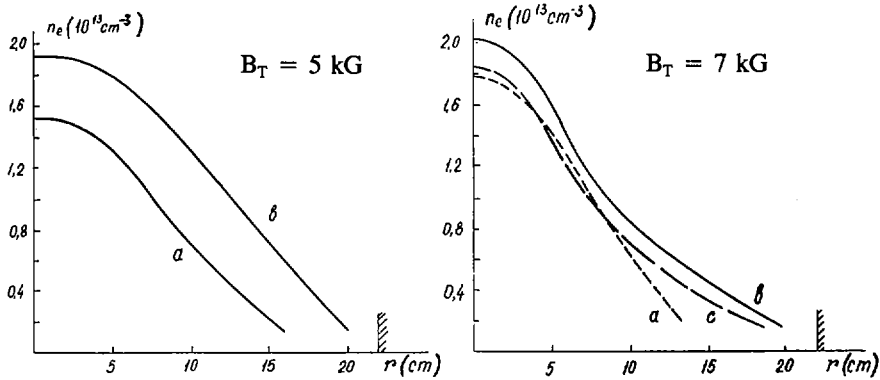


FIG. 4. Radial distributions of density, obtained by Abel inversion of profiles in Fig. 3. Curve a: 25 ms, curve b: 32 ms, curve c: 32 ms of discharge with major radius compression without current rise.

$B_T(0) = 7$  kG (Fig. 3). For the sake of comparison, curve 4 (Fig. 3) presents the chord distribution of the density in the plasma after major radius compression without current rise.  $N$  is only 15% higher than at the initial stage. It should be noted that the increase in the total number of particles is mainly due to an increase in the peripheral density (see the radial profile in Fig. 4). The ion temperature also increases during the current rise as is shown by curves e in Figs 1 and 2. Particularly fast ion heating was observed in the case of low magnetic field.

Of great interest is the time evolution of the electron temperature profiles, which can yield the localization of the heat source in the plasma and, therefore, provides indirect information on the current distribution. Figure 5 shows electron temperature profiles measured in a discharge with  $B_T(0) = 5$  kG at different times. The most striking feature of the profiles obtained on the current front at 1 and 3 ms after the start is the noticeable rise in  $T_e$  at medium radius, whereas the central temperature is virtually the same as at the initial stage. Then, the  $T_e$  profile is flattened ( $t = 6$  ms and  $t = 11$  ms) and later on becomes peaked ( $t = 16$  ms). The evolution of  $T_e(r)$  at  $B_T(0) = 7$  kG does not show any hollow distributions (Fig. 6). The fact of a weaker plasma disturbance, in this case, is also confirmed by a lower loop voltage:  $U_p$  ( $B = 7$  kG) = 2.5–3 V,  $U_p$  ( $B = 5$  kG) = 3.0–4.0 V.

#### 4. DISCUSSION

The experiments have demonstrated the possibility of rapid current input into a tokamak ( $dI/dt = 25$  MA·s<sup>-1</sup>). The current rise time (4 ms) is substantially shorter than the classical time of current penetration into the central part of the plasma

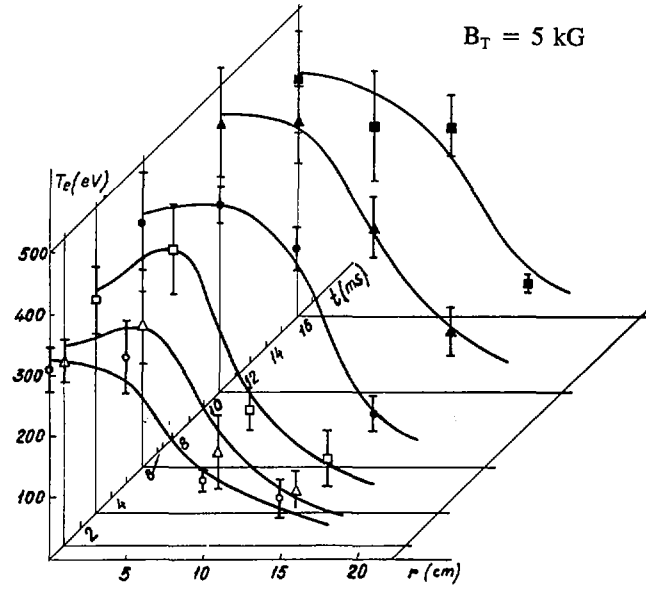


FIG. 5. Evolution of electron temperature profile during current rise at  $B_T = 5 \text{ kG}$ .

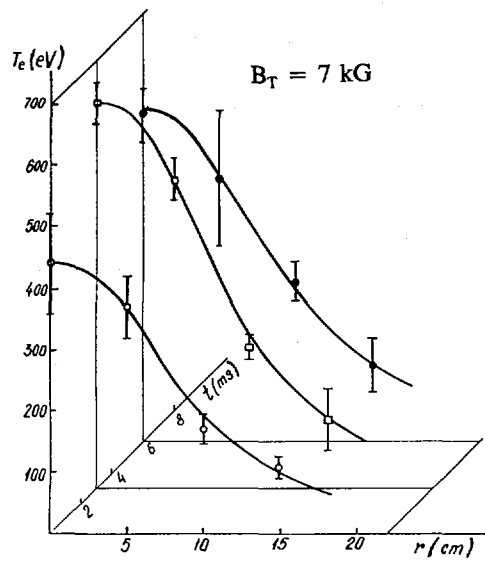


FIG. 6. Evolution of electron temperature profile during current rise at  $B_T = 7 \text{ kG}$ .

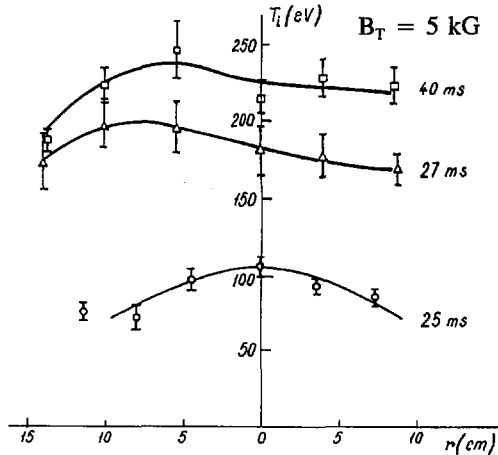


FIG. 7. Radial profile of ion temperature during current rise at  $B_T = 5$  kG.

column. In spite of strong MHD activity during the front of current rise, it is possible to obtain a stable plasma with a low safety factor. At maximum current,  $I_p = 127$  kA, major radius  $R = 53$  cm, toroidal field  $B_T(0) = 5$  kG, the value of  $q$  at the limiter was equal to 1.7, without toroidal correction. With the correction included, we find  $q(a) \approx 2$ .

The data show that a narrow electron temperature profile with cold periphery is necessary for a current rise to take place. Profiles of this kind may be obtained by minor radius compression [1] or by major radius compression such as in the recent experiments. This conclusion is confirmed by the fact that attempts to increase the current in the plasma after a smaller shift or without any shift have ended with disruptions in virtually all cases. A more detailed analysis is needed to understand the mechanism of current density profile redistribution. An MHD stability analysis of the current density profiles obtained from  $\sigma^{\text{neo}}(r)$  as well as from transport simulation is in progress now.

As was mentioned above, discharges at a stronger longitudinal field,  $B_T(0) = 7$  kG, are disturbed by current rise to a lesser extent than at  $B_T(0) = 5$  kG. Only 10% of the discharges ended with a large disruption near the current maximum, whereas at  $B_T(0) = 5$  kG disruptions occurred in 50% of the cases. The radial distributions of  $n_e$  (Fig. 4) and  $T_e$  (Figs 5 and 6) show that the disturbances are substantially higher at lower toroidal fields. Large disturbances of  $n_e(r)$  and  $T_e(r)$  and higher amplitudes of MHD oscillations at  $B_T(0) = 5$  kG may be due to a flattening of the current density distribution.

A fast increase in the ion temperature following plasma shift and current rise was observed in part of the discharges (see Figs 1(e) and 7). The ion temperature

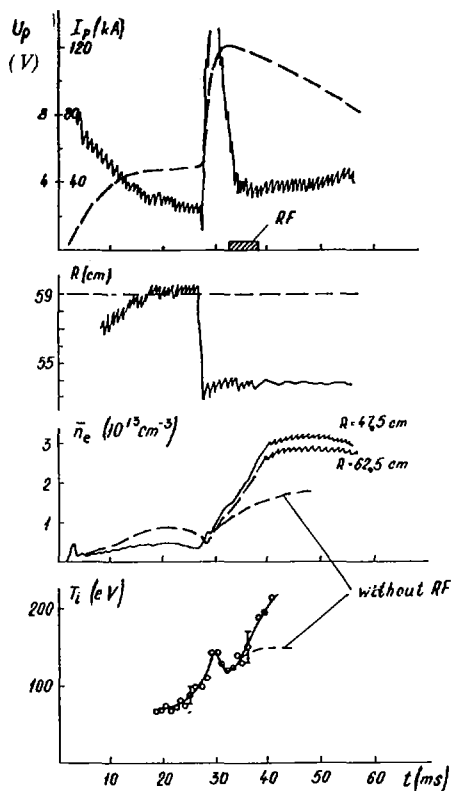


FIG. 8. Time behaviour of different plasma parameters during ICRF heating ( $P < 200$  kW) in discharge with fast shift and current rise.

increased by a factor of two, during 3 to 4 ms. Transport simulation and experiment [1] show that classical energy transfer from electrons to ions and neoclassical ion heat conductivity cannot provide such fast heating, typical times of the  $T_i$  increase being, in these cases, 10–15 ms. Some turbulent mechanism seems to be responsible for fast ion heating during the current rise.

## 5. ION CYCLOTRON HEATING

Experimental results on ion cyclotron heating of a plasma in the quasi-stationary Ohmic heating regime are presented in [5]. At an RF power of  $P < 200$  kW launched into the plasma by a low field side loop antenna, maximum increase in the ion temperature,  $\Delta T_i = 80$  eV, was recorded. Pulse duration and power level were limited by disruptions due to an increase in density during RF heating.

Preliminary experiments on ICH of the plasma formed by shift and fast current rise were performed. The plasma was more stable; disruptions during RF heating were practically absent, in contrast to the previous set of experiments. A maximum density of  $\bar{n}_e = (3-3.5) \times 10^{13} \text{ cm}^{-3}$  at a plasma current of  $I_p = 120 \text{ kA}$  was reached (Fig. 8). At an RF power of  $P < 200 \text{ kW}$ , an ion temperature increase of  $\Delta T_i = 60-80 \text{ eV}$  was observed. The value of  $\Delta T_i$  is consistent with previous results. Now, a special coating of antenna and electrostatic shield is being designed in order to decrease the impurity and hydrogen fluxes originating during the RF pulse.

### REFERENCES

- [1] BENDER, S.E., et al., in *Controlled Fusion and Plasma Physics (Proc. 11th Europ. Conf. Aachen, 1983)*, Vol. 1, European Physical Society (1983) 111.
- [2] FREDRICKSON, E., et al., in *Controlled Fusion and Plasma Heating (Proc. 13th Europ. Conf. Schliersee, 1986)*, Vol. 1, European Physical Society (1986) 148.
- [3] TANGA, A., et al., *ibid.*, p. 264.
- [4] BULYGINSKY, D.G., et al., in *Heating in Toroidal Plasmas (Proc. 4th Int. Symp. Rome, 1984)*, Vol. 2, Int. School of Plasma Physics, Varenna (1984) 961.
- [5] ASKINASI, L.G., et al., in *Controlled Fusion and Plasma Physics (Proc. 12th Europ. Conf. Budapest, 1985)*, Vol. 9F, Part I, European Physical Society (1985) 363.

### DISCUSSION

J.-M. NOTERDAEME: You mentioned that there was need to coat the ICRH antenna. What type of coating are you using?

O.S. PAVLICHENKO: To the best of my knowledge it is a titanium nitride coating.



# ALFVÉN WAVE HEATING AND CURRENT PROFILE MODIFICATION IN TCA

G. BESSON, G.A. COLLINS<sup>1</sup>, B.P. DUVAL,  
 C. HOLLENSTEIN, A.A. HOWLING, B. JOYE, J.B. LISTER,  
 J.-M. MORET, F. RYTER, C.W. SIMM, H. WEISEN  
 Centre de recherches en physique des plasmas,  
 Association Euratom-Confédération Suisse,  
 Ecole polytechnique fédérale de Lausanne,  
 Lausanne, Switzerland

## Abstract

### ALFVÉN WAVE HEATING AND CURRENT PROFILE MODIFICATION IN TCA.

The increase in electron temperature observed during Alfvén wave heating under optimal conditions, near the threshold of the  $(n, m) = (2, 0)$  continuum, leads to a large increase in the sawtooth ramp rate ( $\sim 3 \text{ W/cm}^3$ ) and to a reduction in the loop voltage for several confinement times. The increase in electron density during the pulse moves the resonance surfaces outwards, which probably reduces the heating efficiency. Then, both the temperature increase and the voltage drop disappear. As the rf power is increased, this process becomes more rapid, and the reduction in the loop voltage lasts for only a few milliseconds. The ion temperature increase from 300 to 600 eV can mostly be attributed to the increased electron density, although in some conditions it can precede the density increase, implying some direct ion heating. Besides bulk plasma heating there is evidence of changes in the current profile which are triggered by the appearance of the resonant surfaces. Both increases and decreases of the internal inductance have been produced with frequency programming.

## 1. INTRODUCTION

The paper describes some of the recent results obtained during Alfvén Wave Heating (AWH) experiments on the TCA tokamak ( $R, a = 0.61, 0.18 \text{ m}$ ,  $B_\phi = 1.5 \text{ T}$ ,  $I_p < 170 \text{ kA}$ ) using the full set of eight unshielded antenna groups described in detail elsewhere [1,2]. One set of carbon limiters was used for the experiments described. The quasi-cylindrical condition for the Shear Alfvén Wave resonance is given by:

$$\omega^2(r) = (n+m/q(r))^2 \cdot (B_\phi^2 / \mu_0 \rho(r) R^2) \cdot (1 - \omega^2 / \omega_{ci}^2)$$

in which  $(n, m)$  are the toroidal and poloidal mode numbers, respectively. For the parameters of TCA this resonance condition stipulates a frequency in the range 1-5 MHz, and the work reported here was carried out at 2.3 - 2.7 MHz with  $n = 2$ .

It has been theoretically predicted that a substantial fraction of the input rf power should appear as an inwardly propagating Kinetic Alfvén Wave [3]. We have experimentally

<sup>1</sup> Australian Atomic Energy Research Establishment, Lucas Heights, Australia.

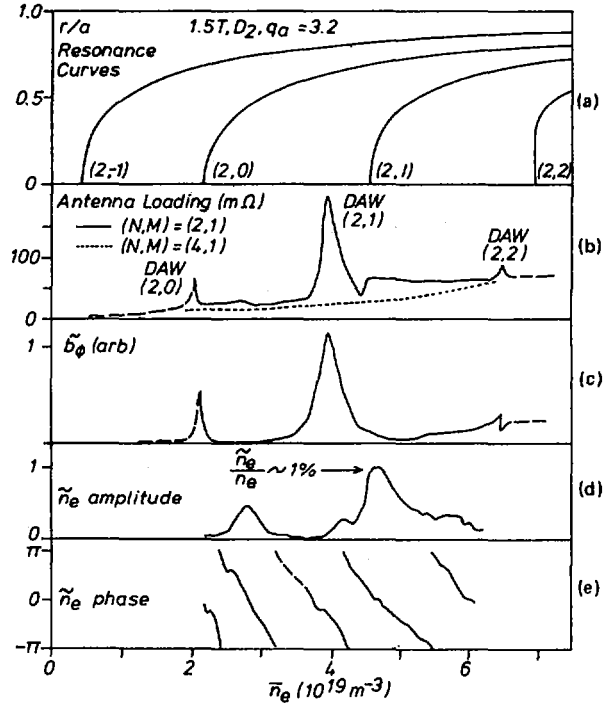


FIG. 1. The main features of the Alfvén wave spectrum excited on TCA.

detected density fluctuations associated with this wave, during the heating experiments, and they exhibit many of the features predicted [4]. Figure 1 summarises the important features of the AWH scheme as a function of the electron density: Fig. 1a shows the calculated positions of the resonance layers for  $n = 2$ ,  $m = 0, \pm 1, 2$ ; Fig. 1b shows the individual antenna loading, varying from 20 - 80 m $\Omega$  in the continua to 200 m $\Omega$  for the Shear Alfvén Wave eigenmodes referred to as Discrete Alfvén Waves (DAW); Fig. 1c shows the  $b_\phi$  component of the rf wavefield measured behind the limiter radius, also showing the continua and the eigenmodes; Fig. 1d shows the amplitude of the synchronous density modulations along a fixed radial chord ( $r \sim a/2$ ) and Fig. 1e the phase of the radially propagating Kinetic Alfvén Wave at this position.

Since the first AWH experiments on TCA, it has been clear that the excited spectrum strongly affects the macroscopic plasma behaviour during the rf pulse. The fact that the resonance condition depends on the plasma density, which increases substantially during the rf pulse, has enabled us to make very detailed spectral scans during the rf pulse. However, it has also limited the high power study to a power level of 570kW in the  $(n,m)=(-2,-1)$

continuum [2]. Even at power levels below this, we observe a power limitation near the AW mode thresholds which are crossed as a result of the density increase.

## 2. PLASMA HEATING

The flow of energy into the Kinetic Alfvén Wave was predicted to heat the electrons via Landau damping. Experimental evidence for heating of the electrons is obtained on TCA from two separate measurements: a reduction in the loop voltage and an increase in the axial electron temperature sawtooth amplitude. Figure 2 shows a summary of the sawtooth modulation results [5]. We obtained a rate of increase of stored energy on axis,  $3/2 \cdot e \cdot n_e(0) dT_e(0)/dt$ , up to  $3 \text{ W/cm}^3$ , equal to 5-8 times the volume averaged rf power, suggesting that the electron power deposition profile must be peaked on axis. The increase in central heating rate is maintained at  $\sim 4.5 \langle P_{rf} \rangle$ , even in the higher density case,  $n_e(0) \sim 10^{20} \text{ m}^{-3}$ .

Figure 3 shows the evolution of the loop resistance during a pulse in which the rf power increases to 200kW,  $P_{rf}/P_{oh} \sim 70\%$ .

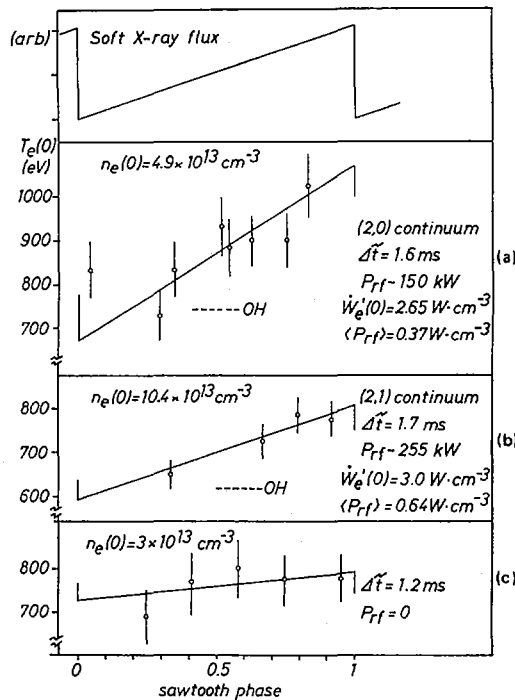


FIG. 2.  $T_e(0)$  sawtooth excursion for: (a) the start of the  $(n, m) = (2, 0)$  continuum, (b) the start of the  $(-2, -1)$  continuum, and (c) a low density target plasma.

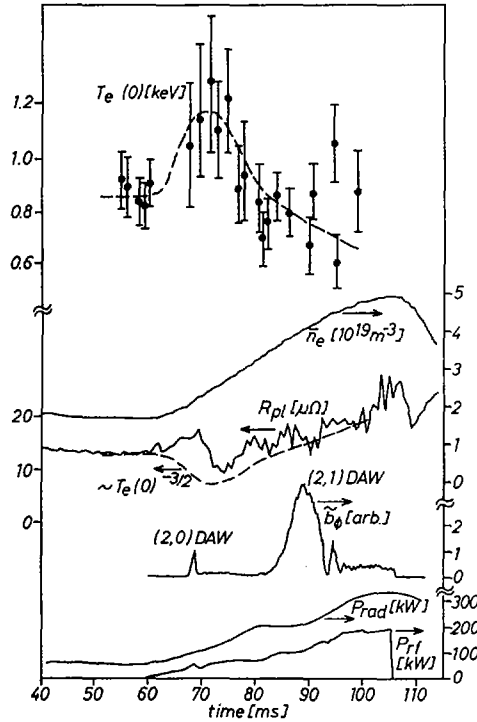


FIG. 3. Increase of electron temperature and reduction of loop resistance with a modest level of rf power.

The density at the start of the rf pulse is chosen so as to maximise the drop in the loop voltage and corresponds to the onset of the toroidally coupled  $(n,m) = (2,0)$  continuum ( $\bar{n}_e = 2 \times 10^{19} \text{ m}^{-3}$ ,  $D_2$ , 2.5 MHz). The 300 eV increase in  $T_e(0)$ , measured by single-point Thomson scattering triggered at the middle of the sawtooth period, leads to a reduction of 0.45 V (25%) in the resistive loop voltage, calculated as  $V_L - L_p dI_p/dt$ . The dashed line through the resistance curve is proportional to  $T_e(0)^{-3/2}$ . The initial voltage increase observed corresponds to a transient inductive effect, due to  $d(\beta + li/2)/dt$ . After 17 msec the resistance returns to the target plasma value and even increases, consistent with the measured increase in  $T_e(0)^{-3/2}$ . The electron confinement time,  $\tau_{Ee} \sim 3.5$  msec, is short compared with the timescale of this evolution. The electron density rises throughout the rf pulse, forcing the resonance layers towards the outside, as seen in Fig. 1, possibly explaining the decrease in  $T_e(0)$ . The appearance of the next continuum threshold  $(-2,-1)$  does not produce a pronounced drop in the loop voltage. This may in part

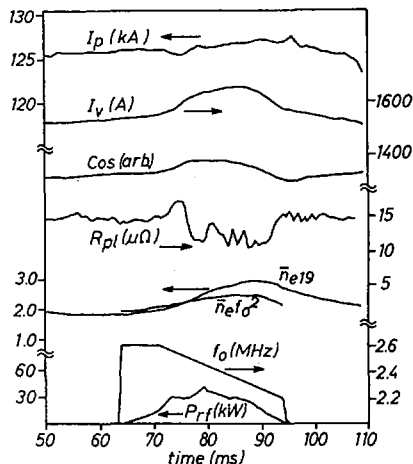


FIG. 4. Prolonged voltage reduction obtained during frequency pre-programming.

be due to the new surface sharing the rf power with the old surface, and partly due to the centrally flat resonance frequency profile of the  $(-2,-1)$  continuum.

Previously, it was assumed that the increase in  $P_{rad}$  (Fig. 3) was responsible for the temperature drop towards the end of the rf pulse. The fractional radiated power has now been reduced to an acceptable level, with  $P_{rad}/(P_{oh}+P_{rf}) \sim 50-60\%$  up to  $(P_{oh}+P_{rf})=0.95\text{MW}$ . It is now difficult to assess whether the increase in the radiated power is due to more than the increased plasma density and the reduction in electron temperature. Measurements of the plasma mass also indicates that most of the increase in plasma density is hydrogenic.

It is noteworthy that if both  $\Delta \bar{n}_e / \bar{n}_e$  and  $\Delta P_{TOT} / P_{OH}$  are of the order of unity then a curious situation arises. A scaling law leading to a progressive decrease in confinement time with additional heating [6], when combined with this large density increase, would predict a decrease in  $\langle T_e + T_i \rangle$ . Since  $\langle T_i \rangle$  already increases considerably, at least by the minimum resulting from the density increase,  $\langle T_e \rangle$  must decrease dramatically if such a scaling is to hold. The lack of stationarity with a significant rf power input still prevents us from accurately assessing the confinement time during the rf pulse.

Since the application of the rf pulse does not lead to a stationary state, the measured loop voltage itself is sensitive to  $d(\beta + li/2)/dt$ , and fast varying poloidal currents can lead to misinterpretation, especially when we suspect the presence of modifications of the current profile. We have prolonged the period of reduced resistive loop voltage to beyond 20 msec ( $\sim 6 \times \tau_{Ee}$ ) by pre-programming the rf generator frequency at low power.

Figure 4 shows such a result, in which the spectral position, given roughly by  $f^2 \bar{n}_e$ , has been partly stabilised by ramping down the frequency at a rate of 17 kHz/msec to compensate for the density rise. The plasma current, vertical field current and plasma current position are quite stable. During this period the error in the loop voltage due to these currents will be small, confirming the reduction, 22% in this case.

As the rf power is increased, the density ramps faster and reduces the time during which  $d(\bar{n}_e f^2)/dt$  is small enough to stabilise the evolution of the spectrum around the optimal region. This explains why the most convincing electron heating results have been obtained at the 100-200 kW level whereas the rf generator has delivered up to 570 kW to the plasma. Work is currently underway to increase the useful frequency sweep range of the rf generator to resolve this question.

An understanding of the increase in electron density is, therefore, still of extreme importance. The magnitude of the increase is relatively insensitive to the excited mode structure, or to the number of active antennas and hence also to the antenna voltages, but it remains a linear function of the total delivered rf power. It also has an almost linear dependence on the plasma current. Detailed analysis of its time evolution using a zero-dimensional model,  $dN/dt = S - N/\tau_{eff}$ , shows that the cause of the increase, a change in either  $S$  or  $\tau_{eff}$ , remains unchanged when the plasma current is reduced. The recycling or pump-out term, which defines the new steady state, increases as the current is reduced, leading to a smaller density increase but with a shorter rise time. The  $H_\alpha + D_\alpha$  emission generally decreases at the start of the rf pulse at high current and remains below the "ohmic" value throughout, suggesting an increase in particle confinement. This decrease disappears as the plasma current is reduced, and we even observe a small increase in  $H_\alpha + D_\alpha$  for  $q_a > 6$ .

In the conditions described, we still observe a large increase in the ion temperature during the rf pulse, typically from 300-600 eV with ~200kW of rf power. In some conditions, preceding a continuum threshold, we observe a fast increase in  $T_i$  which indicates direct ion heating. However, even at the highest powers, the ion temperature never exceeds the electron temperature, suggesting that this direct ion heating must be small.

To summarise, the newest results with naked antennas, carbon limiters and active frequency control have provided further proof of electron heating using Alfvén Waves, by prolonging the period of reduced plasma loop voltage.

### 3. CURRENT PROFILE CHANGES

The predicted local power deposition to the electrons suggests that AWH might be able to modify the current profile, if at all possible. Several experimental results from TCA suggest that this is the case and they are listed below.

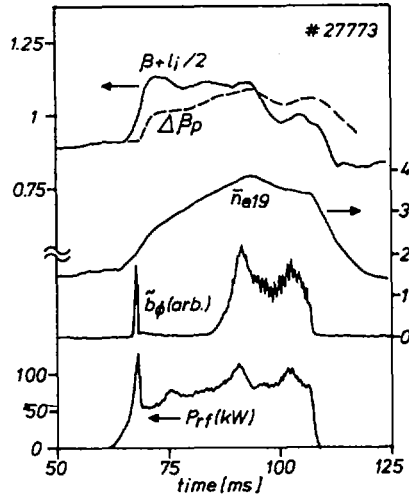


FIG. 5. Evolution of  $\beta_{dia}$  and  $\beta + l_i/2$  during an rf pulse.

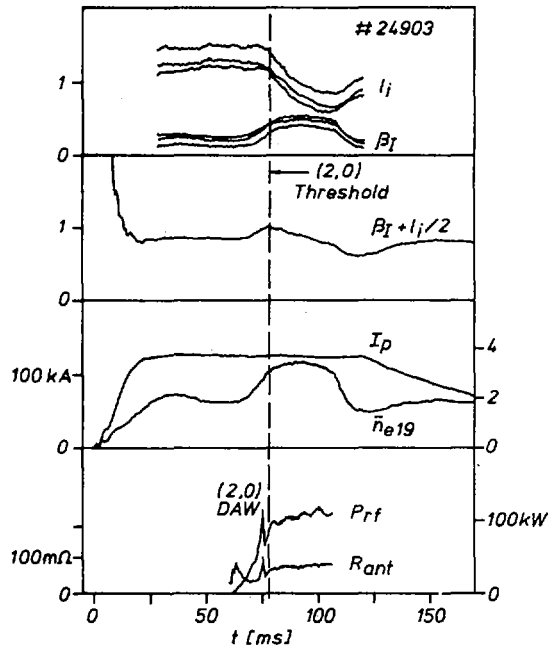


FIG. 6. Reduction in  $l_i$  following the (2, 0) threshold, deduced from  $\beta + l_i/2$ .

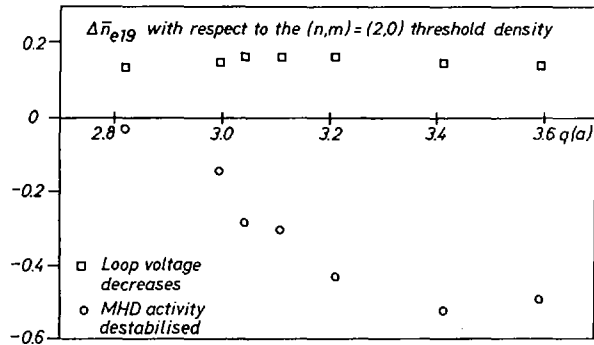


FIG. 7. Occurrence of the voltage drop and onset of Mirnov activity with respect to the (2, 0) threshold density, as the plasma current is varied.

The very rapid rise in  $\beta + l_i/2$  compared with the diamagnetic signal (Fig. 5) suggests a sudden increase in  $l_i/2$  (current peaking) when the rf pulse is first applied. For a given rf power, this increase in  $l_i/2$  depends on the position in the spectrum, being generally larger when the resonance surfaces are in the outer region of the plasma.

The value of  $\beta + l_i/2$  can also decrease during the rf pulse, also seen in Fig. 5. A case is shown in Fig. 6, clearly indicating a reduction in  $l_i$  by more than the value of  $\beta$  in the original target plasma. The magnitude of the decrease is estimated assuming different ohmic scaling laws for the increased density plasma, from which the several curves on the figure are derived. Values in the range  $-\Delta l_i \sim 0.4-0.6$  are obtained.

There is a disruption power limit at fixed points in the spectrum, near the thresholds of the continua, when the increase in  $m=2$  activity at these points exceeds a critical value. The increase in  $m=2$  is attributed to a change in the current profile near the  $q=2$  surface.

There is a change in the details of the DAW spectrum excited, showing up as a hysteresis when the generator frequency is varied [2]. This has been explained by the dependence on  $q(r)$  in the resonance condition.

The origins of these changes are still not fully understood, but it now seems that both the thresholds of the continua and the next outermost surface must play a role.

Figure 7 shows the density difference between the occurrence of the  $(n,m) = (2,0)$  DAW, and a) the occurrence of the drop in loop resistance and b) the increase in  $m=2$  Mirnov activity. The figure shows that, as the plasma current is varied, the loop resistance drop always occurs shortly after the appearance of the  $(2,0)$  threshold, whereas the onset of the destabilization of the MHD activity varies with respect to this threshold. Calculations using assumed plasma current profiles show that the increase in

MHD activity in fact coincides with the approach of the outer resonance surface (2,1) to the estimated position of the  $q=2$  surface, illustrated in Fig. 1.

All these observations indicate that the radial positions of the Shear Alfvén Wave resonance surfaces influence the current profile. Much of the discontinuous behaviour observed during the AWH pulse, and documented in detail elsewhere, could be attributed to these profile changes.

ACKNOWLEDGEMENTS: We gratefully note the continued interest of Professor F. Troyon in our work, as well as the support of the whole TCA team. This work was partly funded by the Fonds National Suisse de la Recherche Scientifique.

### REFERENCES

- [1] COLLINS, G.A., et al., Phys. Fluids **29** (1986) 2260.
- [2] BESSON, G., et al., Plasma Phys. Controll. Fusion **28** (1986) 1291.
- [3] HASEGAWA, A., CHEN, L., Phys. Rev. Lett. **35** (1975) 370.
- [4] BEHN, R., COLLINS, G.A., LISTER, J.B., WEISEN, H., Plasma Phys. Controll. Fusion **29** (1987) 75.
- [5] JOYE, B., et al., Phys. Rev. Lett. **56** (1986) 2481.
- [6] GOLDSTON, R.J., Plasma Phys. Controll. Fusion **26** (1984) 87.

### DISCUSSION

M. ONO: What is the ion temperature behaviour during the regime of large density increase?

J.B. LISTER: The ion temperature increases typically by 300–400 eV, as we have always reported. The question is really whether this is due only to the increase in density, via an increase in  $P_{ei}$ , or whether the RF delivers power directly to the ions. At the 11th European Conference in 1983 we reported a value of  $T_i$  greater than the Ohmic value, and at the 12th European Conference in 1985 we reported values of  $dW_i(0)/dt > P_{ei}(0)$ . The errors in these analyses are large, however, and we consider the question of direct ion heating an open one.



# ANALYSIS OF ICRF HEATING AND CURRENT DRIVE IN TOKAMAKS

A. FUKUYAMA, T. MORISHITA

Department of Electronics,  
Okayama University,  
Okayama

Y. KISHIMOTO, K. HAMAMATSU

Japan Atomic Energy Research Institute,  
Naka-machi, Naka-gun, Ibaraki-ken

S.-I. ITOH

Institute for Fusion Theory,  
Hiroshima University,  
Hiroshima

K. ITOH

Plasma Physics Laboratory,  
Kyoto University,  
Uji, Kyoto

Japan

## Abstract

### ANALYSIS OF ICRF HEATING AND CURRENT DRIVE IN TOKAMAKS.

To analyse ICRF heating and current drive processes in tokamak plasmas, a theoretical model and computational codes are developed. Wave excitation, propagation and absorption, high energy tail formation, thermalization of the absorbed power, and current generation are analysed simultaneously, and the temporal and spatial evolutions of bulk plasma parameters are calculated in a consistent manner and in a realistic geometry. This wave thermalization transport analysis enables a comparison of modelling with experimental results. Through the kinetic treatment of the wave in the ICRF heated plasma, the good accessibility, the controllability of the deposition profile, the sustainment of the high energy particles in the core region, and the current drive ability in the high density regime are confirmed. A study on confinement time and MHD stability is presented. It is found that localized, intensive heating increases the central pressure and invalidates the stability criterion of the internal kink mode.

## 1. INTRODUCTION

Ion cyclotron range of frequency (ICRF) waves have been extensively used as a reliable heating tool and have become a promising candidate for current drive in tokamaks. Analysis of their properties is substantial for an explanation of experimental results and for designing future programmes. To analyse the heating

and current drive processes, we have developed a theoretical model and the computational codes associated with it. Three stages: (1) wave propagation and absorption, (2) relaxation in a velocity space, and (3) spatial transport are systematically analysed according to different time-scales. For given launching conditions, wave field structure, high energy particle generation, power deposition profile, time evolution of temperature profiles and driven current are evaluated in a consistent manner. We examine the confinement characteristics (e.g. the confinement time and attainable temperature), the stability of the internal kink mode and the optimum conditions for the current drive.

## 2. WAVE EXCITATION AND PROPAGATION

We solve Maxwell's equations, using the kinetic conductivity of an inhomogeneous and multicomponent plasma [1, 2]. The following linear processes are described simultaneously: coupling to finite size antennas, wave propagation (reflection, refraction and tunnelling through evanescent layers), mode conversion to ion Bernstein waves, cyclotron damping up to second harmonics, Landau damping as well as transit time magnetic pumping (TTMP). Figure 1 shows the poloidal structures of the wave field (a) and the power deposition profile (b) for two ion hybrid resonance heating in JET (D majority, H minority) [3]. We observe that good accessibility to the central region is obtained, and that 80% of the injected power is absorbed near the plasma centre ( $r \leq 0.2$  m). When a high energy tail component of the minority ion exists, the deposition profile broadens as is shown in (c).

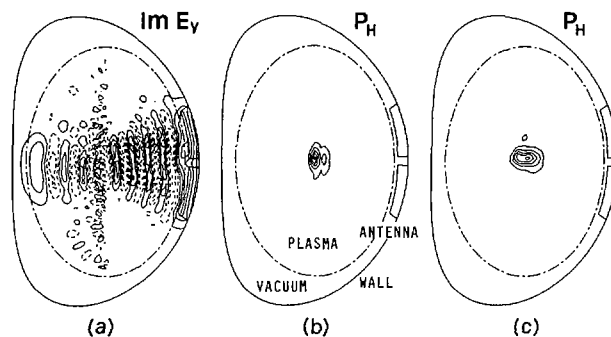


FIG. 1. Poloidal structure for two-ion hybrid resonance heating in JET ( $B_t = 2.04$  T,  $\omega/2\pi = 29.8$  MHz,  $n_{e0} = 2.94 \times 10^{19}$  m $^{-3}$ ,  $T_0 = 2.5$  keV,  $n_H/n_D = 0.1$ , monopole antenna). (a) Wave electric field,  $\text{Im } \vec{E}_y(r, \theta)$ ; (b) power deposition profile to protons; (c) power deposition profile in the presence of a high energy tail component near plasma centre,  $r \leq 0.3$  m.

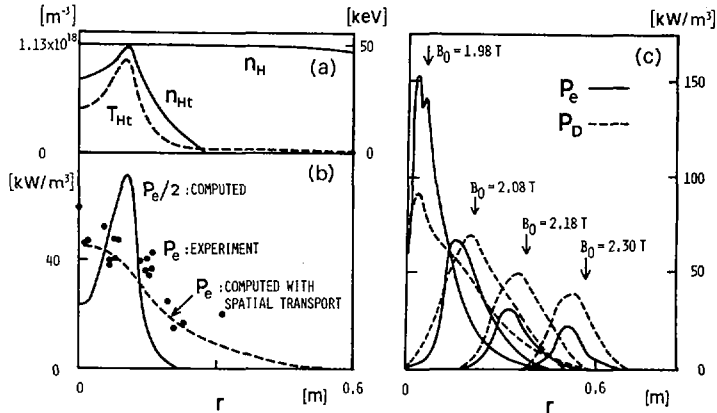


FIG. 2. (a) Radial profiles of  $n_{Ht}$  and  $T_{Ht}$  of hot component at power level of 0.66 MW.  $n_H/n_D = 0.04$ ; other parameters are the same as in Fig. 1; (b) radial profiles of power absorbed by electrons: calculated in the wave thermalization analysis (solid line), computed by coupling with 1-D transport code (dashed line), evaluated from temperature rise in JET (solid circles); (c)  $B_0$  dependence of the absorbed power density. Arrows indicate positions of fundamental cyclotron resonance of proton.

### 3. MODIFICATION OF THE VELOCITY DISTRIBUTION

The velocity distribution of the resonant particles in a heated region is strongly modified, and this modification affects wave propagation and absorption. We describe the time evolution of the local velocity distribution, taking account of the change in the wave structure. The Fokker-Planck analysis [4], including collisional and quasi-linear diffusion, is combined with the 1-D ICRF wave code [1]. We calculate tail formation and power partition through collisional relaxation [5]. In the case of two ion hybrid resonance heating, a high energy tail of the minority ion velocity distribution appears first near the cyclotron resonance. The density  $n_{Ht}$  and the temperature  $T_{Ht}$  of the hot component of the minority ions increase, and the width of the heated region broadens in a collisional time-scale. Figure 2(a) shows the radial profiles of  $n_{Ht}$  and  $T_{Ht}$ , together with the minority density  $n_H$ , for the JET heating experiment. The power deposition profile in Fig. 1(c) is computed on the basis of the distribution of the hot component. The power transferred to electrons through collisions is enhanced near the plasma centre with the increase of the hot component. The spatial profile of the power absorbed by electrons is shown in Fig. 2(b). Solid circles denote the value derived from the temperature rise in JET [3]. The dashed line indicates the initial temperature increment computed by coupling with the 1-D transport code, which is in good agreement with the experiment. Deposition control by frequency change is illustrated in Fig. 2(c) for fixed RF power. As the cyclotron resonance shifts from the plasma centre, the absorbed power density and the tail temperature decrease and the power partition changes.

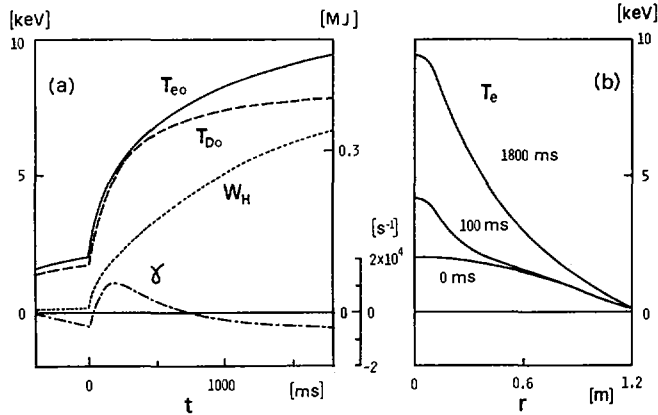


FIG. 3. (a) Temporal evolution of central temperatures,  $T_{e0}$  and  $T_{D0}$ , proton energy content,  $W_H$ , and growth rate of internal kink mode,  $\gamma$ .  $B_0$ ,  $n_{e0}$ ,  $\omega$  are the same as in Fig. 1,  $n_H/n_D = 0.04$  and  $P_{RF} = 3$  MW; (b) electron temperature profile at 0 ms, 100 ms and 1800 ms.

#### 4. SPATIAL TRANSPORT

To study the long time development of plasma profiles, the power deposition is linked to the 1-D transport code. For a given density profile,  $T_e(r,t)$ ,  $T_D(r,t)$  and poloidal magnetic field  $B_p(r,t)$  are computed. An electron energy diffusion coefficient of the ALCATOR-INTOR form ( $\chi_e = 1 \times 10^{19} \text{ n}_e^{-1} \text{ m}^2 \cdot \text{s}^{-1}$ ) is employed. As for the ion energy diffusion coefficient, we use  $\chi_i = 0.5 [\text{m}^2 \cdot \text{s}^{-1}] + \chi_{CH}$  after Doublet III results [6], where  $\chi_{CH}$  is the neoclassical value calculated [7]. Neoclassical resistivity is employed and  $Z_{\text{eff}} = 2.29$ . These coefficients are chosen to reproduce the Ohmic plasma in JET. Figure 3(a) shows the time evolution of the central temperatures,  $T_{e0}$  and  $T_{D0}$ , and the minority energy content  $W_H$ , in the case of 3 MW ICRF input with  $I_p = 2$  MA. The  $T_e$  profiles in the Ohmic phase, in the initial phase of RF heating and in the saturation phase, are shown in Fig. 3(b). In the initial phase,  $T_e$  increases mainly in the central region ( $r \leq 0.3$  m). The ratio of central to average temperature is about 3.4 for  $t > 250$  ms. The confinement time in the saturation phase is 625 ms, which is comparable to that of the Ohmic phase.

#### 5. MHD ACTIVITY

The MHD stability is affected by the localized energy deposition and by the fast ions due to the ICRF heating. We study the stability of the  $m/n = 1/1$  internal kink

mode ( $m/n$ : poloidal/toroidal mode numbers). We employ the simplified stability criterion,  $\delta W_T > 0$  [8], where

$$\delta W_T \approx 3\nu \Delta q \{13/48(\nu+4) - \beta_p^2 [(r_2/r_1)^{\nu-4} - 1]/(\nu-4)\}$$

with

$$\beta_p \equiv -[2\mu_0/B_p^2(r_1)] \int_0^{r_1} (r/r_1)^2 (dp/dr) dr$$

$$q(r_1) = 1 \quad \text{and} \quad q(r_2) = 2$$

The safety factor is fitted as  $q(r) \sim 1 - \Delta q [1 - (r/r_1)^\nu]$  near the axis.

The time evolution of  $\delta W_T$  is given by the wave thermalization transport calculation. With the injected power of 3 MW, we find that  $\beta_p$  increases rapidly and that the mode becomes unstable with a delay time of 35 ms after the onset of RF heating (see Fig. 3(a)). The growth rate  $\gamma$  is about  $10^4 \text{ s}^{-1}$ . This pressure driven internal kink instability may be the origin of the rapid internal disruption which is not accompanied by the precursor oscillations. This delay time seems to be shorter than the experimentally observed period of the giant sawtooth. If we include the finite gyroradius stabilization effects of the tail ions [9], the critical  $\beta_p$  value increases, and the delay time may be longer by a factor of two. We note that the critical  $\beta_p$  value depends weakly on  $n_H/n_e$ . If we assume that  $T_e(r)$  is limited by this instability, the energy confinement time reduces to the order of 100 ms for the parameters of Fig. 3.

## 6. CURRENT DRIVE IN HIGH DENSITY PLASMA

The current drive by using the phase shifted antenna array in the toroidal direction is examined [10]. The Fokker-Planck equation for electrons at each spatial point is combined with the ICRF 1-D wave code [1]. The stationary distribution function is given by

$$F(u) = C \exp \left[ - \int_0^u u du / (1 + D_w/D_c) \right]$$

where  $u = v/v_e$  ( $v_e$  is the electron thermal velocity) and  $D_w$  and  $D_c$  are quasi-linear and collisional diffusion coefficients, respectively [10]. The current is driven by Landau damping and TTMP. Application to JET plasma is given, assuming that seven antennas are installed on the low field side. Figure 4(a) shows the induced current profile and the normalized efficiency  $\eta \equiv (J(x)/P_c(x))(mv_e\nu_0/n_e e)$  [11]

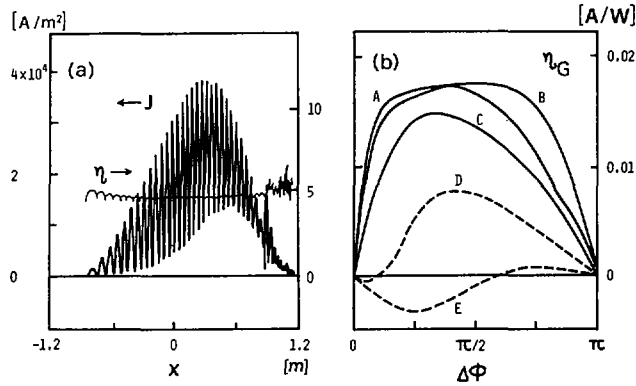


FIG. 4. (a) Induced current profile and normalized efficiency.  $B_i = 2.165$  T,  $\omega/2\pi = 43$  MHz,  $n_{e0} = 8 \times 10^{19} \text{ m}^{-3}$ ,  $T_0 = 10$  keV,  $n_H/n_e = 0.1$ ; (b) phasing and spacing dependence of global efficiency  $\eta_G$  for  $\omega/2\pi = 33$  MHz and  $n_{e0} = 10^{20} \text{ m}^{-3}$ . A:  $\Delta z = 0.126$  m, B:  $\Delta z = 0.188$  m, C:  $\Delta z = 0.295$  m, D:  $\Delta z = 0.377$  m, E:  $\Delta z = 0.589$  m.

(antenna spacing  $\Delta z = 0.188$  m, phase difference  $\Delta\phi = 2\pi/9$ ). At the density of  $n_{e0} = 8 \times 10^{19} \text{ m}^{-3}$ , the current is driven near the plasma centre. About 85% of the incident power is absorbed directly by the electrons. The global efficiency  $\eta_G \equiv I_{\text{RF}}/P_{\text{RF}}$  is 0.025 A/W.

Phasing and spacing dependences are examined (Fig. 4(b)). It is found that  $\Delta z$  has an upper limit to avoid negative current, which is generated by the subpeaks of the radiated RF spectrum. Once the spacing is properly chosen (such as the cases A, B and C), the efficiency is insensitive to the number of antennas. The  $\Delta\phi$  dependence of  $\eta_G$  is weak for  $\pi/4 \lesssim \Delta\phi \lesssim 3\pi/4$ .

## 7. SUMMARY AND DISCUSSION

We have studied an ICRF heated plasma in a tokamak. The wave thermalization transport analysis enables us to deal quantitatively with transport phenomena and stability of the ICRF sustained tokamak plasmas. Through the kinetic treatment of the wave in the ICRF heated plasma, high antenna loading, good accessibility, controllability of deposition profile, sustainment of high energy particles in the core region, and current drive ability in the high density regime are confirmed for present day machines and future designs. The wave thermalization transport code simulates the experimental observation of temperature rise and confinement time. It is found that the central ICRF heating is responsible for the internal kink instability, which may limit global confinement. A future task is to investigate the transport coefficient of ICRF heated tokamaks by applying the analysis to large tokamak experiments.

## ACKNOWLEDGEMENTS

This work was supported by a grant in aid for fusion research and scientific research from the Ministry of Education, Science and Culture of Japan.

## REFERENCES

- [1] FUKUYAMA, A., NISHIYAMA, S., ITOH, S.-I., ITOH, K., Nucl. Fusion **23** (1983) 1005.
- [2] FUKUYAMA, A., GOTO, A., ITOH, S.-I., ITOH, K., Jpn. J. Appl. Phys. **23** (1984) L613; FUKUYAMA, A., ITOH, K., ITOH, S.-I., Computer Phys. Rep. **4** (1986) 137.
- [3] JACQUINOT, J., ANDERSON, R., ARBEZ, D., BARTLETT, D., BEAUMONT, B., et al., Plasma Phys. Controll. Fusion **28** (1986) 1.
- [4] STIX, T.H., Nucl. Fusion **15** (1975) 737.
- [5] MORISHITA, T., FUKUYAMA, A., HAMAMATSU, K., ITOH, S.-I., ITOH, K., Analysis of the Minority Velocity Distribution and the Power Deposition Profile in ICRF Heating in Tokamak, Rep. HIFT-124, Inst. Fusion Theory, Hiroshima (1986).
- [6] GROEBNER, R.J., PFEIFFER, W., BLAU, F.P., BURRELL, K.H., FAIRBANKS, E.S., et al., Nucl. Fusion **26** (1986) 543.
- [7] CHANG, C.S., HINTON, F.L., Phys. Fluids **25** (1982) 1493.
- [8] BUSSAC, M.N., PELLAT, R., EDERY, D., SOULE, J.L., Phys. Rev. Lett. **35** (1975) 1638.
- [9] ITOH, K., ITOH, S.-I., TUDA, T., TOKUDA, S., J. Phys. Soc. Jpn. **53** (1984) 1759.
- [10] KISHIMOTO, Y., HAMAMATSU, K., FUKUYAMA, A., ITOH, S.-I., ITOH, K., ICRF Current Drive by Use of Phase Control of Antennas, Rep. HIFT-120, Inst. Fusion Theory, Hiroshima (1986).
- [11] FISCH, N.J., Phys. Rev. Lett. **41** (1978) 873.



# DOUBLE HELIX $\langle \vec{j} \times \vec{b} \rangle$ CURRENT DRIVE IN THE RF TOKAMAK DEVICE RYTHMAC

M.J. DUTCH, A.L. McCARTHY  
School of Physical Sciences,  
The Flinders University of South Australia,  
Bedford Park, South Australia,  
Australia

## Abstract

DOUBLE HELIX  $\langle \vec{j} \times \vec{b} \rangle$  CURRENT DRIVE IN THE RF TOKAMAK DEVICE RYTHMAC.

Travelling wave fields in  $m = 1$ ,  $n = 4$  double helix structures surrounding a toroidal plasma vessel are used to drive toroidal and poloidal plasma currents by means of the non-linear Hall effect technique  $\langle \vec{j} \times \vec{b} \rangle$  in high power experiments of short duration at 330 kHz. The evolution of the magnetic configuration has been studied using magnetic probe data to calculate and plot the poloidal flux function. Contours of equal driven toroidal current extracted from the same probe data reveal negative toroidal current at a small radius and at early times. This observation is consistent with the model presented. The rapidly rising quasi-steady driven toroidal current distributed over the minor section creates a changing magnetic flux and thus a back electromotive force (emf) observable as the loop voltage. This emf drives negative current along the path of minimum impedance. The configuration approaches a steady state where this back emf and negative current die away without any evidence of disruptions. A series of experiments with 40 ms of current drive is planned to study the equilibrium and stability of the configuration on this longer time-scale, beyond the start-up phase studied here. Extension of the  $\langle \vec{j} \times \vec{b} \rangle$  RF current drive technique to an  $m = +1$  and  $-1$  helical mesh antenna which drives purely toroidal current with no poloidal current is presented. The data for this case are contrasted with those for the  $m = +1$  double helix antenna and the  $m = -1$  double helix antenna applied separately, and a theoretical discussion of the drive by this helical mesh antenna is given.

## 1. INTRODUCTION

To achieve steady operation of a tokamak reactor it is necessary to develop continuous toroidal current drive. Many experimental groups have investigated RF techniques for such continuous current drive and research in this field has been reviewed recently by Jones [1].

We present here data and discussion which gives a detailed account of the start-up phase of our  $m = 1$  double helix driven RF tokamak RYTHMAC, shown schematically in figure 1a, whose experimental operation and theoretical basis in terms of the nonlinear Hall effect  $\langle \vec{j} \times \vec{b} \rangle$  have been previously reported [2,3]. This configuration, which has been reported by Hotta et al [4] to drive toroidal current, is shown here to drive toroidal and poloidal current; the poloidal current, which interacts with the

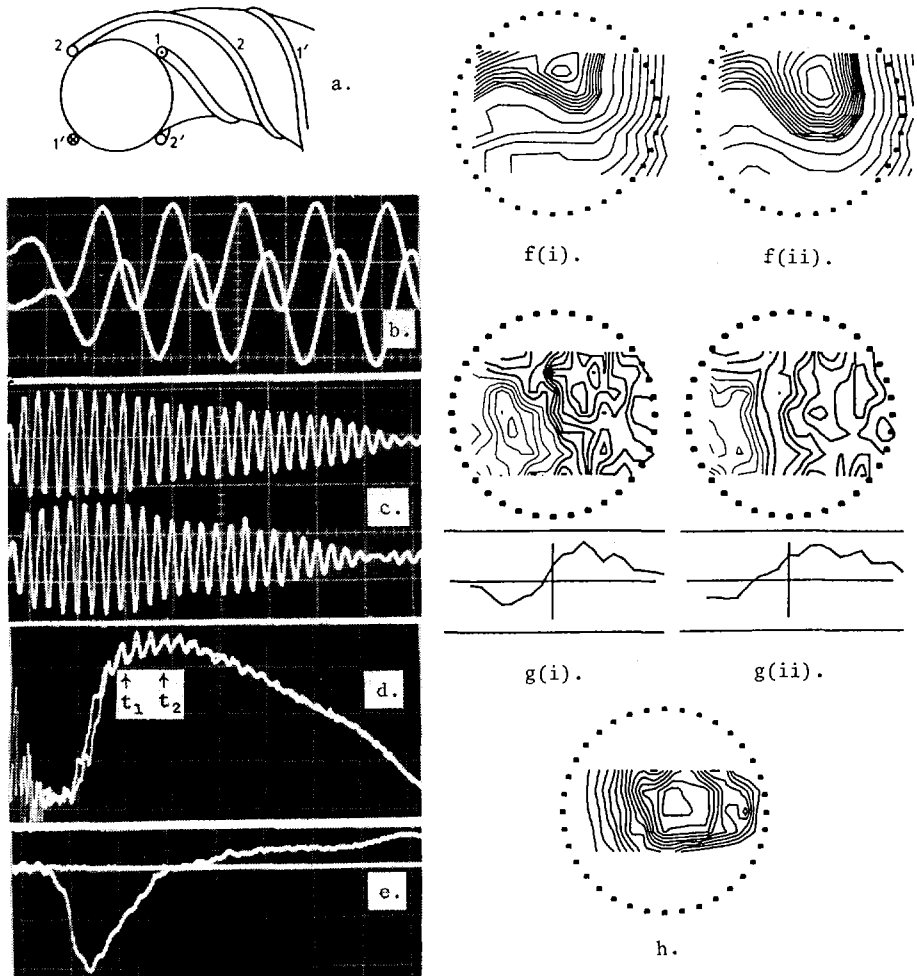


FIG. 1.

- a. Schematic diagram showing the  $m = 1$  double helix structure used to drive toroidal and poloidal currents.
- b. Line generator waveforms at  $2 \mu\text{s}$  per division, showing phase difference and reproducibility.
- c. Line generator waveforms,  $10 \mu\text{s}$  per division.
- d. Rogowski belt measure of toroidal current,  $10 \mu\text{s}$  per division,  $500 \text{ A}$  per division. The spike at  $5 \mu\text{s}$  is spark gap noise at the time the line generators are triggered. Figures 1b and 1d have two shots superposed to show the reproducibility.
- e. Loop voltage; the vertical scale is  $10 \text{ V}$  per division.
- f(i), f(ii). Poloidal flux contours at times  $t_1$  and  $t_2$  marked in d.
- g(i), g(ii). Contours of equal toroidal current density at times  $t_1$  and  $t_2$  marked in d. Heavy contours indicate positive current, light contours negative current. Below are the current profiles in the median plane.
- h. Contours of equal  $\Delta B_\phi$  caused by driven poloidal current.

toroidal field, will take part in the equilibrium and stability and may need to be controlled independently of the toroidal current.

We are led by our detailed study of the  $m = 1$  double helix current drive experiments to develop a new antenna configuration which we call the  $m = +$  and  $-1$  helical mesh antenna, shown schematically in figure 2 in a cylindrical geometry large aspect ratio approximation for clarity. We report observations which demonstrate experimentally that this antenna drives purely toroidal current without poloidal current as does the Synchroak configuration but with an  $m = 0$  antenna [5].

In the section entitled model and theory we give a résumé of the  $\langle \tilde{j} \times \tilde{b} \rangle$  technique of current drive for the  $m = 1$  double helix case. For the  $m = +$  and  $-1$  helical mesh antenna we determine the spatial and temporal dependence of the vacuum magnetic fields. The motion of these fields gives insight into the current drive of this device.

## 2. MODEL AND THEORY

### 2.1. $m = 1$ Double Helix Antenna

To describe the mechanism of steady current drive in our experiments in the simplest model, the ions are assumed immobile and uniformly distributed, and the electrons are treated as an inertialess, pressureless negatively charged fluid. We ignore steady applied magnetic fields. The generalised Ohm's law is written:

$$\underline{E} = \eta \underline{J} + \frac{1}{ne} \underline{J} \times \underline{B} \quad (1)$$

The RF currents in the helical structure of fig. 1a induce screening currents in the plasma which try to exclude the RF fields of the structure. But finite resistivity permits these fields to penetrate. The screening currents  $\tilde{j}$  follow helical paths parallel to the structure currents and because of resistivity have phase different from that of the RF magnetic field  $\tilde{b}$  of the structure. There will thus be a nonlinear Hall effect term consisting of a steady part and a part of frequency  $2\omega$ .

We include the steady parts of these nonlinear Hall effect terms in the components of Ohm's law, using angular brackets to denote the time averages:

$$E_{\phi} = \eta J_{\phi} - \frac{1}{ne} \langle \tilde{j}_{\theta} \tilde{b}_r \rangle \quad (2)$$

$$E_{\theta} = J_{\theta} + \frac{1}{ne} \langle \tilde{j}_{\phi} \tilde{b}_r \rangle \quad (3)$$

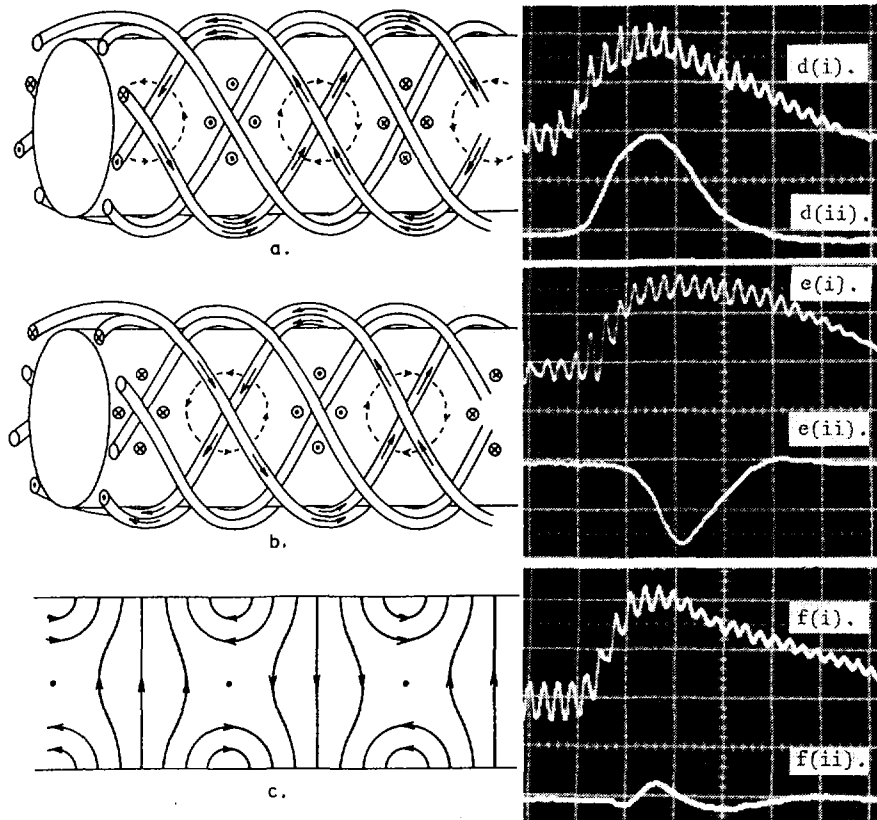


FIG. 2.

- a. Schematic diagram of the  $m = +1$  and  $-1$  helical mesh antenna viewed horizontally. The arrows on the windings show the direction of the RF structure currents at the instant when the current is maximum in phase 1 and zero in phase 2. The symbols  $\odot$  and  $\otimes$  in the plasma vessel indicate the structure of field  $\vec{b}$ . The nature of the screening currents  $\vec{j}$  induced in the plasma is represented by the dashed paths.
- b. The same structure as in a, one quarter of a period later. Now the RF current is zero in phase 1 and maximum in phase 2.
- c. Horizontal cut through the minor axis as seen from above, showing the vacuum travelling magnetic field pattern produced by the helical mesh antenna.
- d. Oscillogram data for  $m = +1$  double helix antenna.
- d(i), e(i), f(i). Steady driven toroidal current  $I_\phi$ , recorded at  $10 \mu\text{s}$  per division. The vertical scale is 450 A per division.
- d(ii), e(ii), f(ii). Change in the toroidal magnetic field on the minor axis,  $\Delta B_\phi(0, 0)$ , caused by the driven poloidal current recorded at  $10 \mu\text{s}$  per division. The vertical scale is about 0.004 T per division.
- e. Data for the  $m = -1$  double helix antenna.
- f. Data for the  $m = +1$  and  $-1$  helical mesh antenna.

From these equations we see that even in the absence of imposed electric fields, such as the inductively coupled  $E_\phi$  of the Tokamak, we would expect the nonlinear Hall effect term to balance the resistive terms to drive not only toroidal current but also poloidal current. We have presented a complete treatment of this problem in helical coordinates, with some analytic and some numerical solutions [3].

## 2.2. $m = +$ and $-1$ Helical Mesh Antenna

We represent the structure currents shown in figures 2a and 2b in the natural helical coordinate systems  $(\hat{r}, \hat{\chi}_{+1}, \hat{\zeta}_{+1})$  and  $(\hat{r}, \hat{\chi}_{-1}, \hat{\zeta}_{-1})$  for the  $m = +1$  and  $m = -1$  conductors, respectively [3].

$$\tilde{j}_{\text{ext}} = \text{Re} \left[ \frac{I_e}{2} e^{i(\omega t + \chi_{+1})} \hat{\zeta}_{+1} + \frac{I_e}{2} e^{i(\omega t - \chi_{-1})} \hat{\zeta}_{-1} \right] \frac{\delta(r - r_0)}{r_0}$$

which can be written in cylindrical coordinates as:

$$\tilde{j}_{\text{ext}} = \text{Re} \left[ \frac{I_e}{2} e^{i(\omega t + \theta + kz)} \left( \frac{-kr \hat{\theta} + \hat{z}}{k_0 r} \right) + \frac{I_e}{2} e^{i(\omega t - \theta + kz)} \left( \frac{kr \hat{\theta} + \hat{z}}{k_0 r} \right) \right] \frac{\delta(r - r_0)}{r_0}$$

and we sum to get

$$\tilde{j}_{\text{ext}} = \frac{I_e}{k_0 r} \left[ kr \sin(\omega t + kz) \sin(\theta) \hat{\theta} + \cos(\omega t + kz) \cos(\theta) \hat{z} \right] \frac{\delta(r - r_0)}{r_0} \quad (4)$$

$I_e$  measures the strength of the RF currents in the helical conductors located at radius  $r_0$  and of pitch length  $\ell = 2\pi/k$ ;  $k_0 = (k^2 + \frac{1}{r^2})^{\frac{1}{2}}$ .

Maxwell's equations in helical coordinates give the total structure field

$$\tilde{b} = \text{Re} \left[ iB_\omega I_1'(kr) \left\{ e^{i(\omega t + \chi_{+1})} + e^{i(\omega t - \chi_{-1})} \right\} \hat{r} - \frac{B k_0}{k} I_1(kr) \left\{ e^{i(\omega t + \chi_{+1})} \hat{\chi}_{+1} - e^{i(\omega t - \chi_{-1})} \hat{\chi}_{-1} \right\} \right]$$

where  $B_{\omega}$  measures the strength of this RF field at  $r=0$  and is proportional to  $I_e$ .  $I_1(kr)$  is a modified Bessel function of order 1.

Expressing this in cylindrical coordinates and summing we get:

$$\tilde{b} = 2B_{\omega} \left[ I_1(kr) \sin(\omega t + kz) \cos(\theta) \hat{r} - \frac{I_1(kr)}{kr} \sin(\omega t + kz) \sin(\theta) \hat{\theta} + I_1(kr) \cos(\omega t + kz) \cos(\theta) \hat{z} \right] \quad (5)$$

from which we may note immediately that all three spatial components of the field progress as a wave on the structure in the axial direction, as indicated by the  $\sin(\omega t + kz)$  dependence, but do not progress in the poloidal direction  $\hat{\theta}$ . Figure 2c shows a partial representation of  $b$ .

Immediately we see from the model of electrons being entrained to move with the field lines (provided  $\frac{eb}{m_i} \ll \omega \ll \frac{e\tilde{b}}{m_e}$ ), while ions remain essentially at rest, that net current can be driven in the axial direction, but no current will be driven in the poloidal direction.

A full analysis using the interaction of the screening currents with the structure fields will be presented elsewhere.

### 3. EXPERIMENTS

#### 3.1. *m = 1 Double Helix antenna experiments*

The experiments were performed in the RYTHMAC device which has a pyrex glass toroidal vessel of major radius 25 cm and minor radius 5 cm. A DC toroidal field of 0.03 Tesla and a vertical field of 0.008 Tesla was applied. The working gas was Argon at 1 millitorr. No preionisation was used.

The antenna is fed by two RF sources which are modified Weibel line generators, giving 16 periods of 330 kHz radio frequency current at a power of about 3.5 Megawatt per line. The duration of each shot is about 50  $\mu$ s.

An externally integrated Rogowski belt measures the total toroidal current. Hall probes which compare the vertical field produced by the driven current  $I_{\phi}$  at the centre of the torus with the DC vertical field give results in excellent

agreement. Poloidal current as well as toroidal current is driven by the double helix antenna structure[3].

In figure 1b,c we display the RF line generator waveforms and in figure 1d we see the quasi steady driven toroidal current as measured by the Rogowski belt. It is important to note that two shots are overlapped in fig. 1b,d, which demonstrates a high degree of reproducibility in the data allowing us to study the plasma configuration by analysing data from several hundred shots. The driven toroidal current in fig. 1d is approximately 1.5 kA.

The magnetic configuration has been studied by measuring the  $B_r$  and  $B_z$  components of the magnetic field on a grid of points in the minor section; from this set of data the poloidal flux function has been calculated. Flux contours for the configuration produced are shown in fig.1f. The driven toroidal current extracted from the magnetic probe data shows, in fig. 1g, negative current at small radius at early times. This is the result of the back emf caused by the flux of the distributed driven toroidal current driving negative current on the path of minimum impedance.

A single-turn loop is used to measure the back emf (see figure 1e). For a vacuum shot with full RF current drive applied the loop voltage  $V_L$  is of course zero, unlike the loop voltage with a vacuum shot for an inductively driven tokamak. The loop voltage to be observed for a non-inductively driven tokamak is a result of the changing flux created by the rapidly rising driven toroidal current. For a non-inductively driven tokamak the forward driving term is localised while the back emf  $V_L = \int \underline{E} \cdot d\underline{\ell} = \frac{-d\Phi_B}{dt}$  is not. The spatial distribution of these terms need not be the same. On the shortest toroidal paths,  $E_\phi$  in  $\int \underline{E} \cdot d\underline{\ell} = \frac{-d\Phi_B}{dt}$  can exceed  $\frac{1}{ne} \langle \tilde{j}_\theta \tilde{b}_r \rangle$  of equation (2)

and negative current will be driven in that part of the minor section. For inductively driven tokamaks, only the net flux changes in the core are important and  $\int \underline{E} \cdot d\underline{\ell} = \frac{-d\Phi_B}{dt}$  has the same sign on all toroidal paths within the plasma.

In this experiment the RF is maintained for a relatively short time because the sources are line generators, and the loop voltage goes to zero as the driven current maximises; the loop voltage changes sign when the driven current falls. This back emf driven negative current dies away as the configuration evolves. If the RF drive were to be maintained, this transient phenomena would cause no problems, but during the start-up phase the interaction of this current contributes to the forces which will determine the equilibrium and stability.

Of more concern for this  $m = 1$  double helix current drive configuration in determining equilibrium is the role played by the driven poloidal current. Evidence for the existence of this current is given in fig. 1h as a contour plot of equal  $\Delta B_\phi$ , the change in toroidal field created by the driven poloidal current. It is important to the discussion that the measured magnitude of the  $\Delta B_\phi$  requires the poloidal current density  $J_\theta$  to be approximately the same as the driven toroidal current density  $J_\phi$ , as expected from the theoretical analysis[3]. It follows that the interaction of  $J_\theta$  with the imposed  $B_\phi$  is a very important term in determining equilibrium, giving approximately three times as large a force as the interaction of the toroidal current with the appropriate vertical field for equilibrium in the absence of driven poloidal current. Unlike the interaction of the negative toroidal current in the start-up phase, the interaction of this driven poloidal current with the toroidal field provides a term in the equilibrium equations which is maintained continuously. Accordingly we sought to control this.

### 3.2. $m = +$ and $-1$ Helical Mesh Antenna Experiment

For these experiments the RYTHMAC machine and plasma conditions were essentially the same as in 3.1, except that the  $m = +$  and  $-1$  helical mesh antenna shown schematically in fig. 2 was built from superposed  $m = +1$  and  $m = -1$  double helix antennas. By making different connections, the windings can be operated as just an  $m = +1$  or just an  $m = -1$  antenna as well as the helical mesh antenna. The impedance presented to each of the RF sources differs in the different configurations, but we choose the operating conditions such that for all the data presented the magnitude of the RF currents in the antenna windings is approximately the same. For the helical mesh antenna, one line generator phase feeds one pair of the  $m = +1$  coils in series with one pair of the  $m = -1$  coils, while the other RF source delayed by one quarter of a period feeds the other pairs similarly.

The data presented compare the results for driven toroidal and poloidal current from the three different antenna configurations;  $m = +1$  double helix in fig. 2d,  $m = -1$  double helix in fig. 2e and the  $m = +$  and  $-1$  helical mesh antenna in fig. 2f. The toroidal current is measured using a calibrated Rogowski belt. Poloidal current is monitored using an integrated wirewound probe placed at the centre of the minor section to measure the change in the toroidal field  $\Delta B_\phi(0,0)$ .

For all three cases the sign of the toroidal current,  $I_\phi$ , is the same; that driven by the helical mesh antenna is slightly

greater in magnitude. The  $\Delta B_\phi(0,0)$  caused by the poloidal current driven by the  $m = -1$  double helix antenna is opposite in sign to that for the  $m = +1$  case, indicating that the poloidal currents flow in opposite directions for these two configurations. The helical mesh antenna makes a much smaller  $\Delta B_\phi(0,0)$ , consistent with a small driven poloidal current relative to that for the other two antennas.

#### 4. SUMMARY

We have made detailed studies of the start-up phase of the  $m = 1$  double helix  $\langle \tilde{j} \times \tilde{b} \rangle$  RF current drive configuration. In approaching problems encountered there, we have built and successfully tested an antenna for  $\langle \tilde{j} \times \tilde{b} \rangle$  RF current drive which produces essentially pure toroidal current of magnitude approximately 900 Amps for the conditions chosen, without driving poloidal current.

#### ACKNOWLEDGEMENTS

The authors are grateful for the loan of the RF sources from Professor I.R. Jones. This work has been supported by grants from the Australian Research Grants Scheme and the Australian Institute of Nuclear Science and Engineering.

#### **REFERENCES**

- [1] JONES, I.R., Comments Plasma Phys. Controll. Fusion **10** 3 (1986).
- [2] DUTCH, M.J., McCARTHY, A.L., Plasma Phys. Controll. Fusion **28** (1986) 695.
- [3] DUTCH, M.J., McCARTHY, A.L., STORER, R.G., Phys. Rev. Lett. **56** (1986) 1563.
- [4] HOTTA, E., SUZUKI, M., OHTA, H., HAYASHI, I., Jpn. J. Appl. Phys. **24** (1985) 110.
- [5] FUKUDA, M., MATSUURA, K., HIRANO, K., MOHRI, A., FUKAO, M., J. Phys. Soc. Jpn. **41** (1976) 1376.



# DEPENDENCE OF POWER ABSORBED IN A PLASMA ON ALFVÉN HEATING ANTENNA PARAMETERS

A.G. KIROV, V.P. SIDOROV, A.G. ELFIMOV,  
S.N. LOZOVSKIJ, L.F. RUCHKO, K.G. KOMOSHVILI,  
V.V. ONISHCHENKO, V.V. DOROKHOV, A.V. SUKACHEV,  
V.D. SAMUSHIA, L.Ya. MALYKH, N.L. GULASARYAN,  
D.A. VOJTENKO

I.N. Vekua Institute of Physics and Technology,  
USSR State Committee for Utilization of Atomic Energy,  
Sukhumi, Union of Soviet Socialist Republics

## Abstract

DEPENDENCE OF POWER ABSORBED IN A PLASMA ON ALFVÉN HEATING ANTENNA PARAMETERS.

The results of theoretical and experimental studies on plasma heating by Alfvén waves are presented for various types of antennas and their parameters. The relation between central and peripheral heating is analysed. Analytic expressions are given for slow Alfvén wave amplitudes on the plasma edge. The new results of the numerical computations are analysed, and conditions for RF power input into the central plasma region for devices of different sizes are formulated. For the R-O device, a high heating efficiency of the poloidal antenna is demonstrated, and the electric field amplitudes inside the plasma column are measured.

## 1. INTRODUCTION

Alfvén heating efficiency and the possibility of controlling the plasma parameters by an Alfvén wave depend on the ratio between the energy input by the slow Alfvén wave at the plasma edge and that by the kinetic Alfvén wave within the conversion zone; these properties also depend on the degree of proximity of the 'helical' resonance frequency to the lower boundary of the Alfvén continuum, when the RF power input occurs near the plasma centre and the active antenna impedance is highest. These conditions depend strongly upon the antenna parameters ( $m$ ,  $n$ ).

These items have already been considered and even partially solved, both theoretically and experimentally [1-6]. In this paper, we present our new results on this subject.

## 2. ANALYTIC CONSIDERATION

RF fields excited by an antenna with RF currents,  $\sim \exp i(\Omega t - m\varphi - k_z z)$ , in a plasma cylinder of radius  $a$  and length  $2\pi R$  placed in a helical magnetic field

$\vec{B}_0$  were determined by means of a technique described in Refs [7, 8]. The assumptions that are made and the notations we apply are the same as in Refs [7, 8]. Except for a certain region near the conversion point  $r_A$ , where  $\epsilon_1 = N_{\parallel}^2$  ( $N_{\parallel}^2 = k_{\parallel}^2 c^2 / \Omega^2$ ,  $k_{\parallel} = k_z (1 + m/nq)$ ),  $n \equiv k_z R$  is the toroidal wavenumber, the amplitudes of the RF electric field components in the plasma may be represented in the form  $\mathcal{E}_j = \bar{\mathcal{E}}_j + \tilde{\mathcal{E}}_j$ , where  $\bar{\mathcal{E}}_j(r)$  is the 'smooth' part of the field connected with the fast (MHD) wave and determined from the solution of a second order MHD equation [9, 10], and  $\tilde{\mathcal{E}}_j(r)$  is the 'fast alternating' part of the field connected with the slow Alfvén wave of small wavelength  $\lambda_A$  or damping depth  $\delta_S$  ( $\delta_S, \lambda_A/2\pi \ll \Delta$ ,  $\Delta \leq a$  is the scale of plasma non-uniformity). In particular, in the 'cold' plasma region, where  $v_{re} < v_{ph} \equiv \Omega/k_z$ ,  $r_A < r_{ph} < r < a$  [10] ( $r_{ph}$  is the 'phase resonance' point, where  $v_{re} = v_{ph}$ ), we find, by a WKB approach and assuming that the conditions  $k_z a / |m| \ll 1$ ,  $\epsilon_1(a) / |m| \bar{\epsilon}_2(a) \gg \lambda_A / 2\pi a$ ,  $\nu_{ei} \ll \Omega$  are fulfilled:

$$\tilde{\mathcal{E}}_r = [(r\bar{\mathcal{E}}_{\varphi})' - (m\bar{\epsilon}_2/\epsilon_1)\bar{\mathcal{E}}_{\varphi}]_{r=a} (f(a)/f(r)) (\varphi(a)/\varphi(r)) \quad (1)$$

where

$$f(r) = \sqrt{r} (\epsilon_1 \epsilon_3)^{1/4} (N_{\parallel}^2 - \epsilon_1)^{1/4}$$

$$\varphi(r) = \sin \left[ 2\pi \int_{r_{ph}}^r \frac{dr}{\lambda_A} + \beta \right]$$

$$\lambda_A(r) = (2\pi c/\Omega) [\epsilon_3 (1 - N_{\parallel}^2/\epsilon_1)]^{-1/2}$$

$$\bar{\epsilon}_2 = \epsilon_2 - \frac{2N_{\parallel}^2}{n + m/q} \frac{1}{2r} \left( \frac{r^2}{q} \right)'$$

$$\text{tg}\beta = \lambda_A (r_{ph} + 0) / 2\pi\delta_S (r_{ph} - 0)$$

for a 'hot' peripheral plasma ( $v_{Te} > v_{ph}$ ),

$$\varphi(r) = \exp \left[ \int \frac{dr}{\delta_S(r)} \right]$$

Assuming that  $|m|\bar{\epsilon}_2(a)/\epsilon_1(a) \geq 1$ ,  $(r\bar{\mathcal{E}}_{\varphi})'_a \sim \bar{\mathcal{E}}_{\varphi}(a)$  and taking, for simplicity,  $q = \text{const}$ , we obtain from (1) that the ratio of slow and fast wave amplitudes at  $r = a$  is of the order of

$$\begin{aligned}
 (\tilde{\mathcal{E}}_r/\mathcal{E}_r)_a &\approx \frac{n_0(r_A)}{n_0(a)} \frac{2m}{m + nq(a)} \frac{\overline{\mathcal{E}}_\varphi(a)}{(r\overline{\mathcal{E}}_\varphi)'_a} \\
 (\tilde{\mathcal{E}}_\varphi/\overline{\mathcal{E}}_\varphi)_a &\approx \left( \frac{\tilde{\mathcal{E}}_r}{\overline{\mathcal{E}}_r} \right)_a \frac{\lambda_A}{2\pi a}
 \end{aligned}
 \tag{2}$$

$n_0(r)$  is the plasma density for a hot peripheral plasma,  $\lambda_A/2\pi a - \delta_S/a$ .

We see from Eq. (2) that, for sufficiently low plasma density at the boundary, the amplitude  $\tilde{\mathcal{E}}_r(a)$  (but not  $\tilde{\mathcal{E}}_\varphi$ ) may reach high values. This effect is essentially connected with the stationary current  $j_z$  and disappears when  $j_z(a) = 0$ .

### 3. NUMERICAL COMPUTATIONS

The antenna active impedances were calculated in cylindrical geometry within the kinetic approach, using the one-dimensional numerical code EPSI, analogous to [3]. It is shown that the maximum impedance and the best RF power input localization occur at  $|k_z a| = 2.5$  for devices with various aspect ratios: INTOR ( $\approx 4.2$ ; circular cross-section), TFTR ( $\approx 3.0$ ) and T-10 ( $\approx 5.1$ ).

In Ref. [4], the RF power absorption maximum had been found, in the MHD approach, at  $|k_z a| = 2.5$  for  $m = -1$ . Here, this effect is found for modes with  $m = \pm 1, -2, -3, -4$ . Figure 1 shows an example of the active plasma impedance versus the position of the local Alfvén resonance point  $X_A$ . The computations have been carried out for INTOR, with the plasma density distributed parabolically and the electron temperature profile given by  $T_e(x) = T_0 \{1 - [1 - (T_1/T_0)^{1/\gamma}]x^2\}^\gamma$ , where  $\gamma = 4/3$ ,  $T_1/T_0 = 0.025$ ,  $q(a) = 2.19$ . Figure 1(b) shows the impedance curves for the  $m = +1$  mode. We see that the direction of wave rotation does not

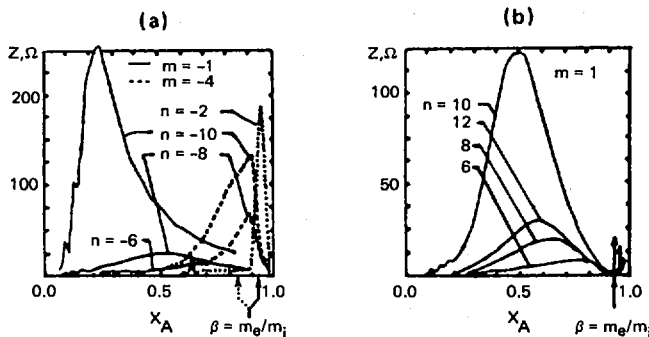


FIG. 1. Plasma impedance versus conversion point position for various INTOR modes (a) for  $m < 0$ ; (b) for  $m > 0$ .

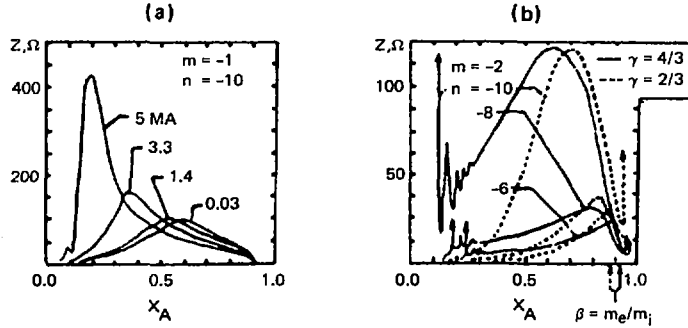


FIG. 2. Plasma impedance versus conversion point position for  $m = -1$ ,  $n = -10$  mode at various values (a) of plasma current, (b) of shear ( $\gamma$  parameter).

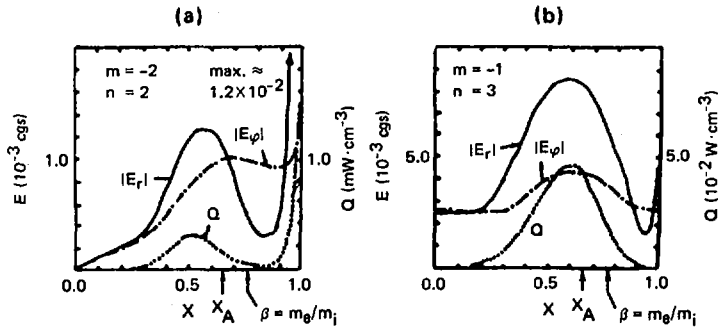


FIG. 3. Radial distribution of electric field and absorbed power in R-O device: (a) for  $m = -n = -2$ ; (b) for  $m = -1$ ,  $n = 3$ .

have any substantial effect on the value of the absorption, which is due to small gyrotropy in INTOR ( $\Omega/\omega_{ci} \lesssim 0.1$ ). The effect of the plasma current on the plasma impedance properties has been studied. The results shown in Fig. 2(a) permit the conclusion that a current value of  $\sim 5$  MA is preferable from the point of view of absorption level and its localization (here,  $\gamma = 2/3$ ).

As is seen from Fig. 2(b), a shear effect of the magnetic field only occurs in that part of the plasma where high-Q kinetic resonances are observed. The parameter  $\gamma$  determines the temperature and the current (through Spitzer's conductivity law) profiles (here,  $q(a) = 1.44$ ).

The 'global' Alfvén modes [4, 5, 10] are studied as a function of  $|k_z a|$ , and it is shown that (1) below the Alfvén continuum threshold, there may exist two and more resonances of the 'global' mode and, (2) in certain conditions, the 'global' mode may penetrate into the continuum for  $|k_z a| \ll 1$  and leave it for  $|k_z a| > 2.5$ .

Fields and absorbed power have been computed for the devices of the R-O type ( $a = 3.5$  cm,  $R = 50$  cm,  $B_0 = 2.5$  kG,  $T_0(0) = 15$  eV,  $n_0(0) = 2 \times 10^{13}$  cm $^{-3}$ ). Figures 3(a,b) show the distributions of the electric fields and absorbed power densities for the  $m = -2$ ,  $n = 2$  and  $m = -1$ ,  $n = 3$  modes, respectively. The conversion point was fixed at  $X_A = 0.65$ . It is seen that, for the  $m = -1$ ,  $n = 3$  mode, the slow Alfvén wave contribution to the power absorbed at the plasma boundary is small and the main portion of the power is absorbed in the central zone. Calculations carried out for various conversion point positions and for frequencies below the Alfvén continuum threshold have shown that the wave amplitudes and the power input at the periphery for the  $m = -1$ ,  $n = 3$  mode are always smaller than for the  $m = -2$ ,  $n = 2$  mode.

#### 4. EXPERIMENTAL STUDIES

The R-O device [1] is an  $\ell = 3$  stellarator with a quartz discharge chamber ( $R = 50$  cm,  $b = 5$  cm,  $a = 3.5-4$  cm,  $B_0 \leq 8$  kG,  $\epsilon \leq 0.8$ ). The helical and poloidal antennas were fed by separate generators with frequencies chosen so as to satisfy the Alfvén resonance condition in radially close regions. For the helical antenna with  $m = +2$ ,  $n = +2$ , the frequency is  $f = 1.25$  MHz, while for the poloidal one with  $m = +1$ ,  $n = +3$ , we have  $f = 2.2$  MHz.

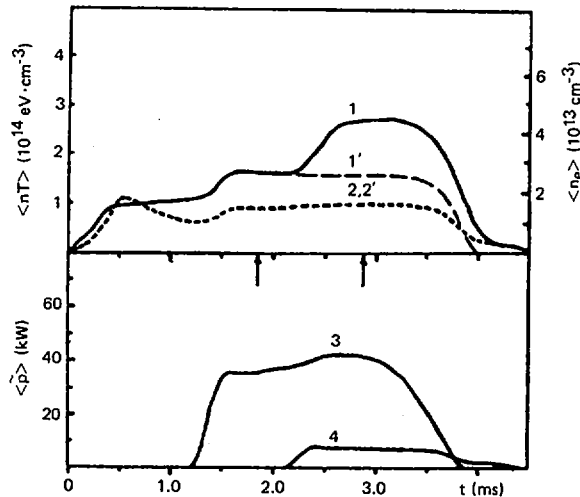


FIG. 4. Energy content (1), plasma density (2) and absorbed RF power due to helical (3) and poloidal (4) antennas: (1, 2 — only helical antenna switched on).  $H_2$ ,  $\nu_0 = 0.4$ ,  $B_0 = 2.6$  kG.

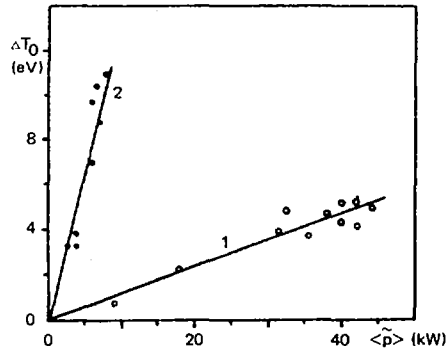


FIG. 5. Temperature increase for helical (1) and poloidal (2) antennas versus absorbed RF power.  $H_2$ ,  $\iota_0 = 0.4$ ,  $B_0 = 2.6$  kG,  $\langle n_e \rangle \approx 1.5 \times 10^{13} \text{ cm}^{-3}$ .

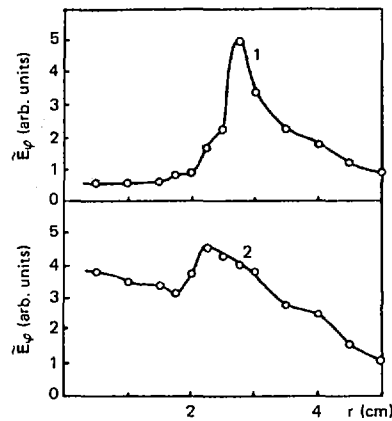


FIG. 6. Radial distribution of RF-field  $E$  component measured at instants of time indicated by arrows in Fig. 4: 1 -  $f = 1.25$  MHz, helical antenna; 2 -  $f = 2.15$  MHz, poloidal antenna;  $H_2$ ,  $\iota_0 = 0.4$ ,  $B_0 = 2.6$  kG.

The principal goal of the experiments was to study the dependence of the relative heating efficiencies and the impedances on  $m$ ,  $n$  and on the types of antennas. The discharge oscillograms are shown in Fig. 4. The special generator produced an initial plasma with  $\bar{n}_0 \sim (1-1.5) \times 10^{13} \text{ cm}^{-3}$  and  $T_e = 5 \text{ eV}$ ; then the helical antenna was switched on and, later, the poloidal antenna with  $m = \pm 1$ ,  $n = \mp 3$  was turned on. From the plasma diamagnetism, density and absorbed power measurements, the temperature increase ( $\Delta T$ ) and, hence, the heating efficiency ( $\eta = (\Delta T/P) n_0(10^{13})$ ) are found. As is seen from Fig. 4, the heating efficiency of the poloidal antenna is many times higher than that of the helical antenna. This effect remained virtually unchanged over a wide range of absorbed powers (Fig. 5).

Estimates of active impedances,  $Z_a = 2P/I^2$ , for both types of antennas were made, and it was found that they depend weakly on the level of power input.

Figure 6 shows the distributions of the electric fields in the plasma (measured by a double electrical probe), excited by helical and poloidal antennas. We see that, for the helical antenna, the electric field amplitudes at the plasma boundary (the separatrix radius is  $r_s = 3.5$  cm) are much larger than in the region of  $r = 2.5$  cm, which was identified as a conversion zone. For the poloidal antenna, the field amplitudes in these regions are comparable. These results indicate that the  $m = \pm 1$ ,  $n = \mp 3$  wave heats the central plasma region quite efficiently while the  $m = \pm 2$ ,  $n = \mp 2$  wave is absorbed mainly in the boundary region as a result of predominant excitation of a peripheral slow Alfvén wave, which accounts for the low efficiency heating by the helical antenna, under the given conditions.

The analytic (Eq. (2)) and numerical (Fig. 3) computations show that, for the  $m = -1$ ,  $n = 3$  mode, the field amplitudes are smaller at the plasma boundary than in the plasma core, and RF power is absorbed mainly in the inner region. In contrast to this, for the  $m = -2$ ,  $n = 2$  mode, the field amplitudes at the boundary are much larger, and power is absorbed predominantly at the periphery.

Thus, the results of the experiments, the numerical and the analytic computations agree qualitatively. The present experiments cannot, however, set forth all possible merits of the kinds of antennas in question since in our experiments this possible effect is masked by the strong dependence of wave generation and absorption on  $m$  and  $n$ .

## 5. CONCLUSIONS

The analytic and numerical calculations and the experimental results presented demonstrate, as a whole, that, for efficient plasma heating, modes with large  $n/m$  ratios should be generated. For a wide class of devices (T-10, INTOR), this ratio varies from 10 to 12. For INTOR, the optimum mode has  $m = -1$ ,  $n = -10$ .

The experiments presented demonstrate a substantial increase in Alfvén heating efficiency, even if one proceeds from  $n/m = -1$  to  $n/m = -3$ .

## REFERENCES

- [1] KIROV, A.G., et al., in Plasma Physics and Controlled Nuclear Fusion Research 1984 (Proc. 10th Int. Conf. London, 1984), Vol. 1, IAEA, Vienna (1985) 643.
- [2] KIROV, A.G., et al., in Controlled Fusion and Plasma Physics (Proc. 12th Europ. Conf. Budapest, 1985), Vol. 2, Part 2, European Physical Society (1985) 260.
- [3] ROSS, D.W., LI, Y., MAHAJAN, S.M., MICHIE, R.B., Nucl. Fusion **26** (1986) 139.
- [4] APPERT, K., VACLAVIK, J., Plasma Phys. **25** (1983) 551.
- [5] APPERT, K., VACLAVIK, J., VILLARD, L., Phys. Fluids **27** (1984) 432.
- [6] DE CHAMBRIER, A., et al., in Plasma Physics and Controlled Nuclear Fusion Research 1984 (Proc. 10th Int. Conf. London, 1984), Vol. 1, IAEA, Vienna (1985) 531.

- [7] LOZOVSKY, S.N., DOROKHOV, V.V., Jr., *Fiz. Plazmy* **11** (1985) 539;  
ELFIMOV, A.G., *Fiz. Plazmy* **11** (1985) 550;  
ELFIMOV, A.G., in *Heating in Toroidal Plasmas* (Proc. 2nd Joint Varenna-Grenoble Int. Symp. Como, 1980), Vol. 2, CEC, Brussels (1980) 683.
- [8] ELFIMOV, A.G., LOZOVSKY, S.N., DOROKHOV, V.V., Jr., *Nucl. Fusion* **24** (1984) 609.
- [9] SOLOVI'EV, L.S., in *Voprosy Teorii Plazmy* (LEONTOVICH, M.A., Ed.), Vol. 6, Moscow, Atomizdat (1972).
- [10] ROSS, D.W., CHEN, G.L., MAHAJAN, S.M., *Phys. Fluids* **25** (1982) 652.

## RECENT ADVANCES IN THE THEORY AND MODELLING OF RF HEATING IN INHOMOGENEOUS PLASMAS

D.G. SWANSON, S. CHO

Department of Physics,  
Auburn University,  
Auburn, Alabama

C.K. PHILLIPS

Princeton Plasma Physics Laboratory,  
Princeton University,  
Princeton, New Jersey

D.Q. HWANG

Department of Applied Science,  
University of California, Davis/Livermore,  
Livermore, California

W. HOULBERG, L. HIVELY

Oak Ridge National Laboratory,  
Oak Ridge, Tennessee

United States of America

### Abstract

RECENT ADVANCES IN THE THEORY AND MODELLING OF RF HEATING IN INHOMOGENEOUS PLASMAS.

Theoretical and numerical modelling of rf heating in inhomogeneous plasmas is discussed. (1) A case is examined near the lower hybrid resonance where two turning points are encountered near one another, first from a cold to a warm wave and then from the warm wave to an ion Bernstein mode. This leads to a sixth order equation which is difficult to solve as it has a quadratic coefficient. (2) Improved asymptotic representations are presented whose accuracy is crucial to the numerical solution of this type of equation. (3) A new method of exact order reduction for higher order equations with no approximations permits generation of a numerical Green function by integrating only second order equations. The differential equation is factored with an asymptotically small source term. The resulting integral equation is more easily solved. (4) A formalism for determining the 2-D structure of the wave fields and the associated power deposition profiles within the mode conversion-absorption layer has been developed by applying the parabolic approximation method to the linearized Vlasov-Maxwell equations. The new method reduces the problem to the solution of one fourth order equation and an associated parabolic diffusion type equation. (5) Time dependent transport simulations of ICRF heated discharges in tokamaks with circular and non-circular cross-sections are presented. The simulations are obtained by interfacing the WHIST 2-D MHD equilibrium and a 1-D flux surface averaged transport code with a ray tracing algorithm.

### 1. Three Wave Mode Conversion Equation

The dispersion relation for lower hybrid waves near ion cyclotron harmonics is approximately given by[1]

$$\frac{k_{\parallel}^2}{k_{Di}^2} \left( 1 - \frac{\omega_{pe}^2}{\omega^2} \right) + \frac{\omega_{ci}^2}{\omega_{pi}^2} \left( 1 + \frac{\omega_{pe}^2}{\omega_{ce}^2} \right) \lambda = \frac{1}{2} \wp Z'(\sqrt{\xi}) + e^{-\lambda} I_{\nu}(\lambda) \pi \nu \cot \pi \nu - \frac{\nu I_n(\lambda) Z'(\zeta_n)}{2e^{\lambda}(\nu - n)} \tag{1}$$

where  $n$  is the harmonic number being considered and  $\nu = \frac{\omega}{\omega_{ci}} \approx \sqrt{m_i/m_e}$ ,  $\lambda = \frac{1}{2} k_{\perp}^2 \rho_{Li}^2$ ,  $\xi = \frac{\nu^2}{2\lambda} = (\omega/k_{\perp} v_i)^2$ , and  $\zeta_n = \frac{\omega - n\omega_{ci}}{k_{\parallel} v_i}$ . With the magnetic field  $B(x) = B_0/(1+x/R)$  where  $R$  is the major radius ( $\nu - n = nx/R$ ), the dispersion relation can be further approximated by the cubic equation in  $\lambda$  or  $k_{\perp}^2$

$$k_{\perp}^6 - (a_4 + b_4 x) k_{\perp}^4 + (a_2 + b_2 x + c_2 x^2) k_{\perp}^2 - (a_0 + b_0 x) = 0 \tag{2}$$

which describes the couplings between the incident lower hybrid wave, the ion plasma wave, and the ion Bernstein wave (cold, warm, and hot wave, respectively). To obtain Eq. (2), we expanded  $\nu$  about  $n$  and  $\lambda$  about  $\lambda_0 (= \frac{1}{2} k_{\perp 0}^2 \rho_{Li}^2)$ , the warm wave value. This approximation is compared to eq. (1) in Fig. 1.

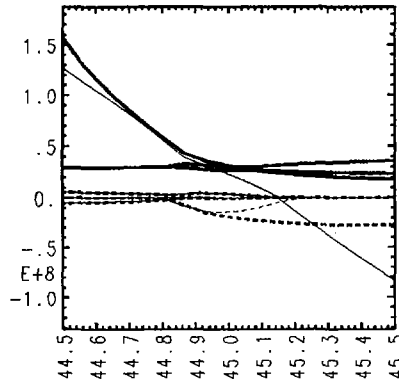


FIG. 1. Comparison of dispersion relations ( $k_{\perp}^2$  versus  $\nu$ ) of Eq. (1) (dark lines) with Eq. (2) (light lines) near the 45th harmonic for typical PLT parameters.

This is converted into the differential equation

$$(P_6 \psi''')''' + (P_4 \psi'')'' + (P_2 \psi')' + P_0 \psi = 0 \tag{3}$$

with suitable  $P_i$  because it has the conserved quantity

$$S = \psi^* (P_6 \psi''')'' - \psi^* (P_6 \psi''')' + \psi''^* (P_6 \psi''') + (\psi^* P_4 \psi'')' - \psi'^* (P_4 \psi'') + P_2 \psi^* \psi' - c.c. \tag{4}$$

rather than replacing  $k_{\perp}$  by  $i\frac{d}{dx}$ , since although the simplified coefficients do not guarantee energy conservation, they do guarantee constant power flow asymptotically and enable one to represent the various amounts of power into various waves.

## 2. Numerical Method

Due to the quadratic term in  $P_2$ , which is essential to describe couplings between all three waves, the Laplace transform method is no longer directly integrable. Thus we use WKBJ approximations and numerical integration.

The asymptotic solutions are:

$$\begin{array}{rcc} -\infty & \longleftarrow x \longrightarrow & +\infty \\ x^{-5/4} e^{\pm \frac{2}{3} i \alpha x^{\frac{3}{2}}} & \longleftarrow \text{hot} \longrightarrow & x^{-5/4} e^{\pm \frac{2}{3} \alpha x^{\frac{3}{2}}} \\ x^{-5/4} e^{\pm \frac{2}{3} \beta x^{\frac{3}{2}}} & \longleftarrow \text{warm} \longrightarrow & x^{-5/4} e^{\pm \frac{2}{3} i \beta x^{\frac{3}{2}}} \\ x^{-3/4} e^{\pm 2\gamma x^{\frac{1}{2}}} & \longleftarrow \text{cold} \longrightarrow & x^{-3/4} e^{\pm 2i\gamma x^{\frac{1}{2}}} \end{array}$$

where  $\alpha = \left[ \left| (b_4/2) - \sqrt{(b_4/2)^2 - c_2} \right| \right]^{\frac{1}{2}}$ ,  $\beta = \left[ \left| (b_4/2) + \sqrt{(b_4/2)^2 - c_2} \right| \right]^{\frac{1}{2}}$ , and  $\gamma = \sqrt{b_0/c_2}$ , with  $b_0, b_4, c_2 < 0$ . Taking the incoming and outgoing cold and warm waves, and the exponentially decaying hot solution as initial conditions as  $x \rightarrow +\infty$ , we integrate five functions until  $x \rightarrow -\infty$ , then find the transfer matrix by expanding those functions in terms of six asymptotic solutions. Tunneling and reflection coefficients for a specific branch may be found by using any basis of asymptotic solutions, while conversion coefficients from one branch to another cannot be found in this way, since the differential equation is homogeneous and solutions may be multiplied by an arbitrary constant which must be determined by a physical quantity we are interested in. Thus, to express conversion of energy from the cold to the warm wave, we must multiply the energy flux ratio,  $\rho_{cw} = S(\psi_w)/S(\psi_c)$ , associated with two waves in a given basis set, by the conversion coefficient obtained numerically, where  $\psi_c$  and  $\psi_w$  are cold and warm asymptotic solutions as  $x \rightarrow \infty$ .

To improve the accuracy of tunneling, reflection, and conversion coefficients, we include higher order terms such as

$$\psi(x) = x^{-3/4} \left( 1 + \frac{p_1}{x^1} + \frac{p_2}{x^2} + \dots \right) \exp \left[ 2i\gamma \left( 1 + \frac{q_1}{x^1} + \frac{q_2}{x^2} + \dots \right) \right] \quad (5)$$

Coefficients up to fourth order are found with the help of the symbolic algebra routine REDUCE. A matrix formulation is being developed to find asymptotic solutions more accurately and efficiently, since the overall accuracy of the coefficients is directly related to the accuracy of the asymptotic basis set.

### 3. Exact Order Reduction in Mode Conversion

Attempts have been made to eliminate the difficulties associated with a class of fourth order differential equations with exponentially growing solutions by reducing the order of the equation[2,3]. While these methods have been successful in evaluating the transmission, reflection and conversion coefficients with approximate equations and no localized absorption, the only successful methods of including the cyclotron absorption are based on fourth order equations[1,4]. An exact method is described whereby only second order differential equations need be solved numerically, avoiding approximations and growing solutions.

The problem is to solve the fourth order differential equation

$$y^{(4)} + b(x)y'' + a(x)y = 0 \quad (6)$$

where the generally complex coefficients  $a(x)$  and  $b(x)$  are real and asymptotically constant plus linear. This equation is then factored by using the WKBJ roots of the equation

$$\left[ \frac{d^2}{dx^2} + k_+^2(x) \right] \left[ \frac{d^2}{dx^2} + k_-^2(x) \right] y = 2(k_-^2)'y' + (k_-^2)''y \quad (7)$$

where  $k_{\pm}^2(x) = [b(x) \pm \sqrt{b^2(x) - 4a(x)}]/2$ ; after a variable change so that  $b \rightarrow \lambda^2 z$  and  $a \rightarrow \lambda^2 z + \gamma$  asymptotically, the roots are *defined* in terms of their asymptotic behavior by the relations  $k_+^2 \approx \lambda^2 z - 1$  and  $k_-^2 \approx 1 + (1 + \gamma)/\lambda^2 z$ . Then Eq. (7), written as  $D_+ D_- y = g(x)$ , is an exact representation of Eq. (6) with solution

$$\psi(x) = \int_{-\infty}^{\infty} G(x, z)g(z)dz \quad (8)$$

This is an inhomogeneous integral equation of the second kind, since  $g(z)$  contains the unknown  $\psi(z)$  and its derivative, and the factors in Eq. (7) have been carefully arranged so that the inhomogeneous term vanishes asymptotically at least as fast as  $z^{-2}$ . Now,  $G(x, z)$  is a fourth order Green function which must be obtained numerically, but *it is constructed from solutions of second order equations only*. The first two solutions of the adjoint equation  $D_- D_+ G = 0$  are the numerical solutions of  $D_+ \Psi = \Psi'' + k_+^2(z)\Psi = 0$ . The other two solutions are constructed from the numerical solutions of  $D_- \Phi = 0$  and  $\Psi_1$  and  $\Psi_2$  since  $D_+ G = \Phi$ , so  $\Psi_3$  and  $\Psi_4$  are obtained from a second order Green function constructed from the first two solutions. Then a fourth order Green function can be constructed to solve Eq. (7). The integral equation has a well behaved kernel and converges by iteration.

### 4. 2D Mode Conversion – Parabolic Approximation

During fast magnetosonic wave heating of tokamaks, mode conversion and absorption processes are generally important only in a thin layer located about

the cyclotron resonance layer. Within this layer, the parabolic approximation method[5] has been used to determine the two-dimensional structure of the propagating finite size wavefronts. The layer may be modeled as a uniform plasma slab in which  $x, y, z$  denote the major radial, vertical, and toroidal directions and the equilibrium magnetic field varies as  $B = B_0(1-x/R)$ , where  $R$  is the major radius. The mode conversion-tunneling equation is derived from the linearized Vlasov-Maxwell equations by following procedures used by Swanson[6] but explicitly retaining  $y$ -derivatives of perturbed quantities. In the limit  $m_e/m_i \rightarrow 0$  and neglecting terms of higher order than  $(k_y/k_x)^2$  and  $(k_x \rho_l)^2$ , where  $k_i$  denotes the  $i^{\text{th}}$  component of the wave vector and  $\rho_l$  is the ion Larmor radius, the wave equation reduces to two coupled pde's for  $E_x$  and  $E_y$ , where  $E$  denotes the wave electric field. Using the paraxial propagation constraint that  $k_y \approx \frac{1}{E} \frac{dE}{dy} \ll k_x \approx \frac{1}{E} \frac{dE}{dx}$ , the wave equation is solved iteratively, yielding an algebraic equation for  $E_x$  in terms of  $E_y$  and a fourth order pde for  $E_y$ . The paraxial propagation constraint also implies that  $E_y$  may be written as  $E_y(x, y) = a(x, y)u(x)$ , where  $u(x)$  is a rapidly varying waveform and  $a(x, y)$  is a slowly varying amplitude factor containing the diffraction effects. Using this ansatz,  $u(x)$  satisfies the usual fourth order mode conversion-tunneling equation for normal incidence[6], while  $a(x, y)$  is determined by a parabolic diffusion type equation:

$$g(x, u(x)) \frac{\partial a}{\partial x} + h(x, u(x)) \frac{\partial a}{\partial y} - \frac{\partial^2 a}{\partial y^2} = 0/. \quad (9)$$

Eq. (9) is easily solved analytically using the separation of variables. Hence, the two-dimensional structure of the wave fields within the kinetic layer can be obtained by solving one fourth order equation and one parabolic diffusion type equation. Computationally, this is more efficient than performing a Fourier decomposition of the fields in  $y$  and solving a fourth order equation for each resulting value of  $k_y$ .

## 5. Transport Simulations of ICRF-heated Tokamaks.

Global time-dependent transport simulations of ICRF-heated tokamaks with circular and noncircular plasma cross-sections have been obtained by interfacing the WHIST 2-D MHD equilibrium/1-D flux surface averaged transport code[7] with an ICRF wave propagation and power deposition package. The ICRF package uses ray tracing/quasilinear damping algorithms, developed initially by Hwang et. al.[8], but generalized to treat 2-D tokamak equilibria. Simulations of PLT experiments[9] and the proposed CIT operating scenario[10] are displayed in Fig. 2. For PLT, the electron thermal conductivity,  $\chi_e$ , is based on L-mode scaling[11] while the ion thermal conductivity,  $\chi_i$ , consists of the neoclassical coefficient plus an anomalous contribution equal to  $0.4\chi_e$ . Comparison of the data with the simulation indicates that the experimental energy confinement is more favorable than L-mode. Since CIT is designed to operate with a divertor,

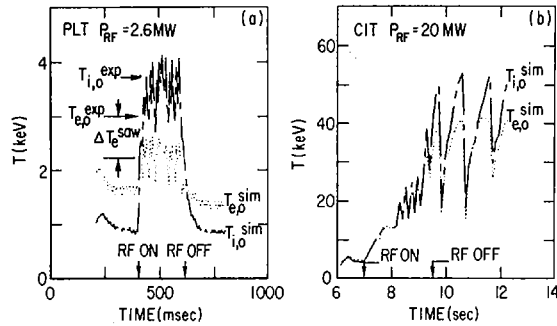


FIG. 2. (a) L-mode simulation of PLT ICRF experiments.  $T_{e,0}^{sim}$  and  $T_{i,0}^{sim}$  are the central electron and ion temperatures from the code results, while  $T_{e,0}^{exp}$  and  $T_{i,0}^{exp}$  are the experimental measurements reported by Mazzucato et al. [9].  $\Delta T_e^{saw}$  indicates the extent of the experimentally observed sawtooth amplitude on  $T_{e,0}$ .

(b) H-mode simulation of CIT plasmas [10]. Ignition is achieved in the simulation with a 2 s pulse of 20 MW of ICRF heating at a frequency of 105 MHz in a D-T-<sup>3</sup>He plasma.

H-mode scaling was assumed for  $\chi_e$  while  $\chi_i$  was the same as for PLT. The simulation indicates that ignition should be possible in CIT with the current design parameters.

### Acknowledgment

This work was supported by the U. S. Department of Energy, Contracts DE-AC02-76-CHO-3073 and DE-AC05-84OR21400, and by Grant DE-FG05-ER53206.

### REFERENCES

- [1] SWANSON, D.G., Phys. Fluids **28** (1985) 2645.
- [2] FUCHS, V., KO, K., BERS, A., Phys. Fluids **24** (1981) 1251.
- [3] CAIRNS, R.A., LASHMORE-DAVIES, C.N., Phys. Fluids **26** (1983) 1268.
- [4] COLESTOCK, P.L., KASHUBA, R.J., Nucl. Fusion **23** (1983) 763.
- [5] PHILLIPS, C.K., PERKINS, F.W., HWANG, D.Q., Phys. Fluids **29** (1986) 1608.
- [6] SWANSON, D.G., Phys. Fluids **24** (1981) 2035.
- [7] HOULBERG, W.A., ATTENBERGER, S.E., LAO, L., in Advances in Mathematical Methods for the Solution of Nuclear Engineering Problems (Proc. Int. Top. Mtg. Karlsruhe, 1981), Vol. 2, Fachinformationszentrum Energie, Physik, Mathematik GmbH, Karlsruhe (1981) 425.
- [8] HWANG, D.Q., et al., Rep. PPPL-1990, Princeton Plasma Physics Lab., Princeton University, Princeton, NJ (1983).
- [9] MAZZUCATO, E., BELL, R., BITTER, M., et al., in Plasma Physics and Controlled Nuclear Fusion Research 1984 (Proc. 10th Int. Conf. London, 1984), Vol. 1, IAEA, Vienna (1985) 433.
- [10] SCHMIDT, J., et al., paper IAEA-CN-47/H-I-2, these Proceedings, Vol. 3.
- [11] KAYE, S.M., GOLDSTON, R.J., Nucl. Fusion **25** (1985) 65.

# ELECTRON CYCLOTRON CURRENT DRIVE AND SUPRA-THERMAL GENERATION IN LARGE TOKAMAKS

T.J. SCHEP, R.W. POLMAN, E. WESTERHOF, L. KLIEB  
Association Euratom-FOM,  
FOM Instituut voor Plasmafysica,  
Rijnhuizen, Nieuwegein,  
Netherlands

## Abstract

### ELECTRON CYCLOTRON CURRENT DRIVE AND SUPRA-THERMAL GENERATION IN LARGE TOKAMAKS.

Top launch of electron cyclotron wave energy into large tokamaks is considered with the aim of investigating the possibilities of spatially localized power deposition in the far tail of the electron distribution function. Such an injection scheme is favourable from the point of view of current drive and generation of a supra-thermal electron population. Oblique injection of the extraordinary mode with a frequency below the local cyclotron frequency is most suitable for this purpose.

## INTRODUCTION

Recent experiments with strong additional heating on JET [1] and TFTR [2] give evidence of a strong correlation between the current and temperature profiles in tokamak discharges. The decoupling of these profiles could clear the way to increase the energy content of the plasma and to improve its confinement. This could be achieved by driving part of the current non-inductively or by carrying the current by a supra-thermal electron population. The noninductive current can be provided by various methods. The shape of the current profile, however, might well be the important factor which determines eventually the efficiency, in terms of plasma energy content and confinement time, of the non-inductive current generation [3]. The favourable feature of electron cyclotron power deposition and current drive is its localized character. This could provide the means for the necessary tailoring of the current profile, even with modest EC-driven currents.

In this paper, power deposition, current drive, and generation of supra-thermal electrons by electron cyclotron waves are discussed for JET and TFTR plasmas. In particular, top launch of RF power in the extraordinary mode is investigated.

## ELECTRON CYCLOTRON RESONANCE AND RAY TRACING

The relativistic electron cyclotron resonance condition is

$$\gamma - \frac{\omega_c}{\omega} - N_{\parallel} p_{\parallel} / mc = 0, \text{ where } \gamma = [1 + p_{\perp}^2 / m^2 c^2 + p_{\parallel}^2 / m^2 c^2]^{1/2}$$

and  $N_{\parallel}$  is the parallel refractive index. All other quantities have their usual meaning. In the  $p_{\parallel}$ - $\gamma$  plane the resonance condition is represented by the straight line  $\gamma - 1 = \Delta + N_{\parallel} p_{\parallel} / mc$ , where  $\Delta = \omega_c / \omega - 1$ , inside the hyperbola  $\gamma = (1 + p_{\perp}^2 / m^2 c^2)^{1/2}$ . The angle between the straight line and the  $p_{\parallel}$ -axis is determined by  $N_{\parallel}$ . The ranges of energies  $E = mc^2(\gamma - 1)$  and parallel momenta of the resonant particles are determined by the intersection points of these curves. The resonance condition implies that electrons with rather large energies can be resonant if waves with down-shifted frequencies ( $\omega < \omega_c$ ) are injected [4]. Under the realistic assumption that the electron distribution function is a decreasing function of energy, most of the RF energy will be deposited near the lower limit ( $E^-$ ) of the energy range.

The ray trajectories and the absorption of electron cyclotron waves injected from a top-port into JET and TFTR are studied with the ray tracing code TORAY [5], which has been extended to calculate ray paths in D-shaped equilibria. The trajectories are calculated from the cold dispersion relation [6]. The power deposition is determined by the absorption coefficient, calculated with the full relativistic cyclotron resonance condition. A contribution due to a supra-thermal electron population is included in the absorption. This population has been modelled by a low density, high energy distribution function which is Maxwellian in a frame moving along the equilibrium magnetic field [7].

The magnetic equilibria have been modelled to present actual discharges in JET and TFTR. In these equilibria the density and

temperature profile are given by  $n_e(\bar{\psi}) = (n_O - n_L)[1 - a_n \bar{\psi}^{b_n}]^{c_n + n_L}$ ,  $T_e(\bar{\psi}) = (T_O - T_L)[1 - a_T \bar{\psi}^{b_T}]^{c_T + T_L}$ , where  $\bar{\psi}^2 = (\psi - \psi_O) / |\psi_L - \psi_O|$ ,  $\psi$  being the poloidal flux function and  $\psi_{L,O}$  its value at the limiter and magnetic axis respectively, with suitable choices for the coefficients  $n_{O,L}$  and  $T_{O,L}$ .

## POWER DEPOSITION IN REAL AND MOMENTUM SPACE

Power deposition in JET along rays that are injected under a variety of angles from several positions into medium ( $n_O = 5 \cdot 10^{19} \text{ m}^{-3}$ ) and high ( $n_O = 10^{20} \text{ m}^{-3}$ ) density Maxwellian plasmas with central temperatures of 5 and 10 keV has been extensively investigated for various equilibria, density profiles, and frequencies [8]. With the proper choice of frequencies the results for JET and TFTR are analogous for standard discharges. In the case of TFTR we have investigated super-shot 23260 because of its broad  $T_e$ -profile and its large shift of the magnetic axis [9]. The special features of this shot lead to interesting results even at the relatively low frequency of 90 GHz.

The direction of the injected rays is specified by the angles  $\theta$  and  $\phi$ , where  $\theta$  is the angle between the ray and the vertical direction, and  $\phi$  is the angle between the projection of the ray on the equatorial plane and the major radius. The dependence of the ray trajectories and of the power deposition on the injection angles is analyzed by scanning in  $\phi$  at fixed  $\theta$  and vice versa. With a proper choice of frequency and launching angles, complete power absorption with good spatial localization can be obtained in both medium and high density plasmas with central temperatures in the range 5-10 keV. Figures 1 and 2 show typical results of a  $\theta$ -scan at  $\phi = -80^\circ$  in JET and TFTR for a Maxwellian plasma. The projections of the ray paths on the poloidal plane are depicted in Figs. 1a and 2a. In Figs. 1b and 2b the bands, in terms of  $\bar{\psi}$  and  $E^-$ , within which the intensity drops from 90% to 10% of the injected value, are plotted versus  $\theta$ . Similar features as in a  $\theta$ -scan are shown by  $\phi$ -scans.

The study yields the following results [8]. The density has only a weak influence on the position where the wave power is absorbed up to densities close to the cut-off value. Only minor changes in the results are found for density profiles with strongly different peaking factors. For higher temperatures the

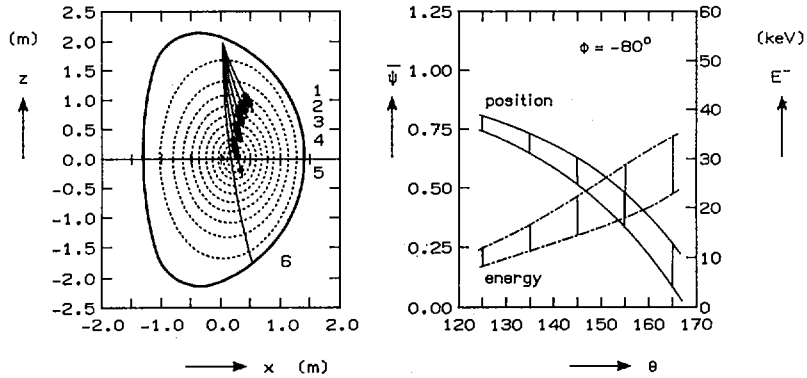


FIG. 1. Results of a scan in  $\theta$  (at  $\phi = -80^\circ$ ) in JET (70 GHz). The rays are launched from  $R = 3.0$  m,  $Z = 1.95$  m. The equilibrium corresponds to JET-3901 with  $n_0 = 5 \times 10^{19} \text{ m}^{-3}$ ,  $T_0 = 5 \text{ keV}$  ( $a_{n,T} = 1$ ,  $b_{n,T} = 2$ ,  $c_{n,T} = 1$ ) and  $B = 3.4$  T at  $R = 2.96$  m.  $\theta = 125^\circ$  (1),  $135^\circ$  (2),  $145^\circ$  (3),  $155^\circ$  (4),  $165^\circ$  (5),  $175^\circ$  (6).

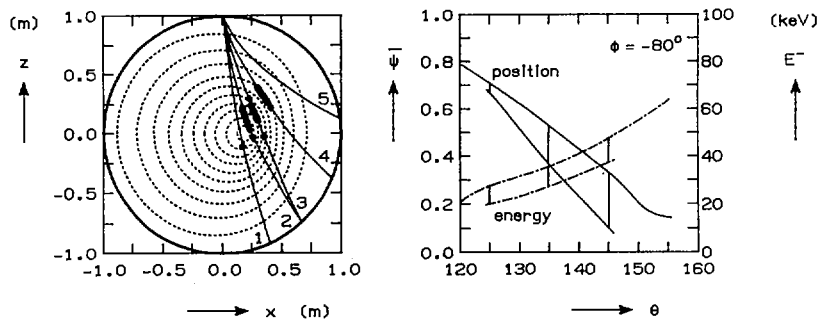


FIG. 2. Results of a scan in  $\theta$  (at  $\phi = -80^\circ$ ) in TFTR (90 GHz). The rays are launched from  $R = 2.55$  m,  $Z = 1.00$  m. Equilibrium and profiles as in TFTR-23260:  $R = 2.46$  m,  $a = 0.80$  m,  $B = 5$  T,  $n_0 = 7 \times 10^{19} \text{ m}^{-3}$  ( $n_L = 7 \times 10^{18} \text{ m}^{-3}$ ,  $a_n = 1$ ,  $b_n = 1.5$ ,  $c_n = 4$ ) and  $T_0 = 7 \text{ keV}$  ( $T_L = 30 \text{ eV}$ ,  $a_T = 1$ ,  $b_T = 2$ ,  $c_T = 1$ ).  $\theta = 155^\circ$  (1),  $145^\circ$  (2),  $135^\circ$  (3),  $125^\circ$  (4),  $115^\circ$  (5).

deposition band narrows somewhat and shifts to higher values of  $\omega_c/\omega$  and rays directed more towards the centre and towards the inboard side show increased absorption. Results for power injection from several positions in a top-port show that rays can be injected more steeply and more towards the high-field side when injected from positions with larger major radii. With a

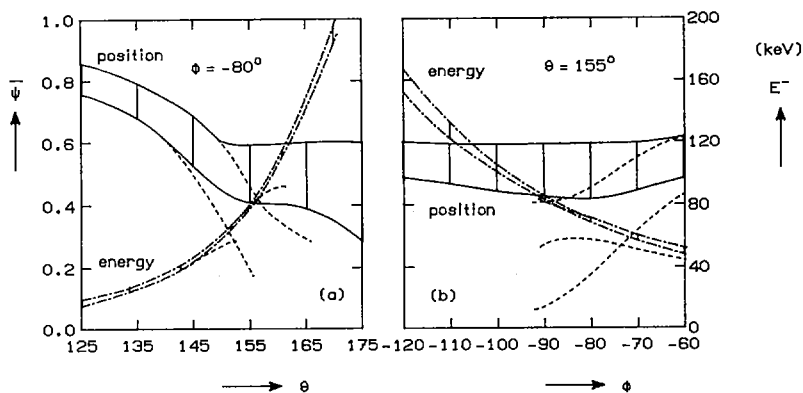


FIG. 3. Ray tracing results in the presence of a supra-thermal population. The dashed bands correspond to a purely Maxwellian plasma. a) a scan in  $\theta$  at  $\phi = -80^\circ$ , b) a scan in  $\phi$  at  $\theta = 155^\circ$ .

proper choice of the injection angles for each launching position, the power can be deposited around the same flux surface and be absorbed by particles in the same energy range. For larger values of  $\omega_c/\omega$  (i.e., lower frequency or higher B-values) the absorption decreases. Also in paramagnetic equilibria (i.e. higher B) the absorption will be lower. Typical values for the resonant energies are given in the Table for near-centre deposition in JET-3901. Similar results are found for TFTR.

In the presence of a supra-thermal electron population the absorption behaviour changes strongly. This is illustrated in Fig. 3 for a paramagnetic equilibrium (the low-q JET shot 7774, rescaled to  $B = 3.43$  T at  $R = 2.96$  m). For a 10 keV,  $n_0 = 5 \cdot 10^{19} \text{ m}^{-3}$  Maxwellian plasma full absorption is obtained up to  $\theta = 155^\circ$  (at  $\phi = -80^\circ$ ) and for  $\phi > -90^\circ$  (at  $\theta = 155^\circ$ ) with particle energies around 50 keV. We assume that the power in these rays produces a supra-thermal population with  $n_s = 5 \cdot 10^{17} \text{ m}^{-3}$ ,  $T_s = 50$  keV and  $\langle v_{\parallel} \rangle = 0.331 c$  inside the surface  $\bar{\psi} = 0.6$  (this value of  $\langle v_{\parallel} \rangle$  is not realistic from the point of view of supra-thermal current, but, here, we consider power absorption). Then, the range in  $\theta$  and  $\phi$  for complete absorption is drastically extended, and the RF power in steeply injected rays is absorbed by particles with energies up to 200 keV in the tail of the supra-thermal distribution.

## CURRENT DRIVE EFFICIENCY

The non-inductive current  $I$ , generated by a point spectrum of electron cyclotron waves, is discussed in Ref. [10]. According to this theory, the current that can be carried by relativistic particles with energy  $mc^2(\gamma-1)$  and parallel momentum  $p_{\parallel}$  is

$$\frac{I}{W} = \frac{1}{2\pi R} \frac{J}{P_d} = \frac{1.05}{R(m)n_{20}} \left| \frac{J}{P_d} \right|_n A/W \quad (1)$$

where  $R$  is the major radius,  $n_{20}$  the density in  $10^{20} \text{ m}^{-3}$ ,  $W$  the RF power and  $(J/P_d)_n$  the normalized efficiency [10]. For the energies under consideration we have  $I/W \approx [6/(5+Z_{\text{eff}})] (I/W)_{Z_{\text{eff}}=1}$ . From Table I and Eq. (1), the following rough estimate is obtained for the efficiency of current drive with near-central power deposition

$$\left. \frac{I}{W} \right|_{Z_{\text{eff}}=1} = \alpha \frac{T_0(10^4 \text{ eV})}{R(m) n_{20}} A/W \quad (2)$$

where  $\alpha \approx 0.15-0.30$  for the temperatures and densities under consideration. Here, we have assumed that all the wave power is absorbed by resonant particles with the lowest energy  $E^-$ .

The profiles of power deposition and current drive for a modelled launching system are given in Fig. 4. In Fig. 4a a magnetic equilibrium similar to JET-7774 has been investigated with  $n_0 = 0.5 \cdot 10^{20} \text{ m}^{-3}$  and  $T_0 = 5 \text{ keV}$ . The toroidal field has been rescaled to  $B = 3.2 \text{ T}$  at  $R = 2.96 \text{ m}$ , which optimizes the absorption around the  $q=1$  surface ( $r \approx 45 \text{ cm}$ ). In Fig. 4b the equilibrium and plasma parameters are chosen to represent TFTR-23260. The large shift of the magnetic axis in this particular discharge does allow for central power deposition and current drive (cf. Fig. 2). The calculations show that  $j(r) \approx P(r)$  which yields an overall efficiency  $I/W \geq 0.05 \text{ A/W}$  in agreement with (2).

TABLE I.  $E^-$  FOR NEAR CENTRE DEPOSITION

$T_0(\text{keV})$	$n_0(\text{m}^{-3})$	$E^-(\text{keV})$	$T_0(\text{keV})$	$n_0(\text{m}^{-3})$	$E^-(\text{keV})$
5	$0.5 \times 10^{20}$	25-35	10	$0.5 \times 10^{20}$	60-80
5	$1 \times 10^{20}$	10-25	10	$1 \times 10^{20}$	35-55

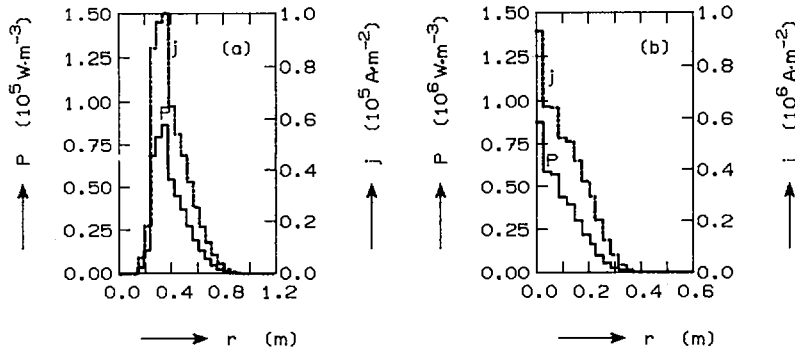


FIG. 4. a) Power deposition and current profile in JET 7774 (70 GHz). Two Gaussian beams (half-width  $5^\circ$ ) of 0.5 MW are launched at  $R = 2.94$  and  $3.06$ . The injection angles of the beam centres are  $\theta = 150^\circ$ ,  $\phi = -80^\circ$  and  $\theta = 155^\circ$ ,  $\phi = -80^\circ$ . b) Power deposition and current profile in TFTR 23260 (90 GHz). 1 MW is launched in a Gaussian beam (half-width  $5^\circ$ ) from the top of the TFTR vessel ( $R = 2.55$ ). The injection angles of the beam centre are  $\theta = 145^\circ$ ,  $\phi = -80^\circ$ .

The widths of the profiles are mainly due to the assumed angular spread of  $5^\circ$  of each beam, and are to a lesser extent the result of the different absorption lengths along the individual rays. Hence, the localization of the power deposition and of the driven current depends to a large extent on the qualities of an actual launching system.

### SUPRA-THERMAL ELECTRON GENERATION

The power deposition and the current drive efficiency are calculated under the assumption that the RF power is absorbed by high-energetic, resonant particles without distorting the tail of the Maxwellian. A necessary condition for the validity of these results is, thus, that collisions are sufficiently frequent so that the RF power can be transferred to the bulk of the distribution function by collisional energy loss of resonant particles. When this condition is not fulfilled, resonant particles will run away in momentum space and strong non-Maxwellian effects are expected [11].

The power lost per unit volume by high energetic particles with density  $n_s$  due to collisions with bulk particles is  $P_{\text{coll}} = n_s m_e v^2 \nu_c(v) = 6 \cdot 10^3 \alpha_s n_{20}^2 / E^{1/2}(\text{keV}) \text{ MW} \cdot \text{m}^{-3}$ , where  $\nu_c = \omega_{pe}^4 \ln \Lambda / 4\pi n v^3$  is the collision frequency ( $\ln \Lambda = 15$  has been

taken), and  $\alpha_s$  is the fraction of resonant particles. Estimating  $\alpha_s$  for a Maxwellian plasma we arrive at

$$P_{\text{coll}} = 0.4 \cdot 10^3 \frac{1}{N_{\parallel}} \frac{e^{-E/T}}{(E/T)^{3/2}} \frac{(\Delta E)_T}{2T} \frac{\Delta E^-}{2T} n_{20}^2 \text{ MW} \cdot \text{m}^{-3} \quad (3)$$

where  $(\Delta E)_T$  is the thermal spread in energy. At the higher temperatures, the spread in energies  $E^-$  is of the order of the thermal spread,  $\Delta E^- \approx (\Delta E)_T = 2T$ ,  $E/T \approx 6-9$  at  $n_{20} = 0.5$  and  $E/T \approx 4-6$  at  $n_{20} = 1$  (see also Table I). The volume in which the RF power is absorbed is of the order of  $10 \text{ m}^3$  when the launching is optimized for near-centre depositions, and about  $2 \text{ m}^3$  when optimized for central deposition. A substitution of these values into (3) shows that with a few MW of RF power, supra-thermal effects can be expected at low densities for near-centre deposition, but also at higher densities for central deposition.

In the run-away regime a depletion of the distribution function will occur unless particles are continuously supplied by the bulk at the lower energy boundary of the resonant population. Resonant particles will accumulate at the high energy boundary and be redistributed by pitch-angle scattering. A non-Maxwellian distribution function will be established in the resonant region. This necessitates a reconsideration of the absorption coefficient. Also the deposition profile and the range of particle energies where the power is absorbed will change drastically, as is illustrated by the results of Fig. 3.

## CONCLUSIONS

The results presented in the preceding Sections lead to the conclusion that electron cyclotron waves at downshifted frequency are completely absorbed in a large tokamak for a wide range of plasma parameters. The RF power is transferred to electrons in the tail of the distribution function. The power deposition is spatially localized for a broad range of injection angles and positions, and plasma parameters.

For real launching systems the localization will be limited by the angular spread of the beams. It is shown by Fig. 4 that all power can be deposited in a volume of  $\sim 2 \text{ m}^3$  for central and in a volume of  $\sim 10 \text{ m}^3$  for near-centre deposition (e.g., around

the  $q=1$  surface). The overall current drive efficiency is predicted to be  $\geq 0.05$  A/W in both cases.

Supra-thermal effects are expected for a few MW of RF power. The creation of suprathermals will drastically alter the absorption by the plasma, and will allow the interaction with higher energetic particles in the tail of the supra-thermal distribution, leading to an increased current drive efficiency.

Thus EC wave injection at down-shifted frequencies from a top-port in a large tokamak (e.g. 70 GHz for  $B_\phi = 3.4$  T (JET) or 90 GHz for  $B_\phi \approx 5$  T (TFTR)) is an attractive tool for current profile control.

### ACKNOWLEDGEMENTS

Fruitful discussions with Prof. Dr. F. Engelmann are gratefully acknowledged. This work was performed under the Euratom-FOM association agreement with financial support from ZWO and Euratom and in part under JET Article 14 Contract no. JJ5/9007.

### REFERENCES

- [1] REBUT, P.H., BRUSATI, M., Plasma Phys. Controll. Fusion **28** (1986) 113.
- [2] MURAKAMI, M., et al., Plasma Phys. Controll. Fusion **28** (1986) 17.
- [3] FURTH, H.P., Plasma Phys. Controll. Fusion **28** (1986) 1305.
- [4] MAZZUCATO, E., FIDONE, I., GIRUZZI, G., KRIVENSKI, V., Nucl. Fusion **26** (1986) 3.
- [5] KRITZ, A.H., HSUAN, H., GOLDFINGER, R.C., BATCHELOR, D.B., Ray-Tracing Study of Electron-Cyclotron Heating in Toroidal Geometry, Rep. PPPL-1980, Princeton Plasma Physics Laboratory (1983).
- [6] BORNATICI, B., CANO, R., De BARBIERI, O., ENGELMANN, F., Nucl. Fusion **23** (1983) 1153.
- [7] BORNATICI, M., RUFFINA, U., WESTERHOF, E., Plasma Phys. Controll. Fusion **28** (1986) 629.
- [8] POLMAN, R.W., SCHEP, T.J., WESTERHOF, E., KLIEB, L., in Report on JET, Article 14, Contract No. JJ5/9007.
- [9] GREK, B., JOHNSON, D., private communication.
- [10] FISCH, N.J., Phys. Rev., A **24** 6 (1981) 3245.
- [11] DEMEIO, L., ENGELMANN, F., in Mathematical Aspects of Fluids and Plasma Dynamics (Proc. Workshop Trieste, 1984) (1984) 201.



## CHAIRMEN OF SESSIONS

### *Volume I*

Session A-I	S. MORI	Japan
Session A-II	D.M. MEADE	USA
Session A-III	J.B. LISTER	Switzerland
Session A-IV	M. KEILHACKER	JET
Session A-V	R.A. GROSS	USA
Session A-VI	L.E. ZAKHAROV	USSR
Session F-I	O.S. PAVLICHENKO	USSR
Session F-II	R.R. PARKER	USA
Session F-III	F.G. PREVOT	France

## SECRETARIAT OF THE CONFERENCE

Scientific Secretaries:	M. LEISER A.A. SHURYGIN	Division of Research and Laboratories, IAEA
Administrative Secretary:	Edith PILLER	Division of External Relations, IAEA
Editors:	J.W. WEIL Maria DEMIR	Division of Publications, IAEA
Records Officer:	J. RICHARDSON	Division of Languages, IAEA



# HOW TO ORDER IAEA PUBLICATIONS

An exclusive sales agent for IAEA publications, to whom all orders and inquiries should be addressed, has been appointed in the following country:

UNITED STATES OF AMERICA    BERNAN – UNIPUB, 4611-F Assembly Drive, Lanham, MD 20706-4391

---

In the following countries IAEA publications may be purchased from the sales agents or booksellers listed or through major local booksellers. Payment can be made in local currency or with UNESCO coupons.

ARGENTINA	Comisión Nacional de Energía Atómica, Avenida del Libertador 8250, RA-1429 Buenos Aires
AUSTRALIA	Hunter Publications, 58 A Gipps Street, Collingwood, Victoria 3066
BELGIUM	Service Courrier UNESCO, 202, Avenue du Roi, B-1060 Brussels
CHILE	Comisión Chilena de Energía Nuclear, Venta de Publicaciones, Amunátegui 95, Casilla 188-D, Santiago
CHINA	IAEA Publications in Chinese: China Nuclear Energy Industry Corporation, Translation Section, P.O. Box 2103, Beijing IAEA Publications other than in Chinese: China National Publications Import & Export Corporation, Deutsche Abteilung, P.O. Box 88, Beijing
CZECHOSLOVAKIA	S.N.T.L., Mikulandska 4, CS-116 86 Prague 1 Alfa, Publishers, Hurbanovo námestie 3, CS-815 89 Bratislava
FRANCE	Office International de Documentation et Librairie, 48, rue Gay-Lussac, F-75240 Paris Cedex 05
HUNGARY	Kultura, Hungarian Foreign Trading Company, P.O. Box 149, H-1389 Budapest 62
INDIA	Oxford Book and Stationery Co., 17, Park Street, Calcutta-700 016 Oxford Book and Stationery Co., Scindia House, New Delhi-110 001
ISRAEL	Heiliger and Co., Ltd, Scientific and Medical Books, 3, Nathan Strauss Street, Jerusalem 94227
ITALY	Libreria Scientifica, Dott. Lucio de Biasio "aeiou", Via Meravigli 16, I-20123 Milan
JAPAN	Maruzen Company, Ltd, P.O. Box 5050, 100-31 Tokyo International
PAKISTAN	Mirza Book Agency, 65, Shahrah Quaid-e-Azam, P.O. Box 729, Lahore 3
POLAND	Ars Polona-Ruch, Centrala Handlu Zagranicznego, Krakowskie Przedmiescie 7, PL-00-068 Warsaw
ROMANIA	Ilexim, P.O. Box 136-137, Bucharest
SOUTH AFRICA	Van Schaik Bookstore (Pty) Ltd, P.O. Box 724, Pretoria 0001
SPAIN	Díaz de Santos, Lagasca 95, E-28006 Madrid Díaz de Santos, Balmes 417, E-08022 Barcelona
SWEDEN	AB Fritzes Kungl. Hovbokhandel, Fredsgatan 2, P.O. Box 16356, S-103 27 Stockholm
UNITED KINGDOM	Her Majesty's Stationery Office, Publications Centre, Agency Section, 51 Nine Elms Lane, London SW8 5DR
USSR	Mezhdunarodnaya Kniga, Smolenskaya-Sennaya 32-34, Moscow G-200
YUGOSLAVIA	Jugoslovenska Knjiga, Terazije 27, P.O. Box 36, YU-11001 Belgrade

---

Orders from countries where sales agents have not yet been appointed and requests for information should be addressed directly to:



Division of Publications  
International Atomic Energy Agency  
Wagramerstrasse 5, P.O. Box 100, A-1400 Vienna, Austria





INTERNATIONAL  
ATOMIC ENERGY AGENCY  
VIENNA, 1987

SUBJECT GROUP: III  
Physics/Plasma Physics, Fusion  
PRICE: Austrian Schillings 1400,—